

Criteria 3

Research, Innovations and Extension

Key Indicator 3.3

Research Publication and Awards

3.3.1 Number of research papers published per teacher in the Journals notified on UGC website during the last five years



Rajarshi Shahu
College of Pharmacy

Journey Towards Academic Excellence

3.3.1 Number of research papers published per teacher in the Journals notified on UGC website during the last five years

2020-2021

Sr. No.	Title of paper	Name of the author/s	Department of the teacher	Name of journal	Impact Factor	Page No. with Link
1	Nanocomposite polymeric materials state of the art in the development of biomedical drug delivery systems and devices	Prakash Kendre , Mrinal Gite, Shrirish Jain, Ajinkya Pote	Pharmaceutics	Polym. Bull. (2021). https://doi.org/10.1007/s00289-021-03985-3 (Springer Nature; Impact Factor: 2.870)	2.843	<u>01</u>
2	Nanocomposite polymeric materials state of the art in the development of biomedical drug delivery systems and devices	Prakash Kendre, Mrinal Gite, Shrirish Jain , Ajinkya Pote	Pharmaceutics	Polym. Bull. (2021). https://doi.org/10.1007/s00289-021-03985-3 (Springer Nature; Impact Factor: 2.870)	2.843	<u>30</u>
3	Stereolithography 3D printing technology in pharmaceuticals: a review	Subhash Deshmane , Prakash Kendre, Hitendra Mahajan, Shirish Jain	Pharmaceutics	Drug Dev Ind Pharm. 2021 Doi: 10.1080/03639045.2021.1994990.	3.727	<u>59</u>
4	Stereolithography 3D printing technology in pharmaceuticals: a review	Subhash Deshmane, Prakash Kendre , Hitendra Mahajan, Shirish Jain	Pharmaceutics	Drug Dev Ind Pharm. 2021 Doi: 10.1080/03639045.2021.1994990.	3.727	<u>71</u>
5	Stereolithography 3D printing technology in pharmaceuticals: a review	Subhash Deshmane, Prakash Kendre, Hitendra Mahajan, Shirish Jain	Pharmaceutics	Drug Dev Ind Pharm. 2021 Doi: 10.1080/03639045.2021.1994990.	3.727	<u>83</u>
6	Identification And Optimization Of Binding Site For An Active Metabolite Of Clopidogrel, Prasugrel And Ticlopidine On Receptor P2y12	Parmeshwar R. Devhare , Shirish Jain, Gajanan Sonwane , Vijay Borkar and Rushikesh Diwre	Pharmaceutical Chemistry	IJPSR, 2021; Vol. 12(8): 4365-4370	0	<u>95</u>

Sr. No.	Title of paper	Name of the author/s	Department of the teacher	Name of journal	Impact Factor	Page No. with Link
7	Identification And Optimization Of Binding Site For An Active Metabolite Of Clopidogrel, Prasugrel And Ticlopidine On Receptor P2y12	Parmeshwar R. Devhare, Shirish Jain , Gajanan Sonwane , Vijay Borkar and Rushikesh Diwre	Pharmaceutical Chemistry	IJPSR, 2021; Vol. 12(8): 4365-4370	0	<u>101</u>
8	Identification And Optimization Of Binding Site For An Active Metabolite Of Clopidogrel, Prasugrel And Ticlopidine On Receptor P2y12	Parmeshwar R. Devhare, Shirish Jain, Gajanan Sonwane , Vijay Borkar and Rushikesh Diwre	Pharmaceutical Chemistry	IJPSR, 2021; Vol. 12(8): 4365-4370	0	<u>107</u>
9	Identification And Optimization Of Binding Site For An Active Metabolite Of Clopidogrel, Prasugrel And Ticlopidine On Receptor P2y12	Parmeshwar R. Devhare, Shirish Jain, Gajanan Sonwane , Vijay Borkar and Rushikesh Diwre	Pharmaceutical Chemistry	IJPSR, 2021; Vol. 12(8): 4365-4370	0	<u>113</u>
10	Evaluation of Antidiabetic Activity Of Echinochloa Colona Plant Extract	Vijay Borkar , Gajanan Sonwane , Parmeshwar Devhare, Rushikesh Diwre and Shirish Jain	Pharmaceutical Chemistry	IJPSR, 2021; Vol. 12(8): 4354-4364.	0	<u>119</u>
11	Evaluation of Antidiabetic Activity Of Echinochloa Colona Plant Extract	Vijay Borkar, Gajanan Sonwane , Parmeshwar Devhare , Rushikesh Diwre and Shirish Jain	Pharmaceutical Chemistry	IJPSR, 2021; Vol. 12(8): 4354-4364.	0	<u>130</u>
12	Evaluation of Antidiabetic Activity Of Echinochloa Colona Plant Extract	Vijay Borkar , Gajanan Sonwane , Parmeshwar Devhare, Rushikesh Diwre and Shirish Jain	Pharmaceutical Chemistry	IJPSR, 2021; Vol. 12(8): 4354-4364.	0	<u>141</u>
13	Evaluation of Antidiabetic Activity Of Echinochloa Colona Plant Extract	Vijay Borkar , Gajanan Sonwane , Parmeshwar Devhare, Rushikesh Diwre and Shirish Jain	Pharmaceutical Chemistry	IJPSR, 2021; Vol. 12(8): 4354-4364.	0	<u>152</u>
14	A Novel Hemizygous Variant in the AFF2 Gene Causing Fragile XE (FRAXE) Syndrome: First Report from Pakistan	Iftikhar Ahmed, Muhammad Ilyas, Gaurav V Harlalka , Asif Mir	Pharmacology	Pak J Med Res Vol. 60, No. 2, 2021, 85-89	0	<u>163</u>

Sr. No.	Title of paper	Name of the author/s	Department of the teacher	Name of journal	Impact Factor	Page No. with Link
15	Lymphatic transport system to circumvent hepatic metabolism for oral delivery of lipid-based nanocarriers	D. R. Telange , A. Rajput, P. Pingale, S. Chalikwar, V. Borse	Pharmaceutics	Journal of Drug Delivery Science and Technology 66 (2021) 102934	5.062	<u>168</u>
16	Use of combined nanocarrier system based on chitosan nanoparticles and phospholipids complex for improved delivery of ferulic acid	D. R. Telange , S P. Jain, A.M. Pethe, P. S. Kharkar, N. R. Rarokar	Pharmaceutics	International Journal of Biological Macromolecules 171 (2021) 288–307	8.025	<u>185</u>
17	Use of combined nanocarrier system based on chitosan nanoparticles and phospholipids complex for improved delivery of ferulic acid	D. R. Telange, S P. Jain , A.M. Pethe, P. S. Kharkar, N. R. Rarokar	Pharmaceutics	International Journal of Biological Macromolecules 171 (2021) 288–307	8.025	<u>205</u>
18	Egg white protein carrier-assisted development of solid dispersion for improved aqueous solubility and permeability of poorly water-soluble hydrochlorothiazide	D. R. Telange , S. P. Jain, A. M. Pethe, P. S. Kharkar	Pharmaceutics	AAPS PharmSciTech, 2021, 8;22(3):94	4.026	<u>225</u>
19	Egg white protein carrier-assisted development of solid dispersion for improved aqueous solubility and permeability of poorly water-soluble hydrochlorothiazide	D. R. Telange, S. P. Jain , A. M. Pethe, P. S. Kharkar	Pharmaceutics	AAPS PharmSciTech, 2021, 8;22(3):94	4.026	<u>240</u>
20	Hypotension: A comprehensive review	Rasika Dnyandeo Bhalke, Mahendra Ashok Giri , Rasal Yash Anil, Narhe Mansi Balasaheb, Parjane Abhishek Nanasaheb and Vishal Vijay Pande	Pharmacology	Journal of Pharmacognosy and Phytochemistry 2021; 10(1): 1945-1947	0	<u>255</u>
21	Tailoring hybrid organic-inorganic film-forming topical gel: A tuneable approach for tramadol HCl delivery	Prakash N. Kendre , Gayatri Dusane, Shirish P. Jain, Mahendra A. Giri & Ajinkya K. Pote	Pharmaceutics	Materials Technology, 2021, 36, 868-882.(Taylor & Francis, Impact Factor: 3.846)	3.297	<u>258</u>

Sr. No.	Title of paper	Name of the author/s	Department of the teacher	Name of journal	Impact Factor	Page No. with Link
22	Tailoring hybrid organic-inorganic film-forming topical gel: A tuneable approach for tramadol HCl delivery	Prakash N. Kendre, Gayatri Dusane, Shirish P. Jain, Mahendra A. Giri & Ajinkya K. Pote	Pharmaceutics	Materials Technology, 2021, 36, 868-882.(Taylor & Francis, Impact Factor: 3.846)	3.297	274
23	Tailoring hybrid organic-inorganic film-forming topical gel: A tuneable approach for tramadol HCl delivery	Prakash N. Kendre, Gayatri Dusane, Shirish P. Jain , Mahendra A. Giri & Ajinkya K. Pote	Pharmaceutics	Materials Technology, 2021, 36, 868-882.(Taylor & Francis, Impact Factor: 3.846)	3.297	290
24	Phospholipid complex-loaded self-assembled phytosomal soft nanoparticles: evidence of enhanced solubility, dissolution rate, ex vivo permeability, oral bioavailability, and antioxidant potential of mangiferin	D. R. Telange , N. K. Sohail, A. T. Hemke, P. S. Kharkar, A. M. Pethe	Pharmaceutics	Drug Delivery and Translational Research, 2021 Jun;11(3):1056-1083	5.671	306
25	Lipiod SPC-3-Based Coprecipitates for the Enhancement of Aqueous Solubility and Permeability of Ranolazine	D. R. Telange , S. A. Ukey, A. T. Hemke, M. J. Umekar, A. M. Pethe, P. S. Kharkar	Pharmaceutics	Journal of Pharmaceutical Innovation volume 16, pages643–658 (2021)	0	334
26	Antimutagenic Activity of Cassia Auriculata Linn Fractions along with Anticancer Activity in Male Albino Mice	Shailesh M. Kewatkar , Dipak V Bhusari, Madhav chakolkar, Amit Joshi, Shirish P. Jain and Chanchal Navin Raj	Pharmacognosy	Journal of Pharmaceutical Research International, 33(59A): 216-228, 2021	0	350
27	Antimutagenic Activity of Cassia Auriculata Linn Fractions along with Anticancer Activity in Male Albino Mice	Shailesh M. Kewatkar, Dipak V Bhusari , Madhav chakolkar, Amit Joshi, Shirish P. Jain and Chanchal Navin Raj	Pharmacognosy	Journal of Pharmaceutical Research International, 33(59A): 216-228, 2021	0	363
28	Antimutagenic Activity of Cassia Auriculata Linn Fractions along with Anticancer Activity in Male Albino Mice	Shailesh M. Kewatkar, Dipak V Bhusari, Madhav chakolkar , Amit Joshi, Shirish P. Jain and Chanchal Navin Raj	Pharmacognosy	Journal of Pharmaceutical Research International, 33(59A): 216-228, 2021	0	376

Sr. No.	Title of paper	Name of the author/s	Department of the teacher	Name of journal	Impact Factor	Page No. with Link
29	Antimutagenic Activity of Cassia Auriculata Linn Fractions along with Anticancer Activity in Male Albino Mice	Shailesh M. Kewatkar, Dipak V Bhusari, Madhav chakolkar, Amit Joshi, Shirish P. Jain and Chanchal Navin Raj	Pharmacognosy	Journal of Pharmaceutical Research International, 33(59A): 216-228, 2021	0	389
30	Evaluation of the Antigenotoxic Potential of Methanolic Leaves Extract of Triticum aestivum in Mice	Gaurav Jain, Shailesh M. Kewatkar , Govind Nayak and Amit Nayak	Pharmacognosy	Journal of Pharmaceutical Research International, 33(47B): 1-9, 2021	0.	402
31	In vitro Antioxidant and Anti-inflammatory activity of Salix alba L. along with simultaneous HPTLC analysis of Salicin and Ferulic acid	Shivatara RS, Dr.Kewatkar SM , Musale R, Lohakare P, Patil D, Choudhary D, Ganu G, Dr. Nagore DH, Dr.Chitlange S	Pharmacognosy	International Journal Of Pharmaceutical Sciences And Research, 2021; Vol. 12(6): 3176-3184.	0	411
32	Antioxidant activity of cassia auriculata and cassia fistula extract along with wound healing activity of its polyherbal formulation.	SM Kewatkar , VV Paithankar, SS Deshpande, SP Jain, DH Nagore	Pharmacognosy	International Journal Of Pharmaceutical Sciences And Research, 2021; Vol. 12(3): 1805-1810.	0	420
33	Antioxidant activity of cassia auriculata and cassia fistula extract along with wound healing activity of its polyherbal formulation.	SM Kewatkar, VV Paithankar, SS Deshpande, SP Jain , DH Nagore	Pharmacognosy	International Journal Of Pharmaceutical Sciences And Research, 2021; Vol. 12(3): 1805-1810.	0	426
34	Comparative Pharmacognostical and Phytochemical Study of Cassia auriculata and Cassia fistula Linn.	Shailesh M. Kewatkar , Vivek V. Paithankar, Supriya S. Deshpande, Shirish P. Jain, Dheeraj H. Nagore, Dipak V. Bhusari, Chanchal Navin Raj, Madhav D. Chakolkar, Trupti A. Nimburka	Pharmacognosy	Journal of Natural Remedies, Vol 2021, 21 (1), 77-85	0	432

Sr. No.	Title of paper	Name of the author/s	Department of the teacher	Name of journal	Impact Factor	Page No. with Link
35	Comparative Pharmacognostical and Phytochemical Study of Cassia auriculata and Cassia fistula Linn.	Shailesh M. Kewatkar, Vivek V. Paithankar, Supriya S. Deshpande, Shirish P. Jain , Dheeraj H. Nagore, Dipak V. Bhusari, Chanchal Navin Raj, Madhav D. Chakolkar, Trupti A. Nimburka	Pharmacognosy	Journal of Natural Remedies, Vol 2021, 21 (1), 77-85	0	441
36	Comparative Pharmacognostical and Phytochemical Study of Cassia auriculata and Cassia fistula Linn.	Shailesh M. Kewatkar,, Vivek V. Paithankar, Supriya S. Deshpande, Shirish P. Jain, Dheeraj H. Nagore, Dipak V. Bhusari , Chanchal Navin Raj, Madhav D. Chakolkar, Trupti A. Nimburka	Pharmacognosy	Journal of Natural Remedies, Vol 2021, 21 (1), 77-85	0	450
37	Comparative Pharmacognostical and Phytochemical Study of Cassia auriculata and Cassia fistula Linn.	Shailesh M. Kewatkar,, Vivek V. Paithankar, Supriya S. Deshpande, Shirish P. Jain, Dheeraj H. Nagore, Dipak V. Bhusari, Chanchal Navin Raj, Madhav D. Chakolkar , Trupti A. Nimburka	Pharmacognosy	Journal of Natural Remedies, Vol 2021, 21 (1), 77-85	0	459
38	Pharmaceutical and biopharmaceutical aspect of quantum dots –An overview	Saddam C. Shaikh , Shweta G. Saboo, Prashant S. Tandale, Fahim S. Memon, Sharad D. Tayade, M. Akiful Haque, Sharuk L. Khan	Pharmaceutics	International Journal of Applied Pharmaceutics, Vol 13, Issue 5, 2021, 44-53	0	468
39	Pharmaceutical and biopharmaceutical aspect of quantum dots –An overview	Saddam C. Shaikh, Shweta G. Saboo, Prashant S. Tandale, Fahim S. Memon, Sharad D. Tayade , M. Akiful Haque, Sharuk L. Khan	Pharmaceutics	International Journal of Applied Pharmaceutics, Vol 13, Issue 5, 2021, 44-53	0	478



DBUGVF's

Rajarshi Shahu College of Pharmacy, Buldana

Approved by AICTE, PCI, New Delhi and affiliated to SantGadge Baba Amravati University, Amravati)

Sr. No.	Title of paper	Name of the author/s	Department of the teacher	Name of journal	Impact Factor	Page No. with Link
40	A Review on: Fast Dissolving oral Film	Mr. Vijay P. Ingle, Prof. Sharad D. Tayade , Dr. Shirish P. Jain	Pharmaceutics	International Journal of Trend in Scientific Research and Development, 2021, 5 (5), 300-310	0	<u>488</u>
41	A Review on: Fast Dissolving oral Film	Mr. Vijay P. Ingle, Prof. Sharad D. Tayade, Dr. Shirish P. Jain	Pharmaceutics	International Journal of Trend in Scientific Research and Development, 2021, 5 (5), 300-310	0	<u>499</u>



Nanocomposite polymeric materials: state of the art in the development of biomedical drug delivery systems and devices

Prakash Namdeo Kendre² · Mrinal Gite¹ · Shirish P. Jain² · Ajinkya Pote²

Received: 21 September 2021 / Revised: 12 November 2021 / Accepted: 18 November 2021
© The Author(s), under exclusive licence to Springer-Verlag GmbH Germany, part of Springer Nature 2021

Abstract

Due to recent advancements in the field of science and technology, it becomes easier to synthesize and produce nanomaterials. These nanomaterials are now better choice to the researchers for the development of various products. Their use in the development of variety of products including biomedical devices and drug delivery systems has much attention to the researchers. Due to change in the physical properties at molecular level, it becomes easier to overcome the hurdles in the development of drug delivery systems with better therapeutic benefit and ease of convenience to the patients. Different carrier systems are useful for the delivery of drugs to the site of action, but nanocarriers systems have attracted due to their particle size, shape, strength and huge surface area. Among these carrier systems, nanocomposite polymeric materials have greater attention for their use in the development of various drug delivery and targeting devices. In many recent studies, their applications in the design of biomedical devices and bone tissue engineering are observed. In this review, the various types nanocomposite polymeric materials, their behaviour during synthesis, evaluation parameters and various applications with critical findings in the field of pharmaceuticals and biomedical sciences are discussed.

Keywords Nanocomposite · Nanomaterials · Biomedical applications · Targeted drug delivery

Introduction

Nanotechnology can be defined as the application of controlling the properties of the matter at the molecular level [1]. In everyday life, nanotechnology is now widely utilized science due to which our routine becomes much easier and

✉ Prakash Namdeo Kendre
prakashkendre@gmail.com

Extended author information available on the last page of the article

comfortable than use of conventional approaches [2]. Nanotechnology is the science which deals with the materials and particles which have at least one dimension in the range of 1–100 nm [3]. Nanocomposites: In recent years, there is huge development in nanotechnology through which the various problems related to drug development have been overcome from which one is the use of nanocomposite materials. Nanocomposites are a broad range of materials which consist of one or more phases embedded in metal, ceramic or polymer matrix at nanometre range [4]. As a material, nanocomposite has so many benefits in drug development and will show great changes in the industrial field [5]. Bansi D. Malhotra, Md Azahar Ali (2018) stated that if different structural units are utilized in individual regimen, then the term “Nanocomposites” is used [4]. According to Jaiswal L et.al. (2019) for creating new and innovative packaging materials, nanocomposites are represented as an inspiring route [6]. Most drugs have problems related with their poor solubility, stability and bioavailability which can be now solved by the use of nanocomposite materials.

Okpala CC. (2013) states that for the better properties of nanocomposites they not only depend on their interfacial characteristic but also depend on their individual parents and their morphology. Nanocomposite improves various properties such as mechanical properties like strength and dimensional stability, thermal stability, solubility, permeability, bioavailability in the drug development [7]. There are two different parts present in nanocomposites: one is continuous phase and another is discontinuous or reinforcing phase. Polymers, ceramic and metals are considered as the three different building blocks for the nanocomposites. Based on the continuous phase, each of these possesses specific properties which may add value in nanocomposites like polymers that provide the insulation, ductility, and also impact resistance, metals provides strangeness ductility and conductivity whereas ceramics provides properties like chemical resistance, brittleness and strangeness. Discontinuous phase includes the nanomaterials with different types which are also called nanofillers dispersed in the continuous phase [8, 9]. Nanocomposites include nanoparticles, nanoclay and nanofibers as nanomaterials to overcome the limitations regarding the microcomposites, and monolithic nanocomposites are represented as new alternative ways [10].

Materials with unique physicochemical characteristics are recently attracted for the development of many biomedical devices. Composite materials exhibiting nanometre scale have proven their applications in the development of implants, drug delivery systems and many engineered nanostructures. Their use in the biomedical field has been increased due to their comprehensive properties like, nanoscale, huge surface area mechanical strength, targeting ability, tissue engineering and biocompatible nature. Metal- and polymer-based nanocomposite materials have increasing demand in the development of biomedical devices, including surgical implants in prosthetic and orthopaedic applications.

This review provides insight on various types nanocomposite polymeric materials, their behaviour during synthesis, evaluation parameters and various applications with critical findings in the field of pharmaceuticals and biomedical sciences.

Advantages of nanocomposites

There are various advantages of nanocomposites over the other composites materials; they are as follows:

- Improved mechanical properties—greater ductility without any loss in strength, and resistance over scratch;
- Small size of fillers and distance between fillers allowed due to the high surface or volume ratio;
- Increased optical properties (as transmission of light and particle size is dependent on each other).

Disadvantages of nanocomposites

As nanocomposites are having various applications in various drug delivery systems, it also has some disadvantages; they are as follows:

- Toughness and impact performance related with the incorporation of nanoparticles to bulk matrix
- Cost effectiveness
- Lack of sufficient understanding between properties, formulation and structural relationship
- Component as well as, long-term stability and service, structural integrity, mechanical properties and corrosion properties, and uncertain cytotoxicity in tissue engineering.

Types of nanocomposites

On the basis of their type of matrix material, nanocomposites are classified into different categories as shown in Fig. 1 [11, 12].

Polymer matrix nanocomposites (PMNC)

In this type of nanocomposites, the polymer and nanoadditives are used as matrix material and reinforcement material, respectively. The additives used are 1D (nanotubes and fibres), 2D (layered materials like clay) or 3D (spherical particles), and due to the better mechanical properties with a small concentration of nanoadditives, they gained considerable attention in academics and as well as in industrial field [13]. Due to easy production, ductility and lower weight properties polymer matrix nanocomposites are widely used in the industries [14]. Properties of these nanocomposite depend on properties of individual component as well as various different parameters like process used in nanocomposite fabrication, degree of mixing of two phases, type of adhesion at the matrix interface, volume fraction of nanoparticles, characteristics of nanoparticles, nature of the

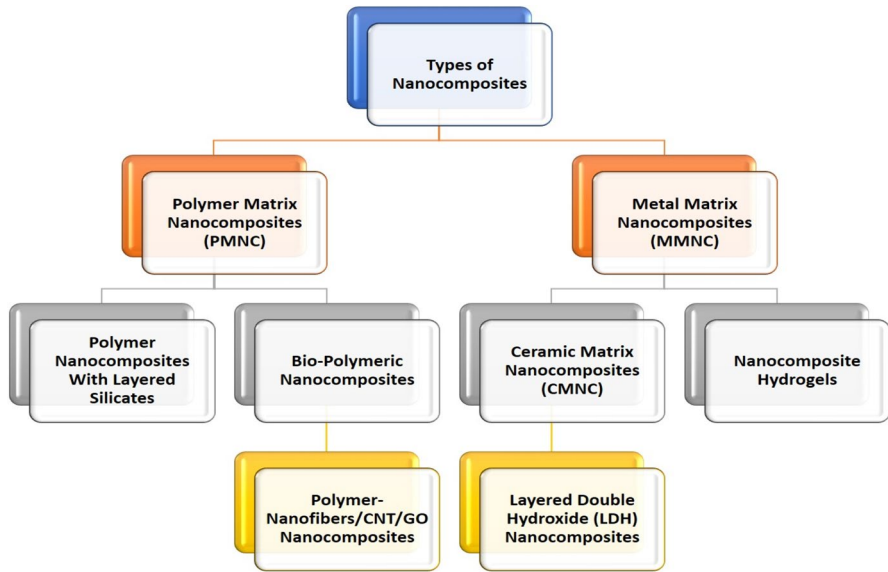


Fig. 1 Broad classification of nanocomposites

interphase developed at matrix interface, size and shape of nanofiller materials and system morphology [13]. The main factor to be considered in the polymeric matrix nanocomposites is the dispersion of the nanofillers in the bulk polymer matrix for resulting in improved properties with the homogeneous distribution of nanomaterials [14]. Examples of polymer matrix nanocomposites are thermo-plastic/thermoset polymer/layered silicates, polyester/ TiO_2 , polymer/CNT, polymer/layered double hydroxides [15].

Ceramic matrix nanocomposites (CMNC)

These are considered as a new generation of engineering materials having huge impact in the industrial application and these nanocomposites consist of one or more phases in the nanometre range. Ceramics are the solid materials in general that possess strong ionic bonding and covalent bonding in few of the cases [13]. For preparation of CMNCs, various methods such as conventional powder method; polymer precursor route; spray pyrolysis; vapour techniques (CVD and PVD) and chemical methods, which include the sol–gel process, colloidal and precipitation approaches and the template synthesis, are included in the many studies [11, 16]. Examples of ceramic matrix nanocomposites are $\text{Al}_2\text{O}_3/\text{SiO}_2$, SiO_2/Ni , $\text{Al}_2\text{O}_3/\text{TiO}_2$ and $\text{Al}_2\text{O}_3/\text{SiC}$. After the discovery of carbon nanotubes (CNT), they were used in the fabrication of nanocomposites. Some common examples of CNT-based ceramic matrix nanocomposite include $\text{Al}_2\text{O}_3/\text{CNT}$, $\text{MgAl}_2\text{O}_4/\text{CNT}$ and MgO/CNT [16].

Metal matrix nanocomposites (MMNC)

In recent years, metal matrix nanocomposites have taken a great area of interest in the various fields due to their special functional and structural applications. From the last two decades, there is considerable interest in the research area generated by the development of new materials [17]. Metal matrix nanocomposites consist of ductile metal/ matrix consisting of alloy and in which the nanosized reinforcement material is implanted [15]. There are various methods for the processing of MMNC such as spray pyrolysis, liquid metal infiltration, vapour technique, rapid solidification, electrode position and some of the chemical methods like colloidal and sol–gel method. Some common examples of metal matrix nanocomposites are Fe–Cr/Al₂O₃, Ni/Al₂O₃, Fe/MgO, Al/CNT and Mg/CNT [16].

Polymer nanocomposites with layered silicates

In this, the polymer incorporated with a low amount of layered silicate which is dispersed at nanoscale level is considered as most promising material which is characterized by physical, chemical and mechanical properties which cannot be obtained with micro- or macroscopic dispersion of inorganic fillers. This polymer layer silicate can be obtained by inserting the polymer molecules in the galleries between the layers of poly-silicate. Insertion of polymer molecules can be done to prepare the ‘intercalation hybrids’ replacing the water hydration molecules into the galleries bipolar functional group containing polymers using ion–dipole method [18]. There are two types of nanoplatelet particle composites: one is graphite and another is silicate clay minerals, and for the preparation of nanocomposites, some of the smectite type layered silicates like montmorillonite (MMT), saponite and hectorite are commonly used [12]. Among these smectite type layered silicate, the montmorillonite is considered as common and best studied clay having 2:1 layer structure which means that it consists of two tetrahedral silica layers which are separated by an octahedral alumina layer [19]. In pharmaceutical engineering, MMT is found to have very extensive applications such as stabilizing and suspending agent along with this it is also used as adsorbent and clarifying agent. Along with MMT, other clay species are also used as drug carrier in drug delivery and tissue regeneration agents for various compounds such as paclitaxel, procainamide, tamoxifen citrate, buspirone, timolol maleate, 5-fluorouracil and epidermal growth factor [20]. Jain S and Datta M (2014) prepared montmorillonite–PLGA nanocomposites effectively for the oral extended drug delivery of the venlafaxine hydrochloride [21].

Polymer nanofibers /CNT/GO nanocomposites

Augmentation of the mechanical properties of polymer obtained by the use of inorganic fillers containing some micrometric dimensions such as calcium carbonate, talc and glass blends in the conventional polymer composite [12]. From the past few years, carbon nanotubes had very much impact in the nanomaterials; in various drug delivery, bio-sensing as well as biomedical imaging, it also has high impact in the design of functional nanocomposites [22]. Justin R. and Chen B. (2014) developed

the strong and conductive chitosan-reduced graphene oxide nanocomposites which is reported for transdermal drug delivery by in situ reduction of graphene oxide in chitosan by heating 37 °C for 72 h and they found increase in mechanical properties of the nanocomposites and the strongest nanocomposite with 1% weight reduced graphene oxide showing increase of 91.3% for Young's modulus and 95.6% for ultimate tensile strength over pristine chitosan while maintaining the elongation at break at 10.8% [23].

Bio-polymeric nanocomposites

For the sake of controlled drug delivery of therapeutically active substances, the biopolymers are considered as best contrasting option to the traditional non-biodegradable polymers [12]. The biopolymers are obtained from the natural sources like plants and animals, considered as environmentally friendly polymers; therefore, they are used in various food packaging materials and also have applications in the formation of biopolymer films [24]. These polymers are classified into three classes: class first includes the polymers which are specially separated from biomass, for example, cellulose or starch. The polymers which are obtained synthetically from bio-based monomers are included in class second like poly (lactic acid). The last classification of the biopolymers consists of polymers which are obtained from microorganisms or microscopic organisms such as poly (hydroxyl alkanooates) [12]. The fabrication of biopolymer nanocomposites is done with the help of biopolymers and bio-fillers which shows different physical, mechanical and thermal properties along with some functionalities like biodegradability and biocompatibility [25].

Starch-based nanocomposites

Starch is abundant, renewable, and having low-cost material containing biodegradable properties and properties like film forming due to this starch is considered as the best alternative option to synthetic materials [12]. For improvement of the mechanical properties and reduction in the hydrophilic character of starch, the blends of starch with natural and synthetic polymers are studied to overcome these problems and also to overcome the aging effect [26]. Cao X. et al. (2008) prepared cellulose nanocrystals suspension from flax fibres by acid hydrolysis and used to reinforce the plasticized starch (PS) with the content of 5–30% nanocomposites. Well dispersion of FCNs fillers in PS matrix and good adhesion at interfacial area was observed in the nanocomposites which are prepared by casting method and also showed increase in the tensile strength, Young's modulus with higher water resistance [27]. Kalambar S.B, Rizvi S.S (2004) successfully prepared nanocomposites with superior properties from starch–polycaprolactone (PCL) blends in the presence of montmorillonite (MMT) nanoclay by using reactive extrusion processing and found that with the addition of a modified nanoclay at 3%wt level increased elongation almost fourfold over that of pristine starch–PCL blends. These nanocomposites showed the better solvent-resistance properties because of resistance to diffusion offered by clay platelets in the polymer matrix [28].

Cellulose-based nanocomposites

Because of the specific properties like non-toxicity, cost effectiveness, low density, combustibility and its biodegradable properties cellulose fibre-reinforced polymer composites received very much attention in the various fields of science [29]. Unique properties like improved chemical reactivity, high specific area, non-toxicity, better mechanical durability, together with biodegradability, biocompatibility nanoscale cellulose have become an excellent candidate for the release applications of the drugs [12]. He Y et al. (2020) prepared the carboxymethyl cellulose (CMC)-based nanocomposites which are reinforced with the montmorillonite (MMT) and ϵ -poly-(lysine) (ϵ -PL) with the help of solvent casting method for antimicrobial active food packaging. They evaluated the activity of CMC/MMT/ ϵ -PL nanocomposites against bacteria and fungi and the result showed the favourable inhibition activity against them. The microbial inhibition rate of CMC/MMT/ ϵ -PL 7.5 wt. % film can reach up to above 90%. They also performed the shelf-life study by coating the strawberries with the film forming solution of CMC/MMT/ ϵ -PL 7.5% and they found the extended shelf life for 2 days under ambient temperature [2].

Guar gum-based nanocomposites

Guar gum is used as biomaterial in a different biological and technological processes due to their specific properties like biocompatibility, non-toxicity and the most important is biodegradable polymer [12]. Mansa R, Detellier C (2013) prepared guar–montmorillonite nanocomposites using neutral guar gum and cationic guar gum by the solution intercalation method. Observed morphology and structure of these nanocomposites shows the dependency on relative amounts of guar gum and montmorillonite used for the preparation of nanocomposites [30]. Palem R.R et al. (2020) synthesized guar gum graft polymer-based silver nanocomposite hydrogels and utilized successfully to explore sustained release of 5-fluorouracil (5-FU) and they also evaluated the antibacterial activity. Their study also suggested the use of these nanocomposites in the applications for wound healing purpose and controlled delivery of drug [31].

Nanocomposite hydrogels

Recently, the interest of researchers has been attracted by the nanocomposite hydrogels as biomaterials and by doing the manipulation in the properties of hydrogels and the composite material properties of these biomaterials can be altered easily [12]. Haraguchi K (2007) reported the novel creation of the nanocomposite hydrogels to overcome the limitations of conventional chemically cross-linked hydrogels and it is possible due to the extraordinary properties like mechanical, optical and swelling. Nanocomposite hydrogels were achieved by allowing the clay platelets to act as multifunctional cross-linkers in the formation of polymer/clay networks [32]. Gaharwar AK et al. (2014) studied nanocomposite hydrogels for the biomedical applications and their study concluded that the nanocomposite hydrogel can potentially be used for various pharmaceutical and biomedical applications such as

drug delivery, sensors, regenerative medicine, and actuators and in other biomedical devices. The nanocomposite hydrogels are found to be superior in their physical, chemical, electrical and biological properties than the properties of conventional polymeric hydrogels [33].

Layered double hydroxide (LDH) nanocomposites

These layered double hydroxide (LDH) plays very vital role in the field of material chemistry due to their extraordinary properties and wide range of applications such as thermal stability, energy applications, food packaging applications, drug delivery, agriculture applications, water purification, photoluminescence and flame retardancy. Due to increase in the extent of exfoliation of LDH nanosheets in the polymer matrices, their high efficiency in these applications can be achieved. But because of the high interlayer interaction arises from high charge density of layers, there is big problem to obtain the remarkable exfoliation. This problem can be overcome by the advancement in the fabrication of LDH–polymer nanocomposites by various methods like melt compounding, solution blending and in situ methods like in situ polymerisation, in situ LDH synthesis and double in situ method [34].

Various materials used in the synthesis of nanocomposites

As we discussed above, nanocomposites are substances in which filler materials are incorporated into matrix and based on matrices they are classified as polymer, ceramic and metal matrix nanocomposites, and for their synthesis, various materials are used like various polymers and clays like montmorillonite, saponite, etc., and for certain synthesis methods, it is very critical for polymer, clays and filler materials to get solubilize into organic and aqueous solvents [35]. The overall thought of nanocomposites is based on the idea of making a huge interface between the nanosized-assembling blocks and polymer matrix. Be that as it may, the properties of nanocomposites are not decided exclusively by the size of interface, yet different elements such as design and interactions also assumed as significant part [36]. Polymers utilized in the synthesis of nanocomposites are of different properties, and in various characteristics, some of them might be biodegradable polymers or some might be used as commodities as general-purpose polymers [37]. Raw materials used for synthesis of primarily include polymers ranging from vinyl polymers to special polymers; compatibility agent (can be a polymer) offers a chemically compatible with polymer and filler materials (may be nanoparticle) [35, 37]. Various materials such as polymers, clays and different filler materials used in synthesis of nanocomposites are discussed below.

Polyvinyl alcohol (PVA)

Polyvinyl alcohol (PVA) is used in synthesis of nanocomposites because of its strong chemical and mechanical properties as well as good thermal properties and resistance. PVA is environmentally safe, cost effective and light weight. Many of

the researchers utilized PVA for preparation of nanocomposites using various filler materials and the results have shown increased thermal properties as well as increased antibacterial activity [38, 39].

Polyvinyl chloride (PVC)

PVC is one of the major thermoplastics along with other standard polymers like polyethylene and polystyrene. However, some of its main characteristics such as plasticity, thermal and photostability are inferior to other standard polymers. Among these various characteristic properties, it also bears property of flexibility and durability with suitable chemical and biological resistance and also because of excellent improvement in toughness, thermal robustness and structural stability PVC-based nanocomposites have attracted much more than other [40–42].

Polyaniline

Polyaniline is most studied polymer in synthesis of nanocomposites used in drug delivery. Binitha N. Narayana et al. (2010) prepared exfoliated nanocomposites with polyaniline and montmorillonite. As compared to intercalative nanocomposites, polyaniline/montmorillonite nanocomposite shows excellent physical properties like strength, stiffness and barrier properties [43]. Polyaniline-based nanocomposites also show better results in the cancer therapy with great *in vivo* or *in vitro* biocompatibility and biodegradability [44].

Polyhydroxybutyrate (PHB)

Polyhydroxybutyrate is a biodegradable polymer, but it has disadvantages like stiffness, fragility and low thermal stability and these disadvantages can be overcome by preparing nanocomposites [37]. Application of PHB in drug delivery is that it has been investigated for bone tissue engineering. Mikael Larsson et al. [45] prepared nanocomposites of polyacrylic acid nanogel and biodegradable polyhydroxybutyrate for bone regeneration and drug delivery and the results indicated that prepared composites may be suitable for biomedical uses as a biodegradable material where use of nanostructure design done to tune mechanism of drug release, from diffusion controlled to degradation controlled. Furthermore, drug release was demonstrated for small lithium ion which together with improved tolerance to deformation suggest that the nanocomposites to be appropriate for bone tissue engineering [45].

Chitosan

Chitosan is a biopolymer characterized by excellent chemical and biological properties that can be used in a wide range of applications, such as food, cosmetics, water treatment, membranes, environmental protection, material development, biomedicine, tissue engineering and has excellent biocompatibility and biodegradability [46, 47]. Chitosan nanocomposites refer to chitosan polymer containing dispersed nanofillers having an average particle size less than 100 nm; however, it contains some

drawbacks and to overcome these drawbacks related with biopolymers nano-reinforcement incorporated into chitosan matrix [47]. Utilization of chitosan in ocular drug delivery is due to some extraordinary properties like biocompatibility, penetration–facilitation, cationic polysaccharide and suitable structure for the ocular problems [48].

Montmorillonite

Various clays that belong to smectite family are mostly utilized for preparation of nanocomposites: one of them is montmorillonite. Montmorillonite is most common and best studied clay used in the preparation of polymer nanocomposites for almost three decades due to biocompatibility and biodegradability along with good mechanical properties [49]. Shilpa Jain and Monika Datta prepared montmorillonite–PLGA nanocomposites as an oral extended drug delivery vehicle for venlafaxine hydrochloride and found controlled release behaviour over a period of 12 h. and effective for oral extended drug delivery resulted in decrease in the dosing frequencies [21].

Saponite

Saponite clay is most easily synthesized smectite clay. It is also used in preparation of clay-based nanocomposites utilized for drug delivery. Inorganic layers of saponite play very crucial role in stabilizing and protecting the surfactant molecules by increasing their thermal stability. Kumaresan S. et.al. (2019) synthesized saponite-based nanocomposites to improve the controlled oral drug release of quinine hydrochloride dihydrate [50, 51]. Along with polymers and clays, various filler (materials incorporated in polymer matrix) materials such as nanoparticles also play important role in the preparation of nanocomposite; they used to improve mechanical strength hardness and stiffness.

Graphene oxide nanoparticles

Nanoparticle fillers have been incorporated into polymer-based nanocomposites of different macroscopic form. Oxygen containing functional groups render graphene oxide a biocompatible and physiologically soluble behaviour, and allow strong interaction with many polymers which leads to development of nacre-like structure, an organization widely explored in the development of tough biomimetic nanocomposites [52]. Hailin Lei et.al. (2016) prepared chitosan/sodium alginate medicated graphene oxide-based nanocomposite as a carrier for drug delivery doxorubicin is used as model drug. They prepared DOX-loaded GO/CS-alginate nanocomposites through self-assembly process. The results showed that chitosan/sodium alginate (SA) modification increased the stability and dispersibility of graphene oxide sheets but also suggested that GO-CS/SA nanocomposites were promising novel vehicles for drug delivery [53].

Hydroxyapatite nanoparticle

Hydroxyapatite nanoparticles are utilized to treat bone infections. Being biocompatible, nanohydroxyapatite is used as drug carrier and biomolecules for various diseases. A.P.S. Prasanna and G. D. Venkatasubbu prepared hydroxyapatite nanocomposites for sustained release of amoxicillin. In this, PVA and sodium alginate are coated layer by layer on the hydroxyapatite nanoparticles. Sustained release of drug observed from nanocomposites for 30 days and drug-loaded nanocomposites showed better antibacterial activity and ensured that it can be used as drug delivery system to treat bone infections [54].

Magnetic nanoparticles

Use of magnetic nanoparticles for drug delivery provides promising and effective approach in animal models for cancer and other diseases. It possesses specific properties, like large surface area, small particle size and super magnetism. Farahnaz Brahuie et.al. (2017) prepared phytic acid-chitosan iron oxide nanocomposite (PTA-CS-MNP) by coating magnetic nanoparticles with chitosan for sustained release of phytic acid (anticancer agent). The released profile of the drug from nanocomposites into phosphate buffer saline was observed in sustained manner with total release equilibrium of 86% and 93% when exposed to environments of pH 7.4 and 4.8 at 127 and 56 h, respectively. The prepared nanocomposites estimated as having good anticancer potential against colon cancer cells with no cytotoxicity to normal fibroblast cells [55, 56].

Polymer nanoparticles

Yu et.al. (2009) developed composite microparticles of chitosan, alginate and pectin for drug delivery using bovine serum albumin as a model drug. The result shows the sustained release of drug at stimulated gastric medium, whereas a fast release was observed in simulated intestinal and colonic media [57]. Rajan et.al. (2016) evaluated in vitro release of cisplatin from poly oxalates cross-linked chitosan nanocomposite and they observed that cisplatin-loaded nanocomposites were able to inhibit the tumour growth up to two times more than free cisplatin [58].

Structural features of nanocomposites

Structure of nanocomposites consists of the matrix in which various reinforcement materials like particles, fibres, nanotubes, etc., are incorporated. Structure of nanocomposites can be classified by the distribution of the particles in polymer matrix, and depends on the processing of the composite materials [59]. Most important phenomenon in nanotube or nanofiller reinforced composites is both aggregation and orientation, while in case of composites containing spherical particles, aggregation is a major problem which may cause due to face-to-face interaction and edge-to-edge

orientation leads to the formation of a silicate network [36]. Nanocomposite often contains large particles and network structure developing at large extent of exfoliation and complexity of structure of nanocomposites depends on type of reinforcement (plates, nanoparticles, nanotubes, etc.) within matrix [60]. Primary condition for obtaining nanocomposites with acceptable properties is homogeneous dispersion of nanoparticles [36]. While discussing structure of polymer/layered silicate nanocomposite, the silicate must be exfoliated means the original particles separated to individual layers. Bhavesh D. Kevadiya et.al (2010) intercalated procainamide hydrochloride (PA) in montmorillonite (MMT) as a carrier for drug delivery. Prepared bio-nanocomposite found to have spherical structure due to coating of chitosan over PA-MMT-AL beads (PA-MMT-AL-CS) [20]. The structure of nanocomposites can be established by the arrangement of particles in the polymer matrix [59]. Depending upon structure of dispersed clay platelets in the polymer matrix, the composites can be classified as intercalated or exfoliated nanocomposites. Intercalated structure of nanocomposites can be recognized with its well-ordered and self-assembled multi-layered structures where the extended polymer chains are inserted into the gallery space of the clays, while in an exfoliated structure, individual silicate sheets lose their layered geometry as a result of delamination, and dispersed as nanoscale platelets in a polymer matrix [61]. Arrangement of particles in spherical or onion-like structures shows that the dispersion behaviour of nanoparticles can be crucially influenced by an organic shell [59]. XRD spectra and TEM study are used in the characterization of structure of nanocomposite, wherein XRD spectra of exfoliated nanocomposite do not show any peak at 2θ value near about 8.9° because exfoliation of clay layers removed parallel arrangement of different layers which leads to no interlayer spacing between them but XRD alone can lead to false interpretation of exfoliated structure of nanocomposites. Therefore in other hand, TEM study is also used which can provide very important information in a localized area on the structure, morphology and the distribution of dispersed phase of the nanocomposites [43, 61]. Some of the types of nanocomposite structure are highlighted in Fig. 2.

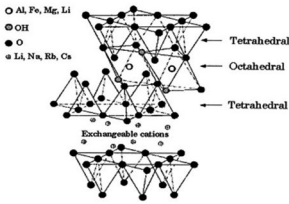
Behaviour of nanocomposites in the developmental stage

Properties of nanocomposites can crucially affect the dispersion state of nanoparticles in a polymer matrix and this situation is dominated with entropy by enthalpy effect where weak role is played by entropy. Recently, the miscibility of nanoparticles in polymer matrix has become a topic of interest for study where the miscibility occurs when the polymer chains present are bigger than the nanoparticles [62]. Table 1 shows various nanocomposite formulations and their physical properties and behaviour.

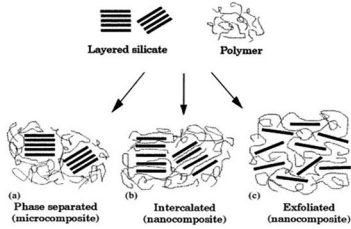
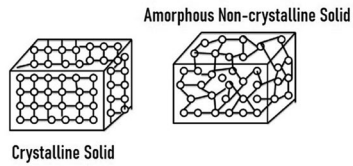
Various applications of nanocomposite materials in pharmaceuticals and biomedical field are highlighted in Table 2, whereas Tables 3 and 4 highlights the critical findings in the development of nanocomposite materials.

Figure 3 shows the various evaluation parameters of prepared nanocomposites based on the critical behaviour of materials used in the synthesis of nanocomposites.

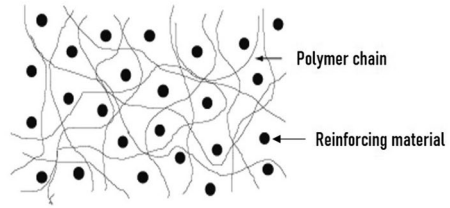
(a) Polymer-layered silicate nanocomposite structure



(b) Ceramic nanocomposites



(c) Other types of nanocomposite structures



(d) Polymer reinforced nanocomposite structure

Fig. 2 Some of the types of nanocomposite structures

Limitations of nanocomposites

- Long-term stability and uncertain cytotoxicity in tissue engineering [108].
- Nanocomposite hydrogels can show undesired dehydration during its use in drug delivery [13].
- Use of natural biopolymer film in industries and wide application of starch-based nanocomposites are limited due to their water vapour barrier properties and poor mechanical properties like brittleness of those films by high intermolecular forces [24].
- Chitosan–aluminosilicate nanocomposite carrier can affect by gastric pH and their ratio [109].
- There are some limitations to the application of chitosan film for packaging, due to its high sensitivity to moisture [110].
- Limitations for both TiO₂ nanocomposite and TiO₂ porous films are that high-temperature process is required to form anatase nanocrystals [111].

Conclusion

Due to diversity in the synthesis of nanocomposite carriers and recent advancements in the field of science and technology, it becomes easier to select the proper material in the design and development of various drug delivery systems and devices. Their use in the development of variety of products including biomedical devices and drug delivery systems has much attention to the researchers. Due to change in the physical properties at molecular level, it becomes easier to overcome the hurdles in the

Table 1 Various nanocomposite formulations and their physical properties and behaviour

Nanocomposite	Method of preparation	Components	Effect on various properties of nanocomposite	References
Chitosan-reduced graphene oxide particles	Biocompatible in situ reduction process	Reduced graphene oxide (rGO) High concentration of rGO in nanocomposites	Increases crystallinity Brittle	[23]
Guar–montmorillonite (MMT) nanocomposites	Solution intercalation method	Guar gum Montmorillonite (MMT)	Increases interlayer space of montmorillonite and TEM study indicates partial exfoliation with MMT	[30]
Guar gum graft polymer-based silver nanocomposite hydrogels	In situ polymerisation method	Acrylamidoglycolic acid chains onto guar gum backbone Cross-linked graft polymer (GGAA) and its silver nanocomposites (GGAA@SNC)	Fractured morphology of nanocomposite hydrogels Cross-linking of borate ions and cis-diol of graft copolymer	[31]
Poly(propylene carbonate)/MMT nanocomposite	Solution intercalation method	Hydrated edge–edge interaction of silicate layers At OMMT 4 wt %	Flocculation of stacks and intercalated layers of silicate High tensile strength and good dispersion into matrix	[63]
Chitosan-g-poly(acrylamide) or zinc nanocomposite	Microwave irradiation method	Polymerisation of acrylamide Inhibition of deoxygenase and periplasmic enzyme activity	Change in surface morphology of chitosan Good antibacterial activity	[64]
pH-sensitive super paramagnetic iron oxide nanocomposite	pH-sensitive acylhydrazone linkage	Addition of 0.1 N HCl Presence of acylhydrazone	Brakeage of acylhydrazone linkage Efficient pH-triggered release of doxorubicin (DOX)	[65]
Calcium phosphate nanocomposites	Rapid precipitation of water in presence of polymer	Addition of drug to all resulting nanocomposites	Hardly affected the spherical shape of nanocomposites	[66]
Layered double hydroxide nanocomposite	Direct mixing of SiO ₂ nanodots with MgAl-LDH nanoparticles	Increase in mass ratio from MgAl-LDH to SiO ₂	Decrease in particle size of nanocomposites	[67]
Carboxymethyl cellulose/graphene oxide bio-nanocomposite hydrogel beads	Simple mixing of graphene oxide and CMC with aqueous dispersion	Addition of graphene oxide	Change in porous structure of GO/CMC monoliths	[68]

Table 1 (continued)

Nanocomposite	Method of preparation	Components	Effect on various properties of nano-composite	References
Chitosan—Locust bean gum (LBG) interpenetrating polymeric network nanocomposite	Glutaraldehyde cross-linking	Variation in polymer concentration of LBG or Chitosan	Decrease in size of composite	[69]
Lecithin and PLGA-based self-assembled nanocomposite	Solution intercalation method	Increase in concentration of polymer/lecithin or high ratio of polymer/lecithin	Increase in size of resulting nano-composite	[70]

Table 2 Applications of nanocomposite materials in pharmaceuticals

Sr. No.	Nanocomposite	Drug development key material	Drug delivery system	Applications	References
1	Amorphous ternary cyclodextrin nanocomposite	Telmisartan	Oral drug delivery system	Improved solubility and reduced pharmacokinetic variability	[71]
2	Silica-based nanocomposites	Al ₂ O ₃ -SiC nanocomposite	Topical drug delivery system	Crack healing and stress relaxation	[72]
3	Inhalable magnetic nanocomposite microparticles	Iron oxide MNPs and D-mannitol	Targeted pulmonary delivery	Inhalation aerosol treatment of lung cancer via targeted hyperthermia	[73]
4	Montmorillonite (M ₁) based PLGA nanocomposites	Venlafaxine hydrochloride	Controlled drug delivery	Effective for the oral extended drug delivery, oral and controlled release carrier for an antidepressant drug	[21]
5	Calcium phosphate nanocomposites	Cisplatin	Controlled drug delivery	Controlled drug release carriers for chemotherapy of cancers, improvement of Anticancer Activity	[66]
6	Hydroxyapatite–chitosan nanocomposite	Celecoxib	Colon targeted drug delivery	Safe vehicle for celecoxib delivery in colon cancer chemotherapy	[74]
7	Hydroxyapatite nanocomposite	Amoxicillin	Sustained release drug delivery	Treatment of bone infection	[54]
8	Polymer nanocomposite	Atorvastatin calcium	Oral drug delivery system	Solubility enhancement of atorvastatin	[75]
9	Hyaluronic acid-based nanocomposite hydrogels	Latanoprost	Ocular drug delivery system	Reducing ocular hypertension by sustained release of latanoprost	[76]
10	Montmorillonite–alginate nanocomposite	Irinotecan	Sustained drug delivery system	Sustained delivery of irinotecan an antineoplastic drug	[77]
11	Chitosan/organic rectorite nanocomposite	Bovine serum albumin	Transdermal drug delivery system	Bactericidal activity of bovine albumin serum	[78]
12	SiO ₂ -layered double hydroxide nanocomposites	Methotrexate (MTX)	Non-viral delivery carrier for in vivo drug and gene delivery	Inhibition of human osteosarcoma cell (U2OS) growth	[67]
13	Montmorillonite/insulin/TiO ₂ hybrid nanocomposite	Insulin	Oral drug delivery system	Oral delivery of insulin	[79]

Table 2 (continued)

Sr. No.	Nanocomposite	Drug development key material	Drug delivery system	Applications	References
14	Sodium alginate/chitosan/hydroxyapatite (SA/CS/HAP) nanocomposite hydrogel	Doxorubicin (DOX)	Oral drug delivery system	Anticancer activity for liver cancer	[80]
15	Chitosan-based nanocomposite films	Metformin	Controlled drug delivery system	Improved hydrophilicity, hydrolytic stability, biocompatibility, mechanical and drug release properties	[81]
16	CS/LBG nanocomposites system	Acetoclofenac	Oral drug delivery	For delivery of acetoclofenac	[68]
17	Graphene oxide/carboxymethyl cellulose nanocomposites	Doxorubicin	Targeted drug delivery system	For controlled release of anticancer drug doxorubicin (DOX)	[69]
18	Lactoferrin-modified graphene oxide iron oxide nanocomposites	Doxorubicin	Targeted drug delivery system	Targeted delivery of doxorubicin in treatment [of glioma	[82]
19	Hollow Fe ₃ O ₄ /graphene oxide nanocomposites	Rapamycin	Targeted drug delivery system	Targeted delivery of rapamycin for prolonged drug release in anticancer therapies	[83]
20	Curcumin-loaded PMMA-PEG/ZnO nanocomposites	Curcumin	Targeted drug delivery	Induce the apoptosis of cancer cells and raises its probability to cure gastric cancer cells	[84]
21	Mesoporous silica/apatite nanocomposite	Atenolol	Controlled local drug delivery	Prevent the rapid release of atenolol during assays	[85]
22	Chitosan/polyacrylic acid/Fe ₃ O ₄ magnetic nanocomposite hydrogel (CS/PAA/Fe ₃ O ₄)	5-fluorouracil (5-FU)	Anticancer drug delivery system	Enhancement in the stability of drug dosing for a long time with controlled release in colon and rectal condition, in DDS as a colon and rectal administration of 5-FU	[86]

Table 2 (continued)

Sr. No.	Nanocomposite	Drug development key material	Drug delivery system	Applications	References
23	Thermo-sensitive poly(<i>N</i> -isopropylacrylamide)/Mesoporous silica nanocomposites	Ibuprofen	Controlled drug delivery system	Loading and release behaviour for drug ibuprofen	[87]
24	Tyrosine-derived polycarbonatesilica xerogel nanocomposites	Rifampicin and bupivacaine	Controlled drug delivery system	Controlled drug delivery of rifampicin and bupivacaine and also attractive biomaterials for applications such as wound dressings, tissue engineering substrates and stents	[88]
25	Micellar nanocomposites hydrogels thin films	Ciprofloxacin hydrochloride (CPX)	Vaginal drug delivery system	Improved antibiotic drug loading and for controlled drug delivery in the infected vaginal pH condition	[89]
26	Montmorillonite-based polyacrylamide nanocomposite hydrogel rings	Methylene blue	Controlled vaginal drug delivery system	Antibacterial applications (efficiently inhibit the growth of <i>E. coli</i>)	[90]
27	Acrylic acid/polyethylene glycol)-zinc oxide mucoadhesive nanocomposites	Propranolol HCl	Buccal drug delivery system	For buccal administration propranolol HCl and they could also be used as mucoadhesive carrier for buccal drug delivery with efficient antibacterial properties	[91]
28	Chitosan-magnesium aluminium silicate nanocomposite films	Nicotine	Buccal drug delivery system	For buccal delivery of nicotine	[92]
29	Lecithin and PLGA-based self-assembled nanocomposite	Daurorubicin (DNR) and lornoxicam (LNX)	Parenteral and oral drug delivery system	Parenteral and oral drug delivery of DNR and LNX in anticancer and anti-inflammatory activity	[70]

Table 3 Critical findings in the development of nanocomposite materials

Sr. No.	Drug	Dosage form	Experimental model	Comments	References
1	Tacrolimus-loaded PLGA nanoparticles	Eye drop	Excised rabbit corneas	The drug concentration was able to be maintained in cornea and conjunctiva for 24 H The uptake of tacrolimus was increased in trans-corneal area The enhancement in $T_{1/2}$ values was observed as compared to conventional dosage form. (1.77 folds) More than twofold enhancement was observed in AUC0-inf, AUMCO-inf and MRT0-inf as detected in aqueous humour	[93]
2	Polymeric PLGA nanoparticles (NPs) of dexibuprofen	Eye drops	In vitro and in vivo ocular irritation assay on chorioallantoic membrane and in rabbits, respectively Ex vivo ocular permeation study in rabbits	Enhancement in interaction between dexibuprofen-NPs and customized corneal membrane was facilitated by PEG Fast release of drug was observed for first 150 min, followed by sustained release	[94]
3	PLGA-NPs of flurbiprofen	Eye drop	Rabbit ocular surface inflammation model	Entrapment efficiency was high Storage stability of 6 months was observed No irritation was observed on ocular tissues Controlled & continuous delivery with excellent anti-inflammatory potential was observed	[95]
4	Proglycosomes modified Liposomal tacrolimus	Eye drop	Ex vivo goat eyes for Trans-corneal permeation study; rabbits for precorneal retention study	Fivefold & 13-fold enhancement in corneal permeation when compared to conventional liposomes	[96]

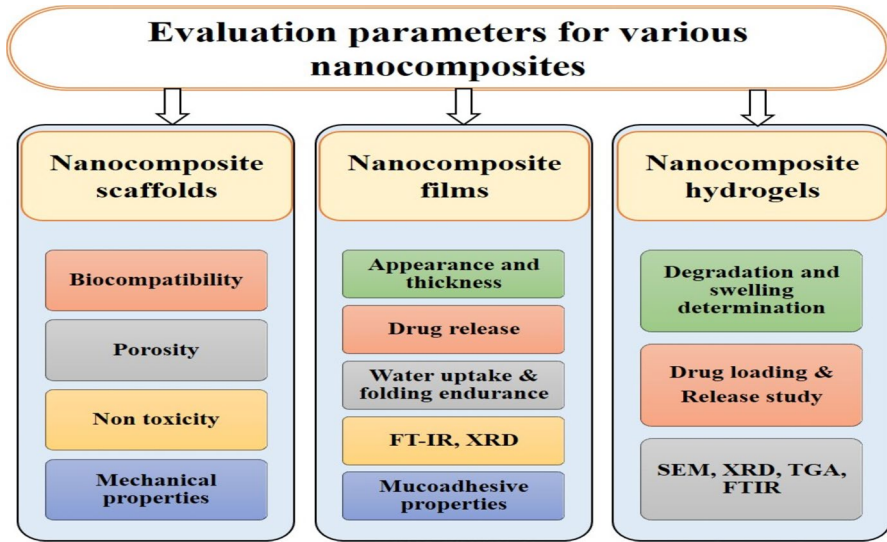


Fig. 3 Various evaluation parameters for nanocomposite materials

development of drug delivery systems with better therapeutic benefit and ease of convenience to the patients. Different carrier systems are useful for the delivery of drugs to the site of action, but nanocarriers systems have attracted due to their particle size, shape, strength and huge surface area.

Table 4 Some critical findings of nanocomposite materials with applications

Sr. No.	Nanocomposite	Critical findings	References
<i>Role of nanocomposite as bioimaging</i>			
1	Silica–cyanine hybrid nanoparticles	Accumulates in the liver after intravenous injection Long retention in tumour after intra-tumour injection High sensitivity, sufficient tissue penetration and high spatial resolution Nearly no cytotoxicity excellent photo-properties	[97]
2	Graphene quantum dot cross-linked carboxymethyl cellulose nanocomposite hydrogel	pH-sensitive swelling and degradation with improved tensile strength Exhibited biocompatibility pH-triggered site-specific & sustained drug delivery system Unique photoluminescent properties suitable for bioimaging applications	[98]
3	Oleyl chitosan, conjugated with folic acid and loaded with quercetin	Contrast agent for MRI & CT scan Preferential activity is observed against Malignant cells Non-hemolytic Biocompatible It functions as dual modality contrast agent for both MRI & CT	[99]
4	AgInZnS–graphene oxide Nanocomposites	Biocompatibility and photostability Exhibited bright and stable photoluminescence Photoluminescence can be tuned based on controlling composition of Zn Potential Bioimage application	[100]
5	Multifunctional mesoporous silica nanocomposite	Carboxyl functionalization made the drug delivery pH dependant Folate functionalization facilitated cellular uptake Water dispersibility was enhanced by PEG Near-infrared fluorescent dye Cy5 made the system effective for bioimaging in live cell	[101]
6	Polymer nanocomposite film made up of calcium oxalate and thionine	Droplet microfluidic approach for intracellular imaging of ascorbic acid in living cells Provides a robust method and ideal platform to study single-cell Promising tool for molecular biology assays in clinical assessment Fast detection & imaging	[102]

Table 4 (continued)

Sr. No.	Nanocomposite	Critical findings	References
<i>Role of nanocomposite in gene delivery</i>			
1	Core-shell polymeric-inorganic hybrid nanocomposite system made up of super paramagnetic iron oxide, polyethylene imine,	<p>Effective platform for MRI-visible gene delivery</p> <p>Effective in MC.DNA-based transfection in HEK293T cells and showed little cytotoxicity</p> <p>Enhanced imaging sensitivity due to high T2 relaxation</p> <p>Transfected cells could be detected by 1.5 T MRI</p> <p>Transfected cell proved to be cell factory for gene product</p>	[103]
2	Core-shell nanosystem consisting of zinc oxide (ZnO) nanocore and a polydopamine (PDA) shell was constructed to integrate chemo- (doxorubicin), gene-(DNAzyme, DZ) and photothermal (PDA layer)	<p>Enhanced anti-tumour efficacy</p> <p>Reduced the side effects of doxorubicin in heart and liver</p> <p>Strategy for synergistic cancer therapy via chemo/gene/photothermal combination</p> <p>ZnO nanocore was designed as a metal cofactor reservoir to release Zn^{2+} in response to intracellular stimuli, which triggered the activation of DZ</p> <p>Strategy to harness DZ as a gene-silencing tool</p> <p>PDA shell could detoxify the ZnO</p>	[104]
3	Aminotetrazole-functionalized magnetic chitosan nanocomposite	Cytotoxicity of N-amino functionalized composite was 35% lower	[105]
4	Cationic magnetic nanocomposites (MNCs) comprising branched poly-ethyleneimine (PEI)-coated iron oxide nanoparticles (IONPs)	<p>Transfection was enhanced by threefold</p> <p>Enhancement of gene expression in the HECK-293 T cell line</p> <p>Biocompatible and biodegradable nanocarrier to cancer cells</p> <p>Excellent DNA condensation and high Transfection efficiencies</p> <p>high stability, targeted gene transfection, control release</p> <p>Ability to penetrate the negatively charged cell wall for the delivery of miR-34a molecules into cancerous cells</p> <p>Transfection efficiency was enhanced through a magnetic field that enabled a very rapid concentration of the completely delivered vector dose onto cells</p> <p>Increased amplification of miR-34a led to the suppression of the MYCN protein</p> <p>Decreased toxicity</p>	[106]

Table 4 (continued)

Sr. No.	Nanocomposite	Critical findings	References
5	Mannose-conjugated layered double hydroxide nanocomposite	<p>More efficient uptake of siRNA by osteosarcoma (U2OS) via receptor-mediated internalization</p> <p>Significantly inhibited U2OS cell growth</p> <p>2D nanoparticles may provide the more efficient internalization by the cells due to their sheet-like morphology</p> <p>Enhanced permeability and retention (EPR) effect</p> <p>Lectin receptor-mediated endocytosis and significantly suppress the cell growth</p> <p>It reveals that mannose-modified LDH is a promising candidate for effective target siRNA/drug delivery for cancer</p>	[107]

Acknowledgements Authors are very thankful to Principal, Rajarshi Shahu College of Pharmacy, Buldana, for providing the library facility for through literature survey. Also, authors are grateful to language editing services by Palladium Documentation, Chennai, India.

Funding This review article is not funded by any funding agency.

Code availability No software application was used in the review article.

Declarations

Conflict of interest Authors declare no financial conflict of interest.

Ethical approval No animal or human volunteers are used.

References

- Mitra SB (2018) Nanoparticles for dental materials: synthesis, analysis, and applications. Emerging nanotechnologies in dentistry, 2nd edn. Elsevier Inc., pp 17–39
- He X, Deng H, Hwang HM (2019) The current application of nanotechnology in food and agriculture. *J Food Drug Anal* 27:1–21. <https://doi.org/10.1016/j.jfda.2018.12.002>
- Calipinar H, Ulas D (2019) Development of nanotechnology in the world and nanotechnology standards in Turkey. *Procedia Comput Sci* 158:1011–1018. <https://doi.org/10.1016/j.procs.2019.09.142>
- Komarneni S (2005) Nanocomposite materials. In: Chemical processing of ceramics, 2nd edn., pp 341–368
- Ouarhim W, Hassani FZSA, Qaiss AEK, Bouhfid R (2019) Rheology of polymer nanocomposites. Rheology of polymer blends and nanocomposites: theory, modelling and applications. Elsevier Inc., pp 73–96
- Jaiswal L, Shankar S, Rhim JW (2019) Applications of nanotechnology in food microbiology. *Methods in microbiology*, 1st edn. Elsevier Ltd., pp 43–60
- Okpala CC (2013) Nanocomposites: an overview. *Int J Eng Res Dev* 8:17–23
- Twardowski T (2007) Introduction to nanocomposite materials : properties, processing, characterization. DEStech Publications, Lancaster
- Parhi R (2018) Nanocomposite for transdermal drug delivery. Applications of nanocomposite materials in drug delivery. Elsevier Inc., pp 353–389
- Omanovi E, Badnjevi A, Kazlagi A, Hajlovac M (2019) Nanocomposites : a brief review. *J Heal Technol*. <https://doi.org/10.1007/s12553-019-00380-x>
- Camargo PHC, Satyanarayana KG, Wypych F (2009) Nanocomposites: synthesis, structure, properties and new application opportunities. *Mater Res* 12:1–39. <https://doi.org/10.1590/S1516-14392009000100002>
- Kaurav H, Manchanda S, Dua K, Kapoor DN (2018) Nanocomposites in controlled & targeted drug delivery systems. *Nano Hybrids Compos* 20:27–45. <https://doi.org/10.4028/www.scientific.net/nhc.20.27>
- Shanbhag PP, Rane D, Chandra R, Lande S, Deshmukh P, Prerna Patil TG (2019) Nanocomposites: a newer technology in drug delivery systems. *Int J Pharm Sci Rev Res* 56:144–154
- Avella M, Errico ME, Martelli S, Martuscelli E (2001) Preparation methodologies of polymer matrix nanocomposites. *Appl Organomet Chem* 15:435–439. <https://doi.org/10.1002/aoc.168>
- Swathi SKR, Krishna KR (2018) A review on types of nanocomposites and their applications. *Int J Adv Res* 4:235–236
- Khan WS, Hamadneh NN, Khan WA (2016) Polymer nanocomposites: synthesis techniques, classification and properties Waseem. In: Science and applications of tailored nanostructures. pp 50–67

17. Saboori A, Dadkhah M, Fino P, Pavese M (2018) An overview of metal matrix nanocomposites reinforced with graphene nanoplatelets; mechanical, electrical and thermophysical properties. *Metals (Basel)* 8:1–33. <https://doi.org/10.3390/met8060423>
18. Zanetti M, Lomakin S, Camino G (2000) Polymer layered silicate nanocomposites: a review. *Macromol Mater Eng* 279:1–9. <https://doi.org/10.3390/ma2030992>
19. Król-Morkisz K, Pieliuchowska K (2018) Thermal decomposition of polymer nanocomposites with functionalized nanoparticles. *Polymer composites with functionalized nanoparticles: synthesis, properties, and applications*. Elsevier Inc., pp 405–435
20. Kevadiya BD, Joshi GV, Bajaj HC (2010) Layered bionanocomposites as carrier for procainamide. *Int J Pharm* 388:280–286. <https://doi.org/10.1016/j.ijpharm.2010.01.002>
21. Jain S, Datta M (2014) Montmorillonite-PLGA nanocomposites as an oral extended drug delivery vehicle for venlafaxine hydrochloride. *Appl Clay Sci* 99:42–47. <https://doi.org/10.1016/j.clay.2014.06.006>
22. Saifuddin N, Raziah AZ, Junzah AR (2013) Carbon nanotubes: a review on structure and their interaction with proteins. *J Chem* 2013:1–18. <https://doi.org/10.1155/2013/676815>
23. Justin R, Chen B (2014) Strong and conductive chitosan-reduced graphene oxide nanocomposites for transdermal drug delivery. *J Mater Chem B* 2:3759–3770. <https://doi.org/10.1039/c4tb00390j>
24. Rhim JW, Ng PKW (2007) Natural biopolymer-based nanocomposite films for packaging applications. *Crit Rev Food Sci Nutr* 47:411–433. <https://doi.org/10.1080/10408390600846366>
25. Othman SH (2014) Bio-nanocomposite materials for food packaging applications: types of biopolymer and nano-sized filler. *Agric Agric Sci Procedia* 2:296–303. <https://doi.org/10.1016/j.aaspro.2014.11.042>
26. Dufresne A (2009) Starch-based nanocomposites. pp 1–288
27. Cao X, Chen Y, Chang PR et al (2008) Starch-based nanocomposites reinforced with flax cellulose nanocrystals. *Express Polym Lett* 2:502–510. <https://doi.org/10.3144/expresspolymlett.2008.60>
28. Kalambur SB, Rizvi SS (2004) Starch-based nanocomposites by reactive extrusion processing. *Polym Int* 53:1413–1416. <https://doi.org/10.1002/pi.1478>
29. Kalia S, Dufresne A, Cherian BM et al (2011) Cellulose-based bio- and nanocomposites: a review. *Int J Polym Sci* 2011:1–35. <https://doi.org/10.1155/2011/837875>
30. Mansa R, Detellier C (2013) Preparation and characterization of guar-montmorillonite nanocomposites. *Materials (Basel)* 6:5199–5216. <https://doi.org/10.3390/ma6115199>
31. Palem RR, Shimoga G, Rao KSVK et al (2020) Guar gum graft polymer-based silver nanocomposite hydrogels: synthesis, characterization and its biomedical applications. *J Polym Res*. <https://doi.org/10.1007/s10965-020-2026-8>
32. Haraguchi K (2007) Nanocomposite hydrogels. *Curr Opin Solid State Mater Sci* 11:47–54. <https://doi.org/10.1016/j.cossms.2008.05.001>
33. Gaharwar AK, Peppas NA, Khademhosseini A (2014) Nanocomposite hydrogels for biomedical applications. *Biotechnol Bioeng* 111:441–453. <https://doi.org/10.1002/bit.25160>
34. Daniel S, Thomas S (2020) Layered double hydroxides: fundamentals to applications. *Layered double hydroxide polymer nanocomposites*. Elsevier Ltd, pp 1–76
35. Ravichandran K, Praseetha PK, Arun T, Gobalakrishnan S (2018) Synthesis of nanocomposites. *Synthesis of inorganic nanomaterials*. Elsevier Ltd., pp 141–168
36. Hári J, Pukánszky B (2011) Nanocomposites: preparation, structure, and properties. In: *Applied plastics engineering handbook*. Elsevier, pp 109–142
37. Morles RB, Marchetti M, Muraviev D, et al (2012) New trends and development. *J Colloid Interface Sci*. 1–16
38. Hajeessa KS, Hussein MA, Anwar Y et al (2018) Nanocomposites containing polyvinyl alcohol and reinforced carbon-based nanofiller: a super effective biologically active material. *Nanobiomedicine* 5:1–12. <https://doi.org/10.1177/1849543518794818>
39. Ghaffari-Moghaddam M, Eslahi H (2014) Synthesis, characterization and antibacterial properties of a novel nanocomposite based on polyaniline/polyvinyl alcohol/Ag. *Arab J Chem* 7:846–855. <https://doi.org/10.1016/j.arabjc.2013.11.011>
40. Gilbert M (2012) Poly(vinyl chloride)(PVC)-based nanocomposites. *Advances in polymer nanocomposites: types and applications*. Woodhead Publishing Limited, pp 216–237
41. Gholami A, Moghadassi AR, Hosseini SM et al (2014) Preparation and characterization of polyvinyl chloride based nanocomposite nanofiltration-membrane modified by iron oxide nanoparticles for lead removal from water. *J Ind Eng Chem* 20:1517–1522. <https://doi.org/10.1016/j.jiec.2013.07.041>

42. Kausar A (2018) Review on polymer/halloysite nanotube nanocomposite. *Polym Plast Technol Eng* 57:548–564. <https://doi.org/10.1080/03602559.2017.1329436>
43. Narayanan BN, Koodathil R, Gangadharan T et al (2010) Preparation and characterization of exfoliated polyaniline/montmorillonite nanocomposites. *Mater Sci Eng B Solid-State Mater Adv Technol* 168:242–244. <https://doi.org/10.1016/j.mseb.2009.12.027>
44. Xia B, Wang B, Shi J et al (2017) Photothermal and biodegradable polyaniline/porous silicon hybrid nanocomposites as drug carriers for combined chemo-photothermal therapy of cancer. *Acta Biomater* 51:197–208. <https://doi.org/10.1016/j.actbio.2017.01.015>
45. Larsson M, Bergstrand A, Mesiah L et al (2014) Nanocomposites of polyacrylic acid nanogels and biodegradable polyhydroxybutyrate for bone regeneration and drug delivery. *J Nanomater* 2014:9–11. <https://doi.org/10.1155/2014/371307>
46. Yassue-Cordeiro PH, Severino P, Souto EB et al (2018) Chitosan-based nanocomposites for drug delivery. Applications of nanocomposite materials in drug delivery. Elsevier Inc., pp 1–26
47. Ali A, Ahmed S (2018) A review on chitosan and its nanocomposites in drug delivery. *Int J Biol Macromol* 109:273–286. <https://doi.org/10.1016/j.ijbiomac.2017.12.078>
48. Ahmad M, Manzoor K, Ikram S (2018) Chitosan based nanocomposites for drug, gene delivery, and bioimaging applications. Applications of nanocomposite materials in drug delivery. Elsevier Inc., pp 27–38
49. Paravastu VKK, Yarraguntla SR, Suvvari A (2019) Role of nanocomposites in drug delivery. *GSC Biol Pharm Sci* 8:094–103. <https://doi.org/10.30574/gscbps.2019.8.3.0150>
50. Kotal M, Bhowmick AK (2015) Polymer nanocomposites from modified clays: recent advances and challenges. *Prog Polym Sci* 51:127–187. <https://doi.org/10.1016/j.progpolymsci.2015.10.001>
51. Kumaresan S, Pawar RR, Kevadiya BD, Bajaj HC (2019) Synthesis of saponite based nanocomposites to improve the controlled oral drug release of model drug quinine hydrochloride dihydrate. *Pharmaceuticals* 12:1–13. <https://doi.org/10.3390/ph12030105>
52. Moura D, Mano JF, Paiva MC, Alves NM (2016) Chitosan nanocomposites based on distinct inorganic fillers for biomedical applications. *Sci Technol Adv Mater* 17:626–643. <https://doi.org/10.1080/14686996.2016.1229104>
53. Lei H, Xie M, Zhao Y et al (2016) Chitosan/sodium alginate modified graphene oxide-based nanocomposite as a carrier for drug delivery. *Ceram Int* 42:17798–17805. <https://doi.org/10.1016/j.ceramint.2016.08.108>
54. Prasanna APS, Venkatasubbu GD (2018) Sustained release of amoxicillin from hydroxyapatite nanocomposite for bone infections. *Prog Biomater* 7:289–296. <https://doi.org/10.1007/s40204-018-0103-4>
55. Kalubowilage M, Janik K, Bossmann SH (2019) Magnetic nanomaterials for magnetically-aided drug delivery and hyperthermia. *Appl Sci* 9:2927. <https://doi.org/10.3390/app9142927>
56. Barahuie F, Dorniani D, Saifullah B et al (2017) Sustained release of anticancer agent phytic acid from its chitosan-coated magnetic nanoparticles for drug-delivery system. *Int J Nanomed* 12:2361–2372. <https://doi.org/10.2147/IJN.S126245>
57. Yu CY, Yin BC, Zhang W et al (2009) Composite microparticle drug delivery systems based on chitosan, alginate and pectin with improved pH-sensitive drug release property. *Colloids Surf B Biointerfaces* 68:245–249. <https://doi.org/10.1016/j.colsurfb.2008.10.013>
58. Rajan M, Murugan M, Ponnamma D et al (2016) Poly-carboxylic acids functionalized chitosan nanocarriers for controlled and targeted anti-cancer drug delivery. *Biomed Pharmacother* 83:201–211. <https://doi.org/10.1016/j.biopha.2016.06.026>
59. Caseri WR (2006) Nanocomposites of polymers and inorganic particles: preparation, structure and properties. *Mater Sci Technol* 22:807–817. <https://doi.org/10.1179/174328406X101256>
60. Keledi G, Hári J, Pukánszky B (2012) Polymer nanocomposites: structure, interaction, and functionality. *Nanoscale* 4:1919–1938. <https://doi.org/10.1039/c2nr11442a>
61. Tjong SC (2006) Structural and mechanical properties of polymer nanocomposites. *Mater Sci Eng R Rep* 53:73–197. <https://doi.org/10.1016/j.mser.2006.06.001>
62. Kumar SK, Krishnamoorti R (2010) Nanocomposites: structure, phase behavior, and properties. *Annu Rev Chem Biomol Eng* 1:37–58. <https://doi.org/10.1146/annurev-chembioeng-073009-100856>
63. Shi X, Gan Z (2007) Preparation and characterization of poly(propylene carbonate)/montmorillonite nanocomposites by solution intercalation. *Eur Polym J* 43:4852–4858. <https://doi.org/10.1016/j.eurpolymj.2007.09.024>

64. Pathania D, Gupta D, Kothiyal NC et al (2016) Preparation of a novel chitosan-g-poly(acrylamide)/Zn nanocomposite hydrogel and its applications for controlled drug delivery of ofloxacin. *Int J Biol Macromol* 84:340–348. <https://doi.org/10.1016/j.ijbiomac.2015.12.041>
65. Zhu L, Wang D, Wei X et al (2013) Multifunctional pH-sensitive superparamagnetic iron-oxide nanocomposites for targeted drug delivery and MR imaging. *J Control Release* 169:228–238. <https://doi.org/10.1016/j.jconrel.2013.02.015>
66. Dan Son K, Kim YJ (2017) Anticancer activity of drug-loaded calcium phosphate nanocomposites against human osteosarcoma. *Biomater Res* 21:1–8. <https://doi.org/10.1186/s40824-017-0099-1>
67. Li L, Gu Z, Gu W et al (2016) Efficient drug delivery using SiO₂-layered double hydroxide nanocomposites. *J Colloid Interface Sci* 470:47–55. <https://doi.org/10.1016/j.jcis.2016.02.042>
68. Rasoulzadeh M, Namazi H (2017) Carboxymethyl cellulose/graphene oxide bio-nanocomposite hydrogel beads as anticancer drug carrier agent. *Carbohydr Polym* 168:320–326. <https://doi.org/10.1016/j.carbpol.2017.03.014>
69. Jana S, Sen KK (2017) Chitosan—Locust bean gum interpenetrating polymeric network nanocomposites for delivery of aceclofenac. *Int J Biol Macromol* 102:878–884. <https://doi.org/10.1016/j.ijbiomac.2017.04.097>
70. Varghese SE, Fariya MK, Rajawat GS et al (2016) Lecithin and PLGA-based self-assembled nanocomposite, Lecithmer: preparation, characterization, and pharmacokinetic/pharmacodynamic evaluation. *Drug Deliv Transl Res* 6:342–353. <https://doi.org/10.1007/s13346-016-0314-y>
71. Sangwai M, Vavia P (2013) Amorphous ternary cyclodextrin nanocomposites of telmisartan for oral drug delivery: improved solubility and reduced pharmacokinetic variability. *Int J Pharm* 453:423–432. <https://doi.org/10.1016/j.ijpharm.2012.08.034>
72. Thompson AM, Chan HM, Harmer MP, Cook RE (1995) Crack healing and stress relaxation in Al₂O₃ SiC “nanocomposites.” *J Am Ceram Soc* 78:567–571
73. Stocke NA, Meenach SA, Arnold SM et al (2015) Formulation and characterization of inhalable magnetic nanocomposite microparticles (MnMs) for targeted pulmonary delivery via spray drying. *Int J Pharm* 479:320–328. <https://doi.org/10.1016/j.ijpharm.2014.12.050>
74. Venkatesan P, Puvvada N, Dash R et al (2011) The potential of celecoxib-loaded hydroxyapatite-chitosan nanocomposite for the treatment of colon cancer. *Biomaterials* 32:3794–3806. <https://doi.org/10.1016/j.biomaterials.2011.01.027>
75. Sonawane DD, Jat RK, Pawar AY, Jhabarmal SJ (2019) Formulation & development of nanocomposites for solubility enhancement of BCS Class II model drug using microwave induced diffusion technique. *Res Rev Int J Multidiscip* 3085:502–512
76. Widjaja LK, Bora M, Chan PNP et al (2014) Hyaluronic acid-based nanocomposite hydrogels for ocular drug delivery applications. *J Biomed Mater Res Part A* 102:3056–3065. <https://doi.org/10.1002/jbm.a.34976>
77. Iliescu RI, Andronescu E, Ghitulica CD et al (2014) Montmorillonite-alginate nanocomposite as a drug delivery system—incorporation and in vitro release of irinotecan. *Int J Pharm* 463:184–192. <https://doi.org/10.1016/j.ijpharm.2013.08.043>
78. Wang X, Du Y, Luo J et al (2007) Chitosan/organic rectorite nanocomposite films: structure, characteristic and drug delivery behaviour. *Carbohydr Polym* 69:41–49. <https://doi.org/10.1016/j.carbpol.2006.08.025>
79. Kamari Y, Ghiaci P, Ghiaci M (2017) Study on montmorillonite/insulin/TiO₂ hybrid nanocomposite as a new oral drug-delivery system. *Mater Sci Eng C* 75:822–828. <https://doi.org/10.1016/j.msec.2017.02.115>
80. Abou Taleb MF, Alkahtani A, Mohamed SK (2015) Radiation synthesis and characterization of sodium alginate/chitosan/hydroxyapatite nanocomposite hydrogels: a drug delivery system for liver cancer. *Polym Bull* 72:725–742. <https://doi.org/10.1007/s00289-015-1301-z>
81. Shariatinia Z, Zahraee Z (2017) Controlled release of metformin from chitosan-based nanocomposite films containing mesoporous MCM-41 nanoparticles as novel drug delivery systems. *J Colloid Interface Sci* 501:60–76. <https://doi.org/10.1016/j.jcis.2017.04.036>
82. Song MM, Xu HL, Liang JX et al (2017) Lactoferrin modified graphene oxide iron oxide nanocomposite for glioma-targeted drug delivery. *Mater Sci Eng C* 77:904–911. <https://doi.org/10.1016/j.msec.2017.03.309>

83. Cao L, Jiang Y, Chen Z (2017) Hollow Fe₃O₄/graphene oxide nanocomposites as novel rapamycin carrier: formulation optimization and in vitro characterization. *J Nanosci Nanotechnol* 18:3067–3076. <https://doi.org/10.1166/jnn.2018.14674>
84. Dhivya R, Ranjani J, Bowen PK et al (2017) Biocompatible curcumin loaded PMMA-PEG/ZnO nanocomposite induce apoptosis and cytotoxicity in human gastric cancer cells. *Mater Sci Eng C* 80:59–68. <https://doi.org/10.1016/j.msec.2017.05.128>
85. Sousa A, Souza KC, Sousa EMB (2008) Mesoporous silica/apatite nanocomposite: special synthesis route to control local drug delivery. *Acta Biomater* 4:671–679. <https://doi.org/10.1016/j.actbio.2007.11.003>
86. Amini-Fazl MS, Mohammadi R, Kheiri K (2019) 5-Fluorouracil loaded chitosan/polyacrylic acid/Fe₃O₄ magnetic nanocomposite hydrogel as a potential anticancer drug delivery system. *Int J Biol Macromol* 132:506–513. <https://doi.org/10.1016/j.ijbiomac.2019.04.005>
87. Tian BS, Yang C (2011) Thermo-sensitive poly(N-isopropylacrylamide)/mesoporous silica nanocomposites as controlled delivery carriers: loading and release behaviors for drug ibuprofen. *J Nanosci Nanotechnol* 11:1871–1879. <https://doi.org/10.1166/jnn.2011.3543>
88. Costache MC, Vaughan AD, Qu H et al (2013) Tyrosine-derived polycarbonate-silica xerogel nanocomposites for controlled drug delivery. *Acta Biomater* 9:6544–6552. <https://doi.org/10.1016/j.actbio.2013.01.034>
89. Adnan M, Santhosh Kumar K, Sreejith L (2020) Micellar nanocomposites hydrogels films for pH sensitive controlled drug delivery. *Mater Lett* 277:128286. <https://doi.org/10.1016/j.matlet.2020.128286>
90. Sharifzadeh G, Hezaveh H, Muhamad II et al (2020) Montmorillonite-based polyacrylamide hydrogel rings for controlled vaginal drug delivery. *Mater Sci Eng C* 110:110609. <https://doi.org/10.1016/j.msec.2019.110609>
91. Mahmoud GA, Ali AEH, Raafat AI et al (2018) Development of (acrylic acid/ polyethylene glycol)-zinc oxide mucoadhesive nanocomposites for buccal administration of propranolol HCl. *Radiat Phys Chem* 147:18–26. <https://doi.org/10.1016/j.radphyschem.2018.01.020>
92. Pongjanyakul T, Khunawattanakul W, Strachan CJ et al (2013) Characterization of chitosan-magnesium aluminum silicate nanocomposite films for buccal delivery of nicotine. *Int J Biol Macromol* 55:24–31. <https://doi.org/10.1016/j.ijbiomac.2012.12.043>
93. Kalam MA, Alshamsan A (2017) Poly (D, L-lactide-co-glycolide) nanoparticles for sustained release of tacrolimus in rabbit eyes. *Biomed Pharmacother* 94:402–411. <https://doi.org/10.1016/j.biopha.2017.07.110>
94. Sánchez-López E, Esteruelas G, Ortiz A et al (2020) Article dexibuprofen biodegradable nanoparticles: one step closer towards a better ocular interaction study. *Nanomaterials* 10:1–24. <https://doi.org/10.3390/nano10040720>
95. Vega E, Egea MA, Valls O, Espina M, García ML (2006) Flurbiprofen loaded biodegradable nanoparticles for ophthalmic administration. *J Pharm Sci* 95:2393–2405. <https://doi.org/10.1002/jps>
96. Garg V, Suri R, Jain GK, Kohli K (2017) Proglycosomes: A novel nano-vesicle for ocular delivery of tacrolimus. *Colloids Surf B Biointerfaces* 157:40–47. <https://doi.org/10.1016/j.colsurfb.2017.05.049>
97. Wu X, Chang S, Sun X, Guo Z, Li Y, Tang J, Shen Y, Shi J, Tian H, Zhu W (2015) Constructing NIR silica-cyanine hybrid nanocomposite for bioimaging in vivo: a breakthrough in photo-stability and bright fluorescence with large Stokes shift. *J Mater Chem C* 3:10715–10722. <https://doi.org/10.1039/b000000x>
98. Rakhshaei R, Namazi H, Hamishehkar H, Rahimi M (2020) Graphene quantum dot cross-linked carboxymethyl cellulose nanocomposite hydrogel for pH-sensitive oral anticancer drug delivery with potential bioimaging properties. *Int J Biol Macromol* 150:1121–1129. <https://doi.org/10.1016/j.ijbiomac.2019.10.118>
99. Hemalatha T, UmaMaheswari T, Anbukkarsi K, Ayyadurai N (2020) Imaging and anti-apoptotic potentials of oleyl chitosan coated quercetin nanocomposite: in vitro perspectives. *Mater Lett* 279:128496. <https://doi.org/10.1016/j.matlet.2020.128496>
100. Zang Z, Zeng X, Wang M et al (2017) Tunable photoluminescence of water-soluble AgInZnS-graphene oxide (GO) nanocomposites and their application in-vivo bioimaging. *Sens Actuators B Chem* 252:1179–1186. <https://doi.org/10.1016/j.snb.2017.07.144>

101. Xie M, Shi H, Li Z et al (2013) A multifunctional mesoporous silica nanocomposite for targeted delivery, controlled release of doxorubicin and bioimaging. *Colloids Surf B Biointerfaces* 110:138–147. <https://doi.org/10.1016/j.colsurfb.2013.04.009>
102. Alizadeh N, Ghasemi F, Salimi A et al (2020) Polymer nanocomposite film for dual colorimetric and fluorescent ascorbic acid detection integrated single-cell bioimaging with droplet microfluidic platform. *Dye Pigment* 173:107875. <https://doi.org/10.1016/j.dyepig.2019.107875>
103. Cai J, Chen G, Jin R et al (2019) A core-shell polymeric-inorganic hybrid nanocomposite system for MRI-visible gene delivery application in cancer immunotherapy. *J Ind Eng Chem* 76:188–196. <https://doi.org/10.1016/j.jiec.2019.03.039>
104. Liu M, Peng Y, Nie Y et al (2020) Co-delivery of doxorubicin and DNase using ZnO@polydopamine core-shell nanocomposites for chemo/gene/photothermal therapy. *Acta Biomater* 110:242–253. <https://doi.org/10.1016/j.actbio.2020.04.041>
105. Irvani Kashkouli K, Torkzadeh-Mahani M, Mosaddegh E (2018) Synthesis and characterization of aminotetrazole-functionalized magnetic chitosan nanocomposite as a novel nanocarrier for targeted gene delivery. *Mater Sci Eng C* 89:166–174. <https://doi.org/10.1016/j.msec.2018.03.032>
106. Mdlovu NV, Lin KS, Chen Y, Wu CM (2021) Formulation of magnetic nanocomposites for intracellular delivery of micro-RNA for MYCN inhibition in neuroblastoma. *Colloids Surf A Physicochem Eng Asp* 615:126264. <https://doi.org/10.1016/j.colsurfa.2021.126264>
107. Li L, Zhang R, Gu W, Xu ZP (2018) Mannose-conjugated layered double hydroxide nanocomposite for targeted siRNA delivery to enhance cancer therapy. *Nanomed Nanotechnol Biol Med* 14:2355–2364. <https://doi.org/10.1016/j.nano.2017.06.006>
108. Liu W, Webster TJ (2016) Toxicity and biocompatibility properties of nanocomposites for musculoskeletal tissue regeneration. *Nanocomposites for musculoskeletal tissue regeneration*. Elsevier Ltd, pp 95–122
109. De Cremer K, Braem A, Gerits E et al (2017) Controlled release of chlorhexidine from a mesoporous silica-containing macroporous titanium dental implant prevents microbial biofilm formation. *Eur Cells Mater* 33:13–27. <https://doi.org/10.22203/eCM.v033a02>
110. Yan H, Wang S, Han L et al (2018) Chlorhexidine-encapsulated mesoporous silica-modified dentin adhesive. *J Dent* 78:83–90. <https://doi.org/10.1016/j.jdent.2018.08.012>
111. Bukara K, Schueller L, Rosier J et al (2016) Ordered mesoporous silica to enhance the bioavailability of poorly water-soluble drugs: proof of concept in man. *Eur J Pharm Biopharm* 108:220–225. <https://doi.org/10.1016/j.ejpb.2016.08.020>

Publisher's Note Springer Nature remains neutral with regard to jurisdictional claims in published maps and institutional affiliations.

Authors and Affiliations

Prakash Namdeo Kendre²  · Mrinal Gite¹ · Shirish P. Jain² · Ajinkya Pote²

Mrinal Gite
mrinalgite1@gmail.com

Shirish P. Jain
principalrscp@gmail.com

Ajinkya Pote
ajinkyapote1996@gmail.com

¹ Department of Pharmaceutics, Rajarshi Shahu College of Pharmacy, Buldana, Maharashtra, India

² Rajarshi Shahu College of Pharmacy, Buldana, Maharashtra, India



Nanocomposite polymeric materials: state of the art in the development of biomedical drug delivery systems and devices

Prakash Namdeo Kendre² · Mrinal Gite¹ · Shirish P. Jain² · Ajinkya Pote²

Received: 21 September 2021 / Revised: 12 November 2021 / Accepted: 18 November 2021
© The Author(s), under exclusive licence to Springer-Verlag GmbH Germany, part of Springer Nature 2021

Abstract

Due to recent advancements in the field of science and technology, it becomes easier to synthesize and produce nanomaterials. These nanomaterials are now better choice to the researchers for the development of various products. Their use in the development of variety of products including biomedical devices and drug delivery systems has much attention to the researchers. Due to change in the physical properties at molecular level, it becomes easier to overcome the hurdles in the development of drug delivery systems with better therapeutic benefit and ease of convenience to the patients. Different carrier systems are useful for the delivery of drugs to the site of action, but nanocarriers systems have attracted due to their particle size, shape, strength and huge surface area. Among these carrier systems, nanocomposite polymeric materials have greater attention for their use in the development of various drug delivery and targeting devices. In many recent studies, their applications in the design of biomedical devices and bone tissue engineering are observed. In this review, the various types nanocomposite polymeric materials, their behaviour during synthesis, evaluation parameters and various applications with critical findings in the field of pharmaceuticals and biomedical sciences are discussed.

Keywords Nanocomposite · Nanomaterials · Biomedical applications · Targeted drug delivery

Introduction

Nanotechnology can be defined as the application of controlling the properties of the matter at the molecular level [1]. In everyday life, nanotechnology is now widely utilized science due to which our routine becomes much easier and

✉ Prakash Namdeo Kendre
prakashkendre@gmail.com

Extended author information available on the last page of the article

comfortable than use of conventional approaches [2]. Nanotechnology is the science which deals with the materials and particles which have at least one dimension in the range of 1–100 nm [3]. Nanocomposites: In recent years, there is huge development in nanotechnology through which the various problems related to drug development have been overcome from which one is the use of nanocomposite materials. Nanocomposites are a broad range of materials which consist of one or more phases embedded in metal, ceramic or polymer matrix at nanometre range [4]. As a material, nanocomposite has so many benefits in drug development and will show great changes in the industrial field [5]. Bansi D. Malhotra, Md Azahar Ali (2018) stated that if different structural units are utilized in individual regimen, then the term “Nanocomposites” is used [4]. According to Jaiswal L et.al. (2019) for creating new and innovative packaging materials, nanocomposites are represented as an inspiring route [6]. Most drugs have problems related with their poor solubility, stability and bioavailability which can be now solved by the use of nanocomposite materials.

Okpala CC. (2013) states that for the better properties of nanocomposites they not only depend on their interfacial characteristic but also depend on their individual parents and their morphology. Nanocomposite improves various properties such as mechanical properties like strength and dimensional stability, thermal stability, solubility, permeability, bioavailability in the drug development [7]. There are two different parts present in nanocomposites: one is continuous phase and another is discontinuous or reinforcing phase. Polymers, ceramic and metals are considered as the three different building blocks for the nanocomposites. Based on the continuous phase, each of these possesses specific properties which may add value in nanocomposites like polymers that provide the insulation, ductility, and also impact resistance, metals provides strangeness ductility and conductivity whereas ceramics provides properties like chemical resistance, brittleness and strangeness. Discontinuous phase includes the nanomaterials with different types which are also called nanofillers dispersed in the continuous phase [8, 9]. Nanocomposites include nanoparticles, nanoclay and nanofibers as nanomaterials to overcome the limitations regarding the microcomposites, and monolithic nanocomposites are represented as new alternative ways [10].

Materials with unique physicochemical characteristics are recently attracted for the development of many biomedical devices. Composite materials exhibiting nanometre scale have proven their applications in the development of implants, drug delivery systems and many engineered nanostructures. Their use in the biomedical field has been increased due to their comprehensive properties like, nanoscale, huge surface area mechanical strength, targeting ability, tissue engineering and biocompatible nature. Metal- and polymer-based nanocomposite materials have increasing demand in the development of biomedical devices, including surgical implants in prosthetic and orthopaedic applications.

This review provides insight on various types nanocomposite polymeric materials, their behaviour during synthesis, evaluation parameters and various applications with critical findings in the field of pharmaceuticals and biomedical sciences.

Advantages of nanocomposites

There are various advantages of nanocomposites over the other composites materials; they are as follows:

- Improved mechanical properties—greater ductility without any loss in strength, and resistance over scratch;
- Small size of fillers and distance between fillers allowed due to the high surface or volume ratio;
- Increased optical properties (as transmission of light and particle size is dependent on each other).

Disadvantages of nanocomposites

As nanocomposites are having various applications in various drug delivery systems, it also has some disadvantages; they are as follows:

- Toughness and impact performance related with the incorporation of nanoparticles to bulk matrix
- Cost effectiveness
- Lack of sufficient understanding between properties, formulation and structural relationship
- Component as well as, long-term stability and service, structural integrity, mechanical properties and corrosion properties, and uncertain cytotoxicity in tissue engineering.

Types of nanocomposites

On the basis of their type of matrix material, nanocomposites are classified into different categories as shown in Fig. 1 [11, 12].

Polymer matrix nanocomposites (PMNC)

In this type of nanocomposites, the polymer and nanoadditives are used as matrix material and reinforcement material, respectively. The additives used are 1D (nanotubes and fibres), 2D (layered materials like clay) or 3D (spherical particles), and due to the better mechanical properties with a small concentration of nanoadditives, they gained considerable attention in academics and as well as in industrial field [13]. Due to easy production, ductility and lower weight properties polymer matrix nanocomposites are widely used in the industries [14]. Properties of these nanocomposite depend on properties of individual component as well as various different parameters like process used in nanocomposite fabrication, degree of mixing of two phases, type of adhesion at the matrix interface, volume fraction of nanoparticles, characteristics of nanoparticles, nature of the

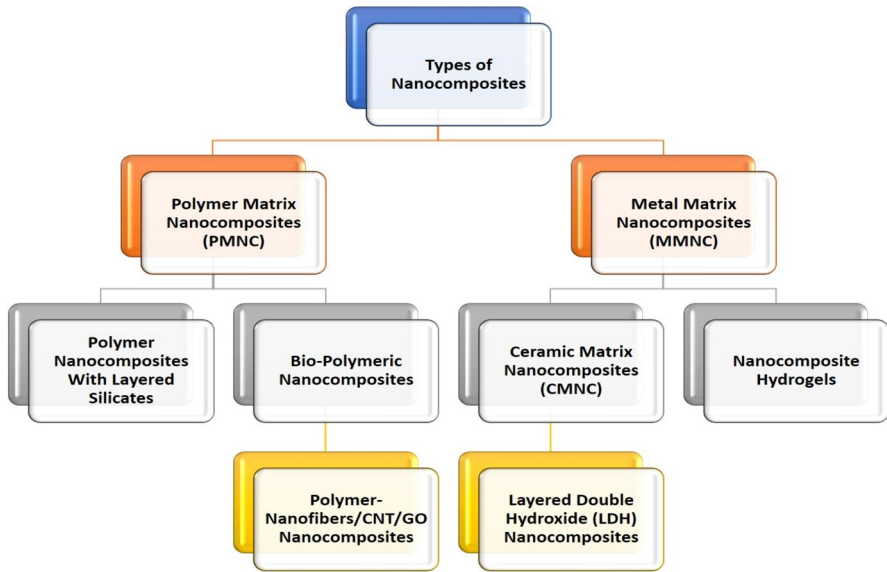


Fig. 1 Broad classification of nanocomposites

interphase developed at matrix interface, size and shape of nanofiller materials and system morphology [13]. The main factor to be considered in the polymeric matrix nanocomposites is the dispersion of the nanofillers in the bulk polymer matrix for resulting in improved properties with the homogeneous distribution of nanomaterials [14]. Examples of polymer matrix nanocomposites are thermo-plastic/thermoset polymer/layered silicates, polyester/ TiO_2 , polymer/CNT, polymer/layered double hydroxides [15].

Ceramic matrix nanocomposites (CMNC)

These are considered as a new generation of engineering materials having huge impact in the industrial application and these nanocomposites consist of one or more phases in the nanometre range. Ceramics are the solid materials in general that possess strong ionic bonding and covalent bonding in few of the cases [13]. For preparation of CMNCs, various methods such as conventional powder method; polymer precursor route; spray pyrolysis; vapour techniques (CVD and PVD) and chemical methods, which include the sol–gel process, colloidal and precipitation approaches and the template synthesis, are included in the many studies [11, 16]. Examples of ceramic matrix nanocomposites are $\text{Al}_2\text{O}_3/\text{SiO}_2$, SiO_2/Ni , $\text{Al}_2\text{O}_3/\text{TiO}_2$ and $\text{Al}_2\text{O}_3/\text{SiC}$. After the discovery of carbon nanotubes (CNT), they were used in the fabrication of nanocomposites. Some common examples of CNT-based ceramic matrix nanocomposite include $\text{Al}_2\text{O}_3/\text{CNT}$, $\text{MgAl}_2\text{O}_4/\text{CNT}$ and MgO/CNT [16].

Metal matrix nanocomposites (MMNC)

In recent years, metal matrix nanocomposites have taken a great area of interest in the various fields due to their special functional and structural applications. From the last two decades, there is considerable interest in the research area generated by the development of new materials [17]. Metal matrix nanocomposites consist of ductile metal/ matrix consisting of alloy and in which the nanosized reinforcement material is implanted [15]. There are various methods for the processing of MMNC such as spray pyrolysis, liquid metal infiltration, vapour technique, rapid solidification, electrode position and some of the chemical methods like colloidal and sol–gel method. Some common examples of metal matrix nanocomposites are Fe–Cr/Al₂O₃, Ni/Al₂O₃, Fe/MgO, Al/CNT and Mg/CNT [16].

Polymer nanocomposites with layered silicates

In this, the polymer incorporated with a low amount of layered silicate which is dispersed at nanoscale level is considered as most promising material which is characterized by physical, chemical and mechanical properties which cannot be obtained with micro- or macroscopic dispersion of inorganic fillers. This polymer layer silicate can be obtained by inserting the polymer molecules in the galleries between the layers of poly-silicate. Insertion of polymer molecules can be done to prepare the ‘intercalation hybrids’ replacing the water hydration molecules into the galleries bipolar functional group containing polymers using ion–dipole method [18]. There are two types of nanoplatelet particle composites: one is graphite and another is silicate clay minerals, and for the preparation of nanocomposites, some of the smectite type layered silicates like montmorillonite (MMT), saponite and hectorite are commonly used [12]. Among these smectite type layered silicate, the montmorillonite is considered as common and best studied clay having 2:1 layer structure which means that it consists of two tetrahedral silica layers which are separated by an octahedral alumina layer [19]. In pharmaceutical engineering, MMT is found to have very extensive applications such as stabilizing and suspending agent along with this it is also used as adsorbent and clarifying agent. Along with MMT, other clay species are also used as drug carrier in drug delivery and tissue regeneration agents for various compounds such as paclitaxel, procainamide, tamoxifen citrate, buspirone, timolol maleate, 5-fluorouracil and epidermal growth factor [20]. Jain S and Datta M (2014) prepared montmorillonite–PLGA nanocomposites effectively for the oral extended drug delivery of the venlafaxine hydrochloride [21].

Polymer nanofibers /CNT/GO nanocomposites

Augmentation of the mechanical properties of polymer obtained by the use of inorganic fillers containing some micrometric dimensions such as calcium carbonate, talc and glass blends in the conventional polymer composite [12]. From the past few years, carbon nanotubes had very much impact in the nanomaterials; in various drug delivery, bio-sensing as well as biomedical imaging, it also has high impact in the design of functional nanocomposites [22]. Justin R. and Chen B. (2014) developed

the strong and conductive chitosan-reduced graphene oxide nanocomposites which is reported for transdermal drug delivery by in situ reduction of graphene oxide in chitosan by heating 37 °C for 72 h and they found increase in mechanical properties of the nanocomposites and the strongest nanocomposite with 1% weight reduced graphene oxide showing increase of 91.3% for Young's modulus and 95.6% for ultimate tensile strength over pristine chitosan while maintaining the elongation at break at 10.8% [23].

Bio-polymeric nanocomposites

For the sake of controlled drug delivery of therapeutically active substances, the biopolymers are considered as best contrasting option to the traditional non-biodegradable polymers [12]. The biopolymers are obtained from the natural sources like plants and animals, considered as environmentally friendly polymers; therefore, they are used in various food packaging materials and also have applications in the formation of biopolymer films [24]. These polymers are classified into three classes: class first includes the polymers which are specially separated from biomass, for example, cellulose or starch. The polymers which are obtained synthetically from bio-based monomers are included in class second like poly (lactic acid). The last classification of the biopolymers consists of polymers which are obtained from microorganisms or microscopic organisms such as poly (hydroxyl alkanooates) [12]. The fabrication of biopolymer nanocomposites is done with the help of biopolymers and bio-fillers which shows different physical, mechanical and thermal properties along with some functionalities like biodegradability and biocompatibility [25].

Starch-based nanocomposites

Starch is abundant, renewable, and having low-cost material containing biodegradable properties and properties like film forming due to this starch is considered as the best alternative option to synthetic materials [12]. For improvement of the mechanical properties and reduction in the hydrophilic character of starch, the blends of starch with natural and synthetic polymers are studied to overcome these problems and also to overcome the aging effect [26]. Cao X. et al. (2008) prepared cellulose nanocrystals suspension from flax fibres by acid hydrolysis and used to reinforce the plasticized starch (PS) with the content of 5–30% nanocomposites. Well dispersion of FCNs fillers in PS matrix and good adhesion at interfacial area was observed in the nanocomposites which are prepared by casting method and also showed increase in the tensile strength, Young's modulus with higher water resistance [27]. Kalambar S.B, Rizvi S.S (2004) successfully prepared nanocomposites with superior properties from starch–polycaprolactone (PCL) blends in the presence of montmorillonite (MMT) nanoclay by using reactive extrusion processing and found that with the addition of a modified nanoclay at 3%wt level increased elongation almost fourfold over that of pristine starch–PCL blends. These nanocomposites showed the better solvent-resistance properties because of resistance to diffusion offered by clay platelets in the polymer matrix [28].

Cellulose-based nanocomposites

Because of the specific properties like non-toxicity, cost effectiveness, low density, combustibility and its biodegradable properties cellulose fibre-reinforced polymer composites received very much attention in the various fields of science [29]. Unique properties like improved chemical reactivity, high specific area, non-toxicity, better mechanical durability, together with biodegradability, biocompatibility nanoscale cellulose have become an excellent candidate for the release applications of the drugs [12]. He Y et al. (2020) prepared the carboxymethyl cellulose (CMC)-based nanocomposites which are reinforced with the montmorillonite (MMT) and ϵ -poly-(lysine) (ϵ -PL) with the help of solvent casting method for antimicrobial active food packaging. They evaluated the activity of CMC/MMT/ ϵ -PL nanocomposites against bacteria and fungi and the result showed the favourable inhibition activity against them. The microbial inhibition rate of CMC/MMT/ ϵ -PL 7.5 wt. % film can reach up to above 90%. They also performed the shelf-life study by coating the strawberries with the film forming solution of CMC/MMT/ ϵ -PL 7.5% and they found the extended shelf life for 2 days under ambient temperature [2].

Guar gum-based nanocomposites

Guar gum is used as biomaterial in a different biological and technological processes due to their specific properties like biocompatibility, non-toxicity and the most important is biodegradable polymer [12]. Mansa R, Detellier C (2013) prepared guar–montmorillonite nanocomposites using neutral guar gum and cationic guar gum by the solution intercalation method. Observed morphology and structure of these nanocomposites shows the dependency on relative amounts of guar gum and montmorillonite used for the preparation of nanocomposites [30]. Palem R.R et al. (2020) synthesized guar gum graft polymer-based silver nanocomposite hydrogels and utilized successfully to explore sustained release of 5-fluorouracil (5-FU) and they also evaluated the antibacterial activity. Their study also suggested the use of these nanocomposites in the applications for wound healing purpose and controlled delivery of drug [31].

Nanocomposite hydrogels

Recently, the interest of researchers has been attracted by the nanocomposite hydrogels as biomaterials and by doing the manipulation in the properties of hydrogels and the composite material properties of these biomaterials can be altered easily [12]. Haraguchi K (2007) reported the novel creation of the nanocomposite hydrogels to overcome the limitations of conventional chemically cross-linked hydrogels and it is possible due to the extraordinary properties like mechanical, optical and swelling. Nanocomposite hydrogels were achieved by allowing the clay platelets to act as multifunctional cross-linkers in the formation of polymer/clay networks [32]. Gaharwar AK et al. (2014) studied nanocomposite hydrogels for the biomedical applications and their study concluded that the nanocomposite hydrogel can potentially be used for various pharmaceutical and biomedical applications such as

drug delivery, sensors, regenerative medicine, and actuators and in other biomedical devices. The nanocomposite hydrogels are found to be superior in their physical, chemical, electrical and biological properties than the properties of conventional polymeric hydrogels [33].

Layered double hydroxide (LDH) nanocomposites

These layered double hydroxide (LDH) plays very vital role in the field of material chemistry due to their extraordinary properties and wide range of applications such as thermal stability, energy applications, food packaging applications, drug delivery, agriculture applications, water purification, photoluminescence and flame retardancy. Due to increase in the extent of exfoliation of LDH nanosheets in the polymer matrices, their high efficiency in these applications can be achieved. But because of the high interlayer interaction arises from high charge density of layers, there is big problem to obtain the remarkable exfoliation. This problem can be overcome by the advancement in the fabrication of LDH–polymer nanocomposites by various methods like melt compounding, solution blending and in situ methods like in situ polymerisation, in situ LDH synthesis and double in situ method [34].

Various materials used in the synthesis of nanocomposites

As we discussed above, nanocomposites are substances in which filler materials are incorporated into matrix and based on matrices they are classified as polymer, ceramic and metal matrix nanocomposites, and for their synthesis, various materials are used like various polymers and clays like montmorillonite, saponite, etc., and for certain synthesis methods, it is very critical for polymer, clays and filler materials to get solubilize into organic and aqueous solvents [35]. The overall thought of nanocomposites is based on the idea of making a huge interface between the nanosized-assembling blocks and polymer matrix. Be that as it may, the properties of nanocomposites are not decided exclusively by the size of interface, yet different elements such as design and interactions also assumed as significant part [36]. Polymers utilized in the synthesis of nanocomposites are of different properties, and in various characteristics, some of them might be biodegradable polymers or some might be used as commodities as general-purpose polymers [37]. Raw materials used for synthesis of primarily include polymers ranging from vinyl polymers to special polymers; compatibility agent (can be a polymer) offers a chemically compatible with polymer and filler materials (may be nanoparticle) [35, 37]. Various materials such as polymers, clays and different filler materials used in synthesis of nanocomposites are discussed below.

Polyvinyl alcohol (PVA)

Polyvinyl alcohol (PVA) is used in synthesis of nanocomposites because of its strong chemical and mechanical properties as well as good thermal properties and resistance. PVA is environmentally safe, cost effective and light weight. Many of

the researchers utilized PVA for preparation of nanocomposites using various filler materials and the results have shown increased thermal properties as well as increased antibacterial activity [38, 39].

Polyvinyl chloride (PVC)

PVC is one of the major thermoplastics along with other standard polymers like polyethylene and polystyrene. However, some of its main characteristics such as plasticity, thermal and photostability are inferior to other standard polymers. Among these various characteristic properties, it also bears property of flexibility and durability with suitable chemical and biological resistance and also because of excellent improvement in toughness, thermal robustness and structural stability PVC-based nanocomposites have attracted much more than other [40–42].

Polyaniline

Polyaniline is most studied polymer in synthesis of nanocomposites used in drug delivery. Binitha N. Narayana et al. (2010) prepared exfoliated nanocomposites with polyaniline and montmorillonite. As compared to intercalative nanocomposites, polyaniline/montmorillonite nanocomposite shows excellent physical properties like strength, stiffness and barrier properties [43]. Polyaniline-based nanocomposites also show better results in the cancer therapy with great *in vivo* or *in vitro* biocompatibility and biodegradability [44].

Polyhydroxybutyrate (PHB)

Polyhydroxybutyrate is a biodegradable polymer, but it has disadvantages like stiffness, fragility and low thermal stability and these disadvantages can be overcome by preparing nanocomposites [37]. Application of PHB in drug delivery is that it has been investigated for bone tissue engineering. Mikael Larsson et al. [45] prepared nanocomposites of polyacrylic acid nanogel and biodegradable polyhydroxybutyrate for bone regeneration and drug delivery and the results indicated that prepared composites may be suitable for biomedical uses as a biodegradable material where use of nanostructure design done to tune mechanism of drug release, from diffusion controlled to degradation controlled. Furthermore, drug release was demonstrated for small lithium ion which together with improved tolerance to deformation suggest that the nanocomposites to be appropriate for bone tissue engineering [45].

Chitosan

Chitosan is a biopolymer characterized by excellent chemical and biological properties that can be used in a wide range of applications, such as food, cosmetics, water treatment, membranes, environmental protection, material development, biomedicine, tissue engineering and has excellent biocompatibility and biodegradability [46, 47]. Chitosan nanocomposites refer to chitosan polymer containing dispersed nanofillers having an average particle size less than 100 nm; however, it contains some

drawbacks and to overcome these drawbacks related with biopolymers nano-reinforcement incorporated into chitosan matrix [47]. Utilization of chitosan in ocular drug delivery is due to some extraordinary properties like biocompatibility, penetration–facilitation, cationic polysaccharide and suitable structure for the ocular problems [48].

Montmorillonite

Various clays that belong to smectite family are mostly utilized for preparation of nanocomposites: one of them is montmorillonite. Montmorillonite is most common and best studied clay used in the preparation of polymer nanocomposites for almost three decades due to biocompatibility and biodegradability along with good mechanical properties [49]. Shilpa Jain and Monika Datta prepared montmorillonite–PLGA nanocomposites as an oral extended drug delivery vehicle for venlafaxine hydrochloride and found controlled release behaviour over a period of 12 h. and effective for oral extended drug delivery resulted in decrease in the dosing frequencies [21].

Saponite

Saponite clay is most easily synthesized smectite clay. It is also used in preparation of clay-based nanocomposites utilized for drug delivery. Inorganic layers of saponite play very crucial role in stabilizing and protecting the surfactant molecules by increasing their thermal stability. Kumaresan S. et.al. (2019) synthesized saponite-based nanocomposites to improve the controlled oral drug release of quinine hydrochloride dihydrate [50, 51]. Along with polymers and clays, various filler (materials incorporated in polymer matrix) materials such as nanoparticles also play important role in the preparation of nanocomposite; they used to improve mechanical strength hardness and stiffness.

Graphene oxide nanoparticles

Nanoparticle fillers have been incorporated into polymer-based nanocomposites of different macroscopic form. Oxygen containing functional groups render graphene oxide a biocompatible and physiologically soluble behaviour, and allow strong interaction with many polymers which leads to development of nacre-like structure, an organization widely explored in the development of tough biomimetic nanocomposites [52]. Hailin Lei et.al. (2016) prepared chitosan/sodium alginate medicated graphene oxide-based nanocomposite as a carrier for drug delivery doxorubicin is used as model drug. They prepared DOX-loaded GO/CS-alginate nanocomposites through self-assembly process. The results showed that chitosan/sodium alginate (SA) modification increased the stability and dispersibility of graphene oxide sheets but also suggested that GO-CS/SA nanocomposites were promising novel vehicles for drug delivery [53].

Hydroxyapatite nanoparticle

Hydroxyapatite nanoparticles are utilized to treat bone infections. Being biocompatible, nanohydroxyapatite is used as drug carrier and biomolecules for various diseases. A.P.S. Prasanna and G. D. Venkatasubbu prepared hydroxyapatite nanocomposites for sustained release of amoxicillin. In this, PVA and sodium alginate are coated layer by layer on the hydroxyapatite nanoparticles. Sustained release of drug observed from nanocomposites for 30 days and drug-loaded nanocomposites showed better antibacterial activity and ensured that it can be used as drug delivery system to treat bone infections [54].

Magnetic nanoparticles

Use of magnetic nanoparticles for drug delivery provides promising and effective approach in animal models for cancer and other diseases. It possesses specific properties, like large surface area, small particle size and super magnetism. Farahnaz Brahuie et.al. (2017) prepared phytic acid-chitosan iron oxide nanocomposite (PTA-CS-MNP) by coating magnetic nanoparticles with chitosan for sustained release of phytic acid (anticancer agent). The released profile of the drug from nanocomposites into phosphate buffer saline was observed in sustained manner with total release equilibrium of 86% and 93% when exposed to environments of pH 7.4 and 4.8 at 127 and 56 h, respectively. The prepared nanocomposites estimated as having good anticancer potential against colon cancer cells with no cytotoxicity to normal fibroblast cells [55, 56].

Polymer nanoparticles

Yu et.al. (2009) developed composite microparticles of chitosan, alginate and pectin for drug delivery using bovine serum albumin as a model drug. The result shows the sustained release of drug at stimulated gastric medium, whereas a fast release was observed in simulated intestinal and colonic media [57]. Rajan et.al. (2016) evaluated in vitro release of cisplatin from poly oxalates cross-linked chitosan nanocomposite and they observed that cisplatin-loaded nanocomposites were able to inhibit the tumour growth up to two times more than free cisplatin [58].

Structural features of nanocomposites

Structure of nanocomposites consists of the matrix in which various reinforcement materials like particles, fibres, nanotubes, etc., are incorporated. Structure of nanocomposites can be classified by the distribution of the particles in polymer matrix, and depends on the processing of the composite materials [59]. Most important phenomenon in nanotube or nanofiller reinforced composites is both aggregation and orientation, while in case of composites containing spherical particles, aggregation is a major problem which may cause due to face-to-face interaction and edge-to-edge

orientation leads to the formation of a silicate network [36]. Nanocomposite often contains large particles and network structure developing at large extent of exfoliation and complexity of structure of nanocomposites depends on type of reinforcement (plates, nanoparticles, nanotubes, etc.) within matrix [60]. Primary condition for obtaining nanocomposites with acceptable properties is homogeneous dispersion of nanoparticles [36]. While discussing structure of polymer/layered silicate nanocomposite, the silicate must be exfoliated means the original particles separated to individual layers. Bhavesh D. Kevadiya et.al (2010) intercalated procainamide hydrochloride (PA) in montmorillonite (MMT) as a carrier for drug delivery. Prepared bio-nanocomposite found to have spherical structure due to coating of chitosan over PA-MMT-AL beads (PA-MMT-AL-CS) [20]. The structure of nanocomposites can be established by the arrangement of particles in the polymer matrix [59]. Depending upon structure of dispersed clay platelets in the polymer matrix, the composites can be classified as intercalated or exfoliated nanocomposites. Intercalated structure of nanocomposites can be recognized with its well-ordered and self-assembled multi-layered structures where the extended polymer chains are inserted into the gallery space of the clays, while in an exfoliated structure, individual silicate sheets lose their layered geometry as a result of delamination, and dispersed as nanoscale platelets in a polymer matrix [61]. Arrangement of particles in spherical or onion-like structures shows that the dispersion behaviour of nanoparticles can be crucially influenced by an organic shell [59]. XRD spectra and TEM study are used in the characterization of structure of nanocomposite, wherein XRD spectra of exfoliated nanocomposite do not show any peak at 2θ value near about 8.9° because exfoliation of clay layers removed parallel arrangement of different layers which leads to no interlayer spacing between them but XRD alone can lead to false interpretation of exfoliated structure of nanocomposites. Therefore in other hand, TEM study is also used which can provide very important information in a localized area on the structure, morphology and the distribution of dispersed phase of the nanocomposites [43, 61]. Some of the types of nanocomposite structure are highlighted in Fig. 2.

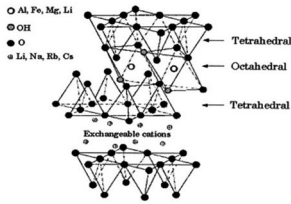
Behaviour of nanocomposites in the developmental stage

Properties of nanocomposites can crucially affect the dispersion state of nanoparticles in a polymer matrix and this situation is dominated with entropy by enthalpy effect where weak role is played by entropy. Recently, the miscibility of nanoparticles in polymer matrix has become a topic of interest for study where the miscibility occurs when the polymer chains present are bigger than the nanoparticles [62]. Table 1 shows various nanocomposite formulations and their physical properties and behaviour.

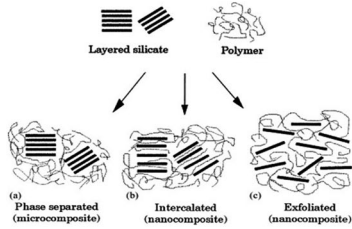
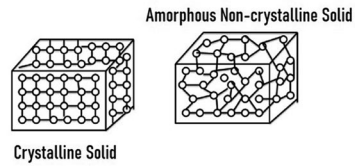
Various applications of nanocomposite materials in pharmaceuticals and biomedical field are highlighted in Table 2, whereas Tables 3 and 4 highlights the critical findings in the development of nanocomposite materials.

Figure 3 shows the various evaluation parameters of prepared nanocomposites based on the critical behaviour of materials used in the synthesis of nanocomposites.

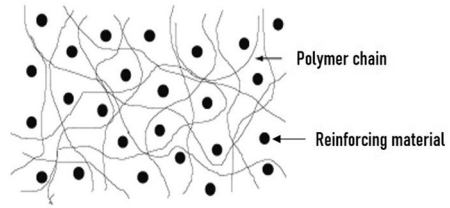
(a) Polymer-layered silicate nanocomposite structure



(b) Ceramic nanocomposites



(c) Other types of nanocomposite structures



(d) Polymer reinforced nanocomposite structure

Fig. 2 Some of the types of nanocomposite structures

Limitations of nanocomposites

- Long-term stability and uncertain cytotoxicity in tissue engineering [108].
- Nanocomposite hydrogels can show undesired dehydration during its use in drug delivery [13].
- Use of natural biopolymer film in industries and wide application of starch-based nanocomposites are limited due to their water vapour barrier properties and poor mechanical properties like brittleness of those films by high intermolecular forces [24].
- Chitosan–aluminosilicate nanocomposite carrier can affect by gastric pH and their ratio [109].
- There are some limitations to the application of chitosan film for packaging, due to its high sensitivity to moisture [110].
- Limitations for both TiO₂ nanocomposite and TiO₂ porous films are that high-temperature process is required to form anatase nanocrystals [111].

Conclusion

Due to diversity in the synthesis of nanocomposite carriers and recent advancements in the field of science and technology, it becomes easier to select the proper material in the design and development of various drug delivery systems and devices. Their use in the development of variety of products including biomedical devices and drug delivery systems has much attention to the researchers. Due to change in the physical properties at molecular level, it becomes easier to overcome the hurdles in the

Table 1 Various nanocomposite formulations and their physical properties and behaviour

Nanocomposite	Method of preparation	Components	Effect on various properties of nanocomposite	References
Chitosan-reduced graphene oxide particles	Biocompatible in situ reduction process	Reduced graphene oxide (rGO) High concentration of rGO in nanocomposites	Increases crystallinity Brittle	[23]
Guar-montmorillonite (MMT) nanocomposites	Solution intercalation method	Guar gum Montmorillonite (MMT)	Increases interlayer space of montmorillonite and TEM study indicates partial exfoliation with MMT	[30]
Guar gum graft polymer-based silver nanocomposite hydrogels	In situ polymerisation method	Acrylamidoglycolic acid chains onto guar gum backbone Cross-linked graft polymer (GGAA) and its silver nanocomposites (GGAA@SNC)	Fractured morphology of nanocomposite hydrogels Cross-linking of borate ions and cis-diol of graft copolymer	[31]
Poly(propylene carbonate)/MMT nanocomposite	Solution intercalation method	Hydrated edge-edge interaction of silicate layers At OMMT 4 wt %	Flocculation of stacks and intercalated layers of silicate High tensile strength and good dispersion into matrix	[63]
Chitosan-g-poly(acrylamide) or zinc nanocomposite	Microwave irradiation method	Polymerisation of acrylamide Inhibition of deoxygenase and periplasmic enzyme activity	Change in surface morphology of chitosan Good antibacterial activity	[64]
pH-sensitive super paramagnetic iron oxide nanocomposite	pH-sensitive acylhydrazone linkage	Addition of 0.1 N HCl Presence of acylhydrazone	Brakeage of acylhydrazone linkage Efficient pH-triggered release of doxorubicin (DOX)	[65]
Calcium phosphate nanocomposites	Rapid precipitation of water in presence of polymer	Addition of drug to all resulting nanocomposites	Hardly affected the spherical shape of nanocomposites	[66]
Layered double hydroxide nanocomposite	Direct mixing of SiO ₂ nanodots with MgAl-LDH nanoparticles	Increase in mass ratio from MgAl-LDH to SiO ₂	Decrease in particle size of nanocomposites	[67]
Carboxymethyl cellulose/graphene oxide bio-nanocomposite hydrogel beads	Simple mixing of graphene oxide and CMC with aqueous dispersion	Addition of graphene oxide	Change in porous structure of GO/CMC monoliths	[68]

Table 1 (continued)

Nanocomposite	Method of preparation	Components	Effect on various properties of nano-composite	References
Chitosan—Locust bean gum (LBG) interpenetrating polymeric network nanocomposite	Glutaraldehyde cross-linking	Variation in polymer concentration of LBG or Chitosan	Decrease in size of composite	[69]
Lecithin and PLGA-based self-assembled nanocomposite	Solution intercalation method	Increase in concentration of polymer/lecithin or high ratio of polymer/lecithin	Increase in size of resulting nano-composite	[70]

Table 2 Applications of nanocomposite materials in pharmaceuticals

Sr. No.	Nanocomposite	Drug development key material	Drug delivery system	Applications	References
1	Amorphous ternary cyclodextrin nanocomposite	Telmisartan	Oral drug delivery system	Improved solubility and reduced pharmacokinetic variability	[71]
2	Silica-based nanocomposites	Al ₂ O ₃ -SiC nanocomposite	Topical drug delivery system	Crack healing and stress relaxation	[72]
3	Inhalable magnetic nanocomposite microparticles	Iron oxide MNPs and D-mannitol	Targeted pulmonary delivery	Inhalation aerosol treatment of lung cancer via targeted hyperthermia	[73]
4	Montmorillonite (M ₁) based PLGA nanocomposites	Venlafaxine hydrochloride	Controlled drug delivery	Effective for the oral extended drug delivery, oral and controlled release carrier for an antidepressant drug	[21]
5	Calcium phosphate nanocomposites	Cisplatin	Controlled drug delivery	Controlled drug release carriers for chemotherapy of cancers, improvement of Anticancer Activity	[66]
6	Hydroxyapatite–chitosan nanocomposite	Celecoxib	Colon targeted drug delivery	Safe vehicle for celecoxib delivery in colon cancer chemotherapy	[74]
7	Hydroxyapatite nanocomposite	Amoxicillin	Sustained release drug delivery	Treatment of bone infection	[54]
8	Polymer nanocomposite	Atorvastatin calcium	Oral drug delivery system	Solubility enhancement of atorvastatin	[75]
9	Hyaluronic acid-based nanocomposite hydrogels	Latanoprost	Ocular drug delivery system	Reducing ocular hypertension by sustained release of latanoprost	[76]
10	Montmorillonite–alginate nanocomposite	Irinotecan	Sustained drug delivery system	Sustained delivery of irinotecan an antineoplastic drug	[77]
11	Chitosan/organic rectorite nanocomposite	Bovine serum albumin	Transdermal drug delivery system	Bactericidal activity of bovine albumin serum	[78]
12	SiO ₂ -layered double hydroxide nanocomposites	Methotrexate (MTX)	Non-viral delivery carrier for in vivo drug and gene delivery	Inhibition of human osteosarcoma cell (U2OS) growth	[67]
13	Montmorillonite/insulin/TiO ₂ hybrid nanocomposite	Insulin	Oral drug delivery system	Oral delivery of insulin	[79]

Table 2 (continued)

Sr. No.	Nanocomposite	Drug development key material	Drug delivery system	Applications	References
14	Sodium alginate/chitosan/hydroxyapatite (SA/CS/HAP) nanocomposite hydrogel	Doxorubicin (DOX)	Oral drug delivery system	Anticancer activity for liver cancer	[80]
15	Chitosan-based nanocomposite films	Metformin	Controlled drug delivery system	Improved hydrophilicity, hydrolytic stability, biocompatibility, mechanical and drug release properties	[81]
16	CS/LBG nanocomposites system	Acceclofenac	Oral drug delivery	For delivery of aceclofenac	[68]
17	Graphene oxide/carboxymethyl cellulose nanocomposites	Doxorubicin	Targeted drug delivery system	For controlled release of anticancer drug doxorubicin (DOX)	[69]
18	Lactoferrin-modified graphene oxide iron oxide nanocomposites	Doxorubicin	Targeted drug delivery system	Targeted delivery of doxorubicin in treatment [of glioma	[82]
19	Hollow Fe ₃ O ₄ /graphene oxide nanocomposites	Rapamycin	Targeted drug delivery system	Targeted delivery of rapamycin for prolonged drug release in anticancer therapies	[83]
20	Curcumin-loaded PMMA-PEG/ZnO nanocomposites	Curcumin	Targeted drug delivery	Induce the apoptosis of cancer cells and raises its probability to cure gastric cancer cells	[84]
21	Mesoporous silica/apatite nanocomposite	Atenolol	Controlled local drug delivery	Prevent the rapid release of atenolol during assays	[85]
22	Chitosan/polyacrylic acid/Fe ₃ O ₄ magnetic nanocomposite hydrogel (CS/PAA/Fe ₃ O ₄)	5-fluorouracil (5-FU)	Anticancer drug delivery system	Enhancement in the stability of drug dosing for a long time with controlled release in colon and rectal condition, in DDS as a colon and rectal administration of 5-FU	[86]

Table 2 (continued)

Sr. No.	Nanocomposite	Drug development key material	Drug delivery system	Applications	References
23	Thermo-sensitive poly(<i>N</i> -isopropylacrylamide)/Mesoporous silica nanocomposites	Ibuprofen	Controlled drug delivery system	Loading and release behaviour for drug ibuprofen	[87]
24	Tyrosine-derived polycarbonate-silica xerogel nanocomposites	Rifampicin and bupivacaine	Controlled drug delivery system	Controlled drug delivery of rifampicin and bupivacaine and also attractive biomaterials for applications such as wound dressings, tissue engineering substrates and stents	[88]
25	Micellar nanocomposites hydrogels thin films	Ciprofloxacin hydrochloride (CPX)	Vaginal drug delivery system	Improved antibiotic drug loading and for controlled drug delivery in the infected vaginal pH condition	[89]
26	Montmorillonite-based polyacrylamide nanocomposite hydrogel rings	Methylene blue	Controlled vaginal drug delivery system	Antibacterial applications (efficiently inhibit the growth of <i>E. coli</i>)	[90]
27	Acrylic acid/polyethylene glycol)-zinc oxide mucoadhesive nanocomposites	Propranolol HCl	Buccal drug delivery system	For buccal administration propranolol HCl and they could also be used as mucoadhesive carrier for buccal drug delivery with efficient antibacterial properties	[91]
28	Chitosan-magnesium aluminium silicate nanocomposite films	Nicotine	Buccal drug delivery system	For buccal delivery of nicotine	[92]
29	Lecithin and PLGA-based self-assembled nanocomposite	Daurorubicin (DNR) and lornoxicam (LNX)	Parenteral and oral drug delivery system	Parenteral and oral drug delivery of DNR and LNX in anticancer and anti-inflammatory activity	[70]

Table 3 Critical findings in the development of nanocomposite materials

Sr. No.	Drug	Dosage form	Experimental model	Comments	References
1	Tacrolimus-loaded PLGA nanoparticles	Eye drop	Excised rabbit corneas	The drug concentration was able to be maintained in cornea and conjunctiva for 24 H The uptake of tacrolimus was increased in trans-corneal area The enhancement in $T_{1/2}$ values was observed as compared to conventional dosage form. (1.77 folds)	[93]
2	Polymeric PLGA nanoparticles (NPs) of dexibuprofen	Eye drops	In vitro and in vivo ocular irritation assay on chorioallantoic membrane and in rabbits, respectively Ex vivo ocular permeation study in rabbits	Enhancement in interaction between dexibuprofen-NPs and customized corneal membrane was facilitated by PEG Fast release of drug was observed for first 150 min, followed by sustained release	[94]
3	PLGA-NPs of flurbiprofen	Eye drop	Rabbit ocular surface inflammation model	Entrapment efficiency was high Storage stability of 6 months was observed No irritation was observed on ocular tissues Controlled & continuous delivery with excellent anti-inflammatory potential was observed	[95]
4	Proglycosomes modified Liposomal tacrolimus	Eye drop	Ex vivo goat eyes for Trans-corneal permeation study; rabbits for precorneal retention study	Fivefold & 13-fold enhancement in corneal permeation when compared to conventional liposomes	[96]

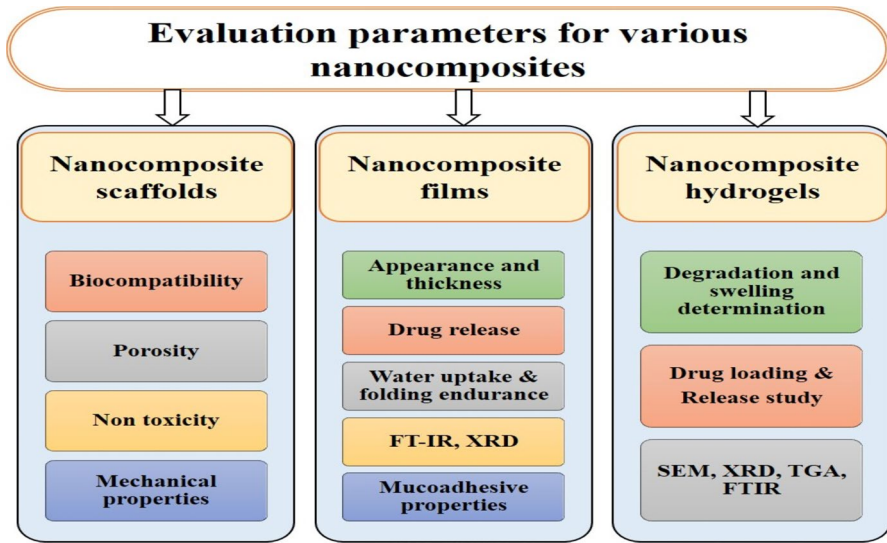


Fig. 3 Various evaluation parameters for nanocomposite materials

development of drug delivery systems with better therapeutic benefit and ease of convenience to the patients. Different carrier systems are useful for the delivery of drugs to the site of action, but nanocarriers systems have attracted due to their particle size, shape, strength and huge surface area.

Table 4 Some critical findings of nanocomposite materials with applications

Sr. No.	Nanocomposite	Critical findings	References
<i>Role of nanocomposite as bioimaging</i>			
1	Silica–cyanine hybrid nanoparticles	Accumulates in the liver after intravenous injection Long retention in tumour after intra-tumour injection High sensitivity, sufficient tissue penetration and high spatial resolution Nearly no cytotoxicity excellent photo-properties	[97]
2	Graphene quantum dot cross-linked carboxymethyl cellulose nanocomposite hydrogel	pH-sensitive swelling and degradation with improved tensile strength Exhibited biocompatibility pH-triggered site-specific & sustained drug delivery system Unique photoluminescent properties suitable for bioimaging applications	[98]
3	Oleyl chitosan, conjugated with folic acid and loaded with quercetin	Contrast agent for MRI & CT scan Preferential activity is observed against Malignant cells Non-hemolytic Biocompatible It functions as dual modality contrast agent for both MRI & CT	[99]
4	AgInZnS–graphene oxide Nanocomposites	Biocompatibility and photostability Exhibited bright and stable photoluminescence Photoluminescence can be tuned based on controlling composition of Zn Potential Bioimage application	[100]
5	Multifunctional mesoporous silica nanocomposite	Carboxyl functionalization made the drug delivery pH dependant Folate functionalization facilitated cellular uptake Water dispersibility was enhanced by PEG Near-infrared fluorescent dye Cy5 made the system effective for bioimaging in live cell	[101]
6	Polymer nanocomposite film made up of calcium oxalate and thionine	Droplet microfluidic approach for intracellular imaging of ascorbic acid in living cells Provides a robust method and ideal platform to study single-cell Promising tool for molecular biology assays in clinical assessment Fast detection & imaging	[102]

Table 4 (continued)

Sr. No.	Nanocomposite	Critical findings	References
<i>Role of nanocomposite in gene delivery</i>			
1	Core-shell polymeric-inorganic hybrid nanocomposite system made up of super paramagnetic iron oxide, polyethylene imine,	<p>Effective platform for MRI-visible gene delivery [103]</p> <p>Effective in MC.DNA-based transfection in HEK293T cells and showed little cytotoxicity</p> <p>Enhanced imaging sensitivity due to high T2 relaxation</p> <p>Transfected cells could be detected by 1.5 T MRI</p> <p>Transfected cell proved to be cell factory for gene product</p>	[103]
2	Core-shell nanosystem consisting of zinc oxide (ZnO) nanocore and a polydopamine (PDA) shell was constructed to integrate chemo- (doxorubicin), gene-(DNAzyme, DZ) and photothermal (PDA layer)	<p>Enhanced anti-tumour efficacy [104]</p> <p>Reduced the side effects of doxorubicin in heart and liver</p> <p>Strategy for synergistic cancer therapy via chemo/gene/photothermal combination</p> <p>ZnO nanocore was designed as a metal cofactor reservoir to release Zn^{2+} in response to intracellular stimuli, which triggered the activation of DZ</p> <p>Strategy to harness DZ as a gene-silencing tool</p> <p>PDA shell could detoxify the ZnO</p>	[104]
3	Aminotetrazole-functionalized magnetic chitosan nanocomposite	<p>Cytotoxicity of N-amino functionalized composite was 35% lower [105]</p> <p>Transfection was enhanced by threefold</p> <p>Enhancement of gene expression in the HECK-293 T cell line</p> <p>Biocompatible and biodegradable nanocarrier to cancer cells</p> <p>Excellent DNA condensation and high Transfection efficiencies</p> <p>high stability, targeted gene transfection, control release</p>	[105]
4	Cationic magnetic nanocomposites (MNCs) comprising branched poly-ethyleneimine (PEI)-coated iron oxide nanoparticles (IONPs)	<p>Ability to penetrate the negatively charged cell wall for the delivery of miR-34a molecules into cancerous cells [106]</p> <p>Transfection efficiency was enhanced through a magnetic field that enabled a very rapid concentration of the completely delivered vector dose onto cells</p> <p>Increased amplification of miR-34a led to the suppression of the MYCN protein</p> <p>Decreased toxicity</p>	[106]

Table 4 (continued)

Sr. No.	Nanocomposite	Critical findings	References
5	Mannose-conjugated layered double hydroxide nanocomposite	<p>More efficient uptake of siRNA by osteosarcoma (U2OS) via receptor-mediated internalization</p> <p>Significantly inhibited U2OS cell growth</p> <p>2D nanoparticles may provide the more efficient internalization by the cells due to their sheet-like morphology</p> <p>Enhanced permeability and retention (EPR) effect</p> <p>Lectin receptor-mediated endocytosis and significantly suppress the cell growth</p> <p>It reveals that mannose-modified LDH is a promising candidate for effective target siRNA/drug delivery for cancer</p>	[107]

Acknowledgements Authors are very thankful to Principal, Rajarshi Shahu College of Pharmacy, Buldana, for providing the library facility for through literature survey. Also, authors are grateful to language editing services by Palladium Documentation, Chennai, India.

Funding This review article is not funded by any funding agency.

Code availability No software application was used in the review article.

Declarations

Conflict of interest Authors declare no financial conflict of interest.

Ethical approval No animal or human volunteers are used.

References

- Mitra SB (2018) Nanoparticles for dental materials: synthesis, analysis, and applications. Emerging nanotechnologies in dentistry, 2nd edn. Elsevier Inc., pp 17–39
- He X, Deng H, Hwang HM (2019) The current application of nanotechnology in food and agriculture. *J Food Drug Anal* 27:1–21. <https://doi.org/10.1016/j.jfda.2018.12.002>
- Calipinar H, Ulas D (2019) Development of nanotechnology in the world and nanotechnology standards in Turkey. *Procedia Comput Sci* 158:1011–1018. <https://doi.org/10.1016/j.procs.2019.09.142>
- Komarneni S (2005) Nanocomposite materials. In: Chemical processing of ceramics, 2nd edn., pp 341–368
- Ouarhim W, Hassani FZSA, Qaiss AEK, Bouhfid R (2019) Rheology of polymer nanocomposites. Rheology of polymer blends and nanocomposites: theory, modelling and applications. Elsevier Inc., pp 73–96
- Jaiswal L, Shankar S, Rhim JW (2019) Applications of nanotechnology in food microbiology. *Methods in microbiology*, 1st edn. Elsevier Ltd., pp 43–60
- Okpala CC (2013) Nanocomposites: an overview. *Int J Eng Res Dev* 8:17–23
- Twardowski T (2007) Introduction to nanocomposite materials : properties, processing, characterization. DEStech Publications, Lancaster
- Parhi R (2018) Nanocomposite for transdermal drug delivery. Applications of nanocomposite materials in drug delivery. Elsevier Inc., pp 353–389
- Omanovi E, Badnjevi A, Kazlagi A, Hajlovac M (2019) Nanocomposites : a brief review. *J Heal Technol*. <https://doi.org/10.1007/s12553-019-00380-x>
- Camargo PHC, Satyanarayana KG, Wypych F (2009) Nanocomposites: synthesis, structure, properties and new application opportunities. *Mater Res* 12:1–39. <https://doi.org/10.1590/S1516-14392009000100002>
- Kaurav H, Manchanda S, Dua K, Kapoor DN (2018) Nanocomposites in controlled & targeted drug delivery systems. *Nano Hybrids Compos* 20:27–45. <https://doi.org/10.4028/www.scientific.net/nhc.20.27>
- Shanbhag PP, Rane D, Chandra R, Lande S, Deshmukh P, Prerna Patil TG (2019) Nanocomposites: a newer technology in drug delivery systems. *Int J Pharm Sci Rev Res* 56:144–154
- Avella M, Errico ME, Martelli S, Martuscelli E (2001) Preparation methodologies of polymer matrix nanocomposites. *Appl Organomet Chem* 15:435–439. <https://doi.org/10.1002/aoc.168>
- Swathi SKR, Krishna KR (2018) A review on types of nanocomposites and their applications. *Int J Adv Res* 4:235–236
- Khan WS, Hamadneh NN, Khan WA (2016) Polymer nanocomposites: synthesis techniques, classification and properties Waseem. In: Science and applications of tailored nanostructures. pp 50–67

17. Saboori A, Dadkhah M, Fino P, Pavese M (2018) An overview of metal matrix nanocomposites reinforced with graphene nanoplatelets; mechanical, electrical and thermophysical properties. *Metals (Basel)* 8:1–33. <https://doi.org/10.3390/met8060423>
18. Zanetti M, Lomakin S, Camino G (2000) Polymer layered silicate nanocomposites: a review. *Macromol Mater Eng* 279:1–9. <https://doi.org/10.3390/ma2030992>
19. Król-Morkisz K, Pieliuchowska K (2018) Thermal decomposition of polymer nanocomposites with functionalized nanoparticles. *Polymer composites with functionalized nanoparticles: synthesis, properties, and applications*. Elsevier Inc., pp 405–435
20. Kevadiya BD, Joshi GV, Bajaj HC (2010) Layered bionanocomposites as carrier for procainamide. *Int J Pharm* 388:280–286. <https://doi.org/10.1016/j.ijpharm.2010.01.002>
21. Jain S, Datta M (2014) Montmorillonite-PLGA nanocomposites as an oral extended drug delivery vehicle for venlafaxine hydrochloride. *Appl Clay Sci* 99:42–47. <https://doi.org/10.1016/j.clay.2014.06.006>
22. Saifuddin N, Raziah AZ, Junzah AR (2013) Carbon nanotubes: a review on structure and their interaction with proteins. *J Chem* 2013:1–18. <https://doi.org/10.1155/2013/676815>
23. Justin R, Chen B (2014) Strong and conductive chitosan-reduced graphene oxide nanocomposites for transdermal drug delivery. *J Mater Chem B* 2:3759–3770. <https://doi.org/10.1039/c4tb00390j>
24. Rhim JW, Ng PKW (2007) Natural biopolymer-based nanocomposite films for packaging applications. *Crit Rev Food Sci Nutr* 47:411–433. <https://doi.org/10.1080/10408390600846366>
25. Othman SH (2014) Bio-nanocomposite materials for food packaging applications: types of biopolymer and nano-sized filler. *Agric Agric Sci Procedia* 2:296–303. <https://doi.org/10.1016/j.aaspro.2014.11.042>
26. Dufresne A (2009) Starch-based nanocomposites. pp 1–288
27. Cao X, Chen Y, Chang PR et al (2008) Starch-based nanocomposites reinforced with flax cellulose nanocrystals. *Express Polym Lett* 2:502–510. <https://doi.org/10.3144/expresspolymlett.2008.60>
28. Kalambur SB, Rizvi SS (2004) Starch-based nanocomposites by reactive extrusion processing. *Polym Int* 53:1413–1416. <https://doi.org/10.1002/pi.1478>
29. Kalia S, Dufresne A, Cherian BM et al (2011) Cellulose-based bio- and nanocomposites: a review. *Int J Polym Sci* 2011:1–35. <https://doi.org/10.1155/2011/837875>
30. Mansa R, Detellier C (2013) Preparation and characterization of guar-montmorillonite nanocomposites. *Materials (Basel)* 6:5199–5216. <https://doi.org/10.3390/ma6115199>
31. Palem RR, Shimoga G, Rao KSVK et al (2020) Guar gum graft polymer-based silver nanocomposite hydrogels: synthesis, characterization and its biomedical applications. *J Polym Res*. <https://doi.org/10.1007/s10965-020-2026-8>
32. Haraguchi K (2007) Nanocomposite hydrogels. *Curr Opin Solid State Mater Sci* 11:47–54. <https://doi.org/10.1016/j.cossms.2008.05.001>
33. Gaharwar AK, Peppas NA, Khademhosseini A (2014) Nanocomposite hydrogels for biomedical applications. *Biotechnol Bioeng* 111:441–453. <https://doi.org/10.1002/bit.25160>
34. Daniel S, Thomas S (2020) Layered double hydroxides: fundamentals to applications. *Layered double hydroxide polymer nanocomposites*. Elsevier Ltd, pp 1–76
35. Ravichandran K, Praseetha PK, Arun T, Gobalakrishnan S (2018) Synthesis of nanocomposites. *Synthesis of inorganic nanomaterials*. Elsevier Ltd., pp 141–168
36. Hári J, Pukánszky B (2011) Nanocomposites: preparation, structure, and properties. In: *Applied plastics engineering handbook*. Elsevier, pp 109–142
37. Morles RB, Marchetti M, Muraviev D, et al (2012) New trends and development. *J Colloid Interface Sci*. 1–16
38. Hajeessa KS, Hussein MA, Anwar Y et al (2018) Nanocomposites containing polyvinyl alcohol and reinforced carbon-based nanofiller: a super effective biologically active material. *Nanobiomedicine* 5:1–12. <https://doi.org/10.1177/1849543518794818>
39. Ghaffari-Moghaddam M, Eslahi H (2014) Synthesis, characterization and antibacterial properties of a novel nanocomposite based on polyaniline/polyvinyl alcohol/Ag. *Arab J Chem* 7:846–855. <https://doi.org/10.1016/j.arabjc.2013.11.011>
40. Gilbert M (2012) Poly(vinyl chloride)(PVC)-based nanocomposites. *Advances in polymer nanocomposites: types and applications*. Woodhead Publishing Limited, pp 216–237
41. Gholami A, Moghadassi AR, Hosseini SM et al (2014) Preparation and characterization of polyvinyl chloride based nanocomposite nanofiltration-membrane modified by iron oxide nanoparticles for lead removal from water. *J Ind Eng Chem* 20:1517–1522. <https://doi.org/10.1016/j.jiec.2013.07.041>

42. Kausar A (2018) Review on polymer/halloysite nanotube nanocomposite. *Polym Plast Technol Eng* 57:548–564. <https://doi.org/10.1080/03602559.2017.1329436>
43. Narayanan BN, Koodathil R, Gangadharan T et al (2010) Preparation and characterization of exfoliated polyaniline/montmorillonite nanocomposites. *Mater Sci Eng B Solid-State Mater Adv Technol* 168:242–244. <https://doi.org/10.1016/j.mseb.2009.12.027>
44. Xia B, Wang B, Shi J et al (2017) Photothermal and biodegradable polyaniline/porous silicon hybrid nanocomposites as drug carriers for combined chemo-photothermal therapy of cancer. *Acta Biomater* 51:197–208. <https://doi.org/10.1016/j.actbio.2017.01.015>
45. Larsson M, Bergstrand A, Mesiah L et al (2014) Nanocomposites of polyacrylic acid nanogels and biodegradable polyhydroxybutyrate for bone regeneration and drug delivery. *J Nanomater* 2014:9–11. <https://doi.org/10.1155/2014/371307>
46. Yassue-Cordeiro PH, Severino P, Souto EB et al (2018) Chitosan-based nanocomposites for drug delivery. Applications of nanocomposite materials in drug delivery. Elsevier Inc., pp 1–26
47. Ali A, Ahmed S (2018) A review on chitosan and its nanocomposites in drug delivery. *Int J Biol Macromol* 109:273–286. <https://doi.org/10.1016/j.ijbiomac.2017.12.078>
48. Ahmad M, Manzoor K, Ikram S (2018) Chitosan based nanocomposites for drug, gene delivery, and bioimaging applications. Applications of nanocomposite materials in drug delivery. Elsevier Inc., pp 27–38
49. Paravastu VKK, Yarraguntla SR, Suvvari A (2019) Role of nanocomposites in drug delivery. *GSC Biol Pharm Sci* 8:094–103. <https://doi.org/10.30574/gscbps.2019.8.3.0150>
50. Kotal M, Bhowmick AK (2015) Polymer nanocomposites from modified clays: recent advances and challenges. *Prog Polym Sci* 51:127–187. <https://doi.org/10.1016/j.progpolymsci.2015.10.001>
51. Kumaresan S, Pawar RR, Kevadiya BD, Bajaj HC (2019) Synthesis of saponite based nanocomposites to improve the controlled oral drug release of model drug quinine hydrochloride dihydrate. *Pharmaceuticals* 12:1–13. <https://doi.org/10.3390/ph12030105>
52. Moura D, Mano JF, Paiva MC, Alves NM (2016) Chitosan nanocomposites based on distinct inorganic fillers for biomedical applications. *Sci Technol Adv Mater* 17:626–643. <https://doi.org/10.1080/14686996.2016.1229104>
53. Lei H, Xie M, Zhao Y et al (2016) Chitosan/sodium alginate modified graphene oxide-based nanocomposite as a carrier for drug delivery. *Ceram Int* 42:17798–17805. <https://doi.org/10.1016/j.ceramint.2016.08.108>
54. Prasanna APS, Venkatasubbu GD (2018) Sustained release of amoxicillin from hydroxyapatite nanocomposite for bone infections. *Prog Biomater* 7:289–296. <https://doi.org/10.1007/s40204-018-0103-4>
55. Kalubowilage M, Janik K, Bossmann SH (2019) Magnetic nanomaterials for magnetically-aided drug delivery and hyperthermia. *Appl Sci* 9:2927. <https://doi.org/10.3390/app9142927>
56. Barahue F, Dorniani D, Saifullah B et al (2017) Sustained release of anticancer agent phytic acid from its chitosan-coated magnetic nanoparticles for drug-delivery system. *Int J Nanomed* 12:2361–2372. <https://doi.org/10.2147/IJN.S126245>
57. Yu CY, Yin BC, Zhang W et al (2009) Composite microparticle drug delivery systems based on chitosan, alginate and pectin with improved pH-sensitive drug release property. *Colloids Surf B Biointerfaces* 68:245–249. <https://doi.org/10.1016/j.colsurfb.2008.10.013>
58. Rajan M, Murugan M, Ponnamma D et al (2016) Poly-carboxylic acids functionalized chitosan nanocarriers for controlled and targeted anti-cancer drug delivery. *Biomed Pharmacother* 83:201–211. <https://doi.org/10.1016/j.biopha.2016.06.026>
59. Caseri WR (2006) Nanocomposites of polymers and inorganic particles: preparation, structure and properties. *Mater Sci Technol* 22:807–817. <https://doi.org/10.1179/174328406X101256>
60. Keledi G, Hári J, Pukánszky B (2012) Polymer nanocomposites: structure, interaction, and functionality. *Nanoscale* 4:1919–1938. <https://doi.org/10.1039/c2nr11442a>
61. Tjong SC (2006) Structural and mechanical properties of polymer nanocomposites. *Mater Sci Eng R Rep* 53:73–197. <https://doi.org/10.1016/j.mser.2006.06.001>
62. Kumar SK, Krishnamoorti R (2010) Nanocomposites: structure, phase behavior, and properties. *Annu Rev Chem Biomol Eng* 1:37–58. <https://doi.org/10.1146/annurev-chembioeng-073009-100856>
63. Shi X, Gan Z (2007) Preparation and characterization of poly(propylene carbonate)/montmorillonite nanocomposites by solution intercalation. *Eur Polym J* 43:4852–4858. <https://doi.org/10.1016/j.eurpolymj.2007.09.024>

64. Pathania D, Gupta D, Kothiyal NC et al (2016) Preparation of a novel chitosan-g-poly(acrylamide)/Zn nanocomposite hydrogel and its applications for controlled drug delivery of ofloxacin. *Int J Biol Macromol* 84:340–348. <https://doi.org/10.1016/j.ijbiomac.2015.12.041>
65. Zhu L, Wang D, Wei X et al (2013) Multifunctional pH-sensitive superparamagnetic iron-oxide nanocomposites for targeted drug delivery and MR imaging. *J Control Release* 169:228–238. <https://doi.org/10.1016/j.jconrel.2013.02.015>
66. Dan Son K, Kim YJ (2017) Anticancer activity of drug-loaded calcium phosphate nanocomposites against human osteosarcoma. *Biomater Res* 21:1–8. <https://doi.org/10.1186/s40824-017-0099-1>
67. Li L, Gu Z, Gu W et al (2016) Efficient drug delivery using SiO₂-layered double hydroxide nanocomposites. *J Colloid Interface Sci* 470:47–55. <https://doi.org/10.1016/j.jcis.2016.02.042>
68. Rasoulzadeh M, Namazi H (2017) Carboxymethyl cellulose/graphene oxide bio-nanocomposite hydrogel beads as anticancer drug carrier agent. *Carbohydr Polym* 168:320–326. <https://doi.org/10.1016/j.carbpol.2017.03.014>
69. Jana S, Sen KK (2017) Chitosan—Locust bean gum interpenetrating polymeric network nanocomposites for delivery of aceclofenac. *Int J Biol Macromol* 102:878–884. <https://doi.org/10.1016/j.ijbiomac.2017.04.097>
70. Varghese SE, Fariya MK, Rajawat GS et al (2016) Lecithin and PLGA-based self-assembled nanocomposite, Lecithmer: preparation, characterization, and pharmacokinetic/pharmacodynamic evaluation. *Drug Deliv Transl Res* 6:342–353. <https://doi.org/10.1007/s13346-016-0314-y>
71. Sangwai M, Vavia P (2013) Amorphous ternary cyclodextrin nanocomposites of telmisartan for oral drug delivery: improved solubility and reduced pharmacokinetic variability. *Int J Pharm* 453:423–432. <https://doi.org/10.1016/j.ijpharm.2012.08.034>
72. Thompson AM, Chan HM, Harmer MP, Cook RE (1995) Crack healing and stress relaxation in Al₂O₃ SiC “nanocomposites.” *J Am Ceram Soc* 78:567–571
73. Stocke NA, Meenach SA, Arnold SM et al (2015) Formulation and characterization of inhalable magnetic nanocomposite microparticles (MnMs) for targeted pulmonary delivery via spray drying. *Int J Pharm* 479:320–328. <https://doi.org/10.1016/j.ijpharm.2014.12.050>
74. Venkatesan P, Puvvada N, Dash R et al (2011) The potential of celecoxib-loaded hydroxyapatite-chitosan nanocomposite for the treatment of colon cancer. *Biomaterials* 32:3794–3806. <https://doi.org/10.1016/j.biomaterials.2011.01.027>
75. Sonawane DD, Jat RK, Pawar AY, Jhabarmal SJ (2019) Formulation & development of nanocomposites for solubility enhancement of BCS Class II model drug using microwave induced diffusion technique. *Res Rev Int J Multidiscip* 3085:502–512
76. Widjaja LK, Bora M, Chan PNP et al (2014) Hyaluronic acid-based nanocomposite hydrogels for ocular drug delivery applications. *J Biomed Mater Res Part A* 102:3056–3065. <https://doi.org/10.1002/jbm.a.34976>
77. Iliescu RI, Andronescu E, Ghitulica CD et al (2014) Montmorillonite-alginate nanocomposite as a drug delivery system—incorporation and in vitro release of irinotecan. *Int J Pharm* 463:184–192. <https://doi.org/10.1016/j.ijpharm.2013.08.043>
78. Wang X, Du Y, Luo J et al (2007) Chitosan/organic rectorite nanocomposite films: structure, characteristic and drug delivery behaviour. *Carbohydr Polym* 69:41–49. <https://doi.org/10.1016/j.carbpol.2006.08.025>
79. Kamari Y, Ghiaci P, Ghiaci M (2017) Study on montmorillonite/insulin/TiO₂ hybrid nanocomposite as a new oral drug-delivery system. *Mater Sci Eng C* 75:822–828. <https://doi.org/10.1016/j.msec.2017.02.115>
80. Abou Taleb MF, Alkahtani A, Mohamed SK (2015) Radiation synthesis and characterization of sodium alginate/chitosan/hydroxyapatite nanocomposite hydrogels: a drug delivery system for liver cancer. *Polym Bull* 72:725–742. <https://doi.org/10.1007/s00289-015-1301-z>
81. Shariatinia Z, Zahraee Z (2017) Controlled release of metformin from chitosan-based nanocomposite films containing mesoporous MCM-41 nanoparticles as novel drug delivery systems. *J Colloid Interface Sci* 501:60–76. <https://doi.org/10.1016/j.jcis.2017.04.036>
82. Song MM, Xu HL, Liang JX et al (2017) Lactoferrin modified graphene oxide iron oxide nanocomposite for glioma-targeted drug delivery. *Mater Sci Eng C* 77:904–911. <https://doi.org/10.1016/j.msec.2017.03.309>

83. Cao L, Jiang Y, Chen Z (2017) Hollow Fe₃O₄/graphene oxide nanocomposites as novel rapamycin carrier: formulation optimization and in vitro characterization. *J Nanosci Nanotechnol* 18:3067–3076. <https://doi.org/10.1166/jnn.2018.14674>
84. Dhivya R, Ranjani J, Bowen PK et al (2017) Biocompatible curcumin loaded PMMA-PEG/ZnO nanocomposite induce apoptosis and cytotoxicity in human gastric cancer cells. *Mater Sci Eng C* 80:59–68. <https://doi.org/10.1016/j.msec.2017.05.128>
85. Sousa A, Souza KC, Sousa EMB (2008) Mesoporous silica/apatite nanocomposite: special synthesis route to control local drug delivery. *Acta Biomater* 4:671–679. <https://doi.org/10.1016/j.actbio.2007.11.003>
86. Amini-Fazl MS, Mohammadi R, Kheiri K (2019) 5-Fluorouracil loaded chitosan/polyacrylic acid/Fe₃O₄ magnetic nanocomposite hydrogel as a potential anticancer drug delivery system. *Int J Biol Macromol* 132:506–513. <https://doi.org/10.1016/j.ijbiomac.2019.04.005>
87. Tian BS, Yang C (2011) Thermo-sensitive poly(N-isopropylacrylamide)/mesoporous silica nanocomposites as controlled delivery carriers: loading and release behaviors for drug ibuprofen. *J Nanosci Nanotechnol* 11:1871–1879. <https://doi.org/10.1166/jnn.2011.3543>
88. Costache MC, Vaughan AD, Qu H et al (2013) Tyrosine-derived polycarbonate-silica xerogel nanocomposites for controlled drug delivery. *Acta Biomater* 9:6544–6552. <https://doi.org/10.1016/j.actbio.2013.01.034>
89. Adnan M, Santhosh Kumar K, Sreejith L (2020) Micellar nanocomposites hydrogels films for pH sensitive controlled drug delivery. *Mater Lett* 277:128286. <https://doi.org/10.1016/j.matlet.2020.128286>
90. Sharifzadeh G, Hezaveh H, Muhamad II et al (2020) Montmorillonite-based polyacrylamide hydrogel rings for controlled vaginal drug delivery. *Mater Sci Eng C* 110:110609. <https://doi.org/10.1016/j.msec.2019.110609>
91. Mahmoud GA, Ali AEH, Raafat AI et al (2018) Development of (acrylic acid/ polyethylene glycol)-zinc oxide mucoadhesive nanocomposites for buccal administration of propranolol HCl. *Radiat Phys Chem* 147:18–26. <https://doi.org/10.1016/j.radphyschem.2018.01.020>
92. Pongjanyakul T, Khunawattanakul W, Strachan CJ et al (2013) Characterization of chitosan-magnesium aluminum silicate nanocomposite films for buccal delivery of nicotine. *Int J Biol Macromol* 55:24–31. <https://doi.org/10.1016/j.ijbiomac.2012.12.043>
93. Kalam MA, Alshamsan A (2017) Poly (D, L-lactide-co-glycolide) nanoparticles for sustained release of tacrolimus in rabbit eyes. *Biomed Pharmacother* 94:402–411. <https://doi.org/10.1016/j.biopha.2017.07.110>
94. Sánchez-López E, Esteruelas G, Ortiz A et al (2020) Article dexibuprofen biodegradable nanoparticles: one step closer towards a better ocular interaction study. *Nanomaterials* 10:1–24. <https://doi.org/10.3390/nano10040720>
95. Vega E, Egea MA, Valls O, Espina M, García ML (2006) Flurbiprofen loaded biodegradable nanoparticles for ophthalmic administration. *J Pharm Sci* 95:2393–2405. <https://doi.org/10.1002/jps>
96. Garg V, Suri R, Jain GK, Kohli K (2017) Proglycosomes: A novel nano-vesicle for ocular delivery of tacrolimus. *Colloids Surf B Biointerfaces* 157:40–47. <https://doi.org/10.1016/j.colsurfb.2017.05.049>
97. Wu X, Chang S, Sun X, Guo Z, Li Y, Tang J, Shen Y, Shi J, Tian H, Zhu W (2015) Constructing NIR silica-cyanine hybrid nanocomposite for bioimaging in vivo: a breakthrough in photo-stability and bright fluorescence with large Stokes shift. *J Mater Chem C* 3:10715–10722. <https://doi.org/10.1039/b000000x>
98. Rakhshaei R, Namazi H, Hamishehkar H, Rahimi M (2020) Graphene quantum dot cross-linked carboxymethyl cellulose nanocomposite hydrogel for pH-sensitive oral anticancer drug delivery with potential bioimaging properties. *Int J Biol Macromol* 150:1121–1129. <https://doi.org/10.1016/j.ijbiomac.2019.10.118>
99. Hemalatha T, UmaMaheswari T, Anbukkarsi K, Ayyadurai N (2020) Imaging and anti-apoptotic potentials of oleyl chitosan coated quercetin nanocomposite: in vitro perspectives. *Mater Lett* 279:128496. <https://doi.org/10.1016/j.matlet.2020.128496>
100. Zang Z, Zeng X, Wang M et al (2017) Tunable photoluminescence of water-soluble AgInZnS-graphene oxide (GO) nanocomposites and their application in-vivo bioimaging. *Sens Actuators B Chem* 252:1179–1186. <https://doi.org/10.1016/j.snb.2017.07.144>

101. Xie M, Shi H, Li Z et al (2013) A multifunctional mesoporous silica nanocomposite for targeted delivery, controlled release of doxorubicin and bioimaging. *Colloids Surf B Biointerfaces* 110:138–147. <https://doi.org/10.1016/j.colsurfb.2013.04.009>
102. Alizadeh N, Ghasemi F, Salimi A et al (2020) Polymer nanocomposite film for dual colorimetric and fluorescent ascorbic acid detection integrated single-cell bioimaging with droplet microfluidic platform. *Dye Pigment* 173:107875. <https://doi.org/10.1016/j.dyepig.2019.107875>
103. Cai J, Chen G, Jin R et al (2019) A core-shell polymeric-inorganic hybrid nanocomposite system for MRI-visible gene delivery application in cancer immunotherapy. *J Ind Eng Chem* 76:188–196. <https://doi.org/10.1016/j.jiec.2019.03.039>
104. Liu M, Peng Y, Nie Y et al (2020) Co-delivery of doxorubicin and DNase using ZnO@polydopamine core-shell nanocomposites for chemo/gene/photothermal therapy. *Acta Biomater* 110:242–253. <https://doi.org/10.1016/j.actbio.2020.04.041>
105. Irvani Kashkouli K, Torkzadeh-Mahani M, Mosaddegh E (2018) Synthesis and characterization of aminotetrazole-functionalized magnetic chitosan nanocomposite as a novel nanocarrier for targeted gene delivery. *Mater Sci Eng C* 89:166–174. <https://doi.org/10.1016/j.msec.2018.03.032>
106. Mdlovu NV, Lin KS, Chen Y, Wu CM (2021) Formulation of magnetic nanocomposites for intracellular delivery of micro-RNA for MYCN inhibition in neuroblastoma. *Colloids Surf A Physicochem Eng Asp* 615:126264. <https://doi.org/10.1016/j.colsurfa.2021.126264>
107. Li L, Zhang R, Gu W, Xu ZP (2018) Mannose-conjugated layered double hydroxide nanocomposite for targeted siRNA delivery to enhance cancer therapy. *Nanomed Nanotechnol Biol Med* 14:2355–2364. <https://doi.org/10.1016/j.nano.2017.06.006>
108. Liu W, Webster TJ (2016) Toxicity and biocompatibility properties of nanocomposites for musculoskeletal tissue regeneration. *Nanocomposites for musculoskeletal tissue regeneration*. Elsevier Ltd, pp 95–122
109. De Cremer K, Braem A, Gerits E et al (2017) Controlled release of chlorhexidine from a mesoporous silica-containing macroporous titanium dental implant prevents microbial biofilm formation. *Eur Cells Mater* 33:13–27. <https://doi.org/10.22203/eCM.v033a02>
110. Yan H, Wang S, Han L et al (2018) Chlorhexidine-encapsulated mesoporous silica-modified dentin adhesive. *J Dent* 78:83–90. <https://doi.org/10.1016/j.jdent.2018.08.012>
111. Bukara K, Schueller L, Rosier J et al (2016) Ordered mesoporous silica to enhance the bioavailability of poorly water-soluble drugs: proof of concept in man. *Eur J Pharm Biopharm* 108:220–225. <https://doi.org/10.1016/j.ejpb.2016.08.020>

Publisher's Note Springer Nature remains neutral with regard to jurisdictional claims in published maps and institutional affiliations.

Authors and Affiliations

Prakash Namdeo Kendre²  · Mrinal Gite¹ · Shirish P. Jain² · Ajinkya Pote²

Mrinal Gite
mrinalgite1@gmail.com

Shirish P. Jain
principalrscp@gmail.com

Ajinkya Pote
ajinkyapote1996@gmail.com

¹ Department of Pharmaceutics, Rajarshi Shahu College of Pharmacy, Buldana, Maharashtra, India

² Rajarshi Shahu College of Pharmacy, Buldana, Maharashtra, India

Stereolithography 3D printing technology in pharmaceuticals: a review

Subhash Deshmane, Prakash Kendre, Hitendra Mahajan & Shirish Jain

To cite this article: Subhash Deshmane, Prakash Kendre, Hitendra Mahajan & Shirish Jain (2021): Stereolithography 3D printing technology in pharmaceuticals: a review, Drug Development and Industrial Pharmacy, DOI: [10.1080/03639045.2021.1994990](https://doi.org/10.1080/03639045.2021.1994990)

To link to this article: <https://doi.org/10.1080/03639045.2021.1994990>



Published online: 29 Oct 2021.



Submit your article to this journal [↗](#)



Article views: 20





View related articles [↗](#)



View Crossmark data [↗](#)

Stereolithography 3D printing technology in pharmaceuticals: a review

Subhash Deshmane^a , Prakash Kendre^a, Hitendra Mahajan^b  and Shirish Jain^a

^aDepartment of Pharmaceutics, Rajarshi Shahu College of Pharmacy, Malvihir, India; ^bDepartment of Pharmaceutics, R. C. Patel Institute of Pharmaceutical Education and Research, Shirpur, India

ABSTRACT

Three-dimensional printing (3DP) technology is an innovative tool used in manufacturing medical devices, producing alloys, replacing biological tissues, producing customized dosage forms and so on. Stereolithography (SLA), a 3D printing technique, is very rapid and highly accurate and produces finished products of uniform quality. 3D formulations have been optimized with a perfect tool of artificial intelligence learning techniques. Complex designs/shapes can be fabricated through SLA using the photopolymerization principle. Different 3DP technologies are introduced and the most promising of these, SLA, and its commercial applications, are focused on. The high speed and effectiveness of SLA are highlighted. The working principle of SLA, the materials used and applications of the technique in a wide range of different sectors are highlighted in this review. An innovative idea of 3D printing customized pharmaceutical dosage forms is also presented. SLA comprises several advantages over other methods, such as cost effectiveness, controlled integrity of materials and greater speed. The development of SLA has allowed the development of printed pharmaceutical devices. Considering the present trends, it is expected that SLA will be used along with conventional methods of manufacturing of 3D model. This 3D printing technology may be utilized as a novel tool for delivering drugs on demand. This review will be useful for researchers working on 3D printing technologies.

ARTICLE HISTORY

Received 7 March 2021
Revised 14 July 2021
Accepted 12 October 2021

KEYWORDS

Additive manufacturing; customized dosage form; photocurable resins; solid freeform fabrication; three-dimensional printing; vat polymerization

Introduction

Three-dimensional printing (3DP) technology has opened new frontiers in pharmaceutical and other sectors. Simple tools and poor-standard object of some materials cannot yield high-quality products from any bulk substances. This is the limitation of typical or common methods of manufacture [1,2]. In contrast, the 3DP technique is sophisticated, rapid, highly automated, easy to use, customized and cost effective [3–6]. The 3DP technology is used to make 3D objects by laying layers on top of each other. Biological materials, alloys, tissues/cells, metals, wood, thermoplastics, etc. are used in making 3D objects [7,8]. Anatomical prostheses, biological tissues, heart valves, hearing aids and different parts or models of machinery are among the well known examples of 3D objects [9–13]. Innovative scanning and printing systems hold promise in the area of medicine [14]. Over the last three decades, pharmaceutical companies have been looking at 3DP technology to understand the roles it will play and how best to use it. Against a background in which new formulations, biomedical devices and medicines were being developed daily, Professor Clive Roberts, from the University of Nottingham, said that many researchers have designed and prepared many different dosage forms using 3DP techniques [15]. As with most complex 3D architectures, medical devices were printed directly using 3DP technology in the early 2000s [16,17]. Devices specific to a patient's anatomy were also fabricated. Optimized tools and techniques are a prerequisite for making formulations of the desired shapes and sizes. In August 2015, Aprelia Pharmaceuticals printed the first 3D drug that was approved by the FDA. This was Spritam (Levetiracetam) [18,19], a porous structure printed layer by layer

and reformulated to treat dysphagia. When it comes in contact with saliva, it dissolves rapidly and delivers a high dose (1 g) of an antiepileptic drug from a tightly packed pill [20]. The non-uniform quality of some finished products is mainly caused by manufacturing processes such as milling, mixing, granulation and compression. Certain tools related to drug release, drug content and product stability are affected by these operations [21,22]. 3DP is proving to be the solution in overcoming such challenges [23].

Now a day's we can serve better with readdressing of artificial intelligence (AI). In the various filed, AI igniting with notice development [24,25]. Minimum time and cost is the new perspectives of AI in optimization of 3D products that, creating interest in the researchers for launching the products in market [26]. Design of experiments is also mostly used in optimization, but computer aided artificial neural network(ANN) have more attention and delight [27]. Extended drug release ibuprofen tablet fabricated with crosslinked polymers printed with artificial neural network [28]. A perfect tool of AI learning techniques develops pharmaceutical formulations in 3DP. Web bases software M3DISEEN [29] and accurate optimal parameters are the best example of AI [30]. 3D printed tablets of atomoxetine fabricated by ANN release the tailored drug release from immediate to prolong [31]. A solid three-dimensional object of any shape can be prepared starting from a digital model through an automated sequential layering process [32]. It means this technique shares the theme of a sequential layer of material addition of 3D envelope [33,34]. 3DP allows more complex designs or shapes to be fabricated compared with conventional manufacturing processes [35]. Objects can be fabricated using 3DP methods through digital files [36–38].

Now 3DP technology is emerging as a technology for designing and preparing personalized medicines and novel formulations [39–42]. 3DP technology increases the speed with which personalized pharmaceutical drugs can be produced, using computer-based drug design systems [43,44]. First 3D printer in the world is launched by FabRx for personalized medicines in 2020. M3DIMAKER™ used from drug development timeline to human clinical trials [45]. Semi-liquid binding solutions are mixed with powder beds to produce adhesive particles in inkjet printing [46]. According to the United States Government Accountability Office, a 3DP method is a layer-by-layer process used for making 3D objects from digital models [47]. Other synonyms for '3DP technology' are 'rapid prototyping,' 'solid free form' and 'additive manufacturing and fabrication' [48,49]. The American Society of Mechanical Engineers has suggested 'additive manufacturing' be used as an alternate term for 3DP for the purposes of pharmaceutical manufacturing processes [50].

Various 3DP technologies are briefly described here.

Thermal ink-jet printing

In this process, the printing materials are deposited on the printed product. The materials applied layer by layer in the form of droplets through small-diameter nozzles, and UV light is used to harden the 3D object. Ink-jet systems comprise two types of technologies, continuous and drop on demand printing [51,52]. Living cells are protected and maintained in an aqueous environment by more biocompatible thermal inkjet 3D printer [53,54].

Fused deposition modeling (FDM)

Hot melt extrusion (HME) based FDM, in which the materials are softened or melted by heating during the printing process [55,56]. FDM 3DP is used to manufacture delayed-release tablets without an outer enteric coating and also provides personalized doses of medicines [57]. The FDM 3DP technique, however, suffers various limitations. These include non-availability of suitable polymers because elevated temperature (~200 °C) may degrade certain polymers and drug also [58], stagnant and often partial drug release (because the drug remains trapped in the polymers) [59,60] and difficulties in evaluating the solubility of the drug and additives in the presence of polymers [61]. Only poly vinyl alcohol (PVA) and poly lactic acid (PLA) is mostly used.

Fused material is extruded as a filament or wire through a nozzle, which turns the flow on and off. It gets heated and melts the material. Extrusion require materials in semisolid form and does not require high temperature, therefore choice for polymers is quite more [58]. It moves horizontally and vertically by computer-aided manufacturing. The sacrificial material is later removed using hot water, a water jet or a solvent. Mainly used filaments are acrylonitrile butadiene styrene and polylactic acid (PLA) [62].

Selective laser sintering

A liquid binder and a powder are used in this technique. The process chamber is filled with the powder and then the binder is introduced uniformly through nozzles at a moderate pressure. The required 3D object is created by gluing the powder particles with the binder [63]. Smooth and accurate parts has been produced using fine particles, which is difficult to spread and handling [64]. Photopolymerization of powder is done in SLS using high power

laser as an energy source. SLS technology has many advantages such as, high strength, speed and chemical resistance [65].

All the methods described have limitations in terms of the technique, quality of the products and properties of the materials. A literature survey revealed that stereolithography is the only method in which the resolution is fine and thermal degradation of substances is avoided.

Stereolithography (SLA)

is the first laser-based printing technology. It was developed in 1980 by Japanese Dr, Kodama and granted the first patent for rapid prototyping and is well known in commerce as the solid freeform fabrication (SFF) process [66,67]. 3D objects are produced by SLA through the superintended solidification of a liquid resin by a photo-polymerization mechanism [68,69]. SLA is used to make different types of production parts, medical models, prototypes, patterns, computer hardware and biomaterials. The term 'SLA' was coined by Chuck Hull in 1984 and a patent was granted in 1986, but research on SLA began in the 1970s. Laser-based SLA and digital light projection are the two types of SLA [70]. In the laser-based method, the product is fabricated in a bottom-up, vector-by-vector manner using a computer-manipulated laser beam system [71] where UV light is passed through the transparent bottom of a vat containing photosensitive resin [72,73]. The stereolithographic technique has a number of unique features [74]. Its fine resolution [75] permits complex structures to be created. During the printing process, the heating is minimal and thereby thermal degradation of drugs is avoided [76]. Hence SLA is particularly useful for thermo-labile drugs [77]. The resolution and accuracy of SLA are superior to those of other techniques [78,79]. With FDM, differences between layers results in anisotropic effects and requires adjustments in the geometry of the object. Thus FDM is unsuitable for certain applications. In contrast, highly isotropic parts can be created using SLA. The integrity of the material is tightly controlled by considering a number of factors in SLA. Better patient compliance, customized formulations, modulated drug release dosage forms and deliver-on-demand medications can all be prepared using SLA [80–82]. SLA is faster than FDM and selective laser sintering (SLS) [83]. Children's of 4-11 years age has prefer 3D printed tablets on visual inspection [84]. SLA also has some limitations. The limited availability of a number of photocrosslinkable polymers is the main drawback of SLA. The available materials require recognition as safe. When the drugs are exposed to laser, they may lead to lung diseases [85]. Another disadvantage of SLA is that it is quite expensive.

Principle of stereolithography

When ultraviolet (UV) radiation is passed through a photosensitive resin, it is photopolymerized totally. This is the basic principle of SLA. Low-power UV radiation (up to 1000 mW) from a He-Cd/Nd:YVO₄ laser solidifies a thin layer of resin on the surface [86]. The platform is the main component of a SLA machine. The 3D object is formed in a bath of liquid resin in which the platform is immersed. The laser source is another important part. It is controlled by a computer. All the parts of the machine can be cleaned using a solvent after a 3D object is made. Any resinous materials on the surface can be removed using the solvent [87]. A UV oven is used to cure the cleaned and finished 3D object and with the help of CAD model [88], every layer of resin is being scanned by laser technique [89]. Pharmaceutical formulation containing higher water content when exposed to visible light

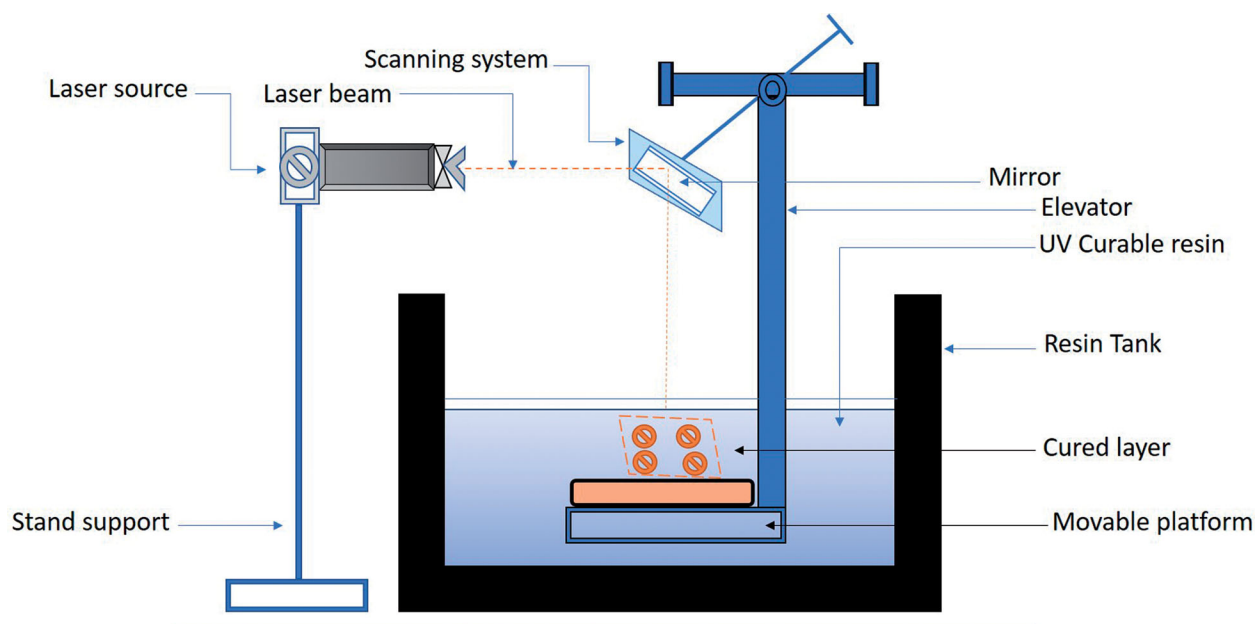


Figure 1. Stereolithographic 3D printer.

irradiation process, results pronounced effect on drug release from 27% to 95% over eight hours [90].

Working of SLA

Stereolithographic is based on the photo-polymerization in which superintended solidification of a liquid resin is executed [55]. A vessel containing the liquid resin (photopolymer) is fixed on the main (fixed) platform (Figure 1). An elevator with a movable platform, located in the vessel, is attached to the main platform. Initially, the movable platform is lifted close to the surface of the liquid resin photopolymer. After one cycle of UV laser treatment, a new photopolymerized layer is formed, and the thickness of the next layer is set by moving the platform down. The 3D object is produced by repeated laser treatments. Due to gravitational force and lateral pressure of subsequent coat, cross section may not precisely form 3D structure. Therefore supporting structure of filaments are form and help in holding the cross section. Filaments support is bring out with the help of CAD model, used on the stereolithography machine during the preparation [91]. Finally, this supports is being removed manually. The manufacturing of pharmaceutical products using SLA allows individualization of medicines. Despite the numerous medical and economic benefits, there are some technical challenges that restrict the extensive commercial use of 3DP. These challenges include the limited number of biocompatible materials in 3DP printing, the stability of active pharmaceutical ingredient, the efficiency as well as reproducibility of the methods, and the quality of the finished products. A computer interprets the information available in STL files and sends it to the 3D printer, where the data are converted into a 3D structure. The kinetics of the curing reactions depends on the scanning speed, the chemistry and the amounts of the monomer and photoinitiators [92,93].

Materials used in stereolithographic printing

The choice of photopolymer is of utmost importance in SLA [94,95]. The lack of approval of photosensitive materials by the regulatory authority (the FDA) limits the use of SLA significantly,

even though photosensitive materials are used in tissue engineering. During the last decade, a number of photocrosslinkable polymers have been developed. Poly(ethylene glycol) diacrylate (PEGDA) [73,96], poly(2-hydroxyethyl methacrylate) (pHEMA) [97], poly(ethylene glycol) dimethacrylate (PEGDMA) [98,99] and poly(propylene fumarate)/diethyl fumarate (PPF/DEF) [100,101] are examples of photocrosslinkable polymers. Biomedical materials have applications in surgical tools, hearing aids, knee joint appliances and dental appliances [102]. The multiple resins for one build showed patterning with PEG-DMA and PEG-DA with fluorescently labeled dextran, fluorescently labeled bioactive PEG or bioactive PEG in different regions of the scaffold [103]. Complex 3D scaffolds can be fabricated using photocrosslinkable poly(propylene fumarate) (PPF) [104,105], which requires reactive diluents containing significant amounts of non-degradable components. N-vinyl-2-pyrrolidone and diethyl fumarate are used as diluents to reduce the viscosity of the resin during processing [106]. Reconstruction of cranial defects in rabbits is possible because of the ability to produce controlled microstructures [89]. Trimethylene carbonate, polycaprolactone and poly(D,L-lactide) are examples of materials used commonly in tissue engineering [107,108].

The essential components of photocurable resins used in SLA are shown in Figure 2. The precursors are liquid molecules that form a solid 3D structure on exposure to light. Because of the high reactivity of acrylate-based resins, 3D structures can be built rapidly. Hence, acrylate-based resins are commonly used in SLA [46,109]. Deformity in printed part is the main disadvantage of acrylate resins. This is due to the high shrinkage of resins during printing [110]. The problem of distortion can be solved by using a combination of an acrylate resin and methacrylates. The polymerization reaction may be inhibited by a resin's sensitivity to oxygen. The shrinkage of epoxy resins is remarkably lower than that of acrylates [111,112]. An acrylate and epoxy-based resins in combination may have an accelerated curing rate and reduced shrinkage [112–114]. Photoinitiators (PIs) are the resin components that normally react with light. A PI attains an excited state ion being irradiated with radiation of the right wavelength. Xenon lamps, mercury arc lamps, LEDs or lasers used as light source. UV (190–400 nm), visible (400–700 nm) or IR (700–1000 nm) range of

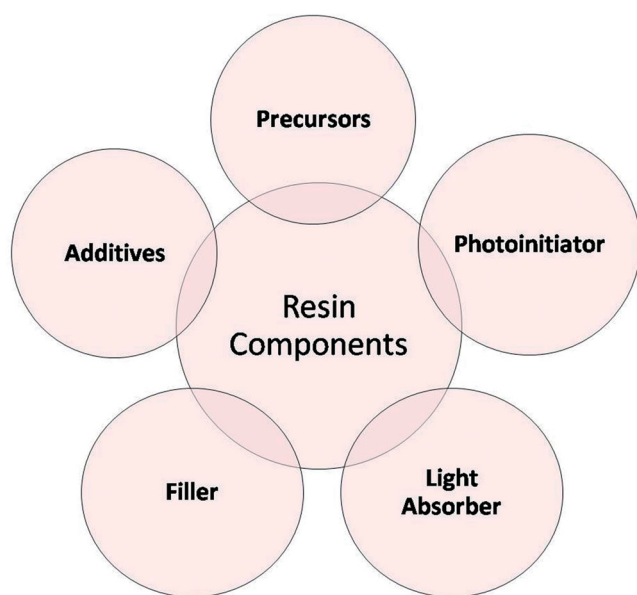


Figure 2. Components of resin for SLA.

wavelength can be used. Visible LEDs are ecofriendly and safe. Water soluble PI, Irgacure 651 has been used in the fabrication of biocompatible hydrogel scaffold [115]. The PI in the excited starts the curing reaction. A suitable photoinitiator is selected on the basis of the precursor utilized. The mechanical properties of device, reaction kinetics, cross-linking density, light dosage required and conversion to printed device depend on the type and amount of PI [116,117]. The light absorber is another material used in SLA processes. A light absorber diminishes the perception of light into the resin and thereby controls the depth to which the resin is cured [118]. The cure depth needs to be precisely defined in complex geometries to prevent unnecessary curing and loss of the features of the model [119,120]. Benzotriazole derivatives are common examples of UV light absorbers [121]. Filling resins with powder, debinding and sintering the printed part or printing the parts is the basic requirement in the fabrication of ceramic materials or metals by SLA [122,123]. In thin structures, the binder burns out easily and fills any cracks or defects that form. A high filler content is recommended for reducing the shrinkage of resins and thereby producing geometrically accurate parts [124]. Optical, thermal, mechanical and electrical properties can be further modified through the use of nano size particles in the SLA resin [125–127]. Long shelf-life (stable) slurries, rheological additives and stabilizers used during the fabrication processes increase the solid loading [128]. A high fraction of solids increases the viscosity of the slurry when the particles are small in size [122]. A high viscosity changes the flow behavior of the resin and interferes with coating mechanisms [129]. This can be overcome by using dispersants such as oligomeric surfactants [130], long-chained oleic acid [131] or phosphine oxides [132].

3DP stereolithography in pharmaceuticals

Stereolithographic 3D printers have been used in various novel and innovative projects. Distinct types of devices, models and dosage forms have been producing using SLA. Researcher used 3D printing applications in fabrication of various dosage forms are mentioned in Table 1.

Pharmaceutical applications of 3D printing technology

SLA can alter elastic silicones for soft model to high strength post cured resins [150,151]. In the field of medical device formation and drug delivery, SLA offers unique applications [152]. Some applications of the SLA 3DP technique are discussed here.

Individualized drug dosing

Today's patient suffers from more than one disease and requires a single multi-dose form of formulation [153,154]. A personalized and accurate dose is required for better compliance. An optimal multi-dose form containing a narrow therapeutics index drug can be given to a patient whose pharmacogenetic profile, age and race are known [65,155]. Fabrication of complete, effective formulations is the second important role of 3D printing technology. One active ingredient can be dispensed in one form as a result [32]. This helps increase the efficacy of the drugs and reduces adverse reactions, if any [156]. Poly(ethylene glycol) diacrylate 700 (PEGDA700) as initial material used in fabrication of patient customized tablets of atomoxetine hydrochloride by digital light processing (DLP) 3D printing technique [157] and Ghost tablets as unique prediction model as future tailored medicines that release entrapped drug without disintegrating [158]. Tailored chewable formulation containing isoleucine fabricated by 3DP offers rapid and feasible approach in hospital setting in maple sirup urine disease [159].

Modified drug release profile

A modified drug release profile requires the preparation of complex geometries containing multiple drugs of porous texture, surrounded by a modulated layer of barriers [160]. A multilayered bone implant based on a pulse release mechanism, with a distinct profile in which rifampicin and isoniazid are released alternately was prepared using 3DP technology. A very small quantity of chloramphenicol maleate could also be released at a predetermined time with perfect accuracy from a cellulose powder substrate using a 3D printing technique [155]. Problem associated with slow and incomplete release of paracetamol has been overcome by sustained released 3D printlet using hydrophilic excipients [161]. Multilayered 3D printed tablets containing four antihypertensive drugs reports, chemical interaction of drug and polymer unexpectedly [162].

Microneedles

Microstructure of microneedles delivers macromolecules through the skin (as in insulin skin delivery) more effectively than does a conventional transdermal dosage form [163]. The stereolithographic method of 3DP allows more complex and sophisticated geometries of microneedles to be fabricated. Ochoa *et al* developed a novel manufacturing process for microneedles with 9.6 μm radius tips. Sharp polymeric microneedles for vaccine delivery were manufactured using the enhanced resolution limit of the 3DP technique [164]. Microstereolithography helped fabricate microneedles through which a 5 weeks' controlled release of the anticancer dacarbazine drug was achieved. Microneedles with a cone-and-pyramid shape were fabricated using a biocompatible resin [165].

Table 1. SLA 3DP applications in pharmaceuticals.

Formulations	Specifications	Reference(s)
4-aminosalicylic (4-ASA) acid and paracetamol-loaded 3D tablets.	Different concentrations of polyethylene glycol diacrylate (PEGDA) and polyethylene glycol have been used in printing solutions	[133]
An anti-acne drug (salicylic acid)-loaded 3D model of a personalized shape nose.	With SLA, there was no drug degradation, and the resolution was higher than with FDM	[134]
A hydrogel of cross-linked polyethylene glycol diacrylate containing ibuprofen.	Because of entrapment of water, pre-wetted, drug loaded hydrogel and devices can be prepared	[135]
Tablets containing a solid dispersion of paracetamol and polyethylene glycol.	A different shape of tablets was unattainable due to powder compaction.	[136]
A mask of higher resolution was produced using SLA.	The drug loading was high, and there was insignificant degradation of salicylic acid.	[137]
Antifouling hybrid hydrogels.	A highly solvated and tough hydrogel increases the gelation rate and the elasticity of the resulting hybrid hydrogel.	[138,139]
Bone tissue engineering is the main prominence area of SLA.	–	[140]
Bone formation	Bone formation was promoted using SLA in rats with cranial defects in <i>in-vivo</i> studies.	[141]
Soft tissue	Bovine chondrocytes, flexible and soft cartilage tissues was fabricated.	[142]
Encapsulation of NIH/3T3	PEG-DMA with human chondrocytes was promoted with an inkjet printer.	[143,144]
Synthesis of novel macromers without any reactive diluents.	–	[145–147]
Polycaprolactone porous structures.	Porous structures scaffolds to release lidocaine more rapidly compared with the solid form.	[148]
Multilayered polypill with variable drug content and shape	Six drugs, paracetamol, naproxen, chloramphenicol, prednisolone and aspirin were printed with different geometries and materials	[149]

Tailored prostheses and implants

Prostheses and implants of any possible shape can be fabricated using 3DP technology. In the present context, translation of MRI images, CT scans, and X-ray images is desirable [156,160,165]. Both complex and standard surgical implants and prosthetic limbs can be prepared in less than 24 h. The Layer Wise Company fabricated spinal, maxillofacial and dental implants [160,166]. The BIOMED Research Institute, Belgium successfully implanted 3D printed mandibular prostheses [165]. Prosthetic ears were made from silver nanoparticles, silicon and chondrocytes using 3DP technology to detect electromagnetic frequencies. The fit of every model is perfect and the price is low thanks to 3DP technology. Nowadays more than 90% of the customized hearing aids are fabricated using 3D printers [156]. Revolutionary localized delivery of lidocaine HCL has been possible by 3DP indwelling bladder device [167]. A 3D printed hearing aid released antibiotics for more than two weeks and inhibits any biofilm and bacterial growth on device [168].

Anatomical models for surgical preparations

There are individual variations in the complex human anatomy. Before performing medical surgery, obtaining knowledge regarding the patient's surgical or anatomical part is important. The size and shape of a specific anatomy requires a complex surgical procedure. 3DP technology provides vital tools for making anatomical models that fit perfectly [160, 169]. Surgeons use calcified aortas manufactured using 3D printers [160]. The airways of premature infants have been fabricated using 3DP methods to evaluate aerosols [160].

Soft materials in the food industry

Traditional food preparation does not produce customized food or recipes for specific nutritional requirements. Food 3D printing

involves premixing and depositing the required nutrients in distinct layers [170]. Different customers (the elderly, pregnant or feeding mothers, children, athletes) require different proportions of carbohydrates, fats and proteins [171]. The use of 3DP to make smooth food for elderly people having difficulties in chewing and swallowing [172,173]. Recently, BeexHex, USA, a 3D printing company, prepared food for National Aeronautics and Space Administration (NASA) astronauts when they were on a mission [174]. The food-containing-drug approach will become the new path food-based pharmaceutical drug delivery systems [175].

Other pharmaceutical dosage forms

Different 3DP technologies are available for the fabricating customized [176] pharmaceutical dosage forms. Some of these dosage forms are focused on here. Accurate and tailored controlled released dosage forms have been fabricated using 3D printers [177]. Also drug can be printed on porous carrier using flexographic printers [178]. 3D printer was used to manufacture highly adjustable, affordable, small delayed-release prednisolone tablets in poly(vinyl alcohol) filaments [179]. An oral pulsatile release capsular model based on erodible hydroxypropyl cellulose was fabricated by Melocchi *et al.* using an FDM 3D printer [180]. Oral dosage forms with accurate and uniform content and excellent dosage control have been fabricated using 3DP technology [181]. A fast-disintegrating tablet in which the microstructure and surface texture are controlled was fabricated using a 3D printer [182]. A matrix tablet with zero-order drug-release characteristics in the radial direction was also manufactured using 3DP technology [183]. A biodegradable implant patch containing a high dose of fluorouracil (drug) and poly-lactic-co-glycolic acid and polycaprolactone (carrier) was fabricated using a 3DP technique for local delivery of anticancer drugs [184,185]. Tablets containing 4-aminosalicylic acid and paracetamol in a combined form were produced using stereolithography. These tablets have a customized drug-

release profile [133]. Making biodegradable patches of customized shapes for delivering drugs exactly at a tumor site is another possibility with 3DP techniques. A sustained-release patch containing an anticancer drug, 5-fluorouracil, and a blend of polycaprolactone and poly(lactide-co-glycolide) was prepared using 3DP, which had site-specific characteristics [186]. A 3D printed poly(lactic-co-glycolic acid), gelatin and chitosan scaffold loaded with anticancer drugs significantly inhibited the recurrence and growth of breast cancer and reduced drug toxicity with a sustained action [187]. Functionally characterized 3D printed chitosan based film prepared with genipin as crosslinker shown promising effect for chronic wound [188]. Two drugs in separate compartments of hollow shell suppository shell prepared by FDM 3DP become advanced model for pediatric patients [189]. 3D printed suppository molds were fabricated to cast the self supporting suppositories [190]. Gummy drug formulation (hydrogel) containing lamotrigine for pediatric patients was fabricated by 3D bioprinter with perspective of future clinical setting [191].

Conclusions

A rapid, sophisticated and highly accurate method of fabricating medical devices, biological tissues, alloys, tailored dosage forms and many more is offered by 3DP technology. Solid forms can be fabricated using the photopolymerization mechanism and photocurable resins. Customized dosage forms produced using the 3DP technique may improve patient compliance. SLA is a very promising technique. It improves the stability and resolution, and degradation of the materials is avoided. The SLA 3DP technology offers significant potential benefits in the manufacture of pharmaceuticals, medical devices and many other devices. 3DP technology is an innovative scanning and printing technology that provides hope that most of the present limitations can be overcome. It is considered one of the most hopeful areas of medicine.

Disclosure statement

No potential conflict of interest was reported by the author(s).

Funding

The author(s) reported there is no funding associated with the work featured in this article.

ORCID

Subhash Deshmane  <http://orcid.org/0000-0002-0563-4075>

Hitendra Mahajan  <http://orcid.org/0000-0001-6648-144X>

References

- [1] Campbell TW, C, Ivanova O, Garrett B. Could 3d printing change the world? Technologies and implications of additive manufacturing. Washington (DC): Atlantic Council; 2012. p. 1–14.
- [2] Hwang HH, Zhu W, Victorine G, et al. 3D-printing of functional biomedical microdevices via light- and Extrusion-Based approaches. *Small Methods*. 2018;2(2):1700277.
- [3] Peterson GI, Larsen MB, Ganter MA, et al. 3D-printed mechanochromic materials. *ACS Appl Mater Interfaces*. 2015;7(1):577–583.
- [4] Anciaux SK, Geiger M, Bowser MT. 3D printed micro free-flow electrophoresis device. *Anal Chem*. 2016;88(15):7675–7682.
- [5] Wang X, Ao Q, Tian X, et al. 3D bioprinting technologies for hard tissue and organ engineering. *Materials*. 2016;9(10):802.
- [6] Noorani R. 3D printing: technology, applications, and selection. 1st ed. Boca Raton (FL): CRC Press; 2017.
- [7] Randolph SA. 3D printing: what are the hazards? *Workplace Health Saf*. 2018;66(3):164–164.
- [8] Kim J, Kong JS, Han W, et al. 3D cell printing of tissue/organ-mimicking constructs for therapeutic and drug testing applications. *IJMS*. 2020;21(20):7757.
- [9] Gong H, Woolley AT, Nordin GP. High density 3D printed microfluidic valves, pumps, and multiplexers. *Lab Chip*. 2016;16(13):2450–2458.
- [10] Macdonald NP, Cabot JM, Smejkal P, et al. Comparing microfluidic performance of three-dimensional (3D) printing platforms. *Anal Chem*. 2017;89(7):3858–3866.
- [11] Johnson AR, Caudill CL, Tumbleston JR, et al. Single-step fabrication of computationally designed microneedles by continuous liquid interface production. *PLoS One*. 2016;11(9):e0162518.
- [12] Chrzan R, Miechowicz S, Urbanik A, et al. Individually fitted hearing aid device manufactured using rapid prototyping based on ear CT. A case report. *Neuroradiol J*. 2009;22(2):209–214.
- [13] Dhir V, Itoi T, Fockens P, et al. Novel ex vivo model for hands-on teaching of and training in EUS-guided biliary drainage: creation of "Mumbai EUS" stereolithography/3D printing bile duct prototype (with videos). *Gastrointest Endosc*. 2015;81(2):440–446.
- [14] Ventola CL. Medical applications for 3D printing: current and projected uses. *P T*. 2014;39(10):704–711.
- [15] Tunnicliffe A. The past, present and future of 3D printing in the pharmaceutical industry. 2020. <https://www.ns-healthcare.com/analysis/additive-manufacturing-3d-printing/>
- [16] Maulvi FA, Shah MJ, Solanki BS, et al. Application of 3D printing technology in the development of novel drug delivery systems. *Int J Drug Dev Res*. 2017;9:44–49. <https://www.ijddr.in/drug-development/application-of-3d-printing-technology-in-the-development-of-novel-drug-delivery-systems.php?aid=18776>
- [17] Park JH, Jung JW, Kang H-W, et al. Indirect three-dimensional printing of synthetic polymer scaffold based on thermal molding process. *Biofabrication*. 2014;6(2):025003.
- [18] Pravin S, Sudhir A. Integration of 3D printing with dosage forms: a new perspective for modern healthcare. *Biomed Pharmacother*. 2018; 107:146–154.
- [19] Prasad LK, Smyth H. 3D printing technologies for drug delivery: a review. *Drug Dev Ind Pharm*. 2016;42(7):1019–1031.
- [20] First 3D-printed pill. *Nat Biotechnol*. 2015;33:1014–1014.
- [21] Ursan ID, Chiu L, Pierce A. Three-dimensional drug printing: a structured review. *J Am Pharm Assoc*. 2013;53(2):136–144.
- [22] O Oyewumi M. 3D printing technology in pharmaceutical drug delivery: prospects and challenges. *J Biomol Res Ther*. 2015;04(04):1–3.
- [23] Larush L, Kaner I, Fluksman A, et al. 3D printing of responsive hydrogels for drug-delivery systems. *J 3D Print Med*. 2017;1(4):219–229.

- [24] Baker D. Artificial intelligence: the future landscape of genomic medical diagnosis: dataset in Silico artificial intelligent clinical information, and machine learning systems. In: Lambert CG, Baker DJ, Patrinos GP, editors. Human genome informatics. San Diego: Academic Press; 2018. p. 223–267.
- [25] Popova M, Isayev O, Tropsha A. Deep reinforcement learning for de novo drug design. *Sci Adv.* 2018;4:eap7885.
- [26] Han R, Xiong H, Ye Z, et al. Predicting physical stability of solid dispersions by machine learning techniques. *J Control Release.* 2019;311–312:16–25.
- [27] Harrer S, Shah P, Antony B, et al. Artificial intelligence for clinical trial design. *Trends Pharmacol Sci.* 2019;40(8): 577–591.
- [28] Madzarevic M, Medarevic D, Vulovic A, et al. Optimization and prediction of ibuprofen release from 3D DLP printlets using artificial neural networks. *Pharmaceutics.* 2019;11: 544.
- [29] Elbadawi M, Muñiz Castro B, Gavins FKH, et al. M3DISEEN: a novel machine learning approach for predicting the 3D printability of medicines. *Int J Pharm.* 2020;590:119837.
- [30] Elbadawi M, McCoubrey LE, Gavins FKH, et al. Harnessing artificial intelligence for the next generation of 3D printed medicines. *Adv Drug Deliv Rev.* 2021;175:113805.
- [31] Stanojević G, Medarević D, Adamov I, et al. Tailoring atomoxetine release rate from DLP 3D-printed tablets using artificial neural networks: influence of tablet thickness and drug loading. *Molecules.* 2020;26(1):111.
- [32] Khaled SA, Burley JC, Alexander MR, et al. 3D printing of tablets containing multiple drugs with defined release profiles. *Int J Pharm.* 2015;494(2):643–650.
- [33] Goyanes A, Robles Martinez P, Buanz A, et al. Effect of geometry on drug release from 3D printed tablets. *Int J Pharm.* 2015;494(2):657–663.
- [34] Awari GK, Thorat CS, Ambade V, et al. Additive manufacturing and 3D printing technology. 1st ed. Boca Raton (FL): CRC Press/Taylor & Francis Group, LLC; 2021.
- [35] Łaszcz M, Witkowska A. Studies of phase transitions in the aripiprazole solid dosage form. *J Pharm Biomed Anal.* 2016;117:298–303.
- [36] Water JJ, Bohr A, Boetker J, et al. Three-dimensional printing of drug-eluting implants: preparation of an antimicrobial polylactide feedstock material. *J Pharm Sci.* 2015; 104(3):1099–1107.
- [37] Yu DG, Zhu LM, Branford-White CJ, et al. Three-dimensional printing in pharmaceuticals: Promises and problems. *J Pharm Sci.* 2008;97(9):3666–3690.
- [38] Bakhatwar M, Chikkala Vnvk SR. Three-dimensional printing in pharmaceutical technology – an overview of innovations. *Innov Pharm Pharmacother.* 2019;7:67–71.
- [39] Zheng F, Huang S. Advances in study on three-dimensional printing in pharmaceuticals. *Chinese Herb Med.* 2016; 8(2):121–125.
- [40] Aimar A, Palermo A, Innocenti B. The role of 3D printing in medical applications: a state of the art. *J Healthc Eng.* 2019;2019:1–10.
- [41] Khan FA, Narasimhan K, Swathi CSV, et al. 3D printing technology in customized drug delivery system: current state of the art, prospective and the challenges. *Curr Pharm Des.* 2018;24(42):5049–5061.
- [42] Zhu X, Li H, Huang L, et al. 3D printing promotes the development of drugs. *Biomed Pharmacother.* 2020;131: 110644.
- [43] Ameeruzzafar Alruwaili NK, Rizwanullah M, et al. 3D printing technology in design of pharmaceutical products. *Curr Pharm Des.* 2019;24:5009–5018.
- [44] Mathew E, Pitzanti G, Larrañeta E, et al. 3D printing of pharmaceuticals and drug delivery devices. *Pharmaceutics.* 2020;12(3):266.
- [45] Trenfield SB. Innovations in 3D printed pharmaceuticals. *ONdrugDelivery Magazine.* 2020;109:45–49.
- [46] Ligon SC, Liska R, Stampfl J, et al. Polymers for 3D printing and customized additive manufacturing. *Chem Rev.* 2017; 117(15):10212–10290.
- [47] Kim GB, Lee S, Kim H, et al. Three-dimensional printing: basic principles and applications in medicine and radiology. *Korean J Radiol.* 2016;17(2):182–197.
- [48] Hodgdon T, Danrad R, Patel MJ, et al. Logistics of three-dimensional printing: primer for radiologists. *Acad Radiol.* 2018;25(1):40–51.
- [49] Chua CK, Leong KF, An J. Introduction to rapid prototyping of biomaterials. In: Narayan R, editor. Rapid prototyping of biomaterials. San Diego: Elsevier; 2014. p. 1–15.
- [50] Tofail SAM, Koumoulos EP, Bandyopadhyay A, et al. Additive manufacturing: scientific and technological challenges, market uptake and opportunities. *Mater Today.* 2018;21(1):22–37.
- [51] Goole J, Amighi K. 3D printing in pharmaceuticals: a new tool for designing customized drug delivery systems. *Int J Pharm.* 2016;499(1–2):376–394.
- [52] Lau G-K, Shrestha M. Ink-jet printing of micro-electromechanical systems (MEMS). *Micromachines.* 2017;8(6):194.
- [53] Cui X, Boland T, D’Lima D, et al. Thermal inkjet printing in tissue engineering and regenerative medicine. *Recent Pat Drug Deliv Formul.* 2012;6(2):149–155.
- [54] Gardin C, Ferroni L, Latremouille C, et al. Recent applications of three dimensional printing in cardiovascular medicine. *Cells.* 2020;9(3):742.
- [55] He D, Han F, Wang Z, et al. A review of 3D printing via fused deposition modeling in pharmaceuticals. *Yao Xue Xue Bao.* 2016;51:1659–1665.
- [56] Long J, Gholizadeh H, Lu J, et al. Application of fused deposition modelling (FDM) method of 3D printing in drug delivery. *Curr Pharm Des.* 2017;23(3):433–439.
- [57] Goyanes A, Fina F, Martorana A, et al. Development of modified release 3D printed tablets (printlets) with pharmaceutical excipients using additive manufacturing. *Int J Pharm.* 2017;527(1–2):21–30.
- [58] Alhnan MA, Okwuosa TC, Sadia M, et al. Emergence of 3D printed dosage forms: opportunities and challenges. *Pharm Res.* 2016;33(8):1817–1832.
- [59] Lim SH, Chia SMY, Kang L, et al. Three-dimensional printing of carbamazepine sustained-release scaffold. *J Pharm Sci.* 2016;105(7):2155–2163.
- [60] Goyanes A, Chang H, Sedough D, et al. Fabrication of controlled-release budesonide tablets via desktop (FDM) 3D printing. *Int J Pharm.* 2015;496(2):414–420.
- [61] Gumaste SG, Gupta SS, Serajuddin ATM. Investigation of polymer-surfactant and polymer-drug-surfactant miscibility for solid dispersion. *AAPS J.* 2016;18(5):1131–1143.
- [62] Gioumouxouzis CI, Baklavaridis A, Katsamenis OL, et al. A 3D printed bilayer oral solid dosage form combining metformin for prolonged and glimepiride for immediate drug delivery. *Eur J Pharm Sci.* 2018;120:40–52.

- [63] Fina F, Madla CM, Goyanes A, et al. Fabricating 3D printed orally disintegrating printlets using selective laser sintering. *Int J Pharm.* 2018;541(1–2):101–107.
- [64] Zhou Y. The recent development and applications of fluidic channels by 3D printing. *J Biomed Sci.* 2017;24(1):80.
- [65] Park BJ, Choi HJ, Moon SJ, et al. Pharmaceutical applications of 3D printing technology: current understanding and future perspectives. *J Pharm Investig.* 2018;49:575–585.
- [66] Hull CW, Arcadia C. Apparatus for production of three-dimensional objects by stereolithography. US Patent, 1984.
- [67] Lonjon C. The history of 3d printer: from rapid prototyping to additive fabrication. <https://www.sculpteo.com/blog/2017/03/01/whos-behind-the-three-main-3d-printing-technologies/>.
- [68] Chia HN, Wu BM. Recent advances in 3D printing of biomaterials. *J Biol Eng.* 2015;9:4.
- [69] Huang B, Wu B, Han L, et al. Preparation of a novel cationic photosensitive resin (3D-SLR01) for stereolithography 3D printing and determination of its some properties. *J Wuhan Univ Technol-Mat Sci Edit.* 2019;34(4):761–768.
- [70] Robles Martinez P, Basit AW, Gaisford S. The history, developments and opportunities of stereolithography. In: *AAPS advances in the pharmaceutical sciences series*. New York: Springer Verlag; 2012. p. 55–79.
- [71] Wang Z, Abdulla R, Parker B, et al. A simple and high-resolution stereolithography-based 3D bioprinting system using visible light crosslinkable bioinks. *Biofabrication.* 2015;7(4):045009.
- [72] ASTM 52921. Standard terminology for additive manufacturing — coordinate systems and test methodologies. Geneva: ASTM Int; 2019.
- [73] Chan V, Zorlutuna P, Jeong JH, et al. Three-dimensional photopatterning of hydrogels using stereolithography for long-term cell encapsulation. *Lab Chip.* 2010;10(16):2062–2070.
- [74] Curti C, Kirby DJ, Russell CA. Stereolithography apparatus evolution: enhancing throughput and efficiency of pharmaceutical formulation development. *Pharmaceutics.* 2021;13(5):616.
- [75] Lim SH, Kathuria H, Bin AM, et al. High resolution photopolymer for 3D printing of personalised microneedle for transdermal delivery of anti-wrinkle small peptide. *J Control Release.* 2020;329:907–918.
- [76] Goyanes A, Buanz ABM, Hatton GB, et al. 3D printing of modified-release aminosalicylate (4-ASA and 5-ASA) tablets. *Eur J Pharm Biopharm.* 2015;89:157–162.
- [77] Konta A, García-Piña M, Serrano D. Personalised 3D printed medicines: which techniques and polymers are more successful? *Bioengineering.* 2017;4(4):79.
- [78] Melchels FPW, Feijen J, Grijpma DW. A review on stereolithography and its applications in biomedical engineering. *Biomaterials.* 2010;31(24):6121–6130.
- [79] Gardan J. Additive manufacturing technologies: state of the art and trends. *Int J Prod Res.* 2016;54(10):3118–3132.
- [80] Norman J, Madurawe RD, Moore CMV, et al. A new chapter in pharmaceutical manufacturing: 3D-printed drug products. *Adv Drug Deliv Rev.* 2017;108:39–50.
- [81] Trenfield SJ, Madla CM, Basit AW, et al. The shape of things to come: emerging applications of 3D printing in healthcare. In: *AAPS advances in the pharmaceutical sciences series*. New York: Springer Verlag; 2012. p. 1–19.
- [82] Osouli-Bostanabad K, Adibkia K. Made-on-demand, complex and personalized 3D-printed drug products. *Bioimpacts.* 2018;8(2):77–79.
- [83] Vitale A, Cabral J. Frontal conversion and uniformity in 3D printing by photopolymerisation. *Materials.* 2016;9(9):760.
- [84] Januskaite P, Xu X, Ranmal SR, et al. I spy with my little eye: a paediatric visual preferences survey of 3D printed tablets. *Pharmaceutics.* 2020;12(11):1100.
- [85] Rattanakit P, Moulton SE, Santiago KS, et al. Extrusion printed polymer structures: a facile and versatile approach to tailored drug delivery platforms. *Int J Pharm.* 2012;422(1–2):254–263.
- [86] Stereolithography-ODM | 3D systems. [cited 2021 Jan 8]. <https://www.3dsystems.com/on-demand-manufacturing/stereolithography-sla>.
- [87] Zhang X, Jiang X, Sun C. Micro-stereolithography of polymeric and ceramic microstructures. *Sensors Actuators A Phys.* 1999;77(2):149–156.
- [88] US4575330A – Apparatus for production of three-dimensional objects by stereolithography - Google Patents. [cited 2021 Jan 31]. <https://patents.google.com/patent/US4575330A/en>.
- [89] Salonitis K, Tsoukantas G, Stavropoulos P, et al. A critical review of stereolithography process modeling. In: Bártolo P, editor. *Virtual modelling and rapid manufacturing – advanced research in virtual and rapid prototyping*. London; New York: Taylor & Francis; 2003.
- [90] Madžarević M, Ibrić S. Evaluation of exposure time and visible light irradiation in LCD 3D printing of ibuprofen extended release tablets. *Eur J Pharm Sci.* 2021;158:105688.
- [91] Venuvinod PK, Ma W. Stereolithography (SL). In: *Rapid prototyping*. Boston (MA): Springer US; 2004. p. 195–244.
- [92] Heller C, Schwentenwein M, Russmueller G, et al. Vinyl esters: low cytotoxicity monomers for the fabrication of biocompatible 3D scaffolds by lithography based additive manufacturing. *J Polym Sci A Polym Chem.* 2009;47(24):6941–6954.
- [93] Patel DK, Sakhaei AH, Layani M, et al. Highly stretchable and UV curable elastomers for digital light processing based 3D printing. *Adv Mater.* 2017;29(15):1606000.
- [94] Noorani R. Materials for 3D printing. In: Noorani R, editor. *3D printing*. Boca Raton (FL): CRC Press; 2017. p. 81–98.
- [95] Choi J-W, Kim H-C, Wicker R. Multi-material stereolithography. *J Mater Process Technol.* 2011;211(3):318–328.
- [96] Vehse M, Petersen S, Sternberg K, et al. Drug delivery from poly(ethylene glycol) diacrylate scaffolds produced by DLC based micro-stereolithography. *Macromol Symp.* 2014;346(1):43–47.
- [97] Hanson Shepherd JN, Parker ST, Shepherd RF, et al. 3D microperiodic hydrogel scaffolds for robust neuronal cultures. *Adv Funct Mater.* 2011;21(1):46–46.
- [98] Arcaute K, Mann BK, Wicker RB. Stereolithography of three-dimensional bioactive poly(ethylene glycol) constructs with encapsulated cells. *Ann Biomed Eng.* 2006;34(9):1429–1441.
- [99] Dhariwala B, Hunt E, Boland T. Rapid prototyping of tissue-engineering constructs, using photopolymerizable hydrogels and stereolithography. *Tissue Eng.* 2004;10(9–10):1316–1322.
- [100] Fisher JP, Dean D, Mikos AG. Photocrosslinking characteristics and mechanical properties of diethyl fumarate/poly

- (propylene fumarate) biomaterials. *Biomaterials*. 2002; 23(22):4333–4343.
- [101] Trachtenberg JE, Placone JK, Smith BT, et al. Extrusion-based 3D printing of poly(propylene fumarate) scaffolds with hydroxyapatite gradients. *J Biomater Sci Polym Ed*. 2017;28(6):532–554.
- [102] Tappa K, Jammalamadaka U. Novel biomaterials used in medical 3D printing techniques. *JFB*. 2018;9(1):17.
- [103] Arcaute K, Mann B, Wicker R. Stereolithography of spatially controlled multi-material bioactive poly(ethylene glycol) scaffolds. *Acta Biomater*. 2010;6(3):1047–1054.
- [104] Lee K-W, Wang S, Fox BC, et al. Poly(propylene fumarate) bone tissue engineering scaffold fabrication using stereolithography: effects of resin formulations and laser parameters. *Biomacromolecules*. 2007;8(4):1077–1084.
- [105] Choi J-W, Wicker R, Lee S-H, et al. Fabrication of 3D biocompatible/biodegradable micro-scaffolds using dynamic mask projection microstereolithography. *J Mater Process Technol*. 2009;209(15-16):5494–5503.
- [106] Jansen J, Melchels FPW, Grijpma DW, et al. Fumaric acid monoethyl ester-functionalized poly(D,L-lactide)/N-vinyl-2-pyrrolidone resins for the preparation of tissue engineering scaffolds by stereolithography. *Biomacromolecules*. 2009;10(2):214–220.
- [107] Skoog SA, Goering PL, Narayan RJ. Stereolithography in tissue engineering. *J Mater Sci Mater Med*. 2014;25(3):845–856.
- [108] Ronca A, Ambrosio L, Grijpma DW. Preparation of designed poly(d,l-lactide)/nanosized hydroxyapatite composite structures by stereolithography. *Acta Biomater*. 2013;9(4):5989–5996.
- [109] Stampfl J, Baudis S, Heller C, et al. Photopolymers with tunable mechanical properties processed by laser-based high-resolution stereolithography. *J Micromech Microeng*. 2008;18(12):125014.
- [110] Murphy EJ, Ansel RK. Method of forming a three-dimensional object by stereolithography and composition therefore. US07429568, US, 1989.
- [111] Esposito Corcione C, Greco A, Maffezzoli A. Photopolymerization kinetics of an epoxy-based resin for stereolithography. *J Appl Polym Sci*. 2004;92(6):3484–3491.
- [112] Lee TY, Carioscia J, Smith Z, et al. Thiol – allyl ether – methacrylate ternary systems. Evolution mechanism of Polymerization-Induced shrinkage stress and mechanical properties. *Macromolecules*. 2007;40(5):1473–1479.
- [113] Zhiwei G, Jianhua M, Shuhuai H, et al. Development of a hybrid photopolymer for stereolithography. *J Wuhan Univ Technol-Mat Sci Edit*. 2006;21(1):99–101.
- [114] Oesterreicher A, Wiener J, Roth M, et al. Tough and degradable photopolymers derived from alkyne monomers for 3D printing of biomedical materials. *Polym Chem*. 2016;7(32):5169–5180.
- [115] Bagheri A, Jin J. Photopolymerization in 3D printing. *ACS Appl Polym Mater*. 2019;1(4):593–611.
- [116] Badev A, Abouliatim Y, Chartier T, et al. Photopolymerization kinetics of a polyether acrylate in the presence of ceramic fillers used in stereolithography. *J Photochem Photobiol A Chem*. 2011;222(1):117–122.
- [117] Bail R, Patel A, Yang H, et al. The effect of a type I photoinitiator on cure kinetics and cell toxicity in Projection-Microstereolithography. *Procedia CIRP*. 2013;5:222–225.
- [118] Han L-H, Mapili G, Chen S, et al. Projection microfabrication of three-dimensional scaffolds for tissue engineering. *J Manuf Sci Eng*. 2008;130:021005.
- [119] Choi J, Wicker RB, Cho S, et al. Cure depth control for complex 3D microstructure fabrication in dynamic mask projection microstereolithography. *Rapid Prototyp J*. 2009; 15(1):59–70.
- [120] Sun C, Fang N, Wu DM, et al. Projection micro-stereolithography using digital micro-mirror dynamic mask. *Sensors Actuators A Phys*. 2005;121(1):113–120.
- [121] Bail R, Hong JY, Chin BD. Effect of a red-shifted benzotriazole UV absorber on curing depth and kinetics in visible light initiated photopolymer resins for 3D printing. *J Ind Eng Chem*. 2016;38:141–145.
- [122] Bartolo PJ, Gaspar J. Metal filled resin for stereolithography metal part. *CIRP Ann*. 2008;57(1):235–238.
- [123] Halloran JW. Ceramic stereolithography: additive manufacturing for ceramics by photopolymerization. *Annu Rev Mater Res*. 2016;46(1):19–40.
- [124] Hinczewski C, Corbel S, Chartier T. Ceramic suspensions suitable for stereolithography. *J Eur Ceram Soc*. 1998; 18(6):583–590.
- [125] Farahani RD, Dubé M, Therriault D. Three-dimensional printing of multifunctional nanocomposites: manufacturing techniques and applications. *Adv Mater*. 2016;28(28): 5794–5821.
- [126] Lin D, Jin S, Zhang F, et al. 3D stereolithography printing of graphene oxide reinforced complex architectures. *Nanotechnology*. 2015;26(43):434003.
- [127] Credi C, Fiorese A, Tironi M, et al. 3D printing of cantilever-type microstructures by stereolithography of ferromagnetic photopolymers. *ACS Appl Mater Interfaces*. 2016;8(39):26332–26342.
- [128] De Hazan Y, Heinecke J, Weber A, et al. High solids loading ceramic colloidal dispersions in UV curable media via comb-polyelectrolyte surfactants. *J Colloid Interface Sci*. 2009;337(1):66–74.
- [129] Huang Y-M, Jiang C-P. On-line force monitoring of platform ascending rapid prototyping system. *J Mater Process Technol*. 2005;159(2):257–264.
- [130] Teng WD, Edirisinghe MJ, Evans JRG. Optimization of dispersion and viscosity of a ceramic jet printing ink. *J Am Ceram Soc*. 2005;80(2):486–494.
- [131] Li K, Zhao Z. The effect of the surfactants on the formulation of UV-curable SLA alumina suspension. *Ceram Int*. 2017;43(6):4761–4767.
- [132] Goswami A, K A, Balashanmugam N, et al. Optimization of rheological properties of photopolymerizable alumina suspensions for ceramic microstereolithography. *Ceram Int*. 2014;40(2):3655–3665.
- [133] Wang J, Goyanes A, Gaisford S, et al. Stereolithographic (SLA) 3D printing of oral modified-release dosage forms. *Int J Pharm*. 2016;503(1–2):207–212.
- [134] Goyanes A, Det-Amornrat U, Wang J, et al. 3D scanning and 3D printing as innovative technologies for fabricating personalized topical drug delivery systems. *J Control Release*. 2016;234:41–48.
- [135] Martinez PR, Goyanes A, Basit AW, et al. Fabrication of drug-loaded hydrogels with stereolithographic 3D printing. *Int J Pharm*. 2017;532(1):313–317.
- [136] Martinez PR, Goyanes A, Basit AW, et al. Influence of geometry on the drug release profiles of

- stereolithographic (SLA) 3D-Printed tablets. *AAPS PharmSciTech*. 2018;19(8):3355–3361.
- [137] Ulery BD, Nair LS, Laurencin CT. Biomedical applications of biodegradable polymers. *J Polym Sci B Polym Phys*. 2011;49(12):832–864.
- [138] Pan W, Wallin TJ, Odent J, et al. Optical stereolithography of antifouling zwitterionic hydrogels. *J Mater Chem B*. 2019;7(17):2855–2864.
- [139] Elomaa L, Pan C-C, Shanjani Y, et al. Three-dimensional fabrication of cell-laden biodegradable poly(ethylene glycol-co-depsipeptide) hydrogels by visible light stereolithography. *J Mater Chem B*. 2015;3(42):8348–8358.
- [140] Kim K, Yeatts A, Dean D, et al. Stereolithographic bone scaffold design parameters: osteogenic differentiation and signal expression. *Tissue Eng Part B Rev*. 2010;16(5):523–539.
- [141] Schüller-Ravoo S, Teixeira SM, Feijen J, et al. Flexible and elastic scaffolds for cartilage tissue engineering prepared by stereolithography using poly(trimethylene carbonate)-based resins. *Macromol Biosci*. 2013;13(12):1711–1719.
- [142] Lee JW, Kang KS, Lee SH, et al. Bone regeneration using a microstereolithography-produced customized poly(propylene fumarate)/diethyl fumarate photopolymer 3D scaffold incorporating BMP-2 loaded PLGA microspheres. *Biomaterials*. 2011;32(3):744–752.
- [143] Bajaj P, Marchwiany D, Duarte C, et al. Patterned three-dimensional encapsulation of embryonic stem cells using dielectrophoresis and stereolithography. *Adv Healthc Mater*. 2013;2(3):450–458.
- [144] Cui X, Breitenkamp K, Finn MG, et al. Direct human cartilage repair using three-dimensional bioprinting technology. *Tissue Eng Part A*. 2012;18(11–12):1304–1312.
- [145] Elomaa L, Teixeira S, Hakala R, et al. Preparation of poly(ϵ -caprolactone)-based tissue engineering scaffolds by stereolithography. *Acta Biomater*. 2011;7(11):3850–3856.
- [146] Melchels FPW, Feijen J, Grijpma DW. A poly(D,L-lactide) resin for the preparation of tissue engineering scaffolds by stereolithography. *Biomaterials*. 2009;30(23–24):3801–3809.
- [147] Seck TM, Melchels FPW, Feijen J, et al. Designed biodegradable hydrogel structures prepared by stereolithography using poly(ethylene glycol)/poly(D,L-lactide)-based resins. *J Control Release*. 2010;148(1):34–41.
- [148] Asikainen S, van Bochove B, Seppälä JV. Drug-releasing biopolymeric structures manufactured via stereolithography. *Biomed Phys Eng Express*. 2019;5(2):025008.
- [149] Robles-Martinez P, Xu X, Trenfield SJ, et al. 3D printing of a multi-layered polypill containing six drugs using a novel stereolithographic method. *Pharmaceutics*. 2019;11(6):274.
- [150] Thrasher CJ, Schwartz JJ, Boydston AJ. Modular elastomer photoresins for digital light processing additive manufacturing. *ACS Appl Mater Interfaces*. 2017;9(45):39708–39716.
- [151] Kuang X, Zhao Z, Chen K, et al. High-speed 3D printing of high-performance thermosetting polymers via two-stage curing. *Macromol Rapid Commun*. 2018;39(7):1700809.
- [152] Xu X, Awad A, Robles-Martinez P, et al. Vat photopolymerization 3D printing for advanced drug delivery and medical device applications. *J Control Release*. 2021;329:743–757.
- [153] Gu Y, Chen X, Lee J-H, et al. Inkjet printed antibiotic- and calcium-eluting bioresorbable nanocomposite micropatterns for orthopedic implants. *Acta Biomater*. 2012;8(1):424–431.
- [154] Liang K, Carmone S, Brambilla D, et al. 3D printing of a wearable personalized oral delivery device: a first-in-human study. *Sci Adv*. 2018;4(5):eaat2544.
- [155] Ozbolat IT, Yu Y. Bioprinting toward organ fabrication: challenges and future trends. *IEEE Trans Biomed Eng*. 2013;60(3):691–699.
- [156] Schubert C, Van Langeveld MC, Donoso LA. Innovations in 3D printing: a 3D overview from optics to organs. *Br J Ophthalmol*. 2014;98(2):159–161.
- [157] Krkobabić M, Medarević D, Pešić N, et al. Digital light processing (DLP) 3D printing of atomoxetine hydrochloride tablets using photoreactive suspensions. *Pharmaceutics*. 2020;12(9):833–817.
- [158] Tagami T, Morimura C, Ozeki T. Effective and simple prediction model of drug release from “ghost tablets” fabricated using a digital light projection-type 3D printer. *Int J Pharm*. 2021;604:120721.
- [159] Goyanes A, Madla CM, Umerji A, et al. Automated therapy preparation of isoleucine formulations using 3D printing for the treatment of MSUD: first single-centre, prospective, crossover study in patients. *Int J Pharm*. 2019;567:118497.
- [160] Lipson H. New world of 3-D printing offers “completely new ways of thinking”: Q&A with author, engineer, and 3-D printing expert Hod Lipson. *IEEE Pulse*. 2013;4(6):12–14.
- [161] Krkobabić M, Medarević D, Cvijić S, et al. Hydrophilic excipients in digital light processing (DLP) printing of sustained release tablets: impact on internal structure and drug dissolution rate. *Int J Pharm*. 2019;572:118790.
- [162] Xu X, Robles-Martinez P, Madla CM, et al. Stereolithography (SLA) 3D printing of an antihypertensive polyprintlet: case study of an unexpected photopolymer-drug reaction. *Addit Manuf*. 2020;33:101071.
- [163] Pere CPP, Economidou SN, Lall G, et al. 3D printed micro-needles for insulin skin delivery. *Int J Pharm*. 2018;544(2):425–432.
- [164] Ochoa M, Zhou J, Rahimi R, et al. Rapid 3D-print-and-shrink fabrication of biodegradable microneedles with complex geometries. 2015 Transducers – 2015 18th International Conference on Solid-State Sensors, Actuators and Microsystems, TRANSDUCERS. Anchorage, AK, 2015. p. 1251–1254.
- [165] Lu Y, Mantha SN, Crowder DC, et al. Microstereolithography and characterization of poly(propylene fumarate)-based drug-loaded microneedle arrays. *Biofabrication*. 2015;7(4):045001.
- [166] Miyazaki T, Hotta Y, Kunii J, et al. A review of dental CAD/CAM: current status and future perspectives from 20 years of experience. *Dent Mater J*. 2009;28(1):44–56.
- [167] Xu X, Goyanes A, Trenfield SJ, et al. Stereolithography (SLA) 3D printing of a bladder device for intravesical drug delivery. *Mater Sci Eng C Mater Biol Appl*. 2021;120:111773.
- [168] Vivero-Lopez M, Xu X, Muras A, et al. Anti-biofilm multi drug-loaded 3D printed hearing aids. *Mater Sci Eng C Mater Biol Appl*. 2021;119:111606.
- [169] Klein GT, Lu Y, Wang MY. 3D printing and neurosurgery-ready for prime time? *World Neurosurg*. 2013;80(3–4):233–235.
- [170] Sun J, Peng Z, Zhou W, et al. A review on 3D printing for customized food fabrication. *Procedia Manuf*. 2015;1:308–319.
- [171] Nathan GL. The future: creating novel foods using 3D printing. <https://www.foodnavigator.com/Article/2010/12/>

- 23/Looking-to-the-future-Creating-novel-foods-using-3D-printing. 2012.
- [172] Michail N. Biozoon's 3D printed smooth foods target Europe's elderly, <https://www.foodnavigator.com/Article/2016/09/26/Biozoon-s-3D-printed-smooth-foods-target-Europe-s-elderly>. 2016.
- [173] Serizawa R, Shitara M, Gong J, et al. 3D jet printer of edible gels for food creation. In: Goulbourne NC, Naguib HE, editors. Behavior and mechanics of multifunctional materials and composites. Bellingham: SPIE; 2015. p. 90580A.
- [174] Gohd C. NASA astronauts can now 3D-print pizzas in space. <https://futurism.com/nasa-astronauts-can-now-3d-print-pizzas-in-space>. 2017.
- [175] Vithani K, Goyanes A, Jannin V, et al. An overview of 3D printing technologies for soft materials and potential opportunities for lipid-based drug delivery systems. *Pharm Res*. 2018;36(1):4.
- [176] Pandey M, Choudhury H, Fern JLC, et al. 3D printing for oral drug delivery: a new tool to customize drug delivery. *Drug Deliv Transl Res*. 2020;10(4):986–1001.
- [177] Ali A, Ahmad U, Akhtar J. 3D printing in pharmaceutical sector: an overview. In: Pharmaceutical formulation design – recent practices. London: IntechOpen; 2020.
- [178] Genina N, Fors D, Vakili H, et al. Tailoring controlled-release oral dosage forms by combining inkjet and flexographic printing techniques. *Eur J Pharm Sci*. 2012;47(3):615–623.
- [179] Skowrya J, Pietrzak K, Alhnan MA. Fabrication of extended-release patient-tailored prednisolone tablets via fused deposition modelling (FDM) 3D printing. *Eur J Pharm Sci*. 2015;68:11–17.
- [180] Melocchi A, Parietti F, Loreti G, et al. 3D printing by fused deposition modeling (FDM) of a swellable/erodible capsular device for oral pulsatile release of drugs. *J Drug Deliv Sci Technol*. 2015;30:360–367.
- [181] Katstra WE, Palazzolo RD, Rowe CW, et al. Oral dosage forms fabricated by three dimensional printing(TM). *J Control Release*. 2000;66(1):1–9.
- [182] Yu DG, Branford-White C, Yang YC, et al. A novel fast disintegrating tablet fabricated by three-dimensional printing. *Drug Dev Ind Pharm*. 2009;35(12):1530–1536.
- [183] Deng GY, Xiang LY, Wei DH, et al. Tablets with material gradients fabricated by three-dimensional printing. *J Pharm Sci*. 2007;96:2446–2456.
- [184] Yi H-G, Choi Y-J, Kang KS, et al. A 3D-printed local drug delivery patch for pancreatic cancer growth suppression. *J Control Release*. 2016;238:231–241.
- [185] Holländer J, Genina N, Jukarainen H, et al. Three-dimensional printed PCL-based implantable prototypes of medical devices for controlled drug delivery. *J Pharm Sci*. 2016;105(9):2665–2676.
- [186] Shim IK, Yi H-J, Yi H-G, et al. Locally-applied 5-fluorouracil-loaded slow-release patch prevents pancreatic cancer growth in an orthotopic mouse model. *Oncotarget*. 2017;8(25):40140–40151.
- [187] Shi X, Cheng Y, Wang J, et al. 3D printed intelligent scaffold prevents recurrence and distal metastasis of breast cancer. *Theranostics*. 2020;10(23):10652–10664.
- [188] Hafezi F, Scoutaris N, Douroumis D, et al. 3D printed chitosan dressing crosslinked with genipin for potential healing of chronic wounds. *Int J Pharm*. 2019;560:406–415.
- [189] Tagami T, Ito E, Hayashi N, et al. Application of 3D printing technology for generating hollow-type suppository shells. *Int J Pharm*. 2020;589:119825.
- [190] Seoane-Viaño I, Trenfield SJ, Basit AW, et al. Translating 3D printed pharmaceuticals: from hype to real-world clinical applications. *Adv Drug Deliv Rev*. 2021;174:553–575.
- [191] Tagami T, Ito E, Kida R, et al. 3D printing of gummy drug formulations composed of gelatin and an HPMC-based hydrogel for pediatric use. *Int J Pharm*. 2021;594:120118.

Stereolithography 3D printing technology in pharmaceuticals: a review

Subhash Deshmane, Prakash Kendre, Hitendra Mahajan & Shirish Jain

To cite this article: Subhash Deshmane, Prakash Kendre, Hitendra Mahajan & Shirish Jain (2021): Stereolithography 3D printing technology in pharmaceuticals: a review, Drug Development and Industrial Pharmacy, DOI: [10.1080/03639045.2021.1994990](https://doi.org/10.1080/03639045.2021.1994990)

To link to this article: <https://doi.org/10.1080/03639045.2021.1994990>



Published online: 29 Oct 2021.



Submit your article to this journal [↗](#)



Article views: 20





View related articles [↗](#)



View Crossmark data [↗](#)

Stereolithography 3D printing technology in pharmaceuticals: a review

Subhash Deshmane^a , Prakash Kendre^a, Hitendra Mahajan^b  and Shirish Jain^a

^aDepartment of Pharmaceutics, Rajarshi Shahu College of Pharmacy, Malvihir, India; ^bDepartment of Pharmaceutics, R. C. Patel Institute of Pharmaceutical Education and Research, Shirpur, India

ABSTRACT

Three-dimensional printing (3DP) technology is an innovative tool used in manufacturing medical devices, producing alloys, replacing biological tissues, producing customized dosage forms and so on. Stereolithography (SLA), a 3D printing technique, is very rapid and highly accurate and produces finished products of uniform quality. 3D formulations have been optimized with a perfect tool of artificial intelligence learning techniques. Complex designs/shapes can be fabricated through SLA using the photopolymerization principle. Different 3DP technologies are introduced and the most promising of these, SLA, and its commercial applications, are focused on. The high speed and effectiveness of SLA are highlighted. The working principle of SLA, the materials used and applications of the technique in a wide range of different sectors are highlighted in this review. An innovative idea of 3D printing customized pharmaceutical dosage forms is also presented. SLA comprises several advantages over other methods, such as cost effectiveness, controlled integrity of materials and greater speed. The development of SLA has allowed the development of printed pharmaceutical devices. Considering the present trends, it is expected that SLA will be used along with conventional methods of manufacturing of 3D model. This 3D printing technology may be utilized as a novel tool for delivering drugs on demand. This review will be useful for researchers working on 3D printing technologies.

ARTICLE HISTORY

Received 7 March 2021
Revised 14 July 2021
Accepted 12 October 2021

KEYWORDS

Additive manufacturing; customized dosage form; photocurable resins; solid freeform fabrication; three-dimensional printing; vat polymerization

Introduction

Three-dimensional printing (3DP) technology has opened new frontiers in pharmaceutical and other sectors. Simple tools and poor-standard object of some materials cannot yield high-quality products from any bulk substances. This is the limitation of typical or common methods of manufacture [1,2]. In contrast, the 3DP technique is sophisticated, rapid, highly automated, easy to use, customized and cost effective [3–6]. The 3DP technology is used to make 3D objects by laying layers on top of each other. Biological materials, alloys, tissues/cells, metals, wood, thermoplastics, etc. are used in making 3D objects [7,8]. Anatomical prostheses, biological tissues, heart valves, hearing aids and different parts or models of machinery are among the well known examples of 3D objects [9–13]. Innovative scanning and printing systems hold promise in the area of medicine [14]. Over the last three decades, pharmaceutical companies have been looking at 3DP technology to understand the roles it will play and how best to use it. Against a background in which new formulations, biomedical devices and medicines were being developed daily, Professor Clive Roberts, from the University of Nottingham, said that many researchers have designed and prepared many different dosage forms using 3DP techniques [15]. As with most complex 3D architectures, medical devices were printed directly using 3DP technology in the early 2000s [16,17]. Devices specific to a patient's anatomy were also fabricated. Optimized tools and techniques are a prerequisite for making formulations of the desired shapes and sizes. In August 2015, Aprelia Pharmaceuticals printed the first 3D drug that was approved by the FDA. This was Spritam (Levetiracetam) [18,19], a porous structure printed layer by layer

and reformulated to treat dysphagia. When it comes in contact with saliva, it dissolves rapidly and delivers a high dose (1 g) of an antiepileptic drug from a tightly packed pill [20]. The non-uniform quality of some finished products is mainly caused by manufacturing processes such as milling, mixing, granulation and compression. Certain tools related to drug release, drug content and product stability are affected by these operations [21,22]. 3DP is proving to be the solution in overcoming such challenges [23].

Now a day's we can serve better with readdressing of artificial intelligence (AI). In the various filed, AI igniting with notice development [24,25]. Minimum time and cost is the new perspectives of AI in optimization of 3D products that, creating interest in the researchers for launching the products in market [26]. Design of experiments is also mostly used in optimization, but computer aided artificial neural network(ANN) have more attention and delight [27]. Extended drug release ibuprofen tablet fabricated with crosslinked polymers printed with artificial neural network [28]. A perfect tool of AI learning techniques develops pharmaceutical formulations in 3DP. Web bases software M3DISEEN [29] and accurate optimal parameters are the best example of AI [30]. 3D printed tablets of atomoxetine fabricated by ANN release the tailored drug release from immediate to prolong [31]. A solid three-dimensional object of any shape can be prepared starting from a digital model through an automated sequential layering process [32]. It means this technique shares the theme of a sequential layer of material addition of 3D envelope [33,34]. 3DP allows more complex designs or shapes to be fabricated compared with conventional manufacturing processes [35]. Objects can be fabricated using 3DP methods through digital files [36–38].

Now 3DP technology is emerging as a technology for designing and preparing personalized medicines and novel formulations [39–42]. 3DP technology increases the speed with which personalized pharmaceutical drugs can be produced, using computer-based drug design systems [43,44]. First 3D printer in the world is launched by FabRx for personalized medicines in 2020. M3DIMAKER™ used from drug development timeline to human clinical trials [45]. Semi-liquid binding solutions are mixed with powder beds to produce adhesive particles in inkjet printing [46]. According to the United States Government Accountability Office, a 3DP method is a layer-by-layer process used for making 3D objects from digital models [47]. Other synonyms for '3DP technology' are 'rapid prototyping,' 'solid free form' and 'additive manufacturing and fabrication' [48,49]. The American Society of Mechanical Engineers has suggested 'additive manufacturing' be used as an alternate term for 3DP for the purposes of pharmaceutical manufacturing processes [50].

Various 3DP technologies are briefly described here.

Thermal ink-jet printing

In this process, the printing materials are deposited on the printed product. The materials applied layer by layer in the form of droplets through small-diameter nozzles, and UV light is used to harden the 3D object. Ink-jet systems comprise two types of technologies, continuous and drop on demand printing [51,52]. Living cells are protected and maintained in an aqueous environment by more biocompatible thermal inkjet 3D printer [53,54].

Fused deposition modeling (FDM)

Hot melt extrusion (HME) based FDM, in which the materials are softened or melted by heating during the printing process [55,56]. FDM 3DP is used to manufacture delayed-release tablets without an outer enteric coating and also provides personalized doses of medicines [57]. The FDM 3DP technique, however, suffers various limitations. These include non-availability of suitable polymers because elevated temperature (~200 °C) may degrade certain polymers and drug also [58], stagnant and often partial drug release (because the drug remains trapped in the polymers) [59,60] and difficulties in evaluating the solubility of the drug and additives in the presence of polymers [61]. Only poly vinyl alcohol (PVA) and poly lactic acid (PLA) is mostly used.

Fused material is extruded as a filament or wire through a nozzle, which turns the flow on and off. It gets heated and melts the material. Extrusion require materials in semisolid form and does not require high temperature, therefore choice for polymers is quite more [58]. It moves horizontally and vertically by computer-aided manufacturing. The sacrificial material is later removed using hot water, a water jet or a solvent. Mainly used filaments are acrylonitrile butadiene styrene and polylactic acid (PLA) [62].

Selective laser sintering

A liquid binder and a powder are used in this technique. The process chamber is filled with the powder and then the binder is introduced uniformly through nozzles at a moderate pressure. The required 3D object is created by gluing the powder particles with the binder [63]. Smooth and accurate parts has been produced using fine particles, which is difficult to spread and handling [64]. Photopolymerization of powder is done in SLS using high power

laser as an energy source. SLS technology has many advantages such as, high strength, speed and chemical resistance [65].

All the methods described have limitations in terms of the technique, quality of the products and properties of the materials. A literature survey revealed that stereolithography is the only method in which the resolution is fine and thermal degradation of substances is avoided.

Stereolithography (SLA)

is the first laser-based printing technology. It was developed in 1980 by Japanese Dr, Kodama and granted the first patent for rapid prototyping and is well known in commerce as the solid freeform fabrication (SFF) process [66,67]. 3D objects are produced by SLA through the superintended solidification of a liquid resin by a photo-polymerization mechanism [68,69]. SLA is used to make different types of production parts, medical models, prototypes, patterns, computer hardware and biomaterials. The term 'SLA' was coined by Chuck Hull in 1984 and a patent was granted in 1986, but research on SLA began in the 1970s. Laser-based SLA and digital light projection are the two types of SLA [70]. In the laser-based method, the product is fabricated in a bottom-up, vector-by-vector manner using a computer-manipulated laser beam system [71] where UV light is passed through the transparent bottom of a vat containing photosensitive resin [72,73]. The stereolithographic technique has a number of unique features [74]. Its fine resolution [75] permits complex structures to be created. During the printing process, the heating is minimal and thereby thermal degradation of drugs is avoided [76]. Hence SLA is particularly useful for thermo-labile drugs [77]. The resolution and accuracy of SLA are superior to those of other techniques [78,79]. With FDM, differences between layers results in anisotropic effects and requires adjustments in the geometry of the object. Thus FDM is unsuitable for certain applications. In contrast, highly isotropic parts can be created using SLA. The integrity of the material is tightly controlled by considering a number of factors in SLA. Better patient compliance, customized formulations, modulated drug release dosage forms and deliver-on-demand medications can all be prepared using SLA [80–82]. SLA is faster than FDM and selective laser sintering (SLS) [83]. Children's of 4-11 years age has prefer 3D printed tablets on visual inspection [84]. SLA also has some limitations. The limited availability of a number of photocrosslinkable polymers is the main drawback of SLA. The available materials require recognition as safe. When the drugs are exposed to laser, they may lead to lung diseases [85]. Another disadvantage of SLA is that it is quite expensive.

Principle of stereolithography

When ultraviolet (UV) radiation is passed through a photosensitive resin, it is photopolymerized totally. This is the basic principle of SLA. Low-power UV radiation (up to 1000 mW) from a He-Cd/Nd:YVO₄ laser solidifies a thin layer of resin on the surface [86]. The platform is the main component of a SLA machine. The 3D object is formed in a bath of liquid resin in which the platform is immersed. The laser source is another important part. It is controlled by a computer. All the parts of the machine can be cleaned using a solvent after a 3D object is made. Any resinous materials on the surface can be removed using the solvent [87]. A UV oven is used to cure the cleaned and finished 3D object and with the help of CAD model [88], every layer of resin is being scanned by laser technique [89]. Pharmaceutical formulation containing higher water content when exposed to visible light

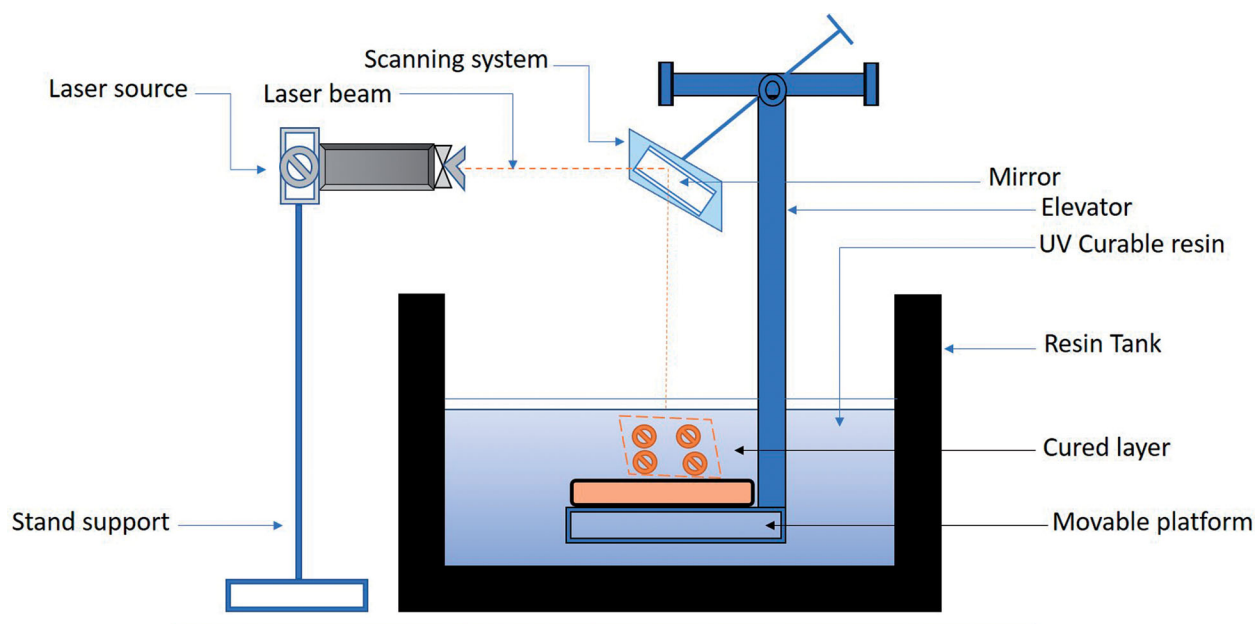


Figure 1. Stereolithographic 3D printer.

irradiation process, results pronounced effect on drug release from 27% to 95% over eight hours [90].

Working of SLA

Stereolithographic is based on the photo-polymerization in which superintended solidification of a liquid resin is executed [55]. A vessel containing the liquid resin (photopolymer) is fixed on the main (fixed) platform (Figure 1). An elevator with a movable platform, located in the vessel, is attached to the main platform. Initially, the movable platform is lifted close to the surface of the liquid resin photopolymer. After one cycle of UV laser treatment, a new photopolymerized layer is formed, and the thickness of the next layer is set by moving the platform down. The 3D object is produced by repeated laser treatments. Due to gravitational force and lateral pressure of subsequent coat, cross section may not precisely form 3D structure. Therefore supporting structure of filaments are form and help in holding the cross section. Filaments support is bring out with the help of CAD model, used on the stereolithography machine during the preparation [91]. Finally, this supports is being removed manually. The manufacturing of pharmaceutical products using SLA allows individualization of medicines. Despite the numerous medical and economic benefits, there are some technical challenges that restrict the extensive commercial use of 3DP. These challenges include the limited number of biocompatible materials in 3DP printing, the stability of active pharmaceutical ingredient, the efficiency as well as reproducibility of the methods, and the quality of the finished products. A computer interprets the information available in STL files and sends it to the 3D printer, where the data are converted into a 3D structure. The kinetics of the curing reactions depends on the scanning speed, the chemistry and the amounts of the monomer and photoinitiators [92,93].

Materials used in stereolithographic printing

The choice of photopolymer is of utmost importance in SLA [94,95]. The lack of approval of photosensitive materials by the regulatory authority (the FDA) limits the use of SLA significantly,

even though photosensitive materials are used in tissue engineering. During the last decade, a number of photocrosslinkable polymers have been developed. Poly(ethylene glycol) diacrylate (PEGDA) [73,96], poly(2-hydroxyethyl methacrylate) (pHEMA) [97], poly(ethylene glycol) dimethacrylate (PEGDMA) [98,99] and poly(propylene fumarate)/diethyl fumarate (PPF/DEF) [100,101] are examples of photocrosslinkable polymers. Biomedical materials have applications in surgical tools, hearing aids, knee joint appliances and dental appliances [102]. The multiple resins for one build showed patterning with PEG-DMA and PEG-DA with fluorescently labeled dextran, fluorescently labeled bioactive PEG or bioactive PEG in different regions of the scaffold [103]. Complex 3D scaffolds can be fabricated using photocrosslinkable poly(propylene fumarate) (PPF) [104,105], which requires reactive diluents containing significant amounts of non-degradable components. N-vinyl-2-pyrrolidone and diethyl fumarate are used as diluents to reduce the viscosity of the resin during processing [106]. Reconstruction of cranial defects in rabbits is possible because of the ability to produce controlled microstructures [89]. Trimethylene carbonate, polycaprolactone and poly(D,L-lactide) are examples of materials used commonly in tissue engineering [107,108].

The essential components of photocurable resins used in SLA are shown in Figure 2. The precursors are liquid molecules that form a solid 3D structure on exposure to light. Because of the high reactivity of acrylate-based resins, 3D structures can be built rapidly. Hence, acrylate-based resins are commonly used in SLA [46,109]. Deformity in printed part is the main disadvantage of acrylate resins. This is due to the high shrinkage of resins during printing [110]. The problem of distortion can be solved by using a combination of an acrylate resin and methacrylates. The polymerization reaction may be inhibited by a resin's sensitivity to oxygen. The shrinkage of epoxy resins is remarkably lower than that of acrylates [111,112]. An acrylate and epoxy-based resins in combination may have an accelerated curing rate and reduced shrinkage [112–114]. Photoinitiators (PIs) are the resin components that normally react with light. A PI attains an excited state ion being irradiated with radiation of the right wavelength. Xenon lamps, mercury arc lamps, LEDs or lasers used as light source. UV (190–400 nm), visible (400–700 nm) or IR (700–1000 nm) range of

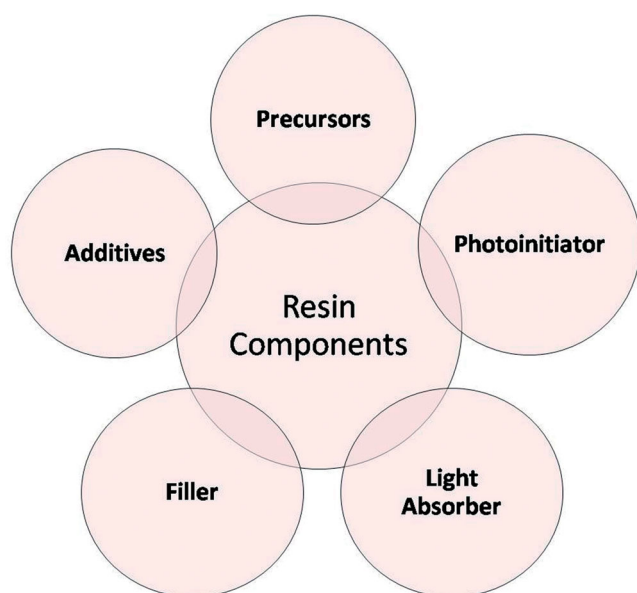


Figure 2. Components of resin for SLA.

wavelength can be used. Visible LEDs are ecofriendly and safe. Water soluble PI, Irgacure 651 has been used in the fabrication of biocompatible hydrogel scaffold [115]. The PI in the excited starts the curing reaction. A suitable photoinitiator is selected on the basis of the precursor utilized. The mechanical properties of device, reaction kinetics, cross-linking density, light dosage required and conversion to printed device depend on the type and amount of PI [116,117]. The light absorber is another material used in SLA processes. A light absorber diminishes the perception of light into the resin and thereby controls the depth to which the resin is cured [118]. The cure depth needs to be precisely defined in complex geometries to prevent unnecessary curing and loss of the features of the model [119,120]. Benzotriazole derivatives are common examples of UV light absorbers [121]. Filling resins with powder, debinding and sintering the printed part or printing the parts is the basic requirement in the fabrication of ceramic materials or metals by SLA [122,123]. In thin structures, the binder burns out easily and fills any cracks or defects that form. A high filler content is recommended for reducing the shrinkage of resins and thereby producing geometrically accurate parts [124]. Optical, thermal, mechanical and electrical properties can be further modified through the use of nano size particles in the SLA resin [125–127]. Long shelf-life (stable) slurries, rheological additives and stabilizers used during the fabrication processes increase the solid loading [128]. A high fraction of solids increases the viscosity of the slurry when the particles are small in size [122]. A high viscosity changes the flow behavior of the resin and interferes with coating mechanisms [129]. This can be overcome by using dispersants such as oligomeric surfactants [130], long-chained oleic acid [131] or phosphine oxides [132].

3DP stereolithography in pharmaceuticals

Stereolithographic 3D printers have been used in various novel and innovative projects. Distinct types of devices, models and dosage forms have been producing using SLA. Researcher used 3D printing applications in fabrication of various dosage forms are mentioned in Table 1.

Pharmaceutical applications of 3D printing technology

SLA can alter elastic silicones for soft model to high strength post cured resins [150,151]. In the field of medical device formation and drug delivery, SLA offers unique applications [152]. Some applications of the SLA 3DP technique are discussed here.

Individualized drug dosing

Today's patient suffers from more than one disease and requires a single multi-dose form of formulation [153,154]. A personalized and accurate dose is required for better compliance. An optimal multi-dose form containing a narrow therapeutics index drug can be given to a patient whose pharmacogenetic profile, age and race are known [65,155]. Fabrication of complete, effective formulations is the second important role of 3D printing technology. One active ingredient can be dispensed in one form as a result [32]. This helps increase the efficacy of the drugs and reduces adverse reactions, if any [156]. Poly(ethylene glycol) diacrylate 700 (PEGDA700) as initial material used in fabrication of patient customized tablets of atomoxetine hydrochloride by digital light processing (DLP) 3D printing technique [157] and Ghost tablets as unique prediction model as future tailored medicines that release entrapped drug without disintegrating [158]. Tailored chewable formulation containing isoleucine fabricated by 3DP offers rapid and feasible approach in hospital setting in maple sirup urine disease [159].

Modified drug release profile

A modified drug release profile requires the preparation of complex geometries containing multiple drugs of porous texture, surrounded by a modulated layer of barriers [160]. A multilayered bone implant based on a pulse release mechanism, with a distinct profile in which rifampicin and isoniazid are released alternately was prepared using 3DP technology. A very small quantity of chloramphenicol maleate could also be released at a predetermined time with perfect accuracy from a cellulose powder substrate using a 3D printing technique [155]. Problem associated with slow and incomplete release of paracetamol has been overcome by sustained released 3D printlet using hydrophilic excipients [161]. Multilayered 3D printed tablets containing four antihypertensive drugs reports, chemical interaction of drug and polymer unexpectedly [162].

Microneedles

Microstructure of microneedles delivers macromolecules through the skin (as in insulin skin delivery) more effectively than does a conventional transdermal dosage form [163]. The stereolithographic method of 3DP allows more complex and sophisticated geometries of microneedles to be fabricated. Ochoa *et al* developed a novel manufacturing process for microneedles with 9.6 μm radius tips. Sharp polymeric microneedles for vaccine delivery were manufactured using the enhanced resolution limit of the 3DP technique [164]. Microstereolithography helped fabricate microneedles through which a 5 weeks' controlled release of the anticancer dacarbazine drug was achieved. Microneedles with a cone-and-pyramid shape were fabricated using a biocompatible resin [165].

Table 1. SLA 3DP applications in pharmaceuticals.

Formulations	Specifications	Reference(s)
4-aminosalicylic (4-ASA) acid and paracetamol-loaded 3D tablets.	Different concentrations of polyethylene glycol diacrylate (PEGDA) and polyethylene glycol have been used in printing solutions	[133]
An anti-acne drug (salicylic acid)-loaded 3D model of a personalized shape nose.	With SLA, there was no drug degradation, and the resolution was higher than with FDM	[134]
A hydrogel of cross-linked polyethylene glycol diacrylate containing ibuprofen.	Because of entrapment of water, pre-wetted, drug loaded hydrogel and devices can be prepared	[135]
Tablets containing a solid dispersion of paracetamol and polyethylene glycol.	A different shape of tablets was unattainable due to powder compaction.	[136]
A mask of higher resolution was produced using SLA.	The drug loading was high, and there was insignificant degradation of salicylic acid.	[137]
Antifouling hybrid hydrogels.	A highly solvated and tough hydrogel increases the gelation rate and the elasticity of the resulting hybrid hydrogel.	[138,139]
Bone tissue engineering is the main prominence area of SLA.	–	[140]
Bone formation	Bone formation was promoted using SLA in rats with cranial defects in <i>in-vivo</i> studies.	[141]
Soft tissue	Bovine chondrocytes, flexible and soft cartilage tissues was fabricated.	[142]
Encapsulation of NIH/3T3	PEG-DMA with human chondrocytes was promoted with an inkjet printer.	[143,144]
Synthesis of novel macromers without any reactive diluents.	–	[145–147]
Polycaprolactone porous structures.	Porous structures scaffolds to release lidocaine more rapidly compared with the solid form.	[148]
Multilayered polypill with variable drug content and shape	Six drugs, paracetamol, naproxen, chloramphenicol, prednisolone and aspirin were printed with different geometries and materials	[149]

Tailored prostheses and implants

Prostheses and implants of any possible shape can be fabricated using 3DP technology. In the present context, translation of MRI images, CT scans, and X-ray images is desirable [156,160,165]. Both complex and standard surgical implants and prosthetic limbs can be prepared in less than 24 h. The Layer Wise Company fabricated spinal, maxillofacial and dental implants [160,166]. The BIOMED Research Institute, Belgium successfully implanted 3D printed mandibular prostheses [165]. Prosthetic ears were made from silver nanoparticles, silicon and chondrocytes using 3DP technology to detect electromagnetic frequencies. The fit of every model is perfect and the price is low thanks to 3DP technology. Nowadays more than 90% of the customized hearing aids are fabricated using 3D printers [156]. Revolutionary localized delivery of lidocaine HCL has been possible by 3DP indwelling bladder device [167]. A 3D printed hearing aid released antibiotics for more than two weeks and inhibits any biofilm and bacterial growth on device [168].

Anatomical models for surgical preparations

There are individual variations in the complex human anatomy. Before performing medical surgery, obtaining knowledge regarding the patient's surgical or anatomical part is important. The size and shape of a specific anatomy requires a complex surgical procedure. 3DP technology provides vital tools for making anatomical models that fit perfectly [160, 169]. Surgeons use calcified aortas manufactured using 3D printers [160]. The airways of premature infants have been fabricated using 3DP methods to evaluate aerosols [160].

Soft materials in the food industry

Traditional food preparation does not produce customized food or recipes for specific nutritional requirements. Food 3D printing

involves premixing and depositing the required nutrients in distinct layers [170]. Different customers (the elderly, pregnant or feeding mothers, children, athletes) require different proportions of carbohydrates, fats and proteins [171]. The use of 3DP to make smooth food for elderly people having difficulties in chewing and swallowing [172,173]. Recently, BeexHex, USA, a 3D printing company, prepared food for National Aeronautics and Space Administration (NASA) astronauts when they were on a mission [174]. The food-containing-drug approach will become the new path food-based pharmaceutical drug delivery systems [175].

Other pharmaceutical dosage forms

Different 3DP technologies are available for the fabricating customized [176] pharmaceutical dosage forms. Some of these dosage forms are focused on here. Accurate and tailored controlled released dosage forms have been fabricated using 3D printers [177]. Also drug can be printed on porous carrier using flexographic printers [178]. 3D printer was used to manufacture highly adjustable, affordable, small delayed-release prednisolone tablets in poly(vinyl alcohol) filaments [179]. An oral pulsatile release capsular model based on erodible hydroxypropyl cellulose was fabricated by Melocchi *et al.* using an FDM 3D printer [180]. Oral dosage forms with accurate and uniform content and excellent dosage control have been fabricated using 3DP technology [181]. A fast-disintegrating tablet in which the microstructure and surface texture are controlled was fabricated using a 3D printer [182]. A matrix tablet with zero-order drug-release characteristics in the radial direction was also manufactured using 3DP technology [183]. A biodegradable implant patch containing a high dose of fluorouracil (drug) and poly-lactic-co-glycolic acid and polycaprolactone (carrier) was fabricated using a 3DP technique for local delivery of anticancer drugs [184,185]. Tablets containing 4-aminosalicylic acid and paracetamol in a combined form were produced using stereolithography. These tablets have a customized drug-

release profile [133]. Making biodegradable patches of customized shapes for delivering drugs exactly at a tumor site is another possibility with 3DP techniques. A sustained-release patch containing an anticancer drug, 5-fluorouracil, and a blend of polycaprolactone and poly(lactide-co-glycolide) was prepared using 3DP, which had site-specific characteristics [186]. A 3D printed poly(lactic-co-glycolic acid), gelatin and chitosan scaffold loaded with anticancer drugs significantly inhibited the recurrence and growth of breast cancer and reduced drug toxicity with a sustained action [187]. Functionally characterized 3D printed chitosan based film prepared with genipin as crosslinker shown promising effect for chronic wound [188]. Two drugs in separate compartments of hollow shell suppository shell prepared by FDM 3DP become advanced model for pediatric patients [189]. 3D printed suppository molds were fabricated to cast the self supporting suppositories [190]. Gummy drug formulation (hydrogel) containing lamotrigine for pediatric patients was fabricated by 3D bioprinter with perspective of future clinical setting [191].

Conclusions

A rapid, sophisticated and highly accurate method of fabricating medical devices, biological tissues, alloys, tailored dosage forms and many more is offered by 3DP technology. Solid forms can be fabricated using the photopolymerization mechanism and photocurable resins. Customized dosage forms produced using the 3DP technique may improve patient compliance. SLA is a very promising technique. It improves the stability and resolution, and degradation of the materials is avoided. The SLA 3DP technology offers significant potential benefits in the manufacture of pharmaceuticals, medical devices and many other devices. 3DP technology is an innovative scanning and printing technology that provides hope that most of the present limitations can be overcome. It is considered one of the most hopeful areas of medicine.

Disclosure statement

No potential conflict of interest was reported by the author(s).

Funding

The author(s) reported there is no funding associated with the work featured in this article.

ORCID

Subhash Deshmane  <http://orcid.org/0000-0002-0563-4075>

Hitendra Mahajan  <http://orcid.org/0000-0001-6648-144X>

References

- [1] Campbell TW, C, Ivanova O, Garrett B. Could 3d printing change the world? Technologies and implications of additive manufacturing. Washington (DC): Atlantic Council; 2012. p. 1–14.
- [2] Hwang HH, Zhu W, Victorine G, et al. 3D-printing of functional biomedical microdevices via light- and Extrusion-Based approaches. *Small Methods*. 2018;2(2):1700277.
- [3] Peterson GI, Larsen MB, Ganter MA, et al. 3D-printed mechanochromic materials. *ACS Appl Mater Interfaces*. 2015;7(1):577–583.
- [4] Anciaux SK, Geiger M, Bowser MT. 3D printed micro free-flow electrophoresis device. *Anal Chem*. 2016;88(15):7675–7682.
- [5] Wang X, Ao Q, Tian X, et al. 3D bioprinting technologies for hard tissue and organ engineering. *Materials*. 2016;9(10):802.
- [6] Noorani R. 3D printing: technology, applications, and selection. 1st ed. Boca Raton (FL): CRC Press; 2017.
- [7] Randolph SA. 3D printing: what are the hazards? *Workplace Health Saf*. 2018;66(3):164–164.
- [8] Kim J, Kong JS, Han W, et al. 3D cell printing of tissue/organ-mimicking constructs for therapeutic and drug testing applications. *IJMS*. 2020;21(20):7757.
- [9] Gong H, Woolley AT, Nordin GP. High density 3D printed microfluidic valves, pumps, and multiplexers. *Lab Chip*. 2016;16(13):2450–2458.
- [10] Macdonald NP, Cabot JM, Smejkal P, et al. Comparing microfluidic performance of three-dimensional (3D) printing platforms. *Anal Chem*. 2017;89(7):3858–3866.
- [11] Johnson AR, Caudill CL, Tumbleston JR, et al. Single-step fabrication of computationally designed microneedles by continuous liquid interface production. *PLoS One*. 2016;11(9):e0162518.
- [12] Chrzan R, Miechowicz S, Urbanik A, et al. Individually fitted hearing aid device manufactured using rapid prototyping based on ear CT. A case report. *Neuroradiol J*. 2009;22(2):209–214.
- [13] Dhir V, Itoi T, Fockens P, et al. Novel ex vivo model for hands-on teaching of and training in EUS-guided biliary drainage: creation of "Mumbai EUS" stereolithography/3D printing bile duct prototype (with videos). *Gastrointest Endosc*. 2015;81(2):440–446.
- [14] Ventola CL. Medical applications for 3D printing: current and projected uses. *P T*. 2014;39(10):704–711.
- [15] Tunnicliffe A. The past, present and future of 3D printing in the pharmaceutical industry. 2020. <https://www.ns-healthcare.com/analysis/additive-manufacturing-3d-printing/>
- [16] Maulvi FA, Shah MJ, Solanki BS, et al. Application of 3D printing technology in the development of novel drug delivery systems. *Int J Drug Dev Res*. 2017;9:44–49. <https://www.ijddr.in/drug-development/application-of-3d-printing-technology-in-the-development-of-novel-drug-delivery-systems.php?aid=18776>
- [17] Park JH, Jung JW, Kang H-W, et al. Indirect three-dimensional printing of synthetic polymer scaffold based on thermal molding process. *Biofabrication*. 2014;6(2):025003.
- [18] Pravin S, Sudhir A. Integration of 3D printing with dosage forms: a new perspective for modern healthcare. *Biomed Pharmacother*. 2018; 107:146–154.
- [19] Prasad LK, Smyth H. 3D printing technologies for drug delivery: a review. *Drug Dev Ind Pharm*. 2016;42(7):1019–1031.
- [20] First 3D-printed pill. *Nat Biotechnol*. 2015;33:1014–1014.
- [21] Ursan ID, Chiu L, Pierce A. Three-dimensional drug printing: a structured review. *J Am Pharm Assoc*. 2013;53(2):136–144.
- [22] O Oyewumi M. 3D printing technology in pharmaceutical drug delivery: prospects and challenges. *J Biomol Res Ther*. 2015;04(04):1–3.
- [23] Larush L, Kaner I, Fluksman A, et al. 3D printing of responsive hydrogels for drug-delivery systems. *J 3D Print Med*. 2017;1(4):219–229.

- [24] Baker D. Artificial intelligence: the future landscape of genomic medical diagnosis: dataset in Silico artificial intelligent clinical information, and machine learning systems. In: Lambert CG, Baker DJ, Patrinos GP, editors. Human genome informatics. San Diego: Academic Press; 2018. p. 223–267.
- [25] Popova M, Isayev O, Tropsha A. Deep reinforcement learning for de novo drug design. *Sci Adv.* 2018;4:eap7885.
- [26] Han R, Xiong H, Ye Z, et al. Predicting physical stability of solid dispersions by machine learning techniques. *J Control Release.* 2019;311–312:16–25.
- [27] Harrer S, Shah P, Antony B, et al. Artificial intelligence for clinical trial design. *Trends Pharmacol Sci.* 2019;40(8): 577–591.
- [28] Madzarevic M, Medarevic D, Vulovic A, et al. Optimization and prediction of ibuprofen release from 3D DLP printlets using artificial neural networks. *Pharmaceutics.* 2019;11: 544.
- [29] Elbadawi M, Muñiz Castro B, Gavins FKH, et al. M3DISEEN: a novel machine learning approach for predicting the 3D printability of medicines. *Int J Pharm.* 2020;590:119837.
- [30] Elbadawi M, McCoubrey LE, Gavins FKH, et al. Harnessing artificial intelligence for the next generation of 3D printed medicines. *Adv Drug Deliv Rev.* 2021;175:113805.
- [31] Stanojević G, Medarević D, Adamov I, et al. Tailoring atomoxetine release rate from DLP 3D-printed tablets using artificial neural networks: influence of tablet thickness and drug loading. *Molecules.* 2020;26(1):111.
- [32] Khaled SA, Burley JC, Alexander MR, et al. 3D printing of tablets containing multiple drugs with defined release profiles. *Int J Pharm.* 2015;494(2):643–650.
- [33] Goyanes A, Robles Martinez P, Buanz A, et al. Effect of geometry on drug release from 3D printed tablets. *Int J Pharm.* 2015;494(2):657–663.
- [34] Awari GK, Thorat CS, Ambade V, et al. Additive manufacturing and 3D printing technology. 1st ed. Boca Raton (FL): CRC Press/Taylor & Francis Group, LLC; 2021.
- [35] Łaszcz M, Witkowska A. Studies of phase transitions in the aripiprazole solid dosage form. *J Pharm Biomed Anal.* 2016;117:298–303.
- [36] Water JJ, Bohr A, Boetker J, et al. Three-dimensional printing of drug-eluting implants: preparation of an antimicrobial polylactide feedstock material. *J Pharm Sci.* 2015; 104(3):1099–1107.
- [37] Yu DG, Zhu LM, Branford-White CJ, et al. Three-dimensional printing in pharmaceuticals: Promises and problems. *J Pharm Sci.* 2008;97(9):3666–3690.
- [38] Bakhatwar M, Chikkala Vnvk SR. Three-dimensional printing in pharmaceutical technology – an overview of innovations. *Innov Pharm Pharmacother.* 2019;7:67–71.
- [39] Zheng F, Huang S. Advances in study on three-dimensional printing in pharmaceuticals. *Chinese Herb Med.* 2016; 8(2):121–125.
- [40] Aimar A, Palermo A, Innocenti B. The role of 3D printing in medical applications: a state of the art. *J Healthc Eng.* 2019;2019:1–10.
- [41] Khan FA, Narasimhan K, Swathi CSV, et al. 3D printing technology in customized drug delivery system: current state of the art, prospective and the challenges. *Curr Pharm Des.* 2018;24(42):5049–5061.
- [42] Zhu X, Li H, Huang L, et al. 3D printing promotes the development of drugs. *Biomed Pharmacother.* 2020;131: 110644.
- [43] Ameeruzzafar Alruwaili NK, Rizwanullah M, et al. 3D printing technology in design of pharmaceutical products. *Curr Pharm Des.* 2019;24:5009–5018.
- [44] Mathew E, Pitzanti G, Larrañeta E, et al. 3D printing of pharmaceuticals and drug delivery devices. *Pharmaceutics.* 2020;12(3):266.
- [45] Trenfield SB. Innovations in 3D printed pharmaceuticals. *ONdrugDelivery Magazine.* 2020;109:45–49.
- [46] Ligon SC, Liska R, Stampfl J, et al. Polymers for 3D printing and customized additive manufacturing. *Chem Rev.* 2017; 117(15):10212–10290.
- [47] Kim GB, Lee S, Kim H, et al. Three-dimensional printing: basic principles and applications in medicine and radiology. *Korean J Radiol.* 2016;17(2):182–197.
- [48] Hodgdon T, Danrad R, Patel MJ, et al. Logistics of three-dimensional printing: primer for radiologists. *Acad Radiol.* 2018;25(1):40–51.
- [49] Chua CK, Leong KF, An J. Introduction to rapid prototyping of biomaterials. In: Narayan R, editor. Rapid prototyping of biomaterials. San Diego: Elsevier; 2014. p. 1–15.
- [50] Tofail SAM, Koumoulos EP, Bandyopadhyay A, et al. Additive manufacturing: scientific and technological challenges, market uptake and opportunities. *Mater Today.* 2018;21(1):22–37.
- [51] Goole J, Amighi K. 3D printing in pharmaceuticals: a new tool for designing customized drug delivery systems. *Int J Pharm.* 2016;499(1–2):376–394.
- [52] Lau G-K, Shrestha M. Ink-jet printing of micro-electromechanical systems (MEMS). *Micromachines.* 2017;8(6):194.
- [53] Cui X, Boland T, D’Lima D, et al. Thermal inkjet printing in tissue engineering and regenerative medicine. *Recent Pat Drug Deliv Formul.* 2012;6(2):149–155.
- [54] Gardin C, Ferroni L, Latremouille C, et al. Recent applications of three dimensional printing in cardiovascular medicine. *Cells.* 2020;9(3):742.
- [55] He D, Han F, Wang Z, et al. A review of 3D printing via fused deposition modeling in pharmaceuticals. *Yao Xue Xue Bao.* 2016;51:1659–1665.
- [56] Long J, Gholizadeh H, Lu J, et al. Application of fused deposition modelling (FDM) method of 3D printing in drug delivery. *Curr Pharm Des.* 2017;23(3):433–439.
- [57] Goyanes A, Fina F, Martorana A, et al. Development of modified release 3D printed tablets (printlets) with pharmaceutical excipients using additive manufacturing. *Int J Pharm.* 2017;527(1–2):21–30.
- [58] Alhnan MA, Okwuosa TC, Sadia M, et al. Emergence of 3D printed dosage forms: opportunities and challenges. *Pharm Res.* 2016;33(8):1817–1832.
- [59] Lim SH, Chia SMY, Kang L, et al. Three-dimensional printing of carbamazepine sustained-release scaffold. *J Pharm Sci.* 2016;105(7):2155–2163.
- [60] Goyanes A, Chang H, Sedough D, et al. Fabrication of controlled-release budesonide tablets via desktop (FDM) 3D printing. *Int J Pharm.* 2015;496(2):414–420.
- [61] Gumaste SG, Gupta SS, Serajuddin ATM. Investigation of polymer-surfactant and polymer-drug-surfactant miscibility for solid dispersion. *AAPS J.* 2016;18(5):1131–1143.
- [62] Gioumouxouzis CI, Baklavaridis A, Katsamenis OL, et al. A 3D printed bilayer oral solid dosage form combining metformin for prolonged and glimepiride for immediate drug delivery. *Eur J Pharm Sci.* 2018;120:40–52.

- [63] Fina F, Madla CM, Goyanes A, et al. Fabricating 3D printed orally disintegrating printlets using selective laser sintering. *Int J Pharm.* 2018;541(1–2):101–107.
- [64] Zhou Y. The recent development and applications of fluidic channels by 3D printing. *J Biomed Sci.* 2017;24(1):80.
- [65] Park BJ, Choi HJ, Moon SJ, et al. Pharmaceutical applications of 3D printing technology: current understanding and future perspectives. *J Pharm Investig.* 2018;49:575–585.
- [66] Hull CW, Arcadia C. Apparatus for production of three-dimensional objects by stereolithography. US Patent, 1984.
- [67] Lonjon C. The history of 3d printer: from rapid prototyping to additive fabrication. <https://www.sculpteo.com/blog/2017/03/01/whos-behind-the-three-main-3d-printing-technologies/>.
- [68] Chia HN, Wu BM. Recent advances in 3D printing of biomaterials. *J Biol Eng.* 2015;9:4.
- [69] Huang B, Wu B, Han L, et al. Preparation of a novel cationic photosensitive resin (3D-SLR01) for stereolithography 3D printing and determination of its some properties. *J Wuhan Univ Technol-Mat Sci Edit.* 2019;34(4):761–768.
- [70] Robles Martinez P, Basit AW, Gaisford S. The history, developments and opportunities of stereolithography. In: *AAPS advances in the pharmaceutical sciences series*. New York: Springer Verlag; 2012. p. 55–79.
- [71] Wang Z, Abdulla R, Parker B, et al. A simple and high-resolution stereolithography-based 3D bioprinting system using visible light crosslinkable bioinks. *Biofabrication.* 2015;7(4):045009.
- [72] ASTM 52921. Standard terminology for additive manufacturing — coordinate systems and test methodologies. Geneva: ASTM Int; 2019.
- [73] Chan V, Zorlutuna P, Jeong JH, et al. Three-dimensional photopatterning of hydrogels using stereolithography for long-term cell encapsulation. *Lab Chip.* 2010;10(16):2062–2070.
- [74] Curti C, Kirby DJ, Russell CA. Stereolithography apparatus evolution: enhancing throughput and efficiency of pharmaceutical formulation development. *Pharmaceutics.* 2021;13(5):616.
- [75] Lim SH, Kathuria H, Bin AM, et al. High resolution photopolymer for 3D printing of personalised microneedle for transdermal delivery of anti-wrinkle small peptide. *J Control Release.* 2020;329:907–918.
- [76] Goyanes A, Buanz ABM, Hatton GB, et al. 3D printing of modified-release aminosalicylate (4-ASA and 5-ASA) tablets. *Eur J Pharm Biopharm.* 2015;89:157–162.
- [77] Konta A, García-Piña M, Serrano D. Personalised 3D printed medicines: which techniques and polymers are more successful? *Bioengineering.* 2017;4(4):79.
- [78] Melchels FPW, Feijen J, Grijpma DW. A review on stereolithography and its applications in biomedical engineering. *Biomaterials.* 2010;31(24):6121–6130.
- [79] Gardan J. Additive manufacturing technologies: state of the art and trends. *Int J Prod Res.* 2016;54(10):3118–3132.
- [80] Norman J, Madurawe RD, Moore CMV, et al. A new chapter in pharmaceutical manufacturing: 3D-printed drug products. *Adv Drug Deliv Rev.* 2017;108:39–50.
- [81] Trenfield SJ, Madla CM, Basit AW, et al. The shape of things to come: emerging applications of 3D printing in healthcare. In: *AAPS advances in the pharmaceutical sciences series*. New York: Springer Verlag; 2012. p. 1–19.
- [82] Osouli-Bostanabad K, Adibkia K. Made-on-demand, complex and personalized 3D-printed drug products. *Bioimpacts.* 2018;8(2):77–79.
- [83] Vitale A, Cabral J. Frontal conversion and uniformity in 3D printing by photopolymerisation. *Materials.* 2016;9(9):760.
- [84] Januskaite P, Xu X, Ranmal SR, et al. I spy with my little eye: a paediatric visual preferences survey of 3D printed tablets. *Pharmaceutics.* 2020;12(11):1100.
- [85] Rattanakit P, Moulton SE, Santiago KS, et al. Extrusion printed polymer structures: a facile and versatile approach to tailored drug delivery platforms. *Int J Pharm.* 2012;422(1–2):254–263.
- [86] Stereolithography-ODM | 3D systems. [cited 2021 Jan 8]. <https://www.3dsystems.com/on-demand-manufacturing/stereolithography-sla>.
- [87] Zhang X, Jiang X, Sun C. Micro-stereolithography of polymeric and ceramic microstructures. *Sensors Actuators A Phys.* 1999;77(2):149–156.
- [88] US4575330A – Apparatus for production of three-dimensional objects by stereolithography - Google Patents. [cited 2021 Jan 31]. <https://patents.google.com/patent/US4575330A/en>.
- [89] Salonitis K, Tsoukantas G, Stavropoulos P, et al. A critical review of stereolithography process modeling. In: Bártolo P, editor. *Virtual modelling and rapid manufacturing – advanced research in virtual and rapid prototyping*. London; New York: Taylor & Francis; 2003.
- [90] Madžarević M, Ibrić S. Evaluation of exposure time and visible light irradiation in LCD 3D printing of ibuprofen extended release tablets. *Eur J Pharm Sci.* 2021;158:105688.
- [91] Venuvinod PK, Ma W. Stereolithography (SL). In: *Rapid prototyping*. Boston (MA): Springer US; 2004. p. 195–244.
- [92] Heller C, Schwentenwein M, Russmueller G, et al. Vinyl esters: low cytotoxicity monomers for the fabrication of biocompatible 3D scaffolds by lithography based additive manufacturing. *J Polym Sci A Polym Chem.* 2009;47(24):6941–6954.
- [93] Patel DK, Sakhaei AH, Layani M, et al. Highly stretchable and UV curable elastomers for digital light processing based 3D printing. *Adv Mater.* 2017;29(15):1606000.
- [94] Noorani R. Materials for 3D printing. In: Noorani R, editor. *3D printing*. Boca Raton (FL): CRC Press; 2017. p. 81–98.
- [95] Choi J-W, Kim H-C, Wicker R. Multi-material stereolithography. *J Mater Process Technol.* 2011;211(3):318–328.
- [96] Vehse M, Petersen S, Sternberg K, et al. Drug delivery from poly(ethylene glycol) diacrylate scaffolds produced by DLC based micro-stereolithography. *Macromol Symp.* 2014;346(1):43–47.
- [97] Hanson Shepherd JN, Parker ST, Shepherd RF, et al. 3D microperiodic hydrogel scaffolds for robust neuronal cultures. *Adv Funct Mater.* 2011;21(1):46–46.
- [98] Arcaute K, Mann BK, Wicker RB. Stereolithography of three-dimensional bioactive poly(ethylene glycol) constructs with encapsulated cells. *Ann Biomed Eng.* 2006;34(9):1429–1441.
- [99] Dhariwala B, Hunt E, Boland T. Rapid prototyping of tissue-engineering constructs, using photopolymerizable hydrogels and stereolithography. *Tissue Eng.* 2004;10(9–10):1316–1322.
- [100] Fisher JP, Dean D, Mikos AG. Photocrosslinking characteristics and mechanical properties of diethyl fumarate/poly

- (propylene fumarate) biomaterials. *Biomaterials*. 2002; 23(22):4333–4343.
- [101] Trachtenberg JE, Placone JK, Smith BT, et al. Extrusion-based 3D printing of poly(propylene fumarate) scaffolds with hydroxyapatite gradients. *J Biomater Sci Polym Ed*. 2017;28(6):532–554.
- [102] Tappa K, Jammalamadaka U. Novel biomaterials used in medical 3D printing techniques. *JFB*. 2018;9(1):17.
- [103] Arcaute K, Mann B, Wicker R. Stereolithography of spatially controlled multi-material bioactive poly(ethylene glycol) scaffolds. *Acta Biomater*. 2010;6(3):1047–1054.
- [104] Lee K-W, Wang S, Fox BC, et al. Poly(propylene fumarate) bone tissue engineering scaffold fabrication using stereolithography: effects of resin formulations and laser parameters. *Biomacromolecules*. 2007;8(4):1077–1084.
- [105] Choi J-W, Wicker R, Lee S-H, et al. Fabrication of 3D biocompatible/biodegradable micro-scaffolds using dynamic mask projection microstereolithography. *J Mater Process Technol*. 2009;209(15-16):5494–5503.
- [106] Jansen J, Melchels FPW, Grijpma DW, et al. Fumaric acid monoethyl ester-functionalized poly(D,L-lactide)/N-vinyl-2-pyrrolidone resins for the preparation of tissue engineering scaffolds by stereolithography. *Biomacromolecules*. 2009;10(2):214–220.
- [107] Skoog SA, Goering PL, Narayan RJ. Stereolithography in tissue engineering. *J Mater Sci Mater Med*. 2014;25(3):845–856.
- [108] Ronca A, Ambrosio L, Grijpma DW. Preparation of designed poly(d,l-lactide)/nanosized hydroxyapatite composite structures by stereolithography. *Acta Biomater*. 2013;9(4):5989–5996.
- [109] Stampfl J, Baudis S, Heller C, et al. Photopolymers with tunable mechanical properties processed by laser-based high-resolution stereolithography. *J Micromech Microeng*. 2008;18(12):125014.
- [110] Murphy EJ, Ansel RK. Method of forming a three-dimensional object by stereolithography and composition therefore. US07429568, US, 1989.
- [111] Esposito Corcione C, Greco A, Maffezzoli A. Photopolymerization kinetics of an epoxy-based resin for stereolithography. *J Appl Polym Sci*. 2004;92(6):3484–3491.
- [112] Lee TY, Carioscia J, Smith Z, et al. Thiol – allyl ether – methacrylate ternary systems. Evolution mechanism of Polymerization-Induced shrinkage stress and mechanical properties. *Macromolecules*. 2007;40(5):1473–1479.
- [113] Zhiwei G, Jianhua M, Shuhuai H, et al. Development of a hybrid photopolymer for stereolithography. *J Wuhan Univ Technol-Mat Sci Edit*. 2006;21(1):99–101.
- [114] Oesterreicher A, Wiener J, Roth M, et al. Tough and degradable photopolymers derived from alkyne monomers for 3D printing of biomedical materials. *Polym Chem*. 2016;7(32):5169–5180.
- [115] Bagheri A, Jin J. Photopolymerization in 3D printing. *ACS Appl Polym Mater*. 2019;1(4):593–611.
- [116] Badev A, Abouliatim Y, Chartier T, et al. Photopolymerization kinetics of a polyether acrylate in the presence of ceramic fillers used in stereolithography. *J Photochem Photobiol A Chem*. 2011;222(1):117–122.
- [117] Bail R, Patel A, Yang H, et al. The effect of a type I photoinitiator on cure kinetics and cell toxicity in Projection-Microstereolithography. *Procedia CIRP*. 2013;5:222–225.
- [118] Han L-H, Mapili G, Chen S, et al. Projection microfabrication of three-dimensional scaffolds for tissue engineering. *J Manuf Sci Eng*. 2008;130:021005.
- [119] Choi J, Wicker RB, Cho S, et al. Cure depth control for complex 3D microstructure fabrication in dynamic mask projection microstereolithography. *Rapid Prototyp J*. 2009; 15(1):59–70.
- [120] Sun C, Fang N, Wu DM, et al. Projection micro-stereolithography using digital micro-mirror dynamic mask. *Sensors Actuators A Phys*. 2005;121(1):113–120.
- [121] Bail R, Hong JY, Chin BD. Effect of a red-shifted benzotriazole UV absorber on curing depth and kinetics in visible light initiated photopolymer resins for 3D printing. *J Ind Eng Chem*. 2016;38:141–145.
- [122] Bartolo PJ, Gaspar J. Metal filled resin for stereolithography metal part. *CIRP Ann*. 2008;57(1):235–238.
- [123] Halloran JW. Ceramic stereolithography: additive manufacturing for ceramics by photopolymerization. *Annu Rev Mater Res*. 2016;46(1):19–40.
- [124] Hinczewski C, Corbel S, Chartier T. Ceramic suspensions suitable for stereolithography. *J Eur Ceram Soc*. 1998; 18(6):583–590.
- [125] Farahani RD, Dubé M, Therriault D. Three-dimensional printing of multifunctional nanocomposites: manufacturing techniques and applications. *Adv Mater*. 2016;28(28): 5794–5821.
- [126] Lin D, Jin S, Zhang F, et al. 3D stereolithography printing of graphene oxide reinforced complex architectures. *Nanotechnology*. 2015;26(43):434003.
- [127] Credi C, Fiorese A, Tironi M, et al. 3D printing of cantilever-type microstructures by stereolithography of ferromagnetic photopolymers. *ACS Appl Mater Interfaces*. 2016;8(39):26332–26342.
- [128] De Hazan Y, Heinecke J, Weber A, et al. High solids loading ceramic colloidal dispersions in UV curable media via comb-polyelectrolyte surfactants. *J Colloid Interface Sci*. 2009;337(1):66–74.
- [129] Huang Y-M, Jiang C-P. On-line force monitoring of platform ascending rapid prototyping system. *J Mater Process Technol*. 2005;159(2):257–264.
- [130] Teng WD, Edirisinghe MJ, Evans JRG. Optimization of dispersion and viscosity of a ceramic jet printing ink. *J Am Ceram Soc*. 2005;80(2):486–494.
- [131] Li K, Zhao Z. The effect of the surfactants on the formulation of UV-curable SLA alumina suspension. *Ceram Int*. 2017;43(6):4761–4767.
- [132] Goswami A, K A, Balashanmugam N, et al. Optimization of rheological properties of photopolymerizable alumina suspensions for ceramic microstereolithography. *Ceram Int*. 2014;40(2):3655–3665.
- [133] Wang J, Goyanes A, Gaisford S, et al. Stereolithographic (SLA) 3D printing of oral modified-release dosage forms. *Int J Pharm*. 2016;503(1–2):207–212.
- [134] Goyanes A, Det-Amornrat U, Wang J, et al. 3D scanning and 3D printing as innovative technologies for fabricating personalized topical drug delivery systems. *J Control Release*. 2016;234:41–48.
- [135] Martinez PR, Goyanes A, Basit AW, et al. Fabrication of drug-loaded hydrogels with stereolithographic 3D printing. *Int J Pharm*. 2017;532(1):313–317.
- [136] Martinez PR, Goyanes A, Basit AW, et al. Influence of geometry on the drug release profiles of

- stereolithographic (SLA) 3D-Printed tablets. *AAPS PharmSciTech*. 2018;19(8):3355–3361.
- [137] Ulery BD, Nair LS, Laurencin CT. Biomedical applications of biodegradable polymers. *J Polym Sci B Polym Phys*. 2011; 49(12):832–864.
- [138] Pan W, Wallin TJ, Odent J, et al. Optical stereolithography of antifouling zwitterionic hydrogels. *J Mater Chem B*. 2019;7(17):2855–2864.
- [139] Elomaa L, Pan C-C, Shanjani Y, et al. Three-dimensional fabrication of cell-laden biodegradable poly(ethylene glycol-co-depsipeptide) hydrogels by visible light stereolithography. *J Mater Chem B*. 2015;3(42):8348–8358.
- [140] Kim K, Yeatts A, Dean D, et al. Stereolithographic bone scaffold design parameters: osteogenic differentiation and signal expression. *Tissue Eng Part B Rev*. 2010;16(5): 523–539.
- [141] Schüller-Ravoo S, Teixeira SM, Feijen J, et al. Flexible and elastic scaffolds for cartilage tissue engineering prepared by stereolithography using poly(trimethylene carbonate)-based resins. *Macromol Biosci*. 2013;13(12):1711–1719.
- [142] Lee JW, Kang KS, Lee SH, et al. Bone regeneration using a microstereolithography-produced customized poly(propylene fumarate)/diethyl fumarate photopolymer 3D scaffold incorporating BMP-2 loaded PLGA microspheres. *Biomaterials*. 2011;32(3):744–752.
- [143] Bajaj P, Marchwiany D, Duarte C, et al. Patterned three-dimensional encapsulation of embryonic stem cells using dielectrophoresis and stereolithography. *Adv Healthc Mater*. 2013;2(3):450–458.
- [144] Cui X, Breitenkamp K, Finn MG, et al. Direct human cartilage repair using three-dimensional bioprinting technology. *Tissue Eng Part A*. 2012;18(11–12):1304–1312.
- [145] Elomaa L, Teixeira S, Hakala R, et al. Preparation of poly(ϵ -caprolactone)-based tissue engineering scaffolds by stereolithography. *Acta Biomater*. 2011;7(11):3850–3856.
- [146] Melchels FPW, Feijen J, Grijpma DW. A poly(D,L-lactide) resin for the preparation of tissue engineering scaffolds by stereolithography. *Biomaterials*. 2009;30(23–24):3801–3809.
- [147] Seck TM, Melchels FPW, Feijen J, et al. Designed biodegradable hydrogel structures prepared by stereolithography using poly(ethylene glycol)/poly(D,L-lactide)-based resins. *J Control Release*. 2010;148(1):34–41.
- [148] Asikainen S, van Bochove B, Seppälä JV. Drug-releasing biopolymeric structures manufactured via stereolithography. *Biomed Phys Eng Express*. 2019;5(2):025008.
- [149] Robles-Martinez P, Xu X, Trenfield SJ, et al. 3D printing of a multi-layered polypill containing six drugs using a novel stereolithographic method. *Pharmaceutics*. 2019;11(6):274.
- [150] Thrasher CJ, Schwartz JJ, Boydston AJ. Modular elastomer photoresins for digital light processing additive manufacturing. *ACS Appl Mater Interfaces*. 2017;9(45): 39708–39716.
- [151] Kuang X, Zhao Z, Chen K, et al. High-speed 3D printing of high-performance thermosetting polymers via two-stage curing. *Macromol Rapid Commun*. 2018;39(7):1700809.
- [152] Xu X, Awad A, Robles-Martinez P, et al. Vat photopolymerization 3D printing for advanced drug delivery and medical device applications. *J Control Release*. 2021;329: 743–757.
- [153] Gu Y, Chen X, Lee J-H, et al. Inkjet printed antibiotic- and calcium-eluting bioresorbable nanocomposite micropatterns for orthopedic implants. *Acta Biomater*. 2012;8(1): 424–431.
- [154] Liang K, Carmone S, Brambilla D, et al. 3D printing of a wearable personalized oral delivery device: a first-in-human study. *Sci Adv*. 2018;4(5):eaat2544.
- [155] Ozbolat IT, Yu Y. Bioprinting toward organ fabrication: challenges and future trends. *IEEE Trans Biomed Eng*. 2013;60(3):691–699.
- [156] Schubert C, Van Langeveld MC, Donoso LA. Innovations in 3D printing: a 3D overview from optics to organs. *Br J Ophthalmol*. 2014;98(2):159–161.
- [157] Krkobabić M, Medarević D, Pešić N, et al. Digital light processing (DLP) 3D printing of atomoxetine hydrochloride tablets using photoreactive suspensions. *Pharmaceutics*. 2020;12(9):833–817.
- [158] Tagami T, Morimura C, Ozeki T. Effective and simple prediction model of drug release from “ghost tablets” fabricated using a digital light projection-type 3D printer. *Int J Pharm*. 2021;604:120721.
- [159] Goyanes A, Madla CM, Umerji A, et al. Automated therapy preparation of isoleucine formulations using 3D printing for the treatment of MSUD: first single-centre, prospective, crossover study in patients. *Int J Pharm*. 2019;567:118497.
- [160] Lipson H. New world of 3-D printing offers “completely new ways of thinking”: Q&A with author, engineer, and 3-D printing expert Hod Lipson. *IEEE Pulse*. 2013;4(6):12–14.
- [161] Krkobabić M, Medarević D, Cvijić S, et al. Hydrophilic excipients in digital light processing (DLP) printing of sustained release tablets: impact on internal structure and drug dissolution rate. *Int J Pharm*. 2019;572:118790.
- [162] Xu X, Robles-Martinez P, Madla CM, et al. Stereolithography (SLA) 3D printing of an antihypertensive polyprintlet: case study of an unexpected photopolymer-drug reaction. *Addit Manuf*. 2020;33:101071.
- [163] Pere CPP, Economidou SN, Lall G, et al. 3D printed micro-needles for insulin skin delivery. *Int J Pharm*. 2018;544(2): 425–432.
- [164] Ochoa M, Zhou J, Rahimi R, et al. Rapid 3D-print-and-shrink fabrication of biodegradable microneedles with complex geometries. 2015 Transducers – 2015 18th International Conference on Solid-State Sensors, Actuators and Microsystems, TRANSDUCERS. Anchorage, AK, 2015. p. 1251–1254.
- [165] Lu Y, Mantha SN, Crowder DC, et al. Microstereolithography and characterization of poly(propylene fumarate)-based drug-loaded microneedle arrays. *Biofabrication*. 2015;7(4):045001.
- [166] Miyazaki T, Hotta Y, Kunii J, et al. A review of dental CAD/CAM: current status and future perspectives from 20 years of experience. *Dent Mater J*. 2009;28(1):44–56.
- [167] Xu X, Goyanes A, Trenfield SJ, et al. Stereolithography (SLA) 3D printing of a bladder device for intravesical drug delivery. *Mater Sci Eng C Mater Biol Appl*. 2021;120: 111773.
- [168] Vivero-Lopez M, Xu X, Muras A, et al. Anti-biofilm multi drug-loaded 3D printed hearing aids. *Mater Sci Eng C Mater Biol Appl*. 2021;119:111606.
- [169] Klein GT, Lu Y, Wang MY. 3D printing and neurosurgery-ready for prime time? *World Neurosurg*. 2013;80(3–4): 233–235.
- [170] Sun J, Peng Z, Zhou W, et al. A review on 3D printing for customized food fabrication. *Procedia Manuf*. 2015;1: 308–319.
- [171] Nathan GL. The future: creating novel foods using 3D printing. <https://www.foodnavigator.com/Article/2010/12/>

- 23/Looking-to-the-future-Creating-novel-foods-using-3D-printing. 2012.
- [172] Michail N. Biozoon's 3D printed smooth foods target Europe's elderly, <https://www.foodnavigator.com/Article/2016/09/26/Biozoon-s-3D-printed-smooth-foods-target-Europe-s-elderly>. 2016.
- [173] Serizawa R, Shitara M, Gong J, et al. 3D jet printer of edible gels for food creation. In: Goulbourne NC, Naguib HE, editors. Behavior and mechanics of multifunctional materials and composites. Bellingham: SPIE; 2015. p. 90580A.
- [174] Gohd C. NASA astronauts can now 3D-print pizzas in space. <https://futurism.com/nasa-astronauts-can-now-3d-print-pizzas-in-space>. 2017.
- [175] Vithani K, Goyanes A, Jannin V, et al. An overview of 3D printing technologies for soft materials and potential opportunities for lipid-based drug delivery systems. *Pharm Res*. 2018;36(1):4.
- [176] Pandey M, Choudhury H, Fern JLC, et al. 3D printing for oral drug delivery: a new tool to customize drug delivery. *Drug Deliv Transl Res*. 2020;10(4):986–1001.
- [177] Ali A, Ahmad U, Akhtar J. 3D printing in pharmaceutical sector: an overview. In: Pharmaceutical formulation design – recent practices. London: IntechOpen; 2020.
- [178] Genina N, Fors D, Vakili H, et al. Tailoring controlled-release oral dosage forms by combining inkjet and flexographic printing techniques. *Eur J Pharm Sci*. 2012;47(3):615–623.
- [179] Skowrya J, Pietrzak K, Alhnan MA. Fabrication of extended-release patient-tailored prednisolone tablets via fused deposition modelling (FDM) 3D printing. *Eur J Pharm Sci*. 2015;68:11–17.
- [180] Melocchi A, Parietti F, Loreti G, et al. 3D printing by fused deposition modeling (FDM) of a swellable/erodible capsular device for oral pulsatile release of drugs. *J Drug Deliv Sci Technol*. 2015;30:360–367.
- [181] Katstra WE, Palazzolo RD, Rowe CW, et al. Oral dosage forms fabricated by three dimensional printing(TM). *J Control Release*. 2000;66(1):1–9.
- [182] Yu DG, Branford-White C, Yang YC, et al. A novel fast disintegrating tablet fabricated by three-dimensional printing. *Drug Dev Ind Pharm*. 2009;35(12):1530–1536.
- [183] Deng GY, Xiang LY, Wei DH, et al. Tablets with material gradients fabricated by three-dimensional printing. *J Pharm Sci*. 2007;96:2446–2456.
- [184] Yi H-G, Choi Y-J, Kang KS, et al. A 3D-printed local drug delivery patch for pancreatic cancer growth suppression. *J Control Release*. 2016;238:231–241.
- [185] Holländer J, Genina N, Jukarainen H, et al. Three-dimensional printed PCL-based implantable prototypes of medical devices for controlled drug delivery. *J Pharm Sci*. 2016;105(9):2665–2676.
- [186] Shim IK, Yi H-J, Yi H-G, et al. Locally-applied 5-fluorouracil-loaded slow-release patch prevents pancreatic cancer growth in an orthotopic mouse model. *Oncotarget*. 2017;8(25):40140–40151.
- [187] Shi X, Cheng Y, Wang J, et al. 3D printed intelligent scaffold prevents recurrence and distal metastasis of breast cancer. *Theranostics*. 2020;10(23):10652–10664.
- [188] Hafezi F, Scoutaris N, Douroumis D, et al. 3D printed chitosan dressing crosslinked with genipin for potential healing of chronic wounds. *Int J Pharm*. 2019;560:406–415.
- [189] Tagami T, Ito E, Hayashi N, et al. Application of 3D printing technology for generating hollow-type suppository shells. *Int J Pharm*. 2020;589:119825.
- [190] Seoane-Viaño I, Trenfield SJ, Basit AW, et al. Translating 3D printed pharmaceuticals: from hype to real-world clinical applications. *Adv Drug Deliv Rev*. 2021;174:553–575.
- [191] Tagami T, Ito E, Kida R, et al. 3D printing of gummy drug formulations composed of gelatin and an HPMC-based hydrogel for pediatric use. *Int J Pharm*. 2021;594:120118.

Stereolithography 3D printing technology in pharmaceuticals: a review

Subhash Deshmane, Prakash Kendre, Hitendra Mahajan & Shirish Jain

To cite this article: Subhash Deshmane, Prakash Kendre, Hitendra Mahajan & Shirish Jain (2021): Stereolithography 3D printing technology in pharmaceuticals: a review, Drug Development and Industrial Pharmacy, DOI: [10.1080/03639045.2021.1994990](https://doi.org/10.1080/03639045.2021.1994990)

To link to this article: <https://doi.org/10.1080/03639045.2021.1994990>



Published online: 29 Oct 2021.



Submit your article to this journal [↗](#)



Article views: 20





View related articles [↗](#)



View Crossmark data [↗](#)

Stereolithography 3D printing technology in pharmaceuticals: a review

Subhash Deshmane^a , Prakash Kendre^a, Hitendra Mahajan^b  and Shirish Jain^a

^aDepartment of Pharmaceutics, Rajarshi Shahu College of Pharmacy, Malvihir, India; ^bDepartment of Pharmaceutics, R. C. Patel Institute of Pharmaceutical Education and Research, Shirpur, India

ABSTRACT

Three-dimensional printing (3DP) technology is an innovative tool used in manufacturing medical devices, producing alloys, replacing biological tissues, producing customized dosage forms and so on. Stereolithography (SLA), a 3D printing technique, is very rapid and highly accurate and produces finished products of uniform quality. 3D formulations have been optimized with a perfect tool of artificial intelligence learning techniques. Complex designs/shapes can be fabricated through SLA using the photopolymerization principle. Different 3DP technologies are introduced and the most promising of these, SLA, and its commercial applications, are focused on. The high speed and effectiveness of SLA are highlighted. The working principle of SLA, the materials used and applications of the technique in a wide range of different sectors are highlighted in this review. An innovative idea of 3D printing customized pharmaceutical dosage forms is also presented. SLA comprises several advantages over other methods, such as cost effectiveness, controlled integrity of materials and greater speed. The development of SLA has allowed the development of printed pharmaceutical devices. Considering the present trends, it is expected that SLA will be used along with conventional methods of manufacturing of 3D model. This 3D printing technology may be utilized as a novel tool for delivering drugs on demand. This review will be useful for researchers working on 3D printing technologies.

ARTICLE HISTORY

Received 7 March 2021
Revised 14 July 2021
Accepted 12 October 2021

KEYWORDS

Additive manufacturing; customized dosage form; photocurable resins; solid freeform fabrication; three-dimensional printing; vat polymerization

Introduction

Three-dimensional printing (3DP) technology has opened new frontiers in pharmaceutical and other sectors. Simple tools and poor-standard object of some materials cannot yield high-quality products from any bulk substances. This is the limitation of typical or common methods of manufacture [1,2]. In contrast, the 3DP technique is sophisticated, rapid, highly automated, easy to use, customized and cost effective [3–6]. The 3DP technology is used to make 3D objects by laying layers on top of each other. Biological materials, alloys, tissues/cells, metals, wood, thermoplastics, etc. are used in making 3D objects [7,8]. Anatomical prostheses, biological tissues, heart valves, hearing aids and different parts or models of machinery are among the well known examples of 3D objects [9–13]. Innovative scanning and printing systems hold promise in the area of medicine [14]. Over the last three decades, pharmaceutical companies have been looking at 3DP technology to understand the roles it will play and how best to use it. Against a background in which new formulations, biomedical devices and medicines were being developed daily, Professor Clive Roberts, from the University of Nottingham, said that many researchers have designed and prepared many different dosage forms using 3DP techniques [15]. As with most complex 3D architectures, medical devices were printed directly using 3DP technology in the early 2000s [16,17]. Devices specific to a patient's anatomy were also fabricated. Optimized tools and techniques are a prerequisite for making formulations of the desired shapes and sizes. In August 2015, Aprelia Pharmaceuticals printed the first 3D drug that was approved by the FDA. This was Spritam (Levetiracetam) [18,19], a porous structure printed layer by layer

and reformulated to treat dysphagia. When it comes in contact with saliva, it dissolves rapidly and delivers a high dose (1 g) of an antiepileptic drug from a tightly packed pill [20]. The non-uniform quality of some finished products is mainly caused by manufacturing processes such as milling, mixing, granulation and compression. Certain tools related to drug release, drug content and product stability are affected by these operations [21,22]. 3DP is proving to be the solution in overcoming such challenges [23].

Now a day's we can serve better with readdressing of artificial intelligence (AI). In the various filed, AI igniting with notice development [24,25]. Minimum time and cost is the new perspectives of AI in optimization of 3D products that, creating interest in the researchers for launching the products in market [26]. Design of experiments is also mostly used in optimization, but computer aided artificial neural network(ANN) have more attention and delight [27]. Extended drug release ibuprofen tablet fabricated with crosslinked polymers printed with artificial neural network [28]. A perfect tool of AI learning techniques develops pharmaceutical formulations in 3DP. Web bases software M3DISEEN [29] and accurate optimal parameters are the best example of AI [30]. 3D printed tablets of atomoxetine fabricated by ANN release the tailored drug release from immediate to prolong [31]. A solid three-dimensional object of any shape can be prepared starting from a digital model through an automated sequential layering process [32]. It means this technique shares the theme of a sequential layer of material addition of 3D envelope [33,34]. 3DP allows more complex designs or shapes to be fabricated compared with conventional manufacturing processes [35]. Objects can be fabricated using 3DP methods through digital files [36–38].

Now 3DP technology is emerging as a technology for designing and preparing personalized medicines and novel formulations [39–42]. 3DP technology increases the speed with which personalized pharmaceutical drugs can be produced, using computer-based drug design systems [43,44]. First 3D printer in the world is launched by FabRx for personalized medicines in 2020. M3DIMAKER™ used from drug development timeline to human clinical trials [45]. Semi-liquid binding solutions are mixed with powder beds to produce adhesive particles in inkjet printing [46]. According to the United States Government Accountability Office, a 3DP method is a layer-by-layer process used for making 3D objects from digital models [47]. Other synonyms for '3DP technology' are 'rapid prototyping,' 'solid free form' and 'additive manufacturing and fabrication' [48,49]. The American Society of Mechanical Engineers has suggested 'additive manufacturing' be used as an alternate term for 3DP for the purposes of pharmaceutical manufacturing processes [50].

Various 3DP technologies are briefly described here.

Thermal ink-jet printing

In this process, the printing materials are deposited on the printed product. The materials applied layer by layer in the form of droplets through small-diameter nozzles, and UV light is used to harden the 3D object. Ink-jet systems comprise two types of technologies, continuous and drop on demand printing [51,52]. Living cells are protected and maintained in an aqueous environment by more biocompatible thermal inkjet 3D printer [53,54].

Fused deposition modeling (FDM)

Hot melt extrusion (HME) based FDM, in which the materials are softened or melted by heating during the printing process [55,56]. FDM 3DP is used to manufacture delayed-release tablets without an outer enteric coating and also provides personalized doses of medicines [57]. The FDM 3DP technique, however, suffers various limitations. These include non-availability of suitable polymers because elevated temperature (~200 °C) may degrade certain polymers and drug also [58], stagnant and often partial drug release (because the drug remains trapped in the polymers) [59,60] and difficulties in evaluating the solubility of the drug and additives in the presence of polymers [61]. Only poly vinyl alcohol (PVA) and poly lactic acid (PLA) is mostly used.

Fused material is extruded as a filament or wire through a nozzle, which turns the flow on and off. It gets heated and melts the material. Extrusion require materials in semisolid form and does not require high temperature, therefore choice for polymers is quite more [58]. It moves horizontally and vertically by computer-aided manufacturing. The sacrificial material is later removed using hot water, a water jet or a solvent. Mainly used filaments are acrylonitrile butadiene styrene and polylactic acid (PLA) [62].

Selective laser sintering

A liquid binder and a powder are used in this technique. The process chamber is filled with the powder and then the binder is introduced uniformly through nozzles at a moderate pressure. The required 3D object is created by gluing the powder particles with the binder [63]. Smooth and accurate parts has been produced using fine particles, which is difficult to spread and handling [64]. Photopolymerization of powder is done in SLS using high power

laser as an energy source. SLS technology has many advantages such as, high strength, speed and chemical resistance [65].

All the methods described have limitations in terms of the technique, quality of the products and properties of the materials. A literature survey revealed that stereolithography is the only method in which the resolution is fine and thermal degradation of substances is avoided.

Stereolithography (SLA)

is the first laser-based printing technology. It was developed in 1980 by Japanese Dr, Kodama and granted the first patent for rapid prototyping and is well known in commerce as the solid freeform fabrication (SFF) process [66,67]. 3D objects are produced by SLA through the superintended solidification of a liquid resin by a photo-polymerization mechanism [68,69]. SLA is used to make different types of production parts, medical models, prototypes, patterns, computer hardware and biomaterials. The term 'SLA' was coined by Chuck Hull in 1984 and a patent was granted in 1986, but research on SLA began in the 1970s. Laser-based SLA and digital light projection are the two types of SLA [70]. In the laser-based method, the product is fabricated in a bottom-up, vector-by-vector manner using a computer-manipulated laser beam system [71] where UV light is passed through the transparent bottom of a vat containing photosensitive resin [72,73]. The stereolithographic technique has a number of unique features [74]. Its fine resolution [75] permits complex structures to be created. During the printing process, the heating is minimal and thereby thermal degradation of drugs is avoided [76]. Hence SLA is particularly useful for thermo-labile drugs [77]. The resolution and accuracy of SLA are superior to those of other techniques [78,79]. With FDM, differences between layers results in anisotropic effects and requires adjustments in the geometry of the object. Thus FDM is unsuitable for certain applications. In contrast, highly isotropic parts can be created using SLA. The integrity of the material is tightly controlled by considering a number of factors in SLA. Better patient compliance, customized formulations, modulated drug release dosage forms and deliver-on-demand medications can all be prepared using SLA [80–82]. SLA is faster than FDM and selective laser sintering (SLS) [83]. Children's of 4-11 years age has prefer 3D printed tablets on visual inspection [84]. SLA also has some limitations. The limited availability of a number of photocrosslinkable polymers is the main drawback of SLA. The available materials require recognition as safe. When the drugs are exposed to laser, they may lead to lung diseases [85]. Another disadvantage of SLA is that it is quite expensive.

Principle of stereolithography

When ultraviolet (UV) radiation is passed through a photosensitive resin, it is photopolymerized totally. This is the basic principle of SLA. Low-power UV radiation (up to 1000 mW) from a He-Cd/Nd:YVO4 laser solidifies a thin layer of resin on the surface [86]. The platform is the main component of a SLA machine. The 3D object is formed in a bath of liquid resin in which the platform is immersed. The laser source is another important part. It is controlled by a computer. All the parts of the machine can be cleaned using a solvent after a 3D object is made. Any resinous materials on the surface can be removed using the solvent [87]. A UV oven is used to cure the cleaned and finished 3D object and with the help of CAD model [88], every layer of resin is being scanned by laser technique [89]. Pharmaceutical formulation containing higher water content when exposed to visible light

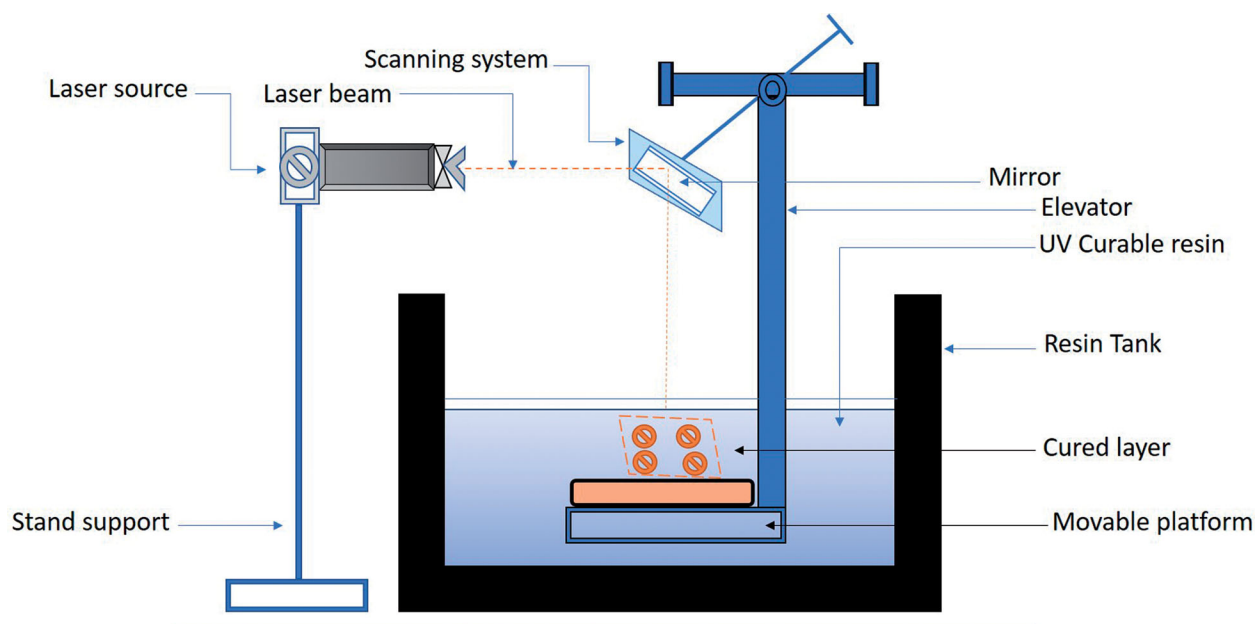


Figure 1. Stereolithographic 3D printer.

irradiation process, results pronounced effect on drug release from 27% to 95% over eight hours [90].

Working of SLA

Stereolithographic is based on the photo-polymerization in which superintended solidification of a liquid resin is executed [55]. A vessel containing the liquid resin (photopolymer) is fixed on the main (fixed) platform (Figure 1). An elevator with a movable platform, located in the vessel, is attached to the main platform. Initially, the movable platform is lifted close to the surface of the liquid resin photopolymer. After one cycle of UV laser treatment, a new photopolymerized layer is formed, and the thickness of the next layer is set by moving the platform down. The 3D object is produced by repeated laser treatments. Due to gravitational force and lateral pressure of subsequent coat, cross section may not precisely form 3D structure. Therefore supporting structure of filaments are form and help in holding the cross section. Filaments support is bring out with the help of CAD model, used on the stereolithography machine during the preparation [91]. Finally, this supports is being removed manually. The manufacturing of pharmaceutical products using SLA allows individualization of medicines. Despite the numerous medical and economic benefits, there are some technical challenges that restrict the extensive commercial use of 3DP. These challenges include the limited number of biocompatible materials in 3DP printing, the stability of active pharmaceutical ingredient, the efficiency as well as reproducibility of the methods, and the quality of the finished products. A computer interprets the information available in STL files and sends it to the 3D printer, where the data are converted into a 3D structure. The kinetics of the curing reactions depends on the scanning speed, the chemistry and the amounts of the monomer and photoinitiators [92,93].

Materials used in stereolithographic printing

The choice of photopolymer is of utmost importance in SLA [94,95]. The lack of approval of photosensitive materials by the regulatory authority (the FDA) limits the use of SLA significantly,

even though photosensitive materials are used in tissue engineering. During the last decade, a number of photocrosslinkable polymers have been developed. Poly(ethylene glycol) diacrylate (PEGDA) [73,96], poly(2-hydroxyethyl methacrylate) (pHEMA) [97], poly(ethylene glycol) dimethacrylate (PEGDMA) [98,99] and poly(propylene fumarate)/diethyl fumarate (PPF/DEF) [100,101] are examples of photocrosslinkable polymers. Biomedical materials have applications in surgical tools, hearing aids, knee joint appliances and dental appliances [102]. The multiple resins for one build showed patterning with PEG-DMA and PEG-DA with fluorescently labeled dextran, fluorescently labeled bioactive PEG or bioactive PEG in different regions of the scaffold [103]. Complex 3D scaffolds can be fabricated using photocrosslinkable poly(propylene fumarate) (PPF) [104,105], which requires reactive diluents containing significant amounts of non-degradable components. N-vinyl-2-pyrrolidone and diethyl fumarate are used as diluents to reduce the viscosity of the resin during processing [106]. Reconstruction of cranial defects in rabbits is possible because of the ability to produce controlled microstructures [89]. Trimethylene carbonate, polycaprolactone and poly(D,L-lactide) are examples of materials used commonly in tissue engineering [107,108].

The essential components of photocurable resins used in SLA are shown in Figure 2. The precursors are liquid molecules that form a solid 3D structure on exposure to light. Because of the high reactivity of acrylate-based resins, 3D structures can be built rapidly. Hence, acrylate-based resins are commonly used in SLA [46,109]. Deformity in printed part is the main disadvantage of acrylate resins. This is due to the high shrinkage of resins during printing [110]. The problem of distortion can be solved by using a combination of an acrylate resin and methacrylates. The polymerization reaction may be inhibited by a resin's sensitivity to oxygen. The shrinkage of epoxy resins is remarkably lower than that of acrylates [111,112]. An acrylate and epoxy-based resins in combination may have an accelerated curing rate and reduced shrinkage [112–114]. Photoinitiators (PIs) are the resin components that normally react with light. A PI attains an excited state ion being irradiated with radiation of the right wavelength. Xenon lamps, mercury arc lamps, LEDs or lasers used as light source. UV (190–400 nm), visible (400–700 nm) or IR (700–1000 nm) range of

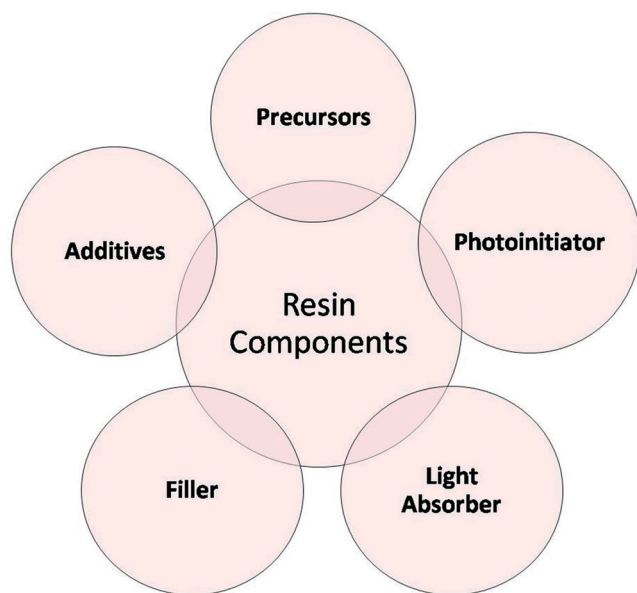


Figure 2. Components of resin for SLA.

wavelength can be used. Visible LEDs are ecofriendly and safe. Water soluble PI, Irgacure 651 has been used in the fabrication of biocompatible hydrogel scaffold [115]. The PI in the excited starts the curing reaction. A suitable photoinitiator is selected on the basis of the precursor utilized. The mechanical properties of device, reaction kinetics, cross-linking density, light dosage required and conversion to printed device depend on the type and amount of PI [116,117]. The light absorber is another material used in SLA processes. A light absorber diminishes the perception of light into the resin and thereby controls the depth to which the resin is cured [118]. The cure depth needs to be precisely defined in complex geometries to prevent unnecessary curing and loss of the features of the model [119,120]. Benzotriazole derivatives are common examples of UV light absorbers [121]. Filling resins with powder, debinding and sintering the printed part or printing the parts is the basic requirement in the fabrication of ceramic materials or metals by SLA [122,123]. In thin structures, the binder burns out easily and fills any cracks or defects that form. A high filler content is recommended for reducing the shrinkage of resins and thereby producing geometrically accurate parts [124]. Optical, thermal, mechanical and electrical properties can be further modified through the use of nano size particles in the SLA resin [125–127]. Long shelf-life (stable) slurries, rheological additives and stabilizers used during the fabrication processes increase the solid loading [128]. A high fraction of solids increases the viscosity of the slurry when the particles are small in size [122]. A high viscosity changes the flow behavior of the resin and interferes with coating mechanisms [129]. This can be overcome by using dispersants such as oligomeric surfactants [130], long-chained oleic acid [131] or phosphine oxides [132].

3DP stereolithography in pharmaceuticals

Stereolithographic 3D printers have been used in various novel and innovative projects. Distinct types of devices, models and dosage forms have been producing using SLA. Researcher used 3D printing applications in fabrication of various dosage forms are mentioned in Table 1.

Pharmaceutical applications of 3D printing technology

SLA can alter elastic silicones for soft model to high strength post cured resins [150,151]. In the field of medical device formation and drug delivery, SLA offers unique applications [152]. Some applications of the SLA 3DP technique are discussed here.

Individualized drug dosing

Today's patient suffers from more than one disease and requires a single multi-dose form of formulation [153,154]. A personalized and accurate dose is required for better compliance. An optimal multi-dose form containing a narrow therapeutics index drug can be given to a patient whose pharmacogenetic profile, age and race are known [65,155]. Fabrication of complete, effective formulations is the second important role of 3D printing technology. One active ingredient can be dispensed in one form as a result [32]. This helps increase the efficacy of the drugs and reduces adverse reactions, if any [156]. Poly(ethylene glycol) diacrylate 700 (PEGDA700) as initial material used in fabrication of patient customized tablets of atomoxetine hydrochloride by digital light processing (DLP) 3D printing technique [157] and Ghost tablets as unique prediction model as future tailored medicines that release entrapped drug without disintegrating [158]. Tailored chewable formulation containing isoleucine fabricated by 3DP offers rapid and feasible approach in hospital setting in maple sirup urine disease [159].

Modified drug release profile

A modified drug release profile requires the preparation of complex geometries containing multiple drugs of porous texture, surrounded by a modulated layer of barriers [160]. A multilayered bone implant based on a pulse release mechanism, with a distinct profile in which rifampicin and isoniazid are released alternately was prepared using 3DP technology. A very small quantity of chloramphenicol maleate could also be released at a predetermined time with perfect accuracy from a cellulose powder substrate using a 3D printing technique [155]. Problem associated with slow and incomplete release of paracetamol has been overcome by sustained released 3D printlet using hydrophilic excipients [161]. Multilayered 3D printed tablets containing four antihypertensive drugs reports, chemical interaction of drug and polymer unexpectedly [162].

Microneedles

Microstructure of microneedles delivers macromolecules through the skin (as in insulin skin delivery) more effectively than does a conventional transdermal dosage form [163]. The stereolithographic method of 3DP allows more complex and sophisticated geometries of microneedles to be fabricated. Ochoa *et al* developed a novel manufacturing process for microneedles with 9.6 μm radius tips. Sharp polymeric microneedles for vaccine delivery were manufactured using the enhanced resolution limit of the 3DP technique [164]. Microstereolithography helped fabricate microneedles through which a 5 weeks' controlled release of the anticancer dacarbazine drug was achieved. Microneedles with a cone-and-pyramid shape were fabricated using a biocompatible resin [165].

Table 1. SLA 3DP applications in pharmaceuticals.

Formulations	Specifications	Reference(s)
4-aminosalicylic (4-ASA) acid and paracetamol-loaded 3D tablets.	Different concentrations of polyethylene glycol diacrylate (PEGDA) and polyethylene glycol have been used in printing solutions	[133]
An anti-acne drug (salicylic acid)-loaded 3D model of a personalized shape nose.	With SLA, there was no drug degradation, and the resolution was higher than with FDM	[134]
A hydrogel of cross-linked polyethylene glycol diacrylate containing ibuprofen.	Because of entrapment of water, pre-wetted, drug loaded hydrogel and devices can be prepared	[135]
Tablets containing a solid dispersion of paracetamol and polyethylene glycol.	A different shape of tablets was unattainable due to powder compaction.	[136]
A mask of higher resolution was produced using SLA.	The drug loading was high, and there was insignificant degradation of salicylic acid.	[137]
Antifouling hybrid hydrogels.	A highly solvated and tough hydrogel increases the gelation rate and the elasticity of the resulting hybrid hydrogel.	[138,139]
Bone tissue engineering is the main prominence area of SLA.	–	[140]
Bone formation	Bone formation was promoted using SLA in rats with cranial defects in <i>in-vivo</i> studies.	[141]
Soft tissue	Bovine chondrocytes, flexible and soft cartilage tissues was fabricated.	[142]
Encapsulation of NIH/3T3	PEG-DMA with human chondrocytes was promoted with an inkjet printer.	[143,144]
Synthesis of novel macromers without any reactive diluents.	–	[145–147]
Polycaprolactone porous structures.	Porous structures scaffolds to release lidocaine more rapidly compared with the solid form.	[148]
Multilayered polypill with variable drug content and shape	Six drugs, paracetamol, naproxen, chloramphenicol, prednisolone and aspirin were printed with different geometries and materials	[149]

Tailored prostheses and implants

Prostheses and implants of any possible shape can be fabricated using 3DP technology. In the present context, translation of MRI images, CT scans, and X-ray images is desirable [156,160,165]. Both complex and standard surgical implants and prosthetic limbs can be prepared in less than 24 h. The Layer Wise Company fabricated spinal, maxillofacial and dental implants [160,166]. The BIOMED Research Institute, Belgium successfully implanted 3D printed mandibular prostheses [165]. Prosthetic ears were made from silver nanoparticles, silicon and chondrocytes using 3DP technology to detect electromagnetic frequencies. The fit of every model is perfect and the price is low thanks to 3DP technology. Nowadays more than 90% of the customized hearing aids are fabricated using 3D printers [156]. Revolutionary localized delivery of lidocaine HCL has been possible by 3DP indwelling bladder device [167]. A 3D printed hearing aid released antibiotics for more than two weeks and inhibits any biofilm and bacterial growth on device [168].

Anatomical models for surgical preparations

There are individual variations in the complex human anatomy. Before performing medical surgery, obtaining knowledge regarding the patient's surgical or anatomical part is important. The size and shape of a specific anatomy requires a complex surgical procedure. 3DP technology provides vital tools for making anatomical models that fit perfectly [160, 169]. Surgeons use calcified aortas manufactured using 3D printers [160]. The airways of premature infants have been fabricated using 3DP methods to evaluate aerosols [160].

Soft materials in the food industry

Traditional food preparation does not produce customized food or recipes for specific nutritional requirements. Food 3D printing

involves premixing and depositing the required nutrients in distinct layers [170]. Different customers (the elderly, pregnant or feeding mothers, children, athletes) require different proportions of carbohydrates, fats and proteins [171]. The use of 3DP to make smooth food for elderly people having difficulties in chewing and swallowing [172,173]. Recently, BeexHex, USA, a 3D printing company, prepared food for National Aeronautics and Space Administration (NASA) astronauts when they were on a mission [174]. The food-containing-drug approach will become the new path food-based pharmaceutical drug delivery systems [175].

Other pharmaceutical dosage forms

Different 3DP technologies are available for the fabricating customized [176] pharmaceutical dosage forms. Some of these dosage forms are focused on here. Accurate and tailored controlled released dosage forms have been fabricated using 3D printers [177]. Also drug can be printed on porous carrier using flexographic printers [178]. 3D printer was used to manufacture highly adjustable, affordable, small delayed-release prednisolone tablets in poly(vinyl alcohol) filaments [179]. An oral pulsatile release capsular model based on erodible hydroxypropyl cellulose was fabricated by Melocchi *et al.* using an FDM 3D printer [180]. Oral dosage forms with accurate and uniform content and excellent dosage control have been fabricated using 3DP technology [181]. A fast-disintegrating tablet in which the microstructure and surface texture are controlled was fabricated using a 3D printer [182]. A matrix tablet with zero-order drug-release characteristics in the radial direction was also manufactured using 3DP technology [183]. A biodegradable implant patch containing a high dose of fluorouracil (drug) and poly-lactic-co-glycolic acid and polycaprolactone (carrier) was fabricated using a 3DP technique for local delivery of anticancer drugs [184,185]. Tablets containing 4-aminosalicylic acid and paracetamol in a combined form were produced using stereolithography. These tablets have a customized drug-

release profile [133]. Making biodegradable patches of customized shapes for delivering drugs exactly at a tumor site is another possibility with 3DP techniques. A sustained-release patch containing an anticancer drug, 5-fluorouracil, and a blend of polycaprolactone and poly(lactide-co-glycolide) was prepared using 3DP, which had site-specific characteristics [186]. A 3D printed poly(lactic-co-glycolic acid), gelatin and chitosan scaffold loaded with anticancer drugs significantly inhibited the recurrence and growth of breast cancer and reduced drug toxicity with a sustained action [187]. Functionally characterized 3D printed chitosan based film prepared with genipin as crosslinker shown promising effect for chronic wound [188]. Two drugs in separate compartments of hollow shell suppository shell prepared by FDM 3DP become advanced model for pediatric patients [189]. 3D printed suppository molds were fabricated to cast the self supporting suppositories [190]. Gummy drug formulation (hydrogel) containing lamotrigine for pediatric patients was fabricated by 3D bioprinter with perspective of future clinical setting [191].

Conclusions

A rapid, sophisticated and highly accurate method of fabricating medical devices, biological tissues, alloys, tailored dosage forms and many more is offered by 3DP technology. Solid forms can be fabricated using the photopolymerization mechanism and photocurable resins. Customized dosage forms produced using the 3DP technique may improve patient compliance. SLA is a very promising technique. It improves the stability and resolution, and degradation of the materials is avoided. The SLA 3DP technology offers significant potential benefits in the manufacture of pharmaceuticals, medical devices and many other devices. 3DP technology is an innovative scanning and printing technology that provides hope that most of the present limitations can be overcome. It is considered one of the most hopeful areas of medicine.

Disclosure statement

No potential conflict of interest was reported by the author(s).

Funding

The author(s) reported there is no funding associated with the work featured in this article.

ORCID

Subhash Deshmane  <http://orcid.org/0000-0002-0563-4075>
Hitendra Mahajan  <http://orcid.org/0000-0001-6648-144X>

References

- [1] Campbell TW, C, Ivanova O, Garrett B. Could 3d printing change the world? Technologies and implications of additive manufacturing. Washington (DC): Atlantic Council; 2012. p. 1–14.
- [2] Hwang HH, Zhu W, Victorine G, et al. 3D-printing of functional biomedical microdevices via light- and Extrusion-Based approaches. *Small Methods*. 2018;2(2):1700277.
- [3] Peterson GI, Larsen MB, Ganter MA, et al. 3D-printed mechanochromic materials. *ACS Appl Mater Interfaces*. 2015;7(1):577–583.
- [4] Anciaux SK, Geiger M, Bowser MT. 3D printed micro free-flow electrophoresis device. *Anal Chem*. 2016;88(15):7675–7682.
- [5] Wang X, Ao Q, Tian X, et al. 3D bioprinting technologies for hard tissue and organ engineering. *Materials*. 2016;9(10):802.
- [6] Noorani R. 3D printing: technology, applications, and selection. 1st ed. Boca Raton (FL): CRC Press; 2017.
- [7] Randolph SA. 3D printing: what are the hazards? *Workplace Health Saf*. 2018;66(3):164–164.
- [8] Kim J, Kong JS, Han W, et al. 3D cell printing of tissue/organ-mimicking constructs for therapeutic and drug testing applications. *IJMS*. 2020;21(20):7757.
- [9] Gong H, Woolley AT, Nordin GP. High density 3D printed microfluidic valves, pumps, and multiplexers. *Lab Chip*. 2016;16(13):2450–2458.
- [10] Macdonald NP, Cabot JM, Smejkal P, et al. Comparing microfluidic performance of three-dimensional (3D) printing platforms. *Anal Chem*. 2017;89(7):3858–3866.
- [11] Johnson AR, Caudill CL, Tumbleston JR, et al. Single-step fabrication of computationally designed microneedles by continuous liquid interface production. *PLoS One*. 2016;11(9):e0162518.
- [12] Chrzan R, Miechowicz S, Urbanik A, et al. Individually fitted hearing aid device manufactured using rapid prototyping based on ear CT. A case report. *Neuroradiol J*. 2009;22(2):209–214.
- [13] Dhir V, Itoi T, Fockens P, et al. Novel ex vivo model for hands-on teaching of and training in EUS-guided biliary drainage: creation of "Mumbai EUS" stereolithography/3D printing bile duct prototype (with videos). *Gastrointest Endosc*. 2015;81(2):440–446.
- [14] Ventola CL. Medical applications for 3D printing: current and projected uses. *P T*. 2014;39(10):704–711.
- [15] Tunnicliffe A. The past, present and future of 3D printing in the pharmaceutical industry. 2020. <https://www.ns-healthcare.com/analysis/additive-manufacturing-3d-printing/>
- [16] Maulvi FA, Shah MJ, Solanki BS, et al. Application of 3D printing technology in the development of novel drug delivery systems. *Int J Drug Dev Res*. 2017;9:44–49. <https://www.ijddr.in/drug-development/application-of-3d-printing-technology-in-the-development-of-novel-drug-delivery-systems.php?aid=18776>
- [17] Park JH, Jung JW, Kang H-W, et al. Indirect three-dimensional printing of synthetic polymer scaffold based on thermal molding process. *Biofabrication*. 2014;6(2):025003.
- [18] Pravin S, Sudhir A. Integration of 3D printing with dosage forms: a new perspective for modern healthcare. *Biomed Pharmacother*. 2018; 107:146–154.
- [19] Prasad LK, Smyth H. 3D printing technologies for drug delivery: a review. *Drug Dev Ind Pharm*. 2016;42(7):1019–1031.
- [20] First 3D-printed pill. *Nat Biotechnol*. 2015;33:1014–1014.
- [21] Ursan ID, Chiu L, Pierce A. Three-dimensional drug printing: a structured review. *J Am Pharm Assoc*. 2013;53(2):136–144.
- [22] O Oyewumi M. 3D printing technology in pharmaceutical drug delivery: prospects and challenges. *J Biomol Res Ther*. 2015;04(04):1–3.
- [23] Larush L, Kaner I, Fluksman A, et al. 3D printing of responsive hydrogels for drug-delivery systems. *J 3D Print Med*. 2017;1(4):219–229.

- [24] Baker D. Artificial intelligence: the future landscape of genomic medical diagnosis: dataset in Silico artificial intelligent clinical information, and machine learning systems. In: Lambert CG, Baker DJ, Patrinos GP, editors. Human genome informatics. San Diego: Academic Press; 2018. p. 223–267.
- [25] Popova M, Isayev O, Tropsha A. Deep reinforcement learning for de novo drug design. *Sci Adv.* 2018;4:eap7885.
- [26] Han R, Xiong H, Ye Z, et al. Predicting physical stability of solid dispersions by machine learning techniques. *J Control Release.* 2019;311–312:16–25.
- [27] Harrer S, Shah P, Antony B, et al. Artificial intelligence for clinical trial design. *Trends Pharmacol Sci.* 2019;40(8): 577–591.
- [28] Madzarevic M, Medarevic D, Vulovic A, et al. Optimization and prediction of ibuprofen release from 3D DLP printlets using artificial neural networks. *Pharmaceutics.* 2019;11: 544.
- [29] Elbadawi M, Muñiz Castro B, Gavins FKH, et al. M3DISEEN: a novel machine learning approach for predicting the 3D printability of medicines. *Int J Pharm.* 2020;590:119837.
- [30] Elbadawi M, McCoubrey LE, Gavins FKH, et al. Harnessing artificial intelligence for the next generation of 3D printed medicines. *Adv Drug Deliv Rev.* 2021;175:113805.
- [31] Stanojević G, Medarević D, Adamov I, et al. Tailoring atomoxetine release rate from DLP 3D-printed tablets using artificial neural networks: influence of tablet thickness and drug loading. *Molecules.* 2020;26(1):111.
- [32] Khaled SA, Burley JC, Alexander MR, et al. 3D printing of tablets containing multiple drugs with defined release profiles. *Int J Pharm.* 2015;494(2):643–650.
- [33] Goyanes A, Robles Martinez P, Buanz A, et al. Effect of geometry on drug release from 3D printed tablets. *Int J Pharm.* 2015;494(2):657–663.
- [34] Awari GK, Thorat CS, Ambade V, et al. Additive manufacturing and 3D printing technology. 1st ed. Boca Raton (FL): CRC Press/Taylor & Francis Group, LLC; 2021.
- [35] Łaszcz M, Witkowska A. Studies of phase transitions in the aripiprazole solid dosage form. *J Pharm Biomed Anal.* 2016;117:298–303.
- [36] Water JJ, Bohr A, Boetker J, et al. Three-dimensional printing of drug-eluting implants: preparation of an antimicrobial polylactide feedstock material. *J Pharm Sci.* 2015; 104(3):1099–1107.
- [37] Yu DG, Zhu LM, Branford-White CJ, et al. Three-dimensional printing in pharmaceuticals: Promises and problems. *J Pharm Sci.* 2008;97(9):3666–3690.
- [38] Bakhatwar M, Chikkala Vnvk SR. Three-dimensional printing in pharmaceutical technology – an overview of innovations. *Innov Pharm Pharmacother.* 2019;7:67–71.
- [39] Zheng F, Huang S. Advances in study on three-dimensional printing in pharmaceuticals. *Chinese Herb Med.* 2016; 8(2):121–125.
- [40] Aimar A, Palermo A, Innocenti B. The role of 3D printing in medical applications: a state of the art. *J Healthc Eng.* 2019;2019:1–10.
- [41] Khan FA, Narasimhan K, Swathi CSV, et al. 3D printing technology in customized drug delivery system: current state of the art, prospective and the challenges. *Curr Pharm Des.* 2018;24(42):5049–5061.
- [42] Zhu X, Li H, Huang L, et al. 3D printing promotes the development of drugs. *Biomed Pharmacother.* 2020;131: 110644.
- [43] Ameeruzzafar Alruwaili NK, Rizwanullah M, et al. 3D printing technology in design of pharmaceutical products. *Curr Pharm Des.* 2019;24:5009–5018.
- [44] Mathew E, Pitzanti G, Larrañeta E, et al. 3D printing of pharmaceuticals and drug delivery devices. *Pharmaceutics.* 2020;12(3):266.
- [45] Trenfield SB. Innovations in 3D printed pharmaceuticals. *ONdrugDelivery Magazine.* 2020;109:45–49.
- [46] Ligon SC, Liska R, Stampfl J, et al. Polymers for 3D printing and customized additive manufacturing. *Chem Rev.* 2017; 117(15):10212–10290.
- [47] Kim GB, Lee S, Kim H, et al. Three-dimensional printing: basic principles and applications in medicine and radiology. *Korean J Radiol.* 2016;17(2):182–197.
- [48] Hodgdon T, Danrad R, Patel MJ, et al. Logistics of three-dimensional printing: primer for radiologists. *Acad Radiol.* 2018;25(1):40–51.
- [49] Chua CK, Leong KF, An J. Introduction to rapid prototyping of biomaterials. In: Narayan R, editor. Rapid prototyping of biomaterials. San Diego: Elsevier; 2014. p. 1–15.
- [50] Tofail SAM, Koumoulos EP, Bandyopadhyay A, et al. Additive manufacturing: scientific and technological challenges, market uptake and opportunities. *Mater Today.* 2018;21(1):22–37.
- [51] Goole J, Amighi K. 3D printing in pharmaceuticals: a new tool for designing customized drug delivery systems. *Int J Pharm.* 2016;499(1-2):376–394.
- [52] Lau G-K, Shrestha M. Ink-jet printing of micro-electromechanical systems (MEMS). *Micromachines.* 2017;8(6):194.
- [53] Cui X, Boland T, D’Lima D, et al. Thermal inkjet printing in tissue engineering and regenerative medicine. *Recent Pat Drug Deliv Formul.* 2012;6(2):149–155.
- [54] Gardin C, Ferroni L, Latremouille C, et al. Recent applications of three dimensional printing in cardiovascular medicine. *Cells.* 2020;9(3):742.
- [55] He D, Han F, Wang Z, et al. A review of 3D printing via fused deposition modeling in pharmaceuticals. *Yao Xue Xue Bao.* 2016;51:1659–1665.
- [56] Long J, Gholizadeh H, Lu J, et al. Application of fused deposition modelling (FDM) method of 3D printing in drug delivery. *Curr Pharm Des.* 2017;23(3):433–439.
- [57] Goyanes A, Fina F, Martorana A, et al. Development of modified release 3D printed tablets (printlets) with pharmaceutical excipients using additive manufacturing. *Int J Pharm.* 2017;527(1–2):21–30.
- [58] Alhnan MA, Okwuosa TC, Sadia M, et al. Emergence of 3D printed dosage forms: opportunities and challenges. *Pharm Res.* 2016;33(8):1817–1832.
- [59] Lim SH, Chia SMY, Kang L, et al. Three-dimensional printing of carbamazepine sustained-release scaffold. *J Pharm Sci.* 2016;105(7):2155–2163.
- [60] Goyanes A, Chang H, Sedough D, et al. Fabrication of controlled-release budesonide tablets via desktop (FDM) 3D printing. *Int J Pharm.* 2015;496(2):414–420.
- [61] Gumaste SG, Gupta SS, Serajuddin ATM. Investigation of polymer-surfactant and polymer-drug-surfactant miscibility for solid dispersion. *AAPS J.* 2016;18(5):1131–1143.
- [62] Gioumouxouzis CI, Baklavaridis A, Katsamenis OL, et al. A 3D printed bilayer oral solid dosage form combining metformin for prolonged and glimepiride for immediate drug delivery. *Eur J Pharm Sci.* 2018;120:40–52.

- [63] Fina F, Madla CM, Goyanes A, et al. Fabricating 3D printed orally disintegrating printlets using selective laser sintering. *Int J Pharm.* 2018;541(1–2):101–107.
- [64] Zhou Y. The recent development and applications of fluidic channels by 3D printing. *J Biomed Sci.* 2017;24(1):80.
- [65] Park BJ, Choi HJ, Moon SJ, et al. Pharmaceutical applications of 3D printing technology: current understanding and future perspectives. *J Pharm Investig.* 2018;49:575–585.
- [66] Hull CW, Arcadia C. Apparatus for production of three-dimensional objects by stereolithography. US Patent, 1984.
- [67] Lonjon C. The history of 3d printer: from rapid prototyping to additive fabrication. <https://www.sculpteo.com/blog/2017/03/01/whos-behind-the-three-main-3d-printing-technologies/>.
- [68] Chia HN, Wu BM. Recent advances in 3D printing of biomaterials. *J Biol Eng.* 2015;9:4.
- [69] Huang B, Wu B, Han L, et al. Preparation of a novel cationic photosensitive resin (3D-SLR01) for stereolithography 3D printing and determination of its some properties. *J Wuhan Univ Technol-Mat Sci Edit.* 2019;34(4):761–768.
- [70] Robles Martinez P, Basit AW, Gaisford S. The history, developments and opportunities of stereolithography. In: *AAPS advances in the pharmaceutical sciences series*. New York: Springer Verlag; 2012. p. 55–79.
- [71] Wang Z, Abdulla R, Parker B, et al. A simple and high-resolution stereolithography-based 3D bioprinting system using visible light crosslinkable bioinks. *Biofabrication.* 2015;7(4):045009.
- [72] ASTM 52921. Standard terminology for additive manufacturing — coordinate systems and test methodologies. Geneva: ASTM Int; 2019.
- [73] Chan V, Zorlutuna P, Jeong JH, et al. Three-dimensional photopatterning of hydrogels using stereolithography for long-term cell encapsulation. *Lab Chip.* 2010;10(16):2062–2070.
- [74] Curti C, Kirby DJ, Russell CA. Stereolithography apparatus evolution: enhancing throughput and efficiency of pharmaceutical formulation development. *Pharmaceutics.* 2021;13(5):616.
- [75] Lim SH, Kathuria H, Bin AM, et al. High resolution photopolymer for 3D printing of personalised microneedle for transdermal delivery of anti-wrinkle small peptide. *J Control Release.* 2020;329:907–918.
- [76] Goyanes A, Buanz ABM, Hatton GB, et al. 3D printing of modified-release aminosalicylate (4-ASA and 5-ASA) tablets. *Eur J Pharm Biopharm.* 2015;89:157–162.
- [77] Konta A, García-Piña M, Serrano D. Personalised 3D printed medicines: which techniques and polymers are more successful? *Bioengineering.* 2017;4(4):79.
- [78] Melchels FPW, Feijen J, Grijpma DW. A review on stereolithography and its applications in biomedical engineering. *Biomaterials.* 2010;31(24):6121–6130.
- [79] Gardan J. Additive manufacturing technologies: state of the art and trends. *Int J Prod Res.* 2016;54(10):3118–3132.
- [80] Norman J, Madurawe RD, Moore CMV, et al. A new chapter in pharmaceutical manufacturing: 3D-printed drug products. *Adv Drug Deliv Rev.* 2017;108:39–50.
- [81] Trenfield SJ, Madla CM, Basit AW, et al. The shape of things to come: emerging applications of 3D printing in healthcare. In: *AAPS advances in the pharmaceutical sciences series*. New York: Springer Verlag; 2012. p. 1–19.
- [82] Osouli-Bostanabad K, Adibkia K. Made-on-demand, complex and personalized 3D-printed drug products. *Bioimpacts.* 2018;8(2):77–79.
- [83] Vitale A, Cabral J. Frontal conversion and uniformity in 3D printing by photopolymerisation. *Materials.* 2016;9(9):760.
- [84] Januskaite P, Xu X, Ranmal SR, et al. I spy with my little eye: a paediatric visual preferences survey of 3D printed tablets. *Pharmaceutics.* 2020;12(11):1100.
- [85] Rattanakit P, Moulton SE, Santiago KS, et al. Extrusion printed polymer structures: a facile and versatile approach to tailored drug delivery platforms. *Int J Pharm.* 2012;422(1–2):254–263.
- [86] Stereolithography-ODM | 3D systems. [cited 2021 Jan 8]. <https://www.3dsystems.com/on-demand-manufacturing/stereolithography-sla>.
- [87] Zhang X, Jiang X, Sun C. Micro-stereolithography of polymeric and ceramic microstructures. *Sensors Actuators A Phys.* 1999;77(2):149–156.
- [88] US4575330A – Apparatus for production of three-dimensional objects by stereolithography - Google Patents. [cited 2021 Jan 31]. <https://patents.google.com/patent/US4575330A/en>.
- [89] Salonitis K, Tsoukantas G, Stavropoulos P, et al. A critical review of stereolithography process modeling. In: Bártolo P, editor. *Virtual modelling and rapid manufacturing – advanced research in virtual and rapid prototyping*. London; New York: Taylor & Francis; 2003.
- [90] Madžarević M, Ibrić S. Evaluation of exposure time and visible light irradiation in LCD 3D printing of ibuprofen extended release tablets. *Eur J Pharm Sci.* 2021;158:105688.
- [91] Venuvinod PK, Ma W. Stereolithography (SL). In: *Rapid prototyping*. Boston (MA): Springer US; 2004. p. 195–244.
- [92] Heller C, Schwentenwein M, Russmueller G, et al. Vinyl esters: low cytotoxicity monomers for the fabrication of biocompatible 3D scaffolds by lithography based additive manufacturing. *J Polym Sci A Polym Chem.* 2009;47(24):6941–6954.
- [93] Patel DK, Sakhaei AH, Layani M, et al. Highly stretchable and UV curable elastomers for digital light processing based 3D printing. *Adv Mater.* 2017;29(15):1606000.
- [94] Noorani R. Materials for 3D printing. In: Noorani R, editor. *3D printing*. Boca Raton (FL): CRC Press; 2017. p. 81–98.
- [95] Choi J-W, Kim H-C, Wicker R. Multi-material stereolithography. *J Mater Process Technol.* 2011;211(3):318–328.
- [96] Vehse M, Petersen S, Sternberg K, et al. Drug delivery from poly(ethylene glycol) diacrylate scaffolds produced by DLC based micro-stereolithography. *Macromol Symp.* 2014;346(1):43–47.
- [97] Hanson Shepherd JN, Parker ST, Shepherd RF, et al. 3D microperiodic hydrogel scaffolds for robust neuronal cultures. *Adv Funct Mater.* 2011;21(1):46–46.
- [98] Arcaute K, Mann BK, Wicker RB. Stereolithography of three-dimensional bioactive poly(ethylene glycol) constructs with encapsulated cells. *Ann Biomed Eng.* 2006;34(9):1429–1441.
- [99] Dhariwala B, Hunt E, Boland T. Rapid prototyping of tissue-engineering constructs, using photopolymerizable hydrogels and stereolithography. *Tissue Eng.* 2004;10(9–10):1316–1322.
- [100] Fisher JP, Dean D, Mikos AG. Photocrosslinking characteristics and mechanical properties of diethyl fumarate/poly

- (propylene fumarate) biomaterials. *Biomaterials*. 2002; 23(22):4333–4343.
- [101] Trachtenberg JE, Placone JK, Smith BT, et al. Extrusion-based 3D printing of poly(propylene fumarate) scaffolds with hydroxyapatite gradients. *J Biomater Sci Polym Ed*. 2017;28(6):532–554.
- [102] Tappa K, Jammalamadaka U. Novel biomaterials used in medical 3D printing techniques. *JFB*. 2018;9(1):17.
- [103] Arcaute K, Mann B, Wicker R. Stereolithography of spatially controlled multi-material bioactive poly(ethylene glycol) scaffolds. *Acta Biomater*. 2010;6(3):1047–1054.
- [104] Lee K-W, Wang S, Fox BC, et al. Poly(propylene fumarate) bone tissue engineering scaffold fabrication using stereolithography: effects of resin formulations and laser parameters. *Biomacromolecules*. 2007;8(4):1077–1084.
- [105] Choi J-W, Wicker R, Lee S-H, et al. Fabrication of 3D biocompatible/biodegradable micro-scaffolds using dynamic mask projection microstereolithography. *J Mater Process Technol*. 2009;209(15-16):5494–5503.
- [106] Jansen J, Melchels FPW, Grijpma DW, et al. Fumaric acid monoethyl ester-functionalized poly(D,L-lactide)/N-vinyl-2-pyrrolidone resins for the preparation of tissue engineering scaffolds by stereolithography. *Biomacromolecules*. 2009;10(2):214–220.
- [107] Skoog SA, Goering PL, Narayan RJ. Stereolithography in tissue engineering. *J Mater Sci Mater Med*. 2014;25(3):845–856.
- [108] Ronca A, Ambrosio L, Grijpma DW. Preparation of designed poly(d,l-lactide)/nanosized hydroxyapatite composite structures by stereolithography. *Acta Biomater*. 2013;9(4):5989–5996.
- [109] Stampfl J, Baudis S, Heller C, et al. Photopolymers with tunable mechanical properties processed by laser-based high-resolution stereolithography. *J Micromech Microeng*. 2008;18(12):125014.
- [110] Murphy EJ, Ansel RK. Method of forming a three-dimensional object by stereolithography and composition therefore. US07429568, US, 1989.
- [111] Esposito Corcione C, Greco A, Maffezzoli A. Photopolymerization kinetics of an epoxy-based resin for stereolithography. *J Appl Polym Sci*. 2004;92(6):3484–3491.
- [112] Lee TY, Carioscia J, Smith Z, et al. Thiol – allyl ether – methacrylate ternary systems. Evolution mechanism of Polymerization-Induced shrinkage stress and mechanical properties. *Macromolecules*. 2007;40(5):1473–1479.
- [113] Zhiwei G, Jianhua M, Shuhuai H, et al. Development of a hybrid photopolymer for stereolithography. *J Wuhan Univ Technol-Mat Sci Edit*. 2006;21(1):99–101.
- [114] Oesterreicher A, Wiener J, Roth M, et al. Tough and degradable photopolymers derived from alkyne monomers for 3D printing of biomedical materials. *Polym Chem*. 2016;7(32):5169–5180.
- [115] Bagheri A, Jin J. Photopolymerization in 3D printing. *ACS Appl Polym Mater*. 2019;1(4):593–611.
- [116] Badev A, Abouliatim Y, Chartier T, et al. Photopolymerization kinetics of a polyether acrylate in the presence of ceramic fillers used in stereolithography. *J Photochem Photobiol A Chem*. 2011;222(1):117–122.
- [117] Bail R, Patel A, Yang H, et al. The effect of a type I photoinitiator on cure kinetics and cell toxicity in Projection-Microstereolithography. *Procedia CIRP*. 2013;5:222–225.
- [118] Han L-H, Mapili G, Chen S, et al. Projection microfabrication of three-dimensional scaffolds for tissue engineering. *J Manuf Sci Eng*. 2008;130:021005.
- [119] Choi J, Wicker RB, Cho S, et al. Cure depth control for complex 3D microstructure fabrication in dynamic mask projection microstereolithography. *Rapid Prototyp J*. 2009; 15(1):59–70.
- [120] Sun C, Fang N, Wu DM, et al. Projection micro-stereolithography using digital micro-mirror dynamic mask. *Sensors Actuators A Phys*. 2005;121(1):113–120.
- [121] Bail R, Hong JY, Chin BD. Effect of a red-shifted benzotriazole UV absorber on curing depth and kinetics in visible light initiated photopolymer resins for 3D printing. *J Ind Eng Chem*. 2016;38:141–145.
- [122] Bartolo PJ, Gaspar J. Metal filled resin for stereolithography metal part. *CIRP Ann*. 2008;57(1):235–238.
- [123] Halloran JW. Ceramic stereolithography: additive manufacturing for ceramics by photopolymerization. *Annu Rev Mater Res*. 2016;46(1):19–40.
- [124] Hinczewski C, Corbel S, Chartier T. Ceramic suspensions suitable for stereolithography. *J Eur Ceram Soc*. 1998; 18(6):583–590.
- [125] Farahani RD, Dubé M, Therriault D. Three-dimensional printing of multifunctional nanocomposites: manufacturing techniques and applications. *Adv Mater*. 2016;28(28): 5794–5821.
- [126] Lin D, Jin S, Zhang F, et al. 3D stereolithography printing of graphene oxide reinforced complex architectures. *Nanotechnology*. 2015;26(43):434003.
- [127] Credi C, Fiorese A, Tironi M, et al. 3D printing of cantilever-type microstructures by stereolithography of ferromagnetic photopolymers. *ACS Appl Mater Interfaces*. 2016;8(39):26332–26342.
- [128] De Hazan Y, Heinecke J, Weber A, et al. High solids loading ceramic colloidal dispersions in UV curable media via comb-polyelectrolyte surfactants. *J Colloid Interface Sci*. 2009;337(1):66–74.
- [129] Huang Y-M, Jiang C-P. On-line force monitoring of platform ascending rapid prototyping system. *J Mater Process Technol*. 2005;159(2):257–264.
- [130] Teng WD, Edirisinghe MJ, Evans JRG. Optimization of dispersion and viscosity of a ceramic jet printing ink. *J Am Ceram Soc*. 2005;80(2):486–494.
- [131] Li K, Zhao Z. The effect of the surfactants on the formulation of UV-curable SLA alumina suspension. *Ceram Int*. 2017;43(6):4761–4767.
- [132] Goswami A, K A, Balashanmugam N, et al. Optimization of rheological properties of photopolymerizable alumina suspensions for ceramic microstereolithography. *Ceram Int*. 2014;40(2):3655–3665.
- [133] Wang J, Goyanes A, Gaisford S, et al. Stereolithographic (SLA) 3D printing of oral modified-release dosage forms. *Int J Pharm*. 2016;503(1–2):207–212.
- [134] Goyanes A, Det-Amornrat U, Wang J, et al. 3D scanning and 3D printing as innovative technologies for fabricating personalized topical drug delivery systems. *J Control Release*. 2016;234:41–48.
- [135] Martinez PR, Goyanes A, Basit AW, et al. Fabrication of drug-loaded hydrogels with stereolithographic 3D printing. *Int J Pharm*. 2017;532(1):313–317.
- [136] Martinez PR, Goyanes A, Basit AW, et al. Influence of geometry on the drug release profiles of

- stereolithographic (SLA) 3D-Printed tablets. *AAPS PharmSciTech*. 2018;19(8):3355–3361.
- [137] Ulery BD, Nair LS, Laurencin CT. Biomedical applications of biodegradable polymers. *J Polym Sci B Polym Phys*. 2011;49(12):832–864.
- [138] Pan W, Wallin TJ, Odent J, et al. Optical stereolithography of antifouling zwitterionic hydrogels. *J Mater Chem B*. 2019;7(17):2855–2864.
- [139] Elomaa L, Pan C-C, Shanjani Y, et al. Three-dimensional fabrication of cell-laden biodegradable poly(ethylene glycol-co-depsipeptide) hydrogels by visible light stereolithography. *J Mater Chem B*. 2015;3(42):8348–8358.
- [140] Kim K, Yeatts A, Dean D, et al. Stereolithographic bone scaffold design parameters: osteogenic differentiation and signal expression. *Tissue Eng Part B Rev*. 2010;16(5):523–539.
- [141] Schüller-Ravoo S, Teixeira SM, Feijen J, et al. Flexible and elastic scaffolds for cartilage tissue engineering prepared by stereolithography using poly(trimethylene carbonate)-based resins. *Macromol Biosci*. 2013;13(12):1711–1719.
- [142] Lee JW, Kang KS, Lee SH, et al. Bone regeneration using a microstereolithography-produced customized poly(propylene fumarate)/diethyl fumarate photopolymer 3D scaffold incorporating BMP-2 loaded PLGA microspheres. *Biomaterials*. 2011;32(3):744–752.
- [143] Bajaj P, Marchwiany D, Duarte C, et al. Patterned three-dimensional encapsulation of embryonic stem cells using dielectrophoresis and stereolithography. *Adv Healthc Mater*. 2013;2(3):450–458.
- [144] Cui X, Breitenkamp K, Finn MG, et al. Direct human cartilage repair using three-dimensional bioprinting technology. *Tissue Eng Part A*. 2012;18(11–12):1304–1312.
- [145] Elomaa L, Teixeira S, Hakala R, et al. Preparation of poly(ϵ -caprolactone)-based tissue engineering scaffolds by stereolithography. *Acta Biomater*. 2011;7(11):3850–3856.
- [146] Melchels FPW, Feijen J, Grijpma DW. A poly(D,L-lactide) resin for the preparation of tissue engineering scaffolds by stereolithography. *Biomaterials*. 2009;30(23–24):3801–3809.
- [147] Seck TM, Melchels FPW, Feijen J, et al. Designed biodegradable hydrogel structures prepared by stereolithography using poly(ethylene glycol)/poly(D,L-lactide)-based resins. *J Control Release*. 2010;148(1):34–41.
- [148] Asikainen S, van Bochove B, Seppälä JV. Drug-releasing biopolymeric structures manufactured via stereolithography. *Biomed Phys Eng Express*. 2019;5(2):025008.
- [149] Robles-Martinez P, Xu X, Trenfield SJ, et al. 3D printing of a multi-layered polypill containing six drugs using a novel stereolithographic method. *Pharmaceutics*. 2019;11(6):274.
- [150] Thrasher CJ, Schwartz JJ, Boydston AJ. Modular elastomer photoresins for digital light processing additive manufacturing. *ACS Appl Mater Interfaces*. 2017;9(45):39708–39716.
- [151] Kuang X, Zhao Z, Chen K, et al. High-speed 3D printing of high-performance thermosetting polymers via two-stage curing. *Macromol Rapid Commun*. 2018;39(7):1700809.
- [152] Xu X, Awad A, Robles-Martinez P, et al. Vat photopolymerization 3D printing for advanced drug delivery and medical device applications. *J Control Release*. 2021;329:743–757.
- [153] Gu Y, Chen X, Lee J-H, et al. Inkjet printed antibiotic- and calcium-eluting bioresorbable nanocomposite micropatterns for orthopedic implants. *Acta Biomater*. 2012;8(1):424–431.
- [154] Liang K, Carmone S, Brambilla D, et al. 3D printing of a wearable personalized oral delivery device: a first-in-human study. *Sci Adv*. 2018;4(5):eaat2544.
- [155] Ozbolat IT, Yu Y. Bioprinting toward organ fabrication: challenges and future trends. *IEEE Trans Biomed Eng*. 2013;60(3):691–699.
- [156] Schubert C, Van Langeveld MC, Donoso LA. Innovations in 3D printing: a 3D overview from optics to organs. *Br J Ophthalmol*. 2014;98(2):159–161.
- [157] Krkobabić M, Medarević D, Pešić N, et al. Digital light processing (DLP) 3D printing of atomoxetine hydrochloride tablets using photoreactive suspensions. *Pharmaceutics*. 2020;12(9):833–817.
- [158] Tagami T, Morimura C, Ozeki T. Effective and simple prediction model of drug release from “ghost tablets” fabricated using a digital light projection-type 3D printer. *Int J Pharm*. 2021;604:120721.
- [159] Goyanes A, Madla CM, Umerji A, et al. Automated therapy preparation of isoleucine formulations using 3D printing for the treatment of MSUD: first single-centre, prospective, crossover study in patients. *Int J Pharm*. 2019;567:118497.
- [160] Lipson H. New world of 3-D printing offers “completely new ways of thinking”: Q&A with author, engineer, and 3-D printing expert Hod Lipson. *IEEE Pulse*. 2013;4(6):12–14.
- [161] Krkobabić M, Medarević D, Cvijić S, et al. Hydrophilic excipients in digital light processing (DLP) printing of sustained release tablets: impact on internal structure and drug dissolution rate. *Int J Pharm*. 2019;572:118790.
- [162] Xu X, Robles-Martinez P, Madla CM, et al. Stereolithography (SLA) 3D printing of an antihypertensive polyprintlet: case study of an unexpected photopolymer-drug reaction. *Addit Manuf*. 2020;33:101071.
- [163] Pere CPP, Economidou SN, Lall G, et al. 3D printed micro-needles for insulin skin delivery. *Int J Pharm*. 2018;544(2):425–432.
- [164] Ochoa M, Zhou J, Rahimi R, et al. Rapid 3D-print-and-shrink fabrication of biodegradable microneedles with complex geometries. 2015 Transducers – 2015 18th International Conference on Solid-State Sensors, Actuators and Microsystems, TRANSDUCERS. Anchorage, AK, 2015. p. 1251–1254.
- [165] Lu Y, Mantha SN, Crowder DC, et al. Microstereolithography and characterization of poly(propylene fumarate)-based drug-loaded microneedle arrays. *Biofabrication*. 2015;7(4):045001.
- [166] Miyazaki T, Hotta Y, Kunii J, et al. A review of dental CAD/CAM: current status and future perspectives from 20 years of experience. *Dent Mater J*. 2009;28(1):44–56.
- [167] Xu X, Goyanes A, Trenfield SJ, et al. Stereolithography (SLA) 3D printing of a bladder device for intravesical drug delivery. *Mater Sci Eng C Mater Biol Appl*. 2021;120:111773.
- [168] Vivero-Lopez M, Xu X, Muras A, et al. Anti-biofilm multi drug-loaded 3D printed hearing aids. *Mater Sci Eng C Mater Biol Appl*. 2021;119:111606.
- [169] Klein GT, Lu Y, Wang MY. 3D printing and neurosurgery-ready for prime time? *World Neurosurg*. 2013;80(3–4):233–235.
- [170] Sun J, Peng Z, Zhou W, et al. A review on 3D printing for customized food fabrication. *Procedia Manuf*. 2015;1:308–319.
- [171] Nathan GL. The future: creating novel foods using 3D printing. <https://www.foodnavigator.com/Article/2010/12/>

- 23/Looking-to-the-future-Creating-novel-foods-using-3D-printing. 2012.
- [172] Michail N. Biozoon's 3D printed smooth foods target Europe's elderly, <https://www.foodnavigator.com/Article/2016/09/26/Biozoon-s-3D-printed-smooth-foods-target-Europe-s-elderly>. 2016.
- [173] Serizawa R, Shitara M, Gong J, et al. 3D jet printer of edible gels for food creation. In: Goulbourne NC, Naguib HE, editors. Behavior and mechanics of multifunctional materials and composites. Bellingham: SPIE; 2015. p. 90580A.
- [174] Gohd C. NASA astronauts can now 3D-print pizzas in space. <https://futurism.com/nasa-astronauts-can-now-3d-print-pizzas-in-space>. 2017.
- [175] Vithani K, Goyanes A, Jannin V, et al. An overview of 3D printing technologies for soft materials and potential opportunities for lipid-based drug delivery systems. *Pharm Res*. 2018;36(1):4.
- [176] Pandey M, Choudhury H, Fern JLC, et al. 3D printing for oral drug delivery: a new tool to customize drug delivery. *Drug Deliv Transl Res*. 2020;10(4):986–1001.
- [177] Ali A, Ahmad U, Akhtar J. 3D printing in pharmaceutical sector: an overview. In: Pharmaceutical formulation design – recent practices. London: IntechOpen; 2020.
- [178] Genina N, Fors D, Vakili H, et al. Tailoring controlled-release oral dosage forms by combining inkjet and flexographic printing techniques. *Eur J Pharm Sci*. 2012;47(3):615–623.
- [179] Skowrya J, Pietrzak K, Alhnan MA. Fabrication of extended-release patient-tailored prednisolone tablets via fused deposition modelling (FDM) 3D printing. *Eur J Pharm Sci*. 2015;68:11–17.
- [180] Melocchi A, Parietti F, Loreti G, et al. 3D printing by fused deposition modeling (FDM) of a swellable/erodible capsular device for oral pulsatile release of drugs. *J Drug Deliv Sci Technol*. 2015;30:360–367.
- [181] Katstra WE, Palazzolo RD, Rowe CW, et al. Oral dosage forms fabricated by three dimensional printing(TM). *J Control Release*. 2000;66(1):1–9.
- [182] Yu DG, Branford-White C, Yang YC, et al. A novel fast disintegrating tablet fabricated by three-dimensional printing. *Drug Dev Ind Pharm*. 2009;35(12):1530–1536.
- [183] Deng GY, Xiang LY, Wei DH, et al. Tablets with material gradients fabricated by three-dimensional printing. *J Pharm Sci*. 2007;96:2446–2456.
- [184] Yi H-G, Choi Y-J, Kang KS, et al. A 3D-printed local drug delivery patch for pancreatic cancer growth suppression. *J Control Release*. 2016;238:231–241.
- [185] Holländer J, Genina N, Jukarainen H, et al. Three-dimensional printed PCL-based implantable prototypes of medical devices for controlled drug delivery. *J Pharm Sci*. 2016;105(9):2665–2676.
- [186] Shim IK, Yi H-J, Yi H-G, et al. Locally-applied 5-fluorouracil-loaded slow-release patch prevents pancreatic cancer growth in an orthotopic mouse model. *Oncotarget*. 2017;8(25):40140–40151.
- [187] Shi X, Cheng Y, Wang J, et al. 3D printed intelligent scaffold prevents recurrence and distal metastasis of breast cancer. *Theranostics*. 2020;10(23):10652–10664.
- [188] Hafezi F, Scoutaris N, Douroumis D, et al. 3D printed chitosan dressing crosslinked with genipin for potential healing of chronic wounds. *Int J Pharm*. 2019;560:406–415.
- [189] Tagami T, Ito E, Hayashi N, et al. Application of 3D printing technology for generating hollow-type suppository shells. *Int J Pharm*. 2020;589:119825.
- [190] Seoane-Viaño I, Trenfield SJ, Basit AW, et al. Translating 3D printed pharmaceuticals: from hype to real-world clinical applications. *Adv Drug Deliv Rev*. 2021;174:553–575.
- [191] Tagami T, Ito E, Kida R, et al. 3D printing of gummy drug formulations composed of gelatin and an HPMC-based hydrogel for pediatric use. *Int J Pharm*. 2021;594:120118.



Received on 20 August 2019; received in revised form, 28 January 2021; accepted, 19 May 2021; published 01 August 2021

IDENTIFICATION AND OPTIMIZATION OF BINDING SITE FOR AN ACTIVE METABOLITE OF CLOPIDOGREL, PRASUGREL AND TICLOPIDINE ON RECEPTOR P2Y12

Parmeshwar R. Devhare ^{*1}, Shirish Jain ², Gajanan Sonwane ¹, Vijay Borkar ¹ and Rushikesh Diwre ¹

Department of Pharmaceutical Chemistry ¹, Department of Pharmacology ², Rajarshi Shahu College of Pharmacy, Buldhana - 443001, Maharashtra, India.

Keywords:

Molecular docking, P2Y12, Clopidogrel, Prasugrel, Ticlopidine

Correspondence to Author: Parmeshwar R. Devhare

Assistant Professor,
Rajarshi Shahu College of Pharmacy,
Buldhana - 443001, Maharashtra,
India.

E-mail: parme1717@gmail.com

ABSTRACT: In this article, an attempt was made to develop molecular docking studies on active metabolites of Prasugrel, Clopidogrel, and Ticlopidine acting as protein P2Y12 inhibitors. Molecular docking analysis was performing by using autodock version 4.3 adjoin with discovery studio to better understand the interactions between P2Y12 targets and inhibitors in this series. Hydrophobic and hydrogen bond interactions lead to the identification of active binding sites of P2Y12 protein in the docked complex, signifying the affection of active Metabolite of Prasugrel is more than other active metabolites of ticlopidine and clopidogrel. The present study may lead to the discovery of therapeutically potent agents against clinically very important cardiovascular disorders, including arterial thrombosis, Hypertension, embolism etc. cardiac diseases. Hence the computer-aided drug design docking model proposed in this work can be employed to design the metabolites of Clopidogrel, Prasugrel, and Ticlopidine with specific P2Y12 inhibitory activity and futuristic active metabolites possibilities.

INTRODUCTION: Molecular modeling and computational tools have become a close matching part of experimenting in the understanding of molecular aspects of genetic systems ¹⁻⁴. The computational strategies like molecular docking and quantitative structure-activity relationship (QSAR) are utilized to find the new hits for different helpful targets ⁵⁻⁷. The ongoing report featured the interface between computational methodologies and experiments as an essential tool in the drug discovery technology ^{8,9}.

Using the prominent rising interest in the design of ligand-enzyme inhibitors, this present study is to elucidate the molecular docking study of active metabolites of clopidogrel, prasugrel, and ticlopidine as P2Y12 inhibitor using computational tools that can be applied to understand interactions between inhibitors and their target proteins.

P2Y12 Crystal structures of the human P2Y12 receptor shown in figure 1 have as of late been settled. Structures of the receptor in a complex with the agonists 2-methylthio-adenosine diphosphate (2MeS-ADP) and 2-methylthio-adenosine triphosphate (2MeS-ATP) ^{10, 11} and with the non-nucleotide antagonist ethyl 6-(4-[(benzylsulfonyl) carbamoyl] piperidin-1-yl)-5- cyano-2-methyl-nicotinate (AZD1283) were obtained ^{12, 13}. The P2Y12 receptor represents a successful drug target, with several clinical drugs on the market, including **095**

<p>QUICK RESPONSE CODE</p>	<p>DOI: 10.13040/IJPSR.0975-8232.12(8).4365-70</p> <hr/> <p>The article can be accessed online on www.ijpsr.com</p> <hr/> <p>DOI link: http://dx.doi.org/10.13040/IJPSR.0975-8232.12(8).4365-70</p>
-----------------------------------	--

clopidogrel, prasugrel, ticlopidine, cangrelor, and ticagrelor, and more drugs in clinical trials¹⁴. Along these lines, the advancement of P2Y₁₂ antagonist has been a functioning region of medication improvement, and endeavors have been founded on dynamic metabolites of clopidogrel, prasugrel, and ticlopidine with the plan to maintain a strategic distance from biotransformation of the prodrug.

Docking considers as the structures of progressively potential medication target are explained the open door for the computer to perform beginning binding studies is expanding. By computationally docking a ligand to a protein, one point of confinement worries about examine intricacy, for example, compound solvency and the requirements to keep up broad physical compound libraries.

The goal of computational docking is to decide how atoms of realized structure will collaborate. The molecule may bind to the receptor and modify its function. The docking considers performed between receptor (P2Y₁₂, PDB code: 4NTJ) and ligands by utilizing PyRx-Python solution (adaptation 0.8). 4NTJ **Fig. 1**, recovered from RCSB and arranged by Discovery Studio visualizer rendition 16.1.01

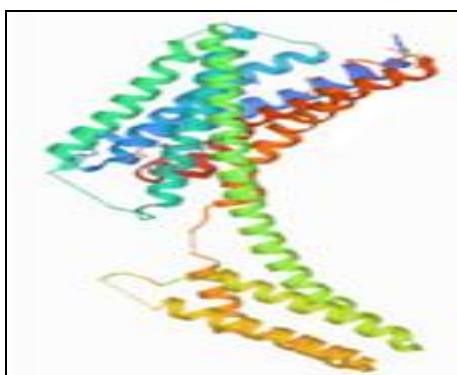


FIG. 1 STRUCTURE OF 4NTJ

Experimental Methods: 3D structure of the enzyme P2Y₁₂ with PDB code: 4NTJ by Zhang *et al.*, and active metabolites are shown in **Fig. 2** of clopidogrel, prasugrel, and ticlopidine were taken from literature^{15, 16}. The protein structure was downloaded from the information base online Protein Data Bank (PDB)^{17, 18}. Two and three-dimensional structure of metabolites drawn utilizing program package ChemDraw Ultra v12.0.2, 2010.

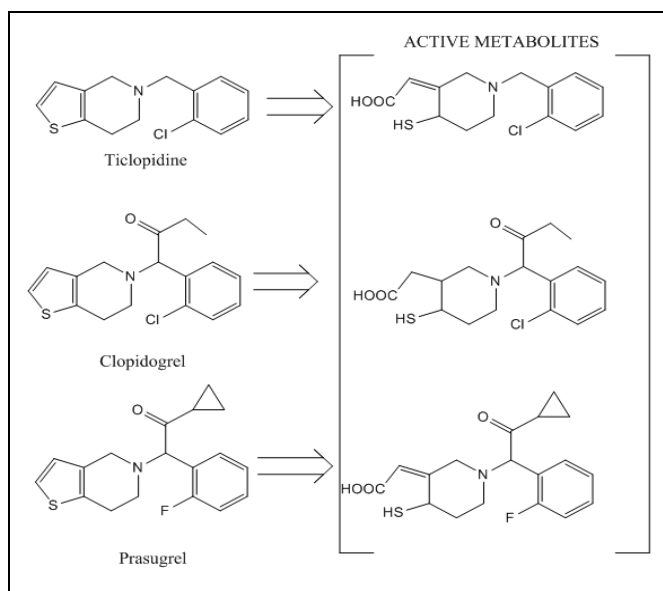


FIG. 2: ACTIVE METABOLITE OF TICLOPIDINE, CLOPIDOGREL AND PRASUGEL

Preparation of Protein Structure: The 3D coordinates of the crystal structure of P2Y₁₂ (PDB ID: 4NTJ) were downloaded from the Protein Data Bank^{19–21}. 4NTJ (chains A) were picked for the docking reenactments. Before docking, all water atoms are ousted from protein document 4NTJ. In the wake of ousting the water molecules, H atom was added to protein for right ionization and tautomeric states of amino corrosive, such as ARG, CYS, LYS, PHE TYR, and VAL.

Preparation of Ligand Structures: The ligands used for the docking study were selected from the literature^{22–24}. The ligand structures were generated using the tool ChemDraw ultra v12.0.2. Three-dimensional optimizations of the ligand structures were done and saved as 'PDB file'. Geometry optimizations of the ligands were performed using the Steepest descent calculation method using Avagdro software. The compounds included in the study are active metabolites of clopidogrel, prasugrel, and ticlopidine; the bioactive compounds considered for the study are listed in **Fig. 2**.

Protein-ligand Interaction using PyRx (Autodock Vina): The docking studies were conceded by PyRx (Autodock vina) tools^{25, 26} version v 0.8 programs. The looking through lattice reached out over the favoured objective proteins; polar hydrogen was added to the ligand moieties. Kollman charges were assigned, and atomic solvation parameters were added. Polar hydrogen

charges of the Gasteiger-type were assigned, and the non-polar hydrogen was merged with the carbons, and the internal degrees of freedom and torsions were set. Active metabolites were docked to target protein complex (4NTJ), with the molecule considered as a rigid body and the ligand being flexible. The search was extended over the whole receptor protein used as blind docking. Affinity maps for all the atom types present, as well as an electrostatic map, were computed with a grid spacing of 0.375 Å. The search was carried out with the Lamarckian Genetic Algorithm; populations of 150 individuals with a mutation rate of 0.02 were evolved for 9 generations. Evaluation of the results was done by sorting the different complexes concerning the predicted binding energy. A cluster analysis based on root mean square deviation values concerning the starting geometry was subsequently performed, and the lowest energy conformation of the more populated cluster was considered as the most trustable solution.

RESULTS AND DISCUSSION: In this present study, to understand the formation of hydrogen bond interactions between the active metabolites and active sites of the crystal structure of P2Y12 (PDB code: 4NTJ) was used to explore their binding mode, and a docking study was performed by using PyRx (Autodock vina)^{27, 28}. Three active metabolites of clopidogrel, prasugrel and ticlopidine were retrieved from literature²⁹. The 3D structure and energy minimization was done by Avogadro software. All these chemical compounds. To date, three crystal structures of P2Y12 in complex with agonist and antagonist have been reported in the literature. In the present study, we have used X-ray crystallography structure of P2Y12 (PDB code: 4NTJ) **Fig. 1** in ternary

complex with the non-nucleotide antagonist ethyl 6-(4-[(benzylsulfonyl) carbamoyl] piperidine-1-yl)-5-cyano-2-methylnicotinate (AZD1283) is used for the docking study.

Binding Site of the Protein: The detection of ligand-binding sites is often the starting point for protein function identification and drug discovery^{30, 31}. In our study, PyRx (autodock vina) predicted the active site of the receptor P2Y12 (4NTJ) with higher average precision. P2Y12 (4NTJ) 's active site comprises amino acid residues such as CYS97, VAL102, TYR105, PHE106, TYR109, MET152, LEU155, SER156, ASN159, HIS187, VAL190, ASN191, CYS194, PHE252, ALA255, ARG256, TYR259, LEU276, AND VAL279. As most of the amino acid residues in the active site are hydrophobic, so they are the main contributors to the receptor and ligand-binding interaction. Amino acid interaction of active metabolite of Ticlopidine, Clopidogrel, and Prasugrel shown in **Fig. 3, 4, and 5** respectively, and standard drug ethyl 6-(4-((benzylsulfonyl) carbamoyl) piperidin- 1- yl)- 5-cyano-2-methylnicotinate amino acid interaction shown in **Fig. 6**.

Interaction between Active Metabolites and 4ntj:

TABLE 1: DOCKING ENERGY OF ACTIVE METABOLITES OF COLPIDOGREL, PRASUGREL, AND TICLOPIDINE

Ligand	Binding Affinity	rmsd/ub	rmsd/lb
Metabolite of Ticlopidine	-7	6.94	1.496
Metabolite of Colpidogrel	-5.7	30.813	29.362
Metabolite of Prasugrel	-7.1	2.378	2.126
Std	-6.8	12.349	11.335

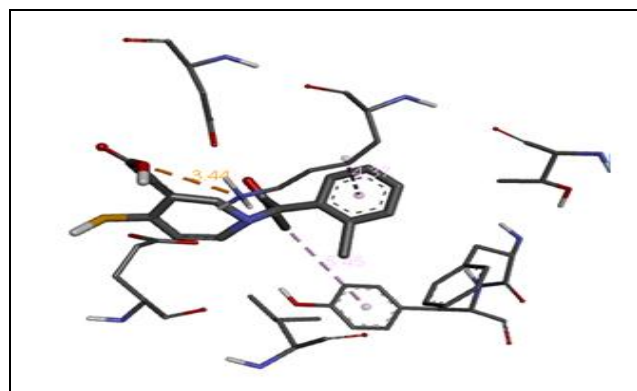
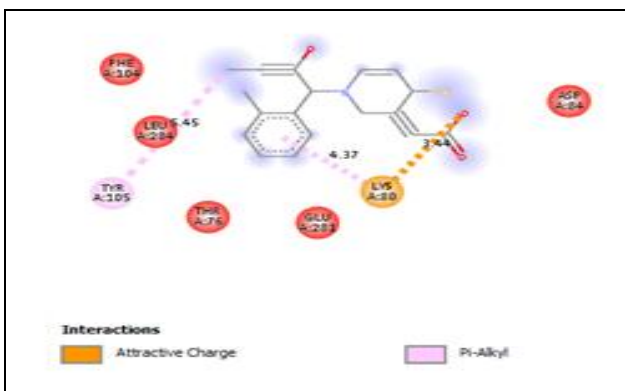


FIG. 3: AMINO ACID INTERACTION WITH TICLOPIDINE LIGAND



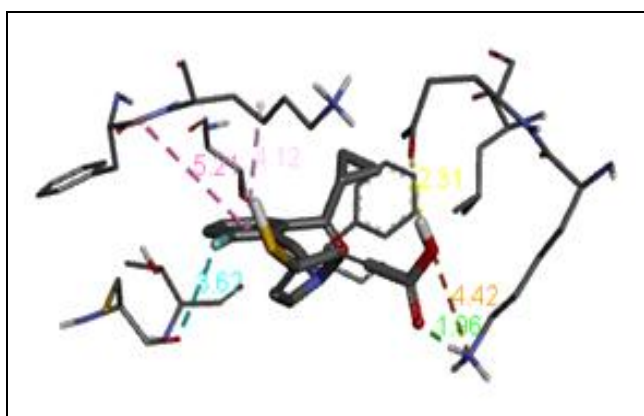


FIG. 4: AMINO ACID INTERACTION WITH COLPIDOGREL LIGAND

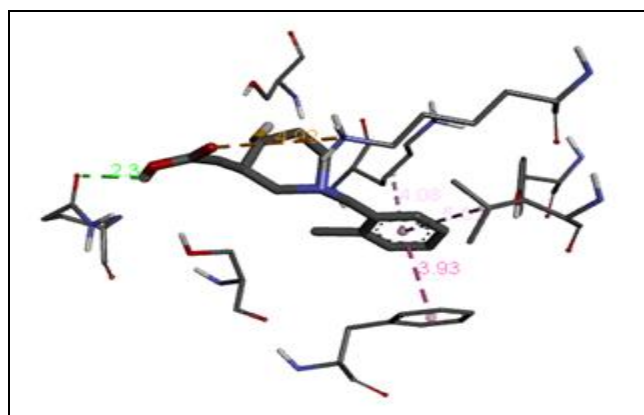
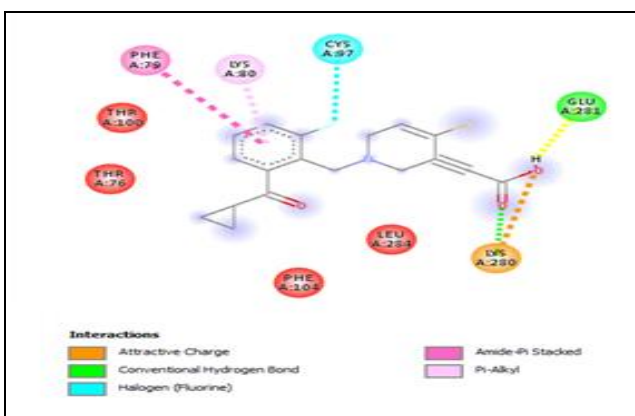


FIG. 5: AMINO ACID INTERACTION WITH PRASUGREL LIGAND

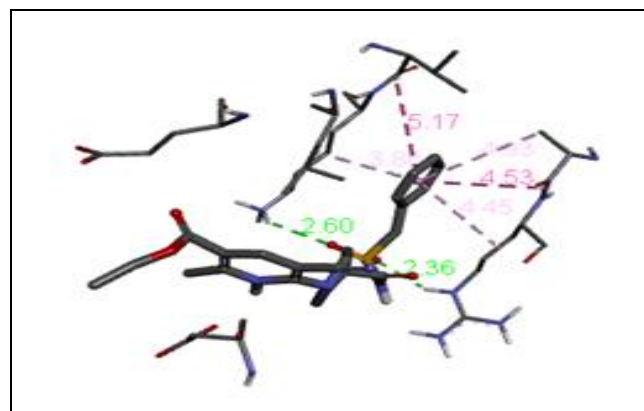
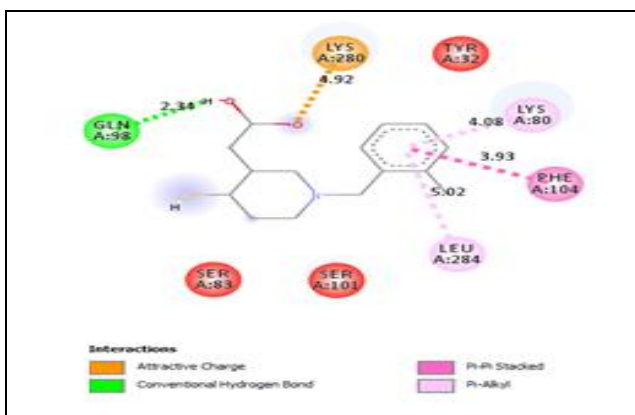
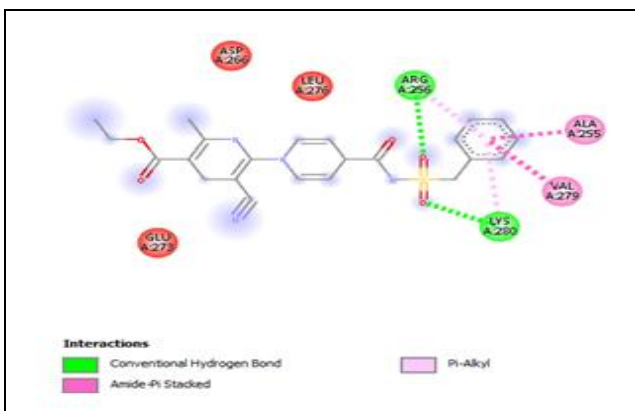


FIG. 6: AMINO ACID INTERACTION WITH STD ETHYL 6-(4-((BENZYSULFONYL) CARBAMOYL) PIPERIDIN-1-YL)-5-CYANO-2-METHYLNICOTINATE LIGAND



CONCLUSION: The P2Y12 receptor is a significant objective of antithrombotic treatment. In PCI patients, new P2Y12 inhibitors decrease all-cause mortality and major ischemic conditions, specifically in PCI for STEMI patients.

These further backings that a more significant level of platelet inhibition than clopidogrel (600 mg) is required for, by far, most of the patients. This study based on binding energy for receptor P2Y12 (4NTJ) of the metabolite of Prasugrel ligand showed better activity than Metabolite of

Ticlopidine Metabolite of Colpidogrel, which may show a better dose regimen with lesser side effects. This research will help for further wetlab Pharmacological investigation of Prasugrel ligand as compared to a metabolite of Ticlopidine and metabolite of Clopidogrel.

ACKNOWLEDGEMENT: Authors are thankful to the Principal, Dr. S.P Jain Sir, Rajarshi Shahu College of Pharmacy, Buldhana (MS), India, for providing the necessary facilities.

CONFLICTS OF INTEREST: Nil**REFERENCES:**

- Wang R, Hozumi Y, Yin C and Wei GW: Decoding SARS-CoV-2 Transmission and Evolution and Ramifications for COVID-19 Diagnosis, Vaccine and Medicine. *Journal of Chemical Information and Modeling* 2020; 1(1): 101-12.
- Villas-Boas GR: The New Coronavirus (SARS-CoV-2): A Comprehensive Review on Immunity and the Application of Bioinformatics and Molecular Modeling to the Discovery of Potential Anti-SARS-CoV-2 Agents. *Molecules* 2020; 1(1): 121-34.
- Mir-Artigues P, Twyman RM, Alvarez D, Cerda Bennasser P, Balcells M, Christou P and Capell TA: Simplified Techno-Economic Model for the Molecular Pharming of Antibodies. *Biotechnology and Bioengineering* 2019; 4(14): 1458-65.
- Martin RW, Butts CT, Cross TJ, Takahashi GR, Diessner EM, Crosby MG, Farahmand V and Zhuang S: Sequence characterization and molecular modeling of clinically relevant variants of the SARS-CoV-2 main protease. *Biochemistry* 2020; 2(2): 151-68.
- De P, Bhayye S, Kumar V and Roy K: *In-silico* modeling for quick prediction of inhibitory activity against 3CLpro enzyme in SARS CoV diseases. *Journal of Biomolecular Structure and Dynamics* 2020; 2(2): 123-35.
- Nesměrák K: Medicinal Chemistry meets electrochemistry: redox potential in the role of endpoint or molecular descriptor in QSAR/QSPR. *Mini-Reviews in Medicinal Chemistry* 2020; 2(3): 201-13.
- Chinen K and Malloy T: QSAR use in REACH analyses of alternatives to predict human health and environmental Toxicity of Alternative Chemical Substances. *Integrated Environmental Assessment and Management* 2020; 2(5): 3-13.
- Hughes JP, Rees S, Kalindjian SB and Philpott KL: Principles of Early Drug Discovery. *British Journal of Pharmacology* 2011; 162 (6): 1239-49.
- Drews J: Drug Discovery: A Historical Perspective. *Science (80-.)* 2000; 3 (2): 135-45.
- Shi C and Kim T: crystal clots as therapeutic target in cholesterol crystal embolism. *Circ Res* 2020; 3 (5): 22-36.
- Neumann A, Müller CE and Namasivayam V: P2Y1-like nucleotide receptors—structures, molecular modeling, mutagenesis, and oligomerization. *wiley interdiscip. Wiley Interdisciplinary Reviews: Computational Molecular Science* 2020; 10 (4): 134-46.
- Kong D, Xue T, Guo B, Cheng J, Liu S, Wei J, Lu Z, Liu H, Gong G, Lan T, Hu W and Yang Y: Optimization of P2Y12 Antagonist Ethyl 6-(4-((Benzylsulfonyl) Carbamoyl) Piperidin-1-Yl)-5-Cyano-2-Methylnicotinate (AZD1283) Led to the Discovery of an Oral Antiplatelet Agent with Improved Druglike Properties. *Journal of Medicinal Chemistry* 2019; 62 (6): 3088-06.
- Van Doren, L, Nguyen N, Garzia C, Fletcher E, Stevenson R, Jaramillo D, Kuliopulos A and Covic L: Blockade of lipid receptor gpr31 suppresses platelet reactivity and thrombosis with minimal effect on hemostasis. *Blood* 2019; 134 (Supplement_1): 1064-64.
- Kaye AD and Manchikanti L: responsible, safe, and effective use of antithrombotics and anticoagulants in patients undergoing interventional techniques: American society of interventional pain physicians (ASIPP) Guidelines. *Pain Physician* 2019; 22(1S): S75-S128.
- Qiu J, Lingna W, Jinghong H and Yongqing Z: Oral administration of leeches (shuizhi): a review of the mechanisms of action on antiplatelet aggregation. *Journal of Ethnopharmacology* 2019; 1(2): 201-22.
- Ticagrelor versus aspirin in ischemic stroke. *Case Med Res* 2019.
- Bank W: How countries are using edtech (including online learning, radio, television, texting) to support access to remote learning during the COVID-19 Pandemic <https://www.worldbank.org/en/topic/edutech/brief/how-countries-are-using-edtech-to-support-remote-learn>. *Worldbank.org* 2020; 1 (1): 1-22.
- Akbar: Snapshot Perbankan Syariah Indonesia. *Snapshot Perbank. syariah* 2018; 1 (1): 1-9.
- Demircuc-Kunt A, Klapper L, Singer D, Ansar S and Hess J: The global finindex database 2017: measuring financial inclusion and the fintech revolution. *glob. finindex database 2017 meas. Financ Incl Fintech Revolut* 2018; 1(1): 121-34.
- Kurbucz MT: A Joint Dataset of Official COVID-19 Reports and the Governance, Trade and Competitiveness Indicators of World Bank Group Platforms. *Data Br* 2020; 31(1): 15-17.
- The Work Bank. Employment in Agriculture (Percentage of Total Employment). *Int. Labour Organ. ILOSTAT database*. Data Retrieved 2014; 1(1): 19-36.
- Vardhan S and Sahoo SK: *In-silico* ADMET and molecular docking study on searching potential inhibitors from limonoids and triterpenoids for COVID-19. *Computers in Biology and Medicine* 2020; 124(1): 135-56.
- Bajgain KT, Badal S, Bajgain BB and Santana MJ: Prevalence of comorbidities among individuals with covid-19: a Rapid Review of Current Literature. *American Journal of Infection Control* 2020; 1(1): 123-45.
- Passarelli PC, Lopez MA, Bonaviri GNM, Garcia-Godoy, F and DâAddona A: Taste and Smell as chemosensory dysfunctions in COVID-19 infection. *American Journal of Dentistry* 2020; 33(3): 135-37.
- Solis-Vasquez L, Santos-Martins D, Koch A and Forli S: Evaluating the energy efficiency of opencl-accelerated autodock molecular docking. in proceedings - 2020 28th Euromicro International Conference on Parallel, Distributed and Network-Based Processing, PDP 2020; 162-66.
- Kumar S, Kashyap P, Chowdhury S, Kumar S, Panwar A and Kumar A: Identification of phytochemicals as potential therapeutic agents that binds to nsp15 protein target of coronavirus (SARS-CoV-2) That Are Capable of Inhibiting Virus Replication. *Phytomedicine* 2020; 1(1): 145-56.
- Gandhi AJ, Rupareliya JD, Shukla VJ, Donga SB and Acharya R: An ayurvedic perspective along with *in-silico* study of the drugs for the management of SARS-CoV-2. *Journal of Ayurv and Integr Medicine* 2020; 1 (1): 145-56.
- Singh V: Structure based docking of secondary metabolites against drpe1 to Treat Tuberculosis. *Int J Res Appl Sci Eng Technol* 2020; 8(6): 2515-20.
- Baqi Y and Müller CE: Antithrombotic P2Y 12 receptor antagonists: recent developments in drug discovery. *Drug Discovery Today* 2019; 24(1): 325-33.
- Jin Z, Du X, Xu Y, Deng Y, Liu M, Zhao Y, Zhang B, Li X, Zhang L, Peng C, Duan Y, Yu J, Wang L, Yang K, Liu F, Jiang R, Yang X, You T, Liu X, Yang X, Bai F, Liu H, Liu X, Guddat LW, Xu W, Xiao G, Qin C, Shi Z, Jiang H, Rao Z and Yang H: Structure of Mpro from SARS-CoV-2 and Discovery of Its Inhibitors. *Nature* 2020; 582 (7811): 289-93.

31. Crommelin D, Stolk P, Besançon L, Shah V, Midha K and Leufkens H: Pharmaceutical Sciences in 2020. Nature

Reviews Drug Discovery 2010; 9(2): 99-00.

How to cite this article:

PR Devhare, Jain S, Sonwane G, Borkar V and Diwre R: Identification and optimization of binding site for an active metabolite of clopidogrel, prasugrel and ticlopidine on receptor P2Y₁₂. Int J Pharm Sci & Res 2021; 12(8): 4365-70. doi: 10.13040/IJPSR.0975-8232.12(8).4365-70.

All © 2013 are reserved by International Journal of Pharmaceutical Sciences and Research. This Journal licensed under a Creative Commons Attribution-NonCommercial-ShareAlike 3.0 Unported License.

This article can be downloaded to **ANDROID OS** based mobile. Scan QR Code using Code/Bar Scanner from your mobile. (Scanners are available on Google Playstore)



Received on 20 August 2019; received in revised form, 28 January 2021; accepted, 19 May 2021; published 01 August 2021

IDENTIFICATION AND OPTIMIZATION OF BINDING SITE FOR AN ACTIVE METABOLITE OF CLOPIDOGREL, PRASUGREL AND TICLOPIDINE ON RECEPTOR P2Y12

Parmeshwar R. Devhare ^{*1}, Shirish Jain ², Gajanan Sonwane ¹, Vijay Borkar ¹ and Rushikesh Diwre ¹

Department of Pharmaceutical Chemistry ¹, Department of Pharmacology ², Rajarshi Shahu College of Pharmacy, Buldhana - 443001, Maharashtra, India.

Keywords:

Molecular docking, P2Y12, Clopidogrel, Prasugrel, Ticlopidine

Correspondence to Author: Parmeshwar R. Devhare

Assistant Professor,
Rajarshi Shahu College of Pharmacy,
Buldhana - 443001, Maharashtra,
India.

E-mail: parme1717@gmail.com

ABSTRACT: In this article, an attempt was made to develop molecular docking studies on active metabolites of Prasugrel, Clopidogrel, and Ticlopidine acting as protein P2Y12 inhibitors. Molecular docking analysis was performing by using autodock version 4.3 adjoin with discovery studio to better understand the interactions between P2Y12 targets and inhibitors in this series. Hydrophobic and hydrogen bond interactions lead to the identification of active binding sites of P2Y12 protein in the docked complex, signifying the affection of active Metabolite of Prasugrel is more than other active metabolites of ticlopidine and clopidogrel. The present study may lead to the discovery of therapeutically potent agents against clinically very important cardiovascular disorders, including arterial thrombosis, Hypertension, embolism etc. cardiac diseases. Hence the computer-aided drug design docking model proposed in this work can be employed to design the metabolites of Clopidogrel, Prasugrel, and Ticlopidine with specific P2Y12 inhibitory activity and futuristic active metabolites possibilities.

INTRODUCTION: Molecular modeling and computational tools have become a close matching part of experimenting in the understanding of molecular aspects of genetic systems ¹⁻⁴. The computational strategies like molecular docking and quantitative structure-activity relationship (QSAR) are utilized to find the new hits for different helpful targets ⁵⁻⁷. The ongoing report featured the interface between computational methodologies and experiments as an essential tool in the drug discovery technology ^{8,9}.

Using the prominent rising interest in the design of ligand-enzyme inhibitors, this present study is to elucidate the molecular docking study of active metabolites of clopidogrel, prasugrel, and ticlopidine as P2Y12 inhibitor using computational tools that can be applied to understand interactions between inhibitors and their target proteins.

P2Y12 Crystal structures of the human P2Y12 receptor shown in figure 1 have as of late been settled. Structures of the receptor in a complex with the agonists 2-methylthio-adenosine diphosphate (2MeS-ADP) and 2-methylthio-adenosine triphosphate (2MeS-ATP) ^{10, 11} and with the non-nucleotide antagonist ethyl 6-(4-[(benzylsulfonyl) carbamoyl] piperidin-1-yl)-5- cyano-2-methyl-nicotinate (AZD1283) were obtained ^{12, 13}. The P2Y12 receptor represents a successful drug target, with several clinical drugs on the market, including **101**

<p>QUICK RESPONSE CODE</p>	<p>DOI: 10.13040/IJPSR.0975-8232.12(8).4365-70</p> <hr/> <p>The article can be accessed online on www.ijpsr.com</p> <hr/> <p>DOI link: http://dx.doi.org/10.13040/IJPSR.0975-8232.12(8).4365-70</p>
-----------------------------------	--

clopidogrel, prasugrel, ticlopidine, cangrelor, and ticagrelor, and more drugs in clinical trials¹⁴. Along these lines, the advancement of P2Y12 antagonist has been a functioning region of medication improvement, and endeavors have been founded on dynamic metabolites of clopidogrel, prasugrel, and ticlopidine with the plan to maintain a strategic distance from biotransformation of the prodrug.

Docking considers as the structures of progressively potential medication target are explained the open door for the computer to perform beginning binding studies is expanding. By computationally docking a ligand to a protein, one point of confinement worries about examine intricacy, for example, compound solvency and the requirements to keep up broad physical compound libraries.

The goal of computational docking is to decide how atoms of realized structure will collaborate. The molecule may bind to the receptor and modify its function. The docking considers performed between receptor (P2Y12, PDB code: 4NTJ) and ligands by utilizing PyRx-Python solution (adaptation 0.8). 4NTJ **Fig. 1**, recovered from RCSB and arranged by Discovery Studio visualizer rendition 16.1.01

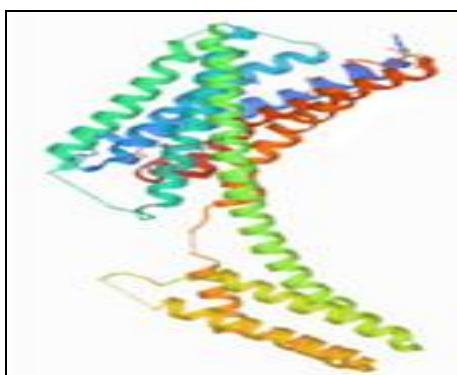


FIG. 1 STRUCTURE OF 4NTJ

Experimental Methods: 3D structure of the enzyme P2Y12 with PDB code: 4NTJ by Zhang *et al.*, and active metabolites are shown in **Fig. 2** of clopidogrel, prasugrel, and ticlopidine were taken from literature^{15, 16}. The protein structure was downloaded from the information base online Protein Data Bank (PDB)^{17, 18}. Two and three-dimensional structure of metabolites drawn utilizing program package ChemDraw Ultra v12.0.2, 2010.

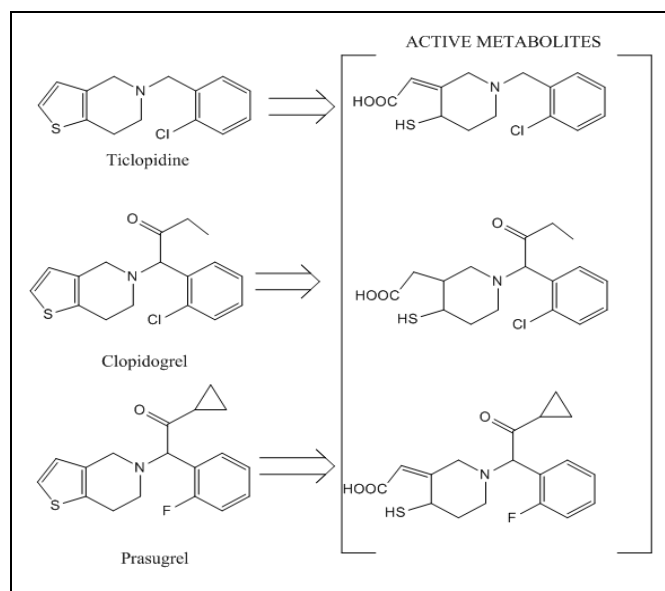


FIG. 2: ACTIVE METABOLITE OF TICLOPIDINE, CLOPIDOGREL AND PRASUGEL

Preparation of Protein Structure: The 3D coordinates of the crystal structure of P2Y12 (PDB ID: 4NTJ) were downloaded from the Protein Data Bank^{19–21}. 4NTJ (chains A) were picked for the docking reenactments. Before docking, all water atoms are ousted from protein document 4NTJ. In the wake of ousting the water molecules, H atom was added to protein for right ionization and tautomeric states of amino corrosive, such as ARG, CYS, LYS, PHE TYR, and VAL.

Preparation of Ligand Structures: The ligands used for the docking study were selected from the literature^{22–24}. The ligand structures were generated using the tool ChemDraw ultra v12.0.2. Three-dimensional optimizations of the ligand structures were done and saved as 'PDB file'. Geometry optimizations of the ligands were performed using the Steepest descent calculation method using Avagdro software. The compounds included in the study are active metabolites of clopidogrel, prasugrel, and ticlopidine; the bioactive compounds considered for the study are listed in **Fig. 2**.

Protein-ligand Interaction using PyRx (Autodock Vina): The docking studies were conceded by PyRx (Autodock vina) tools^{25, 26} version v 0.8 programs. The looking through lattice reached out over the favoured objective proteins; polar hydrogen was added to the ligand moieties. Kollman charges were assigned, and atomic solvation parameters were added. Polar hydrogen

charges of the Gasteiger-type were assigned, and the non-polar hydrogen was merged with the carbons, and the internal degrees of freedom and torsions were set. Active metabolites were docked to target protein complex (4NTJ), with the molecule considered as a rigid body and the ligand being flexible. The search was extended over the whole receptor protein used as blind docking. Affinity maps for all the atom types present, as well as an electrostatic map, were computed with a grid spacing of 0.375 Å. The search was carried out with the Lamarckian Genetic Algorithm; populations of 150 individuals with a mutation rate of 0.02 were evolved for 9 generations. Evaluation of the results was done by sorting the different complexes concerning the predicted binding energy. A cluster analysis based on root mean square deviation values concerning the starting geometry was subsequently performed, and the lowest energy conformation of the more populated cluster was considered as the most trustable solution.

RESULTS AND DISCUSSION: In this present study, to understand the formation of hydrogen bond interactions between the active metabolites and active sites of the crystal structure of P2Y12 (PDB code: 4NTJ) was used to explore their binding mode, and a docking study was performed by using PyRx (Autodock vina)^{27, 28}. Three active metabolites of clopidogrel, prasugrel and ticlopidine were retrieved from literature²⁹. The 3D structure and energy minimization was done by Avogadro software. All these chemical compounds. To date, three crystal structures of P2Y12 in complex with agonist and antagonist have been reported in the literature. In the present study, we have used X-ray crystallography structure of P2Y12 (PDB code: 4NTJ) **Fig. 1** in ternary

complex with the non-nucleotide antagonist ethyl 6-(4-[(benzylsulfonyl) carbamoyl] piperidine-1-yl)-5-cyano-2-methylnicotinate (AZD1283) is used for the docking study.

Binding Site of the Protein: The detection of ligand-binding sites is often the starting point for protein function identification and drug discovery^{30, 31}. In our study, PyRx (autodock vina) predicted the active site of the receptor P2Y12 (4NTJ) with higher average precision. P2Y12 (4NTJ) 's active site comprises amino acid residues such as CYS97, VAL102, TYR105, PHE106, TYR109, MET152, LEU155, SER156, ASN159, HIS187, VAL190, ASN191, CYS194, PHE252, ALA255, ARG256, TYR259, LEU276, AND VAL279. As most of the amino acid residues in the active site are hydrophobic, so they are the main contributors to the receptor and ligand-binding interaction. Amino acid interaction of active metabolite of Ticlopidine, Clopidogrel, and Prasugrel shown in **Fig. 3, 4, and 5** respectively, and standard drug ethyl 6-(4-((benzylsulfonyl) carbamoyl) piperidin- 1- yl)- 5-cyano-2-methylnicotinate amino acid interaction shown in **Fig. 6**.

Interaction between Active Metabolites and 4ntj:

TABLE 1: DOCKING ENERGY OF ACTIVE METABOLITES OF COLPIDOGREL, PRASUGREL, AND TICLOPIDINE

Ligand	Binding Affinity	rmsd/ub	rmsd/lb
Metabolite of Ticlopidine	-7	6.94	1.496
Metabolite of Colpidogrel	-5.7	30.813	29.362
Metabolite of Prasugrel	-7.1	2.378	2.126
Std	-6.8	12.349	11.335

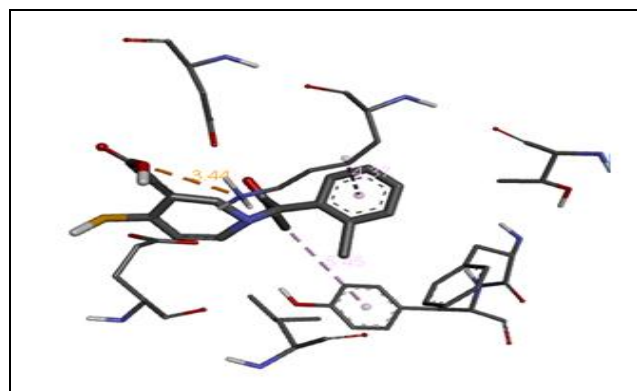
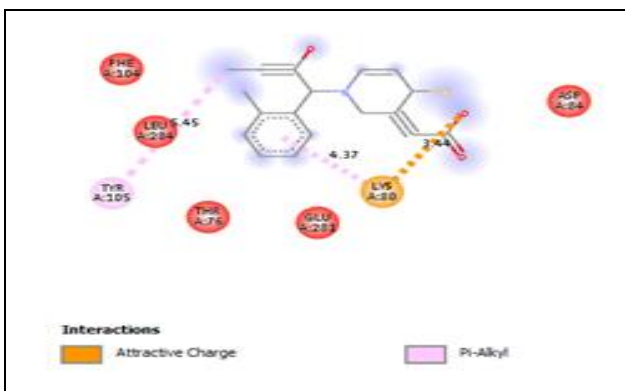


FIG. 3: AMINO ACID INTERACTION WITH TICLOPIDINE LIGAND



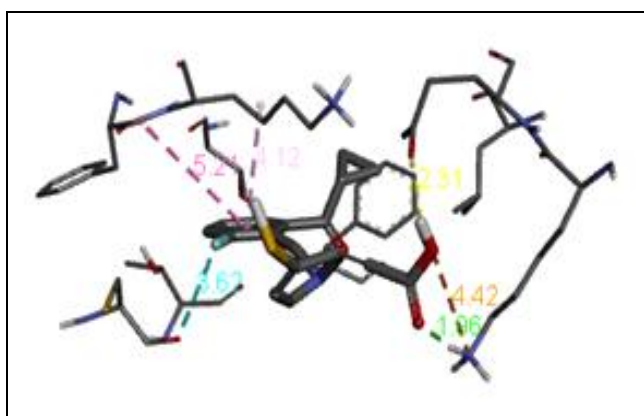


FIG. 4: AMINO ACID INTERACTION WITH COLPIDOGREL LIGAND

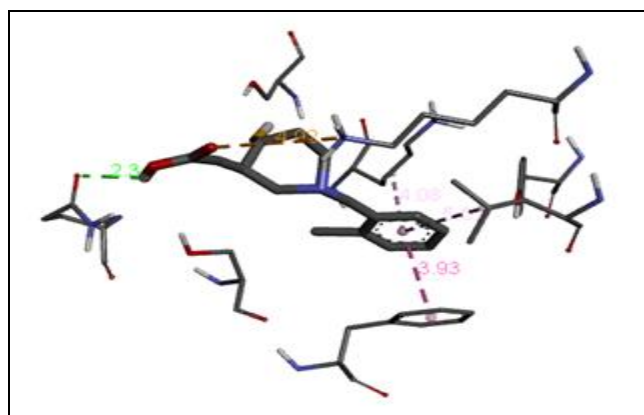
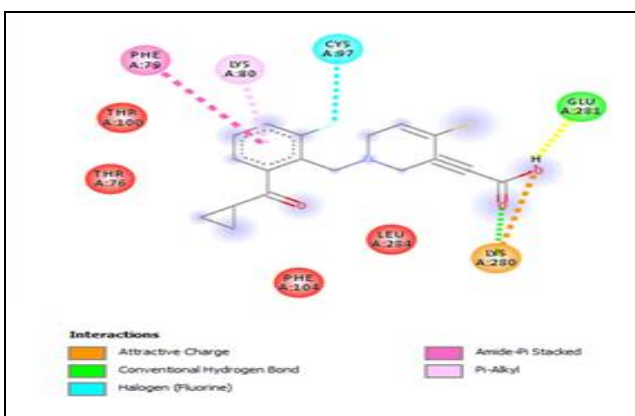


FIG. 5: AMINO ACID INTERACTION WITH PRASUGREL LIGAND

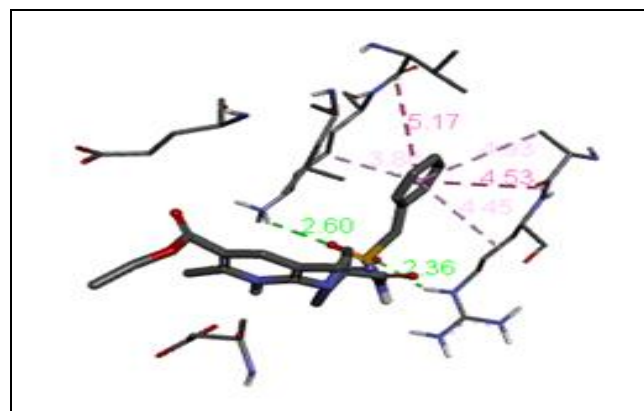
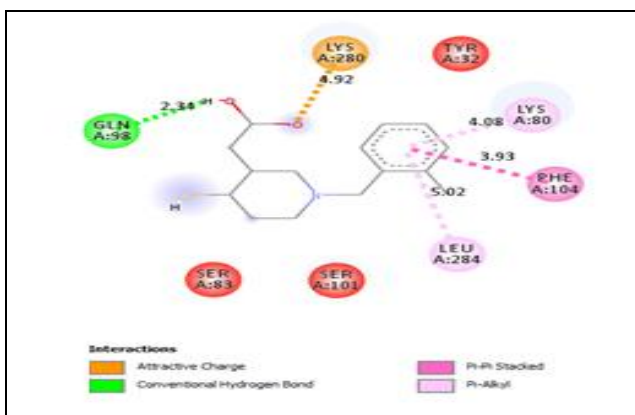
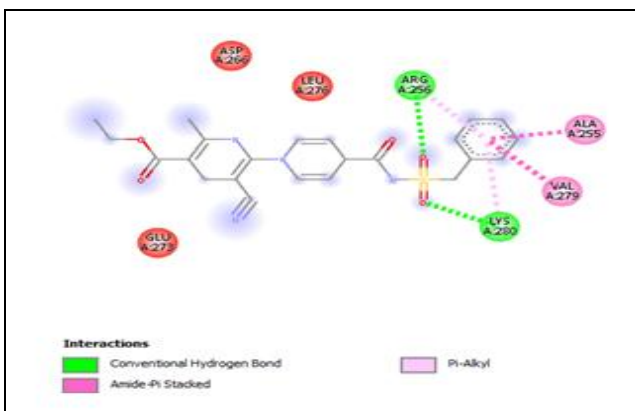


FIG. 6: AMINO ACID INTERACTION WITH STD ETHYL 6-((BENZYSULFONYL) CARBAMOYL) PIPERIDIN-1-YL)-5-CYANO-2-METHYLNICOTINATE LIGAND



CONCLUSION: The P2Y12 receptor is a significant objective of antithrombotic treatment. In PCI patients, new P2Y12 inhibitors decrease all-cause mortality and major ischemic conditions, specifically in PCI for STEMI patients.

These further backings that a more significant level of platelet inhibition than clopidogrel (600 mg) is required for, by far, most of the patients. This study based on binding energy for receptor P2Y12 (4NTJ) of the metabolite of Prasugrel ligand showed better activity than Metabolite of

Ticlopidine Metabolite of Colpidogrel, which may show a better dose regimen with lesser side effects. This research will help for further wetlab Pharmacological investigation of Prasugrel ligand as compared to a metabolite of Ticlopidine and metabolite of Clopidogrel.

ACKNOWLEDGEMENT: Authors are thankful to the Principal, Dr. S.P Jain Sir, Rajarshi Shahu College of Pharmacy, Buldhana (MS), India, for providing the necessary facilities.

CONFLICTS OF INTEREST: Nil**REFERENCES:**

- Wang R, Hozumi Y, Yin C and Wei GW: Decoding SARS-CoV-2 Transmission and Evolution and Ramifications for COVID-19 Diagnosis, Vaccine and Medicine. *Journal of Chemical Information and Modeling* 2020; 1(1): 101-12.
- Villas-Boas GR: The New Coronavirus (SARS-CoV-2): A Comprehensive Review on Immunity and the Application of Bioinformatics and Molecular Modeling to the Discovery of Potential Anti-SARS-CoV-2 Agents. *Molecules* 2020; 1(1): 121-34.
- Mir-Artigues P, Twyman RM, Alvarez D, Cerda Bennasser P, Balcells M, Christou P and Capell TA: Simplified Techno-Economic Model for the Molecular Pharming of Antibodies. *Biotechnology and Bioengineering* 2019; 4(14): 1458-65.
- Martin RW, Butts CT, Cross TJ, Takahashi GR, Diessner EM, Crosby MG, Farahmand V and Zhuang S: Sequence characterization and molecular modeling of clinically relevant variants of the SARS-CoV-2 main protease. *Biochemistry* 2020; 2(2): 151-68.
- De P, Bhayye S, Kumar V and Roy K: *In-silico* modeling for quick prediction of inhibitory activity against 3CLpro enzyme in SARS CoV diseases. *Journal of Biomolecular Structure and Dynamics* 2020; 2(2): 123-35.
- Nesměrák K: Medicinal Chemistry meets electrochemistry: redox potential in the role of endpoint or molecular descriptor in QSAR/QSPR. *Mini-Reviews in Medicinal Chemistry* 2020; 2(3): 201-13.
- Chinen K and Malloy T: QSAR use in REACH analyses of alternatives to predict human health and environmental Toxicity of Alternative Chemical Substances. *Integrated Environmental Assessment and Management* 2020; 2(5): 3-13.
- Hughes JP, Rees S, Kalindjian SB and Philpott KL: Principles of Early Drug Discovery. *British Journal of Pharmacology* 2011; 162 (6): 1239-49.
- Drews J: Drug Discovery: A Historical Perspective. *Science (80-.)* 2000; 3 (2): 135-45.
- Shi C and Kim T: crystal clots as therapeutic target in cholesterol crystal embolism. *Circ Res* 2020; 3 (5): 22-36.
- Neumann A, Müller CE and Namasivayam V: P2Y1-like nucleotide receptors—structures, molecular modeling, mutagenesis, and oligomerization. *wiley interdiscip. Wiley Interdisciplinary Reviews: Computational Molecular Science* 2020; 10 (4): 134-46.
- Kong D, Xue T, Guo B, Cheng J, Liu S, Wei J, Lu Z, Liu H, Gong G, Lan T, Hu W and Yang Y: Optimization of P2Y12 Antagonist Ethyl 6-(4-((Benzylsulfonyl) Carbamoyl) Piperidin-1-Yl)-5-Cyano-2-Methylnicotinate (AZD1283) Led to the Discovery of an Oral Antiplatelet Agent with Improved Druglike Properties. *Journal of Medicinal Chemistry* 2019; 62 (6): 3088-06.
- Van Doren, L, Nguyen N, Garzia C, Fletcher E, Stevenson R, Jaramillo D, Kuliopulos A and Covic L: Blockade of lipid receptor gpr31 suppresses platelet reactivity and thrombosis with minimal effect on hemostasis. *Blood* 2019; 134 (Supplement_1): 1064-64.
- Kaye AD and Manchikanti L: responsible, safe, and effective use of antithrombotics and anticoagulants in patients undergoing interventional techniques: American society of interventional pain physicians (ASIPP) Guidelines. *Pain Physician* 2019; 22(1S): S75-S128.
- Qiu J, Lingna W, Jinghong H and Yongqing Z: Oral administration of leeches (shuizhi): a review of the mechanisms of action on antiplatelet aggregation. *Journal of Ethnopharmacology* 2019; 1(2): 201-22.
- Ticagrelor versus aspirin in ischemic stroke. *Case Med Res* 2019.
- Bank W: How countries are using edtech (including online learning, radio, television, texting) to support access to remote learning during the COVID-19 Pandemic <https://www.worldbank.org/en/topic/edutech/brief/how-countries-are-using-edtech-to-support-remote-learn>. Worldbank.org 2020; 1 (1): 1-22.
- Akbar: Snapshot Perbankan Syariah Indonesia. *Snapshot Perbank. syariah* 2018; 1 (1): 1-9.
- Demircuc-Kunt A, Klapper L, Singer D, Ansar S and Hess J: The global finindex database 2017: measuring financial inclusion and the fintech revolution. *glob. finindex database 2017 meas. Financ Incl Fintech Revolut* 2018; 1(1): 121-34.
- Kurbucz MT: A Joint Dataset of Official COVID-19 Reports and the Governance, Trade and Competitiveness Indicators of World Bank Group Platforms. *Data Br* 2020; 31(1): 15-17.
- The Work Bank. Employment in Agriculture (Percentage of Total Employment). *Int. Labour Organ. ILOSTAT database*. Data Retrieved 2014; 1(1): 19-36.
- Vardhan S and Sahoo SK: *In-silico* ADMET and molecular docking study on searching potential inhibitors from limonoids and triterpenoids for COVID-19. *Computers in Biology and Medicine* 2020; 124(1): 135-56.
- Bajgain KT, Badal S, Bajgain BB and Santana MJ: Prevalence of comorbidities among individuals with covid-19: a Rapid Review of Current Literature. *American Journal of Infection Control* 2020; 1(1): 123-45.
- Passarelli PC, Lopez MA, Bonaviri GNM, Garcia-Godoy, F and DâAddona A: Taste and Smell as chemosensory dysfunctions in COVID-19 infection. *American Journal of Dentistry* 2020; 33(3): 135-37.
- Solis-Vasquez L, Santos-Martins D, Koch A and Forli S: Evaluating the energy efficiency of opencl-accelerated autodock molecular docking. in proceedings - 2020 28th Euromicro International Conference on Parallel, Distributed and Network-Based Processing, PDP 2020; 162-66.
- Kumar S, Kashyap P, Chowdhury S, Kumar S, Panwar A and Kumar A: Identification of phytochemicals as potential therapeutic agents that binds to nsp15 protein target of coronavirus (SARS-CoV-2) That Are Capable of Inhibiting Virus Replication. *Phytomedicine* 2020; 1(1): 145-56.
- Gandhi AJ, Rupareliya JD, Shukla VJ, Donga SB and Acharya R: An ayurvedic perspective along with *in-silico* study of the drugs for the management of SARS-CoV-2. *Journal of Ayurv and Integr Medicine* 2020; 1 (1): 145-56.
- Singh V: Structure based docking of secondary metabolites against drpe1 to Treat Tuberculosis. *Int J Res Appl Sci Eng Technol* 2020; 8(6): 2515-20.
- Baqi Y and Müller CE: Antithrombotic P2Y 12 receptor antagonists: recent developments in drug discovery. *Drug Discovery Today* 2019; 24(1): 325-33.
- Jin Z, Du X, Xu Y, Deng Y, Liu M, Zhao Y, Zhang B, Li X, Zhang L, Peng C, Duan Y, Yu J, Wang L, Yang K, Liu F, Jiang R, Yang X, You T, Liu X, Yang X, Bai F, Liu H, Liu X, Guddat LW, Xu W, Xiao G, Qin C, Shi Z, Jiang H, Rao Z and Yang H: Structure of Mpro from SARS-CoV-2 and Discovery of Its Inhibitors. *Nature* 2020; 582 (7811): 289-93.

31. Crommelin D, Stolk P, Besançon L, Shah V, Midha K and Leufkens H: Pharmaceutical Sciences in 2020. Nature

Reviews Drug Discovery 2010; 9(2): 99-00.

How to cite this article:

PR Devhare, Jain S, Sonwane G, Borkar V and Diwre R: Identification and optimization of binding site for an active metabolite of clopidogrel, prasugrel and ticlopidine on receptor P2Y₁₂. Int J Pharm Sci & Res 2021; 12(8): 4365-70. doi: 10.13040/IJPSR.0975-8232.12(8).4365-70.

All © 2013 are reserved by International Journal of Pharmaceutical Sciences and Research. This Journal licensed under a Creative Commons Attribution-NonCommercial-ShareAlike 3.0 Unported License.

This article can be downloaded to **ANDROID OS** based mobile. Scan QR Code using Code/Bar Scanner from your mobile. (Scanners are available on Google Playstore)



Received on 20 August 2019; received in revised form, 28 January 2021; accepted, 19 May 2021; published 01 August 2021

IDENTIFICATION AND OPTIMIZATION OF BINDING SITE FOR AN ACTIVE METABOLITE OF CLOPIDOGREL, PRASUGREL AND TICLOPIDINE ON RECEPTOR P2Y12

Parmeshwar R. Devhare ^{*1}, Shirish Jain ², Gajanan Sonwane ¹, Vijay Borkar ¹ and Rushikesh Diwre ¹

Department of Pharmaceutical Chemistry ¹, Department of Pharmacology ², Rajarshi Shahu College of Pharmacy, Buldhana - 443001, Maharashtra, India.

Keywords:

Molecular docking, P2Y12, Clopidogrel, Prasugrel, Ticlopidine

Correspondence to Author: Parmeshwar R. Devhare

Assistant Professor,
Rajarshi Shahu College of Pharmacy,
Buldhana - 443001, Maharashtra,
India.

E-mail: parme1717@gmail.com

ABSTRACT: In this article, an attempt was made to develop molecular docking studies on active metabolites of Prasugrel, Clopidogrel, and Ticlopidine acting as protein P2Y12 inhibitors. Molecular docking analysis was performing by using autodock version 4.3 adjoin with discovery studio to better understand the interactions between P2Y12 targets and inhibitors in this series. Hydrophobic and hydrogen bond interactions lead to the identification of active binding sites of P2Y12 protein in the docked complex, signifying the affection of active Metabolite of Prasugrel is more than other active metabolites of ticlopidine and clopidogrel. The present study may lead to the discovery of therapeutically potent agents against clinically very important cardiovascular disorders, including arterial thrombosis, Hypertension, embolism etc. cardiac diseases. Hence the computer-aided drug design docking model proposed in this work can be employed to design the metabolites of Clopidogrel, Prasugrel, and Ticlopidine with specific P2Y12 inhibitory activity and futuristic active metabolites possibilities.

INTRODUCTION: Molecular modeling and computational tools have become a close matching part of experimenting in the understanding of molecular aspects of genetic systems ¹⁻⁴. The computational strategies like molecular docking and quantitative structure-activity relationship (QSAR) are utilized to find the new hits for different helpful targets ⁵⁻⁷. The ongoing report featured the interface between computational methodologies and experiments as an essential tool in the drug discovery technology ^{8,9}.

Using the prominent rising interest in the design of ligand-enzyme inhibitors, this present study is to elucidate the molecular docking study of active metabolites of clopidogrel, prasugrel, and ticlopidine as P2Y12 inhibitor using computational tools that can be applied to understand interactions between inhibitors and their target proteins.

P2Y12 Crystal structures of the human P2Y12 receptor shown in figure 1 have as of late been settled. Structures of the receptor in a complex with the agonists 2-methylthio-adenosine diphosphate (2MeS-ADP) and 2-methylthio-adenosine triphosphate (2MeS-ATP) ^{10, 11} and with the non-nucleotide antagonist ethyl 6-(4-[(benzylsulfonyl) carbamoyl] piperidin-1-yl)-5- cyano-2-methyl-nicotinate (AZD1283) were obtained ^{12, 13}. The P2Y12 receptor represents a successful drug target, with several clinical drugs on the market, including **107**

<p>QUICK RESPONSE CODE</p> 	<p>DOI: 10.13040/IJPSR.0975-8232.12(8).4365-70</p> <hr/> <p>The article can be accessed online on www.ijpsr.com</p> <hr/> <p>DOI link: http://dx.doi.org/10.13040/IJPSR.0975-8232.12(8).4365-70</p>
---	--

clopidogrel, prasugrel, ticlopidine, cangrelor, and ticagrelor, and more drugs in clinical trials¹⁴. Along these lines, the advancement of P2Y12 antagonist has been a functioning region of medication improvement, and endeavors have been founded on dynamic metabolites of clopidogrel, prasugrel, and ticlopidine with the plan to maintain a strategic distance from biotransformation of the prodrug.

Docking considers as the structures of progressively potential medication target are explained the open door for the computer to perform beginning binding studies is expanding. By computationally docking a ligand to a protein, one point of confinement worries about examine intricacy, for example, compound solvency and the requirements to keep up broad physical compound libraries.

The goal of computational docking is to decide how atoms of realized structure will collaborate. The molecule may bind to the receptor and modify its function. The docking considers performed between receptor (P2Y12, PDB code: 4NTJ) and ligands by utilizing PyRx-Python solution (adaptation 0.8). 4NTJ **Fig. 1**, recovered from RCSB and arranged by Discovery Studio visualizer rendition 16.1.01

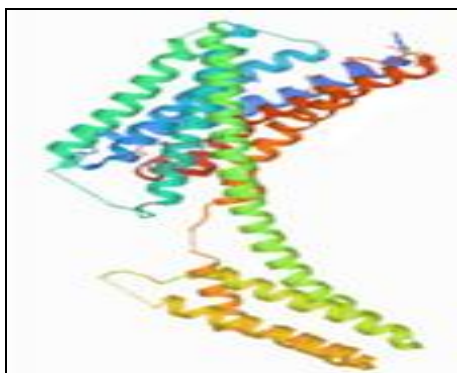


FIG. 1 STRUCTURE OF 4NTJ

Experimental Methods: 3D structure of the enzyme P2Y12 with PDB code: 4NTJ by Zhang *et al.*, and active metabolites are shown in **Fig. 2** of clopidogrel, prasugrel, and ticlopidine were taken from literature^{15, 16}. The protein structure was downloaded from the information base online Protein Data Bank (PDB)^{17, 18}. Two and three-dimensional structure of metabolites drawn utilizing program package ChemDraw Ultra v12.0.2, 2010.

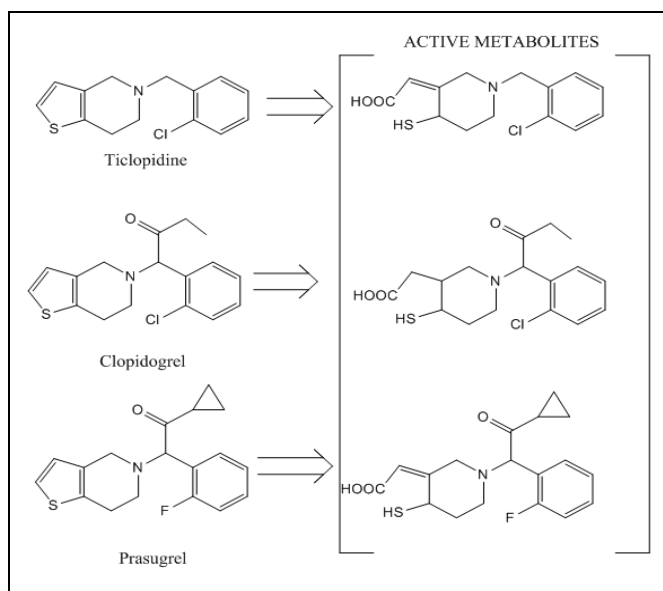


FIG. 2: ACTIVE METABOLITE OF TICLOPIDINE, CLOPIDOGREL AND PRASUGEL

Preparation of Protein Structure: The 3D coordinates of the crystal structure of P2Y12 (PDB ID: 4NTJ) were downloaded from the Protein Data Bank^{19–21}. 4NTJ (chains A) were picked for the docking reenactments. Before docking, all water atoms are ousted from protein document 4NTJ. In the wake of ousting the water molecules, H atom was added to protein for right ionization and tautomeric states of amino corrosive, such as ARG, CYS, LYS, PHE TYR, and VAL.

Preparation of Ligand Structures: The ligands used for the docking study were selected from the literature^{22–24}. The ligand structures were generated using the tool ChemDraw ultra v12.0.2. Three-dimensional optimizations of the ligand structures were done and saved as 'PDB file'. Geometry optimizations of the ligands were performed using the Steepest descent calculation method using Avagdro software. The compounds included in the study are active metabolites of clopidogrel, prasugrel, and ticlopidine; the bioactive compounds considered for the study are listed in **Fig. 2**.

Protein-ligand Interaction using PyRx (Autodock Vina): The docking studies were conceded by PyRx (Autodock vina) tools^{25, 26} version v 0.8 programs. The looking through lattice reached out over the favoured objective proteins; polar hydrogen was added to the ligand moieties. Kollman charges were assigned, and atomic solvation parameters were added. Polar hydrogen

charges of the Gasteiger-type were assigned, and the non-polar hydrogen was merged with the carbons, and the internal degrees of freedom and torsions were set. Active metabolites were docked to target protein complex (4NTJ), with the molecule considered as a rigid body and the ligand being flexible. The search was extended over the whole receptor protein used as blind docking. Affinity maps for all the atom types present, as well as an electrostatic map, were computed with a grid spacing of 0.375 Å. The search was carried out with the Lamarckian Genetic Algorithm; populations of 150 individuals with a mutation rate of 0.02 were evolved for 9 generations. Evaluation of the results was done by sorting the different complexes concerning the predicted binding energy. A cluster analysis based on root mean square deviation values concerning the starting geometry was subsequently performed, and the lowest energy conformation of the more populated cluster was considered as the most trustable solution.

RESULTS AND DISCUSSION: In this present study, to understand the formation of hydrogen bond interactions between the active metabolites and active sites of the crystal structure of P2Y12 (PDB code: 4NTJ) was used to explore their binding mode, and a docking study was performed by using PyRx (Autodock vina)^{27, 28}. Three active metabolites of clopidogrel, prasugrel and ticlopidine were retrieved from literature²⁹. The 3D structure and energy minimization was done by Avogadro software. All these chemical compounds. To date, three crystal structures of P2Y12 in complex with agonist and antagonist have been reported in the literature. In the present study, we have used X-ray crystallography structure of P2Y12 (PDB code: 4NTJ) **Fig. 1** in ternary

complex with the non-nucleotide antagonist ethyl 6-(4-[(benzylsulfonyl) carbamoyl] piperidine-1-yl)-5-cyano-2-methylnicotinate (AZD1283) is used for the docking study.

Binding Site of the Protein: The detection of ligand-binding sites is often the starting point for protein function identification and drug discovery^{30, 31}. In our study, PyRx (autodock vina) predicted the active site of the receptor P2Y12 (4NTJ) with higher average precision. P2Y12 (4NTJ) 's active site comprises amino acid residues such as CYS97, VAL102, TYR105, PHE106, TYR109, MET152, LEU155, SER156, ASN159, HIS187, VAL190, ASN191, CYS194, PHE252, ALA255, ARG256, TYR259, LEU276, AND VAL279. As most of the amino acid residues in the active site are hydrophobic, so they are the main contributors to the receptor and ligand-binding interaction. Amino acid interaction of active metabolite of Ticlopidine, Clopidogrel, and Prasugrel shown in **Fig. 3, 4, and 5** respectively, and standard drug ethyl 6-(4-((benzylsulfonyl) carbamoyl) piperidin- 1- yl)- 5-cyano-2-methylnicotinate amino acid interaction shown in **Fig. 6**.

Interaction between Active Metabolites and 4ntj:

TABLE 1: DOCKING ENERGY OF ACTIVE METABOLITES OF COLPIDOGREL, PRASUGREL, AND TICLOPIDINE

Ligand	Binding Affinity	rmsd/ub	rmsd/lb
Metabolite of Ticlopidine	-7	6.94	1.496
Metabolite of Colpidogrel	-5.7	30.813	29.362
Metabolite of Prasugrel	-7.1	2.378	2.126
Std	-6.8	12.349	11.335

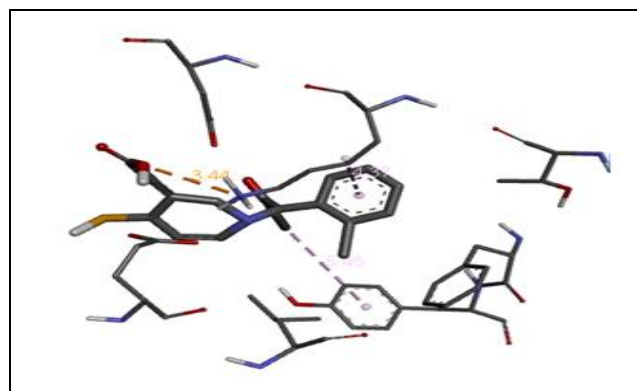
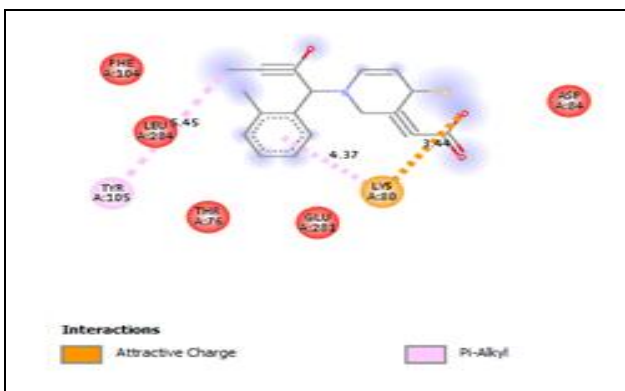


FIG. 3: AMINO ACID INTERACTION WITH TICLOPIDINE LIGAND



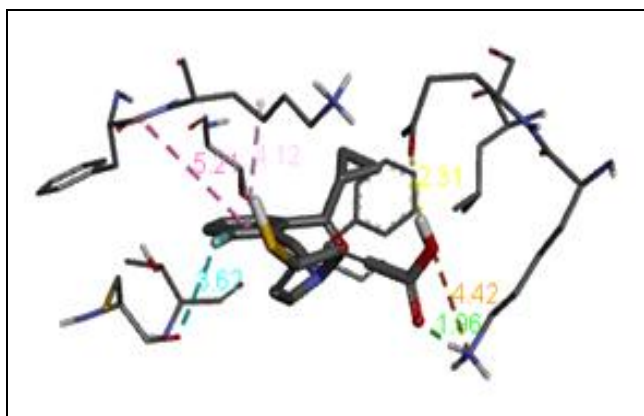


FIG. 4: AMINO ACID INTERACTION WITH COLPIDOGREL LIGAND

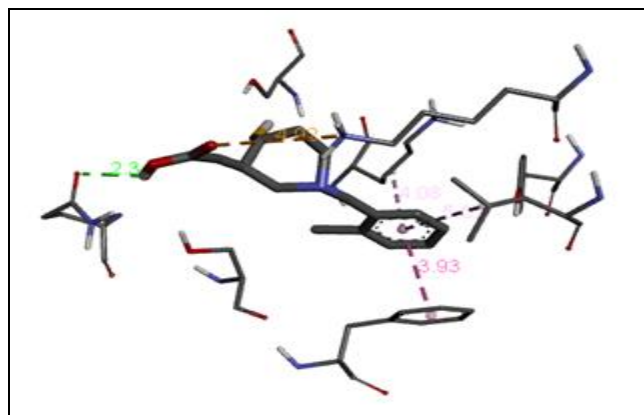
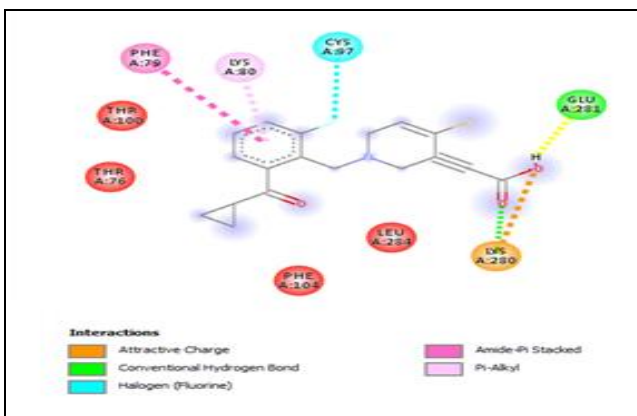


FIG. 5: AMINO ACID INTERACTION WITH PRASUGREL LIGAND

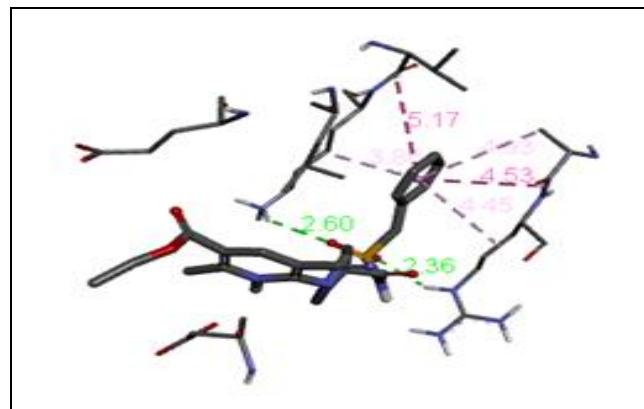
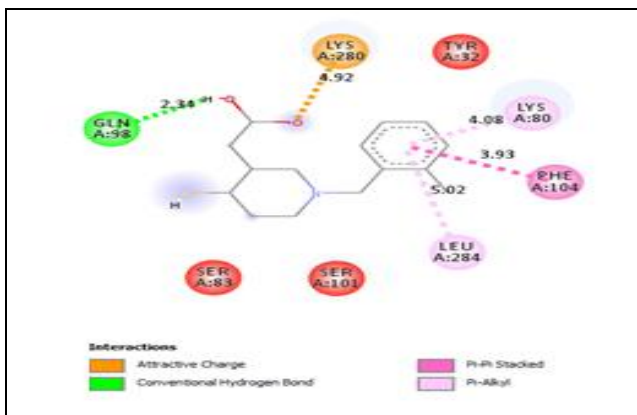
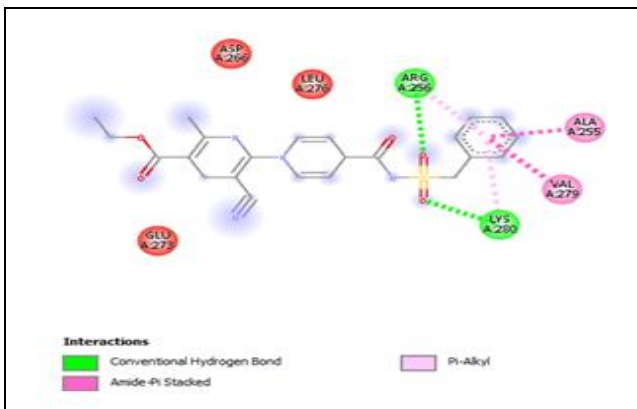


FIG. 6: AMINO ACID INTERACTION WITH STD ETHYL 6-((BENZYSULFONYL) CARBAMOYL) PIPERIDIN-1-YL)-5-CYANO-2-METHYLNICOTINATE LIGAND



CONCLUSION: The P2Y12 receptor is a significant objective of antithrombotic treatment. In PCI patients, new P2Y12 inhibitors decrease all-cause mortality and major ischemic conditions, specifically in PCI for STEMI patients.

These further backings that a more significant level of platelet inhibition than clopidogrel (600 mg) is required for, by far, most of the patients. This study based on binding energy for receptor P2Y12 (4NTJ) of the metabolite of Prasugrel ligand showed better activity than Metabolite of

Ticlopidine Metabolite of Colpidogrel, which may show a better dose regimen with lesser side effects. This research will help for further wetlab Pharmacological investigation of Prasugrel ligand as compared to a metabolite of Ticlopidine and metabolite of Clopidogrel.

ACKNOWLEDGEMENT: Authors are thankful to the Principal, Dr. S.P Jain Sir, Rajarshi Shahu College of Pharmacy, Buldhana (MS), India, for providing the necessary facilities.

CONFLICTS OF INTEREST: Nil**REFERENCES:**

- Wang R, Hozumi Y, Yin C and Wei GW: Decoding SARS-CoV-2 Transmission and Evolution and Ramifications for COVID-19 Diagnosis, Vaccine and Medicine. *Journal of Chemical Information and Modeling* 2020; 1(1): 101-12.
- Villas-Boas GR: The New Coronavirus (SARS-CoV-2): A Comprehensive Review on Immunity and the Application of Bioinformatics and Molecular Modeling to the Discovery of Potential Anti-SARS-CoV-2 Agents. *Molecules* 2020; 1(1): 121-34.
- Mir-Artigues P, Twyman RM, Alvarez D, Cerda Bennasser P, Balcells M, Christou P and Capell TA: Simplified Techno-Economic Model for the Molecular Pharming of Antibodies. *Biotechnology and Bioengineering* 2019; 4(14): 1458-65.
- Martin RW, Butts CT, Cross TJ, Takahashi GR, Diessner EM, Crosby MG, Farahmand V and Zhuang S: Sequence characterization and molecular modeling of clinically relevant variants of the SARS-CoV-2 main protease. *Biochemistry* 2020; 2(2): 151-68.
- De P, Bhayye S, Kumar V and Roy K: *In-silico* modeling for quick prediction of inhibitory activity against 3CLpro enzyme in SARS CoV diseases. *Journal of Biomolecular Structure and Dynamics* 2020; 2(2): 123-35.
- Nesměrák K: Medicinal Chemistry meets electrochemistry: redox potential in the role of endpoint or molecular descriptor in QSAR/QSPR. *Mini-Reviews in Medicinal Chemistry* 2020; 2(3): 201-13.
- Chinen K and Malloy T: QSAR use in REACH analyses of alternatives to predict human health and environmental Toxicity of Alternative Chemical Substances. *Integrated Environmental Assessment and Management* 2020; 2(5): 3-13.
- Hughes JP, Rees S, Kalindjian SB and Philpott KL: Principles of Early Drug Discovery. *British Journal of Pharmacology* 2011; 162 (6): 1239-49.
- Drews J: Drug Discovery: A Historical Perspective. *Science (80-.)* 2000; 3 (2): 135-45.
- Shi C and Kim T: crystal clots as therapeutic target in cholesterol crystal embolism. *Circ Res* 2020; 3 (5): 22-36.
- Neumann A, Müller CE and Namasivayam V: P2Y1-like nucleotide receptors—structures, molecular modeling, mutagenesis, and oligomerization. *wiley interdiscip. Wiley Interdisciplinary Reviews: Computational Molecular Science* 2020; 10 (4): 134-46.
- Kong D, Xue T, Guo B, Cheng J, Liu S, Wei J, Lu Z, Liu H, Gong G, Lan T, Hu W and Yang Y: Optimization of P2Y12 Antagonist Ethyl 6-(4-((Benzylsulfonyl) Carbamoyl) Piperidin-1-Yl)-5-Cyano-2-Methylnicotinate (AZD1283) Led to the Discovery of an Oral Antiplatelet Agent with Improved Druglike Properties. *Journal of Medicinal Chemistry* 2019; 62 (6): 3088-06.
- Van Doren, L, Nguyen N, Garzia C, Fletcher E, Stevenson R, Jaramillo D, Kuliopulos A and Covic L: Blockade of lipid receptor gpr31 suppresses platelet reactivity and thrombosis with minimal effect on hemostasis. *Blood* 2019; 134 (Supplement_1): 1064-64.
- Kaye AD and Manchikanti L: responsible, safe, and effective use of antithrombotics and anticoagulants in patients undergoing interventional techniques: American society of interventional pain physicians (ASIPP) Guidelines. *Pain Physician* 2019; 22(1S): S75-S128.
- Qiu J, Lingna W, Jinghong H and Yongqing Z: Oral administration of leeches (shuizhi): a review of the mechanisms of action on antiplatelet aggregation. *Journal of Ethnopharmacology* 2019; 1(2): 201-22.
- Ticagrelor versus aspirin in ischemic stroke. *Case Med Res* 2019.
- Bank W: How countries are using edtech (including online learning, radio, television, texting) to support access to remote learning during the COVID-19 Pandemic <https://www.worldbank.org/en/topic/edutech/brief/how-countries-are-using-edtech-to-support-remote-learn>. *Worldbank.org* 2020; 1 (1): 1-22.
- Akbar: Snapshot Perbankan Syariah Indonesia. *Snapshot Perbank. syariah* 2018; 1 (1): 1-9.
- Demircuc-Kunt A, Klapper L, Singer D, Ansar S and Hess J: The global finindex database 2017: measuring financial inclusion and the fintech revolution. *glob. finindex database 2017 meas. Financ Incl Fintech Revolut* 2018; 1(1): 121-34.
- Kurbucz MT: A Joint Dataset of Official COVID-19 Reports and the Governance, Trade and Competitiveness Indicators of World Bank Group Platforms. *Data Br* 2020; 31(1): 15-17.
- The Work Bank. Employment in Agriculture (Percentage of Total Employment). *Int. Labour Organ. ILOSTAT database*. Data Retrieved 2014; 1(1): 19-36.
- Vardhan S and Sahoo SK: *In-silico* ADMET and molecular docking study on searching potential inhibitors from limonoids and triterpenoids for COVID-19. *Computers in Biology and Medicine* 2020; 124(1): 135-56.
- Bajgain KT, Badal S, Bajgain BB and Santana MJ: Prevalence of comorbidities among individuals with covid-19: a Rapid Review of Current Literature. *American Journal of Infection Control* 2020; 1(1): 123-45.
- Passarelli PC, Lopez MA, Bonaviri GNM, Garcia-Godoy, F and DâAddona A: Taste and Smell as chemosensory dysfunctions in COVID-19 infection. *American Journal of Dentistry* 2020; 33(3): 135-37.
- Solis-Vasquez L, Santos-Martins D, Koch A and Forli S: Evaluating the energy efficiency of opencl-accelerated autodock molecular docking. in proceedings - 2020 28th Euromicro International Conference on Parallel, Distributed and Network-Based Processing, PDP 2020; 162-66.
- Kumar S, Kashyap P, Chowdhury S, Kumar S, Panwar A and Kumar A: Identification of phytochemicals as potential therapeutic agents that binds to nsp15 protein target of coronavirus (SARS-CoV-2) That Are Capable of Inhibiting Virus Replication. *Phytomedicine* 2020; 1(1): 145-56.
- Gandhi AJ, Rupareliya JD, Shukla VJ, Donga SB and Acharya R: An ayurvedic perspective along with *in-silico* study of the drugs for the management of SARS-CoV-2. *Journal of Ayurv and Integr Medicine* 2020; 1 (1): 145-56.
- Singh V: Structure based docking of secondary metabolites against drpe1 to Treat Tuberculosis. *Int J Res Appl Sci Eng Technol* 2020; 8(6): 2515-20.
- Baqi Y and Müller CE: Antithrombotic P2Y 12 receptor antagonists: recent developments in drug discovery. *Drug Discovery Today* 2019; 24(1): 325-33.
- Jin Z, Du X, Xu Y, Deng Y, Liu M, Zhao Y, Zhang B, Li X, Zhang L, Peng C, Duan Y, Yu J, Wang L, Yang K, Liu F, Jiang R, Yang X, You T, Liu X, Yang X, Bai F, Liu H, Liu X, Guddat LW, Xu W, Xiao G, Qin C, Shi Z, Jiang H, Rao Z and Yang H: Structure of Mpro from SARS-CoV-2 and Discovery of Its Inhibitors. *Nature* 2020; 582 (7811): 289-93.

31. Crommelin D, Stolk P, Besançon L, Shah V, Midha K and Leufkens H: Pharmaceutical Sciences in 2020. Nature

Reviews Drug Discovery 2010; 9(2): 99-00.

How to cite this article:

PR Devhare, Jain S, Sonwane G, Borkar V and Diwre R: Identification and optimization of binding site for an active metabolite of clopidogrel, prasugrel and ticlopidine on receptor P2Y₁₂. Int J Pharm Sci & Res 2021; 12(8): 4365-70. doi: 10.13040/IJPSR.0975-8232.12(8).4365-70.

All © 2013 are reserved by International Journal of Pharmaceutical Sciences and Research. This Journal licensed under a Creative Commons Attribution-NonCommercial-ShareAlike 3.0 Unported License.

This article can be downloaded to **ANDROID OS** based mobile. Scan QR Code using Code/Bar Scanner from your mobile. (Scanners are available on Google Playstore)



Received on 20 August 2019; received in revised form, 28 January 2021; accepted, 19 May 2021; published 01 August 2021

IDENTIFICATION AND OPTIMIZATION OF BINDING SITE FOR AN ACTIVE METABOLITE OF CLOPIDOGREL, PRASUGREL AND TICLOPIDINE ON RECEPTOR P2Y12

Parmeshwar R. Devhare ^{*1}, Shirish Jain ², Gajanan Sonwane ¹, Vijay Borkar ¹ and Rushikesh Diwre ¹

Department of Pharmaceutical Chemistry ¹, Department of Pharmacology ², Rajarshi Shahu College of Pharmacy, Buldhana - 443001, Maharashtra, India.

Keywords:

Molecular docking, P2Y12, Clopidogrel, Prasugrel, Ticlopidine

Correspondence to Author: Parmeshwar R. Devhare

Assistant Professor,
Rajarshi Shahu College of Pharmacy,
Buldhana - 443001, Maharashtra,
India.

E-mail: parme1717@gmail.com

ABSTRACT: In this article, an attempt was made to develop molecular docking studies on active metabolites of Prasugrel, Clopidogrel, and Ticlopidine acting as protein P2Y12 inhibitors. Molecular docking analysis was performing by using autodock version 4.3 adjoin with discovery studio to better understand the interactions between P2Y12 targets and inhibitors in this series. Hydrophobic and hydrogen bond interactions lead to the identification of active binding sites of P2Y12 protein in the docked complex, signifying the affection of active Metabolite of Prasugrel is more than other active metabolites of ticlopidine and clopidogrel. The present study may lead to the discovery of therapeutically potent agents against clinically very important cardiovascular disorders, including arterial thrombosis, Hypertension, embolism etc. cardiac diseases. Hence the computer-aided drug design docking model proposed in this work can be employed to design the metabolites of Clopidogrel, Prasugrel, and Ticlopidine with specific P2Y12 inhibitory activity and futuristic active metabolites possibilities.

INTRODUCTION: Molecular modeling and computational tools have become a close matching part of experimenting in the understanding of molecular aspects of genetic systems ¹⁻⁴. The computational strategies like molecular docking and quantitative structure-activity relationship (QSAR) are utilized to find the new hits for different helpful targets ⁵⁻⁷. The ongoing report featured the interface between computational methodologies and experiments as an essential tool in the drug discovery technology ^{8,9}.

Using the prominent rising interest in the design of ligand-enzyme inhibitors, this present study is to elucidate the molecular docking study of active metabolites of clopidogrel, prasugrel, and ticlopidine as P2Y12 inhibitor using computational tools that can be applied to understand interactions between inhibitors and their target proteins.

P2Y12 Crystal structures of the human P2Y12 receptor shown in figure 1 have as of late been settled. Structures of the receptor in a complex with the agonists 2-methylthio-adenosine diphosphate (2MeS-ADP) and 2-methylthio-adenosine triphosphate (2MeS-ATP) ^{10, 11} and with the non-nucleotide antagonist ethyl 6-(4-[(benzylsulfonyl) carbamoyl] piperidin-1-yl)-5- cyano-2-methyl-nicotinate (AZD1283) were obtained ^{12, 13}. The P2Y12 receptor represents a successful drug target, with several clinical drugs on the market, including **113**

<p>QUICK RESPONSE CODE</p> 	<p>DOI: 10.13040/IJPSR.0975-8232.12(8).4365-70</p> <hr/> <p>The article can be accessed online on www.ijpsr.com</p> <hr/> <p>DOI link: http://dx.doi.org/10.13040/IJPSR.0975-8232.12(8).4365-70</p>
---	--

clopidogrel, prasugrel, ticlopidine, cangrelor, and ticagrelor, and more drugs in clinical trials¹⁴. Along these lines, the advancement of P2Y12 antagonist has been a functioning region of medication improvement, and endeavors have been founded on dynamic metabolites of clopidogrel, prasugrel, and ticlopidine with the plan to maintain a strategic distance from biotransformation of the prodrug.

Docking considers as the structures of progressively potential medication target are explained the open door for the computer to perform beginning binding studies is expanding. By computationally docking a ligand to a protein, one point of confinement worries about examine intricacy, for example, compound solvency and the requirements to keep up broad physical compound libraries.

The goal of computational docking is to decide how atoms of realized structure will collaborate. The molecule may bind to the receptor and modify its function. The docking considers performed between receptor (P2Y12, PDB code: 4NTJ) and ligands by utilizing PyRx-Python solution (adaptation 0.8). 4NTJ **Fig. 1**, recovered from RCSB and arranged by Discovery Studio visualizer rendition 16.1.01

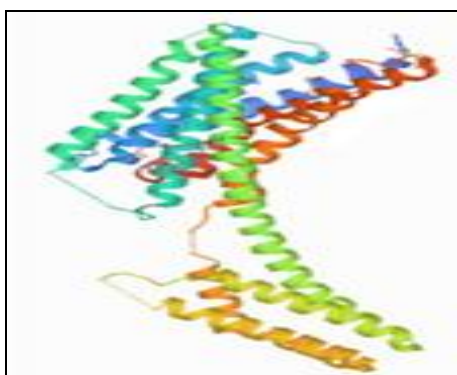


FIG. 1 STRUCTURE OF 4NTJ

Experimental Methods: 3D structure of the enzyme P2Y12 with PDB code: 4NTJ by Zhang *et al.*, and active metabolites are shown in **Fig. 2** of clopidogrel, prasugrel, and ticlopidine were taken from literature^{15, 16}. The protein structure was downloaded from the information base online Protein Data Bank (PDB)^{17, 18}. Two and three-dimensional structure of metabolites drawn utilizing program package ChemDraw Ultra v12.0.2, 2010.

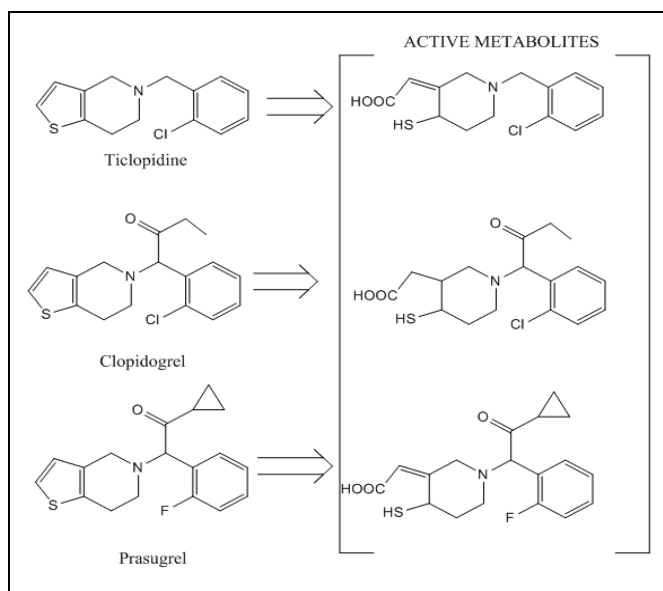


FIG. 2: ACTIVE METABOLITE OF TICLOPIDINE, CLOPIDOGREL AND PRASUGEL

Preparation of Protein Structure: The 3D coordinates of the crystal structure of P2Y12 (PDB ID: 4NTJ) were downloaded from the Protein Data Bank^{19–21}. 4NTJ (chains A) were picked for the docking reenactments. Before docking, all water atoms are ousted from protein document 4NTJ. In the wake of ousting the water molecules, H atom was added to protein for right ionization and tautomeric states of amino corrosive, such as ARG, CYS, LYS, PHE TYR, and VAL.

Preparation of Ligand Structures: The ligands used for the docking study were selected from the literature^{22–24}. The ligand structures were generated using the tool ChemDraw ultra v12.0.2. Three-dimensional optimizations of the ligand structures were done and saved as 'PDB file'. Geometry optimizations of the ligands were performed using the Steepest descent calculation method using Avagdro software. The compounds included in the study are active metabolites of clopidogrel, prasugrel, and ticlopidine; the bioactive compounds considered for the study are listed in **Fig. 2**.

Protein-ligand Interaction using PyRx (Autodock Vina): The docking studies were conceded by PyRx (Autodock vina) tools^{25, 26} version v 0.8 programs. The looking through lattice reached out over the favoured objective proteins; polar hydrogen was added to the ligand moieties. Kollman charges were assigned, and atomic solvation parameters were added. Polar hydrogen

charges of the Gasteiger-type were assigned, and the non-polar hydrogen was merged with the carbons, and the internal degrees of freedom and torsions were set. Active metabolites were docked to target protein complex (4NTJ), with the molecule considered as a rigid body and the ligand being flexible. The search was extended over the whole receptor protein used as blind docking. Affinity maps for all the atom types present, as well as an electrostatic map, were computed with a grid spacing of 0.375 Å. The search was carried out with the Lamarckian Genetic Algorithm; populations of 150 individuals with a mutation rate of 0.02 were evolved for 9 generations. Evaluation of the results was done by sorting the different complexes concerning the predicted binding energy. A cluster analysis based on root mean square deviation values concerning the starting geometry was subsequently performed, and the lowest energy conformation of the more populated cluster was considered as the most trustable solution.

RESULTS AND DISCUSSION: In this present study, to understand the formation of hydrogen bond interactions between the active metabolites and active sites of the crystal structure of P2Y12 (PDB code: 4NTJ) was used to explore their binding mode, and a docking study was performed by using PyRx (Autodock vina)^{27, 28}. Three active metabolites of clopidogrel, prasugrel and ticlopidine were retrieved from literature²⁹. The 3D structure and energy minimization was done by Avogadro software. All these chemical compounds. To date, three crystal structures of P2Y12 in complex with agonist and antagonist have been reported in the literature. In the present study, we have used X-ray crystallography structure of P2Y12 (PDB code: 4NTJ) **Fig. 1** in ternary

complex with the non-nucleotide antagonist ethyl 6-(4-[(benzylsulfonyl) carbamoyl] piperidine-1-yl)-5-cyano-2-methylnicotinate (AZD1283) is used for the docking study.

Binding Site of the Protein: The detection of ligand-binding sites is often the starting point for protein function identification and drug discovery^{30, 31}. In our study, PyRx (autodock vina) predicted the active site of the receptor P2Y12 (4NTJ) with higher average precision. P2Y12 (4NTJ) 's active site comprises amino acid residues such as CYS97, VAL102, TYR105, PHE106, TYR109, MET152, LEU155, SER156, ASN159, HIS187, VAL190, ASN191, CYS194, PHE252, ALA255, ARG256, TYR259, LEU276, AND VAL279. As most of the amino acid residues in the active site are hydrophobic, so they are the main contributors to the receptor and ligand-binding interaction. Amino acid interaction of active metabolite of Ticlopidine, Clopidogrel, and Prasugrel shown in **Fig. 3, 4, and 5** respectively, and standard drug ethyl 6-(4-((benzylsulfonyl) carbamoyl) piperidin- 1- yl)- 5-cyano-2-methylnicotinate amino acid interaction shown in **Fig. 6**.

Interaction between Active Metabolites and 4ntj:

TABLE 1: DOCKING ENERGY OF ACTIVE METABOLITES OF COLPIDOGREL, PRASUGREL, AND TICLOPIDINE

Ligand	Binding Affinity	rmsd/ub	rmsd/lb
Metabolite of Ticlopidine	-7	6.94	1.496
Metabolite of Colpidogrel	-5.7	30.813	29.362
Metabolite of Prasugrel	-7.1	2.378	2.126
Std	-6.8	12.349	11.335

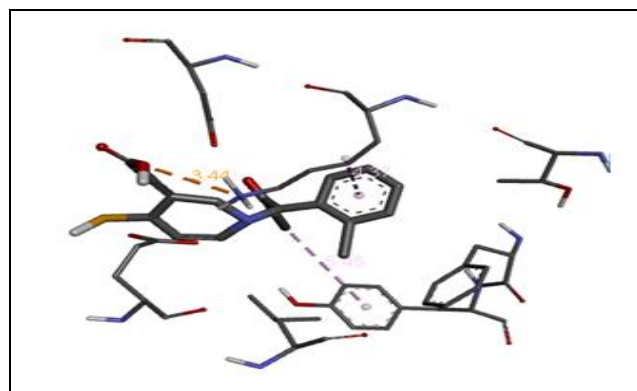
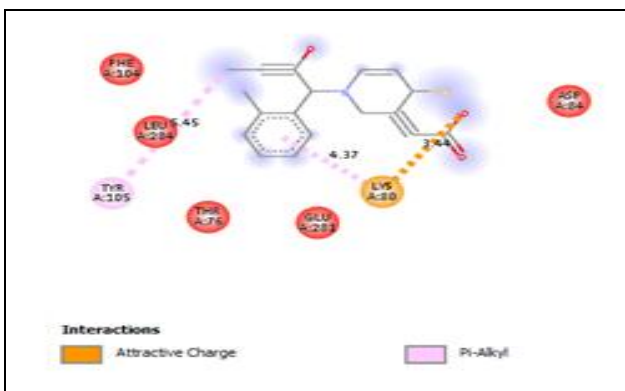


FIG. 3: AMINO ACID INTERACTION WITH TICLOPIDINE LIGAND



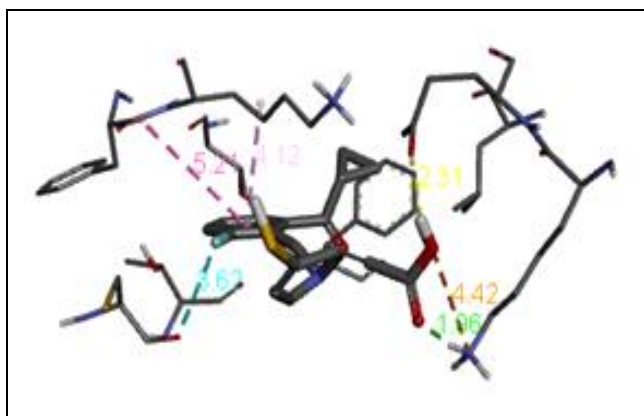


FIG. 4: AMINO ACID INTERACTION WITH COLPIDOGREL LIGAND

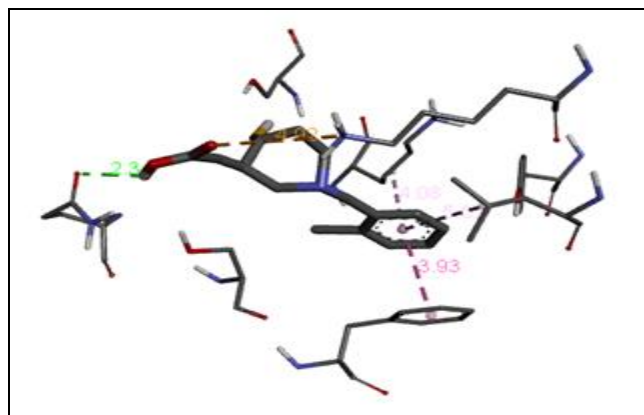
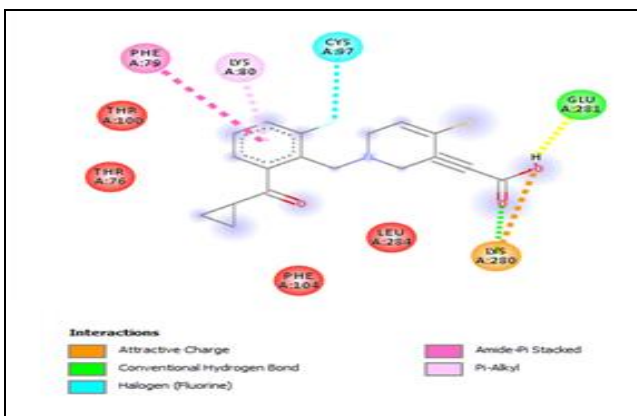


FIG. 5: AMINO ACID INTERACTION WITH PRASUGREL LIGAND

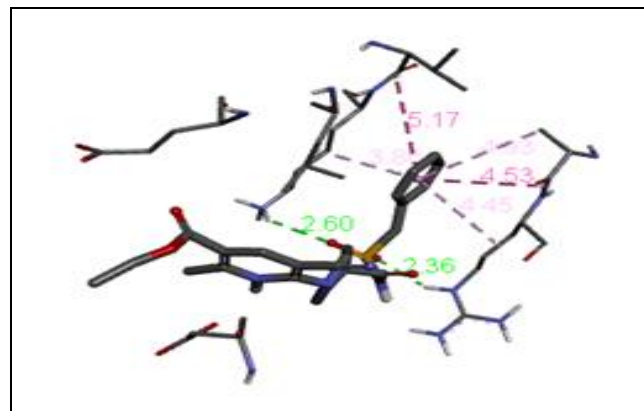
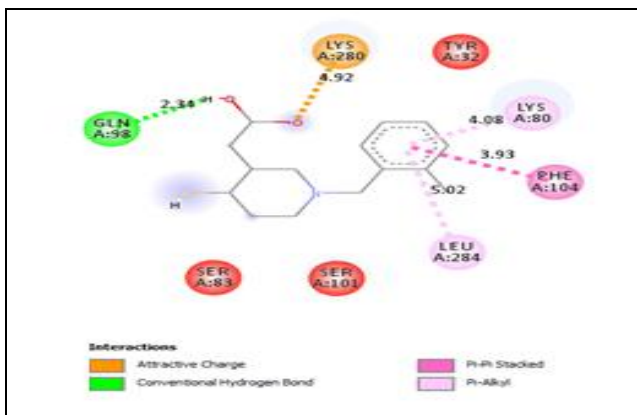
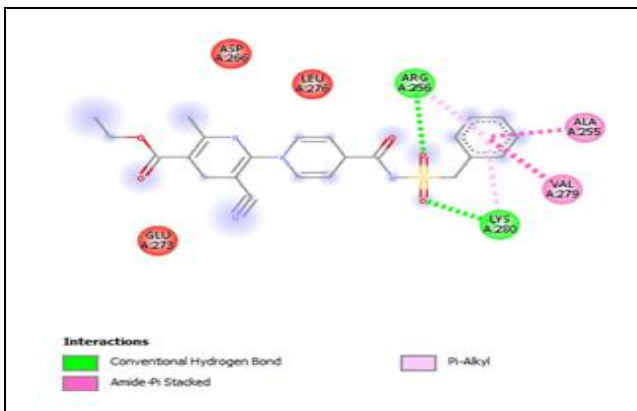


FIG. 6: AMINO ACID INTERACTION WITH STD ETHYL 6-((BENZYSULFONYL) CARBAMOYL) PIPERIDIN-1-YL)-5-CYANO-2-METHYLNICOTINATE LIGAND



CONCLUSION: The P2Y12 receptor is a significant objective of antithrombotic treatment. In PCI patients, new P2Y12 inhibitors decrease all-cause mortality and major ischemic conditions, specifically in PCI for STEMI patients.

These further backings that a more significant level of platelet inhibition than clopidogrel (600 mg) is required for, by far, most of the patients. This study based on binding energy for receptor P2Y12 (4NTJ) of the metabolite of Prasugrel ligand showed better activity than Metabolite of

Ticlopidine Metabolite of Colpidogrel, which may show a better dose regimen with lesser side effects. This research will help for further wetlab Pharmacological investigation of Prasugrel ligand as compared to a metabolite of Ticlopidine and metabolite of Clopidogrel.

ACKNOWLEDGEMENT: Authors are thankful to the Principal, Dr. S.P Jain Sir, Rajarshi Shahu College of Pharmacy, Buldhana (MS), India, for providing the necessary facilities.

CONFLICTS OF INTEREST: Nil**REFERENCES:**

- Wang R, Hozumi Y, Yin C and Wei GW: Decoding SARS-CoV-2 Transmission and Evolution and Ramifications for COVID-19 Diagnosis, Vaccine and Medicine. *Journal of Chemical Information and Modeling* 2020; 1(1): 101-12.
- Villas-Boas GR: The New Coronavirus (SARS-CoV-2): A Comprehensive Review on Immunity and the Application of Bioinformatics and Molecular Modeling to the Discovery of Potential Anti-SARS-CoV-2 Agents. *Molecules* 2020; 1(1): 121-34.
- Mir-Artigues P, Twyman RM, Alvarez D, Cerda Bennasser P, Balcells M, Christou P and Capell TA: Simplified Techno-Economic Model for the Molecular Pharming of Antibodies. *Biotechnology and Bioengineering* 2019; 4(14): 1458-65.
- Martin RW, Butts CT, Cross TJ, Takahashi GR, Diessner EM, Crosby MG, Farahmand V and Zhuang S: Sequence characterization and molecular modeling of clinically relevant variants of the SARS-CoV-2 main protease. *Biochemistry* 2020; 2(2): 151-68.
- De P, Bhayye S, Kumar V and Roy K: *In-silico* modeling for quick prediction of inhibitory activity against 3CLpro enzyme in SARS CoV diseases. *Journal of Biomolecular Structure and Dynamics* 2020; 2(2): 123-35.
- Nesměrák K: Medicinal Chemistry meets electrochemistry: redox potential in the role of endpoint or molecular descriptor in QSAR/QSPR. *Mini-Reviews in Medicinal Chemistry* 2020; 2(3): 201-13.
- Chinen K and Malloy T: QSAR use in REACH analyses of alternatives to predict human health and environmental Toxicity of Alternative Chemical Substances. *Integrated Environmental Assessment and Management* 2020; 2(5): 3-13.
- Hughes JP, Rees S, Kalindjian SB and Philpott KL: Principles of Early Drug Discovery. *British Journal of Pharmacology* 2011; 162 (6): 1239-49.
- Drews J: Drug Discovery: A Historical Perspective. *Science (80-.)* 2000; 3 (2): 135-45.
- Shi C and Kim T: crystal clots as therapeutic target in cholesterol crystal embolism. *Circ Res* 2020; 3 (5): 22-36.
- Neumann A, Müller CE and Namasivayam V: P2Y1-like nucleotide receptors—structures, molecular modeling, mutagenesis, and oligomerization. *wiley interdiscip. Wiley Interdisciplinary Reviews: Computational Molecular Science* 2020; 10 (4): 134-46.
- Kong D, Xue T, Guo B, Cheng J, Liu S, Wei J, Lu Z, Liu H, Gong G, Lan T, Hu W and Yang Y: Optimization of P2Y12 Antagonist Ethyl 6-(4-((Benzylsulfonyl) Carbamoyl) Piperidin-1-Yl)-5-Cyano-2-Methylnicotinate (AZD1283) Led to the Discovery of an Oral Antiplatelet Agent with Improved Druglike Properties. *Journal of Medicinal Chemistry* 2019; 62 (6): 3088-06.
- Van Doren, L, Nguyen N, Garzia C, Fletcher E, Stevenson R, Jaramillo D, Kuliopulos A and Covic L: Blockade of lipid receptor gpr31 suppresses platelet reactivity and thrombosis with minimal effect on hemostasis. *Blood* 2019; 134 (Supplement_1): 1064-64.
- Kaye AD and Manchikanti L: responsible, safe, and effective use of antithrombotics and anticoagulants in patients undergoing interventional techniques: American society of interventional pain physicians (ASIPP) Guidelines. *Pain Physician* 2019; 22(1S): S75-S128.
- Qiu J, Lingna W, Jinghong H and Yongqing Z: Oral administration of leeches (shuizhi): a review of the mechanisms of action on antiplatelet aggregation. *Journal of Ethnopharmacology* 2019; 1(2): 201-22.
- Ticagrelor versus aspirin in ischemic stroke. *Case Med Res* 2019.
- Bank W: How countries are using edtech (including online learning, radio, television, texting) to support access to remote learning during the COVID-19 Pandemic <https://www.worldbank.org/en/topic/edutech/brief/how-countries-are-using-edtech-to-support-remote-learn>. *Worldbank.org* 2020; 1 (1): 1-22.
- Akbar: Snapshot Perbankan Syariah Indonesia. *Snapshot Perbank. syariah* 2018; 1 (1): 1-9.
- Demircuc-Kunt A, Klapper L, Singer D, Ansar S and Hess J: The global finindex database 2017: measuring financial inclusion and the fintech revolution. *glob. finindex database 2017 meas. Financ Incl Fintech Revolut* 2018; 1(1): 121-34.
- Kurbucz MT: A Joint Dataset of Official COVID-19 Reports and the Governance, Trade and Competitiveness Indicators of World Bank Group Platforms. *Data Br* 2020; 31(1): 15-17.
- The Work Bank. Employment in Agriculture (Percentage of Total Employment). *Int. Labour Organ. ILOSTAT database*. Data Retrieved 2014; 1(1): 19-36.
- Vardhan S and Sahoo SK: *In-silico* ADMET and molecular docking study on searching potential inhibitors from limonoids and triterpenoids for COVID-19. *Computers in Biology and Medicine* 2020; 124(1): 135-56.
- Bajgain KT, Badal S, Bajgain BB and Santana MJ: Prevalence of comorbidities among individuals with covid-19: a Rapid Review of Current Literature. *American Journal of Infection Control* 2020; 1(1): 123-45.
- Passarelli PC, Lopez MA, Bonaviri GNM, Garcia-Godoy, F and DâAddona A: Taste and Smell as chemosensory dysfunctions in COVID-19 infection. *American Journal of Dentistry* 2020; 33(3): 135-37.
- Solis-Vasquez L, Santos-Martins D, Koch A and Forli S: Evaluating the energy efficiency of opencl-accelerated autodock molecular docking. in proceedings - 2020 28th Euromicro International Conference on Parallel, Distributed and Network-Based Processing, PDP 2020; 162-66.
- Kumar S, Kashyap P, Chowdhury S, Kumar S, Panwar A and Kumar A: Identification of phytochemicals as potential therapeutic agents that binds to nsp15 protein target of coronavirus (SARS-CoV-2) That Are Capable of Inhibiting Virus Replication. *Phytomedicine* 2020; 1(1): 145-56.
- Gandhi AJ, Rupareliya JD, Shukla VJ, Donga SB and Acharya R: An ayurvedic perspective along with *in-silico* study of the drugs for the management of SARS-CoV-2. *Journal of Ayurv and Integr Medicine* 2020; 1 (1): 145-56.
- Singh V: Structure based docking of secondary metabolites against drpe1 to Treat Tuberculosis. *Int J Res Appl Sci Eng Technol* 2020; 8(6): 2515-20.
- Baqi Y and Müller CE: Antithrombotic P2Y 12 receptor antagonists: recent developments in drug discovery. *Drug Discovery Today* 2019; 24(1): 325-33.
- Jin Z, Du X, Xu Y, Deng Y, Liu M, Zhao Y, Zhang B, Li X, Zhang L, Peng C, Duan Y, Yu J, Wang L, Yang K, Liu F, Jiang R, Yang X, You T, Liu X, Yang X, Bai F, Liu H, Liu X, Guddat LW, Xu W, Xiao G, Qin C, Shi Z, Jiang H, Rao Z and Yang H: Structure of Mpro from SARS-CoV-2 and Discovery of Its Inhibitors. *Nature* 2020; 582 (7811): 289-93.

31. Crommelin D, Stolk P, Besançon L, Shah V, Midha K and Leufkens H: Pharmaceutical Sciences in 2020. Nature

Reviews Drug Discovery 2010; 9(2): 99-00.

How to cite this article:

PR Devhare, Jain S, Sonwane G, Borkar V and Diwre R: Identification and optimization of binding site for an active metabolite of clopidogrel, prasugrel and ticlopidine on receptor P2Y₁₂. Int J Pharm Sci & Res 2021; 12(8): 4365-70. doi: 10.13040/IJPSR.0975-8232.12(8).4365-70.

All © 2013 are reserved by International Journal of Pharmaceutical Sciences and Research. This Journal licensed under a Creative Commons Attribution-NonCommercial-ShareAlike 3.0 Unported License.

This article can be downloaded to **ANDROID OS** based mobile. Scan QR Code using Code/Bar Scanner from your mobile. (Scanners are available on Google Playstore)



Received on 20 August 2019; received in revised form, 29 January 2021; accepted, 19 May 2021; published 01 August 2021

EVALUATION OF ANTIDIABETIC ACTIVITY OF *ECHINOCHLOA COLONA* PLANT EXTRACT

Vijay Borkar ^{*1}, Gajanan Sonwane ¹, Parmeshwar Devhare ¹, Rushikesh Diwre ¹ and Shirish Jain ²

Department of Pharmaceutical Chemistry ¹, Department of Pharmacology ², Rajarshi Shahu College of Pharmacy, Buldana - 443001, Maharashtra, India.

Keywords:

Echinochloa colona, Chromatography, Antidiabetic, Anti diabetic

Correspondence to Author:

Vijay Borkar

Department of Pharmaceutical Chemistry, Rajarshi Shahu College of Pharmacy, Buldana - 443001, Maharashtra, India.

E-mail: sonwane.gajanan@rediffmail.com

ABSTRACT: The current work comprises the assessment of antidiabetic activity of chloroform, ethyl acetate, and ethanol fractions and isolation of some phytoconstituents from chloroform fraction obtained from ethanolic extract of *Echinochloa colona*. The antidiabetic activity was performed using streptozocin induced diabetic model in male Wistar rats (150-200 g). The best restraint results were for metformin, chloroform, ethyl acetate and ethanol fraction was 5.85 ± 0.004 (90.08%), 6.65 ± 0.004 (67.36%), 6.96 ± 0.003 (60.14%) and 7.05 ± 0.004 (58.01%) respectively, comparing controlled diabetic rats which showed a significant reduction of blood glucose level. On total cholesterol level metformin, chloroform, ethyl acetate and ethanol fraction showed decrease in total cholesterol level by 12.16 ± 0.0044 (56.98%), 13.02 ± 0.004 (53.94%), 14.17 ± 0.004 (49.87%) and 16.37 ± 0.004 (42.24%) respectively. Significantly triglyceride was decreased by 10.39 ± 0.0044 (46.49%), 13.16 ± 0.004 (32.23%), 14.06 ± 0.004 (27.60%) and 14.56 ± 0.004 (42.24%) for metformin, chloroform, ethyl acetate and ethanol fraction respectively. Three important phytoconstituents were isolated from chloroform fraction, and structures were elucidated using spectroscopic techniques.

INTRODUCTION: *Echinochloa colona*, regularly known as jungle rice, deccan grass, or awnless farm grass, is a sort of wild grass beginning from tropical Asia. It was some time ago delegated types of *Panicum*. It is the wild precursor of the developed grain crop *Echinochloa frumentacea*, sawa millet. A few taxonomists treat the two taxa as one animal group, in which case the trained structures may likewise be alluded to as *E. colona* ^{1, 3}.

Echinochloa Colona Plant Profile:



Kingdom: Plantae
Division: Angiosperms
Class: Monocots
Order: Poales

QUICK RESPONSE CODE 	DOI: 10.13040/IJPSR.0975-8232.12(8).4354-64
	This article can be accessed online on www.ijpsr.com
DOI link: http://dx.doi.org/10.13040/IJPSR.0975-8232.12(8).4354-64	

Family: Poaceae
Genus: *Echinochloa*
Species: *Echinochloa colona*

Botanical Description: *Echinochloa colona* (Poaceae), commonly known as Jungle rice (awnless barnyard grass) in India, is a yearly upright or decumbent, scattering, rooting from the inferior cutline node. It is a terrestrial, tufted, and erect grass propagates vegetatively but mostly by seeds, extensively spread in tropics & subtropics. It is also observed in South-Southeast Asia and tropical Africa. Leaves are spiral; alternatively, sessile linear more than 2 cm long, apex is acute with clasping base and parallel-veined. It culms ascending, or decumbent 10-100 cm long⁴.

Pharmacognostic Characteristic:

Macroscopy: Culms are 10-70 cm long, lower nodes are glabrous and upper nodes are glabrous. Sheaths are glabrous, ligules absent, blades are 8-10 cm long and cm⁻³⁻⁶ wide. Panicle is cm⁻²⁻¹², erect, rachises. A primary branch is 5-10 cm, erect otherwise ascending, spike-like, distant, devoid of secondary branches, axes glabrous or sparsely hispid. Spikelet is 2-3 mm, disarticulating at maturity, pubescent to hispid. Lower glumes are as long as spiklets; lower florest are sterile occasionally staminate. Lower lemmas are unawned, upper lemmas are 2.6-2.9 mm. Anthers are 0.7-0.8 mm, caryopses are 1.2-1.6 mm, whitish, and embryos are as long as caryopses. It is distributed in tropical and subtropical areas. It is weedy in North America grown in low-lying, damp to wet, including rice fields. Un branched somewhat widely-spaced panicle branches, which make this one of the easier species of the *Echinochloa colona*.

Traditional Uses: As per the literature, in India, seeds of grass are used to prepare a food dish called khichdi and are consumed during festivals, fasting days. The whole plant is used as fodder by grazing animals, and it cures ingestion. *Echinochloa colona*, is a significant crop. It is a reasonable wellspring of protein, which is exceptionally edible; furthermore, it is a fantastic wellspring of dietary fiber with great measures of solvent and insoluble portions. The starch content is low and gradually edible, which makes the *Echinochloa colona*, a characteristic fashioner nourishment. In

the current long periods of expanded diabetes mellitus, *E. colona*, could turn into perfect nourishment.

MATERIALS AND METHODS:

Sample Preparation: *E. colona* samples were collected from a paddy field in Dharmapuri, Tamil Nadu, India province in June 2013 at the flowering stage (red-purple flower). The samples were cleaned and separated into roots and shoots, then air-dried at room temperature and cut into small pieces (5 mm). The *E. colona* samples were extracted using soxhlet extraction methods, previously soaked with n-hexane to remove fatty residue. Then ethanol extract was fractionated (chloroform, acetone, ethyl acetate, ethanol, and methanol) from low to high polarity solvents. The plant parts were extracted using solvent at the rate of 1:5 (w/v) in 1 L beakers and covered with plastic film. The detailed procedure regarding the extraction was described by Gomaa and Abd Elgawad (2012). The beakers were kept in the dark at room temperature for 7 d. The solutions were separated from plant residues and evaporated using a rotary evaporator at 600 °C under reduced pressure. There were six different extracts of *E. colona* from the shoots and roots using n-hexane, extracts from the shoots and roots using chloroform, acetone, ethyl acetate, ethanol, and methanol.

Column Chromatography: The chloroform fraction of *Echinochloa colona* was subjected to column chromatography using silica gel as it has shown better pharmacological effect comparing to ethyl acetate and ethanol fraction and eluted with solvent mixtures of increasing polarity.

While elution, the chromatographic fractions were collected and monitored on TLC. All the fractions showing a single spot were pulled together, purified, and observed for its R_f value using TLC. The solvents like chloroform, acetone, ethyl acetate, ethanol, and methanol used for separation⁵.

Chromatographic Separation of Chloroform Fraction: Slurry of activated silica gel (150 °C for 3 h) was prepared with chloroform, and then the column was packed with slurry. The sample was loaded on the packed silica gel. After stabilization¹²⁰

column was eluted with mobile phase. Fractions were collected and analyzed by TLC.

Preparation of Mobile Phase: All the solvents, chloroform, acetone, ethyl acetate, ethanol, and methanol were distilled and then used for the preparation of the mobile phase. The composition of the mobile phase was made with increasing polarity solvents.

Column Packing: A clean and dry borosil glass column (60 cm, height; 3 cm, diameter) was aligned in a vertical position with the help of clamps attached to metal stand. A piece of cotton soaked in the mobile phase was positioned at the bottom of the column and quietly tamped down by means of a glass rod. The column was then filled about 1/3 volume by the mobile phase. The column was slowly and evenly filled, about 5/6 volumes full with the gradual addition of silica gel slurry. The stopcock was opened to allow the excess mobile phase to drain into the beaker. The side of the column was softly tapped with a cork during the process of packing to compact the silica gel. In the meantime, the stopcock was opened to run down the excess mobile phase. When the packing was finished, the excess mobile phase was drained until it just reaches the top level of silica.

Application of Sample: Weighed quantity of the sample was mixed with 1-2 g of activated silica gel and 3-4 ml of mobile phase to prepare a slurry. The slurry of the sample was added to the top of the packed silica in the column. The stopcock was opened to drain the excess mobile phase until it reaches top level of the sample. A thin disc (column diameter) of filter paper soaked in the mobile phase was placed on top of the bed to prevent disturbing the sample layer after addition of the mobile phase. The column was filled to the top with the mobile phase and allowed to stand for overnight (~24 h) to develop a chromatogram^{6,7}.

Anti Diabetic Activity: Anti-diabetic effect of chloroform, ethyl acetate, and ethanol fractions obtained from ethanolic extract of *Echinochloa colona* was performed using streptozotocin-induced diabetic model in Wistar rats. The doses of the fractions were made at 50 mg /mL. All male Wistar rats (150-200 g) were randomly divided into 7 groups, each containing 5 rats^{8,10}.

- **Group I:** Normal control (normal saline)
- **Group II:** Normal metformin control (150 mg/kg, *i. p.*)
- **Group III:** Diabetic control (normal saline)
- **Group IV:** Diabetic metformin control (150 mg/kg, *i. p.*)
- **Group V:** Diabetic (chloroform fraction)
- **Group VI:** Diabetic (ethyl acetate fraction)
- **Group VII:** Diabetic (ethanol fraction)

The standard drug and test samples were fed orally with an intragastric tube for 24 h experiment. Diabetes was induced (Group III-VII) by intraperitoneal injection (1 mL/kg) of freshly prepared streptozotocin (45 mg/kg), after baseline glucose was estimated.

After 48 h, blood samples were collected from the tail vein of all rats, and the blood glucose level was estimated. Blood glucose levels above ¹¹. 1 mmol/L in animals were selected for the studies considering the condition of diabetes was established.

Biochemical Analysis: After treatment, blood samples were collected with the help of disposable syringes from the tail vein of all rats of all groups before and at 0, 1, 2, 3, 6, 10, 16, and 24th h and analyzed for content of blood glucose using Glucometer (Bio Land, Germany). Then all the rats were sacrificed, and approximately 1-2 mL of blood was collected directly from the heart with the help of disposable syringes.

The blood samples were transferred to centrifuge tubes and allowed to centrifuge at 4000 rpm for 10 min; serum was collected used to determine total cholesterol (TC) and serum triglycerides (TG). Serum total cholesterol and triglycerides were estimated at 505 and 546 nm, respectively, using cholesterol oxidase/ p-amino antipyrine (CHO / PAP) method and glycerol 3- phosphate oxidase (GPO) method, respectively according to manufacturer's protocol^{11,13}.

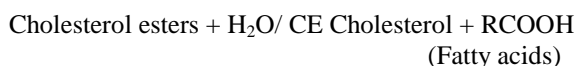
Determination of Total Cholesterol: Total cholesterol was determined by reagents kits of Reckon Diagnostics Pvt. Ltd., Baroda.

Method: CHOD-PAP method was used described by Allain *et al.*, 1974. It is an extremely specific¹²¹

enzymatic colorimetric method for measurements in the visible range (505 nm), well-known for its high flexibility^{14, 15}.

Test Principle: The esters of cholesterol are hydrolyzed to cholesterol by cholesterol esterase (CE). The cholesterol is then oxidized by cholesterol oxidase (CO) to cholesterol 4-en-3-one with the concurrent creation of H₂O₂.

H₂O₂ then reacts with 4-aminoantipyrine (AAP) and phenolic compounds in the presence of peroxidase to give colored complex red at 505 nm (500-540 nm, GREEN filter). The color intensity produced is directly proportional to the concentration of total cholesterol in the test samples.



Sample Material: Serum

Procedure: The three tubes were labeled accordingly as blank, standard, and test. 0.01ml standard and serum were added to the corresponding tubes. 1 mL Cholesterol reagent was placed in all tubes, *i.e.* blank, standard, and test, mixed well, and incubated (10 min at 37 °C). Then absorbance was red of test and standard at 505 nm or with green filter against blank reagent.

Calculations:

Cholesterol (mg/dl) = Absorbance in Test × 200 / Absorbance in Standard

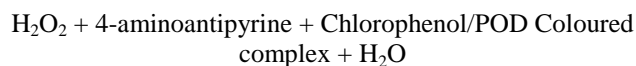
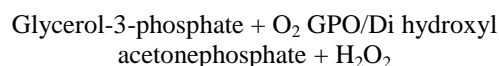
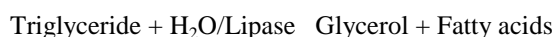
Determination of Triglycerides: Triglyceride was determined by reagents kits of Reckon Diagnostics Pvt. Ltd., Baroda.

Method: High performance enzymatic GPO-PAP method modified according to Fossati 1982; McGowan *et al.*, 1983.

Test Principle: Triglyceride is hydrolyzed sequentially to Di & Monoglycerides and finally to Glycerol by Lipase. Glycerol kinase (GK) by

means of ATP as PO₄ source converts Glycerol to Glycerol-3-phosphate (G-3-Phosphate). G-3-phosphate Oxidase (GPO) oxidised G-3- phosphate to Di-hydroxy acetone phosphate & hydrogen peroxide is formed.

Hydrogen peroxide in presence Peroxidase (POD) oxidised to oxidise 4 amino antipyrine and chlorophenol to a pink coloured complex, which is measured at 546 nm (500-550 nm or with green filter). Absorbance is proportional to Triglycerides concentration.



Sample Material Serum

Procedure: 0.05 mL serum, standard, and distilled water were placed in the tubes marked as a test, standard and blank, respectively.

Then working solution 1 mL of was added to every tube, mixed well, and incubated (20 min at 37 °C). After incubation, 1.5 mL of distilled water was added to every tube, mixed well. Absorbance was red of test and standard against the blank at 546 nm (500-550 nm)

Calculations:

Triglyceride (mg/dl) = Absorbance in Test / Absorbance in Standard × 200

Elution: Elution was carried out with the flow rate (1 ml/min). The mobile phase was added at the top of the column from the solvent reservoir, and fractions were collected in an amber colored bottle.

Fractions were concentrated by evaporating at room temperature until volume was reduced to ¼ of the total volume. TLC of concentrated fractions was carried out to detect similarity between the chromatograms of different fractions.

Source	Fraction	Mobile phase	Abbreviation
<i>E. colona</i>	Chloroform	Chloroform: Ethanol 40:60	EC-I
		Chloroform: Ethanol 30:70	EC-II
		Chloroform: Ethanol 10:90	EC-III

Thin Layer Chromatography (TLC): TLC of each fraction was carried out during column chromatography, and the R_f value for EC-I (0.48), EC-II (0.74), EC-III (0.68) was observed.

Characterization of the Isolated Compounds from *E. Colona*:

EC-I: The EC-I fraction was collected at 40:60 in % ratio of (CHCl₃: C₂H₅OH). The isolated compound was white amorphous powder. The compound was studied for its qualitative properties and found to be positive with the ferric chloride test, and the phenolic nature of the compound was confirmed. The M.P. of the compound was 145-147 °C.

The UV spectrum showed λ_{max} , 220 nm, Ethanol with typical aromatic bands confirming a substituted aromatic benzoic acid. In the FTIR (KBr, cm⁻¹) signal at 3400 (-OH), 2935 (Ar-H), 1688(-COOH), ¹HNMR (CDCl₃, 400 MHz) signals at δ 11.80 (-COOH), 6.5 (Ar-H), 5.10 (Ar-OH), 2.33 (Ar-CH₃) and the peak of molecular ion was observed at m/z 184 matching to C₈H₈O₅, and main peak at 166 [184-(H₂O)]⁺ with other fragments at m/z : 120, 84, 42, 27 were observed.

The above spectral data suggested isolated compound is 2, 3, 4-trihydroxy, 6-methyl benzoic acid. The IR, ¹HNMR, and MASS spectra were shown in following Fig. 1 to 3.

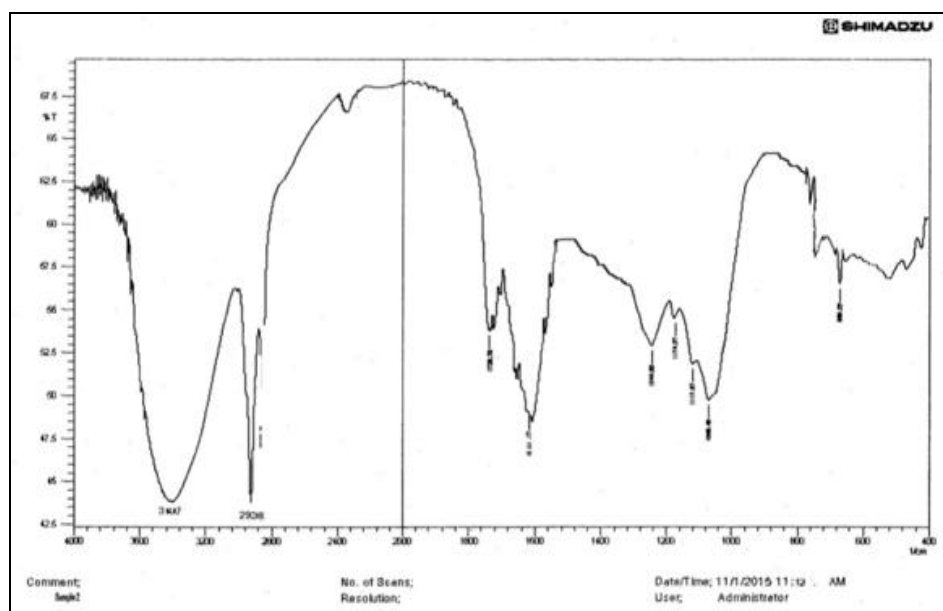


FIG. 1: IR SPECTRA OF EC-I FRACTION ISOLATED FROM *E. COLONA*

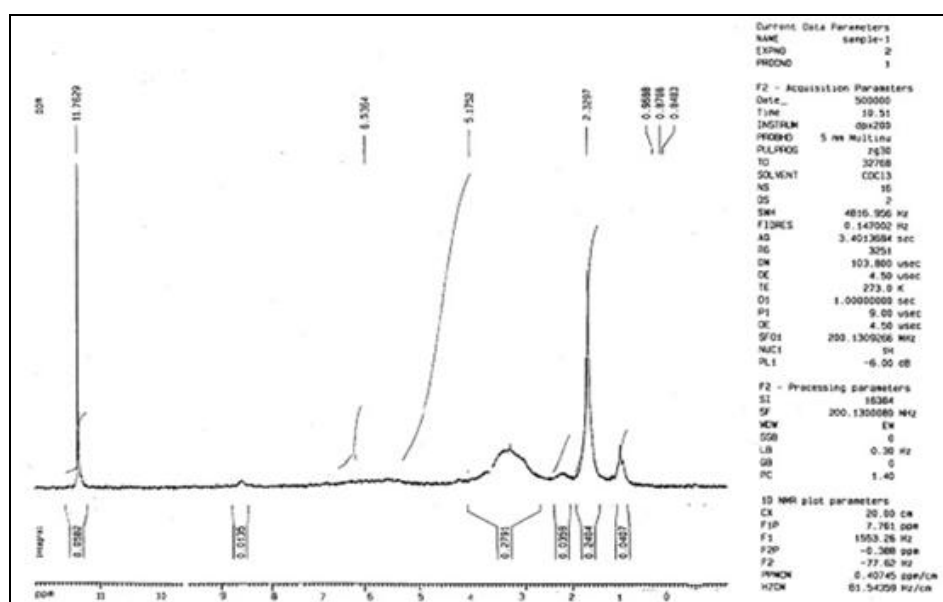


FIG. 2: ¹H NMR SPECTRA OF EC-I FRACTION ISOLATED FROM *E. COLONA*

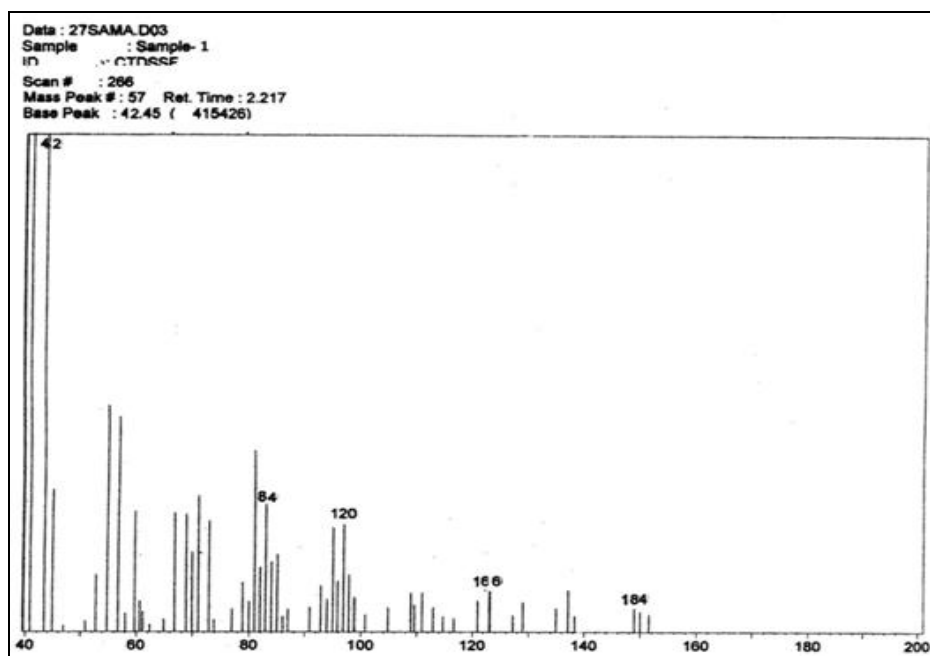


FIG. 3: MASS SPECTRA OF EC-I FRACTION ISOLATED FROM *E. COLONA*

EC-II: The EC-II fraction was collected at 30:70 in % ratio of ($\text{CHCl}_3:\text{C}_2\text{H}_5\text{OH}$). The isolated compound was white crystalline powder with a characteristic odour. The compound was studied for its qualitative properties and found to be positive with the Liebermann-Burchard test, and the steroidal nature of the compound was confirmed. The M.P. of the compound was 137-139 °C. UV spectrum showed λ_{max} , 210 nm, ethanol. In the FTIR (KBr, cm^{-1}) 3545 (-OH), 2931 (-CH₂), 2860 (-CH), 1637 (-C=C-), 1033 (-C-O), ¹HNMR (CDCl_3 , 400 MHz) signals at δ 1.01, 1.04, 1.06,

1.04, 1.17, 1.21(-CH₃), 1.57, 1.98, 1.13, 1.79, 1.24, 1.27, 1.35, 1.34, 1.25, 1.29, (-CH₂-), 3.25(-CH-), 5.37 (H-cyclohexene) and peak of molecular ion was observed at 414.7 corresponding to C₂₉H₅₀O with other characteristic fragmentations of m/z: 414, 396, 381, 330, 290, 273, 255, 212, 199 and 173 were observed. The above spectral data and those reported in the literature support the proposed structure was β -sitosterol 113, 114, 115. The IR, ¹HNMR, and MASS spectra were shown in the following Fig. 4 to 6.

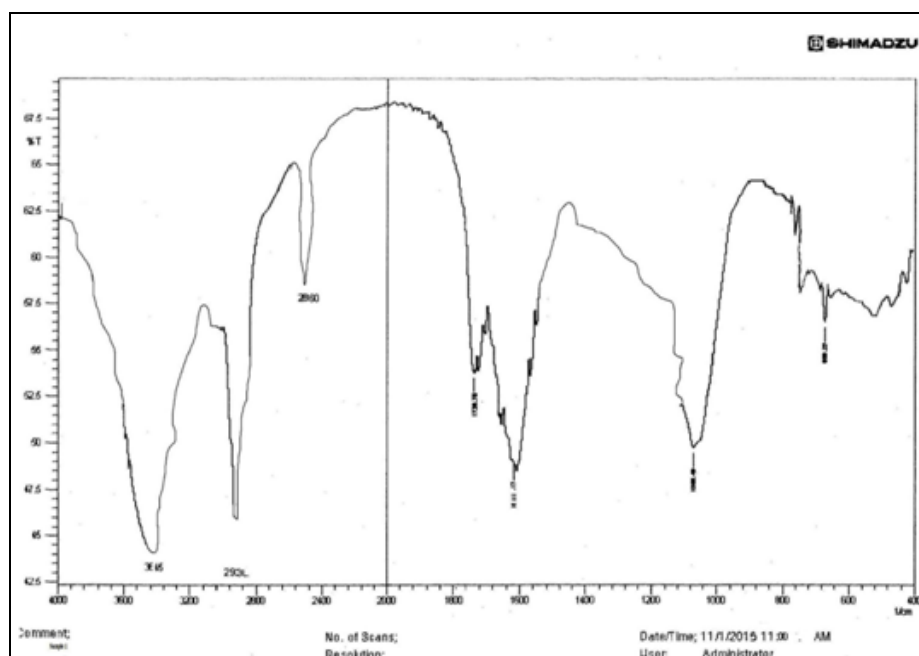


FIG. 4: IR SPECTRA OF EC-II FRACTION ISOLATED FROM *E. COLONA*

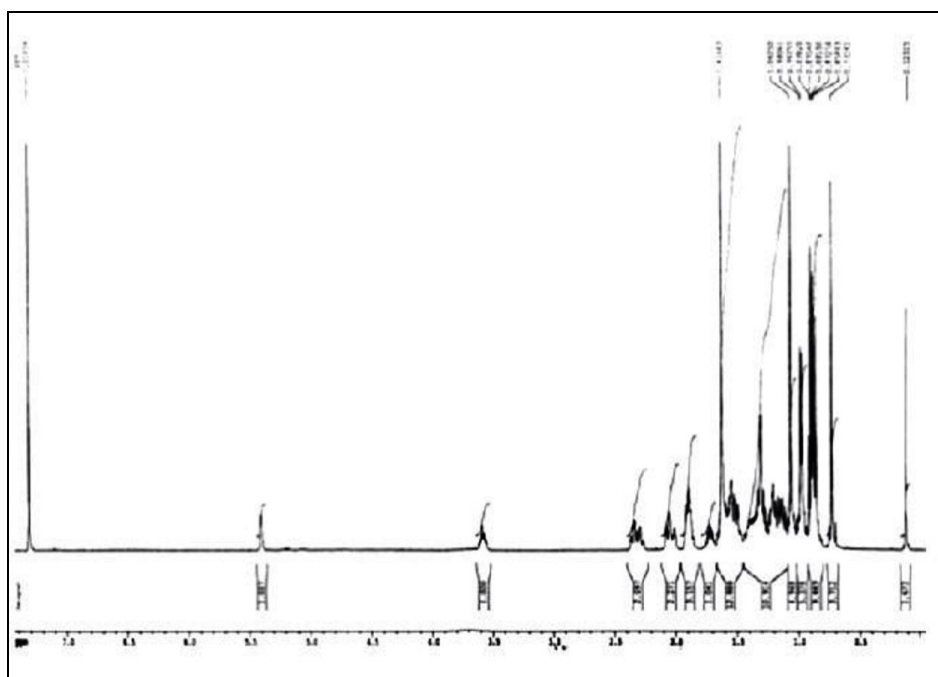


FIG. 5: ^1H NMR SPECTRA OF EC-II FRACTION ISOLATED FROM *E. COLONA*

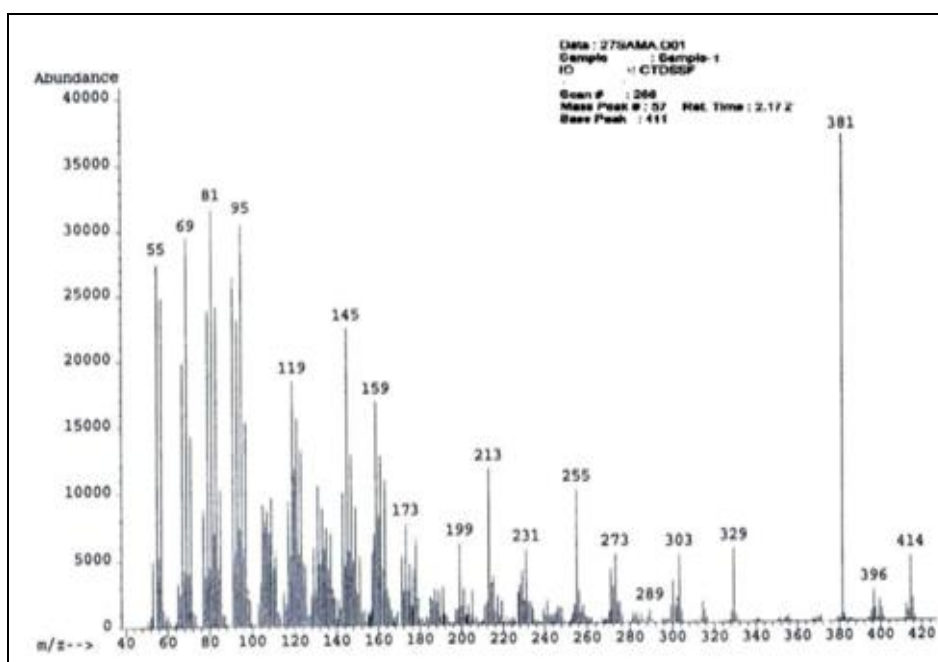


FIG. 6: MASS SPECTRA OF EC-II FRACTION ISOLATED FROM *E. COLONA*

EC-III: The EC-III fraction was collected at 10:90 in % ratio of ($\text{CHCl}_3:\text{C}_2\text{H}_5\text{OH}$). The isolated compound was white crystalline powder with a characteristic odour. The compound was studied for its qualitative properties and found to be positive with the ester test, and the ester nature of the compound was confirmed.

The melting point of the compound was carried out and found to be 150- 152 $^\circ\text{C}$. The UV spectrum showed λ_{max} , 226 nm, methanol. In the FTIR (KBr,

cm^{-1}) band at 1736 (RCOOR) and 3400 (Ar-OH), ^1H NMR (CDCl_3 , 400 MHz) at δ 1.25 (- CH_3), 4.65 (- CH_2 -), 4.58 (Ar-OH) and a peak of molecular ion was observed at m/z 198 correspondings to $\text{C}_9\text{H}_{10}\text{O}_5$ with other fragments at 183, 149 [$183-\text{CH}_3$] $^+$, 129, 111, 97, 83, 69, 57, 43 were observed.

The above spectral data suggested isolated compound was ethyl 3, 4, 5-trihydroxy benzoate. The IR, ^1H NMR, and MASS spectra were shown in the following Fig. 7 to 9.

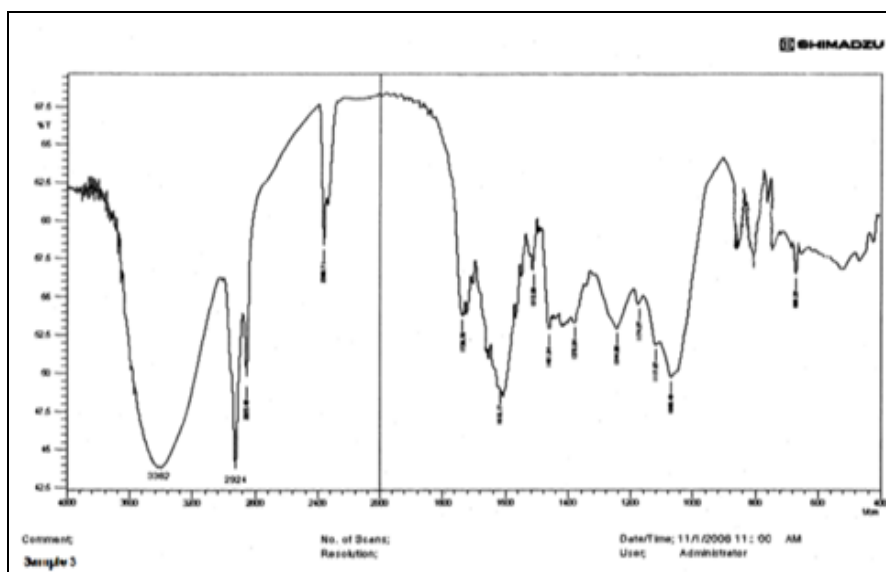


FIG. 7: IR SPECTRA OF EC-III FRACTION ISOLATED FROM *E. COLONA*

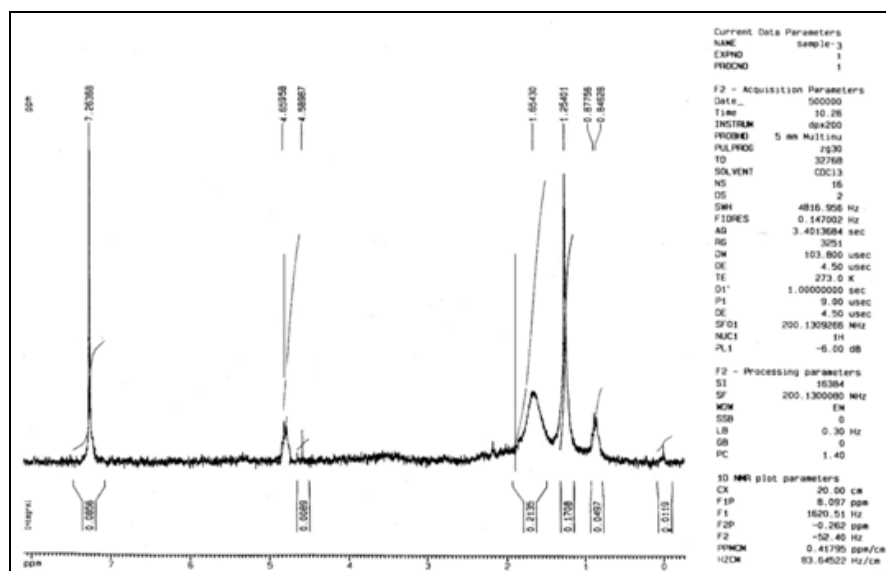


FIG. 8: 1H NMR SPECTRA OF EC-III FRACTION ISOLATED FROM *E. COLONA*

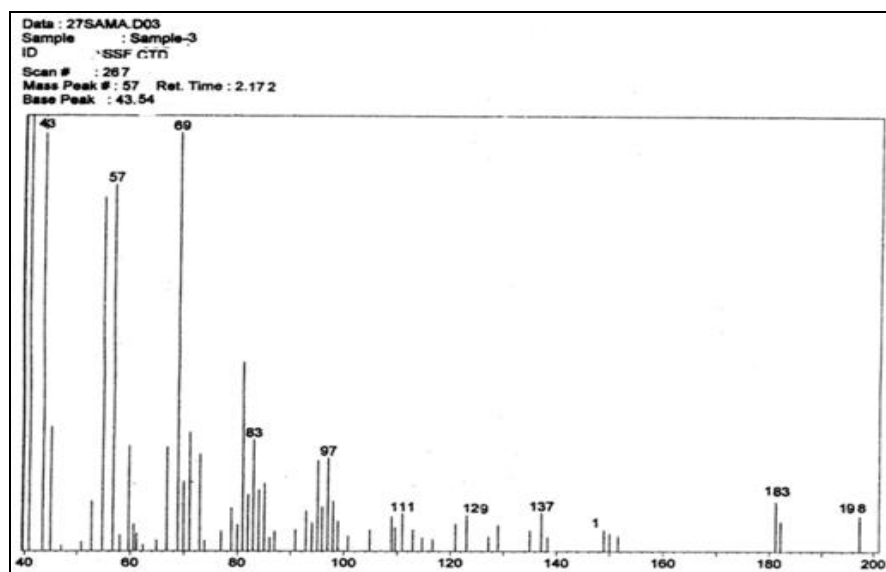


FIG. 9: MASS SPECTRA OF EC-III FRACTION ISOLATED FROM *E. COLONA*

Anti Diabetic Activity: The effects of different fractions (single dose-50 mg/mL) obtained from ethanolic extracts of *E. colonaupon* blood glucose (mmol/L), serum total cholesterol & triglycerides (mmol/L) were investigated within control and streptozotocin induced diabetic rats. Metformin HCl (150 mg/mL) was used as a standard anti-diabetic agent.

Effects of Various Fractions on Blood Glucose: A decrease in blood glucose level was observed in

animals treated with different fractions of *E. colonaat*^{0, 1, 2, 3, 6, 10, 16}, and 24th h **Fig. 1**.

The blood glucose level was significantly reduced at 24th h of the experiment ($p < 0.01$) for metformin, chloroform, ethyl acetate, and ethanol fraction, it was 5.85 ± 0.004 (90.08%) 6.65 ± 0.004 (67.36%), 6.96 ± 0.003 (60.14%) and 7.05 ± 0.004 (58.01%) respectively comparing controlled diabetic rats **Table 1**.

TABLE 1: EFFECT OF DIFFERENT FRACTIONS OF *E. COLONA* ON BLOOD GLUCOSE IN DIABETIC RATS ON ONE DAY TREATMENT

Groups (Treatment)	Blood glucose levels (mmol/L) at Hours							
	0	1	2	3	6	10	16	24
I	7.25 ±	7.26 ±	7.27 ±	7.28 ±	7.29 ±	7.30 ±	7.31 ±	7.32 ±
10 ml saline	0.004	0.004	0.004	0.004	0.004	0.002	0.002	0.004
II	7.26 ±	7.24 ±	7.28 ±	7.20 ±	7.19 ±	6.17 ±	6.05 ±	4.13 ±
150 mg/kg	0.004	0.003	0.004	0.002	0.004	0.004	0.003	0.004
III	11.01 ±	11.50 ±	11.95 ±	12.25 ±	12.75 ±	13.10 ±	13.55 ±	13.95 ±
10 ml saline	0.003	0.003	0.004	0.004	0.004	0.004	0.003	0.003
IV	11.12 ±	10.81 ±	9.05 ±	8.75 ±	6.65 ±	7.08 ±	6.16 ±	5.85 ±
150 mg/kg	0.003	0.20	0.004	0.004	0.004	0.004	0.004	0.004
V	11.13 ±	10.61 ±	10.15 ±	9.95 ±	8.85 ±	7.28 ±	6.96 ±	6.65 ±
50 mg/ml	0.004	0.002	0.008	0.005	0.004	0.004	0.004	0.004
VI	11.13 ±	10.92 ±	10.41 ±	10.31 ±	9.55 ±	7.98 ±	7.86 ±	6.96 ±
50 mg/ml	0.004	0.004	0.004	0.004	0.004	0.003	0.002	0.003
VII	11.14 ±	11.02 ±	10.91 ±	10.71 ±	9.98 ±	9.07 ±	7.66 ±	7.05 ±
50 mg/ml	0.004	0.004	0.005	0.003	0.004	0.004	0.004	0.004

All values are expressed as mean ± SEM, (n=5) in every group, $p < 0.01$, p-values were calculated and compared with control by ANOVA method followed by Dunnett's test

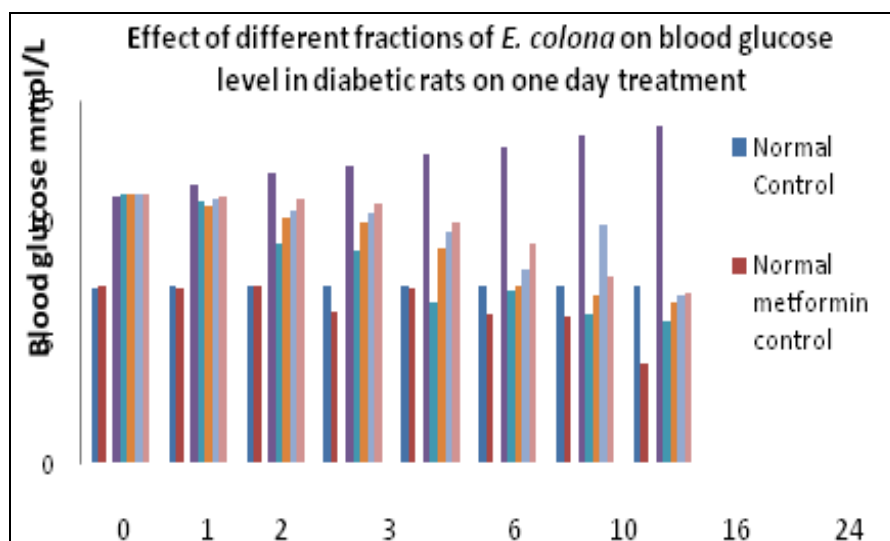


FIG. 10: EFFECT OF DIFFERENT FRACTIONS OF *E. COLONA* ON BLOOD GLUCOSE LEVEL IN DIABETIC RATS ON ONE DAY TREATMENT

Effect of Various Fractions on Total Cholesterol and Triglyceride: After 24 h treatment of different fractions of *E. colona* there was a decrease in total cholesterol and triglyceride in diabetic rats **Fig. 2**.

Metformin, chloroform, ethyl acetate and ethanol fraction showed a decrease in total cholesterol level by 12.16 ± 0.0044 (56.98%) 13.02 ± 0.004 (53.94%) 14.17 ± 0.004 (49.87%) and 16.37 ± 127

0.004 (42.24%) respectively, whereas the triglyceride was decreased by 10.39 ± 0.0044 (46.49%) 13.16 ± 0.004 (32.23%) 14.06 ± 0.004 (27.60%) and 14.56 ± 0.004 (42.24%) for metformin, chloroform, ethyl acetate and ethanol fraction respectively when compared to diabetic control groups **Table 2**.

TABLE 2: EFFECTS OF DIFFERENT FRACTIONS OF *E. COLONA* ON TOTAL CHOLESTEROL & TRIGLYCERIDES IN DIABETIC RAT ON ONE DAY TREATMENT

Parameter (mmol/L)	Groups						
	I	II	III	IV	V	VI	VII
Total Cholesterol	14.37± 0.003	12.24± 0.004*	28.27± 0.004**	12.16± 0.004**	13.02± 0.004**	14.17± 0.004**	16.37± 0.004**
Total Glycerides	12.41± 0.004	10.31± 0.003*	19.42± 0.004*	10.39± 0.004*	13.16± 0.004*	14.06± 0.004*	14.56± 0.004*

All values are expressed as mean \pm SEM, (n=5) in every group, *p <0.01, considered extremely significant, p-values were calculated and compared with control by ANOVA method followed by Dunnett's test.

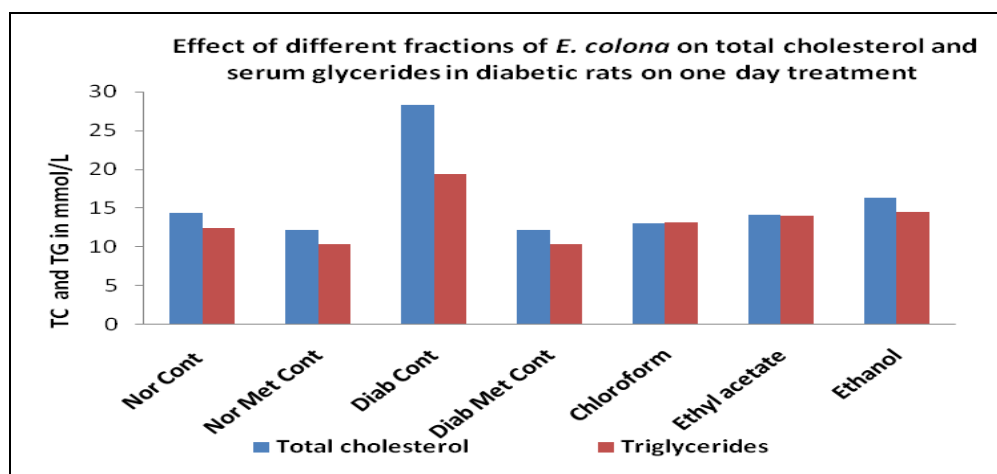


FIG. 11: EFFECTS OF DIFFERENT FRACTIONS OF *E. COLONA* ON TOTAL CHOLESTEROL AND SERUM GLYCERIDES IN DIABETIC RATS ON ONE DAY TREATMENT

CONCLUSION: Given the potent results of the extracts tested in this article against diabetes and the factor responsible for the same (triglycerides). A decrease in blood glucose level was observed in animals treated with different fractions of *E. colona*.

After 24 h treatment of different fractions of *E. colona* there was a significant decrease in total cholesterol and triglyceride on diabetic rats when treated with chloroform fraction. The chloroform fraction exhibiting significant anti-diabetic activity was chromatographed to isolate three phyto constituents 2, 3, 4-trihydroxy, 6-methyl benzoic acid, β -sitosterol, and ethyl 3, 4, 5-trihydroxy benzoate.

ACKNOWLEDGEMENT: Authors are thankful to Principal Rajarshi Shahu College of Pharmacy, Buldhana, for providing the necessary facilities

CONFLICTS OF INTEREST: The authors have not declared any conflict of interest.

REFERENCES:

- Peerzada AM, Bajwa AA, Ali HH and Chauhan BS: Biology, Impact and Management of *Echinochloa Colona* (L.) Link. Crop Prot 2016; 83(1): 56-66.
- Chopra N, Tewari G, Tewari LM, Upreti B and Pandey N: Allelopathic effect of *Echinochloa Colona* L. and *Cyperus iria* l. weed extracts on the seed germination and seedling growth of rice and soyabean. Adv Agric 2017; (1): 1-5.
- Pan L, Yu Q, Han H, Mao L, Nyporko A, Fan LJ, Bai L and Powles S: Aldo-keto reductase metabolizes glyphosate and confers glyphosate resistance in *Echinochloa colona*. Plant Physiol 2019; 1(1): 239-50.
- Chauhan BS and Johnson DE: Seed germination ecology of junglerice (*Echinochloa colona*): a major weed of rice. Weed Sci 2009; 57(3): 235-40.
- Coskun O: Separation techniques chromatography. North Clin Istanbul 2016; 1(1): 123-35.
- Schweiger S, Hinterberger S and Jungbauer A: Column-to-column packing variation of disposable pre-packed columns for protein chromatography. J Chromatogr A 2017; 1527(1): 70-79.
- Mauer L and Reuhs BL: High-performance liquid chromatography bradley. Food Anal 2017; 1(1): 213-26.
- Wang T, yang Li, Q Bi and shun K: Bioactive flavonoids in medicinal plants: structure, activity and biological fate. Asian J Pharm Sci 2018; 13(1): 12-23.
- Anti-Phishing Working Group. Phishing Activity Trends Report 1 Quarter. Most 2010; 1(3); 1-12.

10. Ahad Hussain S, Greeshma Namilikonda M, Karan Chandra T and Arif Pasha M: A review on medi plants with anti-dia activity. Int Journal of Adv Res 2020; 8(3): 902-17.
11. Deng X, Liu B, Li J, Zhang J, Zhao Y and Xu K: Blood biochemical characteristics of patients with coronavirus disease 2019 (covid-19): a systemic review and meta-analysis. Clin Chem Lab Med 2020; 1(1): 145-56.
12. Qian ZP, Mei X, Zhang YY, Zou Y, Zhang ZG, Zhu H, Guo HY, Liu Y, Ling Y, Zhang XY, Wang JF and Lu HZ: Analysis of baseline liver biochemical parameters in 324 cases with novel coronavirus pneumonia in shanghai area. Zhonghua Gan Zang Bing Za Zhi 2020; 28 (3): 229-33.
13. Ali Abd El-Aal Y, Mohamed Abdel-Fattah D and El-Dawy Ahmed K: Some biochemical studies on trans fatty acid-containing diet. Diabetes Metab Syndr Clin Res Rev 2019; 13(3): 1753-57.
14. Kishore J, Gupta N, Kohli C and Kumar N: Prevalence of hypertension and determination of its risk factors in rural delhi. Int J Hypertens 2016; (1): 2016-25.
15. Nordestgaard BG, Langsted A, Mora S and Watts GF: Fasting Is Not routinely required for determination of a lipid profile: clinical and laboratory implications including flagging at desirable concentration cutpoints-a joint consensus statement from the european atherosclerosis soc and european federat. C Chem 2016; 62(7): 930-46.

How to cite this article:

Borkar V, Sonwane G, Devhare P, Diwre R and Jain S: Evaluation of antidiabetic activity of *Echinochloa colona* plant extract. Int J Pharm Sci & Res 2021; 12(8): 4354-64. doi: 10.13040/IJPSR.0975-8232.12(8).4354-64.

All © 2013 are reserved by International Journal of Pharmaceutical Sciences and Research. This Journal licensed under a Creative Commons Attribution-NonCommercial-ShareAlike 3.0 Unported License.

This article can be downloaded to **Android OS** based mobile. Scan QR Code using Code/Bar Scanner from your mobile. (Scanners are available on Google Playstore)



Received on 20 August 2019; received in revised form, 29 January 2021; accepted, 19 May 2021; published 01 August 2021

EVALUATION OF ANTIDIABETIC ACTIVITY OF *ECHINOCHLOA COLONA* PLANT EXTRACT

Vijay Borkar ^{*1}, Gajanan Sonwane ¹, Parmeshwar Devhare ¹, Rushikesh Diwre ¹ and Shirish Jain ²

Department of Pharmaceutical Chemistry ¹, Department of Pharmacology ², Rajarshi Shahu College of Pharmacy, Buldana - 443001, Maharashtra, India.

Keywords:

Echinochloa colona, Chromatography, Antidiabetic, Anti diabetic

Correspondence to Author:

Vijay Borkar

Department of Pharmaceutical Chemistry, Rajarshi Shahu College of Pharmacy, Buldana - 443001, Maharashtra, India.

E-mail: sonwane.gajanan@rediffmail.com

ABSTRACT: The current work comprises the assessment of antidiabetic activity of chloroform, ethyl acetate, and ethanol fractions and isolation of some phytoconstituents from chloroform fraction obtained from ethanolic extract of *Echinochloa colona*. The antidiabetic activity was performed using streptozocin induced diabetic model in male Wistar rats (150-200 g). The best restraint results were for metformin, chloroform, ethyl acetate and ethanol fraction was 5.85 ± 0.004 (90.08%), 6.65 ± 0.004 (67.36%), 6.96 ± 0.003 (60.14%) and 7.05 ± 0.004 (58.01%) respectively, comparing controlled diabetic rats which showed a significant reduction of blood glucose level. On total cholesterol level metformin, chloroform, ethyl acetate and ethanol fraction showed decrease in total cholesterol level by 12.16 ± 0.0044 (56.98%), 13.02 ± 0.004 (53.94%), 14.17 ± 0.004 (49.87%) and 16.37 ± 0.004 (42.24%) respectively. Significantly triglyceride was decreased by 10.39 ± 0.0044 (46.49%), 13.16 ± 0.004 (32.23%), 14.06 ± 0.004 (27.60%) and 14.56 ± 0.004 (42.24%) for metformin, chloroform, ethyl acetate and ethanol fraction respectively. Three important phytoconstituents were isolated from chloroform fraction, and structures were elucidated using spectroscopic techniques.

INTRODUCTION: *Echinochloa colona*, regularly known as jungle rice, deccan grass, or awnless farm grass, is a sort of wild grass beginning from tropical Asia. It was some time ago delegated types of *Panicum*. It is the wild precursor of the developed grain crop *Echinochloa frumentacea*, sawa millet. A few taxonomists treat the two taxa as one animal group, in which case the trained structures may likewise be alluded to as *E. colona* ^{1, 3}.

Echinochloa Colona Plant Profile:



Kingdom: Plantae
Division: Angiosperms
Class: Monocots
Order: Poales

QUICK RESPONSE CODE 	DOI: 10.13040/IJPSR.0975-8232.12(8).4354-64
	This article can be accessed online on www.ijpsr.com
DOI link: http://dx.doi.org/10.13040/IJPSR.0975-8232.12(8).4354-64	

Family: Poaceae
Genus: *Echinochloa*
Species: *Echinochloa colona*

Botanical Description: *Echinochloa colona* (Poaceae), commonly known as Jungle rice (awnless barnyard grass) in India, is a yearly upright or decumbent, scattering, rooting from the inferior cutline node. It is a terrestrial, tufted, and erect grass propagates vegetatively but mostly by seeds, extensively spread in tropics & subtropics. It is also observed in South-Southeast Asia and tropical Africa. Leaves are spiral; alternatively, sessile linear more than 2 cm long, apex is acute with clasping base and parallel-veined. It culms ascending, or decumbent 10-100 cm long⁴.

Pharmacognostic Characteristic:

Macroscopy: Culms are 10-70 cm long, lower nodes are glabrous and upper nodes are glabrous. Sheaths are glabrous, ligules absent, blades are 8-10 cm long and cm⁻³⁻⁶ wide. Panicle is cm⁻²⁻¹², erect, rachises. A primary branch is 5-10 cm, erect otherwise ascending, spike-like, distant, devoid of secondary branches, axes glabrous or sparsely hispid. Spikelet is 2-3 mm, disarticulating at maturity, pubescent to hispid. Lower glumes are as long as spiklets; lower florest are sterile occasionally staminate. Lower lemmas are unawned, upper lemmas are 2.6-2.9 mm. Anthers are 0.7-0.8 mm, caryopses are 1.2-1.6 mm, whitish, and embryos are as long as caryopses. It is distributed in tropical and subtropical areas. It is weedy in North America grown in low-lying, damp to wet, including rice fields. Un branched somewhat widely-spaced panicle branches, which make this one of the easier species of the *Echinochloa colona*.

Traditional Uses: As per the literature, in India, seeds of grass are used to prepare a food dish called khichdi and are consumed during festivals, fasting days. The whole plant is used as fodder by grazing animals, and it cures ingestion. *Echinochloa colona*, is a significant crop. It is a reasonable wellspring of protein, which is exceptionally edible; furthermore, it is a fantastic wellspring of dietary fiber with great measures of solvent and insoluble portions. The starch content is low and gradually edible, which makes the *Echinochloa colona*, a characteristic fashioner nourishment. In

the current long periods of expanded diabetes mellitus, *E. colona*, could turn into perfect nourishment.

MATERIALS AND METHODS:

Sample Preparation: *E. colona* samples were collected from a paddy field in Dharmapuri, Tamil Nadu, India province in June 2013 at the flowering stage (red-purple flower). The samples were cleaned and separated into roots and shoots, then air-dried at room temperature and cut into small pieces (5 mm). The *E. colona* samples were extracted using soxhlet extraction methods, previously soaked with n-hexane to remove fatty residue. Then ethanol extract was fractionated (chloroform, acetone, ethyl acetate, ethanol, and methanol) from low to high polarity solvents. The plant parts were extracted using solvent at the rate of 1:5 (w/v) in 1 L beakers and covered with plastic film. The detailed procedure regarding the extraction was described by Gomaa and Abd Elgawad (2012). The beakers were kept in the dark at room temperature for 7 d. The solutions were separated from plant residues and evaporated using a rotary evaporator at 600 °C under reduced pressure. There were six different extracts of *E. colona* from the shoots and roots using n-hexane, extracts from the shoots and roots using chloroform, acetone, ethyl acetate, ethanol, and methanol.

Column Chromatography: The chloroform fraction of *Echinochloa colona* was subjected to column chromatography using silica gel as it has shown better pharmacological effect comparing to ethyl acetate and ethanol fraction and eluted with solvent mixtures of increasing polarity.

While elution, the chromatographic fractions were collected and monitored on TLC. All the fractions showing a single spot were pulled together, purified, and observed for its R_f value using TLC. The solvents like chloroform, acetone, ethyl acetate, ethanol, and methanol used for separation⁵.

Chromatographic Separation of Chloroform Fraction: Slurry of activated silica gel (150 °C for 3 h) was prepared with chloroform, and then the column was packed with slurry. The sample was loaded on the packed silica gel. After stabilization

column was eluted with mobile phase. Fractions were collected and analyzed by TLC.

Preparation of Mobile Phase: All the solvents, chloroform, acetone, ethyl acetate, ethanol, and methanol were distilled and then used for the preparation of the mobile phase. The composition of the mobile phase was made with increasing polarity solvents.

Column Packing: A clean and dry borosil glass column (60 cm, height; 3 cm, diameter) was aligned in a vertical position with the help of clamps attached to metal stand. A piece of cotton soaked in the mobile phase was positioned at the bottom of the column and quietly tamped down by means of a glass rod. The column was then filled about 1/3 volume by the mobile phase. The column was slowly and evenly filled, about 5/6 volumes full with the gradual addition of silica gel slurry. The stopcock was opened to allow the excess mobile phase to drain into the beaker. The side of the column was softly tapped with a cork during the process of packing to compact the silica gel. In the meantime, the stopcock was opened to run down the excess mobile phase. When the packing was finished, the excess mobile phase was drained until it just reaches the top level of silica.

Application of Sample: Weighed quantity of the sample was mixed with 1-2 g of activated silica gel and 3-4 ml of mobile phase to prepare a slurry. The slurry of the sample was added to the top of the packed silica in the column. The stopcock was opened to drain the excess mobile phase until it reaches top level of the sample. A thin disc (column diameter) of filter paper soaked in the mobile phase was placed on top of the bed to prevent disturbing the sample layer after addition of the mobile phase. The column was filled to the top with the mobile phase and allowed to stand for overnight (~24 h) to develop a chromatogram^{6,7}.

Anti Diabetic Activity: Anti-diabetic effect of chloroform, ethyl acetate, and ethanol fractions obtained from ethanolic extract of *Echinochloa colona* was performed using streptozotocin-induced diabetic model in Wistar rats. The doses of the fractions were made at 50 mg /mL. All male Wistar rats (150-200 g) were randomly divided into 7 groups, each containing 5 rats^{8,10}.

- **Group I:** Normal control (normal saline)
- **Group II:** Normal metformin control (150 mg/kg, *i. p.*)
- **Group III:** Diabetic control (normal saline)
- **Group IV:** Diabetic metformin control (150 mg/kg, *i. p.*)
- **Group V:** Diabetic (chloroform fraction)
- **Group VI:** Diabetic (ethyl acetate fraction)
- **Group VII:** Diabetic (ethanol fraction)

The standard drug and test samples were fed orally with an intragastric tube for 24 h experiment. Diabetes was induced (Group III-VII) by intraperitoneal injection (1 mL/kg) of freshly prepared streptozotocin (45 mg/kg), after baseline glucose was estimated.

After 48 h, blood samples were collected from the tail vein of all rats, and the blood glucose level was estimated. Blood glucose levels above ¹¹. 1 mmol/L in animals were selected for the studies considering the condition of diabetes was established.

Biochemical Analysis: After treatment, blood samples were collected with the help of disposable syringes from the tail vein of all rats of all groups before and at 0, 1, 2, 3, 6, 10, 16, and 24th h and analyzed for content of blood glucose using Glucometer (Bio Land, Germany). Then all the rats were sacrificed, and approximately 1-2 mL of blood was collected directly from the heart with the help of disposable syringes.

The blood samples were transferred to centrifuge tubes and allowed to centrifuge at 4000 rpm for 10 min; serum was collected used to determine total cholesterol (TC) and serum triglycerides (TG). Serum total cholesterol and triglycerides were estimated at 505 and 546 nm, respectively, using cholesterol oxidase/ p-amino antipyrine (CHO / PAP) method and glycerol 3- phosphate oxidase (GPO) method, respectively according to manufacturer's protocol^{11,13}.

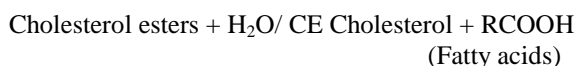
Determination of Total Cholesterol: Total cholesterol was determined by reagents kits of Reckon Diagnostics Pvt. Ltd., Baroda.

Method: CHOD-PAP method was used described by Allain *et al.*, 1974. It is an extremely specific¹³²

enzymatic colorimetric method for measurements in the visible range (505 nm), well-known for its high flexibility^{14, 15}.

Test Principle: The esters of cholesterol are hydrolyzed to cholesterol by cholesterol esterase (CE). The cholesterol is then oxidized by cholesterol oxidase (CO) to cholesterol 4-en-3-one with the concurrent creation of H₂O₂.

H₂O₂ then reacts with 4-aminoantipyrine (AAP) and phenolic compounds in the presence of peroxidase to give colored complex red at 505 nm (500-540 nm, GREEN filter). The color intensity produced is directly proportional to the concentration of total cholesterol in the test samples.



Sample Material: Serum

Procedure: The three tubes were labeled accordingly as blank, standard, and test. 0.01ml standard and serum were added to the corresponding tubes. 1 mL Cholesterol reagent was placed in all tubes, *i.e.* blank, standard, and test, mixed well, and incubated (10 min at 37 °C). Then absorbance was red of test and standard at 505 nm or with green filter against blank reagent.

Calculations:

Cholesterol (mg/dl) = Absorbance in Test × 200 / Absorbance in Standard

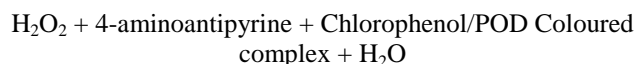
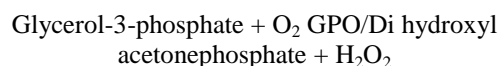
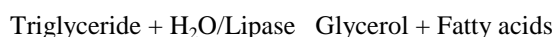
Determination of Triglycerides: Triglyceride was determined by reagents kits of Reckon Diagnostics Pvt. Ltd., Baroda.

Method: High performance enzymatic GPO-PAP method modified according to Fossati 1982; McGowan *et al.*, 1983.

Test Principle: Triglyceride is hydrolyzed sequentially to Di & Monoglycerides and finally to Glycerol by Lipase. Glycerol kinase (GK) by

means of ATP as PO₄ source converts Glycerol to Glycerol-3-phosphate (G-3-Phosphate). G-3-phosphate Oxidase (GPO) oxidised G-3- phosphate to Di-hydroxy acetone phosphate & hydrogen peroxide is formed.

Hydrogen peroxide in presence Peroxidase (POD) oxidised to oxidise 4 amino antipyrine and chlorophenol to a pink coloured complex, which is measured at 546 nm (500-550 nm or with green filter). Absorbance is proportional to Triglycerides concentration.



Sample Material Serum

Procedure: 0.05 mL serum, standard, and distilled water were placed in the tubes marked as a test, standard and blank, respectively.

Then working solution 1 mL of was added to every tube, mixed well, and incubated (20 min at 37 °C). After incubation, 1.5 mL of distilled water was added to every tube, mixed well. Absorbance was red of test and standard against the blank at 546 nm (500-550 nm)

Calculations:

Triglyceride (mg/dl) = Absorbance in Test / Absorbance in Standard × 200

Elution: Elution was carried out with the flow rate (1 ml/min). The mobile phase was added at the top of the column from the solvent reservoir, and fractions were collected in an amber colored bottle.

Fractions were concentrated by evaporating at room temperature until volume was reduced to ¼ of the total volume. TLC of concentrated fractions was carried out to detect similarity between the chromatograms of different fractions.

Source	Fraction	Mobile phase	Abbreviation
<i>E. colona</i>	Chloroform	Chloroform: Ethanol 40:60	EC-I
		Chloroform: Ethanol 30:70	EC-II
		Chloroform: Ethanol 10:90	EC-III

Thin Layer Chromatography (TLC): TLC of each fraction was carried out during column chromatography, and the R_f value for EC-I (0.48), EC-II (0.74), EC-III (0.68) was observed.

Characterization of the Isolated Compounds from *E. Colona*:

EC-I: The EC-I fraction was collected at 40:60 in % ratio of (CHCl₃: C₂H₅OH). The isolated compound was white amorphous powder. The compound was studied for its qualitative properties and found to be positive with the ferric chloride test, and the phenolic nature of the compound was confirmed. The M.P. of the compound was 145-147 °C.

The UV spectrum showed λ_{max} , 220 nm, Ethanol with typical aromatic bands confirming a substituted aromatic benzoic acid. In the FTIR (KBr, cm⁻¹) signal at 3400 (-OH), 2935 (Ar-H), 1688(-COOH), ¹HNMR (CDCl₃, 400 MHz) signals at δ 11.80 (-COOH), 6.5 (Ar-H), 5.10 (Ar-OH), 2.33 (Ar-CH₃) and the peak of molecular ion was observed at m/z 184 matching to C₈H₈O₅, and main peak at 166 [184-(H₂O)]⁺ with other fragments at m/z : 120, 84, 42, 27 were observed.

The above spectral data suggested isolated compound is 2, 3, 4-trihydroxy, 6-methyl benzoic acid. The IR, ¹HNMR, and MASS spectra were shown in following Fig. 1 to 3.

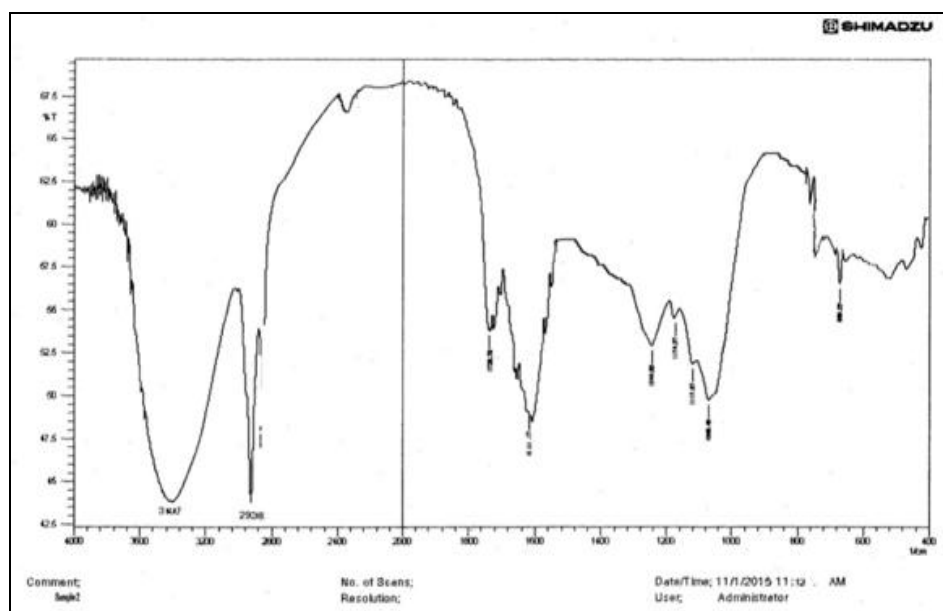


FIG. 1: IR SPECTRA OF EC-I FRACTION ISOLATED FROM *E. COLONA*

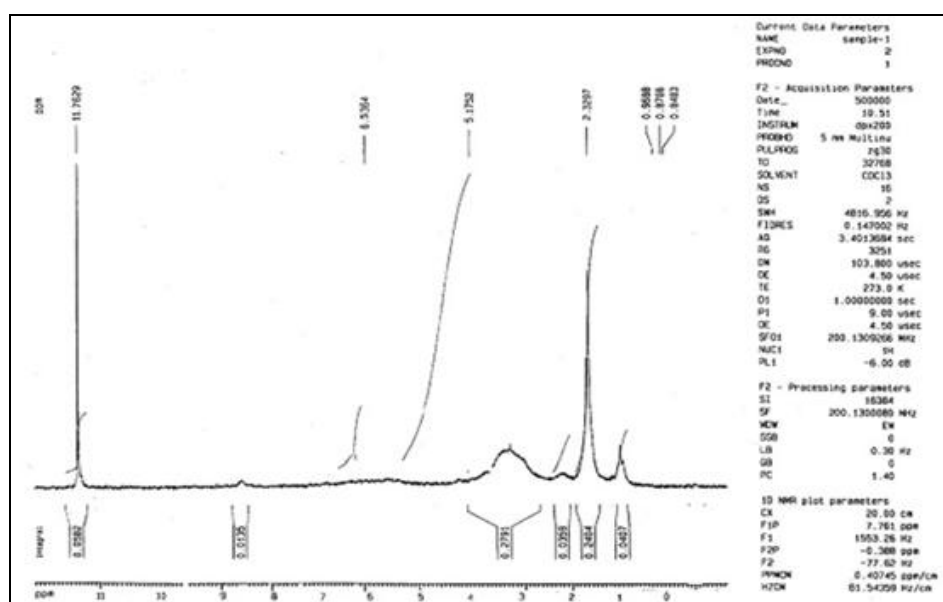


FIG. 2: ¹H NMR SPECTRA OF EC-I FRACTION ISOLATED FROM *E. COLONA*

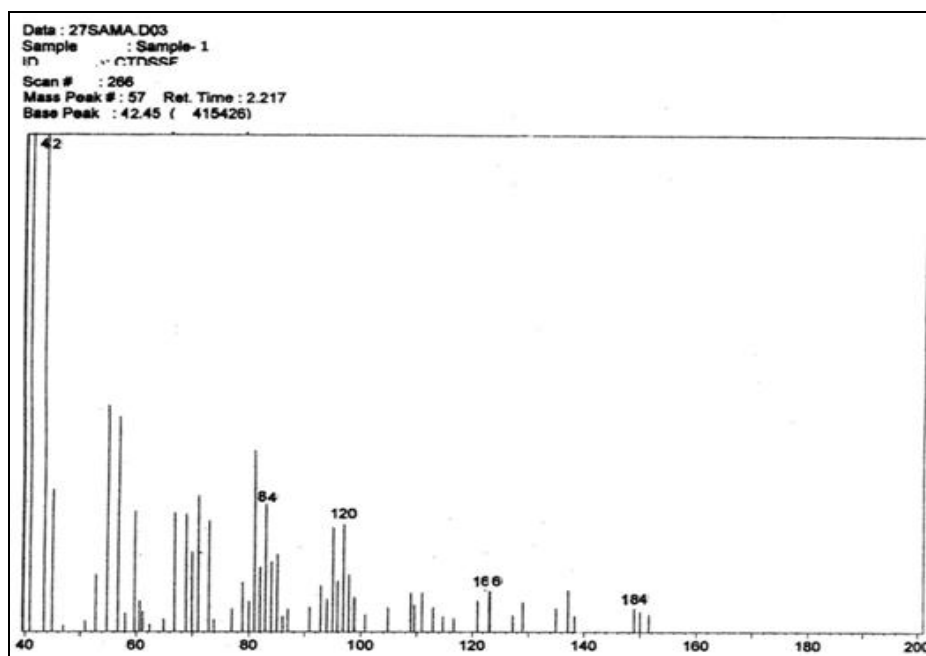


FIG. 3: MASS SPECTRA OF EC-I FRACTION ISOLATED FROM *E. COLONA*

EC-II: The EC-II fraction was collected at 30:70 in % ratio of ($\text{CHCl}_3:\text{C}_2\text{H}_5\text{OH}$). The isolated compound was white crystalline powder with a characteristic odour. The compound was studied for its qualitative properties and found to be positive with the Liebermann-Burchard test, and the steroidal nature of the compound was confirmed. The M.P. of the compound was 137-139 °C. UV spectrum showed λ_{max} , 210 nm, ethanol. In the FTIR (KBr, cm^{-1}) 3545 (-OH), 2931 (-CH₂), 2860 (-CH), 1637 (-C=C-), 1033 (-C-O), ¹HNMR (CDCl_3 , 400 MHz) signals at δ 1.01, 1.04, 1.06,

1.04, 1.17, 1.21(-CH₃), 1.57, 1.98, 1.13, 1.79, 1.24, 1.27, 1.35, 1.34, 1.25, 1.29, (-CH₂-), 3.25(--CH-), 5.37 (H-cyclohexene) and peak of molecular ion was observed at 414.7 corresponding to $\text{C}_{29}\text{H}_{50}\text{O}$ with other characteristic fragmentations of m/z: 414, 396, 381, 330, 290, 273, 255, 212, 199 and 173 were observed. The above spectral data and those reported in the literature support the proposed structure was β -sitosterol 113, 114, 115. The IR, ¹HNMR, and MASS spectra were shown in the following Fig. 4 to 6.

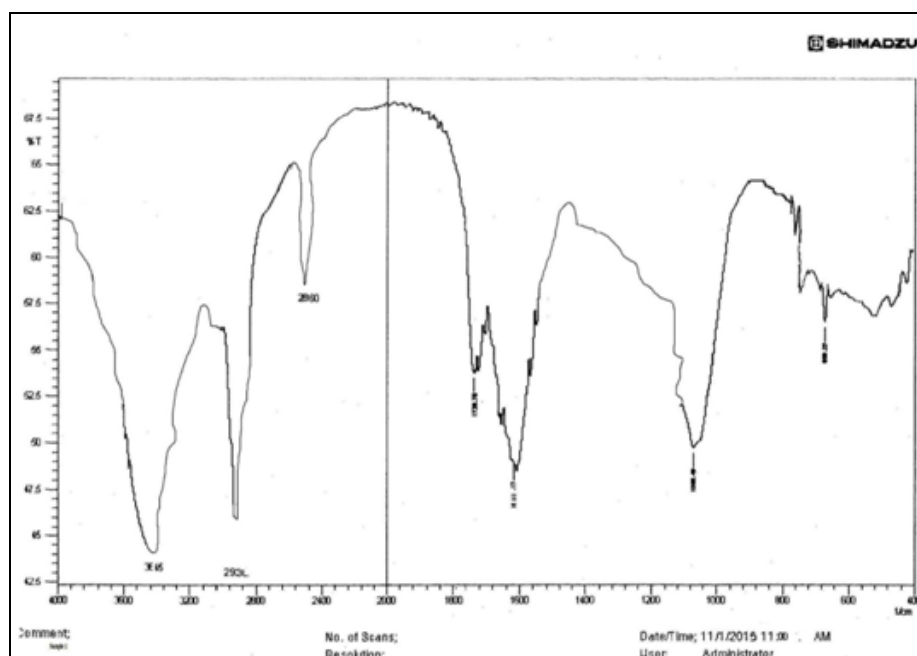


FIG. 4: IR SPECTRA OF EC-II FRACTION ISOLATED FROM *E. COLONA*

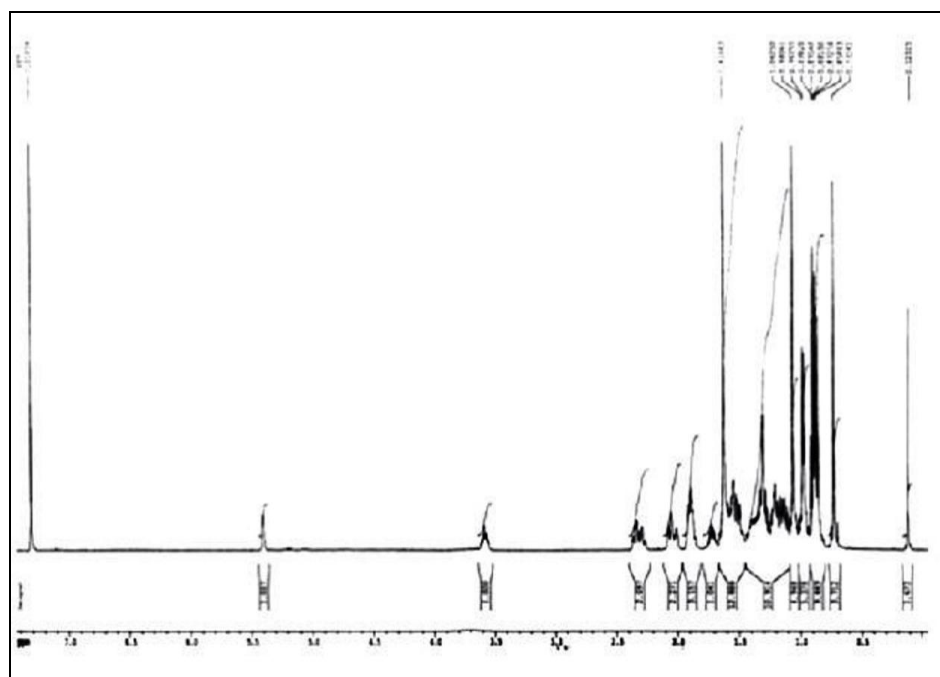


FIG. 5: ^1H NMR SPECTRA OF EC-II FRACTION ISOLATED FROM *E. COLONA*

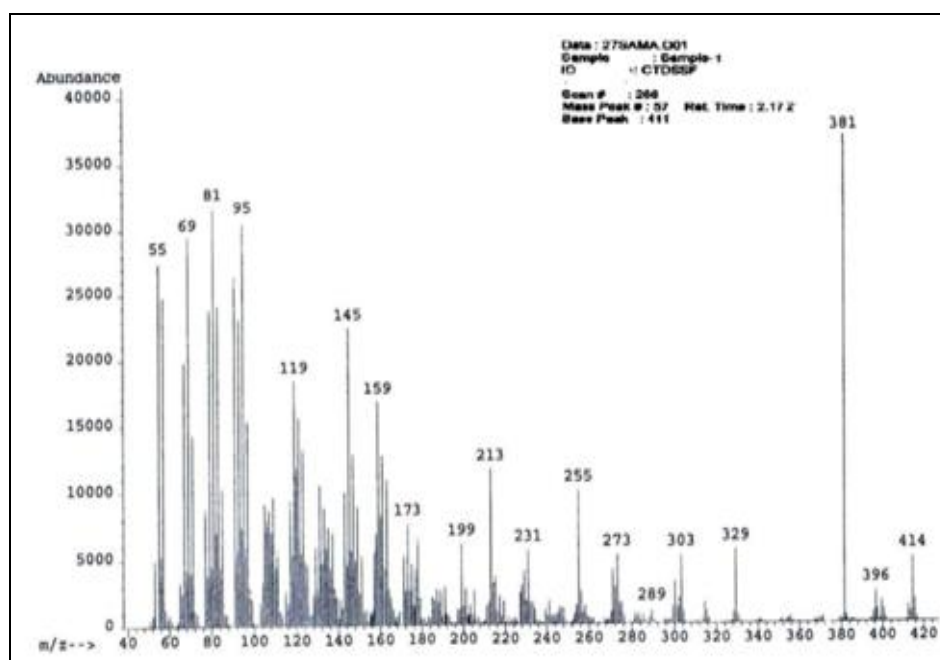


FIG. 6: MASS SPECTRA OF EC-II FRACTION ISOLATED FROM *E. COLONA*

EC-III: The EC-III fraction was collected at 10:90 in % ratio of ($\text{CHCl}_3:\text{C}_2\text{H}_5\text{OH}$). The isolated compound was white crystalline powder with a characteristic odour. The compound was studied for its qualitative properties and found to be positive with the ester test, and the ester nature of the compound was confirmed.

The melting point of the compound was carried out and found to be 150- 152 $^\circ\text{C}$. The UV spectrum showed λ_{max} , 226 nm, methanol. In the FTIR (KBr,

cm^{-1}) band at 1736 (RCOOR) and 3400 (Ar-OH), ^1H NMR (CDCl_3 , 400 MHz) at δ 1.25 (- CH_3), 4.65 (- CH_2 -), 4.58 (Ar-OH) and a peak of molecular ion was observed at m/z 198 correspondings to $\text{C}_9\text{H}_{10}\text{O}_5$ with other fragments at 183, 149 [$183-\text{CH}_3$] $^+$, 129, 111, 97, 83, 69, 57, 43 were observed.

The above spectral data suggested isolated compound was ethyl 3, 4, 5-trihydroxy benzoate. The IR, ^1H NMR, and MASS spectra were shown in the following Fig. 7 to 9.

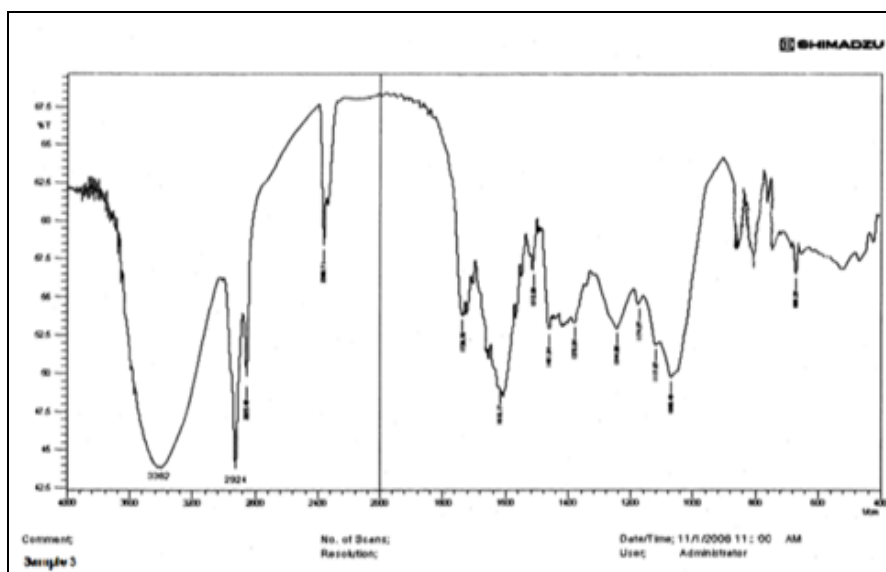


FIG. 7: IR SPECTRA OF EC-III FRACTION ISOLATED FROM *E. COLONA*

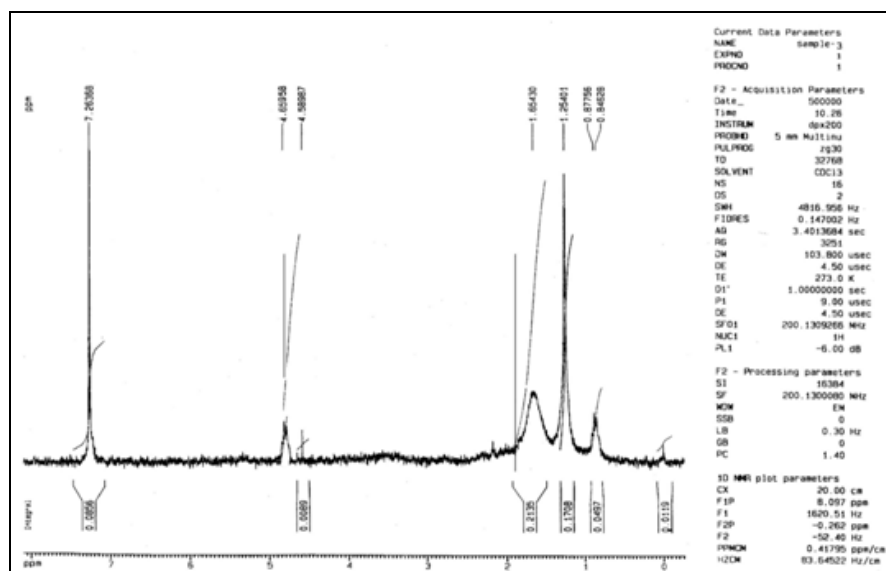


FIG. 8: 1H NMR SPECTRA OF EC-III FRACTION ISOLATED FROM *E. COLONA*

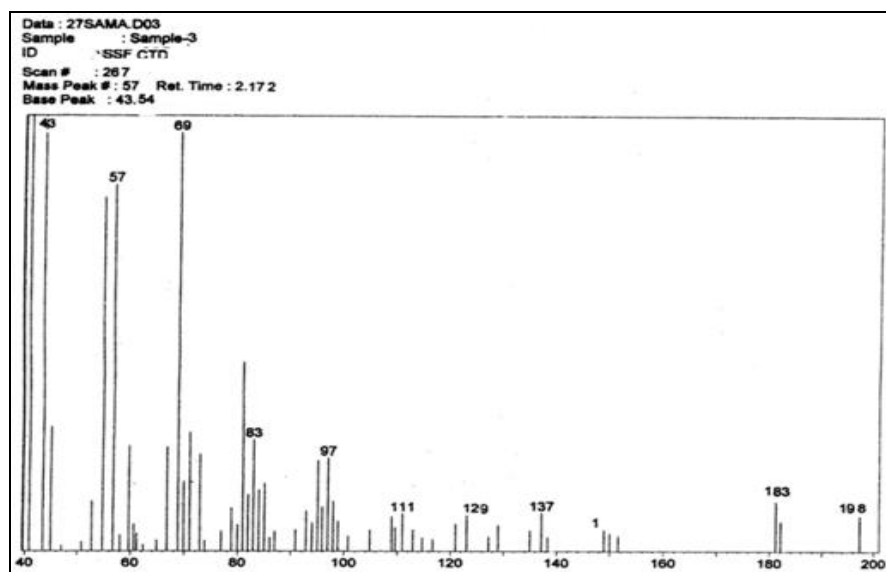


FIG. 9: MASS SPECTRA OF EC-III FRACTION ISOLATED FROM *E. COLONA*

Anti Diabetic Activity: The effects of different fractions (single dose-50 mg/mL) obtained from ethanolic extracts of *E. colonaupon* blood glucose (mmol/L), serum total cholesterol & triglycerides (mmol/L) were investigated within control and streptozotocin induced diabetic rats. Metformin HCl (150 mg/mL) was used as a standard anti-diabetic agent.

Effects of Various Fractions on Blood Glucose: A decrease in blood glucose level was observed in

animals treated with different fractions of *E. colonaat*^{0, 1, 2, 3, 6, 10, 16}, and 24th h **Fig. 1**.

The blood glucose level was significantly reduced at 24th h of the experiment ($p < 0.01$) for metformin, chloroform, ethyl acetate, and ethanol fraction, it was 5.85 ± 0.004 (90.08%) 6.65 ± 0.004 (67.36%), 6.96 ± 0.003 (60.14%) and 7.05 ± 0.004 (58.01%) respectively comparing controlled diabetic rats **Table 1**.

TABLE 1: EFFECT OF DIFFERENT FRACTIONS OF *E. COLONA* ON BLOOD GLUCOSE IN DIABETIC RATS ON ONE DAY TREATMENT

Groups (Treatment)	Blood glucose levels (mmol/L) at Hours							
	0	1	2	3	6	10	16	24
I	7.25 ±	7.26 ±	7.27 ±	7.28 ±	7.29 ±	7.30 ±	7.31 ±	7.32 ±
10 ml saline	0.004	0.004	0.004	0.004	0.004	0.002	0.002	0.004
II	7.26 ±	7.24 ±	7.28 ±	7.20 ±	7.19 ±	6.17 ±	6.05 ±	4.13 ±
150 mg/kg	0.004	0.003	0.004	0.002	0.004	0.004	0.003	0.004
III	11.01 ±	11.50 ±	11.95 ±	12.25 ±	12.75 ±	13.10 ±	13.55 ±	13.95 ±
10 ml saline	0.003	0.003	0.004	0.004	0.004	0.004	0.003	0.003
IV	11.12 ±	10.81 ±	9.05 ±	8.75 ±	6.65 ±	7.08 ±	6.16 ±	5.85 ±
150 mg/kg	0.003	0.20	0.004	0.004	0.004	0.004	0.004	0.004
V	11.13 ±	10.61 ±	10.15 ±	9.95 ±	8.85 ±	7.28 ±	6.96 ±	6.65 ±
50 mg/ml	0.004	0.002	0.008	0.005	0.004	0.004	0.004	0.004
VI	11.13 ±	10.92 ±	10.41 ±	10.31 ±	9.55 ±	7.98 ±	7.86 ±	6.96 ±
50 mg/ml	0.004	0.004	0.004	0.004	0.004	0.003	0.002	0.003
VII	11.14 ±	11.02 ±	10.91 ±	10.71 ±	9.98 ±	9.07 ±	7.66 ±	7.05 ±
50 mg/ml	0.004	0.004	0.005	0.003	0.004	0.004	0.004	0.004

All values are expressed as mean ± SEM, (n=5) in every group, $p < 0.01$, p-values were calculated and compared with control by ANOVA method followed by Dunnett's test

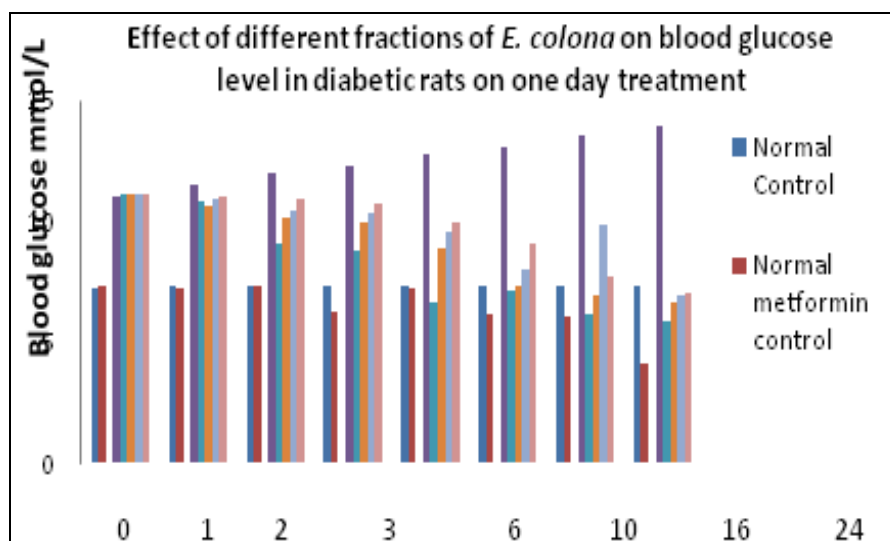


FIG. 10: EFFECT OF DIFFERENT FRACTIONS OF *E. COLONA* ON BLOOD GLUCOSE LEVEL IN DIABETIC RATS ON ONE DAY TREATMENT

Effect of Various Fractions on Total Cholesterol and Triglyceride: After 24 h treatment of different fractions of *E. colona* there was decreased in total cholesterol and triglyceride on diabetic rats **Fig. 2**.

Metformin, chloroform, ethyl acetate and ethanol fraction showed decrease in total cholesterol level by 12.16 ± 0.0044 (56.98%) 13.02 ± 0.004 (53.94%) 14.17 ± 0.004 (49.87%) and 16.37 ± 138

0.004 (42.24%) respectively, whereas the triglyceride was decreased by 10.39 ± 0.0044 (46.49%) 13.16 ± 0.004 (32.23%) 14.06 ± 0.004 (27.60%) and 14.56 ± 0.004 (42.24%) for metformin, chloroform, ethyl acetate and ethanol fraction respectively when compared to diabetic control groups **Table 2**.

TABLE 2: EFFECTS OF DIFFERENT FRACTIONS OF *E. COLONA* ON TOTAL CHOLESTEROL & TRIGLYCERIDES IN DIABETIC RAT ON ONE DAY TREATMENT

Parameter (mmol/L)	Groups						
	I	II	III	IV	V	VI	VII
Total Cholesterol	14.37± 0.003	12.24± 0.004*	28.27± 0.004**	12.16± 0.004**	13.02± 0.004**	14.17± 0.004**	16.37± 0.004**
Total Glycerides	12.41± 0.004	10.31± 0.003*	19.42± 0.004*	10.39± 0.004*	13.16± 0.004*	14.06± 0.004*	14.56± 0.004*

All values are expressed as mean \pm SEM, (n=5) in every group, *p <0.01, considered extremely significant, p-values were calculated and compared with control by ANOVA method followed by Dunnett's test.

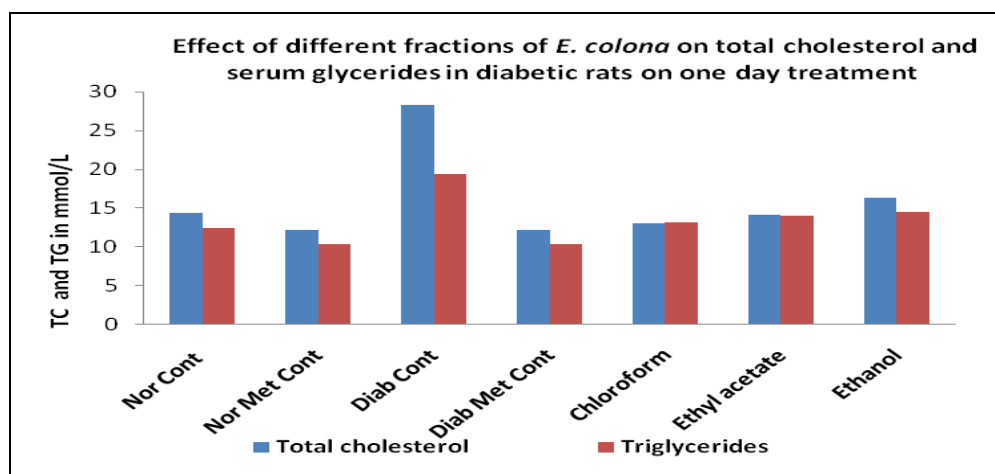


FIG. 11: EFFECTS OF DIFFERENT FRACTIONS OF *E. COLONA* ON TOTAL CHOLESTEROL AND SERUM GLYCERIDES IN DIABETIC RATS ON ONE DAY TREATMENT

CONCLUSION: Given the potent results of the extracts tested in this article against diabetes and the factor responsible for the same (triglycerides). A decrease in blood glucose level was observed in animals treated with different fractions of *E. colona*.

After 24 h treatment of different fractions of *E. colona* there was a significant decrease in total cholesterol and triglyceride on diabetic rats when treated with chloroform fraction. The chloroform fraction exhibiting significant anti-diabetic activity was chromatographed to isolate three phyto constituents 2, 3, 4-trihydroxy, 6-methyl benzoic acid, β -sitosterol, and ethyl 3, 4, 5-trihydroxy benzoate.

ACKNOWLEDGEMENT: Authors are thankful to Principal Rajarshi Shahu College of Pharmacy, Buldhana, for providing the necessary facilities

CONFLICTS OF INTEREST: The authors have not declared any conflict of interest.

REFERENCES:

- Peerzada AM, Bajwa AA, Ali HH and Chauhan BS: Biology, Impact and Management of *Echinochloa Colona* (L.) Link. Crop Prot 2016; 83(1): 56-66.
- Chopra N, Tewari G, Tewari LM, Upreti B and Pandey N: Allelopathic effect of *Echinochloa Colona* L. and *Cyperus iria* l. weed extracts on the seed germination and seedling growth of rice and soyabean. Adv Agric 2017; (1): 1-5.
- Pan L, Yu Q, Han H, Mao L, Nyporko A, Fan LJ, Bai L and Powles S: Aldo-keto reductase metabolizes glyphosate and confers glyphosate resistance in *Echinochloa colona*. Plant Physiol 2019; 1(1): 239-50.
- Chauhan BS and Johnson DE: Seed germination ecology of junglerice (*Echinochloa colona*): a major weed of rice. Weed Sci 2009; 57(3): 235-40.
- Coskun O: Separation techniques chromatography. North Clin Istanbul 2016; 1(1): 123-35.
- Schweiger S, Hinterberger S and Jungbauer A: Column-to-column packing variation of disposable pre-packed columns for protein chromatography. J Chromatogr A 2017; 1527(1): 70-79.
- Mauer L and Reuhs BL: High-performance liquid chromatography bradley. Food Anal 2017; 1(1): 213-26.
- Wang T, yang Li, Q Bi and shun K: Bioactive flavonoids in medicinal plants: structure, activity and biological fate. Asian J Pharm Sci 2018; 13(1): 12-23.
- Anti-Phishing Working Group. Phishing Activity Trends Report 1 Quarter. Most 2010; 1(3): 1-12.

10. Ahad Hussain S, Greeshma Namilikonda M, Karan Chandra T and Arif Pasha M: A review on medi plants with anti-dia activity. Int Journal of Adv Res 2020; 8(3): 902-17.
11. Deng X, Liu B, Li J, Zhang J, Zhao Y and Xu K: Blood biochemical characteristics of patients with coronavirus disease 2019 (covid-19): a systemic review and meta-analysis. Clin Chem Lab Med 2020; 1(1): 145-56.
12. Qian ZP, Mei X, Zhang YY, Zou Y, Zhang ZG, Zhu H, Guo HY, Liu Y, Ling Y, Zhang XY, Wang JF and Lu HZ: Analysis of baseline liver biochemical parameters in 324 cases with novel coronavirus pneumonia in shanghai area. Zhonghua Gan Zang Bing Za Zhi 2020; 28 (3): 229-33.
13. Ali Abd El-Aal Y, Mohamed Abdel-Fattah D and El-Dawy Ahmed K: Some biochemical studies on trans fatty acid-containing diet. Diabetes Metab Syndr Clin Res Rev 2019; 13(3): 1753-57.
14. Kishore J, Gupta N, Kohli C and Kumar N: Prevalence of hypertension and determination of its risk factors in rural delhi. Int J Hypertens 2016; (1): 2016-25.
15. Nordestgaard BG, Langsted A, Mora S and Watts GF: Fasting Is Not routinely required for determination of a lipid profile: clinical and laboratory implications including flagging at desirable concentration cutpoints-a joint consensus statement from the european atherosclerosis soc and european federat. C Chem 2016; 62(7): 930-46.

How to cite this article:

Borkar V, Sonwane G, Devhare P, Diwre R and Jain S: Evaluation of antidiabetic activity of *Echinochloa colona* plant extract. Int J Pharm Sci & Res 2021; 12(8): 4354-64. doi: 10.13040/IJPSR.0975-8232.12(8).4354-64.

All © 2013 are reserved by International Journal of Pharmaceutical Sciences and Research. This Journal licensed under a Creative Commons Attribution-NonCommercial-ShareAlike 3.0 Unported License.

This article can be downloaded to **Android OS** based mobile. Scan QR Code using Code/Bar Scanner from your mobile. (Scanners are available on Google Playstore)



Received on 20 August 2019; received in revised form, 29 January 2021; accepted, 19 May 2021; published 01 August 2021

EVALUATION OF ANTIDIABETIC ACTIVITY OF *ECHINOCHLOA COLONA* PLANT EXTRACT

Vijay Borkar ^{*1}, Gajanan Sonwane ¹, Parmeshwar Devhare ¹, Rushikesh Diwre ¹ and Shirish Jain ²

Department of Pharmaceutical Chemistry ¹, Department of Pharmacology ², Rajarshi Shahu College of Pharmacy, Buldana - 443001, Maharashtra, India.

Keywords:

Echinochloa colona, Chromatography, Antiliidemic, Anti diabetic

Correspondence to Author:

Vijay Borkar

Department of Pharmaceutical Chemistry, Rajarshi Shahu College of Pharmacy, Buldana - 443001, Maharashtra, India.

E-mail: sonwane.gajanan@rediffmail.com

ABSTRACT: The current work comprises the assessment of antidiabetic activity of chloroform, ethyl acetate, and ethanol fractions and isolation of some phytoconstituents from chloroform fraction obtained from ethanolic extract of *Echinochloa colona*. The antidiabetic activity was performed using streptozocin induced diabetic model in male Wistar rats (150-200 g). The best restraint results were for metformin, chloroform, ethyl acetate and ethanol fraction was 5.85 ± 0.004 (90.08%), 6.65 ± 0.004 (67.36%), 6.96 ± 0.003 (60.14%) and 7.05 ± 0.004 (58.01%) respectively, comparing controlled diabetic rats which showed a significant reduction of blood glucose level. On total cholesterol level metformin, chloroform, ethyl acetate and ethanol fraction showed decrease in total cholesterol level by 12.16 ± 0.0044 (56.98%), 13.02 ± 0.004 (53.94%), 14.17 ± 0.004 (49.87%) and 16.37 ± 0.004 (42.24%) respectively. Significantly triglyceride was decreased by 10.39 ± 0.0044 (46.49%), 13.16 ± 0.004 (32.23%), 14.06 ± 0.004 (27.60%) and 14.56 ± 0.004 (42.24%) for metformin, chloroform, ethyl acetate and ethanol fraction respectively. Three important phytoconstituents were isolated from chloroform fraction, and structures were elucidated using spectroscopic techniques.

INTRODUCTION: *Echinochloa colona*, regularly known as jungle rice, deccan grass, or awnless farm grass, is a sort of wild grass beginning from tropical Asia. It was some time ago delegated types of *Panicum*. It is the wild precursor of the developed grain crop *Echinochloa frumentacea*, sawa millet. A few taxonomists treat the two taxa as one animal group, in which case the trained structures may likewise be alluded to as *E. colona* ^{1, 3}.

Echinochloa Colona Plant Profile:



Kingdom: Plantae
Division: Angiosperms
Class: Monocots
Order: Poales

	<p>QUICK RESPONSE CODE</p>
	<p>DOI: 10.13040/IJPSR.0975-8232.12(8).4354-64</p>
<p>This article can be accessed online on www.ijpsr.com</p>	
<p>DOI link: http://dx.doi.org/10.13040/IJPSR.0975-8232.12(8).4354-64</p>	

Family: Poaceae
Genus: *Echinochloa*
Species: *Echinochloa colona*

Botanical Description: *Echinochloa colona* (Poaceae), commonly known as Jungle rice (awnless barnyard grass) in India, is a yearly upright or decumbent, scattering, rooting from the inferior cutline node. It is a terrestrial, tufted, and erect grass propagates vegetatively but mostly by seeds, extensively spread in tropics & subtropics. It is also observed in South-Southeast Asia and tropical Africa. Leaves are spiral; alternatively, sessile linear more than 2 cm long, apex is acute with clasping base and parallel-veined. It culms ascending, or decumbent 10-100 cm long⁴.

Pharmacognostic Characteristic:

Macroscopy: Culms are 10-70 cm long, lower nodes are glabrous and upper nodes are glabrous. Sheaths are glabrous, ligules absent, blades are 8-10 cm long and cm⁻³⁻⁶ wide. Panicle is cm⁻²⁻¹², erect, rachises. A primary branch is 5-10 cm, erect otherwise ascending, spike-like, distant, devoid of secondary branches, axes glabrous or sparsely hispid. Spikelet is 2-3 mm, disarticulating at maturity, pubescent to hispid. Lower glumes are as long as spiklets; lower florest are sterile occasionally staminate. Lower lemmas are unawned, upper lemmas are 2.6-2.9 mm. Anthers are 0.7-0.8 mm, caryopses are 1.2-1.6 mm, whitish, and embryos are as long as caryopses. It is distributed in tropical and subtropical areas. It is weedy in North America grown in low-lying, damp to wet, including rice fields. Un branched somewhat widely-spaced panicle branches, which make this one of the easier species of the *Echinochloa colona*.

Traditional Uses: As per the literature, in India, seeds of grass are used to prepare a food dish called khichdi and are consumed during festivals, fasting days. The whole plant is used as fodder by grazing animals, and it cures ingestion. *Echinochloa colona*, is a significant crop. It is a reasonable wellspring of protein, which is exceptionally edible; furthermore, it is a fantastic wellspring of dietary fiber with great measures of solvent and insoluble portions. The starch content is low and gradually edible, which makes the *Echinochloa colona*, a characteristic fashioner nourishment. In

the current long periods of expanded diabetes mellitus, *E. colona*, could turn into perfect nourishment.

MATERIALS AND METHODS:

Sample Preparation: *E. colona* samples were collected from a paddy field in Dharmapuri, Tamil Nadu, India province in June 2013 at the flowering stage (red-purple flower). The samples were cleaned and separated into roots and shoots, then air-dried at room temperature and cut into small pieces (5 mm). The *E. colona* samples were extracted using soxhlet extraction methods, previously soaked with n-hexane to remove fatty residue. Then ethanol extract was fractionated (chloroform, acetone, ethyl acetate, ethanol, and methanol) from low to high polarity solvents. The plant parts were extracted using solvent at the rate of 1:5 (w/v) in 1 L beakers and covered with plastic film. The detailed procedure regarding the extraction was described by Gomaa and Abd Elgawad (2012). The beakers were kept in the dark at room temperature for 7 d. The solutions were separated from plant residues and evaporated using a rotary evaporator at 600 °C under reduced pressure. There were six different extracts of *E. colona* from the shoots and roots using n-hexane, extracts from the shoots and roots using chloroform, acetone, ethyl acetate, ethanol, and methanol.

Column Chromatography: The chloroform fraction of *Echinochloa colona* was subjected to column chromatography using silica gel as it has shown better pharmacological effect comparing to ethyl acetate and ethanol fraction and eluted with solvent mixtures of increasing polarity.

While elution, the chromatographic fractions were collected and monitored on TLC. All the fractions showing a single spot were pulled together, purified, and observed for its R_f value using TLC. The solvents like chloroform, acetone, ethyl acetate, ethanol, and methanol used for separation⁵.

Chromatographic Separation of Chloroform Fraction: Slurry of activated silica gel (150 °C for 3 h) was prepared with chloroform, and then the column was packed with slurry. The sample was loaded on the packed silica gel. After stabilization¹⁴²

column was eluted with mobile phase. Fractions were collected and analyzed by TLC.

Preparation of Mobile Phase: All the solvents, chloroform, acetone, ethyl acetate, ethanol, and methanol were distilled and then used for the preparation of the mobile phase. The composition of the mobile phase was made with increasing polarity solvents.

Column Packing: A clean and dry borosil glass column (60 cm, height; 3 cm, diameter) was aligned in a vertical position with the help of clamps attached to metal stand. A piece of cotton soaked in the mobile phase was positioned at the bottom of the column and quietly tamped down by means of a glass rod. The column was then filled about 1/3 volume by the mobile phase. The column was slowly and evenly filled, about 5/6 volumes full with the gradual addition of silica gel slurry. The stopcock was opened to allow the excess mobile phase to drain into the beaker. The side of the column was softly tapped with a cork during the process of packing to compact the silica gel. In the meantime, the stopcock was opened to run down the excess mobile phase. When the packing was finished, the excess mobile phase was drained until it just reaches the top level of silica.

Application of Sample: Weighed quantity of the sample was mixed with 1-2 g of activated silica gel and 3-4 ml of mobile phase to prepare a slurry. The slurry of the sample was added to the top of the packed silica in the column. The stopcock was opened to drain the excess mobile phase until it reaches top level of the sample. A thin disc (column diameter) of filter paper soaked in the mobile phase was placed on top of the bed to prevent disturbing the sample layer after addition of the mobile phase. The column was filled to the top with the mobile phase and allowed to stand for overnight (~24 h) to develop a chromatogram^{6,7}.

Anti Diabetic Activity: Anti-diabetic effect of chloroform, ethyl acetate, and ethanol fractions obtained from ethanolic extract of *Echinochloa colona* was performed using streptozotocin-induced diabetic model in Wistar rats. The doses of the fractions were made at 50 mg /mL. All male Wistar rats (150-200 g) were randomly divided into 7 groups, each containing 5 rats^{8,10}.

- **Group I:** Normal control (normal saline)
- **Group II:** Normal metformin control (150 mg/kg, *i. p.*)
- **Group III:** Diabetic control (normal saline)
- **Group IV:** Diabetic metformin control (150 mg/kg, *i. p.*)
- **Group V:** Diabetic (chloroform fraction)
- **Group VI:** Diabetic (ethyl acetate fraction)
- **Group VII:** Diabetic (ethanol fraction)

The standard drug and test samples were fed orally with an intragastric tube for 24 h experiment. Diabetes was induced (Group III-VII) by intraperitoneal injection (1 mL/kg) of freshly prepared streptozotocin (45 mg/kg), after baseline glucose was estimated.

After 48 h, blood samples were collected from the tail vein of all rats, and the blood glucose level was estimated. Blood glucose levels above ¹¹. 1 mmol/L in animals were selected for the studies considering the condition of diabetes was established.

Biochemical Analysis: After treatment, blood samples were collected with the help of disposable syringes from the tail vein of all rats of all groups before and at 0, 1, 2, 3, 6, 10, 16, and 24th h and analyzed for content of blood glucose using Glucometer (Bio Land, Germany). Then all the rats were sacrificed, and approximately 1-2 mL of blood was collected directly from the heart with the help of disposable syringes.

The blood samples were transferred to centrifuge tubes and allowed to centrifuge at 4000 rpm for 10 min; serum was collected used to determine total cholesterol (TC) and serum triglycerides (TG). Serum total cholesterol and triglycerides were estimated at 505 and 546 nm, respectively, using cholesterol oxidase/ p-amino antipyrine (CHO / PAP) method and glycerol 3- phosphate oxidase (GPO) method, respectively according to manufacturer's protocol^{11,13}.

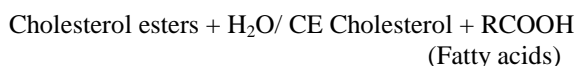
Determination of Total Cholesterol: Total cholesterol was determined by reagents kits of Reckon Diagnostics Pvt. Ltd., Baroda.

Method: CHOD-PAP method was used described by Allain *et al.*, 1974. It is an extremely specific¹⁴³

enzymatic colorimetric method for measurements in the visible range (505 nm), well-known for its high flexibility^{14, 15}.

Test Principle: The esters of cholesterol are hydrolyzed to cholesterol by cholesterol esterase (CE). The cholesterol is then oxidized by cholesterol oxidase (CO) to cholesterol 4-en-3-one with the concurrent creation of H₂O₂.

H₂O₂ then reacts with 4-aminoantipyrine (AAP) and phenolic compounds in the presence of peroxidase to give colored complex red at 505 nm (500-540 nm, GREEN filter). The color intensity produced is directly proportional to the concentration of total cholesterol in the test samples.



Sample Material: Serum

Procedure: The three tubes were labeled accordingly as blank, standard, and test. 0.01ml standard and serum were added to the corresponding tubes. 1 mL Cholesterol reagent was placed in all tubes, *i.e.* blank, standard, and test, mixed well, and incubated (10 min at 37 °C). Then absorbance was red of test and standard at 505 nm or with green filter against blank reagent.

Calculations:

$$\text{Cholesterol (mg/dl)} = \frac{\text{Absorbance in Test} \times 200}{\text{Absorbance in Standard}}$$

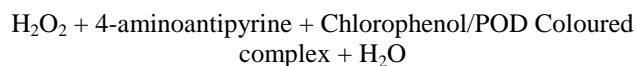
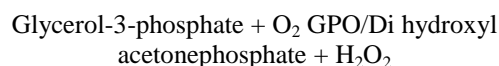
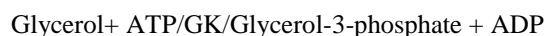
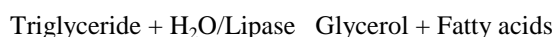
Determination of Triglycerides: Triglyceride was determined by reagents kits of Reckon Diagnostics Pvt. Ltd., Baroda.

Method: High performance enzymatic GPO-PAP method modified according to Fossati 1982; McGowan *et al.*, 1983.

Test Principle: Triglyceride is hydrolyzed sequentially to Di & Monoglycerides and finally to Glycerol by Lipase. Glycerol kinase (GK) by

means of ATP as PO₄ source converts Glycerol to Glycerol-3-phosphate (G-3-Phosphate). G-3-phosphate Oxidase (GPO) oxidised G-3- phosphate to Di-hydroxy acetone phosphate & hydrogen peroxide is formed.

Hydrogen peroxide in presence Peroxidase (POD) oxidised to oxidise 4 amino antipyrine and chlorophenol to a pink coloured complex, which is measured at 546 nm (500-550 nm or with green filter). Absorbance is proportional to Triglycerides concentration.



Sample Material Serum

Procedure: 0.05 mL serum, standard, and distilled water were placed in the tubes marked as a test, standard and blank, respectively.

Then working solution 1 mL of was added to every tube, mixed well, and incubated (20 min at 37 °C). After incubation, 1.5 mL of distilled water was added to every tube, mixed well. Absorbance was red of test and standard against the blank at 546 nm (500-550 nm)

Calculations:

$$\text{Triglyceride (mg/dl)} = \frac{\text{Absorbance in Test}}{\text{Absorbance in Standard}} \times 200$$

Elution: Elution was carried out with the flow rate (1 ml/min). The mobile phase was added at the top of the column from the solvent reservoir, and fractions were collected in an amber colored bottle.

Fractions were concentrated by evaporating at room temperature until volume was reduced to ¼ of the total volume. TLC of concentrated fractions was carried out to detect similarity between the chromatograms of different fractions.

Source	Fraction	Mobile phase	Abbreviation
<i>E. colona</i>	Chloroform	Chloroform: Ethanol 40:60	EC-I
		Chloroform: Ethanol 30:70	EC-II
		Chloroform: Ethanol 10:90	EC-III

Thin Layer Chromatography (TLC): TLC of each fraction was carried out during column chromatography, and the R_f value for EC-I (0.48), EC-II (0.74), EC-III (0.68) was observed.

Characterization of the Isolated Compounds from *E. Colona*:

EC-I: The EC-I fraction was collected at 40:60 in % ratio of (CHCl₃: C₂H₅OH). The isolated compound was white amorphous powder. The compound was studied for its qualitative properties and found to be positive with the ferric chloride test, and the phenolic nature of the compound was confirmed. The M.P. of the compound was 145-147 °C.

The UV spectrum showed λ_{max} , 220 nm, Ethanol with typical aromatic bands confirming a substituted aromatic benzoic acid. In the FTIR (KBr, cm⁻¹) signal at 3400 (-OH), 2935 (Ar-H), 1688(-COOH), ¹HNMR (CDCl₃, 400 MHz) signals at δ 11.80 (-COOH), 6.5 (Ar-H), 5.10 (Ar-OH), 2.33 (Ar-CH₃) and the peak of molecular ion was observed at m/z 184 matching to C₈H₈O₅, and main peak at 166 [184-(H₂O)]⁺ with other fragments at m/z : 120, 84, 42, 27 were observed.

The above spectral data suggested isolated compound is 2, 3, 4-trihydroxy, 6-methyl benzoic acid. The IR, ¹HNMR, and MASS spectra were shown in following Fig. 1 to 3.

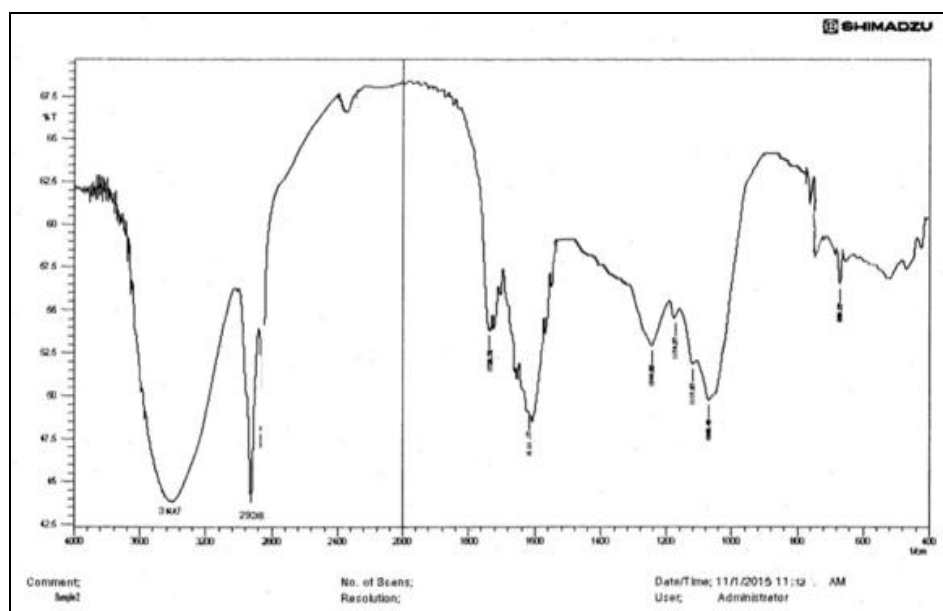


FIG. 1: IR SPECTRA OF EC-I FRACTION ISOLATED FROM *E. COLONA*

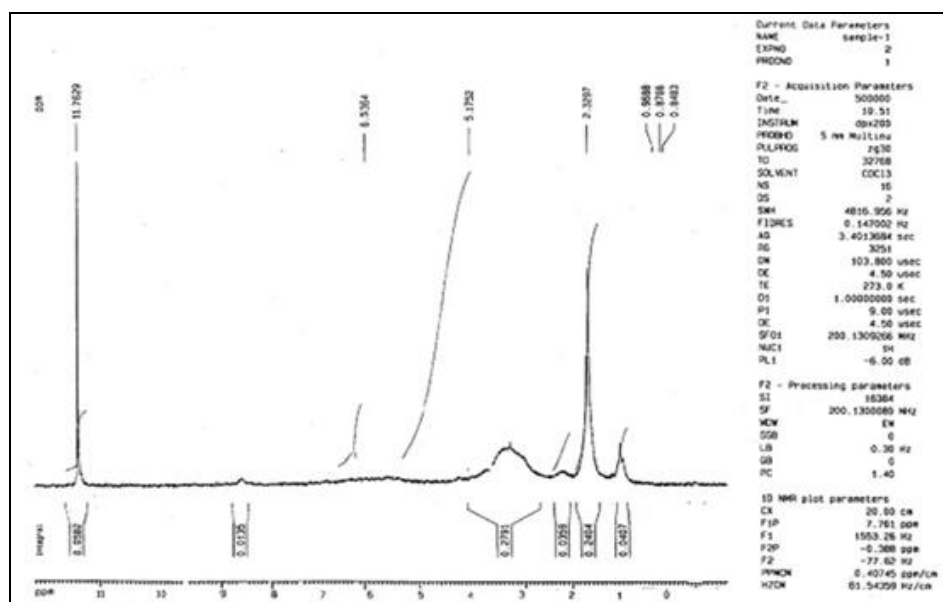


FIG. 2: ¹H NMR SPECTRA OF EC-I FRACTION ISOLATED FROM *E. COLONA*

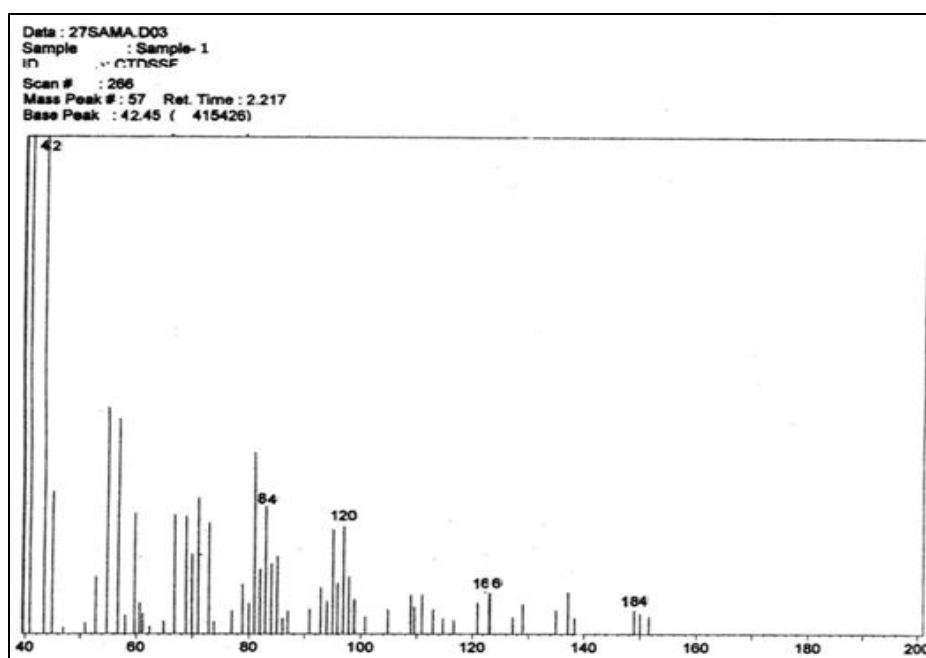


FIG. 3: MASS SPECTRA OF EC-I FRACTION ISOLATED FROM *E. COLONA*

EC-II: The EC-II fraction was collected at 30:70 in % ratio of ($\text{CHCl}_3:\text{C}_2\text{H}_5\text{OH}$). The isolated compound was white crystalline powder with a characteristic odour. The compound was studied for its qualitative properties and found to be positive with the Liebermann-Burchard test, and the steroidal nature of the compound was confirmed. The M.P. of the compound was 137-139 °C. UV spectrum showed λ_{max} , 210 nm, ethanol. In the FTIR (KBr, cm^{-1}) 3545 (-OH), 2931 (-CH₂), 2860 (-CH), 1637 (-C=C-), 1033 (-C-O), ¹HNMR (CDCl_3 , 400 MHz) signals at δ 1.01, 1.04, 1.06,

1.04, 1.17, 1.21(-CH₃), 1.57, 1.98, 1.13, 1.79, 1.24, 1.27, 1.35, 1.34, 1.25, 1.29, (-CH₂-), 3.25(--CH-), 5.37 (H-cyclohexene) and peak of molecular ion was observed at 414.7 corresponding to $\text{C}_{29}\text{H}_{50}\text{O}$ with other characteristic fragmentations of m/z : 414, 396, 381, 330, 290, 273, 255, 212, 199 and 173 were observed. The above spectral data and those reported in the literature support the proposed structure was β -sitosterol 113, 114, 115. The IR, ¹HNMR, and MASS spectra were shown in the following Fig. 4 to 6.

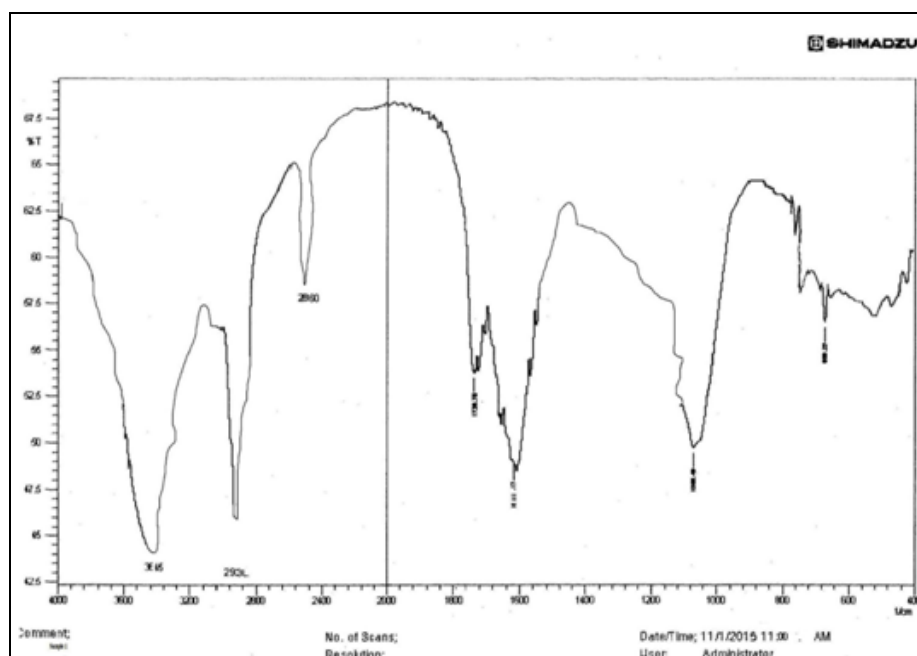


FIG. 4: IR SPECTRA OF EC-II FRACTION ISOLATED FROM *E. COLONA*

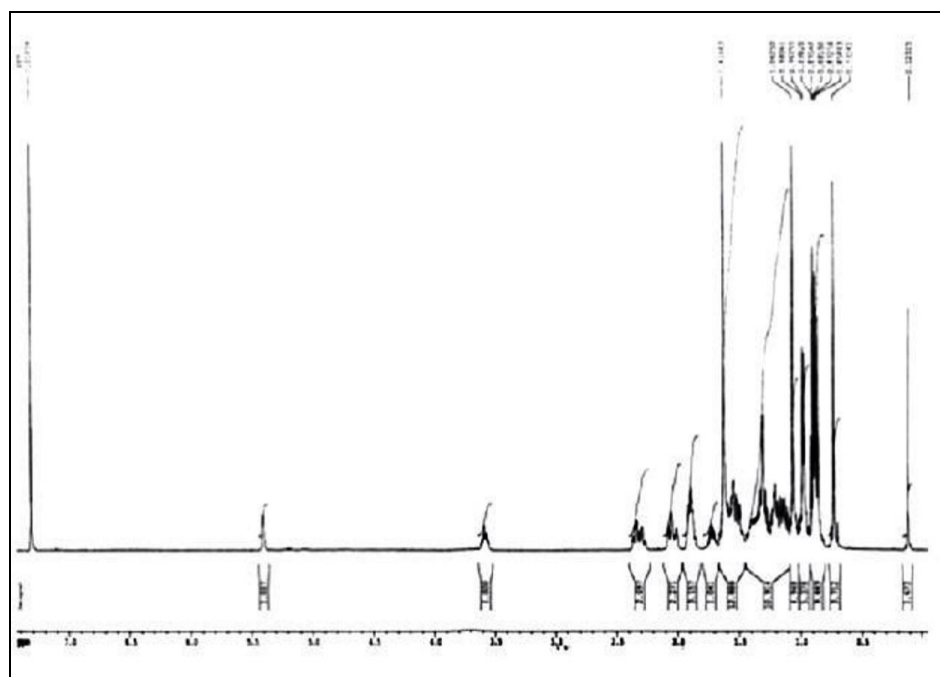


FIG. 5: ^1H NMR SPECTRA OF EC-II FRACTION ISOLATED FROM *E. COLONA*

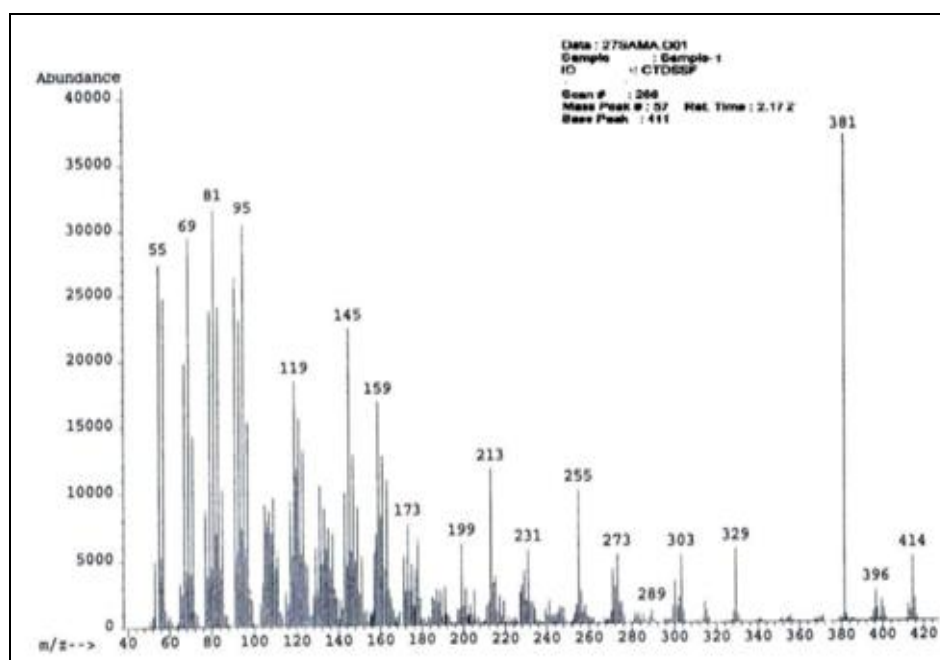


FIG. 6: MASS SPECTRA OF EC-II FRACTION ISOLATED FROM *E. COLONA*

EC-III: The EC-III fraction was collected at 10:90 in % ratio of ($\text{CHCl}_3:\text{C}_2\text{H}_5\text{OH}$). The isolated compound was white crystalline powder with a characteristic odour. The compound was studied for its qualitative properties and found to be positive with the ester test, and the ester nature of the compound was confirmed.

The melting point of the compound was carried out and found to be 150- 152 $^\circ\text{C}$. The UV spectrum showed λ_{max} , 226 nm, methanol. In the FTIR (KBr,

cm^{-1}) band at 1736 (RCOOR) and 3400 (Ar-OH), ^1H NMR (CDCl_3 , 400 MHz) at δ 1.25 (- CH_3), 4.65 (- CH_2 -), 4.58 (Ar-OH) and a peak of molecular ion was observed at m/z 198 correspondings to $\text{C}_9\text{H}_{10}\text{O}_5$ with other fragments at 183, 149 [$183-\text{CH}_3$] $^+$, 129, 111, 97, 83, 69, 57, 43 were observed.

The above spectral data suggested isolated compound was ethyl 3, 4, 5-trihydroxy benzoate. The IR, ^1H NMR, and MASS spectra were shown in the following Fig. 7 to 9.

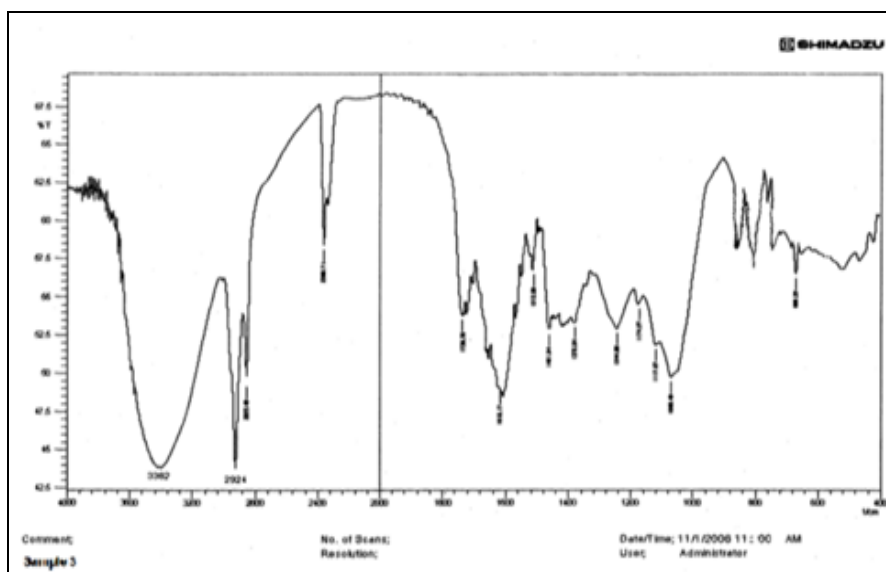


FIG. 7: IR SPECTRA OF EC-III FRACTION ISOLATED FROM *E. COLONA*

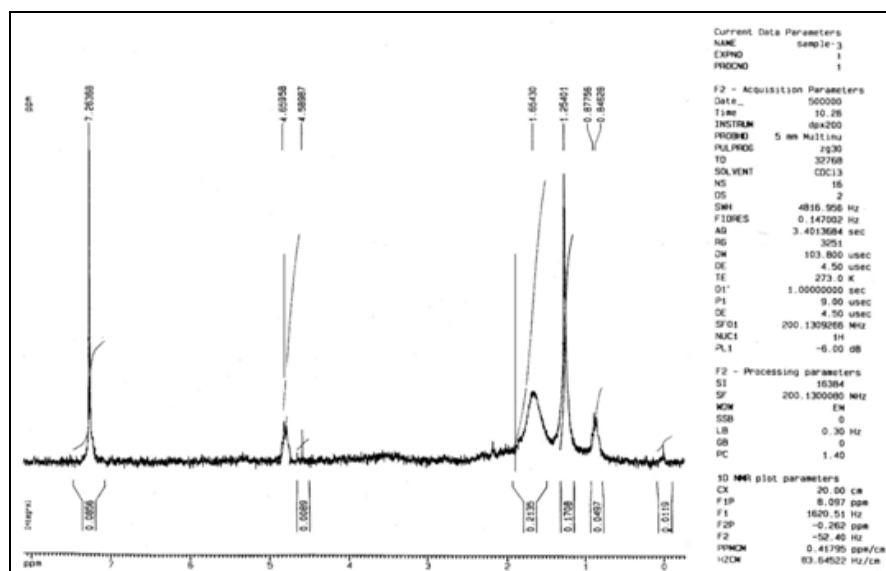


FIG. 8: 1H NMR SPECTRA OF EC-III FRACTION ISOLATED FROM *E. COLONA*

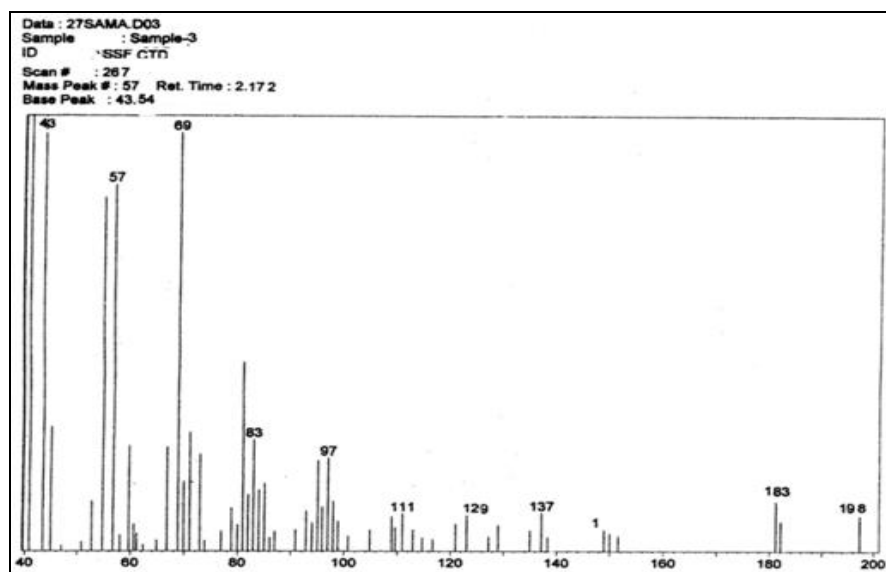


FIG. 9: MASS SPECTRA OF EC-III FRACTION ISOLATED FROM *E. COLONA*

Anti Diabetic Activity: The effects of different fractions (single dose-50 mg/mL) obtained from ethanolic extracts of *E. colonaupon* blood glucose (mmol/L), serum total cholesterol & triglycerides (mmol/L) were investigated within control and streptozotocin induced diabetic rats. Metformin HCl (150 mg/mL) was used as a standard anti-diabetic agent.

Effects of Various Fractions on Blood Glucose: A decrease in blood glucose level was observed in

animals treated with different fractions of *E. colonaat*^{0, 1, 2, 3, 6, 10, 16}, and 24th h **Fig. 1**.

The blood glucose level was significantly reduced at 24th h of the experiment ($p < 0.01$) for metformin, chloroform, ethyl acetate, and ethanol fraction, it was 5.85 ± 0.004 (90.08%) 6.65 ± 0.004 (67.36%), 6.96 ± 0.003 (60.14%) and 7.05 ± 0.004 (58.01%) respectively comparing controlled diabetic rats **Table 1**.

TABLE 1: EFFECT OF DIFFERENT FRACTIONS OF *E. COLONA* ON BLOOD GLUCOSE IN DIABETIC RATS ON ONE DAY TREATMENT

Groups (Treatment)	Blood glucose levels (mmol/L) at Hours							
	0	1	2	3	6	10	16	24
I	7.25 ±	7.26 ±	7.27 ±	7.28 ±	7.29 ±	7.30 ±	7.31 ±	7.32 ±
10 ml saline	0.004	0.004	0.004	0.004	0.004	0.002	0.002	0.004
II	7.26 ±	7.24 ±	7.28 ±	7.20 ±	7.19 ±	6.17 ±	6.05 ±	4.13 ±
150 mg/kg	0.004	0.003	0.004	0.002	0.004	0.004	0.003	0.004
III	11.01 ±	11.50 ±	11.95 ±	12.25 ±	12.75 ±	13.10 ±	13.55 ±	13.95 ±
10 ml saline	0.003	0.003	0.004	0.004	0.004	0.004	0.003	0.003
IV	11.12 ±	10.81 ±	9.05 ±	8.75 ±	6.65 ±	7.08 ±	6.16 ±	5.85 ±
150 mg/kg	0.003	0.20	0.004	0.004	0.004	0.004	0.004	0.004
V	11.13 ±	10.61 ±	10.15 ±	9.95 ±	8.85 ±	7.28 ±	6.96 ±	6.65 ±
50 mg/ml	0.004	0.002	0.008	0.005	0.004	0.004	0.004	0.004
VI	11.13 ±	10.92 ±	10.41 ±	10.31 ±	9.55 ±	7.98 ±	7.86 ±	6.96 ±
50 mg/ml	0.004	0.004	0.004	0.004	0.004	0.003	0.002	0.003
VII	11.14 ±	11.02 ±	10.91 ±	10.71 ±	9.98 ±	9.07 ±	7.66 ±	7.05 ±
50 mg/ml	0.004	0.004	0.005	0.003	0.004	0.004	0.004	0.004

All values are expressed as mean ± SEM, (n=5) in every group, $p < 0.01$, p-values were calculated and compared with control by ANOVA method followed by Dunnett's test

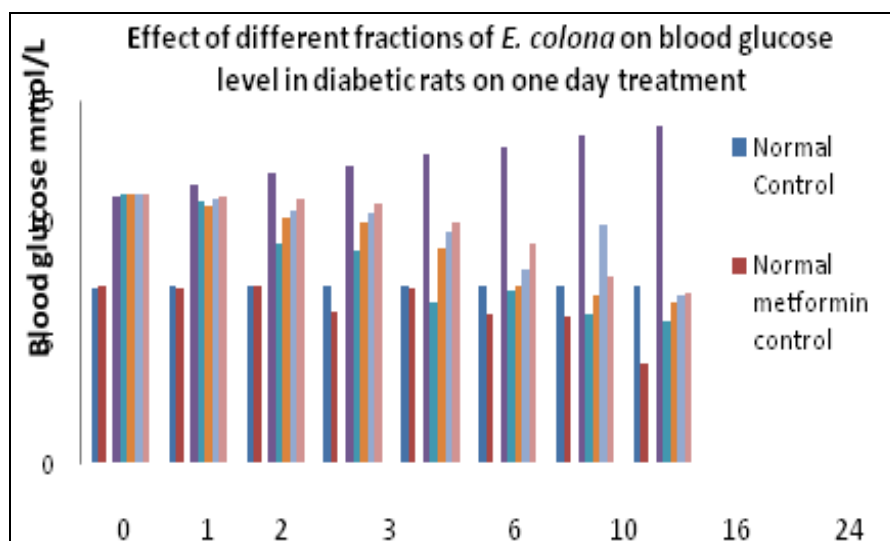


FIG. 10: EFFECT OF DIFFERENT FRACTIONS OF *E. COLONA* ON BLOOD GLUCOSE LEVEL IN DIABETIC RATS ON ONE DAY TREATMENT

Effect of Various Fractions on Total Cholesterol and Triglyceride: After 24 h treatment of different fractions of *E. colona* there was decreased in total cholesterol and triglyceride on diabetic rats **Fig. 2**.

Metformin, chloroform, ethyl acetate and ethanol fraction showed decrease in total cholesterol level by 12.16 ± 0.0044 (56.98%) 13.02 ± 0.004 (53.94%) 14.17 ± 0.004 (49.87%) and 16.37 ± 149

0.004 (42.24%) respectively, whereas the triglyceride was decreased by 10.39 ± 0.0044 (46.49%) 13.16 ± 0.004 (32.23%) 14.06 ± 0.004 (27.60%) and 14.56 ± 0.004 (42.24%) for metformin, chloroform, ethyl acetate and ethanol fraction respectively when compared to diabetic control groups **Table 2**.

TABLE 2: EFFECTS OF DIFFERENT FRACTIONS OF *E. COLONA* ON TOTAL CHOLESTEROL & TRIGLYCERIDES IN DIABETIC RAT ON ONE DAY TREATMENT

Parameter (mmol/L)	Groups						
	I	II	III	IV	V	VI	VII
Total Cholesterol	14.37± 0.003	12.24± 0.004*	28.27± 0.004**	12.16± 0.004**	13.02± 0.004**	14.17± 0.004**	16.37± 0.004**
Total Glycerides	12.41± 0.004	10.31± 0.003*	19.42± 0.004*	10.39± 0.004*	13.16± 0.004*	14.06± 0.004*	14.56± 0.004*

All values are expressed as mean \pm SEM, (n=5) in every group, *p <0.01, considered extremely significant, p-values were calculated and compared with control by ANOVA method followed by Dunnett's test.

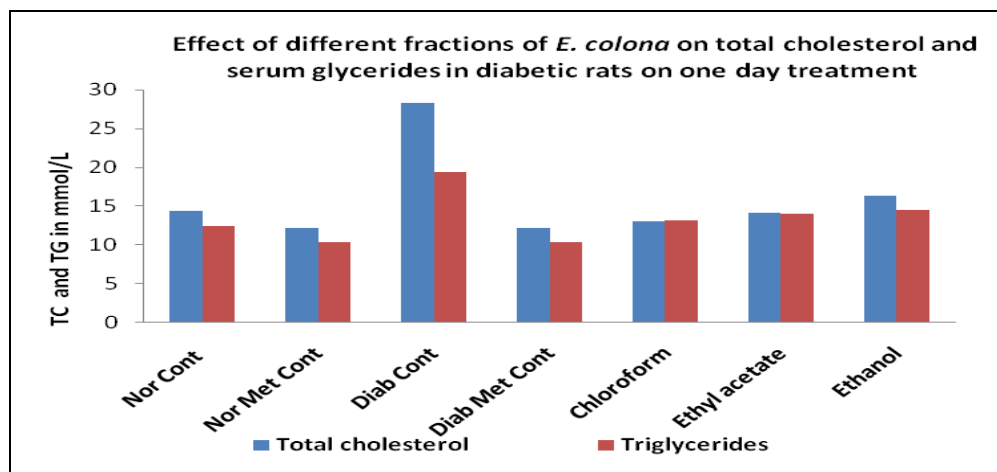


FIG. 11: EFFECTS OF DIFFERENT FRACTIONS OF *E. COLONA* ON TOTAL CHOLESTEROL AND SERUM GLYCERIDES IN DIABETIC RATS ON ONE DAY TREATMENT

CONCLUSION: Given the potent results of the extracts tested in this article against diabetes and the factor responsible for the same (triglycerides). A decrease in blood glucose level was observed in animals treated with different fractions of *E. colona*.

After 24 h treatment of different fractions of *E. colona* there was a significant decrease in total cholesterol and triglyceride on diabetic rats when treated with chloroform fraction. The chloroform fraction exhibiting significant anti-diabetic activity was chromatographed to isolate three phyto constituents 2, 3, 4-trihydroxy, 6-methyl benzoic acid, β -sitosterol, and ethyl 3, 4, 5-trihydroxy benzoate.

ACKNOWLEDGEMENT: Authors are thankful to Principal Rajarshi Shahu College of Pharmacy, Buldhana, for providing the necessary facilities

CONFLICTS OF INTEREST: The authors have not declared any conflict of interest.

REFERENCES:

- Peerzada AM, Bajwa AA, Ali HH and Chauhan BS: Biology, Impact and Management of *Echinochloa Colona* (L.) Link. Crop Prot 2016; 83(1): 56-66.
- Chopra N, Tewari G, Tewari LM, Upreti B and Pandey N: Allelopathic effect of *Echinochloa Colona* L. and *Cyperus iria* l. weed extracts on the seed germination and seedling growth of rice and soyabean. Adv Agric 2017; (1): 1-5.
- Pan L, Yu Q, Han H, Mao L, Nyporko A, Fan LJ, Bai L and Powles S: Aldo-keto reductase metabolizes glyphosate and confers glyphosate resistance in *Echinochloa colona*. Plant Physiol 2019; 1(1): 239-50.
- Chauhan BS and Johnson DE: Seed germination ecology of junglerice (*Echinochloa colona*): a major weed of rice. Weed Sci 2009; 57(3): 235-40.
- Coskun O: Separation techniques chromatography. North Clin Istanbul 2016; 1(1): 123-35.
- Schweiger S, Hinterberger S and Jungbauer A: Column-to-column packing variation of disposable pre-packed columns for protein chromatography. J Chromatogr A 2017; 1527(1): 70-79.
- Mauer L and Reuhs BL: High-performance liquid chromatography bradley. Food Anal 2017; 1(1): 213-26.
- Wang T, yang Li, Q Bi and shun K: Bioactive flavonoids in medicinal plants: structure, activity and biological fate. Asian J Pharm Sci 2018; 13(1): 12-23.
- Anti-Phishing Working Group. Phishing Activity Trends Report 1 Quarter. Most 2010; 1(3); 1-12.

10. Ahad Hussain S, Greeshma Namilikonda M, Karan Chandra T and Arif Pasha M: A review on medi plants with anti-dia activity. Int Journal of Adv Res 2020; 8(3): 902-17.
11. Deng X, Liu B, Li J, Zhang J, Zhao Y and Xu K: Blood biochemical characteristics of patients with coronavirus disease 2019 (covid-19): a systemic review and meta-analysis. Clin Chem Lab Med 2020; 1(1): 145-56.
12. Qian ZP, Mei X, Zhang YY, Zou Y, Zhang ZG, Zhu H, Guo HY, Liu Y, Ling Y, Zhang XY, Wang JF and Lu HZ: Analysis of baseline liver biochemical parameters in 324 cases with novel coronavirus pneumonia in shanghai area. Zhonghua Gan Zang Bing Za Zhi 2020; 28 (3): 229-33.
13. Ali Abd El-Aal Y, Mohamed Abdel-Fattah D and El-Dawy Ahmed K: Some biochemical studies on trans fatty acid-containing diet. Diabetes Metab Syndr Clin Res Rev 2019; 13(3): 1753-57.
14. Kishore J, Gupta N, Kohli C and Kumar N: Prevalence of hypertension and determination of its risk factors in rural delhi. Int J Hypertens 2016; (1): 2016-25.
15. Nordestgaard BG, Langsted A, Mora S and Watts GF: Fasting Is Not routinely required for determination of a lipid profile: clinical and laboratory implications including flagging at desirable concentration cutpoints-a joint consensus statement from the european atherosclerosis soc and european federat. C Chem 2016; 62(7): 930-46.

How to cite this article:

Borkar V, Sonwane G, Devhare P, Diwre R and Jain S: Evaluation of antidiabetic activity of *Echinochloa colona* plant extract. Int J Pharm Sci & Res 2021; 12(8): 4354-64. doi: 10.13040/IJPSR.0975-8232.12(8).4354-64.

All © 2013 are reserved by International Journal of Pharmaceutical Sciences and Research. This Journal licensed under a Creative Commons Attribution-NonCommercial-ShareAlike 3.0 Unported License.

This article can be downloaded to **Android OS** based mobile. Scan QR Code using Code/Bar Scanner from your mobile. (Scanners are available on Google Playstore)



Received on 20 August 2019; received in revised form, 29 January 2021; accepted, 19 May 2021; published 01 August 2021

EVALUATION OF ANTIDIABETIC ACTIVITY OF *ECHINOCHLOA COLONA* PLANT EXTRACT

Vijay Borkar ^{*1}, Gajanan Sonwane ¹, Parmeshwar Devhare ¹, Rushikesh Diwre ¹ and Shirish Jain ²

Department of Pharmaceutical Chemistry ¹, Department of Pharmacology ², Rajarshi Shahu College of Pharmacy, Buldana - 443001, Maharashtra, India.

Keywords:

Echinochloa colona, Chromatography, Antiliidemic, Anti diabetic

Correspondence to Author:

Vijay Borkar

Department of Pharmaceutical Chemistry, Rajarshi Shahu College of Pharmacy, Buldana - 443001, Maharashtra, India.

E-mail: sonwane.gajanan@rediffmail.com

ABSTRACT: The current work comprises the assessment of antidiabetic activity of chloroform, ethyl acetate, and ethanol fractions and isolation of some phytoconstituents from chloroform fraction obtained from ethanolic extract of *Echinochloa colona*. The antidiabetic activity was performed using streptozocin induced diabetic model in male Wistar rats (150-200 g). The best restraint results were for metformin, chloroform, ethyl acetate and ethanol fraction was 5.85 ± 0.004 (90.08%), 6.65 ± 0.004 (67.36%), 6.96 ± 0.003 (60.14%) and 7.05 ± 0.004 (58.01%) respectively, comparing controlled diabetic rats which showed a significant reduction of blood glucose level. On total cholesterol level metformin, chloroform, ethyl acetate and ethanol fraction showed decrease in total cholesterol level by 12.16 ± 0.0044 (56.98%), 13.02 ± 0.004 (53.94%), 14.17 ± 0.004 (49.87%) and 16.37 ± 0.004 (42.24%) respectively. Significantly triglyceride was decreased by 10.39 ± 0.0044 (46.49%), 13.16 ± 0.004 (32.23%), 14.06 ± 0.004 (27.60%) and 14.56 ± 0.004 (42.24%) for metformin, chloroform, ethyl acetate and ethanol fraction respectively. Three important phytoconstituents were isolated from chloroform fraction, and structures were elucidated using spectroscopic techniques.

INTRODUCTION: *Echinochloa colona*, regularly known as jungle rice, deccan grass, or awnless farm grass, is a sort of wild grass beginning from tropical Asia. It was some time ago delegated types of *Panicum*. It is the wild precursor of the developed grain crop *Echinochloa frumentacea*, sawa millet. A few taxonomists treat the two taxa as one animal group, in which case the trained structures may likewise be alluded to as *E. colona* ^{1, 3}.

Echinochloa Colona Plant Profile:



Kingdom: Plantae
Division: Angiosperms
Class: Monocots
Order: Poales

QUICK RESPONSE CODE 	DOI: 10.13040/IJPSR.0975-8232.12(8).4354-64
	This article can be accessed online on www.ijpsr.com
DOI link: http://dx.doi.org/10.13040/IJPSR.0975-8232.12(8).4354-64	

Family: Poaceae
Genus: *Echinochloa*
Species: *Echinochloa colona*

Botanical Description: *Echinochloa colona* (Poaceae), commonly known as Jungle rice (awnless barnyard grass) in India, is a yearly upright or decumbent, scattering, rooting from the inferior cutline node. It is a terrestrial, tufted, and erect grass propagates vegetatively but mostly by seeds, extensively spread in tropics & subtropics. It is also observed in South-Southeast Asia and tropical Africa. Leaves are spiral; alternatively, sessile linear more than 2 cm long, apex is acute with clasping base and parallel-veined. It culms ascending, or decumbent 10-100 cm long⁴.

Pharmacognostic Characteristic:

Macroscopy: Culms are 10-70 cm long, lower nodes are glabrous and upper nodes are glabrous. Sheaths are glabrous, ligules absent, blades are 8-10 cm long and cm⁻³⁻⁶ wide. Panicle is cm⁻²⁻¹², erect, rachises. A primary branch is 5-10 cm, erect otherwise ascending, spike-like, distant, devoid of secondary branches, axes glabrous or sparsely hispid. Spikelet is 2-3 mm, disarticulating at maturity, pubescent to hispid. Lower glumes are as long as spiklets; lower florest are sterile occasionally staminate. Lower lemmas are unawned, upper lemmas are 2.6-2.9 mm. Anthers are 0.7-0.8 mm, caryopses are 1.2-1.6 mm, whitish, and embryos are as long as caryopses. It is distributed in tropical and subtropical areas. It is weedy in North America grown in low-lying, damp to wet, including rice fields. Un branched somewhat widely-spaced panicle branches, which make this one of the easier species of the *Echinochloa colona*.

Traditional Uses: As per the literature, in India, seeds of grass are used to prepare a food dish called khichdi and are consumed during festivals, fasting days. The whole plant is used as fodder by grazing animals, and it cures ingestion. *Echinochloa colona*, is a significant crop. It is a reasonable wellspring of protein, which is exceptionally edible; furthermore, it is a fantastic wellspring of dietary fiber with great measures of solvent and insoluble portions. The starch content is low and gradually edible, which makes the *Echinochloa colona*, a characteristic fashioner nourishment. In

the current long periods of expanded diabetes mellitus, *E. colona*, could turn into perfect nourishment.

MATERIALS AND METHODS:

Sample Preparation: *E. colona* samples were collected from a paddy field in Dharmapuri, Tamil Nadu, India province in June 2013 at the flowering stage (red-purple flower). The samples were cleaned and separated into roots and shoots, then air-dried at room temperature and cut into small pieces (5 mm). The *E. colona* samples were extracted using soxhlet extraction methods, previously soaked with n-hexane to remove fatty residue. Then ethanol extract was fractionated (chloroform, acetone, ethyl acetate, ethanol, and methanol) from low to high polarity solvents. The plant parts were extracted using solvent at the rate of 1:5 (w/v) in 1 L beakers and covered with plastic film. The detailed procedure regarding the extraction was described by Gomaa and Abd Elgawad (2012). The beakers were kept in the dark at room temperature for 7 d. The solutions were separated from plant residues and evaporated using a rotary evaporator at 600 °C under reduced pressure. There were six different extracts of *E. colona* from the shoots and roots using n-hexane, extracts from the shoots and roots using chloroform, acetone, ethyl acetate, ethanol, and methanol.

Column Chromatography: The chloroform fraction of *Echinochloa colona* was subjected to column chromatography using silica gel as it has shown better pharmacological effect comparing to ethyl acetate and ethanol fraction and eluted with solvent mixtures of increasing polarity.

While elution, the chromatographic fractions were collected and monitored on TLC. All the fractions showing a single spot were pulled together, purified, and observed for its R_f value using TLC. The solvents like chloroform, acetone, ethyl acetate, ethanol, and methanol used for separation⁵.

Chromatographic Separation of Chloroform Fraction: Slurry of activated silica gel (150 °C for 3 h) was prepared with chloroform, and then the column was packed with slurry. The sample was loaded on the packed silica gel. After stabilization¹⁵³

column was eluted with mobile phase. Fractions were collected and analyzed by TLC.

Preparation of Mobile Phase: All the solvents, chloroform, acetone, ethyl acetate, ethanol, and methanol were distilled and then used for the preparation of the mobile phase. The composition of the mobile phase was made with increasing polarity solvents.

Column Packing: A clean and dry borosil glass column (60 cm, height; 3 cm, diameter) was aligned in a vertical position with the help of clamps attached to metal stand. A piece of cotton soaked in the mobile phase was positioned at the bottom of the column and quietly tamped down by means of a glass rod. The column was then filled about 1/3 volume by the mobile phase. The column was slowly and evenly filled, about 5/6 volumes full with the gradual addition of silica gel slurry. The stopcock was opened to allow the excess mobile phase to drain into the beaker. The side of the column was softly tapped with a cork during the process of packing to compact the silica gel. In the meantime, the stopcock was opened to run down the excess mobile phase. When the packing was finished, the excess mobile phase was drained until it just reaches the top level of silica.

Application of Sample: Weighed quantity of the sample was mixed with 1-2 g of activated silica gel and 3-4 ml of mobile phase to prepare a slurry. The slurry of the sample was added to the top of the packed silica in the column. The stopcock was opened to drain the excess mobile phase until it reaches top level of the sample. A thin disc (column diameter) of filter paper soaked in the mobile phase was placed on top of the bed to prevent disturbing the sample layer after addition of the mobile phase. The column was filled to the top with the mobile phase and allowed to stand for overnight (~24 h) to develop a chromatogram^{6,7}.

Anti Diabetic Activity: Anti-diabetic effect of chloroform, ethyl acetate, and ethanol fractions obtained from ethanolic extract of *Echinochloa colona* was performed using streptozotocin-induced diabetic model in Wistar rats. The doses of the fractions were made at 50 mg /mL. All male Wistar rats (150-200 g) were randomly divided into 7 groups, each containing 5 rats^{8,10}.

- **Group I:** Normal control (normal saline)
- **Group II:** Normal metformin control (150 mg/kg, *i. p.*)
- **Group III:** Diabetic control (normal saline)
- **Group IV:** Diabetic metformin control (150 mg/kg, *i. p.*)
- **Group V:** Diabetic (chloroform fraction)
- **Group VI:** Diabetic (ethyl acetate fraction)
- **Group VII:** Diabetic (ethanol fraction)

The standard drug and test samples were fed orally with an intragastric tube for 24 h experiment. Diabetes was induced (Group III-VII) by intraperitoneal injection (1 mL/kg) of freshly prepared streptozotocin (45 mg/kg), after baseline glucose was estimated.

After 48 h, blood samples were collected from the tail vein of all rats, and the blood glucose level was estimated. Blood glucose levels above ¹¹. 1 mmol/L in animals were selected for the studies considering the condition of diabetes was established.

Biochemical Analysis: After treatment, blood samples were collected with the help of disposable syringes from the tail vein of all rats of all groups before and at 0, 1, 2, 3, 6, 10, 16, and 24th h and analyzed for content of blood glucose using Glucometer (Bio Land, Germany). Then all the rats were sacrificed, and approximately 1-2 mL of blood was collected directly from the heart with the help of disposable syringes.

The blood samples were transferred to centrifuge tubes and allowed to centrifuge at 4000 rpm for 10 min; serum was collected used to determine total cholesterol (TC) and serum triglycerides (TG). Serum total cholesterol and triglycerides were estimated at 505 and 546 nm, respectively, using cholesterol oxidase/ p-amino antipyrine (CHO / PAP) method and glycerol 3- phosphate oxidase (GPO) method, respectively according to manufacturer's protocol^{11,13}.

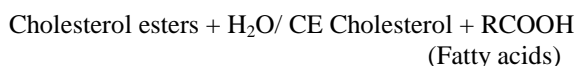
Determination of Total Cholesterol: Total cholesterol was determined by reagents kits of Reckon Diagnostics Pvt. Ltd., Baroda.

Method: CHOD-PAP method was used described by Allain *et al.*, 1974. It is an extremely specific¹⁵⁴

enzymatic colorimetric method for measurements in the visible range (505 nm), well-known for its high flexibility^{14, 15}.

Test Principle: The esters of cholesterol are hydrolyzed to cholesterol by cholesterol esterase (CE). The cholesterol is then oxidized by cholesterol oxidase (CO) to cholesterol 4-en-3-one with the concurrent creation of H₂O₂.

H₂O₂ then reacts with 4-aminoantipyrine (AAP) and phenolic compounds in the presence of peroxidase to give colored complex red at 505 nm (500-540 nm, GREEN filter). The color intensity produced is directly proportional to the concentration of total cholesterol in the test samples.



Sample Material: Serum

Procedure: The three tubes were labeled accordingly as blank, standard, and test. 0.01ml standard and serum were added to the corresponding tubes. 1 mL Cholesterol reagent was placed in all tubes, *i.e.* blank, standard, and test, mixed well, and incubated (10 min at 37 °C). Then absorbance was red of test and standard at 505 nm or with green filter against blank reagent.

Calculations:

Cholesterol (mg/dl) = Absorbance in Test × 200 / Absorbance in Standard

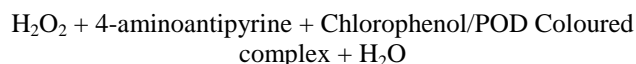
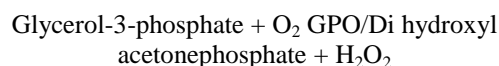
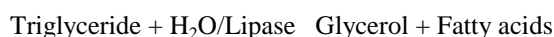
Determination of Triglycerides: Triglyceride was determined by reagents kits of Reckon Diagnostics Pvt. Ltd., Baroda.

Method: High performance enzymatic GPO-PAP method modified according to Fossati 1982; McGowan *et al.*, 1983.

Test Principle: Triglyceride is hydrolyzed sequentially to Di & Monoglycerides and finally to Glycerol by Lipase. Glycerol kinase (GK) by

means of ATP as PO₄ source converts Glycerol to Glycerol-3-phosphate (G-3-Phosphate). G-3-phosphate Oxidase (GPO) oxidised G-3- phosphate to Di-hydroxy acetone phosphate & hydrogen peroxide is formed.

Hydrogen peroxide in presence Peroxidase (POD) oxidised to oxidise 4 amino antipyrine and chlorophenol to a pink coloured complex, which is measured at 546 nm (500-550 nm or with green filter). Absorbance is proportional to Triglycerides concentration.



Sample Material Serum

Procedure: 0.05 mL serum, standard, and distilled water were placed in the tubes marked as a test, standard and blank, respectively.

Then working solution 1 mL of was added to every tube, mixed well, and incubated (20 min at 37 °C). After incubation, 1.5 mL of distilled water was added to every tube, mixed well. Absorbance was red of test and standard against the blank at 546 nm (500-550 nm)

Calculations:

Triglyceride (mg/dl) = Absorbance in Test / Absorbance in Standard × 200

Elution: Elution was carried out with the flow rate (1 ml/min). The mobile phase was added at the top of the column from the solvent reservoir, and fractions were collected in an amber colored bottle.

Fractions were concentrated by evaporating at room temperature until volume was reduced to ¼ of the total volume. TLC of concentrated fractions was carried out to detect similarity between the chromatograms of different fractions.

Source	Fraction	Mobile phase	Abbreviation
<i>E. colona</i>	Chloroform	Chloroform: Ethanol 40:60	EC-I
		Chloroform: Ethanol 30:70	EC-II
		Chloroform: Ethanol 10:90	EC-III

Thin Layer Chromatography (TLC): TLC of each fraction was carried out during column chromatography, and the R_f value for EC-I (0.48), EC-II (0.74), EC-III (0.68) was observed.

Characterization of the Isolated Compounds from *E. Colona*:

EC-I: The EC-I fraction was collected at 40:60 in % ratio of (CHCl₃: C₂H₅OH). The isolated compound was white amorphous powder. The compound was studied for its qualitative properties and found to be positive with the ferric chloride test, and the phenolic nature of the compound was confirmed. The M.P. of the compound was 145-147 °C.

The UV spectrum showed λ_{max} , 220 nm, Ethanol with typical aromatic bands confirming a substituted aromatic benzoic acid. In the FTIR (KBr, cm⁻¹) signal at 3400 (-OH), 2935 (Ar-H), 1688(-COOH), ¹HNMR (CDCl₃, 400 MHz) signals at δ 11.80 (-COOH), 6.5 (Ar-H), 5.10 (Ar-OH), 2.33 (Ar-CH₃) and the peak of molecular ion was observed at m/z 184 matching to C₈H₈O₅, and main peak at 166 [184-(H₂O)]⁺ with other fragments at m/z : 120, 84, 42, 27 were observed.

The above spectral data suggested isolated compound is 2, 3, 4-trihydroxy, 6-methyl benzoic acid. The IR, ¹HNMR, and MASS spectra were shown in following Fig. 1 to 3.

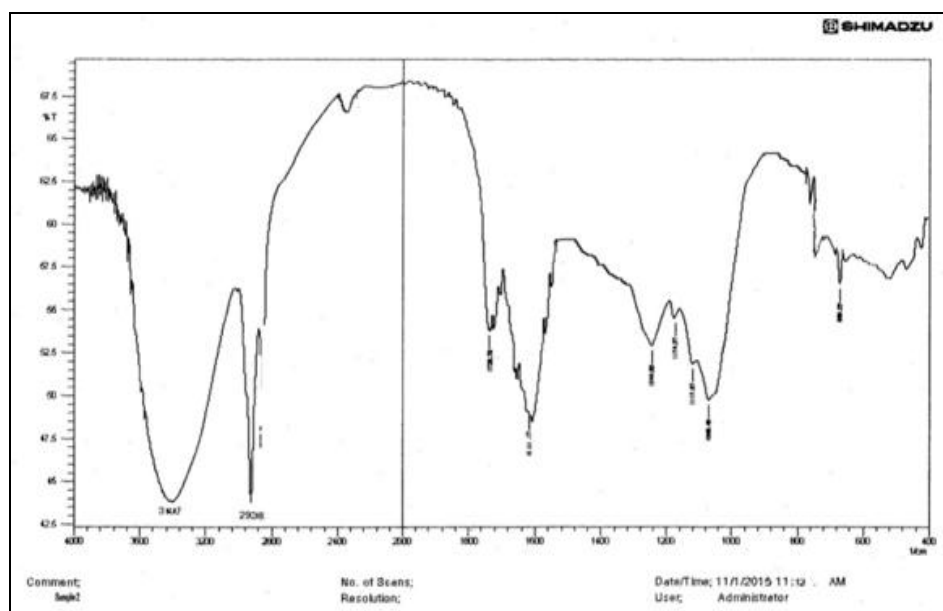


FIG. 1: IR SPECTRA OF EC-I FRACTION ISOLATED FROM *E. COLONA*

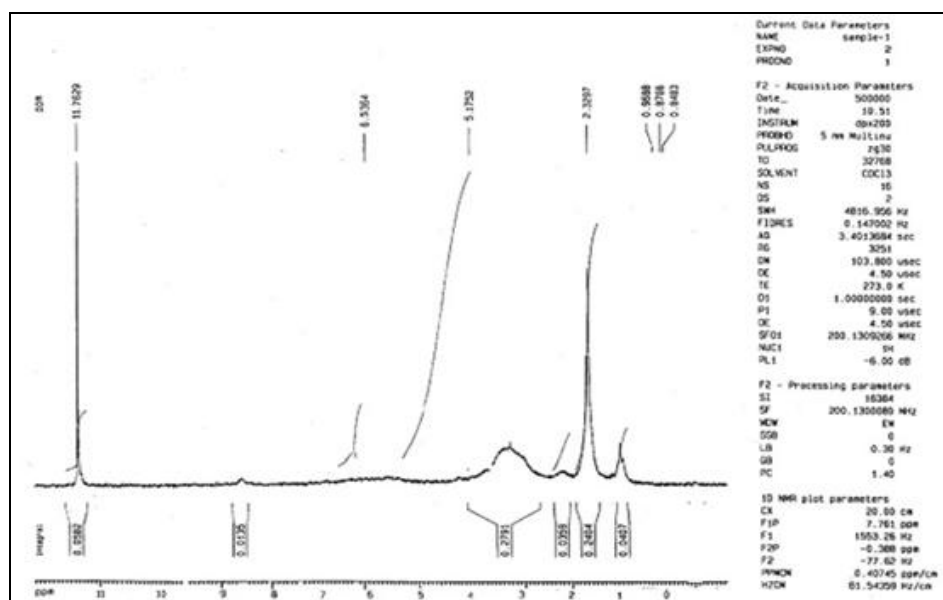


FIG. 2: ¹H NMR SPECTRA OF EC-I FRACTION ISOLATED FROM *E. COLONA*

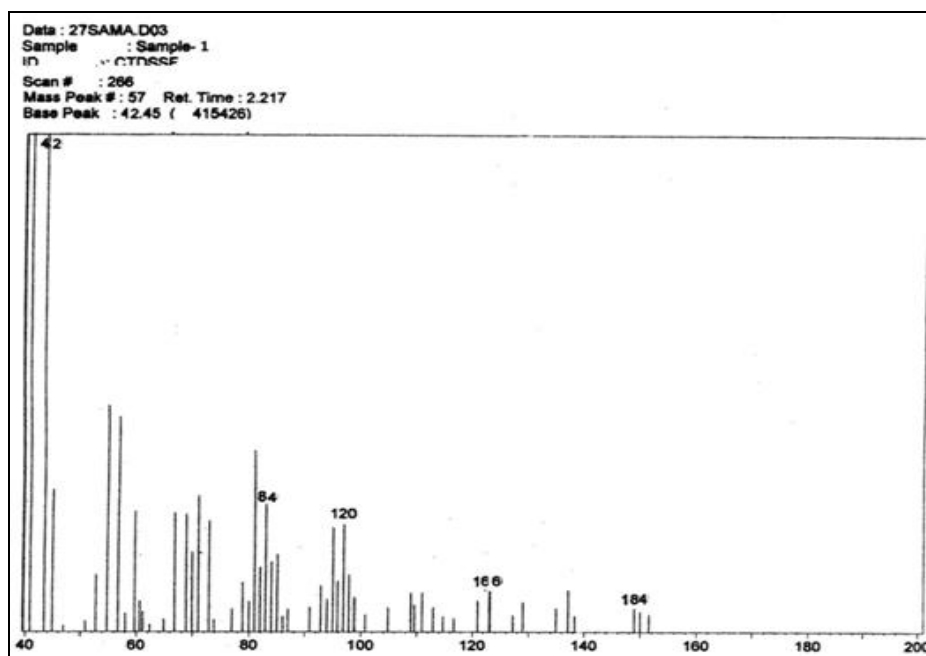


FIG. 3: MASS SPECTRA OF EC-I FRACTION ISOLATED FROM *E. COLONA*

EC-II: The EC-II fraction was collected at 30:70 in % ratio of ($\text{CHCl}_3:\text{C}_2\text{H}_5\text{OH}$). The isolated compound was white crystalline powder with a characteristic odour. The compound was studied for its qualitative properties and found to be positive with the Liebermann-Burchard test, and the steroidal nature of the compound was confirmed. The M.P. of the compound was 137-139 °C. UV spectrum showed λ_{max} , 210 nm, ethanol. In the FTIR (KBr, cm^{-1}) 3545 (-OH), 2931 (-CH₂), 2860 (-CH), 1637 (-C=C-), 1033 (-C-O), ¹HNMR (CDCl_3 , 400 MHz) signals at δ 1.01, 1.04, 1.06,

1.04, 1.17, 1.21(-CH₃), 1.57, 1.98, 1.13, 1.79, 1.24, 1.27, 1.35, 1.34, 1.25, 1.29, (-CH₂-), 3.25(--CH-), 5.37 (H-cyclohexene) and peak of molecular ion was observed at 414.7 corresponding to C₂₉H₅₀O with other characteristic fragmentations of m/z: 414, 396, 381, 330, 290, 273, 255, 212, 199 and 173 were observed. The above spectral data and those reported in the literature support the proposed structure was β -sitosterol 113, 114, 115. The IR, ¹HNMR, and MASS spectra were shown in the following Fig. 4 to 6.

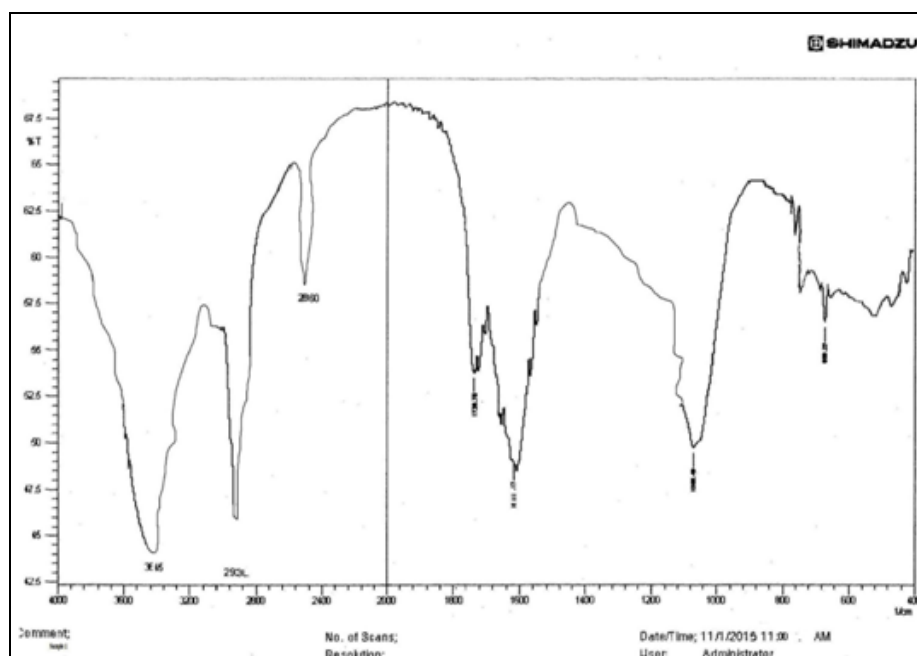


FIG. 4: IR SPECTRA OF EC-II FRACTION ISOLATED FROM *E. COLONA*

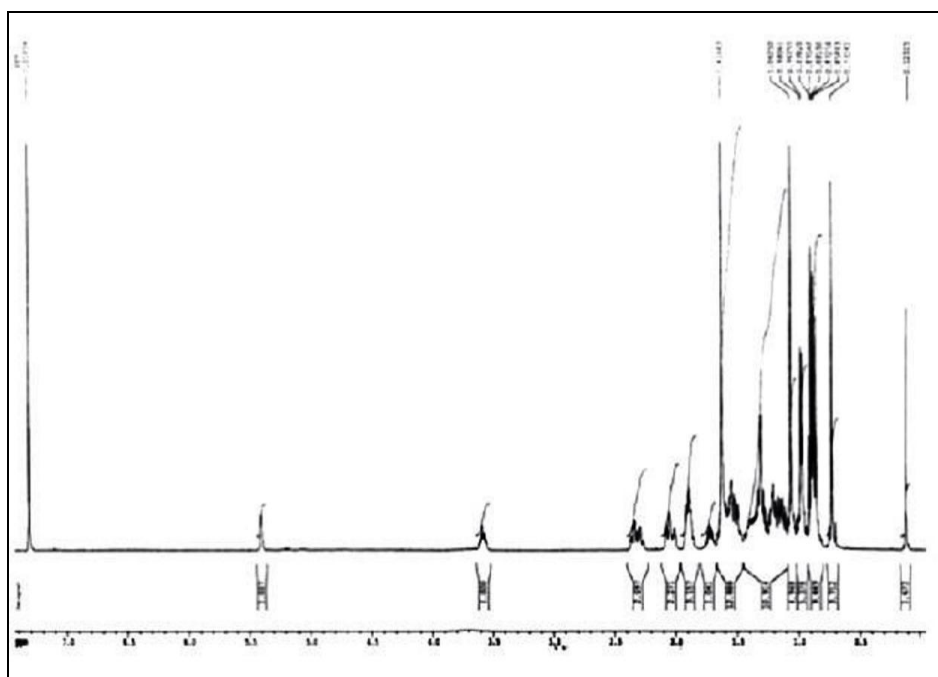


FIG. 5: ¹H NMR SPECTRA OF EC-II FRACTION ISOLATED FROM *E. COLONA*

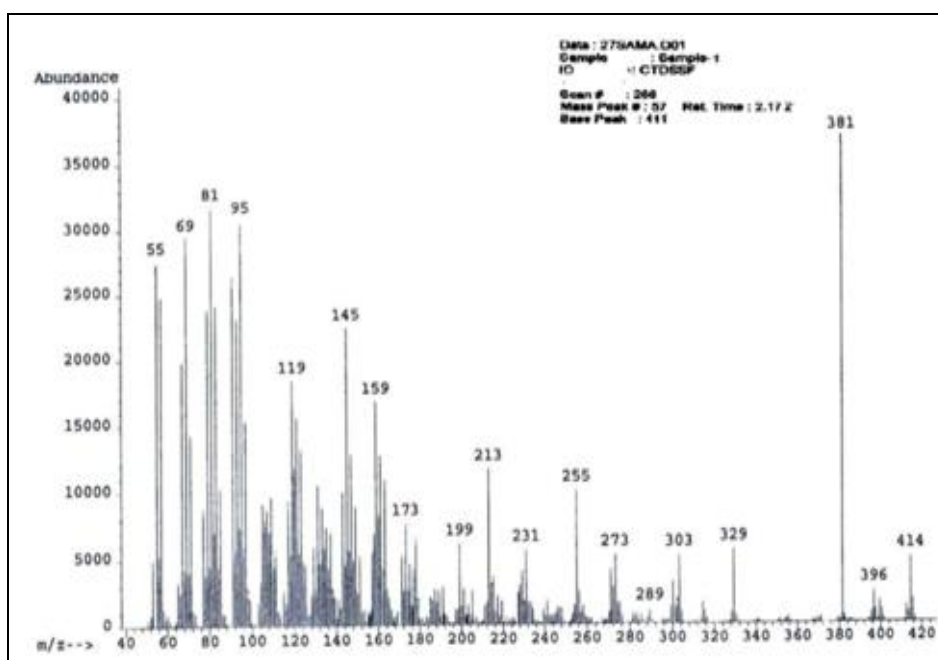


FIG. 6: MASS SPECTRA OF EC-II FRACTION ISOLATED FROM *E. COLONA*

EC-III: The EC-III fraction was collected at 10:90 in % ratio of (CHCl₃:C₂H₅OH). The isolated compound was white crystalline powder with a characteristic odour. The compound was studied for its qualitative properties and found to be positive with the ester test, and the ester nature of the compound was confirmed.

The melting point of the compound was carried out and found to be 150- 152 °C. The UV spectrum showed λ_{\max} , 226 nm, methanol. In the FTIR (KBr,

cm⁻¹) band at 1736 (RCOOR) and 3400 (Ar-OH), ¹HNMR (CDCl₃, 400 MHz) at δ 1.25 (-CH₃), 4.65 (-CH₂-), 4.58 (Ar-OH) and a peak of molecular ion was observed at m/z 198 correspondings to C₉H₁₀O₅ with other fragments at 183, 149 [183-CH₃]⁺, 129, 111, 97, 83, 69, 57, 43 were observed.

The above spectral data suggested isolated compound was ethyl 3, 4, 5-trihydroxy benzoate. The IR, ¹HNMR, and MASS spectra were shown in the following Fig. 7 to 9.

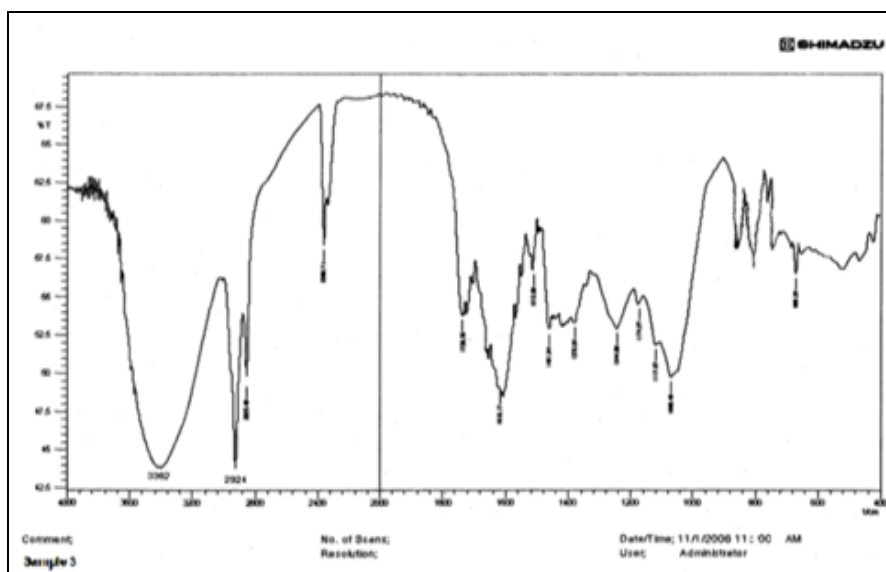


FIG. 7: IR SPECTRA OF EC-III FRACTION ISOLATED FROM *E. COLONA*

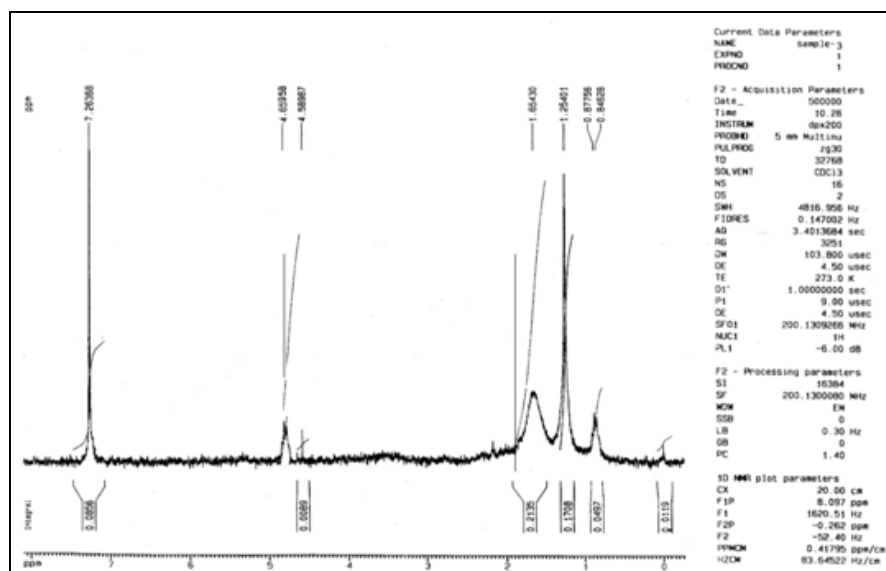


FIG. 8: 1H NMR SPECTRA OF EC-III FRACTION ISOLATED FROM *E. COLONA*

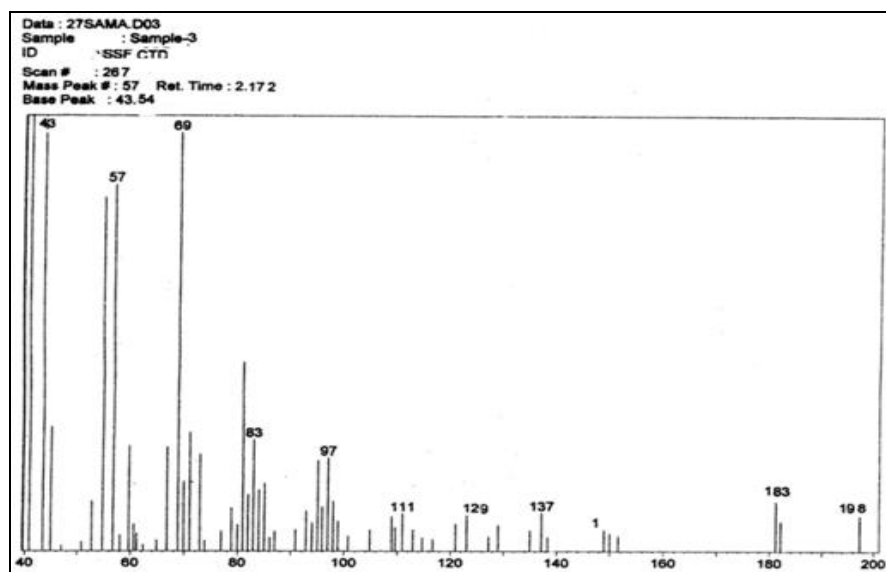


FIG. 9: MASS SPECTRA OF EC-III FRACTION ISOLATED FROM *E. COLONA*

Anti Diabetic Activity: The effects of different fractions (single dose-50 mg/mL) obtained from ethanolic extracts of *E. colonaupon* blood glucose (mmol/L), serum total cholesterol & triglycerides (mmol/L) were investigated within control and streptozotocin induced diabetic rats. Metformin HCl (150 mg/mL) was used as a standard anti-diabetic agent.

Effects of Various Fractions on Blood Glucose: A decrease in blood glucose level was observed in

animals treated with different fractions of *E. colonaat*^{0, 1, 2, 3, 6, 10, 16}, and 24th h **Fig. 1**.

The blood glucose level was significantly reduced at 24th h of the experiment ($p < 0.01$) for metformin, chloroform, ethyl acetate, and ethanol fraction, it was 5.85 ± 0.004 (90.08%) 6.65 ± 0.004 (67.36%), 6.96 ± 0.003 (60.14%) and 7.05 ± 0.004 (58.01%) respectively comparing controlled diabetic rats **Table 1**.

TABLE 1: EFFECT OF DIFFERENT FRACTIONS OF *E. COLONA* ON BLOOD GLUCOSE IN DIABETIC RATS ON ONE DAY TREATMENT

Groups (Treatment)	Blood glucose levels (mmol/L) at Hours							
	0	1	2	3	6	10	16	24
I	7.25 ±	7.26 ±	7.27 ±	7.28 ±	7.29 ±	7.30 ±	7.31 ±	7.32 ±
10 ml saline	0.004	0.004	0.004	0.004	0.004	0.002	0.002	0.004
II	7.26 ±	7.24 ±	7.28 ±	7.20 ±	7.19 ±	6.17 ±	6.05 ±	4.13 ±
150 mg/kg	0.004	0.003	0.004	0.002	0.004	0.004	0.003	0.004
III	11.01 ±	11.50 ±	11.95 ±	12.25 ±	12.75 ±	13.10 ±	13.55 ±	13.95 ±
10 ml saline	0.003	0.003	0.004	0.004	0.004	0.004	0.003	0.003
IV	11.12 ±	10.81 ±	9.05 ±	8.75 ±	6.65 ±	7.08 ±	6.16 ±	5.85 ±
150 mg/kg	0.003	0.20	0.004	0.004	0.004	0.004	0.004	0.004
V	11.13 ±	10.61 ±	10.15 ±	9.95 ±	8.85 ±	7.28 ±	6.96 ±	6.65 ±
50 mg/ml	0.004	0.002	0.008	0.005	0.004	0.004	0.004	0.004
VI	11.13 ±	10.92 ±	10.41 ±	10.31 ±	9.55 ±	7.98 ±	7.86 ±	6.96 ±
50 mg/ml	0.004	0.004	0.004	0.004	0.004	0.003	0.002	0.003
VII	11.14 ±	11.02 ±	10.91 ±	10.71 ±	9.98 ±	9.07 ±	7.66 ±	7.05 ±
50 mg/ml	0.004	0.004	0.005	0.003	0.004	0.004	0.004	0.004

All values are expressed as mean ± SEM, (n=5) in every group, $p < 0.01$, p-values were calculated and compared with control by ANOVA method followed by Dunnett's test

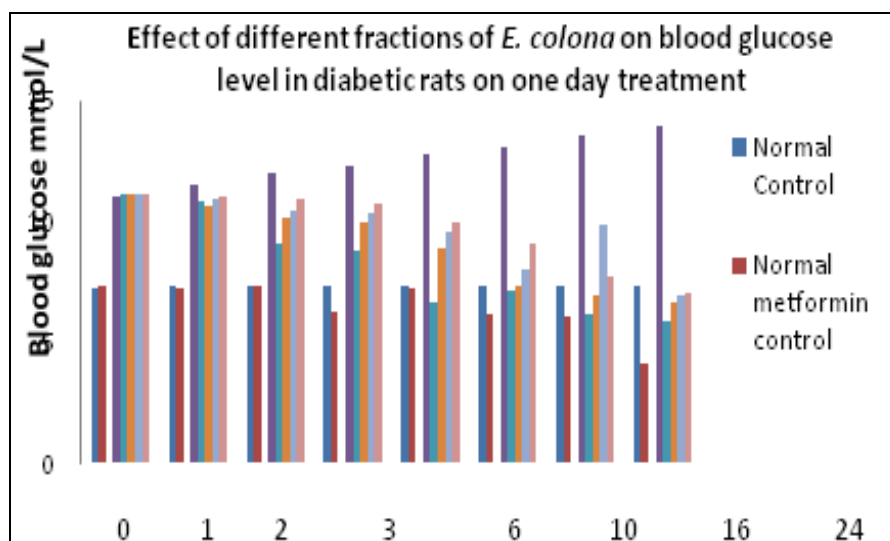


FIG. 10: EFFECT OF DIFFERENT FRACTIONS OF *E. COLONA* ON BLOOD GLUCOSE LEVEL IN DIABETIC RATS ON ONE DAY TREATMENT

Effect of Various Fractions on Total Cholesterol and Triglyceride: After 24 h treatment of different fractions of *E. colona* there was a decrease in total cholesterol and triglyceride in diabetic rats **Fig. 2**.

Metformin, chloroform, ethyl acetate and ethanol fraction showed a decrease in total cholesterol level by 12.16 ± 0.0044 (56.98%) 13.02 ± 0.004 (53.94%) 14.17 ± 0.004 (49.87%) and 16.37 ± 160

0.004 (42.24%) respectively, whereas the triglyceride was decreased by 10.39 ± 0.0044 (46.49%) 13.16 ± 0.004 (32.23%) 14.06 ± 0.004 (27.60%) and 14.56 ± 0.004 (42.24%) for metformin, chloroform, ethyl acetate and ethanol fraction respectively when compared to diabetic control groups **Table 2**.

TABLE 2: EFFECTS OF DIFFERENT FRACTIONS OF *E. COLONA* ON TOTAL CHOLESTEROL & TRIGLYCERIDES IN DIABETIC RAT ON ONE DAY TREATMENT

Parameter (mmol/L)	Groups						
	I	II	III	IV	V	VI	VII
Total Cholesterol	14.37± 0.003	12.24± 0.004*	28.27± 0.004**	12.16± 0.004**	13.02± 0.004**	14.17± 0.004**	16.37± 0.004**
Total Glycerides	12.41± 0.004	10.31± 0.003*	19.42± 0.004*	10.39± 0.004*	13.16± 0.004*	14.06± 0.004*	14.56± 0.004*

All values are expressed as mean \pm SEM, (n=5) in every group, *p <0.01, considered extremely significant, p-values were calculated and compared with control by ANOVA method followed by Dunnett's test.

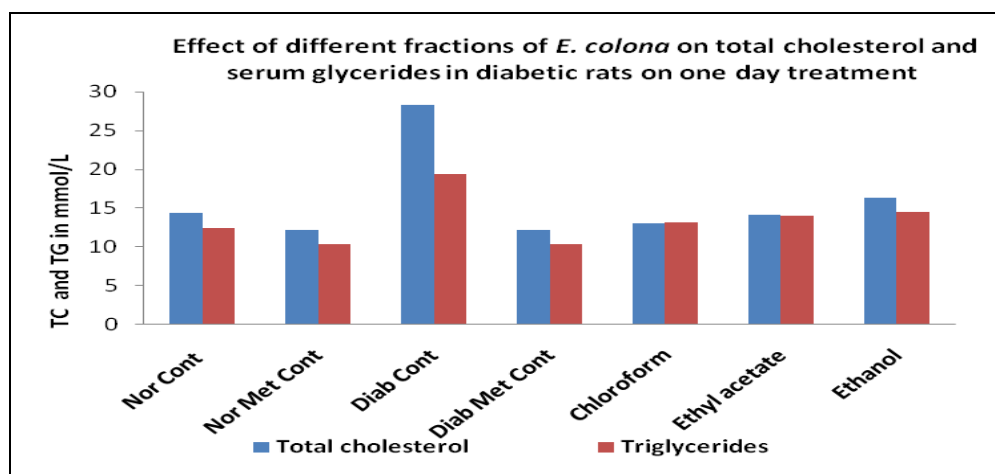


FIG. 11: EFFECTS OF DIFFERENT FRACTIONS OF *E. COLONA* ON TOTAL CHOLESTEROL AND SERUM GLYCERIDES IN DIABETIC RATS ON ONE DAY TREATMENT

CONCLUSION: Given the potent results of the extracts tested in this article against diabetes and the factor responsible for the same (triglycerides). A decrease in blood glucose level was observed in animals treated with different fractions of *E. colona*.

After 24 h treatment of different fractions of *E. colona* there was a significant decrease in total cholesterol and triglyceride on diabetic rats when treated with chloroform fraction. The chloroform fraction exhibiting significant anti-diabetic activity was chromatographed to isolate three phyto constituents 2, 3, 4-trihydroxy, 6-methyl benzoic acid, β -sitosterol, and ethyl 3, 4, 5-trihydroxy benzoate.

ACKNOWLEDGEMENT: Authors are thankful to Principal Rajarshi Shahu College of Pharmacy, Buldhana, for providing the necessary facilities

CONFLICTS OF INTEREST: The authors have not declared any conflict of interest.

REFERENCES:

- Peerzada AM, Bajwa AA, Ali HH and Chauhan BS: Biology, Impact and Management of *Echinochloa Colona* (L.) Link. Crop Prot 2016; 83(1): 56-66.
- Chopra N, Tewari G, Tewari LM, Upreti B and Pandey N: Allelopathic effect of *Echinochloa Colona* L. and *Cyperus iria* l. weed extracts on the seed germination and seedling growth of rice and soyabean. Adv Agric 2017; (1): 1-5.
- Pan L, Yu Q, Han H, Mao L, Nyporko A, Fan LJ, Bai L and Powles S: Aldo-keto reductase metabolizes glyphosate and confers glyphosate resistance in *Echinochloa colona*. Plant Physiol 2019; 1(1): 239-50.
- Chauhan BS and Johnson DE: Seed germination ecology of junglerice (*Echinochloa colona*): a major weed of rice. Weed Sci 2009; 57(3): 235-40.
- Coskun O: Separation techniques chromatography. North Clin Istanbul 2016; 1(1): 123-35.
- Schweiger S, Hinterberger S and Jungbauer A: Column-to-column packing variation of disposable pre-packed columns for protein chromatography. J Chromatogr A 2017; 1527(1): 70-79.
- Mauer L and Reuhs BL: High-performance liquid chromatography bradley. Food Anal 2017; 1(1): 213-26.
- Wang T, yang Li, Q Bi and shun K: Bioactive flavonoids in medicinal plants: structure, activity and biological fate. Asian J Pharm Sci 2018; 13(1): 12-23.
- Anti-Phishing Working Group. Phishing Activity Trends Report 1 Quarter. Most 2010; 1(3): 1-12.

10. Ahad Hussain S, Greeshma Namilikonda M, Karan Chandra T and Arif Pasha M: A review on medi plants with anti-dia activity. Int Journal of Adv Res 2020; 8(3): 902-17.
11. Deng X, Liu B, Li J, Zhang J, Zhao Y and Xu K: Blood biochemical characteristics of patients with coronavirus disease 2019 (covid-19): a systemic review and meta-analysis. Clin Chem Lab Med 2020; 1(1): 145-56.
12. Qian ZP, Mei X, Zhang YY, Zou Y, Zhang ZG, Zhu H, Guo HY, Liu Y, Ling Y, Zhang XY, Wang JF and Lu HZ: Analysis of baseline liver biochemical parameters in 324 cases with novel coronavirus pneumonia in shanghai area. Zhonghua Gan Zang Bing Za Zhi 2020; 28 (3): 229-33.
13. Ali Abd El-Aal Y, Mohamed Abdel-Fattah D and El-Dawy Ahmed K: Some biochemical studies on trans fatty acid-containing diet. Diabetes Metab Syndr Clin Res Rev 2019; 13(3): 1753-57.
14. Kishore J, Gupta N, Kohli C and Kumar N: Prevalence of hypertension and determination of its risk factors in rural delhi. Int J Hypertens 2016; (1): 2016-25.
15. Nordestgaard BG, Langsted A, Mora S and Watts GF: Fasting Is Not routinely required for determination of a lipid profile: clinical and laboratory implications including flagging at desirable concentration cutpoints-a joint consensus statement from the european atherosclerosis soc and european federat. C Chem 2016; 62(7): 930-46.

How to cite this article:

Borkar V, Sonwane G, Devhare P, Diwre R and Jain S: Evaluation of antidiabetic activity of *Echinochloa colona* plant extract. Int J Pharm Sci & Res 2021; 12(8): 4354-64. doi: 10.13040/IJPSR.0975-8232.12(8).4354-64.

All © 2013 are reserved by International Journal of Pharmaceutical Sciences and Research. This Journal licensed under a Creative Commons Attribution-NonCommercial-ShareAlike 3.0 Unported License.

This article can be downloaded to **Android OS** based mobile. Scan QR Code using Code/Bar Scanner from your mobile. (Scanners are available on Google Playstore)

A Novel Hemizygous Variant in the *AFF2* Gene Causing Fragile XE (FRAXE) Syndrome: First Report from Pakistan

Iftikhar Ahmed¹, Muhammad Ilyas¹, Gaurav V Harlalka^{2,3}, Asif Mir¹

Department of Biological Science, International Islamic University¹, H-10, Islamabad, College of Medicine and Health, University of Exeter², Exeter, Devon, UK, Department of Pharmacology, Rajarshi Shahu College of Pharmacy³, Malvihar, Buldana, Maharashtra, India.

Abstract

Background: Fragile XE (FRAXE) is an X-linked recessive condition that affects 1 in 50,000 of new born males with intellectual disability (ID). It is characterized by mild Intellectual disability (ID), speech delay cognitive impairment, and in some cases with phenotypes of Autism Spectrum disorder (ASD).

Methodology: In this study, a family was investigated with two male siblings having neuro developmental delay. Whole exome sequencing analysis (WES) was carried out to identify the pathogenic variant. Sanger sequencing was performed in normal and affected family members and co-segregation analysis was done.

Results: Two probands were affected in a family diagnosed with intellectual disability. A novel hemizygous variant (c.3348G>T, p.Asp1150Tyr) in *AFF2* gene was identified as the causal variant cause in affected individuals. This variant was novel from Pakistani population.

Conclusion: In this study, a novel hemizygous variant (c.3348G>T, p.Asp1150Tyr) identified in *AFF2*. These findings paved the way for further studies on genetic and clinical spectrum of rare X-linked recessive disease involved in ID.

Key words: *AFF2*, hemizygous, intellectual disability, neurological disorders.

Introduction

Cognition is the result of cellular, biological and multiple molecular events in the nervous system. Minor defect in any of these events can results in intellectual disability or cognitive impairment.^{1,2} It can also be termed as neuro-development disorder as it results from defect in synapse formation.^{3,4}

Overall, in general population, the prevalence of intellectual disability (ID) is 2-3%.^{5,6} Its clinical and genetic heterogeneity make the diagnosis challenging for scientists and

physicians.^{7,8} More than 900 genes are reported to cause intellectual disability so far.^{9,10}

The X-linked intellectual disability is a heterogeneous group of genetic disorders. There are more than 141 genes linked with disease located on x-chromosome.¹¹ Its prevalence is high in males as x-chromosome genes contribute to cognition. Among x-linked intellectual disability, Fragile X syndrome (FXS) is common and characterized by moderate to severe disability (OMIM - 309548).¹² There is high repeat expansion of a CGG in *FMR1* gene which cause methylation, that ultimately halts the production of *FMR1* protein leads to (FXS) syndrome.¹³

The *AFF2* gene (also as *FMR2* gene) cause non-specific x-lined intellectual disability with prevalence as 1/25,000 to 100,000 in new born male. Micro deletion in *AFF2* genes leads to Fragile XE (FRAXE) syndrome [14]. It is characterized by mild to moderate intellectual disability.¹⁵

In FRAXE syndrome, learning, thinking ability and cognitive function, affected badly. Also there is delay in speech; hyperactivity, poor writing skills, and very short attention span are common symptoms of people affected with this syndrome. It

Corresponding Author:

Asif Mir

Department of Biological Sciences
International Islamic University, Islamabad.
Email: asif.mir@iiu.edu.pk

Received: 13 September 2020, Accepted: 30 April 2021,

Published: 08 July 2021

Authors Contribution

IA, GVH & AM conceptualized the project and drafting, revision & writing of manuscript. IA & MI did the literature search and data collection. IA, MI & AM performed the statistical analysis.

Copyright © 2021 The Author(s). This is an Open Access article under the CC BY-NC 4.0 license.

is reported that autistic behavior (intense interest in a particular subject, hand flapping, repetitive behavior) were displayed by some individuals. In FRAXE syndrome, cognitive function does not decrease with age as compared to other ID types.¹⁶

Additionally, some phenotypes are found to be variable among patients including mild facial dysmorphic features, long narrow face, nasal abnormalities, irregular teeth's and thick lips. The *AFF2* protein expression resulted in high expression in mouse model in brain area (involved in memory and learning) that provide impact of the gene.¹⁷. Chromosomal abnormalities were also reported to cause disruption of *AFF2* gene leading to ID as reported in patients.¹⁸ Micro deletion in *AFF2* gene causing ID was also reported in two patients which provides further evidence of involvement of this gene in ID.¹⁹

Methodology

The blood samples were collected and DNA extracted by using phenol chloroform method. The suspected family was approached as per convenient sampling. Informed consent was taken from adults and in case of children; consent was taken from parents prior to enrolment.

Microarray genotyping was carried out using Illumina cytoSNP-12v2.0 arrays in both probands to identify the known genes in the family. The microarray typing was done by specialized bead chip to detect cytogenetic abnormalities relevant to human diseases. Whole exome sequencing (WES) was performed commercially on Illumina platform from Macrogen, Seoul, South Korea. WES was performed on two samples (one in each family) by Agilent Sure Select human all exon; V4 exome enrichment kit. Sequence reads aligned to the reference genome UCSC: hg19/ GRCH37 NCBI. GATK (Genome analysis tool kit) tool was used to do the sequence realignment and base quality recalibration. Sam tool methods were used to determine the read depth of the sequences. This software was also used to detect insertion and deletions and single nucleotide variations (SNVs).^{19,20} The annotation of data was carried out by Annovar.²¹ Primers were designed by primer3plus tool.²²

PCR (polymerase chain reaction) was performed on genomic DNA of the patient (proband) and family members and PCR products were purified. Sequencing was performed by using Big Dye terminator kit (Applied Biosystems). The

purified sequencing reactions were performed. Sequences were reviewed manually and comparison was made to reference sequence NM_002025.4 of *AFF2* gene using Codon Aligner software.

Psipred²³ and I-Tasser^{24,25} models were used to predict secondary and three dimensional protein models. The reliability of predicted models was checked by using RAMPAGE.²⁶ Visualization of models were done by UCSF Chimera.²⁷ The protein pockets on three dimensional structure of protein was identified by CASTp server.^{28,29} The impact of protein stability was checked by Meta SNP,³⁰ I-mutant 2.0³¹ and PREDICT SNP³² Different in-silico tools were used to determine the pathogenicity of the variant. Multiple sequence alignment was performed using Clustal Omega.

The Ethical approval was obtained from the Ethical Review Committee of International Islamic University, Islamabad.

Results

A family was enrolled with size of 06 members containing two probands. The probands are named as IV: 2 and IV: 3 (Figure-1A).

Proband IV:2

The Proband (IV:2) was male and aged 08 years old. He was born with normal gestational age. The birth weight, birth length and OFC (occipitofrontal circumference) were 2.2 kg, 41.6 cm and 31 cm, respectively at birth.

Few early developmental milestones were delayed in first 2 years of life. At 14 months, he was able to walk, but could not speak single word. He started uttering few words and crying at need when he was at 02 years of age. The cranial MRI performed at 3 years was normal. Speech testing and language evaluation indicated lack of expressive speech. At 04 years, he was referred to a local hospital for neurological checkup. His parents were having consanguineous marriage, but no other genetic disorders were reported in the family. The weight was 11.56 kg and height was 88.6 cm; with head circumferences as 46.5 cm. There was learning disability, speech delay and flattening of occiput with clinical characteristics of ID. Also other features like large ears and nasal tip was noted. He joined school for special children at 04 years and required support for social, communication skills and cognition.

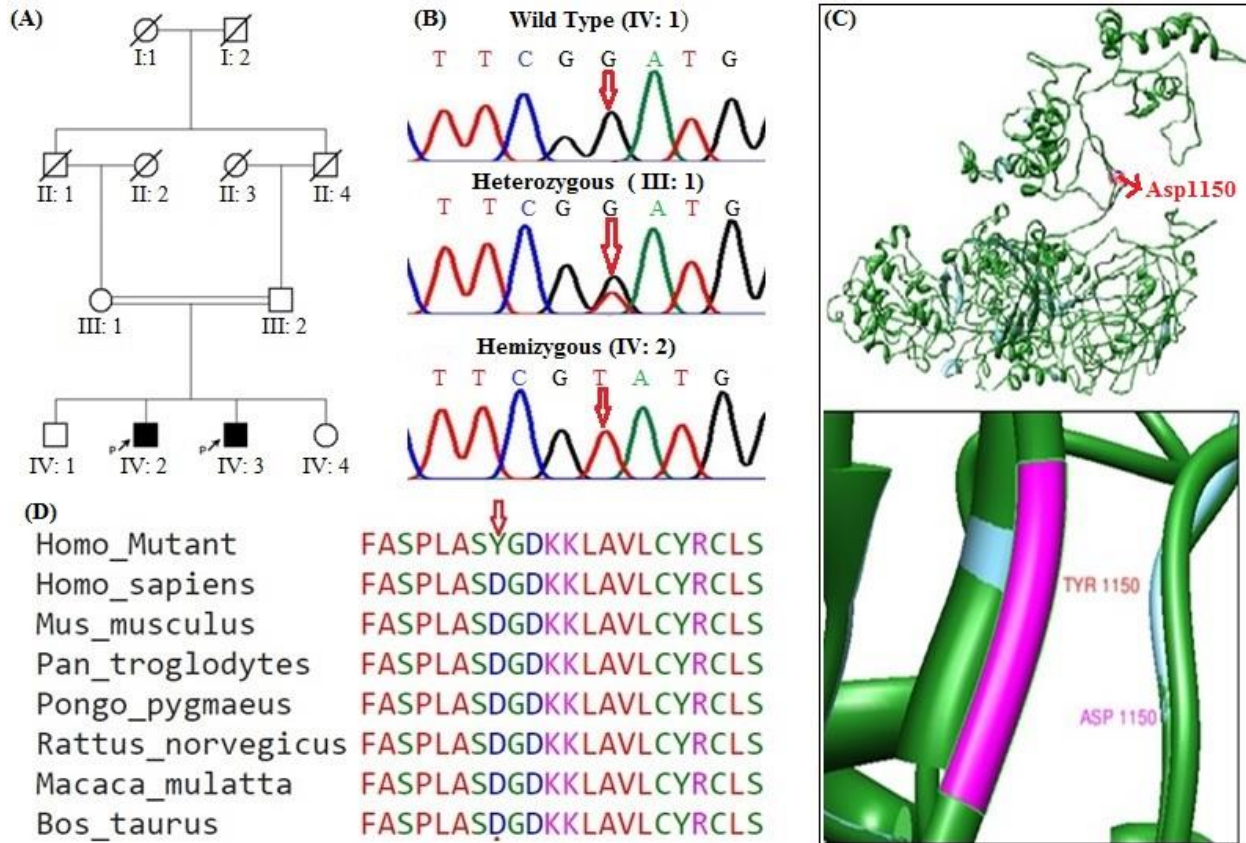


Figure: Figure-1A Pedigree of the family with probands indicated in black filled blocks. (B) Chromatograms showing variant of *AFF2* (c.3448G>A,p.Asp1150Tyr) in heterozygous (III: 1), wild type (IV: 1), and affected individual (IV: 2) in *AFF2* gene, exon 17. (C) The Superimposed *AFF2* structure (normal and mutant) highlighting substitution of variant of Asp (magenta color) with Tyr (red color) at position 1150. Protein structure in green and cornflower blue color showing wild and mutant types respectively. (D) Multiple alignment of mutated protein showing conservation in nearby amino acid.

Patient IV: 3

The second patient (proband) was male, 06 years old and born after uneventful pregnancy. His parents were having consanguineous marriage. His weight and OFC at birth was 3 kg and 30 cm. He started walking with few steps at 18 months, utter few words at 2.5 years with cognitive and motor milestones were not fine.

He was admitted to the district hospital Dera Ismail Khan, KPK at 3 years age for neurological examination. He has speech delay, global developmental delay and behavioral problems. He also exhibited behavioral problems, including aggression, agitation with attention deficits. Hand flapping was also noted during clinical examination but seizures were not reported by the parents. Intellectual disability was indicated in proband with developmental delay.

Genetic analysis

Whole Exome sequencing was performed in the selected patient (IV:2). Genomic library was

prepared by using exon kit (Sure Select, Agilent, Santa Clara, CA) and enrichment of exome was performed on illumina HiSeq4000. The variants were annotated and aligned with human reference genome (GRCH37). The filtration was carried out by variant type, allelic frequency and mode of inheritance for selection of causal variants. Firstly, the variants that were more common were removed on the basis of frequency. The duplicate alignments were removed and variants with allelic frequency <0.005 were retained. This resulted in 4 candid variants. The frequency of variants was checked in gnomAD and HGMD. The variants were not found in South Asian population category of gnomAD database (<https://gnomad.broadinstitute.org/>). The ACMG guidelines were followed to classify the variants. [33]. Benign and likely benign variants were excluded and one variant (NM_002025.4: c.3448G>T; p.Asp1150Tyr) in the *AFF2* gene was selected (OMIM: 309548) for further analysis.

In-silico results indicated that the variant (p.Asp1150Tyr) is deleterious and disease causing.

The pathogenicity of the variant with different software predictions are mentioned in Table. Sanger sequencing analysis was carried out.

Co-segregation analysis was performed in normal and affected members of the family. The analysis revealed complete co-segregating with family members. Two affected males (IV: 2 and IV: 3) were found hemizygous for mutant allele of *AFF2* gene mother (III: 1) was heterozygous and the other family members (IV: 1 and IV: 5) were of wild type (Figure-1B). The Amino acid (aspartic acid) which was converted into tyrosine, was found present in evolutionary conserved position (p.Asp1150Tyr) as per UCSC Human Genome (GRCh37/hg19).

Table: Software predictions for the variant.

Pathogenicity software	Prediction	Score
FATHMM-MKL	Damaging	0.88
DEGEN2	Damaging	-
PROVEAN	Damaging	-2.75
DANN and	Damaging	0.99
GERP	Damaging	5.98

Effect of variant on protein

The pathogenicity of p.Asp1150Tyr variant was assessed by using I-TASSER Tool for the structure of *AFF2* protein using template 6R80 [34] (Figure-1C). The result revealed that template triggers the release of polymerase II enzyme from promoter proximal pausing site. Paused polymerase-II played role in the maintenance of structure of promoter region. The loss of protein structure with no change in protein length was observed. The paused polymerase II also showed alteration in protein conformation and loss of c-terminal helices. Therefore the variant p.Asp1150tyr is probably pathogenic for the family.

Multiple sequence alignment showed conservation of mutated amino acid (p.Asp1150Try) and nearby amino acids in 7 different species. Variant site denoted with red arrow (Figure-1D).

Discussion

X linked intellectual disability is a heterogeneous group of genetic disorder with different clinical manifestations. The features include developmental delay, cognitive impairment and low IQ in males mostly. Most common cause of this disorders an expansion of CGG repeats in the UTR region of the *FMR1* gene.³⁵ About 141 genes were reported to be responsible for this disorder.¹¹ Micro deletion and variants in *FMR2* (*AFF2*) genes leads to FRAXE syndrome in the absence of CGG repeats expansion.¹⁴

Fragile XE (FRAXE) is an x-linked syndrome characterized by speech delay, cognitive impairment, and autistic behavior. The gene (*AFF2*) is responsible for protein present in the cell's nucleus. This protein serves as a transcription factor, binds to specific regions of DNA and helps in controlling activity of other genes.³⁶ In this study, a family with two sibling patients (probands) showing symptoms of FRAXE syndrome. The common symptoms were speech impairment, behavioral problems, hand flapping and developmental delay. Genetic testing showed novel missense variant i.e. c.3448G>T (p.Asp1150Tyr) in coding exon 17 of *AFF2* gene.

The high prevalence of fragile x syndrome was reported from Spain, Chile and Columbia.³⁷ It has been reported that pharmacological, behavior and cognitive interventions are important for improvement in the quality of life of patients.³⁸ There is a need to conduct large scale studies to determine the prevalence and identify the public health burden of fragile x syndrome. Diagnosis and timely screening is also important for early diagnosis of the disease to prevent morbidity in future. Our physicians and health care provider need to be trained to provide genetic counseling to the patient.³⁹

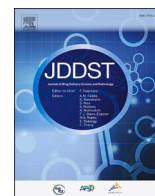
Genetic analysis identified a novel missense variant (c.3448G>T; p.Asp1150Tyr) in the coding exon 17 of *AFF2* gene as the pathogenic variant in a family identified as FRAXE syndrome. Combinational approach of exome sequencing and Sanger sequencing can provide better clinical diagnosis of the ID families.

Conflict of interest: None declared.

References

- Chelly J, Khelifaoui M, Francis F, Chérif B, Bienvenu T. Genetics and pathophysiology of mental retardation. *Eur J Hum Genet* 2006; 14(6): 701-13.
- Wieczorek D. Autosomal dominant intellectual disability. *Medizinische Genet* 2018; 30(3): 318-22.
- Fedulov V, Rex CS, Simmons DA, Palmer L, Gall CM, Lynch G. Evidence that long-term potentiation occurs within individual hippocampal synapses during learning. *J Neurosci* 2007; 27(30): 8031-9.
- Ilyas M, Efthymiou S, Salpietro V, Noureen N, Zafar F, Rauf S, et al. Novel variants underlying autosomal recessive intellectual disability in Pakistani consanguineous families. *BMC Med Genet* 2020; 21: 1-8.
- Uyguner O, Kayserili H, Li Y, Karaman B, Nürnberg G, Hennies HC, et al. A new locus for autosomal recessive non-syndromic mental retardation maps to 1p21.1-p13.3. *Clinl Ggenet* 2007; 71(3): 212-9.
- McKenzie K, Milton M, Smith G, Ouellette-Kuntz H. Systematic review of the prevalence and incidence of

- intellectual disabilities: current trends and issues. *Curr Developmen Disord Rep* 2016; 3(2): 104-15.
7. Inlow JK, Restifo LL. Molecular and comparative genetics of mental retardation. *Genetics* 2004; 166(2): 835-81.
 8. Basel-Vanagaite L. Clinical approaches to genetic mental retardation. *Isr Med Assoc J* 2008; 10(11): 821-6.
 9. Opitz J. Historiography of the causal analysis of mental retardation. In: *Speech to the 29th Annual Gatlinburg Conference on Research and Theory in Mental Retardation, Gatlinburg, TN, 1996.*
 10. Castellví-Bel S, Mila M. Genes responsible for nonspecific mental retardation. *Mol Genet Metab* 2001; 72(2): 104-8.
 11. Tejada MI, Ibarluzea N. Non-syndromic X linked intellectual disability: Current knowledge in light of the recent advances in molecular and functional studies. *Clin Genet* 2020; 97(5): 677-87.
 12. Sahoo T, Theisen A, Marble M, Tervo R, Rosenfeld JA, Torchia BS, et al. Microdeletion of Xq28 involving the AFF2 (FMR2) gene in two unrelated males with developmental delay. *Am J Med Genet Part A* 2011; 155(12): 3110-15.
 13. Rousseau F, Rouillard P, Morel ML, Khandjian EW, Morgan K. Prevalence of carriers of premutation-size alleles of the FMR1 gene--and implications for the population genetics of the fragile X syndrome. *Am J Hum Genet* 1995; 57(5): 1006.
 14. Stettner GM, Shoukier M, Höger C, Brockmann K, Auber B. Familial intellectual disability and autistic behavior caused by a small FMR2 gene deletion. *Ame J Med Genet Part A* 2011; 155(8): 2003-7.
 15. Youings SA, Murray A, Dennis N, Ennis S, Lewis C, McKechnie N, et al. FRAXA and FRAXE: the results of a five year survey. *J Med Genet* 2000; 37(6): 415-21.
 16. Handt M, Epplen A, Hoffjan S, Mese K, Epplen JT, Dekomien G. Point mutation frequency in the FMR1 gene as revealed by fragile X syndrome screening. *Mol Cell Probes* 2014; 28(5-6): 279-83.
 17. Chakrabarti L, Bristulf J, Foss GS, Davies KE. Expression of the murine homologue of FMR2 in mouse brain and during development. *Hum Mol Genet* 1998; 7(3): 441-8.
 18. Honda S, Hayashi S, Kato M, Niida Y, Hayasaka K, Okuyama T, Imoto I, Mizutani S. Clinical and molecular cytogenetic characterization of two patients with non-mutational aberrations of the FMR2 gene. *Am J Med Genet Part A* 2007; 143(7): 687-93.
 19. Quinlan A, Kindlon N. bedtools: A powerful toolset for genome arithmetic. 2017. Accessed on 10h June 2021) Available from URL: <https://bedtools.readthedocs.io/en/latest/>
 20. Li H, Handsaker B, Wysoker A, Fennell T, Ruan J, Homer N, et al. The sequence alignment/map format and SAMtools. *Bioinformatics* 2009; 25(16): 2078-9.
 21. Wang K, Li M, Hakonarson H. ANNOVAR: functional annotation of genetic variants from high-throughput sequencing data. *Nucleic Acids Res* 2010; 38(16): e164.
 22. Untergasser A, Cutcutache I, Koressaar T, Ye J, Faircloth BC, Remm M, et al. Primer3—new capabilities and interfaces. *Nucleic Acids Res* 2012; 40(15): e115.
 23. McGuffin LJ, Bryson K, Jones DT. The PSIPRED protein structure prediction server. *Bioinformatics* 2000; 16(4): 404-5.
 24. Zhang Y. I-TASSER server for protein 3D structure prediction. *BMC Bioinformatics* 2008; 9(1): 40.
 25. Roy A, Kucukural A, Zhang Y: I-TASSER: a unified platform for automated protein structure and function prediction. *Nature Protocols* 2010; 5(4): 725.
 26. Lovell S, Davis I, Arendall W, de Bakker P, Word J, Prisant M, et al. Structure validation by Calpha geometry: phi, psi and Cbeta deviation. *Proteins* 2003;50(3): 437-50.
 27. Pettersen EF, Goddard TD, Huang CC, Couch GS, Greenblatt DM, Meng EC, et al. UCSF Chimera—a visualization system for exploratory research and analysis. *J Comput Chem* 2004; 25(13): 1605-12.
 28. Binkowski TA, Naghibzadeh S, Liang J. CASTp: computed atlas of surface topography of proteins. *Nucleic Acids Res* 2003; 31(13): 3352-5.
 29. Dundas J, Ouyang Z, Tseng J, Binkowski A, Turpaz Y, Liang J. CASTp: computed atlas of surface topography of proteins with structural and topographical mapping of functionally annotated residues. *Nucleic Acids Res* 2006; 34(suppl-2): W116-8.
 30. Capriotti E, Altman RB, Bromberg Y. Collective judgment predicts disease-associated single nucleotide variants. *BMC Genomics* 2013, 14(S3): S2.
 31. Emidio C, Piero F, Rita C. I-Mutant2. 0: predicting stability changes upon mutation from the protein sequence or structure. *Nucleic acids research* 2005; 33: 306-10.
 32. Bendl J, Stourac J, Salanda O, Pavelka A, Wieben ED, Zundulka J, et al. PredictSNP: robust and accurate consensus classifier for prediction of disease-related mutations. *PLoS Comput Biol* 2014, 10(1): e1003440.
 33. Kopanos C, Tsiolkas V, Kouris A, Chapple CE, Aguilera MA, et al. VarSome: the human genomic variant search engine. *Bioinformatics* 2019; 35(11): 1978-80.
 34. Chen Y, Cramer P. Structure of the super-elongation complex subunit AFF4 C-terminal homology domain reveals requirements for AFF homo- and heterodimerization. *J Biol Chem* 2019; 294(27): 10663-73.
 35. Garber KB, Visootsak J, Warren ST: Fragile X syndrome. *Eu J Hum Genet* 2008; 16(6): 666-72.
 36. Bensaid M, Melko M, Bechara EG, Davidovic L, Berretta A, Catania MV, et al. FRAXE-associated mental retardation protein (FMR2) is an RNA-binding protein with high affinity for G-quartet RNA forming structure. *Nucleic Acids Res* 2009, 37(4): 1269-79.
 37. Salcedo-Arellano MJ, Hagerman RJ, Martinez-Cerdeno V. Fragile X syndrome: clinical presentation, pathology and treatment. *Gaceta Med de Mexico* 2020; 156(1): 60-6.
 38. Bagni C, Tassone F, Neri G, Hagerman R. Fragile X syndrome: causes, diagnosis, mechanisms, and therapeutics. *J Clin Invest* 2012; 122(12): 4314-22.
 39. Riley C, Wheeler A. Assessing the Fragile X Syndrome Newborn Screening Landscape. *Pediatrics* 2017; 139(Suppl-3): S207-15.



Lymphatic transport system to circumvent hepatic metabolism for oral delivery of lipid-based nanocarriers

Amarjitsing Rajput^{a,b}, Prashant Pingale^c, Darshan Telange^d, Shailesh Chalikwar^{e,*},¹, Vivek Borse^{f,**},¹

^a Nanomedicine Laboratory, Department of Biosciences and Bioengineering, Indian Institute of Technology Bombay, Powai, 400076, Mumbai, Maharashtra, India

^b Department of Pharmaceutics, Poona College of Pharmacy, Bharti Vidyapeeth Deemed University, Erandwane, Pune, 411038, Pune, Maharashtra, India

^c Department of Pharmaceutics, GES's Sir Dr. M. S. Gosavi College of Pharmaceutical Education and Research, Nashik, 422005, Maharashtra, India

^d Department of Pharmaceutics, Rajarshi Shahu College of Pharmacy, Buldhana, 443001, Maharashtra, India

^e Department of Pharmaceutical Quality Assurance, R. C. Patel Institute of Pharmaceutical Education & Research, Karwand Naka, Shirpur, 425405, Dist.-Dhule, Maharashtra, India

^f NanoBioSens Lab, Department of Medical Devices, National Institute of Pharmaceutical Education & Research (NIPER), Hyderabad, Department of Pharmaceutics, Ministry of Chemicals and Fertilizers, Govt. of India, NH 9, Kukatpally, Industrial Estate, Balanagar, Hyderabad, 500037, Telangana, India

ARTICLE INFO

Keywords:

Lipid-based nanocarriers
Hepatic first-pass metabolism
Lymphatic transport
Presystemic metabolism
Oral delivery of nanoparticles
Research models

ABSTRACT

The oral route of administration for lipid-based nanocarriers is of immense importance for the drugs having low bioavailability because of extensive first-pass metabolism. These drug delivery systems have reportedly improved oral bioavailability via lymphatic transport. The solubility issues of a drug are addressed by directly encapsulating them into the lipid. Subsequently, various lipid-based nanocarriers have enhanced the therapeutic activity of drugs via lymphatic transport with negligible side effects. Animal studies have depicted significant improvement in the oral bioavailability of drugs by avoiding first-pass metabolism. A detailed clinical study for large animals is needed to investigate the safety and efficacy of various lipid-based nanocarriers. In this review, we have described the potential and pertinence of the oral route of administration for lipid-based nanocarriers. The importance of lymphatic transport systems as a liver bypass transport system is also described herein. Various carriers such as liposomes, nanostructured lipid carriers, lipid-drug conjugate, etc. are discussed in brief with recent examples. The transport of lipids and absorption of drugs across the lymphatic pathway and various factors associated with nanocarriers affecting the lymph node targeting are also highlighted. Various *in vivo* and *in vitro* research models along with a brief focus on *in silico* prediction of the lymphatic transfer are described. The insights on future perspectives with an emphasis on the translational barriers may help the researchers working in this area.

1. Introduction

Lymph biology is being explored as an alternative to blood biology regarding the orally administered drug delivery systems. Presently, the lymphatic system is studied vigorously with greater consideration for drug delivery. The lymphatic system is considered as the drain of the vasculature, submissively filtering fluid and proteins from the interstitial spaces along with lipid from the intestine into the blood [1]. The structure and function of lymphatics differ for various organs. Lymphatics in intestines carry out the transport of lipid-soluble vitamins,

fats, and maintain an aqueous balance [2]. The oral route of administration is the most commonly used as compared to various other routes such as intravenous, subcutaneous, pulmonary, transdermal, nasal, etc. Certainly, there are numerous advantages of using oral formulations such as easy administration, convenience, patient compliance, cost-effectiveness, etc. But it also has a major unavoidable disadvantage i.e., low bioavailability due to gastric sensitivity, reduced intestinal absorption, and hepatic first-pass metabolism. The molecular size and solubility of a drug are critical parameters that decide the route of administration. Upon oral administration, the drug is absorbed in the

* Corresponding author.

** Corresponding author.

E-mail addresses: pharmashailesh@rediffmail.com (S. Chalikwar), vivek.borse@niperhyd.ac.in (V. Borse).

¹ Both the corresponding authors have contributed equally.

small intestine and enters into the intestinal portal vein or lymphatic system. Intestines have a profuse supply of blood as well as a lymph capillary network. The drug may preferably enter blood capillaries, as the portal blood flow is 500 times more than intestinal lymph, and undergo hepatic first-pass metabolism [3]. In another pathway, the drug enters lymph capillaries. The highly lipophilic and micro-sized drug molecules are delivered through the portal vein. The drugs undergo enzymatic breakdown in the liver reducing its bioavailability. The lymphatic pathway is preferred to overcome this issue and deliver the drug directly into the systemic circulation. Utilizing the lymphatic pathway, the hepatic first-pass metabolism is bypassed resulting in a significant increase in the bioavailability of drugs [4]. As the lymphatic system is involved in the transport of fats and lipids, lipid-based drug formulations are mainly transported through the lymphatic system [5].

Nanotechnology is regarded as an advanced discipline of the twenty-first century. Nanotechnology has revolutionized all the science and technology areas in the past twenty years, including the pharmaceutical sector [6]. This is attributed to the theoretical as well as practical integration of physics, chemistry, biology, materials, mechanics, and engineering at the nanometer level. Nanoparticles are most suited to reach sub-cellular levels; therefore, the cellular uptake is greater for nanoparticles compared to microparticles. Extending applications of nanotechnology, several colloidal drug delivery systems such as solid lipid nanoparticles (SLNs), polymeric nanoparticles, nanostructured lipid carriers (NLCs), liposomes, dendrimers, etc. have been fabricated. Novel methods and formulations have transformed the present and future of medicine intended for targeted drug delivery [7].

Recently, various nanocarriers have been developed that are based on lipid nanoparticle (LNP) technology. The potential of LNP technology for lymphatic drug delivery is already discussed in the literature [8]. Lipid-based formulations have reportedly enhanced oral absorption of lipophilic drugs via the lymphatic transport system. Thus, the use of lipidic vehicles has significantly improved the oral bioavailability of lipophilic drugs. Lipid-based nanocarriers also prevent the chemical degradation of a drug after oral administration [9,10]. SLNs are nanoparticles made up of multiple lipids such as short, medium, and

long-chain triglycerides. SLNs were discovered in the 1990s as a substitute colloidal carrier for existing traditional carriers, especially for lipid-soluble drug molecules [11]. Further, the advanced version of SLNs was developed, labeled as NLC, which consists of additional component liquid lipid (oil) mixed with solid lipid. The need to classify more potent lead compounds ever causes the increasingly lipophilic drug candidates [12]. Compounds with physicochemical characteristics like $\log P > 5$ and long-chain triglyceride solubility >50 mg/g are potential drug candidates for lymphatic transport (liver bypass) drug delivery [13]. The development of SLN and NLC overcome the various difficulties associated with traditional nanoparticulate-based drug delivery systems [11]. Delivery of lipophilic drugs to the lymph nodes (LNs) using lipid-based nanocarriers is the most promising approach. The particle size and surface properties are important parameters for the delivery of drugs to the LNs. In a particular example, particle size around 20–50 nm was found to be ideal for LNs targeting [14–16]. In this review, we have described the potential and pertinence of the oral route of administration for lipid-based nanocarriers for delivery to LNs.

2. The physiological barriers affecting oral drug delivery

The gastrointestinal tract (GIT) considerably limits the bioavailability of an orally administered drug. The GI anatomy, biochemistry, and metabolism process majorly regulate the fate of oral drug delivery systems. The absorption of drugs is determined by the various physicochemical property of drugs and local factors such as pH, enzymes, mucous membranes, drug residence time, and GIT surface area [17].

2.1. Mucosal diffusion barrier

Mucus acts as a natural barrier to contaminants and molecules and protects mucosal tissue. A pH on the luminal surface varies from 1 to 2 to almost neutral pH on the surface of the epithelium in the stomach [18]. The mucus comprises mucin protein compounds and water covered with proteoglycans; thus, mucus has a negative charge [19]. The thickest mucus layer of GIT is present in the stomach and colon, with a

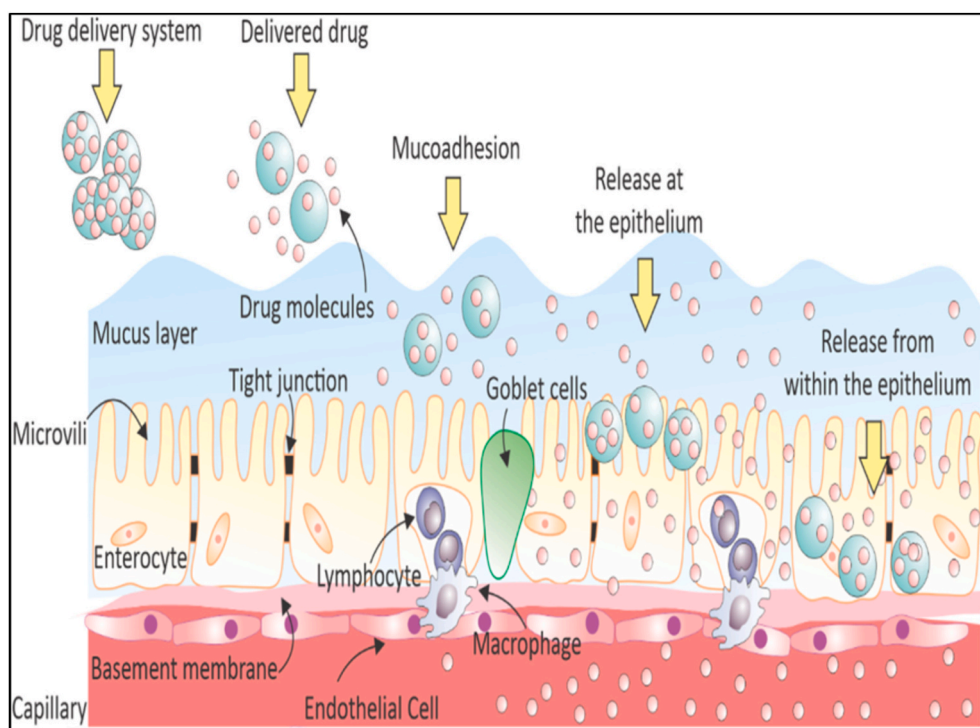


Fig. 1. Schematic illustration of drug release and absorption mechanisms for orally delivered drugs in the large surface area of the human intestinal epithelium. Reproduced with permission, from reference [Ahadian et al., 2020].

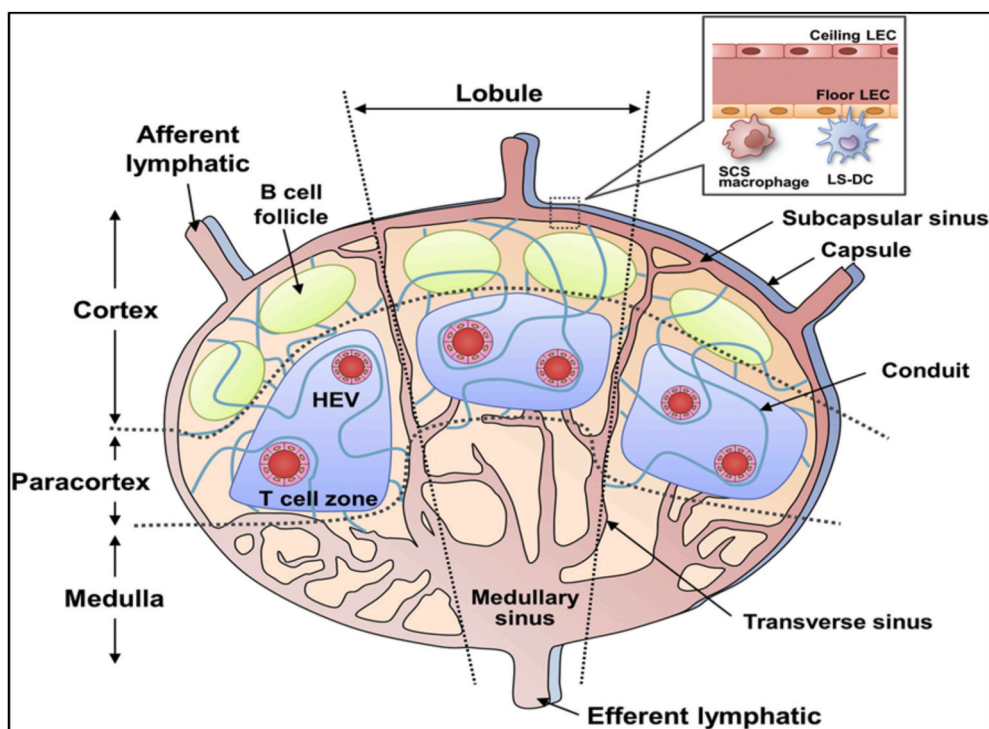


Fig. 2. Architecture of lymph nodes (LNs). LNs have afferent lymphatic and efferent lymphatic as an entrance and an exit, respectively. The multiple lymphoid lobules are covered with SCS. In the SCS, SCS macrophages, and LS-DCs survey the lumen. The area of LNs is divided into the cortex, paracortex, and medulla. The conduit system spreads in the cortex and paracortex. Reproduced with permission, from reference [Nakamura et al., 2020].

double-layer system of mucus. The mucus system is composed of an interior bound mucus layer and an unbound loose mucus portion to the exterior. The mouth and the esophagus have no distinct mucus membrane but are isolated from the salivary glands by mucus, while the small intestine has a sort of loose and unattached mucus [20].

2.2. Biochemical barrier

Owing to separate enzyme function, i.e., suppression or activation, genetic polymorphisms, or even disease state, there is a considerable interindividual variation throughout the drug metabolism processes. The mammalian enzymes are functional within the lumen and inside the enterocytes. The microflora enzymes are found in the ileum and colon [21].

2.2.1. Metabolizing enzymes

The major metabolic obstruction to any drug is hydrochloric acid and proteolytic pepsin present in the lumen of the stomach. The acidic conditions (pH 2–5) induces peptide and protein hydrolysis. The primary enzymatic barrier is peptidases located in the enterocyte cytosol and along the brush line. Variability in enzymatic activity may also affect the degradation of drug molecules such as peptide and protein drugs [21].

2.2.2. Transporters and efflux pumps

Transporters exist in the intestinal barrier, and some of these transporters are permeable to dipeptides and tripeptides. The transfer of peptides into the cell is an energy-dependent process and subjected to saturation, which is receptor-mediated transfer characteristics. P-glycoprotein (P-gp) is an efflux pump located at the brush boundaries of small and large intestine villus tips. P-gp receptors also manifest themselves in other biological boundaries and act as a defense mechanism against xenobiotics. The efflux pump prevents the entry of small molecules (e.g., natural substances, artificial colors, and anticancer drugs) and peptides across the membrane [22].

2.3. Cellular permeability barrier

Orally administered drugs can be absorbed into four categories of trails, i.e., transcellular, paracellular, carrier-mediated transcellular, and facilitated transport. Among these trails, the transcellular route is considered a crucial pathway for absorbing the drug into the GIT. It is typically directly related to the solubility (lipid) of the drug molecules. The paths of drug absorption or drug efficacy are not completely restricted by the barriers met in the gut. But, later there are hepatic barriers as they enter the vessels in the intestinal epithelium. The drugs are permeated passively through paracellular diffusion (among the cells) and transcellular diffusion (over the cell) or actively through endocytosis interceded by receptors and carrier-mediated transport. The drug molecules are absorbed preferably in a non-ionized form (lipophilic) than in an ionized form. Nanoparticles typically undergo cellular absorption in the GIT through the transcellular pathway. Nanoparticles can also be translocated by paracellular transport and vision through gaps or holes at the villous tips [19,22]. Fig. 1 shows the illustration of drug release and absorption mechanism in the large surface area of the human intestinal epithelium for the drugs administered orally.

3. Lymphatic transport systems as a bypass to liver

The lymphatic system is a vasculature structure that actively removes components (fluid and proteins) from interstitial spaces, together with fat from the intestine into the blood [23]. The lymphatic system comprises extremely permeable capillaries inside the tissue and carries lymph-containing lipoproteins, lymphocytes, and cellular proteins [24]. Theoretically, nanoparticles can either undergo indirect transport through the hepatic portal system to the systemic circulation or direct transport through the intestinal lymph system to the systemic circulation. Systemic intestinal lymph can be targeted through lacteal, which will be capillary lymph vessels [25,26].

3.1. Physiology of the intestinal lymphatic system

Gasparo Aselli first described the lymphatic system in 1627 [23] by observing the presence of white vessels in a mesentery of a well-fed dog [27]. The lymph system is made up of lymph, capillary fluid, blood flow, and lymph duct and lymph organs like the LN, thymus, and spleen. Its function is essential to help defend tissues from infection by extracting toxins from the lymph and fostering lymphocyte activities that offer defense or immunity to the disease-causing infectious agents. The primary function of the lymph system is to maintain the normal level of water in body [28].

3.1.1. Organization of the lymphatic system

The lymphatic capillaries have specific permeability and usually remain non-permeable to interstitial molecules. Lymph and interstitial fluid are made up of similar protein structures. The difference is, lymph includes a large volume of intestinal fat. This lymph is a milky, turbid, and white emulsion known as chyle. As blood flows from the branching arteries to the tiniest capillaries, plasma fluid and proteins join the interstitial layer. These exudates are again consumed in the post-capillary venules. Yet, there's a slight net fluid flow out of the vasculature due to the osmotic forces arising from protein extravasations. This consists mainly of endothelial cell layers formed in the cross-section of strongly attenuated cells. The lymph capillaries have a typical diameter of 10–60 μm [27]. The most important restructural units of gut-associated lymphoid tissue in a lymphatic system are the Peyer's patches, a set of organized lymphoid tissues lining the intestinal tract. They are the primary triggers of mucosal immunity and the target sites for oral vaccine delivery [28]. The lymphatic system has five major parts i.e., the capillaries, circulating vessels, lymph nodes, trunks, and ducts as shown in Fig. 2. The interstitial fluid passes through the capillaries of the lymph to form the lymph. Often classified as original or final lymphatics, the lymph capillaries do not have unique structures.

3.1.2. Mechanism of lymph formation and transport

The two components contribute to the net lymphatic flow rate: lymph development (i.e., the transmission of fluid from interstitium to initial lymphatics) and lymph transport (i.e., the transmission of lymph from initial lymphatics via the lymph vessels via the blood). Local driving forces for lymph development are interstitial fluid pressure and extracellular matrix tension. In contrast, lymphatic propulsion is caused by respiration, blood pressure, and exercise on the other side [27].

3.1.3. Solute uptake

The scale of nanoparticles is one of the most crucial variables for lymphatic absorption and survival in LNs [27]. Particulate size from 10 to 100 nm is used for lymphatic absorption, while particles smaller than 10 nm are preferentially reabsorbed into the blood capillaries. Liposomes of size less than 60 nm are absorbed more efficiently by the intestinal lymphatics than liposomes between 400 and 500 nm [29]. The structural composition of a particle is also one of the essential variables in assessing bowel lymphatic uptake. Colloidal and lipid-containing particles are absorbed proficiently. Several drugs are encapsulated in the lipid to form stable lipid nanoparticles having greater absorption efficiencies than the product in a traditional dosage type [30].

3.2. Transport of lipids and lymphatic absorption of the drug

In recent years, the highly lipophilic drugs that are absorbed through the intestinal lymphatic system are of great research interest. The intestinal lymphatic distribution mechanism improves the bioavailability of a large number of lipophilic drugs that are administered orally. There is specific binding of the drug to lymphoid tissue and indirect binding of particular sites linked to low-density lipoprotein receptors [31]. For 100–150 g of fat, an adult digestive system is strong enough to break down 60–80 g. Additional 40–60 g of fat is endogenous that comprises

phospholipids and cholesterol. Intraluminal processing is critical for drug solubilization in the GIT and bioavailability. The *in vivo* passage of lipids from the GI lumen to the systemic circulation is greatly influenced in presence of the digestive system. The fate of lipid-based drug delivery within the human body is complicated, and thus, the actual absorption mechanism of a drug into the enterocyte and its future remains unknown. Three processing phases summarize the principle of lymphatic transport and the absorption of lipid-based formulations [32].

3.2.1. Digestive phase

Upon ingestion, lipid-based formulations are dispersed in the stomach and the lipids are cleaved by the gastric juices. Shearing forces in the stomach helps in the emulsification process of formulation. This is an important stage where the drug release occurs because of the precipitation or dissolution and resolubilized as micelles into gastric media [32]. The enhanced bile salt concentration results in lipid solubilization. Thus, this digestion and solubilization product is captured into a colloidal structure, consisting of different micelles (unilamellar, multilamellar, and mixed micelles) [10]. Overall, the digestive process enhances the lipid and drug solubilization into the small intestine, which is essential for improved bioavailability [33].

3.2.2. Absorptive phase

The absorption step includes the intracellular removal of intact lipids. The 2-monoglyceride (2-MG) pathway and the glycerol-3 phosphate (G3P) pathway are predominantly responsible for the lymphatic transport of the drug [34]. The triglycerides and fatty acids are transported through the apical membrane of the enterocyte. These lipids are transferred to the blood circulation portal or transferred to the channel of 2-MG or G3P. The lipoprotein is transferred to the Golgi system and completes the process, where the lipoprotein is exocytosed from the enterocyte and uses the process for intestinal lymphatic transportation. Most lipids from this pool are expected to leave the enterocyte as folic acid (FA). Thus, the lipid pool transported through the portal route from the enterocyte is called the portal lipid precursor pool [10,13].

3.2.3. Circulatory uptake

A substantial number of drugs administered orally are delivered via systemic circulation to portal plasma. However, medications with a high log P value of more than 5 and more than 50 mg/mL solubility in triglyceride are transferred via the lymphatic path to the systemic circulation, inhibiting the metabolism (first-pass) hepatic system. Drugs show improved bioavailability in the presence of lipids necessary for the production of lipoproteins. Thus, transport of drugs through the lymphatic system requires co-administration of lipid, so that lipoprotein formation is enhanced [32,35].

3.3. Lymph node targeting by lipid-based nanocarriers

The LN targeting was studied over a long period with various lipid-based nanocarriers such as lipid emulsion, lipid nanoparticles, and liposomes [36]. Particle size, surface charge, modification using polyethylene glycol (PEG) as well as an antigen-presenting cell (APC), are the various factors associated with effective targeting of lipid-based nanocarriers to LNs [37].

3.3.1. Effect of particle size

Several studies have focused on the effective entry of lipid-based carriers through cell-mediated or direct transport to LNs. Numerous researchers have been studying the effect of particle size on targeting LNs. Engineered liposomes and SLN have been utilized for lymphatic delivery. SLNs are administered subcutaneously and the particle size is found to be a critical factor for uptake of SLN in intestinal fluid [38,39]. The interstitium is a small structure with a 100 nm diameter aqueous channel. Hence, SLN of size range 10–100 nm can easily pass through aqueous channels from administration to the target site, i.e., lymphatics.

The particles with a particle size of more than 100 nm will be retained at the injection site, and particles with particle diameter < than 10 nm are subjected to reabsorption into the blood capillaries.

Oussoren et al. prepared different non-sized liposomes (400 nm, 170 nm, 70 nm, 40 nm) using the extrusion method [39]. The smaller size liposomes (40 nm) resulted in higher uptake by the lymphatic system after subcutaneous administration than more giant and non-sized liposomes. The lower uptake by the lymphatic system (<20%) was observed for liposomes sized 400 nm. Liposomes in the size range 40 nm were poorly held in the LNs than bigger and non-sized liposomes. It was concluded that smaller size liposomes (40 nm) increase LN transitivity, although a high affinity towards LNs was observed in large-size liposomes compared to small-sized liposomes. Kato et al. fabricated 111In laden lipid emulsion of various sizes (25 nm and 67 nm) and compared its lymphatic uptake and confinement in the LNs from the site of intramuscular administration [40]. The lymphatic uptake was compared and it was found that emulsions having a size of 67 nm showed more retention into the LNs than the size of 25 nm. Hence, it was observed that larger size particles have more retention in LNs. It was also reported that larger size particles i.e., 520 nm had been transported to the subcapsular sinus (SCS) after administration directly to lymphatic vessels [41]. Liposomal formulation having a particle size less than 100 nm displayed great permeability *in vitro* as well as *ex vivo*; improved drug bioavailability was also reported upon oral administration [42]. The nano-emulsion of particle size of less than 100 nm has shown enhanced solubility and oral absorption of lipophilic drugs [43].

3.3.2. Effect of surface charge

Several limitations restrict the entry of drugs administered orally, subcutaneously, and intravenously to the lymphatic system. The presence of glycosaminoglycans imparts a negative surface charge on the lymphatic interstitium [44]. Because of this local negative charge, the nanocarriers that carry neutral or negative charge are permeable to the lymphatic system. On contrary, because of electrostatic interaction, the cationic nanocarriers are mostly retained at the target site [45]. The charge also affects the process of passage and delivery to the LNs in another way [46]. The phosphatidylserine component of the anionic liposomes resulted in increased cellular uptake by APCs. LNPs of size 30 nm with anionic charge showed significant aggregation of the particles in the LNs as compared to cationic and neutral particles [37]. The drug delivery systems such as liposomes, nanoparticles, NLCs, etc., possess a positive charge on their surface, resulting in higher retention at the injection site because of interactions with negatively charged interstitium molecules.

3.3.3. Effect of PEGylation in lipid-based nanocarriers

The biomimicking membrane coating, Zwitterion coating, alteration in physicochemical properties, and blockade of the reticuloendothelial system pre-administration are few approaches used to bypass accelerated blood clearance [47–51]. But, conjugation using PEG (i.e., PEGylation) is one of the most commonly used approaches to develop the nanocarriers with an enhanced half-life (plasma), pharmacokinetics, and biodistribution [52]. PEGylated liposomes currently serve as a promising approach to LN targeting agonists for the stimulator interferon genes (STING) [53]. The STING route is the primary mode for starting antitumor immunity versus the immunogenic tumor [54], and it results in the stimulation of the STING route, which activates APC ripening and Type I Interferon generation [55,56]. Although there are advantages offered by the PEGylation process, the cellular uptake due to the increase in the size of lipid-based nanocarriers may remain a challenge.

3.3.4. Effect of ligand alteration in lipid-based nanocarriers

Alteration of the ligand in lipid-based nanocarriers is one of the critical parameters for LN targeting in addition to PEGylation. Modification of the surface of LNPs using ligand may change the oral

absorption and transportation. Studies have reported a significant increase in lymphatic uptake and oral bioavailability of the SLNs coated with N-carboxymethyl chitosan [57,58]. Liposomes are altered using the class II anti-major histocompatibility complex (MHC) Fab' to attack APCs, enhancing aggregation of nanocarriers in LNs following subcutaneous injection [59]. The altered liposomes using MHC class Fab' fragment is smaller in size (around 85 nm) and easy to be delivered through lymphatics. After altering the PEG side onto liposomes (size-134 nm) with ligand (Immunoglobulins, i.e., IgG), it further increases the targeting to the LNs [60]. The nanocarriers alteration using ligand also increases the uptake of cells by dendritic cells (DCs) at the injection site. The liposomes loaded with gold nanocages (90 nm size) altered using ligand (CD11c antibody) for targeting to DCs, helps in cellular by DCs, and carry to the LNs [61]. However, the alteration in mannose (multi-valent) is also useful for targeting the DCs. Le Moignic et al. suggested a lipid-polymer complex with trimannosylates would be a promising and a possible solution for cancer messenger RNA (mRNA) vaccine targeting LN [62]. In another study, it was reported that the increase in length of the lipid chain improves lymphatic transport, and the lipids with long chains were found to be highly efficient carriers [63].

4. Drug solubility in lipid-based vehicles

The selection of lipids is a vital parameter to be considered in designing lipid-based nanocarriers. Lipids must be selected based upon the solubility of the drug in them. A drug molecule solubility in lipid is an absolute measurement of its dissolution in equilibrium with its pure form [64]. There may be chances that the drug has a high log P-value. Still, it is not necessarily highly soluble in a particular oil or lipid. On the contrary, drugs in oil or lipid can be very soluble but have a relatively low log P value [63]. However, no specific method is reported yet to assess the solubility of a drug in solid lipid. Chakraborty et al. reported the method to quantify the amount of drug solubilized into the solid lipid. This is obtained by solubilizing the highest amount of drug in the molten lipid, mainly heated overhead the glass transition temperature of that lipid. The optical intensity and powdered X-ray diffraction (XRD) experiments are performed on the cooled samples. This helps to quantify the appearance of drug crystals [32]. Another method consists of preparing drug and lipid solutions in a commonly used solvent, and the film is dried, and the film was analyzed using a microscope or with the XRD technique. But this approach is not convenient for lipids with a high melting point. The saturation of drug solubility was noted at partition temperature and above the glass transition temperature of lipid. This is based on the assumption that lipid solubilization capability decreases as temperature decreases [65].

Venkateswarlu et al. evaluated the partition coefficient of clozapine for glyceryl monostearate, i.e., GMO (imwitor 900), a lipidic group, Stearic acid with Tribehnin (Compritol 888). In this method, 10 mg quantity of the drug was suspended in a mixture of 1 g of melted lipid and 1 mL of distilled water (hot). The mixture was stirred using a magnetic stirrer for half an hour. The lipidic phase was separated from the aqueous phase. The amount of drug in the lipid phase was evaluated using HPLC and thus, the partition coefficient of the drug in particular lipid was calculated [66]. Nankervis et al. reported another technique to evaluate the number of drugs in lipid. In this technique, 1 mL of different oil samples were used for the study. About 5–10 mg of drug was dispersed in each oil, and the mixture was sonicated for 30 min on an ultrasonic water bath where the temperature increased gradually from 24 °C to 60 °C. Then, each oil sample was visually inspected for any signs of precipitation. The samples were subjected to centrifugation, and HPLC analyzed the amount of drug in the oil phase. For the oil in which no precipitation was observed, the same procedure was followed with the addition of drugs until precipitation was observed [63].

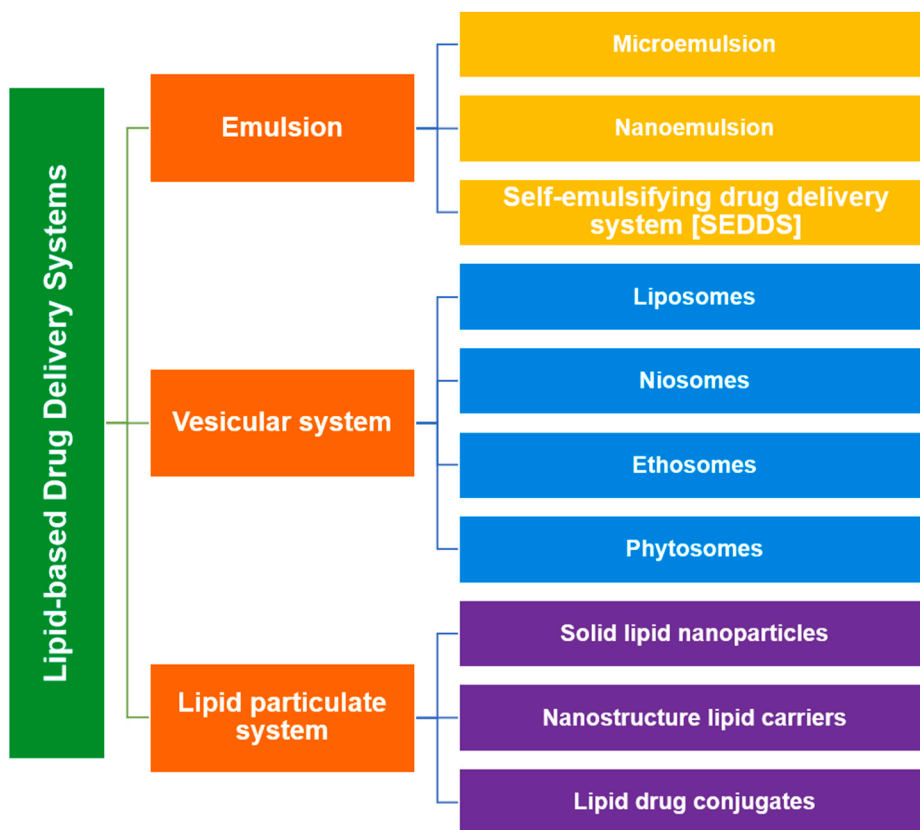


Fig. 3. Categorization of the lipid-based drug delivery system.

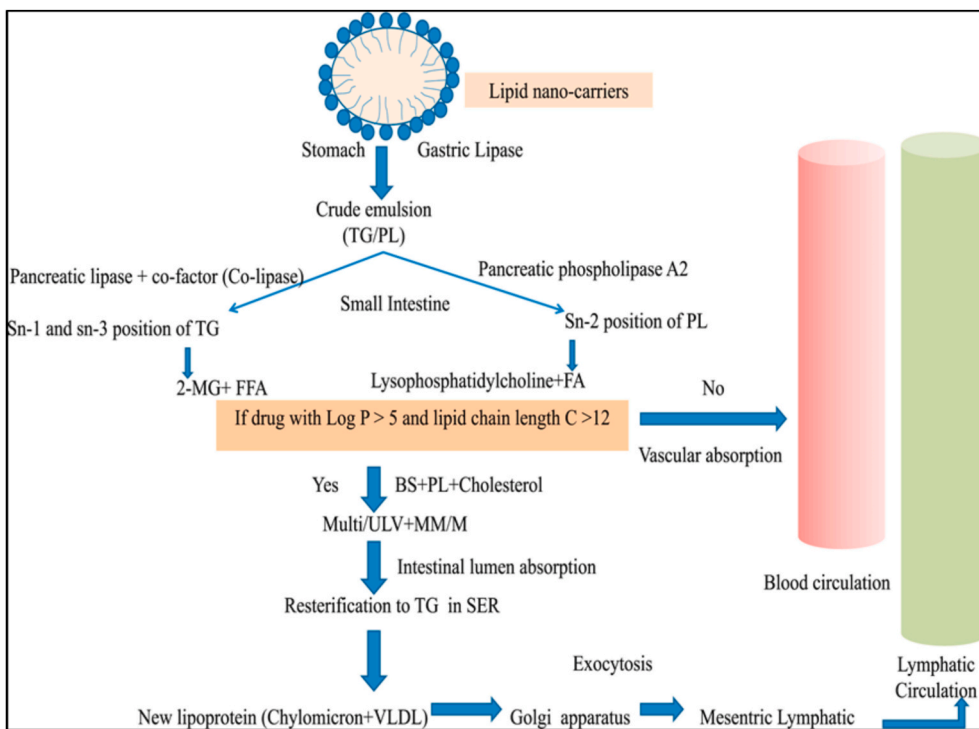


Fig. 4. Schematic representations for the sequence of events depicting in-vivo processing of lipid drug carriers and subsequent lymphatic transport. TG = Triglyceride; PL=Phospholipid; MG = Mono-glyceride; FFA=Free fatty acids; BS=Bile salts; ULV=Unilamellar vesicle; MM = Mixed Micelles; M = Micelles; SER=S-smooth endoplasmic reticulum; VLDL=Very low-density lipoproteins. Reproduced with permission, from reference [Chaturvedi et al., 2020].

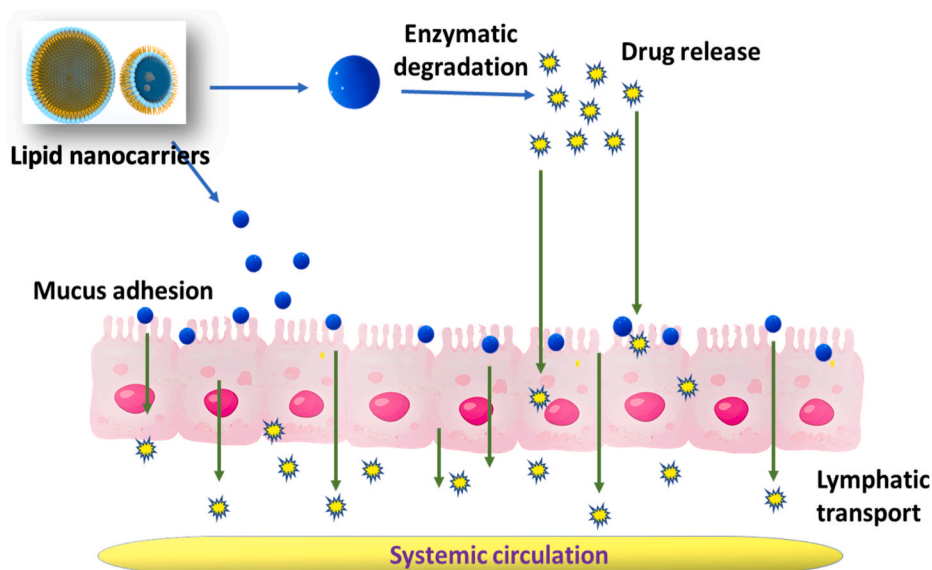


Fig. 5. Representation of the absorption mechanisms of a drug from lipid nanocarrier in the gastrointestinal tract (GIT).

5. Lipid-based drug delivery systems for oral administration

The oral route is widely preferred for the administration of drugs compared to other routes. The benefits are pain-free, convenient administration, higher acceptability, and usefulness for outpatients [67]. However, GIT barriers such as chemical and enzymatic degradation influence the drug delivery effectiveness via the oral route. The epithelial cell monolayer present in the GIT membrane is also responsible for the poor permeability of several compounds [68]. Products based on nanotechnology like NLCs, SLNs, liposomes, etc., result in enhanced oral distribution through improved bioavailability, decreased adverse effects, and ameliorated food impact [21]. The nanocarriers also play an important role in enhancing the degree to which poorly soluble drugs are absorbed into the GIT. It also increases the GIT stability of many drugs by encapsulating and preventing them from chemical and enzymatic degradation in the tract [69]. Fig. 3 shows the schematics for different types of systems categorized under a lipid-based drug delivery system.

Drug delivery via the lymphatic route is an emerging strategy to avoid the first-pass metabolism by delivering a drug into the intestine [70]. The lipid-based nanocarriers are suitable for delivering the drug into the lymph [34]. Nanocarriers can reach the lymphatic system through microfold cells (M cells). The nanocarriers increase oral bioavailability by draining lymph vessels particularly into the thoracic duct and venous blood [71].

5.1. Lipid-based nanocarriers for LN targeting

The Discovery of novel lipophilic molecules has increased the demand to formulate an effective drug carrier system for poorly water-soluble drugs. The various lipidic nanocarriers, such as phytosomes, SLNs, NLCs, and lipid drug conjugates, may be useful for targeting LNs. These lipid-based nanocarriers are functional in LN targeting because of their lipophilic nature. Thus, lipid-based drug delivery systems are well-studied and reported to have enhanced the oral absorption of several drugs [72].

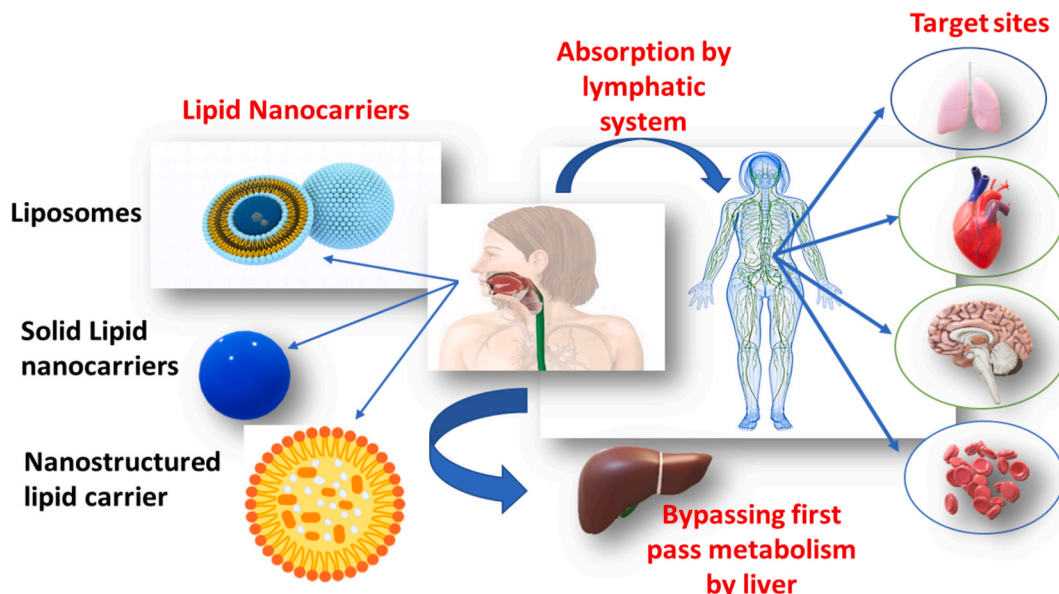


Fig. 6. Various lipid-based nanocarriers for targeting via the lymphatic pathway.

5.2. Challenges in formulating lipid-based drug delivery systems

Various challenges affect the formulation of a lipid-based drug delivery system among which the solubility of lipid drugs remains the most difficult to tackle. Subsequently, lower absorption and bioavailability of lipophilic drugs restrict their applicability via the oral route of administration. The physicochemical properties of lipidic excipients are also a critical consideration while formulating lipid-based nanocarriers. There is a range of lipidic carriers, excipients, and lipophilic drugs presented for formulation development. A large number of compounds are available for use in each of the categories, which adds up an extra effort to sort the compatibility of these individual components. Physicochemical stability of lipid-based nanocarriers is an important challenge as modest oxidation could also cause a detrimental effect on the formulation. The bioavailability of the few drugs is improved when co-administered with food [9]. For example, the bioavailability of some compounds such as griseofulvin [73], halofantrine [74], and danazol [75] is affected by food. The diet-dependent bioavailability could be affected by the utilization of lipid-based formulations of various drug molecules [76]. Many compounds (e.g., biopharmaceutical classification system (BCS) class I) have very little interaction with food. Absorption is improved in the case of BCS class II compounds when administered with food. The underlying explanation for increased bioavailability may be correlated with increased permeability, solubility, residence period in GIT, secretions (biliary and pancreatic), decreased metabolism and efflux activity, and passage via a lymphatic pathway in the existence of food material [9,77,78]. Fig. 4 represents a sequence of events depicting *in vivo* processing of lipid-based nanocarriers and subsequent lymphatic transport. The lipid components in lipid-based nanocarriers aid in molecular solubilization, permeation, and lymphatic transport of lipophilic drugs and reduce the side effects [9,79,80]. The lipid-based formulations are biocompatible, scalable, and industrially applicable. It evades various physiological barriers like the first-pass effect, breakdown in GIT, P-gp efflux, and problems associated with permeation [76,81]. The mechanisms of drug absorption from lipid-based nanocarrier in GIT are as shown in Fig. 5.

5.3. Lipid-based drug delivery systems

The schematic in Fig. 6 shows various lipid-based nanocarriers for targeting via a lymphatic pathway.

5.3.1. Liposomes

Liposomes are nano-sized spherical particles consists of a lipid bilayer vesicle enclosed by an aqueous core. Liposomes can be loaded with drugs (hydrophilic or lipophilic), where lipophilic drugs remain in the lipid bilayer and hydrophilic drugs in an aqueous core [82,83]. Managuli et al. fabricated the surface engineered asenapine maleate (ASPM) nanoliposomes for lymphatic delivery. The liposomes were conjugated with RGD peptide to target Payer's patches in the intestine for direct entry into the lymphatic system, which improved the oral bioavailability of the ASPM. The sustained release performance of drugs from prepared liposomes was studied. The optimized batch of liposomes with particle size less than 100 nm showed higher *in vitro* permeation for the Caco-2 + Raji B co-culture model. The liposomes also improvised oral bioavailability and efficacy compared to the plain drug [42]. Yazdi et al. have reported PEGylated liposomes with folate targeting to deliver insulin by the oral route. The liposomes were synthesized using phospholipid with high transition temperature, having particle size 150–210 nm. These particles have a negative charge due to the PEGylation process. It resulted in the enhancement of stability of liposomes with high penetration potential. The cell uptake study results showed higher insulin uptake due to folic acid conjugation. The biodistribution study of PEGylated liposomes showed higher residence time in the stomach and intestine with more blood and liver concentration. The *in vivo* anti-diabetic study of liposomes displayed increased insulin levels with decreased blood glucose levels. The study concluded that phospholipids

of high transition temperature with the PEGylation and conjugation with ligand could enhance liposomal oral delivery [84]. Singh et al. have reported that the PEGylation of liposomes improves the permeability and solubility of drugs. The exemestane (EXE) loaded conventional, and PEGylated liposomes were fabricated and characterized by various parameters. The PEGylation of liposomes prevented the breakdown of a drug in the GIT as compared to the conventional liposomal formulation. The PEGylated liposomal formulation also showed high intracellular uptake, *ex vivo* gut permeability, and improved oral bioavailability [85]. Bile acid conjugated partially uncapped liposomes have shown improved intestinal uptake and lymphatic transport of insulin. The study has shown promising results for the application of modified liposomes in the oral delivery of insulin [86].

5.3.2. Self-nanoemulsifying drug delivery systems (SNEDDS)

SNEDDS are nanocarriers composed of lipids, which are nowadays used to deliver several drugs via oral pathways [87]. It is considered a recent and innovative technology to increase the bioavailability of lipophilic drugs [88]. SNEDDS also helps improve dissolution, solubility, and oral absorption of poorly water-soluble drugs [13,89]. It is also considered an effective and patient-friendly drug delivery system [90]. The self-emulsifying drug delivery system (SEDDS) consists of oil, surfactant, co-surfactant, and drug molecules. It possesses the ability to form nanoemulsion post oral administration in the GIT. This nanoemulsion is having a particle size of less than 100 nm that can enhance the solubility and absorption of lipophilic drugs [43]. The advantages of SNEDDS include its ability to avoid the hepatic first-pass metabolism and improve the lymphatic transmission of lipophilic drugs, reduce cytochrome-P450 enzyme degradation in the gut enterocyte community, and resolve enterohepatic recirculation [87,91–93]. The delivery of SNEDDS is achieved mainly via lymphatic passage through Peyer's patches together with GIT [94].

Garg et al. reported a study of self-nanoemulsifying oils comprising long-chain fatty acids to enhance the oral delivery of darunavir to the lymphatic system for complete inhibition of the human immunodeficiency virus (HIV). The quality by design (QbD) approach was used with various parameters such as critical quality attributes (CQA) and quality target product profile (QTTP) to achieve formulation development in minimum trials. The preformulation study involved phase diagram study, solubility study, and risk evaluation by failure mode effect analysis (FMEA). The FMEA study recognizes Tween 80, Lauroglycol 90, and Transcutol HP as an emulsifying agent, lipid, and co-solvent, respectively, for the self-nanoemulsifying oily formulation of darunavir. The formulation was systematically optimized, and the optimized batch was selected based on the numerical desirability function. The optimized batch showed 50 nm globule diameter, >85% release in 15 min, and >75% penetration of drug in 45 min. *In vivo* studies, including lymph cannulation and *in situ* intestinal diffusion study, demonstrated a significant enhancement in the absorption of drug-using self-nanoemulsifying oily formulations through a lymphatic way because of the existence of triglycerides (long-chain). Similarly, *in vivo* pharmacokinetic study performed in the rat confirmed the enhancement in the drug bioavailability in the plasma for advanced formulation dosing than the pure drug administration. The study concluded that there is a significant increase in the biopharmaceutical parameters of the self-nanoemulsifying oily formulation of darunavir used orally to treat the viral loads [95].

Singh et al. have studied *trans*-resveratrol SNEDDS using long-chain triglycerides (LCTs) to address the various issues associated with its oral delivery. The solubility study results showed components useful for formulating the SNEDDS like Lauroglycol FCC (lipid), Transcutol P, and Labrasol (surfactants). The 32 central composite design (CCD) was used to optimize formulation and select the optimized batch using an overlay plot. The particle size in the nanometer range and higher zeta potential values of developed SNEDDS indicated the non-coalescent nature of the formulation. An optimized batch showed a significant enhancement in

the release profile of the drug than a pure drug. The pharmacokinetic study of optimized formulation also demonstrated drastic improvement absorption rate constant (K_a) 3.29-time and area under the curve (AUC) 4.31-fold compared to pure drug. Similarly, *in situ* perfusion study in Wistar rats showed an increment in the permeability and absorptivity factors of SNEDDS versus the pure drug compound. The study suggested a remarkable improvement in the absorption and oral bioavailability of *trans*-resveratrol using SNEDDS [96].

5.3.3. Phytosomes

Phytosomes or phytoconstituents–phospholipids complex is lipid compatible molecular complex or aggregates of phytoconstituents or drugs and phospholipids [97]. Phytosomes contain the phytoconstituents of herbs that are bioactive and form a strong complex with a polar head of phospholipids through intermolecular forces of interactions viz., hydrogen bonding and van der Waals forces. Phytosomes in drug delivery have certain advantages such as enhancement of complexation rate, drug loading capacity, drug stability, encapsulation efficiency, and most importantly, inhibition of drug expulsion [91, 98–100]. According to its composition, the phospholipids are the chief component of this drug delivery system due to its higher phosphatidylcholine (PC) contents, i.e., 76%, cylindrical shape with higher entropy, amphiphilicity, and biocompatibility nature with the mammalian cell membrane [101,102], and thus, assists in improving the oral bioavailability of drugs and bioactive via crossing lipid-rich bio-membrane [97]. Phytosomes are obtained from a stoichiometric chemical reaction (e.g., solvent evaporation, salting out, and lyophilization method) between the active constituents and phospholipids non-polar solvents such as dichloromethane, 1,4-dioxane, tetrahydrofuran, and ethanol, etc. [103–105]. Phytosomes were first developed by Indena in 1989 and have been commercialized with the name of PHYTOSOMES® in the market [106].

Telange et al. have developed the phytosomal soft nanoparticle-loaded mangiferin–phospholipids complex (MPLC SNPs) to improve the biopharmaceutical properties of mangiferin. The CCD produced optimal values of mangiferin: phospholipids ratio (X_1 , 1: 1.76 w: w), reaction temperature (X_2 , 50.55 °C), and reaction time (X_3 , 2.02 h) revealed lower particle size ~ 507 nm, polydispersity index (PDI) ~ 0.43 and zeta potential ~ -12.53 mV, however, after nanoprecipitation and lyophilization (~2% w/w sucrose) enhanced the particle size to ~ 907 nm, PDI of 0.50 but maintained the same zeta potential value (-12 mV). The authors reported that obtained phospholipids complex and MPLC SNPs resulted in improved aqueous solubility, dissolution rate, *ex vivo* permeation rate, and *in vivo* antioxidant activity compared to plain mangiferin. Differential scanning calorimetry (DSC), powder x-ray diffractometry (PXRD), FT-IR, and ¹H NMR studies confirmed the complex formation and reported that there is the involvement of weak intermolecular forces between mangiferin and phospholipids. Pharmacokinetics studies at 60 mg/kg in albino rats reported that MPLC SNPs compared to phospholipids complex showed significantly improved oral bioavailability ~53.29% by enhancing the C_{max} , T_{max} , and AUC of mangiferin. The stability study concludes with nonsignificant particle size changes, PDI, drug loading, and entrapment efficiency after six months [107].

Li et al. formulated, evaluated, and pharmacologically characterized the mangoflorine-phospholipids complex in the chronic unpredictable mild stress animal model. The blood-brain distribution and *in vivo* antidepressant activity studies were carried out in male ICR mice in eight and four groups. At the end of the study and 30 min post intravenous injection, the study demonstrates that the complex (17 mg/kg) enhanced the blood-brain barrier permeability compared to pure mangoflorine. Similarly, the complex treated ICR mice (7 mg/kg) appreciably showed the antidepressant-like response [108].

Biswas et al. fabricated a phospholipids complex using response surface methodology to enhance ursolic acid absorption and oral bioavailability. The animal study was carried out with the carbon

tetrachloride (CCl₄) induced intoxicated rat model. The optimal values of formulation and process variables, i.e., ursolic acid: Hydrogenated soy phosphatidylcholine (HSPC) ratio, reaction time, and reaction temperature of ursolic – phospholipids complex by the application of Box-Behnken Design was observed to be 1:1.96, 1.7 h and 55.2 °C respectively. The optimized complex resulted in enhance aqueous solubility (1.3-fold), oil-water partition coefficient, and *in vitro* dissolution performance in both gastric and intestinal juice for 12 h of study. *In vivo* study concludes that at a dose of 20 mg/kg, the ursolic acid – HSPC complex in the CCl₄-treated animals offered the hepatoprotection by restoring the *in vivo* antioxidant marker enzyme levels [109].

Jain et al. prepared raloxifene-phospholipids complex (RLX-C) and studied its effects on phase solubility, *in vitro* release, cell cytotoxicity, and pharmacokinetics of raloxifene. The phase solubility study demonstrated that RLX-C at stoichiometric ratio (7:3) shows a higher Gibbs free energy value because a higher value indicates higher solubility in water. The release study concluded that RLX on complexation with phospholipids follows the non-Fickian release. Cell viability study performed on MCF-7 cells, and their results demonstrated that RLX-C reduced the cell viability (4-folds) compared to pure RLX, suggested the cytotoxicity of RLX-C formulations. The flow cytometry study revealed that RLX-C treated MCF-7 cells at a 12.50 µg/mL concentration show early phase apoptosis (78.26%) compared to late phase apoptosis (69.09%) for pure RLX. However, the late apoptosis phase was found to be increased from 2.92 to 11.26% for reference control, RLX, and RLX-C, respectively. A pharmacokinetic study (60 mg/kg) revealed that RLX-C improves the C_{max} , T_{max} . In contrast, it also reduced the other parameters such as half-life ($t_{1/2}$) and residence time in blood circulation indicated an overall improvement in the biopharmaceutical profile of RLX [110].

Ravi et al. developed a nano-lipid complex of rutin at a molar ratio of (1:1, 1:2, and 1:3) using solvent evaporation, salting out, and lyophilization method. Authors have studied its effect on hepatoprotective, antioxidant, and oral bioavailability in rats. The results showed that the lyophilization method at a molar ratio of (1:2) using a combination of dimethyl sulfoxide (DMSO) and *t*-butyl alcohol as an optimal solvent system improved the particle size, zeta potential, and release behavior of rutin. *In vivo* study was performed in CCl₄-induced intoxicated rats for seven days. After seven days, the results revealed that rutin-lipid complex at ratio (1:2) at a dose of (100 mg/kg and 200 mg/kg) significantly restored enzyme levels compared to pure rutin. The oral bioavailability of this optimized complex was found to be 86.23% compared to pure rutin. It was concluded that the lyophilization method can be a suitable strategy for preparing nano-lipid complex and enhancing the absorption and permeation profile of rutin [111].

5.3.4. Solid lipid nanoparticles (SLN)

SLNs are colloidal dispersion of small (<100 nm), medium (100–300 nm), and large size (up to 1000 nm) particles [112]. SLNs comprise active pharmaceutical ingredients (API) and solid lipids with a monolayer coating of surfactant or co-surfactant [113]. The appropriate amount of solid lipids around ~0.1–30% w/w and surfactants and co-surfactants around ~0.5–5% w/v along with suitable manufacturing method, produce the SLNs with desired parameters such as particle size, shape, surface charge, short and long-term stability, drug loading and controlled release of APIs. The low solubility and high permeability profile of APIs from anesthetics, analgesics, antipyretics, anxiolytics, antipsychotics, antibiotics, and antiparasitic antiretroviral, anticancer, and antihypertensive represent the most favorable candidate for SLN [114]. SLN provides numerous benefits such as improved biopharmaceutical features of nanoparticles following oral administration, reduction in particle size helps to modify the release patterns (i.e., controlled and targeted release), a superior drug loading capacity of API, improved drug stability, ease to prepare at large scale, reduced toxicity, encapsulation of water-soluble and lipid-soluble drug with different physicochemical and biological properties, easy to carry small as well as large bio-macromolecules, vaccine, and antigen [11,115–120]. Moreover,

the lipid nature and devoid of organic solvent in SLN make it more biocompatible with the cellular membrane absorption [121].

Ban et al. studied the effect of tristearin and PEGylated emulsifiers (PEG10SE or PEG100SE) on the controlled oral absorption of curcumin-loaded SLN. The curcumin-loaded SLN was prepared using the oil-in-water emulsion technique and characterized. The employed emulsifiers (e.g., PEG10SE or PEG100SE) at 46.9 mM concentration resulted in stabilized, spherical, and opaque SLN. Compared to PEG10SE, the PEG100SE significantly influence the particle size, zeta potential, yield, and emulsifier surface, respectively. The GIT absorption study concluded that the PEG100SE modulates the digestion of SLN formulation via changing its interface thickness, particle size, and emulsifier surface load results in the highest curcumin solubility of formed mixed micelles. This resulted in prolonged lipolysis of SLN formulation and assisted in increase the oral bioavailability of curcumin. Hence, the obtained results suggested that PEG100SE is a better emulsifier for controlling curcumin absorption like valuable molecules with therapeutic value [122].

Jain et al. investigated the impact of lipid component mixture GMS: Gelucire 50/13 on oral bioavailability and therapeutic efficacy of beta-carotene loaded SLN prepared using hot homogenization technique. The author reported that lipid component mixture (GMS: Gelucire 50/13), when used at an equal ratio of (1:1), produced the beta-carotene loaded SLN with particle size ~ 203 nm, PDI ~ 0.185, and zeta potential ~ -7.21 mV, respectively. The lipid component mixture ratio increases the entrapment efficiency by ~68.3% and drug loading capacity around ~13% that was attributed to the high solubility of beta carotene in the selected lipid mixture compared to the ratio 1:0.5 and 1:2, respectively. *In vitro* dissolution study of formulation revealed that at first 1 h, a burst release ~28.34% followed by a slower and controlled release around 80% by the end of 48 h indicates selected lipid mixture Gelucire increases the controlled release of beta carotene from SLN formulations. Cytotoxicity study revealed that beta-carotene loaded SLN between the concentration range 10–40 $\mu\text{M}/\text{mL}$ for 48 h and 72 h incubation, reduced the survival rate of MCF-7 cell, indicated that nanometer size support with the controlled release of drug from SLN penetrated the cancer cell and showed cytotoxicity effect [123].

Pandya et al. prepared olmesartan medoxomil loaded SLN using a hot homogenization method and optimized using CCD to treat hypertension. A CCD based study reported that SLN formulation with optimized GMO concentration (X1, 108.94 mg) and surfactant concentration (X2, Pluronic 407P: Tween 80, 1:1% w/w) produced the desired particle size (113.10 nm) spherical shape, with higher entrapment efficiency (94.09%) and zeta potential (-22.80 mV). The lyophilization using trehalose at (1:4) weight ratio shows the increase in particle size from 113.10 nm to 152.40 nm, whereas the zeta potential remains unaffected. The *in vitro* release study revealed that optimized SLN formulation extends the release of olmesartan medoxomil for 24 h (72.49%) in phosphate buffer saline (PBS pH 6.8 (1% sodium lauryl sulfate, i.e., SLS) compared to low release SLN formulation around 5% in 0.1 N HCl (1% SLS) respectively. Similarly, *ex vivo* diffusion studies demonstrate that optimized SLN formulation in the duodenum by the end of 8 h shows the enhanced drug release compare to in the stomach for 2 h only. The pharmacokinetic study was conducted in male Wister rats at a dose of 1.023 mg/kg; it demonstrates that SLN formulation improved the oral bioavailability of olmesartan medoxomil 2.3-fold via increasing C_{max} (1610 ng/mL) and AUC₀₋₂₇ (15492.50 ng/mL and 5527.75 ng/mL), respectively. Stability study revealed that refrigerated condition (2–8 °C) preserves the particle size of optimized drug-loaded SLN, while room temperature influences the same formulation after two months followed by precipitation at the end of 3 months [124].

5.3.5. Nanostructured lipid carriers (NLC)

Nanostructured lipid carriers (NLCs) are advanced nanoparticle carriers made up of solid lipids, liquid lipids, surfactants, and co-surfactants. The appropriate combination of these blends produces a

partially crystallized or less ordered lipid matrix providing high loading capacity and preventing leaching of the drug from the nano-systems throughout the storage [125]. The NLCs system provides multiple advantages such as controlled release performance, enhanced targeting efficiency, improved stability, site-specific transport through different administration routes, easy to prepare, feasibility scale-up, biocompatibility, biodegradability, and non-toxicity [126]. Additionally, NLCs are developed to overwhelm the shortcomings of SLN, such as low drug loading caused by crystallized lipids and drug expulsion because of phase transition (i.e., β - modification) of lipids gelation throughout the storage [127–129].

Oshiro-Junior et al. evaluated the potential of phthalocyanine (photosensitizer-PS)-loaded NLCs functionalized with folic acid (NLC-FA-PS) as a carrier for photodynamic therapy (PDT) breast cancer. Pluronic-folic acid synthetic polymer (PF127-FA) was synthesized at a molar ratio of (1:4) was confirmed by infrared and proton nuclear magnetic resonance (¹H NMR) spectroscopy. The added PF127 (3.5%) in NLCs at sonication amplitude of 8% for 20 min at an interval period of 20 s obtained homogeneously distributed particles, i.e., low particle size <112 nm and PDI <0.2. However, more than >4% amplitude increases the probe temperature, which resulted in homogenous nanometer-scale particles. Moreover, the PF127-FA based NLCs reported stability up to 90 days without any precipitation, creaming, and phase separation, but the addition of PS, i.e., phthalocyanine, showed a change in coloration from blue to green. The encapsulation study reported ~63% w/w incorporation of phthalocyanine efficiency into NLCs. It depends on the simultaneous incorporation of this drug with the lipid phase followed by centrifugation and filtration to prevent precipitation and aggregation upon addition into an aqueous phase. The hydrodynamic diameter, PDI, and zeta potential values of NLC-FA-PS were found in between the range of ~165.3–181.3 nm, 0.23 to 0.18, and -17.3 to -19.9 mV, respectively, which also confirmed its suitability for the treatment of solid tumors due to easy accumulation and retention of these particles for showing enhanced permeability and retention effect. The photobleaching study demonstrated that at 500 $\mu\text{g}/\text{mL}$ of PS in NLC-FA-PS showed a 25% reduction of photobleaching rate and increases the aqueous dispersion rate of PS, which causes to generate higher reactive oxygen species and shows cellular and tissue damage cell. The PS dissolved around 4.13% and 28% by the end of 30 min and 7 days, suggested its sustained release behavior attributes to its nanosystems and photobleaching. The MTT assay concluded that NLC-FA-PS at a concentration of 0.91 μM following 90 s of light exposure showed only 57% of cell viability. Results indicated that PF127-FA assisted NLCs with a PDT combination could provide a potential approach for photosensitizer in breast cancer treatment [130].

Singh et al. fabricated exemestane-loaded NLCs (EXE-loaded NLCs) using Precirol® ATO (solid lipid) and flaxseed oil (liquid lipid) using the ultrasonication method. The formulation was optimized using a CCD. Results showed that Precirol® ATO, flaxseed oil, and surfactants (e.g., poloxamer 188: Tween® 80: Tween® 20, 2:1:1) were the best combination for the EXE-loaded NLCs. The optimized concentration of process and formulation variables, i.e., high lipid, surfactant concentration, and sonication time, reports the significant outcomes of particle size (131 nm), PDI (0.20), entrapment efficiency (87% w/w), and drug loading (40.12% w/w) respectively. DSC, PXRD, and scanning electron microscopy (SEM), and transmission electron microscopy (TEM) studies revealed that selected lipids and surfactants reduced the crystalline nature of EXE and provide high encapsulation with lipid matrix, which finally appears as a spherical shape and smooth surface. The early burst release and subsequently sustained-release (84%) with Fickian diffusion release compared to free EXE suspension (34%) for 24 h designates that significant impact of solid lipid and liquid lipid on the EXE-loaded NLCs. Intestinal permeation study concluded that solid and liquid-solid as digestive lipids and surfactants as a P-gp inhibitor in the gastrointestinal system increase the intestinal permeability (Papp ~ 3.15 cm/min) of this formulation. The higher cell penetration sustained release, and high

accumulation of EXE from NLCs resulted in high cytotoxicity in-between the range of (IC₅₀-6.25–100 μ M) in MCF-7 cell lines. The pharmacokinetics study concludes that the nanosize of this formulation has enhanced the oral bioavailability significantly through effective contact with enterocytes, resulting in EXE uptake from NLCs into the blood circulation. The study suggests that the lipid mixture with a surfactant ratio can be utilized as a suitable component for the preparation of NLCs with high entrapment and loading efficiency of EXE [131].

Cavalcanti et al. developed and evaluated the hot ultrasonication and microwave-based NLCs for the oral delivery of zidovudine (NLC-AZT and M-NLC-AZT). The study reported that Precirol® ATO 5 (solid lipid) and Miglyol® 812 (liquid lipid) in the ratio (1:40 w/w) and (1:50 w/w) for conventional and microwave methods are the suitable lipids for higher solubility of AZT as well as sufficient particle size and PDI value of NLCs. The full factorial design (FFD) study revealed a low level of sonication time. The quantity of Tween® 20 and a high level of solid lipids critically influenced the loading capacity of AZT. The CCD reported the best optimal values for sonication time (2 min 20 s) and the amount of Tween® 80 (31 mg) for optimized loading capacity, particle size, and PDI of AZT-NLCs. For microwave-based NLCs, the CCD also provide the best optimal values for the quantity of Tween 80 (158 mg) and amount of solid lipid (73 mg) for optimized loading capacity, whereas the quantity of Tween® 80 (150 mg) and amount of solid lipids (75 mg) for the optimized value of PDI. Obtained lower particle size \sim 113 nm, PDI \sim 0.21, zeta potential \sim -20 mV, EE \sim 22% w/w, and higher loading capacity \sim 1.41% w/w for M-AZT-NLCs compared to AZT-NLCs indicates long circulating time particles, uniform, and monodisperse particles and with good stability. The release study concluded that in simulated physiological solutions, the AZT-NLCs and M-AZT-NLCs reported the controlled release performance for more than 24 h via a controlled diffusion mechanism. Stability study revealed that up to 45 days, both the NLCs formulation preserved the particle size between the range (\sim 100–300 nm), PDI value (\sim 0.3), and zeta potential ($>$ -20 mV), respectively. Comparative results in this study suggested that the microwave method could be a promising approach over the conventional one to prepare NLCs [132].

5.3.6. Lipid drug conjugates (LDCs)

LDCs are lipid-based carriers synthesized by conjugation of drug molecules with lipids. The lipids are the essential components of this system and based on this, various lipids, for instance, fatty acids, steroids, glycerides, and phospholipids, have been used in conjugation with drug molecules via chemical bonds such as ester, amide, hydrazone, disulfide, and other bonds. The LDCs alter the physicochemical properties of drug molecules and improve their lipophilic performance. LDCs enhance oral bioavailability, permeability into the brain, targetability to the tumors and lymphatic system, higher drug loading, extended drug release, and reduce toxicity [133].

Ding et al. have developed nicotine-loaded LDC SLN using Kolliwax®, stearic acid, and hydrogenated sunflower oil. The stearic acid: lipid nicotine conjugate (SA-LDC) and Kolliwax®: lipid nicotine conjugate (K-LDC) at molar ratio (1.2:1) and (1:1) was formulated using a simple melting method, whereas the W-SA-LDC-SLN, B-K-LDC-SLN, W-SLN, and B-SLN was prepared using high-pressure homogenization method (HPH, homogenization cycles \sim 1, 5, 3 and 3 respectively) and reported the significant encapsulation efficiency of nicotine into lipid mold with an enhancement of its lipophilicity log P \sim - 2.4. The HPH method produced a significant effect on the particle size of these formulations, and therefore, the particle size of W-SLN and B-SLN was observed to be \sim 300 nm. In contrast, W-SA-LDC-SLN and B-K-LDC-SLN reported different particle sizes around \sim 251 and 137 nm that were attributed to a difference in lipid composition and smaller droplets by HPH, suggests that additional homogenization cycles may be used to reduce the particle size of W-SA-LDC-SLN. The DSC study showed that the shifting of the melting peak of LDC and SLN to lower temperatures provided a controlled release of nicotine from the lipid matrix into the

oral cavity. LDC formulation reported \sim 50% w/w of entrapment efficiency, whereas non-LDC formulation reported only \sim 6 and 8% w/w [134].

Soni et al. designed and characterized lipid-drug conjugate NPs carriers for oral delivery of pemetrexed diacid (PTX). The conjugation of PTX with stearic acid (SA) was carried out by the ethanol-based solvent evaporation technique. The LDC NPs were prepared using a cold homogenization method and optimized by three levels of Box-Behnken design. An optimization result concludes that middle concentration of SA (4% w/v), lower concentration of surfactant (0.8% w/v) and middle HPH cycle (12) as optimal values showed lower particle size \sim 121 nm, PDI \sim 0.35, high zeta potential \sim - 51.6 mV, high entrapment efficiency \sim 81% w/w and drug loading \sim 80% w/w respectively. The lower particle size with its uniform distribution within the LDC NPs was confirmed by TEM studies. The DSC, FT-IR, and PXRD studies found that the PTX is completely dissolved into SA resulted in formation conjugation between PTX and SA via amide bond formation. The PTX release from LDC NPs was burst release \sim 25% w/w at initial 2 h, followed by sustained release around \sim 84% w/w after 24 h and follows first-order kinetic with Fickian diffusion release mechanism. The intestinal permeability (Papp) was increased for LDC NPs loaded PTX \sim 3.065 cm/min than plain PTX solution \sim 0.5082 cm/min, and this permeation was confirmed by confocal laser scanning microscopy. MTT assay was carried out on human lung adenocarcinoma cell lines (A 549) and reported that LDC NPs loaded PTX showed significant cytotoxicity at 25, 50, and 100 μ g/mL, respectively, compared to plain PTX solution because of the biphasic release performance of PTX from optimized LDC NPs. A pharmacokinetic study was studied using a non-compartmental method and reported that LDC NPs loaded PTX at 20 mg/kg showed significant enhancement of C_{max}, T_{max}, and AUC₀₋₂₄ compared to plain PTX solution suggest controlled release of PTX from LDC NPs responsible for the enhancement of oral bioavailability of PTX [135].

Ashwini Kumar et al. have developed 5-fluorouracil-palmitic acid conjugate (5-FUDIPAL) incorporated in polyester nanoparticles using the dual technique, i.e., double emulsion-solvent evaporation method, and evaluated its efficacy for controlled release and cytotoxicity in HCT-116 cell line (colon cancer). Compared to PLGA (Poly (lactide-co-glycolide) and PLA (polylactic acid), the PCL (polycaprolactone) demonstrated higher encapsulation efficiency and yield of 5-FUDIPAL around \sim 97% w/w and 96.3%, respectively. These higher encapsulation values also confirmed that PCL possesses inherent structural hydrophobicity. The physicochemical analysis concluded that 5-FUDIPAL particles are monodisperse and homogeneously distributed within all nanoparticles. It was supported by particle size \sim < 150 nm, acceptable PDI \sim 0.15–0.19, and low zeta potential value \sim - 8.6 to - 17.7 mV, respectively. The spherical and smooth surface nature of all nanoparticles was found in the microscopic analysis; however, the good NPs separation and aggregation were reported in TEM and SEM. The physicochemical studies suggested the homogenous dispersion of 5-FUDIPAL within the polymeric matrix indicates a complete missing of its characteristics. The controlled release study concluded that all three NPs displayed burst release for the initial 60 min, after that; PCL showed slow release for 900 min, PLGA displayed elevated release for 300 min, and PLA exhibited elevated release of 5-FUDIPAL between the time points of 300–900 min. The cytotoxicity study showed that all NPs loaded with 5-FUDIPAL conjugate exhibited higher inhibitory activity against HCT-116 cell lines. However, the PLGA NPs after 24, 48, and 72 h at 50 and 75 μ M showed significant inhibitory activity around \sim 63%, 86%, and 87%, respectively, compared to PCL and PLA NPs [136].

Neupane et al. have reported the LDC NPs of decitabine (DCB) and studied its effect on the permeability of DCB using *ex vivo* gut permeation studies. The LDC conjugate between DCB and SA was prepared using a salt formation method, and subsequently, its NPs were developed using a cold homogenization method. The obtained middle-level values of lipid concentration (X1, 8% w/v), surfactant concentration (X2, 5% w/v), and a number of homogenization cycle (X3, 12) based on

BBD for LDC NPs reported the desired particle size ~ 202.6 nm, lower PDI ~ 0.33 , EE $\sim 69\%$ w/w. Higher zeta potential values ~ -34 mV respectively indicated homogenous dispersion of DCB within the LDC NPs prevents its degradation and, thus, showed maximum stability. The high solubility of DCB in lipid, lipid matrix, partition coefficient, and particle size showed the burst release of $\sim 26\%$ in 2 h followed by sustained release of around 77% w/w by the end of 24 h reported by LDC NPs of DCB compared to the fast release of plain DC. The stability study concludes that LDC NPs of DCB indicated no precipitation, phase separation, and good dispersibility upon six months of storage. The optimized SA and surfactant concentration in LDC NPs reported an enhanced intestinal permeability ~ 1.464 cm/min and mitigated the intestinal efflux. The study suggested that the SA can be utilized as a promising LDC NPs carrier for enhancing the oral bioavailability of DCB [137].

Paliwal et al. have developed methotrexate-lipid drug conjugate nanoparticles (MTX-LDC NPs) as autolymphotrophs for enhanced oral bioavailability and reduced gastrointestinal toxicity. The MTX-LDC-NPs formulation showed low particle size ~ 152 nm, acceptable zeta potential ~ -22 mV, and high entrapment efficiency $\sim 83\%$ w/w, respectively; however, other NPs formulations, i.e., MTX-LDC-NPs3, also showed the same values for these parameters. Lower particle size in all the formulations confirmed its uptake via the lymphatic system, increased its residence time, improved oral bioavailability, and reduced gastrointestinal toxicity of MTX. The bioavailability study concludes that the lymphatic transport mechanism was the dominant mechanism responsible for the enhanced oral bioavailability of MTX-LDC-NPs formulations [138].

6. Research models

The use of specific research models is needed to investigate intestinal lymphatic transport and accurately predict improved oral lipophilic formulations with *in vitro* and *in vivo* studies. The transportation of lipid-soluble compounds through intestinal lymphatics mainly takes place with the biosynthesis of lipoprotein. Thus, co-administration of lipid is the most common way for maximizing lymphatic drug transport [139]. Portal blood absorption is faster than that of intestinal lymphatic transport owing to the series of complex events. Thus, the plasma profile of the absorbed drug is large, indicating the slow intake of lipoproteins. This also causes double peaks in plasma profile, although gastric emptying or resolubilisation impact resulted in portal blood absorption [140]. The comparison between data sets is difficult because there is a massive difference in the method and animal model used [141]. The intestinal lymphatic transport is a complex system in both anatomical and physiological aspects. Thus, animal models should be specific, easy to handle & reliable for easily finding intestinal lymphatic transport [142].

6.1. *In vivo* models

The intestinal lymphatic specific targeting and transport have been studied with *in vivo* lymph duct cannulated animal models. The rat, mouse, and dog are commonly used animals. *In vivo* models are necessary for predicting intestinal lymphatic transport of LNPs, the fate of the lipid, and lipid-based nanocarriers inside the human body. In contrast, such transport of intestinal lymphatic drugs cannot be investigated thoroughly in humans [143].

6.1.1. Small animal models

Several animals can be used in studying intestinal lymphatic drug transport. The bulk of studies were carried out in anesthetized rats to appraise diverse formulation parameters and experimental factors [144]. The unconscious rat model is most predominantly used in the drug lymphatic transport study. These are reasonably easy to source and house in a small laboratory. Sometimes the unconscious rat model is also

used, but some differences exist for cannulation and lymph fistulation [145]. There are several advantages of the unconscious rat model as there is no rat movement during lymph collection, and there is no occlusion of cannula draining the lymph. However, the rate of absorption is slow for the drugs, which are suitable for intestinal lymphatic drug transport [146]. The lymph flow rate in the rat model is affected by the state in which the animal is present; for anesthetized rats, it lies between 0.1 and 0.6 mL/h and in the conscious rats, it lies between 1 and 2 mL/h. This is due to there is a reduction in motility and function of GIT. Also, there are chances of animal mortality during experimentation because of the higher time of anesthesia required [147]. The lipidic nanoparticle formulations have to be administered through the cannula implanted in the duodenum, which makes the process slightly cumbersome [148]. Conscious restrained rat models have been commonly used in lymphatic drug transport studies. After recovery from the anesthesia, the animals are strapped in a harness that contains changeable lymph collection bottles or positioned in a restraining cage [144].

6.1.2. Large animal models

Large animal models such as pigs and dogs were used to accurately assess the intestinal lymphatic transport of drugs. Large animal models have advantages, such as they are the right candidate for full-sized human dosage forms. Thus, the dosing capacity of the large animal model is equivalent to the human dosage form [149]. The fed and fasted state can be adjusted in the large animal models required for the study purpose. In contrast with rodents, the GIT, transit profile, and biliary secretion pattern of dogs and pigs are identical to humans [150]. The major disadvantages of the large animal models include the complexity of animals, and the cost of larger animals typically limits its experimental use [151].

6.1.3. Alternate *in vivo* approach

An alternative *in vivo* approach was developed in which systemic drug exposure is calculated post administration of the drug in the presence and absence of an intestinal chylomicron flow inhibitor such as Pluronic-L81 or Colchicine [152]. The importance of intestinal lymphatic for overall bioavailability is underlined in the existence or non-existence of intestinal lymph structure with the use of these agents [153]. The major advantage of this model is that it does not require surgical interventions, which are a vital requirement in lymph duct cannulation. The issues related to chylomicron flow and intestinal lipid processing are discussed in Ref. [154].

6.2. *In vitro* models

Successful drug targeting and prediction of nanoparticle drug delivery could be achieved through a better understanding of *in vitro* models used for the study. Caco-2 cells are commonly used as an intestinal epithelium model *in vitro* and estimate permeability characteristics. In lipid biochemistry, the caco-2 cells were also used to investigate the characteristics of intracellular lipoprotein assembly [155,156]. It is the potential *in vitro* model to study the impact of various lipids along with other lipid excipients on drug encapsulation in the lymphatic system (i.e., lipoproteins and lymphatic transport) [157]. The *ex vivo* association of the drug with chylomicron as a simple, productive means for estimating the lymphatic transport can also be utilized as an *in vitro* method [158]. Another method for *in vitro* model uses the dialysis membrane. The dialysis membrane retains nanoparticles and allows the free drug to remain in the dissolution media within a range of 8000–14,000 MW cut-offs [159]. The dialysis membrane is usually soaked in the double-distilled water for 12 h before use [160]. For the determination of intestinal lymphatic transport, 5–6 mL of SLN dispersion and ~ 2.5 mL of phosphate buffer of pH 6.8 are poured on the membrane, with the two ends of the membrane are fixed by clamps [161]. The membranes are placed in a suitable conical flask, and the receiving phase was added suitably. The dialysis was continued for 12 h, and the medium in the



Fig. 7. Challenges in the translation or commercialization of the lipid-based nanocarriers.

conical flask was removed intermittently for analysis [162,163].

7. *In silico* prediction of intestinal lymphatic transfer

The progress of combinatorial chemistry and high throughput screening methods have directed the discovery of a large number of lipophilic molecules. The inherent properties of drug molecules affect their pharmacokinetic profile, many molecules fail to proceed with their clinical development [164]. The popular method to enhance the bioavailability of these molecules is incorporating them into the lipidic vesicles such as lipids like stearic acid, oleic acid, compritol, etc. The mechanism underlying the intestinal lymphatic transfer is still not clear. Ichihashi et al. have therefore checked the correlation among the partition ratio of different drugs absorbed into either the lymphatic system or systemic circulation when administered to lymphatic cannulated rats using long and medium-chain triglycerides [165]. It was suggested that the lipid-soluble property is a crucial parameter to estimate the amount that follows intestinal lymphatic transport [166].

In silico methods have been used previously to predict passive absorption, thus the *in silico* prediction can also be applied to lymphatic transport. This could be achieved by developing a quantitative structure-lymphatic transfer correlation [167]. Holm et al. have used extended conformations of molecular models developed with the Sybyl molecular modeling framework (version 6.1). The authors have computed the molecular descriptors using Vol Surf software (version 2). The log P values were calculated using the log Kow online version [168]. The important relationship between structure and property was identified employing partial least squares and statistical projection of latent

structures [169]. Charman et al. proposed to have log P > 4.6 and triglyceride solubility >50 mg/mL for the drug candidates for lymphatic transport [170]. Holm & Hoest have developed a model that is an easily available device for assessing effective lymphatic transmission and focused on factors that influence intestinal lymphatic transportation other than common physicochemical properties such as log P and triglyceride solubility [168].

8. Conclusion and future perspectives in oral drug delivery via a lymphatic pathway

The lymphatic transport system enhances the bioavailability of lipophilic drugs delivered using lipid-based nanocarriers via the oral route of administration. Various drugs that are lipophilic, have solubility restrictions, prone to hepatic first-pass metabolism, and have low bioavailability could be delivered using LNPs and transported to the lymphatic system. Stability, flow properties, drug loading efficiency, etc. are few issues associated with lipid-based nanocarriers that affect formulation design. Importantly, for application in oral drug delivery, the LNPs that are usually available in powder form, the ultimate aim would be to have a conventional dosage form such as tablets and capsules. Various synthesis methods used for the preparation of lipid-based nanocarriers and the use of complex *in vivo* research models for pharmacokinetic studies of formulation significantly influence the functionality of lipid-based nanocarriers. The investigation is much needed on the precise mechanism of lymphatic transport of LNPs along with various factors affecting it. The larger preformulation and clinical study data may certainly aid in the optimization and scaling up of the

formulation. Although several studies have reported the improvement and enhancement in lymphatic transport, drug encapsulation, controlled drug release, bioavailability, drug efficacy, etc., substantial clinical studies are required. Very few studies have shown the translational and commercialization potential of the lipid-based nanocarriers for oral drug delivery via lymphatics. There are several barriers associated with the commercial viability and scalability of lipid-based nanocarriers. Fig. 7 shows challenges in the translation or commercialization of lipid-based nanocarriers. The formulation stability, scaling up to the industrial level manufacturing, dependable pharmacokinetic and pharmacodynamics activity, toxic and side effects, *in vivo* stability, target specific functionalization, reliable clinical data, etc. are the important barriers that need to be tackled. Taking into consideration the involvement of all activities for the development of a lipid-based nanocarrier formulation, expecting the cost of formulation comparative to conventional formulation would be mistaken. Another important challenge in the commercialization of lipid-based formulations is regulatory aspects. The safety and quality parameters related to preclinical and clinical studies need to be addressed prudently. Thus, translation of the lipid-based nanocarriers into products, and going beyond, their acceptance in clinical practice seems very challenging. The recent advancements in the field that are coupled with the design of experiments technology may certainly assist pharmaceutical industries to estimate, optimize, and elevate the scalability of lipid-based formulations.

Declaration of competing interest

The authors declare that they have no known competing financial interests or personal relationships that could have appeared to influence the work reported in this paper.

Acknowledgment

This review article is the motivational compilation against our regular research work on lipidic drug delivery systems. The authors extend their gratitude to the management and principal Dr. S. J. Surana of R. C. Patel Institute of Pharmaceutical Education and Research, Shirpur for providing necessary library facilities. Dr. Vivek Borse would like to acknowledge the Department of Science and Technology, Ministry of Science and Technology, Government of India for the INSPIRE Faculty Award (IFA18-ENG266, DST/INSPIRE/04/2018/000991).

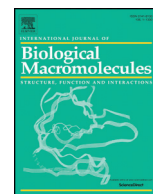
References

- [1] L. Alderfer, A. Wei, D. Hanjaya-putra, Lymphatic tissue engineering and regeneration, *J. Biol. Eng.* 12 (2018) 32, <https://doi.org/10.1186/s13036-018-0122-7>.
- [2] M. Al-Kofahi, J.W. Yun, A. Minagar, J.S. Alexander, Anatomy and roles of lymphatics in inflammatory diseases, *Clin. Exp. Neuroimmunol.* 8 (2017) 199–214, <https://doi.org/10.1111/cen3.12400>.
- [3] J.A. Yáñez, S.W.J. Wang, I.W. Knemeyer, M.A. Wirth, K.B. Alton, Intestinal lymphatic transport for drug delivery, *Adv. Drug Deliv. Rev.* 63 (2011) 923–942, <https://doi.org/10.1016/j.addr.2011.05.019>.
- [4] H. Ahn, J.H. Park, Liposomal delivery systems for intestinal lymphatic drug transport, *Biomater. Res.* 20 (2016) 36, <https://doi.org/10.1186/s40824-016-0083-1>.
- [5] M. Markovic, S. Ben-Shabat, A. Aponick, Lipids and Lipid-Processing Pathways in Drug Delivery and Therapeutics, 2020, p. 21, <https://doi.org/10.3390/ijms21093248>.
- [6] J. Jeevanandam, A. Barhoum, Y.S. Chan, A. Dufresne, M.K. Danquah, Review on nanoparticles and nanostructured materials: history, sources, toxicity and regulations, *Beilstein J. Nanotechnol.* 9 (2018) 1050–1074, <https://doi.org/10.3762/bjnano.9.98>.
- [7] V. Mishra, K.K. Bansal, A. Verma, N. Yadav, S. Thakur, K. Sudhakar, J. M. Rosenholm, Solid lipid nanoparticles: emerging colloidal nano drug delivery systems, *Pharmaceutics* 10 (2018) 191, <https://doi.org/10.3390/pharmaceutics10040191>.
- [8] T. Nakamura, H. Harashima, Dawn of lipid nanoparticles in lymph node targeting: potential in cancer immunotherapy, *Adv. Drug Deliv. Rev.* 167 (2020) 78–88, <https://doi.org/10.1016/j.addr.2020.06.003>.
- [9] S. Kalepu, M. Manthina, V. Padavala, Oral lipid-based drug delivery systems—an overview, *Acta Pharm. Sin. B.* 3 (2013) 361–372, <https://doi.org/10.1016/j.apsb.2013.10.001>.
- [10] C.J.H. Porter, N.L. Trevaskis, W.N. Charman, Lipids and lipid-based formulations: optimizing the oral delivery of lipophilic drugs, *Nat. Rev. Drug Discov.* 6 (2007) 231–248, <https://doi.org/10.1038/nrd2197>.
- [11] P. Ghasemiyeh, S. Mohammadi-Samani, Solid lipid nanoparticles and nanostructured lipid carriers as novel drug delivery systems: applications, advantages and disadvantages, *Res. Pharm. Sci.* 13 (2018) 288–303, <https://doi.org/10.4103/1735-5362.235156>.
- [12] C. I, Y. M, V. M, S. AP, I. Chauhan, M. Yasir, M. Verma, A.P. Singh, Nanostructured lipid carriers: a groundbreaking approach for transdermal drug delivery, *Adv. Pharmaceut. Bull.* 10 (2020) 150, <https://doi.org/10.34172/APB.2020.021>.
- [13] C.W. Pouton, C.J.H. Porter, Formulation of lipid-based delivery systems for oral administration: materials, methods and strategies, *Adv. Drug Deliv. Rev.* 60 (2008) 625–637, <https://doi.org/10.1016/j.addr.2007.10.010>.
- [14] V. Manolova, A. Flace, M. Bauer, K. Schwarz, P. Saudan, M.F.F. Bachmann, Nanoparticles target distinct dendritic cell populations according to their size, *Eur. J. Immunol.* 38 (2008) 1404–1413, <https://doi.org/10.1002/eji.200737984>.
- [15] S.T. Reddy, A. Rehor, H.G. Schmoedel, J.A. Hubbell, M.A. Swartz, *In vivo* targeting of dendritic cells in lymph nodes with poly(propylene sulfide) nanoparticles, *J. Contr. Release* 112 (2006) 26–34, <https://doi.org/10.1016/j.jconrel.2006.01.006>.
- [16] S.T. Reddy, A.J. van der Vlies, E. Simeoni, V. Angeli, G.J. Randolph, C.P. O'Neil, L.K. Lee, M.A. Swartz, J.A. Hubbell, Exploiting lymphatic transport and complement activation in nanoparticle vaccines, *Nat. Biotechnol.* 25 (2007) 1159–1164, <https://doi.org/10.1038/nbt1332>.
- [17] S. Ahadian, J.A. Finbloom, M. Mofidfar, S.E. Dilemiz, F. Nasrollahi, E. Davoodi, V. Hosseini, I. Mylonaki, S. Sangabathuni, H. Montazerian, K. Fetah, R. Nasiri, M. R. Dokmeci, M.M. Stevens, T.A. Desai, A. Khademhosseini, Micro and nanoscale technologies in oral drug delivery, *Adv. Drug Deliv. Rev.* 157 (2020) 37–62, <https://doi.org/10.1016/j.addr.2020.07.012>.
- [18] J. Leal, H.D.C. Smyth, D. Ghosh, Physicochemical properties of mucus and their impact on transmucosal drug delivery, *Int. J. Pharm.* 532 (2017) 555–572, <https://doi.org/10.1016/j.ijpharm.2017.09.018>.
- [19] B. Homayun, X. Lin, H.-J. Choi, Challenges and recent progress in oral drug delivery systems for biopharmaceuticals, *Pharmaceutics* 11 (2019) 129, <https://doi.org/10.3390/pharmaceutics11030129>.
- [20] M.E.V. Johansson, H. Sjövall, G.C. Hansson, The gastrointestinal mucus system in health and disease, *Nat. Rev. Gastroenterol. Hepatol.* 10 (2013) 352–361, <https://doi.org/10.1038/nrgastro.2013.35>.
- [21] B. Hu, X. Liu, C. Zhang, X. Zeng, Food macromolecule based nanodelivery systems for enhancing the bioavailability of polyphenols, *J. Food Drug Anal.* 25 (2017) 3–15, <https://doi.org/10.1016/j.jfda.2016.11.004>.
- [22] S. Hua, Advances in oral drug delivery for regional targeting in the gastrointestinal tract - influence of physiological, pathophysiological and pharmaceutical factors, *Front. Pharmacol.* 11 (2020) 524, <https://doi.org/10.3389/fphar.2020.00524>.
- [23] J.B. Dixon, Lymphatic lipid transport: sewer or subway? *Trends Endocrinol. Metabol.* 21 (2010) 480–487, <https://doi.org/10.1016/j.tem.2010.04.003>.
- [24] M.A. Burchill, A.R. Goldberg, B.A.J. Tamburini, Emerging roles for lymphatics in chronic liver disease, *Front. Physiol.* 10 (2020), <https://doi.org/10.3389/fphys.2019.01579>.
- [25] D.M. Denbow, Gastrointestinal anatomy and physiology, in: *Sturkie's Avian Physiol*, sixth ed., Elsevier, 2015, pp. 337–366, <https://doi.org/10.1016/B978-0-12-407160-5.00014-2>.
- [26] R.S. Managuli, S.Y. Raut, M.S. Reddy, S. Mutalik, Targeting the intestinal lymphatic system: a versatile path for enhanced oral bioavailability of drugs, *Expet Opin. Drug Deliv.* 15 (2018) 787–804, <https://doi.org/10.1080/17425247.2018.1503249>.
- [27] M.A. Swartz, The physiology of the lymphatic system, *Adv. Drug Deliv. Rev.* 50 (2001) 3–20, [https://doi.org/10.1016/S0169-409X\(01\)00150-8](https://doi.org/10.1016/S0169-409X(01)00150-8).
- [28] Y. Nishioka, H. Yoshino, Lymphatic targeting with nanoparticulate system, *Adv. Drug Deliv. Rev.* 47 (2001) 55–64, [https://doi.org/10.1016/S0169-409X\(00\)00121-6](https://doi.org/10.1016/S0169-409X(00)00121-6).
- [29] G. Vandermeulen, T. Athanasopoulos, A. Trundley, K. Foster, V. Pr at, R.J. Y anez-Mu oz, G. Dickson, Highly potent delivery method of gp160 envelope vaccine combining lentivirus-like particles and DNA electrotransfer, *J. Contr. Release* 159 (2012) 376–383, <https://doi.org/10.1016/j.jconrel.2012.01.035>.
- [30] S. Saraf, A. Ghosh, C.D. Kaur, S. Saraf, Novel modified nanosystem based lymphatic targeting, *Res. J. Nanosci. Nanotechnol.* 1 (2011) 60–74, <https://doi.org/10.3923/rjnn.2011.60.74>.
- [31] A. Dahan, A. Mendelman, S. Amsili, N. Ezov, A. Hoffman, The effect of general anesthesia on the intestinal lymphatic transport of lipophilic drugs: comparison between anesthetized and freely moving conscious rat models, *Eur. J. Pharmaceut. Sci.* 32 (2007) 367–374, <https://doi.org/10.1016/j.ejps.2007.09.005>.
- [32] S. Chakraborty, D. Shukla, B. Mishra, S. Singh, Lipid - an emerging platform for oral delivery of drugs with poor bioavailability, *Eur. J. Pharm. Biopharm.* 73 (2009) 1–15, <https://doi.org/10.1016/j.ejpb.2009.06.001>.
- [33] M. Kazi, Lipid-based nano-delivery for oral administration of poorly water soluble drugs (PWSDs): design, optimization and *in vitro* assessment, in: *Adv. Technol. Deliv. Ther.*, InTech, 2017, p. 31, <https://doi.org/10.5772/65710>.

- [34] S. Chaudhary, T. Garg, R.S.R. Murthy, G. Rath, A.K. Goyal, Recent approaches of lipid-based delivery system for lymphatic targeting via oral route, *J. Drug Target.* 22 (2014) 871–882, <https://doi.org/10.3109/1061186X.2014.950664>.
- [35] N.L. Trevasakis, D.M. Shackelford, W.N. Charman, G.A. Edwards, A. Gardin, S. Appel-Dingemanse, O. Kretz, B. Galli, C.J.H. Porter, Intestinal lymphatic transport enhances the post-prandial oral bioavailability of a novel cannabinoid receptor agonist via avoidance of first-pass metabolism, *Pharm. Res. (N. Y.)* 26 (2009) 1486–1495, <https://doi.org/10.1007/s11095-009-9860-z>.
- [36] V.I. Kaledin, N.A. Matienko, V.P. Nikolin, Y.V. Gruntenko, V.G. Budker, T. E. Vakhruševa, Subcutaneously injected radiolabeled liposomes: transport to the lymph nodes in mice, *J. Natl. Cancer Inst.* 69 (1982) 67–71, <https://doi.org/10.1093/jnci/69.1.67>.
- [37] T. Nakamura, M. Kawai, Y. Sato, M. Maeki, M. Tokeshi, H. Harashima, The effect of size and charge of lipid nanoparticles prepared by microfluidic mixing on their lymph node transitivity and distribution, *Mol. Pharm.* 17 (2020) 944–953, <https://doi.org/10.1021/acs.molpharmaceut.9b01182>.
- [38] A.E. Hawley, S.S. Davis, L. Illum, Targeting of colloids to lymph nodes: influence of lymphatic physiology and colloidal characteristics, *Adv. Drug Deliv. Rev.* 17 (1995) 129–148, [https://doi.org/10.1016/0169-409X\(95\)00045-9](https://doi.org/10.1016/0169-409X(95)00045-9).
- [39] C. Oussoren, J. Zuidema, D.J.A. Crommelin, G. Storm, Lymphatic uptake and biodistribution of liposomes after subcutaneous injection I. Influence of the anatomical site of injection, *J. Liposome Res.* 7 (1997) 85–99, <https://doi.org/10.3109/08982109709035487>.
- [40] Y.-C. Tseng, Z. Xu, K. Guley, H. Yuan, L. Huang, Lipid–calcium phosphate nanoparticles for delivery to the lymphatic system and SPECT/CT imaging of lymph node metastases, *Biomaterials* 35 (2014) 4688–4698, <https://doi.org/10.1016/j.biomaterials.2014.02.030>.
- [41] S. Kato, Y. Shirai, C. Motozono, H. Kanzaki, S. Mori, T. Kodama, In vivo delivery of an exogenous molecule into murine T lymphocytes using a lymphatic drug delivery system combined with sonoporation, *Biochem. Biophys. Res. Commun.* 525 (2020) 1025–1031, <https://doi.org/10.1016/j.bbrc.2020.02.174>.
- [42] R.S. Managuli, J.T.-W. Wang, F.M. Faruqi, A. Pandey, S. Jain, K.T. Al-Jamal, S. Mutalik, Surface engineered nanoliposomal platform for selective lymphatic uptake of asenapine maleate: in vitro and in vivo studies, *Mater. Sci. Eng. C* 109 (2020) 110620, <https://doi.org/10.1016/j.msec.2019.110620>.
- [43] A. Dahan, A. Hoffman, Rationalizing the selection of oral lipid based drug delivery systems by an in vitro dynamic lipolysis model for improved oral bioavailability of poorly water soluble drugs, *J. Contr. Release* 129 (2008) 1–10, <https://doi.org/10.1016/j.jconrel.2008.03.021>.
- [44] D.N. McLennan, C.J.H. Porter, S.A. Charman, Subcutaneous drug delivery and the role of the lymphatics, *Drug Discov. Today Technol.* 2 (2005) 89–96, <https://doi.org/10.1016/j.ddtec.2005.05.006>.
- [45] G.M. Ryan, L.M. Kaminskas, C.J.H. Porter, Nano-chemotherapeutics: maximising lymphatic drug exposure to improve the treatment of lymph-metastatic cancers, *J. Contr. Release* 193 (2014) 241–256, <https://doi.org/10.1016/j.jconrel.2014.04.051>.
- [46] N.L. Trevasakis, L.M. Kaminskas, C.J.H. Porter, From sewer to saviour-targeting the lymphatic system to promote drug exposure and activity, *Nat. Rev. Drug Discov.* 14 (2015) 781–803, <https://doi.org/10.1038/nrd4608>.
- [47] J. Zhao, Z. Qin, J. Wu, L. Li, Q. Jin, J. Ji, Zwitterionic stealth peptide-protected gold nanoparticles enable long circulation without the accelerated blood clearance phenomenon, *Biomater. Sci.* 6 (2018) 200–206, <https://doi.org/10.1039/C7BM00747G>.
- [48] R.M. de Kruijff, R. Raavé, A. Kip, J. Molkenboer-Kuening, S.J. Roobol, J. Essers, S. Heskamp, A.G. Denkova, Elucidating the influence of tumor presence on the polymersome circulation time in mice, *Pharmaceutics* 11 (2019) 241, <https://doi.org/10.3390/pharmaceutics11050241>.
- [49] I.B. Magaña, R.B. Yendluri, P. Adhikari, G.P. Goodrich, J.A. Schwartz, E. A. Sherer, D.P. O'Neal, Suppression of the reticuloendothelial system using λ -carrageenan to prolong the circulation of gold nanoparticles, *Ther. Deliv.* 6 (2015) 777–783, <https://doi.org/10.4155/tde.15.33>.
- [50] Z. Wu, B. Chen, Z. Gan, F. Chen, X. Luo, Exogenous vitamin C-triggered surface charge conversion of pH/reduction-responsive micelles for the enhanced tumor-specific activity of loaded doxorubicin, *Mol. Pharm.* 17 (2020) 954–964, <https://doi.org/10.1021/acs.molpharmaceut.9b01183>.
- [51] D. Wang, H. Dong, M. Li, Y. Cao, F. Yang, K. Zhang, W. Dai, C. Wang, X. Zhang, Erythrocyte-cancer hybrid membrane camouflaged hollow copper sulfide nanoparticles for prolonged circulation life and homotypic-targeting photothermal/chemotherapy of melanoma, *ACS Nano* 12 (2018) 5241–5252, <https://doi.org/10.1021/acsnano.7b08355>.
- [52] J.S. Suk, Q. Xu, N. Kim, J. Hanes, L.M. Ensign, PEGylation as a strategy for improving nanoparticle-based drug and gene delivery, *Adv. Drug Deliv. Rev.* 99 (2016) 28–51, <https://doi.org/10.1016/j.addr.2015.09.012>.
- [53] M.C. Hanson, M.P. Crespo, W. Abraham, K.D. Moynihan, G.L. Szeto, S.H. Chen, M.B. Melo, S. Mueller, D.J. Irvine, Nanoparticulate STING agonists are potent lymph node-targeted vaccine adjuvants, *J. Clin. Invest.* 125 (2015) 2532–2546, <https://doi.org/10.1172/JCI79915>.
- [54] S.R. Woo, M.B. Fuertes, L. Corrales, S. Spranger, M.J. Furdyna, M.Y.K. Leung, R. Duggan, Y. Wang, G.N. Barber, K.A. Fitzgerald, M.L. Alegre, T.F. Gajewski, STING-dependent cytosolic DNA sensing mediates innate immune recognition of immunogenic tumors, *Immunity* 41 (2014) 830–842, <https://doi.org/10.1016/j.immuni.2014.10.017>.
- [55] G.N. Barber, STING: infection, inflammation and cancer, *Nat. Rev. Immunol.* 15 (2015) 760–770, <https://doi.org/10.1038/nri3921>.
- [56] Q. Chen, L. Sun, Z.J. Chen, Regulation and function of the cGAS-STING pathway of cytosolic DNA sensing, *Nat. Immunol.* 17 (2016) 1142–1149, <https://doi.org/10.1038/ni.3558>.
- [57] Z. Zhang, Y. Lu, J. Qi, W. Wu, An update on oral drug delivery via intestinal lymphatic transport, *Acta Pharm. Sin. B* (2021), <https://doi.org/10.1016/J.APSB.2020.12.022>.
- [58] J.S. Baek, C.W. Cho, Surface modification of solid lipid nanoparticles for oral delivery of curcumin: improvement of bioavailability through enhanced cellular uptake, and lymphatic uptake, *Eur. J. Pharm. Biopharm.* 117 (2017) 132–140, <https://doi.org/10.1016/j.ejpb.2017.04.013>.
- [59] I. Dufresne, A. Désormeaux, J. Bestman-Smith, P. Gourde, M.J. Tremblay, M. G. Bergeron, Targeting lymph nodes with liposomes bearing anti-HLA-DR Fab' fragments, *Biochim. Biophys. Acta Biomembr.* 1421 (1999) 284–294, [https://doi.org/10.1016/S0005-2736\(99\)00137-6](https://doi.org/10.1016/S0005-2736(99)00137-6).
- [60] S.M. Moghimi, M. Moghimi, Enhanced lymph node retention of subcutaneously injected IgG1-PEG2000-liposomes through pentameric IgM antibody-mediated vesicular aggregation, *Biochim. Biophys. Acta Biomembr.* 1778 (2008) 51–55, <https://doi.org/10.1016/j.bbmem.2007.08.033>.
- [61] R. Liang, J. Xie, J. Li, K. Wang, L. Liu, Y. Gao, M. Hussain, G. Shen, J. Zhu, J. Tao, Liposomes-coated gold nanocages with antigens and adjuvants targeted delivery to dendritic cells for enhancing antitumor immune response, *Biomaterials* 149 (2017) 41–50, <https://doi.org/10.1016/j.biomaterials.2017.09.029>.
- [62] A. Le Moignon, V. Malard, T. Benvenne, L. Lemiègre, M. Berchel, P.A. Jaffrès, C. Bailloy, M. Delost, R. Macedo, J. Rochefort, G. Lescaille, C. Pichon, F. M. Lemoine, P. Midoux, V. Mateo, Preclinical evaluation of mRNA trimannosylated lipopolyplexes as therapeutic cancer vaccines targeting dendritic cells, *J. Contr. Release* 278 (2018) 110–121, <https://doi.org/10.1016/j.jconrel.2018.03.035>.
- [63] R. Nankervis, S.S. Davis, N.H. Day, P.N. Shaw, Effect of lipid vehicle on the intestinal lymphatic transport of isotretinoin in the rat, *Int. J. Pharm.* 119 (1995) 173–181, [https://doi.org/10.1016/0378-5173\(94\)00390-Q](https://doi.org/10.1016/0378-5173(94)00390-Q).
- [64] V. Jannin, J. Musakhanian, D. Marchaud, Approaches for the development of solid and semi-solid lipid-based formulations, *Adv. Drug Deliv. Rev.* 60 (2008) 734–746, <https://doi.org/10.1016/j.addr.2007.09.006>.
- [65] S.S. Rane, B.D. Anderson, What determines drug solubility in lipid vehicles: is it predictable? *Adv. Drug Deliv. Rev.* 60 (2008) 638–656, <https://doi.org/10.1016/j.addr.2007.10.015>.
- [66] V. Venkateswarlu, K. Manjunath, Preparation, characterization and in vitro release kinetics of clozapine solid lipid nanoparticles, *J. Contr. Release* 95 (2004) 627–638, <https://doi.org/10.1016/j.jconrel.2004.01.005>.
- [67] B.F. Choonara, Y.E. Choonara, P. Kumar, D. Bijukumar, L.C. du Toit, V. Pillay, A review of advanced oral drug delivery technologies facilitating the protection and absorption of protein and peptide molecules, *Biotechnol. Adv.* 32 (2014) 1269–1282, <https://doi.org/10.1016/j.biotechadv.2014.07.006>.
- [68] L.M. Ensign, R. Cone, J. Hanes, Oral drug delivery with polymeric nanoparticles: the gastrointestinal mucus barriers, *Adv. Drug Deliv. Rev.* 64 (2012) 557–570, <https://doi.org/10.1016/j.addr.2011.12.009>.
- [69] A. Bernkop-Schnürch, Reprint of: nanocarrier systems for oral drug delivery: do we really need them? *Eur. J. Pharmaceut. Sci.* 50 (2013) 2–7, <https://doi.org/10.1016/j.ejps.2013.06.011>.
- [70] S. Saraf, R. Rathi, C.D. Kaur, S. Saraf, Colloidosomes an advanced vesicular system in drug delivery, *Asian J. Sci. Res.* 4 (2011) 1–15, <https://doi.org/10.3923/ajsr.2011.1.15>.
- [71] J. Mudassir, Y. Darwis, S. Muhamad, A.A. Khan, Self-assembled insulin and nanogels polyelectrolyte complex (Ins/NGs-PEC) for oral insulin delivery: characterization, lyophilization and in-vivo evaluation, *Int. J. Nanomed.* 14 (2019) 4895, <https://doi.org/10.2147/IJN.S199507>.
- [72] H. Ali, S.K. Singh, Biological voyage of solid lipid nanoparticles: a proficient carrier in nanomedicine, *Ther. Deliv.* 7 (2016) 691–709, <https://doi.org/10.4155/tde-2016-0038>.
- [73] N. Aoyagi, H. Ogata, N. Kaniwa, A. Ejima, Effect of food on the bioavailability of griseofulvin from microsize and peg ultramicrosize (Gris-Pegr) plain tablets, *J. Pharmacobio-Dyn* 5 (1982) 120–124, <https://doi.org/10.1248/bpb1978.5.120>.
- [74] A.J. Humberstone, C.J. Porter, W.N. Charman, A physicochemical basis for the effect of food on the absolute oral bioavailability of halofantrine, *J. Pharmacol. Sci.* 85 (1996) 525–529, <https://doi.org/10.1021/js950472p>.
- [75] W.N. Charman, M.C. Rogge, A.W. Boddy, B.M. Berger, Effect of food and a monoglyceride emulsion formulation on danazol bioavailability, *J. Clin. Pharmacol.* 33 (1993) 381–386, <https://doi.org/10.1002/j.1552-4604.1993.tb04673.x>.
- [76] R. Ghadi, N. Dand, BCS class IV drugs: highly notorious candidates for formulation development, *J. Contr. Release* 248 (2017) 71–95, <https://doi.org/10.1016/j.jconrel.2017.01.014>.
- [77] M.E. Washington, M. Reillo, Food and beverage compositions infused with lipophilic active agents and methods of use thereof, *World Intellect. Prop. Organ.* (2015). <https://patents.google.com/patent/US9839612B2/en>.
- [78] S. Kollipara, R.K. Gandhi, Pharmacokinetic aspects and in vitro-in vivo correlation potential for lipid-based formulations, *Acta Pharm. Sin. B* 4 (2014) 333–349, <https://doi.org/10.1016/j.apsb.2014.09.001>.
- [79] K. Čerpnjak, A. Zvonar, M. Gašperlin, F. Vrečer, Lipid-based systems as a promising approach for enhancing the bioavailability of poorly water-soluble drugs, *Acta Pharm.* 63 (2013) 427–445, <https://doi.org/10.2478/acph-2013-0040>.

- [80] D.G. Fatouros, D.M. Karpf, F.S. Nielsen, A. Mullertz, Clinical studies with oral lipid based formulations of poorly soluble compounds, *Therapeut. Clin. Risk Manag.* 3 (2007) 591–604. <https://pubmed.ncbi.nlm.nih.gov/18472981>.
- [81] K. Thanki, R.P. Gangwal, A.T. Sangamwar, S. Jain, Oral delivery of anticancer drugs: challenges and opportunities, *J. Contr. Release* 170 (2013) 15–40. <https://doi.org/10.1016/j.jconrel.2013.04.020>.
- [82] T.M. Allen, P.R. Cullis, Liposomal drug delivery systems: from concept to clinical applications, *Adv. Drug Deliv. Rev.* 65 (2013) 36–48. <https://doi.org/10.1016/j.addr.2012.09.037>.
- [83] R. Dutta, R.I. Mahato, Recent advances in hepatocellular carcinoma therapy, *Pharmacol. Ther.* 173 (2017) 106–117. <https://doi.org/10.1016/j.pharmthera.2017.02.010>.
- [84] J.R. Yazdi, M. Tafaghodi, K. Sadri, M. Mashreghi, A.R. Nikpoor, S. Nikoofal-Sahlabadi, J. Chamani, R. Vakili, S.A. Moosavian, M.R. Jaafari, Folate targeted PEGylated liposomes for the oral delivery of insulin: in vitro and in vivo studies, *Colloids Surf. B Biointerfaces* 194 (2020) 111203. <https://doi.org/10.1016/j.colsurfb.2020.111203>.
- [85] A. Singh, Y.R. Neupane, S. Shafi, B. Mangla, K. Kohli, PEGylated liposomes as an emerging therapeutic platform for oral nanomedicine in cancer therapy: in vitro and in vivo assessment, *J. Mol. Liq.* 303 (2020) 112649. <https://doi.org/10.1016/j.molliq.2020.112649>.
- [86] K.S. Kim, D.S. Kwag, H.S. Hwang, E.S. Lee, Y.H. Bae, Immense insulin intestinal uptake and lymphatic transport using bile acid conjugated partially uncapped liposome, *Mol. Pharm.* 15 (2018) 4756–4763. <https://doi.org/10.1021/acs.molpharmaceut.8b00708>.
- [87] Y. Elnaggar, Abdallah, Elsheikh Gohar, Nanoemulsion liquid preconcentrates for raloxifene hydrochloride: optimization and in vivo appraisal, *Int. J. Nanomed.* 7 (2012) 3787. <https://doi.org/10.2147/IJN.S33186>.
- [88] E.B. Basalious, N. Shawky, S.M. Badr-Eldin, SNEDDS containing bioenhancers for improvement of dissolution and oral absorption of lacidipine. I: development and optimization, *Int. J. Pharm.* 391 (2010) 203–211. <https://doi.org/10.1016/j.ijpharm.2010.03.008>.
- [89] K. Mohsin, M.A. Long, C.W. Pouton, Design of lipid-based formulations for oral administration of poorly water-soluble drugs: precipitation of drug after dispersion of formulations in aqueous solution, *J. Pharmaceut. Sci.* 98 (2009) 3582–3595.
- [90] M. Kazi, M. Al-Swairi, A. Ahmad, M. Raish, F.K. Alanazi, M.M. Badran, A.A. Khan, A.M. Alanazi, M.D. Hussain, Evaluation of self-nanoemulsifying drug delivery systems (SNEDDS) for poorly water-soluble talinolol: preparation, in vitro and in vivo assessment, *Front. Pharmacol.* 10 (2019) 459. <https://doi.org/10.3389/fphar.2019.00459>.
- [91] P. Balakrishnan, B.J. Lee, D.H. Oh, J.O. Kim, M.J. Hong, J.P. Jee, J.A. Kim, B. K. Yoo, J.S. Woo, C.S. Yong, H.G. Choi, Enhanced oral bioavailability of dexibuprofen by a novel solid Self-emulsifying drug delivery system (SEDDS), *Eur. J. Pharm. Biopharm.* 72 (2009) 539–545. <https://doi.org/10.1016/j.ejpb.2009.03.001>.
- [92] A.A. Date, N. Desai, R. Dixit, M. Nagarsenker, Self-nanoemulsifying drug delivery systems: formulation insights, applications and advances, *Nanomedicine* 5 (2010) 1595–1616. <https://doi.org/10.2217/nmm.10.126>.
- [93] C.J.H. Porter, W.N. Charman, Intestinal lymphatic drug transport: an update, *Adv. Drug Deliv. Rev.* 50 (2001) 61–80. [https://doi.org/10.1016/S0169-409X\(01\)00151-X](https://doi.org/10.1016/S0169-409X(01)00151-X).
- [94] K. Balakumar, C.V. Raghavan, N.T. selvan, R.H. prasad, S. Abdu, Self nanoemulsifying drug delivery system (SNEDDS) of Rosuvastatin calcium: design, formulation, bioavailability and pharmacokinetic evaluation, *Colloids Surf. B Biointerfaces* 112 (2013) 337–343. <https://doi.org/10.1016/j.colsurfb.2013.08.025>.
- [95] B. Garg, S. Beg, R. Kaur, R. Kumar, O.P. Katara, B. Singh, Long-chain triglycerides-based self-nanoemulsifying oily formulations (SNEOFs) of darunavir with improved lymphatic targeting potential, *J. Drug Target.* 26 (2018) 252–266. <https://doi.org/10.1080/1061186X.2017.1365875>.
- [96] G. Singh, R.S. Pai, Trans-resveratrol self-nano-emulsifying drug delivery system (SNEDDS) with enhanced bioavailability potential: optimization, pharmacokinetics and in situ single pass intestinal perfusion (SPIP) studies, *Drug Deliv.* 22 (2015) 522–530. <https://doi.org/10.3109/10717544.2014.885616>.
- [97] A. Semalty, M. Semalty, M.S.M. Rawat, F. Franceschi, Supramolecular phospholipids–polyphenolics interactions: the PHYTOSOME® strategy to improve the bioavailability of phytochemicals, *Fitoterapia* 81 (2010) 306–314. <https://doi.org/10.1016/j.fitote.2009.11.001>.
- [98] E. Bombardelli, S.B. Curri, R. Della Loggia, P. Del Negro, P. Gariboldi, A. Tubaro, Anti-inflammatory activity of 18- β -glycyrrhetic acid in phytosome form, *Fitoterapia* 60 (1989) 29–37.
- [99] A. Semalty, M. Semalty, B.S. Rawat, D. Singh, M.S.M. Rawat, Pharmacosomes: the lipid-based new drug delivery system, *Expet Opin. Drug Deliv.* 6 (2009) 599–612. <https://doi.org/10.1517/17425240902967607>.
- [100] J.N. Yu, Y. Zhu, L. Wang, M. Peng, S.S. Tong, X. Cao, H. Qiu, X.M. Xu, Enhancement of oral bioavailability of the poorly water-soluble drug silybin by sodium cholate/phospholipid-mixed micelles, *Acta Pharmacol. Sin.* 31 (2010) 759–764. <https://doi.org/10.1038/aps.2010.55>.
- [101] A.A. Khan, J. Mudassar, N. Mohtar, Y. Darwis, Advanced drug delivery to the lymphatic system: lipid-based nanoformulations, *Int. J. Nanomed.* 8 (2013) 2733–2744. <https://doi.org/10.2147/IJN.S41521>.
- [102] K. Kuche, N. Bhargavi, C.P. Dora, S. Jain, Drug-phospholipid complex—a go through strategy for enhanced oral bioavailability, *AAPS PharmSciTech* 20 (2019) 43. <https://doi.org/10.1208/s12249-018-1252-4>.
- [103] S. Bhattacharyya, S.M. Ahammed, B.P. Saha, P.K. Mukherjee, The gallic acid-phospholipid complex improved the antioxidant potential of gallic acid by enhancing its bioavailability, *AAPS PharmSciTech* 14 (2013) 1025–1033. <https://doi.org/10.1208/s12249-013-9991-8>.
- [104] D.R. Telange, A.T. Patil, A.M. Pethe, H. Fegade, S. Anand, V.S. Dave, Formulation and characterization of an apigenin-phospholipid phytosome (APLC) for improved solubility, in vivo bioavailability, and antioxidant potential, *Eur. J. Pharmaceut. Sci.* 108 (2017) 36–49. <https://doi.org/10.1016/j.ejps.2016.12.009>.
- [105] J. Zhang, Q. Tang, X. Xu, N. Li, Development and evaluation of a novel phytosome-loaded chitosan microsphere system for curcumin delivery, *Int. J. Pharm.* 448 (2013) 168–174. <https://doi.org/10.1016/j.ijpharm.2013.03.021>.
- [106] P.M. Kidd, Bioavailability and activity of phytosome complexes from botanical polyphenols: the silymarin, curcumin, green tea, and grape seed extracts, *Alternative Med. Rev.* 14 (2009) 226–246. <http://www.ncbi.nlm.nih.gov/pubmed/19803548>.
- [107] D.R. Telange, N.K. Sohail, A.T. Hemke, P.S. Kharkar, A.M. Pethe, Phospholipid complex-loaded self-assembled phytosomal soft nanoparticles: evidence of enhanced solubility, dissolution rate, ex vivo permeability, oral bioavailability, and antioxidant potential of mangiferin, *Drug Deliv. Transl. Res.* (2020). <https://doi.org/10.1007/s13346-020-00822-4>.
- [108] B. Li, L. Han, B. Cao, X. Yang, X. Zhu, B. Yang, H. Zhao, W. Qiao, Use of magnoflorine-phospholipid complex to permeate blood-brain barrier and treat depression in the CUMS animal model, *Drug Deliv.* 26 (2019) 566–574. <https://doi.org/10.1080/10717544.2019.1616236>.
- [109] S. Biswas, P.K. Mukherjee, R.K. Harwansh, S. Bannerjee, P. Bhattacharjee, Enhanced bioavailability and hepatoprotectivity of optimized ursolic acid–phospholipid complex, *Drug Dev. Ind. Pharm.* 45 (2019) 946–958. <https://doi.org/10.1080/03639045.2019.1583755>.
- [110] A. Jain, S. Saini, R. Kumar, T. Sharma, R. Swami, O.P. Katara, B. Singh, Phospholipid-based complex of raloxifene with enhanced biopharmaceutical potential: synthesis, characterization and preclinical assessment, *Int. J. Pharm.* 571 (2019) 118698. <https://doi.org/10.1016/j.ijpharm.2019.118698>.
- [111] G.S. Ravi, R.N. Charyulu, A. Dubej, P. Prabhu, S. Hebbar, A.C. Mathias, Nano-lipid complex of rutin: development, characterisation and in vivo investigation of hepatoprotective, antioxidant activity and bioavailability study in rats, *AAPS PharmSciTech* 19 (2018) 3631–3649. <https://doi.org/10.1208/s12249-018-1195-9>.
- [112] S. Cunha, M.H. Amaral, J.M. Sousa Lobo, A.C. Silva, Lipid nanoparticles for nasal/intranasal drug delivery, *Crit. Rev. Ther. Drug Carrier Syst.* 34 (2017) 257–282. <https://doi.org/10.1615/CritRevTherDrugCarrierSyst.2017018693>.
- [113] G. Anderluzzi, G. Lou, Y. Su, Y. Perrie, Scalable manufacturing processes for solid lipid nanoparticles, *Pharm. Nanotechnol.* 7 (2019) 444–459. <https://doi.org/10.2174/2211738507666190925112942>.
- [114] A. Gordillo-Galeano, C.E. Mora-Huertás, Solid lipid nanoparticles and nanostructured lipid carriers: a review emphasizing on particle structure and drug release, *Eur. J. Pharm. Biopharm.* 133 (2018) 285–308. <https://doi.org/10.1016/j.ejpb.2018.10.017>.
- [115] L. Battaglia, L. Serpe, E. Muntoni, G.P. Zara, M. Trotta, M. Gallarate, Methotrexate-loaded SLNs prepared by coacervation technique: in vitro cytotoxicity and in vivo pharmacokinetics and biodistribution, *Nanomedicine* 6 (2011) 1561–1573. <https://doi.org/10.2217/nmm.11.52>.
- [116] S.S. Chalikwar, V.S. Belgamwar, V.R. Talele, S.J. Surana, M.U. Patil, Formulation and evaluation of Nimodipine-loaded solid lipid nanoparticles delivered via lymphatic transport system, *Colloids Surf. B Biointerfaces* 97 (2012) 109–116. <https://doi.org/10.1016/j.colsurfb.2012.04.027>.
- [117] W. Mehnert, K. Mäder, Solid lipid nanoparticles: production, characterization and applications, *Adv. Drug Deliv. Rev.* 64 (2012) 83–101. <https://doi.org/10.1016/j.addr.2012.09.021>.
- [118] A. zur Mühlen, C. Schwarz, W. Mehnert, Solid lipid nanoparticles (SLN) for controlled drug delivery – drug release and release mechanism, *Eur. J. Pharm. Biopharm.* 45 (1998) 149–155. [https://doi.org/10.1016/S0939-6411\(97\)00150-1](https://doi.org/10.1016/S0939-6411(97)00150-1).
- [119] R. Paliwal, S.R. Paliwal, G.P. Agrawal, S.P. Vyas, Biomimetic solid lipid nanoparticles for oral bioavailability enhancement of low molecular weight heparin and its lipid conjugates: in vitro and in vivo evaluation, *Mol. Pharm.* 8 (2011) 1314–1321. <https://doi.org/10.1021/mp200109m>.
- [120] S.P. Vyas, R. Shivani, P. Rishi, N.G. Prem, K. Kapil, K.G. Amit, V. Bhuvaneshwar, Solid lipid nanoparticles (SLNs) as a rising tool in drug delivery science: one step up in nanotechnology, *Curr. Nanosci.* 4 (2008) 30–44. <https://doi.org/10.2174/157341308783591816>.
- [121] R.H. Müller, W. Mehnert, J.S. Lucks, C. Schwarz, A. Zur Mühlen, H. Weyhers, C. Freitas, D. Ruhl, Solid lipid nanoparticles (SLN) - an alternative colloidal carrier system for controlled drug delivery, *Eur. J. Pharm. Biopharm.* 41 (1995) 62–69.
- [122] C. Ban, M. Jo, Y.H. Park, J.H. Kim, J.Y. Han, K.W. Lee, D.H. Kweon, Y.J. Choi, Enhancing the oral bioavailability of curcumin using solid lipid nanoparticles, *Food Chem.* 302 (2020) 125328. <https://doi.org/10.1016/j.foodchem.2019.125328>.
- [123] A. Jain, G. Sharma, K. Thakur, K. Raza, U.S. Shivhare, G. Ghoshal, O.P. Katara, Beta-carotene-Encapsulated solid lipid nanoparticles (BC-SLNs) as promising vehicle for cancer: an investigative assessment, *AAPS PharmSciTech* 20 (2019) 100. <https://doi.org/10.1208/s12249-019-1301-7>.
- [124] N.T. Pandya, P. Jani, J. Vanza, H. Tandell, Solid lipid nanoparticles as an efficient drug delivery system of olmesartan medoxomil for the treatment of hypertension, *Colloids Surf. B Biointerfaces* 165 (2018) 37–44. <https://doi.org/10.1016/j.colsurfb.2018.02.011>.

- [125] R.N. Saha, S. Vasanthakumar, G. Bende, M. Snehalatha, Nanoparticulate drug delivery systems for cancer chemotherapy, *Mol. Membr. Biol.* 27 (2010) 215–231, <https://doi.org/10.3109/09687688.2010.510804>.
- [126] A. Khosa, S. Reddi, R.N. Saha, Nanostructured lipid carriers for site-specific drug delivery, *Biomed. Pharmacother.* 103 (2018) 598–613, <https://doi.org/10.1016/j.biopha.2018.04.055>.
- [127] S. Martins, B. Sarmento, D.C. Ferreira, E.B. Souto, Lipid-based colloidal carriers for peptide and protein delivery—liposomes versus lipid nanoparticles, *Int. J. Nanomed.* 2 (2007) 595–607, <http://europepmc.org/abstract/MED/18203427>.
- [128] S. Das, A. Chaudhury, Recent advances in lipid nanoparticle formulations with solid matrix for oral drug delivery, *AAPS PharmSciTech* 12 (2011) 62–76, <https://doi.org/10.1208/s12249-010-9563-0>.
- [129] S. Weber, A. Zimmer, J. Pardeike, Solid lipid nanoparticles (SLN) and nanostructured lipid carriers (NLC) for pulmonary application: a review of the state of the art, *Eur. J. Pharm. Biopharm.* 86 (2014) 7–22, <https://doi.org/10.1016/j.ejpb.2013.08.013>.
- [130] J.A. Oshiro-Junior, M.R. Sato, F.I. Boni, K.L.M. Santos, K.T. de Oliveira, L.M. de Freitas, C.R. Fontana, D. Nicholas, A. McHale, J.F. Callan, M. Chorilli, Phthalocyanine-loaded nanostructured lipid carriers functionalized with folic acid for photodynamic therapy, *Mater. Sci. Eng. C* 108 (2020) 110462, <https://doi.org/10.1016/j.msec.2019.110462>.
- [131] A. Singh, Y.R. Neupane, B. Mangla, K. Kohli, Nanostructured lipid carriers for oral bioavailability enhancement of exemestane: formulation design, in vitro, ex vivo, and in vivo studies, *J. Pharmaceut. Sci.* 108 (2019) 3382–3395, <https://doi.org/10.1016/j.xphs.2019.06.003>.
- [132] S.M.T. Cavalcanti, C. Nunes, S.A. Costa Lima, J.L. Soares-Sobrinho, S. Reis, Optimization of nanostructured lipid carriers for Zidovudine delivery using a microwave-assisted production method, *Eur. J. Pharmaceut. Sci.* 122 (2018) 22–30, <https://doi.org/10.1016/j.ejps.2018.06.017>.
- [133] D. Irby, C. Du, F. Li, Lipid–drug conjugate for enhancing drug delivery, *Mol. Pharm.* 14 (2017) 1325–1338, <https://doi.org/10.1021/acs.molpharmaceut.6b01027>.
- [134] Y. Ding, K.A. Nielsen, B.P. Nielsen, N.W. Bøje, R.H. Müller, S.M. Pyo, Lipid-drug-conjugate (LDC) solid lipid nanoparticles (SLN) for the delivery of nicotine to the oral cavity – optimization of nicotine loading efficiency, *Eur. J. Pharm. Biopharm.* 128 (2018) 10–17, <https://doi.org/10.1016/j.ejpb.2018.03.004>.
- [135] K. Soni, A. Mujtaba, K. Kohli, Lipid drug conjugate nanoparticle as a potential nanocarrier for the oral delivery of pemetrexed diacid: formulation design, characterization, ex vivo, and in vivo assessment, *Int. J. Biol. Macromol.* 103 (2017) 139–151, <https://doi.org/10.1016/j.ijbiomac.2017.05.015>.
- [136] N. Ashwanikumar, N.A. Kumar, S. Asha Nair, G.S. Vinod Kumar, 5-Fluorouracil-lipid conjugate: potential candidate for drug delivery through encapsulation in hydrophobic polyester-based nanoparticles, *Acta Biomater.* 10 (2014) 4685–4694, <https://doi.org/10.1016/j.actbio.2014.07.032>.
- [137] Y.R. Neupane, M.D. Sabir, N. Ahmad, M. Ali, K. Kohli, Lipid drug conjugate nanoparticle as a novel lipid nanocarrier for the oral delivery of decitabine: ex vivo gut permeation studies, *Nanotechnology* 24 (2013) 415102, <https://doi.org/10.1088/0957-4484/24/41/415102>.
- [138] R. Paliwal, S. Rai, S. Vyas, Lipid drug conjugate (LDC) nanoparticles as autolymphtrophs for oral delivery of methotrexate, *J. Biomed. Nanotechnol.* 7 (2011) 130–131, <https://doi.org/10.1166/jbnn.2011.1235>.
- [139] J.S. Alexander, V.C. Ganta, P.A. Jordan, M.H. Witte, Gastrointestinal lymphatics in health and disease, *Pathophysiology* 17 (2010) 315–335, <https://doi.org/10.1016/j.pathophys.2009.09.003>.
- [140] P.I. Korner, B. Morris, F.C. Courtice, An analysis of factors affecting lymph flow and protein composition during gastric absorption of food and fluids, and during intravenous infusion, *Aust. J. Exp. Biol. Med. Sci.* 32 (1954) 301–320, <https://doi.org/10.1038/icb.1954.33>.
- [141] M. Ionac, T. Laskay, D. Labahn, G. Geisslinger, W. Solbach, Improved technique for cannulation of the murine thoracic duct: a valuable tool for the dissection of immune responses, *J. Immunol. Methods* 202 (1997) 35–40, [https://doi.org/10.1016/S0022-1759\(96\)00226-8](https://doi.org/10.1016/S0022-1759(96)00226-8).
- [142] S.A. Charman, A.M. Segrave, G.A. Edwards, C.J.H. Porter, Systemic availability and lymphatic transport of human growth hormone administered by subcutaneous injection, *J. Pharmaceut. Sci.* 89 (2000) 168–177, [https://doi.org/10.1002/\(SICI\)1520-6017\(200002\)89:2<168::AID-JPS4>3.0.CO;2-Q](https://doi.org/10.1002/(SICI)1520-6017(200002)89:2<168::AID-JPS4>3.0.CO;2-Q).
- [143] G.A. Edwards, C.J.H. Porter, S.M. Caliph, S.-M. Khoo, W.N. Charman, Animal models for the study of intestinal lymphatic drug transport, *Adv. Drug Deliv. Rev.* 50 (2001) 45–60, [https://doi.org/10.1016/S0169-409X\(01\)00148-X](https://doi.org/10.1016/S0169-409X(01)00148-X).
- [144] D.J. Hauss, S.E. Fogal, J.V. Ficorilli, C.A. Price, T. Roy, A.A. Jayaraj, J.J. Keirns, Lipid-based delivery systems for improving the bioavailability and lymphatic transport of a poorly water-soluble LTB4 inhibitor, *J. Pharmaceut. Sci.* 87 (1998) 164–169, <https://doi.org/10.1021/js970300n>.
- [145] S.G. Turner, J.A. Barrowman, Intestinal lymph flow and lymphatic transport of protein during fat absorption, *Q. J. Exp. Physiol. Cogn. Med. Sci.* 62 (1977) 175–180, <https://doi.org/10.1113/expphysiol.1977.sp002387>.
- [146] D.G. White, M.J. Story, S.G. Barnwell, An experimental animal model for studying the effects of a novel lymphatic drug delivery system for propranolol, *Int. J. Pharm.* 69 (1991) 169–174, [https://doi.org/10.1016/0378-5173\(91\)90221-9](https://doi.org/10.1016/0378-5173(91)90221-9).
- [147] A. Dahan, A. Hoffman, Evaluation of a chylomicron flow blocking approach to investigate the intestinal lymphatic transport of lipophilic drugs, *Eur. J. Pharmaceut. Sci.* 24 (2005) 381–388, <https://doi.org/10.1016/j.ejps.2004.12.006>.
- [148] P. Gershkovich, A. Hoffman, Uptake of lipophilic drugs by plasma derived isolated chylomicrons: linear correlation with intestinal lymphatic bioavailability, *Eur. J. Pharmaceut. Sci.* 26 (2005) 394–404, <https://doi.org/10.1016/j.ejps.2005.07.011>.
- [149] M. Onizuka, T. Flatebo, G. Nicolaysen, Lymph flow pattern in the intact thoracic duct in sheep, *J. Physiol.* 503 (1997) 223–234, <https://doi.org/10.1111/j.1469-7793.1997.223bi.x>.
- [150] L.T. Jensen, H.P. Olesen, J. Risteli, I. Lorenzen, External thoracic duct-venous shunt in conscious pigs for long term studies of connective tissue metabolites in lymph, *Lab. Anim. Sci.* 40 (1990) 620–624, <http://www.ncbi.nlm.nih.gov/pubmed/2172627>.
- [151] J.C. Fish, H.E. Sarles, A.T. Mattingly, M.V. Ross, A.R. Remmers, Preparation of chronic thoracic duct lymph fistulas in man and laboratory animals, *J. Surg. Res.* 9 (1969) 101–106, [https://doi.org/10.1016/0022-4804\(69\)90038-9](https://doi.org/10.1016/0022-4804(69)90038-9).
- [152] T. Ichihashi, H. Kinoshita, H. Yamada, Absorption and disposition of epithiosteroids in rats (2): avoidance of first-pass metabolism of mefiprostane by lymphatic absorption, *Xenobiotica* 21 (1991) 873–880, <https://doi.org/10.3109/00498259109039527>.
- [153] P. Tso, J.A. Balint, Formation and transport of chylomicrons by enterocytes to the lymphatics, *Am. J. Physiol. Gastrointest. Liver Physiol.* 250 (1986) G715–G726, <https://doi.org/10.1152/ajpgi.1986.250.6.g715>.
- [154] H. Lennernäs, Intestinal drug absorption and bioavailability: beyond involvement of single transport function, *J. Pharm. Pharmacol.* 55 (2003) 429–433, <https://doi.org/10.1211/002235702973>.
- [155] S. Chaturvedi, A. Garg, A. Verma, Nano lipid based carriers for lymphatic voyage of anti-cancer drugs: an insight into the in-vitro, ex-vivo, in-situ and in-vivo study models, *J. Drug Deliv. Sci. Technol.* 59 (2020) 101899, <https://doi.org/10.1016/j.jddst.2020.101899>.
- [156] D.M. Karpf, R. Holm, C. Garafalo, E. Levy, J. Jacobsen, A. Müllertz, Effect of different surfactants in biorelevant medium on the secretion of a lipophilic compound in lipoproteins using Caco-2 cell culture, *J. Pharmaceut. Sci.* 95 (2006) 45–55, <https://doi.org/10.1002/jps.20431>.
- [157] F. Seeballuck, E. Lawless, M.B. Ashford, C.M. O'Driscoll, Stimulation of triglyceride-rich lipoprotein secretion by polysorbate 80: in vitro and in vivo correlation using caco-2 cells and a cannulated rat intestinal lymphatic model, *Pharm. Res. (N. Y.)* 21 (2004) 2320–2326, <https://doi.org/10.1007/s11095-004-7684-4>.
- [158] P. Tso, V. Pitts, D.N. Granger, Role of lymph flow in intestinal chylomicron transport, *Am. J. Physiol. Gastrointest. Liver Physiol.* 12 (1985) G21–G28, <https://doi.org/10.1152/ajpgi.1985.249.1.g21>.
- [159] J. Varshosaz, M. Minayian, E. Moazen, Enhancement of oral bioavailability of pentoxifylline by solid lipid nanoparticles, *J. Liposome Res.* 20 (2010) 115–123, <https://doi.org/10.3109/08982100903161456>.
- [160] N.P. Aditya, S. Patankar, B. Madhusudhan, R.S.R. Murthy, E.B. Souto, Arthemeter-loaded lipid nanoparticles produced by modified thin-film hydration: pharmacokinetics, toxicological and in vivo anti-malarial activity, *Eur. J. Pharmaceut. Sci.* 40 (2010) 448–455, <https://doi.org/10.1016/j.ejps.2010.05.007>.
- [161] J. Varshosaz, M. Tabbakhian, M.Y. Mohammadi, Formulation and optimization of solid lipid nanoparticles of buspirone HCl for enhancement of its oral bioavailability, *J. Liposome Res.* 20 (2010) 286–296, <https://doi.org/10.3109/08982100903443065>.
- [162] L. Harivardhan Reddy, K. Vivek, N. Bakshi, R.S.R. Murthy, Tamoxifen citrate loaded solid lipid nanoparticles (SLNTM): preparation, characterization, in vitro drug release, and pharmacokinetic evaluation, *Pharmaceut. Dev. Technol.* 11 (2006) 167–177, <https://doi.org/10.1080/10837450600561265>.
- [163] S. Chakraborty, D. Shukla, P.R. Vuddanda, B. Mishra, S. Singh, Utilization of adsorption technique in the development of oral delivery system of lipid based nanoparticles, *Colloids Surf. B Biointerfaces* 81 (2010) 563–569, <https://doi.org/10.1016/j.colsurfb.2010.07.058>.
- [164] C.W. Andrews, L. Bennett, L.X. Yu, Predicting human oral bioavailability of a compound: development of a novel quantitative structure-bioavailability relationship, *Pharm. Res. (N. Y.)* 17 (2000) 639–644, <https://doi.org/10.1023/A:1007556711109>.
- [165] T. Ichihashi, H. Kinoshita, Y. Takagishi, H. Yamada, Intrinsic lymphatic partition rate of mefiprostane, epiostanol, and oleic acid absorbed from rat intestine, *Pharm. Res. (N. Y.)* 8 (1991) 1302–1306, <https://doi.org/10.1023/A:1015864131681>.
- [166] T. Ichihashi, T. Nagasaki, Y. Takagishi, H. Yamada, A quantitative concept of the mechanism of intestinal lymphatic transfer of lipophilic molecules, *Pharm. Res. (N. Y.)* 11 (1994) 508–512, <https://doi.org/10.1023/A:1018954213469>.
- [167] C.A. Lipinski, F. Lombardo, B.W. Dominy, P.J. Feeney, Experimental and computational approaches to estimate solubility and permeability in drug discovery and development settings, *Adv. Drug Deliv. Rev.* 23 (1997) 3–25, [https://doi.org/10.1016/S0169-409X\(96\)00423-1](https://doi.org/10.1016/S0169-409X(96)00423-1).
- [168] R. Holm, J. Hoest, Successful in silico predicting of intestinal lymphatic transfer, *Int. J. Pharm.* 272 (2004) 189–193, <https://doi.org/10.1016/j.ijpharm.2003.12.017>.
- [169] S. Wold, M. Sjöström, L. Eriksson, Partial least squares projections to latent structures (PLS) in chemistry, in: *Encycl. Comput. Chem.*, John Wiley & Sons, Ltd, Chichester, UK, 2002, <https://doi.org/10.1002/0470845015.cpa012>.
- [170] W.N.A. Charman, V.J. Stella, Estimating the maximal potential for intestinal lymphatic transport of lipophilic drug molecules, *Int. J. Pharm.* 34 (1986) 175–178, [https://doi.org/10.1016/0378-5173\(86\)90027-X](https://doi.org/10.1016/0378-5173(86)90027-X).



Use of combined nanocarrier system based on chitosan nanoparticles and phospholipids complex for improved delivery of ferulic acid

Darshan R. Telange ^{a,*}, Shirish P. Jain ^a, Anil M. Pethe ^b, Prashant S. Kharkar ^c, Nilesh R. Rarokar ^d

^a Rajarshi Shahu College of Pharmacy, Malvihi, Botha Road, Buldhana 443301, M.S., India

^b School of Pharmacy and Technology Management, SVKM's NMIMS (Deemed to be University), Pollepally SEZ, Jadcherla, Mehbubnagar, Hyderabad 509301, India

^c Department of Pharmaceutical Sciences and Technology, Institute of Chemical Technology, Mumbai 400019, M.S., India

^d Department of Pharmaceutical Sciences, Rashtrasant Tukadoji Maharaj Nagpur University, Nagpur, 440033, M.S., India

ARTICLE INFO

Article history:

Received 16 November 2020

Received in revised form 17 December 2020

Accepted 29 December 2020

Available online 05 January 2021

Keywords:

Ferulic acid
Chitosan nanoparticles
Phospholipids complex
Oral bioavailability
Antioxidant activity

ABSTRACT

A novel nanocarrier system of phospholipids complex loaded chitosan nanoparticles (FAPLC CNPs) was developed to improve the oral bioavailability and antioxidant potential of FA. FAPLC CNPs were optimized using a Box-Behnken Design (BBD). FAPLC CNPs were characterized using differential scanning calorimetry, Fourier transforms infrared spectroscopy, powder x-ray diffractometry, proton nuclear magnetic resonance, solubility, in vitro dissolution, ex vivo permeation, and in vivo antioxidant activity in carbon tetrachloride (CCl₄)-induced albino rat model. The characterization studies indicated a formation of the complex as well as FAPLC CNPs. The FAPLC CNPs exhibited a lower particle size ~123.27 nm, PDI value ~0.31, and positive zeta potential ~32 mV respectively. Functional characterization studies revealed a significant improvement in the aqueous solubility, dissolution, and permeation rate of FAPLC and FAPLC CNPs compared to FA and FA CNPs. The FAPLC CNPs showed significant enhancement of in vivo antioxidant activity of FA by restoring the elevated marker enzymes in the CCl₄-intoxicated rat model compared to FA CNPs. Moreover, the pharmacokinetic analysis demonstrated a significant enhancement of oral bioavailability of FA from FAPLC CNPs compared to FA CNPs. These findings show that FAPLC CNPs could be used as an effective nanocarrier for improving the oral delivery of FA.

© 2021 Elsevier B.V. All rights reserved.

1. Introduction

Ferulic acid (FA) (IUPAC name: [E]-3-[4-hydroxy-3-methoxy-phenyl] prop-2-enoic acid), a phenolic acid derivative, found in wheat, rice, barley, citrus, and some beverages such as coffee and beer. It is a potent free radical scavenger [1,2]. FA produces several biological activities such as antioxidant [3], neurodegenerative disorder [4], antidiabetic [5], anticancer [6], and pulmonary protective effect [7], etc. The antioxidant activity of FA attributes to the presence of unsaturated side chain, phenolic nucleus, hydroxyl and methoxy group attached to the phenyl ring, which ultimately provides stabilization to the structure via resonance [8]. Moreover, FA has low toxicity and therefore, it has been widely used in the pharmaceutical and food industry [9]. Despite these potential medical applications, FA exhibits low bioavailability, rapid metabolism, and elimination via oral administration [10]. Additionally, being a BCS class II drug (low solubility and high permeability), FA shows a poor absorption profile from the gastrointestinal tract via conventional delivery systems. Therefore, we need to develop novel and smart

nanocarriers which can improve the biopharmaceutical properties of FA.

Literature analysis demonstrated that only some nanoformulations have been attempted by the authors for enhancing the biopharmaceutical properties of FA. These include nanostructured lipid carrier (NLCs) [11], conjugates [12], phospholipids complex [13], hydrogel [14], and PLGA nanoparticles [15]. Analysis of these work demonstrated only partial improvement in the dissolution rate of FA, whereas, optimization, solubility, permeability, oral bioavailability, and antioxidant activity evaluation were found to have lacked. Likewise, the findings of phospholipids complex work have shown the limited improvement of FA solubility ~ (3-fold only) without analysis of dissolution rate, permeability, oral bioavailability, and antioxidant status of FA [13]. Moreover, the obtained low solubility of FA in employed soy lecithin based phospholipids can form strong aggregates and agglomeration product, which could exhibit low dissolution of FA from this phospholipids complex. The existed drawbacks of these single nanocarriers were overcome in the present research work by the formation of novel nanocarriers using a combination of phospholipids complex and chitosan nanoparticles through solvent evaporation and ionic gelation technology, which can accomplish the benefits of each carrier and circumvent their limitations.

* Corresponding author at: Rajarshi Shahu College of Pharmacy, Malvihi, Botha Road, 443001 Maharashtra, India.

E-mail address: telange.darshan@gmail.com (D.R. Telange).

Phospholipids complexation technology has been considered as one of the best techniques for enhancing the biopharmaceutical attributes of bioactive as compared to others, due to the simple preparation method, high drug loading ability, and long terms stability of the drug. Based on this, many researchers have used this expertise and reported a significant improvement in the solubility, permeability, and oral bioavailability of scores of bioactive such as ursolic acid [16], rutin [17], mangoflorine [18], and capsaicin [19]. These significant improvements in the bioactives are depending upon the composition of the phospholipids complex. The phospholipids complex consists of phospholipids, bioactive, and/or synthetic drug and preparation methods i.e. solvent evaporation method, the most widely used method. In this study, the LIPOID® SPC-3 (LSPC-3) was used as phospholipids. This lipid-like class of phospholipids also shows biocompatibility, biodegradability, metabolic activity, and low toxicity, and thus, it acts as suitable nanocarriers for translocation of bioactive across the biological membrane [20–22]. Moreover, being biocompatible due to similarity in lipid content of this lipid with the amphiphilic mammalian cell membrane, it exhibits higher miscibility towards each other and facilitates the effective permeation of bioactive. The amphiphilic nature of LSPC-3 also demonstrates aqueous as well as lipid solubility [23,24]. The LSPC-3 containing hydroxyl group can form interaction with the active hydrogen atom of any lipophilic drug through the esterification process, convert into amphiphilic compounds, facilitate its transportation across the biological membrane and finally, improve the therapeutic efficiency of drugs [25]. The same mechanism also occurred in the phospholipids complex, where phospholipids can form polar and hydrogen bonding interaction with bioactive and enhances their biopharmaceutical properties to a great extent [26–28].

Chitosan nanoparticles (CNPs) are natural materials that show physico-chemical, antimicrobial, and biological properties [29]. It can permeate into the interstitial spaces and increases the cellular uptake of drugs [30]. It is prepared from chitosan, which is a modified biopolymer, polycationic copolymer, and nitrogenous polysaccharide, obtained by total or partial deacetylation of chitin [31]. It contains one amino (-NH₂) and two hydroxyls (OH)₂ groups in the glucosidic residual chain. It is biocompatible and shows non-toxicity to the living tissues. It shows gel-forming ability, high adsorption capacity, and biodegradability properties. These properties of chitosan make it a potential nanocarrier for improving the encapsulation efficiency and sustained release properties of drugs [32]. The affinity of the positive charge of CNPs (due to cationic amino group) towards the negative charge of FAPLC complex (anionic group) forms strong electrostatic interaction, leading to increases in the encapsulation of phospholipids complex into CNPs and forms combined delivery system i.e. FAPLC CNPs, which prevents its exposure and provide a controlled release of a drug [33]. Additionally, the outside positive charge of FAPLC CNPs can also form interaction with the negative charge of the plasma membrane and mucosa, resulting into increase in their interaction, adhesion, and retention to the intestinal epithelial cells and enhances the permeability and absorption of drugs via opening the tight junction between the cells [34,35]. Earlier reports have shown that the encapsulation of phospholipids complex into the nanosystem i.e. nanoparticles can considerably improve the biopharmaceutical attributes of bioactive [36,37]. Therefore, based on the evidence, the developed FAPLC CNPs can be considered as promising combined drug delivery nanocarriers for improving the delivery and absorption of bioactive.

In this work, we developed FAPLC CNPs using FAPLC and CNPs via solvent evaporation and ionic gelation technology. The FAPLC was optimized using the quality by design (QbD) based Design of Experiment (DOE). Following this, the FAPLC CNPs were characterized for physico-chemical and functional parameters of particle size analysis, differential scanning calorimetry, Fourier transforms infrared spectroscopy, powder x-ray diffractometry, solubility analysis, in vitro dissolution, and ex vivo permeation studies. Moreover, the FAPLC CNPs were also investigated for in vivo antioxidant potential in the CCl₄-induced albino rat model.

2. Materials and methods

2.1. Chemicals

FA (HPLC purity > 99%) was obtained as a gift sample from Sisco Research Laboratories Pvt. Ltd. Mumbai, India. LIPOID® SPC-3 was obtained from Lipoid GmbH, Ludwigshafen, Germany. Chitosan (molecular weight = 340 kDa and degree of deacetylation = 75 – 80%) was purchased from HiMedia Laboratories Pvt. Ltd., Mumbai, India. Acetic acid, carbon tetrachloride, chloroform, ethanol, methanol, sodium chloride, sodium lauryl sulfate, sodium tripolyphosphate, and Tween® 20 were purchased from Loba Chemicals Pvt. Ltd., Mumbai, India. Disodium hydrogen phosphate, potassium dihydrogen phosphate, n-Hexane, and n-octanol were purchased from Sigma Chemicals, Sigma-Aldrich Corporation, St. Louis, MO. All other chemicals used in this study were based on analytical grade.

2.2. Preparation of ferulic acid – LIPOID® SPC-3 complex (FAPLC)

The ferulic acid – LIPOID® SPC-3 complex (FAPLC) was prepared as per the molar ratio of (1:1.5) using the ethanol-based solvent evaporation method described previously [33]. Briefly, the FA (194.20 mg) and LIPOID® SPC-3 (LSPC-3) (1173 mg) were individually weighed as per the above-mentioned molar ratio and transferred into a 100 mL round bottom flask. The weighed ingredients were mixed and dissolved in 20 mL of absolute ethanol. The solution in the flask was refluxed at a controlled temperature of 50 °C using a water bath (DSY-2-2, Aiqixia Apparatus Center, China) for 2 h respectively. The heated solution was concentrated to get 2–3 mL of liquid residue. This was then poured into 10 mL of n-hexane resulted in precipitation of FAPLC. The obtained complex was filtered and dried under vacuum at 40 °C for 12 h to remove traces of residual solvent if any. The dried FAPLC (yield ~92% w/w) was transferred to amber-colored (light protected) glass vials, purged with N₂, and stored at room temperature (RT) until further analysis.

2.3. Screening of phospholipids

The screening of four different grades of phospholipids such as Phospholipon® 80H, Phospholipon® 90H, Phospholipon® 90G, and LSPC-3 was carried out based on drug content and physico-chemical properties of the FAPLC. Among all, the LSPC-3 was selected as optimized phospholipids and used in the preparation of FAPLC as per the molar ratio of (1:1.5) using the solvent evaporation method.

2.4. Determination of extent of complexation of FA in FAPLC

A UV-based method previously described by Tan et al. [39] was used for the determination of the extent of the complexation of FA in FAPLC. Briefly, an approximate amount of FAPLC (equivalent to ~50 mg of FA) was weighed and transferred into 10 mL of the beaker. The weighed FAPLC powder was dispersed in 5 mL of chloroform and stirred well resulted in the formation of dispersion. In this dispersion, the FAPLC and LSPC-3 both were dissolved, while, FA remained as insoluble residue. This residue was filtered and dried at room RT. The dried residue was dissolved in methanol, diluted suitably, and analyzed for absorbance at (λ_{max} ~311 nm) using a UV-visible spectrophotometer (Model: V-630, JASCO International Co., Ltd., Tokyo, Japan). The extent of complexation was calculated using the below-described equation.

$$\text{Extent of complexation rate (\%)} = \frac{(C_t - C_f)}{C_t} \times 100 \quad (1)$$

where, C_t indicates the theoretical concentration of FA in FAPLC, and C_f represents the observed concentration of FA in the filtrate.

2.5. Preparation of FAPLC loaded chitosan nanoparticles (FAPLC CNPs)

The ionic gelation method described earlier was employed for the preparation of FAPLC CNPs with slight modifications [33]. This nanoparticle was prepared using FAPLC, acetic acid solution (2%, w/v), chitosan, and sodium tripolyphosphate (STPP) respectively. Briefly, the FAPLC (equivalent to ~10 mg of FA) and chitosan (200, 400, or 600 mg) were weighed and dispersed in the freshly prepared acetic acid solution. The developed complex-polymer dispersion was added in a dropwise manner at a flow rate of 2 mL/min using a nozzle (diameter ~2 mm) attached to the peristaltic pump (Model: PP 50 V, Electrolab India Pvt. Ltd., Mumbai, India) into continuously stirred 400 mL of STPP solution (0.2, 0.3 or 0.4 % w/v). The dispersion was stirred using a magnetic stirrer at a speed of (800, 1000, or 1200 RPM). This complex-polymer-STPP cross-linking mechanism resulted in the formation of FAPLC CNPs. The obtained nanoparticles were kept aside in the STPP solution in the dark overnight. Consequently, the nanoparticles were filtered (syringe filter, 0.22 µm), washed using deionized water, and oven-dried at 40 °C. Dried FAPLC CNPs were stored in light-protected glass vials, purged with N₂, and kept at RT until further analysis. Likewise, the FA CNPs, as well as blank CNPs (free of FAPLC) were also prepared using the same method as described above.

2.6. The rationale for selecting independent, dependent variables and their ranges

The preliminary experiments and supporting literature were used for the selection of independent, dependent variables and their ranges for the optimization of FAPLC CNPs. The nanoparticles were prepared using the same method as described above. The prepared nanoparticles were tested for encapsulation efficiency, and based on their results; the independent, dependent variables and their ranges were selected. Moreover, to explore further the range of independent variables, the FAPLC CNPs were optimized at three levels (-) low, (0) middle, and (+1) higher using Box-Behnken Design.

2.7. Box-Behnken Design (BBD)

Quality by Design (QbD) is a systematic, scientific and risk-based approach that commences with predefined objectives of the final product, and based on this, it identifies the critical parameters of the manufacturing process and/or formulation components that affect the quality of the product, translates these parameters into critical materials attributes (CMA) and/or critical process attributes (CPA) and finally establish these attributes in the form of experimental trials to consistently produce a product with desired characteristics [38]. In this study, the QbD-based Design of Experiments (DOE) i.e. Box-Behnken Design (BBD) (Design-Expert®, Version 10.0.4.0, Stat-Ease Inc., Minneapolis, Minnesota, USA) was employed to optimize CMA and/or CPA in less number of experimental trials to achieve the desired FAPLC CNPs. Based on preliminary experiments and supporting literature, the three independent variables i.e. chitosan (mg, X₁), STPP concentration (% w/v, X₂), and stirring speed (RPM, X₃) respectively were selected. Likewise, the encapsulation efficiency (% w/w) was selected as dependent variables. The selected independent variables were investigated at three levels and coded as (-1) low, (0) middle, and (+1) higher respectively. The BBD generated 17# possible experimental trials along with a statistical model i.e. polynomial equation as shown below. The equation containing the coefficient of magnitude, interaction terms, and generated positive and/or negative sign was used for the optimization of the FAPLC CNPs.

$$Y = b_0 + b_1X_1 + b_2X_2 + b_3X_3 + b_{11}X_1^2 + b_{22}X_2^2 + b_{33}X_3^2 + b_{12}X_1X_2 + b_{13}X_1X_3 + b_{23}X_2X_3 \quad (2)$$

where Y, is the encapsulation efficiency (% w/w) and b₀ is the coefficient of the independent variable of X. The X₁, X₂, and X₃ represent the main

effects of the study. The interaction terms i.e. X₁X₂, X₂X₃, and X₁X₃ indicate the combined effect of the independent variables on the encapsulation efficiency. The polynomial terms i.e. X₁², X₂², and X₃² show the non-linearity response of the dependent variables. The coded and real values of the independent and dependent variables are shown in Table 1, whereas, the possible experimental trials with an estimated value of encapsulation efficiency (% w/w) are depicted in Table 2.

2.8. Estimation of n encapsulation efficiency

The estimation of the encapsulation efficiency of FA within the FAPLC CNPs was carried out using the spectrophotometric method described previously [40,41]. Briefly, a certain amount of FAPLC CNPs was weighed and dispersed in 5 mL of 0.1 M HCl. The resulting dispersion in 1.5 mL of microcentrifuge tube was ultracentrifuged at 15,000 RPM at 4 °C for 40 min. Next, the supernatant was collected, diluted approximately, and analyzed at a maximum wavelength (λ_{max} ~311) on a UV-visible spectrophotometer against the blank. The encapsulation efficiency and drug loading were calculated using the equation described below.

$$\text{Encapsulation efficiency (\%)} = \frac{\text{Total amount of FA} - \text{Free FA}}{\text{Total amount of FA}} \times 100 \quad (3)$$

$$\text{Drug loading (\%)} = \frac{\text{Total amount of FA} - \text{Free FA}}{\text{Weight of nanoparticles}} \times 100 \quad (4)$$

2.9. Physical-chemical characterization of FAPLC and FAPLC CNPs

2.9.1. Particle size and zeta potential

Particle size and zeta potential are the most widely used indicator for the determination of release behavior and physical stability of a multi particulate system dispersed in the liquid medium. In this study, the particle size and size distribution of FA within FAPLC or FAPLC CNPs were evaluated using Photon Cross-Correlation Spectroscopy (PCCS) equipped with Dynamic Light Scattering (DLS) technology. Briefly, the aqueous dispersion of FAPLC or FAPLC CNPs was analyzed for particle size within the sensitivity range of 1 nm to 10 µm using a particle size analyzer (Model: Nanophox Sympatec, GmbH, Clausthal-Zellerfeld, Germany). The same dispersion of formulation was also used for the analysis of zeta potential within the sensitivity range of - 200 to +200 mV using Nano Particle Analyzer (Model: NanoPlus™-2, Particulate System, Norcross, GA, USA). The detailed procedure for the preparation of the sample and its evaluation has been reported earlier by our group [42].

2.9.2. Scanning electron microscopy (SEM)

The samples of FA, LSPC-3, FAPLC, and FAPLC CNPs were analyzed to study their surface characterization using a scanning electron microscope (Model: Supra®, Carl Zeiss NTS Ltd., Germany) according to the method described previously in the literature [43]. Briefly, the samples (~50 mg) were weighed and spread as a thin layer on double-faced carbon tape and then loaded into the sample chamber of the SEM. After

Table 1
Coded levels and real values for each independent variable.

Variables	Coded levels		
	-1	0	+1
Independent	Real values		
Chitosan (X ₁ , mg)	200	400	600
STPP concentration (X ₂ , % w/v)	0.2	0.3	0.4
Stirring speed (X ₃ , RPM)	800	1000	1200
Dependent			
Encapsulation efficiency (% w/w)			

Table 2

Box Behnken Design experimental trial formulation batches with obtained encapsulation efficiency values (% w/w).

Experimental trials	X ₁	X ₂	X ₃	Encapsulation efficiency ^a (% w/w)
1	0	0	0	78.73 ± 1.17
2	0	-1	+1	50.52 ± 1.54
3	+1	0	-1	65.11 ± 1.56
4	+1	-1	0	62.08 ± 1.12
5	0	0	0	89.76 ± 1.90
6	0	0	0	76.92 ± 1.61
7	-1	+1	0	83.24 ± 0.78
8	+1	+1	0	96.04 ± 1.20
9	+1	0	+1	85.20 ± 1.78
10	0	+1	-1	85.60 ± 1.29
11	0	+1	+1	93.37 ± 1.34
12	0	-1	-1	58.27 ± 1.87
13	-1	-1	0	54.17 ± 0.87
14	0	0	0	91.21 ± 1.76
15	-1	0	-1	68.19 ± 1.54
16	0	0	0	90.47 ± 1.85
17	-1	0	+1	70.23 ± 0.34

^a Values are presented as mean ± SD (n = 3).

loading, the sample was coated using gold (~400°) via a sputter coating technique. The coated sample was scanned at an accelerating voltage of 10 kV. The scanned image of each sample at various magnifications was analyzed using instrument attached software (Smart@SEM V05.06).

2.9.3. Fourier transforms infrared spectroscopy (FT-IR)

FT-IR is a valuable analytical tool often used in the identification of functional group interaction between the formulation components. The FA, LSPC-3, physical mixture (PM) of FA and LSPC-3, FAPLC, chitosan, and FAPLC CNPs were analyzed using the FT-IR spectrophotometer (Model: FT-IR-8300, Shimadzu, Kyoto, Japan). Briefly, the powder mixture of samples and FT-IR grade of potassium bromide was compressed into thin transparent discs using Mini Hand Press Machine (Model: MHP-1, P/N-200-66, 747-91, Shimadzu, Kyoto, Japan). This disc was then scanned at a wavenumber range of 400 to 4000 cm⁻¹ under the scanning resolution of 4 cm⁻¹. The scanned image of each FT-IR sample was analyzed and interpreted using instrument accompanied software (IRSolution, version 1.10). The above procedure for the FT-IR analysis has been reported previously [44].

2.9.4. Differential scanning calorimetry (DSC)

The FA, LSPC-3, PM, FAPLC, chitosan, FA CNPs, and FAPLC CNPs were analyzed to investigate their thermal properties using differential scanning calorimeter (Model: DSC-1821e, Mettler-Toledo AG, Analytical, Schwerzenbach, Switzerland). Briefly, the sample (~2 mg) was weighed and loaded into a previously calibrated and N₂ purged analyzing area. The loaded sample was subjected to heating at a rate of 10 °C/min in the heating range of 0 to 400 °C. Following heating, the generated DSC thermograms of each sample were read using instrument attached software (Universal Analysis 2000, V4.5A, Build 4.5.0.5). The adopted DSC procedure has been reported by our group earlier [45,46].

2.9.5. Powder x-ray diffractometry (PXRD)

A powder x-ray diffractometer (Model: D8 ADVANCE, Bruker AXS, Inc., Madison, WI, USA) was employed for the comparative analysis of crystal characteristics of FA, LSPC-3, PM, FAPLC, chitosan, FA CNPs, and FAPLC CNPs respectively. Briefly, samples (~50 mg) were loaded into a sample analyzing area and irradiated using the CuK β radiation source ($\lambda = 1.5406\text{\AA}$). The irradiated sample was scanned and detected using a dimensional silicon strip based technology detector (LYNXEYE™). The obtained diffraction spectra on the 2 θ angle between the ranges of 3 to 60° at a count rate of 5 s were interpreted using PXRD accompanied software. An earlier published procedure by our group has been followed for the PXRD analysis of samples [47].

2.9.6. Proton nuclear magnetic resonance spectroscopy (¹H NMR)

The carbon-hydrogen structures, as well as chemical shift values of the above-mentioned formulation components, were analyzed using a 400 MHz FT-NMR spectrophotometer (Model: Bruker Advance II, Bruker BioSpin, Billerica, USA). The detailed procedure for the preparation of the sample, their analysis, and evaluation has been reported previously [46].

2.9.7. Solubility studies

A method earlier described by Singh et al. was used for the solubility analysis of pure FA, PM, FAPLC, FA CNPs, and FAPLC CNPs respectively [48]. Briefly, the above-mentioned samples in an excess quantity were dispersed in 5 mL of distilled water or n-octanol in sealed glass vials. The content in the vials was then agitated using a shaker (Model: RSB-12, Remi House, Mumbai, India) for 24 h. After agitation, the developed dispersion was centrifuged at 1500 rpm for 25 min followed by filtration using a 0.45 μ membrane filter. The filtrate was suitably diluted and analyzed the solution at the maximum wavelength of ($\lambda_{\text{max}} = \sim 311$ nm) against the blank to determine the solubility of each sample in water or n-octanol. The sample absorbance was recorded using a UV-visible spectrophotometer (Model: V-630, JASCO International Co., Ltd., Tokyo, Japan).

2.10. Functional characterization of FAPLC and FAPLC CNPs

2.10.1. In vitro dissolution studies

A dissolution method similar to that previously described by Maiti et al. was employed for the comparative evaluation of release performance of FA suspension, FA CNPs, FAPLC, or FAPLC CNPs respectively [49]. Briefly, an approximate amount of the above-mentioned samples containing ~2 mg of FA was weighed and dispersed in 2 mL of phosphate buffer. This dispersion was sonicated and then loaded into the dialysis bag. The dialysis bag with a requirement of average diameter ~21.55 mm, average flat width ~32.34, loading capacity ~3.63 mL, and molecular size cut off ~12,000–14,000 kDa was used in the dissolution studies. Moreover, the dialysis bag was rinsed as per the manufacturer's guidelines. The loaded samples in the dialysis bag were suspended vertically in the dissolution flask containing freshly prepared phosphate buffer (200 mL, pH 6.8) with Tween® 20 (1% v/v) dissolution media. The media in the flask was continuously stirred at 50 RPM using a magnetic stirrer and maintained at 37 ± 1 °C for 12 h. At a predetermined time interval, the samples were removed from the flask and compensate with the same quantity of fresh dissolution media. The removed samples were diluted suitably and analyzed the solution absorbance at maximum wavelength of ($\lambda_{\text{max}} \sim 311$ nm) on a UV-visible 188

spectrophotometer (Model: V-630, JASCO International Co., Ltd., Tokyo, Japan) against the blank. The recorded absorbance of samples was further used for the estimation of the cumulative release of FA.

2.10.2. Ex vivo permeation studies

The comparative permeation pattern of pure FA from FA suspension, FAPLC, FA CNPs, or FAPLC CNPs across a biological membrane was analyzed using a previously described *everted rat intestine* method [50]. The detailed procedure related to the procurement of animals, isolation, and preparation of rat intestine to *everted rat intestine* has been reported previously and the same was followed in this study. Briefly, the prepared everted rat intestine membrane was mounted between the two supporting ends of the apparatus followed by filling the same apparatus with the freshly prepared Krebs solution. After this, the entire apparatus was inserted vertically into a 250 mL beaker containing formulations i.e. FA suspension (100 µg/mL), FAPLC (100 µg/mL), FA CNPs (100 µg/mL) or FAPLC CNPs (100 µg/mL) prepared in the Krebs solution. The contents in the beaker were stirred at 25 RPM using a magnetic stirrer, maintained at a temperature of 37 ± 0.5 °C, and aerated using a mixture of carbogen (95% O₂ and 5% CO₂) throughout the permeation period i.e. 12 h. The samples were withdrawn from the assembly at an interval of 10 min, diluted suitably, and analyzed for absorbance at a maximum wavelength (λ_{max} ~311 nm) using a UV-visible spectrophotometer (Model: V-630, JASCO International Co., Ltd., Tokyo, Japan) against the blank. The measured absorbance of the permeated samples was further used for the estimation of cumulative permeation of FA and it was estimated using the below described equation.

$$\text{Apparent permrability} = [V/A \times T] \times C_1/C_0 \quad (5)$$

In the above equation, *V* shows the serosal content (mL), *A* represents the surface area of the intestinal sac (cm²), *T* represents the time of incubation (sec), *C*₀ displays the initial concentration on the mucosal side, whereas, *C*₁ displays the concentration of on the serosal side after time *T*.

2.11. In vivo antioxidant activity

2.11.1. Animals

The FA CNPs or FAPLC CNPs were evaluated for in vivo antioxidant potential using chloroform (CCl₄) - intoxicated rat model as per the procedure reported earlier [3,49]. The animal protocol (RSCOP/IAEC/2018-19 dated August 19, 2018) for the study was approved and sanctioned by Rajarshi Shahu College of Pharmacy, Buldhana. The animals (male and female albino rats, Wister strain) weighing about 150–200 g were used and preserved in clean colony cages under the controlled temperature (25 ± 5 °C) and relative humidity ($50 \pm 5\%$ RH) for 12 h light/dark cycle. Following this, the animals were nourished with food (pellet chow, Brooke Bond, Lipton, India) and water ad libitum. The entire study was carried out according to the ethical guidelines provided by the committee for the purpose of control and supervision of experiments on animals (CPCSEA).

2.11.2. Dosing

The animals used for in vivo antioxidant activity were divided into four groups containing six animals each. Group I animals administered only Tween® 20 (1% v/v, p.o.) for seven days and considered as a negative control, whereas, group II animals administered Tween® 20 (1% v/v, p.o.) for seven days and on the same day, the group II also received a single dose of an equal mixture of CCl₄ and olive oil (1:1, 5 mL/kg, i.p.) and considered as a positive control. Group III and IV animals administered FA CNPs or optimized FAPLC CNPs (20 mg/kg, p.o.) in Tween® 20 (1% v/v, p.o.) for seven days. Subsequently, on the seventh day, group III and IV animals also administered a single dose of an equal mixture of CCl₄ and olive oil (1:1, 5 mL/kg, p.o.) and left them for further observations. After 24 h of formulation and CCl₄ dosing, all the animals

were anesthetized using light ether. From these animals, the blood samples from the retro-orbital plexus were collected in a tube containing heparin and then centrifuged using microcentrifuge (Model: RM-12C, Angle Rotor Head, Remi House, Goregaon (E), Mumbai, India). The obtained supernatant plasma samples were further used for the assessment of liver function tests. Following this, the animals were euthanized using the cervical decapitation technique followed by isolation of the livers. The livers were washed in ice-cold saline solution and homogenized in 0.1 M PBS (pH 7.4) solution. The clear supernatant was analyzed to observe the overall influence of the formulations on the performance of in vivo antioxidant marker enzymes.

2.11.3. Estimation of the liver and in vivo antioxidant marker enzymes

The performance of liver function marker enzymes of serum glutamic oxaloacetic transaminase (SGOT) and serum glutamic pyruvic transaminase (SGPT) [51], alkaline phosphate (ALP) [52], and total bilirubin [53] in rat plasma samples were determined against FA CNPs or FAPLC CNPs using UV-visible spectrophotometer. Likewise, the antioxidant effect of FA CNPs or FAPLC CNPs on in vivo antioxidant marker enzymes of glutathione peroxidase (GSH) [54], superoxide dismutase (SOD) [55], lipid peroxidase (LPO) [56] and catalase (CAT) [57] present in rat liver homogenate was also determined using UV-visible spectrophotometer.

2.12. Oral bioavailability studies

2.12.1. Bioanalytical method development

An accurate amount of FA (~10 mg) was weighed and dissolved in a sufficient quantity of acetonitrile to get a final concentration of 200 mg/L. This stock solution was stored at 4 °C until further analysis. From this solution, different dilutions of FA were prepared and spiked with 50 µL blank plasma results in the formation of final concentrations in the range of 0.5–800 ng/mL. These diluted solutions were then used for the preparation of quality control (QC) samples at three different concentrations such as low (1.0 ng/mL), medium (20 ng/mL), and higher (640 ng/mL) respectively. The calibrated as well as QC samples were stored at –20 °C till further characterization.

An LC-MS/MS method previously described by Zhang et al. was used for the quantitative estimation of FA in rat plasma samples [58]. Briefly, the LC-MS/MS instruments (Model: ACQUITY UPLC™, Water Corporation, Milford, MA, USA) equipped with Tandem Quadrupole (TQ) detector, cooling auto-sampler, and column oven for controlling the temperature of analytical column was employed in this study. The separation was carried out on the stationary phase consisted of the BEH C18 column (50 mm × 2.1 mm, particle size ~1.7 µm, ACQUITY UPLC™, Water Corporation, Milford, MA, USA) and its column temperature was maintained at 35 °C. The chromatographic separation was carried out using a mobile phase composed of acetonitrile and water and the flow rate was set at 0.2 mL/min throughout the study. The run time for the sample was set at 3.5 min. The docetaxel (DXT) was used as an internal standard (IN) due to its structural similarity with the FA. The samples were analyzed in both, negative and positive ionization mode using multiple reaction monitoring (MRM). The ion source temperature was 120 °C. The target ions were scanned at an *m/z* ratio of 193 for FA and 808 for DXT respectively. Other supporting parameters such as data acquisition and peak integration were analyzed using instrument associated software (Masslynx 4.1 software).

2.12.2. Extraction of FA and sample preparation

A previously described liquid-liquid extraction (LLE) method was followed for the extraction of the FA from rat plasma samples [58]. The diethyl ether and formic acid (0.5%) was used as an extracting solvent and showed higher extraction recovery and reproducibility. Briefly, the extraction of FA was started with the oral administration of formulations to the animals. The animals were divided into groups I and II containing six animals each. Group I animals received FA CNPs (20 mg/kg)

p.o.) and group II animals received FAPLC CNPs (~20 mg/kg, p.o.) respectively. Following administration, all the animals were anesthetized at a pre-determined schedule and withdrawn their blood samples from retro-orbital plexus into the clean Eppendorf® Safe-Lock microcentrifuge tube (1.5 mL) containing heparin. The heparinized blood samples were centrifuged at 800 ×g for 10 min followed by a collection of plasma and preserved at –20 °C till further analysis.

2.12.3. Validation of the extraction and quantification method

International Conference on Harmonization (ICH) guidelines was followed for the validation of the developed LC-MS/MS method. The intra-day accuracy and precision analysis were performed using prepared QC samples on the same day ($n = 6$). The inter-day accuracy and precision were analyzed using the same QC samples on three subsequent days ($n = 6$). The extraction of FA from tissue samples and standard solution were performed and compared concerning extraction recoveries. Moreover, stability studies i.e. long term (24 h) and short term (14 days) were carried out on the prepared QC samples.

2.12.4. Study of pharmacokinetic parameters

Following administration of testing formulations, extraction, and LC-MS/MS analysis, the pharmacokinetic parameters of FA such as half-life ($t_{1/2}$), area under the plasma concentration-time curve (AUC) from zero to time of final measured sample (AUC_{0-t}) and from zero to infinity ($AUC_{0-\infty}$), mean residence time (MRT) were estimated using program-based WinNonlin® software (Version 4.1, Certara USA Inc., Princeton, NJ, USA). Moreover, C_{max} and T_{max} were estimated using the plasma concentration-time curve.

2.13. Statistical analysis

The extent of complexation rate, solubility, and in vitro release data was reported as a mean ± standard deviation. Additionally, the animal studies report i.e. liver function tests, in vivo antioxidant study, and pharmacokinetic analysis data were reported as mean ± standard error of the mean. The statistical differences between the animals treated groups were determined using a one-way analysis of variance (ANOVA). The obtained p -value of less than 0.05 was considered a significant one.

3. Results and discussion

3.1. Preparation of FAPLC and FAPLC CNPs

In this study, the FAPLC was prepared using ethanol based-solvent evaporation method. Before this experiment, the preliminary solubility analysis was conducted for FA and LSPC-3. It was found that both of these compounds are lipophilic and show higher solubility in organic solvents [59]. This physico-chemical property of FA was utilized in this study and prepared the phospholipids complex using the solvent evaporation method. The phospholipids complex are lipid compatible molecular aggregates of drug and/or bioactive and phospholipids and their formation is depending upon the complete dissolution of a drug as well as phospholipids in common solvents results in the formation of stable phospholipids complex. Previous literature reported the use of dichloromethane [16], 1, 4 – dioxane [46], and tetrahydrofuran (THF) [60] as a choice of solvents for the preparation of stable

phospholipids complex. These solvents were tested and found that FA as well as LSPC-3, both showed low solubility and precipitation problems during the formation of a complex. This solubility problem was overcome by using ethanol as a choice of solvents because of its semi-polar nature, class III solvent with a low toxicity profile, and provides higher solubility for FA and LSPC-3. Therefore, based on solubility, the ethanol was chosen as an optimal solvent for the preparation of stable FAPLC.

Following this, the FAPLC was loaded into chitosan nanoparticles and developed FAPLC CNPs using the ionic gelation method. Chitosan nanoparticles are formed due to the establishment of strong electrostatic interaction between dissolved polycationic chitosan and negatively charged STPP in a common solvent. Chitosan is an amphiphilic and polycationic polymer that demonstrates good solubility at below pH 6.8 due to the protonation of the amino group.

3.2. Screening of phospholipids

The screening of phospholipids was carried out based on high phosphatidylcholine (PC) and drug content and their results are presented in Table 3. As seen in the table, the LSPC-3 demonstrated higher PC content compared to Phospholipon® 80H, Phospholipon® 90H and Phospholipon® 90G indicate its suitability for the formation of a stable complex with FA. Moreover, the high PC content of LSPC-3 also showed higher drug content ($92.61 \pm 0.20\%$ w/w) compared to other phospholipids also suggested that higher PC could favorably interact with FA resulting in the formation of stable FAPLC with better physical form.

3.3. The rationale for selection of independent, dependent variables and their ranges

According to the ionic gelation method, the FAPLC CNPs was prepared at a laboratory scale, and based on that, the chitosan, STPP concentration, and stirring speed were selected as independent variables, and the influence of these variables was found significantly on the encapsulation efficiency, hence; it was selected as dependent variables. After this, the range of selected independent variables was finalized and it was done by using previously published reports which suggest that the optimal values ~100 mg, 4% w/v, and 700 RPM of the chitosan, STPP concentration, and stirring speed to produce the stable chitosan nanoparticles [61]. In this study, these values were used, synthesized the FAPLC CNPs, and tested for encapsulation efficiency. The tested results showed that synthesized FAPLC CNPs lowered the value of encapsulation efficiency. To improve this, the reported optimal values of independent variables were shifted from 100 to 200 mg, 4 to 0.2% w/v, and 700 to 800 RPM respectively. The shifted values produced the various experimental trials of FAPLC CNPs and demonstrated appreciable enhancement of encapsulation efficiency. Based on the positive results and to get more information about formulation in less number of trials, the range of variables at three levels was explored using BBD because it provides strong coefficient estimates near the center of the design space and more efficiency. Moreover, BBD offers an economic choice to central composite design (CCD) for the fitting of quadratic models that require three levels for each variable. Hence, based on the advantages of BBD, the chitosan, STPP concentration, and stirring speed were studied at three levels i.e. (–1) low, (0) middle, and (+) higher respectively.

Table 3
Screening of phospholipids for the preparation of FAPLC.

Lipids	Drug to lipids ratio	Drug content (% w/w)	Physical form
Phospholipon® 80H	1:1.5	73.24 ± 1.22	Sticky and aggregates
Phospholipon® 90H	1:1.5	79.40 ± 0.41	Sticky and aggregates
Phospholipon® 90G	1:1.5	86.52 ± 0.34	Sticky and aggregates
Lipoid® SPC-3 (LSPC-3)	1:1.5	91.61 ± 0.20	Powder

Table 4
Fit statistics of dependent variables of BBD.

Fit statistics	Std. Dev.	Mean	C.V. %	R ²	Adjusted R ²	Predicted R ²	Adeq precision
Encapsulation efficiency	6.23	76.42	8.16	0.9203	0.8179	0.6290	8.7111

C.V.: coefficient of variation.

3.4. Box Behnken Design

The generated experimental trials of FAPLC CNPs using selected independent variables produced a considerable impact on the encapsulation efficiency, and its results are presented in Table 2. The encapsulation efficiency value shows a significant variation and based on this, the lowest and highest efficiency values were 50.52% and 96.04% respectively. The obtained seventeen trials represent the interaction between selected independent variables. Subsequent interaction and analysis of data, the BBD exhibited the results in the form of fit statistics (Table 4), ANOVA data, diagnostic results, and model graphs respectively. Supporting this, the BBD also displayed the polynomial equation which shows the influence of independent variables on the encapsulation efficiency as well as the presence of coefficient of magnitude and positive and negative sign also demonstrated a strong impact on the encapsulations efficiency. These parameters of the polynomial equation were used further to optimize the FAPLC CNPs.

$$Y = +85.42 + 4.08X_1 + 16.65X_2 + 2.77X_3 - 5.65X_1^2 - 5.89X_2^2 - 7.59X_3^2 + 1.22X_1X_2 + 4.51X_1X_3 + 3.88X_2X_3 \quad (6)$$

Based on the ANOVA data (Table 5), the coefficient of magnitude i.e. b_2 and b_{33} represents the significant terms, while, the b_0 , b_1 , b_3 , b_{11} , b_{22} , b_{12} , b_{13} , and b_{23} represents non-significant terms ($p > 0.05$). Moreover, the obtained quadratic model for the FAPLC CNPs using BBD indicates the best fit model. Other parameters such as F-value and p -value found to be ~ 8.98 (>1) and 0.05 respectively suggest that the quadratic model is the best fit model. The lack of fit value ~ 0.53 (>0.05) indicates the suitability of the quadratic model for these trial formulations. Supporting this, the adequate precision value ~ 8.7111 (>4) and the difference between the adjusted & predicted correlation coefficient value $\sim <0.2$ indicates the quadratic model is significant and thus, can be used to navigate the design space. Additionally, the generated PRESS value ~ 1540.02 also suggests the suitability of the quadratic model. The polynomial equation containing a positive and negative sign of the coefficient of magnitude, and their impact on the encapsulation efficiency also demonstrated that as the concentration of X_1 , X_2 and X_3 increases to the middle level, the efficiency increases

Table 5
Summary of ANOVA used for data analysis of dependent variables of BBD.

Source	Sum of squares	df	Mean square	F-value	P-value	Remark
ANOVA: encapsulation efficiency (quadratic model)						
Model	3142.61	9	349.18	8.98	0.0043	Significant
A – chitosan	132.85	1	132.85	3.42	0.1070	
B – STPP concentration	2218.11	1	2218.11	57.07	0.0001	
C – stirring speed	61.33	1	61.33	1.58	0.2494	
AB	5.98	1	5.98	0.1538	0.7066	
AC	81.45	1	81.45	2.10	0.1910	
BC	60.22	1	60.22	1.55	0.2533	
A ²	134.24	1	134.24	3.45	0.1055	
B ²	146.02	1	146.02	3.76	0.0938	
C ²	242.50	1	242.50	6.24	0.0411	
Residual	272.03	7	38.87			
Cor total	3414.70	16				

df: degree of freedom.

and thereafter, found to reduce as the concentration of variables reduces concurrently indicates that middle-level concentration of above variables could be an optimal value for the optimization of FAPLC CNPs. The influence of X_1 , X_2 , and X_3 on encapsulation efficiency is presented in (Fig. 1A and B) respectively.

The optimization of FAPLC CNPs was conducted using numerical and graphical optimization methods. In the numerical method, the applied constraints for independent variables of X_1 , X_2 , and X_3 were in the range of ~ 200 to 600 mg, ~ 0.2 to 0.4 , and 800 to 1200 RPM respectively, whereas, the constraints for encapsulation efficiency was in the range of ~ 90.01 to 96.04% . The applied data showed one solution with the recommended values of independent variables as well as encapsulation efficiency. The possible solution also displayed the desirability value close to 1 indicates the suitability of constraints values and its results are shown in (Fig. 1C). In the graphical method, the same constraints were used and it exhibited the results in the form design space overlay plot (Fig. 1D). The design space also recommended the possible values of independent variables and encapsulation efficiency. Therefore, based on the desirability value and design space overlay plot, the optimal values for chitosan (X_1), STPP concentration (X_2), and stirring speed (X_3) were found to be 338.42 mg, 0.35% w/v, and 1003.52 RPM respectively. Moreover, the post-analysis results also showed close agreement between the experimental and predicted values, which further confirms the validity of the selected design (Table 6).

3.5. Validation of the model

An additional FAPLC CNPs trial using design – generated optimal values of X_1 , X_2 , and X_3 was prepared, evaluated, and compared against model-predicted yield values. The comparative results demonstrated a good agreement between the actual and model-predicted yield values. Moreover, bias (%) between these two yields was calculated using the below-described equation and it was found to be less than 3% indicates the suitability of the BBD for the optimization of FAPLC CNPs. Additionally, the obtained higher correlation coefficient value ~ 0.9203 also confirms the right selection of design and model.

$$\text{Bias (\%)} = \frac{\text{Predicted value} - \text{observed value}}{\text{Predicted value}} \times 100 \quad (7)$$

3.6. Physico-chemical characterization of FAPLC and FAPLC CNPs

3.6.1. Particle size and zeta potential

Particle size and zeta potential are typically considered as physical stability indicators of a multiparticulate system. The results of particle size and zeta potential of FAPLC and FAPLC CNPs are discussed below. As is reported previously, the LSPC-3 based diosmin phospholipids complex at the molar ratio of (1:1, 1:2, and 1:4) produced higher particle size (around ~ 536 nm, ~ 316 nm, and ~ 350 nm) accompanied with higher solubility, intestinal absorption, and bioavailability [62]. As a result, the obtained average particle size of FAPLC was around $\sim 4208 \pm 1.40$ nm with a low polydispersity index (PDI) value $\sim 0.39 \pm 0.04$ indicates narrow particle size distribution of FA within the matrix of LSPC-3 and suitability for oral administration. The higher particle size of FAPLC was likely attributed to excessive aggregation of LSPC-3 around FA molecules which could lead to remarkable complexation between them and produced higher particle size and low PDI value [62]. Zeta potential (ζ) is another physical property of a multi particulate system that provides information about the surface charges around the particle in suspension. The FAPLC displayed the zeta potential around $\sim -12.15 \pm 0.20$ mV. The zeta potential value higher than ± 10 mV is indicative of considerable stability of the system [63,64] and the zeta potential value of complex was higher than -10 mV designates better physical stability of the complex. This achieved value could be explained by the fact that a small contribution of LSPC-3 towards complexation m

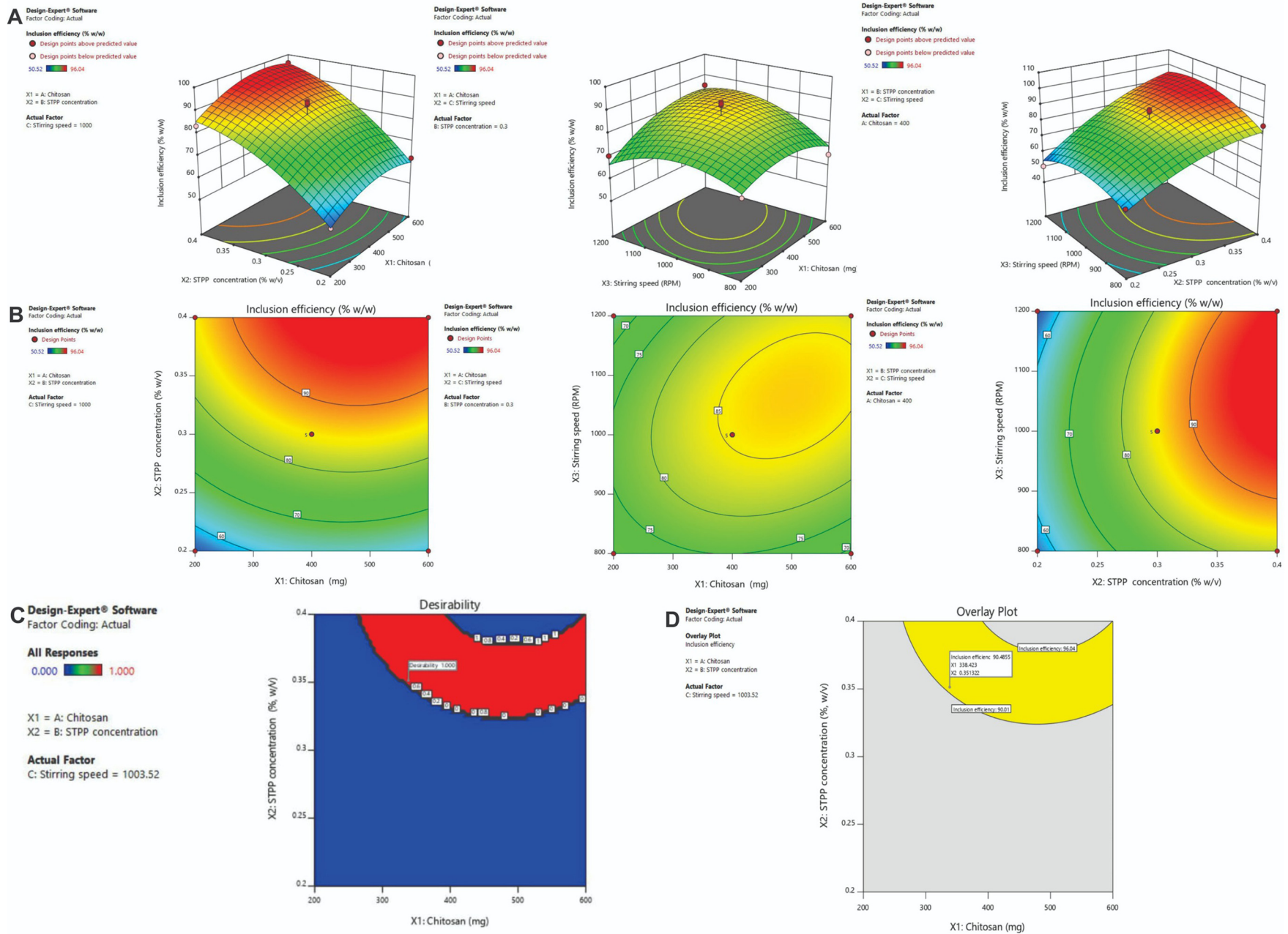


Fig. 1. (A) Counter plot, (B) 3D response surface plot, (C) desirability plot, and (D) design space plot describes the influence of independent variables of chitosan (X_1 , mg), STPP concentration (X_2 , % w/v) and stirring speed (X_3 , RPM) on inclusion efficiency (% w/w).

Table 6
Post analysis confirmation at two tailed 95% confidence level.

Response	Predicted mean	Predicted median	Std. Dev.	n	SE Pred	95% PI low	95% PI high
Encapsulation efficiency	90.4865	90.4865	6.2345	3	6.8221	74.3547	106.61

cause to produce a negative charge on the complex in neutral pH aqueous media, which could result in lower zeta potential values. It was also suggested that the employed phospholipids (its composition and type) could significantly change the zeta potential values [46].

In addition to this, the particle size and zeta potential of FAPLC CNPs were also evaluated by PCCS and their results are discussed below. The average particle size and PDI value of FAPLC CNPs were found to be $\sim 123.27 \pm 1.11$ nm and 0.31 ± 0.08 . The results are in consistent with earlier published reports which suggest that prepared chitosan nanoparticles using the ionic gelation method with particle size $\sim 142 \pm 1.51$ nm and PDI value $\sim 0.20 \pm 0.09$ are appropriate for oral delivery due to low toxicity, low immunogenicity, and high biocompatibility of chitosan [65]. The distribution of surface charge of FAPLC CNPs was found to be $\sim 32 \pm 1.28$ mV. The obtained value was more than reported $+30$ mV indicates excellent stability of the chitosan nanoparticles. It was likely attributed to a positive amino group of chitosan [66]. Thus, the lower particle size, low PDI, and positive surface charge value suggest excellent stability of FAPLC CNPs.

3.6.2. Scanning electron microscopy

Fig. 2(A–D) shows the surface morphology of FA, LSPC-3, FAPLC, and FAPLC CNPs respectively. The FA (Fig. 2A) exhibited as large crystalline needle-shaped particles with well-defined edges and faces. The

appearances of these particles are following earlier reports [13]. SEM image of LSPC-3 particles (Fig. 2B) appeared as clusters of small and large particles with ill-defined surface characteristics. The FAPLC SEM morphology (Fig. 2C) exhibited as large and non-uniform particles with a smooth surface. This particle morphology also shows the complete absence of FA particles suggesting that FA dispersed entirely in the LSPC-3 could result in a disappearance of FA particles. Compared to all, the SEM analysis of FAPLC CNPs (Fig. 2D) particles appeared as small spherical shaped particles with heterogeneous and porous surface suggesting that favorable interaction between complex – chitosan in STPP solution could result in the formation of spherical shape chitosan nanoparticles. Additionally, it was also suggested that a combination of solvent evaporation and ionic gelation technology could be demonstrated as strong interaction between the complex, chitosan, and STPP which was resulted in the formation of spherical nanoparticles.

3.6.3. Fourier transform infrared spectroscopy

FT-IR analysis provides vital information about functional group identification and their interaction with other components used in the formulations. Fig. 3(A–F) shows the FT-IR spectrum of FA, LSPC-3, PM, FAPLC, chitosan, and FAPLC CNPs respectively. The FT-IR spectrum of FA (Fig. 3A) shows the presence of absorption peak at ~ 3436.6 (OH stretching), 1617.7 (C = C stretching), 1464.8 (C = C aromatic stretching vibration), 1688.5 (C = O stretching), 1664.1 (C = C stretching) and found consistent with earlier published reports [13]. The FT-IR spectrum of LSPC-3 displays in (Fig. 3B). As shown in the figure, the LSPC-3 showing the characteristics absorption peak at ~ 3328.5 (OH stretching), 2914.8 and 2829.0 (C-H stretching of long fatty acid chain), 1736.9 (C = O stretching of fatty acid ester), 1237.5 (P = O stretching), 1062.3 (P-O-C stretching) and 902.0 [N+ - (CH₂)₃] [67]. PM FT-IR spectrum shows in (Fig. 3C). The PM exhibits an absorption

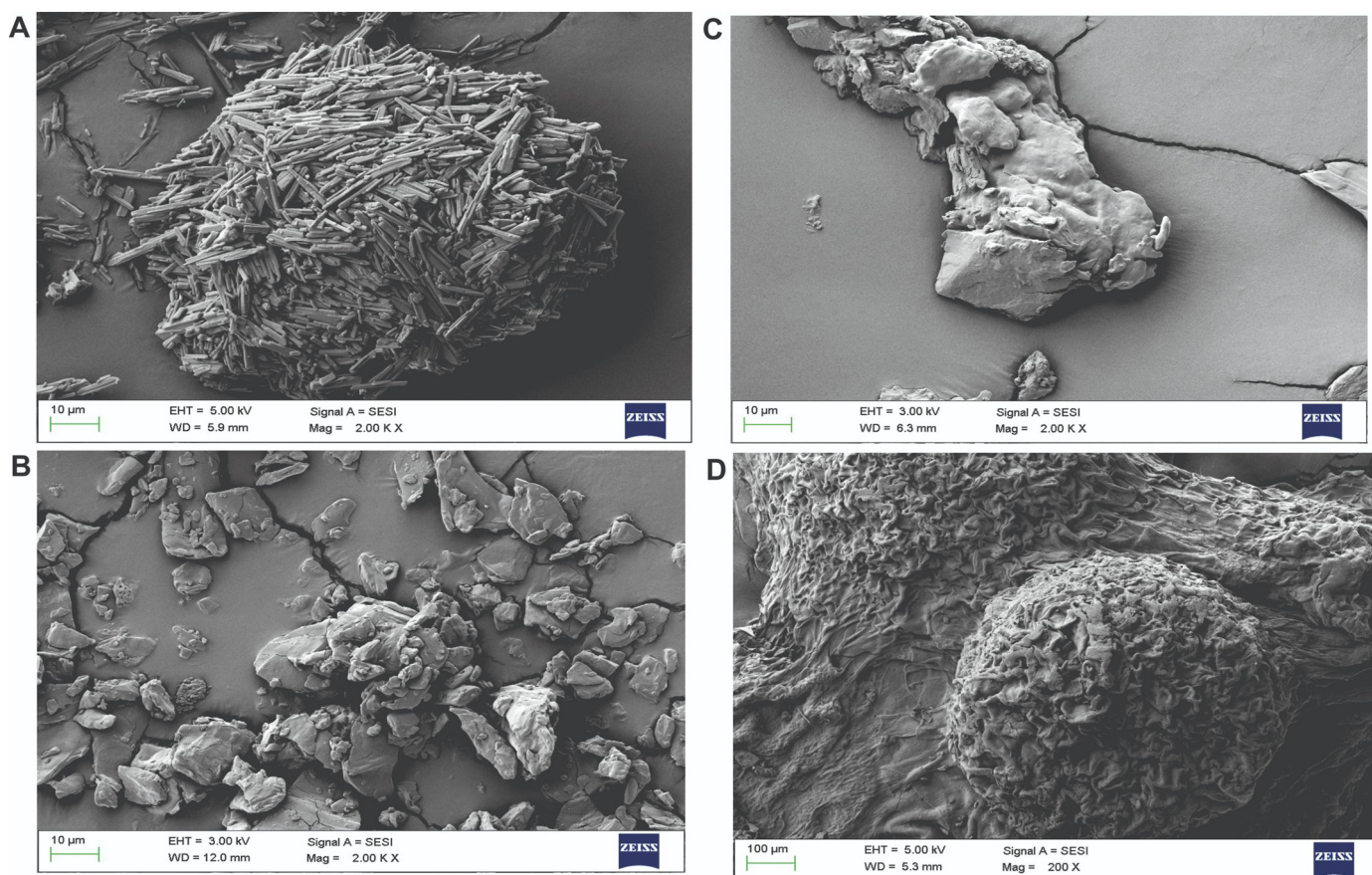


Fig. 2. SEM image of (A) FA, (B) LSPC-3, (C) FAPLC, and (D) FAPLC CNPs formulations.

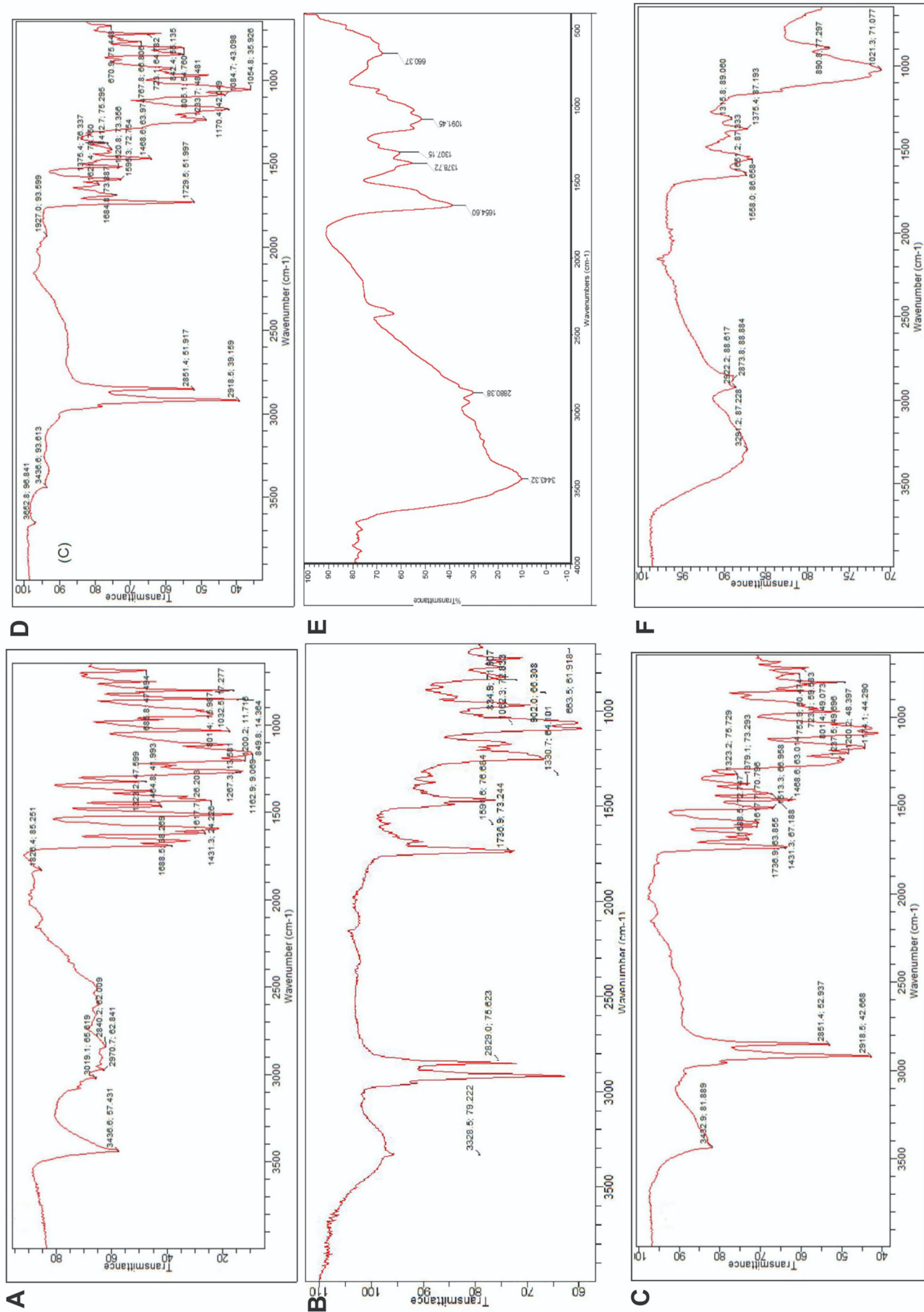


Fig. 3. FT-IR spectra of (A) FA, (B) LSPC-3, (C) PM, (D) FAPLC, (E) chitosan, and (F) FAPLC CNPs formulations.

peak at ~ 3432.9 , 1617.7 , 1468.6 , 1688.5 , 2918.5 , 2851.4 , 1736.9 , and 1237.5 indicates additive peaks of FA and LSPC-3. The slight shifting of the above peaks compared to the original one suggesting some interaction between FA and LSPC-3. The FT-IR spectrum of FAPLC (Fig. 3D) revealed a complete shifting of absorption peaks. The obtained narrow peak at ~ 3652.8 was shifted from ~ 3362.1 indicates hydroxyl group interaction between the FA and LSPC-3. It must be also emphasized that the peak position of FA was the same as appeared in the original spectra; however, it became narrow suggesting that the hydroxyl group of FA could be actively involved in the interaction mechanism with LSPC-3. The absence of a peak at ~ 1617.7 and 1464.8 correspondings to $C = C$ stretching and $C = C$ aromatic ring stretching suggesting shielding of these groups as a result of phospholipids complexation. Moreover, the disappearance of peaks at ~ 1688.5 and 1664.1 was likely due to affinity between the negative ($C = O$) group of FA and the positive (N^+) group of LSPC-3 [13]. The peak at ~ 1736.9 and 1062.3 related to LSPC-3 was also shifted to 1729.5 and 1084.7 in complex indicating an involvement of these groups in the complexation process. The shifted peak at ~ 1233.7 from ~ 1237.5 in the complex suggesting that ($P = O$) group of LSPC-3 could be interacted with (OH) group of FA via hydrogen bonding, van der Waals and ion-dipole forces resulted in the successful formation of FAPLC.

FT-IR spectrum of chitosan (Fig. 3E) presented a significant absorption peak at ~ 3443.32 (O-H stretching), 2880.38 (C-H stretching), 1654.60 (N-H stretching), 1378.32 (amide group), and 1091.45 ($C=O$ stretching in C-O-C) respectively. The FAPLC CNPs FT-IR spectra (Fig. 3F) revealed the absorption of a peak at ~ 3291.2 , 2922.2 , 2873.8 , 1651.2 , 1375.4 , and 1021.3 respectively. The shifting of these peaks

from their original spectrum could be explained on the basis that positive (N-H) functional groups of chitosan interacted with negative charge ($C = O$) group of FA, LSPC-3, and FAPLC via weak intermolecular and ionic interaction forces, which could result in the formation of chitosan nanoparticles loaded with FAPLC. Therefore, it can be concluded that weak and ionic interaction forces between FAPLC and chitosan resulted in the formation of FAPLC CNPs.

3.6.4. Differential scanning calorimetry

DSC is a valuable tool particularly used to determine the physical and/or solid-state interaction (i.e. appearance, disappearance, shifting, and/or alter the peak position and area) between the components of formulations. The developed interaction can provide information regarding the formation of a complex. The DSC curve of FA, LSPC-3, PM, FAPLC, chitosan, FA CNPs, and FAPLC CNPs are shown in Fig. 4(A–G) respectively. The FA DSC curve (Fig. 4A) displayed a high-intensity endothermic peak around ~ 174.25 °C with an enthalpy value ~ 105.16 J/g indicates polymorphic form I of FA [13,59]. (Fig. 4B) shows the DSC curve of LSPC-3. The LSPC-3 showed three small intensity diffused endothermic peaks around ~ 78.18 °C, 110.88 °C, and 183.08 °C respectively. The associated enthalpies of these peaks were ~ 11.82 J/g, 5.58 J/g, and 1.05 J/g respectively. The earliest two peaks could be attributed to the melting of a polar component of LSPC-3, while, the later one was probably attributed to a change of physical state of the hydrophobic part of LSPC-3 from gel-like state to crystalline state due to increasing the temperature of the LSPC-3 [33,67]. The DSC curve of PM (Fig. 4C) exhibited a series of endothermic peaks appeared at ~ 75.25 °C, 143.58 °C, 185.95 °C, 235.58 °C and 254.45 °C respectively indicating additive characteristics

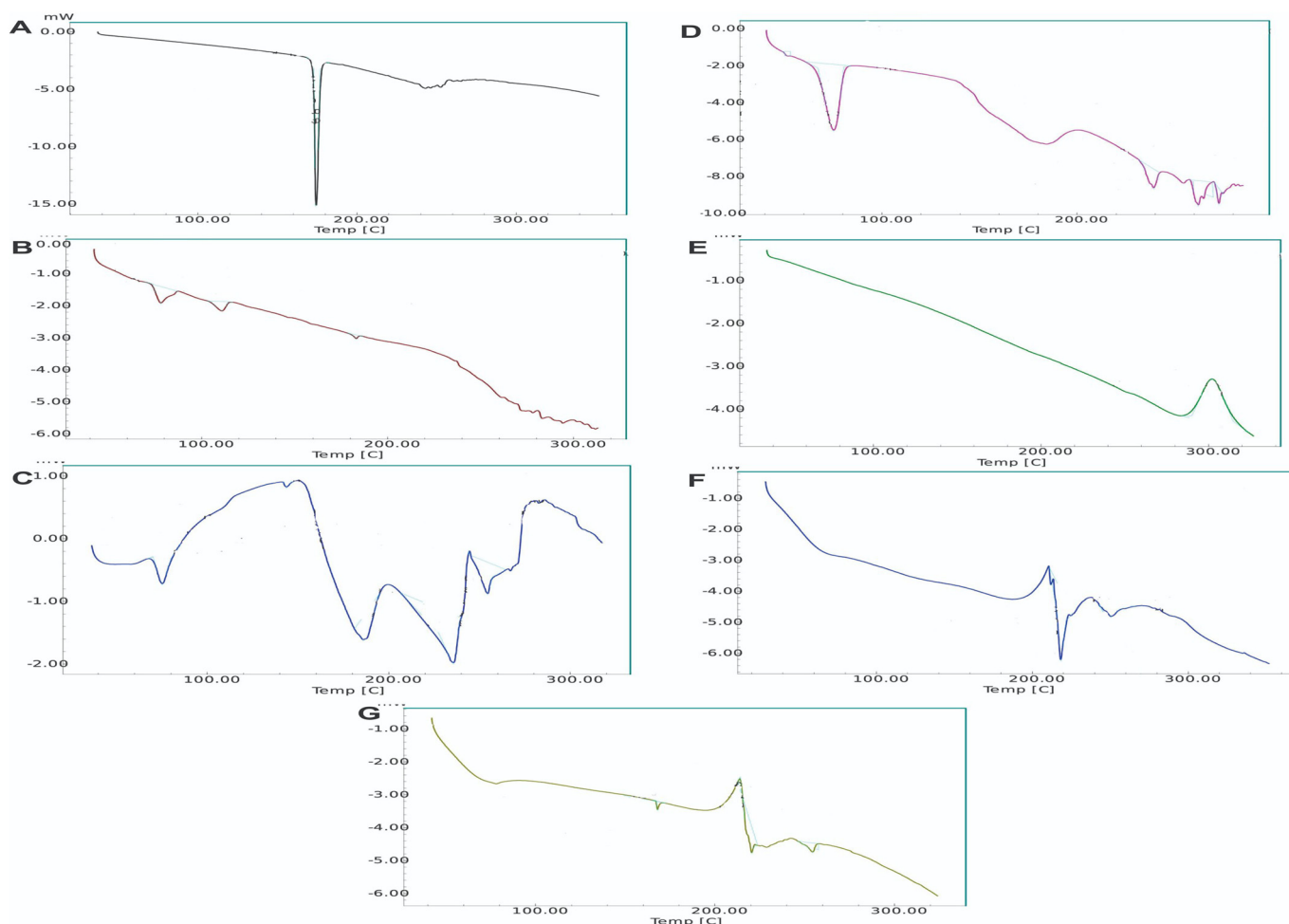


Fig. 4. DSC curves of (A) FA, (B) LSPC-3 (C) PM (D) FAPLC (E) chitosan (F) FA CNPs and (G) FAPLC CNPs formulations.

of FA and LSPC-3, suggesting that the increasing temperature melted the PM, form partial in situ mixture, which could lower the peak intensity as compared to original peaks. The high-intensity peak of FA was shifted to a low-intensity peak around ~143.58 °C indicates favorable interaction between the FA and LSPC-3. Moreover, the presence of a low amount

of FA ratio in the PM could also be the reason for showing such a low-intensity peak. Also, two more peaks i.e. 235.58 °C and 254.45 °C appeared in this curve indicates it is related to LSPC-3. The appearance of these peaks also shows the promising interaction between the components. The DSC curve of FAPLC (Fig. 4D) exhibited a novel, broad and

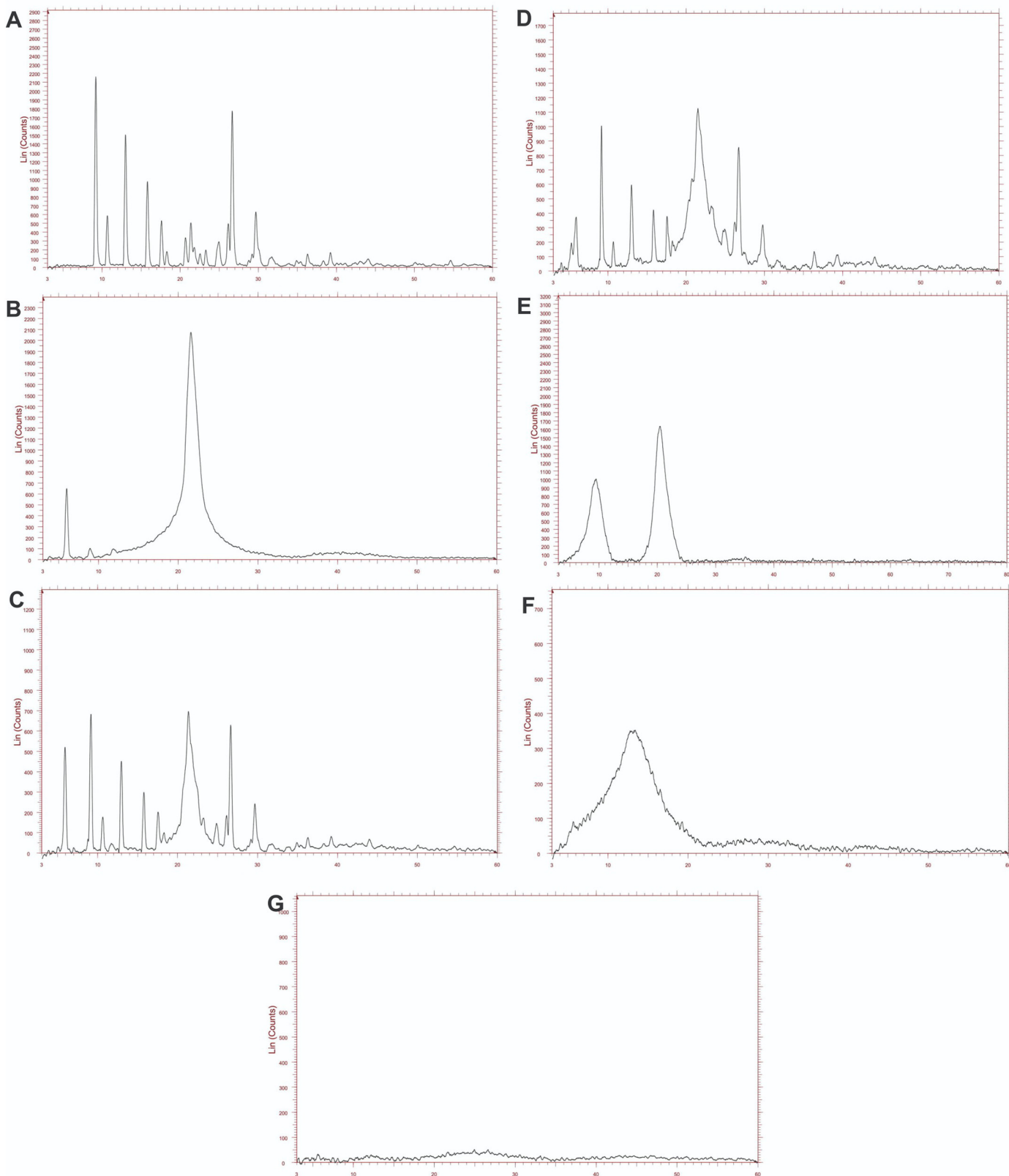


Fig. 5. PXRD spectra of (A) FA, (B) LSPC-3 (C) PM (D) FAPLC (E) chitosan (F) FA CNPs and (G) FAPLC CNPs formulations.

small intensity endothermic peak around $\sim 75.32^\circ\text{C}$ with enthalpy value $\sim 66.90\text{ J/g}$ and disappeared the original peaks of the components indicates a complete amorphization of FA by LSPC-3 [68]. Moreover, it is also suggested that polar segment form I of FA and LSPC-3 could interact via weak intermolecular forces, improved the dispersibility of FA within LSPC-3, and thus, resulted in the formation of a stable complex. The hydrophobic interaction ascribed to the aromatic ring of FA may also contribute to the formation of a complex with LSPC-3 [69]. Additionally, the obtained different enthalpy values of FA and complex also suggest the formation of FAPLC.

The chitosan DSC curve (Fig. 4E) displayed a single and sharp endothermic peak around $\sim 302.04^\circ\text{C}$ with an enthalpy value of $\sim 55.61\text{ J/g}$ indicates the melting of chitosan. This peak can be obtained due to the decomposition of the amino group and it is consistent with previous reports [70]. The DSC curve of FA CNPs (Fig. 4F) displayed three small intensity endothermic peaks around $\sim 183.12^\circ\text{C}$, 218.23°C , and $\sim 250.49^\circ\text{C}$ respectively corresponding to FA and chitosan. The broad endothermic peak of FA at $\sim 183.12^\circ\text{C}$ indicates the presence of microcrystalline form I of FA in the chitosan nanoparticles; however, its intensity was reduced compared to the original peak due to interaction with chitosan. The remaining two peaks of chitosan may be attributed to a possible change in the physical state of chitosan due to the presence of STPP as cross-linking agents. Finally, the DSC curve of FAPLC CNPs (Fig. 4G) showed the low-intensity endothermic peak at $\sim 168.02^\circ\text{C}$ with enthalpy value $\sim 0.82\text{ J/g}$ indicating conversion of crystalline form I to amorphous FA, suggesting that when complex introduced into chitosan solution, the protonated chitosan may show strong affinity towards negative charge FAPLC, further established interaction, reduces its crystallinity and converts into chitosan nanoparticles with different peak characteristics. Thus, based on comparative DSC curves, it can be concluded that weak intermolecular forces between FA and LSPC-3 and strong interaction between complex and chitosan results in the formation of FAPLC and FAPLC CNPs.

3.6.5. Powder x-ray diffractometry

PXRD is a unique characterization technique used widely for the evaluation of the crystalline state of a drug within the matrix of the carrier. PXRD spectra of FA, LSPC-3, PM, FAPLC, chitosan, FA CNPs, and FAPLC CNPs are shown in Fig. 5(A–G) respectively. The PXRD spectra of FA (Fig. 5A) showed a series of sharp and mixed intensity peaks at ~ 9.19 (Lin counts on y-axis ~ 2150), 8.32 (~ 600), 12.96 (~ 1500), 15.77 (~ 950), 17.57 (~ 500), 21.34 (~ 500), 26.65 (~ 1750) and 29.68 (~ 600) respectively indicate polymorphic form I of FA. This spectrum is found to be consistent with earlier reports of FA [71]. The diffractograms of LSPC-3 (Fig. 5B) displayed two unrelated peaks. The first low-intensity peak appeared at ~ 6.01 (~ 650), while, the second high and broad intensity peak appeared at ~ 21.1 (~ 2050) indicates the amorphous nature of LSPC-3 [36]. The diffractograms of PM (Fig. 5C) exhibited a peak of FA and LSPC-3. The peak intensity of FA in between 5 and 10° was reduced slightly compared to the original one due to the low amount of FA in PM as well achievable interaction with LSPC-3, at the same time, the peak intensity of LSPC-3 in between the region of 20 to 25° was also reduced compared to original one due to formation of a partial mixture with FA which may cause to from PM powder with lower peak characteristics. The PXRD spectrum of FAPLC (Fig. 5D) exhibits very few peaks of FA accompanied with low intensity. The complex in between the region of 3 to 17° shows only four low-intensity peaks compared to higher intensity peak in pure FA and PM, whereas, in the region between 17 and 30° , the more broad LSPC-3 peak was appeared in complex compared to higher, sharp, and narrow range of peak in PM indicating that maximum amorphization of FA due to a higher amount of LSPC-3 available for complexation, suggesting that when FA comes in contact with higher amount of LSPC-3, the molecular interaction occurred between them due to hydrogen bonding and ion-dipole forces may cause to increase the dispersibility of FA into a polar head group of LSPC-3 matrix, reduced its crystallinity and form an amorphous complex powder. This

result concludes that molecular interaction and thereafter, the reduction of crystallinity of FA also confirms the formation of a complex.

The PXRD of chitosan (Fig. 5E) displays two dissimilar, broad, and high-intensity peaks at $\sim 10^\circ$ (~ 1000 count) and 20° (~ 1600 counts). These peaks could be caused by crystallinity and developed H-bonding with the amino groups of chitosan [72]. PXRD spectrum of FA CNPs (Fig. 5F) shows the presence of broad chitosan dominated peaks with complete disappearance of FA peak indicates partial amorphization of FA. This observable fact could be caused by the dispersion of FA in the chitosan matrix could result in the amorphization of FA [73,74]. (Fig. 5G) shows the PXRD of FAPLC CNPs. As seen in the figure, these spectra show the absolute disappearance of crystalline peaks of FA indicates total amorphization of FA by chitosan as well as LSPC-3. This result could be explained on the basis that the amino group of chitosan interacted with the polar part of FA and FAPLC through hydrogen bonding and van der Waals forces, this favorable interaction could facilitate the dispersibility of complex into chitosan polymer resulted in the formation of amorphous chitosan nanoparticles. Thus, it can be suggested that interaction between chitosan and complex could be responsible for the preparation of chitosan nanoparticles.

3.6.6. Proton nuclear magnetic resonance

^1H NMR is used to determine the physico-chemical interaction between the formulation components and provide information about the formation of complex and nanoparticles. ^1H NMR spectra of FA, LSPC-3, PM, and FAPLC are shown in Fig. 6(A, B, C, and D). ^1H NMR of FA (Fig. 6A) shows chemical shift values at $\sim \delta 3.813\text{ s}$ (3H for three CH_3 groups, 10 Hz), $\delta 6.340\text{ d}$ (1H, 10 Hz), $\delta 6.803\text{ d}$ (1H, C-H of aromatic ring), $\delta 7.076\text{ s}$ (1H, C-H), $\delta 7.508\text{ d}$ (1H, C-H) and $\delta 9.570\text{ s}$ (1H, OH) [71]. LSPC-3 ^1H NMR spectra (Fig. 6B) exhibited chemical shift values around $\sim \delta 4.40$ (1H, s), $\delta 4.09 - \delta 3.94$ (br s, 1H), $\delta 3.93 - \delta 3.75$ (s, 2H), $\delta 3.32$ (s, 1H), $\delta 2.95$ (H-8, $J = 8$ Hz), $\delta 2.27$ (s, 1H), $\delta 0.89$ (s, 3H) [75]. The ^1H NMR spectra of PM (Fig. 6C) showed the chemical shift values corresponding to FA and LSPC-3 signifies interaction between them. (Fig. 6D) displays the chemical shift values of FAPLC around $\sim \delta 6.339\text{ d} - \delta 6.379\text{ d}$ (1H, 10 Hz), $\delta 6.801\text{ d}$ (1H, for C-H), $\delta 7.507\text{ s}$ (1H, C-H) and $\delta 9.572\text{ s}$ (1H, OH) indicates remarkable shifting of chemical shift values towards downfield region i.e. ($\delta > 7$). This shifting could be attributed to molecular interaction of specific phenolic hydroxyl group of FA with the polar part of LSPC-3 by the means of hydrogen bonding and van der Waals forces resulting in the formation of a complex. Findings are following earlier reports [36]. This comparative result concludes that molecular-level interaction could be the main reason for the establishment of the complex.

3.6.7. Solubility studies

The solubility analysis of FA, FA CNPs, PM, FAPLC, and FAPLC CNPs in water or *n*-octanol are shown in Table 7. The pure FA showed low aqueous solubility around $\sim 0.71\text{ mg/mL}$, whereas, in *n*-octanol, the solubility of FA was increased $\sim 1.85\text{ mg/mL}$ respectively. The obtained results are not surprising because FA is a BCS II drug, which shows low solubility and high permeability [15]. The PM exhibits higher aqueous solubility and *n*-octanol solubility around ~ 1.83 and $\sim 3.20\text{ mg/mL}$ compared to pure FA. This could be attributed to close contact of negative charge ($\text{C}=\text{O}$) of FA and positive charge (N^+) of LSPC-3 followed by their interaction resulted in modest enhancement of aqueous solubility of FA. The FAPLC revealed higher aqueous solubility around $\sim 5.80\text{ mg/mL}$ (8-fold higher) compared to pure FA and PM. The solubility result was found significant ($p < 0.05$). This improved aqueous solubility could be explained by the following mechanism i.e. close association, interaction, dispersion, and followed by amorphization of FA due to the amphiphilic nature of LSPC-3. Moreover, it may be also suggested that the enwrapping of two long fatty acid chains of LSPC-3 onto the polar head of LSPC-3 enclose with FA resulted in maximum dispersion and amorphization of FA, which could result in enhancing aqueous solubility. The enhanced *n*-octanol solubility was likely due to the lipophilic

Table 7
Solubility results of FA, FA CNPs, PM, FAPLC and FAPLC CNPs in water and n-octanol.

Samples	Aqueous solubility (mg/mL) ^a	n-Octanol solubility (mg/mL) ^a
Pure FA	0.71 ± 0.09	1.85 ± 0.46
FA CNPs	1.83 ± 0.52	3.20 ± 0.37
PM	5.80 ± 1.14	8.43 ± 1.24
FAPLC	2.14 ± 0.47	4.67 ± 1.11
FAPLC CNPs	8.22 ± 1.20	12.10 ± 2.34

^a Values are presented as mean ± SD (n = 3).

character of LSPC-3. On the other hand, the FA CNPs and FAPLC CNPs demonstrate higher aqueous and n-octanol solubility compared to pure FA and PM. The FA CNPs displayed higher aqueous solubility approximately ~2.14 mg/mL (3-fold) compared to pure FA indicating that conversion of crystalline to an amorphous form of FA, suggesting that interaction between the protonated amino group of chitosan and negative oxygen group of FA may reduce its crystallinity and thereby, increase its dispersibility into chitosan, which resulted in improved aqueous solubility [76]. The FAPLC CNPs significantly improved the aqueous solubility around ~8.22 mg/mL (12-fold) compared to FA CNPs and this could be attributed to the attraction between two opposite charge of phospholipids complex and chitosan polymer, which form complex-polymer interaction, and this may increase the dispersion, amorphization and finally aqueous solubility of FA.

3.6.8. *In vitro* dissolution studies

The *in vitro* dissolution studies show the performance of the formulation at a molecular level. Fig. 7 shows the dissolution performance of FA from its suspension, FA CNPs, FAPLC, and FAPLC CNPs respectively. The FA suspension displays only ~29% FA dissolution at the end of 12 h attributes to low aqueous solubility of FA and it is correlated with the solubility studies. In the case of FAPLC, the dissolution rate of FA, by the end of first 5 h was found to be ~53% and, thereafter also, it released continuously and reached to a maximum around ~83% indicates sustained release behavior of FAPLC, suggesting that the enhanced aqueous solubility, as well as wettability of FAPLC, could increase the release of FA via formation of the homogenous aqueous dispersion and thus, enhanced its dissolution rate [36,77]. Moreover, it may be also suggested that partial amorphization and structural modification owing to interaction with a positive nitrogen group of LSPC-3 may increase the wetting of FA in aqueous media resulted in enhancement of the dissolution rate of FA. Compared to this, the FA CNPs and FAPLC CNPs demonstrated a higher dissolution rate of FA. The FA CNPs by the end of 5 h exhibited a rapid release of approximately ~30% and then, showed only ~54% of drug released. The rapid release of FA CNPs could be attributed to the absorption of FA on the loose surface of chitosan nanoparticles as suggested by Zhang et al. [33]. Additionally, it was also indicated that the protonation of the amino group of chitosan in presence of phosphate buffer (pH 6.8) could facilitate the swelling and then the dissolution of chitosan. The FAPLC CNPs revealed that the dissolution rate of the FA in the initial 5 h was approximately ~71% indicates burst release, while, at the end of 12 h, the same formulation showed maximum release around ~97% indicates sustained release. The burst effect could be caused by dissociation of FA from chitosan nanoparticles due to its weak attachment with chitosan [15], while, the sustained release effect could be attributed to secure interaction between negative charge of FAPLC and positive charge of chitosan, which inhibit its dissociation from the chitosan nanoparticles and sustain the release of FA. Similarly, the interaction between the negative oxygen charge of FA and the positive nitrogen charge of LSPC-3 could also retard the release rate of FA. Moreover, it was also suggested that the utilization of an amino group of chitosan by FAPLC during nanoparticle formation may restrict its protonation in an aqueous environment results in sustained release of FA. The obtained results suggest that FAPLC CNPs could provide a sustained release of FA over to that of FA CNPs and PM.

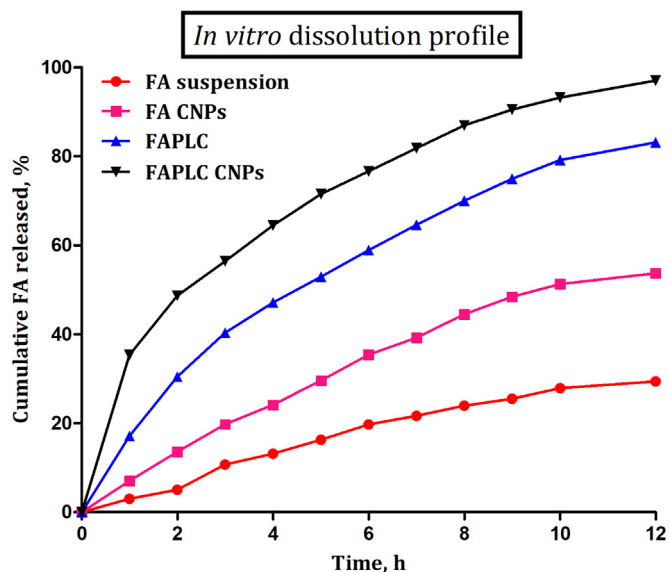


Fig. 7. *In vitro* dissolution pattern of FA from FA suspension, FAPLC, FA CNPs and FAPLC CNPs respectively. Values are presented as mean ± SD (n = 3).

The obtained release data of all the formulations were fitted into different kinetic models such as zero order, first order, Higuchi model, and Korsmeyer-Peppas model and evaluated for kinetic performance. Following analysis, the FAPLC, FA CNPs and FAPLC CNPs displayed Higuchi as best-fit kinetic model based on obtained higher correlation coefficient value ($R^2 = 0.9823, 0.9887$ and 0.9764) as compared to lower zero-order ($R^2 = 0.9655, 0.9478$ and 0.9245) and first-order values ($R^2 = 0.9033, 0.9154$ and 0.9018). The obtained Higuchi model suggests diffusion is the mechanism responsible for the release of FA from these formulations. Moreover, the obtained release exponent value of all the formulations was found to be <0.5 , which also suggests that, the diffusion mechanism mainly responsible for the release of FA from FAPLC, FA CNPs, and FAPLC CNPs respectively. The release mechanism of FA from FAPLC could be described by two steps: 1) the FA dissociated from FAPLC and, 2) the dissociated FA was diffused through the matrix of LSPC-3. In the case of FA CNPs, the release mechanism is governed by diffusion of FA from the matrix of chitosan, whereas, the release mechanism of FA from FAPLC CNPs could be described by two steps; 1) the FAPLC released from chitosan nanoparticles and then, 2) the FA released from the matrix of FAPLC. The findings were following earlier published reports [78].

3.6.9. *Ex vivo* permeation studies

Permeability is a complex kinetic process used to determine the speed at which a dissolved drug passes from the intestinal wall to the systemic blood circulation [80]. The *ex vivo* permeation pattern of FA from its suspension, FAPLC, FA CNPs, and FAPLC CNPs are shown in Fig. 8. The permeation efficiency of FA from its suspension at the end of 12 h was found close to ~26% indicates low permeability of FA. The intestinal permeability coefficient (P_{app}) value of FA suspension was found to be around $\sim(0.92 \pm 0.02 \times 10^{-6} \text{ cm/s})$ also indicates low permeability of FA. Compared to suspension, the FA CNPs by the end of 12 h, showed only ~52% FA permeation. The same formulation also displayed a permeability coefficient value around $\sim(2.12 \pm 0.33 \times 10^{-6} \text{ cm/s})$ suggests a modest increase of FA permeability from FA CNPs due to interaction between chitosan and phospholipids. The complex as well as optimized FAPLC CNPs both revealed a high permeation rate of FA. The permeation rate and permeability coefficient value of FA from FAPLC was found to be ~81%, and $\sim(3.22 \pm 0.46 \times 10^{-6} \text{ cm/s})$ respectively attributes to increase miscibility of FAPLC with the biological cell membrane, whereas, from FAPLC CNPs the permeation rate and permeability coefficient value was ~95% and $\sim(3.46 \pm 0.11 \times 10^{-6} \text{ cm/s})$.

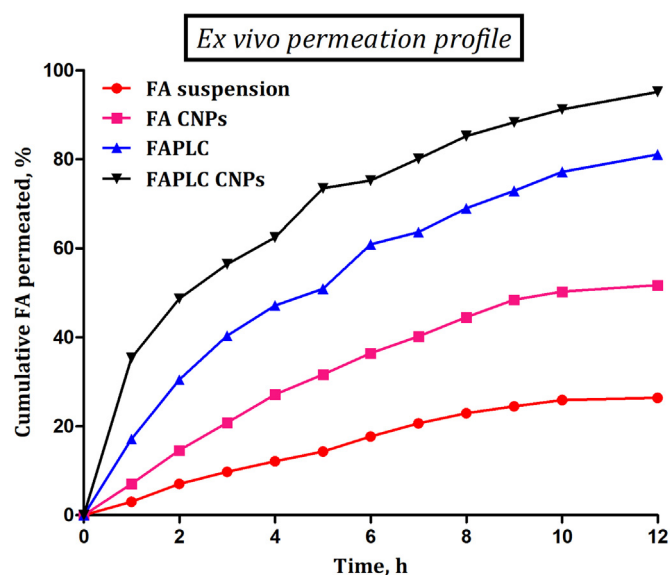


Fig. 8. Ex vivo permeation profile of FA from FA suspension, FAPLC, FA CNPs and FAPLC CNPs across everted rat intestine membrane. Values are presented as mean \pm SD ($n = 3$).

s) respectively compared to suspension, FA CNPs, and FAPLC. This more significant enhancement was likely due to the tight junction opening ability of chitosan nanoparticles. Moreover, the high degree of deacetylation of chitosan could also contribute to enhancing the permeability of FA.

The permeability of drug substance is often dependent upon three main factors such as physiological, physico-chemical parameters of drug substance, and bio-physicochemical parameters of the gastrointestinal tract [79]. In this study, the successful permeation of FA was achieved using a combination of phospholipids complex and chitosan nanoparticles. Phospholipids complex are reported to enhance the aqueous solubility and permeability of phytoconstituents through increasing its amphiphilicity. Similarly, the LSPC-3 based FAPLC also improved the aqueous solubility and permeability of FA via amorphization and increasing the amphiphilic nature of FA as evidenced by solubility studies. Also, the reported similarity of the lipid content of mammalian cell membrane (containing amphiphilic phospholipids bilayer) with the structure of LSPC-3 offers excellent biocompatibility towards each other [80], and based on this we believe that the amphiphilic FAPLC could increase its miscibility with the biological cell membrane (the fluid mosaic model proposed by S. J. Singer and G. L. Nicolson in 1972) resulted in an efficient permeation of FA. Compared to this, there is a significant permeation pattern difference was observed between FA CNPs and FAPLC CNPs respectively. In the case of FA CNPs, the established interaction between the positive charge of chitosan nanoparticles and negative charge of phospholipids bilayer of the cell membrane can increase their adhesion as well as retention to the

intestinal epithelium, however, the unfavorable interaction between the same negative charge of FA and LSPC-3 presents in the cell membrane may restrict its entry across the cell membrane and this could be the main reason for its low permeability through chitosan nanoparticles. Moreover, the partial amorphization of FA by chitosan nanoparticles as clearly seen in DSC, PXRD, and solubility studies could help to increase its permeability across the cell membrane. In the case of FAPLC CNPs, the developed interaction between the positive charge of chitosan and negative charge of phospholipids membrane could allow maximum adhesion and retention of chitosan nanoparticles with the epithelium for a maximum time leading to release and contact of FAPLC with the amphiphilic phospholipids bilayer of a biological membrane, increase its miscibility with the cell membrane resulted in noteworthy enhancement of FA permeability via paracellular and transcellular pathways. In supporting to phospholipids complex, the chitosan nanoparticles with their ability to temporarily opening of the tight junction of intestinal epithelium cells can also help to increase the FA permeability [35]. The obtained results conclude that FA CNPs and FAPLC improve the permeability of FA, however, a combination of phospholipids complex and chitosan polymer and their further favorable interaction drastically increases the permeation rate as well as bio-availability of FA.

3.7. In vivo antioxidant activity

3.7.1. Liver function tests

CCl_4 , a well-known hepatotoxin rapidly metabolized by CYP450 enzymes into various reactive oxygen species (ROS) i.e. free radicals. These radicals rapidly react with the macromolecules of the body, induce lipid peroxidation and finally damage the cellular membrane of hepatic cells, which in turn, leading to the release of liver function enzymes like SGOT, SGPT, total bilirubin, and SALP [81]. The release and presence of these enzymes in the blood signify the hepatic damage. The results of the antioxidant potential of FA CNPs and FAPLC CNPs on liver function liver marker enzymes are shown in Table 8. As seen, the SGOT, SGPT, total bilirubin, and ALP enzymes were elevated significantly in CCl_4 induced albino rat model. In response to this, the FA CNPs (20 mg/kg, p.o.) significantly reduced ($p < 0.05$) the elevated level of enzyme compared to the CCl_4 treated group indicates the hepatoprotective potential of FA. Additionally, the FAPLC CNPs more significantly ($p < 0.01$) restored the liver marker enzymes at the same dose level indicating that FAPLC CNPs provide more hepatoprotection over to that of FA CNPs, suggesting that, opposite charge attraction between FAPLC and CNPs provide effective interaction, adhesion, and retention on the hepatic cell membrane, which could improve the permeation and thereby, antioxidant efficacy of FA.

3.7.2. In vivo antioxidant marker enzymes estimation

Fig. 9 displays the effect of FA CNPs and FAPLC CNPs on the in vivo antioxidant marker enzymes such as GSH, SOD, CAT, and LPO respectively. The hepatotoxin CCl_4 remarkably reduced the GSH level

Table 8

Effect of FA CNPs and FAPLC CNPs on liver function test parameters (SGOT, SGPT, SALP and total bilirubin) in CCl_4 -induced rats.

Treatment groups with samples	SGPT (IU/L) ^a	SGOT (IU/L) ^a	SALP (IU/L) ^a	Total bilirubin (mg/dL)
Group I: Normal [Tween® 20 (1%, v/v, p.o.)]	50.11 \pm 2.20**	72.33 \pm 2.38**	120.50 \pm 3.58**	0.70 \pm 0.04**
Group II: Control [CCl_4 and olive oil (1:1, 5 mL/kg, i.p.)]	107.45 \pm 3.42	140.74 \pm 4.57	190.29 \pm 3.19	1.56 \pm 0.60
Group III: FA CNPs (~20 mg/kg, p.o.) [CCl_4 and olive oil (1:1, 5 mL/kg, i.p. for 7 days)]	76.02 \pm 2.27*	102.45 \pm 3.65*	148.39 \pm 2.36*	0.91 \pm 0.07*
Group IV: FAPLC CNPs (~20 mg/kg of MGN, p.o.) [CCl_4 and olive oil (1:1, 5 mL/kg, i.p. for 7 days)]	61.41 \pm 2.47**	86.71 \pm 3.15**	131.46 \pm 3.14**	0.82 \pm 0.08**

All values are Mean \pm SEM ($n = 6$).

^a IU/L – International Units/Liter of plasma.

* $p < 0.05$.

** $p < 0.01$ (significant with respect to control group).

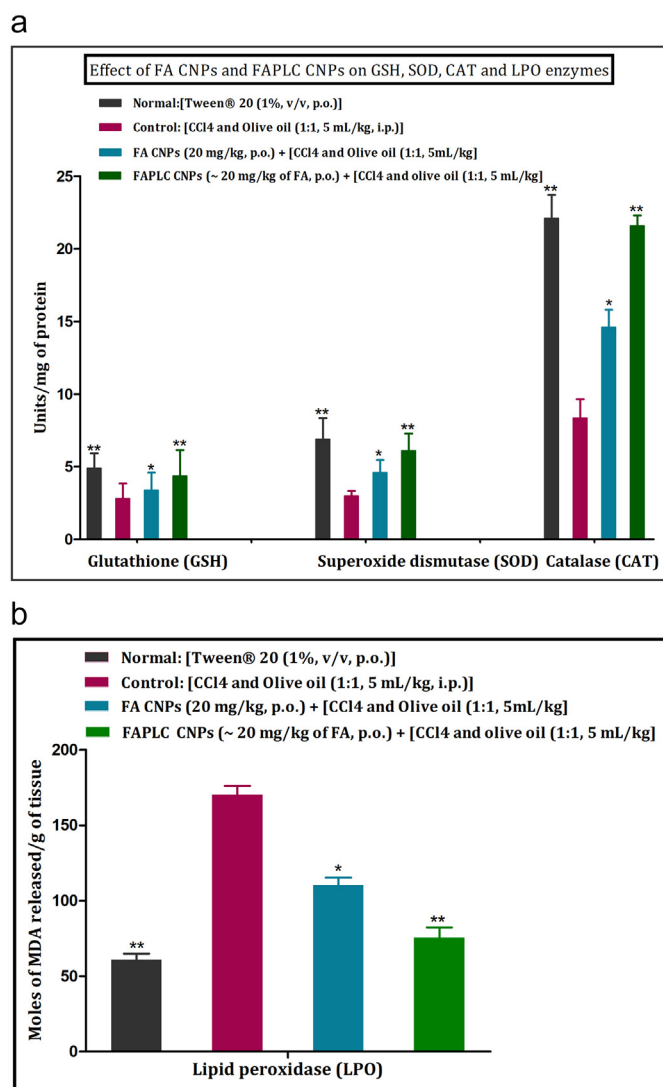


Fig. 9. Effect of FA CNPs and FAPLC CNPs on rat liver antioxidant marker enzymes, such as glutathione reductase (GSH) (nmoles/mg of protein), superoxide dismutase (SOD) (units/mg protein), catalase (CAT) (units/mg protein), and lipid peroxidase (LPO) (nmoles of MDA released/g tissue). Values are Mean \pm SEM ($n = 6$). * $p < 0.05$, ** $p < 0.01$ (significant with respect to control groups).

compared to the normal group. The same group on the administration of FA CNPs (20 mg/kg, p.o.) significantly ($p < 0.05$) enhanced the GSH level, whereas, the FAPLC CNPs more significantly ($p < 0.01$) elevated the GSH level at the same dose level. The level of SOD was found to be reduced in the CCl₄-intoxicated albino rat model. The FA CNPs at a dose of (20 mg/kg, p.o.) significantly ($p < 0.05$) improved the SOD level. In contrast to this, the FAPLC CNPs at the same dose more considerably ($p < 0.01$) enhanced the SOD level. CAT, another important enzyme was also found to have lowered following CCl₄ administration as compared to normal groups. The animal group treated with FA CNPs significantly ($p < 0.05$) elevated the CAT enzyme in the blood, while, the FAPLC CNPs at a dose of (20 mg/kg, p.o.) appreciably improved its level as well as activity against the developed free radicals. The significance of this result was ($p < 0.01$). The CCl₄-treated groups increased the lipid peroxidation level over to that of normal groups. However, on the administration of FA CNPs, the LPO level was reduced drastically. The FAPLC CNPs more notably reduced the LPO level. The level of significance of this study was found to be ($p < 0.01$). Therefore, the comparative result concludes that FAPLC CNPs demonstrate appreciable antioxidant activity compared to FA CNPs indicates that the FAPLC CNPs improved the antioxidant potential of FA and this could be

ascribed to the following reasons. First, the reported antioxidant and free radical scavenger potential of FA inhibit the formation of ROS by donating their electron to the free radicals, neutralize them and form less toxic phenolic and quinone methide radical. The chelate forming ability of FA with the protonated copper and iron metals prevent its conversion into toxic hydroxyl radicals, inhibit the lipid peroxidation, thereby, increase its antioxidant status (14). Second, the developed combined nanocarriers system could modify the FA resulted in the improvement of its solubility, dissolution, and permeation rate. This modified property of FA could be able to react with free radical and forms resonance-stabilized phenoxyl radical, which is mainly responsible for its antioxidant activity. The offering of extended conjugation by FAPLC CNPs to the resonance stabilized phenoxyl radical may also account for the strong antioxidant activity of FA. Third, the adhesion and retention property of FAPLC CNPs on epithelium could increase the miscibility of FAPLC with amphiphilic phospholipids bilayer of cell membrane increasing FA permeability via paracellular and transcellular routes and subsequently enhance the antioxidant status of FA. Fourth, the tight junction (intestinal epithelium cells) opening ability of chitosan nanoparticles may also increase the permeation rate of FAPLC into the damaged hepatic cells and restored the antioxidant status of liver cells. Sixth, the enhanced C_{max} , T_{max} , and biological half-life ($t_{1/2}$) of FA due to FAPLC CNPs could increase its circulation time in blood as well as utilization by hepatic cells could improve antioxidant activity of FA. Seventh, the sustained release property of FAPLC CNPs could also offer more exposure of FA to damaged hepatic cells, which in turn, provide strong antioxidant potential against free radicals. Finally, the amorphization, as well as improved amphiphilicity of FAPLC CNPs may increase the permeation of FA across the membrane and thus, provide an antioxidant effect. Obtained results concluded that FAPLC CNPs can offer better hepatoprotection against CCl₄ over to that of FA CNPs.

3.8. LC-MS/MS method validation

The obtained validation parameters of the LC-MS/MS method are discussed below. The selected concentration in the range of (0.5–800 ng/mL) displayed a good linearity with correlation coefficient value was ($r^2 = 0.9965$). The lower limit of detection and lower limit of quantification value following validation were found to be around ~0.15 and 0.5 ng/mL respectively. The intra-day and inter-day precision values were observed to be lower than <5%, whereas, the extraction recovery of FA from plasma samples was observed between the ranges of ~74.2–79.1% respectively. The stability studies showed no degradability

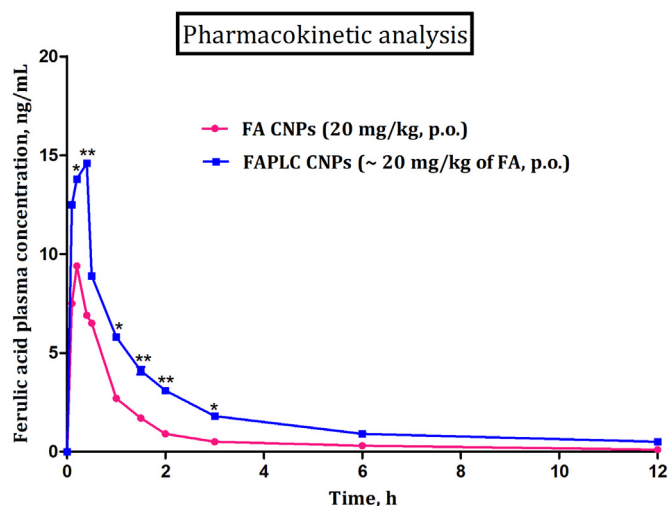


Fig. 10. Mean plasma concentration-time profile curve following oral administration of FA CNPs (20 mg/kg, p.o.) and FAPLC CNPs (~20mg/kg of FA, p.o.). Values are mean \pm SEM ($n = 6$). * $p < 0.05$ and ** $p < 0.01$ (significant with respect to FA CNPs treated group).

Table 9

Results of pharmacokinetic parameters obtained in group of animals following oral administration of FA CNPs (~20 mg/kg, p.o.) and FAPLC CNPs (~20 mg/kg, p.o.).

Pharmacokinetic parameters	Formulations	
	FA CNPs	FAPLC CNPs
C_{max} (ng/mL)	9.40 ± 1.33	14.61 ± 2.34
T_{max} (h)	0.20 ± 0.05	0.40 ± 0.09
$t_{1/2el}$ (h)	0.30 ± 0.02	0.50 ± 0.04
AUC_{0-t} (ng h/mL)	10.60 ± 2.59	24.80 ± 2.31
$AUC_{0-\infty}$ (ng h/mL)	18.60 ± 1.52	29.40 ± 2.65
MRT (0–12 h) (h)	1.30 ± 0.60	2.08 ± 1.24
MRT (0–∞) (h)	3.19 ± 1.02	2.70 ± 1.36

All the values are mean ± SEM (n = 6).

of FA under the influence of the selected temperature indicates its excellent stability.

3.9. Pharmacokinetic parameters

The plasma concentration vs. time profile curve of FA CNPs and FAPLC CNPs at a dose of (20 mg/kg, p.o.) are shown in Fig. 10. The FA CNPs showed a C_{max} value around ~ (9.40 ng/mL), whereas, the FAPLC CNPs displayed the higher C_{max} value ~ (14.6 ng/mL), and thereafter, the plasma concentration of FA was reduced significantly in both the formulations. The FAPLC CNPs demonstrated a higher t_{max} value around ~ (0.40 min), while, FA CNPs exhibited a lower t_{max} value around ~ (0.20 min). Moreover, the half-life ($t_{1/2}$) value of FAPLC CNPs was around ~ (0.50 h) as compared to the lower value ~ (0.30 h) in FA CNPs. These results could be caused by the sustained release property of FA present in FAPLC CNPs. In addition to this, other pharmacokinetic parameters were also estimated using WinNonlin® software (Version 4.1, Certara USA Inc., Princeton, NJ, USA) and are shown in Table 9. As seen in the table, the FAPLC CNPs showed higher AUC_{0-t} and $AUC_{0-\infty}$ values around ~ (24.80 and 29.40 ng h/mL) over to that lower value ~ (10.60 and 18.60 ng h/mL) of FA CNPs indicates the enhancement of oral bioavailability of FA. The mean residence time was increased significantly around ~ (2.08 h) in FAPLC CNPs, while, in the case of FA CNPs, the mean residence time was lowered ~ (1.30 h) indicates the availability of FA in the body for a maximum time. Obtained results suggested that developed interaction between negative charge of FAPLC and positive charge of CNPs may provide overall modification of FA and this modification could result in improvement of absorption and oral bioavailability of FA.

4. Conclusion

The current work demonstrated a successful preparation of FAPLC CNPs using a combination of phospholipids complex and chitosan nanoparticles via solvent evaporation and ionic gelation methodology. BBD study demonstrated a successful optimization of FAPLC CNPs using the design space and desirability plot. Characterization results indicated the formation of FAPLC and FAPLC CNPs through the contribution of hydrogen bonding and van der Waals forces between FA, LSPC-3, phospholipids complex, and chitosan nanoparticles. Moreover, the affinity of the negative charge of FAPLC towards the positive charge of chitosan revealed evidence for the formation of FAPLC CNPs. SEM and particle size analysis of FAPLC CNPs exhibited spherical shape morphology and its fitness for oral administration. Solubility study showed that FAPLC CNPs remarkably enhanced the aqueous solubility of FA around ~ (12-fold) over to that of FA CNPs ~ (3-fold). In vitro dissolution results revealed biphasic release performance (initial burst and then sustained release) of FA from FAPLC CNPs as compared to FA CNPs. Likewise, the permeation rate of FA from FAPLC CNPs was enhanced noteworthy as compared to FA CNPs. In vivo, the antioxidant potential of FAPLC CNPs at a dose of (20 mg/kg, p.o.) showed significant absorption of FA into the damaged hepatic cells and restored the marker enzymes compared

to FA CNPs at the same dose level. Pharmacokinetic analysis revealed an appreciable improvement of oral bioavailability of FA from FAPLC CNPs compared to FA CNPs. Obtained results suggested that FAPLC CNPs could be served as a promising nanocarriers system for the enhancement of oral bioavailability and antioxidant activity of FA.

CRedit authorship contribution statement

All the authors and co-authors of this manuscript declare that this manuscript is original and has not been published before.

We confirm that the submitted manuscript has been read, revised and approved by all the contributed authors. We also confirmed that the order of authors mentioned and listed in the manuscript has been approved by all of us.

We undersigned that the corresponding author is the only author contact for the editorial process. He is mainly responsible for communicating with all the authors about progress, submission of revisions and final approval of proofs.

Also, the current research work is completed without support of government funding.

Declaration of competing interest

The contributed authors have no competing interest to declare.

Acknowledgment

The corresponding authors of this manuscript express their sincere thanks to Dr. Shirish P. Jain, Principal, Rajarshi Shahu College of Pharmacy, Buldhana for providing financial and technical support.

Ethics statement

The animal protocol (RSCOP/IAEC/2018–19 dated August 19, 2018) for the study was approved and sanctioned by Rajarshi Shahu College of Pharmacy, Buldhana.

Funding

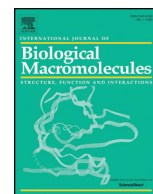
The conducted research work did not receive any funding from government agencies.

References

- [1] N.R. Prasad, S. Ramachandran, K.V. Pugalendi, V.P. Menon, Ferulic acid inhibits UV-induced oxidative stress in human lymphocytes, *Nutr. Res.* 27 (2007) 559–564, <https://doi.org/10.1016/j.nutres.2007.06.011>.
- [2] C. Mancuso, R. Santangelo, Ferulic acid: pharmacological and toxicological aspects, *Food Chem. Toxicol.* 65 (2014) 185–195, <https://doi.org/10.1016/j.fct.2013.12.024>.
- [3] M. Srinivasan, R. Rukkumani, A.R. Sudheer, V.P. Menon, Ferulic acid, a natural protector against carbon tetra chloride-induced toxicity, *Fundamental and Clin. Pharmacol.* 19 (2005) 491–496, <https://doi.org/10.1111/j.1472-8206.2005.00332.x>.
- [4] A. Sgarbossa, D. Giacomazza, M. di Carlo, Ferulic acid: a hope for Alzheimer's disease therapy from plants, *Nutr* 7 (2015) 5764–5782, <https://doi.org/10.3390/nu7075246>.
- [5] M.S. Balasubhashini, R. Rukkumani, P. Vishwanathan, V.P. Menon, Ferulic acid alleviates lipid peroxidation in diabetic rats, *Phytother. Res.* 18 (2004) 310–314, <https://doi.org/10.1002/ptr.1440>.
- [6] K. Kawabata, T. Yamamoto, A. Hara, M. Shimizu, Y. Yamada, K. Matsunaga, T. Tanaka, H. Mori, Modifying effects of ferulic acid on azoxymethane-induced colon carcinogenesis in F344 rats, *Cancer Let.* 157 (2000) 15–21, [https://doi.org/10.1016/S0304-3835\(00\)00461-4](https://doi.org/10.1016/S0304-3835(00)00461-4).
- [7] A.R. Sudheer, C. Kalpana, M. Srinivasan, V.P. Menon, Ferulic acid modulates lipid profiles, and prooxidant/antioxidant status in circulation during nicotine-induced toxicity: a dose dependent study, *Toxicol. Mech. Methods* 15 (2005) 375–381, <https://doi.org/10.1080/15376520500194783>.
- [8] N. Kumar, V. Purthi, Potential application of ferulic acid from natural sources, *Biotechnol. Rep.* 4 (2014) 86–93, <https://doi.org/10.1016/j.btre.2014.09.002>.
- [9] K. Zdunska, A. Dana, A. Kolodziejczak, H. Rotsztein, Antioxidant properties of ferulic acid and its possible application, *Skin Pharmacol. Physiol.* 31 (2018) 332–336, <https://doi.org/10.1159/000491755>.
- [10] N. Yan, Z. Tang, Y. Xu, X. Li, Q. Wang, Pharmacokinetic study of ferulic acid following transdermal or intragastric administration in rats, *AAPS PharmSciTech* 21 (2020) 1–7, <https://doi.org/10.1208/s12249-020-01709-w>.

- [11] Y. Zhang, Z. Li, K. Zhang, G. Yang, Z. Wang, J. Zhao, R. Hu, N. Feng, Ethyl oleate-containing nanostructured lipid carriers improve oral bioavailability of trans-ferulic acid as compared with conventional solid lipid nanoparticles, *Int. J. Pharm.* 115 (1) (2016) 57–64, <https://doi.org/10.1016/j.ijpharm.2016.06.131>.
- [12] C. Li, J.-B. Li, Preparation of chitosan-ferulic acid conjugate: structure characterization and in the application of pharmaceuticals, *Int. J. Biol. Macromol.* 43 (2017) 1539–1543, <https://doi.org/10.1016/j.ijbiomac.2017.04.103>.
- [13] Li. Li, Y. Liu, Y. Xue, J. Zhu, X. Wang, Y. Dong, Preparation of the ferulic acid-phospholipids complex to improve solubility, dissolution, and B16F10 cellular melanogenesis inhibition activity, *Chem. Central J.* 11 (26) (2017) 2–8, <https://doi.org/10.1186/s13065-017-0254-8>.
- [14] G.-C. Dong, C.-Y. Kuan, S. Subramaniam, J.-Y. Zhao, S. Savitasubramaniam, H.-Y. Chang, F.-H. Lin, A potent inhibition of oxidative stress-induced gene expression in neural cells by sustained ferulic acid release from a chitosan-based hydrogel, *Materials Sci. Engg. C.* 49 (2015) 691–699, <https://doi.org/10.1016/j.msc.2015.01.030>.
- [15] I.A. de Lima, N.M. Khalil, T.T. Tominaga, A. Lechanteur, B. Sermento, R.M. Mairandes, Mucoadhesive chitosan-coated PLGA nanoparticles for oral delivery of ferulic acid, *Artificial Cells, Nanomed. Biotechnol.* 46 (2018) 993–1002, <https://doi.org/10.1080/21691401.2018.1477788>.
- [16] S. Biswas, P.K. Mukherjee, R.K. Harwarwash, S. Banerjee, P. Bhattacherjee, Enhanced bioavailability, and hepatoprotectivity of optimized ursolic acid-phospholipids complex, *Drug Dev. Ind. Pharm.* 45 (6) (2019) 946–958, <https://doi.org/10.1080/03639045.2019.1583755>.
- [17] G.S. Ravi, R.N. Charyulu, A. Dubey, P. Prabhu, S. Hebbar, A.C. Mathias, Nano-lipid complex of rutin: development, characterization and in vivo investigation of hepatoprotective antioxidant activity and bioavailability study in rats, *AAPS PharmSciTech* 19 (8) (2018) 3631–3649, <https://doi.org/10.1208/s12249-018-1195-9>.
- [18] B. Li, L. Han, B. Cao, X. Yang, X. Zhu, B. Yang, H. Zhao, W. Qiao, Use of the mangoflorine-phospholipids complex to permeate blood-brain barrier and treat depression in the CUMS animal model, *Drug Delivery* 26 (1) (2019) <https://doi.org/10.1080/10717544.2019.1616236>.
- [19] R. Mondal, Y. Bobde, B. Ghosh, T.K. Giri, Development, and characterization of a phospholipids complex for effective delivery of capsaicin, *Ind. J. Pharm. Sci* 81 (6) (2019) 1011–1019.
- [20] U. Citeresi, M. Sciacchitano, Phospholipids/active ingredient complexes, *Cosm. Toil.* 110 (1995) 57–68.
- [21] S. Bhattacharyya, Phytosomes: emerging strategy in the delivery of herbal drugs and nutraceuticals, *Pharma. Times* 41 (2009) 9–12.
- [22] E. Fahy, S. Subramanian, H.A. Brown, A comprehensive classification system for lipids, *J. Lipid Res.* 46 (2005) 839–861, <https://doi.org/10.1194/jlr.E400004-JLR200>.
- [23] P.P. Constantinidas, M.V. Chaubal, R. Shorr, Advances in lipid nanodispersion for parenteral drug delivery and targeting, *Adv. Drug Deliv. Rev.* 60 (6) (2008) 757–767, <https://doi.org/10.1016/j.addr.2007.10.013>.
- [24] P.M. Kidd, Bioavailability and active phytosomes complexes from botanical polyphenols: the silymarin, curcumin, green tea, and grape seed extracts, *Alter. Med. Rev* 14 (3) (2009) 226–246.
- [25] L. Bildstein, C. Dubernet, P. Couvreur, Prodrug-based intracellular delivery of anticancer agents, *Adv. Drug Deliv. Rev.* 63 (1–2) (2011) 3–23, <https://doi.org/10.1016/j.addr.2010.12.005>.
- [26] E. Bombardelli, Phytosome: new drug delivery system, *Boll. Chem. Farm* 130 (11) (1991) 431–438.
- [27] D. Peer, J. Karp, S. Hong, Nanocarriers as an emerging platform for cancer therapy, *Nat. Nanotech.* 2 (2007) 751–760.
- [28] E. Sousa, S. Cassel, M. Blanzet, I. Rico-lattes, Drug delivery by soft matter: matrix and vascular carriers, *Angew. Chem. Int. Ed.* 48 (2) (2009) 274–278.
- [29] H.J. Malmiri, M.A.G. Jahanian, A. Berenjian, Potential applications of chitosan nanoparticles as novel support in enzyme immobilization, *Am. J. Biochem. Biotechnol.* 8 (4) (2012) 203–219, <https://doi.org/10.3844/ajbbsp.2012.203.219>.
- [30] L.L. Chaves, S.A. Costa Lima, A.C.C. Vieira, Development of PLGA nanoparticles loaded with clofazimine for oral delivery: assessment of formulation variables and intestinal permeability, *Eur. J. Pharm. Sci.* 112 (2018) 28–37.
- [31] M.E.I. Badawy, E.I. Rabea, A biopolymer chitosan and its derivatives as promising antimicrobial agents against plant pathogens and their applications in crop protection, *Int. J. Carbohydr. Chem.* (2011) 1–29, <https://doi.org/10.1155/2011/460381>.
- [32] M. Dash, F. Chiellini, R.M. Ottenbrite, E. Chiellini, Chitosan—a versatile semi-synthetic polymer in biomedical applications, *Prog. Polym. Sci.* 36 (8) (2011) 981–1014, <https://doi.org/10.1016/j.progpolymsci.2011.02.001>.
- [33] J. Zhang, Q. Tang, X. Xu, N. Li, Development and evaluation of a novel phytosome-loaded chitosan microsphere for curcumin delivery, *Int. J. Pharm.* 448 (2013) 168–174, <https://doi.org/10.1016/j.ijpharm.2013.03.021>.
- [34] L. Chronopoulou, M. Massimi, M.F. Giardi, Chitosan-coated PLGA nanoparticles: a sustained drug release strategy for cell cultures, *Colloids Surf B Biointerfaces* 103 (2013) 310–317, <https://doi.org/10.1016/j.colsurfb.2012.10.063>.
- [35] F. Araujo, N. Shrestha, M.A. Shahbazi, The impact of nanoparticles on the mucosal translocation and transport of GLP-1 across the intestinal epithelium, *Biomaterials* 35 (2014) 9199–9207, <https://doi.org/10.1016/j.biomaterials.2014.07.026>.
- [36] D.R. Telange, N.K. Sohail, A.T. Hemke, P.S. Kharkar, A.M. Pethe, Phospholipids complex-loaded self-assembled phytosomal soft nanoparticles: evidence of enhanced solubility, dissolution rate, ex vivo permeability, oral bioavailability and antioxidant potential of mangiferin, *Drug Deliv. Transl. Res.* (2020) 1–28, <https://doi.org/10.1007/s13346-020-00822-4>.
- [37] R.K. Khurana, A.K. Bansal, S. Beg, A.J. Burrow, O.P. Katara, K.K. Singh, Enhancing bio-pharmaceutical attributes of phospholipid complex-loaded nanostructured lipidic carriers of mangiferin: systematic development, characterization, and evaluation, *Int. J. Pharm.* 518 (2017) 289–306, <https://doi.org/10.1016/j.ijpharm.2016.12.044>.
- [38] L.X. Yu, Pharmaceutical quality by design: product and process development, understanding, and control, *Pharm. Res.* 25 (4) (2008) 781–791, <https://doi.org/10.1007/s11095-007-9511-1>.
- [39] Q. Tan, S. Liu, X. Chen, M. Wu, H. Wang, H. Yin, Design and evaluation of a novel evodiamine-phospholipid complex for improved oral bioavailability, *AAPS PharmSciTech* 13 (2012) 534–547, <https://doi.org/10.1208/s12249-012-9772-9>.
- [40] S. Alam, J.J. Panda, V.S. Chauha, Novel dipeptide nanoparticles for effective curcumin delivery, *Int. J. Nanomedicine* 7 (2012) <https://doi.org/10.2147/IJN.S330154207-4022>.
- [41] M.D. Shadab, R.A. Khan, G. Mustafa, K. Chuttani, S. Baboota, J.K. Sahni, Bromocriptine loaded chitosan nanoparticles intended for a direct nose to brain delivery: pharmacodynamic, pharmacokinetic and scintigraphy study in mice model, *Eur. J. Pharm. Sci.* 48 (2013) 393–405, <https://doi.org/10.1016/j.ejps.2012.12.007>.
- [42] D.R. Telange, R. Denge, A.T. Patil, M.J. Umekar, S.V. Gupta, V.S. Dave, Pentaerythritol as an excipient/solid dispersion carrier for improved solubility and permeability of ursodeoxycholic acid, *J. Excipient. Food Chem.* 9 (2018) 80–95.
- [43] D.R. Telange, S.B. Bhagat, A.T. Patil, M.J. Umekar, A.M. Pethe, N.A. Raut, V.S. Dave, Glucosamine HCl-based solid dispersion to enhance the biopharmaceutical properties of acyclovir, *J. Excipient. Food Chem* 10 (2019) 65–80.
- [44] D.R. Telange, S.B. Nirgulkar, M.J. Umekar, A.T. Patil, A.M. Pethe, N.R. Bali, Enhanced transdermal permeation and anti-inflammatory potential of phospholipids complex – loaded matrix film of umbelliferone: formulation development, physico-chemical and functional characterization, *Eur. J. Pharm. Sci.* 131 (2019) 23–38, <https://doi.org/10.1016/j.ejps.2019.02.006>.
- [45] D.R. Telange, A.T. Patil, A.M. Pethe, A.A. Tatode, S. Anand, V.S. Dave, Kaempferol-phospholipids complex: formulation and evaluation of improved solubility, in vivo bioavailability and antioxidant potential of kaempferol, *J. Excipient. Food Chem* 7 (2016) 89–120.
- [46] D.R. Telange, A.T. Patil, A.M. Pethe, H. Fegade, S. Anand, V.S. Dave, Formulation and characterization of an apigenin-phospholipid phytosome (APLC) for improved solubility, in vivo bioavailability, and antioxidant potential, *Eur. J. Pharm. Sci.* 15 (2017) 36–49, <https://doi.org/10.1016/j.ejps.2016.12.009>.
- [47] D.R. Telange, S.A. Ukey, A.T. Hemke, M.J. Umekar, A.M. Pethe, P.S. Kharkar, LIPOID SPC-3 based coprecipitates for the enhancement of aqueous solubility and permeability of ranolazine, *J. Pharm. Innov.* (2020) 1–16, <https://doi.org/10.1007/s12247-020-09477-7>.
- [48] D. Singh, M.S.M. Rawat, A. Semalty, M. Semalty, Chrysophanol–phospholipid complex: a drug delivery strategy in herbal novel drug delivery system, *J. Therm. Anal. Calorim.* 111 (2012) 2069–2077, <https://doi.org/10.1007/s10973-012-2448-6>.
- [49] M.K. Mukherjee, V. Murugan, B.P. Saha, P.K. Mukherjee, Exploring the effect of hesperetin-HSPC complex—a novel drug delivery system on the in vitro release, therapeutic efficacy, and pharmacokinetics, *AAPS PharmSciTech* 10 (2009) 943–950, <https://doi.org/10.1208/s12249-009-9282-6>.
- [50] P. Dixit, D.K. Jain, J. Dumbwani, Standardization of an ex vivo method for determination of intestinal permeability of drugs using everted rat intestine apparatus, *J. Pharmacol. Toxicol. Methods* 65 (2012) 13–17, <https://doi.org/10.1016/j.vascn.2011.11.001>.
- [51] S. Reitman, S. Frankel, A colorimetric method for the determination of serum glutamic oxaloacetic and glutamic pyruvic transaminases, *Am. J. Clin. Pathol.* 28 (1) (1957) 56–63, <https://doi.org/10.1093/ajcp/28.1.56>.
- [52] P.R. Kind, E.J. King, Estimation of plasma phosphatase by determination of hydrolyzed phenol with amino-antipyrine, *J. Clin. Pathol.* 7 (1954) 322–326, <https://doi.org/10.1136/jcp.7.4.322>.
- [53] H.T. Malloy, K.A. Evelyn, The determination of bilirubin with the photoelectric colorimeter, *J. Biol. Chem.* 119 (1937) 481–490.
- [54] G.L. Ellman, Tissue sulfhydryl groups, *Arch. Biochem. Biophys.* 82 (1959) 70–77, [https://doi.org/10.1016/0003-9861\(59\)90090-6](https://doi.org/10.1016/0003-9861(59)90090-6).
- [55] S. Marklund, G. Marklund, Involvement of the superoxide anion radical in the autoxidation of pyrogallol and a convenient assay for superoxide dismutase, *Eur. J. Biochem.* 47 (1974) 469–474, <https://doi.org/10.1111/j.1432-1033.1974.tb03714.x>.
- [56] J. Stocks, T.L. Dormandy, The autoxidation of human red cell lipids induced by hydrogen peroxide, *Br. J. Haematol.* 20 (1971) 95–111, <https://doi.org/10.1111/j.1365-2141.1971.tb00790.x>.
- [57] R.F. Beers, I.W. Sizer, A spectrophotometric method for measuring the breakdown of hydrogen peroxide by catalase, *J. Biol. Chem.* 195 (1) (1952) 133–140.
- [58] T. Zhang, X. Yang, P. Zhang, M. Zhu, Z. He, K. Bi, Determination of ferulic acid in rat plasma by liquid chromatography-tandem mass spectrometry method: application to a pharmacokinetic study, *Anal. Letters.* 42 (2009) 2157–2169, <https://doi.org/10.1080/00032710903137418>.
- [59] F. Shakeel, M.M. Salem-Bekhit, N. Haq, N.A. Siddiqui, Solubility, and thermodynamics of ferulic acid in different neat solvents: measurement, correlation, and molecular interactions, *J. Mol. Lipids.* 236 (2017) 144–150, <https://doi.org/10.1016/j.molliq.2017.04.014>.
- [60] J. Zhang, Q. Peng, S. Shi, Q. Zhang, X. Sun, T. Gong, H. Zhang, Preparation, characterization and in vivo evaluation of a self-nano emulsifying drug delivery system (SNEEDS) loaded with morin phospholipids complex, *Int. J. Nanomedicine* 6 (2011) 3405–3415, <https://doi.org/10.2147/IJN.S25824>.
- [61] N.R. Pani, S. Acharya, S. Patra, Development and validation of RP-HPLC method for quantification of glipizide in biological macromolecules, *Int. J. Biol. Macromol.* 65 (2014) 65–71, <https://doi.org/10.1016/j.ijbiomac.2014.01.007>.
- [62] M.S. Freag, Y.S.R. Elnaggar, O.Y. Abdallah, Lyophilized phytosomal nanocarriers as platforms for enhanced diosmin delivery: optimization and ex vivo permeation, *Int. J. Nanomedicine* 8 (2013) 2385–2397, <https://doi.org/10.2147/IJN.S45231>.
- [63] A. Mazumdar, A. Dwivedi, J.L. Du Preez, J. du Plessis, In vitro wound healing and cytotoxic effects of sinigrin – phytosomes complex, *Int. J. Pharm.* 498 (2016) 283–293, <https://doi.org/10.1016/j.ijpharm.2015.12.027>.

- [64] K. Pate, P. Safier, Chemical metrology methods for CMP quality, *Adv. Chem. Mech. Planazn.* (2016) 299–325.
- [65] N. Othman, M.S. Masaruddin, C.Y. Kuen, N.A. Dasuan, L.C. Abdullah, S.N.A.Md. Jamil, Synthesis, and optimization of chitosan nanoparticles loaded with L-ascorbic acid and thymoquinone, *Nanomaterials* 8 (2020) 2–19, <https://doi.org/10.3390/nano8110920>.
- [66] A.I. Barbosa, S.A.C. Lima, S. Reis, Development of methotrexate loaded fucoidan/chitosan nanoparticles with anti-inflammatory potential and enhanced skin permeation, *Int. J. Biol. Macromol.* 124 (2019) 1115–1122, <https://doi.org/10.1016/j.ijbiomac.2018.12.014>.
- [67] J. Li, P. Liu, J.-P. Liu, J.-K. Yang, W.-L. Zhang, Y.-Q. Fan, S.-L. Kan, Y. Cui, W.-J. Zhang, Bioavailability, and foam cells permeability enhancement of salvianolic acid B pellets based on drug-phospholipids complex technique, *Eur. J. Pharm. Biopharm.* 83 (2013) 76–86, <https://doi.org/10.1016/j.ejpb.2012.09.021>.
- [68] S.D. Saoji, N.A. Raut, P.W. Dhore, C.D. Borkar, M. Popielarczyk, V.S. Dave, Preparation and evaluation of phospholipids based complex of standardized Centella extract (SCE) for the enhanced delivery of phytoconstituents, *AAPS Journal*. 18 (2016) 102–114, <https://doi.org/10.1016/j.ejpb.2012.09.021>.
- [69] Z. Hou, Y. Li, Y. Huang, C. Zhou, J. Lin, Y. Wang, F. Cui, S. Zhou, M. Jia, S. Ye, Q. Zhang, Phytosomes loaded with mitomycin C – soybean phosphatidylcholine complex developed for drug delivery, *Mol. Pharm.* 10 (2013) 90–101, <https://doi.org/10.1021/mp300489p>.
- [70] B.B. Seghir, M.H. Benhamza, Preparation, optimization, and characterization of chitosan polymer from shrimp shells, *J. Food Measurement and Characterization*. 11 (2017) 1137–1147, <https://doi.org/10.1007/s11694-017-9490-9>.
- [71] C. Anselmi, M. Centini, M. Ricci, A. Bounocore, P. Granata, T. Tsuno, R.M. Facino, Analytical characterization of a ferulic acid/cyclodextrin inclusion complex, *J. Pharm. Biomed. Anal.* 40 (2006) 875–881, <https://doi.org/10.1016/j.jpba.2005.08.019>.
- [72] C.V. Pardeshi, V.S. Belgamwar, Controlled synthesis of N, N, N-trimethyl chitosan for modulated bio adhesion and nasal membrane permeability, *Int. J. Biol. Macromol.* 82 (2016) 933–944, <https://doi.org/10.1016/j.ijbiomac.2015.11.012>.
- [73] V.S. Belgamwar, H.S. Patel, A.S. Joshi, A. Agrawal, S.J. Surana, A.R. Tekade, Design and development of nasal mucoadhesive microspheres containing tramadol HCl for CNS targeting, *Drug Delivery* 18 (5) (2011) 353–360, <https://doi.org/10.3109/10717544.2011.557787>.
- [74] S. Patil, A. Babbar, R. Mathur, A. Mishra, K. Sawant, Mucoadhesive chitosan microspheres of carvedilol for nasal administration, *J. Drug Target.* 18 (4) (2010) 321–331, <https://doi.org/10.3109/10611861003663523>.
- [75] S. Sharma, R.K. Roy, B. Shrivastava, Antiproliferative effect of phytosome complex of methanolic extract of Terminalia arjuna bark on human breast cancer cell lines (mcf-7), *Int. J. Drug Dev. Res.* 7 (2015) (2015) 173–182.
- [76] S. Mutalik, K. Manoj, M.S. Reddy, P. Kushtagi, A.N. Usha, P. Anju, A.K. Ranjith, N. Udupa, Chitosan and enteric polymer-based once daily sustained release tablets of aceclofenac: in vitro and in vivo studies, *AAPS PharmSciTech* 9 (2008) 1–8, <https://doi.org/10.1208/s12249-008-9075-3>.
- [77] M. Perrut, J. Jung, F. Leboeuf, Enhancement of dissolution rate of poorly soluble active ingredients by supercritical fluid processes, *Int. J. Pharm.* 288 (2004) 3–10, <https://doi.org/10.1016/j.ijpharm.2004.09.007>.
- [78] S.S. Feng, G. Ruan, Q.T. Li, Fabrication and characterizations of a novel drug delivery device liposomes-in-microsphere (LIM), *Biomaterials* 25 (2004) 5181–5189, <https://doi.org/10.1016/j.biomaterials.2003.12.013>.
- [79] P.A. Cardenas, J.M. Kratz, A. Hernandez, G.M. Costa, L.F. Ospina, Y. Baena, C.M.O. Simoes, M. Aragon, In vitro intestinal permeability studies, pharmacokinetics and tissue distribution of 6-methyl coumarin after oral intraperitoneal administration in Wister rats, *Braz. J. Pharm. Sci* 53 (1) (2017) 1–9, <https://doi.org/10.1590/s2175-97902017000116081>.
- [80] G.L. Nicolson, The fluid–mosaic model of membrane structure: still relevant to understanding the structure, function, and dynamics of biological membranes after more than 40 years, *Biochim. Biophys. Acta* 1838 (6) (2014) 1451–1466, <https://doi.org/10.1016/j.bbame.2013.10.019>.
- [81] S. Martin-Aragón, D.L. Heras, M.I. Sanchez-Reus, Pharmacological modification of endogenous antioxidant enzymes by ursolic acid on tetrachloride-induced liver damage in rats and primary cultures of rat hepatocytes, *Exp. Toxicol. Pathol.* 53 (2001) 199–206, <https://doi.org/10.1078/0940-2993-00185>.



Use of combined nanocarrier system based on chitosan nanoparticles and phospholipids complex for improved delivery of ferulic acid

Darshan R. Telange ^{a,*}, Shirish P. Jain ^a, Anil M. Pethe ^b, Prashant S. Kharkar ^c, Nilesh R. Rarokar ^d

^a Rajarshi Shahu College of Pharmacy, Malvihi, Botha Road, Buldhana 443301, M.S., India

^b School of Pharmacy and Technology Management, SVKM's NMIMS (Deemed to be University), Pollepally SEZ, Jadcherla, Mehbubnagar, Hyderabad 509301, India

^c Department of Pharmaceutical Sciences and Technology, Institute of Chemical Technology, Mumbai 400019, M.S., India

^d Department of Pharmaceutical Sciences, Rashtrasant Tukadoji Maharaj Nagpur University, Nagpur, 440033, M.S., India

ARTICLE INFO

Article history:

Received 16 November 2020

Received in revised form 17 December 2020

Accepted 29 December 2020

Available online 05 January 2021

Keywords:

Ferulic acid
Chitosan nanoparticles
Phospholipids complex
Oral bioavailability
Antioxidant activity

ABSTRACT

A novel nanocarrier system of phospholipids complex loaded chitosan nanoparticles (FAPLC CNPs) was developed to improve the oral bioavailability and antioxidant potential of FA. FAPLC CNPs were optimized using a Box-Behnken Design (BBD). FAPLC CNPs were characterized using differential scanning calorimetry, Fourier transforms infrared spectroscopy, powder x-ray diffractometry, proton nuclear magnetic resonance, solubility, in vitro dissolution, ex vivo permeation, and in vivo antioxidant activity in carbon tetrachloride (CCl₄)-induced albino rat model. The characterization studies indicated a formation of the complex as well as FAPLC CNPs. The FAPLC CNPs exhibited a lower particle size ~123.27 nm, PDI value ~0.31, and positive zeta potential ~32 mV respectively. Functional characterization studies revealed a significant improvement in the aqueous solubility, dissolution, and permeation rate of FAPLC and FAPLC CNPs compared to FA and FA CNPs. The FAPLC CNPs showed significant enhancement of in vivo antioxidant activity of FA by restoring the elevated marker enzymes in the CCl₄-intoxicated rat model compared to FA CNPs. Moreover, the pharmacokinetic analysis demonstrated a significant enhancement of oral bioavailability of FA from FAPLC CNPs compared to FA CNPs. These findings show that FAPLC CNPs could be used as an effective nanocarrier for improving the oral delivery of FA.

© 2021 Elsevier B.V. All rights reserved.

1. Introduction

Ferulic acid (FA) (IUPAC name: [E]-3-[4-hydroxy-3-methoxy-phenyl] prop-2-enoic acid), a phenolic acid derivative, found in wheat, rice, barley, citrus, and some beverages such as coffee and beer. It is a potent free radical scavenger [1,2]. FA produces several biological activities such as antioxidant [3], neurodegenerative disorder [4], antidiabetic [5], anticancer [6], and pulmonary protective effect [7], etc. The antioxidant activity of FA attributes to the presence of unsaturated side chain, phenolic nucleus, hydroxyl and methoxy group attached to the phenyl ring, which ultimately provides stabilization to the structure via resonance [8]. Moreover, FA has low toxicity and therefore, it has been widely used in the pharmaceutical and food industry [9]. Despite these potential medical applications, FA exhibits low bioavailability, rapid metabolism, and elimination via oral administration [10]. Additionally, being a BCS class II drug (low solubility and high permeability), FA shows a poor absorption profile from the gastrointestinal tract via conventional delivery systems. Therefore, we need to develop novel and smart

nanocarriers which can improve the biopharmaceutical properties of FA.

Literature analysis demonstrated that only some nanoformulations have been attempted by the authors for enhancing the biopharmaceutical properties of FA. These include nanostructured lipid carrier (NLCs) [11], conjugates [12], phospholipids complex [13], hydrogel [14], and PLGA nanoparticles [15]. Analysis of these work demonstrated only partial improvement in the dissolution rate of FA, whereas, optimization, solubility, permeability, oral bioavailability, and antioxidant activity evaluation were found to have lacked. Likewise, the findings of phospholipids complex work have shown the limited improvement of FA solubility ~ (3-fold only) without analysis of dissolution rate, permeability, oral bioavailability, and antioxidant status of FA [13]. Moreover, the obtained low solubility of FA in employed soy lecithin based phospholipids can form strong aggregates and agglomeration product, which could exhibit low dissolution of FA from this phospholipids complex. The existed drawbacks of these single nanocarriers were overcome in the present research work by the formation of novel nanocarriers using a combination of phospholipids complex and chitosan nanoparticles through solvent evaporation and ionic gelation technology, which can accomplish the benefits of each carrier and circumvent their limitations.

* Corresponding author at: Rajarshi Shahu College of Pharmacy, Malvihi, Botha Road, 443001 Maharashtra, India.

E-mail address: telange.darshan@gmail.com (D.R. Telange).

Phospholipids complexation technology has been considered as one of the best techniques for enhancing the biopharmaceutical attributes of bioactive as compared to others, due to the simple preparation method, high drug loading ability, and long terms stability of the drug. Based on this, many researchers have used this expertise and reported a significant improvement in the solubility, permeability, and oral bioavailability of scores of bioactive such as ursolic acid [16], rutin [17], mangoflorine [18], and capsaicin [19]. These significant improvements in the bioactives are depending upon the composition of the phospholipids complex. The phospholipids complex consists of phospholipids, bioactive, and/or synthetic drug and preparation methods i.e. solvent evaporation method, the most widely used method. In this study, the LIPOID® SPC-3 (LSPC-3) was used as phospholipids. This lipid-like class of phospholipids also shows biocompatibility, biodegradability, metabolic activity, and low toxicity, and thus, it acts as suitable nanocarriers for translocation of bioactive across the biological membrane [20–22]. Moreover, being biocompatible due to similarity in lipid content of this lipid with the amphiphilic mammalian cell membrane, it exhibits higher miscibility towards each other and facilitates the effective permeation of bioactive. The amphiphilic nature of LSPC-3 also demonstrates aqueous as well as lipid solubility [23,24]. The LSPC-3 containing hydroxyl group can form interaction with the active hydrogen atom of any lipophilic drug through the esterification process, convert into amphiphilic compounds, facilitate its transportation across the biological membrane and finally, improve the therapeutic efficiency of drugs [25]. The same mechanism also occurred in the phospholipids complex, where phospholipids can form polar and hydrogen bonding interaction with bioactive and enhances their biopharmaceutical properties to a great extent [26–28].

Chitosan nanoparticles (CNPs) are natural materials that show physico-chemical, antimicrobial, and biological properties [29]. It can permeate into the interstitial spaces and increases the cellular uptake of drugs [30]. It is prepared from chitosan, which is a modified biopolymer, polycationic copolymer, and nitrogenous polysaccharide, obtained by total or partial deacetylation of chitin [31]. It contains one amino (-NH₂) and two hydroxyls (OH)₂ groups in the glucosidic residual chain. It is biocompatible and shows non-toxicity to the living tissues. It shows gel-forming ability, high adsorption capacity, and biodegradability properties. These properties of chitosan make it a potential nanocarrier for improving the encapsulation efficiency and sustained release properties of drugs [32]. The affinity of the positive charge of CNPs (due to cationic amino group) towards the negative charge of FAPLC complex (anionic group) forms strong electrostatic interaction, leading to increases in the encapsulation of phospholipids complex into CNPs and forms combined delivery system i.e. FAPLC CNPs, which prevents its exposure and provide a controlled release of a drug [33]. Additionally, the outside positive charge of FAPLC CNPs can also form interaction with the negative charge of the plasma membrane and mucosa, resulting into increase in their interaction, adhesion, and retention to the intestinal epithelial cells and enhances the permeability and absorption of drugs via opening the tight junction between the cells [34,35]. Earlier reports have shown that the encapsulation of phospholipids complex into the nanosystem i.e. nanoparticles can considerably improve the biopharmaceutical attributes of bioactive [36,37]. Therefore, based on the evidence, the developed FAPLC CNPs can be considered as promising combined drug delivery nanocarriers for improving the delivery and absorption of bioactive.

In this work, we developed FAPLC CNPs using FAPLC and CNPs via solvent evaporation and ionic gelation technology. The FAPLC was optimized using the quality by design (QbD) based Design of Experiment (DOE). Following this, the FAPLC CNPs were characterized for physico-chemical and functional parameters of particle size analysis, differential scanning calorimetry, Fourier transforms infrared spectroscopy, powder x-ray diffractometry, solubility analysis, in vitro dissolution, and ex vivo permeation studies. Moreover, the FAPLC CNPs were also investigated for in vivo antioxidant potential in the CCl₄-induced albino rat model.

2. Materials and methods

2.1. Chemicals

FA (HPLC purity > 99%) was obtained as a gift sample from Sisco Research Laboratories Pvt. Ltd. Mumbai, India. LIPOID® SPC-3 was obtained from Lipoid GmbH, Ludwigshafen, Germany. Chitosan (molecular weight = 340 kDa and degree of deacetylation = 75 – 80%) was purchased from HiMedia Laboratories Pvt. Ltd., Mumbai, India. Acetic acid, carbon tetrachloride, chloroform, ethanol, methanol, sodium chloride, sodium lauryl sulfate, sodium tripolyphosphate, and Tween® 20 were purchased from Loba Chemicals Pvt. Ltd., Mumbai, India. Disodium hydrogen phosphate, potassium dihydrogen phosphate, n-Hexane, and n-octanol were purchased from Sigma Chemicals, Sigma-Aldrich Corporation, St. Louis, MO. All other chemicals used in this study were based on analytical grade.

2.2. Preparation of ferulic acid – LIPOID® SPC-3 complex (FAPLC)

The ferulic acid – LIPOID® SPC-3 complex (FAPLC) was prepared as per the molar ratio of (1:1.5) using the ethanol-based solvent evaporation method described previously [33]. Briefly, the FA (194.20 mg) and LIPOID® SPC-3 (LSPC-3) (1173 mg) were individually weighed as per the above-mentioned molar ratio and transferred into a 100 mL round bottom flask. The weighed ingredients were mixed and dissolved in 20 mL of absolute ethanol. The solution in the flask was refluxed at a controlled temperature of 50 °C using a water bath (DSY-2-2, Aiqixia Apparatus Center, China) for 2 h respectively. The heated solution was concentrated to get 2–3 mL of liquid residue. This was then poured into 10 mL of n-hexane resulted in precipitation of FAPLC. The obtained complex was filtered and dried under vacuum at 40 °C for 12 h to remove traces of residual solvent if any. The dried FAPLC (yield ~92% w/w) was transferred to amber-colored (light protected) glass vials, purged with N₂, and stored at room temperature (RT) until further analysis.

2.3. Screening of phospholipids

The screening of four different grades of phospholipids such as Phospholipon® 80H, Phospholipon® 90H, Phospholipon® 90G, and LSPC-3 was carried out based on drug content and physico-chemical properties of the FAPLC. Among all, the LSPC-3 was selected as optimized phospholipids and used in the preparation of FAPLC as per the molar ratio of (1:1.5) using the solvent evaporation method.

2.4. Determination of extent of complexation of FA in FAPLC

A UV-based method previously described by Tan et al. [39] was used for the determination of the extent of the complexation of FA in FAPLC. Briefly, an approximate amount of FAPLC (equivalent to ~50 mg of FA) was weighed and transferred into 10 mL of the beaker. The weighed FAPLC powder was dispersed in 5 mL of chloroform and stirred well resulted in the formation of dispersion. In this dispersion, the FAPLC and LSPC-3 both were dissolved, while, FA remained as insoluble residue. This residue was filtered and dried at room RT. The dried residue was dissolved in methanol, diluted suitably, and analyzed for absorbance at (λ_{max} ~311 nm) using a UV-visible spectrophotometer (Model: V-630, JASCO International Co., Ltd., Tokyo, Japan). The extent of complexation was calculated using the below-described equation.

$$\text{Extent of complexation rate (\%)} = \frac{(C_t - C_f)}{C_t} \times 100 \quad (1)$$

where, C_t indicates the theoretical concentration of FA in FAPLC, and C_f represents the observed concentration of FA in the filtrate.

2.5. Preparation of FAPLC loaded chitosan nanoparticles (FAPLC CNPs)

The ionic gelation method described earlier was employed for the preparation of FAPLC CNPs with slight modifications [33]. This nanoparticle was prepared using FAPLC, acetic acid solution (2%, w/v), chitosan, and sodium tripolyphosphate (STPP) respectively. Briefly, the FAPLC (equivalent to ~10 mg of FA) and chitosan (200, 400, or 600 mg) were weighed and dispersed in the freshly prepared acetic acid solution. The developed complex-polymer dispersion was added in a dropwise manner at a flow rate of 2 mL/min using a nozzle (diameter ~2 mm) attached to the peristaltic pump (Model: PP 50 V, Electrolab India Pvt. Ltd., Mumbai, India) into continuously stirred 400 mL of STPP solution (0.2, 0.3 or 0.4 % w/v). The dispersion was stirred using a magnetic stirrer at a speed of (800, 1000, or 1200 RPM). This complex-polymer-STPP cross-linking mechanism resulted in the formation of FAPLC CNPs. The obtained nanoparticles were kept aside in the STPP solution in the dark overnight. Consequently, the nanoparticles were filtered (syringe filter, 0.22 µm), washed using deionized water, and oven-dried at 40 °C. Dried FAPLC CNPs were stored in light-protected glass vials, purged with N₂, and kept at RT until further analysis. Likewise, the FA CNPs, as well as blank CNPs (free of FAPLC) were also prepared using the same method as described above.

2.6. The rationale for selecting independent, dependent variables and their ranges

The preliminary experiments and supporting literature were used for the selection of independent, dependent variables and their ranges for the optimization of FAPLC CNPs. The nanoparticles were prepared using the same method as described above. The prepared nanoparticles were tested for encapsulation efficiency, and based on their results; the independent, dependent variables and their ranges were selected. Moreover, to explore further the range of independent variables, the FAPLC CNPs were optimized at three levels (-) low, (0) middle, and (+1) higher using Box-Behnken Design.

2.7. Box-Behnken Design (BBD)

Quality by Design (QbD) is a systematic, scientific and risk-based approach that commences with predefined objectives of the final product, and based on this, it identifies the critical parameters of the manufacturing process and/or formulation components that affect the quality of the product, translates these parameters into critical materials attributes (CMA) and/or critical process attributes (CPA) and finally establish these attributes in the form of experimental trials to consistently produce a product with desired characteristics [38]. In this study, the QbD-based Design of Experiments (DOE) i.e. Box-Behnken Design (BBD) (Design-Expert®, Version 10.0.4.0, Stat-Ease Inc., Minneapolis, Minnesota, USA) was employed to optimize CMA and/or CPA in less number of experimental trials to achieve the desired FAPLC CNPs. Based on preliminary experiments and supporting literature, the three independent variables i.e. chitosan (mg, X₁), STPP concentration (% w/v, X₂), and stirring speed (RPM, X₃) respectively were selected. Likewise, the encapsulation efficiency (% w/w) was selected as dependent variables. The selected independent variables were investigated at three levels and coded as (-1) low, (0) middle, and (+1) higher respectively. The BBD generated 17# possible experimental trials along with a statistical model i.e. polynomial equation as shown below. The equation containing the coefficient of magnitude, interaction terms, and generated positive and/or negative sign was used for the optimization of the FAPLC CNPs.

$$Y = b_0 + b_1X_1 + b_2X_2 + b_3X_3 + b_{11}X_1^2 + b_{22}X_2^2 + b_{33}X_3^2 + b_{12}X_1X_2 + b_{13}X_1X_3 + b_{23}X_2X_3 \quad (2)$$

where Y, is the encapsulation efficiency (% w/w) and b₀ is the coefficient of the independent variable of X. The X₁, X₂, and X₃ represent the main

effects of the study. The interaction terms i.e. X₁X₂, X₂X₃, and X₁X₃ indicate the combined effect of the independent variables on the encapsulation efficiency. The polynomial terms i.e. X₁², X₂², and X₃² show the non-linearity response of the dependent variables. The coded and real values of the independent and dependent variables are shown in Table 1, whereas, the possible experimental trials with an estimated value of encapsulation efficiency (% w/w) are depicted in Table 2.

2.8. Estimation of n encapsulation efficiency

The estimation of the encapsulation efficiency of FA within the FAPLC CNPs was carried out using the spectrophotometric method described previously [40,41]. Briefly, a certain amount of FAPLC CNPs was weighed and dispersed in 5 mL of 0.1 M HCl. The resulting dispersion in 1.5 mL of microcentrifuge tube was ultracentrifuged at 15,000 RPM at 4 °C for 40 min. Next, the supernatant was collected, diluted approximately, and analyzed at a maximum wavelength (λ_{max} ~311) on a UV-visible spectrophotometer against the blank. The encapsulation efficiency and drug loading were calculated using the equation described below.

$$\text{Encapsulation efficiency (\%)} = \frac{\text{Total amount of FA} - \text{Free FA}}{\text{Total amount of FA}} \times 100 \quad (3)$$

$$\text{Drug loading (\%)} = \frac{\text{Total amount of FA} - \text{Free FA}}{\text{Weight of nanoparticles}} \times 100 \quad (4)$$

2.9. Physical-chemical characterization of FAPLC and FAPLC CNPs

2.9.1. Particle size and zeta potential

Particle size and zeta potential are the most widely used indicator for the determination of release behavior and physical stability of a multi particulate system dispersed in the liquid medium. In this study, the particle size and size distribution of FA within FAPLC or FAPLC CNPs were evaluated using Photon Cross-Correlation Spectroscopy (PCCS) equipped with Dynamic Light Scattering (DLS) technology. Briefly, the aqueous dispersion of FAPLC or FAPLC CNPs was analyzed for particle size within the sensitivity range of 1 nm to 10 µm using a particle size analyzer (Model: Nanophox Sympatec, GmbH, Clausthal-Zellerfeld, Germany). The same dispersion of formulation was also used for the analysis of zeta potential within the sensitivity range of - 200 to +200 mV using Nano Particle Analyzer (Model: NanoPlus™-2, Particulate System, Norcross, GA, USA). The detailed procedure for the preparation of the sample and its evaluation has been reported earlier by our group [42].

2.9.2. Scanning electron microscopy (SEM)

The samples of FA, LSPC-3, FAPLC, and FAPLC CNPs were analyzed to study their surface characterization using a scanning electron microscope (Model: Supra®, Carl Zeiss NTS Ltd., Germany) according to the method described previously in the literature [43]. Briefly, the samples (~50 mg) were weighed and spread as a thin layer on double-faced carbon tape and then loaded into the sample chamber of the SEM. After

Table 1
Coded levels and real values for each independent variable.

Variables	Coded levels		
	-1	0	+1
Independent	Real values		
Chitosan (X ₁ , mg)	200	400	600
STPP concentration (X ₂ , % w/v)	0.2	0.3	0.4
Stirring speed (X ₃ , RPM)	800	1000	1200
Dependent			
Encapsulation efficiency (% w/w)			

Table 2

Box Behnken Design experimental trial formulation batches with obtained encapsulation efficiency values (% w/w).

Experimental trials	X ₁	X ₂	X ₃	Encapsulation efficiency ^a (% w/w)
1	0	0	0	78.73 ± 1.17
2	0	-1	+1	50.52 ± 1.54
3	+1	0	-1	65.11 ± 1.56
4	+1	-1	0	62.08 ± 1.12
5	0	0	0	89.76 ± 1.90
6	0	0	0	76.92 ± 1.61
7	-1	+1	0	83.24 ± 0.78
8	+1	+1	0	96.04 ± 1.20
9	+1	0	+1	85.20 ± 1.78
10	0	+1	-1	85.60 ± 1.29
11	0	+1	+1	93.37 ± 1.34
12	0	-1	-1	58.27 ± 1.87
13	-1	-1	0	54.17 ± 0.87
14	0	0	0	91.21 ± 1.76
15	-1	0	-1	68.19 ± 1.54
16	0	0	0	90.47 ± 1.85
17	-1	0	+1	70.23 ± 0.34

^a Values are presented as mean ± SD (n = 3).

loading, the sample was coated using gold (~400°) via a sputter coating technique. The coated sample was scanned at an accelerating voltage of 10 kV. The scanned image of each sample at various magnifications was analyzed using instrument attached software (Smart@SEM V05.06).

2.9.3. Fourier transforms infrared spectroscopy (FT-IR)

FT-IR is a valuable analytical tool often used in the identification of functional group interaction between the formulation components. The FA, LSPC-3, physical mixture (PM) of FA and LSPC-3, FAPLC, chitosan, and FAPLC CNPs were analyzed using the FT-IR spectrophotometer (Model: FT-IR-8300, Shimadzu, Kyoto, Japan). Briefly, the powder mixture of samples and FT-IR grade of potassium bromide was compressed into thin transparent discs using Mini Hand Press Machine (Model: MHP-1, P/N-200-66, 747-91, Shimadzu, Kyoto, Japan). This disc was then scanned at a wavenumber range of 400 to 4000 cm⁻¹ under the scanning resolution of 4 cm⁻¹. The scanned image of each FT-IR sample was analyzed and interpreted using instrument accompanied software (IRSolution, version 1.10). The above procedure for the FT-IR analysis has been reported previously [44].

2.9.4. Differential scanning calorimetry (DSC)

The FA, LSPC-3, PM, FAPLC, chitosan, FA CNPs, and FAPLC CNPs were analyzed to investigate their thermal properties using differential scanning calorimeter (Model: DSC-1821e, Mettler-Toledo AG, Analytical, Schwerzenbach, Switzerland). Briefly, the sample (~2 mg) was weighed and loaded into a previously calibrated and N₂ purged analyzing area. The loaded sample was subjected to heating at a rate of 10 °C/min in the heating range of 0 to 400 °C. Following heating, the generated DSC thermograms of each sample were read using instrument attached software (Universal Analysis 2000, V4.5A, Build 4.5.0.5). The adopted DSC procedure has been reported by our group earlier [45,46].

2.9.5. Powder x-ray diffractometry (PXRD)

A powder x-ray diffractometer (Model: D8 ADVANCE, Bruker AXS, Inc., Madison, WI, USA) was employed for the comparative analysis of crystal characteristics of FA, LSPC-3, PM, FAPLC, chitosan, FA CNPs, and FAPLC CNPs respectively. Briefly, samples (~50 mg) were loaded into a sample analyzing area and irradiated using the CuK β radiation source ($\lambda = 1.5406\text{\AA}$). The irradiated sample was scanned and detected using a dimensional silicon strip based technology detector (LYNXEYE™). The obtained diffraction spectra on the 2 θ angle between the ranges of 3 to 60° at a count rate of 5 s were interpreted using PXRD accompanied software. An earlier published procedure by our group has been followed for the PXRD analysis of samples [47].

2.9.6. Proton nuclear magnetic resonance spectroscopy (¹H NMR)

The carbon-hydrogen structures, as well as chemical shift values of the above-mentioned formulation components, were analyzed using a 400 MHz FT-NMR spectrophotometer (Model: Bruker Advance II, Bruker BioSpin, Billerica, USA). The detailed procedure for the preparation of the sample, their analysis, and evaluation has been reported previously [46].

2.9.7. Solubility studies

A method earlier described by Singh et al. was used for the solubility analysis of pure FA, PM, FAPLC, FA CNPs, and FAPLC CNPs respectively [48]. Briefly, the above-mentioned samples in an excess quantity were dispersed in 5 mL of distilled water or n-octanol in sealed glass vials. The content in the vials was then agitated using a shaker (Model: RSB-12, Remi House, Mumbai, India) for 24 h. After agitation, the developed dispersion was centrifuged at 1500 rpm for 25 min followed by filtration using a 0.45 μ membrane filter. The filtrate was suitably diluted and analyzed the solution at the maximum wavelength of ($\lambda_{\text{max}} = \sim 311$ nm) against the blank to determine the solubility of each sample in water or n-octanol. The sample absorbance was recorded using a UV-visible spectrophotometer (Model: V-630, JASCO International Co., Ltd., Tokyo, Japan).

2.10. Functional characterization of FAPLC and FAPLC CNPs

2.10.1. In vitro dissolution studies

A dissolution method similar to that previously described by Maiti et al. was employed for the comparative evaluation of release performance of FA suspension, FA CNPs, FAPLC, or FAPLC CNPs respectively [49]. Briefly, an approximate amount of the above-mentioned samples containing ~2 mg of FA was weighed and dispersed in 2 mL of phosphate buffer. This dispersion was sonicated and then loaded into the dialysis bag. The dialysis bag with a requirement of average diameter ~21.55 mm, average flat width ~32.34, loading capacity ~3.63 mL, and molecular size cut off ~12,000–14,000 kDa was used in the dissolution studies. Moreover, the dialysis bag was rinsed as per the manufacturer's guidelines. The loaded samples in the dialysis bag were suspended vertically in the dissolution flask containing freshly prepared phosphate buffer (200 mL, pH 6.8) with Tween® 20 (1% v/v) dissolution media. The media in the flask was continuously stirred at 50 RPM using a magnetic stirrer and maintained at 37 ± 1 °C for 12 h. At a predetermined time interval, the samples were removed from the flask and compensate with the same quantity of fresh dissolution media. The removed samples were diluted suitably and analyzed the solution absorbance at maximum wavelength of ($\lambda_{\text{max}} \sim 311$ nm) on a UV-visible 208

spectrophotometer (Model: V-630, JASCO International Co., Ltd., Tokyo, Japan) against the blank. The recorded absorbance of samples was further used for the estimation of the cumulative release of FA.

2.10.2. Ex vivo permeation studies

The comparative permeation pattern of pure FA from FA suspension, FAPLC, FA CNPs, or FAPLC CNPs across a biological membrane was analyzed using a previously described *everted rat intestine* method [50]. The detailed procedure related to the procurement of animals, isolation, and preparation of rat intestine to *everted rat intestine* has been reported previously and the same was followed in this study. Briefly, the prepared everted rat intestine membrane was mounted between the two supporting ends of the apparatus followed by filling the same apparatus with the freshly prepared Krebs solution. After this, the entire apparatus was inserted vertically into a 250 mL beaker containing formulations i.e. FA suspension (100 µg/mL), FAPLC (100 µg/mL), FA CNPs (100 µg/mL) or FAPLC CNPs (100 µg/mL) prepared in the Krebs solution. The contents in the beaker were stirred at 25 RPM using a magnetic stirrer, maintained at a temperature of 37 ± 0.5 °C, and aerated using a mixture of carbogen (95% O₂ and 5% CO₂) throughout the permeation period i.e. 12 h. The samples were withdrawn from the assembly at an interval of 10 min, diluted suitably, and analyzed for absorbance at a maximum wavelength (λ_{max} ~311 nm) using a UV-visible spectrophotometer (Model: V-630, JASCO International Co., Ltd., Tokyo, Japan) against the blank. The measured absorbance of the permeated samples was further used for the estimation of cumulative permeation of FA and it was estimated using the below described equation.

$$\text{Apparent permrability} = [V/A \times T] \times C_1/C_0 \quad (5)$$

In the above equation, *V* shows the serosal content (mL), *A* represents the surface area of the intestinal sac (cm²), *T* represents the time of incubation (sec), *C*₀ displays the initial concentration on the mucosal side, whereas, *C*₁ displays the concentration of on the serosal side after time *T*.

2.11. In vivo antioxidant activity

2.11.1. Animals

The FA CNPs or FAPLC CNPs were evaluated for in vivo antioxidant potential using chloroform (CCl₄) - intoxicated rat model as per the procedure reported earlier [3,49]. The animal protocol (RSCOP/IAEC/2018-19 dated August 19, 2018) for the study was approved and sanctioned by Rajarshi Shahu College of Pharmacy, Buldhana. The animals (male and female albino rats, Wister strain) weighing about 150–200 g were used and preserved in clean colony cages under the controlled temperature (25 ± 5 °C) and relative humidity ($50 \pm 5\%$ RH) for 12 h light/dark cycle. Following this, the animals were nourished with food (pellet chow, Brooke Bond, Lipton, India) and water ad libitum. The entire study was carried out according to the ethical guidelines provided by the committee for the purpose of control and supervision of experiments on animals (CPCSEA).

2.11.2. Dosing

The animals used for in vivo antioxidant activity were divided into four groups containing six animals each. Group I animals administered only Tween® 20 (1% v/v, p.o.) for seven days and considered as a negative control, whereas, group II animals administered Tween® 20 (1% v/v, p.o.) for seven days and on the same day, the group II also received a single dose of an equal mixture of CCl₄ and olive oil (1:1, 5 mL/kg, i.p.) and considered as a positive control. Group III and IV animals administered FA CNPs or optimized FAPLC CNPs (20 mg/kg, p.o.) in Tween® 20 (1% v/v, p.o.) for seven days. Subsequently, on the seventh day, group III and IV animals also administered a single dose of an equal mixture of CCl₄ and olive oil (1:1, 5 mL/kg, p.o.) and left them for further observations. After 24 h of formulation and CCl₄ dosing, all the animals

were anesthetized using light ether. From these animals, the blood samples from the retro-orbital plexus were collected in a tube containing heparin and then centrifuged using microcentrifuge (Model: RM-12C, Angle Rotor Head, Remi House, Goregaon (E), Mumbai, India). The obtained supernatant plasma samples were further used for the assessment of liver function tests. Following this, the animals were euthanized using the cervical decapitation technique followed by isolation of the livers. The livers were washed in ice-cold saline solution and homogenized in 0.1 M PBS (pH 7.4) solution. The clear supernatant was analyzed to observe the overall influence of the formulations on the performance of in vivo antioxidant marker enzymes.

2.11.3. Estimation of the liver and in vivo antioxidant marker enzymes

The performance of liver function marker enzymes of serum glutamic oxaloacetic transaminase (SGOT) and serum glutamic pyruvic transaminase (SGPT) [51], alkaline phosphate (ALP) [52], and total bilirubin [53] in rat plasma samples were determined against FA CNPs or FAPLC CNPs using UV-visible spectrophotometer. Likewise, the antioxidant effect of FA CNPs or FAPLC CNPs on in vivo antioxidant marker enzymes of glutathione peroxidase (GSH) [54], superoxide dismutase (SOD) [55], lipid peroxidase (LPO) [56] and catalase (CAT) [57] present in rat liver homogenate was also determined using UV-visible spectrophotometer.

2.12. Oral bioavailability studies

2.12.1. Bioanalytical method development

An accurate amount of FA (~10 mg) was weighed and dissolved in a sufficient quantity of acetonitrile to get a final concentration of 200 mg/L. This stock solution was stored at 4 °C until further analysis. From this solution, different dilutions of FA were prepared and spiked with 50 µL blank plasma results in the formation of final concentrations in the range of 0.5–800 ng/mL. These diluted solutions were then used for the preparation of quality control (QC) samples at three different concentrations such as low (1.0 ng/mL), medium (20 ng/mL), and higher (640 ng/mL) respectively. The calibrated as well as QC samples were stored at –20 °C till further characterization.

An LC-MS/MS method previously described by Zhang et al. was used for the quantitative estimation of FA in rat plasma samples [58]. Briefly, the LC-MS/MS instruments (Model: ACQUITY UPLC™, Water Corporation, Milford, MA, USA) equipped with Tandem Quadrupole (TQ) detector, cooling auto-sampler, and column oven for controlling the temperature of analytical column was employed in this study. The separation was carried out on the stationary phase consisted of the BEH C18 column (50 mm × 2.1 mm, particle size ~1.7 µm, ACQUITY UPLC™, Water Corporation, Milford, MA, USA) and its column temperature was maintained at 35 °C. The chromatographic separation was carried out using a mobile phase composed of acetonitrile and water and the flow rate was set at 0.2 mL/min throughout the study. The run time for the sample was set at 3.5 min. The docetaxel (DXT) was used as an internal standard (IN) due to its structural similarity with the FA. The samples were analyzed in both, negative and positive ionization mode using multiple reaction monitoring (MRM). The ion source temperature was 120 °C. The target ions were scanned at an *m/z* ratio of 193 for FA and 808 for DXT respectively. Other supporting parameters such as data acquisition and peak integration were analyzed using instrument associated software (Masslynx 4.1 software).

2.12.2. Extraction of FA and sample preparation

A previously described liquid-liquid extraction (LLE) method was followed for the extraction of the FA from rat plasma samples [58]. The diethyl ether and formic acid (0.5%) was used as an extracting solvent and showed higher extraction recovery and reproducibility. Briefly, the extraction of FA was started with the oral administration of formulations to the animals. The animals were divided into groups I and II containing six animals each. Group I animals received FA CNPs (20 mg/kg, p.o.)

p.o.) and group II animals received FAPLC CNPs (~20 mg/kg, p.o.) respectively. Following administration, all the animals were anesthetized at a pre-determined schedule and withdrawn their blood samples from retro-orbital plexus into the clean Eppendorf® Safe-Lock microcentrifuge tube (1.5 mL) containing heparin. The heparinized blood samples were centrifuged at 800 ×g for 10 min followed by a collection of plasma and preserved at -20 °C till further analysis.

2.12.3. Validation of the extraction and quantification method

International Conference on Harmonization (ICH) guidelines was followed for the validation of the developed LC-MS/MS method. The intra-day accuracy and precision analysis were performed using prepared QC samples on the same day ($n = 6$). The inter-day accuracy and precision were analyzed using the same QC samples on three subsequent days ($n = 6$). The extraction of FA from tissue samples and standard solution were performed and compared concerning extraction recoveries. Moreover, stability studies i.e. long term (24 h) and short term (14 days) were carried out on the prepared QC samples.

2.12.4. Study of pharmacokinetic parameters

Following administration of testing formulations, extraction, and LC-MS/MS analysis, the pharmacokinetic parameters of FA such as half-life ($t_{1/2}$), area under the plasma concentration-time curve (AUC) from zero to time of final measured sample (AUC_{0-t}) and from zero to infinity ($AUC_{0-\infty}$), mean residence time (MRT) were estimated using program-based WinNonlin® software (Version 4.1, Certara USA Inc., Princeton, NJ, USA). Moreover, C_{max} and T_{max} were estimated using the plasma concentration-time curve.

2.13. Statistical analysis

The extent of complexation rate, solubility, and in vitro release data was reported as a mean ± standard deviation. Additionally, the animal studies report i.e. liver function tests, in vivo antioxidant study, and pharmacokinetic analysis data were reported as mean ± standard error of the mean. The statistical differences between the animals treated groups were determined using a one-way analysis of variance (ANOVA). The obtained p -value of less than 0.05 was considered a significant one.

3. Results and discussion

3.1. Preparation of FAPLC and FAPLC CNPs

In this study, the FAPLC was prepared using ethanol based-solvent evaporation method. Before this experiment, the preliminary solubility analysis was conducted for FA and LSPC-3. It was found that both of these compounds are lipophilic and show higher solubility in organic solvents [59]. This physico-chemical property of FA was utilized in this study and prepared the phospholipids complex using the solvent evaporation method. The phospholipids complex are lipid compatible molecular aggregates of drug and/or bioactive and phospholipids and their formation is depending upon the complete dissolution of a drug as well as phospholipids in common solvents results in the formation of stable phospholipids complex. Previous literature reported the use of dichloromethane [16], 1, 4 - dioxane [46], and tetrahydrofuran (THF) [60] as a choice of solvents for the preparation of stable

phospholipids complex. These solvents were tested and found that FA as well as LSPC-3, both showed low solubility and precipitation problems during the formation of a complex. This solubility problem was overcome by using ethanol as a choice of solvents because of its semi-polar nature, class III solvent with a low toxicity profile, and provides higher solubility for FA and LSPC-3. Therefore, based on solubility, the ethanol was chosen as an optimal solvent for the preparation of stable FAPLC.

Following this, the FAPLC was loaded into chitosan nanoparticles and developed FAPLC CNPs using the ionic gelation method. Chitosan nanoparticles are formed due to the establishment of strong electrostatic interaction between dissolved polycationic chitosan and negatively charged STPP in a common solvent. Chitosan is an amphiphilic and polycationic polymer that demonstrates good solubility at below pH 6.8 due to the protonation of the amino group.

3.2. Screening of phospholipids

The screening of phospholipids was carried out based on high phosphatidylcholine (PC) and drug content and their results are presented in Table 3. As seen in the table, the LSPC-3 demonstrated higher PC content compared to Phospholipon® 80H, Phospholipon® 90H and Phospholipon® 90G indicate its suitability for the formation of a stable complex with FA. Moreover, the high PC content of LSPC-3 also showed higher drug content ($92.61 \pm 0.20\%$ w/w) compared to other phospholipids also suggested that higher PC could favorably interact with FA resulting in the formation of stable FAPLC with better physical form.

3.3. The rationale for selection of independent, dependent variables and their ranges

According to the ionic gelation method, the FAPLC CNPs was prepared at a laboratory scale, and based on that, the chitosan, STPP concentration, and stirring speed were selected as independent variables, and the influence of these variables was found significantly on the encapsulation efficiency, hence; it was selected as dependent variables. After this, the range of selected independent variables was finalized and it was done by using previously published reports which suggest that the optimal values ~100 mg, 4% w/v, and 700 RPM of the chitosan, STPP concentration, and stirring speed to produce the stable chitosan nanoparticles [61]. In this study, these values were used, synthesized the FAPLC CNPs, and tested for encapsulation efficiency. The tested results showed that synthesized FAPLC CNPs lowered the value of encapsulation efficiency. To improve this, the reported optimal values of independent variables were shifted from 100 to 200 mg, 4 to 0.2% w/v, and 700 to 800 RPM respectively. The shifted values produced the various experimental trials of FAPLC CNPs and demonstrated appreciable enhancement of encapsulation efficiency. Based on the positive results and to get more information about formulation in less number of trials, the range of variables at three levels was explored using BBD because it provides strong coefficient estimates near the center of the design space and more efficiency. Moreover, BBD offers an economic choice to central composite design (CCD) for the fitting of quadratic models that require three levels for each variable. Hence, based on the advantages of BBD, the chitosan, STPP concentration, and stirring speed were studied at three levels i.e. (-1) low, (0) middle, and (+) higher respectively.

Table 3
Screening of phospholipids for the preparation of FAPLC.

Lipids	Drug to lipids ratio	Drug content (% w/w)	Physical form
Phospholipon® 80H	1:1.5	73.24 ± 1.22	Sticky and aggregates
Phospholipon® 90H	1:1.5	79.40 ± 0.41	Sticky and aggregates
Phospholipon® 90G	1:1.5	86.52 ± 0.34	Sticky and aggregates
Lipoid® SPC-3 (LSPC-3)	1:1.5	91.61 ± 0.20	Powder

Table 4
Fit statistics of dependent variables of BBD.

Fit statistics	Std. Dev.	Mean	C.V. %	R ²	Adjusted R ²	Predicted R ²	Adeq precision
Encapsulation efficiency	6.23	76.42	8.16	0.9203	0.8179	0.6290	8.7111

C.V.: coefficient of variation.

3.4. Box Behnken Design

The generated experimental trials of FAPLC CNPs using selected independent variables produced a considerable impact on the encapsulation efficiency, and its results are presented in Table 2. The encapsulation efficiency value shows a significant variation and based on this, the lowest and highest efficiency values were 50.52% and 96.04% respectively. The obtained seventeen trials represent the interaction between selected independent variables. Subsequent interaction and analysis of data, the BBD exhibited the results in the form of fit statistics (Table 4), ANOVA data, diagnostic results, and model graphs respectively. Supporting this, the BBD also displayed the polynomial equation which shows the influence of independent variables on the encapsulation efficiency as well as the presence of coefficient of magnitude and positive and negative sign also demonstrated a strong impact on the encapsulations efficiency. These parameters of the polynomial equation were used further to optimize the FAPLC CNPs.

$$Y = +85.42 + 4.08X_1 + 16.65X_2 + 2.77X_3 - 5.65X_1^2 - 5.89X_2^2 - 7.59X_3^2 + 1.22X_1X_2 + 4.51X_1X_3 + 3.88X_2X_3 \quad (6)$$

Based on the ANOVA data (Table 5), the coefficient of magnitude i.e. b_2 and b_{33} represents the significant terms, while, the b_0 , b_1 , b_3 , b_{11} , b_{22} , b_{12} , b_{13} , and b_{23} represents non-significant terms ($p > 0.05$). Moreover, the obtained quadratic model for the FAPLC CNPs using BBD indicates the best fit model. Other parameters such as F-value and p -value found to be ~ 8.98 (>1) and 0.05 respectively suggest that the quadratic model is the best fit model. The lack of fit value ~ 0.53 (>0.05) indicates the suitability of the quadratic model for these trial formulations. Supporting this, the adequate precision value ~ 8.7111 (>4) and the difference between the adjusted & predicted correlation coefficient value $\sim <0.2$ indicates the quadratic model is significant and thus, can be used to navigate the design space. Additionally, the generated PRESS value ~ 1540.02 also suggests the suitability of the quadratic model. The polynomial equation containing a positive and negative sign of the coefficient of magnitude, and their impact on the encapsulation efficiency also demonstrated that as the concentration of X_1 , X_2 and X_3 increases to the middle level, the efficiency increases

Table 5
Summary of ANOVA used for data analysis of dependent variables of BBD.

Source	Sum of squares	df	Mean square	F-value	P-value	Remark
ANOVA: encapsulation efficiency (quadratic model)						
Model	3142.61	9	349.18	8.98	0.0043	Significant
A – chitosan	132.85	1	132.85	3.42	0.1070	
B – STPP concentration	2218.11	1	2218.11	57.07	0.0001	
C – stirring speed	61.33	1	61.33	1.58	0.2494	
AB	5.98	1	5.98	0.1538	0.7066	
AC	81.45	1	81.45	2.10	0.1910	
BC	60.22	1	60.22	1.55	0.2533	
A ²	134.24	1	134.24	3.45	0.1055	
B ²	146.02	1	146.02	3.76	0.0938	
C ²	242.50	1	242.50	6.24	0.0411	
Residual	272.03	7	38.87			
Cor total	3414.70	16				

df: degree of freedom.

and thereafter, found to reduce as the concentration of variables reduces concurrently indicates that middle-level concentration of above variables could be an optimal value for the optimization of FAPLC CNPs. The influence of X_1 , X_2 , and X_3 on encapsulation efficiency is presented in (Fig. 1A and B) respectively.

The optimization of FAPLC CNPs was conducted using numerical and graphical optimization methods. In the numerical method, the applied constraints for independent variables of X_1 , X_2 , and X_3 were in the range of ~ 200 to 600 mg, ~ 0.2 to 0.4 , and 800 to 1200 RPM respectively, whereas, the constraints for encapsulation efficiency was in the range of ~ 90.01 to 96.04% . The applied data showed one solution with the recommended values of independent variables as well as encapsulation efficiency. The possible solution also displayed the desirability value close to 1 indicates the suitability of constraints values and its results are shown in (Fig. 1C). In the graphical method, the same constraints were used and it exhibited the results in the form design space overlay plot (Fig. 1D). The design space also recommended the possible values of independent variables and encapsulation efficiency. Therefore, based on the desirability value and design space overlay plot, the optimal values for chitosan (X_1), STPP concentration (X_2), and stirring speed (X_3) were found to be 338.42 mg, 0.35% w/v, and 1003.52 RPM respectively. Moreover, the post-analysis results also showed close agreement between the experimental and predicted values, which further confirms the validity of the selected design (Table 6).

3.5. Validation of the model

An additional FAPLC CNPs trial using design – generated optimal values of X_1 , X_2 , and X_3 was prepared, evaluated, and compared against model-predicted yield values. The comparative results demonstrated a good agreement between the actual and model-predicted yield values. Moreover, bias (%) between these two yields was calculated using the below-described equation and it was found to be less than 3% indicates the suitability of the BBD for the optimization of FAPLC CNPs. Additionally, the obtained higher correlation coefficient value ~ 0.9203 also confirms the right selection of design and model.

$$\text{Bias (\%)} = \frac{\text{Predicted value} - \text{observed value}}{\text{Predicted value}} \times 100 \quad (7)$$

3.6. Physico-chemical characterization of FAPLC and FAPLC CNPs

3.6.1. Particle size and zeta potential

Particle size and zeta potential are typically considered as physical stability indicators of a multiparticulate system. The results of particle size and zeta potential of FAPLC and FAPLC CNPs are discussed below. As is reported previously, the LSPC-3 based diosmin phospholipids complex at the molar ratio of (1:1, 1:2, and 1:4) produced higher particle size (around ~ 536 nm, ~ 316 nm, and ~ 350 nm) accompanied with higher solubility, intestinal absorption, and bioavailability [62]. As a result, the obtained average particle size of FAPLC was around $\sim 4208 \pm 1.40$ nm with a low polydispersity index (PDI) value $\sim 0.39 \pm 0.04$ indicates narrow particle size distribution of FA within the matrix of LSPC-3 and suitability for oral administration. The higher particle size of FAPLC was likely attributed to excessive aggregation of LSPC-3 around FA molecules which could lead to remarkable complexation between them and produced higher particle size and low PDI value [62]. Zeta potential (ζ) is another physical property of a multi particulate system that provides information about the surface charges around the particle in suspension. The FAPLC displayed the zeta potential around $\sim -12.15 \pm 0.20$ mV. The zeta potential value higher than ± 10 mV is indicative of considerable stability of the system [63,64] and the zeta potential value of complex was higher than -10 mV designates better physical stability of the complex. This achieved value could be explained by the fact that a small contribution of LSPC-3 towards complexation m

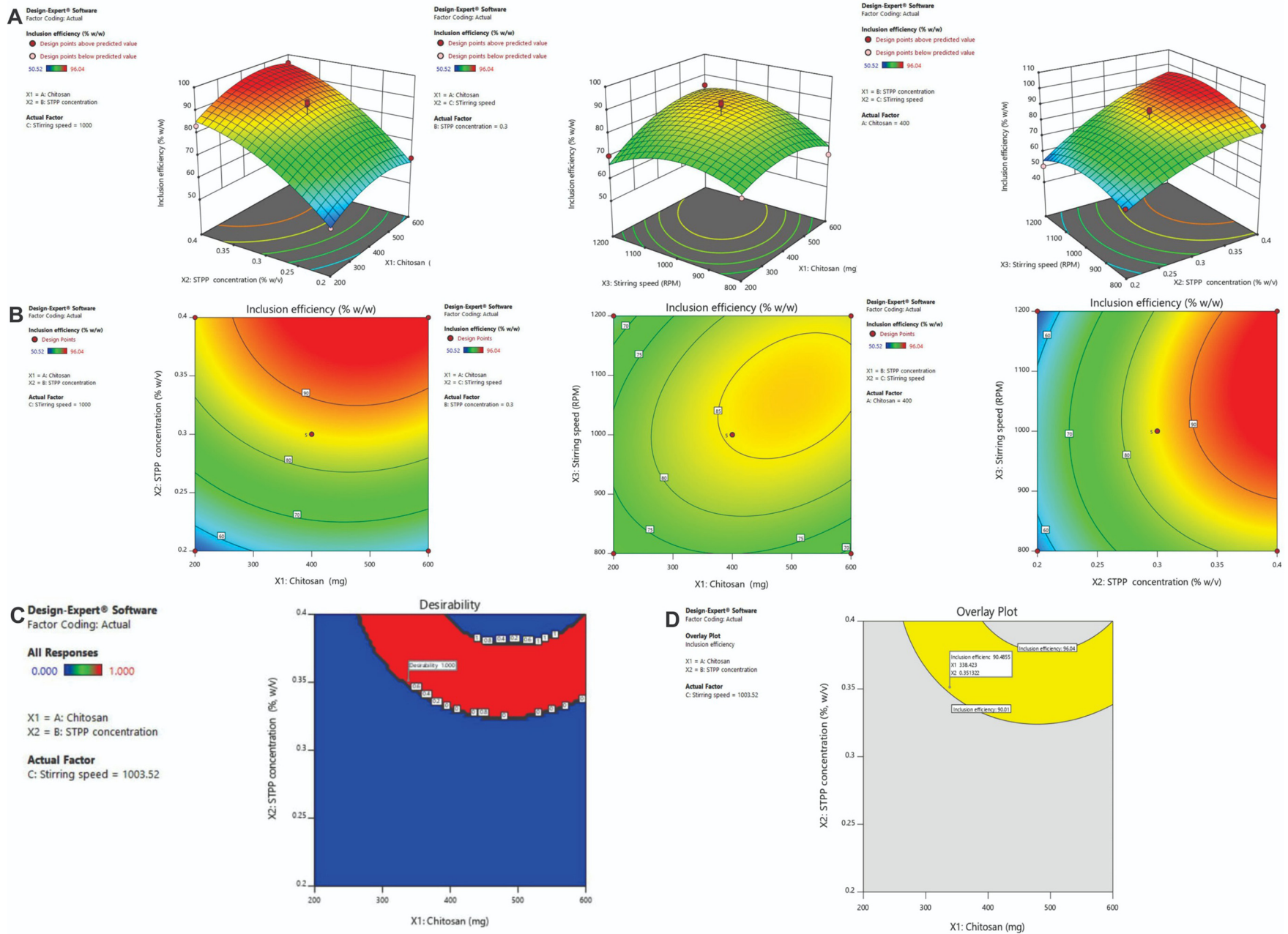


Fig. 1. (A) Counter plot, (B) 3D response surface plot, (C) desirability plot, and (D) design space plot describes the influence of independent variables of chitosan (X_1 , mg), STPP concentration (X_2 , % w/v) and stirring speed (X_3 , RPM) on inclusion efficiency (% w/w).

Table 6
Post analysis confirmation at two tailed 95% confidence level.

Response	Predicted mean	Predicted median	Std. Dev.	n	SE Pred	95% PI low	95% PI high
Encapsulation efficiency	90.4865	90.4865	6.2345	3	6.8221	74.3547	106.61

cause to produce a negative charge on the complex in neutral pH aqueous media, which could result in lower zeta potential values. It was also suggested that the employed phospholipids (its composition and type) could significantly change the zeta potential values [46].

In addition to this, the particle size and zeta potential of FAPLC CNPs were also evaluated by PCCS and their results are discussed below. The average particle size and PDI value of FAPLC CNPs were found to be $\sim 123.27 \pm 1.11$ nm and 0.31 ± 0.08 . The results are in consistent with earlier published reports which suggest that prepared chitosan nanoparticles using the ionic gelation method with particle size $\sim 142 \pm 1.51$ nm and PDI value $\sim 0.20 \pm 0.09$ are appropriate for oral delivery due to low toxicity, low immunogenicity, and high biocompatibility of chitosan [65]. The distribution of surface charge of FAPLC CNPs was found to be $\sim 32 \pm 1.28$ mV. The obtained value was more than reported $+30$ mV indicates excellent stability of the chitosan nanoparticles. It was likely attributed to a positive amino group of chitosan [66]. Thus, the lower particle size, low PDI, and positive surface charge value suggest excellent stability of FAPLC CNPs.

3.6.2. Scanning electron microscopy

Fig. 2(A–D) shows the surface morphology of FA, LSPC-3, FAPLC, and FAPLC CNPs respectively. The FA (Fig. 2A) exhibited as large crystalline needle-shaped particles with well-defined edges and faces. The

appearances of these particles are following earlier reports [13]. SEM image of LSPC-3 particles (Fig. 2B) appeared as clusters of small and large particles with ill-defined surface characteristics. The FAPLC SEM morphology (Fig. 2C) exhibited as large and non-uniform particles with a smooth surface. This particle morphology also shows the complete absence of FA particles suggesting that FA dispersed entirely in the LSPC-3 could result in a disappearance of FA particles. Compared to all, the SEM analysis of FAPLC CNPs (Fig. 2D) particles appeared as small spherical shaped particles with heterogeneous and porous surface suggesting that favorable interaction between complex – chitosan in STPP solution could result in the formation of spherical shape chitosan nanoparticles. Additionally, it was also suggested that a combination of solvent evaporation and ionic gelation technology could be demonstrated as strong interaction between the complex, chitosan, and STPP which was resulted in the formation of spherical nanoparticles.

3.6.3. Fourier transform infrared spectroscopy

FT-IR analysis provides vital information about functional group identification and their interaction with other components used in the formulations. Fig. 3(A–F) shows the FT-IR spectrum of FA, LSPC-3, PM, FAPLC, chitosan, and FAPLC CNPs respectively. The FT-IR spectrum of FA (Fig. 3A) shows the presence of absorption peak at ~ 3436.6 (OH stretching), 1617.7 (C = C stretching), 1464.8 (C = C aromatic stretching vibration), 1688.5 (C = O stretching), 1664.1 (C = C stretching) and found consistent with earlier published reports [13]. The FT-IR spectrum of LSPC-3 displays in (Fig. 3B). As shown in the figure, the LSPC-3 showing the characteristics absorption peak at ~ 3328.5 (OH stretching), 2914.8 and 2829.0 (C-H stretching of long fatty acid chain), 1736.9 (C = O stretching of fatty acid ester), 1237.5 (P = O stretching), 1062.3 (P-O-C stretching) and 902.0 [N+ - (CH₂)₃] [67]. PM FT-IR spectrum shows in (Fig. 3C). The PM exhibits an absorption

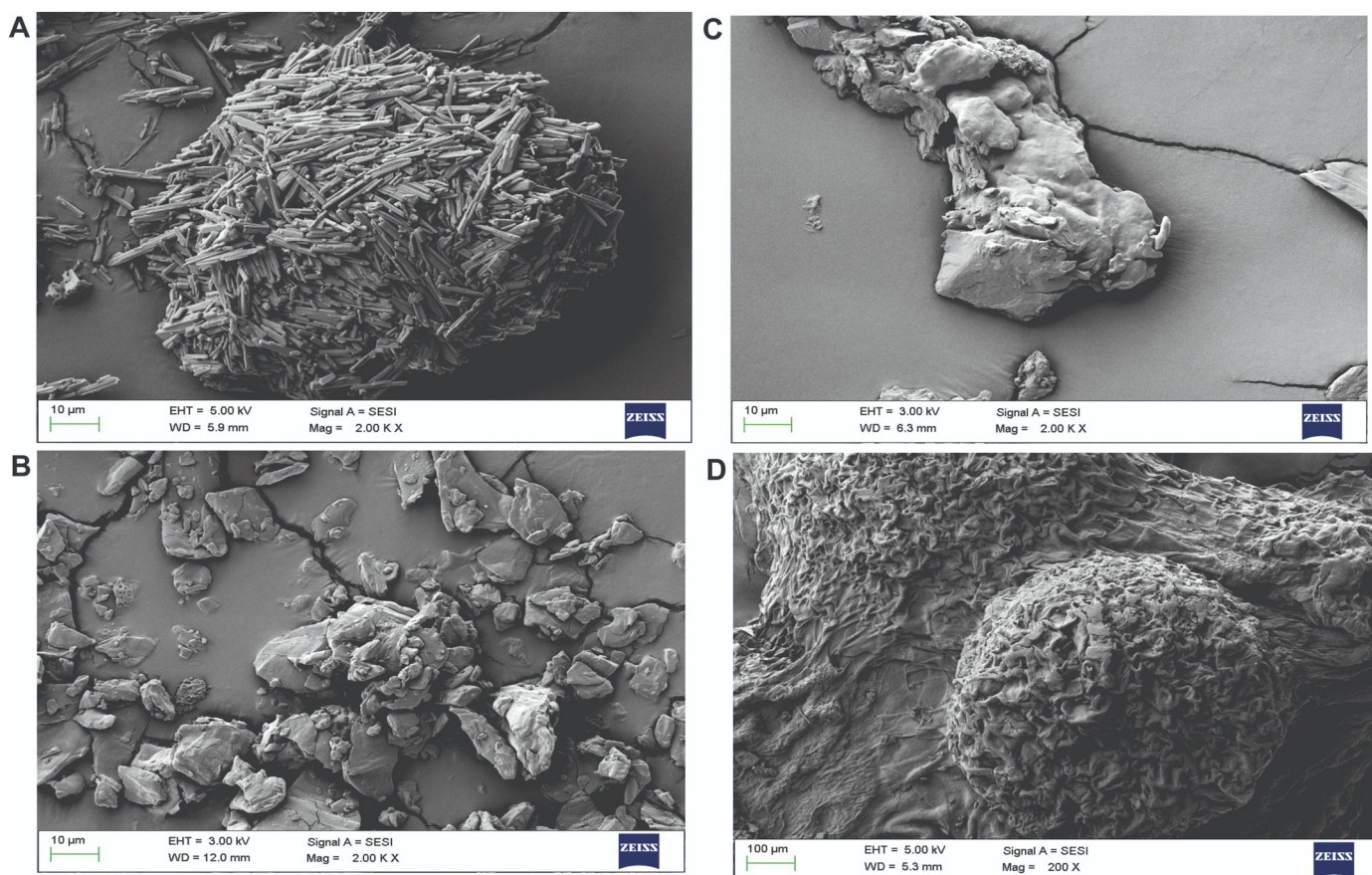


Fig. 2. SEM image of (A) FA, (B) LSPC-3, (C) FAPLC, and (D) FAPLC CNPs formulations.

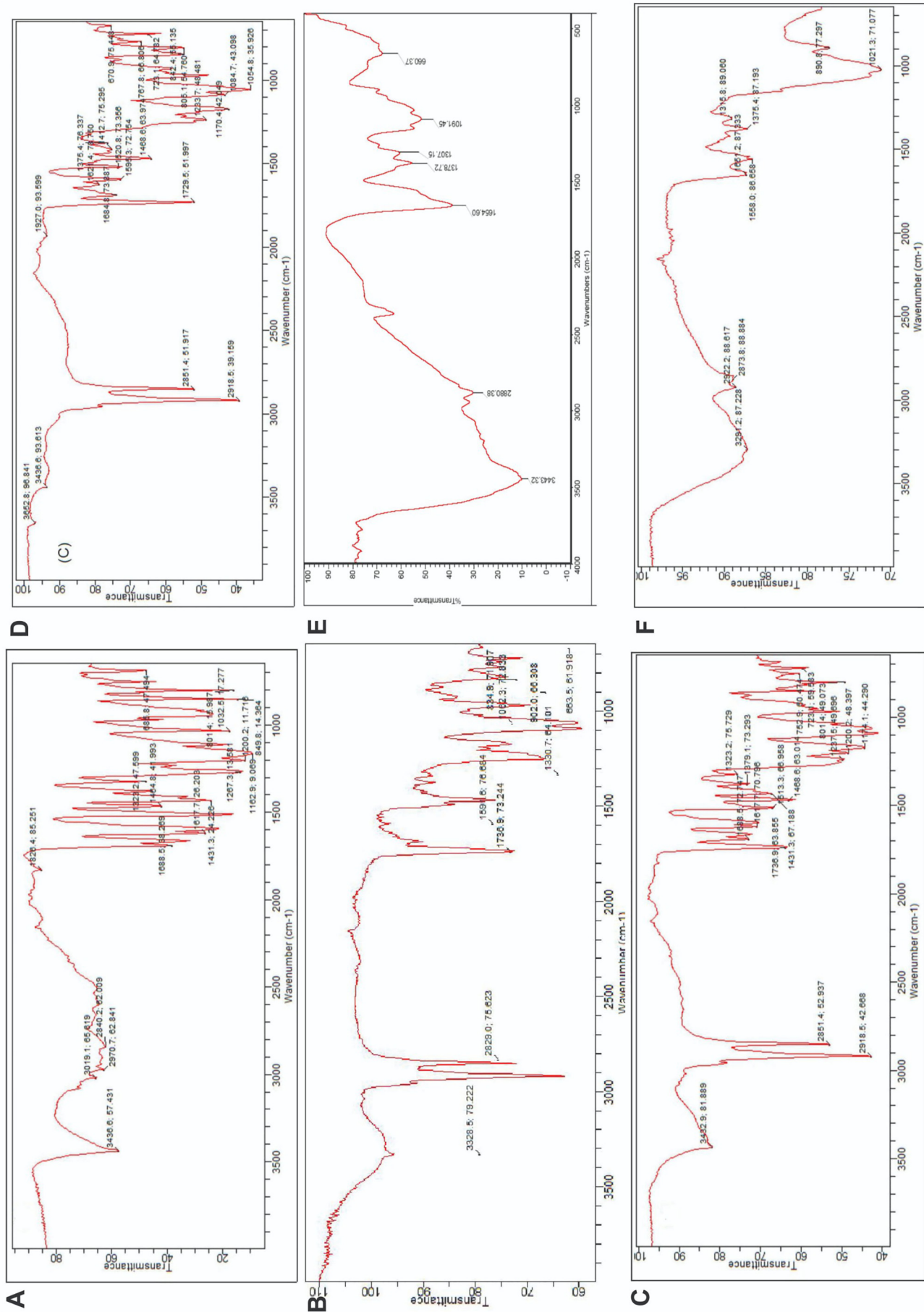


Fig. 3. FT-IR spectra of (A) FA, (B) LSPC-3, (C) PM, (D) FAPLC, (E) chitosan, and (F) FAPLC CNPs formulations.

peak at ~ 3432.9 , 1617.7 , 1468.6 , 1688.5 , 2918.5 , 2851.4 , 1736.9 , and 1237.5 indicates additive peaks of FA and LSPC-3. The slight shifting of the above peaks compared to the original one suggesting some interaction between FA and LSPC-3. The FT-IR spectrum of FAPLC (Fig. 3D) revealed a complete shifting of absorption peaks. The obtained narrow peak at ~ 3652.8 was shifted from ~ 3362.1 indicates hydroxyl group interaction between the FA and LSPC-3. It must be also emphasized that the peak position of FA was the same as appeared in the original spectra; however, it became narrow suggesting that the hydroxyl group of FA could be actively involved in the interaction mechanism with LSPC-3. The absence of a peak at ~ 1617.7 and 1464.8 correspondings to $C = C$ stretching and $C = C$ aromatic ring stretching suggesting shielding of these groups as a result of phospholipids complexation. Moreover, the disappearance of peaks at ~ 1688.5 and 1664.1 was likely due to affinity between the negative ($C = O$) group of FA and the positive (N^+) group of LSPC-3 [13]. The peak at ~ 1736.9 and 1062.3 related to LSPC-3 was also shifted to 1729.5 and 1084.7 in complex indicating an involvement of these groups in the complexation process. The shifted peak at ~ 1233.7 from ~ 1237.5 in the complex suggesting that ($P = O$) group of LSPC-3 could be interacted with (OH) group of FA via hydrogen bonding, van der Waals and ion-dipole forces resulted in the successful formation of FAPLC.

FT-IR spectrum of chitosan (Fig. 3E) presented a significant absorption peak at ~ 3443.32 (O-H stretching), 2880.38 (C-H stretching), 1654.60 (N-H stretching), 1378.32 (amide group), and 1091.45 ($C=O$ stretching in C-O-C) respectively. The FAPLC CNPs FT-IR spectra (Fig. 3F) revealed the absorption of a peak at ~ 3291.2 , 2922.2 , 2873.8 , 1651.2 , 1375.4 , and 1021.3 respectively. The shifting of these peaks

from their original spectrum could be explained on the basis that positive (N-H) functional groups of chitosan interacted with negative charge ($C = O$) group of FA, LSPC-3, and FAPLC via weak intermolecular and ionic interaction forces, which could result in the formation of chitosan nanoparticles loaded with FAPLC. Therefore, it can be concluded that weak and ionic interaction forces between FAPLC and chitosan resulted in the formation of FAPLC CNPs.

3.6.4. Differential scanning calorimetry

DSC is a valuable tool particularly used to determine the physical and/or solid-state interaction (i.e. appearance, disappearance, shifting, and/or alter the peak position and area) between the components of formulations. The developed interaction can provide information regarding the formation of a complex. The DSC curve of FA, LSPC-3, PM, FAPLC, chitosan, FA CNPs, and FAPLC CNPs are shown in Fig. 4(A–G) respectively. The FA DSC curve (Fig. 4A) displayed a high-intensity endothermic peak around ~ 174.25 °C with an enthalpy value ~ 105.16 J/g indicates polymorphic form I of FA [13,59]. (Fig. 4B) shows the DSC curve of LSPC-3. The LSPC-3 showed three small intensity diffused endothermic peaks around ~ 78.18 °C, 110.88 °C, and 183.08 °C respectively. The associated enthalpies of these peaks were ~ 11.82 J/g, 5.58 J/g, and 1.05 J/g respectively. The earliest two peaks could be attributed to the melting of a polar component of LSPC-3, while, the later one was probably attributed to a change of physical state of the hydrophobic part of LSPC-3 from gel-like state to crystalline state due to increasing the temperature of the LSPC-3 [33,67]. The DSC curve of PM (Fig. 4C) exhibited a series of endothermic peaks appeared at ~ 75.25 °C, 143.58 °C, 185.95 °C, 235.58 °C and 254.45 °C respectively indicating additive characteristics

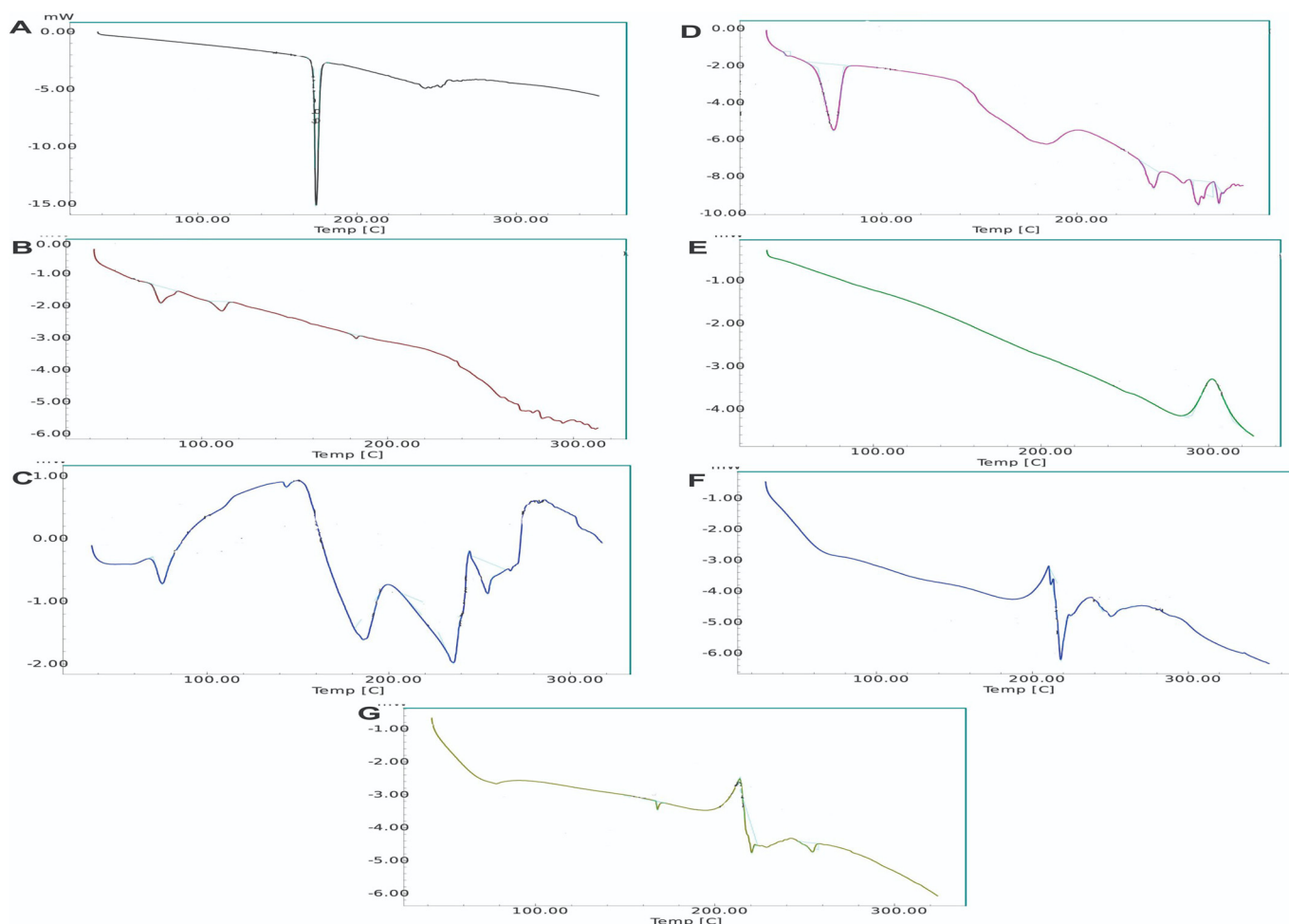


Fig. 4. DSC curves of (A) FA, (B) LSPC-3 (C) PM (D) FAPLC (E) chitosan (F) FA CNPs and (G) FAPLC CNPs formulations.

of FA and LSPC-3, suggesting that the increasing temperature melted the PM, form partial in situ mixture, which could lower the peak intensity as compared to original peaks. The high-intensity peak of FA was shifted to a low-intensity peak around ~143.58 °C indicates favorable interaction between the FA and LSPC-3. Moreover, the presence of a low amount

of FA ratio in the PM could also be the reason for showing such a low-intensity peak. Also, two more peaks i.e. 235.58 °C and 254.45 °C appeared in this curve indicates it is related to LSPC-3. The appearance of these peaks also shows the promising interaction between the components. The DSC curve of FAPLC (Fig. 4D) exhibited a novel, broad and

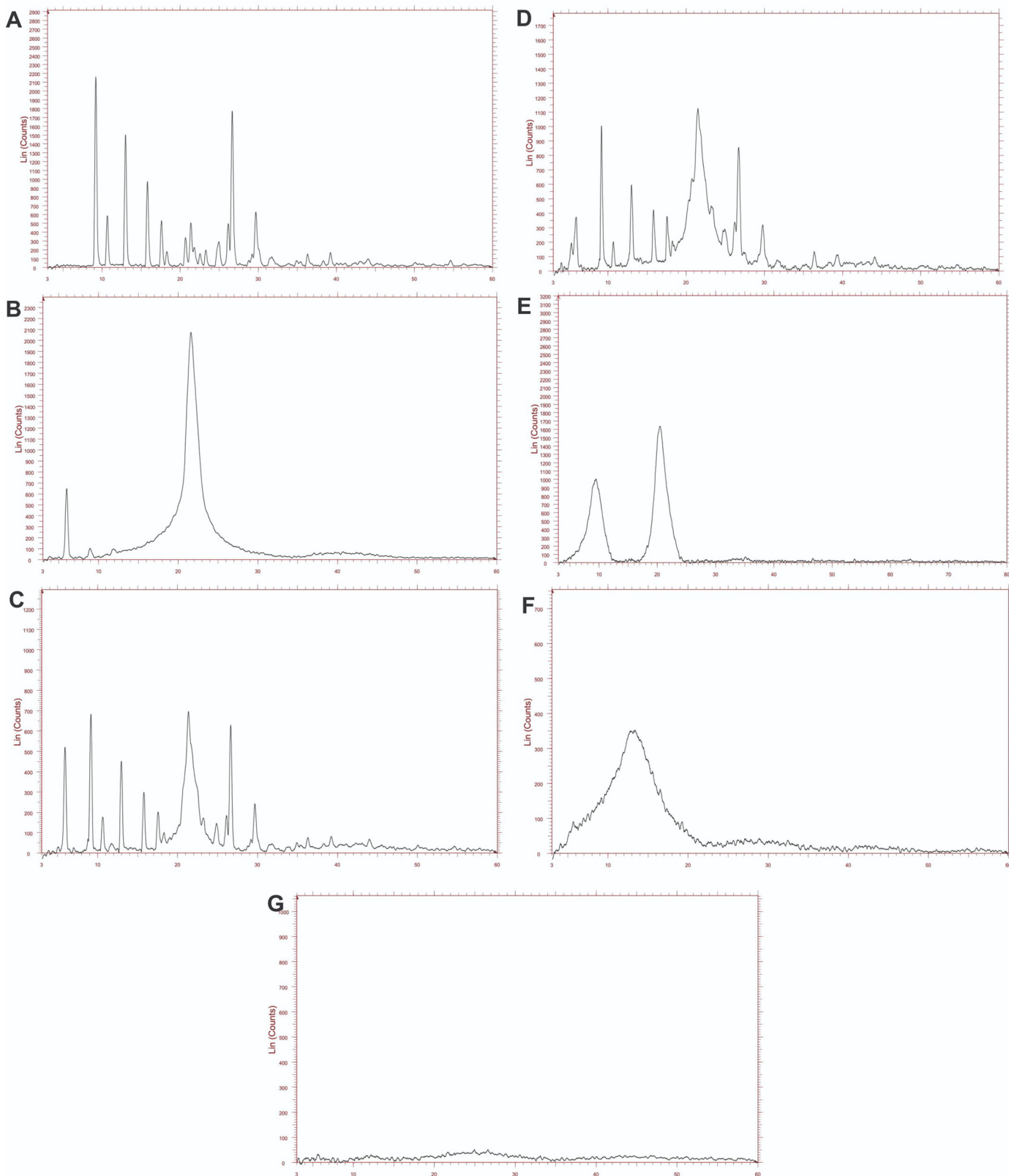


Fig. 5. PXRD spectra of (A) FA, (B) LSPC-3 (C) PM (D) FAPLC (E) chitosan (F) FA CNPs and (G) FAPLC CNPs formulations.

small intensity endothermic peak around -75.32°C with enthalpy value -66.90 J/g and disappeared the original peaks of the components indicates a complete amorphization of FA by LSPC-3 [68]. Moreover, it is also suggested that polar segment form I of FA and LSPC-3 could interact via weak intermolecular forces, improved the dispersibility of FA within LSPC-3, and thus, resulted in the formation of a stable complex. The hydrophobic interaction ascribed to the aromatic ring of FA may also contribute to the formation of a complex with LSPC-3 [69]. Additionally, the obtained different enthalpy values of FA and complex also suggest the formation of FAPLC.

The chitosan DSC curve (Fig. 4E) displayed a single and sharp endothermic peak around -302.04°C with an enthalpy value of -55.61 J/g indicates the melting of chitosan. This peak can be obtained due to the decomposition of the amino group and it is consistent with previous reports [70]. The DSC curve of FA CNPs (Fig. 4F) displayed three small intensity endothermic peaks around -183.12°C , 218.23°C , and -250.49°C respectively corresponding to FA and chitosan. The broad endothermic peak of FA at -183.12°C indicates the presence of microcrystalline form I of FA in the chitosan nanoparticles; however, its intensity was reduced compared to the original peak due to interaction with chitosan. The remaining two peaks of chitosan may be attributed to a possible change in the physical state of chitosan due to the presence of STPP as cross-linking agents. Finally, the DSC curve of FAPLC CNPs (Fig. 4G) showed the low-intensity endothermic peak at -168.02°C with enthalpy value -0.82 J/g indicating conversion of crystalline form I to amorphous FA, suggesting that when complex introduced into chitosan solution, the protonated chitosan may show strong affinity towards negative charge FAPLC, further established interaction, reduces its crystallinity and converts into chitosan nanoparticles with different peak characteristics. Thus, based on comparative DSC curves, it can be concluded that weak intermolecular forces between FA and LSPC-3 and strong interaction between complex and chitosan results in the formation of FAPLC and FAPLC CNPs.

3.6.5. Powder x-ray diffractometry

PXRD is a unique characterization technique used widely for the evaluation of the crystalline state of a drug within the matrix of the carrier. PXRD spectra of FA, LSPC-3, PM, FAPLC, chitosan, FA CNPs, and FAPLC CNPs are shown in Fig. 5(A–G) respectively. The PXRD spectra of FA (Fig. 5A) showed a series of sharp and mixed intensity peaks at -9.19 (Lin counts on y-axis ~ 2150), 8.32 (~ 600), 12.96 (~ 1500), 15.77 (~ 950), 17.57 (~ 500), 21.34 (~ 500), 26.65 (~ 1750) and 29.68 (~ 600) respectively indicate polymorphic form I of FA. This spectrum is found to be consistent with earlier reports of FA [71]. The diffractograms of LSPC-3 (Fig. 5B) displayed two unrelated peaks. The first low-intensity peak appeared at -6.01 (~ 650), while, the second high and broad intensity peak appeared at -21.1 (~ 2050) indicates the amorphous nature of LSPC-3 [36]. The diffractograms of PM (Fig. 5C) exhibited a peak of FA and LSPC-3. The peak intensity of FA in between 5 and 10° was reduced slightly compared to the original one due to the low amount of FA in PM as well achievable interaction with LSPC-3, at the same time, the peak intensity of LSPC-3 in between the region of 20 to 25° was also reduced compared to original one due to formation of a partial mixture with FA which may cause to from PM powder with lower peak characteristics. The PXRD spectrum of FAPLC (Fig. 5D) exhibits very few peaks of FA accompanied with low intensity. The complex in between the region of 3 to 17° shows only four low-intensity peaks compared to higher intensity peak in pure FA and PM, whereas, in the region between 17 and 30° , the more broad LSPC-3 peak was appeared in complex compared to higher, sharp, and narrow range of peak in PM indicating that maximum amorphization of FA due to a higher amount of LSPC-3 available for complexation, suggesting that when FA comes in contact with higher amount of LSPC-3, the molecular interaction occurred between them due to hydrogen bonding and ion-dipole forces may cause to increase the dispersibility of FA into a polar head group of LSPC-3 matrix, reduced its crystallinity and form an amorphous complex powder. This

result concludes that molecular interaction and thereafter, the reduction of crystallinity of FA also confirms the formation of a complex.

The PXRD of chitosan (Fig. 5E) displays two dissimilar, broad, and high-intensity peaks at $\sim 10^{\circ}$ (~ 1000 count) and 20° (~ 1600 counts). These peaks could be caused by crystallinity and developed H-bonding with the amino groups of chitosan [72]. PXRD spectrum of FA CNPs (Fig. 5F) shows the presence of broad chitosan dominated peaks with complete disappearance of FA peak indicates partial amorphization of FA. This observable fact could be caused by the dispersion of FA in the chitosan matrix could result in the amorphization of FA [73,74]. (Fig. 5G) shows the PXRD of FAPLC CNPs. As seen in the figure, these spectra show the absolute disappearance of crystalline peaks of FA indicates total amorphization of FA by chitosan as well as LSPC-3. This result could be explained on the basis that the amino group of chitosan interacted with the polar part of FA and FAPLC through hydrogen bonding and van der Waals forces, this favorable interaction could facilitate the dispersibility of complex into chitosan polymer resulted in the formation of amorphous chitosan nanoparticles. Thus, it can be suggested that interaction between chitosan and complex could be responsible for the preparation of chitosan nanoparticles.

3.6.6. Proton nuclear magnetic resonance

^1H NMR is used to determine the physico-chemical interaction between the formulation components and provide information about the formation of complex and nanoparticles. ^1H NMR spectra of FA, LSPC-3, PM, and FAPLC are shown in Fig. 6(A, B, C, and D). ^1H NMR of FA (Fig. 6A) shows chemical shift values at $-\delta 3.813\text{ s}$ (3H for three CH_3 groups, 10 Hz), $\delta 6.340\text{ d}$ (1H, 10 Hz), $\delta 6.803\text{ d}$ (1H, C-H of aromatic ring), $\delta 7.076\text{ s}$ (1H, C-H), $\delta 7.508\text{ d}$ (1H, C-H) and $\delta 9.570\text{ s}$ (1H, OH) [71]. LSPC-3 ^1H NMR spectra (Fig. 6B) exhibited chemical shift values around $-\delta 4.40$ (1H, s), $\delta 4.09 - \delta 3.94$ (br s, 1H), $\delta 3.93 - \delta 3.75$ (s, 2H), $\delta 3.32$ (s, 1H), $\delta 2.95$ (H-8, $J = 8$ Hz), $\delta 2.27$ (s, 1H), $\delta 0.89$ (s, 3H) [75]. The ^1H NMR spectra of PM (Fig. 6C) showed the chemical shift values corresponding to FA and LSPC-3 signifies interaction between them. (Fig. 6D) displays the chemical shift values of FAPLC around $-\delta 6.339\text{ d} - \delta 6.379\text{ d}$ (1H, 10 Hz), $\delta 6.801\text{ d}$ (1H, for C-H), $\delta 7.507\text{ s}$ (1H, C-H) and $\delta 9.572\text{ s}$ (1H, OH) indicates remarkable shifting of chemical shift values towards downfield region i.e. ($\delta > 7$). This shifting could be attributed to molecular interaction of specific phenolic hydroxyl group of FA with the polar part of LSPC-3 by the means of hydrogen bonding and van der Waals forces resulting in the formation of a complex. Findings are following earlier reports [36]. This comparative result concludes that molecular-level interaction could be the main reason for the establishment of the complex.

3.6.7. Solubility studies

The solubility analysis of FA, FA CNPs, PM, FAPLC, and FAPLC CNPs in water or *n*-octanol are shown in Table 7. The pure FA showed low aqueous solubility around $\sim 0.71\text{ mg/mL}$, whereas, in *n*-octanol, the solubility of FA was increased $\sim 1.85\text{ mg/mL}$ respectively. The obtained results are not surprising because FA is a BCS II drug, which shows low solubility and high permeability [15]. The PM exhibits higher aqueous solubility and *n*-octanol solubility around ~ 1.83 and $\sim 3.20\text{ mg/mL}$ compared to pure FA. This could be attributed to close contact of negative charge ($\text{C}=\text{O}$) of FA and positive charge (N^+) of LSPC-3 followed by their interaction resulted in modest enhancement of aqueous solubility of FA. The FAPLC revealed higher aqueous solubility around $\sim 5.80\text{ mg/mL}$ (8-fold higher) compared to pure FA and PM. The solubility result was found significant ($p < 0.05$). This improved aqueous solubility could be explained by the following mechanism i.e. close association, interaction, dispersion, and followed by amorphization of FA due to the amphiphilic nature of LSPC-3. Moreover, it may be also suggested that the enwrapping of two long fatty acid chains of LSPC-3 onto the polar head of LSPC-3 enclose with FA resulted in maximum dispersion and amorphization of FA, which could result in enhancing aqueous solubility. The enhanced *n*-octanol solubility was likely due to the lipophilic

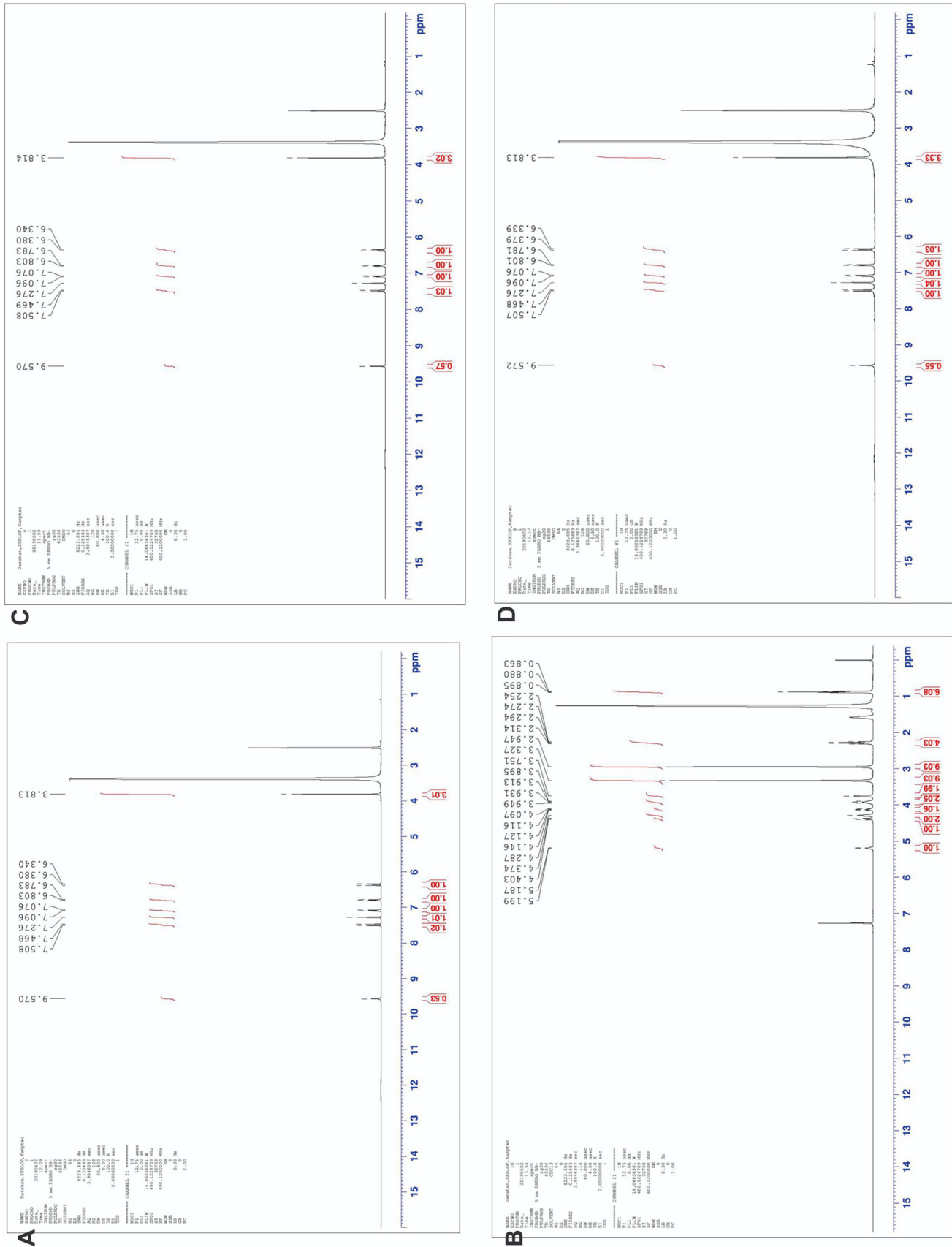


Fig. 6. ¹H-NMR spectra of (A) FA, (B) LSPC-3 (C) PM, and (D) FAPIC formulations.

Table 7
Solubility results of FA, FA CNPs, PM, FAPLC and FAPLC CNPs in water and n-octanol.

Samples	Aqueous solubility (mg/mL) ^a	n-Octanol solubility (mg/mL) ^a
Pure FA	0.71 ± 0.09	1.85 ± 0.46
FA CNPs	1.83 ± 0.52	3.20 ± 0.37
PM	5.80 ± 1.14	8.43 ± 1.24
FAPLC	2.14 ± 0.47	4.67 ± 1.11
FAPLC CNPs	8.22 ± 1.20	12.10 ± 2.34

^a Values are presented as mean ± SD (n = 3).

character of LSPC-3. On the other hand, the FA CNPs and FAPLC CNPs demonstrate higher aqueous and n-octanol solubility compared to pure FA and PM. The FA CNPs displayed higher aqueous solubility approximately ~2.14 mg/mL (3-fold) compared to pure FA indicating that conversion of crystalline to an amorphous form of FA, suggesting that interaction between the protonated amino group of chitosan and negative oxygen group of FA may reduce its crystallinity and thereby, increase its dispersibility into chitosan, which resulted in improved aqueous solubility [76]. The FAPLC CNPs significantly improved the aqueous solubility around ~8.22 mg/mL (12-fold) compared to FA CNPs and this could be attributed to the attraction between two opposite charge of phospholipids complex and chitosan polymer, which form complex-polymer interaction, and this may increase the dispersion, amorphization and finally aqueous solubility of FA.

3.6.8. In vitro dissolution studies

The in vitro dissolution studies show the performance of the formulation at a molecular level. Fig. 7 shows the dissolution performance of FA from its suspension, FA CNPs, FAPLC, and FAPLC CNPs respectively. The FA suspension displays only ~29% FA dissolution at the end of 12 h attributes to low aqueous solubility of FA and it is correlated with the solubility studies. In the case of FAPLC, the dissolution rate of FA, by the end of first 5 h was found to be ~53% and, thereafter also, it released continuously and reached to a maximum around ~83% indicates sustained release behavior of FAPLC, suggesting that the enhanced aqueous solubility, as well as wettability of FAPLC, could increase the release of FA via formation of the homogenous aqueous dispersion and thus, enhanced its dissolution rate [36,77]. Moreover, it may be also suggested that partial amorphization and structural modification owing to interaction with a positive nitrogen group of LSPC-3 may increase the wetting of FA in aqueous media resulted in enhancement of the dissolution rate of FA. Compared to this, the FA CNPs and FAPLC CNPs demonstrated a higher dissolution rate of FA. The FA CNPs by the end of 5 h exhibited a rapid release of approximately ~30% and then, showed only ~54% of drug released. The rapid release of FA CNPs could be attributed to the absorption of FA on the loose surface of chitosan nanoparticles as suggested by Zhang et al. [33]. Additionally, it was also indicated that the protonation of the amino group of chitosan in presence of phosphate buffer (pH 6.8) could facilitate the swelling and then the dissolution of chitosan. The FAPLC CNPs revealed that the dissolution rate of the FA in the initial 5 h was approximately ~71% indicates burst release, while, at the end of 12 h, the same formulation showed maximum release around ~97% indicates sustained release. The burst effect could be caused by dissociation of FA from chitosan nanoparticles due to its weak attachment with chitosan [15], while, the sustained release effect could be attributed to secure interaction between negative charge of FAPLC and positive charge of chitosan, which inhibit its dissociation from the chitosan nanoparticles and sustain the release of FA. Similarly, the interaction between the negative oxygen charge of FA and the positive nitrogen charge of LSPC-3 could also retard the release rate of FA. Moreover, it was also suggested that the utilization of an amino group of chitosan by FAPLC during nanoparticle formation may restrict its protonation in an aqueous environment results in sustained release of FA. The obtained results suggest that FAPLC CNPs could provide a sustained release of FA over to that of FA CNPs and PM.

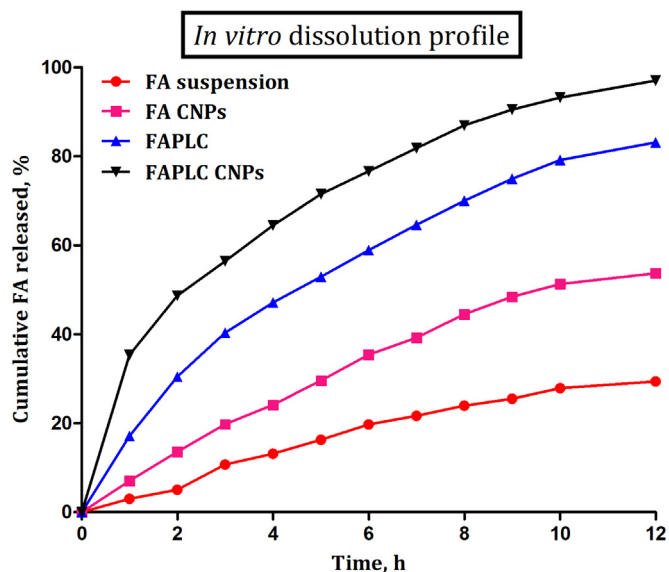


Fig. 7. In vitro dissolution pattern of FA from FA suspension, FAPLC, FA CNPs and FAPLC CNPs respectively. Values are presented as mean ± SD (n = 3).

The obtained release data of all the formulations were fitted into different kinetic models such as zero order, first order, Higuchi model, and Korsmeyer-Peppas model and evaluated for kinetic performance. Following analysis, the FAPLC, FA CNPs and FAPLC CNPs displayed Higuchi as best-fit kinetic model based on obtained higher correlation coefficient value ($R^2 = 0.9823, 0.9887$ and 0.9764) as compared to lower zero-order ($R^2 = 0.9655, 0.9478$ and 0.9245) and first-order values ($R^2 = 0.9033, 0.9154$ and 0.9018). The obtained Higuchi model suggests diffusion is the mechanism responsible for the release of FA from these formulations. Moreover, the obtained release exponent value of all the formulations was found to be <0.5 , which also suggests that, the diffusion mechanism mainly responsible for the release of FA from FAPLC, FA CNPs, and FAPLC CNPs respectively. The release mechanism of FA from FAPLC could be described by two steps: 1) the FA dissociated from FAPLC and, 2) the dissociated FA was diffused through the matrix of LSPC-3. In the case of FA CNPs, the release mechanism is governed by diffusion of FA from the matrix of chitosan, whereas, the release mechanism of FA from FAPLC CNPs could be described by two steps; 1) the FAPLC released from chitosan nanoparticles and then, 2) the FA released from the matrix of FAPLC. The findings were following earlier published reports [78].

3.6.9. Ex vivo permeation studies

Permeability is a complex kinetic process used to determine the speed at which a dissolved drug passes from the intestinal wall to the systemic blood circulation [80]. The ex vivo permeation pattern of FA from its suspension, FAPLC, FA CNPs, and FAPLC CNPs are shown in Fig. 8. The permeation efficiency of FA from its suspension at the end of 12 h was found close to ~26% indicates low permeability of FA. The intestinal permeability coefficient ($Papp$) value of FA suspension was found to be around $\sim(0.92 \pm 0.02 \times 10^{-6} \text{ cm/s})$ also indicates low permeability of FA. Compared to suspension, the FA CNPs by the end of 12 h, showed only ~52% FA permeation. The same formulation also displayed a permeability coefficient value around $\sim(2.12 \pm 0.33 \times 10^{-6} \text{ cm/s})$ suggests a modest increase of FA permeability from FA CNPs due to interaction between chitosan and phospholipids. The complex as well as optimized FAPLC CNPs both revealed a high permeation rate of FA. The permeation rate and permeability coefficient value of FA from FAPLC was found to be ~81%, and $\sim(3.22 \pm 0.46 \times 10^{-6} \text{ cm/s})$ respectively attributes to increase miscibility of FAPLC with the biological cell membrane, whereas, from FAPLC CNPs the permeation rate and permeability coefficient value was ~95% and $\sim(3.46 \pm 0.11 \times 10^{-6} \text{ cm/s})$.

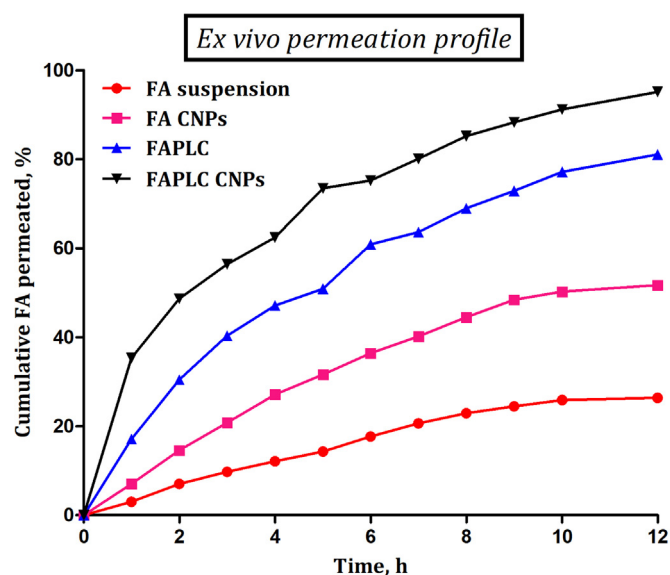


Fig. 8. Ex vivo permeation profile of FA from FA suspension, FAPLC, FA CNPs and FAPLC CNPs across everted rat intestine membrane. Values are presented as mean \pm SD ($n = 3$).

s) respectively compared to suspension, FA CNPs, and FAPLC. This more significant enhancement was likely due to the tight junction opening ability of chitosan nanoparticles. Moreover, the high degree of deacetylation of chitosan could also contribute to enhancing the permeability of FA.

The permeability of drug substance is often dependent upon three main factors such as physiological, physico-chemical parameters of drug substance, and bio-physicochemical parameters of the gastrointestinal tract [79]. In this study, the successful permeation of FA was achieved using a combination of phospholipids complex and chitosan nanoparticles. Phospholipids complex are reported to enhance the aqueous solubility and permeability of phytoconstituents through increasing its amphiphilicity. Similarly, the LSPC-3 based FAPLC also improved the aqueous solubility and permeability of FA via amorphization and increasing the amphiphilic nature of FA as evidenced by solubility studies. Also, the reported similarity of the lipid content of mammalian cell membrane (containing amphiphilic phospholipids bilayer) with the structure of LSPC-3 offers excellent biocompatibility towards each other [80], and based on this we believe that the amphiphilic FAPLC could increase its miscibility with the biological cell membrane (the fluid mosaic model proposed by S. J. Singer and G. L. Nicolson in 1972) resulted in an efficient permeation of FA. Compared to this, there is a significant permeation pattern difference was observed between FA CNPs and FAPLC CNPs respectively. In the case of FA CNPs, the established interaction between the positive charge of chitosan nanoparticles and negative charge of phospholipids bilayer of the cell membrane can increase their adhesion as well as retention to the

intestinal epithelium, however, the unfavorable interaction between the same negative charge of FA and LSPC-3 presents in the cell membrane may restrict its entry across the cell membrane and this could be the main reason for its low permeability through chitosan nanoparticles. Moreover, the partial amorphization of FA by chitosan nanoparticles as clearly seen in DSC, PXRD, and solubility studies could help to increase its permeability across the cell membrane. In the case of FAPLC CNPs, the developed interaction between the positive charge of chitosan and negative charge of phospholipids membrane could allow maximum adhesion and retention of chitosan nanoparticles with the epithelium for a maximum time leading to release and contact of FAPLC with the amphiphilic phospholipids bilayer of a biological membrane, increase its miscibility with the cell membrane resulted in noteworthy enhancement of FA permeability via paracellular and transcellular pathways. In supporting to phospholipids complex, the chitosan nanoparticles with their ability to temporarily opening of the tight junction of intestinal epithelium cells can also help to increase the FA permeability [35]. The obtained results conclude that FA CNPs and FAPLC improve the permeability of FA, however, a combination of phospholipids complex and chitosan polymer and their further favorable interaction drastically increases the permeation rate as well as bio-availability of FA.

3.7. In vivo antioxidant activity

3.7.1. Liver function tests

CCl_4 , a well-known hepatotoxin rapidly metabolized by CYP450 enzymes into various reactive oxygen species (ROS) i.e. free radicals. These radicals rapidly react with the macromolecules of the body, induce lipid peroxidation and finally damage the cellular membrane of hepatic cells, which in turn, leading to the release of liver function enzymes like SGOT, SGPT, total bilirubin, and SALP [81]. The release and presence of these enzymes in the blood signify the hepatic damage. The results of the antioxidant potential of FA CNPs and FAPLC CNPs on liver function liver marker enzymes are shown in Table 8. As seen, the SGOT, SGPT, total bilirubin, and ALP enzymes were elevated significantly in CCl_4 induced albino rat model. In response to this, the FA CNPs (20 mg/kg, p.o.) significantly reduced ($p < 0.05$) the elevated level of enzyme compared to the CCl_4 treated group indicates the hepatoprotective potential of FA. Additionally, the FAPLC CNPs more significantly ($p < 0.01$) restored the liver marker enzymes at the same dose level indicating that FAPLC CNPs provide more hepatoprotection over to that of FA CNPs, suggesting that, opposite charge attraction between FAPLC and CNPs provide effective interaction, adhesion, and retention on the hepatic cell membrane, which could improve the permeation and thereby, antioxidant efficacy of FA.

3.7.2. In vivo antioxidant marker enzymes estimation

Fig. 9 displays the effect of FA CNPs and FAPLC CNPs on the in vivo antioxidant marker enzymes such as GSH, SOD, CAT, and LPO respectively. The hepatotoxin CCl_4 remarkably reduced the GSH level

Table 8

Effect of FA CNPs and FAPLC CNPs on liver function test parameters (SGOT, SGPT, SALP and total bilirubin) in CCl_4 -induced rats.

Treatment groups with samples	SGPT (IU/L) ^a	SGOT (IU/L) ^a	SALP (IU/L) ^a	Total bilirubin (mg/dL)
Group I: Normal [Tween® 20 (1%, v/v, p.o.)]	50.11 \pm 2.20**	72.33 \pm 2.38**	120.50 \pm 3.58**	0.70 \pm 0.04**
Group II: Control [CCl_4 and olive oil (1:1, 5 mL/kg, i.p.)]	107.45 \pm 3.42	140.74 \pm 4.57	190.29 \pm 3.19	1.56 \pm 0.60
Group III: FA CNPs (~20 mg/kg, p.o.) [CCl_4 and olive oil (1:1, 5 mL/kg, i.p. for 7 days)]	76.02 \pm 2.27*	102.45 \pm 3.65*	148.39 \pm 2.36*	0.91 \pm 0.07*
Group IV: FAPLC CNPs (~20 mg/kg of MGN, p.o.) [CCl_4 and olive oil (1:1, 5 mL/kg, i.p. for 7 days)]	61.41 \pm 2.47**	86.71 \pm 3.15**	131.46 \pm 3.14**	0.82 \pm 0.08**

All values are Mean \pm SEM ($n = 6$).

^a IU/L – International Units/Liter of plasma.

* $p < 0.05$.

** $p < 0.01$ (significant with respect to control group).

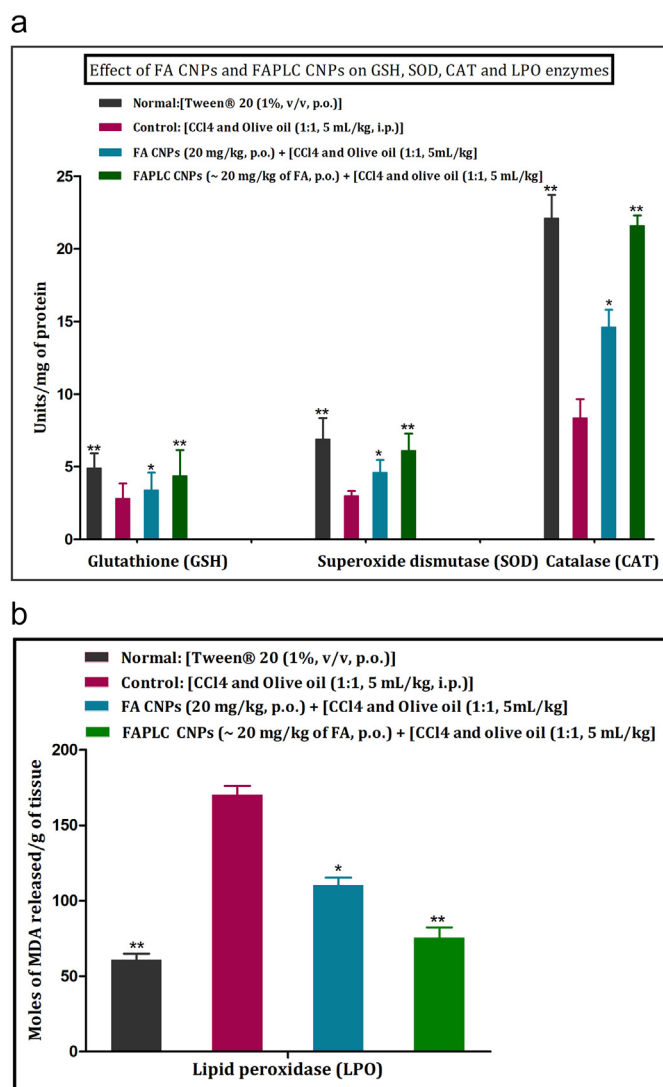


Fig. 9. Effect of FA CNPs and FAPLC CNPs on rat liver antioxidant marker enzymes, such as glutathione reductase (GSH) (nmol/mg of protein), superoxide dismutase (SOD) (units/mg protein), catalase (CAT) (units/mg protein), and lipid peroxidase (LPO) (nmol of MDA released/g tissue). Values are Mean \pm SEM ($n = 6$). * $p < 0.05$, ** $p < 0.01$ (significant with respect to control groups).

compared to the normal group. The same group on the administration of FA CNPs (20 mg/kg, p.o.) significantly ($p < 0.05$) enhanced the GSH level, whereas, the FAPLC CNPs more significantly ($p < 0.01$) elevated the GSH level at the same dose level. The level of SOD was found to be reduced in the CCl₄-intoxicated albino rat model. The FA CNPs at a dose of (20 mg/kg, p.o.) significantly ($p < 0.05$) improved the SOD level. In contrast to this, the FAPLC CNPs at the same dose more considerably ($p < 0.01$) enhanced the SOD level. CAT, another important enzyme was also found to have lowered following CCl₄ administration as compared to normal groups. The animal group treated with FA CNPs significantly ($p < 0.05$) elevated the CAT enzyme in the blood, while, the FAPLC CNPs at a dose of (20 mg/kg, p.o.) appreciably improved its level as well as activity against the developed free radicals. The significance of this result was ($p < 0.01$). The CCl₄-treated groups increased the lipid peroxidation level over to that of normal groups. However, on the administration of FA CNPs, the LPO level was reduced drastically. The FAPLC CNPs more notably reduced the LPO level. The level of significance of this study was found to be ($p < 0.01$). Therefore, the comparative result concludes that FAPLC CNPs demonstrate appreciable antioxidant activity compared to FA CNPs indicates that the FAPLC CNPs improved the antioxidant potential of FA and this could be

ascribed to the following reasons. First, the reported antioxidant and free radical scavenger potential of FA inhibit the formation of ROS by donating their electron to the free radicals, neutralize them and form less toxic phenolic and quinone methide radical. The chelate forming ability of FA with the protonated copper and iron metals prevent its conversion into toxic hydroxyl radicals, inhibit the lipid peroxidation, thereby, increase its antioxidant status (14). Second, the developed combined nanocarriers system could modify the FA resulted in the improvement of its solubility, dissolution, and permeation rate. This modified property of FA could be able to react with free radical and forms resonance-stabilized phenoxyl radical, which is mainly responsible for its antioxidant activity. The offering of extended conjugation by FAPLC CNPs to the resonance stabilized phenoxyl radical may also account for the strong antioxidant activity of FA. Third, the adhesion and retention property of FAPLC CNPs on epithelium could increase the miscibility of FAPLC with amphiphilic phospholipids bilayer of cell membrane increasing FA permeability via paracellular and transcellular routes and subsequently enhance the antioxidant status of FA. Fourth, the tight junction (intestinal epithelium cells) opening ability of chitosan nanoparticles may also increase the permeation rate of FAPLC into the damaged hepatic cells and restored the antioxidant status of liver cells. Sixth, the enhanced C_{max} , T_{max} , and biological half-life ($t_{1/2}$) of FA due to FAPLC CNPs could increase its circulation time in blood as well as utilization by hepatic cells could improve antioxidant activity of FA. Seventh, the sustained release property of FAPLC CNPs could also offer more exposure of FA to damaged hepatic cells, which in turn, provide strong antioxidant potential against free radicals. Finally, the amorphization, as well as improved amphiphilicity of FAPLC CNPs may increase the permeation of FA across the membrane and thus, provide an antioxidant effect. Obtained results concluded that FAPLC CNPs can offer better hepatoprotection against CCl₄ over to that of FA CNPs.

3.8. LC-MS/MS method validation

The obtained validation parameters of the LC-MS/MS method are discussed below. The selected concentration in the range of (0.5–800 ng/mL) displayed a good linearity with correlation coefficient value was ($r^2 = 0.9965$). The lower limit of detection and lower limit of quantification value following validation were found to be around ~0.15 and 0.5 ng/mL respectively. The intra-day and inter-day precision values were observed to be lower than <5%, whereas, the extraction recovery of FA from plasma samples was observed between the ranges of ~74.2–79.1% respectively. The stability studies showed no degradability

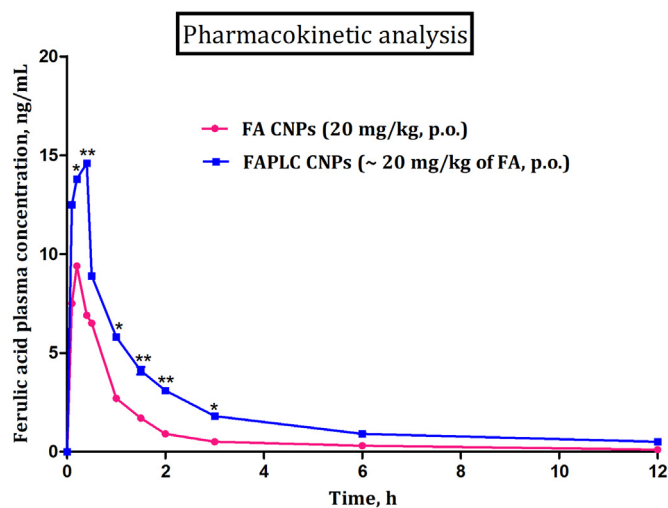


Fig. 10. Mean plasma concentration-time profile curve following oral administration of FA CNPs (20 mg/kg, p.o.), and FAPLC CNPs (~20mg/kg of FA, p.o.). Values are mean \pm SEM ($n = 6$). * $p < 0.05$ and ** $p < 0.01$ (significant with respect to FA CNPs treated group).

Table 9

Results of pharmacokinetic parameters obtained in group of animals following oral administration of FA CNPs (~20 mg/kg, p.o.) and FAPLC CNPs (~20 mg/kg, p.o.).

Pharmacokinetic parameters	Formulations	
	FA CNPs	FAPLC CNPs
C_{max} (ng/mL)	9.40 ± 1.33	14.61 ± 2.34
T_{max} (h)	0.20 ± 0.05	0.40 ± 0.09
$t_{1/2el}$ (h)	0.30 ± 0.02	0.50 ± 0.04
AUC_{0-t} (ng h/mL)	10.60 ± 2.59	24.80 ± 2.31
$AUC_{0-\infty}$ (ng h/mL)	18.60 ± 1.52	29.40 ± 2.65
MRT (0–12 h) (h)	1.30 ± 0.60	2.08 ± 1.24
MRT (0–∞) (h)	3.19 ± 1.02	2.70 ± 1.36

All the values are mean ± SEM (n = 6).

of FA under the influence of the selected temperature indicates its excellent stability.

3.9. Pharmacokinetic parameters

The plasma concentration vs. time profile curve of FA CNPs and FAPLC CNPs at a dose of (20 mg/kg, p.o.) are shown in Fig. 10. The FA CNPs showed a C_{max} value around ~ (9.40 ng/mL), whereas, the FAPLC CNPs displayed the higher C_{max} value ~ (14.6 ng/mL), and thereafter, the plasma concentration of FA was reduced significantly in both the formulations. The FAPLC CNPs demonstrated a higher t_{max} value around ~ (0.40 min), while, FA CNPs exhibited a lower t_{max} value around ~ (0.20 min). Moreover, the half-life ($t_{1/2}$) value of FAPLC CNPs was around ~ (0.50 h) as compared to the lower value ~ (0.30 h) in FA CNPs. These results could be caused by the sustained release property of FA present in FAPLC CNPs. In addition to this, other pharmacokinetic parameters were also estimated using WinNonlin® software (Version 4.1, Certara USA Inc., Princeton, NJ, USA) and are shown in Table 9. As seen in the table, the FAPLC CNPs showed higher AUC_{0-t} and $AUC_{0-\infty}$ values around ~ (24.80 and 29.40 ng h/mL) over to that lower value ~ (10.60 and 18.60 ng h/mL) of FA CNPs indicates the enhancement of oral bioavailability of FA. The mean residence time was increased significantly around ~ (2.08 h) in FAPLC CNPs, while, in the case of FA CNPs, the mean residence time was lowered ~ (1.30 h) indicates the availability of FA in the body for a maximum time. Obtained results suggested that developed interaction between negative charge of FAPLC and positive charge of CNPs may provide overall modification of FA and this modification could result in improvement of absorption and oral bioavailability of FA.

4. Conclusion

The current work demonstrated a successful preparation of FAPLC CNPs using a combination of phospholipids complex and chitosan nanoparticles via solvent evaporation and ionic gelation methodology. BBD study demonstrated a successful optimization of FAPLC CNPs using the design space and desirability plot. Characterization results indicated the formation of FAPLC and FAPLC CNPs through the contribution of hydrogen bonding and van der Waals forces between FA, LSPC-3, phospholipids complex, and chitosan nanoparticles. Moreover, the affinity of the negative charge of FAPLC towards the positive charge of chitosan revealed evidence for the formation of FAPLC CNPs. SEM and particle size analysis of FAPLC CNPs exhibited spherical shape morphology and its fitness for oral administration. Solubility study showed that FAPLC CNPs remarkably enhanced the aqueous solubility of FA around ~ (12-fold) over to that of FA CNPs ~ (3-fold). In vitro dissolution results revealed biphasic release performance (initial burst and then sustained release) of FA from FAPLC CNPs as compared to FA CNPs. Likewise, the permeation rate of FA from FAPLC CNPs was enhanced noteworthy as compared to FA CNPs. In vivo, the antioxidant potential of FAPLC CNPs at a dose of (20 mg/kg, p.o.) showed significant absorption of FA into the damaged hepatic cells and restored the marker enzymes compared

to FA CNPs at the same dose level. Pharmacokinetic analysis revealed an appreciable improvement of oral bioavailability of FA from FAPLC CNPs compared to FA CNPs. Obtained results suggested that FAPLC CNPs could be served as a promising nanocarriers system for the enhancement of oral bioavailability and antioxidant activity of FA.

CRedit authorship contribution statement

All the authors and co-authors of this manuscript declare that this manuscript is original and has not been published before.

We confirm that the submitted manuscript has been read, revised and approved by all the contributed authors. We also confirmed that the order of authors mentioned and listed in the manuscript has been approved by all of us.

We undersigned that the corresponding author is the only author contact for the editorial process. He is mainly responsible for communicating with all the authors about progress, submission of revisions and final approval of proofs.

Also, the current research work is completed without support of government funding.

Declaration of competing interest

The contributed authors have no competing interest to declare.

Acknowledgment

The corresponding authors of this manuscript express their sincere thanks to Dr. Shirish P. Jain, Principal, Rajarshi Shahu College of Pharmacy, Buldhana for providing financial and technical support.

Ethics statement

The animal protocol (RSCOP/IAEC/2018–19 dated August 19, 2018) for the study was approved and sanctioned by Rajarshi Shahu College of Pharmacy, Buldhana.

Funding

The conducted research work did not receive any funding from government agencies.

References

- [1] N.R. Prasad, S. Ramachandran, K.V. Pugalendi, V.P. Menon, Ferulic acid inhibits UV-induced oxidative stress in human lymphocytes, *Nutr. Res.* 27 (2007) 559–564, <https://doi.org/10.1016/j.nutres.2007.06.011>.
- [2] C. Mancuso, R. Santangelo, Ferulic acid: pharmacological and toxicological aspects, *Food Chem. Toxicol.* 65 (2014) 185–195, <https://doi.org/10.1016/j.fct.2013.12.024>.
- [3] M. Srinivasan, R. Rukkumani, A.R. Sudheer, V.P. Menon, Ferulic acid, a natural protector against carbon tetra chloride-induced toxicity, *Fundamental and Clin. Pharmacol.* 19 (2005) 491–496, <https://doi.org/10.1111/j.1472-8206.2005.00332.x>.
- [4] A. Sgarbossa, D. Giacomazza, M. di Carlo, Ferulic acid: a hope for Alzheimer's disease therapy from plants, *Nutr* 7 (2015) 5764–5782, <https://doi.org/10.3390/nu7075246>.
- [5] M.S. Balasubhashini, R. Rukkumani, P. Vishwanathan, V.P. Menon, Ferulic acid alleviates lipid peroxidation in diabetic rats, *Phytother. Res.* 18 (2004) 310–314, <https://doi.org/10.1002/ptr.1440>.
- [6] K. Kawabata, T. Yamamoto, A. Hara, M. Shimizu, Y. Yamada, K. Matsunaga, T. Tanaka, H. Mori, Modifying effects of ferulic acid on azoxymethane-induced colon carcinogenesis in F344 rats, *Cancer Let.* 157 (2000) 15–21, [https://doi.org/10.1016/S0304-3835\(00\)00461-4](https://doi.org/10.1016/S0304-3835(00)00461-4).
- [7] A.R. Sudheer, C. Kalpana, M. Srinivasan, V.P. Menon, Ferulic acid modulates lipid profiles, and prooxidant/antioxidant status in circulation during nicotine-induced toxicity: a dose dependent study, *Toxicol. Mech. Methods* 15 (2005) 375–381, <https://doi.org/10.1080/15376520500194783>.
- [8] N. Kumar, V. Purthi, Potential application of ferulic acid from natural sources, *Biotechnol. Rep.* 4 (2014) 86–93, <https://doi.org/10.1016/j.btre.2014.09.002>.
- [9] K. Zdunska, A. Dana, A. Kolodziejczak, H. Rotsztein, Antioxidant properties of ferulic acid and its possible application, *Skin Pharmacol. Physiol.* 31 (2018) 332–336, <https://doi.org/10.1159/000491755>.
- [10] N. Yan, Z. Tang, Y. Xu, X. Li, Q. Wang, Pharmacokinetic study of ferulic acid following transdermal or intragastric administration in rats, *AAPS PharmSciTech* 21 (2020) 1–7, <https://doi.org/10.1208/s12249-020-01709-w>.

- [11] Y. Zhang, Z. Li, K. Zhang, G. Yang, Z. Wang, J. Zhao, R. Hu, N. Feng, Ethyl oleate-containing nanostructured lipid carriers improve oral bioavailability of trans-ferulic acid as compared with conventional solid lipid nanoparticles, *Int. J. Pharm.* 115 (1) (2016) 57–64, <https://doi.org/10.1016/j.ijpharm.2016.06.131>.
- [12] C. Li, J.-B. Li, Preparation of chitosan-ferulic acid conjugate: structure characterization and in the application of pharmaceuticals, *Int. J. Biol. Macromol.* 43 (2017) 1539–1543, <https://doi.org/10.1016/j.ijbiomac.2017.04.103>.
- [13] Li. Li, Y. Liu, Y. Xue, J. Zhu, X. Wang, Y. Dong, Preparation of the ferulic acid-phospholipids complex to improve solubility, dissolution, and B16F10 cellular melanogenesis inhibition activity, *Chem. Central J.* 11 (26) (2017) 2–8, <https://doi.org/10.1186/s13065-017-0254-8>.
- [14] G.-C. Dong, C.-Y. Kuan, S. Subramaniam, J.-Y. Zhao, S. Savitasubramaniam, H.-Y. Chang, F.-H. Lin, A potent inhibition of oxidative stress-induced gene expression in neural cells by sustained ferulic acid release from a chitosan-based hydrogel, *Materials Sci. Engg. C.* 49 (2015) 691–699, <https://doi.org/10.1016/j.msc.2015.01.030>.
- [15] I.A. de Lima, N.M. Khalil, T.T. Tominaga, A. Lechanteur, B. Sermento, R.M. Mairandes, Mucoadhesive chitosan-coated PLGA nanoparticles for oral delivery of ferulic acid, *Artificial Cells, Nanomed. Biotechnol.* 46 (2018) 993–1002, <https://doi.org/10.1080/21691401.2018.1477788>.
- [16] S. Biswas, P.K. Mukherjee, R.K. Harwarwash, S. Banerjee, P. Bhattacherjee, Enhanced bioavailability, and hepatoprotectivity of optimized ursolic acid-phospholipids complex, *Drug Dev. Ind. Pharm.* 45 (6) (2019) 946–958, <https://doi.org/10.1080/03639045.2019.1583755>.
- [17] G.S. Ravi, R.N. Charyulu, A. Dubey, P. Prabhu, S. Hebbar, A.C. Mathias, Nano-lipid complex of rutin: development, characterization and in vivo investigation of hepatoprotective antioxidant activity and bioavailability study in rats, *AAPS PharmSciTech* 19 (8) (2018) 3631–3649, <https://doi.org/10.1208/s12249-018-1195-9>.
- [18] B. Li, L. Han, B. Cao, X. Yang, X. Zhu, B. Yang, H. Zhao, W. Qiao, Use of the mangoflorine-phospholipids complex to permeate blood-brain barrier and treat depression in the CUMS animal model, *Drug Delivery* 26 (1) (2019) <https://doi.org/10.1080/10717544.2019.1616236>.
- [19] R. Mondal, Y. Bobde, B. Ghosh, T.K. Giri, Development, and characterization of a phospholipids complex for effective delivery of capsaicin, *Ind. J. Pharm. Sci* 81 (6) (2019) 1011–1019.
- [20] U. Citeresi, M. Sciacchitano, Phospholipids/active ingredient complexes, *Cosm. Toil.* 110 (1995) 57–68.
- [21] S. Bhattacharyya, Phytosomes: emerging strategy in the delivery of herbal drugs and nutraceuticals, *Pharma. Times* 41 (2009) 9–12.
- [22] E. Fahy, S. Subramanian, H.A. Brown, A comprehensive classification system for lipids, *J. Lipid Res.* 46 (2005) 839–861, <https://doi.org/10.1194/jlr.E400004-JLR200>.
- [23] P.P. Constantinidas, M.V. Chaubal, R. Shorr, Advances in lipid nanodispersion for parenteral drug delivery and targeting, *Adv. Drug Deliv. Rev.* 60 (6) (2008) 757–767, <https://doi.org/10.1016/j.addr.2007.10.013>.
- [24] P.M. Kidd, Bioavailability and active phytosomes complexes from botanical polyphenols: the silymarin, curcumin, green tea, and grape seed extracts, *Alter. Med. Rev* 14 (3) (2009) 226–246.
- [25] L. Bildstein, C. Dubernet, P. Couvreur, Prodrug-based intracellular delivery of anticancer agents, *Adv. Drug Deliv. Rev.* 63 (1–2) (2011) 3–23, <https://doi.org/10.1016/j.addr.2010.12.005>.
- [26] E. Bombardelli, Phytosome: new drug delivery system, *Boll. Chem. Farm* 130 (11) (1991) 431–438.
- [27] D. Peer, J. Karp, S. Hong, Nanocarriers as an emerging platform for cancer therapy, *Nat. Nanotech.* 2 (2007) 751–760.
- [28] E. Sousa, S. Cassel, M. Blanzet, I. Rico-lattes, Drug delivery by soft matter: matrix and vascular carriers, *Angew. Chem. Int. Ed.* 48 (2) (2009) 274–278.
- [29] H.J. Malmiri, M.A.G. Jahanian, A. Berenjian, Potential applications of chitosan nanoparticles as novel support in enzyme immobilization, *Am. J. Biochem. Biotechnol.* 8 (4) (2012) 203–219, <https://doi.org/10.3844/ajbbsp.2012.203.219>.
- [30] L.L. Chaves, S.A. Costa Lima, A.C.C. Vieira, Development of PLGA nanoparticles loaded with clofazimine for oral delivery: assessment of formulation variables and intestinal permeability, *Eur. J. Pharm. Sci.* 112 (2018) 28–37.
- [31] M.E.I. Badawy, E.I. Rabea, A biopolymer chitosan and its derivatives as promising antimicrobial agents against plant pathogens and their applications in crop protection, *Int. J. Carbohydr. Chem.* (2011) 1–29, <https://doi.org/10.1155/2011/460381>.
- [32] M. Dash, F. Chiellini, R.M. Ottenbrite, E. Chiellini, Chitosan—a versatile semi-synthetic polymer in biomedical applications, *Prog. Polym. Sci.* 36 (8) (2011) 981–1014, <https://doi.org/10.1016/j.progpolymsci.2011.02.001>.
- [33] J. Zhang, Q. Tang, X. Xu, N. Li, Development and evaluation of a novel phytosome-loaded chitosan microsphere for curcumin delivery, *Int. J. Pharm.* 448 (2013) 168–174, <https://doi.org/10.1016/j.ijpharm.2013.03.021>.
- [34] L. Chronopoulou, M. Massimi, M.F. Giardi, Chitosan-coated PLGA nanoparticles: a sustained drug release strategy for cell cultures, *Colloids Surf B Biointerfaces* 103 (2013) 310–317, <https://doi.org/10.1016/j.colsurfb.2012.10.063>.
- [35] F. Araujo, N. Shrestha, M.A. Shahbazi, The impact of nanoparticles on the mucosal translocation and transport of GLP-1 across the intestinal epithelium, *Biomaterials* 35 (2014) 9199–9207, <https://doi.org/10.1016/j.biomaterials.2014.07.026>.
- [36] D.R. Telange, N.K. Sohail, A.T. Hemke, P.S. Kharkar, A.M. Pethe, Phospholipids complex-loaded self-assembled phytosomal soft nanoparticles: evidence of enhanced solubility, dissolution rate, ex vivo permeability, oral bioavailability and antioxidant potential of mangiferin, *Drug Deliv. Transl. Res.* (2020) 1–28, <https://doi.org/10.1007/s13346-020-00822-4>.
- [37] R.K. Khurana, A.K. Bansal, S. Beg, A.J. Burrow, O.P. Katara, K.K. Singh, Enhancing bio-pharmaceutical attributes of phospholipid complex-loaded nanostructured lipidic carriers of mangiferin: systematic development, characterization, and evaluation, *Int. J. Pharm.* 518 (2017) 289–306, <https://doi.org/10.1016/j.ijpharm.2016.12.044>.
- [38] L.X. Yu, Pharmaceutical quality by design: product and process development, understanding, and control, *Pharm. Res.* 25 (4) (2008) 781–791, <https://doi.org/10.1007/s11095-007-9511-1>.
- [39] Q. Tan, S. Liu, X. Chen, M. Wu, H. Wang, H. Yin, Design and evaluation of a novel evodiamine-phospholipid complex for improved oral bioavailability, *AAPS PharmSciTech* 13 (2012) 534–547, <https://doi.org/10.1208/s12249-012-9772-9>.
- [40] S. Alam, J.J. Panda, V.S. Chauha, Novel dipeptide nanoparticles for effective curcumin delivery, *Int. J. Nanomedicine* 7 (2012) <https://doi.org/10.2147/IJN.S330154207-4022>.
- [41] M.D. Shadab, R.A. Khan, G. Mustafa, K. Chuttani, S. Baboota, J.K. Sahni, Bromocriptine loaded chitosan nanoparticles intended for a direct nose to brain delivery: pharmacodynamic, pharmacokinetic and scintigraphy study in mice model, *Eur. J. Pharm. Sci.* 48 (2013) 393–405, <https://doi.org/10.1016/j.ejps.2012.12.007>.
- [42] D.R. Telange, R. Denge, A.T. Patil, M.J. Umekar, S.V. Gupta, V.S. Dave, Pentaerythritol as an excipient/solid dispersion carrier for improved solubility and permeability of ursodeoxycholic acid, *J. Excipient. Food Chem.* 9 (2018) 80–95.
- [43] D.R. Telange, S.B. Bhagat, A.T. Patil, M.J. Umekar, A.M. Pethe, N.A. Raut, V.S. Dave, Glucosamine HCl-based solid dispersion to enhance the biopharmaceutical properties of acyclovir, *J. Excipient. Food Chem* 10 (2019) 65–80.
- [44] D.R. Telange, S.B. Nirgulkar, M.J. Umekar, A.T. Patil, A.M. Pethe, N.R. Bali, Enhanced transdermal permeation and anti-inflammatory potential of phospholipids complex – loaded matrix film of umbelliferone: formulation development, physico-chemical and functional characterization, *Eur. J. Pharm. Sci.* 131 (2019) 23–38, <https://doi.org/10.1016/j.ejps.2019.02.006>.
- [45] D.R. Telange, A.T. Patil, A.M. Pethe, A.A. Tatode, S. Anand, V.S. Dave, Kaempferol-phospholipids complex: formulation and evaluation of improved solubility, in vivo bioavailability and antioxidant potential of kaempferol, *J. Excipient. Food Chem* 7 (2016) 89–120.
- [46] D.R. Telange, A.T. Patil, A.M. Pethe, H. Fegade, S. Anand, V.S. Dave, Formulation and characterization of an apigenin-phospholipid phytosome (APLC) for improved solubility, in vivo bioavailability, and antioxidant potential, *Eur. J. Pharm. Sci.* 15 (2017) 36–49, <https://doi.org/10.1016/j.ejps.2016.12.009>.
- [47] D.R. Telange, S.A. Ukey, A.T. Hemke, M.J. Umekar, A.M. Pethe, P.S. Kharkar, LIPOID SPC-3 based coprecipitates for the enhancement of aqueous solubility and permeability of ranolazine, *J. Pharm. Innov.* (2020) 1–16, <https://doi.org/10.1007/s12247-020-09477-7>.
- [48] D. Singh, M.S.M. Rawat, A. Semalty, M. Semalty, Chrysophanol–phospholipid complex: a drug delivery strategy in herbal novel drug delivery system, *J. Therm. Anal. Calorim.* 111 (2012) 2069–2077, <https://doi.org/10.1007/s10973-012-2448-6>.
- [49] M.K. Mukherjee, V. Murugan, B.P. Saha, P.K. Mukherjee, Exploring the effect of hesperetin-HSPC complex—a novel drug delivery system on the in vitro release, therapeutic efficacy, and pharmacokinetics, *AAPS PharmSciTech* 10 (2009) 943–950, <https://doi.org/10.1208/s12249-009-9282-6>.
- [50] P. Dixit, D.K. Jain, J. Dumbwani, Standardization of an ex vivo method for determination of intestinal permeability of drugs using everted rat intestine apparatus, *J. Pharmacol. Toxicol. Methods* 65 (2012) 13–17, <https://doi.org/10.1016/j.vascn.2011.11.001>.
- [51] S. Reitman, S. Frankel, A colorimetric method for the determination of serum glutamic oxaloacetic and glutamic pyruvic transaminases, *Am. J. Clin. Pathol.* 28 (1) (1957) 56–63, <https://doi.org/10.1093/ajcp/28.1.56>.
- [52] P.R. Kind, E.J. King, Estimation of plasma phosphatase by determination of hydrolyzed phenol with amino-antipyrine, *J. Clin. Pathol.* 7 (1954) 322–326, <https://doi.org/10.1136/jcp.7.4.322>.
- [53] H.T. Malloy, K.A. Evelyn, The determination of bilirubin with the photoelectric colorimeter, *J. Biol. Chem.* 119 (1937) 481–490.
- [54] G.L. Ellman, Tissue sulfhydryl groups, *Arch. Biochem. Biophys.* 82 (1959) 70–77, [https://doi.org/10.1016/0003-9861\(59\)90090-6](https://doi.org/10.1016/0003-9861(59)90090-6).
- [55] S. Marklund, G. Marklund, Involvement of the superoxide anion radical in the autoxidation of pyrogallol and a convenient assay for superoxide dismutase, *Eur. J. Biochem.* 47 (1974) 469–474, <https://doi.org/10.1111/j.1432-1033.1974.tb03714.x>.
- [56] J. Stocks, T.L. Dormandy, The autoxidation of human red cell lipids induced by hydrogen peroxide, *Br. J. Haematol.* 20 (1971) 95–111, <https://doi.org/10.1111/j.1365-2141.1971.tb00790.x>.
- [57] R.F. Beers, I.W. Sizer, A spectrophotometric method for measuring the breakdown of hydrogen peroxide by catalase, *J. Biol. Chem.* 195 (1) (1952) 133–140.
- [58] T. Zhang, X. Yang, P. Zhang, M. Zhu, Z. He, K. Bi, Determination of ferulic acid in rat plasma by liquid chromatography-tandem mass spectrometry method: application to a pharmacokinetic study, *Anal. Letters.* 42 (2009) 2157–2169, <https://doi.org/10.1080/00032710903137418>.
- [59] F. Shakeel, M.M. Salem-Bekhit, N. Haq, N.A. Siddiqui, Solubility, and thermodynamics of ferulic acid in different neat solvents: measurement, correlation, and molecular interactions, *J. Mol. Lipids.* 236 (2017) 144–150, <https://doi.org/10.1016/j.molliq.2017.04.014>.
- [60] J. Zhang, Q. Peng, S. Shi, Q. Zhang, X. Sun, T. Gong, H. Zhang, Preparation, characterization and in vivo evaluation of a self-nano emulsifying drug delivery system (SNEEDS) loaded with morin phospholipids complex, *Int. J. Nanomedicine* 6 (2011) 3405–3415, <https://doi.org/10.2147/IJN.S25824>.
- [61] N.R. Pani, S. Acharya, S. Patra, Development and validation of RP-HPLC method for quantification of glipizide in biological macromolecules, *Int. J. Biol. Macromol.* 65 (2014) 65–71, <https://doi.org/10.1016/j.ijbiomac.2014.01.007>.
- [62] M.S. Freag, Y.S.R. Elnaggar, O.Y. Abdallah, Lyophilized phytosomal nanocarriers as platforms for enhanced diosmin delivery: optimization and ex vivo permeation, *Int. J. Nanomedicine* 8 (2013) 2385–2397, <https://doi.org/10.2147/IJN.S45231>.
- [63] A. Mazumdar, A. Dwivedi, J.L. Du Preez, J. du Plessis, In vitro wound healing and cytotoxic effects of sinigrin – phytosomes complex, *Int. J. Pharm.* 498 (2016) 283–293, <https://doi.org/10.1016/j.ijpharm.2015.12.027>.

- [64] K. Pate, P. Safier, Chemical metrology methods for CMP quality, *Adv. Chem. Mech. Planazn.* (2016) 299–325.
- [65] N. Othman, M.S. Masaruddin, C.Y. Kuen, N.A. Dasuan, L.C. Abdullah, S.N.A.Md. Jamil, Synthesis, and optimization of chitosan nanoparticles loaded with L-ascorbic acid and thymoquinone, *Nanomaterials* 8 (2020) 2–19, <https://doi.org/10.3390/nano8110920>.
- [66] A.I. Barbosa, S.A.C. Lima, S. Reis, Development of methotrexate loaded fucoidan/chitosan nanoparticles with anti-inflammatory potential and enhanced skin permeation, *Int. J. Biol. Macromol.* 124 (2019) 1115–1122, <https://doi.org/10.1016/j.ijbiomac.2018.12.014>.
- [67] J. Li, P. Liu, J.-P. Liu, J.-K. Yang, W.-L. Zhang, Y.-Q. Fan, S.-L. Kan, Y. Cui, W.-J. Zhang, Bioavailability, and foam cells permeability enhancement of salvianolic acid B pellets based on drug-phospholipids complex technique, *Eur. J. Pharm. Biopharm.* 83 (2013) 76–86, <https://doi.org/10.1016/j.ejpb.2012.09.021>.
- [68] S.D. Saoji, N.A. Raut, P.W. Dhore, C.D. Borkar, M. Popielarczyk, V.S. Dave, Preparation and evaluation of phospholipids based complex of standardized Centella extract (SCE) for the enhanced delivery of phytoconstituents, *AAPS Journal*. 18 (2016) 102–114, <https://doi.org/10.1016/j.ejpb.2012.09.021>.
- [69] Z. Hou, Y. Li, Y. Huang, C. Zhou, J. Lin, Y. Wang, F. Cui, S. Zhou, M. Jia, S. Ye, Q. Zhang, Phytosomes loaded with mitomycin C – soybean phosphatidylcholine complex developed for drug delivery, *Mol. Pharm.* 10 (2013) 90–101, <https://doi.org/10.1021/mp300489p>.
- [70] B.B. Seghir, M.H. Benhamza, Preparation, optimization, and characterization of chitosan polymer from shrimp shells, *J. Food Measurement and Characterization*. 11 (2017) 1137–1147, <https://doi.org/10.1007/s11694-017-9490-9>.
- [71] C. Anselmi, M. Centini, M. Ricci, A. Bounocore, P. Granata, T. Tsuno, R.M. Facino, Analytical characterization of a ferulic acid/cyclodextrin inclusion complex, *J. Pharm. Biomed. Anal.* 40 (2006) 875–881, <https://doi.org/10.1016/j.jpba.2005.08.019>.
- [72] C.V. Pardeshi, V.S. Belgamwar, Controlled synthesis of N, N, N-trimethyl chitosan for modulated bio adhesion and nasal membrane permeability, *Int. J. Biol. Macromol.* 82 (2016) 933–944, <https://doi.org/10.1016/j.ijbiomac.2015.11.012>.
- [73] V.S. Belgamwar, H.S. Patel, A.S. Joshi, A. Agrawal, S.J. Surana, A.R. Tekade, Design and development of nasal mucoadhesive microspheres containing tramadol HCl for CNS targeting, *Drug Delivery* 18 (5) (2011) 353–360, <https://doi.org/10.3109/10717544.2011.557787>.
- [74] S. Patil, A. Babbar, R. Mathur, A. Mishra, K. Sawant, Mucoadhesive chitosan microspheres of carvedilol for nasal administration, *J. Drug Target.* 18 (4) (2010) 321–331, <https://doi.org/10.3109/10611861003663523>.
- [75] S. Sharma, R.K. Roy, B. Shrivastava, Antiproliferative effect of phytosome complex of methanolic extract of Terminalia arjuna bark on human breast cancer cell lines (mcf-7), *Int. J. Drug Dev. Res.* 7 (2015) (2015) 173–182.
- [76] S. Mutalik, K. Manoj, M.S. Reddy, P. Kushtagi, A.N. Usha, P. Anju, A.K. Ranjith, N. Udupa, Chitosan and enteric polymer-based once daily sustained release tablets of aceclofenac: in vitro and in vivo studies, *AAPS PharmSciTech* 9 (2008) 1–8, <https://doi.org/10.1208/s12249-008-9075-3>.
- [77] M. Perrut, J. Jung, F. Leboeuf, Enhancement of dissolution rate of poorly soluble active ingredients by supercritical fluid processes, *Int. J. Pharm.* 288 (2004) 3–10, <https://doi.org/10.1016/j.ijpharm.2004.09.007>.
- [78] S.S. Feng, G. Ruan, Q.T. Li, Fabrication and characterizations of a novel drug delivery device liposomes-in-microsphere (LIM), *Biomaterials* 25 (2004) 5181–5189, <https://doi.org/10.1016/j.biomaterials.2003.12.013>.
- [79] P.A. Cardenas, J.M. Kratz, A. Hernandez, G.M. Costa, L.F. Ospina, Y. Baena, C.M.O. Simoes, M. Aragon, In vitro intestinal permeability studies, pharmacokinetics and tissue distribution of 6-methyl coumarin after oral intraperitoneal administration in Wister rats, *Braz. J. Pharm. Sci* 53 (1) (2017) 1–9, <https://doi.org/10.1590/s2175-97902017000116081>.
- [80] G.L. Nicolson, The fluid–mosaic model of membrane structure: still relevant to understanding the structure, function, and dynamics of biological membranes after more than 40 years, *Biochim. Biophys. Acta* 1838 (6) (2014) 1451–1466, <https://doi.org/10.1016/j.bbamem.2013.10.019>.
- [81] S. Martin-Aragón, D.L. Heras, M.I. Sanchez-Reus, Pharmacological modification of endogenous antioxidant enzymes by ursolic acid on tetrachloride-induced liver damage in rats and primary cultures of rat hepatocytes, *Exp. Toxicol. Pathol.* 53 (2001) 199–206, <https://doi.org/10.1078/0940-2993-00185>.



Research Article

Egg White Protein Carrier-Assisted Development of Solid Dispersion for Improved Aqueous Solubility and Permeability of Poorly Water Soluble Hydrochlorothiazide

Darshan R. Telange,^{1,4} Shirish P. Jain,¹ Anil M. Pethe,² and Prashant S. Kharkar³

Received 5 December 2020; accepted 19 February 2021; published online 8 March 2021

Abstract. Hydrochlorothiazide (HTZ) is a first-line drug used in the treatment of hypertension suffered from low oral bioavailability due to poor aqueous solubility and permeability. Hence, lyophilized egg white protein-based solid dispersion (HTZ-EWP SD) was developed to explore its feasibility as a solid dispersion carrier for enhanced aqueous solubility and permeability of HTZ. The HTZ-EWP SD was prepared using the kneading method. HTZ-EWP SD was characterized using scanning electron microscopy (SEM), differential scanning calorimetry (DSC), Fourier transforms infrared spectroscopy (FT-IR), powder X-ray diffractometer (PXRD), solubility, *in vitro* dissolution, and *ex vivo* permeation studies. The physico-chemical evaluation suggested the formation of the solid dispersion. Optimized HTZ-EWP SD4 drastically enhanced (~32-fold) aqueous solubility ($\sim 16.12 \pm 0.08$ mg/mL) over to pure HTZ ($\sim 0.51 \pm 0.03$ mg/mL). The dissolution study in phosphate buffer media (pH 6.8) revealed that HTZ-EWP SD4 significantly enhanced the release rate of HTZ (~ 87 %) over to HTZ (~ 25 %). The permeation rate of HTZ from optimized HTZ-EWP SD4 was enhanced significantly (~ 84 %) compared to pure HTZ (~ 24 %). Optimized HTZ-EWP-SD4 enhanced the rate of HTZ dissolution (~ 86 %) in FeSSIF (fed state simulated intestinal fluid), compared to a low dissolution rate (~ 72 %) in FaSSIF (fasted state simulated intestinal fluid) state after 2-h study. Obtained results conclude that lyophilized egg white protein can be utilized as an alternative solid dispersion carrier for enhancing the solubility and permeability of HTZ.

KEY WORDS: complexation; dissolution; egg white protein; permeability; solubility.

INTRODUCTION

Hydrochlorothiazide (HTZ, Fig. 1) (IUPAC Name: [6-chloro-1, 1-dioxo-3, 4-dihydro-2H-1, 2, 4-benzothiadiazine-7-sulphonamide], a thiazide diuretic, is employed as first-line therapy in the management of hypertension alone and blend with other cardiovascular drugs (1). HTZ produces the antihypertensive action by reducing the reabsorption of Na⁺ and Cl⁻ ion in the distal tubule with Na-Cl co-transporter, which increases the excretion of Na⁺, K⁺, H⁺ and water (2). Despite the health benefit of HTZ, its medical application is confined by low aqueous solubility (~ 0.72 mg/mL), slow dissolution rate, low membrane permeability (logP = - 0.15)

(3), rapid metabolism to hydrolysis product of HTZ, and shorter half-life (~ 6 h) (4, 5). Moreover, the Biopharmaceutical Classification System (BCS) is categorized BCS class IV drug, i.e., low solubility and low permeability (6). Following oral administration, HTZ demonstrates low and variable oral bioavailability in the range of (~ 60 – 80%) (7). Therefore, HTZ, a potential drug candidate, was selected as a model drug to improve its low aqueous solubility and permeability.

Literature analysis revealed that several formulations have been developed and explored for enhancing the solubility and permeability of HTZ. These include pellets (8, 9), β -cyclodextrin complex (10, 11), micelles (12), nanoparticles (3), solid dispersion (13), nanoemulsion (14), self-nano emulsified drug delivery system (SNEDDS) (1), and microsphere (2). The outcome of these studies has shown that none of the authors has investigated the solubility and permeability of HTZ, however, in its place; they investigated the pharmacological activity of HTZ. Hence, there is an alternative formulation strategy is required to overcome the solubility and permeability of HTZ.

Among the reported formulations, the solid dispersion approach has been considered as a preferable approach for

¹Rajarshi Shahu College of Pharmacy, Malvihi, Botha Road, Buldhana, Maharashtra, India.

²School of Pharmacy & Technology Management, NMIMS (Deemed to be University), Hyderabad Campus, Hyderabad, Telangana, India.

³Institute of Chemical Technology, Mumbai, Maharashtra, India.

⁴To whom correspondence should be addressed. (e-mail: telange.darshan@gmail.com)

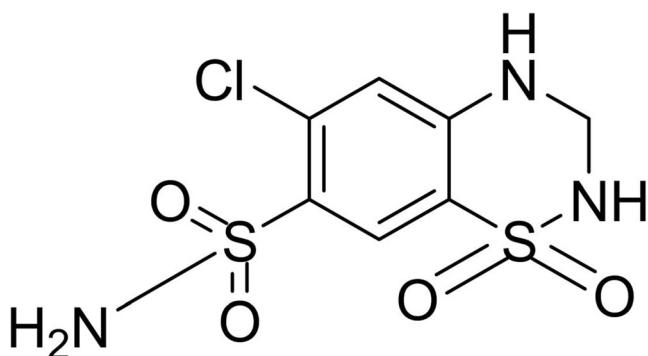


Fig. 1. Chemical structure of HTZ

improving the solubility, dissolution rate, and permeability of BCS class II and IV drugs (15–17). Solid dispersions are the formulation of active pharmaceutical ingredients (API) and hydrophilic matrix carriers. In which the API (one or more) is dispersed into the matrix of the carrier using thermal, mechanical, co-solubilization, and a combination of similar methods (18–20). Following dispersion, the prepared solid dispersion improve the solubility and dissolution rate of API by reducing its particle size to sub-micron and smaller particles increases surface area for dissolution, transformation of the crystalline drug to an amorphous one (high energy state), and enhancing the wettability and porosity of API, resulting to an increase its aqueous solubility (21). The present study deals with the preparation and comprehensive evaluation of solid dispersion of HTZ using lyophilized egg white protein (EWP). Moreover, the combination of the kneading method and lyophilized EWP can physico-chemically modifies the drug, causing a change in particle size, surface area, and crystalline nature of the drug results in an increase in solubility and dissolution rate of HTZ. The carrier, EWP, is a colloidal system composed of ovalbumin (54%), ovotransferrin (12%), ovomucoid (11%), ovomucin (3.5%), and lysozyme (3.5%) (22). The ovalbumin proteins are macromolecules with a molecular weight of 45 kDa containing 386 numbers of amino acids (23). Ovalbumin is multiple binding proteins that form a strong complex with water-insoluble drugs and bioactive through molecular-level interactions. Complex formation involves the entry of drug and bioactive into the hydrophobic pocket of protein *via* hydrophobic interaction, where this interaction further increases by hydrogen bonds. These combined interactions cause a change in the secondary structure of a protein, resulting in a stable water-soluble complex between drug and protein, which improves the aqueous solubility of the drug (24, 25). Moreover, the amphiphilic ovalbumin of EWP has been extensively used as strong emulsifying agents due to containing > 50% of hydrophobic amino acids (26, 27). Due to this property, EWP can rapidly adsorb at the oil-water interface. It self-aggregates *via* molecular interactions, reduces interfacial tension, and forms a continuous membrane around the oil droplet, resulting in a stabilized emulsion. The EWP-assisted stabilized emulsion forms a small droplet particle size with good distribution, superior stability, biocompatibility, and biosafety facilitates the rapid absorption of lipophilic drugs (28). EWP also contains ovomucin (3.5%), another water-soluble protein, which can also act as a complex carrier for improving the drug's solubility (29, 30).

Similar to biopolymers, EWP is reported as natural biopolymers with the same function as that of surface-active agents in enhancing the solubility of poorly water-soluble drugs (31–33). Despite the potential drug delivery benefits of EWP, its use and medical application as a solid dispersion carrier remain unexplored. Based on this, only a few publications have been reported by the group of authors of Imai *et al.* on this protein as a solid dispersion carrier (34, 35). The reported studies have lacked systematic characterization and functional analysis of prepared formulations. Therefore, this study was undertaken to explore the feasibility of lyophilized EWP as a solid dispersion carrier for enhancing the solubility and permeability of poorly water-soluble HTZ.

The present work shows the “proof of concept” type of study. We prepared lyophilized EWP-based solid dispersion of HTZ and evaluated its feasibility as a solid dispersion carrier using physical and functional characterization parameters. The study was carried out in two steps; first, the lyophilized EWP carrier was prepared, and second, the lyophilized carrier-based solid dispersion of HTZ was formulated using the kneading method. Optimized formulation was physico-chemically and functionally characterized using scanning electron microscopy, particle size, and zeta potential, differential scanning calorimetry, Fourier transform infrared spectroscopy, powder X-ray diffractometry, solubility study, *in vitro* dissolution, and *ex vivo* permeation studies. Moreover, the optimized formulation was also assessed for preliminary stability studies under the impact of controlled storage temperature and relative humidity.

MATERIALS AND METHODS

Materials

HTZ (> 98% purity) was received as a gift sample from Alkem Laboratories Ltd. (Mumbai, India). Infertile eggs were obtained from a local vendor. Absolute ethanol (EtOH), acetic acid (glacial, 99.5%) acetone, chloroform, dichloromethane, diethyl ether, 1, 4-dioxane, distilled water, hydrochloric acid (1 N), and methanol was purchased from Loba Chemicals Pvt. Ltd. (Mumbai, India). Lecithin, methylene chloride, potassium dihydrogen phosphate, sodium chloride, sodium dihydrogen phosphate, sodium taurocholate, and sodium hydroxide were purchased from Sigma-Aldrich (St. Louis, MO, USA).

Preparation of Lyophilized EWP

The lyophilized EWP powder was prepared using the procedure described earlier in the literature with some modifications (36). Briefly, the infertile eggs were purchased from local sources. The eggs were washed and boiled. The boiled egg white was separated and cut into small pieces. The pieces were subjected to homogenization for 20 min using a small amount of distilled water, acidified up to (pH 5.5) using 1 N HCl, and centrifuged (Model: R-12C Plus, REMI Laboratory Instruments, Remi House, Mumbai, India) at 1000 rpm for 10 min. The obtained supernatant was diluted with an equal volume of distilled water, transferred into a dialysis bag (molecular weight cut off ~12 kDa, HiMedia, Mumbai, India), and then dialyzed against double distilled

water for 24 h to remove other impurities. The resulting solution was then subjected to freeze-drying at a heating temperature of 50°C, cold trap temperature of -40°C, and vacuum pressure of 100 Pa employing lyophilizer (Model: MSW-137, Macro Scientific Works Pvt. Ltd., New Delhi, India) for 12 h (37). The obtained lyophilized porous mass as a carrier was used to prepare solid dispersion preparation.

Preparation of HTZ-EWP SD

The kneading method was done according to the reference for the preparation of HTZ-EWP SD with many changes (34). Briefly, lyophilized EWP, as a carrier and HTZ, was accurately weighed as per stoichiometric ratios (1:1, 1:2, 1:4, 1:6, and 1:8) and then transferred into clean mortar and pestle. The added mixture was mixed with 10 ml of a mixture of ethanol: water (1:1), obtaining a thick paste. It was then kneaded for 20 min and dried at 40°C in an oven for 24 h. The dried powder was pulverized and passed through a sieve (#60 mesh size) to get homogeneous solid dispersion powder. Afterward, the powder was also dried under vacuum at 40°C for 24 h and stored in an amber-colored airtight container flushed with nitrogen. The composition of the formulations is depicted in Table I.

Preparation of the Physical Mixture

As per the ratios mentioned above, the HTZ and EWP were individually weighed and mixed thoroughly in mortar and pestle. The prepared physical mixtures were sieved using (#60 mesh size) and used for further characterization studies after mixing.

Characterization of HTZ-EWP SD

SEM

Three samples of HTZ, EWP, and optimized HTZ-EWP SD4 were analyzed to study their comparative surface morphology using a scanning electron microscope (Model: Supra[®]55, Carl Zeiss NTS Ltd., Germany). Briefly, the individual weighed samples (~50 mg) were uniformly spread over the double-sided carbon tape and then transferred to the sample holder of the instrument. The samples were sputter-coated using a thin layer of gold (~400 Å⁰). The coating time with gold was set at 10 s. The coated samples were examined under the microscope at an accelerating

voltage of 10 kV, and images were recorded at different magnifications using instrument attached software (Smart[®]SEM V05.06). The detailed procedure for SEM analysis has been reported by our group (38).

DSC

A differential scanning calorimeter (Model: DSC-1821e, Mettler Toledo AG, Analytical, Schwerzenbach, Switzerland) was used to analyze the thermal performance of formulation components of pure HTZ, EWP, physical mixture (PM) of HTZ and EWP (1:6), and HTZ-EWP SD4 respectively. Briefly, an approximate quantity of samples (~2.0 ± 0.2 mg) was weighed, sealed in an aluminum pan using a lid with a crimper, and transferred into a sample analyzing area. The analyzing area was cleaned from air entrapped moisture, and it is done by purging dried nitrogen gas (N₂) at a rate of 50 mL/min. The DSC instrument was calibrated using standard Indium (In) for heat flow and heat capacity. After calibration, the samples were subjected to heating in a temperature range of 0 to 400°C at a heating rate of 10°C/min. The DSC curves of each sample were interpreted by the software (Universal Analysis 2000, V4.5A, build 4.5.0.5) accompanied by the instrument. The detailed procedure has been reported earlier by our group (39, 40).

FT-IR

The FT-IR spectrum of pure HTZ, EWP, PM (1:6), and HTZ-EWP SD4 was obtained on the FT-IR spectrophotometer (Model: FTIR-8300, Shimadzu, Kyoto, Japan). This study was carried out to understand the molecular level functional group interactions between the above-mentioned samples. Briefly, the individual samples and FT-IR grade of potassium bromide (KBr) were weighed and mixed properly to get a uniform mixture. This mixture was compressed into a thin disc using Mini Hand Press Machine (Model: MHP-1, P/N-200-66747-91, Shimadzu, Kyoto, Japan) and scanned between the wavenumber region of 4000 cm⁻¹ to 400 cm⁻¹, at a resolution of 4 cm⁻¹ with an average scan of 45. After scanning, the generated FT-IR spectra for each sample were compared and read using instrument-associated software (IRSolution, FT-IR Control Software, Version 1.10). The procedure published by our group has been followed for the FT-IR analysis (41).

PXRD

The samples of pure HTZ, EWP, PM (1:6), and HTZ-EWP SD4 were analyzed to study their comparative polymorphic nature using a powder X-ray diffractometer (Model: D8 Advance, Bruker AXS, Inc., Madison, WI, USA). Our group's earlier published report has been followed to prepare the sample, evaluation, and interpretation (42).

Determination of Drug Content

The percent drug content was analyzed using the method described earlier in the literature (43). Briefly, an accurate amount of HTZ-EWP SD formulations (~50 mg of HTZ) was weighed and dissolved into 100 mL of phosphate buffer

Table I. Composition and HTZ Content of the HTZ-EWP SD

Formulations	HTZ (mg)	EWP (mg)	Drug content (% w/w)*
HTZ-EWP SD1	50	50	88.65 ± 1.39
HTZ-EWP SD2	50	100	90.12 ± 1.30
HTZ-EWP SD3	50	200	91.49 ± 1.75
HTZ-EWP SD4	50	300	94.89 ± 1.54
HTZ-EWP SD5	50	400	92.28 ± 0.51

HTZ-EWP SD, hydrochlorothiazide-egg white protein solid dispersion; HTZ, hydrochlorothiazide; EWP, egg white protein
*All the values are mean ± Std. Dev.; (n = 3)

(0.05 M, pH 6.8) using a magnetic stirrer. After dissolution, the contents were filtered (membrane filter 0.45 μm), diluted suitably, and analyzed the resulting solution for absorbance on UV-Visible spectrophotometer (Model: V-630, JASCO International Co., Ltd., Tokyo, Japan) at a maximum wavelength of 270 nm. While analyzing, the added carrier interference was removed by preparing the carrier solution with the same procedure and compared against the sample solution. Equation (1) described below was used for the calculation of HTZ content in the solid dispersion.

$$\text{HTZ content (\%)} = \frac{\text{Total HTZ (mg)} - \text{free drug (mg)}}{\text{total HTZ (mg)}} \times 100 \quad (1)$$

Saturation Solubility Studies

The aqueous solubility of pure HTZ, PM, and HTZ-EWP SD formulations was carried out as per the procedure described previously in the literature (43). Briefly, an excess quantity of individual samples was weighed and dispersed in 10 mL of distilled water in a screw cap glass vials. The prepared aqueous dispersion was agitated on a rotary shaker (Model: RS-24 BL, REMI Laboratory Instruments, Remi House, Mumbai, India) at 37°C for 24 h. Following agitation, the contents were filtered using a membrane filter (0.45 μm). The filtrate was collected, diluted, and analyzed for absorbance on a UV-Visible spectrophotometer (Model: V-630, JASCO International Co., Ltd., Tokyo, Japan) at a wavelength of 272 nm against the blank. The solubility procedure was carried out at room temperature.

In Vitro Drug Release Studies

The comparative *in vitro* dissolution performance of pure HTZ, PM (1:6), or optimized HTZ-EWP SD4 in phosphate buffer was evaluated using paddle (USP Type II) dissolution test apparatus (Model: TDT-08LX, Electrolab India Pvt. Ltd., Mumbai, India). The procedure described earlier in the literature was employed to dissolve HTZ-EWP SD4 formulations (43). Briefly, the phosphate buffer (0.05 M, pH 6.8) dissolution media was used in this study. The dissolution samples of pure HTZ (~50 mg), PM (~50 mg of pure HTZ), or optimized HTZ-EWP SD4 (~50 mg of pure HTZ) were accurately weighed and dispersed into 900 mL of media in a dissolution flask. After dispersing the samples, the contents were stirred at a speed of 100 rpm, and the temperature of the media was maintained at 37 \pm 0.5°C throughout the study. While dissolution, the samples were removed from the flask at an interval of 10 min and filtered using a membrane filter (0.45 μm). At the same time, the sink condition was also maintained by replenishing the media into the flask as equal to that of withdrawing volume from the flask for the entire dissolution study. Filtered samples were suitably diluted and analyzed for HTZ absorbance using a UV-Visible spectrophotometer (Model: V-630, JASCO International Co., Ltd., Tokyo, Japan) wavelength of 271 nm against the blank. The recorded absorbance values for both formulations were

compared and converted into percentage cumulative HTZ release.

Dissolution Efficiency

The DE of pure HTZ and optimized HTZ-EWP SD4 in phosphate buffer (0.05 M, pH 6.8) was estimated using Eq. (2) described earlier in the literature (44).

$$DE = 1 + \frac{\int_{t_1}^{t_2} y \cdot dt}{y_{100} \times (t_2 - t_1)} \times 100 \quad (2)$$

In which y represents the percentage of HTZ dissolved, and DE represents the area under the dissolution curve in between the time points of t_1 and t_2 , and it is expressed in percentage of the curve at maximum dissolution, y_{100} , over the same period. The numerator part of the above equation was calculated using Eq. (3), as shown below.

$$AUC = \sum_{i=1}^{i=n} - \frac{(t_1 - t_i - 1)(Y_i - 1 + Y_i)}{2} \quad (3)$$

In this equation, t_i is the i th time point, and Y_i is the percentage of dissolved HTZ at time t_i . The dissolution software (DDSolver[®]) was employed to calculate and compare DE between the pure HTZ and optimized formulation.

Fasted Versus Fed State Dissolution Comparison

The comparative release pattern of pure HTZ or optimized HTZ-EWP SD4 was also evaluated under the influence of food effect (media) in paddle (USP Type II) dissolution test apparatus (Model: TDT-08LX, Electrolab India Pvt. Ltd., Mumbai, India). The food media, i.e., fasted state simulated intestinal fluid (FaSSIF) and fed state simulated intestinal fluid (FeSSIF), were prepared and used in this study. The procedure for the preparation of media and dissolution studies was followed as per reports published earlier in the literature (45). Briefly, the pure HTZ (~50 mg) or HTZ-EWP SD4 (~50 mg of pure HTZ) was accurately weighed and dispersed into FaSSIF (500 mL) or FeSSIF (1000 mL) media, respectively. The flask content was stirred at 50 rpm, and media temperature was set at 37 \pm 0.5°C. The dissolution studies were carried out for 120 minutes. While dissolution, the samples were pipette out at a set interval of 10 min, diluted suitably, and analyzed for HTZ absorbance using UV-Visible absorbance (Model: V-630, JASCO International Co., Ltd., Tokyo, Japan) at a maximum wavelength of 271 nm for FaSSIF or 315 nm for FeSSIF media against the blank. The final values of absorbance were reported in the percentage cumulative of HTZ release.

Ex Vivo Permeability Studies

The permeation efficiency of pure HTZ, PM (1:6), or optimized HTZ-EWP SD4 across the biological membrane was analyzed using an *everted rat intestine* method. The entire

study was performed on the same kind of apparatus described previously in the literature (46). Moreover, the isolated tissue was everted using a well-established glass-rod procedure reported earlier (47). The Institutional Animal Ethics Committee (IAEC) of Rajarshi Shahu College of Pharmacy, Buldhana, sanctioned the protocol (RSCOP/IAEC/2019-20, dated August 19, 2019). The study was performed under the guidelines provided by the Committee for the Purpose of Control and Supervision of Experiments on Animals (CPCSEA). Briefly, the everted rat intestine membrane with the cross-sectional area ($\sim 5.80 \text{ cm}^2$) and thickness ($\sim 110 \mu\text{m}$) was washed and then mounted carefully between the two tapered ends of the apparatus. After mounting the tissue, the apparatus was filled with freshly prepared Krebs solution and placed in contact with pure HTZ ($\sim 100 \mu\text{g/mL}$), PM ($\sim 100 \mu\text{g/mL}$), or HTZ-EWP SD4 ($\sim 100 \mu\text{g/mL}$) formulations prepared in Krebs solution respectively. The solution was stirred at 50 rpm, temperature maintained at $37 \pm 0.5^\circ\text{C}$, and aerated using carbogen (95% O_2 and 5% CO_2) for 120 min. The samples were removed at a designated time intervals, diluted, and analyzed for HTZ absorbance at a wavelength of 271 nm on UV-Visible spectrophotometry (Model: V-630, JASCO International Co., Ltd., Tokyo, Japan). The recorded absorbance values were calculated and reported in terms of the percentage cumulative of HTZ permeation.

Preliminary Functional Stability Evaluation

The optimized HTZ-EWP SD4 (ratio 1:4) were evaluated functionally (i.e., *in vitro* dissolution and *ex vivo* permeation) under the impact of controlled storage temperature ($25 \pm 5^\circ\text{C}$) as well as relative humidity ($60 \pm 5\%$ RH) conditions for six months. Briefly, the formulations mentioned above were packed in screw-capped, amber-colored glass vials and stored in a temperature and relative humidity controlled stability chamber (Model: TS00002009, Mumbai, Maharashtra, India) for 6 months. After 6 months of storage, the samples were removed and analyzed for functional testes with the same procedure described in previous sections.

RESULTS AND DISCUSSION

Preparation of HTZ-EWP SD

The physicochemical property of HTZ shows that it is a strong lipophilic compound and demonstrates maximum solubility in most of the organic solvents (48). This basic property is used in the current study for the preparation of solid dispersion using lyophilized EWP *via* the kneading method. Previous work has shown the effective use of ethanol as the choice of solvent to prepare solid dispersion using the kneading method (49). The same concept was also utilized in the current work; however, the HTZ and carrier both exhibited low solubility, while dissolution caused precipitation of the product. Moreover, due to the high evaporation rate of ethanol, it forms an immediate dried thick paste of drug and carrier before kneading that results in the failure of preparation of the formulation. This solubility and drying problem was solved by exploring the various combinations of binary solvents, including acetone: ethanol, 1, 4-dioxane: ethanol, propylene glycol: ethanol, and ethanol: water in (1:1) ratio,

respectively. The binary solvents of acetone: ethanol and propylene glycol: ethanol in (1:1) ratio demonstrated good solubility of EWP carrier, and poor solubility of HTZ resulted in precipitation of formulation components. Compared to this, 1, 4-dioxane: ethanol (1:1) displayed fair solubility of HTZ and EWP carrier, indicating that physico-chemical properties of 1, 4-dioxane, and ethanol could interact with each other resulted in improvement of HTZ and EWP solubility. However, the reported toxicity profile of 1, 4-dioxane in humans, its further utilization in the formulation was taken away and explored for other suitable solvents. After this, we tested the ethanol: water solvent system and found that this system in (1:1) ratio enhanced the solubility of formulation components and reduced the drying problem to a great extent caused to the formation of amorphous solid dispersion. It was suggested that semi-polar, class III solvent, and low toxicity profile of ethanol could form strong hydrogen bonding with water solvent and assist in complete solubilization of formulation components, reduced drying problem, and formation of amorphous HTZ-EWP SD. Moreover, Ghareeb *et al.* have also shown the utility of the binary solvent to prepare solid dispersion (50). Hence, we have chosen binary solvent of ethanol: water in (1:1) ratio as an optimal solvent system to prepare HTZ-EWP SD.

Characterization of HTZ-EWP SD

SEM

The surface characterization of pure HTZ, EWP, and optimized HTZ-EWP SD4 is depicted in (Fig. 2a, b, and c), respectively. The particles of pure HTZ (Fig. 2a) appeared as small and large crystals with ill-defined morphological characteristics. The morphology of EWP (Fig. 2b) exhibited small, non-uniform, and amorphous particles with heterogeneous and porous surfaces. The HTZ-EWP SD4 (Fig. 2c) particles appeared as fused particles with the characteristics of large particles of pure HTZ and porous particles EWP suggesting that the complex-forming ability of the EWP could result in the development of fused particles. The formation of such types of particles with the addition of carriers has been reported earlier in the literature (49). This comparison confirms the formation of a solid dispersion of HTZ using the kneading method.

DSC

The solid-state interactions between formulation components are quantitatively investigated by DSC in terms of appearance, disappearance, shifting, or changes in the onset and relative area of the peak concerning heat function. These developed interactions can signify the melting, degradation, glass rubber transitions, and complex formation between the components. The DSC curves of pure HTZ, EWP, the PM (1:6), and optimized HTZ-EWP SD4 are presented (Fig. 3a, b, c, and d) respectively. DSC curve of pure HTZ (Fig. 3a) presented the sharp endothermic peak around $\sim 275.05^\circ\text{C}$, indicates a melting temperature of pure HTZ (51). The DSC curve of EWP (Fig. 3b) shows two broad endothermic peaks around $\sim 88.65^\circ\text{C}$ (high intensity) and $\sim 203.06^\circ\text{C}$ (low intensity), indicates the vaporization of moisture from EWP

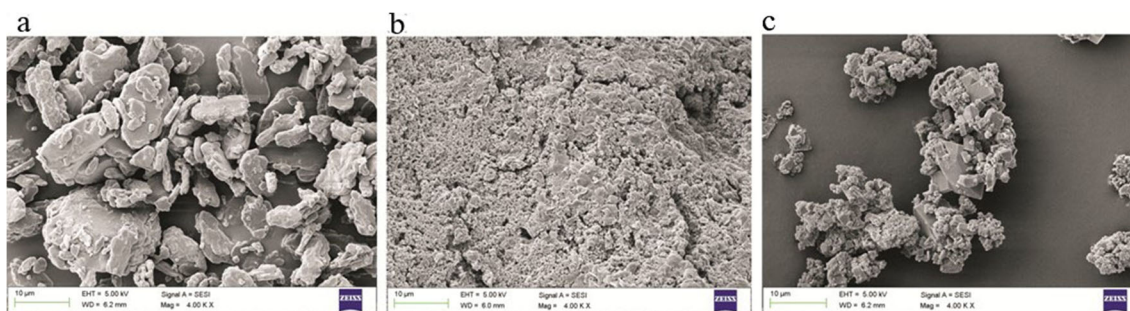


Fig. 2. SEM image of a pure HTZ, b EWP carrier, and c optimized HTZ-EWP SD4

during heating. Findings were consistent with previously published reports (34). EWP also displayed the series of undersized small intensity peaks in the range of $\sim 300^{\circ}\text{C}$ to 400°C . This is likely due to the thermal degradation of the carrier. PM (Fig. 3c) DSC curve exhibited numerous small and high-intensity endothermic peaks in the range of ~ 50 to 300°C indicates that these peaks corresponded to pure HTZ and EWP. In this curve, the peak intensity of pure HTZ was reduced around $\sim 272.27^{\circ}\text{C}$ compared to pure drugs. The reduced peak was likely attributed to the possible interaction between HTZ and EWP, as well as a lower amount of drug present in the optimized mixture ratio. Moreover, the EWP peaks were also reduced completely compared to the original DSC curve of EWP suggested that the carrier could interact well with the HTZ resulted in the formation of PM with fewer intensity peaks. Finally, the DSC curve of optimized HTZ-EWP SD4 is shown in (Fig. 3d). It displayed a straight DSC curve with complete disappearance of the sharp melting peak of HTZ indicates that there was a possible amorphization of HTZ due to strong interaction with the EWP (34). These results suggested that the complex-forming ability of the EWP could encapsulate the HTZ into its hydrophobic pocket and form a complex *via* hydrophobic, electrostatic and hydrogen-bonding interactions caused complete molecular dispersion of HTZ within the matrix of the carrier, resulting in amorphization of HTZ with the formation of the amorphous solid dispersion (24, 25). Moreover, the pure HTZ and optimized formulation demonstrated different enthalpy of fusion (ΔH) values, i.e., 116.54 J/g and 19.09 J/g also suggested the formation of the amorphous solid dispersion.

FT-IR

Figure 4a, b, c, and d represents the FT-IR spectrum of pure HTZ, EWP, PM (1:6), and HTZ-EWP SD4, respectively. As seen in (Fig. 4a), the FT-IR spectrum of pure HTZ presented the absorption peaks at ~ 3358.3 , 3281.4 , and $3164.5/\text{cm}$ for (N-H stretching), 2944.8 and $2832.8/\text{cm}$ for ($-\text{CH}_2$ stretching), $1520.8/\text{cm}$ for ($\text{C}=\text{C}$ stretching), $1427.6/\text{cm}$ for (SO_2 asymmetric stretching), 1371.7 – $1315.8/\text{cm}$ for ($\text{N}=\text{C}$ stretching), $1148.0/\text{cm}$ for (aromatic $\text{C}=\text{H}$ stretching), $1068.6/\text{cm}$ for (SO_2 symmetric stretching), $775.3/\text{cm}$ for (benzene ring deformation), and $674.6/\text{cm}$ for (aliphatic $\text{C}=\text{H}$ band). This spectrum was in agreement with earlier published reports (52, 53). FT-IR spectrum of EWP is shown in (Fig. 4b). It displays the absorption peak at $\sim 3257.7/\text{cm}$ for amide I ($\text{N}=\text{H}$ stretching), $1636.3/\text{cm}$ for ($\text{C}=\text{O}$ amide I), and $1528.2/\text{cm}$ for ($\text{C}-\text{N}$ stretch with $\text{N}-\text{H}$ bending mode due to amide II).

Obtained carrier peaks are well justified with earlier reports (54–56). FT-IR spectrum of PM is shown in (Fig. 4c). It exhibits the additive absorption peaks at $\sim 3358.3/\text{cm}$, $3261.4/\text{cm}$, $3164.5/\text{cm}$, $2944.6/\text{cm}$, $1528.2/\text{cm}$, and $1636.1/\text{cm}$ of pure HTZ as well as EWP indicates strong physico-chemical interaction between the HTZ and EWP. These results also suggested the physical mixing of both ingredients could generate the close associated mixture, which results in the formation of the spectrum with a combination of peaks. As compared to PM, the HTZ-EWP SD4 (Fig. 4d) showed a completely different FT-IR spectrum. It displayed shifting of peaks around $\sim 3265.1/\text{cm}$, $3168.2/\text{cm}$, and $2940.9/\text{cm}$ from $3281.4/\text{cm}$, $3164.2/\text{cm}$, and $2944.6/\text{cm}$ in pure HTZ and PM spectrum.. These absorption peak changes in HTZ-EWP-SD4 were likely attributed to weak intermolecular forces of interaction (hydrogen bonding and van der Waals interactions) between pure HTZ and EWP results in solid dispersion formation (25). Therefore, the above comparison concluded that the weak intermolecular forces of interaction between the HTZ and EWP might be liable for the formation of the HTZ-EWP-SD.

PXRD

The crystalline properties of pure HTZ, EWP, PM (1:6), and HTZ-EWP SD4 were determined using the PXRD diffractometer, and their spectrums are shown in (Fig. 5a–d). Diffraction pattern of pure HTZ (Fig. 5a) exhibited the sharply-pointed peaks at $\sim 16.67^{\circ}$, 19.51° , 20.98° , 21.51° , 24.69° , 28.15° , 28.90° , 33.59° , and 35.97° on 2θ scale. The intensity (counts on the y-axis) of these peaks appeared around ~ 1250 , 1300 , 1050 , 750 , 650 , 350 , 600 , and 300 , respectively, indicates the crystalline nature of pure HTZ. Results were consistent with findings reported earlier (52). EWP diffraction pattern (Fig. 5b) showed the absence of sharp peaks. However, few undersized peaks were detected in the range of $\sim 25^{\circ}$ – 35° on the 2θ scale. The intensity of these peaks appeared at ~ 150 , 180 , and 100 , respectively. The appearance of such types of peaks suggesting that EWP has an amorphous character. This spectrum was similar to earlier published literature (35). PM diffraction pattern is shown in (Fig. 5c). This spectrum revealed a combination of peaks corresponding to pure HTZ and EWP. However, the number and intensity of peaks of HTZ were reduced compared to pure HTZ. The reduced number of peaks was likely attributed to drug amorphization. In contrast, the peak intensity was reduced due to a lower amount of HTZ in the formulation ratio. Moreover, the peak/height intensity in

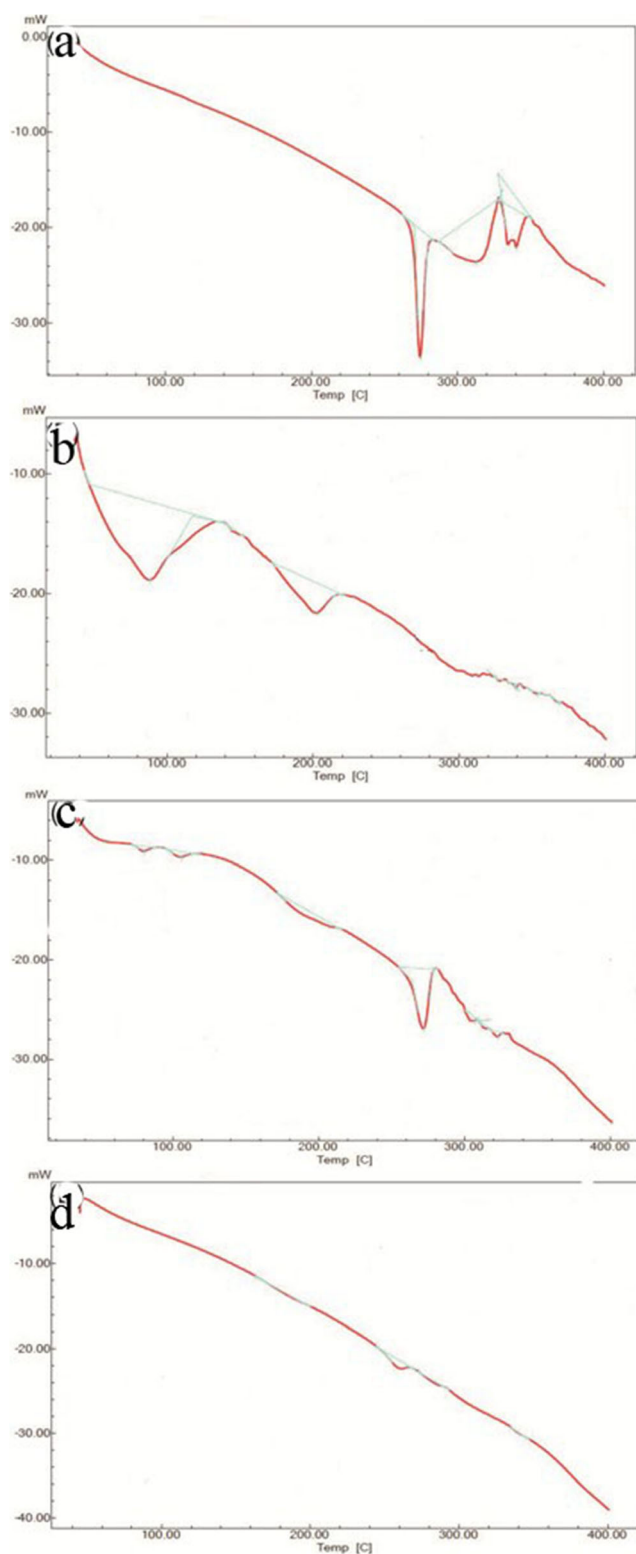


Fig. 3. DSC thermograms of a pure HTZ, b EWP carrier, c PM of HTZ: EWP (1:6), and d optimized HTZ-EWP SD4

between the region of 15° to 30° and 31° to 35° for pure HTZ and EWP were reduced around ~ 600 , 450 , 580 , 300 , 380 , 300 , 100 , and 50 counts, respectively, compared to the original spectrum indicates interaction between HTZ and EWP. (Fig.

5d) shows the diffraction pattern of HTZ-EWP SD4. It revealed peaks similar to that of the diffraction pattern of PM. Although peaks similar to PM, the intensity of retained peaks in the formulation spectrum was reduced significantly around ~ 500 , 420 , 470 , 250 , and 300 compared to pure HTZ and PM. Moreover, some crystalline peaks of HTZ were still noticed even after reduced its peak intensity indicating that HTZ crystalline form existed in the solid dispersion. These results may be explained by the fact that HTZ could disperse as separated crystals instead of molecularly dispersed form in the matrix of EWP, resulting in partial amorphization of HTZ. It was also suggested that non-covalent interactions (i.e., hydrophobic, electrostatic, and hydrogen-bonding interactions) between EWP and HTZ could dispersing HTZ as separated crystals within the matrix of EWP, reduced its partial crystallinity, results in the formation of the solid dispersion (24, 25, 34). Thus, the partial amorphization of HTZ due to the complex forming ability of the EWP confirmed the formation of the solid dispersion.

Determination of Drug Content

Table I shows the content of HTZ in the prepared HTZ-EWP SD formulations. The HTZ-EWP SD4 in the ratio of 1:6 shows the higher HTZ content around $\sim 94.89 \pm 1.54$ % w/w. Other formulations, i.e., HTZ-EWP SD1, SD2, SD3, and SD5 in the ratios of 1:1, 1:2, 1:4, and 1:8 exhibits lower HTZ content around $\sim 88.65 \pm 1.39$, 90.12 ± 1.30 , 91.49 ± 1.75 , and 92.28 ± 0.51 % w/w respectively. The HTZ-EWP SD4 (1:64) was considered optimized formulations and used for remaining characterization studies based on the drug content values. Additionally, it was also suggested that the lyophilized EWP carrier and kneading method are thought to be an appropriate and robust approach for preparing EWP-based solid dispersion with a high content of HTZ.

Saturation Solubility Studies

Pure HTZ, PM, and HTZ-EWP SD formulations were analyzed for solubility analysis, and their results are presented in Table II. Pure HTZ demonstrated low aqueous solubility around ~ 0.51 mg/mL, which indicates poor water solubility and low permeability of the HTZ, i.e., it is categorized into BCS class IV drug (57). Compared to this, all PMs exhibited some improvement in the aqueous solubility of HTZ, and their solubility range was found to be ~ 0.67 to ~ 2.01 mg/mL. These values demonstrate about ~ 4 -fold increase in the aqueous solubility of HTZ. The statistical significance of this improvement was ($p < 0.05$). It has been observed that, when the EWP ratios increased from 1:1 to 1:6, the PM formulations showed an improvement in the aqueous solubility of HTZ, suggesting that physical mixing may cause to increase in the interaction between HTZ and EWP, which could lead to slightly modify the crystalline properties of the HTZ resulting to enhance the solubility of HTZ in the PM. Moreover, the final PM with an EWP ratio of 1:8 displayed lower aqueous solubility of HTZ, suggesting that a large amount of EWP particles could restrict HTZ particle's access into the aqueous media which could result in a lowering of aqueous solubility of HTZ. The HTZ-EWP SD formulations showed a significant improvement in the aqueous solubility of

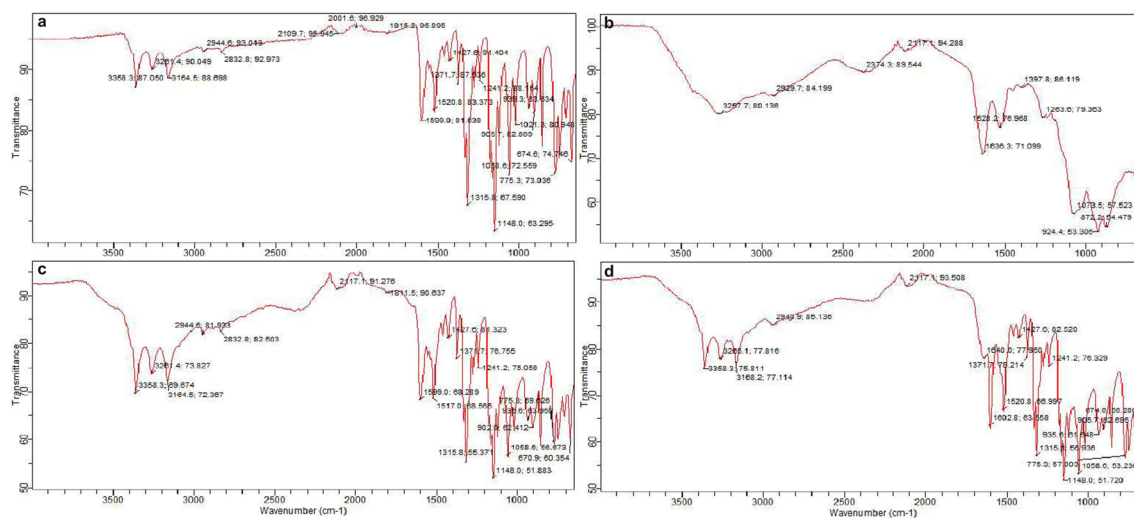


Fig. 4. FT-IR spectra of **a** pure HTZ, **b** EWP carrier, **c** PM of HTZ: EWP (1:6), and **d** optimized HTZ-EWP SD4

HTZ, and their range was found to be ~ 9.24 to ~ 16.12 mg/mL. Despite the crystalline form of HTZ exists in the solid dispersion as reflected in the PXRD spectrum, the optimized HTZ-EWP SD4 significantly ($p < 0.01$) improved the aqueous solubility of HTZ about ~ 32 -fold, and its value was appeared to be ~ 16.12 mg/mL compared to pure HTZ and PM, suggesting that, when HTZ entered into the hydrophobic pocket of EWP *via* hydrophobic interactions formed inadequate hydrogen bonding interaction with the available binding sites of EWP and complete interaction with the binding sites of ovomucin (another water-soluble protein in EWP also responsible for complex formation and improve drug water solubility), caused to absolute change in the secondary structure of EWP with the formation of the stable water-soluble complex resulting in significant improvement of HTZ-EWP SD4 aqueous solubility (24, 25, 29, 30). It was also suggested that the employed higher amount of EWP (1:6) in an optimized HTZ-EWP SD4 could act as a surfactant and thus assist in enhancing an aqueous solubility of HTZ (31–34). Thus, it can be concluded that hydrophobic and hydrogen bonding interaction between HTZ, EWP, and ovomucin could be accountable for enhancing HTZ aqueous solubility.

In Vitro Drug Release Dissolution Studies

The comparative dissolution release of HTZ from pure HTZ, PM (1:6), and optimized HTZ-EWP SD4 is shown in (Fig. 6). The pure HTZ at the end of the 120 min dissolution period released only $\sim 25\%$ of the drug in dissolution media. It could be attributed to its low water solubility, which was also reflected in the tested solubility study. Compared to this, the PM demonstrated a higher rate and extent of drug release, around $\sim 35\%$ at the end of the 120 min dissolution period. This small improvement might be attributed to HTZ and EWP's close association that may cause the formation of a partial water-soluble complex with an improved dissolution rate of HTZ. Despite crystalline HTZ existence in the prepared solid dispersion, an optimized HTZ-EWP SD4 displayed the higher rate and extent of release of HTZ compared to pure HTZ and PM. The formulation exhibited

around $\sim 87\%$ of HTZ released by the end of the release period. These findings suggested that the use of EWP, the kneading method, and water solvent could enhance the dissolution rate of HTZ in the dissolution media. These results indicated that the hydrophilic property of EWP allowed encapsulating the HTZ into its hydrophobic cavity through hydrophobic interactions, and then HTZ may form inadequate hydrogen bonding interaction with the available binding sites of EWP and complete interaction with the known binding sites of ovomucin, lead to a change in the conformation of the secondary structure of EWP, which resulted in noteworthy enhancement of solubility and dissolution rate of HTZ (24, 29, 30). The enhanced dissolution rate of HTZ-EWP SD4 could be attributed to a higher amount of lyophilized EWP in the ratio (1:6), which may entirely encapsulate the small amount of HTZ *via* hydrophobic and hydrogen bonding interaction producing water-soluble complex and subsequently improves the dissolution rate of HTZ and the results are consistent with earlier published reports (34). The reported surfactant property of EWP may also improve HTZ aqueous solubility (31–33). Moreover, the partial amorphization of HTZ due to the complex forming ability of EWP could also increase the dissolution rate of HTZ (58). The lyophilized particles of the EWP could prevent the particles aggregation and inhibit the crystal growth of drug particles and thereby increases the dissolution rate of drugs (59). The complex-forming ability of the EWP with HTZ may also enclose the drug within the matrix of EWP and cause to inhibit the aggregation of drug particles. This interaction increases the surface area of particles with rapid contact with dissolution media; ultimately, improve the wetting of particles and, subsequently, the dissolution rate of the drug (60). The solubilizing effect of EWP could also enhance the dissolution rate of the drug (61). The improved wettability of drugs *via* amorphization could also improve drug dissolution rate (62). The kneading method is also known to modify the size and shape of the drug crystals during formulation. It may cause to amorphization of drug crystals with an increase in its surface area and thereby increase the dissolution rate of the drug from the solid dispersion (35). Moreover, the water solvent is reported to

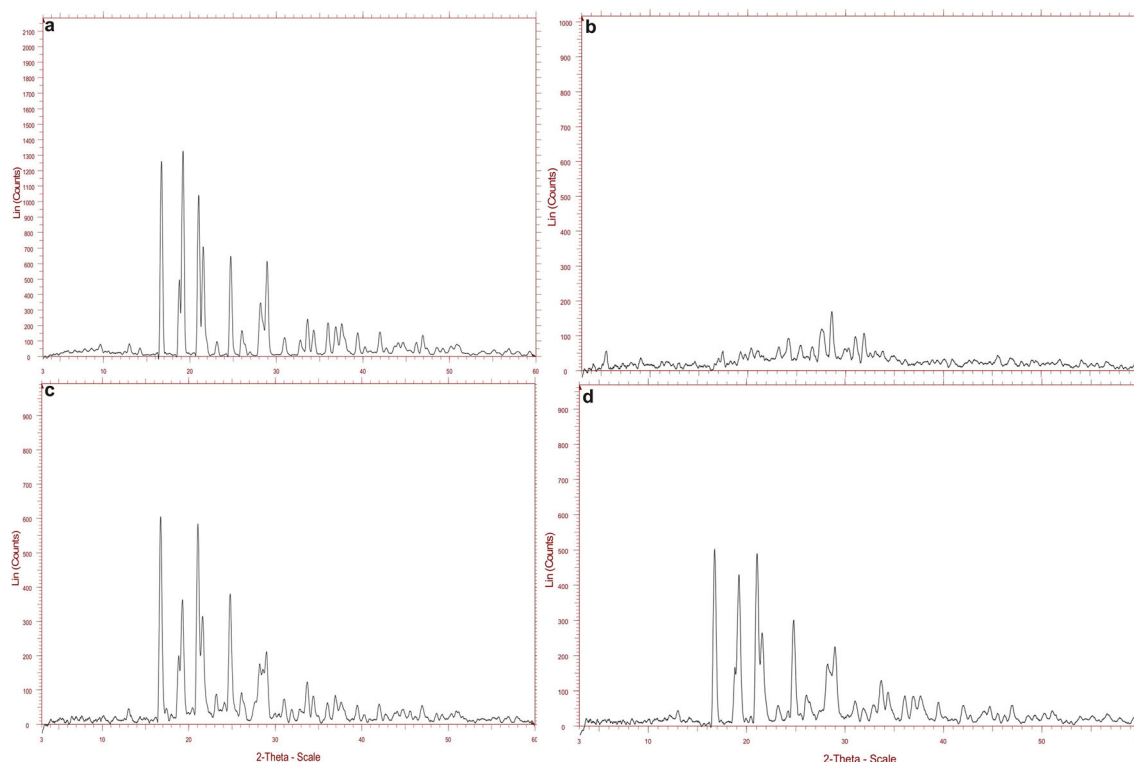


Fig. 5. PXRD pattern of **a** pure HTZ, **b** EWP carrier, **c** PM of HTZ: EWP (1:6), and **d** optimized HTZ-EWP SD4

form hydrogen bonding with the polar groups of drugs and carriers during formulation. It could also help in enhancing the dissolution rate of the drug. Additionally, the HTZ may form strong intermolecular bonding with EWP and change the physico-chemical properties of both these compounds results in significant enhancement of drug dissolution (63). The dissolution and release mechanism of HTZ from optimized formulation was determined by fitting the obtained release data into various kinetic models and analyzed (64). After analysis, the optimized HTZ-EWP SD4 exhibited a higher correlation coefficient value ($R^2 = 0.9840$) for the Higuchi model compared to zero-order ($R^2 = 0.9450$) and

Table II. Solubility Data of Pure HTZ, the Physical Mixture (PM) of Pure HTZ and EWP Carrier, and HTZ-EWP SD Formulations

Formulations	Aqueous solubility (mg/mL)*
Pure HTZ	0.51 ± 0.02
PM-1	0.67 ± 0.08
PM-2	0.74 ± 0.05
PM-3	1.39 ± 0.03
PM-4	2.01 ± 0.08
PM-5	1.10 ± 0.04
HTZ-EWP SD1	9.24 ± 0.05
HTZ-EWP SD2	12.65 ± 0.02
HTZ-EWP SD3	14.20 ± 0.06
HTZ-EWP SD4	16.12 ± 0.02
HTZ-EWP SD5	14.11 ± 0.08

Pure HTZ, pure hydrochlorothiazide; PM, physical mixture; HTZ-EWP SD, hydrochlorothiazide-egg white protein solid dispersion
*Data expressed as mean ± Std. Dev.; ($n = 3$)

first-order ($R^2 = 9230$), indicates that Higuchi is the best-fit model for the dissolution mechanism of the optimized formulation. Additionally, the same formulation showed a release exponent value ($n = 0.49$), suggesting diffusion is the primary mechanism for the release of HTZ from HTZ-EWP SD4.

Dissolution Efficiency

The DE value for pure HTZ was appeared to be $6.74 \pm 0.19\%$. PM (1:6) exhibited a somewhat higher DE value, and it was found to be around $\sim 20.66 \pm 1.42\%$. Compared to this, the DE value for optimized HTZ-EWP SD4 was found to be $\sim 57.12 \pm 1.60\%$ suggests that improved aqueous solubility of HTZ in lyophilized EWP carrier could enhance the DE of optimized HTZ-EWP SD4 compared to pure HTZ and PM, respectively.

Fasted Versus Fed State Dissolution Comparison

The effect of fasted *versus* fed state on the comparative *in vitro* dissolution performance of pure HTZ and optimized HTZ-EWP SD4 formulations is illustrated in (Fig. 7). The dissolution rate of pure HTZ in the FaSSIF state was appeared to be only $\sim 26\%$, while the same drug in the FeSSIF state demonstrated the dissolution of the HTZ around $\sim 36\%$ by the end of 120 min dissolution testing, suggesting the food content could have promoted the release of the drug in the media. In response to this, the optimized HTZ-EWP SD4 exhibits a higher rate and extent of dissolution in the fed and fasted state. However, on close observation, it was found that the optimized formulations in the FeSSIF state enhanced the dissolution of HTZ around \sim

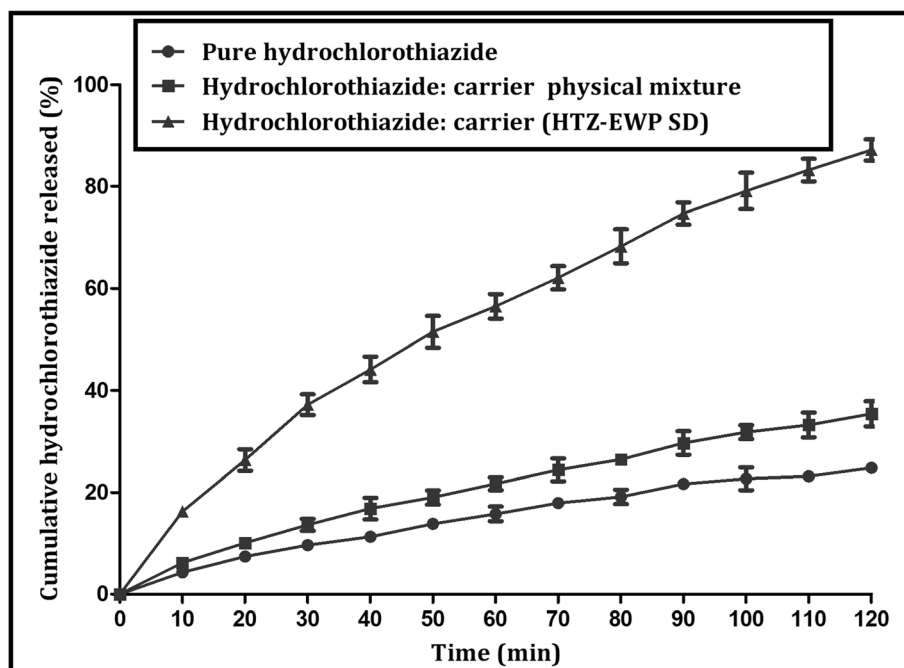


Fig. 6. *In vitro* dissolution profile of pure HTZ, the PM and optimized HTZ-EWP SD4

86% compared to lower dissolution around ~ 72% by the same formulation in the FaSSIF state at the end of dissolution testing. This result suggested the positive effect of food significantly increases the rate and extent of dissolution of drugs, and this finding was in agreement with earlier reports (45, 63). While dissolution, the formation of taurocholate-HTZ micelles and taurocholate-EWP-HTZ micelles in the FeSSIF state could have enhanced the dissolution rate HTZ from prepared HTZ-EWP SD4 (65). This concludes that food condition increases the dissolution rate of the pure drug and formulations.

Ex Vivo Permeability Studies

Figure 8 describes the permeation behavior of HTZ from pure HTZ, PM (1:6), and optimized HTZ-EWP SD4 in Krebs solution for 120 min. Initially, in the first 60 min, the permeation rate of pure HTZ was ~ 12%, and after that, it permeated only ~ 24% at the end of 120 min. This lower permeation could be attributed to the poor membrane permeability of HTZ ($\log P = -0.15$) (3). The PM demonstrated a higher rate and extent of HTZ permeation over to that of pure HTZ. The PM exhibited around ~ 20% of HTZ

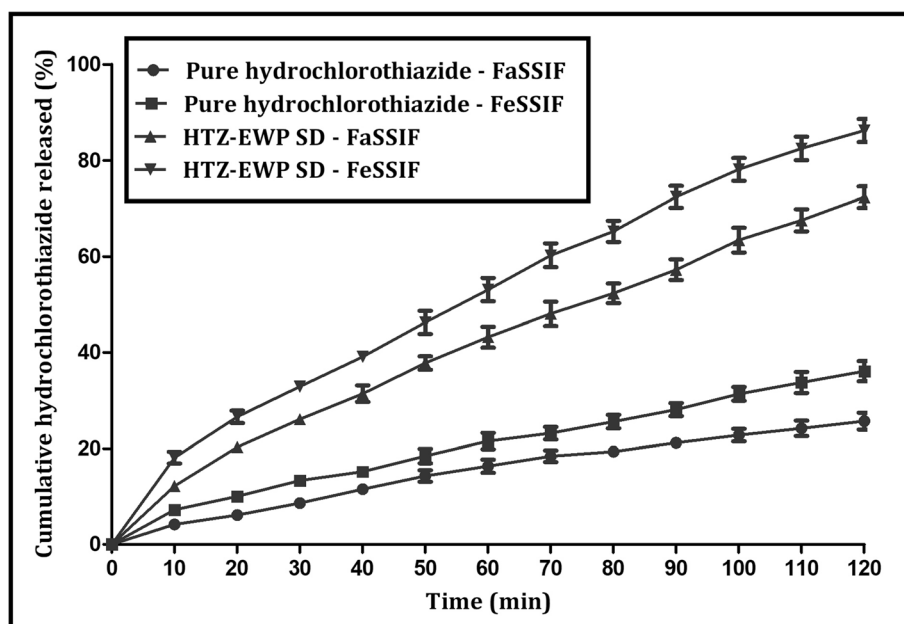


Fig. 7. Comparative *in vitro* dissolution profile of pure HTZ and optimized HTZ-EWP SD4 in "FaSSIF" and "FeSSIF" dissolution media

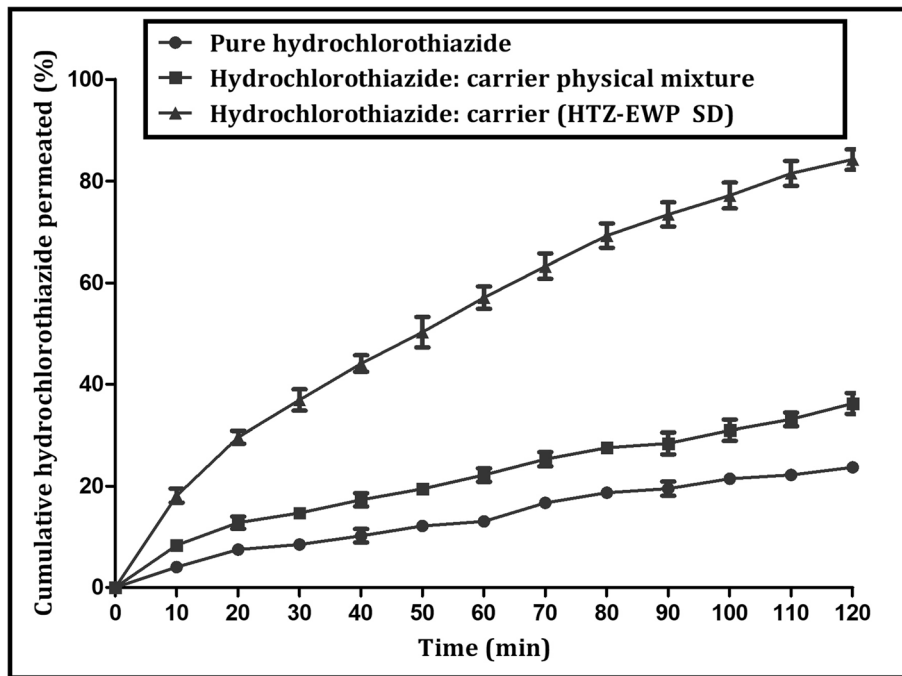


Fig. 8. Ex vivo permeability profile of pure HTZ, the PM and optimized HTZ-EWP SD4

permeation by the end of 60 min, and then it slowly enhanced the permeation rate around ~ 36% over the same testing period. In contrast to this, the permeation rate of optimized HTZ-EWP SD4 (ratio 1:6) at the end of 60 min was observed to be only ~ 50%; however, after this period, the same formulation showed continuous permeation and reached maximum permeation of HTZ around ~ 84% by the end of

120 min. This enhanced permeation rate of HTZ from optimized HTZ-EWP SD4 was likely attributed to EWP carrier, which can act as same protein to that of amphiphilic membrane protein of biological membrane could form covalent and noncovalent interactions with the carrier which in turn, show higher miscibility and thereby, increase the permeation rate of the drug across the biological membrane

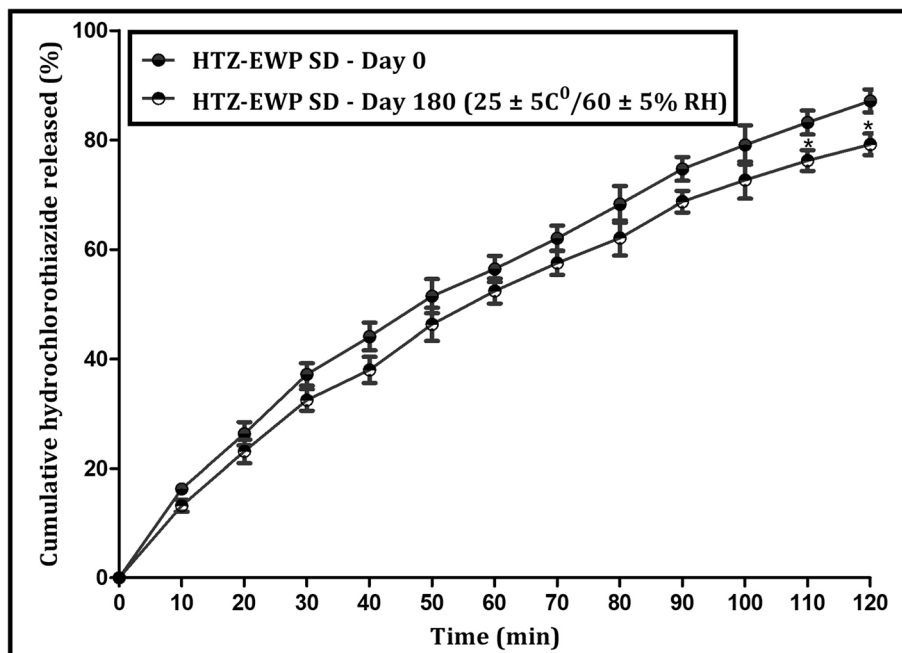


Fig. 9. Comparison of in vitro dissolution profile of optimized HTZ-EWP SD4 before and after six month storage at 25 ± 5°C/60 ± 5% RH

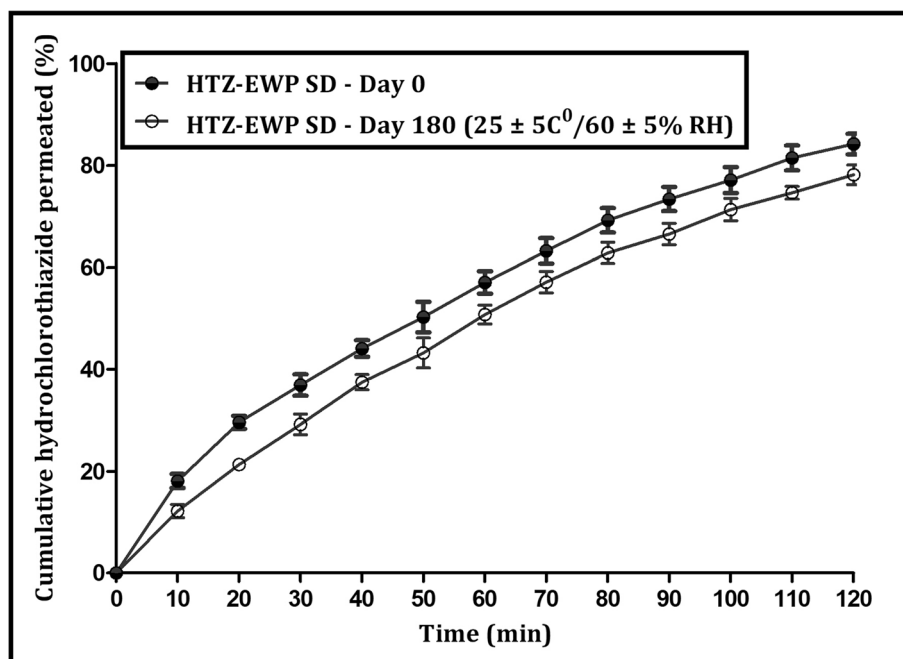


Fig. 10. Comparison of *ex vivo* permeability profile of optimized HTZ-EWP SD4 before and after six month storage at 25 ± 5°C/60 ± 5% RH

(66). The reported amphiphilic and emulsifying property of EWP forms a continuous membrane around the small size droplets *via* molecular interactions and contributes towards rapid permeation and absorption (67–69). In conclusion, the interaction forming ability of EWP with membrane protein could be responsible for increasing the miscibility and permeation of HTZ across the biological membrane.

Preliminary Functional Stability Evaluation

Figures 9 and 10 depict the influence of controlled temperature and relative humidity on the *in vitro* dissolution and *ex vivo* permeation of HTZ from stored (at day 180) optimized HTZ-EWP SD4. As seen in (Fig. 9), the release pattern of stored HTZ-EWP SD4 (at day 180) was found to be reduced significantly at the end of the 110 and 120 min dissolution period compared to the initial HTZ-EWP SD4 (at day 0). Their level of significance was observed to be ($p < 0.05$). Moreover, on close observation, it was found that the stored formulation at day180 decreased the rate and extent of HTZ release by around ~ 80% compared to the initial formulation HTZ release of around ~ 87%. *Ex vivo* permeation is another crucial functional parameter that was also assessed under the influence of storage conditions, and their results are shown in (Fig. 10). At the end of the 120 min permeation period, the initial and stored formulation at days 0 and 180 demonstrated a parallel permeation rate of HTZ without any significant difference. However, on close examination of data, it was observed that the stored formulation at day 180 permeated only ~ 78% of HTZ over to that of initial formulation at day 0 permeation around ~ 84% of HTZ. The possible reason for the lowering of the dissolution and permeation rate of HTZ from stored optimized formulation at day 180 was likely due to the impact of relative humidity and some other unclear factors. Therefore, some extra

characterization studies are required to be carried out on stored formulation to better understand the mechanism of storage conditions.

CONCLUSION

In this work, the feasibility of EWP as a solid dispersion carrier for enhancing the solubility and permeability of HTZ, BCS class IV drug was explored successfully. The HTZ-EWP SD was developed using the kneading method. Preparation of solid dispersion suggested that binary solvent (ethanol: water) in a 1:1 ratio formed the stable and amorphous solid dispersion. Physico-chemical characterization studies suggested the formation of a water-soluble solid dispersion *via* the contribution of hydrophobic and hydrogen bonding interactions. Solubility study suggested that HTZ-EWP SD4 (ratio 1:6) significantly enhanced the solubility of HTZ compared to pure HTZ and PM. *In vitro* dissolution and *ex vivo*, permeation results suggested that optimized HTZ-EWP SD4 enhanced the rate and extent of HTZ dissolution and permeation compared to pure HTZ and PM. The fed vs. fasted dissolution study showed that optimized HTZ-EWP SD4 significantly enhanced the rate and extent of HTZ dissolution in the fed state compared to the fasted state. Under the influence of storage conditions, the HTZ-EWP SD4 was stable and robust; however, at the end of the six months study, the storage conditions have reduced the dissolution and permeation rate either of drug and formulation to some extent. The unclear reason affecting this is still under investigation, and hence, some extra physico-chemical studies must be required to study the stability samples in detail. In conclusion, the obtained results have suggested that the development of HTZ solid dispersion using a lyophilized EWP carrier can be employed as a promising strategy for enhancing BCS class IV drugs solubility and permeability.

ACKNOWLEDGEMENTS

The corresponding author would like to thank Dr. Shirish P. Jain, Principal, Rajarshi Shahu College of Pharmacy, Buldhana, for the technical support to submit this manuscript.

DECLARATIONS

Conflict of Interest The authors declare that they have no conflict of interest.

REFERENCES

- Mendes C, Buttchevitz A, Kruger JH, *et al.* Self-nanoemulsified drug delivery system of HTZ for increasing dissolution rate and diuretic activity. *AAPS PharmSciTech.* 2017;18(7):2494–504. <https://doi.org/10.1208/s12249-017-0735-z>.
- Larbi OC, Merine H, Ramli Y, *et al.* Enhancement of the dissolution profile of the diuretic HTZ by elaboration of microspheres. *J Serb Chem Soc.* 2018;83(11):1243–59. <https://doi.org/10.2298/JSC171112065L>.
- Chadha R, Bhandari S, Kataria D, Gupta G, Jain DS. Exploring the potential of lecithin/chitosan nanoparticles in enhancement of antihypertensive efficacy of hydrochlorothiazide. *J Microencapsul.* 2012;29(8):805–12. <https://doi.org/10.3109/02652048.2012.692399>.
- Barbhaiya RH, Craig WA, Corrick-West P, Welling PG. Pharmacokinetics of hydrochlorothiazide in Fasted and Nonfasted Subjects: A Comparison of Plasma Level and Urinary Excretion Methods. *J Pharm Sci.* 1982;71(2):245–8. <https://doi.org/10.1002/jps.2600710226>.
- Patel RB, Patel UR, Rogge MC, Shah VP, Selen A, Welling PG. Bioavailability of hydrochlorothiazide from tablets and suspensions. *J Pharm Sci.* 1984;73(3):359–61. <https://doi.org/10.1002/jps.2600730317>.
- Yu LX, Amidon GL, Polli JE, *et al.* Biopharmaceutics classification system: the scientific basis for biowaiver extensions. *Pharm Res.* 2002;19(7):921–5. <https://doi.org/10.1023/a:1016473601633>.
- Yadav PS, Yadav E, Verma A, Amin S. Development, characterization, and pharmacodynamic evaluation of hydrochlorothiazide loaded self-nanoemulsifying drug delivery systems. *Sci World J.* 2014;1–10. <https://doi.org/10.1155/2014/274823>.
- Vervae C, Baert L, Remon JP. Enhancement of in vitro drug release by using polyethylene glycol 400 and PEG-40 hydrogenated castor oil in pellets made by extrusion/spheronisation. *Int J Pharm.* 1994;108:207–12. [https://doi.org/10.1016/0378-5173\(94\)90129-5](https://doi.org/10.1016/0378-5173(94)90129-5).
- Vervae C, Remon JP. Bioavailability of hydrochlorothiazide from pellets, made by extrusion/spheronization, containing polyethylene glycol 400 as a dissolution enhancer. *Pharm Res.* 1997;14(11):1644–6. <https://doi.org/10.1023/A:1012151006742>.
- Pires MAS, dos Santos RAS, Sinisterra RD. Pharmaceutical composition of HTZ: β -cyclodextrin: preparation by three different methods, physico-chemical characterization, and in vivo diuretic activity evaluation. *Molecules.* 2011; 16:4482–4499. <https://doi.org/10.3390/molecules16064482>.
- Altamimi MA, Elzayat EM, Alhowyan AA, Alshehri S, Shakeel F. Effect of β -cyclodextrin and different surfactants on solubility stability, and permeability of hydrochlorothiazide. *J Mol Liq.* 2018;250:323–8. <https://doi.org/10.1016/j.molliq.2017.12.006>.
- Kadam Y, Yerramilli U, Bahadur A, Bahadur P. Micelles from PEO-PPO-PEO block copolymers as nanocontainers for solubilization of a poorly water soluble drug hydrochlorothiazide. *Colloids Surf B: Biointerfaces.* 2011;83:49–57. <https://doi.org/10.1016/j.colsurfb.2010.10.041>.
- Sangeetha E, Rao VU, Sudhakar M, Manisha S. Enhancement of solubility and bioavailability of hydrochlorothiazide using solid dispersion technique. *American J Adv Drug Deli.* 2015;3:308–16.
- Mendes C, Buttchevitz A, Kruger JH, *et al.* Chitosan microencapsulation of the dispersed phase of an O/W nanoemulsion to hydrochlorothiazide delivery. *J of Microemulsion.* 2017;34:611–22. <https://doi.org/10.1080/02652048.2017.1373155>.
- Karavas E, Georarakis E, Sigalas MP, Avgoustakis K, Bikiaris D. Investigation of the release mechanism of a sparingly water-soluble drug from solid dispersions in hydrophilic carriers based on physical state of drug, particle size distribution and drug-polymer interactions. *Eur J Pharm Biopharm.* 2007;66:334–47. <https://doi.org/10.1016/j.ejpb.2006.11.020>.
- Bikiaris D, Papageorgiou GZ, Stergiou A, *et al.* Physicochemical studies on solid dispersions of poorly water-soluble drugs Evaluation of capabilities and limitations of thermal analysis techniques. *Thermochim Acta.* 2005;439:58–67. <https://doi.org/10.1016/j.tca.2005.09.011>.
- Al-Hamidi H, Edwards AA, Mohammad MA, Nikhodchi A. To enhance the dissolution rate of poorly water-soluble drugs: glucosamine hydrochloride as a potential carrier in solid dispersion formulations. *Colloids Surf B: Biointerfaces.* 2010;76(1):170–8. <https://doi.org/10.1016/j.colsurfb.2009.10.030>.
- Chiou WL, Riegelman S. Pharmaceutical applications of solid dispersion systems. *J Pharm Sci.* 1971;60:1281–302. <https://doi.org/10.1002/jps.2600600902>.
- Serajuddin ATM. Solid dispersion of poorly water soluble drugs: Early promises, subsequent problems, and recent breakthroughs. *J Pharm Sci.* 1999;88(10):1058–66. <https://doi.org/10.1021/js9804031>.
- Huang YG, Dai. Fundamental aspects of solid dispersion technology for poorly soluble drugs. *Acta Pharm Sin B.* 2014;4(1):18–25. <https://doi.org/10.1016/j.apsb.2013.11.001>.
- Vasconcelos T, Sarmento B, Costa P. Solid dispersions as a strategy to improve oral bioavailability of poor water soluble drugs. *Drug Discov Today.* 2007;12:1068–75. <https://doi.org/10.1016/j.drudis.2007.09.005>.
- Kovacs-Nolan JKN, Phillips M, Mine Y. Advances in the value of eggs and egg components for human health. *J Agric Food Chem.* 2005;53:8421–31. <https://doi.org/10.1021/jf050964f>.
- Huntington JA, Stein PE. Structure and properties of ovalbumin. *J Chromatogr B Biomed Sci Appl.* 2001;756:189–98. [https://doi.org/10.1016/S0378-4347\(01\)00108-6](https://doi.org/10.1016/S0378-4347(01)00108-6).
- Liu Y, Cai Y, Ying D, Fu Y, Xiong Y, Le X. Ovalbumin as a carrier to significantly enhance the aqueous solubility and photostability of curcumin: Interaction and binding mechanism study. *Int J Biol Macromol* 2018; 116:893–900. <https://doi.org/10.1016/j.ijbiomac.2018.05.089>.
- Chen Y, Hu J, Yi X, Ding B, Sun W, Yan F, *et al.* Interactions and emulsifying properties of ovalbumin with tannic acid. *LWT Food Sci Technol.* 2018;95:282–8. <https://doi.org/10.1016/j.lwt.2018.04.088>.
- Jia W, Cui B, Ye T, Lin L, Zheng H, Yan X, *et al.* Phase behavior of ovalbumin and carboxymethylcellulose composite system. *Carbohydr Polym.* 2014;109:64–70. <https://doi.org/10.1016/j.carbpol.2014.03.026>.
- Li Z, Kuang H, Yang J, Hu J, Ding B, Sun W, *et al.* Improving emulsion stability based on ovalbumin-carboxymethyl cellulose complexes with thermal treatment near ovalbumin isoelectric point. *Sci Rep.* 2020;10:34–56. <https://doi.org/10.1038/s41598-020-60455-y>.
- He W, Tan Y, Tian Z, Chen L, Hu F, Wu W. Food protein-stabilized nanoemulsions as potential delivery systems for poorly water-soluble drugs: preparation, in vitro characterization, and pharmacokinetics in rats. *Int J Nanomedicine.* 2011;6:521–33. <https://doi.org/10.2147/IJN.S17282>.
- Omana DA, Wang J, Wu J. Co-extraction of egg white proteins using ion-exchange chromatography from ovomucin-removed egg whites. *J Chromatogr B.* 2010;878:1771–6. <https://doi.org/10.1016/j.jchromb.2010.04.037>.
- Hiidenhovi J, Aro HS, Kankare V. Separation of ovomucin subunits by gel filtration: enhanced resolution of subunits by

- using a dual-column system. *J Agric Food Chem.* 1999;47:1004–8. <https://doi.org/10.1021/jf9811774>.
31. Iqbal S, Batool J, Ajaz M, Ambree N, Akhlaq M. Impact of egg white protein on the quality and stability of corn oil-in-water emulsion. *J Chem Soc Pak.* 2017;39:911–8.
 32. Wang S, Marcone MF, Barbut S, Lim L-T. Fortification of dietary biopolymers-based packaging material with bioactive plant extracts. *Food Res Int.* 2012;49:80–91. <https://doi.org/10.1016/j.foodres.2012.07.023>.
 33. Baloch MK, Hameed G, Iqbal S, Bano A, Rehman W. Extension of the Taylor equation for oil-water surfactant system and investigating the impact of surfactant concentration over the quality of emulsion. *J Dispers Sci Technol.* 2011;32:498–506. <https://doi.org/10.1080/01932691003756845>.
 34. Imai T, Saito Y, Matsumoto H, Satosh T, Otagiri M. Influence of egg albumin on dissolution of several drugs. *Int J Pharm.* 1989;53:7–12. [https://doi.org/10.1016/0378-5173\(89\)90355-4](https://doi.org/10.1016/0378-5173(89)90355-4).
 35. Imai T, Nohdoi K, Acarturk F, Otagiri M. Enhancement of dissolution and absorption of mefenamic acid by egg albumin. *J Pharm Sci.* 1991;80:484–7. <https://doi.org/10.1002/jps.2600800517>.
 36. Li CP, Salvador AS, Ibrahim HR, Sugimoto Y, Aoki T. Phosphorylation of egg white proteins by dry-heating in the presence of phosphate. *J Agric Food Chem.* 2003;51:6808–15. <https://doi.org/10.1021/jf030043+>.
 37. Zhou B, Zhang M, Fang Z, Liu Y. A combination of freeze drying and microwave vacuum drying of duck egg white protein powders. *Drying Tech.* 2014;32:1840–7. <https://doi.org/10.1080/07373937.2014.952380>.
 38. Telange DR, Bhagat SB, Patil AT, Umekar MJ, Pethe AM, Raut NA. Glucosamine HCl-based solid dispersions to enhance the biopharmaceutical properties of acyclovir. *J Excipients and Food Chem.* 2019;10(3):65–81.
 39. Telange DR, Sohail NK, Hemke AT, Kharkar PS, Pethe AM. Phospholipids complex – loaded self-assembled phytosomal soft nanoparticles: evidence of enhanced solubility, dissolution rate, ex vivo permeability, oral bioavailability and antioxidant potential of mangiferin. *Drug Deliv Transl Res.* 2020;1–28. <https://doi.org/10.1007/s13346-020-00822-4>.
 40. Telange DR, Patil AT, Pethe AM, Tatode AA, Anand S, Dave VS. Kaempferol-phospholipid complex: formulation, and evaluation of improved solubility, in vivo bioavailability, and antioxidant potential of kaempferol. *J Excipients and Food Chem.* 2016;7(4):89–116.
 41. Telange DR, Patil AT, Pethe AM, Fegade H, Anand S, Dave VS. Formulation and characterization of an apigenin-phospholipid phytosome (APLC) for improved solubility, in vivo bioavailability, and antioxidant potential. *Eur J Pharm Sci.* 2017;108:36–49. <https://doi.org/10.1016/j.ejps.2016.12.009>.
 42. Telange DR, Nirgulkar SB, Umekar MJ, Patil AT, Pethe AM, Bali NR. Enhanced transdermal permeation and anti-inflammatory potential of phospholipids complex-loaded matrix film of umbelliferone: Formulation development, physico-chemical and functional characterization. *Eur J Pharm Sci.* 2019;131:23–38. <https://doi.org/10.1016/j.ejps.2019.02.006>.
 43. Dhore PW, Dave VS, Saoji SD, Bobde YS, Mack C, Raut NA. Enhancement of the aqueous solubility and permeability of a poorly water soluble drug ritonavir via lyophilized milk-based solid dispersions. *Pharm Dev Technol.* 2017;22(1):90–102. <https://doi.org/10.1080/10837450.2016.1193193>.
 44. Anderson NH, Bauer M, Boussac N, Khan-Malek R, Munden P, Sardaro M. An evaluation of fit factors and dissolution efficiency for the comparison of in vitro dissolution profiles. *J Pharm Biomed Anal.* 1998;17:811–22. [https://doi.org/10.1016/S0731-7085\(98\)00011-9](https://doi.org/10.1016/S0731-7085(98)00011-9).
 45. Klein S. The use of biorelevant dissolution media to forecast the in vivo performance of a drug. *AAPS J.* 2010;12:397–406. <https://doi.org/10.1208/s12248-010-9203-3>.
 46. Dixit P, Jain DK, Dumbwani J. Standardization of an ex vivo method for determination of intestinal permeability of drugs using everted rat intestine apparatus. *J Pharmacol Toxicol Methods.* 2012;65:13–7. <https://doi.org/10.1016/j.jvascn.2011.11.001>.
 47. Hamilton KL, Butt AG. Glucose transport into everted sacs of the small intestine of mice. *Adv Physiol Educ.* 2013;37:415–26. <https://doi.org/10.1152/advan.00017.2013>.
 48. Vaculikova E, Cernikova A, Placha D, *et al.* Preparation of hydrochlorothiazide nanoparticles for solubility enhancement. *Molecules.* 2016;21:2–8. <https://doi.org/10.3390/molecules21081005>.
 49. Telange DR, Denge R, Patil AT, Umekar MJ, Gupta SV, Dave VS. Pentaerythritol as an excipient/solid-dispersion carrier for improved solubility and permeability of ursodeoxycholic acid. *J Excipients and Food Chem.* 2018;9(3):80–95.
 50. Ghareeb MM, Abdulrasool AA, Hussein AA, Noordin M. Kneading technique for preparation of binary solid dispersion of meloxicam with poloxamer 188. *AAPS PharmSciTech.* 2009;10:1206–15. <https://doi.org/10.1208/s12249-009-9316-0>.
 51. Huanbutta K, Limmatvapirat S, Sungthongjeen S, Sriamornsak P. Novel strategy to fabricate floating drug delivery system based on sublimation technique. *AAPS PharmSciTech.* 2015;17(3):693–9. <https://doi.org/10.1208/s12249-015-0398-6>.
 52. Arafa MF, A S. El-Gizawy, *et al.* Sucralose as co-crystal co-former for hydrochlorothiazide: development of oral disintegrating tablets. *Drug Dev Ind Pharm.* 2015;42:1225–33. <https://doi.org/10.3109/03639045.2015.1118495>.
 53. Sirisha PL, Babu GK, Babu PS. Conceptuation, formulation, and evaluation of sustained-release floating tablets of captopril compression coated with gastric dispersible hydrochlorothiazide using 2³ factorial design. *Int J Pharm Invest.* 2014;4(2):77–87. <https://doi.org/10.4103/2230-973X.133055>.
 54. Thiyagarajan K, Bharti VK, Tyagi S, *et al.* Synthesis of non-toxic, biocompatible, and colloidal stable silver nanoparticle using egg-white protein as capping and reducing agents for sustainable antibacterial application. *RSC Adv.* 2018;8:23213–29. <https://doi.org/10.1039/C8RA03649G>.
 55. Mahobia S, Bajpai J, Bajpai AK. An in-vitro investigation of swelling controlled delivery of insulin from egg albumin nanocarriers. *Iran J of Pharm Res.* 2016;15(4):695–711.
 56. Zhao Y, Chen Z, Li J, *et al.* Formation mechanism of ovalbumin gel induced by alkali. *Food Hydrocoll.* 2016;61:390–8. <https://doi.org/10.1016/j.foodhyd.2016.04.041>.
 57. Sanphui P, Devi VK, Clara D, *et al.* Cocrystals of hydrochlorothiazide: Solubility and diffusion/permeability enhancements through drug-coformer interactions. *Mol Pharm.* 2015;12(5):1615–22. <https://doi.org/10.1021/acs.molpharmaceut.5b00020>.
 58. Acarturk F, Kqlal O, Celebi N. The effect of some natural polymers on the solubility and dissolution characteristics of nifedipine. *Int J of Pharm.* 1992; 85: 1-6. [https://doi.org/10.1016/0378-5173\(92\)90127-N](https://doi.org/10.1016/0378-5173(92)90127-N).
 59. Patel M, Tekade A, Gattani S, Surana S. Solubility enhancement of lovastatin by modified locust bean gum using solid dispersion techniques. *AAPS PharmSciTech.* 2008;9:1262–9. <https://doi.org/10.1208/s12249-008-9171-4>.
 60. Shazly GA, Ibrahim MA, Badran MM, Zoheir KMA. Utilizing pluronic F-127 and gelucire 50/13 solid dispersions for enhanced skin delivery of flufenamic acid. *Drug Dev Res.* 2012;73(6):299–307. <https://doi.org/10.1002/ddr.21013>.
 61. Kratz F. Albumin as a drug carrier: Design of prodrugs, drug conjugates, and nanoparticles. *J Control Release.* 2008;132:171–83. <https://doi.org/10.1016/j.jconrel.2008.05.010>.
 62. Imai T, Nodomi K, Shameem M, *et al.* Mutual effect of egg albumin and fatty acids on the bioavailability of dl- α -tocopherol. *Int J Pharm.* 1997;155:45–52. [https://doi.org/10.1016/S0378-5173\(97\)00160-9](https://doi.org/10.1016/S0378-5173(97)00160-9).
 63. Hussain MD, Saxena V, Brausch JF, Talukder RM. Ibuprofen-phospholipids solid dispersion: improved dissolution and gastric tolerance. *Int J Pharm.* 2012;422:290–4. <https://doi.org/10.1016/j.ijpharm.2011.11.011>.
 64. Costa P, Manuel J, Lobô S. Modeling and comparison of dissolution profiles. *Eur J Pharm Sci.* 2001;13:123–33. [https://doi.org/10.1016/S0928-0987\(01\)00095-1](https://doi.org/10.1016/S0928-0987(01)00095-1).
 65. Raman S, Polli JE. Prediction of positive food effect: Bioavailability enhancement of BCS class II drugs. *Int J Pharm.* 2016;506(1-2):110–5. [https://doi.org/10.1016/S0928-0987\(01\)00095-1](https://doi.org/10.1016/S0928-0987(01)00095-1).
 66. Fong SYK, Ibisogly A, Bauer-Brandl A. Solubility enhancement of BCS Class II drug by solid phospholipids dispersions:

- spray drying vs freeze-drying. *Int J Pharm.* 2015;496(2):382–91. [https://doi.org/10.1016/S0928-0987\(01\)00095-1](https://doi.org/10.1016/S0928-0987(01)00095-1).
67. Almén MS, Nordström KJV, Fredriksson R, Schioth HB. Mapping the human membrane proteome: a majority of the human membrane proteins can be classified according to function and evolutionary origin. *BMC Biol.* 2009;7(50):1–14. <https://doi.org/10.1186/1741-7007-7-50>.
68. Chen L, Remondetto GE, Subirade M. Food protein-based materials as nutraceutical delivery systems. *Trends Food Sci Technol.* 2006;17(5):272–83. <https://doi.org/10.1016/j.tifs.2005.12.011>.
69. Davis JP, Foegeding EA. Foaming and interfacial properties of polymerized whey protein isolate. *J Food Sci.* 2004;69(5):404–10. <https://doi.org/10.1111/j.1365-2621.2004.tb10706.x>.

Publisher's Note Springer Nature remains neutral with regard to jurisdictional claims in published maps and institutional affiliations.



Research Article

Egg White Protein Carrier-Assisted Development of Solid Dispersion for Improved Aqueous Solubility and Permeability of Poorly Water Soluble Hydrochlorothiazide

Darshan R. Telange,^{1,4} Shirish P. Jain,¹ Anil M. Pethe,² and Prashant S. Kharkar³

Received 5 December 2020; accepted 19 February 2021; published online 8 March 2021

Abstract. Hydrochlorothiazide (HTZ) is a first-line drug used in the treatment of hypertension suffered from low oral bioavailability due to poor aqueous solubility and permeability. Hence, lyophilized egg white protein-based solid dispersion (HTZ-EWP SD) was developed to explore its feasibility as a solid dispersion carrier for enhanced aqueous solubility and permeability of HTZ. The HTZ-EWP SD was prepared using the kneading method. HTZ-EWP SD was characterized using scanning electron microscopy (SEM), differential scanning calorimetry (DSC), Fourier transforms infrared spectroscopy (FT-IR), powder X-ray diffractometer (PXRD), solubility, *in vitro* dissolution, and *ex vivo* permeation studies. The physico-chemical evaluation suggested the formation of the solid dispersion. Optimized HTZ-EWP SD4 drastically enhanced (~32-fold) aqueous solubility ($\sim 16.12 \pm 0.08$ mg/mL) over to pure HTZ ($\sim 0.51 \pm 0.03$ mg/mL). The dissolution study in phosphate buffer media (pH 6.8) revealed that HTZ-EWP SD4 significantly enhanced the release rate of HTZ (~ 87 %) over to HTZ (~ 25 %). The permeation rate of HTZ from optimized HTZ-EWP SD4 was enhanced significantly (~ 84 %) compared to pure HTZ (~ 24 %). Optimized HTZ-EWP-SD4 enhanced the rate of HTZ dissolution (~ 86 %) in FeSSIF (fed state simulated intestinal fluid), compared to a low dissolution rate (~ 72 %) in FaSSIF (fasted state simulated intestinal fluid) state after 2-h study. Obtained results conclude that lyophilized egg white protein can be utilized as an alternative solid dispersion carrier for enhancing the solubility and permeability of HTZ.

KEY WORDS: complexation; dissolution; egg white protein; permeability; solubility.

INTRODUCTION

Hydrochlorothiazide (HTZ, Fig. 1) (IUPAC Name: [6-chloro-1, 1-dioxo-3, 4-dihydro-2H-1, 2, 4-benzothiadiazine-7-sulphonamide], a thiazide diuretic, is employed as first-line therapy in the management of hypertension alone and blend with other cardiovascular drugs (1). HTZ produces the antihypertensive action by reducing the reabsorption of Na⁺ and Cl⁻ ion in the distal tubule with Na-Cl co-transporter, which increases the excretion of Na⁺, K⁺, H⁺ and water (2). Despite the health benefit of HTZ, its medical application is confined by low aqueous solubility (~ 0.72 mg/mL), slow dissolution rate, low membrane permeability (logP = - 0.15)

(3), rapid metabolism to hydrolysis product of HTZ, and shorter half-life (~ 6 h) (4, 5). Moreover, the Biopharmaceutical Classification System (BCS) is categorized BCS class IV drug, i.e., low solubility and low permeability (6). Following oral administration, HTZ demonstrates low and variable oral bioavailability in the range of (~ 60 – 80%) (7). Therefore, HTZ, a potential drug candidate, was selected as a model drug to improve its low aqueous solubility and permeability.

Literature analysis revealed that several formulations have been developed and explored for enhancing the solubility and permeability of HTZ. These include pellets (8, 9), β -cyclodextrin complex (10, 11), micelles (12), nanoparticles (3), solid dispersion (13), nanoemulsion (14), self-nano emulsified drug delivery system (SNEDDS) (1), and microsphere (2). The outcome of these studies has shown that none of the authors has investigated the solubility and permeability of HTZ, however, in its place; they investigated the pharmacological activity of HTZ. Hence, there is an alternative formulation strategy is required to overcome the solubility and permeability of HTZ.

Among the reported formulations, the solid dispersion approach has been considered as a preferable approach for

¹Rajarshi Shahu College of Pharmacy, Malvihi, Botha Road, Buldhana, Maharashtra, India.

²School of Pharmacy & Technology Management, NMIMS (Deemed to be University), Hyderabad Campus, Hyderabad, Telangana, India.

³Institute of Chemical Technology, Mumbai, Maharashtra, India.

⁴To whom correspondence should be addressed. (e-mail: telange.darshan@gmail.com)

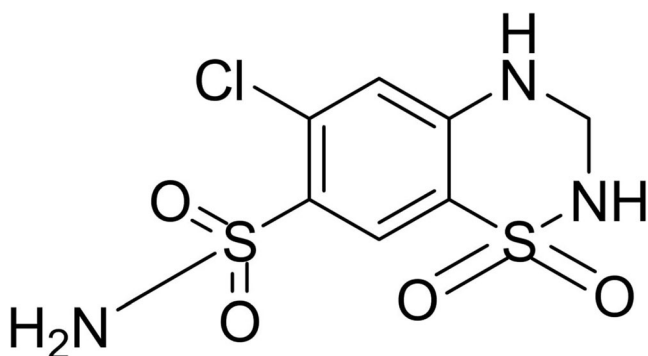


Fig. 1. Chemical structure of HTZ

improving the solubility, dissolution rate, and permeability of BCS class II and IV drugs (15–17). Solid dispersions are the formulation of active pharmaceutical ingredients (API) and hydrophilic matrix carriers. In which the API (one or more) is dispersed into the matrix of the carrier using thermal, mechanical, co-solubilization, and a combination of similar methods (18–20). Following dispersion, the prepared solid dispersion improve the solubility and dissolution rate of API by reducing its particle size to sub-micron and smaller particles increases surface area for dissolution, transformation of the crystalline drug to an amorphous one (high energy state), and enhancing the wettability and porosity of API, resulting to an increase its aqueous solubility (21). The present study deals with the preparation and comprehensive evaluation of solid dispersion of HTZ using lyophilized egg white protein (EWP). Moreover, the combination of the kneading method and lyophilized EWP can physico-chemically modifies the drug, causing a change in particle size, surface area, and crystalline nature of the drug results in an increase in solubility and dissolution rate of HTZ. The carrier, EWP, is a colloidal system composed of ovalbumin (54%), ovotransferrin (12%), ovomucoid (11%), ovomucin (3.5%), and lysozyme (3.5%) (22). The ovalbumin proteins are macromolecules with a molecular weight of 45 kDa containing 386 numbers of amino acids (23). Ovalbumin is multiple binding proteins that form a strong complex with water-insoluble drugs and bioactive through molecular-level interactions. Complex formation involves the entry of drug and bioactive into the hydrophobic pocket of protein *via* hydrophobic interaction, where this interaction further increases by hydrogen bonds. These combined interactions cause a change in the secondary structure of a protein, resulting in a stable water-soluble complex between drug and protein, which improves the aqueous solubility of the drug (24, 25). Moreover, the amphiphilic ovalbumin of EWP has been extensively used as strong emulsifying agents due to containing > 50% of hydrophobic amino acids (26, 27). Due to this property, EWP can rapidly adsorb at the oil-water interface. It self-aggregates *via* molecular interactions, reduces interfacial tension, and forms a continuous membrane around the oil droplet, resulting in a stabilized emulsion. The EWP-assisted stabilized emulsion forms a small droplet particle size with good distribution, superior stability, biocompatibility, and biosafety facilitates the rapid absorption of lipophilic drugs (28). EWP also contains ovomucin (3.5%), another water-soluble protein, which can also act as a complex carrier for improving the drug's solubility (29, 30).

Similar to biopolymers, EWP is reported as natural biopolymers with the same function as that of surface-active agents in enhancing the solubility of poorly water-soluble drugs (31–33). Despite the potential drug delivery benefits of EWP, its use and medical application as a solid dispersion carrier remain unexplored. Based on this, only a few publications have been reported by the group of authors of Imai *et al.* on this protein as a solid dispersion carrier (34, 35). The reported studies have lacked systematic characterization and functional analysis of prepared formulations. Therefore, this study was undertaken to explore the feasibility of lyophilized EWP as a solid dispersion carrier for enhancing the solubility and permeability of poorly water-soluble HTZ.

The present work shows the “proof of concept” type of study. We prepared lyophilized EWP-based solid dispersion of HTZ and evaluated its feasibility as a solid dispersion carrier using physical and functional characterization parameters. The study was carried out in two steps; first, the lyophilized EWP carrier was prepared, and second, the lyophilized carrier-based solid dispersion of HTZ was formulated using the kneading method. Optimized formulation was physico-chemically and functionally characterized using scanning electron microscopy, particle size, and zeta potential, differential scanning calorimetry, Fourier transform infrared spectroscopy, powder X-ray diffractometry, solubility study, *in vitro* dissolution, and *ex vivo* permeation studies. Moreover, the optimized formulation was also assessed for preliminary stability studies under the impact of controlled storage temperature and relative humidity.

MATERIALS AND METHODS

Materials

HTZ (> 98% purity) was received as a gift sample from Alkem Laboratories Ltd. (Mumbai, India). Infertile eggs were obtained from a local vendor. Absolute ethanol (EtOH), acetic acid (glacial, 99.5%) acetone, chloroform, dichloromethane, diethyl ether, 1, 4-dioxane, distilled water, hydrochloric acid (1 N), and methanol was purchased from Loba Chemicals Pvt. Ltd. (Mumbai, India). Lecithin, methylene chloride, potassium dihydrogen phosphate, sodium chloride, sodium dihydrogen phosphate, sodium taurocholate, and sodium hydroxide were purchased from Sigma-Aldrich (St. Louis, MO, USA).

Preparation of Lyophilized EWP

The lyophilized EWP powder was prepared using the procedure described earlier in the literature with some modifications (36). Briefly, the infertile eggs were purchased from local sources. The eggs were washed and boiled. The boiled egg white was separated and cut into small pieces. The pieces were subjected to homogenization for 20 min using a small amount of distilled water, acidified up to (pH 5.5) using 1 N HCl, and centrifuged (Model: R-12C Plus, REMI Laboratory Instruments, Remi House, Mumbai, India) at 1000 rpm for 10 min. The obtained supernatant was diluted with an equal volume of distilled water, transferred into a dialysis bag (molecular weight cut off ~12 kDa, HiMedia, Mumbai, India), and then dialyzed against double distilled

water for 24 h to remove other impurities. The resulting solution was then subjected to freeze-drying at a heating temperature of 50°C, cold trap temperature of -40°C, and vacuum pressure of 100 Pa employing lyophilizer (Model: MSW-137, Macro Scientific Works Pvt. Ltd., New Delhi, India) for 12 h (37). The obtained lyophilized porous mass as a carrier was used to prepare solid dispersion preparation.

Preparation of HTZ-EWP SD

The kneading method was done according to the reference for the preparation of HTZ-EWP SD with many changes (34). Briefly, lyophilized EWP, as a carrier and HTZ, was accurately weighed as per stoichiometric ratios (1:1, 1:2, 1:4, 1:6, and 1:8) and then transferred into clean mortar and pestle. The added mixture was mixed with 10 ml of a mixture of ethanol: water (1:1), obtaining a thick paste. It was then kneaded for 20 min and dried at 40°C in an oven for 24 h. The dried powder was pulverized and passed through a sieve (#60 mesh size) to get homogeneous solid dispersion powder. Afterward, the powder was also dried under vacuum at 40°C for 24 h and stored in an amber-colored airtight container flushed with nitrogen. The composition of the formulations is depicted in Table I.

Preparation of the Physical Mixture

As per the ratios mentioned above, the HTZ and EWP were individually weighed and mixed thoroughly in mortar and pestle. The prepared physical mixtures were sieved using (#60 mesh sizes) and used for further characterization studies after mixing.

Characterization of HTZ-EWP SD

SEM

Three samples of HTZ, EWP, and optimized HTZ-EWP SD4 were analyzed to study their comparative surface morphology using a scanning electron microscope (Model: Supra[®]55, Carl Zeiss NTS Ltd., Germany). Briefly, the individual weighed samples (~50 mg) were uniformly spread over the double-sided carbon tape and then transferred to the sample holder of the instrument. The samples were sputter-coated using a thin layer of gold (~400 Å⁰). The coating time with gold was set at 10 s. The coated samples were examined under the microscope at an accelerating

voltage of 10 kV, and images were recorded at different magnifications using instrument attached software (Smart[®]SEM V05.06). The detailed procedure for SEM analysis has been reported by our group (38).

DSC

A differential scanning calorimeter (Model: DSC-1821e, Mettler Toledo AG, Analytical, Schwerzenbach, Switzerland) was used to analyze the thermal performance of formulation components of pure HTZ, EWP, physical mixture (PM) of HTZ and EWP (1:6), and HTZ-EWP SD4 respectively. Briefly, an approximate quantity of samples (~2.0 ± 0.2 mg) was weighed, sealed in an aluminum pan using a lid with a crimper, and transferred into a sample analyzing area. The analyzing area was cleaned from air entrapped moisture, and it is done by purging dried nitrogen gas (N₂) at a rate of 50 mL/min. The DSC instrument was calibrated using standard Indium (In) for heat flow and heat capacity. After calibration, the samples were subjected to heating in a temperature range of 0 to 400°C at a heating rate of 10°C/min. The DSC curves of each sample were interpreted by the software (Universal Analysis 2000, V4.5A, build 4.5.0.5) accompanied by the instrument. The detailed procedure has been reported earlier by our group (39, 40).

FT-IR

The FT-IR spectrum of pure HTZ, EWP, PM (1:6), and HTZ-EWP SD4 was obtained on the FT-IR spectrophotometer (Model: FTIR-8300, Shimadzu, Kyoto, Japan). This study was carried out to understand the molecular level functional group interactions between the above-mentioned samples. Briefly, the individual samples and FT-IR grade of potassium bromide (KBr) were weighed and mixed properly to get a uniform mixture. This mixture was compressed into a thin disc using Mini Hand Press Machine (Model: MHP-1, P/N-200-66747-91, Shimadzu, Kyoto, Japan) and scanned between the wavenumber region of 4000 cm⁻¹ to 400 cm⁻¹, at a resolution of 4 cm⁻¹ with an average scan of 45. After scanning, the generated FT-IR spectra for each sample were compared and read using instrument-associated software (IRSolution, FT-IR Control Software, Version 1.10). The procedure published by our group has been followed for the FT-IR analysis (41).

PXRD

The samples of pure HTZ, EWP, PM (1:6), and HTZ-EWP SD4 were analyzed to study their comparative polymorphic nature using a powder X-ray diffractometer (Model: D8 Advance, Bruker AXS, Inc., Madison, WI, USA). Our group's earlier published report has been followed to prepare the sample, evaluation, and interpretation (42).

Determination of Drug Content

The percent drug content was analyzed using the method described earlier in the literature (43). Briefly, an accurate amount of HTZ-EWP SD formulations (~50 mg of HTZ) was weighed and dissolved into 100 mL of phosphate buffer

Table I. Composition and HTZ Content of the HTZ-EWP SD

Formulations	HTZ (mg)	EWP (mg)	Drug content (% w/w)*
HTZ-EWP SD1	50	50	88.65 ± 1.39
HTZ-EWP SD2	50	100	90.12 ± 1.30
HTZ-EWP SD3	50	200	91.49 ± 1.75
HTZ-EWP SD4	50	300	94.89 ± 1.54
HTZ-EWP SD5	50	400	92.28 ± 0.51

HTZ-EWP SD, hydrochlorothiazide-egg white protein solid dispersion; HTZ, hydrochlorothiazide; EWP, egg white protein
*All the values are mean ± Std. Dev.; (n = 3)

(0.05 M, pH 6.8) using a magnetic stirrer. After dissolution, the contents were filtered (membrane filter 0.45 μm), diluted suitably, and analyzed the resulting solution for absorbance on UV-Visible spectrophotometer (Model: V-630, JASCO International Co., Ltd., Tokyo, Japan) at a maximum wavelength of 270 nm. While analyzing, the added carrier interference was removed by preparing the carrier solution with the same procedure and compared against the sample solution. Equation (1) described below was used for the calculation of HTZ content in the solid dispersion.

$$\text{HTZ content (\%)} = \frac{\text{Total HTZ (mg)} - \text{free drug (mg)}}{\text{total HTZ (mg)}} \times 100 \quad (1)$$

Saturation Solubility Studies

The aqueous solubility of pure HTZ, PM, and HTZ-EWP SD formulations was carried out as per the procedure described previously in the literature (43). Briefly, an excess quantity of individual samples was weighed and dispersed in 10 mL of distilled water in a screw cap glass vials. The prepared aqueous dispersion was agitated on a rotary shaker (Model: RS-24 BL, REMI Laboratory Instruments, Remi House, Mumbai, India) at 37°C for 24 h. Following agitation, the contents were filtered using a membrane filter (0.45 μm). The filtrate was collected, diluted, and analyzed for absorbance on a UV-Visible spectrophotometer (Model: V-630, JASCO International Co., Ltd., Tokyo, Japan) at a wavelength of 272 nm against the blank. The solubility procedure was carried out at room temperature.

In Vitro Drug Release Studies

The comparative *in vitro* dissolution performance of pure HTZ, PM (1:6), or optimized HTZ-EWP SD4 in phosphate buffer was evaluated using paddle (USP Type II) dissolution test apparatus (Model: TDT-08LX, Electrolab India Pvt. Ltd., Mumbai, India). The procedure described earlier in the literature was employed to dissolve HTZ-EWP SD4 formulations (43). Briefly, the phosphate buffer (0.05 M, pH 6.8) dissolution media was used in this study. The dissolution samples of pure HTZ (~50 mg), PM (~50 mg of pure HTZ), or optimized HTZ-EWP SD4 (~50 mg of pure HTZ) were accurately weighed and dispersed into 900 mL of media in a dissolution flask. After dispersing the samples, the contents were stirred at a speed of 100 rpm, and the temperature of the media was maintained at 37 \pm 0.5°C throughout the study. While dissolution, the samples were removed from the flask at an interval of 10 min and filtered using a membrane filter (0.45 μm). At the same time, the sink condition was also maintained by replenishing the media into the flask as equal to that of withdrawing volume from the flask for the entire dissolution study. Filtered samples were suitably diluted and analyzed for HTZ absorbance using a UV-Visible spectrophotometer (Model: V-630, JASCO International Co., Ltd., Tokyo, Japan) wavelength of 271 nm against the blank. The recorded absorbance values for both formulations were

compared and converted into percentage cumulative HTZ release.

Dissolution Efficiency

The DE of pure HTZ and optimized HTZ-EWP SD4 in phosphate buffer (0.05 M, pH 6.8) was estimated using Eq. (2) described earlier in the literature (44).

$$DE = 1 + \frac{\int_{t_1}^{t_2} y \cdot dt}{y_{100} \times (t_2 - t_1)} \times 100 \quad (2)$$

In which y represents the percentage of HTZ dissolved, and DE represents the area under the dissolution curve in between the time points of t_1 and t_2 , and it is expressed in percentage of the curve at maximum dissolution, y_{100} , over the same period. The numerator part of the above equation was calculated using Eq. (3), as shown below.

$$AUC = \sum_{i=1}^{i=n} - \frac{(t_1 - t_i - 1)(Y_i - 1 + Y_i)}{2} \quad (3)$$

In this equation, t_i is the i th time point, and Y_i is the percentage of dissolved HTZ at time t_i . The dissolution software (DDSolver[®]) was employed to calculate and compare DE between the pure HTZ and optimized formulation.

Fasted Versus Fed State Dissolution Comparison

The comparative release pattern of pure HTZ or optimized HTZ-EWP SD4 was also evaluated under the influence of food effect (media) in paddle (USP Type II) dissolution test apparatus (Model: TDT-08LX, Electrolab India Pvt. Ltd., Mumbai, India). The food media, i.e., fasted state simulated intestinal fluid (FaSSIF) and fed state simulated intestinal fluid (FeSSIF), were prepared and used in this study. The procedure for the preparation of media and dissolution studies was followed as per reports published earlier in the literature (45). Briefly, the pure HTZ (~50 mg) or HTZ-EWP SD4 (~50 mg of pure HTZ) was accurately weighed and dispersed into FaSSIF (500 mL) or FeSSIF (1000 mL) media, respectively. The flask content was stirred at 50 rpm, and media temperature was set at 37 \pm 0.5°C. The dissolution studies were carried out for 120 minutes. While dissolution, the samples were pipette out at a set interval of 10 min, diluted suitably, and analyzed for HTZ absorbance using UV-Visible absorbance (Model: V-630, JASCO International Co., Ltd., Tokyo, Japan) at a maximum wavelength of 271 nm for FaSSIF or 315 nm for FeSSIF media against the blank. The final values of absorbance were reported in the percentage cumulative of HTZ release.

Ex Vivo Permeability Studies

The permeation efficiency of pure HTZ, PM (1:6), or optimized HTZ-EWP SD4 across the biological membrane was analyzed using an *everted rat intestine* method. The entire

study was performed on the same kind of apparatus described previously in the literature (46). Moreover, the isolated tissue was everted using a well-established glass-rod procedure reported earlier (47). The Institutional Animal Ethics Committee (IAEC) of Rajarshi Shahu College of Pharmacy, Buldhana, sanctioned the protocol (RSCOP/IAEC/2019-20, dated August 19, 2019). The study was performed under the guidelines provided by the Committee for the Purpose of Control and Supervision of Experiments on Animals (CPCSEA). Briefly, the everted rat intestine membrane with the cross-sectional area ($\sim 5.80 \text{ cm}^2$) and thickness ($\sim 110 \mu\text{m}$) was washed and then mounted carefully between the two tapered ends of the apparatus. After mounting the tissue, the apparatus was filled with freshly prepared Krebs solution and placed in contact with pure HTZ ($\sim 100 \mu\text{g/mL}$), PM ($\sim 100 \mu\text{g/mL}$), or HTZ-EWP SD4 ($\sim 100 \mu\text{g/mL}$) formulations prepared in Krebs solution respectively. The solution was stirred at 50 rpm, temperature maintained at $37 \pm 0.5^\circ\text{C}$, and aerated using carbogen (95% O_2 and 5% CO_2) for 120 min. The samples were removed at a designated time intervals, diluted, and analyzed for HTZ absorbance at a wavelength of 271 nm on UV-Visible spectrophotometry (Model: V-630, JASCO International Co., Ltd., Tokyo, Japan). The recorded absorbance values were calculated and reported in terms of the percentage cumulative of HTZ permeation.

Preliminary Functional Stability Evaluation

The optimized HTZ-EWP SD4 (ratio 1:4) were evaluated functionally (i.e., *in vitro* dissolution and *ex vivo* permeation) under the impact of controlled storage temperature ($25 \pm 5^\circ\text{C}$) as well as relative humidity ($60 \pm 5\%$ RH) conditions for six months. Briefly, the formulations mentioned above were packed in screw-capped, amber-colored glass vials and stored in a temperature and relative humidity controlled stability chamber (Model: TS00002009, Mumbai, Maharashtra, India) for 6 months. After 6 months of storage, the samples were removed and analyzed for functional testes with the same procedure described in previous sections.

RESULTS AND DISCUSSION

Preparation of HTZ-EWP SD

The physicochemical property of HTZ shows that it is a strong lipophilic compound and demonstrates maximum solubility in most of the organic solvents (48). This basic property is used in the current study for the preparation of solid dispersion using lyophilized EWP *via* the kneading method. Previous work has shown the effective use of ethanol as the choice of solvent to prepare solid dispersion using the kneading method (49). The same concept was also utilized in the current work; however, the HTZ and carrier both exhibited low solubility, while dissolution caused precipitation of the product. Moreover, due to the high evaporation rate of ethanol, it forms an immediate dried thick paste of drug and carrier before kneading that results in the failure of preparation of the formulation. This solubility and drying problem was solved by exploring the various combinations of binary solvents, including acetone: ethanol, 1, 4-dioxane: ethanol, propylene glycol: ethanol, and ethanol: water in (1:1) ratio,

respectively. The binary solvents of acetone: ethanol and propylene glycol: ethanol in (1:1) ratio demonstrated good solubility of EWP carrier, and poor solubility of HTZ resulted in precipitation of formulation components. Compared to this, 1, 4-dioxane: ethanol (1:1) displayed fair solubility of HTZ and EWP carrier, indicating that physico-chemical properties of 1, 4-dioxane, and ethanol could interact with each other resulted in improvement of HTZ and EWP solubility. However, the reported toxicity profile of 1, 4-dioxane in humans, its further utilization in the formulation was taken away and explored for other suitable solvents. After this, we tested the ethanol: water solvent system and found that this system in (1:1) ratio enhanced the solubility of formulation components and reduced the drying problem to a great extent caused to the formation of amorphous solid dispersion. It was suggested that semi-polar, class III solvent, and low toxicity profile of ethanol could form strong hydrogen bonding with water solvent and assist in complete solubilization of formulation components, reduced drying problem, and formation of amorphous HTZ-EWP SD. Moreover, Ghareeb *et al.* have also shown the utility of the binary solvent to prepare solid dispersion (50). Hence, we have chosen binary solvent of ethanol: water in (1:1) ratio as an optimal solvent system to prepare HTZ-EWP SD.

Characterization of HTZ-EWP SD

SEM

The surface characterization of pure HTZ, EWP, and optimized HTZ-EWP SD4 is depicted in (Fig. 2a, b, and c), respectively. The particles of pure HTZ (Fig. 2a) appeared as small and large crystals with ill-defined morphological characteristics. The morphology of EWP (Fig. 2b) exhibited small, non-uniform, and amorphous particles with heterogeneous and porous surfaces. The HTZ-EWP SD4 (Fig. 2c) particles appeared as fused particles with the characteristics of large particles of pure HTZ and porous particles EWP suggesting that the complex-forming ability of the EWP could result in the development of fused particles. The formation of such types of particles with the addition of carriers has been reported earlier in the literature (49). This comparison confirms the formation of a solid dispersion of HTZ using the kneading method.

DSC

The solid-state interactions between formulation components are quantitatively investigated by DSC in terms of appearance, disappearance, shifting, or changes in the onset and relative area of the peak concerning heat function. These developed interactions can signify the melting, degradation, glass rubber transitions, and complex formation between the components. The DSC curves of pure HTZ, EWP, the PM (1:6), and optimized HTZ-EWP SD4 are presented (Fig. 3a, b, c, and d) respectively. DSC curve of pure HTZ (Fig. 3a) presented the sharp endothermic peak around $\sim 275.05^\circ\text{C}$, indicates a melting temperature of pure HTZ (51). The DSC curve of EWP (Fig. 3b) shows two broad endothermic peaks around $\sim 88.65^\circ\text{C}$ (high intensity) and $\sim 203.06^\circ\text{C}$ (low intensity), indicates the vaporization of moisture from EWP

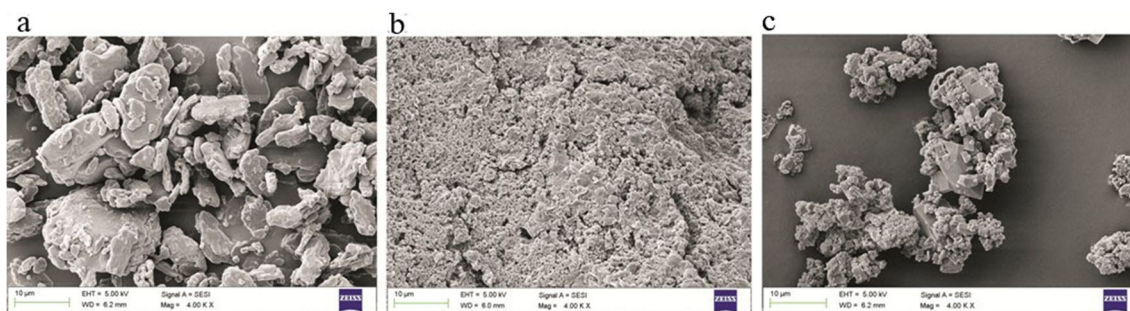


Fig. 2. SEM image of a pure HTZ, b EWP carrier, and c optimized HTZ-EWP SD4

during heating. Findings were consistent with previously published reports (34). EWP also displayed the series of undersized small intensity peaks in the range of $\sim 300^\circ\text{C}$ to 400°C . This is likely due to the thermal degradation of the carrier. PM (Fig. 3c) DSC curve exhibited numerous small and high-intensity endothermic peaks in the range of ~ 50 to 300°C indicates that these peaks corresponded to pure HTZ and EWP. In this curve, the peak intensity of pure HTZ was reduced around $\sim 272.27^\circ\text{C}$ compared to pure drugs. The reduced peak was likely attributed to the possible interaction between HTZ and EWP, as well as a lower amount of drug present in the optimized mixture ratio. Moreover, the EWP peaks were also reduced completely compared to the original DSC curve of EWP suggested that the carrier could interact well with the HTZ resulted in the formation of PM with fewer intensity peaks. Finally, the DSC curve of optimized HTZ-EWP SD4 is shown in (Fig. 3d). It displayed a straight DSC curve with complete disappearance of the sharp melting peak of HTZ indicates that there was a possible amorphization of HTZ due to strong interaction with the EWP (34). These results suggested that the complex-forming ability of the EWP could encapsulate the HTZ into its hydrophobic pocket and form a complex *via* hydrophobic, electrostatic and hydrogen-bonding interactions caused complete molecular dispersion of HTZ within the matrix of the carrier, resulting in amorphization of HTZ with the formation of the amorphous solid dispersion (24, 25). Moreover, the pure HTZ and optimized formulation demonstrated different enthalpy of fusion (ΔH) values, i.e., 116.54 J/g and 19.09 J/g also suggested the formation of the amorphous solid dispersion.

FT-IR

Figure 4a, b, c, and d represents the FT-IR spectrum of pure HTZ, EWP, PM (1:6), and HTZ-EWP SD4, respectively. As seen in (Fig. 4a), the FT-IR spectrum of pure HTZ presented the absorption peaks at ~ 3358.3 , 3281.4 , and $3164.5/\text{cm}$ for (N-H stretching), 2944.8 and $2832.8/\text{cm}$ for ($-\text{CH}_2$ stretching), $1520.8/\text{cm}$ for ($\text{C}=\text{C}$ stretching), $1427.6/\text{cm}$ for (SO_2 asymmetric stretching), 1371.7 – $1315.8/\text{cm}$ for ($\text{N}=\text{C}$ stretching), $1148.0/\text{cm}$ for (aromatic $\text{C}=\text{H}$ stretching), $1068.6/\text{cm}$ for (SO_2 symmetric stretching), $775.3/\text{cm}$ for (benzene ring deformation), and $674.6/\text{cm}$ for (aliphatic $\text{C}=\text{H}$ band). This spectrum was in agreement with earlier published reports (52, 53). FT-IR spectrum of EWP is shown in (Fig. 4b). It displays the absorption peak at $\sim 3257.7/\text{cm}$ for amide I ($\text{N}=\text{H}$ stretching), $1636.3/\text{cm}$ for ($\text{C}=\text{O}$ amide I), and $1528.2/\text{cm}$ for ($\text{C}-\text{N}$ stretch with $\text{N}-\text{H}$ bending mode due to amide II).

Obtained carrier peaks are well justified with earlier reports (54–56). FT-IR spectrum of PM is shown in (Fig. 4c). It exhibits the additive absorption peaks at $\sim 3358.3/\text{cm}$, $3261.4/\text{cm}$, $3164.5/\text{cm}$, $2944.6/\text{cm}$, $1528.2/\text{cm}$, and $1636.1/\text{cm}$ of pure HTZ as well as EWP indicates strong physico-chemical interaction between the HTZ and EWP. These results also suggested the physical mixing of both ingredients could generate the close associated mixture, which results in the formation of the spectrum with a combination of peaks. As compared to PM, the HTZ-EWP SD4 (Fig. 4d) showed a completely different FT-IR spectrum. It displayed shifting of peaks around $\sim 3265.1/\text{cm}$, $3168.2/\text{cm}$, and $2940.9/\text{cm}$ from $3281.4/\text{cm}$, $3164.2/\text{cm}$, and $2944.6/\text{cm}$ in pure HTZ and PM spectrum.. These absorption peak changes in HTZ-EWP-SD4 were likely attributed to weak intermolecular forces of interaction (hydrogen bonding and van der Waals interactions) between pure HTZ and EWP results in solid dispersion formation (25). Therefore, the above comparison concluded that the weak intermolecular forces of interaction between the HTZ and EWP might be liable for the formation of the HTZ-EWP-SD.

PXRD

The crystalline properties of pure HTZ, EWP, PM (1:6), and HTZ-EWP SD4 were determined using the PXRD diffractometer, and their spectrums are shown in (Fig. 5a–d). Diffraction pattern of pure HTZ (Fig. 5a) exhibited the sharply-pointed peaks at $\sim 16.67^\circ$, 19.51° , 20.98° , 21.51° , 24.69° , 28.15° , 28.90° , 33.59° , and 35.97° on 2θ scale. The intensity (counts on the y-axis) of these peaks appeared around ~ 1250 , 1300 , 1050 , 750 , 650 , 350 , 600 , and 300 , respectively, indicates the crystalline nature of pure HTZ. Results were consistent with findings reported earlier (52). EWP diffraction pattern (Fig. 5b) showed the absence of sharp peaks. However, few undersized peaks were detected in the range of $\sim 25^\circ$ – 35° on the 2θ scale. The intensity of these peaks appeared at ~ 150 , 180 , and 100 , respectively. The appearance of such types of peaks suggesting that EWP has an amorphous character. This spectrum was similar to earlier published literature (35). PM diffraction pattern is shown in (Fig. 5c). This spectrum revealed a combination of peaks corresponding to pure HTZ and EWP. However, the number and intensity of peaks of HTZ were reduced compared to pure HTZ. The reduced number of peaks was likely attributed to drug amorphization. In contrast, the peak intensity was reduced due to a lower amount of HTZ in the formulation ratio. Moreover, the peak/height intensity in

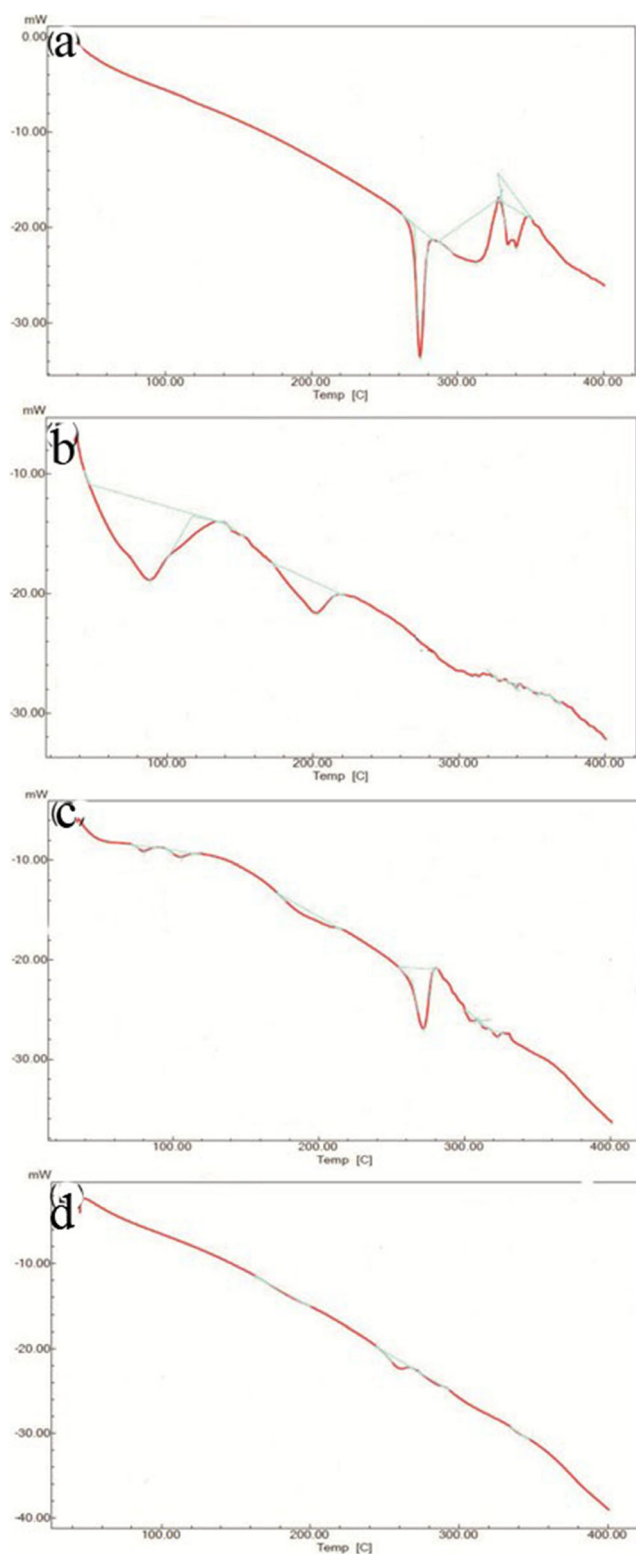


Fig. 3. DSC thermograms of a pure HTZ, b EWP carrier, c PM of HTZ: EWP (1:6), and d optimized HTZ-EWP SD4

between the region of 15° to 30° and 31° to 35° for pure HTZ and EWP were reduced around ~ 600 , 450 , 580 , 300 , 380 , 300 , 100 , and 50 counts, respectively, compared to the original spectrum indicates interaction between HTZ and EWP. (Fig.

5d) shows the diffraction pattern of HTZ-EWP SD4. It revealed peaks similar to that of the diffraction pattern of PM. Although peaks similar to PM, the intensity of retained peaks in the formulation spectrum was reduced significantly around ~ 500 , 420 , 470 , 250 , and 300 compared to pure HTZ and PM. Moreover, some crystalline peaks of HTZ were still noticed even after reduced its peak intensity indicating that HTZ crystalline form existed in the solid dispersion. These results may be explained by the fact that HTZ could disperse as separated crystals instead of molecularly dispersed form in the matrix of EWP, resulting in partial amorphization of HTZ. It was also suggested that non-covalent interactions (i.e., hydrophobic, electrostatic, and hydrogen-bonding interactions) between EWP and HTZ could dispersing HTZ as separated crystals within the matrix of EWP, reduced its partial crystallinity, results in the formation of the solid dispersion (24, 25, 34). Thus, the partial amorphization of HTZ due to the complex forming ability of the EWP confirmed the formation of the solid dispersion.

Determination of Drug Content

Table I shows the content of HTZ in the prepared HTZ-EWP SD formulations. The HTZ-EWP SD4 in the ratio of 1:6 shows the higher HTZ content around $\sim 94.89 \pm 1.54$ % w/w. Other formulations, i.e., HTZ-EWP SD1, SD2, SD3, and SD5 in the ratios of 1:1, 1:2, 1:4, and 1:8 exhibits lower HTZ content around $\sim 88.65 \pm 1.39$, 90.12 ± 1.30 , 91.49 ± 1.75 , and 92.28 ± 0.51 % w/w respectively. The HTZ-EWP SD4 (1:64) was considered optimized formulations and used for remaining characterization studies based on the drug content values. Additionally, it was also suggested that the lyophilized EWP carrier and kneading method are thought to be an appropriate and robust approach for preparing EWP-based solid dispersion with a high content of HTZ.

Saturation Solubility Studies

Pure HTZ, PM, and HTZ-EWP SD formulations were analyzed for solubility analysis, and their results are presented in Table II. Pure HTZ demonstrated low aqueous solubility around ~ 0.51 mg/mL, which indicates poor water solubility and low permeability of the HTZ, i.e., it is categorized into BCS class IV drug (57). Compared to this, all PMs exhibited some improvement in the aqueous solubility of HTZ, and their solubility range was found to be ~ 0.67 to ~ 2.01 mg/mL. These values demonstrate about ~ 4 -fold increase in the aqueous solubility of HTZ. The statistical significance of this improvement was ($p < 0.05$). It has been observed that, when the EWP ratios increased from 1:1 to 1:6, the PM formulations showed an improvement in the aqueous solubility of HTZ, suggesting that physical mixing may cause to increase in the interaction between HTZ and EWP, which could lead to slightly modify the crystalline properties of the HTZ resulting to enhance the solubility of HTZ in the PM. Moreover, the final PM with an EWP ratio of 1:8 displayed lower aqueous solubility of HTZ, suggesting that a large amount of EWP particles could restrict HTZ particle's access into the aqueous media which could result in a lowering of aqueous solubility of HTZ. The HTZ-EWP SD formulations showed a significant improvement in the aqueous solubility of

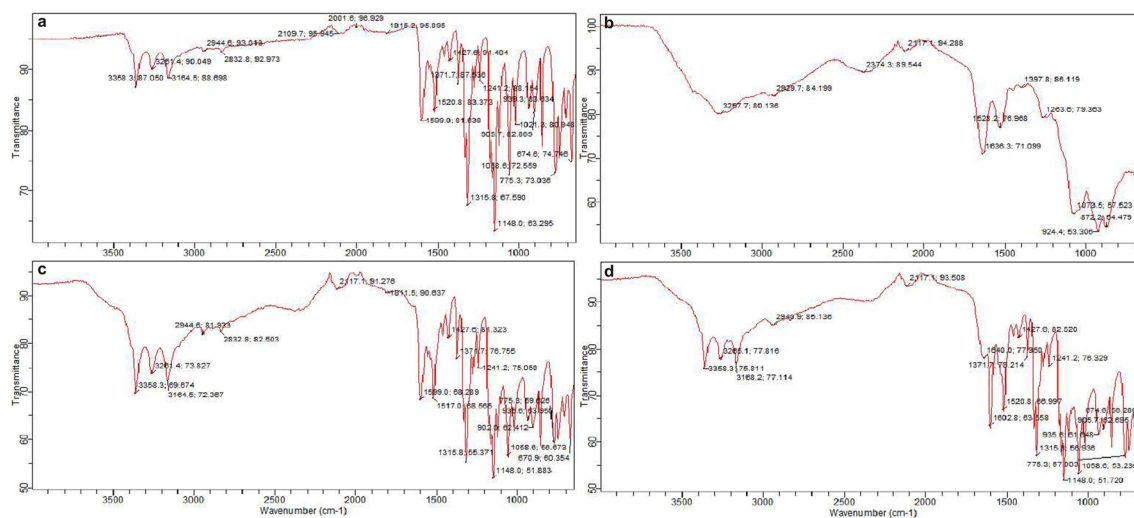


Fig. 4. FT-IR spectra of **a** pure HTZ, **b** EWP carrier, **c** PM of HTZ: EWP (1:6), and **d** optimized HTZ-EWP SD4

HTZ, and their range was found to be ~ 9.24 to ~ 16.12 mg/mL. Despite the crystalline form of HTZ exists in the solid dispersion as reflected in the PXRD spectrum, the optimized HTZ-EWP SD4 significantly ($p < 0.01$) improved the aqueous solubility of HTZ about ~ 32 -fold, and its value was appeared to be ~ 16.12 mg/mL compared to pure HTZ and PM, suggesting that, when HTZ entered into the hydrophobic pocket of EWP *via* hydrophobic interactions formed inadequate hydrogen bonding interaction with the available binding sites of EWP and complete interaction with the binding sites of ovomucin (another water-soluble protein in EWP also responsible for complex formation and improve drug water solubility), caused to absolute change in the secondary structure of EWP with the formation of the stable water-soluble complex resulting in significant improvement of HTZ-EWP SD4 aqueous solubility (24, 25, 29, 30). It was also suggested that the employed higher amount of EWP (1:6) in an optimized HTZ-EWP SD4 could act as a surfactant and thus assist in enhancing an aqueous solubility of HTZ (31–34). Thus, it can be concluded that hydrophobic and hydrogen bonding interaction between HTZ, EWP, and ovomucin could be accountable for enhancing HTZ aqueous solubility.

In Vitro Drug Release Dissolution Studies

The comparative dissolution release of HTZ from pure HTZ, PM (1:6), and optimized HTZ-EWP SD4 is shown in (Fig. 6). The pure HTZ at the end of the 120 min dissolution period released only $\sim 25\%$ of the drug in dissolution media. It could be attributed to its low water solubility, which was also reflected in the tested solubility study. Compared to this, the PM demonstrated a higher rate and extent of drug release, around $\sim 35\%$ at the end of the 120 min dissolution period. This small improvement might be attributed to HTZ and EWP's close association that may cause the formation of a partial water-soluble complex with an improved dissolution rate of HTZ. Despite crystalline HTZ existence in the prepared solid dispersion, an optimized HTZ-EWP SD4 displayed the higher rate and extent of release of HTZ compared to pure HTZ and PM. The formulation exhibited

around $\sim 87\%$ of HTZ released by the end of the release period. These findings suggested that the use of EWP, the kneading method, and water solvent could enhance the dissolution rate of HTZ in the dissolution media. These results indicated that the hydrophilic property of EWP allowed encapsulating the HTZ into its hydrophobic cavity through hydrophobic interactions, and then HTZ may form inadequate hydrogen bonding interaction with the available binding sites of EWP and complete interaction with the known binding sites of ovomucin, lead to a change in the conformation of the secondary structure of EWP, which resulted in noteworthy enhancement of solubility and dissolution rate of HTZ (24, 29, 30). The enhanced dissolution rate of HTZ-EWP SD4 could be attributed to a higher amount of lyophilized EWP in the ratio (1:6), which may entirely encapsulate the small amount of HTZ *via* hydrophobic and hydrogen bonding interaction producing water-soluble complex and subsequently improves the dissolution rate of HTZ and the results are consistent with earlier published reports (34). The reported surfactant property of EWP may also improve HTZ aqueous solubility (31–33). Moreover, the partial amorphization of HTZ due to the complex forming ability of EWP could also increase the dissolution rate of HTZ (58). The lyophilized particles of the EWP could prevent the particles aggregation and inhibit the crystal growth of drug particles and thereby increases the dissolution rate of drugs (59). The complex-forming ability of the EWP with HTZ may also enclose the drug within the matrix of EWP and cause to inhibit the aggregation of drug particles. This interaction increases the surface area of particles with rapid contact with dissolution media; ultimately, improve the wetting of particles and, subsequently, the dissolution rate of the drug (60). The solubilizing effect of EWP could also enhance the dissolution rate of the drug (61). The improved wettability of drugs *via* amorphization could also improve drug dissolution rate (62). The kneading method is also known to modify the size and shape of the drug crystals during formulation. It may cause to amorphization of drug crystals with an increase in its surface area and thereby increase the dissolution rate of the drug from the solid dispersion (35). Moreover, the water solvent is reported to

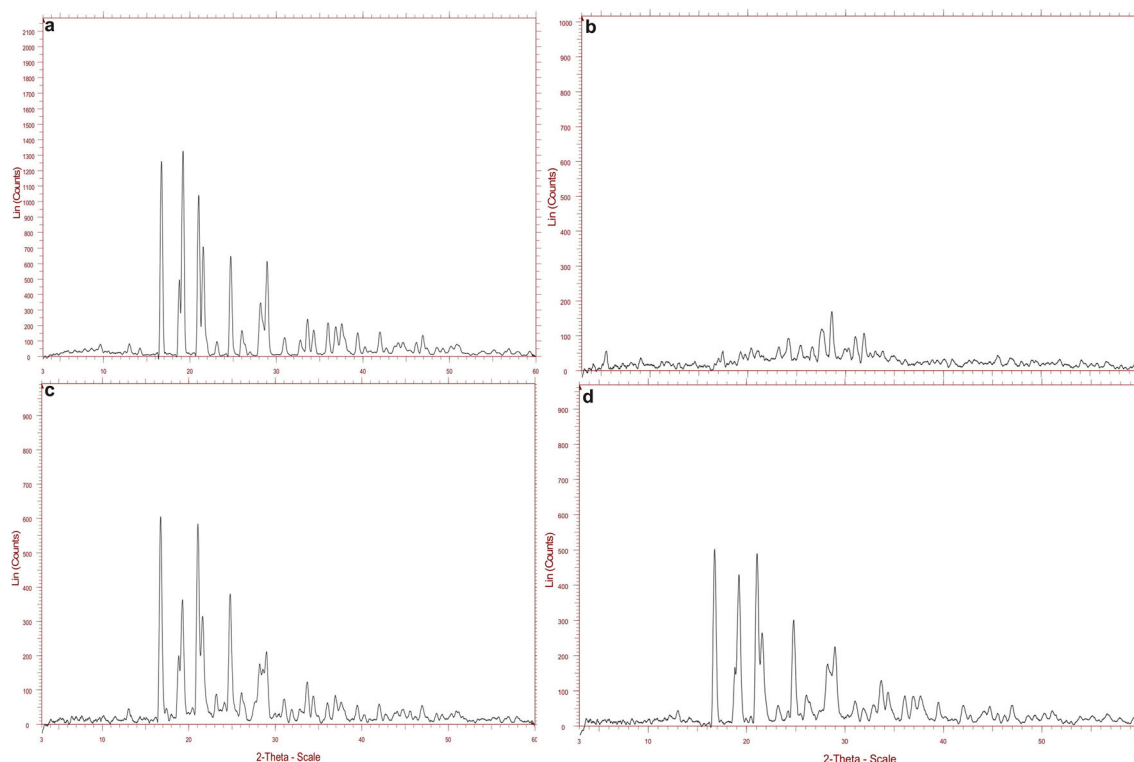


Fig. 5. PXRD pattern of **a** pure HTZ, **b** EWP carrier, **c** PM of HTZ: EWP (1:6), and **d** optimized HTZ-EWP SD4

form hydrogen bonding with the polar groups of drugs and carriers during formulation. It could also help in enhancing the dissolution rate of the drug. Additionally, the HTZ may form strong intermolecular bonding with EWP and change the physico-chemical properties of both these compounds results in significant enhancement of drug dissolution (63). The dissolution and release mechanism of HTZ from optimized formulation was determined by fitting the obtained release data into various kinetic models and analyzed (64). After analysis, the optimized HTZ-EWP SD4 exhibited a higher correlation coefficient value ($R^2 = 0.9840$) for the Higuchi model compared to zero-order ($R^2 = 0.9450$) and

first-order ($R^2 = 0.9230$), indicates that Higuchi is the best-fit model for the dissolution mechanism of the optimized formulation. Additionally, the same formulation showed a release exponent value ($n = 0.49$), suggesting diffusion is the primary mechanism for the release of HTZ from HTZ-EWP SD4.

Dissolution Efficiency

The DE value for pure HTZ was appeared to be $6.74 \pm 0.19\%$. PM (1:6) exhibited a somewhat higher DE value, and it was found to be around $\sim 20.66 \pm 1.42\%$. Compared to this, the DE value for optimized HTZ-EWP SD4 was found to be $\sim 57.12 \pm 1.60\%$ suggests that improved aqueous solubility of HTZ in lyophilized EWP carrier could enhance the DE of optimized HTZ-EWP SD4 compared to pure HTZ and PM, respectively.

Table II. Solubility Data of Pure HTZ, the Physical Mixture (PM) of Pure HTZ and EWP Carrier, and HTZ-EWP SD Formulations

Formulations	Aqueous solubility (mg/mL)*
Pure HTZ	0.51 ± 0.02
PM-1	0.67 ± 0.08
PM-2	0.74 ± 0.05
PM-3	1.39 ± 0.03
PM-4	2.01 ± 0.08
PM-5	1.10 ± 0.04
HTZ-EWP SD1	9.24 ± 0.05
HTZ-EWP SD2	12.65 ± 0.02
HTZ-EWP SD3	14.20 ± 0.06
HTZ-EWP SD4	16.12 ± 0.02
HTZ-EWP SD5	14.11 ± 0.08

Pure HTZ, pure hydrochlorothiazide; PM, physical mixture; HTZ-EWP SD, hydrochlorothiazide-egg white protein solid dispersion
*Data expressed as mean \pm Std. Dev.; ($n = 3$)

Fasted Versus Fed State Dissolution Comparison

The effect of fasted *versus* fed state on the comparative *in vitro* dissolution performance of pure HTZ and optimized HTZ-EWP SD4 formulations is illustrated in (Fig. 7). The dissolution rate of pure HTZ in the FaSSIF state was appeared to be only $\sim 26\%$, while the same drug in the FeSSIF state demonstrated the dissolution of the HTZ around $\sim 36\%$ by the end of 120 min dissolution testing, suggesting the food content could have promoted the release of the drug in the media. In response to this, the optimized HTZ-EWP SD4 exhibits a higher rate and extent of dissolution in the fed and fasted state. However, on close observation, it was found that the optimized formulations in the FeSSIF state enhanced the dissolution of HTZ around \sim

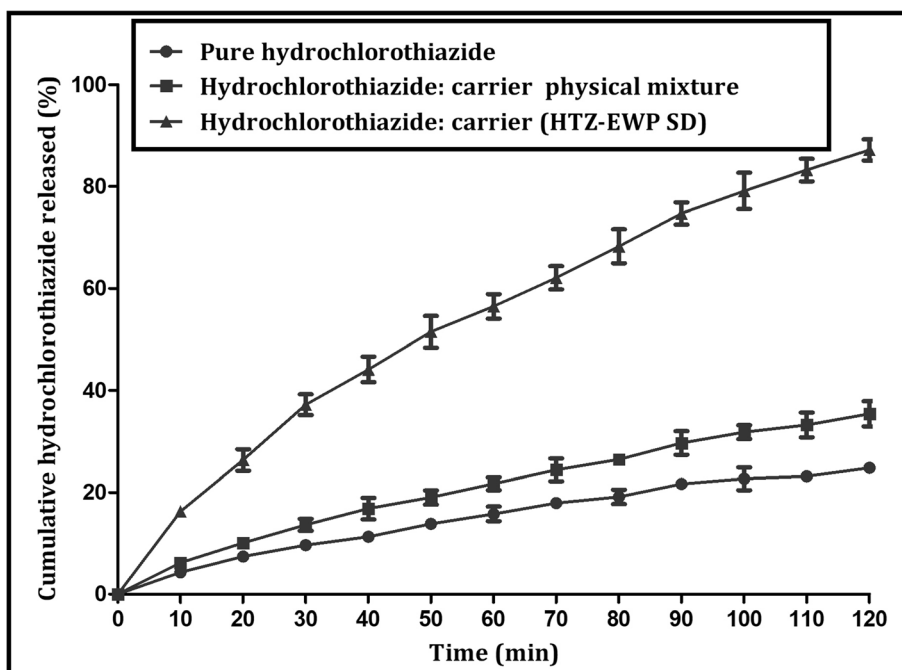


Fig. 6. *In vitro* dissolution profile of pure HTZ, the PM and optimized HTZ-EWP SD4

86% compared to lower dissolution around ~ 72% by the same formulation in the FaSSIF state at the end of dissolution testing. This result suggested the positive effect of food significantly increases the rate and extent of dissolution of drugs, and this finding was in agreement with earlier reports (45, 63). While dissolution, the formation of taurocholate-HTZ micelles and taurocholate-EWP-HTZ micelles in the FeSSIF state could have enhanced the dissolution rate HTZ from prepared HTZ-EWP SD4 (65). This concludes that food condition increases the dissolution rate of the pure drug and formulations.

Ex Vivo Permeability Studies

Figure 8 describes the permeation behavior of HTZ from pure HTZ, PM (1:6), and optimized HTZ-EWP SD4 in Krebs solution for 120 min. Initially, in the first 60 min, the permeation rate of pure HTZ was ~ 12%, and after that, it permeated only ~ 24% at the end of 120 min. This lower permeation could be attributed to the poor membrane permeability of HTZ ($\log P = -0.15$) (3). The PM demonstrated a higher rate and extent of HTZ permeation over to that of pure HTZ. The PM exhibited around ~ 20% of HTZ

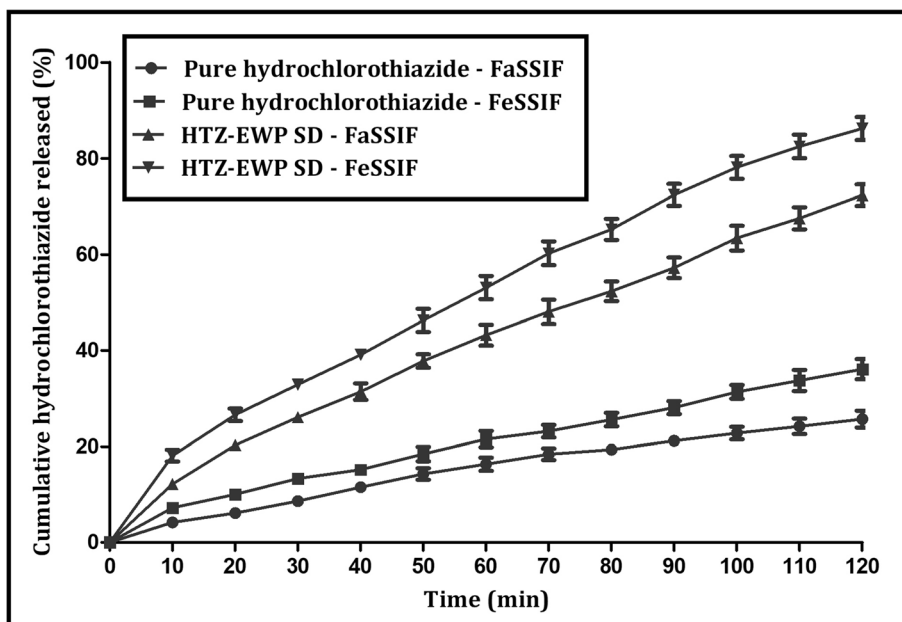


Fig. 7. Comparative *in vitro* dissolution profile of pure HTZ and optimized HTZ-EWP SD4 in "FaSSIF" and "FeSSIF" dissolution media

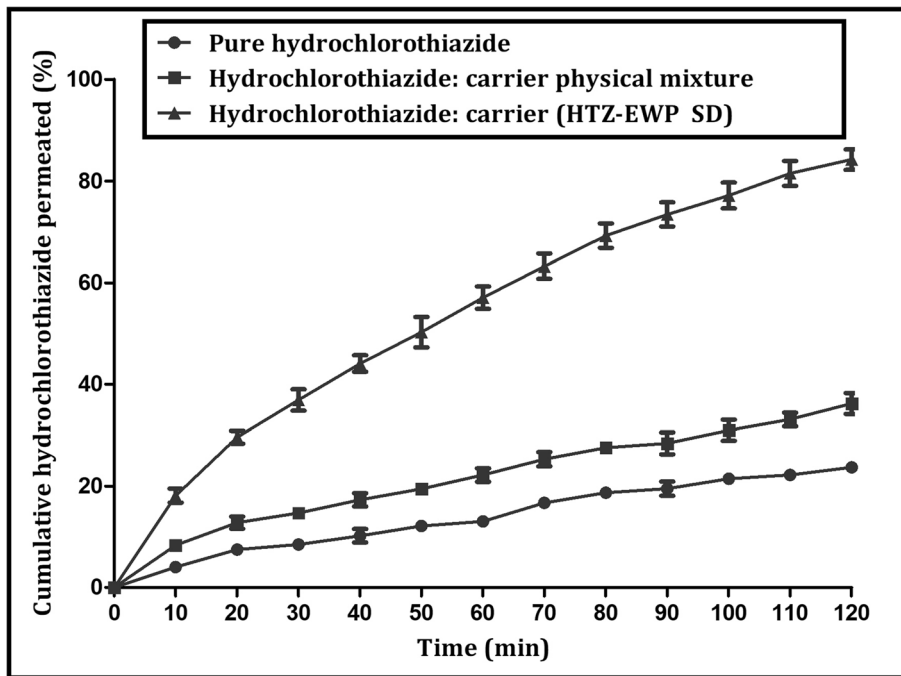


Fig. 8. *Ex vivo* permeability profile of pure HTZ, the PM and optimized HTZ-EWP SD4

permeation by the end of 60 min, and then it slowly enhanced the permeation rate around ~ 36% over the same testing period. In contrast to this, the permeation rate of optimized HTZ-EWP SD4 (ratio 1:6) at the end of 60 min was observed to be only ~ 50%; however, after this period, the same formulation showed continuous permeation and reached maximum permeation of HTZ around ~ 84% by the end of

120 min. This enhanced permeation rate of HTZ from optimized HTZ-EWP SD4 was likely attributed to EWP carrier, which can act as same protein to that of amphiphilic membrane protein of biological membrane could form covalent and noncovalent interactions with the carrier which in turn, show higher miscibility and thereby, increase the permeation rate of the drug across the biological membrane

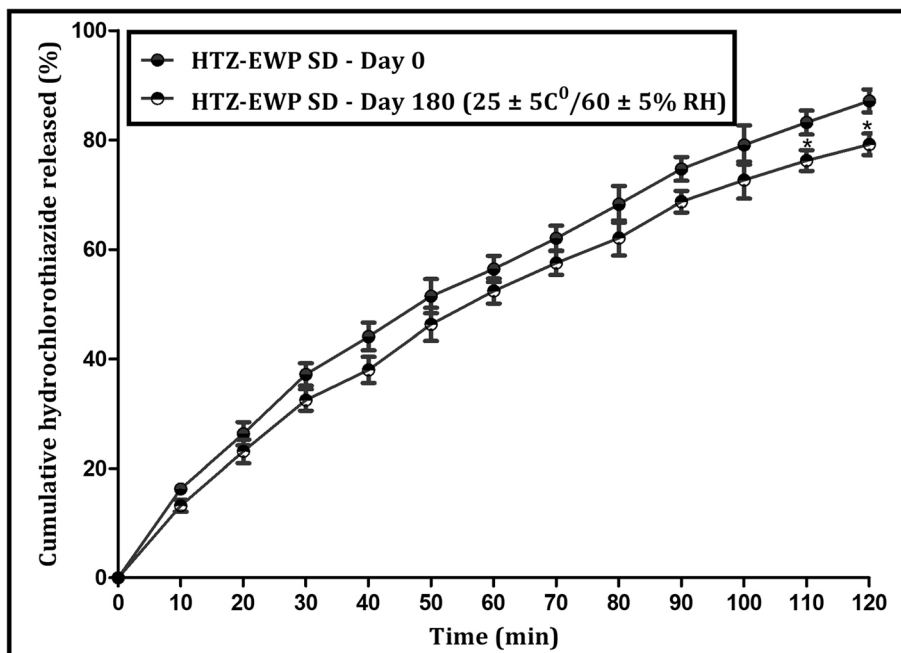


Fig. 9. Comparison of *in vitro* dissolution profile of optimized HTZ-EWP SD4 before and after six month storage at 25 ± 5°C/60 ± 5% RH

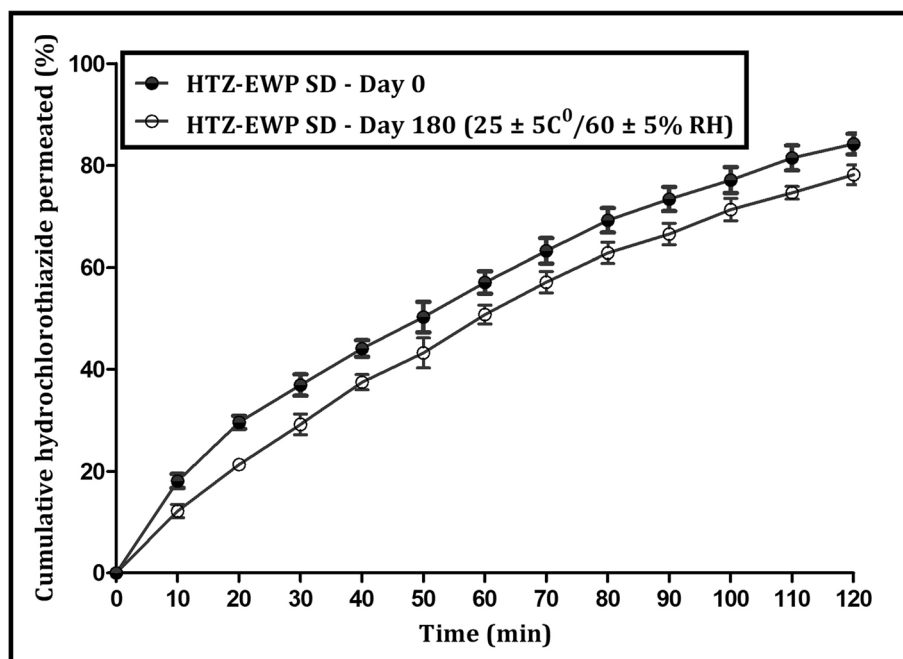


Fig. 10. Comparison of *ex vivo* permeability profile of optimized HTZ-EWP SD4 before and after six month storage at $25 \pm 5^\circ\text{C}/60 \pm 5\% \text{RH}$

(66). The reported amphiphilic and emulsifying property of EWP forms a continuous membrane around the small size droplets *via* molecular interactions and contributes towards rapid permeation and absorption (67–69). In conclusion, the interaction forming ability of EWP with membrane protein could be responsible for increasing the miscibility and permeation of HTZ across the biological membrane.

Preliminary Functional Stability Evaluation

Figures 9 and 10 depict the influence of controlled temperature and relative humidity on the *in vitro* dissolution and *ex vivo* permeation of HTZ from stored (at day 180) optimized HTZ-EWP SD4. As seen in (Fig. 9), the release pattern of stored HTZ-EWP SD4 (at day 180) was found to be reduced significantly at the end of the 110 and 120 min dissolution period compared to the initial HTZ-EWP SD4 (at day 0). Their level of significance was observed to be ($p < 0.05$). Moreover, on close observation, it was found that the stored formulation at day180 decreased the rate and extent of HTZ release by around ~ 80% compared to the initial formulation HTZ release of around ~ 87%. *Ex vivo* permeation is another crucial functional parameter that was also assessed under the influence of storage conditions, and their results are shown in (Fig. 10). At the end of the 120 min permeation period, the initial and stored formulation at days 0 and 180 demonstrated a parallel permeation rate of HTZ without any significant difference. However, on close examination of data, it was observed that the stored formulation at day 180 permeated only ~ 78% of HTZ over to that of initial formulation at day 0 permeation around ~ 84% of HTZ. The possible reason for the lowering of the dissolution and permeation rate of HTZ from stored optimized formulation at day 180 was likely due to the impact of relative humidity and some other unclear factors. Therefore, some extra

characterization studies are required to be carried out on stored formulation to better understand the mechanism of storage conditions.

CONCLUSION

In this work, the feasibility of EWP as a solid dispersion carrier for enhancing the solubility and permeability of HTZ, BCS class IV drug was explored successfully. The HTZ-EWP SD was developed using the kneading method. Preparation of solid dispersion suggested that binary solvent (ethanol: water) in a 1:1 ratio formed the stable and amorphous solid dispersion. Physico-chemical characterization studies suggested the formation of a water-soluble solid dispersion *via* the contribution of hydrophobic and hydrogen bonding interactions. Solubility study suggested that HTZ-EWP SD4 (ratio 1:6) significantly enhanced the solubility of HTZ compared to pure HTZ and PM. *In vitro* dissolution and *ex vivo*, permeation results suggested that optimized HTZ-EWP SD4 enhanced the rate and extent of HTZ dissolution and permeation compared to pure HTZ and PM. The fed vs. fasted dissolution study showed that optimized HTZ-EWP SD4 significantly enhanced the rate and extent of HTZ dissolution in the fed state compared to the fasted state. Under the influence of storage conditions, the HTZ-EWP SD4 was stable and robust; however, at the end of the six months study, the storage conditions have reduced the dissolution and permeation rate either of drug and formulation to some extent. The unclear reason affecting this is still under investigation, and hence, some extra physico-chemical studies must be required to study the stability samples in detail. In conclusion, the obtained results have suggested that the development of HTZ solid dispersion using a lyophilized EWP carrier can be employed as a promising strategy for enhancing BCS class IV drugs solubility and permeability.

ACKNOWLEDGEMENTS

The corresponding author would like to thank Dr. Shirish P. Jain, Principal, Rajarshi Shahu College of Pharmacy, Buldhana, for the technical support to submit this manuscript.

DECLARATIONS

Conflict of Interest The authors declare that they have no conflict of interest.

REFERENCES

- Mendes C, Buttchevitz A, Kruger JH, *et al.* Self-nanoemulsified drug delivery system of HTZ for increasing dissolution rate and diuretic activity. *AAPS PharmSciTech*. 2017;18(7):2494–504. <https://doi.org/10.1208/s12249-017-0735-z>.
- Larbi OC, Merine H, Ramli Y, *et al.* Enhancement of the dissolution profile of the diuretic HTZ by elaboration of microspheres. *J Serb Chem Soc*. 2018;83(11):1243–59. <https://doi.org/10.2298/JSC171112065L>.
- Chadha R, Bhandari S, Kataria D, Gupta G, Jain DS. Exploring the potential of lecithin/chitosan nanoparticles in enhancement of antihypertensive efficacy of hydrochlorothiazide. *J Microencapsul*. 2012;29(8):805–12. <https://doi.org/10.3109/02652048.2012.692399>.
- Barbhaiya RH, Craig WA, Corrick-West P, Welling PG. Pharmacokinetics of hydrochlorothiazide in Fasted and Nonfasted Subjects: A Comparison of Plasma Level and Urinary Excretion Methods. *J Pharm Sci*. 1982;71(2):245–8. <https://doi.org/10.1002/jps.2600710226>.
- Patel RB, Patel UR, Rogge MC, Shah VP, Selen A, Welling PG. Bioavailability of hydrochlorothiazide from tablets and suspensions. *J Pharm Sci*. 1984;73(3):359–61. <https://doi.org/10.1002/jps.2600730317>.
- Yu LX, Amidon GL, Polli JE, *et al.* Biopharmaceutics classification system: the scientific basis for biowaiver extensions. *Pharm Res*. 2002;19(7):921–5. <https://doi.org/10.1023/a:1016473601633>.
- Yadav PS, Yadav E, Verma A, Amin S. Development, characterization, and pharmacodynamic evaluation of hydrochlorothiazide loaded self-nanoemulsifying drug delivery systems. *Sci World J*. 2014;1–10. <https://doi.org/10.1155/2014/274823>.
- Vervae C, Baert L, Remon JP. Enhancement of in vitro drug release by using polyethylene glycol 400 and PEG-40 hydrogenated castor oil in pellets made by extrusion/spheronisation. *Int J Pharm*. 1994;108:207–12. [https://doi.org/10.1016/0378-5173\(94\)90129-5](https://doi.org/10.1016/0378-5173(94)90129-5).
- Vervae C, Remon JP. Bioavailability of hydrochlorothiazide from pellets, made by extrusion/spheronization, containing polyethylene glycol 400 as a dissolution enhancer. *Pharm Res*. 1997;14(11):1644–6. <https://doi.org/10.1023/A:1012151006742>.
- Pires MAS, dos Santos RAS, Sinisterra RD. Pharmaceutical composition of HTZ: β -cyclodextrin: preparation by three different methods, physico-chemical characterization, and in vivo diuretic activity evaluation. *Molecules*. 2011; 16:4482–4499. <https://doi.org/10.3390/molecules16064482>.
- Altamimi MA, Elzayat EM, Alhowyan AA, Alshehri S, Shakeel F. Effect of β -cyclodextrin and different surfactants on solubility stability, and permeability of hydrochlorothiazide. *J Mol Liq*. 2018;250:323–8. <https://doi.org/10.1016/j.molliq.2017.12.006>.
- Kadam Y, Yerramilli U, Bahadur A, Bahadur P. Micelles from PEO-PPO-PEO block copolymers as nanocontainers for solubilization of a poorly water soluble drug hydrochlorothiazide. *Colloids Surf B: Biointerfaces*. 2011;83:49–57. <https://doi.org/10.1016/j.colsurfb.2010.10.041>.
- Sangeetha E, Rao VU, Sudhakar M, Manisha S. Enhancement of solubility and bioavailability of hydrochlorothiazide using solid dispersion technique. *American J Adv Drug Deli*. 2015;3:308–16.
- Mendes C, Buttchevitz A, Kruger JH, *et al.* Chitosan microencapsulation of the dispersed phase of an O/W nanoemulsion to hydrochlorothiazide delivery. *J of Microemulsion*. 2017;34:611–22. <https://doi.org/10.1080/02652048.2017.1373155>.
- Karavas E, Georarakis E, Sigalas MP, Avgoustakis K, Bikiaris D. Investigation of the release mechanism of a sparingly water-soluble drug from solid dispersions in hydrophilic carriers based on physical state of drug, particle size distribution and drug-polymer interactions. *Eur J Pharm Biopharm*. 2007;66:334–47. <https://doi.org/10.1016/j.ejpb.2006.11.020>.
- Bikiaris D, Papageorgiou GZ, Stergiou A, *et al.* Physicochemical studies on solid dispersions of poorly water-soluble drugs Evaluation of capabilities and limitations of thermal analysis techniques. *Thermochim Acta*. 2005;439:58–67. <https://doi.org/10.1016/j.tca.2005.09.011>.
- Al-Hamidi H, Edwards AA, Mohammad MA, Nikhodchi A. To enhance the dissolution rate of poorly water-soluble drugs: glucosamine hydrochloride as a potential carrier in solid dispersion formulations. *Colloids Surf B: Biointerfaces*. 2010;76(1):170–8. <https://doi.org/10.1016/j.colsurfb.2009.10.030>.
- Chiou WL, Riegelman S. Pharmaceutical applications of solid dispersion systems. *J Pharm Sci*. 1971;60:1281–302. <https://doi.org/10.1002/jps.2600600902>.
- Serajuddin ATM. Solid dispersion of poorly water soluble drugs: Early promises, subsequent problems, and recent breakthroughs. *J Pharm Sci*. 1999;88(10):1058–66. <https://doi.org/10.1021/js9804031>.
- Huang YG, Dai. Fundamental aspects of solid dispersion technology for poorly soluble drugs. *Acta Pharm Sin B*. 2014;4(1):18–25. <https://doi.org/10.1016/j.apsb.2013.11.001>.
- Vasconcelos T, Sarmento B, Costa P. Solid dispersions as a strategy to improve oral bioavailability of poor water soluble drugs. *Drug Discov Today*. 2007;12:1068–75. <https://doi.org/10.1016/j.drudis.2007.09.005>.
- Kovacs-Nolan JKN, Phillips M, Mine Y. Advances in the value of eggs and egg components for human health. *J Agric Food Chem*. 2005;53:8421–31. <https://doi.org/10.1021/jf050964f>.
- Huntington JA, Stein PE. Structure and properties of ovalbumin. *J Chromatogr B Biomed Sci Appl*. 2001;756:189–98. [https://doi.org/10.1016/S0378-4347\(01\)00108-6](https://doi.org/10.1016/S0378-4347(01)00108-6).
- Liu Y, Cai Y, Ying D, Fu Y, Xiong Y, Le X. Ovalbumin as a carrier to significantly enhance the aqueous solubility and photostability of curcumin: Interaction and binding mechanism study. *Int J Biol Macromol*. 2018; 116:893–900. <https://doi.org/10.1016/j.ijbiomac.2018.05.089>.
- Chen Y, Hu J, Yi X, Ding B, Sun W, Yan F, *et al.* Interactions and emulsifying properties of ovalbumin with tannic acid. *LWT Food Sci Technol*. 2018;95:282–8. <https://doi.org/10.1016/j.lwt.2018.04.088>.
- Jia W, Cui B, Ye T, Lin L, Zheng H, Yan X, *et al.* Phase behavior of ovalbumin and carboxymethylcellulose composite system. *Carbohydr Polym*. 2014;109:64–70. <https://doi.org/10.1016/j.carbpol.2014.03.026>.
- Li Z, Kuang H, Yang J, Hu J, Ding B, Sun W, *et al.* Improving emulsion stability based on ovalbumin-carboxymethyl cellulose complexes with thermal treatment near ovalbumin isoelectric point. *Sci Rep*. 2020;10:34–56. <https://doi.org/10.1038/s41598-020-60455-y>.
- He W, Tan Y, Tian Z, Chen L, Hu F, Wu W. Food protein-stabilized nanoemulsions as potential delivery systems for poorly water-soluble drugs: preparation, in vitro characterization, and pharmacokinetics in rats. *Int J Nanomedicine*. 2011;6:521–33. <https://doi.org/10.2147/IJN.S17282>.
- Omana DA, Wang J, Wu J. Co-extraction of egg white proteins using ion-exchange chromatography from ovomucin-removed egg whites. *J Chromatogr B*. 2010;878:1771–6. <https://doi.org/10.1016/j.jchromb.2010.04.037>.
- Hiidenhovi J, Aro HS, Kankare V. Separation of ovomucin subunits by gel filtration: enhanced resolution of subunits by

- using a dual-column system. *J Agric Food Chem*. 1999;47:1004–8. <https://doi.org/10.1021/jf9811774>.
31. Iqbal S, Batool J, Ajaz M, Ambree N, Akhlaq M. Impact of egg white protein on the quality and stability of corn oil-in-water emulsion. *J Chem Soc Pak*. 2017;39:911–8.
 32. Wang S, Marcone MF, Barbut S, Lim L-T. Fortification of dietary biopolymers-based packaging material with bioactive plant extracts. *Food Res Int*. 2012;49:80–91. <https://doi.org/10.1016/j.foodres.2012.07.023>.
 33. Baloch MK, Hameed G, Iqbal S, Bano A, Rehman W. Extension of the Taylor equation for oil-water surfactant system and investigating the impact of surfactant concentration over the quality of emulsion. *J Dispers Sci Technol*. 2011;32:498–506. <https://doi.org/10.1080/01932691003756845>.
 34. Imai T, Saito Y, Matsumoto H, Satosh T, Otagiri M. Influence of egg albumin on dissolution of several drugs. *Int J Pharm*. 1989;53:7–12. [https://doi.org/10.1016/0378-5173\(89\)90355-4](https://doi.org/10.1016/0378-5173(89)90355-4).
 35. Imai T, Nohdoi K, Acarturk F, Otagiri M. Enhancement of dissolution and absorption of mefenamic acid by egg albumin. *J Pharm Sci*. 1991;80:484–7. <https://doi.org/10.1002/jps.2600800517>.
 36. Li CP, Salvador AS, Ibrahim HR, Sugimoto Y, Aoki T. Phosphorylation of egg white proteins by dry-heating in the presence of phosphate. *J Agric Food Chem*. 2003;51:6808–15. <https://doi.org/10.1021/jf030043+>.
 37. Zhou B, Zhang M, Fang Z, Liu Y. A combination of freeze drying and microwave vacuum drying of duck egg white protein powders. *Drying Tech*. 2014;32:1840–7. <https://doi.org/10.1080/07373937.2014.952380>.
 38. Telange DR, Bhagat SB, Patil AT, Umekar MJ, Pethe AM, Raut NA. Glucosamine HCl-based solid dispersions to enhance the biopharmaceutical properties of acyclovir. *J Excipients and Food Chem*. 2019;10(3):65–81.
 39. Telange DR, Sohail NK, Hemke AT, Kharkar PS, Pethe AM. Phospholipids complex – loaded self-assembled phytosomal soft nanoparticles: evidence of enhanced solubility, dissolution rate, ex vivo permeability, oral bioavailability and antioxidant potential of mangiferin. *Drug Deliv Transl Res*. 2020;1–28. <https://doi.org/10.1007/s13346-020-00822-4>.
 40. Telange DR, Patil AT, Pethe AM, Tatode AA, Anand S, Dave VS. Kaempferol-phospholipid complex: formulation, and evaluation of improved solubility, in vivo bioavailability, and antioxidant potential of kaempferol. *J Excipients and Food Chem*. 2016;7(4):89–116.
 41. Telange DR, Patil AT, Pethe AM, Fegade H, Anand S, Dave VS. Formulation and characterization of an apigenin-phospholipid phytosome (APLC) for improved solubility, in vivo bioavailability, and antioxidant potential. *Eur J Pharm Sci*. 2017;108:36–49. <https://doi.org/10.1016/j.ejps.2016.12.009>.
 42. Telange DR, Nirgulkar SB, Umekar MJ, Patil AT, Pethe AM, Bali NR. Enhanced transdermal permeation and anti-inflammatory potential of phospholipids complex-loaded matrix film of umbelliferone: Formulation development, physico-chemical and functional characterization. *Eur J Pharm Sci*. 2019;131:23–38. <https://doi.org/10.1016/j.ejps.2019.02.006>.
 43. Dhore PW, Dave VS, Saoji SD, Bobde YS, Mack C, Raut NA. Enhancement of the aqueous solubility and permeability of a poorly water soluble drug ritonavir via lyophilized milk-based solid dispersions. *Pharm Dev Technol*. 2017;22(1):90–102. <https://doi.org/10.1080/10837450.2016.1193193>.
 44. Anderson NH, Bauer M, Boussac N, Khan-Malek R, Munden P, Sardaro M. An evaluation of fit factors and dissolution efficiency for the comparison of in vitro dissolution profiles. *J Pharm Biomed Anal*. 1998;17:811–22. [https://doi.org/10.1016/S0731-7085\(98\)00011-9](https://doi.org/10.1016/S0731-7085(98)00011-9).
 45. Klein S. The use of biorelevant dissolution media to forecast the in vivo performance of a drug. *AAPS J*. 2010;12:397–406. <https://doi.org/10.1208/s12248-010-9203-3>.
 46. Dixit P, Jain DK, Dumbwani J. Standardization of an ex vivo method for determination of intestinal permeability of drugs using everted rat intestine apparatus. *J Pharmacol Toxicol Methods*. 2012;65:13–7. <https://doi.org/10.1016/j.jvascn.2011.11.001>.
 47. Hamilton KL, Butt AG. Glucose transport into everted sacs of the small intestine of mice. *Adv Physiol Educ*. 2013;37:415–26. <https://doi.org/10.1152/advan.00017.2013>.
 48. Vaculikova E, Cernikova A, Placha D, et al. Preparation of hydrochlorothiazide nanoparticles for solubility enhancement. *Molecules*. 2016;21:2–8. <https://doi.org/10.3390/molecules21081005>.
 49. Telange DR, Denge R, Patil AT, Umekar MJ, Gupta SV, Dave VS. Pentaerythritol as an excipient/solid-dispersion carrier for improved solubility and permeability of ursodeoxycholic acid. *J Excipients and Food Chem*. 2018;9(3):80–95.
 50. Ghareeb MM, Abdulrasool AA, Hussein AA, Noordin M. Kneading technique for preparation of binary solid dispersion of meloxicam with poloxamer 188. *AAPS PharmSciTech*. 2009;10:1206–15. <https://doi.org/10.1208/s12249-009-9316-0>.
 51. Huanbutta K, Limmatvapirat S, Sungthongjeen S, Sriamornsak P. Novel strategy to fabricate floating drug delivery system based on sublimation technique. *AAPS PharmSciTech*. 2015;17(3):693–9. <https://doi.org/10.1208/s12249-015-0398-6>.
 52. Arafa MF, A S. El-Gizawy, et al. Sucralose as co-crystal co-former for hydrochlorothiazide: development of oral disintegrating tablets. *Drug Dev Ind Pharm*. 2015;42:1225–33. <https://doi.org/10.3109/03639045.2015.1118495>.
 53. Sirisha PL, Babu GK, Babu PS. Conceptuation, formulation, and evaluation of sustained-release floating tablets of captopril compression coated with gastric dispersible hydrochlorothiazide using 2³ factorial design. *Int J Pharm Invest*. 2014;4(2):77–87. <https://doi.org/10.4103/2230-973X.133055>.
 54. Thiyagarajan K, Bharti VK, Tyagi S, et al. Synthesis of non-toxic, biocompatible, and colloidal stable silver nanoparticle using egg-white protein as capping and reducing agents for sustainable antibacterial application. *RSC Adv*. 2018;8:23213–29. <https://doi.org/10.1039/C8RA03649G>.
 55. Mahobia S, Bajpai J, Bajpai AK. An in-vitro investigation of swelling controlled delivery of insulin from egg albumin nanocarriers. *Iran J of Pharm Res*. 2016;15(4):695–711.
 56. Zhao Y, Chen Z, Li J, et al. Formation mechanism of ovalbumin gel induced by alkali. *Food Hydrocoll*. 2016;61:390–8. <https://doi.org/10.1016/j.foodhyd.2016.04.041>.
 57. Sanphui P, Devi VK, Clara D, et al. Cocrystals of hydrochlorothiazide: Solubility and diffusion/permeability enhancements through drug-coformer interactions. *Mol Pharm*. 2015;12(5):1615–22. <https://doi.org/10.1021/acs.molpharmaceut.5b00020>.
 58. Acarturk F, Kqlal O, Celebi N. The effect of some natural polymers on the solubility and dissolution characteristics of nifedipine. *Int J of Pharm*. 1992; 85: 1-6. [https://doi.org/10.1016/0378-5173\(92\)90127-N](https://doi.org/10.1016/0378-5173(92)90127-N).
 59. Patel M, Tekade A, Gattani S, Surana S. Solubility enhancement of lovastatin by modified locust bean gum using solid dispersion techniques. *AAPS PharmSciTech*. 2008;9:1262–9. <https://doi.org/10.1208/s12249-008-9171-4>.
 60. Shazly GA, Ibrahim MA, Badran MM, Zoheir KMA. Utilizing pluronic F-127 and gelucire 50/13 solid dispersions for enhanced skin delivery of flufenamic acid. *Drug Dev Res*. 2012;73(6):299–307. <https://doi.org/10.1002/ddr.21013>.
 61. Kratz F. Albumin as a drug carrier: Design of prodrugs, drug conjugates, and nanoparticles. *J Control Release*. 2008;132:171–83. <https://doi.org/10.1016/j.jconrel.2008.05.010>.
 62. Imai T, Nodomi K, Shameem M, et al. Mutual effect of egg albumin and fatty acids on the bioavailability of dl- α -tocopherol. *Int J Pharm*. 1997;155:45–52. [https://doi.org/10.1016/S0378-5173\(97\)00160-9](https://doi.org/10.1016/S0378-5173(97)00160-9).
 63. Hussain MD, Saxena V, Brausch JF, Talukder RM. Ibuprofen-phospholipids solid dispersion: improved dissolution and gastric tolerance. *Int J Pharm*. 2012;422:290–4. <https://doi.org/10.1016/j.jipharm.2011.11.011>.
 64. Costa P, Manuel J, Lobô S. Modeling and comparison of dissolution profiles. *Eur J Pharm Sci*. 2001;13:123–33. [https://doi.org/10.1016/S0928-0987\(01\)00095-1](https://doi.org/10.1016/S0928-0987(01)00095-1).
 65. Raman S, Polli JE. Prediction of positive food effect: Bioavailability enhancement of BCS class II drugs. *Int J Pharm*. 2016;506(1-2):110–5. [https://doi.org/10.1016/S0928-0987\(01\)00095-1](https://doi.org/10.1016/S0928-0987(01)00095-1).
 66. Fong SYK, Ibisogly A, Bauer-Brandl A. Solubility enhancement of BCS Class II drug by solid phospholipids dispersions:

- spray drying vs freeze-drying. *Int J Pharm.* 2015;496(2):382–91. [https://doi.org/10.1016/S0928-0987\(01\)00095-1](https://doi.org/10.1016/S0928-0987(01)00095-1).
67. Almén MS, Nordström KJV, Fredriksson R, Schioth HB. Mapping the human membrane proteome: a majority of the human membrane proteins can be classified according to function and evolutionary origin. *BMC Biol.* 2009;7(50):1–14. <https://doi.org/10.1186/1741-7007-7-50>.
68. Chen L, Remondetto GE, Subirade M. Food protein-based materials as nutraceutical delivery systems. *Trends Food Sci Technol.* 2006;17(5):272–83. <https://doi.org/10.1016/j.tifs.2005.12.011>.
69. Davis JP, Foegeding EA. Foaming and interfacial properties of polymerized whey protein isolate. *J Food Sci.* 2004;69(5):404–10. <https://doi.org/10.1111/j.1365-2621.2004.tb10706.x>.

Publisher's Note Springer Nature remains neutral with regard to jurisdictional claims in published maps and institutional affiliations.



E-ISSN: 2278-4136

P-ISSN: 2349-8234

www.phytojournal.com

JPP 2021; 10(1): 1945-1947

Received: 25-11-2020

Accepted: 27-12-2020

Rasika Dnyandeo BhalkeSanjivani College of
Pharmaceutical Education and
Research Kopergaon,
Maharashtra, India**Mahendra Ashok Giri**Rajashri Shahu College of
Pharmacy, Buldana,
Maharashtra, India**Rasal Yash Anil**Sanjivani College of
Pharmaceutical Education and
Research Kopergaon,
Maharashtra, India**Narhe Mansi Balasaheb**Sanjivani College of
Pharmaceutical Education and
Research Kopergaon,
Maharashtra, India**Parjane Abhishek Nanasaheb**Sanjivani College of
Pharmaceutical Education and
Research Kopergaon,
Maharashtra, India**Vishal Vijay Pande**NN Sattha College of Pharmacy,
Ahmednagar, Maharashtra,
India**Corresponding Author:****Rasika Dnyandeo Bhalke**Sanjivani College of
Pharmaceutical Education and
Research Kopergaon,
Maharashtra, India

Hypotension: A comprehensive review

Rasika Dnyandeo Bhalke, Mahendra Ashok Giri, Rasal Yash Anil, Narhe Mansi Balasaheb, Parjane Abhishek Nanasaheb and Vishal Vijay Pande**Abstract**

Hypotension is a decrease in systemic blood pressure below accepted low values. While there is not an accepted standard hypotensive value, pressures less than 90/60 are recognized as hypotensive. Hypotension is a relatively benign condition that is under-recognized mainly because it is typically asymptomatic. It only becomes a concern once pumping pressure is not sufficient to perfuse key organs with oxygenated blood. This leads to symptoms impacting the quality of life of a patient. Hypotension is classified based on the biometric parameters of the blood pressure measurement. It may be absolute with changes in systolic blood pressure to less than 90 mm Hg or mean arterial pressure of less than 65 mm Hg. It may be relative to a decrease in diastolic blood pressure to less than 40 mm Hg. It may be orthostatic with a decrease in systolic pressure or 20 mm Hg or greater or a decrease in diastolic pressure of 10 mm Hg or greater on positional change from lying to standing. It may be profound which is defined as being medication-dependent. In acute conditions, the hypotensive shock is a possible and life-threatening condition.

Keywords: Genetic combining ability, specific combining ability, okra, variance, growth, yield and quality

Introduction

Low blood pressure is known as Hypotension. It is the blood pressure low enough that flow of blood to the organ of the body is inadequate. Normal blood pressure is 120/80mm of Hg whereas hypotension blood pressure is 90/60mm of Hg.

Types of hypotension

1. Chronic Asymptomatic hypotension.
2. Orthostatic hypotension.
3. Neurally Mediated hypotension.

Chronic Asymptomatic Hypotension

It has no signs or symptoms & needs no treatment.

Orthostatic Hypotension (OH)

It occurs when standing up from a sitting down position. It can give a dizzy feel. Orthostatic hypotension occurs if your body isn't able to adjust blood pressure and blood flow fast enough for the change in position. This type of low blood pressure usually lasts for only a few seconds or minutes after immediate standing. After sitting or lying down for a short time brings blood pressure to normal. It may occur in all age groups.

Orthostatic Hypotension causes

Two types of causes

I. Non neurogenic causes

It is caused by cardiac impairment, hypovolemia, venous pooling. It is of the following two types.

a. Acute non neurogenic

In this type hypotension is frequently caused by decrease in intravascular blood flow. It is accompanied by myocardial infarction.

b. Chronic non neurogenic causes

It is associated with disorders causing cardiac impairment, anemia, diabetic insipidus.

II. Neurogenic causes

It is associated with central and peripheral autonomic disorder. There are two types:

a. Acute neurogenic

It is a breakdown of autonomic regulatory mechanisms. In this type parasympathetic and sympathetic nervous systems are affected.

b. Chronic neurogenic

It is associated with neurodegenerative disease which is interrupted with sympathetic reflex arc. The adrenergic response is abnormal.

These are again subdivided into two types

Primary chronic neurogenic

Failure of autonomic mechanism caused by peripheral or sympathetic dysfunction which is associated with low level of norepinephrine.

Secondary chronic neurogenic

It is usually associated with disease and syndrome which are inherited and acquired.

Prevalence: The prevalence of orthostatic hypotension is between 5% and 30% for healthy communities, increases with age, and may be present in up to 50% of long-term-care residents.

Signs & Symptoms

Hypotension has symptoms like weakness, fatigue, nausea, palpitations, headache, syncope, dyspnea, chest pain, lightheadedness, dizziness and changes in vision. Neck and shoulder pain are also possible but occur less frequently [1-2, 9-10].

Pathophysiology of orthostatic Hypotension

Changing position from lying to standing there is change in blood pressure i.e. systolic pressure remains unchanged or drops slightly and diastolic pressure rises slightly. The drop in blood pressure is related to the dependent pool of blood in veins of liver, organs, intestines, legs and feet. Venous return and stroke volume decrease because of pooled blood. Therefore, cardiac output becomes compromised and arterial blood pressure drops. By sudden standing, the blood rushes to feet by gravity thus further decreasing venous return. Once venous return and stroke volume is compromised, the body activated baroreceptor located in the aorta and carotid arteries Baroreceptor works constantly to maintain normal range of blood pressure. Baroreceptors stimulated by pressure excreted upon them by blood in vessels. When upper body vessel pressure falls, baroreceptor stimulation stops and this information is transmitted to the brain. The medulla reacts by initiating vasoconstriction, increasing heart rate and cardiac output to raise blood pressure. When the sympathetic nervous system increases heart rate increases, contractility, and increases vasomotor tone of the capacitance vessels. Simultaneous parasympathetic inhibition also increases heart rate. Therefore, there is activation of renin-angiotensin-aldosterone-system (RAAS) and vasopressin (ADH) secretion cause sodium and water retention and increase circulating blood volume.

Factors affect blood pressure in patients with OH

Age: The pumping action of heart loses efficiency and blood

vessels stiffen and weaken, causing decreased cardiac output. Additional baroreceptor becomes less sensitive to pressure changes thus the signal transmitted to medulla is not effective.

Hypertension: It decreases baroreceptor compensatory mechanism. This increases the risk of OH. The afferent pathway transfers information from arterial baroreceptors in the carotid artery and the aortic arch. This information reaches the vasomotor centre in the medulla oblongata. The afferent pathway regulates two basic cardiovascular responses: heart rate and vascular tone. The hypothalamus can then activate vasopressin release, which is an additional regulatory mechanism. Higher brain functions can modulate autonomic cardiovascular responses [3].

Numbers of medications can also cause OH particularly drugs used to treat high blood pressure:

1. Diuretic
2. Beta blocker
3. Calcium channel blocker
4. Angiotensin converting enzyme inhibitors
5. Antidepressants
6. Drug used to treat Parkinson's disease
7. Erectile dysfunction

Treatment on orthostatic hypotension [4]

a. Nonpharmacological treatment

The first line of defense is those avoiding carbohydrate rich meals & adding sodium-rich foods or sodium tablets to the diet & limiting alcohol intake.

b. Pharmacologic treatment

1. **Mineralocorticoids & Fludrocortisone:** It is necessary for regulation of salt and water in the body & it increases sodium reabsorption by an action on the distal tubules of the kidney and thus raising blood pressure.
2. **Midodrine:** It works on narrowing the blood vessels and increasing blood pressure. Thus it is used to treat low blood pressure.
3. **α -adrenoceptor agonists (systemic vasoconstrictors):** Methoxamine and phenylephrine are used as pressor agents in treating hypotension and shock.
4. **Fluid & salt:** (Volume expansion)

Neurally Mediated Hypotension

In this hypotension after standing for a long time, blood pressure drops. Person may feel dizzy, faint, or sick. It is also called as fainting reflex/neurocardiogenic syncope/vasodepressor syncope/autonomic dysfunction/vaso-fatal reflex.

Neurally mediated hypotension is a complication that occurs due to unnatural reflex action between the brain and heart, though they are structurally normal. It is a disorder of the autonomic regulation of postural tone, which results in hypotension, bradycardia and loss of consciousness. Symptoms included are nausea, lightheadedness, abdominal discomfort, difficulty in concentration, temporary impairment of blood circulation in the brain and anemia.

Cause of Neurally mediated hypotension

Low blood pressure from faulty brain signals (neurally mediated hypotension). This disorder, which causes a blood pressure drop after standing for long periods, mostly affects young adults and children. It seems to occur because of a miscommunication between the heart and the brain.

Pathophysiology

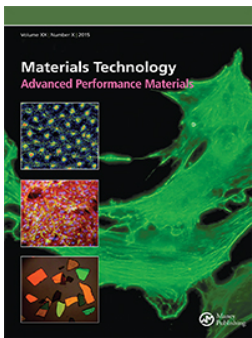
In normal person's body

Human body has remarkable ability to maintain stable blood pressure in fact of changing forces that constantly shift & redistribution the circulated blood volume. To achieve this stable blood pressure reflex mechanism continuously works & adjusts the vascular tone and cardiac output. Small change in posture there is shifting of blood from thorax to abdomen and further to lower extremities; this shifting decreases the cardiac output. The decrease of cardiac output sensed by arterial baroreceptors located in the carotid sinus and aortic arch. The receptor transmits the signal to the nervous system and results in reflex-increased sympathetic output. In addition, the vascular system responds locally restricting blood flow to non-vital organs such as skin, adipose tissue, muscle etc. Clinically this response manifests as an increase in heart rate, which is mediated, increase in sympathetic output, and diastolic pressure increase, which is mediated by local vasoconstriction.

In NMS person's, NMS is caused by hypersensitivity of ANS, which over respond to different stimuli Eg: NMS is trigger by orthostatic stress ^[5-10].

References

1. Fortinsky RH, Baker D, Gottschalk M *et al.* Extent of implementation of evidence-based fall prevention practices for older patients in home health care. *Journal of the American Geriatrics Society* 2008;56(4):737-743.
2. Poon IO, Braun U. High prevalence of orthostatic hypotension and its correlation with potentially causative medications among elderly veterans. *J Clin Pharm Ther* 2005;30(2):173-8.
3. Ricci F, De Caterina R, Fedorowski A. Orthostatic hypotension: Epidemiology, prognosis, and treatment. *J Am Coll Cardiol* 2015;66(7):848-60.
4. Lanier JB, Mote MB, Clay EC. Evaluation and management of orthostatic hypotension. *Am Fam Physician* 2011;84(5):527-36.
5. Thomson HL, Atherton JJ, Khafagi FA, Frenneaux MP. Failure of reflex venoconstriction during exercise in patients with vasovagal syncope. *Circulation* 1996;93(5):953-9.
6. Mark AL. The Bezold-Jarisch reflex revisited: clinical implications of inhibitory reflexes originating in the heart. *J Am Coll Cardiol* 1983;1(1):90-102.
7. Jacobsen TN, Morgan BJ, Scherrer U, Vissing SF, Lange RA, Johnson N *et al.* Relative contributions of cardiopulmonary and sinoaortic baroreflexes in causing sympathetic activation in the human skeletal muscle circulation during orthostatic stress. *Circ Res* 1993;73(2):367-78.
8. Grubb BP, Karas B. Clinical disorders of the autonomic nervous system associated with orthostatic intolerance: an overview of classification, clinical evaluation, and management. *Pacing Clin Electrophysiol* 1999;22(5):798-810.
9. Tripathi KD. *Essentials of Medical Pharmacology*, Jaypee Brothers Medical publishers, edition 8th, 604p.
10. Barar FSK. *Essentials of Pharmacotherapeutics*, S. Chand and Company Ltd, Edition 1st, 239p.



Tailoring hybrid organic-inorganic film-forming topical gel: a tuneable approach for tramadol HCl delivery

Prakash N. Kendre , Gayatri Dusane , Shirish P. Jain , Mahendra A. Giri & Ajinkya K. Pote

To cite this article: Prakash N. Kendre , Gayatri Dusane , Shirish P. Jain , Mahendra A. Giri & Ajinkya K. Pote (2020): Tailoring hybrid organic-inorganic film-forming topical gel: a tuneable approach for tramadol HCl delivery, Materials Technology, DOI: [10.1080/10667857.2020.1802839](https://doi.org/10.1080/10667857.2020.1802839)

To link to this article: <https://doi.org/10.1080/10667857.2020.1802839>



Published online: 07 Aug 2020.



Submit your article to this journal [↗](#)



View related articles [↗](#)



View Crossmark data [↗](#)



Tailoring hybrid organic-inorganic film-forming topical gel: a tuneable approach for tramadol HCl delivery

Prakash N. Kendre^a, Gayatri Dusane^b, Shirish P. Jain^c, Mahendra A. Giri^b and Ajinkya K. Pote^a

^aDepartment of Pharmaceutics, Rajarshi Shahu College of Pharmacy, Buldana, India; ^bDepartment of Pharmaceutics, Sanjivani College of Pharmaceutical Education & Research, Kopergaon, Maharashtra, India; ^cRajarshi Shahu College of Pharmacy, Buldana, India

ABSTRACT

Drug release properties for transdermal route can be better modified as per requirement which is mostly dependent upon the carrier system. In case of organic film-forming systems, the physical properties may not be achieved for successful delivery of drug through transdermal route. A novel organic-inorganic hybrid film-forming gel may fulfil these expectations to many extend. The present study focuses on the development of the organic-inorganic hybrid film-forming gel. A smooth, transparent, clear film-forming gel of tramadol was prepared for application on the intact skin with better comfort and modified drug release rate properties. The key properties of the adhesive films produced from the hybrid gels were investigated and the results showed that the incorporation of appropriate PVA: TEOS: Glycerine: HCl in the ratio of 46:12.5:25.5:6 respectively. Resultant hybrid film-forming gel has modified the physical properties and improved drug release properties. Furthermore, the investigations of skin irritation suggested no irritation to skin after topical application. This study has provided an alternative to the presently available organic gel and films for transdermal delivery of drugs with better patient compliance and modified physical and chemical stability.

ARTICLE HISTORY

Received 9 April 2020
Accepted 27 July 2020

KEYWORDS

TEOS; PVA; hybrid-organic-inorganic film-forming gel; tramadol HCl; transdermal route etc

Introduction

Many of the drug delivery systems have been developed till date by many researchers with different characteristics. Efficient drug delivery systems can be developed further by doing modifications in the available drug delivery systems. These modifications can be possible using variety of compatible polymeric components. These modifications may include grafting of polymers, cross-linking of polymers and many more other approaches using various techniques.

Hybrid systems are made-up of composites of two different materials with different physical and or chemical properties. Hybrid film-forming gels refers to the combination of organic and inorganic components in one system either at macroscopic level or molecular level [1].

Single hybrid system is a homogenous phase of both organic and inorganic materials and shows characteristics that are different at their individual level. These resultant characteristics may be beneficial based upon the appropriate contributions of both the materials combined together using suitable methodology and techniques. Mechanical properties of hybrid systems are so improved so that patient acceptance will enhance with excellent drug release properties and stability of the final formulation. Mostly inorganic

phase provides mechanical strength while organic phase delivers bonding. The word hybrid comes from the Latin word 'hybrida', which is related to the meaning 'mongrel'. The easy way to construct transparent and homogeneous hybrid materials is to increase the affinity between organic polymer and inorganic phases [2].

Optical transparency is the most important characteristic of these hybrids and it arises because dispersion of material in the matrix is in the order of tens of nanometres, far less than the wavelength of visible and ultraviolet light. As a result, light is not lost due to scattering.

Moreover, the hybrid materials offer the advantages like higher flexibility and mechanical strength, greater temperature, range of usability, increased durability, improved electrical, magnetic or redox properties [3–5].

The synthesis of hybrid materials includes two methodologies:

- (A) Building block approach
- (B) *In-situ* formation of the components
 - a. In situ formation of inorganic materials
 - b. Formation of organic polymers in presence of preformed inorganic materials

- c. Hybrid materials by simultaneous formation of both components.

Wang et al. have prepared the hybrid injectable hydrogels consisting of gelatin and nanocrystalline cellulose. These hydrogels were processed using adaptation of interpenetrated network of alginate-gelatin, ionic cross-linking and supramolecular interaction approach. Due to this approach mechanical properties were changed and resembles native tissue structure. This approach has been used for delivery of cells in tissue engineering [6].

In another study, the researchers have synthesised microgels via cross-linking of chitosan and gelatin with succinimide-end polyethylene glycol (PEG). The presence of PEG provided thermoresponsiveness to microgels due to which the size of microgels was significantly changed at elevated temperature [7].

Another cross-linking aspect of modified form of materials used to prepare biocompatible injectable hydrogels. In this approach, different gelation techniques like, physical cross-link, chemical cross-link, ionic cross-link and supramolecular interaction were used to prepare chitosan-based injectable hydrogels to be formed. These gelation approaches have significant impact on the structure and properties of hydrogels, which directs their use as tissue engineering scaffold and drug delivery vehicle [8].

Chitosan-based controlled and extended drug release nanoparticles were prepared using expandable layered aluminosilicate as an inorganic material. This hybrid form of nanoparticles has significant impact on the drug release rate properties due to change in the structural morphology and swelling behaviour. The study has revealed its application in the biomedical and tissue engineering for controlled drug delivery [9].

Another study suggested the preparation of chitosan-encapsulated ZnO quantum dots loaded with drug for anti-cancer treatment. Study has demonstrated its use for tumour-targeted delivery of anti-cancer agents [10].

In one more study, chitosan-grafted-copolymer has been used to prepare stimuli-responsive magnetic nanoparticle drug carrier. This grafted chitosan has significant impact on the drug release property which was extended in a controlled fashion that responds to the change in temperature and pH with characteristics of longer circulation time and reduced side effects [11].

Transdermal drug delivery system has been proved to be an alternative to the many oral as well as injectables preparations avoiding first-pass-metabolism and painful irritations respectively.

In first generation, this route has been used for delivery of lipophilic and low-dose drugs. In second generation, using chemical permeation enhancers, iontophoresis, sonophoresis etc. In third generation,

microneedle injection, electroporation and cavitation ultra sound approach has been used for delivery of drugs.

Transdermal delivery system is a desirable alternative administration route for tramadol hydrochloride for patients with chronic pain. To overcome skin barrier property, organic-inorganic (hybrid) film-forming gel approaches have been chosen in this study [12–14].

Hybrid material offers multiple benefits and its use in drug delivery system is itself a novel approach. Based on these considerations the current work has aimed to prepare a novel organic-inorganic (hybrid) film-forming gel for transdermal drug delivery of tramadol HCl, a non-invasive drug administration route and offers potential benefits of simplicity, efficacy and patient acceptance by maintaining a constant blood drug concentration for an extended period [15].

In addition, the transdermal delivery system can decrease the possible abuse and addiction potential of tramadol by avoiding peak and trough plasma concentrations and by reducing the total amount of medication input [16].

Materials and method

Materials

Tramadol HCl was obtained from IPCA laboratories, Mumbai; polyvinyl alcohol (PVA), tetraethylorthosilicate (TEOS), were obtained from Research Fine Chem Industries, Mumbai. All other chemicals glycerine, hydrochloric acid (HCl) etc. used were of analytical grade.

Method

Preparation of hybrid-organic-inorganic film-forming gel

Preparation of hybrid-film-forming gel was prepared in two steps as mentioned below. Both the phases were prepared separately as organic and inorganic phase and mixed together to form homogenous gel with improved physical, chemical properties and modified drug release properties. Different concentration and levels of components in the formulation are highlighted in Table 1.

Preparation of organic phase. Initially the organic phase was prepared using typical synthesis, weighed amount of PVA was added to double distilled water which is preheated at 90 °C with continuous stirring till PVA was completely mixed in the water. The resultant homogenous blend of PVA was allowed to cool at room temperature.

Table 1. Formulation batches of organic-inorganic hybrid gel.

Ingredient (%)	HG-1	HG-2	HG-3	HG-4	HG-5	HG-6	HG-7	HG-8	HG-9	HG-10
Tramadol HCl	5	5	5	5	5	5	5	5	5	5
PVA	50.87	47.18	64.43	62.49	62.49	71.95	44.76	46.5	46	45
TEOS	18.46	18.46	14.77	11.81	11.81	10	11.5	12	12.5	12.5
Glycerine	14.77	18.46	4.90	9.80	9.80	3.05	28.24	25.5	25.5	25.5
HCl	5.90	5.90	5.90	5.90	5.90	5	5.5	6	6	7
Distilled Water	5	5	5	5	5	5	5	5	5	5

*HG = Hybrid Gel

Preparation of inorganic phase and catalyst mixture.

In this step required amount of 0.1 N HCl was added dropwise in the weighed amount of Tetraethyl orthosilicate (TEOS). Initially, separate phase of globules was observed which disappeared with continuous stirring and finally a clear transparent solution was formed. Heat was evolved at the end due to exothermic reaction.

In the later step, inorganic phase was added to the organic phase in a dropwise manner with continuous mixing till homogenous system was formed. This mixture was then added to another previously prepared mixture of glycerine, water and drug to form the final formulation.

As shown in above Table 1, various batches of hybrid film-forming gel were prepared.

The optimised batch was selected by the self-developed method as described below. The prepared hybrid gel was poured on a uniform surfaced glass slide. The gel was allowed to form a thin layer on the slide. Once the film was formed it was slowly peeled off from the slide. According to the visual observation and experience, manual peeling force required, spreadability of solution on glass slide and texture of film, the best hybrid film-forming gel batch was selected and further characterised for different physical and chemical parameters using various tools and techniques. It has made easy job to deal with only selective formulation batch out of initially formulated batches for further characterisation and testing.

Preparation of PVA-based gel

In typical synthesis, the weighed amount of PVA was dissolved in double distilled water preheated at 90°C under stirring. After complete dissolution of PVA, fixed amount of drug was added to the mixture upon cooling at room temperature. Various batches with concentration of PVA from 1 % W/V to 30% W/V were prepared to get final desired formulation of PVA gel. Final formulation batch was selected using self-developed method. On one glass slide; prepared PVA solution was poured and tried to spread evenly that leads to formation thin layer on the glass slide. The formed film was dried for 5 minutes and peeled out to check the peel ability. Final concentration of PVA was determined on the basis of their physical parameters

like spreadability of PVA solution, peeling force required after drying and texture properties of formed film.

Characterisation of film-forming gel

All the batches of Tramadol HCl organic-inorganic hybrid film-forming gel formulations were observed for appearance, pH, colour and consistency etc.

pH

Accurately weighed 1 gm of gel was and dispersed in 100 ml of distilled water. The pH of dispersion was measured using digital pH metre. All the readings were taken in triplicate and noted.

Rheological study

a Brookfield digital RST-CC Rheometer (7,120,128) was used to determine rheology and viscosity of the formulations. The viscosity was measured by 12 MP in 4 blocks (UID-140).

Drug content

Drug content study was conducted for organic-inorganic hybrid film-forming gel as well as PVA-based gel.

Accurately weighed amount of (500 mg) of Tramadol HCl containing organic-inorganic hybrid film-forming gel was added to 50 ml of phosphate buffer (pH 7.4). Resultant solution was kept for sonication for 10 minutes to dissolved the gel completely. Absorbance of solution was checked at 271 nm against blank as a phosphate buffer solution. Thus, percentage drug content was calculated. All the readings were taken in triplicate and noted. Same method was implemented to determine the drug in the PVA organic gel.

FT-IR study

Tramadol HCl was identified and confirmed by using the FT-IR (8400, Shimadzu, Japan), Drug:KBr (1:100) ratio was taken and mixture was gently grinded in the mortar pestle, then translucent pellet was made by using the pellet press method, then pellet was placed in the sample holder, then instrument was run and gotten the FTIR spectra of the Acitretin. The samples were tested at R.C. Patel College of Pharmacy, Shirpur, India. In the same way, Physical blends of drug and

other excipients were also analysed for compatibility testing and suitability for the preparation of final formulation.

Differential scanning calorimetry (DSC) study

Shimadzu DSC-60 plus was used for DSC study of selected hybrid organic-inorganic gel as well as PVA organic gel. Small amount of 3–6 mg sample was taken on aluminium pan. The sample was covered with the aluminium lead and crimping was carried out with the help of crimping tool. The crimped pan was installed at the sample holder point. The test was carried out and the thermogram was recorded in TW-60 software

Texture analysis

Texture analysis of PVA-based gel and organic-inorganic hybrid gel was performed using a CT3 Texture Analyser in TPA mode. Formulations were transferred into lower cone taking care to avoid the introduction of air into the samples. A conical analytical probe (45°C) was forced down into each sample at a defined test speed (2 mm/s) and to a defined depth (12 mm). At least five replicate analyses of each sample were performed at temperatures of 25°C and 30°C. From the resulting force–time plots, the hardness (the force required to attain a given deformation), compressibility (the work required to deform the product during the first pass of the probe) and adhesiveness (the work necessary to overcome the attractive forces between the surface of the sample and the surface of the probe) were derived [17–19].

Appearance and miscibility study

All the batches of Tramadol HCl organic-inorganic hybrid film formulations were observed for appearance and transparency.

The structural properties and the unique functions of the blend-type polymer gels, were dependent on the miscibility, chemical structure and interaction between mixture components. No macro-phase separation occurring between the organic polymer and inorganic is indicated by the high transparency in the film [20].

Ex-vivo drug diffusion study of hybrid gel

Investigation of the amount of drug released from a tramadol HCl organic-inorganic hybrid gel was performed using *Ex-vivo* drug diffusion study. A fresh goat skin was used as a diffusion membrane. Goat skin was positioned between the two cell halves of a glass chamber. The two compartments were held together with a clamp, 10 ml of phosphate buffer pH 7.4 was added to the receiver/receptor compartment. The donor compartment was loaded with 0.5 gm of formulation which was spread evenly on the membrane. The receptor phase (phosphate buffer pH 7.4) was continuously stirred with the help of magnetic stirrer at 300 rpm

and maintained at 37°C using a circulating water bath. Samples of 1 ml were collected at the interval of every 20 minutes for 3 hours study from the receiver compartment at predetermined time intervals and replaced with fresh buffer solution. The samples collected were analysed for drug content using UV-spectrometric method at 271 nm wavelength and finally graph was plotted as percentage cumulative drug permeation Verses time [19].

Animal activity

Skin irritation study. Skin irritation study was conducted using healthy rats. The protocol of the study was sanctioned by the Institutional Animal Ethical Committee and permission was granted to conduct the study using healthy rats monitored as per the guidelines of animal ethical committee. The rats ($n = 9$) were randomly divided into three equal groups for application of standard irritant, optimised formulation or test and control (no application). Hairs were removed by bend scissor from an area (2 cm²) on the dorsal side of the albino rats to make a hairless area. The optimised formulation was applied to group 2 of rats ($n = 3$) for assessing any kind of irritation at specified sites. Formulation was removed after 48 hours and skin was examined for any signs of erythema and oedema [20,21].

Analgesic activity. Analgesic activity was conducted using healthy mice. The protocol of the study was sanctioned by the Institutional Animal Ethical Committee and permission was granted to conduct the study using healthy rats monitored as per the guidelines of animal ethical committee. Mice weighing 25–30 gm were divided in two groups of five each. The hot plate was maintained at $56 \pm 1^\circ\text{C}$. Formulation was applied on the animals and placed into a glass cylinder of 24 cm diameter on the heated surface. The time between placement and licking the paws or jumping was recorded as response latency. The reaction time was recorded for control mice treated with Tramadol HCl (5 %) at 0, 15, 30, 60 and 90 minutes. The test was terminated at 15 seconds to prevent tissue damage. The statistical analysis was carried out using Graph-Pad-Prism 3.03 software. The *t*-test was selected as the test for significance and *P* value less than 0.05 was considered statistically significant [22].

Stability study of film-forming gels

Stability study was conducted according to the ICH guidelines at $40 \pm 2^\circ\text{C}$ and $75 \pm 5\%$ RH for 3 months. The samples were withdrawn at beginning, after 30, 60 and 90 days and analysed for any physical and chemical changes.

Characterisation of tramadol HCl organic-inorganic hybrid film

In order to characterise the film quantitatively, it was characterised with the help of the following parameters. All the batches of tramadol HCl organic-inorganic hybrid film formulations were observed for appearance and transparency.

X-Ray diffraction study (XRD)

Bruker Model D8 Advance was used to check the crystallinity of formulation. This test was done from Sophisticated Test and Instrumentation Centre, Kochi University, Kochi, Kerala, India. The sample was smeared over low back ground sample holder (amorphous silica holder) and fixed on the sample stage in goniometer. The instrument was set with B-B geometry. The current and voltage was set to 40 mV and 35 mA and data was collected.

Drug content study of film-forming gels

Uniform thickness organic-inorganic hybrid gel film of $1 \times 1 \text{ cm}^2$ size was dissolved in 50 ml of phosphate buffer (pH 7.4). Resultant solution was kept for sonication for 10 minutes to dissolved the gel completely. The solution was filtered through the Whatman filter media and clear solution was checked for absorbance at 271 nm against blank as a phosphate buffer solution, pH 7.4. Thus, percentage drug content was calculated. All the readings were taken in triplicate and noted. Same method was implemented to determine the drug in the PVA organic gel film.

Moisture uptake study

The films were put in a desiccator with silica gel for 24 hours and weighed (W_i). The films were then transferred to another desiccator containing saturated NaCl solution (relative humidity 75%) at 25°C until a constant weight was obtained. After equilibrium was attained, the films were taken out and weighed (W_m). Moisture uptake capacity was calculated according to the following Equation (1) [23]:

$$\begin{aligned} \text{Moisture uptake capacity (\%)} \\ = (W_m - W_i / W_i) \times 100 \end{aligned} \quad (1)$$

Moisture content study

Both the organic PVA film and hybrid organic-inorganic films were evaluated for moisture content study. The prepared films were weighed initially (W_i) and kept in the desiccator containing silica gel at 25°C and is continuously weighed until it shows constant weight (W_d).

The moisture content is calculated using following Equation (2) [23]:

$$\text{Moisture content (\%)} = (W_d - W_i / W_i) \times 100 \quad (2)$$

Water uptake and swelling study

This study was performed to find out water uptake capacity of the prepared films. In this method, the prepared films of uniform size and thickness were fixed to the plain stainless-steel surface and slowly immersed in a beaker containing 25 ml distilled water at room temperature for 3 hours. After 3 hours the films were slowly removed and excess of water was wiped slowly with the help of soft filter paper. This experiment was discontinued at the observation of point when film begins to disintegrate or dissolve. Finally, the water uptake and swelling of film was calculated by the following Equation (3) [23]:

$$\text{Moisture content (\%)} = (W_s - W_i / W_i) \times 100 \quad (3)$$

Where, W_s is weight of film after swelling; W_i is the initial weight of film before water uptake and swelling.

Folding endurance study

a specific area of strip was cut and repeatedly folded at the same place till it broke. The number of times the film could be folded without breaking gave the value of folding endurance.

Weight variation test and thickness measurement

For each formulation, three film samples ($10 \times 40 \text{ mm}$) were used. Each film sample was weighed individually and the average weight was calculated.

Thickness of both organic-gel film and hybrid-gel film was measured using digital Vernier calliper (Mitutoyo, Japan). Thickness was measure at all the corner and centre of the film, multiple observations were noted and finally, average value was considered as $\pm\text{SD}$, $n = 3$.

Drying time

For the assessment of the drying time the formulation was applied to the glass slide. After 2 minutes a glass slide was placed on the film without pressure. If no remains of liquid were visible on the glass slide after removal, the film was considered dry. If remains of liquid were visible on the glass slide the experiment was repeated until the film was found to be completely dried [5].

Surface morphology study of organic-inorganic hybrid film of tramadol HCl

Surface morphology study of organic-inorganic hybrid film containing tramadol HCl was determined using Scanning electron microscopy (SEM).

SEM analysis carried out for surface morphology of film. Jeol, JSM 6390LA was used to check the smeared

on a small piece of adhesive carbon tape which was fixed on a brass stub. The sample was then subjected to gold coating using sputtering unit (model: JFC1600) for 10 sec at 10 mA of current. The gold coated sample placed in chamber of SEM (Jeol, JSM 6390LA) and secondary electron/Back Scattered electron images were recorded.

In-vitro drug permeation study of organic PVA film and organic-inorganic hybrid film

Drug permeation study of both organic PVA film and organic-inorganic hybrid film was conducted using fresh goat as a diffusion membrane. Goat skin was positioned between the two cell halves of a glass chamber. The two compartments were held together with a clamp. About 10 ml of phosphate buffer pH 7.4 was added to the receiver/receptor compartment. The film (25 mm in diameter) were mounted over the goat membrane and integrity was checked visually with proper equilibration. The receptor phase (phosphate buffer pH 7.4) was continuously stirred with the help of magnetic stirrer at 300 rpm and maintained at 37°C using a circulating water bath. Samples of 1 ml were collected at the interval of every hour for 24 hours study from the receiver compartment at predetermined time intervals and replaced with fresh buffer solution. The samples collected were analysed for drug content using UV spectrometric method at 271 nm wavelength and finally graph was plotted as cumulative drug permeation Verses time [19].

Stability study of organic and hybrid films

Stability study of film was performed in the same way as mentioned above for organic-inorganic hybrid gel.

Result and discussion

Pre-formulation study and characterisation of film-forming gels

As discussed in the methods section 2.2.1, the final organic-inorganic hybrid film-forming gel formulation was selected and further characterised for various physical and chemical parameters discussed below.

FT-IR study

The FT-IR spectra of PVA, TEOS, Tramadol HCl and blend of all these ingredients are presented in the Figure 1. The spectra of tramadol HCl shown major peaks indicating the basic functional groups at 3065.3; 2861.84; 2514.72, 2605.36; 3306.36; 1271.82; 1578.45; 1045.23 consisting of C-H stretching (aromatic), C-H stretching (aliphatic), C-H stretching of -CH₂ and -CH₃ groups, N-H stretching, C-N stretching respectively. Same peaks were retained in the Spectra of physical blend of all the ingredients indicating the no interactions among the them without affecting any changes in the tramadol HCl [24].

Differential scanning calorimetry (DSC)

The DSC thermogram of organic-inorganic hybrid gel (HG-9 formulation) shown in Figure 2 and interpretation are mentioned below:

1st peak. Exhibiting endothermic peak at -27.92°C,

- Corresponding to its melting and decomposition reported peak temperature was -16.95°C to -27.92°C.
- Enthalpy of fusion found to be -110.11 J/g

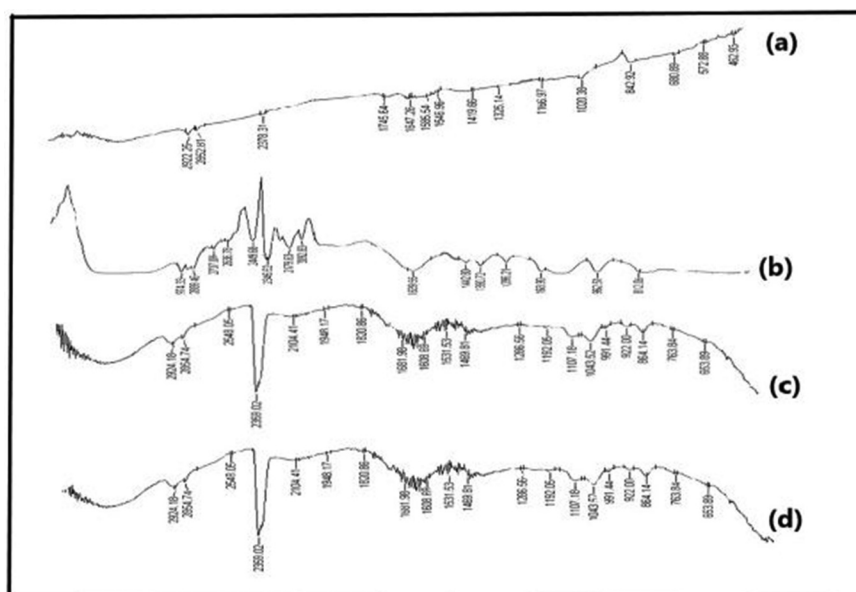


Figure 1. FT-IR study: PVA (a); TEOS (b); Tramadol HCl (c); Blend of PVA+TEOS+ Tramadol HCl (d).

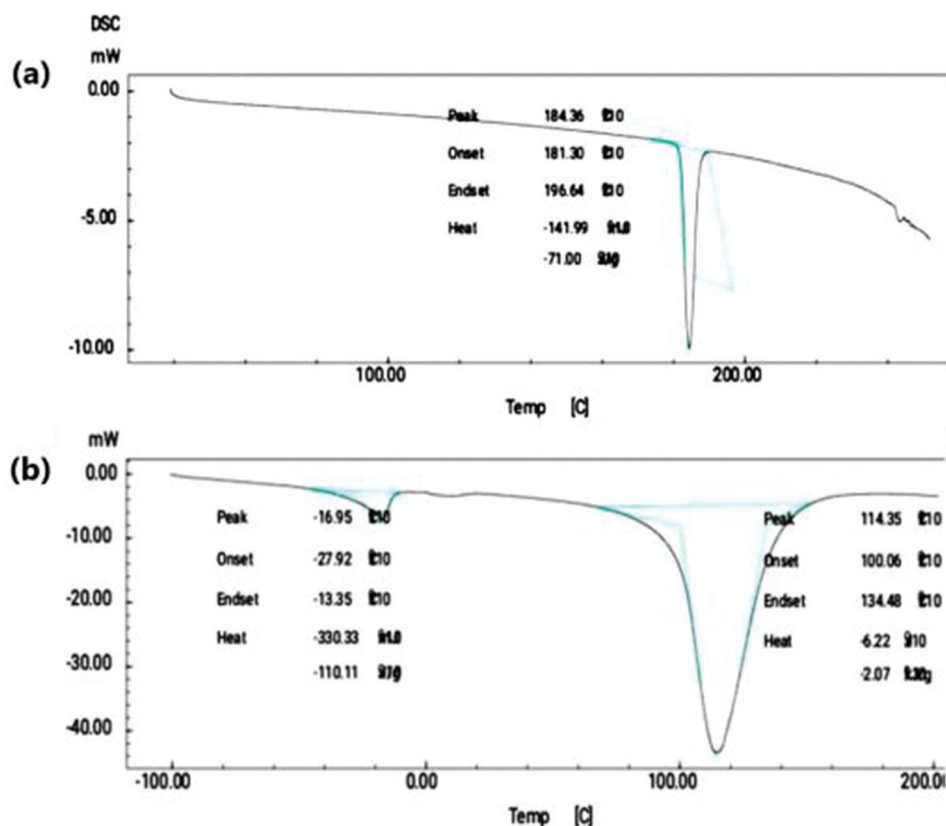


Figure 2. DSC study: Spectra of tramadol HCl (a); Spectra of Hybrid-organic-inorganic-film (b).

2nd peak. Exhibiting an endothermic peak at 114.35°C,

- (a) Corresponding to its melting and decomposition reported peak temperature was 100.04°C to 134.48°C
- (b) Enthalpy of fusion found to be -2.07 J/g

As shown in Figure 2, 1st peak indicates that formation of eutectic mixture and 2nd peak is broad asymmetric melting peak. Cross-linking increases in hybrid organic-inorganic gel due to formation of eutectic mixture. Decreased in melting point is indication of formation of eutectic mixture which promotes cross-linking of the resultant blend. Resultant melting of its blend is lower than their individual melting point. Because of reaction between organic and inorganic polymer there is formation of eutectic mixture, the melting point of resultant formulation was decrease and found to be 114.35°C and is less than that of original melting point of drug 184.36°C and polymer which is used [25].

Appearance and pH

As shown in Figure 3 the tramadol HCl formulation was observed under dark background, which shows transparent viscous preparation with smooth, homogenous, consistent.

All the organic-inorganic hybrid gel formulations were tested for pH and were found to be in the range

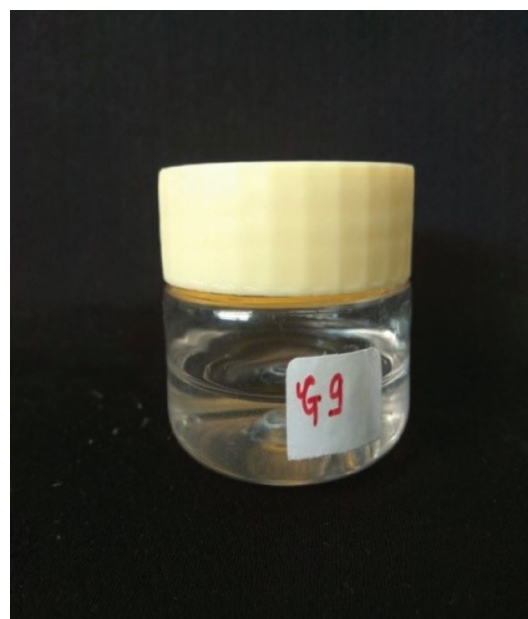


Figure 3. Appearance of tramadol HCl containing organic-inorganic hybrid gel (HG-9).

of 6.6–7.1. The pH of the final selected batch HG-9 was 6.9.

Rheological behaviour of film-forming gels

As shown in Figure 4(a) viscosity of hybrid gel (HG-9) found to be 231.2 Pa.s with respect to temperature condition. Resultant viscosity is sufficient for application to skin and leads to good spreadability

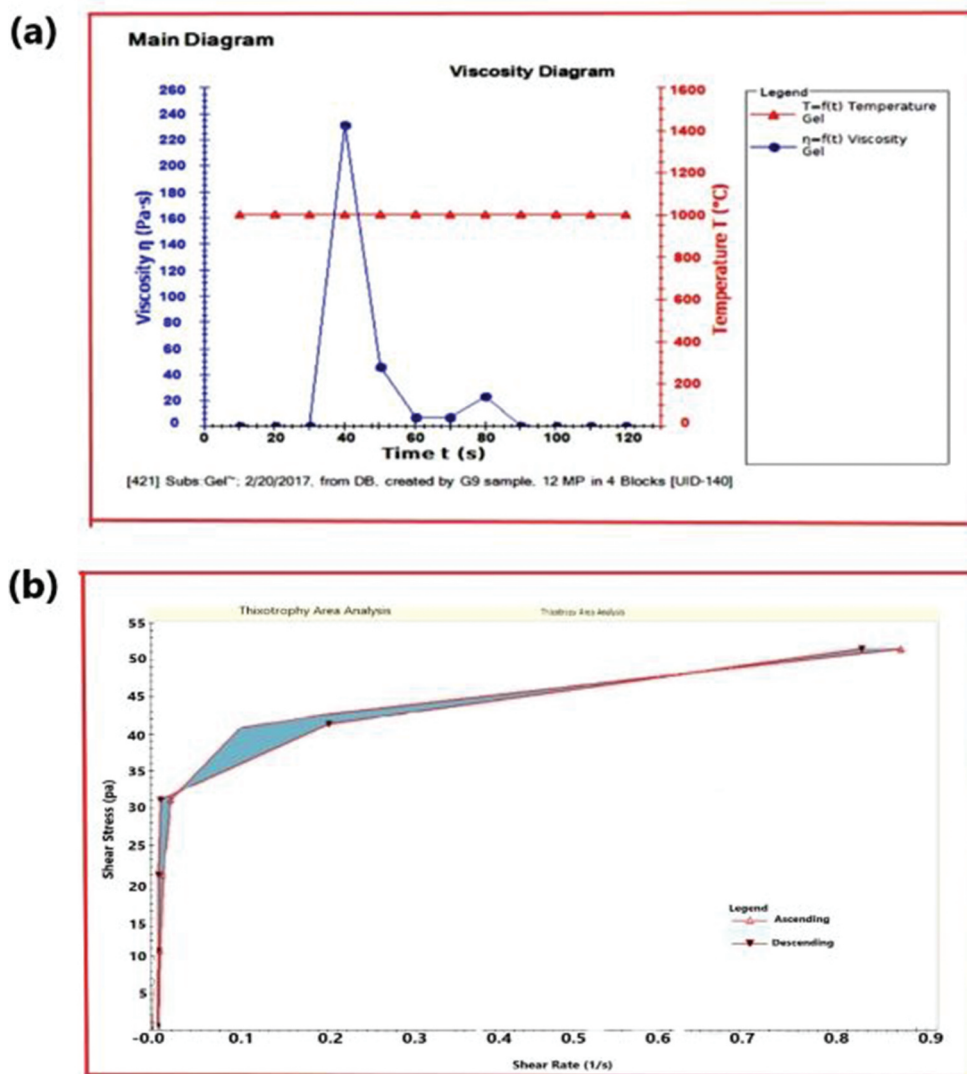


Figure 4. Rheological behaviour of hybrid-organic-inorganic film-forming gel: Viscosity study (a); Thixotropy study (b).

property. As per given in the Figure 4(a) it was observed that viscosity of final HG-9 formulation was increasing with increased in temperature up to certain value of 1400°C but later on as time laps, it again goes on decreasing with decreased in temperature condition, so this type of behaviour indicates the temperature dependability of the formulation with change in viscosity at certain shear rate value. This type of observation indicates thixotropic behaviour of system. All the detailed data of viscosity study is presented in Table 2.

According to Figure 4(b), the formulation showed thixotropy behaviour and change in viscosity with respect to certain values of shear rate and shear stress in which the shear rate steadily increases at constant rate from zero to some maximum value and then decreased at the same rate to zero again, a hysteresis loop form was shown in the Figure 4(b). The height, shape and enclosed area of hysteresis loop depend on the duration of shearing, the rate of increase/decrease

Table 2. Detailed data of viscosity study.

Sr. No.	Time t (sec)	Shear stress (pa) τ	Shear rate(1/s) $\dot{\gamma}$	Viscosity
1.	10	0.000	0.000	0.0
2.	20	9.984	0.001	0.0
3.	30	19.989	0.005	0.0
4.	40	29.993	0.013	231.265
5.	50	39.998	0.088	45.354
6.	60	49.982	0.764	6.543
7.	70	49.982	0.724	6.906
8.	80	39.998	0.175	22.845
9.	90	29.993	0.003	0.0
10.	100	19.989	0.000	0.0
11.	110	9.984	0.000	0.0
12.	120	0.000	-0.001	0.0

of shear rate and the past kinematic history of the sample. The sample has taken fixed time to return more viscous state, it is called Non-Newtonian pseudo plastic fluid

showing a time dependant change in viscosity. As this is time dependant system, viscosity of the formulation gradually becomes loss the internal structure of material was broken down.

Table 3. Detailed data of thixotropy study.

Block index	Time (s)	Shear rate (1/s)	Shear stress (Pa)	Shear rate (1/s)	Shear stress (Pa)
0	10	0.0	0.0	0.0	0.0
0	20	0.0	9.998	0.001	9.984
0	30	0.01	19.99	0.05	19.989
0	40	0.01	29.99	0.013	29.993
0	50	0.09	40.00	0.088	39.998
0	60	0.76	49.98	0.764	49.982
0	70	0.72	49.98	0.724	49.982
1	80	0.18	40.0	0.175	39.998
1	90	0.00	29.99	0.003	29.993
1	100	0.00	19.99	0.00	19.989
1	110	0.00	9.98	0.00	9.984
1	120	0.00	0.00	-0.001	0.000

All the detailed data of thixotropy study is presented in Table 3 [5,26].

Drug content study of film-forming gels

The drug content of the PVA-based gel and final organic-inorganic film-forming gel formulation (HG-9) gel was determined in triplicate and from standard deviation drug content was found to be of $88.4 \pm 3.178\%$ and $95.1 \pm 2.31\%$ respectively. The drug content of hybrid gel was found to be more than that of organic PVA-based gel. Hence uniformity of drug content was found to be satisfactory.

Texture profile analysis

a higher peak load (firmness) and hardness work done value indicate a less spreadable sample. Conversely, a lower peak load (firmness) value coupled with a lower hardness work done value indicates a more spreadable sample. The observations for spreadability of PVA-based gel and organic-inorganic hybrid (HG-9) gel is shown in Figure 5. Comparison of mechanical properties between PVA-based gel and hybrid gel were presented in Table 4.

Animal activity

Skin irritation test. The result of skin irritation study based on visual observation, it has revealed that hybrid gel (HG-9) formulation was non-sensitising and safe

Table 4. Comparison of mechanical properties between PVA-based gel and hybrid gel.

Sr. no.	Parameters	Resultant value of PVA-based gel (OG)	Resultant value of hybrid gel (HG-9)
1.	Adhesiveness	0.70 mJ	3.40 mJ
2.	Stringiness Length	0.00 mm	0.56 mm
3.	Fracturability	10.00 g with 1% of load sensitivity	14.00 g with 1% of load sensitivity
4.	Cohesiveness	1.26	0.81

*OG = Organic Gel; *HG = Hybrid Gel

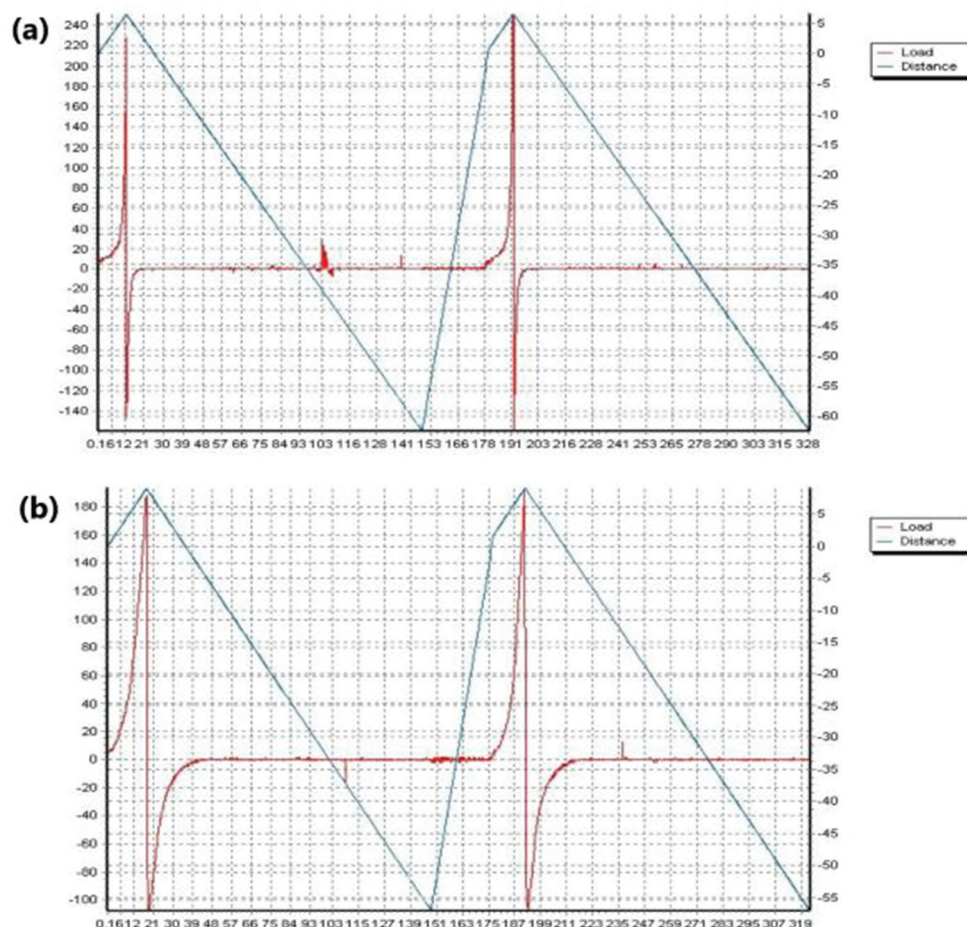


Figure 5. Texture analysis: Mechanical properties and spreadability study of PVA organic gel (a) and Hybrid organic-inorganic gel (b).



Figure 6. Skin irritation study using rats as animals.

Table 5. Skin irritation study data.

Test material ^a	Skin reaction ^b	Mean irritation score		
		12 hours	24 hours	48 hours
Hybrid-organic-inorganic film (HGF-9)	Erythema	0	0	0.1
	Oedema	0	0	0

^aTest material was applied on rat skin

^bErythema and oedema, the mean irritation score was the summation of each irritation score divided by the number of animals (rats)

for use, as there was no significant irritation produced after application of hybrid gel (HG-9) formulation on the rat’s skin. Following observation were depicted from the skin irritation and photographs of animals undergoing skin irritation study are presented in Figure 6. The erythema and oedema irritation matrix score was presented in Table 5.

Analgesic activity. Final HG-9 formulation possesses very significant analgesic effect according to statistical analysis. Statistical *t*-test was applied and statistical data was generated as mentioned in Figure 7.

Ex-vivo drug permeation study of tramadol HCl organic-inorganic hybrid gel

The *ex-vivo* drug permeation of Tramadol HCl organic-inorganic hybrid gel was evaluated by *ex-vivo* diffusion study using Franz diffusion cell, using a fresh goat skin as a diffusion membrane at pH 7.4. Cumulative % of drug permeated are mentioned in Figure 8. Formulations with higher concentration of PVA shown less amount of drug

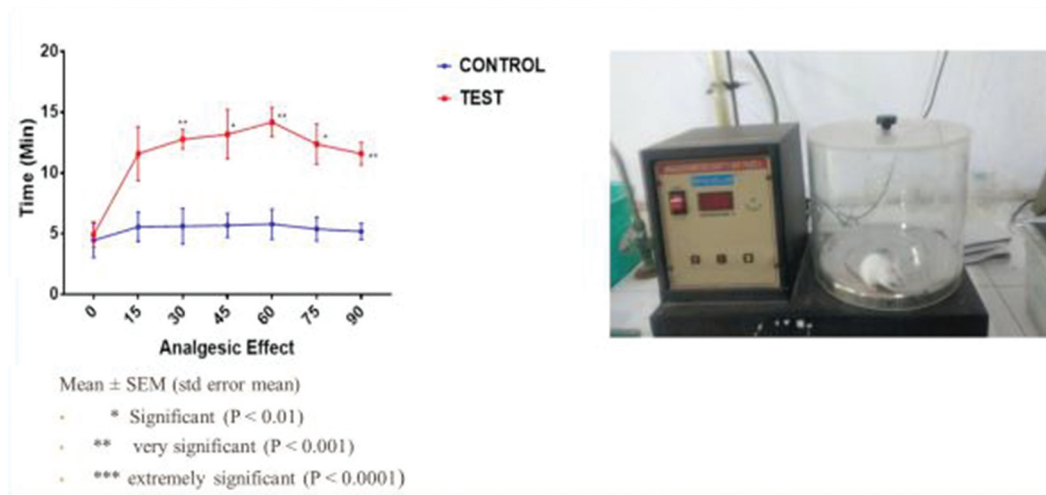


Figure 7. Analgesic activity in mice.

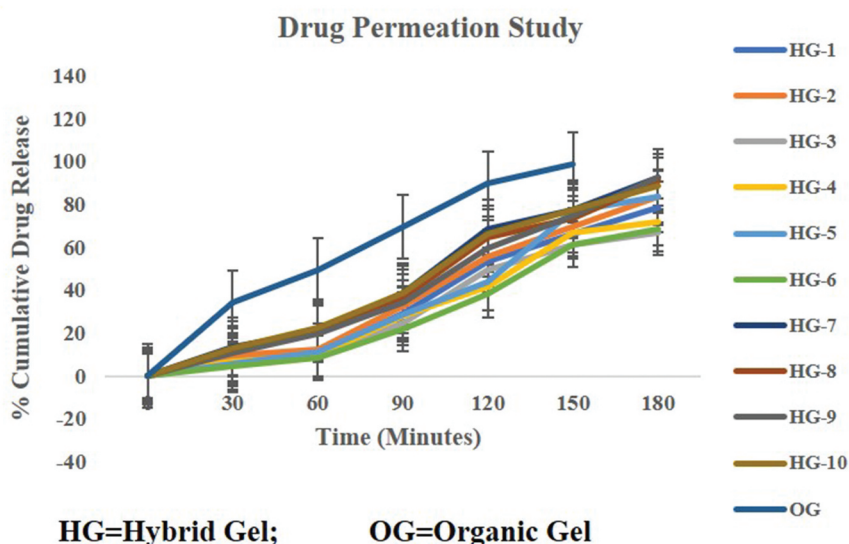


Figure 8. Cumulative drug permeation study of both organic and hybrid film-forming gel.

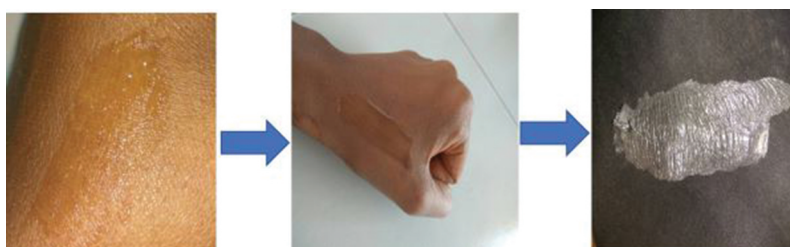


Figure 9. Appearance of prepared and applied dried film.

release after 3 hours of time period. Hence, in first few formulations, HG-1 to HG-6, less amount of drug release was observed, showing 78.66%, 83.55%, 66.55%, 71.45%, 83.25% and 68.58% respectively. This may happen due to extent of cross-linking interaction between PVA and TEOS in the presence of HCl [5]. There was little difference of drug release was found among the formulations HG-7 to HG-10 due to presence of nearly same amount of PVA and TEOS showing, 92.5%, 90.58%, 92.36% and 88.68% respectively. Finally, HG-9 formulation was

considered to be optimised based on the initial results observed and as identified which was already discussed in method section 2.2.1.

Appearance and miscibility study

For the blend-type polymer gels, the structural properties and the unique functions were dependent on the miscibility, chemical structure and interaction between mixture components. PVA and glycerine have excellent compatibility due to the well-known observation of PVA solubility in glycerol. The high transparency of the film in Figure 9 indicated that there may be no macro-

Table 6. Stability study hybrid-organic-inorganic film-forming gel.

Duration	Temperature and relative humidity	Appearance	*pH	*Drug content
1 month	40°C, 75%RH	Transparent, smooth, viscous	7.0 ± 0.2	95.9 ± 0.58%
2 months	40°C, 75%RH	Transparent, smooth, viscous	6.9 ± 0.4	95.0 ± 0.84%
3 months	40°C, 75%RH	Transparent, smooth, viscous	7.0 ± 0.2	96.01 ± 1.02%

*All the observations were taken in triplicate as ±SD ($n = 3$).

phase separation occurring between the organic polymer and inorganic TEOS.

Stability study

The storage of tramadol HCl organic-inorganic hybrid gel containing of an optimised batch for 3 months at room temperature and relative humidity (40°C, 75%) showed no change in appearance of the system was explained in Table 6.

Stability study was performed for 1, 2 and 3 months which did not show any major changes in appearance, pH, drug content.

Characterisation of tramadol HCl organic-inorganic hybrid film

The organic-inorganic hybrid film of tramadol HCl was evaluated for various physical and chemical parameters in order to ensure the quality of the film for continuous release of tramadol HCl in the management of pain on affected area by transdermal route. Simultaneously, the organic PVA film containing tramadol HCl was also evaluated XRD study.

The XRD was used to investigate the influence of TEOS on the crystalline property of the hybrid films, which was shown in fig. As seen, pure PVA film possessed distinctly higher crystalline intensity than its hybrid films, and results showed the main diffraction peaks of PVA film containing Tramadol HCl and PVA-TEOS hybrid film containing Tramadol HCl were around $2\theta = 6.14$ and 5.360 respectively. In the XRD patterns, this can be ascribed to the crystalline regions of PVA due to strong hydrogen bonds between the hydroxyl groups. Furthermore, peak intensities of PVA hybrid films decreased

continuously with incorporation of TEOS. Namely, there was a significant decrease in crystalline regions and increase in amorphous regions in the hybrid film, which can indicate that the introduction of TEOS led to the destruction, to some extent, of the crystalline region of PVA film [11]. Figure 10 shows the interpretation of the XRD peaks observed for both organic PVA film and hybrid film.

All the observations of thickness, drug content, moisture content, moisture uptake capacity and swelling index study are presented in Table 7 and discussed below.

The drug content of the optimised Formulation (HG-9) film and PVA film was carried out in triplicate and average drug content was found to be of 87.20% and 81.3% respectively. The drug content of hybrid film was found more than the organic PVA film. Hence uniformity of drug content was found to be satisfactory.

In moisture content study, selective films final formulations were evaluated and average moisture was found to be $1.07 \pm 0.04\%$. These values show the percent moisture uptake capacity of films. The

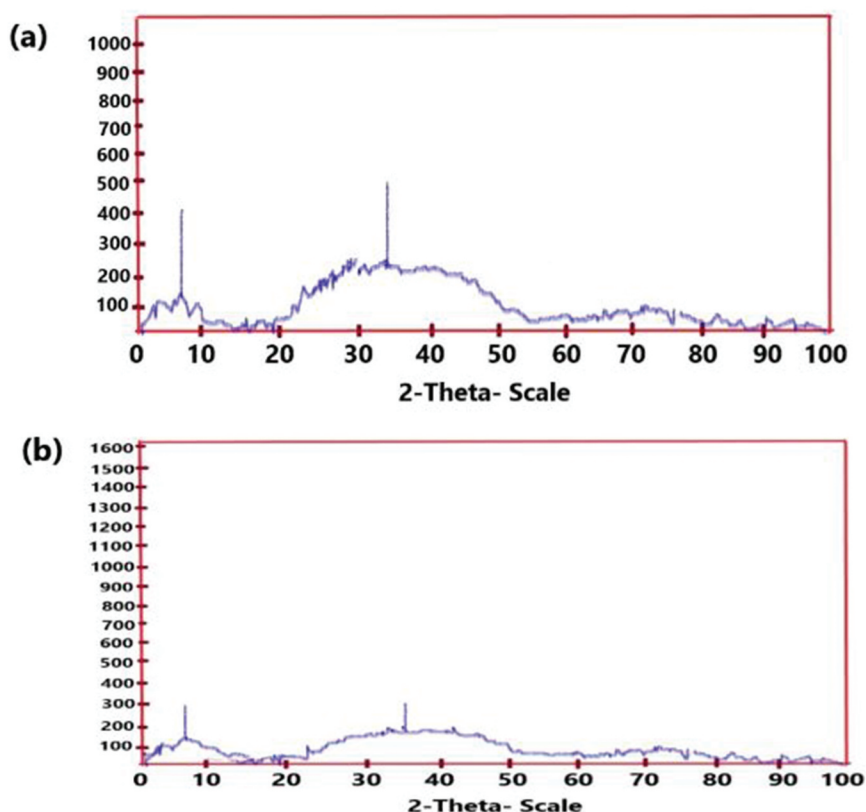


Figure 10. XRD graph of PVA-organic film (a) and hybrid-organic-inorganic film (b) containing tramadol HCl.

Table 7.: Evaluation of tramadol HCl films for various parameters.

Sr. no.	Type of formulation	*Thickness (mm)	*Drug content (%)	*Moisture content (%)	*Moisture uptake capacity (%)	*Swelling index (%)
1.	PVA Organic Film (OGF)	0.584 ± 0.014	81.3 ± 0.55	2.13 ± 0.12	2.55 ± 0.45	78.28 ± 0.14
2.	Hybrid Organic-inorganic Film (HG-9)	0.458 ± 0.032	87.20 ± 0.24	1.07 ± 0.04	1.65 ± 0.16	89.45 ± 0.23

*All the experiments were conducted triplicate \pm SD ($n = 3$).

moisture uptake of the films was generally low; this will help the films to remain stable and protect them from microbial contamination. Generally, the moisture uptake capacity of films increases with increasing hydrophilicity of the polymer or plasticiser and the levels of hydrophilic polymers as well. Moisture uptake capacity of PVA-organic film was higher than the hybrid film whereas the swelling index values of hybrid film was found to be little higher than the PVA-organic film. Extent of swelling was also depending upon the hydrophilicity of film and proportion of such components in the formulation.

In folding endurance study, a specific area of strip was cut and repeatedly folded at the same place till it broke. The number of times the film was folded without breaking gave the value of folding endurance. Films were folded for more than 300 times it did not show any sign of cracks. It was taken as end point and confirmed the physical stability of formed film of organic-inorganic hybrid gel.

For weight variation study, films formed from final organic-inorganic hybrid gel were selected and average weight of films were considered as final weight of the films. In this study, average weight of film (10×40mm size) was found to be 0.21 ± 0.007 g. Readings were taken in triplicate for accuracy.

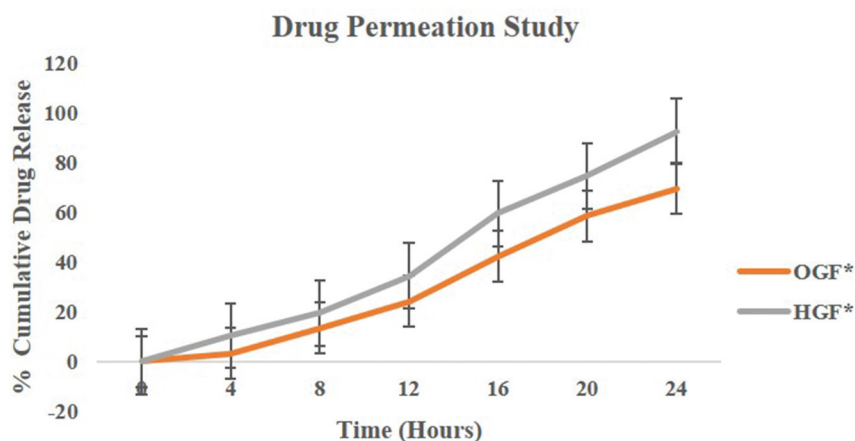
It is very important to know about the drying time of the gel to form the film after application on the intact skin. For this purpose, a simple observation technique was implemented as discussed above. a glass slide was placed on the film without pressure and after 2 minutes glass slide was removed from film and it was observed that no liquid form of gel was visible on the glass slide, this has indicated that the film was dried immediately.

Both organic as well as hybrid-organic-inorganic films were subjected to the drug permeation study as discussed in the method section. For this study optimised formulation GHF was selected as hybrid dried

film and PVA organic film (OGF). In this study, both results were compared and it was found that the PVA organic (OGF) has shown less amount of 69.55% drug release whereas hybrid film (HGF) has shown 92.36% drug release in the 24 hours of study. This huge difference in the drug release among both the formulation was due to the fact the nature of PVA organic film little hydrophilic with high level of concentration in the formulation. But strong interaction between PVA and TEOS make weak C-OH peak and formation of Si-O-C peaks in the XRD study. Due to this crystallinity of the PVA decreases resulting more soluble and transparent film formation and hence hybrid film has shown higher percentage of drug release as compare to the plain PVA organic film [11,27]. The cumulative drug release profile of both the organic PVA (OGF) and hybrid organic-inorganic film is highlighted in Figure 11.

Surface morphology of both the organic PVA film and hybrid organic-inorganic film was checked visually as well as using scanning electron microscopy (SEM). SEM can provide

direct visual evidence of the influence of TEOS on surface morphology of the hybrid films. SEM photographs of surface sections of pure PVA and its hybrid are displayed in Figure 12. From these micrographs, it can be seen that the surface of PVA film was both homogeneous and smooth. Moreover, the addition of TEOS significantly affected the surface morphology. However, no visible phase separation between PVA and silica in all hybrid films can be observed. The hybrid HG-9 film exhibited a homogeneous granular structure. The presence of silica microparticles can be attributed to the reaction between PVA and the hydrolysed silanol of TEOS in the sol-gel process, which may play an important role in destroying regular crystalline arrangement of PVA chains and consequently decreasing the crystalline regions in PVA films. In



*OGF=Organic-Gel-Film;

*HGF=Hybrid-Gel-Film

Figure 11. Cumulative drug permeation study of both organic and hybrid dried films.

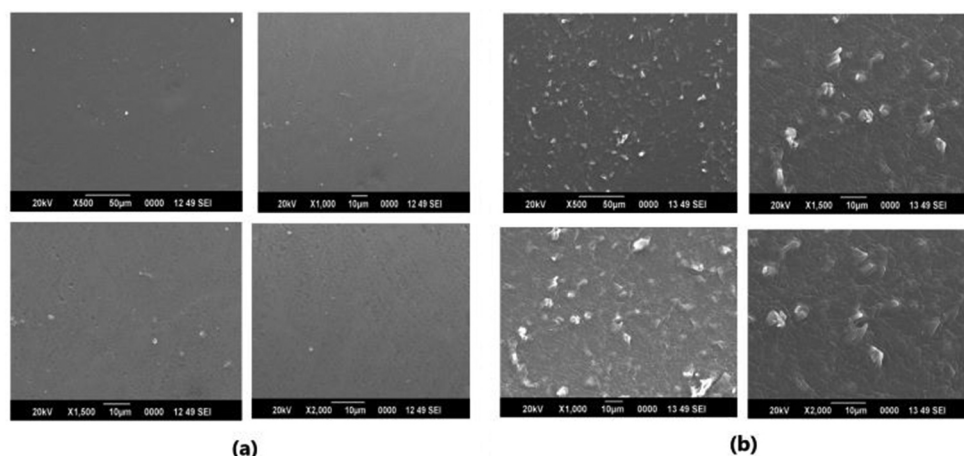


Figure 12.: Scanning electron microscopic photographs showing morphology of prepared film at different resolution.

Table 8.: Stability study hybrid-organic-inorganic film.

Duration	Storage condition	Appearance	*Drug Content
1 month	40°C, 75%RH	Transparent, thin, no brittleness	84.23 ± 1.05%
2 months	40°C, 75%RH	Transparent, thin, no brittleness	83.20 ± 1.15%
3 months	40°C, 75%RH	Transparent, thin, no brittleness	83.28 ± 0.89%

**All the observations were conducted triplicate ±SD ($n = 3$)

addition, the surface morphology of hybrid film became rough and uneven, which was due to the polycondensation of excessive TEOS leading to conglomeration and aggregation in the matrix. This conglomeration and aggregation may result in the film more compact that does not favour the diffusion of the drug molecule in the film.

Stability study was performed for 1, 2 and 3 months which does not show any major changes in appearance, drug content. Results of stability study of hybrid film is presented in Table 8.

Conclusion

Transdermal drug delivery systems have gained many benefits and are better alternatives for other conventional routes of administrations like oral to avoid GI irritation, first-pass effect and undesired drug release pattern. Conventional available transdermal/topical formulations are not capable to modify the drug release property and other physical properties and have many disadvantages. In this study, an attempt was made to prepare a novel organic–inorganic hybrid film-forming gel formulation, which showed enhanced adhesion, cross-linking and better drug release property with ease of application on skin and formation of flexible, comfortable film than plain PVA films. More importantly, use of inorganic phase in PVA matrix not only significantly improved mechanical strength and skin adhesion properties, but also

decreased the crystalline regions of PVA and hence facilitate the diffusion of drug and water.

So, from this study it was concluded that formulation of organic-inorganic film-forming gel is the challenging and excellent new approach for transdermal delivery of drug with better patient compliance as compare to the existed organic material-based transdermal formulations.

Acknowledgements

Authors are very thankful to the IPCA laboratories, Mumbai for providing Tramadol HCl.

Also grateful to the Principal of our institute for providing facilities and support to conduct this research study. At the last, authors are very thankful to all those who have cooperated to complete this work successfully.

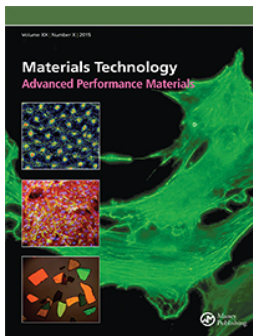
Disclosure statement

Authors declare no conflict of interest.

References

- [1] Yu YY, Chen CY, Chen WC. Synthesis and characterization of organic–inorganic hybrid thin films from poly(acrylic) and monodispersed colloidal silica. *Polymer*. 2003;44:593–601.
- [2] Novak BM. Hybrid nanocomposite materials-between inorganic glasses and organic polymers. *Adv Mater*. 1993;5:422–433.
- [3] Otsuka T, Poly CY. (methyl methacrylate) (PMMA)-based hybrid materials with reactive zirconium oxide nanocrystals. *Polym J*. 2010;42:58–65.
- [4] Ibrahim H, Ibrahim S. Study some properties of hybrids silica/PVA using sol gel method. *Chem Bio Phy Sci Sec C*. 2015;5(2):1950–1957.
- [5] Guo R, Xiaoyan D, Zhang R, et al. Bioadhesive film formed from a novel organic–inorganic hybrid gel for transdermal drug delivery system. *Eur J Pharm Biopharm*. 2011;79:574–583.
- [6] Wang K, Nune KC, Misra RDK. The functional response of alginate-gelatin-nanocrystalline injectable

- hydrogels toward delivery of cells and bioactive molecules. *Acta Biomaterialia*. 2016;36:143–154
- [7] Wang K, Lin S, Nune KC, et al. Chitosan-gelation based microgel for sustained drug delivery. *J Biomat Sci*. 2016;27:441–453.
- [8] Wang K, Buschle-Diller MRDK. Chitosan-based injectable hydrogels for biomedical applications. *Materials Technol*. 2015;30:198–205.
- [9] Yuan Q, Shah J, Hein S, et al. Controlled and extended drug release behavior of chitosan-based nanoparticle carrier. *Acta Biomaterialia*. 2010;6:1140–1148.
- [10] Yuan Q, Hein S, Misra RDK. New generation of chitosan-encapsulated ZnO quantum dots loaded with drug: synthesis, characterization and in vitro drug delivery response. *Acta Biomater*. 2010;6:2732–2739.
- [11] Yuan Q, Subramanian R, Hein S, et al. Stimuli-responsive magnetic nanoparticle drug carrier: magnetite encapsulated with chitosan-grafted-copolymer. *Acta Biomater*. 2008;4:1024–1037.
- [12] Prausnitz MR, Langer R. Transdermal drug delivery. *Nat Biotechnol*. 2008;26:1261–1268.
- [13] Berner B, John VA. Pharmacokinetic characterization of transdermal delivery systems. *Clin Pharmacokinet*. 1994;26:121–134.
- [14] Setouhy DA, Ashmony SM. Ketorolac tramadol topical formulations: release behaviour, physical characterization, skin permeation, efficacy and gastric safety. *J Pharm Pharmacol*. 2010;62:25–34.
- [15] Klotz U. Tramadol-the impact of its pharmacokinetic and pharmacodynamic properties on the clinical management of pain. *Arzne imittel for schung*. 2003;53:681–687.
- [16] Raffa RB. Basic pharmacology relevant to drug abuse assessment: tramadol as example. *J Clin Pharm Ther*. 2008;33:101–108.
- [17] 24 December 2019. Available from: <http://www.brookfieldengineering.com/education/learn-about-texture.asp>
- [18] 24 December 2019. Available from: <http://www.brookfieldengineering.com/education/applications/texture-analysis.asp>
- [19] 24 December 2019. Available from: <http://www.brookfieldengineering.com/education/applications/texture-jelly-cup.asp>
- [20] Reddy MS, Mutalik S, Rao G, et al. Preparation and evaluation of minoxidil gels for topical application in alopecia. *Indian J Pharm Sci*. 2006;68(4):432–436.
- [21] More BH, Sakharwade SN, Tembhurne SV, et al. Evaluation for Skin irritancy testing of developed formulations containing extract of *Butea monosperma* for its topical application. *Int J Toxicol Appl Pharmacol*. 2013;3(1):10–13.
- [22] Kasture SB. A handbook of experiments in pre-clinical pharmacology. 1st ed. Career publication; 2006. p. 72–73.
- [23] Ammar HO, Ghorab M, El-Nahhas SA, et al. Polymeric matrix system for prolonged delivery of tramadol hydrochloride, part I: physicochemical evaluation. *AAPS Pharm Sci Tech*. 2009;10:7–20.
- [24] Dyer JR. Applications of absorption spectroscopy of organic compounds. Prentice Hall of India; 2004. p. 33–38.
- [25] Skoog DA, West DM. Fundamentals of analytical chemistry. 8th ed. Singapore: Thomson Brooks/Cole; 2004. p. 906–946.
- [26] Chhabra RP, Richardson JF. Non-Newtonian flow in the process industries: fundamentals and engineering applications. Butterworth-Heinemann; 1999.
- [27] Hu P, Jia M, Zuo Y, et al. A silica/PVA adhesive hybrid material with high transparency, thermostability and mechanical strength. *RSC Adv*. 2017;7:2450–2459.



Tailoring hybrid organic-inorganic film-forming topical gel: a tuneable approach for tramadol HCl delivery

Prakash N. Kendre , Gayatri Dusane , Shirish P. Jain , Mahendra A. Giri & Ajinkya K. Pote

To cite this article: Prakash N. Kendre , Gayatri Dusane , Shirish P. Jain , Mahendra A. Giri & Ajinkya K. Pote (2020): Tailoring hybrid organic-inorganic film-forming topical gel: a tuneable approach for tramadol HCl delivery, Materials Technology, DOI: [10.1080/10667857.2020.1802839](https://doi.org/10.1080/10667857.2020.1802839)

To link to this article: <https://doi.org/10.1080/10667857.2020.1802839>



Published online: 07 Aug 2020.



Submit your article to this journal [↗](#)



View related articles [↗](#)



View Crossmark data [↗](#)



Tailoring hybrid organic-inorganic film-forming topical gel: a tuneable approach for tramadol HCl delivery

Prakash N. Kendre^a, Gayatri Dusane^b, Shirish P. Jain^c, Mahendra A. Giri^b and Ajinkya K. Pote^a

^aDepartment of Pharmaceutics, Rajarshi Shahu College of Pharmacy, Buldana, India; ^bDepartment of Pharmaceutics, Sanjivani College of Pharmaceutical Education & Research, Kopergaon, Maharashtra, India; ^cRajarshi Shahu College of Pharmacy, Buldana, India

ABSTRACT

Drug release properties for transdermal route can be better modified as per requirement which is mostly dependent upon the carrier system. In case of organic film-forming systems, the physical properties may not be achieved for successful delivery of drug through transdermal route. A novel organic-inorganic hybrid film-forming gel may fulfil these expectations to many extend. The present study focuses on the development of the organic-inorganic hybrid film-forming gel. A smooth, transparent, clear film-forming gel of tramadol was prepared for application on the intact skin with better comfort and modified drug release rate properties. The key properties of the adhesive films produced from the hybrid gels were investigated and the results showed that the incorporation of appropriate PVA: TEOS: Glycerine: HCl in the ratio of 46:12.5:25.5:6 respectively. Resultant hybrid film-forming gel has modified the physical properties and improved drug release properties. Furthermore, the investigations of skin irritation suggested no irritation to skin after topical application. This study has provided an alternative to the presently available organic gel and films for transdermal delivery of drugs with better patient compliance and modified physical and chemical stability.

ARTICLE HISTORY

Received 9 April 2020
Accepted 27 July 2020

KEYWORDS

TEOS; PVA; hybrid-organic-inorganic film-forming gel; tramadol HCl; transdermal route etc

Introduction

Many of the drug delivery systems have been developed till date by many researchers with different characteristics. Efficient drug delivery systems can be developed further by doing modifications in the available drug delivery systems. These modifications can be possible using variety of compatible polymeric components. These modifications may include grafting of polymers, cross-linking of polymers and many more other approaches using various techniques.

Hybrid systems are made-up of composites of two different materials with different physical and or chemical properties. Hybrid film-forming gels refers to the combination of organic and inorganic components in one system either at macroscopic level or molecular level [1].

Single hybrid system is a homogenous phase of both organic and inorganic materials and shows characteristics that are different at their individual level. These resultant characteristics may be beneficial based upon the appropriate contributions of both the materials combined together using suitable methodology and techniques. Mechanical properties of hybrid systems are so improved so that patient acceptance will enhance with excellent drug release properties and stability of the final formulation. Mostly inorganic

phase provides mechanical strength while organic phase delivers bonding. The word hybrid comes from the Latin word 'hybrida', which is related to the meaning 'mongrel'. The easy way to construct transparent and homogeneous hybrid materials is to increase the affinity between organic polymer and inorganic phases [2].

Optical transparency is the most important characteristic of these hybrids and it arises because dispersion of material in the matrix is in the order of tens of nanometres, far less than the wavelength of visible and ultraviolet light. As a result, light is not lost due to scattering.

Moreover, the hybrid materials offer the advantages like higher flexibility and mechanical strength, greater temperature, range of usability, increased durability, improved electrical, magnetic or redox properties [3–5].

The synthesis of hybrid materials includes two methodologies:

- (A) Building block approach
- (B) *In-situ* formation of the components
 - a. In situ formation of inorganic materials
 - b. Formation of organic polymers in presence of preformed inorganic materials

- c. Hybrid materials by simultaneous formation of both components.

Wang et al. have prepared the hybrid injectable hydrogels consisting of gelatin and nanocrystalline cellulose. These hydrogels were processed using adaptation of interpenetrated network of alginate-gelatin, ionic cross-linking and supramolecular interaction approach. Due to this approach mechanical properties were changed and resembles native tissue structure. This approach has been used for delivery of cells in tissue engineering [6].

In another study, the researchers have synthesised microgels via cross-linking of chitosan and gelatin with succinimide-end polyethylene glycol (PEG). The presence of PEG provided thermoresponsiveness to microgels due to which the size of microgels was significantly changed at elevated temperature [7].

Another cross-linking aspect of modified form of materials used to prepare biocompatible injectable hydrogels. In this approach, different gelation techniques like, physical cross-link, chemical cross-link, ionic cross-link and supramolecular interaction were used to prepare chitosan-based injectable hydrogels to be formed. These gelation approaches have significant impact on the structure and properties of hydrogels, which directs their use as tissue engineering scaffold and drug delivery vehicle [8].

Chitosan-based controlled and extended drug release nanoparticles were prepared using expandable layered aluminosilicate as an inorganic material. This hybrid form of nanoparticles has significant impact on the drug release rate properties due to change in the structural morphology and swelling behaviour. The study has revealed its application in the biomedical and tissue engineering for controlled drug delivery [9].

Another study suggested the preparation of chitosan-encapsulated ZnO quantum dots loaded with drug for anti-cancer treatment. Study has demonstrated its use for tumour-targeted delivery of anti-cancer agents [10].

In one more study, chitosan-grafted-copolymer has been used to prepare stimuli-responsive magnetic nanoparticle drug carrier. This grafted chitosan has significant impact on the drug release property which was extended in a controlled fashion that responds to the change in temperature and pH with characteristics of longer circulation time and reduced side effects [11].

Transdermal drug delivery system has been proved to be an alternative to the many oral as well as injectables preparations avoiding first-pass-metabolism and painful irritations respectively.

In first generation, this route has been used for delivery of lipophilic and low-dose drugs. In second generation, using chemical permeation enhancers, iontophoresis, sonophoresis etc. In third generation,

microneedle injection, electroporation and cavitation ultra sound approach has been used for delivery of drugs.

Transdermal delivery system is a desirable alternative administration route for tramadol hydrochloride for patients with chronic pain. To overcome skin barrier property, organic-inorganic (hybrid) film-forming gel approaches have been chosen in this study [12–14].

Hybrid material offers multiple benefits and its use in drug delivery system is itself a novel approach. Based on these considerations the current work has aimed to prepare a novel organic-inorganic (hybrid) film-forming gel for transdermal drug delivery of tramadol HCl, a non-invasive drug administration route and offers potential benefits of simplicity, efficacy and patient acceptance by maintaining a constant blood drug concentration for an extended period [15].

In addition, the transdermal delivery system can decrease the possible abuse and addiction potential of tramadol by avoiding peak and trough plasma concentrations and by reducing the total amount of medication input [16].

Materials and method

Materials

Tramadol HCl was obtained from IPCA laboratories, Mumbai; polyvinyl alcohol (PVA), tetraethylorthosilicate (TEOS), were obtained from Research Fine Chem Industries, Mumbai. All other chemicals glycerine, hydrochloric acid (HCl) etc. used were of analytical grade.

Method

Preparation of hybrid-organic-inorganic film-forming gel

Preparation of hybrid-film-forming gel was prepared in two steps as mentioned below. Both the phases were prepared separately as organic and inorganic phase and mixed together to form homogenous gel with improved physical, chemical properties and modified drug release properties. Different concentration and levels of components in the formulation are highlighted in Table 1.

Preparation of organic phase. Initially the organic phase was prepared using typical synthesis, weighed amount of PVA was added to double distilled water which is preheated at 90 °C with continuous stirring till PVA was completely mixed in the water. The resultant homogenous blend of PVA was allowed to cool at room temperature.

Table 1. Formulation batches of organic-inorganic hybrid gel.

Ingredient (%)	HG-1	HG-2	HG-3	HG-4	HG-5	HG-6	HG-7	HG-8	HG-9	HG-10
Tramadol HCl	5	5	5	5	5	5	5	5	5	5
PVA	50.87	47.18	64.43	62.49	62.49	71.95	44.76	46.5	46	45
TEOS	18.46	18.46	14.77	11.81	11.81	10	11.5	12	12.5	12.5
Glycerine	14.77	18.46	4.90	9.80	9.80	3.05	28.24	25.5	25.5	25.5
HCl	5.90	5.90	5.90	5.90	5.90	5	5.5	6	6	7
Distilled Water	5	5	5	5	5	5	5	5	5	5

*HG = Hybrid Gel

Preparation of inorganic phase and catalyst mixture.

In this step required amount of 0.1 N HCl was added dropwise in the weighed amount of Tetraethyl orthosilicate (TEOS). Initially, separate phase of globules was observed which disappeared with continuous stirring and finally a clear transparent solution was formed. Heat was evolved at the end due to exothermic reaction.

In the later step, inorganic phase was added to the organic phase in a dropwise manner with continuous mixing till homogenous system was formed. This mixture was then added to another previously prepared mixture of glycerine, water and drug to form the final formulation.

As shown in above Table 1, various batches of hybrid film-forming gel were prepared.

The optimised batch was selected by the self-developed method as described below. The prepared hybrid gel was poured on a uniform surfaced glass slide. The gel was allowed to form a thin layer on the slide. Once the film was formed it was slowly peeled off from the slide. According to the visual observation and experience, manual peeling force required, spreadability of solution on glass slide and texture of film, the best hybrid film-forming gel batch was selected and further characterised for different physical and chemical parameters using various tools and techniques. It has made easy job to deal with only selective formulation batch out of initially formulated batches for further characterisation and testing.

Preparation of PVA-based gel

In typical synthesis, the weighed amount of PVA was dissolved in double distilled water preheated at 90°C under stirring. After complete dissolution of PVA, fixed amount of drug was added to the mixture upon cooling at room temperature. Various batches with concentration of PVA from 1 % W/V to 30% W/V were prepared to get final desired formulation of PVA gel. Final formulation batch was selected using self-developed method. On one glass slide; prepared PVA solution was poured and tried to spread evenly that leads to formation thin layer on the glass slide. The formed film was dried for 5 minutes and peeled out to check the peel ability. Final concentration of PVA was determined on the basis of their physical parameters

like spreadability of PVA solution, peeling force required after drying and texture properties of formed film.

Characterisation of film-forming gel

All the batches of Tramadol HCl organic-inorganic hybrid film-forming gel formulations were observed for appearance, pH, colour and consistency etc.

pH

Accurately weighed 1 gm of gel was and dispersed in 100 ml of distilled water. The pH of dispersion was measured using digital pH metre. All the readings were taken in triplicate and noted.

Rheological study

a Brookfield digital RST-CC Rheometer (7,120,128) was used to determine rheology and viscosity of the formulations. The viscosity was measured by 12 MP in 4 blocks (UID-140).

Drug content

Drug content study was conducted for organic-inorganic hybrid film-forming gel as well as PVA-based gel.

Accurately weighed amount of (500 mg) of Tramadol HCl containing organic-inorganic hybrid film-forming gel was added to 50 ml of phosphate buffer (pH 7.4). Resultant solution was kept for sonication for 10 minutes to dissolved the gel completely. Absorbance of solution was checked at 271 nm against blank as a phosphate buffer solution. Thus, percentage drug content was calculated. All the readings were taken in triplicate and noted. Same method was implemented to determine the drug in the PVA organic gel.

FT-IR study

Tramadol HCl was identified and confirmed by using the FT-IR (8400, Shimadzu, Japan), Drug:KBr (1:100) ratio was taken and mixture was gently grinded in the mortar pestle, then translucent pellet was made by using the pellet press method, then pellet was placed in the sample holder, then instrument was run and gotten the FTIR spectra of the Acitretin. The samples were tested at R.C. Patel College of Pharmacy, Shirpur, India. In the same way, Physical blends of drug and

other excipients were also analysed for compatibility testing and suitability for the preparation of final formulation.

Differential scanning calorimetry (DSC) study

Shimadzu DSC-60 plus was used for DSC study of selected hybrid organic-inorganic gel as well as PVA organic gel. Small amount of 3–6 mg sample was taken on aluminium pan. The sample was covered with the aluminium lead and crimping was carried out with the help of crimping tool. The crimped pan was installed at the sample holder point. The test was carried out and the thermogram was recorded in TW-60 software

Texture analysis

Texture analysis of PVA-based gel and organic-inorganic hybrid gel was performed using a CT3 Texture Analyser in TPA mode. Formulations were transferred into lower cone taking care to avoid the introduction of air into the samples. A conical analytical probe (45°C) was forced down into each sample at a defined test speed (2 mm/s) and to a defined depth (12 mm). At least five replicate analyses of each sample were performed at temperatures of 25°C and 30°C. From the resulting force–time plots, the hardness (the force required to attain a given deformation), compressibility (the work required to deform the product during the first pass of the probe) and adhesiveness (the work necessary to overcome the attractive forces between the surface of the sample and the surface of the probe) were derived [17–19].

Appearance and miscibility study

All the batches of Tramadol HCl organic-inorganic hybrid film formulations were observed for appearance and transparency.

The structural properties and the unique functions of the blend-type polymer gels, were dependent on the miscibility, chemical structure and interaction between mixture components. No macro-phase separation occurring between the organic polymer and inorganic is indicated by the high transparency in the film [20].

Ex-vivo drug diffusion study of hybrid gel

Investigation of the amount of drug released from a tramadol HCl organic-inorganic hybrid gel was performed using *Ex-vivo* drug diffusion study. A fresh goat skin was used as a diffusion membrane. Goat skin was positioned between the two cell halves of a glass chamber. The two compartments were held together with a clamp, 10 ml of phosphate buffer pH 7.4 was added to the receiver/receptor compartment. The donor compartment was loaded with 0.5 gm of formulation which was spread evenly on the membrane. The receptor phase (phosphate buffer pH 7.4) was continuously stirred with the help of magnetic stirrer at 300 rpm

and maintained at 37°C using a circulating water bath. Samples of 1 ml were collected at the interval of every 20 minutes for 3 hours study from the receiver compartment at predetermined time intervals and replaced with fresh buffer solution. The samples collected were analysed for drug content using UV-spectrometric method at 271 nm wavelength and finally graph was plotted as percentage cumulative drug permeation Verses time [19].

Animal activity

Skin irritation study. Skin irritation study was conducted using healthy rats. The protocol of the study was sanctioned by the Institutional Animal Ethical Committee and permission was granted to conduct the study using healthy rats monitored as per the guidelines of animal ethical committee. The rats ($n = 9$) were randomly divided into three equal groups for application of standard irritant, optimised formulation or test and control (no application). Hairs were removed by bend scissor from an area (2 cm²) on the dorsal side of the albino rats to make a hairless area. The optimised formulation was applied to group 2 of rats ($n = 3$) for assessing any kind of irritation at specified sites. Formulation was removed after 48 hours and skin was examined for any signs of erythema and oedema [20,21].

Analgesic activity. Analgesic activity was conducted using healthy mice. The protocol of the study was sanctioned by the Institutional Animal Ethical Committee and permission was granted to conduct the study using healthy rats monitored as per the guidelines of animal ethical committee. Mice weighing 25–30 gm were divided in two groups of five each. The hot plate was maintained at $56 \pm 1^\circ\text{C}$. Formulation was applied on the animals and placed into a glass cylinder of 24 cm diameter on the heated surface. The time between placement and licking the paws or jumping was recorded as response latency. The reaction time was recorded for control mice treated with Tramadol HCl (5 %) at 0, 15, 30, 60 and 90 minutes. The test was terminated at 15 seconds to prevent tissue damage. The statistical analysis was carried out using Graph-Pad-Prism 3.03 software. The *t*-test was selected as the test for significance and *P* value less than 0.05 was considered statistically significant [22].

Stability study of film-forming gels

Stability study was conducted according to the ICH guidelines at $40 \pm 2^\circ\text{C}$ and $75 \pm 5\%$ RH for 3 months. The samples were withdrawn at beginning, after 30, 60 and 90 days and analysed for any physical and chemical changes.

Characterisation of tramadol HCl organic-inorganic hybrid film

In order to characterise the film quantitatively, it was characterised with the help of the following parameters. All the batches of tramadol HCl organic-inorganic hybrid film formulations were observed for appearance and transparency.

X-Ray diffraction study (XRD)

Bruker Model D8 Advance was used to check the crystallinity of formulation. This test was done from Sophisticated Test and Instrumentation Centre, Kochi University, Kochi, Kerala, India. The sample was smeared over low back ground sample holder (amorphous silica holder) and fixed on the sample stage in goniometer. The instrument was set with B-B geometry. The current and voltage was set to 40 mV and 35 mA and data was collected.

Drug content study of film-forming gels

Uniform thickness organic-inorganic hybrid gel film of $1 \times 1 \text{ cm}^2$ size was dissolved in 50 ml of phosphate buffer (pH 7.4). Resultant solution was kept for sonication for 10 minutes to dissolved the gel completely. The solution was filtered through the Whatman filter media and clear solution was checked for absorbance at 271 nm against blank as a phosphate buffer solution, pH 7.4. Thus, percentage drug content was calculated. All the readings were taken in triplicate and noted. Same method was implemented to determine the drug in the PVA organic gel film.

Moisture uptake study

The films were put in a desiccator with silica gel for 24 hours and weighed (W_i). The films were then transferred to another desiccator containing saturated NaCl solution (relative humidity 75%) at 25°C until a constant weight was obtained. After equilibrium was attained, the films were taken out and weighed (W_m). Moisture uptake capacity was calculated according to the following Equation (1) [23]:

$$\begin{aligned} \text{Moisture uptake capacity (\%)} \\ = (W_m - W_i / W_i) \times 100 \end{aligned} \quad (1)$$

Moisture content study

Both the organic PVA film and hybrid organic-inorganic films were evaluated for moisture content study. The prepared films were weighed initially (W_i) and kept in the desiccator containing silica gel at 25°C and is continuously weighed until it shows constant weight (W_d).

The moisture content is calculated using following Equation (2) [23]:

$$\text{Moisture content (\%)} = (W_d - W_i / W_i) \times 100 \quad (2)$$

Water uptake and swelling study

This study was performed to find out water uptake capacity of the prepared films. In this method, the prepared films of uniform size and thickness were fixed to the plain stainless-steel surface and slowly immersed in a beaker containing 25 ml distilled water at room temperature for 3 hours. After 3 hours the films were slowly removed and excess of water was wiped slowly with the help of soft filter paper. This experiment was discontinued at the observation of point when film begins to disintegrate or dissolve. Finally, the water uptake and swelling of film was calculated by the following Equation (3) [23]:

$$\text{Moisture content (\%)} = (W_s - W_i / W_i) \times 100 \quad (3)$$

Where, W_s is weight of film after swelling; W_i is the initial weight of film before water uptake and swelling.

Folding endurance study

a specific area of strip was cut and repeatedly folded at the same place till it broke. The number of times the film could be folded without breaking gave the value of folding endurance.

Weight variation test and thickness measurement

For each formulation, three film samples ($10 \times 40 \text{ mm}$) were used. Each film sample was weighed individually and the average weight was calculated.

Thickness of both organic-gel film and hybrid-gel film was measured using digital Vernier calliper (Mitutoyo, Japan). Thickness was measure at all the corner and centre of the film, multiple observations were noted and finally, average value was considered as $\pm\text{SD}$, $n = 3$.

Drying time

For the assessment of the drying time the formulation was applied to the glass slide. After 2 minutes a glass slide was placed on the film without pressure. If no remains of liquid were visible on the glass slide after removal, the film was considered dry. If remains of liquid were visible on the glass slide the experiment was repeated until the film was found to be completely dried [5].

Surface morphology study of organic-inorganic hybrid film of tramadol HCl

Surface morphology study of organic-inorganic hybrid film containing tramadol HCl was determined using Scanning electron microscopy (SEM).

SEM analysis carried out for surface morphology of film. Jeol, JSM 6390LA was used to check the smeared

on a small piece of adhesive carbon tape which was fixed on a brass stub. The sample was then subjected to gold coating using sputtering unit (model: JFC1600) for 10 sec at 10 mA of current. The gold coated sample placed in chamber of SEM (Jeol, JSM 6390LA) and secondary electron/Back Scattered electron images were recorded.

In-vitro drug permeation study of organic PVA film and organic-inorganic hybrid film

Drug permeation study of both organic PVA film and organic-inorganic hybrid film was conducted using fresh goat as a diffusion membrane. Goat skin was positioned between the two cell halves of a glass chamber. The two compartments were held together with a clamp. About 10 ml of phosphate buffer pH 7.4 was added to the receiver/receptor compartment. The film (25 mm in diameter) were mounted over the goat membrane and integrity was checked visually with proper equilibration. The receptor phase (phosphate buffer pH 7.4) was continuously stirred with the help of magnetic stirrer at 300 rpm and maintained at 37°C using a circulating water bath. Samples of 1 ml were collected at the interval of every hour for 24 hours study from the receiver compartment at predetermined time intervals and replaced with fresh buffer solution. The samples collected were analysed for drug content using UV spectrometric method at 271 nm wavelength and finally graph was plotted as cumulative drug permeation Verses time [19].

Stability study of organic and hybrid films

Stability study of film was performed in the same way as mentioned above for organic-inorganic hybrid gel.

Result and discussion

Pre-formulation study and characterisation of film-forming gels

As discussed in the methods section 2.2.1, the final organic-inorganic hybrid film-forming gel formulation was selected and further characterised for various physical and chemical parameters discussed below.

FT-IR study

The FT-IR spectra of PVA, TEOS, Tramadol HCl and blend of all these ingredients are presented in the Figure 1. The spectra of tramadol HCl shown major peaks indicating the basic functional groups at 3065.3; 2861.84; 2514.72, 2605.36; 3306.36; 1271.82; 1578.45; 1045.23 consisting of C-H stretching (aromatic), C-H stretching (aliphatic), C-H stretching of -CH₂ and -CH₃ groups, N-H stretching, C-N stretching respectively. Same peaks were retained in the Spectra of physical blend of all the ingredients indicating the no interactions among the them without affecting any changes in the tramadol HCl [24].

Differential scanning calorimetry (DSC)

The DSC thermogram of organic-inorganic hybrid gel (HG-9 formulation) shown in Figure 2 and interpretation are mentioned below:

1st peak. Exhibiting endothermic peak at -27.92°C,

- Corresponding to its melting and decomposition reported peak temperature was -16.95°C to -27.92°C.
- Enthalpy of fusion found to be -110.11 J/g

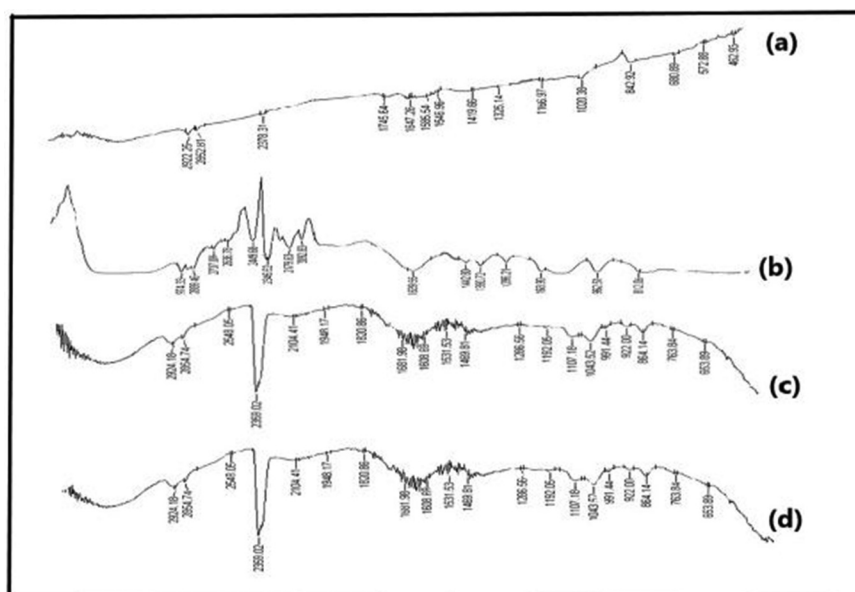


Figure 1. FT-IR study: PVA (a); TEOS (b); Tramadol HCl (c); Blend of PVA+TEOS+ Tramadol HCl (d).

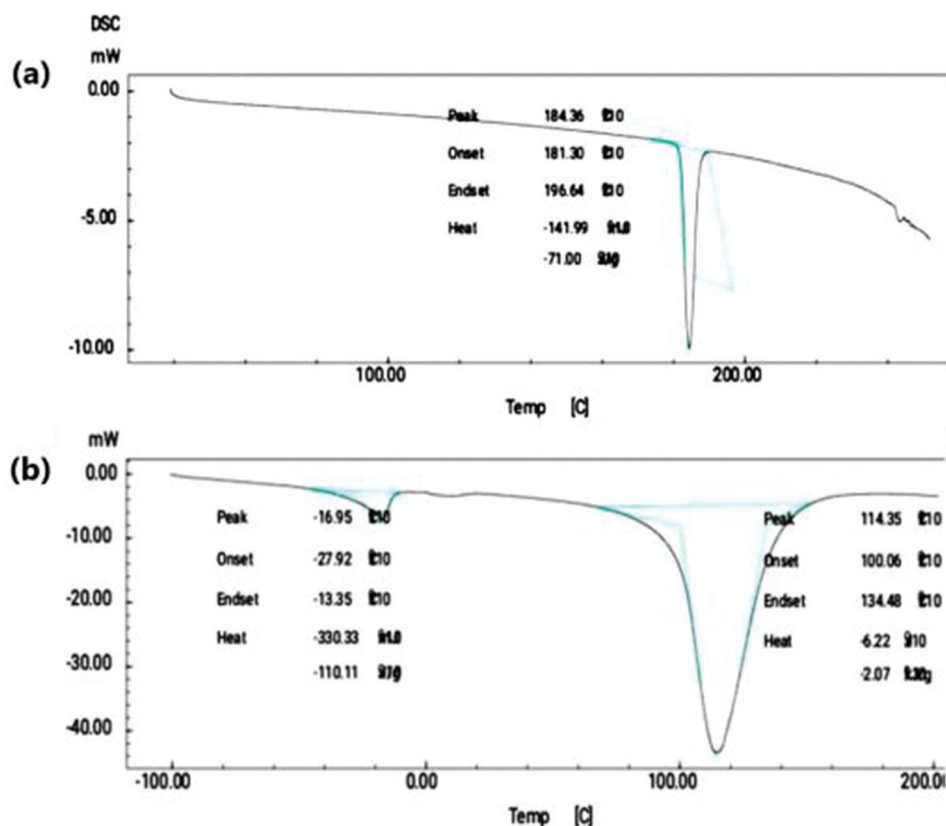


Figure 2. DSC study: Spectra of tramadol HCl (a); Spectra of Hybrid-organic-inorganic-film (b).

2nd peak. Exhibiting an endothermic peak at 114.35°C,

- (a) Corresponding to its melting and decomposition reported peak temperature was 100.04°C to 134.48°C
- (b) Enthalpy of fusion found to be -2.07 J/g

As shown in Figure 2, 1st peak indicates that formation of eutectic mixture and 2nd peak is broad asymmetric melting peak. Cross-linking increases in hybrid organic-inorganic gel due to formation of eutectic mixture. Decreased in melting point is indication of formation of eutectic mixture which promotes cross-linking of the resultant blend. Resultant melting of its blend is lower than their individual melting point. Because of reaction between organic and inorganic polymer there is formation of eutectic mixture, the melting point of resultant formulation was decrease and found to be 114.35°C and is less than that of original melting point of drug 184.36°C and polymer which is used [25].

Appearance and pH

As shown in Figure 3 the tramadol HCl formulation was observed under dark background, which shows transparent viscous preparation with smooth, homogenous, consistent.

All the organic-inorganic hybrid gel formulations were tested for pH and were found to be in the range

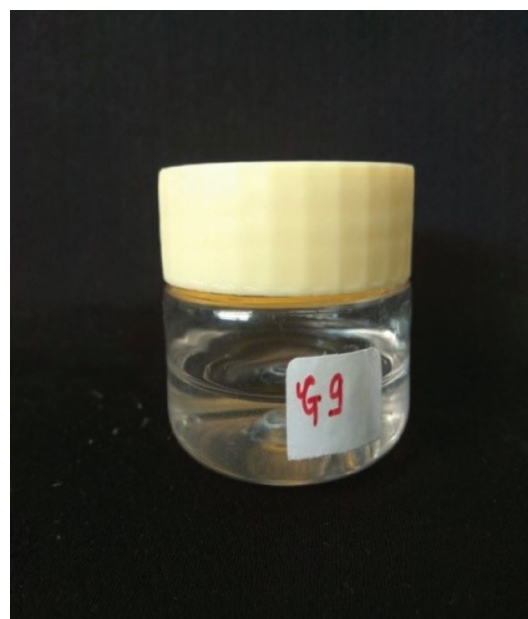


Figure 3. Appearance of tramadol HCl containing organic-inorganic hybrid gel (HG-9).

of 6.6–7.1. The pH of the final selected batch HG-9 was 6.9.

Rheological behaviour of film-forming gels

As shown in Figure 4(a) viscosity of hybrid gel (HG-9) found to be 231.2 Pa.s with respect to temperature condition. Resultant viscosity is sufficient for application to skin and leads to good spreadability

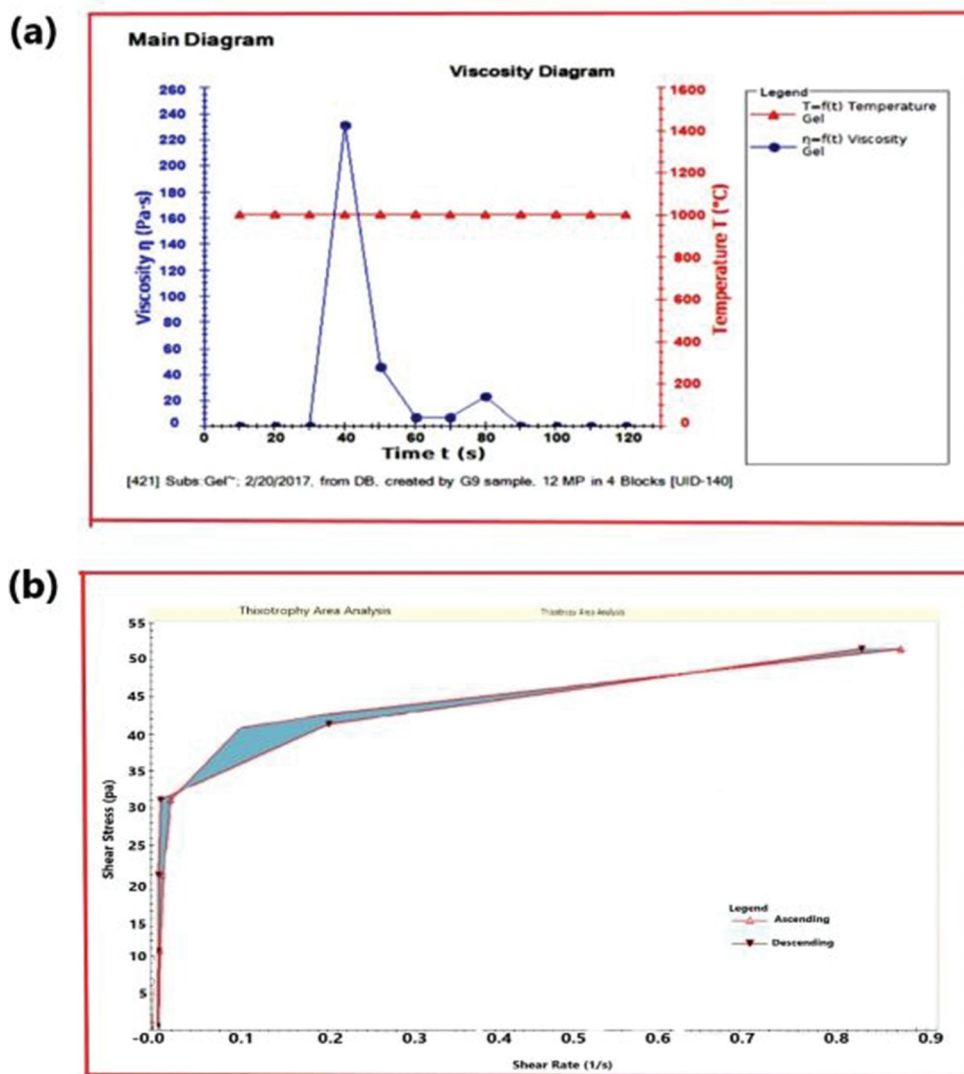


Figure 4. Rheological behaviour of hybrid-organic-inorganic film-forming gel: Viscosity study (a); Thixotropy study (b).

property. As per given in the Figure 4(a) it was observed that viscosity of final HG-9 formulation was increasing with increased in temperature up to certain value of 1400°C but later on as time laps, it again goes on decreasing with decreased in temperature condition, so this type of behaviour indicates the temperature dependability of the formulation with change in viscosity at certain shear rate value. This type of observation indicates thixotropic behaviour of system. All the detailed data of viscosity study is presented in Table 2.

According to Figure 4(b), the formulation showed thixotropy behaviour and change in viscosity with respect to certain values of shear rate and shear stress in which the shear rate steadily increases at constant rate from zero to some maximum value and then decreased at the same rate to zero again, a hysteresis loop form was shown in the Figure 4(b). The height, shape and enclosed area of hysteresis loop depend on the duration of shearing, the rate of increase/decrease

Table 2. Detailed data of viscosity study.

Sr. No.	Time t (sec)	Shear stress (pa) τ	Shear rate(1/s) $\dot{\gamma}$	Viscosity
1.	10	0.000	0.000	0.0
2.	20	9.984	0.001	0.0
3.	30	19.989	0.005	0.0
4.	40	29.993	0.013	231.265
5.	50	39.998	0.088	45.354
6.	60	49.982	0.764	6.543
7.	70	49.982	0.724	6.906
8.	80	39.998	0.175	22.845
9.	90	29.993	0.003	0.0
10.	100	19.989	0.000	0.0
11.	110	9.984	0.000	0.0
12.	120	0.000	-0.001	0.0

of shear rate and the past kinematic history of the sample. The sample has taken fixed time to return more viscous state, it is called Non-Newtonian pseudo plastic fluid

showing a time dependant change in viscosity. As this is time dependant system, viscosity of the formulation gradually becomes loss the internal structure of material was broken down.

Table 3. Detailed data of thixotropy study.

Block index	Time (s)	Shear rate (1/s)	Shear stress (Pa)	Shear rate (1/s)	Shear stress (Pa)
0	10	0.0	0.0	0.0	0.0
0	20	0.0	9.998	0.001	9.984
0	30	0.01	19.99	0.05	19.989
0	40	0.01	29.99	0.013	29.993
0	50	0.09	40.00	0.088	39.998
0	60	0.76	49.98	0.764	49.982
0	70	0.72	49.98	0.724	49.982
1	80	0.18	40.0	0.175	39.998
1	90	0.00	29.99	0.003	29.993
1	100	0.00	19.99	0.00	19.989
1	110	0.00	9.98	0.00	9.984
1	120	0.00	0.00	-0.001	0.000

All the detailed data of thixotropy study is presented in Table 3 [5,26].

Drug content study of film-forming gels

The drug content of the PVA-based gel and final organic-inorganic film-forming gel formulation (HG-9) gel was determined in triplicate and from standard deviation drug content was found to be of $88.4 \pm 3.178\%$ and $95.1 \pm 2.31\%$ respectively. The drug content of hybrid gel was found to be more than that of organic PVA-based gel. Hence uniformity of drug content was found to be satisfactory.

Texture profile analysis

a higher peak load (firmness) and hardness work done value indicate a less spreadable sample. Conversely, a lower peak load (firmness) value coupled with a lower hardness work done value indicates a more spreadable sample. The observations for spreadability of PVA-based gel and organic-inorganic hybrid (HG-9) gel is shown in Figure 5. Comparison of mechanical properties between PVA-based gel and hybrid gel were presented in Table 4.

Animal activity

Skin irritation test. The result of skin irritation study based on visual observation, it has revealed that hybrid gel (HG-9) formulation was non-sensitising and safe

Table 4. Comparison of mechanical properties between PVA-based gel and hybrid gel.

Sr. no.	Parameters	Resultant value of PVA-based gel (OG)	Resultant value of hybrid gel (HG-9)
1.	Adhesiveness	0.70 mJ	3.40 mJ
2.	Stringiness Length	0.00 mm	0.56 mm
3.	Fracturability	10.00 g with 1% of load sensitivity	14.00 g with 1% of load sensitivity
4.	Cohesiveness	1.26	0.81

*OG = Organic Gel; *HG = Hybrid Gel

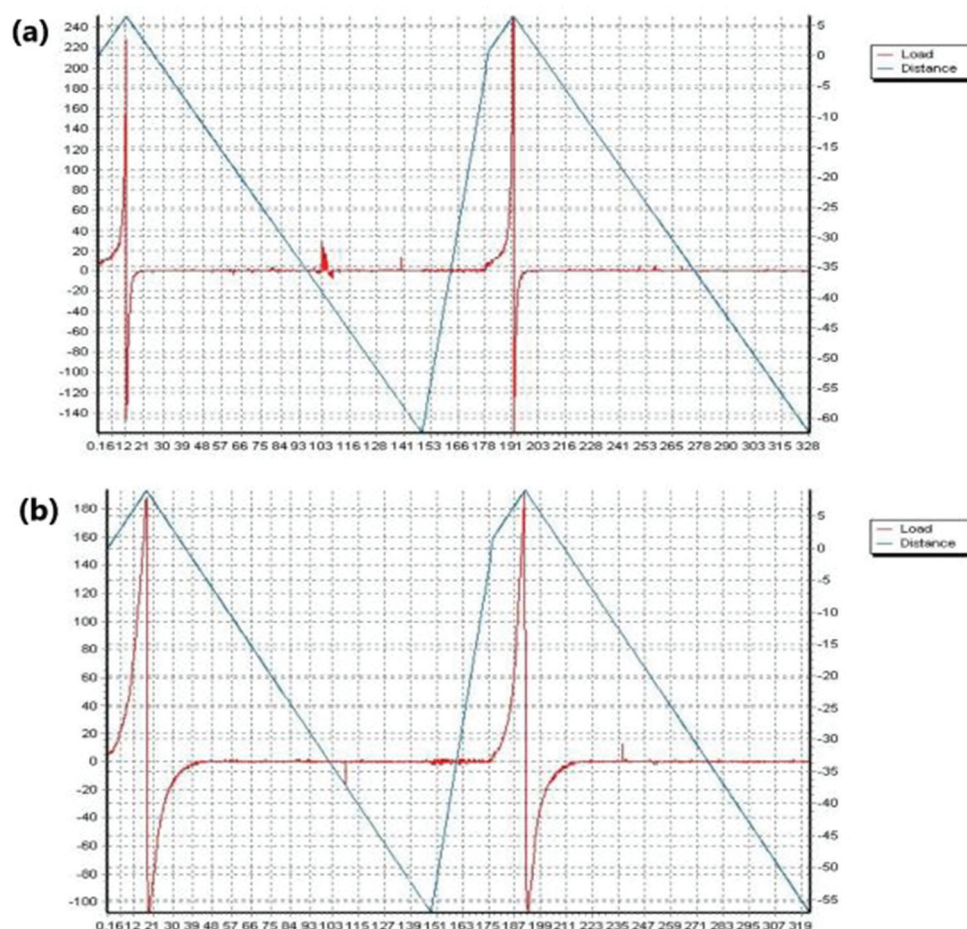


Figure 5. Texture analysis: Mechanical properties and spreadability study of PVA organic gel (a) and Hybrid organic-inorganic gel (b).



Figure 6. Skin irritation study using rats as animals.

Table 5. Skin irritation study data.

Test material ^a	Skin reaction ^b	Mean irritation score		
		12 hours	24 hours	48 hours
Hybrid-organic-inorganic film (HGF-9)	Erythema	0	0	0.1
	Oedema	0	0	0

^aTest material was applied on rat skin

^bErythema and oedema, the mean irritation score was the summation of each irritation score divided by the number of animals (rats)

for use, as there was no significant irritation produced after application of hybrid gel (HG-9) formulation on the rat’s skin. Following observation were depicted from the skin irritation and photographs of animals undergoing skin irritation study are presented in Figure 6. The erythema and oedema irritation matrix score was presented in Table 5.

Analgesic activity. Final HG-9 formulation possesses very significant analgesic effect according to statistical analysis. Statistical *t*-test was applied and statistical data was generated as mentioned in Figure 7.

Ex-vivo drug permeation study of tramadol HCl organic-inorganic hybrid gel

The *ex-vivo* drug permeation of Tramadol HCl organic-inorganic hybrid gel was evaluated by *ex-vivo* diffusion study using Franz diffusion cell, using a fresh goat skin as a diffusion membrane at pH 7.4. Cumulative % of drug permeated are mentioned in Figure 8. Formulations with higher concentration of PVA shown less amount of drug

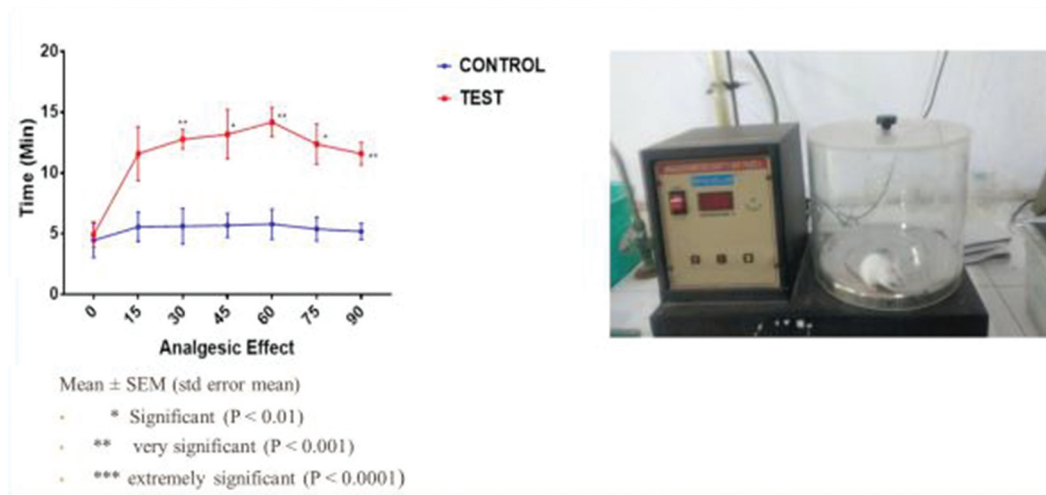


Figure 7. Analgesic activity in mice.

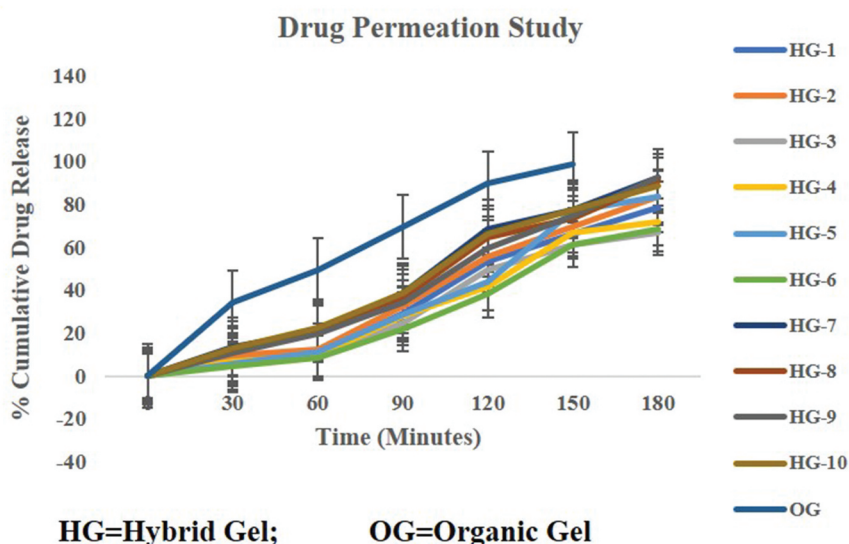


Figure 8. Cumulative drug permeation study of both organic and hybrid film-forming gel.

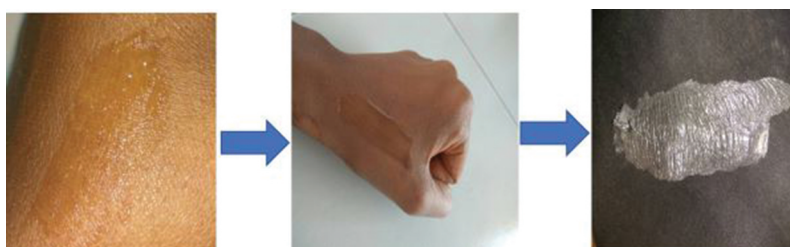


Figure 9. Appearance of prepared and applied dried film.

release after 3 hours of time period. Hence, in first few formulations, HG-1 to HG-6, less amount of drug release was observed, showing 78.66%, 83.55%, 66.55%, 71.45%, 83.25% and 68.58% respectively. This may happen due to extent of cross-linking interaction between PVA and TEOS in the presence of HCl [5]. There was little difference of drug release was found among the formulations HG-7 to HG-10 due to presence of nearly same amount of PVA and TEOS showing, 92.5%, 90.58%, 92.36% and 88.68% respectively. Finally, HG-9 formulation was

considered to be optimised based on the initial results observed and as identified which was already discussed in method section 2.2.1.

Appearance and miscibility study

For the blend-type polymer gels, the structural properties and the unique functions were dependent on the miscibility, chemical structure and interaction between mixture components. PVA and glycerine have excellent compatibility due to the well-known observation of PVA solubility in glycerol. The high transparency of the film in Figure 9 indicated that there may be no macro-

Table 6. Stability study hybrid-organic-inorganic film-forming gel.

Duration	Temperature and relative humidity	Appearance	*pH	*Drug content
1 month	40°C, 75%RH	Transparent, smooth, viscous	7.0 ± 0.2	95.9 ± 0.58%
2 months	40°C, 75%RH	Transparent, smooth, viscous	6.9 ± 0.4	95.0 ± 0.84%
3 months	40°C, 75%RH	Transparent, smooth, viscous	7.0 ± 0.2	96.01 ± 1.02%

*All the observations were taken in triplicate as ±SD ($n = 3$).

phase separation occurring between the organic polymer and inorganic TEOS.

Stability study

The storage of tramadol HCl organic-inorganic hybrid gel containing of an optimised batch for 3 months at room temperature and relative humidity (40°C, 75%) showed no change in appearance of the system was explained in Table 6.

Stability study was performed for 1, 2 and 3 months which did not show any major changes in appearance, pH, drug content.

Characterisation of tramadol HCl organic-inorganic hybrid film

The organic-inorganic hybrid film of tramadol HCl was evaluated for various physical and chemical parameters in order to ensure the quality of the film for continuous release of tramadol HCl in the management of pain on affected area by transdermal route. Simultaneously, the organic PVA film containing tramadol HCl was also evaluated XRD study.

The XRD was used to investigate the influence of TEOS on the crystalline property of the hybrid films, which was shown in fig. As seen, pure PVA film possessed distinctly higher crystalline intensity than its hybrid films, and results showed the main diffraction peaks of PVA film containing Tramadol HCl and PVA-TEOS hybrid film containing Tramadol HCl were around $2\theta = 6.14$ and 5.360 respectively. In the XRD patterns, this can be ascribed to the crystalline regions of PVA due to strong hydrogen bonds between the hydroxyl groups. Furthermore, peak intensities of PVA hybrid films decreased

continuously with incorporation of TEOS. Namely, there was a significant decrease in crystalline regions and increase in amorphous regions in the hybrid film, which can indicate that the introduction of TEOS led to the destruction, to some extent, of the crystalline region of PVA film [11]. Figure 10 shows the interpretation of the XRD peaks observed for both organic PVA film and hybrid film.

All the observations of thickness, drug content, moisture content, moisture uptake capacity and swelling index study are presented in Table 7 and discussed below.

The drug content of the optimised Formulation (HG-9) film and PVA film was carried out in triplicate and average drug content was found to be of 87.20% and 81.3% respectively. The drug content of hybrid film was found more than the organic PVA film. Hence uniformity of drug content was found to be satisfactory.

In moisture content study, selective films final formulations were evaluated and average moisture was found to be $1.07 \pm 0.04\%$. These values show the percent moisture uptake capacity of films. The

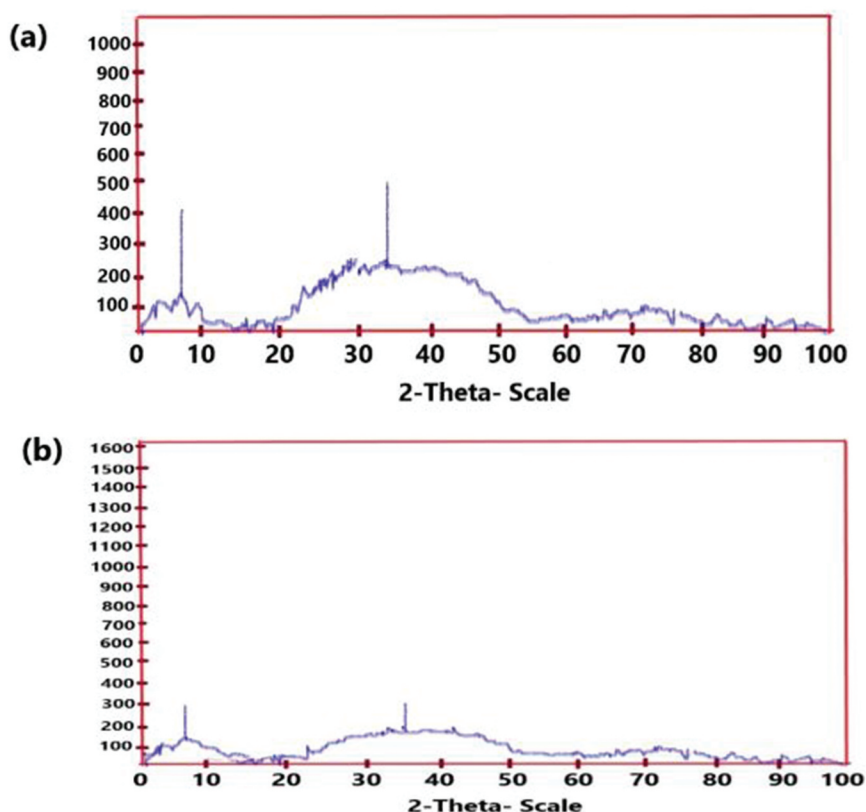


Figure 10. XRD graph of PVA-organic film (a) and hybrid-organic-inorganic film (b) containing tramadol HCl.

Table 7.: Evaluation of tramadol HCl films for various parameters.

Sr. no.	Type of formulation	*Thickness (mm)	*Drug content (%)	*Moisture content (%)	*Moisture uptake capacity (%)	*Swelling index (%)
1.	PVA Organic Film (OGF)	0.584 ± 0.014	81.3 ± 0.55	2.13 ± 0.12	2.55 ± 0.45	78.28 ± 0.14
2.	Hybrid Organic-inorganic Film (HG-9)	0.458 ± 0.032	87.20 ± 0.24	1.07 ± 0.04	1.65 ± 0.16	89.45 ± 0.23

*All the experiments were conducted triplicate \pm SD ($n = 3$).

moisture uptake of the films was generally low; this will help the films to remain stable and protect them from microbial contamination. Generally, the moisture uptake capacity of films increases with increasing hydrophilicity of the polymer or plasticiser and the levels of hydrophilic polymers as well. Moisture uptake capacity of PVA-organic film was higher than the hybrid film whereas the swelling index values of hybrid film was found to be little higher than the PVA-organic film. Extent of swelling was also depending upon the hydrophilicity of film and proportion of such components in the formulation.

In folding endurance study, a specific area of strip was cut and repeatedly folded at the same place till it broke. The number of times the film was folded without breaking gave the value of folding endurance. Films were folded for more than 300 times it did not show any sign of cracks. It was taken as end point and confirmed the physical stability of formed film of organic-inorganic hybrid gel.

For weight variation study, films formed from final organic-inorganic hybrid gel were selected and average weight of films were considered as final weight of the films. In this study, average weight of film (10×40mm size) was found to be 0.21 ± 0.007 g. Readings were taken in triplicate for accuracy.

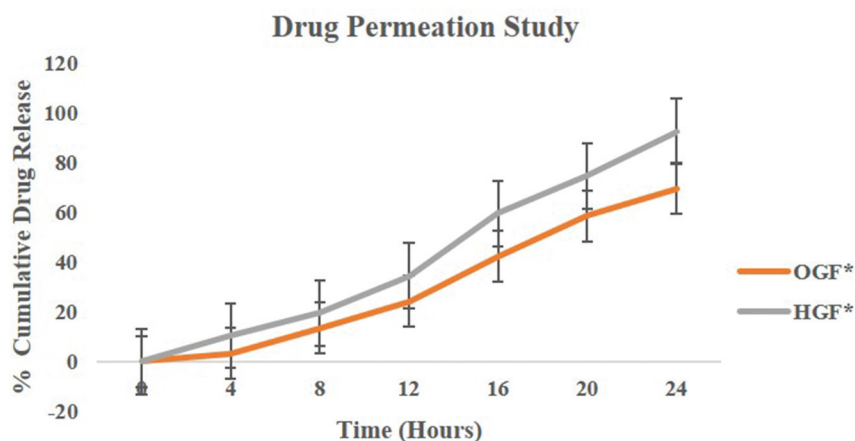
It is very important to know about the drying time of the gel to form the film after application on the intact skin. For this purpose, a simple observation technique was implemented as discussed above. a glass slide was placed on the film without pressure and after 2 minutes glass slide was removed from film and it was observed that no liquid form of gel was visible on the glass slide, this has indicated that the film was dried immediately.

Both organic as well as hybrid-organic-inorganic films were subjected to the drug permeation study as discussed in the method section. For this study optimised formulation GHF was selected as hybrid dried

film and PVA organic film (OGF). In this study, both results were compared and it was found that the PVA organic (OGF) has shown less amount of 69.55% drug release whereas hybrid film (HGF) has shown 92.36% drug release in the 24 hours of study. This huge difference in the drug release among both the formulation was due to the fact the nature of PVA organic film little hydrophilic with high level of concentration in the formulation. But strong interaction between PVA and TEOS make weak C-OH peak and formation of Si-O-C peaks in the XRD study. Due to this crystallinity of the PVA decreases resulting more soluble and transparent film formation and hence hybrid film has shown higher percentage of drug release as compare to the plain PVA organic film [11,27]. The cumulative drug release profile of both the organic PVA (OGF) and hybrid organic-inorganic film is highlighted in Figure 11.

Surface morphology of both the organic PVA film and hybrid organic-inorganic film was checked visually as well as using scanning electron microscopy (SEM). SEM can provide

direct visual evidence of the influence of TEOS on surface morphology of the hybrid films. SEM photographs of surface sections of pure PVA and its hybrid are displayed in Figure 12. From these micrographs, it can be seen that the surface of PVA film was both homogeneous and smooth. Moreover, the addition of TEOS significantly affected the surface morphology. However, no visible phase separation between PVA and silica in all hybrid films can be observed. The hybrid HG-9 film exhibited a homogeneous granular structure. The presence of silica microparticles can be attributed to the reaction between PVA and the hydrolysed silanol of TEOS in the sol-gel process, which may play an important role in destroying regular crystalline arrangement of PVA chains and consequently decreasing the crystalline regions in PVA films. In



*OGF=Organic-Gel-Film;

*HGF=Hybrid-Gel-Film

Figure 11. Cumulative drug permeation study of both organic and hybrid dried films.

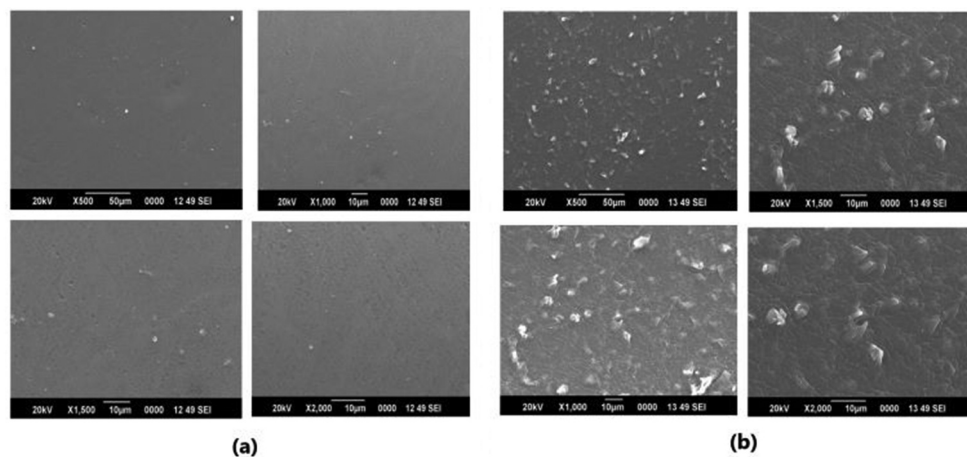


Figure 12.: Scanning electron microscopic photographs showing morphology of prepared film at different resolution.

Table 8.: Stability study hybrid-organic-inorganic film.

Duration	Storage condition	Appearance	*Drug Content
1 month	40°C, 75%RH	Transparent, thin, no brittleness	84.23 ± 1.05%
2 months	40°C, 75%RH	Transparent, thin, no brittleness	83.20 ± 1.15%
3 months	40°C, 75%RH	Transparent, thin, no brittleness	83.28 ± 0.89%

**All the observations were conducted triplicate ±SD ($n = 3$)

addition, the surface morphology of hybrid film became rough and uneven, which was due to the polycondensation of excessive TEOS leading to conglomeration and aggregation in the matrix. This conglomeration and aggregation may result in the film more compact that does not favour the diffusion of the drug molecule in the film.

Stability study was performed for 1, 2 and 3 months which does not show any major changes in appearance, drug content. Results of stability study of hybrid film is presented in Table 8.

Conclusion

Transdermal drug delivery systems have gained many benefits and are better alternatives for other conventional routes of administrations like oral to avoid GI irritation, first-pass effect and undesired drug release pattern. Conventional available transdermal/topical formulations are not capable to modify the drug release property and other physical properties and have many disadvantages. In this study, an attempt was made to prepare a novel organic–inorganic hybrid film-forming gel formulation, which showed enhanced adhesion, cross-linking and better drug release property with ease of application on skin and formation of flexible, comfortable film than plain PVA films. More importantly, use of inorganic phase in PVA matrix not only significantly improved mechanical strength and skin adhesion properties, but also

decreased the crystalline regions of PVA and hence facilitate the diffusion of drug and water.

So, from this study it was concluded that formulation of organic-inorganic film-forming gel is the challenging and excellent new approach for transdermal delivery of drug with better patient compliance as compare to the existed organic material-based transdermal formulations.

Acknowledgements

Authors are very thankful to the IPCA laboratories, Mumbai for providing Tramadol HCl.

Also grateful to the Principal of our institute for providing facilities and support to conduct this research study. At the last, authors are very thankful to all those who have cooperated to complete this work successfully.

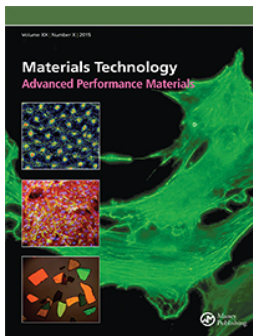
Disclosure statement

Authors declare no conflict of interest.

References

- [1] Yu YY, Chen CY, Chen WC. Synthesis and characterization of organic–inorganic hybrid thin films from poly(acrylic) and monodispersed colloidal silica. *Polymer*. 2003;44:593–601.
- [2] Novak BM. Hybrid nanocomposite materials-between inorganic glasses and organic polymers. *Adv Mater*. 1993;5:422–433.
- [3] Otsuka T, Poly CY. (methyl methacrylate) (PMMA)-based hybrid materials with reactive zirconium oxide nanocrystals. *Polym J*. 2010;42:58–65.
- [4] Ibrahim H, Ibrahim S. Study some properties of hybrids silica/PVA using sol gel method. *Chem Bio Phy Sci Sec C*. 2015;5(2):1950–1957.
- [5] Guo R, Xiaoyan D, Zhang R, et al. Bioadhesive film formed from a novel organic–inorganic hybrid gel for transdermal drug delivery system. *Eur J Pharm Biopharm*. 2011;79:574–583.
- [6] Wang K, Nune KC, Misra RDK. The functional response of alginate-gelatin-nanocrystalline injectable

- hydrogels toward delivery of cells and bioactive molecules. *Acta Biomaterialia*. 2016;36:143–154
- [7] Wang K, Lin S, Nune KC, et al. Chitosan-gelation based microgel for sustained drug delivery. *J Biomat Sci*. 2016;27:441–453.
- [8] Wang K, Buschle-Diller MRDK. Chitosan-based injectable hydrogels for biomedical applications. *Materials Technol*. 2015;30:198–205.
- [9] Yuan Q, Shah J, Hein S, et al. Controlled and extended drug release behavior of chitosan-based nanoparticle carrier. *Acta Biomaterialia*. 2010;6:1140–1148.
- [10] Yuan Q, Hein S, Misra RDK. New generation of chitosan-encapsulated ZnO quantum dots loaded with drug: synthesis, characterization and in vitro drug delivery response. *Acta Biomater*. 2010;6:2732–2739.
- [11] Yuan Q, Subramanian R, Hein S, et al. Stimuli-responsive magnetic nanoparticle drug carrier: magnetite encapsulated with chitosan-grafted-copolymer. *Acta Biomater*. 2008;4:1024–1037.
- [12] Prausnitz MR, Langer R. Transdermal drug delivery. *Nat Biotechnol*. 2008;26:1261–1268.
- [13] Berner B, John VA. Pharmacokinetic characterization of transdermal delivery systems. *Clin Pharmacokinet*. 1994;26:121–134.
- [14] Setouhy DA, Ashmony SM. Ketorolac tramadol topical formulations: release behaviour, physical characterization, skin permeation, efficacy and gastric safety. *J Pharm Pharmacol*. 2010;62:25–34.
- [15] Klotz U. Tramadol-the impact of its pharmacokinetic and pharmacodynamic properties on the clinical management of pain. *Arzne imittel for schung*. 2003;53:681–687.
- [16] Raffa RB. Basic pharmacology relevant to drug abuse assessment: tramadol as example. *J Clin Pharm Ther*. 2008;33:101–108.
- [17] 24 December 2019. Available from: <http://www.brookfieldengineering.com/education/learn-about-texture.asp>
- [18] 24 December 2019. Available from: <http://www.brookfieldengineering.com/education/applications/texture-analysis.asp>
- [19] 24 December 2019. Available from: <http://www.brookfieldengineering.com/education/applications/texture-jelly-cup.asp>
- [20] Reddy MS, Mutalik S, Rao G, et al. Preparation and evaluation of minoxidil gels for topical application in alopecia. *Indian J Pharm Sci*. 2006;68(4):432–436.
- [21] More BH, Sakharwade SN, Tembhurne SV, et al. Evaluation for Skin irritancy testing of developed formulations containing extract of *Butea monosperma* for its topical application. *Int J Toxicol Appl Pharmacol*. 2013;3(1):10–13.
- [22] Kasture SB. *A handbook of experiments in pre-clinical pharmacology*. 1st ed. Career publication; 2006. p. 72–73.
- [23] Ammar HO, Ghorab M, El-Nahhas SA, et al. Polymeric matrix system for prolonged delivery of tramadol hydrochloride, part I: physicochemical evaluation. *AAPS Pharm Sci Tech*. 2009;10:7–20.
- [24] Dyer JR. *Applications of absorption spectroscopy of organic compounds*. Prentice Hall of India; 2004. p. 33–38.
- [25] Skoog DA, West DM. *Fundamentals of analytical chemistry*. 8th ed. Singapore: Thomson Brooks/Cole; 2004. p. 906–946.
- [26] Chhabra RP, Richardson JF. *Non-Newtonian flow in the process industries: fundamentals and engineering applications*. Butterworth-Heinemann; 1999.
- [27] Hu P, Jia M, Zuo Y, et al. A silica/PVA adhesive hybrid material with high transparency, thermostability and mechanical strength. *RSC Adv*. 2017;7:2450–2459.



Tailoring hybrid organic-inorganic film-forming topical gel: a tuneable approach for tramadol HCl delivery

Prakash N. Kendre , Gayatri Dusane , Shirish P. Jain , Mahendra A. Giri & Ajinkya K. Pote

To cite this article: Prakash N. Kendre , Gayatri Dusane , Shirish P. Jain , Mahendra A. Giri & Ajinkya K. Pote (2020): Tailoring hybrid organic-inorganic film-forming topical gel: a tuneable approach for tramadol HCl delivery, Materials Technology, DOI: [10.1080/10667857.2020.1802839](https://doi.org/10.1080/10667857.2020.1802839)

To link to this article: <https://doi.org/10.1080/10667857.2020.1802839>



Published online: 07 Aug 2020.



Submit your article to this journal [↗](#)



View related articles [↗](#)



View Crossmark data [↗](#)



Tailoring hybrid organic-inorganic film-forming topical gel: a tuneable approach for tramadol HCl delivery

Prakash N. Kendre^a, Gayatri Dusane^b, Shirish P. Jain^c, Mahendra A. Giri^b and Ajinkya K. Pote^a

^aDepartment of Pharmaceutics, Rajarshi Shahu College of Pharmacy, Buldana, India; ^bDepartment of Pharmaceutics, Sanjivani College of Pharmaceutical Education & Research, Kopergaon, Maharashtra, India; ^cRajarshi Shahu College of Pharmacy, Buldana, India

ABSTRACT

Drug release properties for transdermal route can be better modified as per requirement which is mostly dependent upon the carrier system. In case of organic film-forming systems, the physical properties may not be achieved for successful delivery of drug through transdermal route. A novel organic-inorganic hybrid film-forming gel may fulfil these expectations to many extend. The present study focuses on the development of the organic-inorganic hybrid film-forming gel. A smooth, transparent, clear film-forming gel of tramadol was prepared for application on the intact skin with better comfort and modified drug release rate properties. The key properties of the adhesive films produced from the hybrid gels were investigated and the results showed that the incorporation of appropriate PVA: TEOS: Glycerine: HCl in the ratio of 46:12.5:25.5:6 respectively. Resultant hybrid film-forming gel has modified the physical properties and improved drug release properties. Furthermore, the investigations of skin irritation suggested no irritation to skin after topical application. This study has provided an alternative to the presently available organic gel and films for transdermal delivery of drugs with better patient compliance and modified physical and chemical stability.

ARTICLE HISTORY

Received 9 April 2020
Accepted 27 July 2020

KEYWORDS

TEOS; PVA; hybrid-organic-inorganic film-forming gel; tramadol HCl; transdermal route etc

Introduction

Many of the drug delivery systems have been developed till date by many researchers with different characteristics. Efficient drug delivery systems can be developed further by doing modifications in the available drug delivery systems. These modifications can be possible using variety of compatible polymeric components. These modifications may include grafting of polymers, cross-linking of polymers and many more other approaches using various techniques.

Hybrid systems are made-up of composites of two different materials with different physical and or chemical properties. Hybrid film-forming gels refers to the combination of organic and inorganic components in one system either at macroscopic level or molecular level [1].

Single hybrid system is a homogenous phase of both organic and inorganic materials and shows characteristics that are different at their individual level. These resultant characteristics may be beneficial based upon the appropriate contributions of both the materials combined together using suitable methodology and techniques. Mechanical properties of hybrid systems are so improved so that patient acceptance will enhance with excellent drug release properties and stability of the final formulation. Mostly inorganic

phase provides mechanical strength while organic phase delivers bonding. The word hybrid comes from the Latin word 'hybrida', which is related to the meaning 'mongrel'. The easy way to construct transparent and homogeneous hybrid materials is to increase the affinity between organic polymer and inorganic phases [2].

Optical transparency is the most important characteristic of these hybrids and it arises because dispersion of material in the matrix is in the order of tens of nanometres, far less than the wavelength of visible and ultraviolet light. As a result, light is not lost due to scattering.

Moreover, the hybrid materials offer the advantages like higher flexibility and mechanical strength, greater temperature, range of usability, increased durability, improved electrical, magnetic or redox properties [3–5].

The synthesis of hybrid materials includes two methodologies:

- (A) Building block approach
- (B) *In-situ* formation of the components
 - a. In situ formation of inorganic materials
 - b. Formation of organic polymers in presence of preformed inorganic materials

- c. Hybrid materials by simultaneous formation of both components.

Wang et al. have prepared the hybrid injectable hydrogels consisting of gelatin and nanocrystalline cellulose. These hydrogels were processed using adaptation of interpenetrated network of alginate-gelatin, ionic cross-linking and supramolecular interaction approach. Due to this approach mechanical properties were changed and resembles native tissue structure. This approach has been used for delivery of cells in tissue engineering [6].

In another study, the researchers have synthesised microgels via cross-linking of chitosan and gelatin with succinimide-end polyethylene glycol (PEG). The presence of PEG provided thermoresponsiveness to microgels due to which the size of microgels was significantly changed at elevated temperature [7].

Another cross-linking aspect of modified form of materials used to prepare biocompatible injectable hydrogels. In this approach, different gelation techniques like, physical cross-link, chemical cross-link, ionic cross-link and supramolecular interaction were used to prepare chitosan-based injectable hydrogels to be formed. These gelation approaches have significant impact on the structure and properties of hydrogels, which directs their use as tissue engineering scaffold and drug delivery vehicle [8].

Chitosan-based controlled and extended drug release nanoparticles were prepared using expandable layered aluminosilicate as an inorganic material. This hybrid form of nanoparticles has significant impact on the drug release rate properties due to change in the structural morphology and swelling behaviour. The study has revealed its application in the biomedical and tissue engineering for controlled drug delivery [9].

Another study suggested the preparation of chitosan-encapsulated Zn quantum dots loaded with drug for anti-cancer treatment. Study has demonstrated its use for tumour-targeted delivery of anti-cancer agents [10].

In one more study, chitosan-grafted-copolymer has been used to prepare stimuli-responsive magnetic nanoparticle drug carrier. This grafted chitosan has significant impact on the drug release property which was extended in a controlled fashion that responds to the change in temperature and pH with characteristics of longer circulation time and reduced side effects [11].

Transdermal drug delivery system has been proved to be an alternative to the many oral as well as injectables preparations avoiding first-pass-metabolism and painful irritations respectively.

In first generation, this route has been used for delivery of lipophilic and low-dose drugs. In second generation, using chemical permeation enhancers, iontophoresis, sonophoresis etc. In third generation,

microneedle injection, electroporation and cavitation ultra sound approach has been used for delivery of drugs.

Transdermal delivery system is a desirable alternative administration route for tramadol hydrochloride for patients with chronic pain. To overcome skin barrier property, organic-inorganic (hybrid) film-forming gel approaches have been chosen in this study [12–14].

Hybrid material offers multiple benefits and its use in drug delivery system is itself a novel approach. Based on these considerations the current work has aimed to prepare a novel organic-inorganic (hybrid) film-forming gel for transdermal drug delivery of tramadol HCl, a non-invasive drug administration route and offers potential benefits of simplicity, efficacy and patient acceptance by maintaining a constant blood drug concentration for an extended period [15].

In addition, the transdermal delivery system can decrease the possible abuse and addiction potential of tramadol by avoiding peak and trough plasma concentrations and by reducing the total amount of medication input [16].

Materials and method

Materials

Tramadol HCl was obtained from IPCA laboratories, Mumbai; polyvinyl alcohol (PVA), tetraethylorthosilicate (TEOS), were obtained from Research Fine Chem Industries, Mumbai. All other chemicals glycerine, hydrochloric acid (HCl) etc. used were of analytical grade.

Method

Preparation of hybrid-organic-inorganic film-forming gel

Preparation of hybrid-film-forming gel was prepared in two steps as mentioned below. Both the phases were prepared separately as organic and inorganic phase and mixed together to form homogenous gel with improved physical, chemical properties and modified drug release properties. Different concentration and levels of components in the formulation are highlighted in Table 1.

Preparation of organic phase. Initially the organic phase was prepared using typical synthesis, weighed amount of PVA was added to double distilled water which is preheated at 90 °C with continuous stirring till PVA was completely mixed in the water. The resultant homogenous blend of PVA was allowed to cool at room temperature.

Table 1. Formulation batches of organic-inorganic hybrid gel.

Ingredient (%)	HG-1	HG-2	HG-3	HG-4	HG-5	HG-6	HG-7	HG-8	HG-9	HG-10
Tramadol HCl	5	5	5	5	5	5	5	5	5	5
PVA	50.87	47.18	64.43	62.49	62.49	71.95	44.76	46.5	46	45
TEOS	18.46	18.46	14.77	11.81	11.81	10	11.5	12	12.5	12.5
Glycerine	14.77	18.46	4.90	9.80	9.80	3.05	28.24	25.5	25.5	25.5
HCl	5.90	5.90	5.90	5.90	5.90	5	5.5	6	6	7
Distilled Water	5	5	5	5	5	5	5	5	5	5

*HG = Hybrid Gel

Preparation of inorganic phase and catalyst mixture.

In this step required amount of 0.1 N HCl was added dropwise in the weighed amount of Tetraethyl orthosilicate (TEOS). Initially, separate phase of globules was observed which disappeared with continuous stirring and finally a clear transparent solution was formed. Heat was evolved at the end due to exothermic reaction.

In the later step, inorganic phase was added to the organic phase in a dropwise manner with continuous mixing till homogenous system was formed. This mixture was then added to another previously prepared mixture of glycerine, water and drug to form the final formulation.

As shown in above Table 1, various batches of hybrid film-forming gel were prepared.

The optimised batch was selected by the self-developed method as described below. The prepared hybrid gel was poured on a uniform surfaced glass slide. The gel was allowed to form a thin layer on the slide. Once the film was formed it was slowly peeled off from the slide. According to the visual observation and experience, manual peeling force required, spreadability of solution on glass slide and texture of film, the best hybrid film-forming gel batch was selected and further characterised for different physical and chemical parameters using various tools and techniques. It has made easy job to deal with only selective formulation batch out of initially formulated batches for further characterisation and testing.

Preparation of PVA-based gel

In typical synthesis, the weighed amount of PVA was dissolved in double distilled water preheated at 90°C under stirring. After complete dissolution of PVA, fixed amount of drug was added to the mixture upon cooling at room temperature. Various batches with concentration of PVA from 1 % W/V to 30% W/V were prepared to get final desired formulation of PVA gel. Final formulation batch was selected using self-developed method. On one glass slide; prepared PVA solution was poured and tried to spread evenly that leads to formation thin layer on the glass slide. The formed film was dried for 5 minutes and peeled out to check the peel ability. Final concentration of PVA was determined on the basis of their physical parameters

like spreadability of PVA solution, peeling force required after drying and texture properties of formed film.

Characterisation of film-forming gel

All the batches of Tramadol HCl organic-inorganic hybrid film-forming gel formulations were observed for appearance, pH, colour and consistency etc.

pH

Accurately weighed 1 gm of gel was and dispersed in 100 ml of distilled water. The pH of dispersion was measured using digital pH metre. All the readings were taken in triplicate and noted.

Rheological study

a Brookfield digital RST-CC Rheometer (7,120,128) was used to determine rheology and viscosity of the formulations. The viscosity was measured by 12 MP in 4 blocks (UID-140).

Drug content

Drug content study was conducted for organic-inorganic hybrid film-forming gel as well as PVA-based gel.

Accurately weighed amount of (500 mg) of Tramadol HCl containing organic-inorganic hybrid film-forming gel was added to 50 ml of phosphate buffer (pH 7.4). Resultant solution was kept for sonication for 10 minutes to dissolved the gel completely. Absorbance of solution was checked at 271 nm against blank as a phosphate buffer solution. Thus, percentage drug content was calculated. All the readings were taken in triplicate and noted. Same method was implemented to determine the drug in the PVA organic gel.

FT-IR study

Tramadol HCl was identified and confirmed by using the FT-IR (8400, Shimadzu, Japan), Drug:KBr (1:100) ratio was taken and mixture was gently grinded in the mortar pestle, then translucent pellet was made by using the pellet press method, then pellet was placed in the sample holder, then instrument was run and gotten the FTIR spectra of the Acitretin. The samples were tested at R.C. Patel College of Pharmacy, Shirpur, India. In the same way, Physical blends of drug and

other excipients were also analysed for compatibility testing and suitability for the preparation of final formulation.

Differential scanning calorimetry (DSC) study

Shimadzu DSC-60 plus was used for DSC study of selected hybrid organic-inorganic gel as well as PVA organic gel. Small amount of 3–6 mg sample was taken on aluminium pan. The sample was covered with the aluminium lead and crimping was carried out with the help of crimping tool. The crimped pan was installed at the sample holder point. The test was carried out and the thermogram was recorded in TW-60 software

Texture analysis

Texture analysis of PVA-based gel and organic-inorganic hybrid gel was performed using a CT3 Texture Analyser in TPA mode. Formulations were transferred into lower cone taking care to avoid the introduction of air into the samples. A conical analytical probe (45°C) was forced down into each sample at a defined test speed (2 mm/s) and to a defined depth (12 mm). At least five replicate analyses of each sample were performed at temperatures of 25°C and 30°C. From the resulting force–time plots, the hardness (the force required to attain a given deformation), compressibility (the work required to deform the product during the first pass of the probe) and adhesiveness (the work necessary to overcome the attractive forces between the surface of the sample and the surface of the probe) were derived [17–19].

Appearance and miscibility study

All the batches of Tramadol HCl organic-inorganic hybrid film formulations were observed for appearance and transparency.

The structural properties and the unique functions of the blend-type polymer gels, were dependent on the miscibility, chemical structure and interaction between mixture components. No macro-phase separation occurring between the organic polymer and inorganic is indicated by the high transparency in the film [20].

Ex-vivo drug diffusion study of hybrid gel

Investigation of the amount of drug released from a tramadol HCl organic-inorganic hybrid gel was performed using *Ex-vivo* drug diffusion study. A fresh goat skin was used as a diffusion membrane. Goat skin was positioned between the two cell halves of a glass chamber. The two compartments were held together with a clamp, 10 ml of phosphate buffer pH 7.4 was added to the receiver/receptor compartment. The donor compartment was loaded with 0.5 gm of formulation which was spread evenly on the membrane. The receptor phase (phosphate buffer pH 7.4) was continuously stirred with the help of magnetic stirrer at 300 rpm

and maintained at 37°C using a circulating water bath. Samples of 1 ml were collected at the interval of every 20 minutes for 3 hours study from the receiver compartment at predetermined time intervals and replaced with fresh buffer solution. The samples collected were analysed for drug content using UV-spectrometric method at 271 nm wavelength and finally graph was plotted as percentage cumulative drug permeation Verses time [19].

Animal activity

Skin irritation study. Skin irritation study was conducted using healthy rats. The protocol of the study was sanctioned by the Institutional Animal Ethical Committee and permission was granted to conduct the study using healthy rats monitored as per the guidelines of animal ethical committee. The rats ($n = 9$) were randomly divided into three equal groups for application of standard irritant, optimised formulation or test and control (no application). Hairs were removed by bend scissor from an area (2 cm²) on the dorsal side of the albino rats to make a hairless area. The optimised formulation was applied to group 2 of rats ($n = 3$) for assessing any kind of irritation at specified sites. Formulation was removed after 48 hours and skin was examined for any signs of erythema and oedema [20,21].

Analgesic activity. Analgesic activity was conducted using healthy mice. The protocol of the study was sanctioned by the Institutional Animal Ethical Committee and permission was granted to conduct the study using healthy rats monitored as per the guidelines of animal ethical committee. Mice weighing 25–30 gm were divided in two groups of five each. The hot plate was maintained at $56 \pm 1^\circ\text{C}$. Formulation was applied on the animals and placed into a glass cylinder of 24 cm diameter on the heated surface. The time between placement and licking the paws or jumping was recorded as response latency. The reaction time was recorded for control mice treated with Tramadol HCl (5 %) at 0, 15, 30, 60 and 90 minutes. The test was terminated at 15 seconds to prevent tissue damage. The statistical analysis was carried out using Graph-Pad-Prism 3.03 software. The *t*-test was selected as the test for significance and *P* value less than 0.05 was considered statistically significant [22].

Stability study of film-forming gels

Stability study was conducted according to the ICH guidelines at $40 \pm 2^\circ\text{C}$ and $75 \pm 5\%$ RH for 3 months. The samples were withdrawn at beginning, after 30, 60 and 90 days and analysed for any physical and chemical changes.

Characterisation of tramadol HCl organic-inorganic hybrid film

In order to characterise the film quantitatively, it was characterised with the help of the following parameters. All the batches of tramadol HCl organic-inorganic hybrid film formulations were observed for appearance and transparency.

X-Ray diffraction study (XRD)

Bruker Model D8 Advance was used to check the crystallinity of formulation. This test was done from Sophisticated Test and Instrumentation Centre, Kochi University, Kochi, Kerala, India. The sample was smeared over low back ground sample holder (amorphous silica holder) and fixed on the sample stage in goniometer. The instrument was set with B-B geometry. The current and voltage was set to 40 mV and 35 mA and data was collected.

Drug content study of film-forming gels

Uniform thickness organic-inorganic hybrid gel film of $1 \times 1 \text{ cm}^2$ size was dissolved in 50 ml of phosphate buffer (pH 7.4). Resultant solution was kept for sonication for 10 minutes to dissolved the gel completely. The solution was filtered through the Whatman filter media and clear solution was checked for absorbance at 271 nm against blank as a phosphate buffer solution, pH 7.4. Thus, percentage drug content was calculated. All the readings were taken in triplicate and noted. Same method was implemented to determine the drug in the PVA organic gel film.

Moisture uptake study

The films were put in a desiccator with silica gel for 24 hours and weighed (W_i). The films were then transferred to another desiccator containing saturated NaCl solution (relative humidity 75%) at 25°C until a constant weight was obtained. After equilibrium was attained, the films were taken out and weighed (W_m). Moisture uptake capacity was calculated according to the following Equation (1) [23]:

$$\begin{aligned} \text{Moisture uptake capacity (\%)} \\ = (W_m - W_i / W_i) \times 100 \end{aligned} \quad (1)$$

Moisture content study

Both the organic PVA film and hybrid organic-inorganic films were evaluated for moisture content study. The prepared films were weighed initially (W_i) and kept in the desiccator containing silica gel at 25°C and is continuously weighed until it shows constant weight (W_d).

The moisture content is calculated using following Equation (2) [23]:

$$\text{Moisture content (\%)} = (W_d - W_i / W_i) \times 100 \quad (2)$$

Water uptake and swelling study

This study was performed to find out water uptake capacity of the prepared films. In this method, the prepared films of uniform size and thickness were fixed to the plain stainless-steel surface and slowly immersed in a beaker containing 25 ml distilled water at room temperature for 3 hours. After 3 hours the films were slowly removed and excess of water was wiped slowly with the help of soft filter paper. This experiment was discontinued at the observation of point when film begins to disintegrate or dissolve. Finally, the water uptake and swelling of film was calculated by the following Equation (3) [23]:

$$\text{Moisture content (\%)} = (W_s - W_i / W_i) \times 100 \quad (3)$$

Where, W_s is weight of film after swelling; W_i is the initial weight of film before water uptake and swelling.

Folding endurance study

a specific area of strip was cut and repeatedly folded at the same place till it broke. The number of times the film could be folded without breaking gave the value of folding endurance.

Weight variation test and thickness measurement

For each formulation, three film samples ($10 \times 40 \text{ mm}$) were used. Each film sample was weighed individually and the average weight was calculated.

Thickness of both organic-gel film and hybrid-gel film was measured using digital Vernier calliper (Mitutoyo, Japan). Thickness was measure at all the corner and centre of the film, multiple observations were noted and finally, average value was considered as $\pm\text{SD}$, $n = 3$.

Drying time

For the assessment of the drying time the formulation was applied to the glass slide. After 2 minutes a glass slide was placed on the film without pressure. If no remains of liquid were visible on the glass slide after removal, the film was considered dry. If remains of liquid were visible on the glass slide the experiment was repeated until the film was found to be completely dried [5].

Surface morphology study of organic-inorganic hybrid film of tramadol HCl

Surface morphology study of organic-inorganic hybrid film containing tramadol HCl was determined using Scanning electron microscopy (SEM).

SEM analysis carried out for surface morphology of film. Jeol, JSM 6390LA was used to check the smeared

on a small piece of adhesive carbon tape which was fixed on a brass stub. The sample was then subjected to gold coating using sputtering unit (model: JFC1600) for 10 sec at 10 mA of current. The gold coated sample placed in chamber of SEM (Jeol, JSM 6390LA) and secondary electron/Back Scattered electron images were recorded.

In-vitro drug permeation study of organic PVA film and organic-inorganic hybrid film

Drug permeation study of both organic PVA film and organic-inorganic hybrid film was conducted using fresh goat as a diffusion membrane. Goat skin was positioned between the two cell halves of a glass chamber. The two compartments were held together with a clamp. About 10 ml of phosphate buffer pH 7.4 was added to the receiver/receptor compartment. The film (25 mm in diameter) were mounted over the goat membrane and integrity was checked visually with proper equilibration. The receptor phase (phosphate buffer pH 7.4) was continuously stirred with the help of magnetic stirrer at 300 rpm and maintained at 37°C using a circulating water bath. Samples of 1 ml were collected at the interval of every hour for 24 hours study from the receiver compartment at predetermined time intervals and replaced with fresh buffer solution. The samples collected were analysed for drug content using UV spectrometric method at 271 nm wavelength and finally graph was plotted as cumulative drug permeation Verses time [19].

Stability study of organic and hybrid films

Stability study of film was performed in the same way as mentioned above for organic-inorganic hybrid gel.

Result and discussion

Pre-formulation study and characterisation of film-forming gels

As discussed in the methods section 2.2.1, the final organic-inorganic hybrid film-forming gel formulation was selected and further characterised for various physical and chemical parameters discussed below.

FT-IR study

The FT-IR spectra of PVA, TEOS, Tramadol HCl and blend of all these ingredients are presented in the Figure 1. The spectra of tramadol HCl shown major peaks indicating the basic functional groups at 3065.3; 2861.84; 2514.72, 2605.36; 3306.36; 1271.82; 1578.45; 1045.23 consisting of C-H stretching (aromatic), C-H stretching (aliphatic), C-H stretching of -CH₂ and -CH₃ groups, N-H stretching, C-N stretching respectively. Same peaks were retained in the Spectra of physical blend of all the ingredients indicating the no interactions among the them without affecting any changes in the tramadol HCl [24].

Differential scanning calorimetry (DSC)

The DSC thermogram of organic-inorganic hybrid gel (HG-9 formulation) shown in Figure 2 and interpretation are mentioned below:

1st peak. Exhibiting endothermic peak at -27.92°C,

- Corresponding to its melting and decomposition reported peak temperature was -16.95°C to -27.92°C.
- Enthalpy of fusion found to be -110.11 J/g

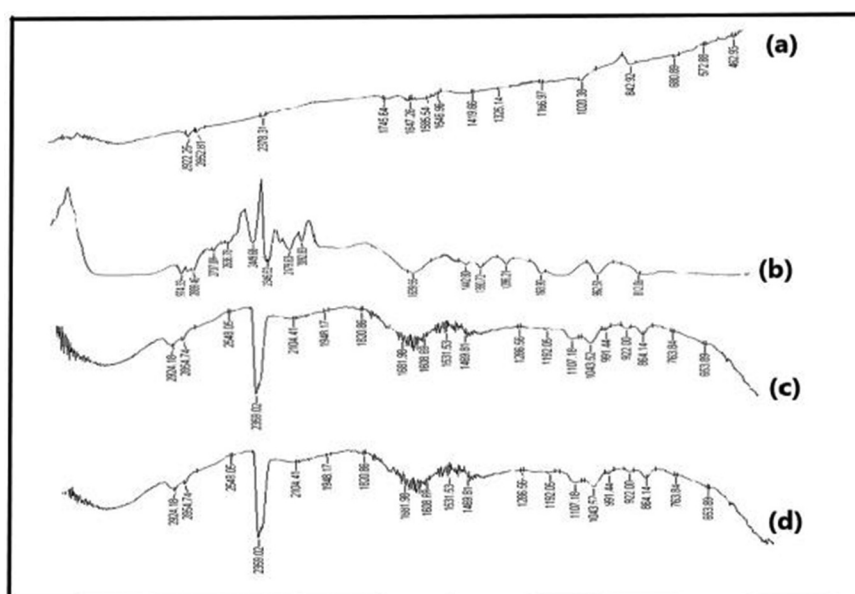


Figure 1. FT-IR study: PVA (a); TEOS (b); Tramadol HCl (c); Blend of PVA+TEOS+ Tramadol HCl (d).

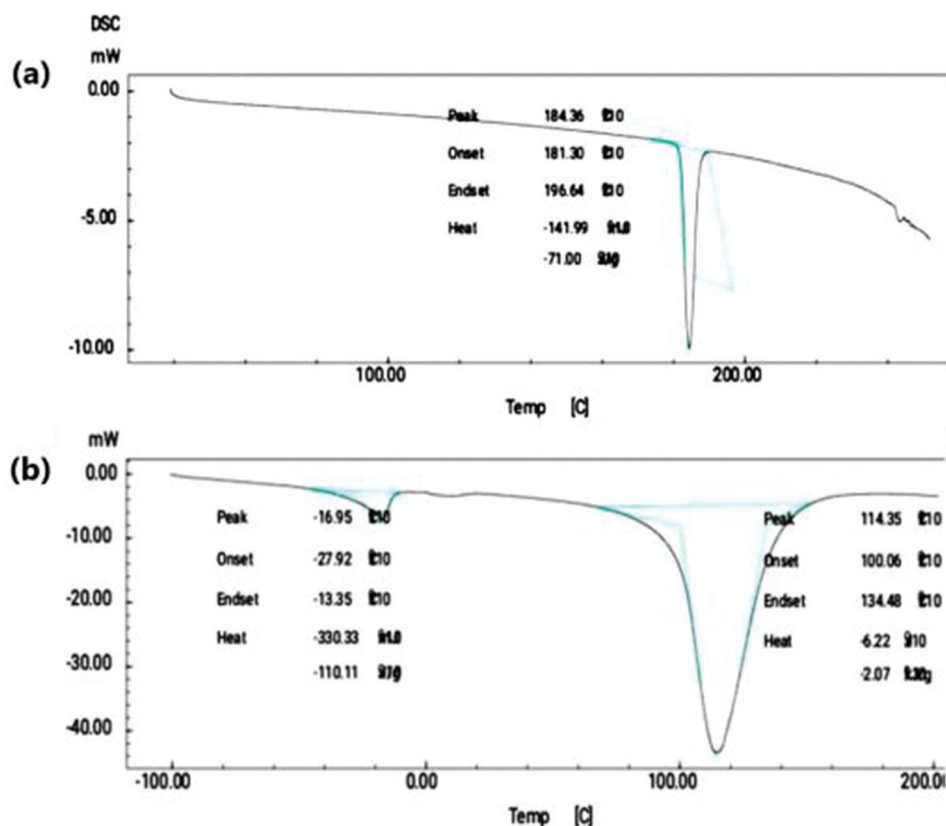


Figure 2. DSC study: Spectra of tramadol HCl (a); Spectra of Hybrid-organic-inorganic-film (b).

2nd peak. Exhibiting an endothermic peak at 114.35°C,

- (a) Corresponding to its melting and decomposition reported peak temperature was 100.04°C to 134.48°C
- (b) Enthalpy of fusion found to be -2.07 J/g

As shown in Figure 2, 1st peak indicates that formation of eutectic mixture and 2nd peak is broad asymmetric melting peak. Cross-linking increases in hybrid organic-inorganic gel due to formation of eutectic mixture. Decreased in melting point is indication of formation of eutectic mixture which promotes cross-linking of the resultant blend. Resultant melting of its blend is lower than their individual melting point. Because of reaction between organic and inorganic polymer there is formation of eutectic mixture, the melting point of resultant formulation was decrease and found to be 114.35°C and is less than that of original melting point of drug 184.36°C and polymer which is used [25].

Appearance and pH

As shown in Figure 3 the tramadol HCl formulation was observed under dark background, which shows transparent viscous preparation with smooth, homogenous, consistent.

All the organic-inorganic hybrid gel formulations were tested for pH and were found to be in the range

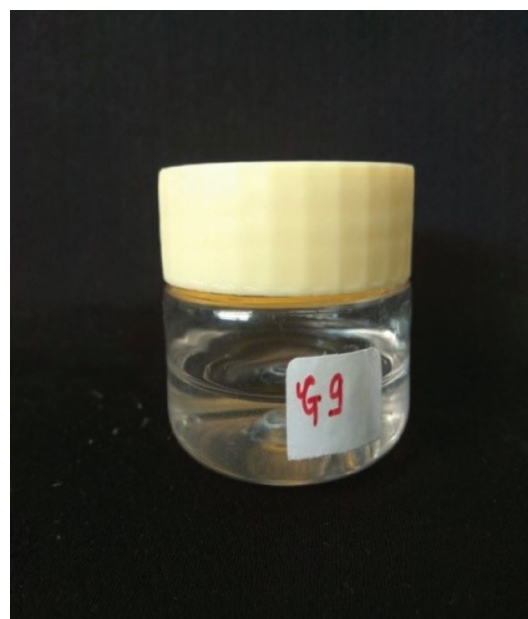


Figure 3. Appearance of tramadol HCl containing organic-inorganic hybrid gel (HG-9).

of 6.6–7.1. The pH of the final selected batch HG-9 was 6.9.

Rheological behaviour of film-forming gels

As shown in Figure 4(a) viscosity of hybrid gel (HG-9) found to be 231.2 Pa.s with respect to temperature condition. Resultant viscosity is sufficient for application to skin and leads to good spreadability

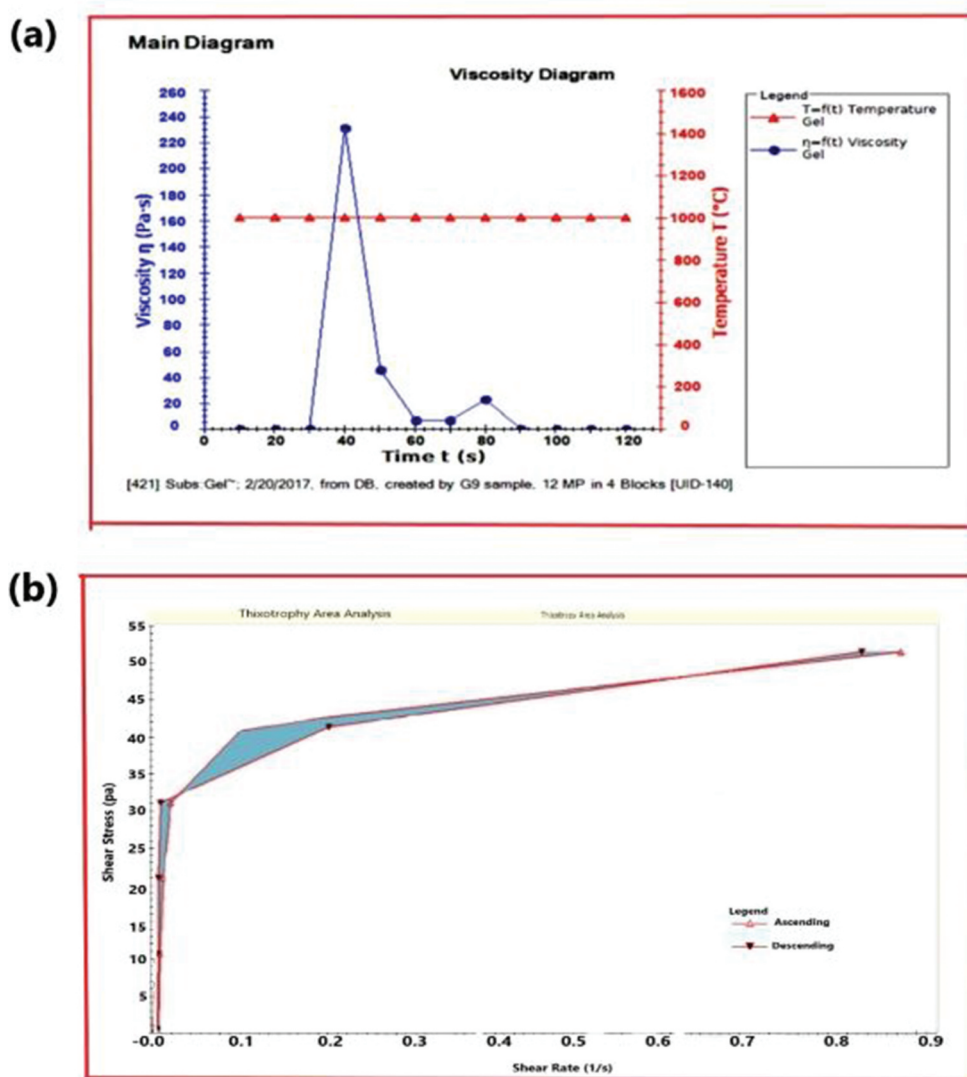


Figure 4. Rheological behaviour of hybrid-organic-inorganic film-forming gel: Viscosity study (a); Thixotropy study (b).

property. As per given in the Figure 4(a) it was observed that viscosity of final HG-9 formulation was increasing with increased in temperature up to certain value of 1400°C but later on as time laps, it again goes on decreasing with decreased in temperature condition, so this type of behaviour indicates the temperature dependability of the formulation with change in viscosity at certain shear rate value. This type of observation indicates thixotropic behaviour of system. All the detailed data of viscosity study is presented in Table 2.

According to Figure 4(b), the formulation showed thixotropy behaviour and change in viscosity with respect to certain values of shear rate and shear stress in which the shear rate steadily increases at constant rate from zero to some maximum value and then decreased at the same rate to zero again, a hysteresis loop form was shown in the Figure 4(b). The height, shape and enclosed area of hysteresis loop depend on the duration of shearing, the rate of increase/decrease

Table 2. Detailed data of viscosity study.

Sr. No.	Time t (sec)	Shear stress (pa) τ	Shear rate(1/s) $\dot{\gamma}$	Viscosity
1.	10	0.000	0.000	0.0
2.	20	9.984	0.001	0.0
3.	30	19.989	0.005	0.0
4.	40	29.993	0.013	231.265
5.	50	39.998	0.088	45.354
6.	60	49.982	0.764	6.543
7.	70	49.982	0.724	6.906
8.	80	39.998	0.175	22.845
9.	90	29.993	0.003	0.0
10.	100	19.989	0.000	0.0
11.	110	9.984	0.000	0.0
12.	120	0.000	-0.001	0.0

of shear rate and the past kinematic history of the sample. The sample has taken fixed time to return more viscous state, it is called Non-Newtonian pseudo plastic fluid

showing a time dependant change in viscosity. As this is time dependant system, viscosity of the formulation gradually becomes loss the internal structure of material was broken down.

Table 3. Detailed data of thixotropy study.

Block index	Time (s)	Shear rate (1/s)	Shear stress (Pa)	Shear rate (1/s)	Shear stress (Pa)
0	10	0.0	0.0	0.0	0.0
0	20	0.0	9.998	0.001	9.984
0	30	0.01	19.99	0.05	19.989
0	40	0.01	29.99	0.013	29.993
0	50	0.09	40.00	0.088	39.998
0	60	0.76	49.98	0.764	49.982
0	70	0.72	49.98	0.724	49.982
1	80	0.18	40.0	0.175	39.998
1	90	0.00	29.99	0.003	29.993
1	100	0.00	19.99	0.00	19.989
1	110	0.00	9.98	0.00	9.984
1	120	0.00	0.00	-0.001	0.000

All the detailed data of thixotropy study is presented in Table 3 [5,26].

Drug content study of film-forming gels

The drug content of the PVA-based gel and final organic-inorganic film-forming gel formulation (HG-9) gel was determined in triplicate and from standard deviation drug content was found to be of $88.4 \pm 3.178\%$ and $95.1 \pm 2.31\%$ respectively. The drug content of hybrid gel was found to be more than that of organic PVA-based gel. Hence uniformity of drug content was found to be satisfactory.

Texture profile analysis

a higher peak load (firmness) and hardness work done value indicate a less spreadable sample. Conversely, a lower peak load (firmness) value coupled with a lower hardness work done value indicates a more spreadable sample. The observations for spreadability of PVA-based gel and organic-inorganic hybrid (HG-9) gel is shown in Figure 5. Comparison of mechanical properties between PVA-based gel and hybrid gel were presented in Table 4.

Animal activity

Skin irritation test. The result of skin irritation study based on visual observation, it has revealed that hybrid gel (HG-9) formulation was non-sensitising and safe

Table 4. Comparison of mechanical properties between PVA-based gel and hybrid gel.

Sr. no.	Parameters	Resultant value of PVA-based gel (OG)	Resultant value of hybrid gel (HG-9)
1.	Adhesiveness	0.70 mJ	3.40 mJ
2.	Stringiness Length	0.00 mm	0.56 mm
3.	Fracturability	10.00 g with 1% of load sensitivity	14.00 g with 1% of load sensitivity
4.	Cohesiveness	1.26	0.81

*OG = Organic Gel; *HG = Hybrid Gel

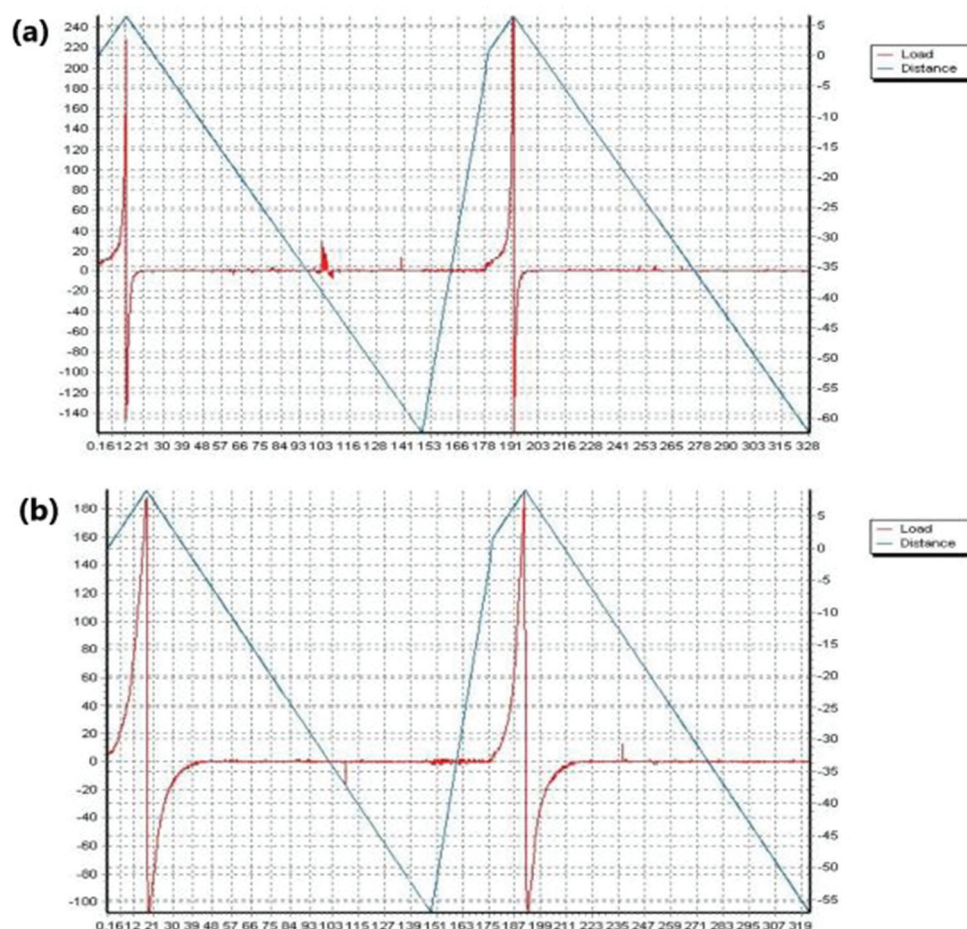


Figure 5. Texture analysis: Mechanical properties and spreadability study of PVA organic gel (a) and Hybrid organic-inorganic gel (b).



Figure 6. Skin irritation study using rats as animals.

Table 5. Skin irritation study data.

Test material ^a	Skin reaction ^b	Mean irritation score		
		12 hours	24 hours	48 hours
Hybrid-organic-inorganic film (HGF-9)	Erythema	0	0	0.1
	Oedema	0	0	0

^aTest material was applied on rat skin

^bErythema and oedema, the mean irritation score was the summation of each irritation score divided by the number of animals (rats)

for use, as there was no significant irritation produced after application of hybrid gel (HG-9) formulation on the rat’s skin. Following observation were depicted from the skin irritation and photographs of animals undergoing skin irritation study are presented in Figure 6. The erythema and oedema irritation matrix score was presented in Table 5.

Analgesic activity. Final HG-9 formulation possesses very significant analgesic effect according to statistical analysis. Statistical *t*-test was applied and statistical data was generated as mentioned in Figure 7.

Ex-vivo drug permeation study of tramadol HCl organic-inorganic hybrid gel

The *ex-vivo* drug permeation of Tramadol HCl organic-inorganic hybrid gel was evaluated by *ex-vivo* diffusion study using Franz diffusion cell, using a fresh goat skin as a diffusion membrane at pH 7.4. Cumulative % of drug permeated are mentioned in Figure 8. Formulations with higher concentration of PVA shown less amount of drug

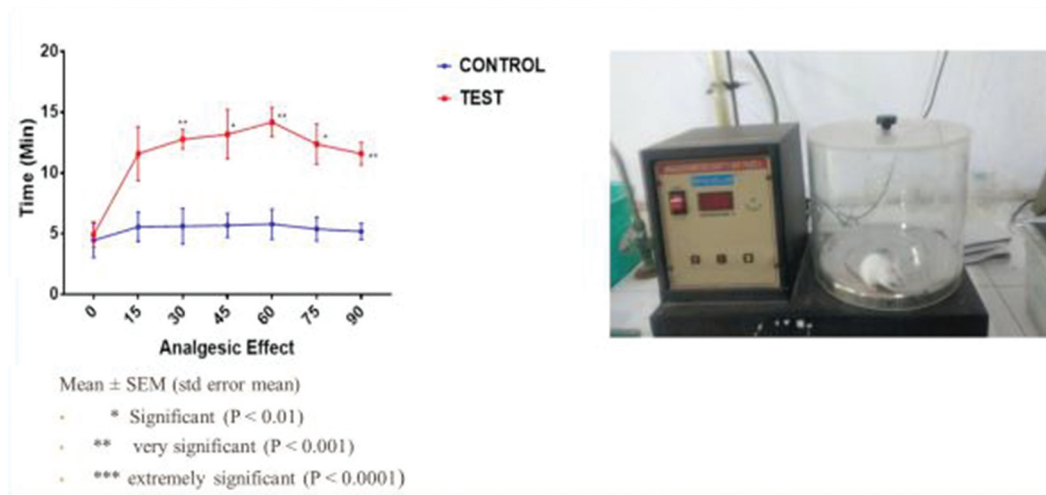


Figure 7. Analgesic activity in mice.

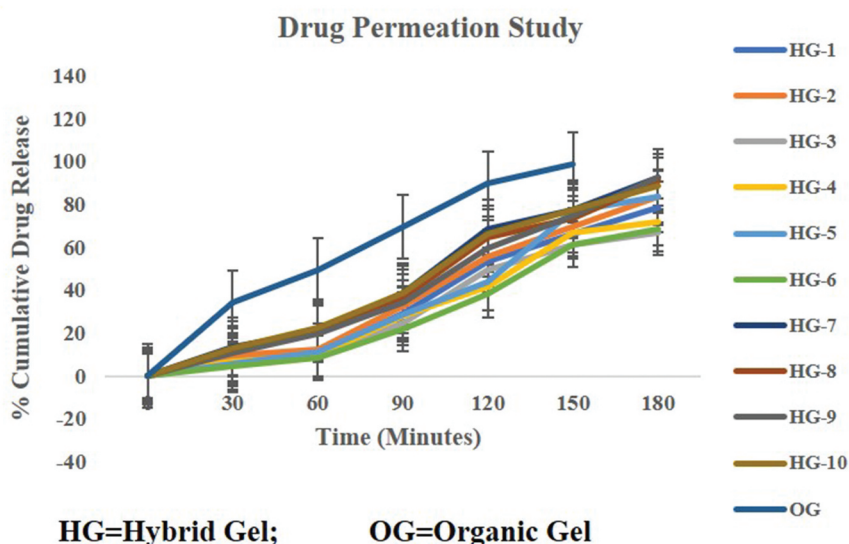


Figure 8. Cumulative drug permeation study of both organic and hybrid film-forming gel.

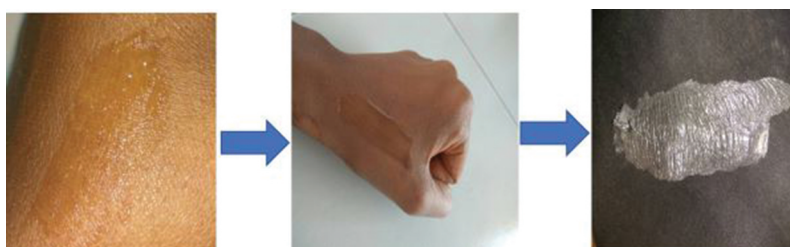


Figure 9. Appearance of prepared and applied dried film.

release after 3 hours of time period. Hence, in first few formulations, HG-1 to HG-6, less amount of drug release was observed, showing 78.66%, 83.55%, 66.55%, 71.45%, 83.25% and 68.58% respectively. This may happen due to extent of cross-linking interaction between PVA and TEOS in the presence of HCl [5]. There was little difference of drug release was found among the formulations HG-7 to HG-10 due to presence of nearly same amount of PVA and TEOS showing, 92.5%, 90.58%, 92.36% and 88.68% respectively. Finally, HG-9 formulation was

considered to be optimised based on the initial results observed and as identified which was already discussed in method section 2.2.1.

Appearance and miscibility study

For the blend-type polymer gels, the structural properties and the unique functions were dependent on the miscibility, chemical structure and interaction between mixture components. PVA and glycerine have excellent compatibility due to the well-known observation of PVA solubility in glycerol. The high transparency of the film in Figure 9 indicated that there may be no macro-

Table 6. Stability study hybrid-organic-inorganic film-forming gel.

Duration	Temperature and relative humidity	Appearance	*pH	*Drug content
1 month	40°C, 75%RH	Transparent, smooth, viscous	7.0 ± 0.2	95.9 ± 0.58%
2 months	40°C, 75%RH	Transparent, smooth, viscous	6.9 ± 0.4	95.0 ± 0.84%
3 months	40°C, 75%RH	Transparent, smooth, viscous	7.0 ± 0.2	96.01 ± 1.02%

*All the observations were taken in triplicate as ±SD (n = 3).

phase separation occurring between the organic polymer and inorganic TEOS.

Stability study

The storage of tramadol HCl organic-inorganic hybrid gel containing of an optimised batch for 3 months at room temperature and relative humidity (40°C, 75%) showed no change in appearance of the system was explained in Table 6.

Stability study was performed for 1, 2 and 3 months which did not show any major changes in appearance, pH, drug content.

Characterisation of tramadol HCl organic-inorganic hybrid film

The organic-inorganic hybrid film of tramadol HCl was evaluated for various physical and chemical parameters in order to ensure the quality of the film for continuous release of tramadol HCl in the management of pain on affected area by transdermal route. Simultaneously, the organic PVA film containing tramadol HCl was also evaluated XRD study.

The XRD was used to investigate the influence of TEOS on the crystalline property of the hybrid films, which was shown in fig. As seen, pure PVA film possessed distinctly higher crystalline intensity than its hybrid films, and results showed the main diffraction peaks of PVA film containing Tramadol HCl and PVA-TEOS hybrid film containing Tramadol HCl were around $2\theta = 6.14$ and 5.360 respectively. In the XRD patterns, this can be ascribed to the crystalline regions of PVA due to strong hydrogen bonds between the hydroxyl groups. Furthermore, peak intensities of PVA hybrid films decreased

continuously with incorporation of TEOS. Namely, there was a significant decrease in crystalline regions and increase in amorphous regions in the hybrid film, which can indicate that the introduction of TEOS led to the destruction, to some extent, of the crystalline region of PVA film [11]. Figure 10 shows the interpretation of the XRD peaks observed for both organic PVA film and hybrid film.

All the observations of thickness, drug content, moisture content, moisture uptake capacity and swelling index study are presented in Table 7 and discussed below.

The drug content of the optimised Formulation (HG-9) film and PVA film was carried out in triplicate and average drug content was found to be of 87.20% and 81.3% respectively. The drug content of hybrid film was found more than the organic PVA film. Hence uniformity of drug content was found to be satisfactory.

In moisture content study, selective films final formulations were evaluated and average moisture was found to be $1.07 \pm 0.04\%$. These values show the percent moisture uptake capacity of films. The

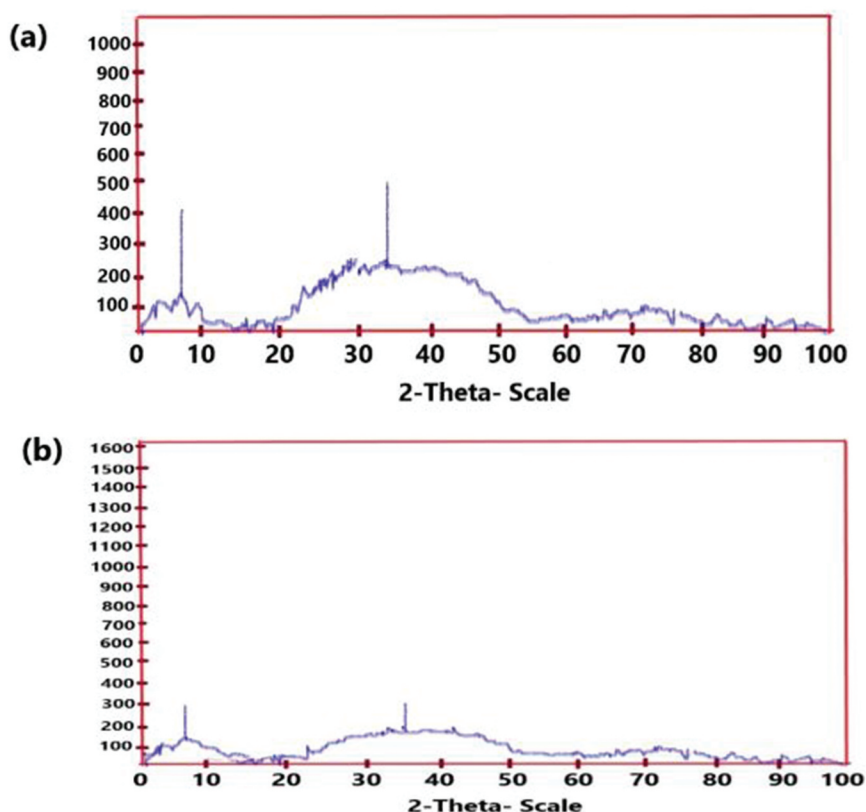


Figure 10. XRD graph of PVA-organic film (a) and hybrid-organic-inorganic film (b) containing tramadol HCl.

Table 7.: Evaluation of tramadol HCl films for various parameters.

Sr. no.	Type of formulation	*Thickness (mm)	*Drug content (%)	*Moisture content (%)	*Moisture uptake capacity (%)	*Swelling index (%)
1.	PVA Organic Film (OGF)	0.584 ± 0.014	81.3 ± 0.55	2.13 ± 0.12	2.55 ± 0.45	78.28 ± 0.14
2.	Hybrid Organic-inorganic Film (HG-9)	0.458 ± 0.032	87.20 ± 0.24	1.07 ± 0.04	1.65 ± 0.16	89.45 ± 0.23

*All the experiments were conducted triplicate \pm SD ($n = 3$).

moisture uptake of the films was generally low; this will help the films to remain stable and protect them from microbial contamination. Generally, the moisture uptake capacity of films increases with increasing hydrophilicity of the polymer or plasticiser and the levels of hydrophilic polymers as well. Moisture uptake capacity of PVA-organic film was higher than the hybrid film whereas the swelling index values of hybrid film was found to be little higher than the PVA-organic film. Extent of swelling was also depending upon the hydrophilicity of film and proportion of such components in the formulation.

In folding endurance study, a specific area of strip was cut and repeatedly folded at the same place till it broke. The number of times the film was folded without breaking gave the value of folding endurance. Films were folded for more than 300 times it did not show any sign of cracks. It was taken as end point and confirmed the physical stability of formed film of organic-inorganic hybrid gel.

For weight variation study, films formed from final organic-inorganic hybrid gel were selected and average weight of films were considered as final weight of the films. In this study, average weight of film (10×40mm size) was found to be 0.21 ± 0.007 g. Readings were taken in triplicate for accuracy.

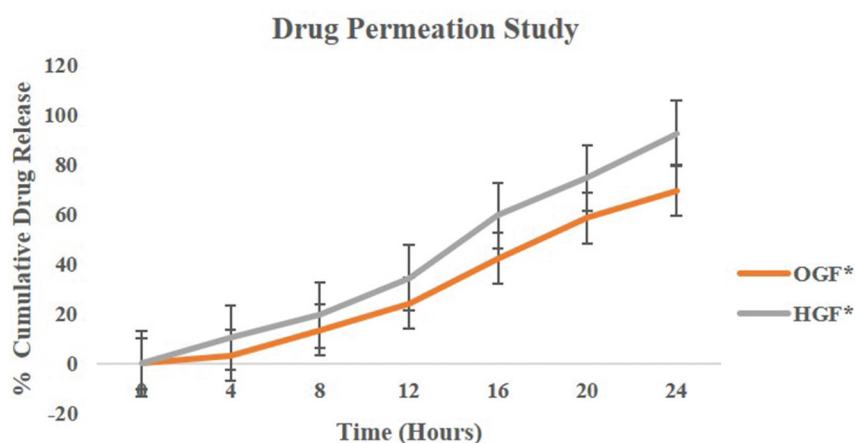
It is very important to know about the drying time of the gel to form the film after application on the intact skin. For this purpose, a simple observation technique was implemented as discussed above. a glass slide was placed on the film without pressure and after 2 minutes glass slide was removed from film and it was observed that no liquid form of gel was visible on the glass slide, this has indicated that the film was dried immediately.

Both organic as well as hybrid-organic-inorganic films were subjected to the drug permeation study as discussed in the method section. For this study optimised formulation GHF was selected as hybrid dried

film and PVA organic film (OGF). In this study, both results were compared and it was found that the PVA organic (OGF) has shown less amount of 69.55% drug release whereas hybrid film (HGF) has shown 92.36% drug release in the 24 hours of study. This huge difference in the drug release among both the formulation was due to the fact the nature of PVA organic film little hydrophilic with high level of concentration in the formulation. But strong interaction between PVA and TEOS make weak C-OH peak and formation of Si-O-C peaks in the XRD study. Due to this crystallinity of the PVA decreases resulting more soluble and transparent film formation and hence hybrid film has shown higher percentage of drug release as compare to the plain PVA organic film [11,27]. The cumulative drug release profile of both the organic PVA (OGF) and hybrid organic-inorganic film is highlighted in Figure 11.

Surface morphology of both the organic PVA film and hybrid organic-inorganic film was checked visually as well as using scanning electron microscopy (SEM). SEM can provide

direct visual evidence of the influence of TEOS on surface morphology of the hybrid films. SEM photographs of surface sections of pure PVA and its hybrid are displayed in Figure 12. From these micrographs, it can be seen that the surface of PVA film was both homogeneous and smooth. Moreover, the addition of TEOS significantly affected the surface morphology. However, no visible phase separation between PVA and silica in all hybrid films can be observed. The hybrid HG-9 film exhibited a homogeneous granular structure. The presence of silica microparticles can be attributed to the reaction between PVA and the hydrolysed silanol of TEOS in the sol-gel process, which may play an important role in destroying regular crystalline arrangement of PVA chains and consequently decreasing the crystalline regions in PVA films. In



*OGF=Organic-Gel-Film;

*HGF=Hybrid-Gel-Film

Figure 11. Cumulative drug permeation study of both organic and hybrid dried films.

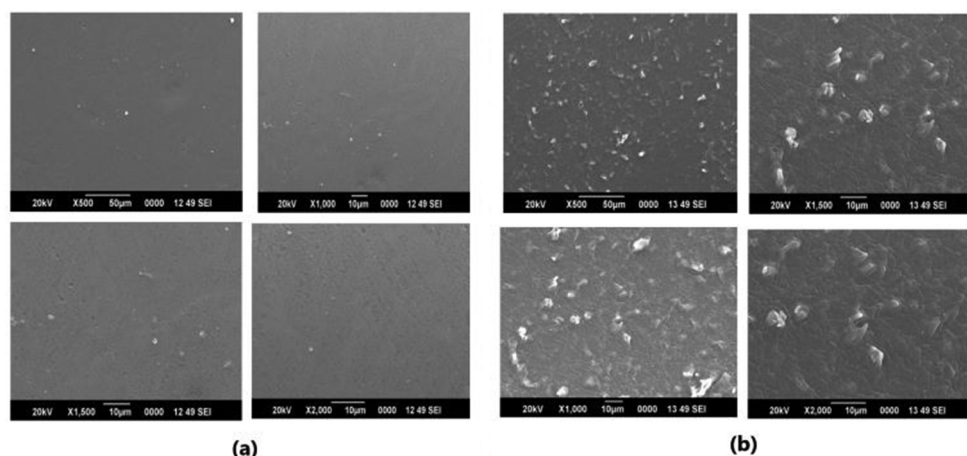


Figure 12.: Scanning electron microscopic photographs showing morphology of prepared film at different resolution.

Table 8.: Stability study hybrid-organic-inorganic film.

Duration	Storage condition	Appearance	*Drug Content
1 month	40°C, 75%RH	Transparent, thin, no brittleness	84.23 ± 1.05%
2 months	40°C, 75%RH	Transparent, thin, no brittleness	83.20 ± 1.15%
3 months	40°C, 75%RH	Transparent, thin, no brittleness	83.28 ± 0.89%

**All the observations were conducted triplicate ±SD ($n = 3$)

addition, the surface morphology of hybrid film became rough and uneven, which was due to the polycondensation of excessive TEOS leading to conglomeration and aggregation in the matrix. This conglomeration and aggregation may result in the film more compact that does not favour the diffusion of the drug molecule in the film.

Stability study was performed for 1, 2 and 3 months which does not show any major changes in appearance, drug content. Results of stability study of hybrid film is presented in Table 8.

Conclusion

Transdermal drug delivery systems have gained many benefits and are better alternatives for other conventional routes of administrations like oral to avoid GI irritation, first-pass effect and undesired drug release pattern. Conventional available transdermal/topical formulations are not capable to modify the drug release property and other physical properties and have many disadvantages. In this study, an attempt was made to prepare a novel organic–inorganic hybrid film-forming gel formulation, which showed enhanced adhesion, cross-linking and better drug release property with ease of application on skin and formation of flexible, comfortable film than plain PVA films. More importantly, use of inorganic phase in PVA matrix not only significantly improved mechanical strength and skin adhesion properties, but also

decreased the crystalline regions of PVA and hence facilitate the diffusion of drug and water.

So, from this study it was concluded that formulation of organic-inorganic film-forming gel is the challenging and excellent new approach for transdermal delivery of drug with better patient compliance as compare to the existed organic material-based transdermal formulations.

Acknowledgements

Authors are very thankful to the IPCA laboratories, Mumbai for providing Tramadol HCl.

Also grateful to the Principal of our institute for providing facilities and support to conduct this research study. At the last, authors are very thankful to all those who have cooperated to complete this work successfully.

Disclosure statement

Authors declare no conflict of interest.

References

- [1] Yu YY, Chen CY, Chen WC. Synthesis and characterization of organic–inorganic hybrid thin films from poly(acrylic) and monodispersed colloidal silica. *Polymer*. 2003;44:593–601.
- [2] Novak BM. Hybrid nanocomposite materials-between inorganic glasses and organic polymers. *Adv Mater*. 1993;5:422–433.
- [3] Otsuka T, Poly CY. (methyl methacrylate) (PMMA)-based hybrid materials with reactive zirconium oxide nanocrystals. *Polym J*. 2010;42:58–65.
- [4] Ibrahim H, Ibrahim S. Study some properties of hybrids silica/PVA using sol gel method. *Chem Bio Phy Sci Sec C*. 2015;5(2):1950–1957.
- [5] Guo R, Xiaoyan D, Zhang R, et al. Bioadhesive film formed from a novel organic–inorganic hybrid gel for transdermal drug delivery system. *Eur J Pharm Biopharm*. 2011;79:574–583.
- [6] Wang K, Nune KC, Misra RDK. The functional response of alginate-gelatin-nanocrystalline injectable

- hydrogels toward delivery of cells and bioactive molecules. *Acta Biomaterialia*. 2016;36:143–154
- [7] Wang K, Lin S, Nune KC, et al. Chitosan-gelation based microgel for sustained drug delivery. *J Biomat Sci*. 2016;27:441–453.
- [8] Wang K, Buschle-Diller MRDK. Chitosan-based injectable hydrogels for biomedical applications. *Materials Technol*. 2015;30:198–205.
- [9] Yuan Q, Shah J, Hein S, et al. Controlled and extended drug release behavior of chitosan-based nanoparticle carrier. *Acta Biomaterialia*. 2010;6:1140–1148.
- [10] Yuan Q, Hein S, Misra RDK. New generation of chitosan-encapsulated ZnO quantum dots loaded with drug: synthesis, characterization and in vitro drug delivery response. *Acta Biomater*. 2010;6:2732–2739.
- [11] Yuan Q, Subramanian R, Hein S, et al. Stimuli-responsive magnetic nanoparticle drug carrier: magnetite encapsulated with chitosan-grafted-copolymer. *Acta Biomater*. 2008;4:1024–1037.
- [12] Prausnitz MR, Langer R. Transdermal drug delivery. *Nat Biotechnol*. 2008;26:1261–1268.
- [13] Berner B, John VA. Pharmacokinetic characterization of transdermal delivery systems. *Clin Pharmacokinet*. 1994;26:121–134.
- [14] Setouhy DA, Ashmony SM. Ketorolac tramadol topical formulations: release behaviour, physical characterization, skin permeation, efficacy and gastric safety. *J Pharm Pharmacol*. 2010;62:25–34.
- [15] Klotz U. Tramadol-the impact of its pharmacokinetic and pharmacodynamic properties on the clinical management of pain. *Arzne imittel for schung*. 2003;53:681–687.
- [16] Raffa RB. Basic pharmacology relevant to drug abuse assessment: tramadol as example. *J Clin Pharm Ther*. 2008;33:101–108.
- [17] 24 December 2019. Available from: <http://www.brookfieldengineering.com/education/learn-about-texture.asp>
- [18] 24 December 2019. Available from: <http://www.brookfieldengineering.com/education/applications/texture-analysis.asp>
- [19] 24 December 2019. Available from: <http://www.brookfieldengineering.com/education/applications/texture-jelly-cup.asp>
- [20] Reddy MS, Mutalik S, Rao G, et al. Preparation and evaluation of minoxidil gels for topical application in alopecia. *Indian J Pharm Sci*. 2006;68(4):432–436.
- [21] More BH, Sakharwade SN, Tembhurne SV, et al. Evaluation for Skin irritancy testing of developed formulations containing extract of *Butea monosperma* for its topical application. *Int J Toxicol Appl Pharmacol*. 2013;3(1):10–13.
- [22] Kasture SB. A handbook of experiments in pre-clinical pharmacology. 1st ed. Career publication; 2006. p. 72–73.
- [23] Ammar HO, Ghorab M, El-Nahhas SA, et al. Polymeric matrix system for prolonged delivery of tramadol hydrochloride, part I: physicochemical evaluation. *AAPS Pharm Sci Tech*. 2009;10:7–20.
- [24] Dyer JR. Applications of absorption spectroscopy of organic compounds. Prentice Hall of India; 2004. p. 33–38.
- [25] Skoog DA, West DM. Fundamentals of analytical chemistry. 8th ed. Singapore: Thomson Brooks/Cole; 2004. p. 906–946.
- [26] Chhabra RP, Richardson JF. Non-Newtonian flow in the process industries: fundamentals and engineering applications. Butterworth-Heinemann; 1999.
- [27] Hu P, Jia M, Zuo Y, et al. A silica/PVA adhesive hybrid material with high transparency, thermostability and mechanical strength. *RSC Adv*. 2017;7:2450–2459.



Phospholipid complex-loaded self-assembled phytosomal soft nanoparticles: evidence of enhanced solubility, dissolution rate, ex vivo permeability, oral bioavailability, and antioxidant potential of mangiferin

Darshan R. Telange¹ · Nazish K. Sohail² · Atul T. Hemke² · Prashant S. Kharkar³ · Anil M. Pethe⁴

© Controlled Release Society 2020

Abstract

In this study, self-assembled phytosomal soft nanoparticles encapsulated with phospholipid complex (MPLC SNPs) using a combination of solvent evaporation and nanoprecipitation method were developed to enhance the biopharmaceutical and antioxidant potential of MGN. The mangiferin-Phospholipon® 90H complex (MPLC) was produced by the solvent evaporation method and optimized using central composite design (CCD). The optimized MPLC was converted into MPLC SNPs using the nanoprecipitation method. The physicochemical and functional characterization of MPLC and MPLC SNPs was carried out by differential scanning calorimetry (DSC), thermogravimetric analysis (TGA), Fourier-transform infrared spectroscopy (FT-IR), powder X-ray diffractometer (PXRD), proton nuclear magnetic resonance (¹H-NMR), solubility, in vitro dissolution, oral bioavailability, and in vivo antioxidant studies. A CCD formed stable MPLC with the optimal values of 1:1.76, 50.55 °C, and 2.02 h, respectively. Characterization studies supported the formation of a complex. MPLC and MPLC SNPs both enhanced the aqueous solubility (~32-fold and ~39-fold), dissolution rate around ~98% via biphasic release pattern, and permeation rate of ~97%, respectively, compared with MGN and MGN SNPs. Liver function tests and in vivo antioxidant studies exhibited that MPLC SNPs significantly preserved the CCl₄-intoxicated liver marker and antioxidant marker enzymes, compared with MGN SNPs. The oral bioavailability of MPLC SNPs was increased appreciably up to ~10-fold by increasing the main pharmacokinetic parameters such as C_{max} , T_{max} , and AUC. Thus, MPLC SNPs could be engaged as a nanovesicle delivery system for improving the biopharmaceutical and antioxidant potential of MGN.

Keywords Mangiferin · Solubility · In vitro dissolution rate · Oral bioavailability and in vivo antioxidant potential

Introduction

Mangiferin (MGN), a xanthonoid predominantly found in the leaves, bark, fruits, and root bark of plants such as *Mangifera indica* (Family: Anacardiaceae) and others, is a super-antioxidant [1–6]. Following oral administration, it offers a score of health benefits such as antioxidants [7], blood lipid-lowering agents [8], anti-proliferative [9], skeletal muscle contractile [10], and brain oxygenation [11]. Recently Imran et al. [4] have extensively reviewed the potential of MGN in managing lifestyle-related disorders. Enormous literature reports are available demonstrating the utility of MGN in a variety of diseases and disorders. MGN is being consistently explored in life sciences, particularly during the last decade or so, as seen from the number of published papers. Yang et al. reported the protective effect of MGN on cerebral ischemia-reperfusion

✉ Darshan R. Telange
telange.darshan@gmail.com

¹ Rajarshi Shahu College of Pharmacy, Malvihir, Botha Road, Buldhana, Maharashtra, India

² Smt. Kishoritai Bhoyar College of Pharmacy, Nagpur, Maharashtra, India

³ Shobhaben Pratapbhai Patel School of Pharmacy and Technology Management, SVKM's NMIMS (Deemed to be University), V.L.Mehta Road, Vile Parle (W), Mumbai, Maharashtra, India

⁴ School of Pharmacy and Technology Management, SVKM's NMIMS (Deemed to be University), Polepally SEZ, Jadcherla, Mahbubnagar, Hyderabad, Telangana, India

injury via enhancing the activation of the Nrf2/HO-1 pathway [12]. Bhatt et al. reported the cardioprotective activity of MGN against cyclophosphamide-induced cardiotoxicity via enhancing lipid profile, antioxidant level, and electrocardiographic parameters [13]. Szandurk et al. investigated the protective effect of MGN on trinitrobenzene sulfonic acid-induced colitis in rats and found that MGN at 30 and 100 mg/kg improved the colitis condition in rats by reducing TNF- α and IL-17 concentration [14]. Sahu et al. investigated the defensive role of MGN against cisplatin-induced nephrotoxicity. Results demonstrated that MGN at a dose of 20 and 40 mg/kg appreciably reversed the renal function [15]. Despite the potential offered by MGN as a medicinal agent and a nutraceutical, its benefits are strongly confined by its nearly undesirable biopharmaceutical and pharmacokinetic properties such as low aqueous solubility (0.1 to 0.3 mg/mL), deprived lipophilicity (logP 0.56), limited and variable oral bioavailability (1.5 to 5%), rapid phase II metabolism (glucuronidation), shorter half-life ($t_{1/2}$) (1.71 h), and fast clearance from the human body [16–20]. It is categorized as the Biopharmaceutical Classification System (BCS) class IV drug. The presence of four phenolic -OH groups contribute significantly to its extensive glucuronidation, following oral administration [21], compromising its oral bioavailability and subsequent therapeutic benefits.

A significant number of formulation strategies have been explored so far to overcome the above biopharmaceutical challenges associated with MGN. These attempts include β -cyclodextrin (β -CD) inclusion complexation [22], salt formation [23], phospholipid complexation [17, 18], nanostructured lipid carrier system [24], and spray-dried formulation [25]. A detailed analysis of these formulation trials demonstrated variable and limited success. Moreover, the phospholipid complexation work of Khurana et al. [17, 18] has shown the limited improvements in solubility (25-fold only) and dissolution studies without investigating optimization, entrapment efficiency, oral bioavailability, and in vivo antioxidant activity of complex and/or nanostructured lipid carriers (NLCs). Additionally, the author has used Phospholipon® 90G, for the preparation of phospholipid complex even though it exhibits low solubility for MGN. Phospholipon® 90G is reported to form strong aggregates and agglomeration with drug and/or bioactive which, in turn, results to the decrease in the solubility and dissolution performance of drug and/or bioactive [26]. With the consideration of this, we, therefore, used a novel dual-formulation approach to overcoming the observed limitations of the previously reported formulations and/or drug delivery systems (DDS), by designing and developing an alternate formulation or DDS addressing the existing pain-in-the-brain biopharmaceutical issues associated with MGN.

Of the several strategies for enhancing the aqueous solubility of poorly water-soluble drugs in general and BCS class IV drugs in particular, complexation with phospholipids presents

a unique and appropriate strategy. Previously, this modality has been used successfully for improving the poor aqueous solubility, in vitro release rate, and most importantly, the oral bioavailability of plant-based bioactive such as daidzein [27], salvianolic acid B [28], chlorogenic acid [19], kaempferol, and apigenin [29, 30]. Moreover, a phospholipid-based system, i.e., formulation, offers several benefits such as ease of preparation, high drug loading capacity, and long-term stability, to name a few. Furthermore, the utilized Phospholipon® 90H and nanoprecipitation method in the current study convert the system into soft nanoparticles with significant improvement in solubility, dissolution, absorption, and finally oral bioavailability of MGN.

Self-assembled phytosomal soft nanoparticles (SNPs) are lipid-compatible molecular aggregates that form a micelle-like spherical structure. This delivery system has created significant interest among researchers due to several benefits such as controlled release, maximization of therapeutic efficacy, minimization of side effects, gastric protection from luminal enzymes, ease of fabrication, drug stability, and, most importantly, transportation of drugs across the biological barriers. SNPs are consisting of bioactive and phospholipids. Phospholipids are compound lipids, which act as a major part of the biomembrane as well as a precursor in the formation of platelet activation factor, arachidonic acid, and secondary messengers used in the process of signal transduction [31–33]. As a part of the biomembrane, phospholipids demonstrate good biocompatibility and, thus, serve as excellent drug delivery carriers in the transportation of drugs across the biological barrier [34]. The presence of positive and negative charges in the phospholipid compound makes it amphiphilic, which shows lipid as well as water solubility to a greater extent [35, 36]. The presence of hydroxyl group (-OH) of phospholipids can make successful interactions with active hydrogen part of any lipophilic drug via esterification process, leading to produce an amphiphilic compound which further can improve the therapeutic activity of drug molecule via facilitating its transportation across lipid-rich biomembrane [37]. Moreover, this physicochemical property of phospholipids is also employed in the formation of a complex with bioactive through polar and hydrogen bonding interactions [38–40]. Earlier literature has shown that phospholipid complex improved the aqueous solubility, permeability, stability, and site specificity, thereby enhancing the oral bioavailability and efficacy and reducing the toxic side effects of hydrophobic drugs [41]. Additionally, the formation of self-assembled amphiphilic structure [42], biocompatibility [43], emulsifying [44], and wetting characteristics [42] of phospholipids provide a base material for the preparation of nanoparticles' drug delivery system. Nanoprecipitation technology is a nanoparticle preparation technique, in which the SNPs are prepared by diffusing the organic phase containing complex into the continuous water phase leading to the formation of o/w suspension. Further

rapid diffusion leads to a decreased interfacial tension and evaporation of the organic solvent, resulting in the formation of self-assembled phytosomal SNPs as nanodroplets loaded with phospholipid complex. Formations of SNPs using this technology can result in amphiphilic nanoparticles which can entrap bioactive and phospholipid complex to a greater extent and facilitate the transfer of complex loaded into SNPs from water-soluble location to the lipid-soluble location of cell membrane for exhibiting high drug efficacy [45]. Therefore, self-assembled phytosomal SNPs are considered to be the promising dual-formulation technology for improving the biopharmaceutical attributes of many bioactive. Many pharmaceutical scientists devised a combined formulation strategy involving two or more carriers such as polymer gel [46], phospholipid complex loaded in microspheres [47], and phospholipid complex-loaded matrix film [48]. These unique formulations exhibited significant improvement in the biopharmaceutical profile of the loaded drug or phytoconstituents. Previously, it was demonstrated that a noteworthy enhancement of biopharmaceutical properties of drugs relied upon the successful incorporation of the phospholipid complex into the nanosystems [49–51]. To the best of our knowledge, such a novel formulation strategy has not been reported so far in the literature.

In the present study, we report a systematic and comprehensive study of novel dual-formulation strategy for improving the biopharmaceutical profile of a super-antioxidant MGN, with a potential impact on its bioavailability and therapeutic utility. The formulations were optimized using the design of experiments (DoE) methodology, followed by the physicochemical and biopharmaceutical characterization (particle size, zeta potential, detailed thermal, spectroscopic, powder X-ray diffraction, solubility, in vitro dissolution studies, etc.). Finally, the optimized formulations were functionally evaluated for their antioxidant potential in vivo in carbon tetrachloride (CCl₄)-intoxicated albino rat model.

Materials and methods

Mangiferin (HPLC purity >99%) was obtained from Sisco Research Laboratories Pvt. Ltd. Mumbai, India. Phospholipon® 90H was obtained from Lipoid GmbH, Ludwigshafen, Germany. Carbon tetrachloride, chloroform, ethylenediaminetetraacetic acid (EDTA), 5,5'-dithiobis-2-nitro benzoic acid (DTNB), sodium chloride, sodium lauryl sulfate, and Tween® 20 were obtained from Loba Chemicals Pvt. Ltd., Mumbai, India. n-Hexane, 1-octanol, metaphosphoric acid, thiobarbituric acid, and trichloroacetic acid were obtained from Sigma Chemicals, Sigma-Aldrich Corporation, St. Louis, MO. All other chemicals were of analytical grade unless otherwise mentioned.

Formulation of mangiferin-phospholipid complex (MPLC)

A well-established solvent evaporation method described previously by Zhang et al. [47] was used for the preparation of MPLC. Briefly, MGN (MW, 422.33 g/mol) and Phospholipon® 90H (MW, 790 g/mol) were individually weighed in molar ratios 1:0.51, 1:1.02, 1:1.76, 1:2.5, or 1:3 and then transferred to a clean 100-mL round-bottom flask. The contents of the flask were dissolved in absolute EtOH (20 mL) and stirred well. The solution was heated under controlled conditions 40.14/44.2/50.15/56.1/60.15 °C on water bath (DSY-2-2, Aiqixia Apparatus Center, China) for 1.01/1.42/2.01/2.6 or 3.0 h, respectively. The solvent was evaporated and the residue was mixed with n-hexane (10 mL), leading to precipitation of MPLC. Further subsequent filtration and drying under vacuum at 40 °C for 12 h yielded the product, which was stored at room temperature (RT) in an amber-colored glass vial, previously flushed with nitrogen (N₂), until further use.

The rationale for selecting independent, dependent variables and their ranges

The independent, dependent variables and their ranges were selected based on preliminary experiments, supporting literature, and central composite design. A phytosome (drug-phospholipid complex) is a molecular aggregate of the drug-phospholipid complex. Therefore, MPLC was prepared using the same procedure as mentioned above [35] and explored for the selection of independent, dependent variables and their ranges. After the selection of variables and their range, the MPLC was optimized at five levels using the above-mentioned design.

Central composite design (CCD)

The MPLC formulation was optimized using CCD (Design-Expert®, Version 10.0.4.0, Stat-Ease Inc., Minneapolis, MN, USA) to obtain precise information on the formulation/process variables with a reasonably lower number of experimental trials. In the present study, we have chosen three independent variables, namely, MGN/phospholipids ratio (X_1 , w:w), reaction temperature (X_2 , °C), and reaction time (X_3 , h), respectively. The chosen variables were investigated at five levels and were coded as -1.73, -1, 0, +1, and +1.73. The extent of the complexation rate or yield (%) was chosen as a dependent (response) variable. The detailed analysis led to 20 possible runs. These formulations were prepared and assessed one by one for the dependent variable, i.e., yield (%). Upon fitting the data, a statistical model, i.e., a polynomial equation along with a desirability plot, was obtained. The

model (Eq. 1) listed the coefficients of the variables and the quadratic and interaction terms having a significant influence on the dependent variable:

$$Y = b_0 + b_1X_1 + b_2X_2 + b_3X_3 + b_{11}X_1^2 + b_{22}X_2^2 + b_{33}X_3^2 + b_{12}X_1X_2 + b_{23}X_2X_3 + b_{13}X_1X_3 \quad (1)$$

where Y is the dependent variable, b_0 , the intercept of the arithmetic average of 20 experimental trials, and b_1 to b_{13} represents the calculated coefficients of (X_i , $i = X_1, X_2$, and X_3). X_1 , X_2 , and X_3 are the main effects. The interaction terms X_1X_2 , X_2X_3 , and X_1X_3 are the combined effects of the independent variables, while polynomial terms X_1^2 , X_2^2 , and X_3^2 signify the nonlinear dependency of the response variable on the inputs. Table 1 lists the details of the experimental trials along with the coded and real values of both, the independent and dependent variables. The CCD and the experimental trials with calculated values of yield (%) are given in Table 2.

Estimation of the extent of MGN complexation in prepared MPLC (% yield)

The extent of MGN complexation in MPLC formulations was determined using UV-visible spectroscopy [52]. Briefly, MPLC (equivalent to ~50 mg of MGN) was transferred to a beaker, followed by mixing with chloroform (5 mL). In the resulting dispersion, the MPLC and Phospholipon® 90H were dissolved completely while MGN precipitated out. The insoluble MGN was allowed to settle and the dispersion is filtered using Whatman® quantitative filter paper (ashless, Grade 41, Sigma-Aldrich Corporation, St. Louis, MO), dried, dissolved in methanol, suitably diluted, and assayed at the detection wavelength (~259 nm) using a UV-visible spectrophotometer (Model: V-630, JASCO International Co., Ltd., Tokyo, Japan). The extent of the complexation of MGN with phospholipids was calculated by Eq. 2:

$$\text{Extent of complexation (\%)} = (c_t - c_f) / c_t \times 100 \quad (2)$$

where c_t is the theoretical concentration of MGN in MPLC

Table 2 Central composite design experimental trial formulation batches with obtained yield values (% w/w)

Experimental trials	X_1	X_2	X_3	Extent of complexation, or yield* (% w/w)
1	-1	+1	-1	59.20 ± 0.11
2	+1	-1	-1	84.02 ± 0.09
3	-1	-1	+1	78.30 ± 0.43
4	+1	+1	-1	82.10 ± 0.26
5	0	0	0	91.30 ± 0.56
6	+1.73	0	0	87.24 ± 0.51
7	0	0	0	90.16 ± 0.63
8	+1	+1	+1	86.26 ± 0.17
9	0	0	0	88.12 ± 0.24
10	0	0	+1.73	97.71 ± 0.33
11	-1	-1	-1	72.38 ± 0.40
12	0	0	0	90.18 ± 0.20
13	0	0	-1.73	93.41 ± 0.29
14	0	+1.73	0	89.29 ± 0.14
15	-1.73	0	0	70.23 ± 0.50
16	-1	+1	+1	67.17 ± 0.49
17	0	0	0	89.51 ± 0.58
18	0	-1.73	0	68.89 ± 0.41
19	+1	-1	+1	93.41 ± 0.09
20	0	0	0	90.28 ± 0.25

*Values are represented as mean ± SD ($n = 3$)

and c_f is the observed concentration of MGN in the filtrate.

Preparation of MPLC-loaded soft nanoparticles (MPLC SNPs)

The MPLC SNPs were prepared by the nanoprecipitation method reported previously [45]. Briefly, MGN (10 mg) or MPLC (equiv. to 10 mg of MGN) was accurately weighed and mixed with dichloromethane (10 mL) using a magnetic stirrer until a clear solution was obtained. It was then introduced dropwise (0.2 mL/min) into a magnetically stirred distilled water (40 mL). The dispersed

Table 1 Coded levels and real values for each independent variable studied

Variables	Levels				
	-1.73	-1	0	+1	+1.73
<i>Independent</i>					
MGN:Phospholipon® 90H ratio (X_1 , w:w)	1: 0.51	1:1.02	1:1.76	1:2.50	1:3.00
Reaction temperature (X_2 , °C)	40.14	44.2	50.15	56.1	60.15
Reaction time (X_3 , h)	1.01	1.42	2.01	2.6	3.00
<i>Dependent</i>					
Extent of complexation or yield (Y, % w/w)					

phase was then gradually evaporated while stirring, resulting in the formation of MGN SNPs or MPLC SNPs suspension with light green opalescence. The resultant suspension was then freeze-dried using a lyophilizer (Model: MSW-137, Macro Scientific Works Pvt. Ltd., New Delhi, India) under the conditions of controlled condenser temperature of $-80\text{ }^{\circ}\text{C}$ and vacuum of 10 Pa. Finally, the lyophilized MPLC SNPs were stored in amber-colored (light-protected) glass vials, flushed with N_2 , and kept at $4\text{ }^{\circ}\text{C}$ until further use. The MGN SNPs (free of MPLC) were also prepared using the same procedure, stored, and evaluated.

Estimation of encapsulation efficiency and drug loading

A method previously described by Sahni et al. [53] and Alam et al. [54] was used for the estimation of drug loading and encapsulation efficiency of MGN within MPLC SNPs formulations, before and after lyophilization. Briefly, the prepared MPLC SNP suspension was transferred into a clean Eppendorf® Safe-Lock microcentrifuge tube (1.5 mL) and ultracentrifuged at 15,000 rpm at $4\text{ }^{\circ}\text{C}$ for 40 min. The supernatant was collected, diluted suitably, and analyzed for the absorbance of the final solution at (λ_{max} , $\sim 259\text{ nm}$) using a UV-visible spectrophotometer. The encapsulation efficiency and drug loading were calculated using the equations described below:

Encapsulation efficiency (%)

$$= \frac{\text{Total amount of MGN} - \text{Free MGN}}{\text{Total amount of MGN}} \times 100 \quad (3)$$

Drug loading (%)

$$= \frac{\text{Total amount of MGN} - \text{Free MGN}}{\text{Weight of nanoparticles}} \times 100 \quad (4)$$

Physicochemical characterization of MPLC and MPLC SNPs

Scanning electron microscopy (SEM)

The comparative surface morphology of pure MGN, MPLC, and MPLC SNPs formulations was studied using a scanning electron microscope (Model: Supra®55, Carl Zeiss NTS Ltd., Germany). Briefly, the sample for SEM (scanning electron microscopy) analysis was prepared by weighing an individual sample ($\sim 50\text{ mg}$) and spread uniformly over the double-sided carbon tape attached to the sample holder. Loaded samples were sputter-coated using a thin layer of gold ($\sim 400^{\circ}$) and then examined under the microscope at an accelerating

voltage of 10 kV. The captured images at different magnifications were read by the attached software (Smart®SEM V05.06).

Particle size and zeta potential

The particle size and size distribution of MGN in MPLC and MPLC SNPs were analyzed using Photon Cross-Correlation Spectroscopy (PCCS) equipped with dynamic light scattering (DLC) technique reported earlier by us [55]. Briefly, MPLC or MPLC SNPs ($\sim 5\text{ mg}$) were accurately weighed and dispersed in deionized water (10 mL). The aqueous dispersion was then placed in the sample chamber of particle size analyzer (Model: NANOPHOX Sympatec, GmbH, Clausthal-Zellerfeld, Germany). The particle size analysis (range: 1 nm to 10 μm) was carried out by adjusting the sample vial position for optimizing the count rate as determined by the software. The resultant aqueous dispersion of MPLC or MPLC SNPs was used similarly for measuring the zeta potential using a Nano Particle Analyzer (Model: NanoPlus™-2, Particulate system, Norcross, GA, USA) loaded with dynamic light scattering (DLS) setup. A complete analysis was carried out at RT with a sensitivity range of -200 to $+200\text{ mV}$.

Thermal analysis

The thermal behavior of the formulation components such as pure MGN, Phospholipon® 90H, the physical mixture (PM) of MGN and Phospholipon® 90H, and MPLC was comparatively analyzed by differential scanning calorimeter (DSC) and thermogravimetric analysis (TGA) (Model: DSC-1821e, Mettler-Toledo AG, Analytical, Schwerzenbach, Switzerland) as per the protocol reported by us earlier [56]. Briefly, the DSC was calibrated using high-purity standard indium (In) concerning heat flow and heat capacity. The sample analyzing area was continuously purged with dried N_2 at a flow rate of 50 mL/min. The samples ($2.0 \pm 0.2\text{ mg}$ each) were accurately weighed and subjected to heating in the range of 40 to 400 $^{\circ}\text{C}$ at a rate of 10 $^{\circ}\text{C}/\text{min}$. The generated data were analyzed and interpreted by the instrument software (Universal Analysis 2000, V4.5A, Build 4.5.0.5).

Fourier-transform infrared spectroscopy (FT-IR)

Pure MGN, Phospholipon® 90H, PM of MGN and Phospholipon® 90H, and MPLC were analyzed by the FT-IR spectrophotometer (Model: FTIR-8300, Shimadzu, Kyoto, Japan) according to the previously reported protocols [57]. Briefly, a homogenous mixture of previously air-dried samples ($\sim 2\text{ mg}$) with FT-IR grade potassium bromide (KBr, $\sim 200\text{ mg}$) in an agate mortar and pestle was prepared, followed by compression into a thin transparent disc using Mini Hand Press Machine (Model: MHP-1, P/N-200-66,747-91,

Shimadzu, Kyoto, Japan) at a pressure of 10 ton/Nm². The prepared sample discs were scanned at a wavenumber range of 4000 to 400 cm⁻¹. The scanning resolution was fixed at 4 cm⁻¹. After scanning, the obtained individual sample spectra were interpreted using the peaks assigned by the FT-IR software (IR solution, version 1.10).

Powder X-ray diffraction (PXRD)

The comparative crystalline nature of the four samples pure MGN, Phospholipon® 90H, PM, and the MPLC was analyzed using a powder X-ray diffractometer (Model: D8 ADVANCE, Bruker AXS, Inc., Madison, WI, USA). The PXRD spectra of the samples were recorded on a 2θ scale according to a previously reported procedure [30].

Proton nuclear magnetic resonance spectroscopy (1H-NMR)

The ¹H-NMR spectra of formulation components, i.e., pure MGN, Phospholipon® 90H, and optimized MPLC formulations, were analyzed to study their carbon-hydrogen framework using a 400-MHz FT-NMR spectrophotometer (Model: Bruker Advance II, Bruker, Rheinstetten, Germany). The analysis was carried out at room temperature.

Solubility studies

The solubility of pure MGN, MGN SNPs, PM of MGN, and Phospholipon® 90H, MPLC, and MPLC SNPs was determined using a method previously described by Singh et al. [50]. Briefly, the samples were added in an excess amount to a sealed glass vial containing either purified water (5 mL) or 1-octanol (5 mL) which was further agitated using a shaker (Model: RSB-12, Remi House, Mumbai, India) for 24 h. The resulting dispersion was then centrifuged at 1500 rpm for 25 min. The supernatant was filtered using a 0.45- μ membrane filter to get a clear solution. The aliquot was suitably diluted using purified water or methanol and the absorbance of the solution was recorded to quantitate MGN (λ_{\max} ~259 nm) on a UV-visible spectrophotometer. The solubility analysis was conducted at RT.

Functional characterization of MPLC and MPLC SNPs

In vitro dissolution studies

The comparative in vitro dissolution profile of MGN suspension, MGN SNPs, MPLC, or MPLC SNPs was analyzed using a previously reported method [58]. Briefly, the dialysis membrane (LA395, dialysis membrane-110, HiMedia Laboratories, Mumbai, India) with an average diameter of ~21.55 mm, average flat width ~32.34 mm, and capacity ~3.63 mL was used for the dissolution study. The molecular

size cutoff was 12,000–14,000 Da. The membrane was washed and rinsed according to the manufacturer's guidelines. Furthermore, the dialysis bags were prepared and the formulation samples such as MGN suspension (containing ~2 mg of MGN), MGN SNPs (~2 mg of MGN), MPLC (~2 mg of MGN), or MPLC SNPs (~2 mg of MGN) were placed into the dialysis bags and tied up with the thread. The bags were then suspended vertically into a beaker filled with dissolution medium, i.e., phosphate-buffered saline (PBS, 200 mL, pH 7.4) with Tween® 20 (1%, v/v). The contents of the beaker were continuously stirred (50 rpm, 37.0 ± 2.0 °C, 12 h) using a magnetic stirrer. Samples (5 mL) were withdrawn at regular intervals while maintaining the sink conditions. The samples were suitably diluted and the absorbance recorded (λ_{\max} ~ 259 nm) using UV-visible spectrophotometer. The cumulative amount of MGN released from the respective formulations was determined from the measured absorbance.

Ex vivo permeability studies

The comparative permeation efficiency of MGN from MGN SNPs and MPLC SNPs across a biological membrane was evaluated using an *everted rat intestine*, as described previously [55, 56, 59]. The study was performed using the intestine isolated carefully from albino rats of either sex with (150–200 g). On the day of the experiment, the overnight fasted animals were euthanized using a cervical dislocation method. The abdomen was incised carefully and the ileocecal part of the intestine was removed. The jejunal section of the intestine around ~7-cm long was carefully separated without any damage. The tissue was continuously washed with the freshly prepared Krebs solution. The intestine was then everted using a well-established, glass-rod procedure, described previously by Hamilton and Butt [60]. The everted intestine was kept in the freshly prepared Krebs solution until the permeation experiment.

The tissue was carefully mounted between the two tapered ends of the apparatus. Subsequently, the apparatus was filled with the freshly prepared Krebs solution and inserted carefully in a vertical position in a 250-mL beaker. The beaker was filled with the sample solution, MGN SNPs (100 μ g/mL), or MPLC SNPs formulations (100 μ g/mL) prepared in the Krebs solution. The whole assembly was placed on a magnetic stirrer and the contents of the beaker are stirred continuously at 25 rpm (37 ± 0.5 °C) for a period of 12 h. The Krebs solution in the apparatus as well as in the beaker was under constant aeration. At pre-determined intervals, samples were withdrawn and diluted appropriately, and the absorbance at (λ_{\max} ~ 259 nm) is recorded using a UV-visible spectrophotometer. The apparent permeability was calculated by Eq. 5:

$$\text{Apparent permeability} = [V/(A \times T)] \times c_1/c_0 \quad (5)$$

where V represents the volume of serosal content (mL); A , the surface area of the intestinal sac (cm²); T , time of incubation (sec); c_0 , the initial concentration of on the mucosal side; and c_1 , the concentration on the serosal side after time T .

In vivo antioxidant studies

The antioxidant potential of MGN SNPs and MPLC SNPs was evaluated in albino rats (male or female) using the CCl₄-induced oxidative stress model reported previously [58, 61].

Animals

Male and female albino rats (Wistar strain, bred in-house) weighing 150–200 g were used. The animals were kept under controlled conditions of temperature (25 ± 5 °C) and relative humidity (50 ± 5 %RH) with a 12-h light/dark cycle. They were nourished with pellet chaw (Brooke Bond, Lipton, India) and water ad libitum. The Institutional Animal Ethical Committee (IAEC) of Smt. Kishoritai Bhoyar College of Pharmacy, New Kamptee, Nagpur, sanctioned and approved the experimental protocols (*SKBCOP/IAEC/2017–2018, dated August 13, 2018*) for the current study. The studies were carried out according to the ethical guidelines available by the Committee for Purpose of Control and Supervision of Experiments on Animals (CPCSEA).

Dosing

The animals were divided randomly into four groups of six animals each. Group I animals received only Tween® 20 (1% v/v, p.o.) for 7 days and served as blank negative control. Group II animals also received Tween® 20 (1% v/v, p.o.) for 7 days. On the seventh day, group II animals received a single dose of a mixture of CCl₄ and olive oil (1:1, 5 mL/kg, i.p.) and served as a positive control. Group III animals received pure MGN SNP suspension at a dose of ~60 mg/kg of MGN, p.o., in distilled water with Tween® 20 (1%, v/v, p.o.) for 7 days. Group IV received MPLC SNPs at a dose of ~60 mg/kg of MGN, p.o., in distilled water with Tween® 20 (1%, v/v) for 7 days. After administration of the respective formulations to the animals, on the seventh day, the same groups also received a single dose of a mixture of CCl₄ and olive oil (1:1, 5 mL/kg, i.p.).

On the eighth day, the animals with CCl₄ intoxication were anesthetized using light ether anesthesia. The blood samples were collected from the retro-orbital plexus into tubes containing heparin and then centrifuged using a microcentrifuge (Model:

RM-12C, Angle Rotor Head, Remi House, Goregaon (E), Mumbai, India) to obtain clear plasma samples. These were then used for the estimation of liver marker enzyme (liver function tests). Afterward, all the animals were euthanized by cervical decapitation and their livers were removed immediately and washed in ice-cold saline solution. The isolated livers were homogenized in 0.1 M PBS (pH 7.4) and then centrifuged to get a clear supernatant, which was further used for the estimation of antioxidant marker enzymes.

Liver marker enzyme estimation (liver function test)

The liver function marker enzymes such as serum glutamic oxaloacetic transaminase (SGOT), serum glutamic pyruvic transaminase (SGPT), alkaline phosphate (ALP), and total bilirubin were measured quantitatively to compare the influence of pure MGN SNPs and MPLC SNPs on liver function of the rats. The SGOT and SGPT in rat plasma were evaluated by the previously outlined method [62]. Briefly, SGOT substrate (0.5 mL) [α -L-alanine (200 mM) and SGPT substrate (0.5 mL) [L-aspartate (200 mM) with 2 mM α -ketoglutarate] were added in a clean test tube and incubated for 5 min at 37 °C. After incubation, the investigational rat plasma samples (100 μ L) were added into the respective test tubes and the final volume was adjusted to 1 mL using phosphate buffer (pH 7.4, 0.1 M). The prepared mixture was then incubated further for 60 min (SGOT) or 30 min (SGPT) followed by the addition of 2,4-dinitrophenyl hydrazine as an indicator and incubated again for an additional 30 min. Following this, the freshly prepared sodium hydroxide solution (5 mL, 0.4 N) was added and the absorbance is measured at 505 nm.

The Grifols-Lucas method previously reported by Kind and King [63] was used to determine the ALP levels in the rat plasma. Briefly, the reaction mixture was prepared by the addition of phenyl phosphate buffer (1 mL, 0.5 N) to bicarbonate buffer (1 mL, pH 10) and then incubated at 37 °C for 3 min. To this solution, a rat plasma sample (100 μ L) was added and incubated further for 30 min. Subsequently, the freshly prepared sodium hydroxide (0.8 mL, 0.5 N), NaHCO₃ (1.2 mL, 0.5 N), and amino-antipyrine (1 mL, 0.6%) solutions were introduced in the above reaction mixture and mixed well. The absorbance of the final solution was recorded at 520 nm.

Total bilirubin was determined from rat plasma using a previously reported method [64]. Briefly, in a test tube containing rat plasma (250 μ L), the sulfanilic acid solution (5 mL, 4 mmol/L) and NaNO₂ (0.1 mL, 144 mmol/L) were added and the contents incubated at 37 °C for 10 min. After incubation, the absorbance was recorded at 670 nm.

In vivo antioxidant marker enzyme estimation

The antioxidant status of pure MGN SNPs and MPLC SNPs was assessed by measuring its influence on in vivo antioxidant

marker enzymes, viz., glutathione peroxidase (GSH), superoxide dismutase (SOD), catalase (CAT), and lipid peroxidase (LPO) present in the prepared rat liver homogenate. The antioxidant marker GSH was quantitatively determined using a well-known method [65]. Briefly, the reaction mixture was prepared by the addition of liver homogenate supernatant (200 μ L), distilled water (1.8 mL), and precipitating mixture (0.3 mL) to a clean test tube, mixed well and centrifuged by using a microcentrifuge at 5000 rpm for 5 min to get clear supernatant, 1 mL of which was mixed with phosphate buffer (1.5 mL, 0.1 M) and 5,5'-dithiobis-(2-nitrobenzoic acid) (DTNB, Ellman's reagent, 0.5 mL). The resulting solution was analyzed for absorbance at 412 nm. The obtained value was expressed as μ g/mg of protein.

In the rat liver homogenate, the SOD level was estimated as described previously [66]. Briefly, in a test tube containing liver supernatant (20 μ L), Tris-HCl buffer (2 mL, 75 mM, pH 8.2) and freshly prepared pyrogallol solution (0.5 mL, 30 mM) were mixed. The resultant solution was recorded for an increase in absorbance for 3 min. at an interval of 30 s. at 420 nm. The rate of auto-oxidation of the pyrogallol solution with 50% inhibition by SOD was considered as one unit enzyme activity. The value was expressed as units/mg of protein.

A method earlier described by Stocks and Dormandy [67] was employed for the estimation of LPO in the prepared liver homogenate. Briefly, to rat liver supernatant (500 μ L), the freshly prepared sodium lauryl sulfate (0.2 mL, 0.8% w/v), trichloroacetic acid (1 mL, 20% w/v), and thiobarbituric acid (1.5 mL, 0.85 w/v) were added, mixed, and then heated at 100 $^{\circ}$ C for a period of 1 h. The solution was cooled to RT and diluted with distilled water (1 mL). The mixture was centrifuged to separate the organic layer from the aqueous one. The organic layer was carefully collected in a cuvette and its absorbance is measured at 532 nm. The molar extinction coefficient of malondialdehyde (MDA) ($1.56 \times 10^5 \text{ M}^{-1} \text{ cm}^{-1}$) was used for the calculation of lipid peroxidation. The LPO enzyme activity was expressed as MDA (nM/g) in hemoglobin.

Similarly, the CAT enzyme level in the liver supernatant was determined using the method described by Beers and Sizer [68]. Briefly, the prepared liver supernatant (100 μ L) was mixed with phosphate buffer (1.9 mL, 50 mM, pH 7.4) and the freshly prepared H_2O_2 solution (1 mL, 30 mM). This mixture was then analyzed at 240 nm. The enzyme activity was correlated with the extent of H_2O_2 decomposition.

Histopathological studies

At the end of dosing of formulations and CCl_4 intoxication, all the animals were euthanized by cervical decapitation method. Subsequently, their livers were removed immediately, washed in ice-cold saline, and preserved in a neutral buffered formalin (10% v/v) solution till further processing. The livers were sectioned and stained using a hematoxylin-eosin reagent.

The stained sections were observed under an optical microscope (Model: DM2500, Leica Microsystems Inc., Buffalo Grove, IL). The observed and suitable images were captured using an attached digital camera at a magnification of $\times 400$.

Oral bioavailability studies

Bioanalytical method development

Method development was started by preparing the stock solution of standard MGN. Briefly, an approximate amount of MGN (~ 10 mg) was dissolved in sufficient amount of methanol and the solution with a concentration of 1000 μ g/mL is prepared. The prepared solution was stored at 4 $^{\circ}$ C until analysis. From this, different concentrations of solutions were prepared and spiked with blank plasma to get the final solution in the range of 0.05–10 μ g/mL, respectively. These solutions were used for the preparation of quality control (QC) samples at a concentration of low (0.05 μ g/mL), medium (0.5 μ g/mL), and higher (10 μ g/mL), respectively. In these solutions, the freshly prepared nitrophenol as internal standard (IN, 4 μ g/mL) and a 3 mL of acetonitrile were added and mixed well. The developed reaction mixture solution was vortexed and then centrifuged at a condition of $800 \times g$ for 10 min to get clear supernatant. The obtained supernatant was collected, evaporated, and reconstituted using 100- μ L mobile phase. This solution was injected into HPLC (Thermo Scientific™ Ultimate™ 3000, Thermo Scientific, San Jose, CA, USA), the peak areas of standard plasma spiked with various concentration of MGN are determined, and then the ratio of peak areas of IN and MGN against the concentration of MGN is plotted. Following this, the calibration curve was prepared and linearity was calculated.

A chromatographic method described earlier by Chen et al. [69] was also followed for the quantification of MGN in the collected plasma samples. Briefly, the MGN estimation in plasma was carried out using the same HPLC system as mentioned in the above method development section. This system is equipped with a photodiode array detector (Thermo Scientific, San Jose, CA, USA). The stationary phase consisted of the Hypersil GOLD™ C18 selectivity LC column (100 \times 4.6 mm) with a particle size of 5 μ m. Acetonitrile and acetic acid (3%) in MilliQ water were used as the mobile phase for gradient elution. During the entire analysis, the flow rate of the optimized mobile phase as well as the column temperature was maintained at 1.0 mL/min and 30 $^{\circ}$ C, respectively. The detection was performed at 259 nm. Nitrophenol was used as an IN due to its structural similarity to MGN. The optimized mobile phase was used for the effective resolution of MGN peaks in the HPLC chromatograms. The peaks were analyzed and interpreted using a software associated with the HPLC system.

Extraction of MGN from plasma and sample preparation

The extraction of MGN from rat plasma was carried out by the liquid-liquid extraction (LLE) method described previously [61]. The LLE exhibits high recovery and reproducibility from the biological matrix. Briefly, male and female albino rats were divided into two groups containing six animals each (overnight fasting with free access to water). Group I animals received pure MGN SNP suspension at a single dose of ~60 mg/kg of MGN, p.o., and group II received MPLC SNPs (~60 mg/kg, p.o. of MGN). Afterward, the animals were anesthetized at designated time intervals, and then blood samples were collected from their retro-orbital plexus. Collected blood samples were transferred into clean heparinized Eppendorf® Safe-Lock microcentrifuge tubes (1.5 mL). The tubes containing samples were centrifuged at 800 *g* for 10 min. to separate the plasma, which was stored at -20 °C till further analysis.

The MGN from plasma samples was extracted by spiking plasma samples (500 µL) of respective formulations with 20 µL of IN and of acetonitrile (3 mL). The mixture was vortexed for 1 min and centrifuged at 800 *g* for 10 min. The supernatant was carefully collected and transferred to another clean tube. The solvent was allowed to evaporate in a vacuum desiccator and then the residue reconstituted (mobile phase, 100 µL). A 20-µL sample was injected for the quantitation of MGN.

Validation of the extraction and quantification method

The guidelines as suggested by the International Conference on Harmonization (ICH) were used for carrying out validation of the developed HPLC method. The validation parameters, i.e., intra-day accuracy and precision, were determined for prepared QC samples on the same day ($n = 6$), while, inter-day accuracy and precision were determined for the same QC samples on three following days. Moreover, the extraction recoveries of MGN from extracted tissue samples and standard solutions at the same concentration were tested and compared. The short-term (for 24 h) and long-term (for 14 days) stability studies were also performed on QC samples.

Study of pharmacokinetic parameters

The pharmacokinetic parameters such as C_{max} and T_{max} were determined from the plasma concentration time profile. Other parameters such as half-life ($t_{1/2}$), area under the plasma concentration time curve (AUC) from zero to time of final measured sample (AUC_{0-t}) and from zero to infinity ($AUC_{0-\infty}$), clearance (Cl/F), the volume of distribution, and relative bioavailability (F) were estimated using WinNonlin® statistical software (Version 4.1, Certara USA Inc., Princeton, NJ, USA).

Stability studies

According to the ICH guidelines, the long-term stability studies were carried out on lyophilized MPLC SNPs formulations. Briefly, the lyophilized formulation was sealed in clear glass vials and stored at RT (25 °C) and 4 °C, respectively, for the period of 6 months. At designated intervals (i.e., 0, 3, and 6 months), the samples were removed and analyzed for particle size, PDI, zeta potential, and entrapment efficiency of MPLC SNP formulations.

Statistical analysis of data

The results of solubility and in vitro dissolution and stability studies were reported as mean ± standard deviation (SD). Similarly, the results of liver function tests, the in vivo antioxidant activity, and pharmacokinetic studies were represented as mean ± standard error of the mean (SEM). One-way analysis of variance (ANOVA) followed by Dunnett's test was used for estimating the statistical differences between treatment groups. An obtained P value < 0.05 was considered to be statistically significant.

Results and discussion

Formulation of MPLC and MPLC SNPs

MGN is a well-known xanthonoid exhibiting fair solubility in most organic solvents and poor solubility in water [18, 21]. The present study aimed at improving the aqueous solubility of MGN by incorporating it in the form of MPLC. We and others have previously shown that the flavonoid-phospholipid complexes could be successfully prepared by using 1,4-dioxane [30], CH_2Cl_2 [19], and tetrahydrofuran (THF) [70] (solvent evaporation method). Based on these studies, we have also used these solvents for the preparation of phospholipid complex. However, while preparation, we found that both MGN and phospholipids exhibited poor solubility in the abovementioned solvents, which further results in precipitation of both the formulation components. To overcome these inherent solubility issues, we tested other organic solvents for the solubilization of MGN and phospholipids. Out of all the solvents tried, absolute ethanol showed better suitability. Given the semi-polar nature of this class III solvent with a low-toxicity profile, we chose to formulate MGN with phospholipids using ethanol as a solvent with the hope that it would result in the stable MPLC formulation.

On the other hand, MPLC SNPs were prepared using dichloromethane as a solvent by the nanoprecipitation technique in four steps: (i) formation of o/w dispersion (of organic phase in continuous aqueous phase); (ii) dramatic reduction in the interfacial tension between the two phases, leading to the

lowered droplet size of MPLC; (iii) formation of soft nanoparticles due to evaporation of the organic solvent; and (iv) precipitation of nanodroplets from the aqueous environment with the formation of self-assembled MPLC SNPs.

The rationale for selecting independent, dependent variables and their ranges

Based on the preliminary experiments, the independent, dependent variables and their ranges were selected and used in the formulation of MPLC. It was prepared using a solvent evaporation method, and based on this, three independent variables were selected, i.e., MGN/Phospholipon® 90H ratio, reaction temperature, and reaction time. The ratio acts as the basic composition of MPLC. Reaction temperature helps in the establishment of a complex between MGN and Phospholipon® 90H, while reaction time provides the maximum contact between MGN and Phospholipon® 90H, resulting in the formation of stable MPLC. The extent of complexation was selected as the dependent variable. After the selection of these variables, their experimental ranges were selected. According to Semalty et al., the drug/Phospholipon® 90H ratio (1:1), reaction temperature (40 °C), and reaction time (1 h) are the suitable range for the successful preparation of phospholipid complex [71]. So, we utilized the same range for the preparation, resulting in the formation of MPLC with limited solubility and a low extent of complexation. To improve these parameters, we increased the MGN/Phospholipon® 90H ratio from 1:1 to 1:2, the reaction temperature from 40 to 50 °C, and the reaction time from 1 to 2 h, respectively, which resulted in the formation of various MPLCs with significant enhancement in its solubility and extent of complexation. However, to explore further the range of independent variables at various levels, we selected CCD as one of the best optimization tools, because it provides the chance to explore the largest possible processing space at five levels, i.e., extremely lower level (−1.73), low (−1), middle (0), higher (+1), and extremely higher level (+1.73), respectively. The obtained experimental trials by using these levels showed a significant impact on the response variables. Hence, we have chosen three independent variables and studied their range at five levels using CCD.

CCD

Table 2 lists the results of the extent of complexation or yield (% w/w) for the respective experimental trial formulations of MPLC obtained using a combination of studied independent variables. As seen from Table 2, the yield (%) was in the range of 59.2 to 97.71%, indicating the significant impact of independent variables of MGN/Phospholipon® 90H ratio (X_1), reaction temperature (X_2), and reaction time (X_3) on the response variable. At the end of the formulation trials, the following polynomial equation (Eq. 6) was obtained. It was

further used for formulation optimization. Moreover, the generated positive and negative (+ or −) signs associated with the coefficient of magnitude were also used to study the influence of independent variables on the yield as well as for the optimization of the same variables:

$$Y = 90.13 + 7.13X_1 + 0.0680X_2 + 2.54X_3 - 5.28X_1^2 - 5.15X_2^2 - 0.668X_3^2 + 1.90X_1X_2 - 0.3975X_2X_3 - 0.0425X_1X_3 \quad (6)$$

The output of the CCD trials, i.e., fit summary, ANOVA data, polynomial equation, counter, and 3D response graphs, was critically analyzed wherein the quadratic model was found to be the best-fit model. It correlated well with the polynomial equation. The coefficients b_1 , b_{11} , and b_{12} were statistically significant ($p < 0.05$). Other coefficients b_0 , b_2 , b_3 , b_{13} , b_{22} , b_{23} , and b_{33} were statistically non-significant. The model *F-value* (3.21) indicates the suitability of the quadratic model for experimental trial formulations. Additionally, the adequate precision value was greater than > 4 (i.e., 8.133) and the correlation coefficient value (R^2) between adjusted and predicted appeared less than < 0.2 , which suggests that the quadratic model is the best-fit model, and therefore, this model can be used to navigate the design space. The model summary statistics showed that the PRESS value for response yield was ~ 4087.42 , which also indicates the suitability of quadratic model as the best-fit model. The developed positive sign (+) in the coefficient of the magnitude of X_1 , X_2 , and X_3 showed that as the concentration of X_1 , X_2 , and X_3 increases, the yield also increases simultaneously, indicating a direct correlation between the independent and dependent variables. The overall influence of independent variables (X_1 , X_2 , and X_3) on yield is shown as counter and 3D response plot Fig. 1a and b. As seen in this figure, at constant reaction time, the yield was found to increase, as the X_1 and X_2 increase to the middle level and then decreased. Moreover, at the fixed reaction temperature, the yield increased, increasing the X_1 and X_3 to the middle level and then decreased. Also, at fixed MGN/Phospholipon® 90H ratio, the yield also increased, as the X_2 and X_3 increase to the middle level and then decreased, respectively. Therefore, it can be concluded that the middle values of X_1 , X_2 , and X_3 may be found as an optimal value for achieving higher yield.

The optimization of the suitable experimental trial with higher yield was achieved by following numerical and graphical optimization techniques. In both techniques, the constraints were applied to independent and dependent variables to get the desired and optimized formulation. The constraints for independent variables

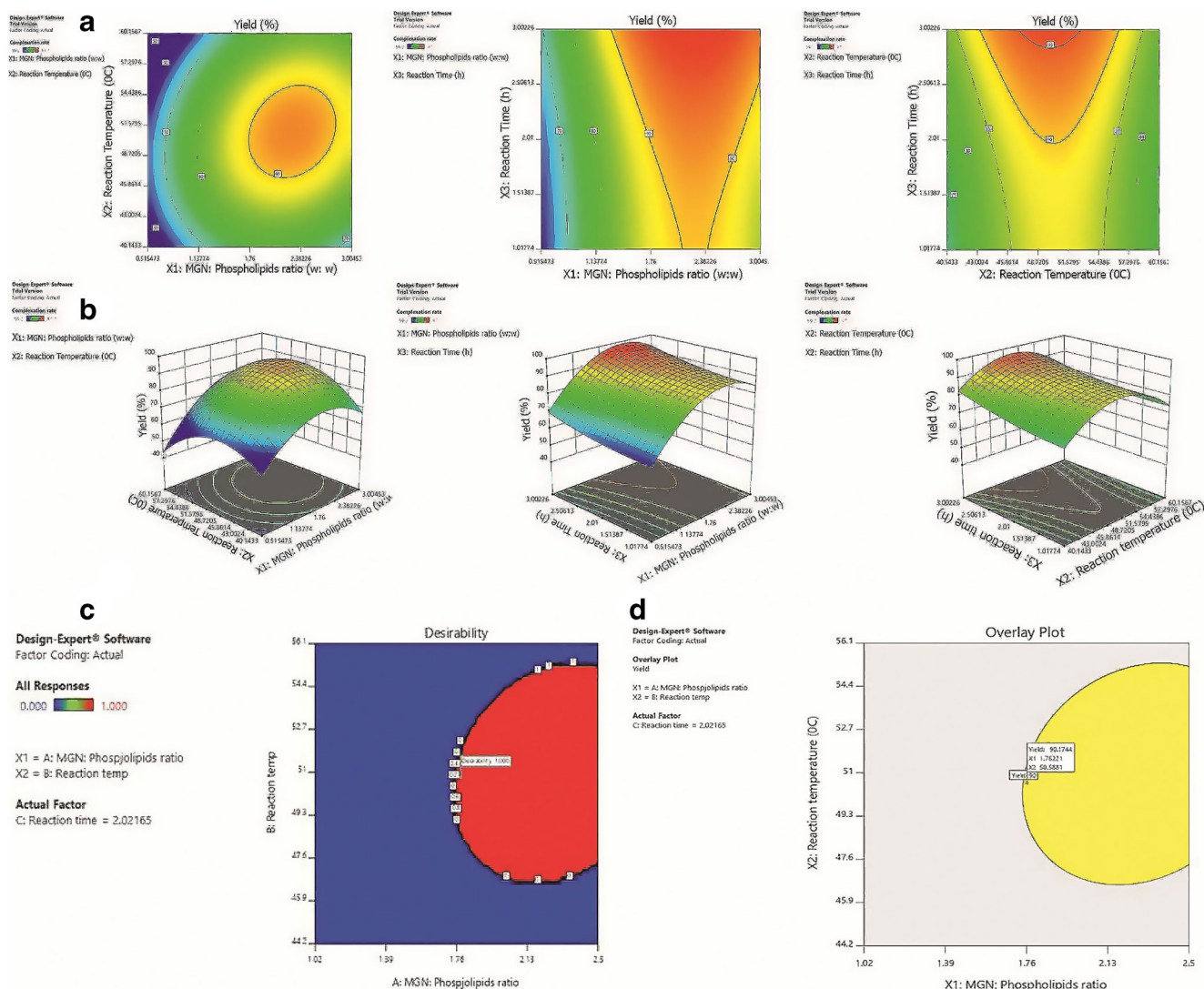


Fig. 1 **a** Contour plot, **b** 3D response surface plot, **c** desirability plots, and **d** design space of extent of complexation or yield (Y, %) as a function of MGN and Phospholipon® 90H ratio (X_1 , w: w), reaction temperature (X_2 , °C), and reaction time (X_3 , h)

of X_1 , X_2 , and X_3 were in the range of 1:1.02 to 1:2.5 (w: w), 44.2–56.1 °C, and 1.42–2.6 h, whereas the constraints for yield were in the range of 90.0–96.10 (%), respectively. Following the analysis, the design provided one possible solution of the experimental trial, which showed recommended values of independent variables as well as desirability value close to 1. The results of this analysis are shown as desirability plot (Fig. 1c). In graphical optimization, the constraints used for yield were the same as that used in numerical optimization, and based on this, it showed the design space in the form of overlay plot (Fig. 1d). The suggested values of the design space were used for the preparation of optimized formulation. Overall, the combination of desirability and design space overlay plot provided the optimal values of ~1:1.76 (w:w), 50.55 (°C), and 2.02 (h) for the independent variables of MGN/

Phospholipon® 90H ratio (X_1), reaction temperature (X_2), and reaction time (X_3), respectively.

Validation of model optimization

The validation of the CCD-generated model was carried out by preparing an additional trial formulation of MPLC using optimal values of X_1 , X_2 , and X_3 . The actual yield of MPLC (~90.35%) was found in a close agreement with the predicted value (~90.14%). The experimental confirmation, in a way, validated the robustness of the design-generated quadratic model. The predicted error or bias (%) between these two yields was calculated using Eq. 7. It was found to be <3% (0.21). Overall, the CCD helped in optimizing the MPLC formulation successfully:

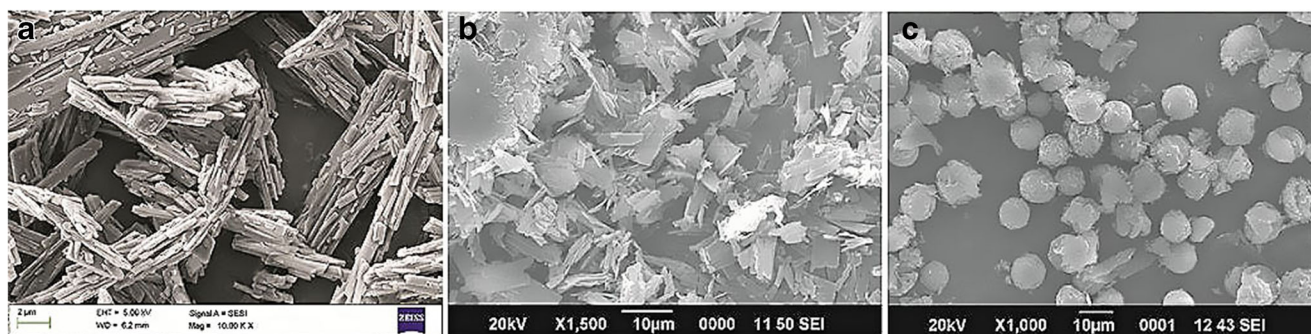


Fig. 2 SEM image of **a** pure MGN, **b** MPLC, and **c** MPLC SNPs formulations

$$\text{Bias (\%)} = \frac{\text{predicted value} - \text{observed value}}{\text{predicted value}} \times 100 \quad (7)$$

Physicochemical characterization of MPLC and MPLC SNPs

SEM

The SEM analysis of pure MGN, MPLC, and lyophilized MPLC SNPs formulations is shown in Fig. 2a, b, and c, respectively. The particles of pure MGN (Fig. 2a) appeared as a blend of small and large needle-shaped particles with ill-defined edges. SEM image of optimized MPLC in (Fig. 2b) exhibited as large, fused, and irregularly shaped particles with heterogeneous surface suggests the formation of a complex between pure MGN and Phospholipon® 90H. Compared with pure MGN and MPLC, the SEM morphology of lyophilized MPLC SNPs (Fig. 2c) appeared as spherical shaped particles with heterogeneous surface, suggesting that the implementation of nanoprecipitation coupled with lyophilization technology could result in the formation of spherical particles.

Particle size and zeta potential

The physical stability of the sub-micron particles in a liquid medium is mostly dependent on two parameters—particle size distribution and zeta potential. Previously, Telange et al. prepared apigenin-phospholipid complex (APLC) and reported particle size and PDI value around $\sim 107.08 \pm 1.30$ nm and 0.37 as narrow particle size distribution. The APLC enhanced aqueous solubility and bioavailability following oral administration [30]. The same author also developed umbelliferone-phospholipid complex (UPLC) and its particle size and PDI values were found to be higher around $\sim 7134.79 \pm 0.67$ nm and 0.53. The UPLC with these parameters significantly enhanced the solubility, permeation, and anti-inflammatory potential of umbelliferone [48]. Figure 3a shows the particle size distribution of MPLC with mean particle size of 507.55 ± 0.40 nm and polydispersity index (PDI) of 0.43 ± 0.10 ,

indicating relatively wide particle size distribution of MGN within MPLC. However, upon comparison with APLC and UPLC, the particle size and PDI value of MPLC was found to be in between them, suggesting that MPLC particles are acceptable smaller particle size and thus found to be suitable for oral administration. Moreover, the particle size of pharmaceutical processed materials is found to be inversely proportional to their surface area/volume (SA/V) ratio, which means that the smaller the particle size, the higher is the SA/V. This concept is found to apply to MPLC, as the smaller particle size of MPLC shows a higher SA/V ratio, resulting in increased solubility and release rate of MGN from MPLC via diffusion and surface erosion [72]. It is well accepted that smaller particles (size < 500 nm) are usually taken up by endocytosis during their transit across the biological membranes. In contrast, larger particles < 5 mm are easily absorbed by the lymphatic system [73, 74].

Zeta potential (ζ) is yet another significant measure specifically used for the determination of surface charges (+ or -). This has a direct impact on the physical stability of the multiparticulate systems. Earlier reports have suggested that zeta potential of values greater than ± 10 mV is indicative of considerable physical stability of the multiparticulate systems [75, 76]. The measured zeta potential of the optimized MPLC formulations is shown in (Fig. 3b). The observed value of zeta potential of MPLC formulations was found to be -12.53 ± 0.17 mV, which is higher than -10 mV, indicating a physical stability of MPLC formulations. The obtained zeta potential value of MPLC could potentially be attributed to the small portion of phospholipids involved in the complexation process with the generation of negative charges in an aqueous environment with near-neutral pH value. This mechanism could provide sufficient negative charges on the surface of MPLC, making it considerably stable in the aqueous state. Moreover, the phospholipid composition and its type may also influence the zeta potential values significantly [30]. Therefore, the results demonstrated that the MPLC formulation of better physical stability was obtained.

Similarly, the measured particle size distribution and zeta potential of MPLC SNPs are shown in Fig. 3c and d, respectively. Lyophilization of the MPLC SNPs was carried out using

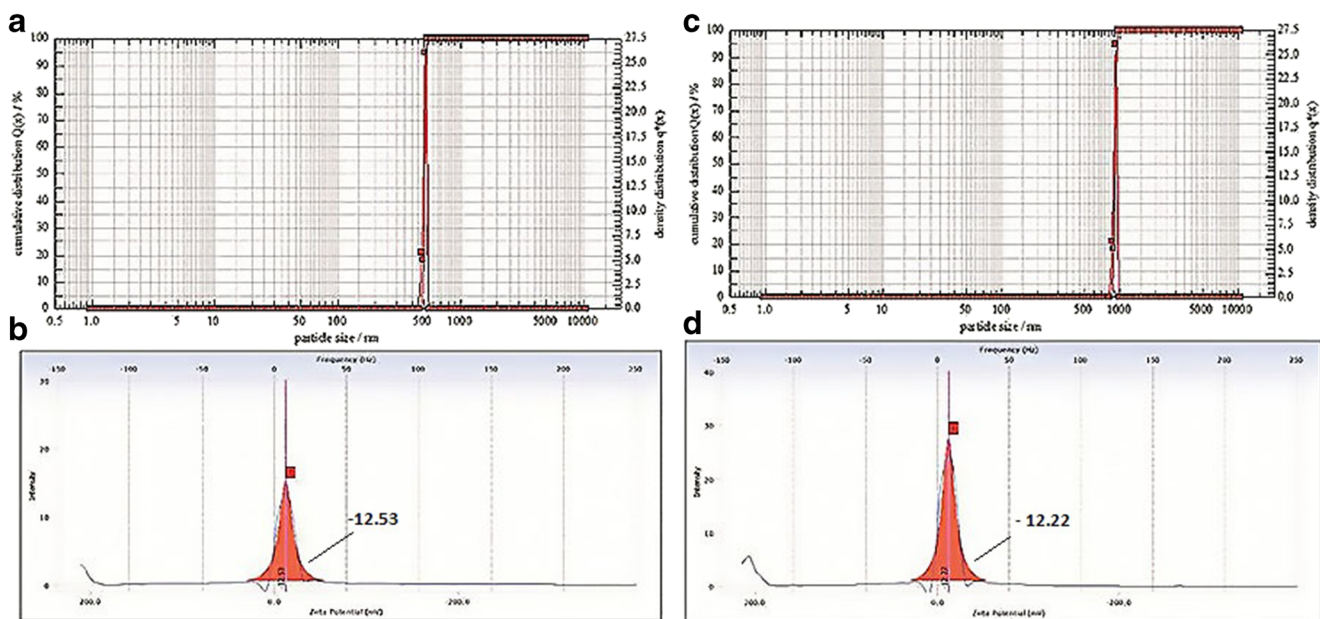


Fig. 3 **a** Particle size distribution, **b** zeta potential of the optimized MPLC formulation before lyophilization, **c** particle size distribution, and **d** zeta potential of MPLC SNPs after lyophilization

sucrose (2% w/w) as cryoprotectant. The formulation exhibited higher average particle size and PDI value of 906.69 ± 0.20 nm and 0.50 ± 0.19 , respectively (Fig. 3c). The zeta potential of the lyophilized formulation was comparable to the one before lyophilization, i.e., -12.22 ± 0.33 mV (Fig. 3d), indicating that the lyophilization technique preserved the physical, chemical, and, most likely, biological stability of the formulation. This is going to be beneficial by preventing the leakage of MGN from MPLC-loaded SNPs under realistic conditions of use in vivo. The results were found to be consistent with an earlier report [45]. Overall, the comparative results of particle size, PDI, and zeta potential values before and after lyophilization are shown in Table 3.

In this study, the MPLC SNPs were prepared using the nanoprecipitation method followed by lyophilization. Lyophilization is the most widely used method which converts solution or suspension into a lyophilized solid form with improved stability and particle size of nanoparticles. However, the freezing, primary drying, and secondary drying steps of the lyophilization process may create stressful conditions (i.e., formation of ice crystal and particle aggregation via crystallization) that can result in destabilization of nanoparticles. To reduce this mechanical stress as well as increase the

stability of nanoparticles, the optimization of the lyophilization process is needed and it is done by introducing the cryoprotectant, which can act as protective agents and prevents the aggregation and/or fusion of nanoparticles during lyophilization and enhances its stability. The same optimization was also carried out for MPLC SNPs using various cryoprotectants at different concentrations. According to earlier reported studies, the total seven cryoprotectants, i.e., glucose, fructose (as monosaccharides), trehalose, maltose, and sucrose (as disaccharides), PVA, and PVP (as a polymer) were studied at four concentrations of 0.5, 1, 2 and 5% (w/w), respectively, and investigate their effect on particle size and PDI of MPLC SNPs [77]. In the following analysis, the PVP and PVA at all concentration range significantly increased the particle size and PDI value of MPLC SNPs around ~ 941.10 and ~ 0.74 nm, respectively. It may be attributed to the complete absence of a thick layer of this polymer at these concentrations on the surface of nanoparticles, which causes the fusion of particles and increases the particle size and PDI values of MPLC SNPs [77]. After lyophilization, all monosaccharides at lower concentration (0.5 and 1%) maintain the same particle size and PDI value as that of polymer, while at higher concentration (2 and 5%), it marginally reduces the particle size

Table 3 Encapsulation efficiency, drug loading, particle size, PDI, and zeta potential values of MPLC SNPs formulations before and after lyophilization

MPLC SNPs formulations	Encapsulation efficiency (%)*	Drug loading (%)*	Particle size (nm)	PDI	Zeta potential (mV)
Before lyophilization	82.23 ± 0.37	17.48 ± 0.19	507.55 ± 0.40	0.43 ± 0.10	-12.53 ± 0.17
After lyophilization	81.63 ± 0.41	16.91 ± 0.30	906.69 ± 0.20	0.50 ± 0.19	-12.22 ± 0.33

*Data are represented as mean \pm SD ($n = 3$)

around ~ 936.39 and ~ 0.68 nm, respectively, compared with polymer, suggesting that the crystallization of these excipients during lyophilization may lose its ability and/or form weak interaction with nanoparticles which results in lowering of particle aggregation to some extent and reduces the particle size and PDI value of MPLC SNPs [77]. Compared with polymer and monosaccharides, the trehalose and maltose at lower concentration (0.5 and 1%) displayed nearly about the same value as that of values shown by monosaccharides at lower concentration, i.e., ~ 939.06 and 0.70 nm, respectively, whereas, at higher concentration (2 and 5%), it marginally reduces the particle size and PDI value of MPLC SNPs around ~ 931.50 and ~ 0.62 nm, respectively, suggesting the solidification of these materials while lyophilization increases the interaction with nanoparticles and, thus, reduces the particle size and PDI value of MPLC SNPs [78, 79]. Among all disaccharides, the sucrose displayed best and more significant results. At lower concentrations, sucrose showed the same results as that of a lower concentration of disaccharides. At 5% concentration, sucrose marginally reduces the particle size and PDI value around ~ 923.42 and ~ 0.56 nm, respectively. However, sucrose at 2% concentration, after lyophilization, more appreciably reduces the particle size and PDI value of MPLC SNPs around ~ 906.69 and ~ 0.50 , respectively, with the appearance of spherical shaped particles as shown in SEM studies. This significant result was likely due to the lyophilized amorphous nature of sucrose, which can form strong H-bonding interactions with developed nanoparticles, preserves it in pseudo-hydrated form, and improves stability of nanoparticles [80]. Moreover, the low hygroscopic nature of sucrose attracts the water molecules from the surrounding environment which form hydrogen bonding with nanoparticles, resulting in the reduction of the particle size and preserving the stability of nanoparticles [81]. Additionally, the phase transformation behavior of sucrose at higher temperatures could provide a favorable environment to lyophilization, forming a stable lyophilized amorphous cake, which shows high redispersibility, lower residual moisture content, and long-term stabilization on storage [82, 83]. Based on these results, the sucrose at 2% (w/w) was chosen as optimum cryoprotectant improving the stability, particle size, and PDI value of MPLC SNPs.

Encapsulation efficiency and drug loading

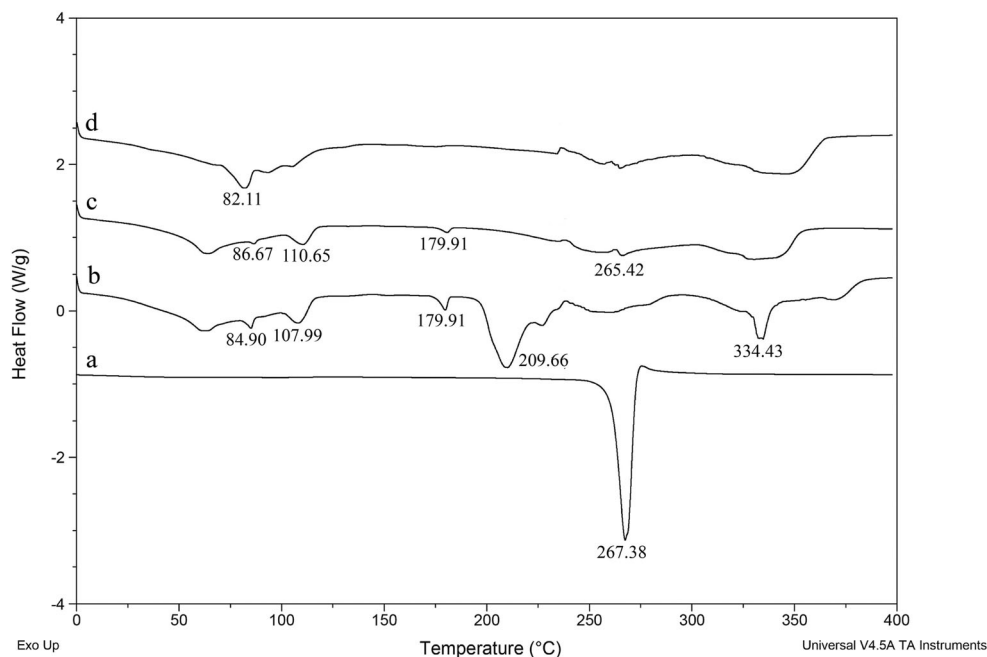
Encapsulation efficiency and drug loading analysis for the MPLC SNPs formulations before and after the lyophilization are presented in Table 3 with the respective values before lyophilization as 82.23 ± 0.37 and $17.48 \pm 0.19\%$. However, after lyophilization, the MPLC SNPs exhibited no significant change in encapsulation efficiency ($81.63 \pm 0.41\%$) and drug loading ($16.91 \pm 0.30\%$). The results indicate that the adopted combined formulation strategy had no remarkable influence

on the quite important encapsulation efficiency and drug content. This is very crucial since the potentially sustained drug release performance was without any sign of drug leakage.

Thermal analysis

Thermograms of pure MGN, Phospholipon® 90H, PM of pure MGN and Phospholipon 90H®, and the MPLC are depicted in Fig. 4a, b, c, and d, respectively. As seen from (Fig. 4a), pure MGN exhibited a sharp, high-intensity melting peak at 267.38 °C. Such sharp peaks are indicative of high purity and the crystalline nature of the substances. The peak was similar to the one reported previously [61]. Phospholipon® 90H showed multiple (#5) endothermic peaks (Fig. 4b). Out of the five peaks, the initial three low-intensity, broad, and diffused peaks (84.90 , 107.99 , and 179.91 °C) indicated the melting of the polar region of the phospholipids. The latter two peaks appeared at 209.66 and 334.43 °C, possibly due to thermal scrambling in the hydrophobic tails of the phospholipids leading to the transformation of the gel-like structure to a crystalline state. These observations were in agreement with the earlier reports [28, 47]. The PM thermograms showed four endothermic peaks at 86.67 , 110.65 , 179.91 , and 265.42 °C (Fig. 4c). The first three peaks were contributed by Phospholipon 90H®, whereas the fourth peak was contributed by pure MGN, demonstrating the additive nature of pure MGN and Phospholipon 90H®. These peaks resulted from the melting of the PM at higher temperatures with the partial formation of the complex, which exhibited lower melting temperature compared with the original formulation. Moreover, the peak intensity of pure MGN in PM thermograms was lower compared with the corresponding peak in pure MGN. However, on close observation, it appeared that, like other small intensity peaks of Phospholipon® 90H, the low-intensity peak of MGN is also detected and this could be due to the remnant MGN while the major amount interacted with Phospholipon® 90H [84]. The thermogram of MPLC (Fig. 4d) displayed a new low-intensity endothermic peak at 82.11 °C, which was completely different from the original peaks observed for pure MGN and Phospholipon® 90H. Moreover, the sharp melting peak of MGN disappeared completely, indicating the amorphization of pure MGN [30, 72]. A completely different DSC melting behavior indicated the occurrence of weak intermolecular interactions such as H-bonding, van der Waals forces, or ion-dipole forces between pure MGN and Phospholipon 90H®. Thus, it is suggested that the formulation process completely dispersed MGN within the phospholipid matrix, leading to the formation of amorphous and stable MPLC [85, 86]. Moreover, the pure MGN and MPLC both exhibited enthalpy of fusion (ΔH) of 29.27 and 152.8 J/g, respectively. This observed difference in enthalpy of fusion for MGN and MPLC further confirmed the formation of the complex.

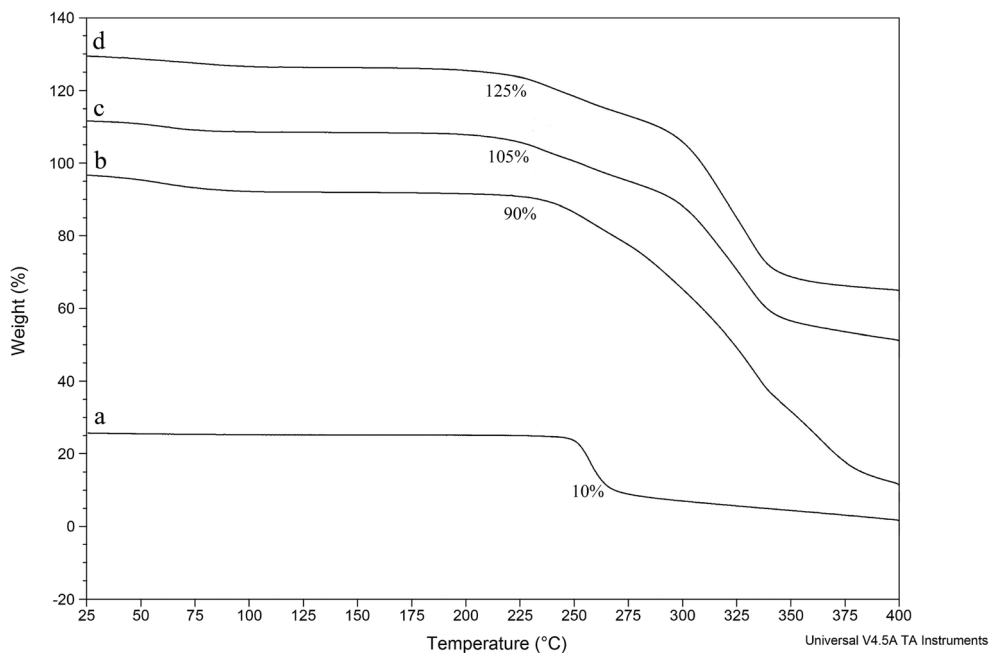
Fig. 4 DSC thermograms of **a** pure MGN, **b** Phospholipon® 90H, **c** the physical mixture (1:1.76) of pure MGN and Phospholipon® 90H, and **d** MPLC formulations



In addition to DSC, the thermogravimetric analysis (TGA) is yet another valuable technique also employed for the investigation of the thermal performance of the formulation. The TGA curves of pure MGN, Phospholipon® 90H, PM, and the MPLC are shown in Fig. 5a, b, c, and d, respectively. Pure MGN (Fig. 5a) exhibited a pointed decrease in weight loss (~10%) in the temperature range 250–275 °C, corresponding to the melting (endothermic peak) of pure MGN. Beyond 275 °C, a continued weight loss was observed, indicating the thermal degradation of MGN. The TGA curves of Phospholipon® 90H (Fig. 5b) displayed a sharp loss in weight

(~90%) around 225 °C. Beyond this point, the curve showed consistent lowering. This could be attributed to the physicochemical transformation of the phospholipids from the gel-like structure to the crystalline state. Figure 5c showed the TGA curve of the PM. It displayed a weight loss (~105%) between the ranges of 225 and 350 °C. Beyond 350 °C, PM showed rapid weight loss. In contrast to this, MPLC (Fig. 5d) exhibited a weight loss (~125%) between the same ranges as mentioned for PM; however, on close observations; it was found that the MPLC beyond 350 °C exhibits slow rate of weight loss compared with rapid weight loss of PM, which

Fig. 5 TGA curves of **a** pure MGN, **b** Phospholipon® 90H, **c** the physical mixture (1:1.76) of pure MGN and Phospholipon® 90H, and **d** MPLC formulations



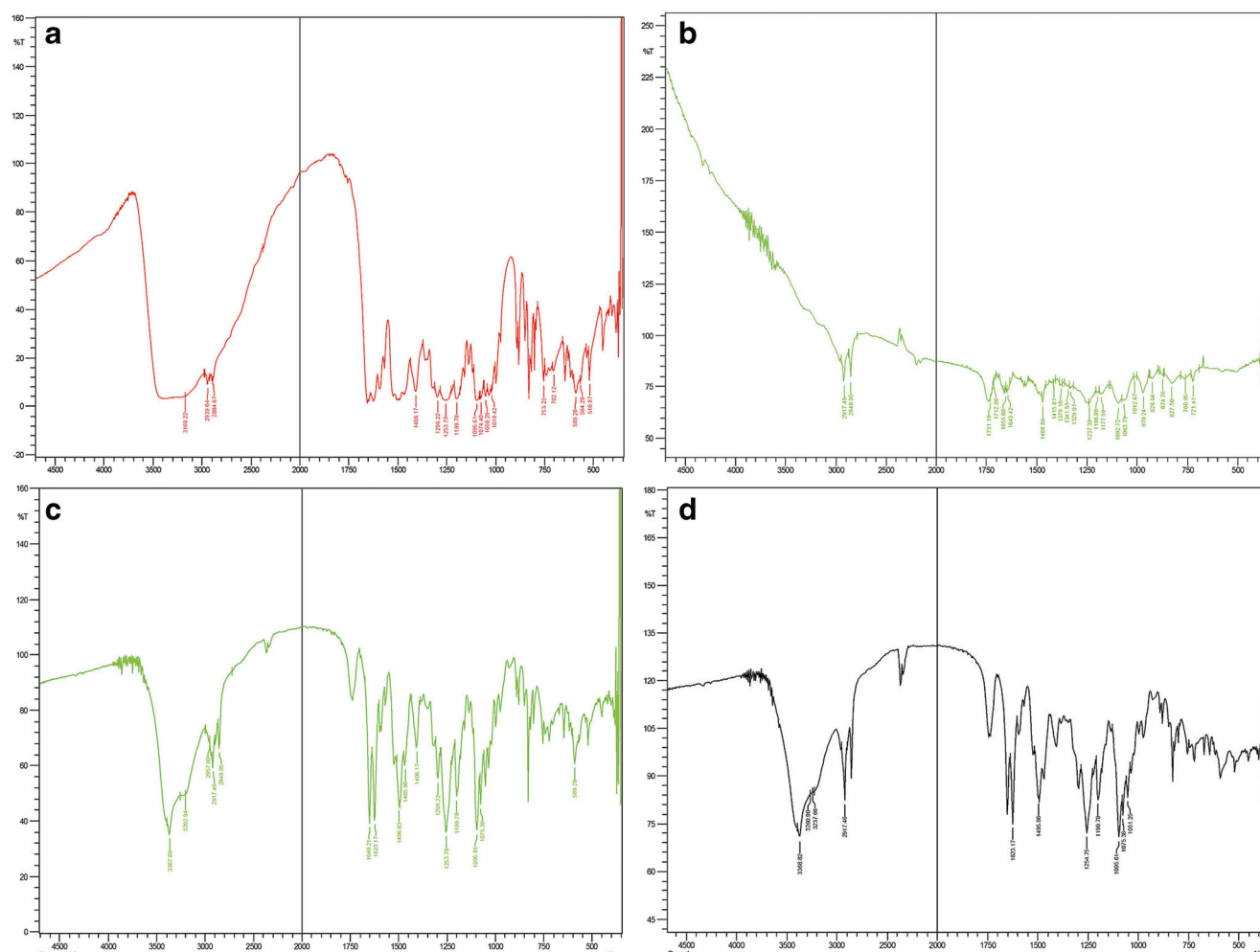


Fig. 6 FT-IR spectra of **a** pure MGN, **b** Phospholipon® 90H, **c** the physical mixture (1:1.76) of pure MGN and Phospholipon® 90H, and **d** MPLC formulations

indicates an improved thermal stability of MGN due to the formation of MPLC complex [87]. This result suggested that the molecular interaction of MGN with the polar head of Phospholipon® 90H via polar and hydrogen bonding interactions could increase their affinity toward each other and increase the stability of MPLC.

FT-IR

Figure 6 (a, b, c, and d) depicts the FT-IR spectra for pure MGN, Phospholipon® 90H, PM, and MPLC formulation, respectively. As seen in (Fig. 6a), pure MGN displayed distinctive absorption signals at 3367.86 and 3168.22 cm^{-1} corresponding to the O-H stretching, 2939.64 cm^{-1} for aliphatic C-H stretching, 1648.66 and 1622.56 cm^{-1} for C=O stretching, 1253.78 and 1095.61 cm^{-1} for aryl ether C-O-C stretching, 1406.17 cm^{-1} for C=C stretching, and 702.12 and 589.28 cm^{-1} for aromatic bending vibrations. These signals were consistent with the earlier published reports [61]. The FT-IR spectrum of Phospholipon®

90H (Fig. 6b) marked the presence of multiple characteristic absorption signals, which appeared at 2917.46 and 2849.95 cm^{-1} (C-H stretching of long fatty acid chain) and 1731.19 cm^{-1} for C=O stretching vibration of fatty acid ester. Besides these, some additional signals were also observed at 1237.39 and 1092.72 cm^{-1} (for P=O and P-O-C stretching) and 970.24 cm^{-1} for $[-\text{N}^+(\text{CH}_3)_3]$. These FT-IR peaks were in agreement with the previous reports for Phospholipon® 90H [28, 50, 88]. The characteristic FT-IR signals exhibited by the PM are shown in (Fig. 6c). The signals appeared at 3367.86, 3202.94, 2957.00, 2917.46, 2849.95, 1725.10, 1649.21, 1623.17, 1253.78, 1095.61, and 589.28 cm^{-1} . The appearance of these peaks in the FT-IR spectrum indicated a strong alliance between pure MGN and Phospholipon 90H®. Finally, the MPLC FT-IR spectrum (Fig. 6d) showed the absorption signals at 3368.82, 3260.80, 3237.66, and 1623.17 cm^{-1} . In addition to this, no new extra peaks were seen. These signals were shifted from lower to higher frequencies specific to the functional groups O-H and C=O. The shifting of peaks in MPLC compared with pure MGN suggested that the presence of weak

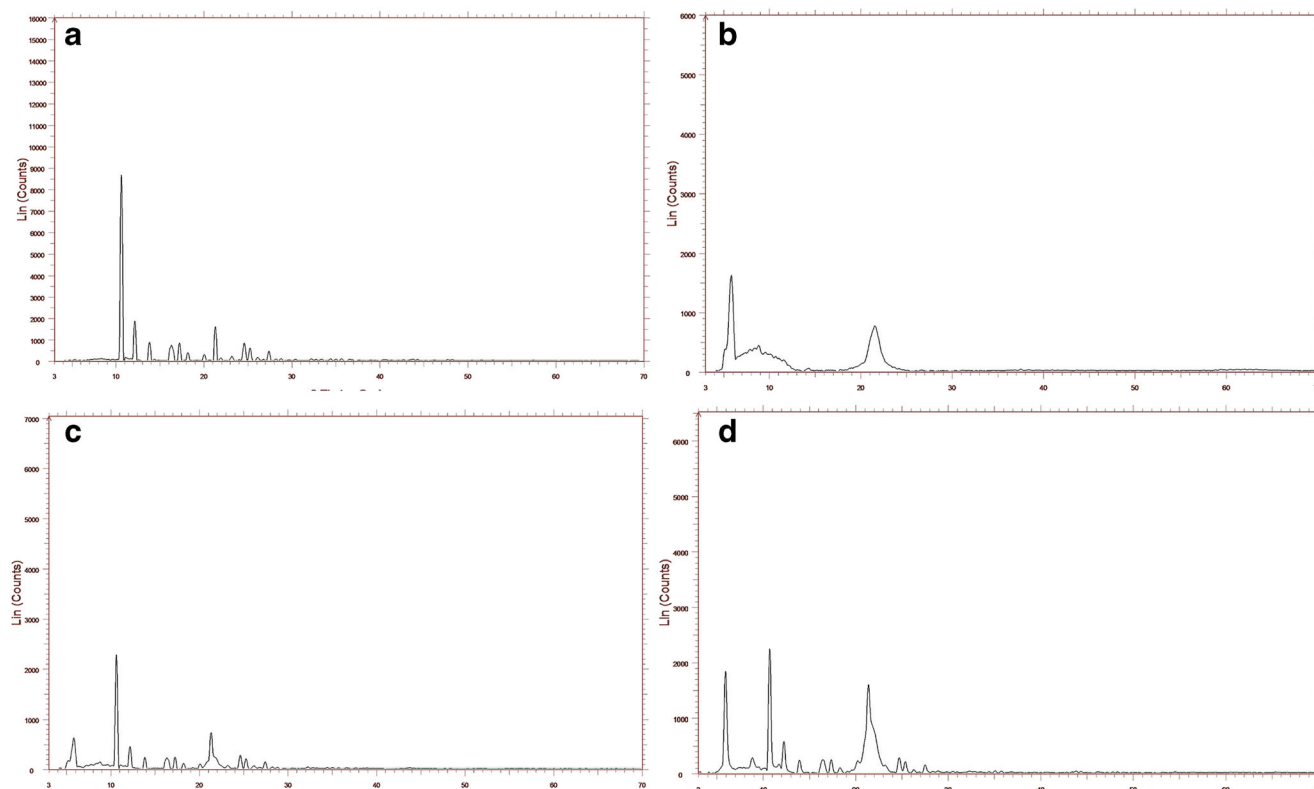


Fig. 7 The X-ray diffractograms of **a** pure MGN, **b** Phospholipon® 90H, **c** the physical mixture (1:1.76) of pure MGN and Phospholipon® 90H, and **d** MPLC formulations

intermolecular interactions, i.e., H-bonding, van der Waals forces, and/or ion-dipole forces, is involved in the formation of MPLC.

PXRD

The diffractograms for pure MGN, Phospholipon® 90H, PM, and the MPLC formulation are shown in Fig. 7a, b, c, and d, respectively. On the 2θ scale, multiple diffraction peaks were shown by pure MGN (Fig. 7a). Three sharp peaks were seen at 10° , 12° , and 21° , and their intensity was found to be higher around ~ 8500 , 2000 , and 1000 counts on y -axis. Moreover, some additional low-intensity peaks appeared at 13.5° , 16° , 17° , 18° , 20° , 24° , 25° , and 27° . These peaks signified the crystalline nature of pure MGN [17]. The Phospholipon® 90H diffraction spectrum (Fig. 7b) exhibited two peaks. The first peak appeared at 5° , while the second one was seen at 21° . The intensities of these peaks were around ~ 1600 and 800 counts on the y -axis scale, respectively. Moreover, the absence of sharp and intense peaks in this diffractogram indicated its amorphous nature [29, 30, 48]. Abundant diffraction signals were displayed in diffractograms of the PM (Fig. 7c). These signals were seen at 5° , 10° , 12° , 13° , 16° , 17° , 18° , 21° , 22° , and 23° , indicating a partial interaction between MGN and Phospholipon 90H®. The intensity of the MGN peak in the physical mixture was lower around ~ 2100 and 500 counts

on the y -axis, compared with the pure MGN, possibly indicating a lower fraction of pure MGN and hindrance of phospholipids and in situ formation of partial aggregates. It was evident that the PM exhibited a relatively different diffractogram compared with those of MGN and Phospholipon® 90H individually [47]. As depicted in (Fig. 7d), MPLC exhibited more or less similar diffraction pattern as that of the PM. However, the intensity of phospholipid-dominated peaks was increased, whereas the MGN-dominated peak intensity was suppressed around ~ 2350 and 600 counts on the y -axis. Moreover, the third intense peak of MGN disappeared completely in MPLC, which might be attributed to the merging of the third peak into the phospholipid-dominated peak. Therefore, based on the changes in peak intensities in MPLC compared with pure MGN, it could be ascertained that the complexation proceeded successfully, wherein the crystalline MGN dispersed into the phospholipid matrix resulting in the conversion of crystalline MGN to amorphous MPLC; the complex is stabilized by weak intermolecular interactions.

$^1\text{H-NMR}$

The $^1\text{H-NMR}$ spectra of pure MGN, Phospholipon® 90H, and optimized MPLC are recorded on the δ scale and their spectrums are depicted in Fig. 8 (a, b, c, and d), respectively. Pure MGN (Fig. 8a) exhibited chemical shift values around

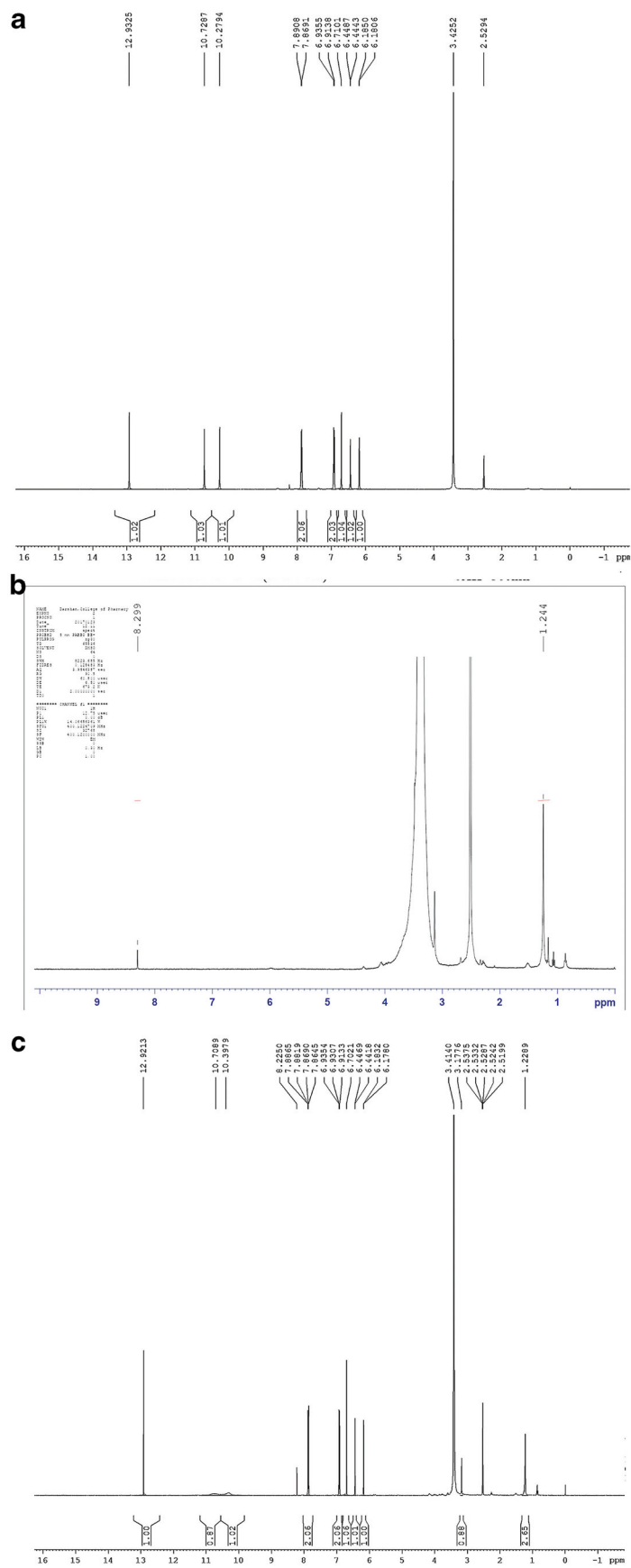


Fig. 8 $^1\text{H-NMR}$ spectra of **a** pure MGN, **b** Phospholipon® 90H, and **c** MPLC formulations

$\sim \delta$ 12.93 (1H, s, 1-OH), δ 10.73 (1H, s, 6-OH), δ 10.28 (1H, s, 3-OH, and 7-OH), δ 7.88 (1H, s, H-8), δ 6.92 (1H, s, H-5), and δ 6.44 (1H, s, H-4, and H-6). Results are consistent with earlier published literature [89]. Chemical shift values of Phospholipon® 90 (Fig. 8b) appeared around $\sim \delta$ 4.85 (1H, s), δ 4.08– δ 3.96 (br s, 1H), δ 3.83– δ 3.62 (s, 2H), δ 3.38 (s, 1H), δ 3.07 (s, 15H), δ 2.95 (H-8, J = 8 Hz), δ 2.27 (s, 1H), δ 1.26 (s, 2H, s), δ 0.95 (s, 23H), and δ 0.57 (s, 3H, s) [90]. The $^1\text{H-NMR}$ spectrum of optimized MPLC formulation is shown in (Fig. 8c). It exhibited values around $\sim \delta$ 12.92 (1H, s, 1-OH), δ 10.70 (1H, s, 6-OH), δ 10.39 (1H, s, 3-OH, and 7-OH), δ 8.225 (2H), δ 7.88 (1H, s, H-8), δ 6.93 (1H, s, H-5), δ 6.44 (1H, s, H-4, and H-6), δ 3.17 (s, 3H), and δ 1.23 (s, 3H), respectively. Upon comparison, it was observed that there is a significant shifting of proton signals in downfield ($\delta > 7$) and upfield ($\delta < 4$) aromatic region of the MPLC, indicating the formation of a molecular complex between the specific phenolic (3-OH, 6-OH, and 1-OH) group of MGN with the polar head of Phospholipon® 90H through the involvement of hydrogen bonding, ion-dipole, and van der Waals forces of interaction (29, 48). This conclusion suggests the weak intermolecular forces are the main mechanism involved in the formation of stable MPLC.

Solubility studies

The results obtained from the solubility studies of pure MGN, MGN SNPs, PM, optimized MPLC, and MPLC SNPs formulation in water or n-octanol are shown in Table 4. It is seen that pure MGN and MGN SNPs possessed low aqueous solubility (0.34 and 0.37 $\mu\text{g/mL}$), while the observed solubility in n-octanol was 178- and 182-fold higher (60.78 and 64.20 $\mu\text{g/mL}$). It was not surprising given the BCS class IV status of MGN [91]. The outcome of PM solubility studies was a moderate increase (up to 10-fold) in aqueous solubility (3.41 $\mu\text{g/mL}$) over pure MGN. This observation was statistically significant ($p < 0.05$). In contrast to aqueous solubility, the PM did not show significant improvement in solubility in n-octanol. The considerable improvement in aqueous solubility of the PM was attributed to the close association of amphiphilic Phospholipon® 90H with pure MGN during the complexation process. Interestingly, the solubility of MPLC

formulation in water increased significantly (10.79 $\mu\text{g/mL}$, \sim 32-fold) over pure MGN and the PM. Additionally, the solubility of MPLC formulation in n-octanol was observed to be 257.15 $\mu\text{g/mL}$. This was attributed to the physicochemical modification as well as the amorphization of pure MGN during complexation with amphiphilic Phospholipon® 90H. The MPLC SNPs showed a significant ($p < 0.001$) increase in aqueous solubility (13.39 $\mu\text{g/mL}$, \sim 39-fold) over pure MGN. From this comparative solubility analysis, it could be concluded that the MPLC SNPs significantly improved the aqueous solubility of MGN, and it was likely due to the amorphized and amphiphilic-assisted nanosized nature of MPLC SNPs.

Functional characterization of MPLC and MPLC SNPs

In vitro dissolution studies The comparative in vitro release pattern of pure MGN suspension, MGN SNPs, MPLC, and MPLC SNPs in PBS (pH 7.4) using dialysis method is shown in (Fig. 9). The dissolution pattern of MGN suspension and MGN SNPs exhibited \sim 27 and \sim 30% release (0–5 h) and \sim 41 and \sim 43% release at the end of 12 h. This could be due to poor aqueous solubility of MGN. These results correlated well with the solubility studies [91]. In comparison, both the MPLC and MPLC SNPs demonstrated a sharp enhancement in the rate and extent of dissolution of MGN. For the initial phase (0–5 h), the MPLC exhibited \sim 53% release, and subsequently, the MGN release increased significantly and reached \sim 85% at the end of the 12-h testing period. The increased MPLC dissolution was likely due to the increased solubility and wettability of MGN in MPLC owing to the complex formation with Phospholipon® 90H, resulting in uniform dispersion in the dissolution medium. These findings agreed with the earlier reports [48, 92]. The release profile of MGN from MPLC SNPs showed that the MGN displayed a burst release (\sim 71%) in the initial phase (0–5 h). However, after 5 h, around \sim 98% of the sustained release of MGN was observed. The MPLC SNPs exhibited a more sustained release and it was indicated by the initial burst release and latter prolonged-release behavior. The initial burst release was attributed to the absorption of MPLC on the surface of soft nanoparticles that undergo dissociation of MGN and released in free form in

Table 4 Solubility analysis of pure MGN, MGN SNPs, the physical mixture (1:1.76) of MGN and Phospholipon® 90H (PM), design-optimized MPLC, and lyophilized MPLC SNPs

Samples	Aqueous solubility ($\mu\text{g/mL}$)*	n-octanol solubility ($\mu\text{g/mL}$)*
Pure MGN	0.34 \pm 0.09	60.78 \pm 0.21
MGN SNPs	0.37 \pm 0.12	64.20 \pm 0.36
PM	3.41 \pm 0.17	67.42 \pm 0.43
MPLC	10.79 \pm 0.32	109.08 \pm 0.20
MPLC SNPs	13.39 \pm 0.22	117.20 \pm 0.44

*Data are represented as mean \pm SD ($n = 3$)

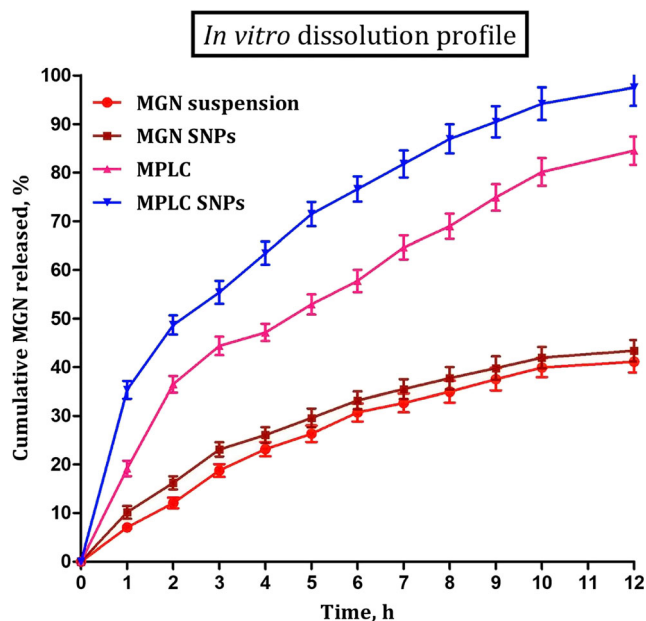


Fig. 9 The in vitro dissolution profiles of MGN release from MGN suspension, MGN SNPs, prepared MPLC, and MPLC SNPs formulations. Values are presented as mean \pm Std. Dev. ($n = 3$)

dissolution medium, whereas prolonged-release was attributed to the presence of stabilized MPLC within the core space of soft nanoparticles, and from this, the MGN showed diffusion-controlled sustained release via two stages: firstly, the MGN dissociated from MPLC, and secondly, the dissociated MGN within the core space diffused through the skeleton of soft nanoparticles. These outcomes indicate that MGN is stable and release in a sustained manner for a long period attributed to the formation of MPLC and following its incorporation into SNPs. Results are well supported by previous reports [45]. The comparative release profile indicated that MPLC SNPs provided a sustained release of MGN for longer periods, compared with that of MPLC and suspension. This only

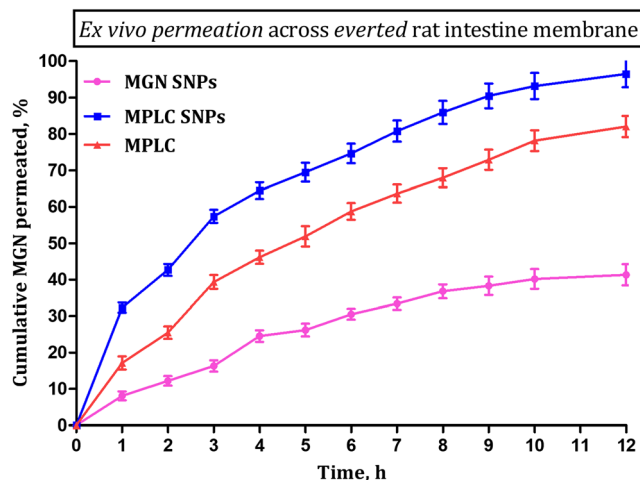


Fig. 10 Ex vivo permeation profiles of MGN permeated from MGN SNPs, MPLC, and prepared MPLC SNPs across everted rat intestine membrane. Values are presented as mean \pm Std. Dev. ($n = 3$)

emphasized that MPLC SNPs could be an effective nanovesicle drug delivery system for the oral administration of MGN.

The release kinetics of MGN from the formulation was estimated by the fitting of the observed release data into various kinetic models, i.e., first-order, zero-order, Higuchi, and Korsmeyer-Peppas models [93]. The MPLC-loaded SNPs exhibited correlation coefficient value ($R^2 = 0.983$). Based on this result, the Higuchi model was found to be the best-fit kinetic model, which described the underlying dissolution mechanism. Moreover, the same formulation ($n = 0.49$) indicated that the MPLC SNPs followed diffusion as the main mechanism for MGN release. It is essentially described as a two-step process—(i) MGN was released from MPLC and (ii) free MGN then diffused through the phytosomal matrix into the surrounding medium.

Ex vivo permeability studies The permeability of pure MGN from MGN SNPs, MPLC, and MPLC SNPs formulations across the everted rat intestine membrane was studied using a specially designed apparatus, and the generated results are depicted in (Fig. 10). At the end of the 12-h permeation period, MGN from MGN SNPs exhibited only $\sim 41\%$ of permeation across the everted rat intestinal membrane. This was likely due to the low permeability of MGN following the earlier reports. Compared with the MGN SNPs, the MPLC and MPLC SNPs showed a higher rate and extent of permeation across the intestinal membrane. By the end of the 12-h permeation period, the MPLC demonstrated around $\sim 82\%$ of MGN permeation, whereas the MPLC SNP formulation demonstrated $\sim 97\%$ of MGN permeation. The results are correlated with dissolution studies.

The observed difference in permeation studies could be attributed to the formulation methods and phospholipids. In this study, the MPLC and MPLC SNPs were prepared from the same phospholipids, and as reported earlier, the phospholipids on complexation with bioactive improved its permeability via increasing the amphiphilic nature of bioactive. Moreover, the similarity of the structural component of employed phospholipids with the lipid content of mammalian cell membrane exhibits biocompatibility toward each other [94]. The biological cell membrane is also made up of phospholipid bilayer and shows the amphiphilic character (the fluid mosaic model proposed by S. J. Singer and G. L. Nicolson in 1972). So it may be assumed that the improved amphiphilicity of MGN using the Phospholipon® 90H could show higher miscibility with the biological cell membrane and facilitate effective permeation of MGN [72]. The soft nanoparticles, i.e., MPLC SNPs, prepared using a combination of solvent evaporation and nanoprecipitation method have modified the MGN physicochemically, resulting in an increase of lipophilicity followed by permeation. According to previous studies, it has been reported that the nanoparticles prepared

using phospholipids increase their affinity toward the biological cell membrane and maximize the drug permeation [95–97]. In MPLC SNPs, the presence of the excess amount of MPLC as well as amphiphilic nature of soft nanoparticles could also increase strong affinity toward the cell membrane and allow greater miscibility within the phospholipid bilayer of the cell membrane, significantly enhancing the permeability of MPLC SNPs compared with MPLC and MGN. Moreover, the affinity of MPLC SNPs toward the plasma membrane provides strong interaction between them, which may cause destabilization of the membrane as well as the formation of pore within the membrane, resulting in the translocation and permeation of nanoparticles via exchanging of coating lipids between MPLC SNPs and lipid bilayer [98]. Additionally, the adhesion (i.e., partial wrapping) and complete wrapping and internalization of MPLC SNPs within the plasma membrane and, subsequently, membrane pore formation may also be answerable for the enhancement of MGN permeation [99]. The permeation study indicated that MPLC enhances the permeation of MGN, but in the form of soft nanoparticles, their strong affinity to the cell membrane as well as lipid exchange mechanism could enhance their permeation to a greater extent and subsequently increase the oral bioavailability of MGN.

In vivo antioxidant activity The influence of orally administered formulations containing MGN on CCl₄-induced albino rats is discussed below.

Liver function test

The damage to the hepatic tissue in all groups of animals was induced by a well-known hepatotoxin, CCl₄. After oral administration, the CCl₄ was metabolized to reactive oxygen species (ROS), i.e., free radicals, mediated via CYP450 enzymes. The generated ROS further biochemically reacted with

various biological macromolecules such as lipids, proteins, and carbohydrates, which in turn led to oxidative damage.

Table 5 lists the results obtained from the antioxidant studies of MGN SNPs suspension and MPLC SNPs on liver function tests. The marker enzymes such as SGOT, SGPT, total bilirubin, and SALP were elevated significantly following induction by CCl₄. However, this elevation in the marker enzymes was restored by the administration of antioxidant formulations to the animals. The MGN SNPs suspension (dose: 60 mg/kg, p.o.) exhibited a significant ($p < 0.05$) reduction in SGOT, SGPT, total bilirubin, and SALP. In contrast to this, the MPLC SNPs demonstrated a more significant ($p < 0.01$) reduction in the marker enzymes at the same dose level. In conclusion, the MPLC SNPs exhibited a significant hepatoprotective activity, compared with the MGN SNPs suspension.

In vivo antioxidant marker enzyme estimation

The performance of orally administered formulations containing MGN on the in vivo antioxidant marker enzymes such as GSH, SOD, CAT, and LPO in CCl₄-induced albino rats is shown in (Fig. 11). After CCl₄ administration, the GSH level in rat liver homogenate was reduced rapidly compared with the normal group. In contrast, the MGN SNP-treated animals (dose: 60 mg/kg, p.o.) significantly ($p < 0.05$) increased the GSH levels. Compared with the MGN SNP suspension, a more significant ($p < 0.01$) enhancement in the GSH level was produced by the MPLC SNPs at the same dose level. Reduction in the SOD level was observed compared to the positive control. The MGN SNPs suspension increased the SOD significantly ($p < 0.05$) at the dose level of (~ 60 mg/kg, p.o.). The MPLC SNPs (dose: 60 mg/kg of MGN, p.o.) showed an improvement ($p < 0.01$) in SOD levels, compared to the MGN SNPs. Reduction in the CAT level in the rat liver homogenate was observed following the oral administration of CCl₄. A significant ($p < 0.05$) increase in the CAT level was

Table 5 Effect of MGN SNPs and lyophilized MPLC SNPs on CCl₄-intoxicated liver function marker enzymes, SGOT, SGPT, SALP, and total bilirubin

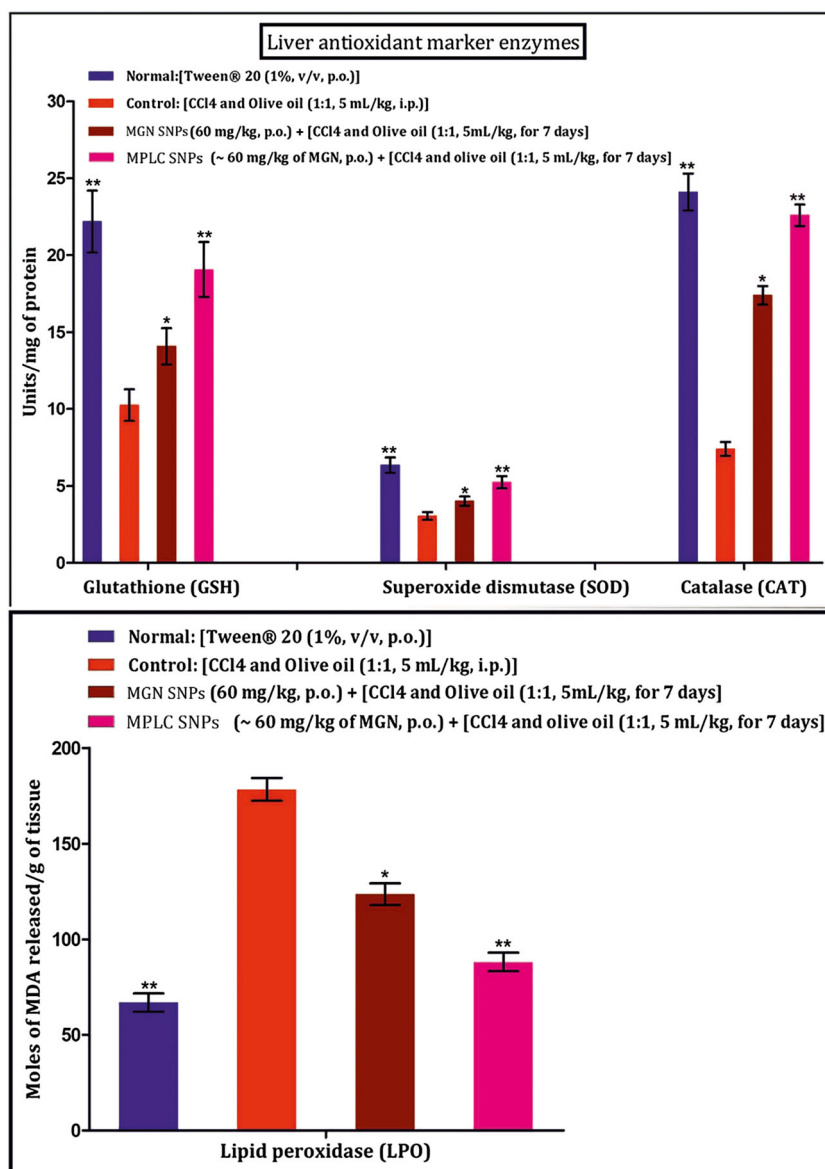
Treatment groups	SGPT (IU/L) ^a	SGOT (IU/L) ^a	SALP (IU/L) ^a	Total bilirubin (mg/dL)
Group I: Normal [Tween® 20 (1%, v/v, p.o.)]	28.03 ± 1.06**	31.10 ± 1.22**	144.31 ± 2.18**	0.30 ± 0.06**
Group II: Control [CCl ₄ and olive oil (1:1, 5 mL/kg, i.p.)]	61.27 ± 2.02	79.42 ± 3.51	187.34 ± 4.08	0.87 ± 0.03
Group III: MGN SNPs (~ 60 mg/kg, p.o.) [CCl ₄ and olive oil (1:1, 5 mL/kg, i.p. for 7 days)]	50.14 ± 2.30*	64.19 ± 1.86*	175.49 ± 2.39*	0.67 ± 0.09*
Group IV: MPLC SNPs (~ 60 mg/kg of MGN, p.o.) [CCl ₄ and olive oil (1:1, 5 mL/kg, i.p. for 7 days)]	34.54 ± 1.17**	42.28 ± 1.60**	151.20 ± 2.59**	0.46 ± 0.08**

^a IU/L International Units/Liter of plasma

All values are Mean ± Std. Error of Mean ($n = 6$)

* $p < 0.05$, ** $p < 0.01$ (significant with respect to control group)

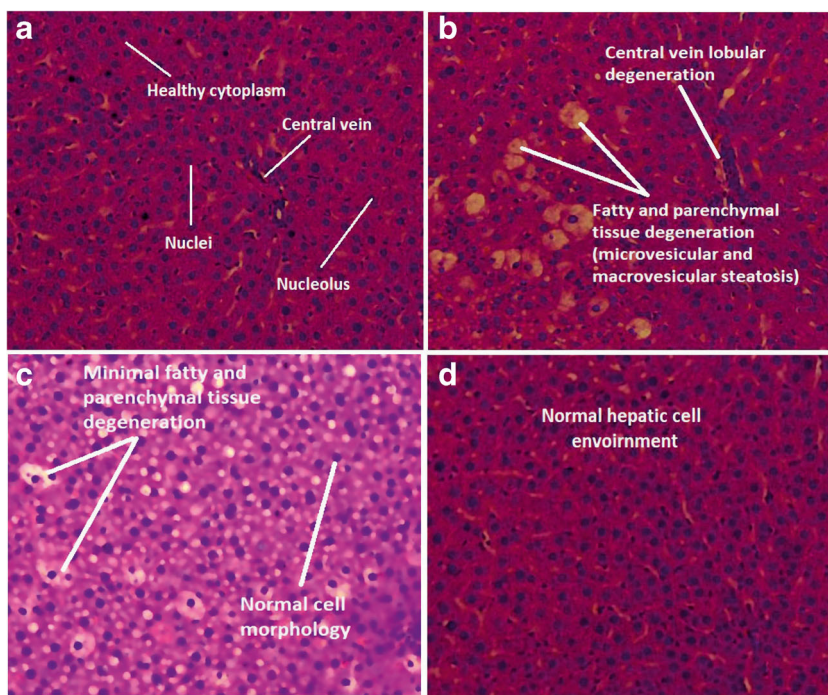
Fig. 11 Effect of MGN SNPs and MPLC SNPs on rat liver antioxidant marker enzymes, such as glutathione reductase (GSH) (nmoles/mg of protein), superoxide dismutase (SOD) (units/mg protein), catalase (CAT) (units/mg protein), and lipid peroxidase (LPO) (nmoles of MDA released/g tissue). Values are Mean \pm Std. Error of Mean ($n = 6$). * $p < 0.05$, ** $p < 0.01$ (significant with respect to control groups)



recorded in the case of pure MGN SNP suspension at a dose of ~ 60 mg/kg, p.o. A further increase in the CAT level in liver homogenate was seen more significantly ($p < 0.01$) after oral administration of MPLC SNPs at the same dose level. In the case of LPO, the MGN SNP suspension lowered its level ($p < 0.05$) in liver homogenate at (~ 60 mg/kg, p.o.) dosing. The MPLC SNP-treated animals at a dose of ~ 60 mg/kg of MGN, p.o. exhibited higher and significant ($p < 0.01$) elevation in the LPO levels in rat liver homogenate. The overall study indicated that MPLC SNPs provide more significant hepatoprotection against CCl₄ intoxication. CCl₄ is a well-known causative agent for the liver. Following administration, CCl₄ metabolized into trichloromethyl radical [100], which causes an increase in lipid peroxidation and lowering of some enzyme functionality [101], resulting in the production of hepatocellular degeneration and centrilobular necrosis in the

liver [102, 103]. Earlier reports have shown that numerous bioactive compounds produce a significant antioxidant activity against CCl₄-induced hepatotoxicity. MGN, a xanthone compound, also produces an antioxidant activity against CCl₄-induced liver damage. Moreover, it is also reported as a potent free radical scavenger, which scavenges the free radical and, subsequently, protects the liver [4]. However, poor bioavailability, poor absorption, and low lipophilicity of MGN limited its antioxidant activity. In this study, the above major issue of MGN was solved by converting it into soft nanoparticles loaded with MPLC and evaluated its activity against MGN SNPs. The MGN SNPs are soft nanoparticles loaded with MGN without complex that still showed significant results in liver function test and in vivo antioxidant studies attributed to slight improvements in aqueous as well as lipid solubility and its results are reflected in Table 4.

Fig. 12 Histopathology micrographs of ($\times 400$) of rat livers. **a** Normal: Tween® 20 (1%, v/v, p.o.), **b** control: CCl₄ + olive oil (1:1, 5 mL/kg, i.p.), **c** MGN SNPs (60 mg/kg, p.o.) + [CCl₄ + olive oil (1:1, 5 mL/kg, i.p. for 7 days], and **d** MPLC SNPs (~60 mg/kg of MGN, p.o.) + [CCl₄ + olive oil (1:1, 5 mL/kg, i.p. for 7 days]



Compared with MGN SNPs, the MPLC SNPs show more significant effects. The positive results of MPLC SNPs were attributed to the following factors that may be involved. First, the affinity of MPLC SNPs toward the plasma membrane can provide complete wrapping, internalization, and formation of the pore of nanoparticles within the membrane, resulting in the enhancement of permeation of MGN and, thus, increasing the in vivo antioxidant activity. Second, the lipid exchange mechanism between coating lipids of MPLC SNPs and bilayer may enhance the translocation and permeation of MGN into

hepatic cells leading to the increase of antioxidant enzyme levels. Third, the improved biological half-life of MGN by converting into MPLC SNPs also increases its effective time in systemic circulation, resulting in more utilization of MGN by damaged hepatic cells. Forth, the sustained release characteristics of MPLC SNPs may provide a prolonged exposure of the damaged hepatic cells to MGN, leading to the enhancement of the hepatoprotection against CCl₄. Finally, the improved lipophilicity of MPLC SNPs can increase its miscibility with lipid content of biological membrane; facilitate its effective transportation across the membrane, subsequently, entering the hepatic cells; and show an effective antioxidant

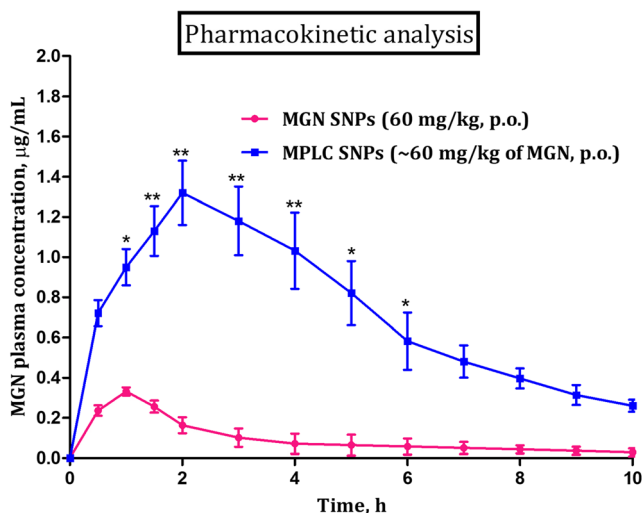


Fig. 13 Mean plasma concentration time profile curve after oral administration of MGN SNPs (60 mg/kg, p.o.) and MPLC SNPs (~60 mg/kg of MGN, p.o.). Values are mean \pm Std. Error of Mean. ($n = 6$). * $p < 0.05$ and ** $p < 0.01$ (significant with respect to MGN SNPs-treated group)

Table 6 Pharmacokinetic parameters for group of animals after oral administration of MGN SNPs (60 mg/kg, p.o.) or MPLC SNPs (~60 mg/kg of MGN, p.o.)

Pharmacokinetic parameters	Treatment	
	MGN SNPs	MPLC SNPs
C_{max} ($\mu\text{g mL}^{-1}$)	0.33 ± 0.10	1.32 ± 0.40
T_{max} (h)	1.00 ± 0.31	2.00 ± 0.19
AUC_{0-t} ($\mu\text{g h mL}^{-1}$)	0.74 ± 0.07	7.11 ± 1.43
AUC_{0-} ($\mu\text{g h mL}^{-1}$)	0.96 ± 0.58	7.30 ± 1.65
$t_{1/2el}$ (h)	2.82 ± 1.29	3.22 ± 1.04
K_{el} (h^{-1})	0.39 ± 0.04	0.19 ± 0.09
cl/F [$(\text{mg}/\mu\text{g mL}^{-1} \text{ h}^{-1})$]	74.22 ± 2.41	9.39 ± 1.71
Vz/F (L/kg)	302.41 ± 1.28	43.64 ± 2.45
Relative bioavailability (F)	–	53.29

All values are Mean \pm Std. Error of Mean ($n = 6$)

Table 7 Stability studies of lyophilized MPLC SNPs at 4 and 25 °C

Parameters	At 4 °C			At 25 °C	
	0 months	3 months	6 months	3 months	6 months
Particle size (nm)	906.69 ± 0.20	910.18 ± 2.10	915.08 ± 1.18	920.21 ± 2.34	931.28 ± 2.46
PDI	0.50 ± 0.19	0.56 ± 0.04	0.61 ± 0.19	0.65 ± 0.39	0.73 ± 0.11
Zeta potential (mV)	-12.22 ± 0.33	-14.05 ± 1.49	-15.56 ± 2.65	-16.21 ± 1.388	-20.43 ± 1.05
Entrapment efficiency (%)	81.63 ± 0.41	79.86 ± 1.41	77.91 ± 2.10	76.66 ± 1.54	67.58 ± 1.77

All values are mean ± SD ($n = 3$)

activity. So, this study suggested that MPLC SNPs could be a promising delivery system in the enhancement of the in vivo antioxidant activity of MGN compared with MGN SNPs.

Histopathological studies

The investigations of CCl₄-induced liver damage of rats in hematoxylin-eosin-stained microscopic ($\times 400$) images from groups of animals treated with vehicle (Tween® 20), CCl₄ only, CCl₄ and MGN SNP suspension, and CCl₄ and MPLC SNPs are shown in Fig. 12 (a, b, c, and d), respectively. As seen in (Fig. 12a), there were no gross pathological changes in the vehicle-treated animals. In sharp contrast, the CCl₄-treated animals (Fig. 12b) exhibited pathological changes such as damage to the fat (steatosis) as well as parenchymal cells. Additionally, CCl₄ also damaged the central lobular vein extensively. Animals treated with MGN SNP suspension (Fig. 12c) demonstrated a significant hepatoprotective activity with modest tissue recovery. Compared with MGN SNPs, the MPLC SNPs (Fig. 12d) demonstrated a highly significant recovery to the damaged hepatic tissue by protecting for longer periods. These results confirmed that the MPLC SNPs offered a significant hepatoprotection to the CCl₄-exposed hepatic cells, likely due to the nanosized nature of the drug delivery system.

HPLC method validation

The results obtained from the HPLC method validation studies are discussed below. The concentration range (0.05–10 µg/mL) showed good linear relation between the selected concentration range and correlation coefficient ($r^2 = 0.9970$). The results of the limit of detection and limit of quantification appeared around ~ 10 and 32 ng/mL, respectively. The results of intra-day and inter-day precision were found to be within the value of ~ 4%. The absolute extraction recoveries of MGN from rat plasma samples were observed to be in the range of ~ 95.2–96.6%, respectively. After freeze-thaw cycles, the MGN demonstrated excellent stability, and the variation content of MGN was found to be ~ 8%. At the end of short-term and long-term stability studies, the MGN appeared to be stable.

The variation of MGN content was found to be ~ 7 and 16%, respectively.

Pharmacokinetic analysis

The mean plasma concentration time profile obtained following oral administration of MGN SNPs (60 mg/kg, p.o.) or MPLC SNPs (60 mg/kg of MGN, p.o.) to a group of animals is shown in (Fig. 13). The MGN SNPs displayed C_{max} (0.3 µg/mL) within 1 h, following which there was a consistent decrease in mean plasma concentration up to 10 h. In contrast to this, the MPLC SNPs demonstrated C_{max} (0.95 µg/mL) within 1 h. The MGN concentration further increased to 1.3 µg/mL at 2 h. However, beyond this period, the MGN plasma concentration decreased at a much slower rate up to 10 h. From this observation, it is clear that the MPLC SNPs increased the MGN plasma concentration to a great extent, compared with the MGN SNPs. This observation validated our original objective of improving the biopharmaceutical profile of MGN significantly.

The obtained pharmacokinetic data were analyzed using the WinNonlin® (Version 4.1, Certara USA Inc., Princeton, NJ, USA) software. The detailed analyses are shown in Table 6. The orally administrated MPLC SNPs (dose: 60 mg/kg of MGN, p.o.) displayed a higher C_{max} (1.32 µg/mL), T_{max} (2.0 h), and $AUC_{0-\infty}$ (7.3 µg mL⁻¹ h) compared with the MGN SNPs. Likewise, the elimination half-life value ($t_{1/2el}$) was also found to be higher around 3.22 h for MPLC SNPs compared with MGN SNPs. Moreover, the clearance (Cl/F), elimination rate constant (K_{el}), and volume of distribution (V_z/F) for MPLC SNPs were found to be lowered around 9.39 µg mL⁻¹ h⁻¹, 0.191 h⁻¹, and 43.64 L, respectively, compared with the MGN SNPs. The calculated bioavailability value (F) for MPLC SNPs was 53.29%. Based on the differences in pharmacokinetic parameters for both formulations, it indicates that MPLC SNPs significantly modified the MGN due to complexation with Phospholipon® 90H along with the nanoformulation.

Stability studies

The results of long-term stability studies are shown in Table 7. As seen in the table, the MPLC SNPs at both temperature of 25 and 4 °C demonstrated no significant change in the particle size, PDI, zeta potential, and entrapment efficiency of final formulation, indicating the presence of sucrose at 2% w/w as a cryoprotectant in lyophilized formulation could enhance the stability of the formulation. This result also suggested that the molecularly interacted MGN with the polar head of Phospholipon® 90H in lyophilized MPLC SNPs formulations could increase their affinity toward each other as well as the lipophilicity of MPLC, thus, enhancing the stability of MPLC SNPs.

Conclusions

The developed self-assembled MPLC SNPs using a combination of solvent evaporation and nanoprecipitation method significantly improved the aqueous solubility, in vitro dissolution rate, oral bioavailability, and in vivo antioxidant potential of MGN. The characterization studies confirmed the formation of MPLC and MPLC SNPs through the contribution of weak intermolecular forces of interactions, such as H-bonding, ion-dipole forces, van der Waals forces, etc., between the polar parts of MGN and the Phospholipon® 90H. The MPLC SNPs exhibited a smaller particle size and favorable zeta potential, indicating its suitability for oral administration. Overall, the MPLC and MPLC SNPs drastically enhanced the aqueous solubility (~32-fold and ~39-fold) of MGN compared with the MGN SNPs. The results of the in vitro dissolution studies showed that MPLC SNPs significantly enhanced the rate and extent of MGN release via burst and then sustained release about ~98% at the end of the 12-h dissolution testing, over to that of MGN SNPs. The MPLC SNPs exhibited a higher rate and extent of permeation around ~97%, compared with the MGN SNPs. The in vivo antioxidant potential of MPLC SNPs was enhanced significantly ($p < 0.001$) in the CCl₄-induced hepatotoxicity in rats when compared with the MGN SNPs. Moreover, the MPLC SNPs (dose: 60 mg/kg of MGN, p.o.) improved the oral bioavailability considerably over MGN SNPs. The final formulation demonstrated an excellent antioxidant potential in vivo by offering significant restoration of the hepatic cellular microenvironment. Overall, the promising results evidenced that the developed self-assembled MPLC SNPs offered an effective nanovesicle delivery system for enhancing the biopharmaceutical and in vivo antioxidant potential of MGN.

Acknowledgments The corresponding author is thankful to Dr. Milind J. Umekar, Principal, Smt. Kishoritai Bhoyar College of Pharmacy, New Kamptee, Nagpur, for providing instrument facilities to complete this research work. The author is also thankful to Dr. Shirish P. Jain,

Principal, Rajarshi Shahu College of Pharmacy, Buldhana, for constant financial and technical support to complete this manuscript on time.

Author contribution Darshan Telange: conceptualization, investigation, methodology, writing of the original draft, writing the review, and editing

Nazish Sohail: methodology, investigation, and data curation

Atul Hemke: validation and data curation

Prashant Kharkar: investigation, methodology, and writing of the original draft

Anil Pethe: conceptualization, supervision, investigation, and visualization

Funding information The current research work did not receive any funding from government agencies.

Compliance with ethical standards

Conflict of interest The authors declared that they have no conflict of interest.

Ethical approval The Institutional Animal Ethical Committee (IAEC) of Smt. Kishoritai Bhoyar College of Pharmacy, New Kamptee, Nagpur, sanctioned and approved the experimental protocols (*SKBCOP/IAEC/2017–2018, dated August 13, 2018*) for the current study. The studies were carried out according to the ethical guidelines available by the Committee for Purpose of Control and Supervision of Experiments on Animals (CPCSEA).

References

1. Yoshimi N, Matsunaga K, Katayama M, Yamada Y, Kuno T, Qiao Z, et al. The inhibitory effects of mangiferin, a naturally occurring glucosyl xanthone, in bowel carcinogenesis of male F344 rats. *Cancer Lett.* 2001;163(2):163–70. [https://doi.org/10.1016/s0304-3835\(00\)00678-9](https://doi.org/10.1016/s0304-3835(00)00678-9).
2. Yoshikawa M, Ninomiya K, Shimoda H, Nishida N, Matsuda H. Hepatoprotective and antioxidative properties of *Salacia reticulata*: preventive effects of phenolic constituents on CCl₄-induced liver injury in mice. *Biol Pharm Bull.* 2002;25:72–6. <https://doi.org/10.1248/bpb.25.72>.
3. Das J, Ghosh J, Roy A, Sil PC. Mangiferin exerts hepatoprotective activity against D-galactosamine induced acute toxicity and oxidative/nitrosative stress via Nrf2-NFκB pathways. *Toxicol Appl Pharmacol.* 2012;260:35–47. <https://doi.org/10.1016/j.taap.2012.01.015>.
4. Imran M, Arshad MS, Butt MS, Kwon JH, Arshad MU, Sultan MT. Mangiferin: a natural miracle bioactive compound against lifestyle-related disorders. *Lipids Health Dis.* 2017;16:1–17. <https://doi.org/10.1186/s12944-017-0449-y>.
5. Moreira RRD, Carlos IZ, Vilegas W. Release of intermediate reactive hydrogen peroxide by macrophage cells activated by natural products. *Biol Pharm Bull.* 2002;24:201–4. <https://doi.org/10.1248/bpb.24.201>.
6. Ghosh J, Das J, Manna P, Sil PC. The protective role of arjunolic acid against doxorubicin-induced intracellular ROS dependent JNK-p38 and p53-mediated cardiac apoptosis. *Biomaterials.* 2011;32:4857–66. <https://doi.org/10.1016/j.biomaterials.2011.03.048>.
7. Rodeiro I, Delgado R, Garrido G. Effects of a *Mangifera indica* L. stem bark extract and mangiferin on radiation-induced DNA damage in human lymphocytes and lymphoblastoid cells. *Cell Prolif.* 2014;47:48–55. <https://doi.org/10.1111/cpr.12078>.

8. Na L, Zhang Q, Jiang S, Shanshan D, Zhang W, Li Y, et al. Mangiferin supplementation improves serum lipid profiles in overweight patients with hyperlipidemia: a double-blind randomized controlled trial. *Sci Rep*. 2015;5:1–9. <https://doi.org/10.1038/srep10344>.
9. Henca I, Kokotkiewicz A, Luczkiewicz P, Bryla E, Luczkiewicz M, Witkowski JM. Naturally occurring xanthone and benzophenone derivatives exert significant anti-proliferative and proapoptotic effects in vitro on synovial fibroblasts and macrophages from rheumatoid arthritis patients. *Int Immunopharmacol*. 2017;49:148–54. <https://doi.org/10.1016/j.intimp.2017.05.034>.
10. Gelabert-Rebato M, Wiebe JC, Martin-Rincon M, et al. *Mangifera indica* L. leaf extract in combination with luteolin or quercetin enhances vo2peak and peak power output and preserves skeletal muscle function during ischemia-reperfusion in humans. *Front Physiol*. 2018;9:1–15. <https://doi.org/10.3389/fphys.2018.00740>.
11. Gelabert-Rebato M, Wiebe JC, Martin-Rincon M, Galvan-Alvarez V, Curtelin D, Perez-Valera M, et al. Enhancement of exercise performance by 48 hours, and 15-day supplementation with mangiferin and luteolin in men. *Nutrients*. 2019;11:2–24. <https://doi.org/10.3390/nu11020344>.
12. Yang Z, Weian C, Susu H, Hamim W. Protective effects of mangiferin on cerebral ischemia-reperfusion injury and its mechanism. *Eur J Pharmacol*. 2015;771:145–51. <https://doi.org/10.1016/j.ejphar.2015.12.003>.
13. Bhatt L, Sebastian B, Joshi V. Mangiferin protects rat myocardial tissue against cyclophosphamide-induced cardiotoxicity. *J Ayurveda Integr Med*. 2017;8(2):62–7. <https://doi.org/10.1016/j.jaim.2017.04.006>.
14. Szandurk M, Mervid-Lad A, Szelag A. The impact of mangiferin from *belamcanda chinensis* on experimental colitis in rats. *Inflammopharmacology*. 2018;26(2):571–81. <https://doi.org/10.1016/j.jaim.2017.04.006>.
15. Sahu AK, Verma VK, Mutneja E, Malik S, Nag TC, Dinda AK, et al. Mangiferin attenuates cisplatin-induced acute kidney injury in rats mediating modulation of MAPK pathway. *Mol Cell Biochem*. 2019;452(1–2):141–52. <https://doi.org/10.1007/s11010-018-3420-y>.
16. Basheer L, Kerem Z. Interactions between CYP3A4 and dietary polyphenols. *Oxidative Med Cell Longev*. 2015;2015:1–15. <https://doi.org/10.1155/2015/854015>.
17. Khurana RK, Bansal AK, Beg S, Burrow AJ, Katare OP, Singh KK, et al. Enhancing biopharmaceutical attributes of phospholipid complex-loaded nanostructured lipid carriers of mangiferin: systematic development, characterization, and evaluation. *Int J Pharm*. 2017;518:289–306. <https://doi.org/10.1016/j.ijpharm.2016.12.044>.
18. Khurana RK, Gaspar BL, Welsby G, Katare OP, Singh KK, Singh B. Improving the biopharmaceutical attributes of mangiferin using vitamin E-TPGS co-loaded self-assembled phospholipid nano-mixed micellar systems. *Drug Deliv Transl Res*. 2018;8:617–32. <https://doi.org/10.1007/s13346-018-0498-4>.
19. Bhattacharyya S, Majhi S, Saha BP, Mukherjee PK. Chlorogenic acid – phospholipid complex improve protection against UVA-induced oxidative stress. *J Photochem Photobiol B Biol*. 2014;130:293–8. <https://doi.org/10.1016/j.jphotobiol.2013.11.020>.
20. Wang Q, Yang J, Cui W, Chen L, Lv F, Wen X, et al. Pharmacokinetic study of major bioactive components in rats after oral administration of extract of *Ilex hainanensis* by high-performance liquid chromatography/electrospray ionization mass spectrometry. *J Pharm Biomed Anal*. 2013;77:21–8. <https://doi.org/10.1016/j.jpba.2013.01.011>.
21. Ferreira F d R, Valentim IB, Ramones ELC, Trevisan MTS, Olea-Azar C, Perez-Cruz F, et al. Antioxidant activity of the mangiferin inclusion complex with β -cyclodextrin. *LWT Food Sci Technol*. 2013;51:129–34. <https://doi.org/10.1016/j.lwt.2012.09.032>.
22. Yang X, Zhao Y, Chen Y, Liao X, Gao C, Xiao D, et al. Host-guest inclusion system of mangiferin with β -cyclodextrin and its derivatives. *Mater Sci Eng C Mater Biol Appl*. 2013;33:2386–91. <https://doi.org/10.1016/j.msec.2013.02.002>.
23. Wang C, Jiang JD, Wu W, Kong WJ. The compound of mangiferin-berberine salt has potent activities in modulating lipid and glucose metabolisms in HepG2 cells. *Biomed Res Int*. 2016;2016:1–14. <https://doi.org/10.1155/2016/8753436>.
24. Liu R, Liu Z, Zhang C, Zhang B. Nanostructured lipid carriers as a novel ophthalmic delivery system for mangiferin: improving in vivo ocular bioavailability. *J Pharm Sci*. 2012;101(10):3833–44. <https://doi.org/10.1002/jps.23251>.
25. de Souza JRR, Feitosa JPA, Ricardo NMPS, Trevisan MTS, de Paula HCB, Ulrich CM, et al. Spray-drying encapsulation of mangiferin using natural polymers. *Food Hydrocoll*. 2013;33:10–8. <https://doi.org/10.1016/j.foodhyd.2013.02.017>.
26. Zhou Y, Dong W, Ye J, Hao H, Zhou J, Wang R, et al. A novel matrix dispersion based on phospholipid complex for improving oral bioavailability of baicalin: preparation, in vitro and in vivo evaluations. *Drug Deliv*. 2017;24:720–8. <https://doi.org/10.1080/10717544.2017.1311968>.
27. Zhang Z, Huang Y, Gao F, Bu H, Gu W, Li Y. Daidzein-phospholipid complex loaded lipid nanocarriers improved oral absorption: in vitro characteristics and in vivo behavior in rats. *Nanoscale*. 2011;3:1780–7. <https://doi.org/10.1039/c0nr00879f>.
28. Zhang WL, Cui Y, Fan Y-Q, Yang J-K, Liu P, Liu J-P, et al. Bioavailability, and foam cells permeability enhancement of salvianolic acid B pellets based on drug-phospholipids complex technique. *Eur J Pharm Biopharm*. 2012;83:76–86. <https://doi.org/10.1016/j.ejpb.2012.09.021>.
29. Telange DR, Patil AT, Pethe AM, Tatode AA, Anand S, Dave VS. Kaempferol-phospholipid complex: formulation, and evaluation of improved solubility, in vivo bioavailability, and antioxidant potential of kaempferol. *J Excipients Food Chem*. 2016;7(4):89–120.
30. Telange DR, Patil AT, Pethe AM, Fegade H, Anand S, Dave VS. Formulation and characterization of an apigenin-phospholipid phytosome (APLC) for improved solubility, in vivo bioavailability, and antioxidant potential. *Eur J Pharm Sci*. 2017;108:36–49. <https://doi.org/10.1016/j.ejps.2016.12.009>.
31. Citernes U, Sciacchitano M. Phospholipids/active ingredient complexes. *Cosm Toil*. 1995;110:57–68.
32. Bhattacharya S. Phytosomes: emerging strategy in the delivery of herbal drugs and nutraceuticals. *Pharma Times*. 2009;41:9–12.
33. Fahy E, Subramanian S, Brown HA. A comprehensive classification system for lipids. *J Lipid Res*. 2005;46:839–61. <https://doi.org/10.1194/jlr.E400004-JLR200>.
34. Renukuntla J, Vadlapudi AD, Patel A, Boddu SHS, Mitra AK. Approaches for enhancing oral bioavailability of peptides and proteins. *Int J Pharm*. 2013;447:75–93. <https://doi.org/10.1016/j.ijpharm.2013.02.030>.
35. Constantinides PP, Chaubal MV, Shorr R. Advances in lipid nanodispersions for parenteral drug delivery and targeting. *Adv Drug Deliv Rev*. 2008;60(6):757–67. <https://doi.org/10.1016/j.addr.2007.10.013>.
36. Kidd PM. Bioavailability and activity of phytosome complexes from botanical polyphenols: the silymarin, curcumin, green tea, and grape seed extracts. *Altern Med Rev*. 2009;14(3):226–46.
37. L. Bildstein, C. Dubernet, P. Couvreur, Prodrug-based intracellular delivery of anticancer agents. *Adv. Drug Delivery Rev*. 63 (1–2)(2011) 3–23. doi: <https://doi.org/10.1016/j.addr.2010.12.005>.
38. Bombardelli E. Phytosome: new cosmetic delivery system. *Boll Chim Farm*. 1991;130(11):431–8.

39. Peer D, Karp J, Hong S, et al. Nanocarriers as an emerging platform for cancer therapy. *Nat Nanotech.* 2007;2:751–60. <https://doi.org/10.1038/nnano.2007.387>.
40. Soussan E, Cassel S, Blanzat M, Rico-Lattes I. Drug delivery by soft matter: matrix and vesicular carriers. *Angew Chem Int Ed.* 2009;48(2):274–88. <https://doi.org/10.1002/anie.200802453>.
41. Pathan RA, Bhandari U. Preparation and characterization of the embelin-phospholipids complex as effective drug delivery tool. *J Incl Phenom Macrocycl Chem.* 2011;69:139–47. <https://doi.org/10.1007/s10847-010-9824-2>.
42. Singh RP, Gangadharappa HV, Mruthunjaya K. Phospholipids: unique carriers for drug delivery systems. *J Drug Deliv Sci Technol.* 2017;39:166–79. <https://doi.org/10.1016/j.jddst.2017.03.027>.
43. Cullis PR, De Kruijff B. Lipid polymorphism and the functional roles of lipids in biological membranes. *Biochim Biophys Acta.* 1979;559:399–420. [https://doi.org/10.1016/0304-4157\(79\)90012-1](https://doi.org/10.1016/0304-4157(79)90012-1).
44. Yang R, Zhang X, Li F. Role of phospholipids and copolymers in enhancing stability and controlling degradation of intravenous lipid emulsions. *Colloid Surf A Physicochem Eng Asp.* 2013;436:434–42. <https://doi.org/10.1016/j.colsurfa.2013.07.022>.
45. Hou Z, Li Y, Huang Y, Zhou C, Lin J, Wang Y, et al. Phytosomes loaded with mitomycin C-soybean phosphatidylcholine complex developed for drug delivery. *Mol Pharm.* 2013;10:90–101. <https://doi.org/10.1021/mp300489p>.
46. Cai X, Luan Y, Jiang Y, Song A, Shao W, Li Z, et al. Huperzine A-phospholipid complex-loaded biodegradable thermosensitive polymer gel for controlled drug release. *Int J Pharm.* 2012;433:102–11. <https://doi.org/10.1016/j.ijpharm.2012.05.009>.
47. Zhang J, Tang Q, Xu X, Li N. Development and evaluation of a novel phytosome-loaded chitosan microsphere system for curcumin delivery. *Int J Pharm.* 2013;448:168–74. <https://doi.org/10.1016/j.ijpharm.2013.03.021>.
48. Telange DR, Nirgulkar SB, Umekar MJ, Patil AT, Pethe AM, Bali NR. Enhanced transdermal permeation and anti-inflammatory potential of phospholipids complex-loaded matrix film of umbelliferone: formulation development, physicochemical and functional characterization. *Eur J Pharm Sci.* 2019;131:23–38. <https://doi.org/10.1016/j.ejps.2019.02.006>.
49. Singh D, Rawat M, Semalty A, Semalty M. Rutin-phospholipid complex: an innovative technique in novel drug delivery system-NDDS. *Curr Drug Deliv.* 2012;9:305–14.
50. Singh D, Rawat MSM, Semalty A, Semalty M. Chrysophanol-phospholipid complex. *J Therm Anal Calorim.* 2012;111:2069–77. <https://doi.org/10.1007/s10973-012-2448-6>.
51. Jin C, Zhang Z, Xia H, Hu, Jia X. A novel phospholipid complex enriched with micelles: preparation and evaluation in vitro and in vivo. *Int J Nanomedicine.* 2013;545. <https://doi.org/10.2147/ijn.s39526>.
52. Tan Q, Liu S, Chen X, Wu M, Wang H, Yin H, et al. Design and evaluation of a novel evodiamine-phospholipid complex for improved oral bioavailability. *AAPS PharmSciTech.* 2012;13:534–47. <https://doi.org/10.1208/s12249-012-9772-9>.
53. Alam S, Panda JJ, Chauhan VS. Novel dipeptide nanoparticles for effective curcumin delivery. *Int J Nanomedicine.* 2012;7:4207–22. <https://doi.org/10.2147/IJN.S33015>.
54. Shadab MD, Khan RA, Mustafa G, Chuttani K, Baboota S, Sahni JK, et al. Bromocriptine loaded chitosan nanoparticles intended for a direct nose to brain delivery: pharmacodynamic, pharmacokinetic and scintigraphy study in mice model. *Eur J Pharm Sci.* 2013;48:393–405. <https://doi.org/10.1016/j.ejps.2012.12.007>.
55. Telange DR, Wavare KD, Patil AT, Umekar MJ, Anand S, Dave VS. Drug-phospholipid complex-loaded matrix film formulation for enhanced transdermal delivery of quercetin. *J Excipients Food Chem.* 2018;9(2):31–50.
56. Dave V, Telange D, Denge R, Patil A, Umekar M, Gupta SV. Pentaerythritol as an excipient/solid-dispersion carrier for improved solubility and permeability of ursodeoxycholic acid. *J Excipients Food Chem.* 2018;9:80–95.
57. Telange DR, Bhagat SB, Patil AT, Umekar MJ, Pethe AM, Raut NA, et al. Glucosamine HCL-based solid dispersions to enhance the biopharmaceutical properties of acyclovir. *J Excipients Food Chem.* 2019;10:65–81.
58. Maiti K, Mukherjee K, Murugan V, Saha BP, Mukherjee PK. Exploring the effect of hesperetin-HSPC complex-a novel drug delivery system on the in vitro release, therapeutic efficacy and pharmacokinetics. *AAPS PharmSciTech.* 2009;10:943–50. <https://doi.org/10.1208/s12249-009-9282-6>.
59. Dixit P, Jain DK, Dumbwani J. Standardization of an ex vivo method for determination of intestinal permeability of drugs using everted rat intestine apparatus. *J Pharmacol Toxicol Methods.* 2012;65:13–7. <https://doi.org/10.1016/j.vascn.2011.11.001>.
60. Hamilton KL, Butt AG. Glucose transport into everted sacs of the small intestine of mice. *Adv Physiol Educ.* 2013;37:415–26. <https://doi.org/10.1152/advan.00017.2013>.
61. Bhattacharyya S, Ahmed SM, Saha BP, Mukherjee PK. Soya phospholipids complex of mangiferin enhances its hepatoprotectivity by improving its bioavailability and pharmacokinetics. *J Sci Food Agric.* 2014;94:1380–8. <https://doi.org/10.1002/jsfa.6422>.
62. Reitman S, Frankel S. A colorimetric method for the determination of serum glutamic oxalacetic and glutamic pyruvic transaminases. *Am J Clin Pathol.* 1957;28(1):56–63.
63. Kind PR, King EJ. Estimation of plasma phosphatase by determination of hydrolyzed phenol with amino-antipyrine. *J Clin Pathol.* 1954;7:322–6. <https://doi.org/10.1136/jcp.7.4.322>.
64. Malloy HT, Evelyn KA. The determination of bilirubin with the photoelectric colorimeter. *J Biol Chem.* 1937;119:481–90.
65. Ellman GL. Tissue sulfhydryl groups. *Arch Biochem Biophys.* 1959;82:70–7.
66. Marklund S, Marklund G. Involvement of the superoxide anion radical in the autoxidation of pyrogallol and a convenient assay for superoxide dismutase. *Eur J Biochem.* 1974;47:469–74. <https://doi.org/10.1111/j.1432-1033.1974.tb03714.x>.
67. Stocks J, Dormandy TL. The autoxidation of human red cell lipids induced by hydrogen peroxide. *Br J Haematol.* 1971;20:95–111. <https://doi.org/10.1111/j.1365-2141.1971.tb00790.x>.
68. Beers RF, Sizer IW. A spectrophotometric method for measuring the breakdown of hydrogen peroxide by catalase. *J Biol Chem.* 1952;195(1):133–40.
69. Chen ZP, Sun J, Chen HX, Xiao YY, Liu D, Chen J, et al. Comparative pharmacokinetics and bioavailability studies of quercetin, kaempferol and isorhamnetin after oral administration of Ginkgo biloba extracts, Ginkgo biloba extract phospholipid complexes and Ginkgo biloba extract solid dispersions in rats. *Fitoterapia.* 2010;81:1045–52. <https://doi.org/10.1016/j.fitote.2010.06.028>.
70. Zhang Q, Sun X, Peng Q, Shi S, Gong T, Zhang J. Preparation, characterization, and in vivo evaluation of a self-nano emulsifying drug delivery system (SNEDDS) loaded with morin-phospholipid complex. *Int J Nanomedicine.* 2011;3405. <https://doi.org/10.2147/ijn.s25824>.
71. Semalty A, Semalty M, Singh D, Rawat MSM. Development and physicochemical evaluation of pharmacosomes of diclofenac. *Acta Pharma.* 2009;59:335–44. <https://doi.org/10.2478/v10007-009-0023-x>.
72. Saoji SD, Belgamvar VS, Dharashivkar SS, Rode AA, Mack C, Dave VS. The study of the influence of formulation and process variables on the functional attributes of simvastatin-phospholipids complex. *J Pharm Innov.* 2016;11:264–78. <https://doi.org/10.1007/s12247-016-9256-7>.

73. Lefevre ME, Olivo R, Vanderhoff JW, Joel ADD. Accumulation of latex in Peyer's patches and its subsequent appearance in villi and mesenteric lymph nodes. *Proc Soc Exp Biol Med.* 1978;159:298–302.
74. Savić R, Luo L, Eisenberg A, Maysinger D. Micellar nanocontainers distribute to defined cytoplasmic organelles. *Science.* 2003;300:615–8. <https://doi.org/10.1126/science.1078192>.
75. Mazumdar A, Dwivedi A, Du Preez JL, du Plessis J. In vitro wound healing and cytotoxic effects of sinigrin - phytosomes complex. *Int J Pharm.* 2016;498:283–93. <https://doi.org/10.1016/j.ijpharm.2015.12027>.
76. Pate K, Safier P. Chemical metrology methods for CMP quality. *Adv Chem Mech Planazn.* 2016;299–325. <https://doi.org/10.1016/B978-0-08-100165-3.00012-7>.
77. Howard MD, Lu X, Jay M, Dziubla TD. Optimization of the lyophilization process for long-term stability of solid lipid nanoparticles. *Drug Dev Ind Pharm.* 2012;38(10):1270–9. <https://doi.org/10.3109/03639045.2011.645835>.
78. Kamiya S, Nozawa Y, Miyagishima A, Kurita T, Sadzuka Y, Sonobe T. Physical characteristics of freeze-dried griseofulvin lipids nanoparticles. *Chem Pharm Bull.* 2006;54:181–4. <https://doi.org/10.1248/cpb.54.181>.
79. Ohshima H, Miyagishima A, Kurita T, Makino Y, Wao Y, Sonobe T. Freeze-dried nifedipine-lipid nanoparticles with long-term nano-dispersion stability after reconstitution. *Int J Pharm.* 2009;377:180–4. <https://doi.org/10.1016/j.ijpharm.2009.05.004>.
80. Rampino A, Borgogna M, Blasi P, Bellich B, Cesaro A. Chitosan nanoparticles: preparation, size evolution and stability. *Int J Pharm.* 2013;455:219–28. <https://doi.org/10.1016/j.ijpharm.2013.07.034>.
81. Crowe LM, Reid DS, Crowe JH. Is trehalose special for preserving dry biomaterials? *Biophys J.* 1996;71:2087–93. [https://doi.org/10.1016/S0006*3495\(96\)79407-9](https://doi.org/10.1016/S0006*3495(96)79407-9).
82. Franks F. Freeze-drying of bi-products: putting principles into practice. *Eur J Pharm Biopharm.* 1998;45:221–9. [https://doi.org/10.1016/S0939-6411\(98\)00004-6](https://doi.org/10.1016/S0939-6411(98)00004-6).
83. Izutsu KI, Fujimaki Y, Kuwabara A, Aoyagi N. Effect of counterions on the physical properties of L-arginine in frozen solutions and freeze-dried solids. *Int J Pharm.* 2005;301:161–9. <https://doi.org/10.1016/j.ijpharm.2005.05.019>.
84. Ruan J, Liu J, Zhu D, Gong T, Yang F, Hao X, et al. Preparation and evaluation of self-nano emulsified drug delivery systems (SNEDDSs) of matrine based on a drug-phospholipid complex technique. *Int J Pharm.* 2010;386:282–90. <https://doi.org/10.1016/j.ijpharm.2009.11.026>.
85. Venema FR, Weringa WD. The interactions of phospholipid vesicles with some anti-inflammatory agents. *J Colloid Interface Sci.* 1988;125(2):484–92.
86. Lasonder E, Weringa WD. An NMR and DSC study of the interaction of phospholipid vesicles with some anti-inflammatory agents. *J Colloid Interface Sci.* 1990;139:469–78. [https://doi.org/10.1016/0021-9797\(90\)90119-9](https://doi.org/10.1016/0021-9797(90)90119-9).
87. Dhore PW, Dave VS, Saoji SD, Bobde YS, Mack C, Raut NA. Enhancement of aqueous solubility and permeability of poorly water-soluble drug ritonavir via lyophilized milk-based solid dispersions. *Pharm Dev Technol.* 2017;22(1):90–102. <https://doi.org/10.1080/10837450.2016.1193193>.
88. Zhang WJ, Yang M, Zhu WF, Yue PF, Cai PL, Yuan HL, et al. Process optimization, characterization and pharmacokinetic evaluation in rats of ursodeoxycholic acid-phospholipids complex. *AAPS PharmSciTech.* 2008;9:322–9. <https://doi.org/10.1208/s12249-088-9040-1>.
89. Hara H, Ise Y, Morimota N, Shimazawa M, Ichihashi K, Ohyama M, et al. Laxative effects of agawood leaves and its mechanism. *Biosci Biotechnol Biochem.* 2008;72(2):335–45. <https://doi.org/10.1271/bbb.70361>.
90. Sharma S, Roy RR, Shrivastava B. Antiproliferative effect of phytosome complex of methanolic extract of terminalia arjuna bark on human breast cancer cell lines (MCF-7). *Int J Drug Dev Res.* 2015;7(1):173–82.
91. van der Merwe JD, Joubert E, Manley M, de Beer D, Malherbe CJ, Gelderblom WCA. Mangiferin glucuronidation: important hepatic modulation of antioxidant activity. *Food Chem Toxicol.* 2012;50:808–15. <https://doi.org/10.1016/j.fct.2011.11.018>.
92. Perrut M, Jung J, Leboeuf F. Enhancement of dissolution rate of poorly soluble active ingredients by supercritical fluid processes. *Int J Pharm.* 2004;288:3–10. <https://doi.org/10.1016/j.ijpharm.2004.09.007>.
93. Costa P, Manuel J, Lobô S. Modeling, and comparison of dissolution profiles. *Eur J Pharm Sci.* 2001;13:123–33.
94. Nicolson GL. The fluid—mosaic model of membrane structure: still relevant to understanding the structure, function, and dynamics of biological membranes after more than 40 years. *Biochim Biophys Acta.* 2014;1838(6):1451–66. <https://doi.org/10.1016/j.bbmem.2013.10.019>.
95. Soma CE, Dubernet C, Barratt G, Benita S, Couvreur P. Investigation of the role of macrophages on the cytotoxicity of doxorubicin and doxorubicin-loaded nanoparticles on M5076 cells in vitro. *J Control Release.* 2008;68(2):283–9. [https://doi.org/10.1016/s0168-3659\(00\)00269-8](https://doi.org/10.1016/s0168-3659(00)00269-8).
96. Partlow KC, Lanza GM, Wickline SA. Exploiting lipid raft transport with membrane-targeted nanoparticles: a strategy for cytosolic drug delivery. *Biomaterials.* 2008;29(23):3367–75. <https://doi.org/10.1016/j.biomaterials.2008.04.030>.
97. Xiong XB, Huang Y, Lu WL, Zhang X, Zhang H, Nagai T. Enhanced intracellular delivery and improved antitumor efficacy of doxorubicin by sterically stabilized liposomes modified with a synthetic RGD mimetic. *J Control Release.* 2005;107(2):262–75. <https://doi.org/10.1016/j.jconrel.2005.03.030>.
98. Guo Y, Terazzi E, Seemann R, Fleury RB, Baulin VA. Direct proof of spontaneous translocation of lipid covering hydrophobic nanoparticles through a phospholipids bilayer. *Sci Adv.* 2016;2(11):1–10. <https://doi.org/10.1126/sciadv.1600261>.
99. Contini C, Schneemilch M, Gaisford S, Quirke N. Nanoparticle-membrane interactions. *J Exp Nanosci.* 2018;13(1):62–81. <https://doi.org/10.1080/17458080.2017.1413253>.
100. Recknagel RO, Glende EA, Dolak JA, Waller RL. Mechanisms of carbon tetrachloride toxicity. *Pharmacol Ther.* 1989;43:139–54. [https://doi.org/10.1016/0163-7258\(89\)90050-8](https://doi.org/10.1016/0163-7258(89)90050-8).
101. Glende EA, Hruszewycz AM, Recknagel RO. Critical role of lipid peroxidation in carbon tetrachloride-induced loss of aminopyrine demethylase, cytochrome P-450, and glucose-6-phosphatase. *Biochem Pharmacol.* 1976;25:2163–70. [https://doi.org/10.1016/0006-2952\(76\)90128-3](https://doi.org/10.1016/0006-2952(76)90128-3).
102. Kim HJ, Bruckner JV, Dallas CE, Gallo GM. Effects of dosing vehicles on the pharmacokinetics of orally administered carbon tetrachlorides in rats. *Toxicol Appl Pharmacol.* 1990;102:50–60. [https://doi.org/10.1016/0041-008x\(90\)90082-6](https://doi.org/10.1016/0041-008x(90)90082-6).
103. Valles EG, De Castro CR, De Castro JA. N-Acetylcysteine is an early but also a late preventive agent against carbon tetrachloride-induced liver necrosis. *Toxicol Lett.* 1994;71:87–95. [https://doi.org/10.1016/0378-4274\(94\)90202-x](https://doi.org/10.1016/0378-4274(94)90202-x).

Publisher's note Springer Nature remains neutral with regard to jurisdictional claims in published maps and institutional affiliations.



LIPOID SPC-3-Based Coprecipitates for the Enhancement of Aqueous Solubility and Permeability of Ranolazine

Darshan R. Telange¹ · Sarita A. Ukey² · Atul T. Hemke² · Milind J. Umekar² · Anil M. Pethe³ · Prashant S. Kharkar⁴

© Springer Science+Business Media, LLC, part of Springer Nature 2020

Abstract

Purpose The study was aimed at exploring the feasibility of LIPOID SPC-3 as a coprecipitate carrier to enhance the aqueous solubility and permeability of ranolazine, a BCS class II drug.

Methods LIPOID SPC-3-based coprecipitates of ranolazine (RNZ-SPC-CP) were developed using the solvent method. The developed formulation was physico-chemically characterized using scanning electron microscopy (SEM), differential scanning calorimetry (DSC), Fourier transform infrared spectroscopy (FT-IR), powder x-ray diffractometry (PXRD), and drug content. Functional evaluation of RNZ-SPC-CP formulations was carried out by solubility analysis, in vitro dissolution studies, fed vs. fasted state dissolution comparison, and ex vivo permeation studies.

Results The SEM studies revealed dissimilar morphological characteristics of pure ranolazine, LSPC-3, and RNZ-SPC-CP formulations. The physico-chemical analysis confirmed the formation of the coprecipitate. Optimized RNZ-SPC-CP1 demonstrated a noteworthy increase (~18-fold) in water solubility (92.23 ± 1.02 µg/mL) over that of pure ranolazine (4.94 ± 0.06 µg/mL) and physical mixture (PM) (30.21 ± 2.12 µg/mL). Optimized RNZ-SPC-CP1 appreciably enhanced the rate and extent of ranolazine dissolution (~85%), compared with that of pure ranolazine (~21%) and PM (~35%). Similarly, the permeation rate of ranolazine from optimized RNZ-SPC-CP1 formulation was found to be enhanced significantly (~83%) over that of pure ranolazine (~19%) and PM (~32%). In the fed state, the RNZ-SPC-CP1 improved the rate and extent of ranolazine dissolution, compared with those of fasted state dissolution.

Conclusions The results conclude that RNZ-SPC-CP could be used as a promising approach for enhancing the aqueous solubility and permeation rate of ranolazine.

Keywords Coprecipitates · Dissolution · Permeability · Phospholipids · Solubility

Introduction

Ranolazine (IUPAC name: *N*-(2,6-dimethyl phenyl)-2-[4-[2-hydroxy-3-(2-methoxy phenoxy) propyl]-propyl] piperazine-

acetamide]), a piperazine derivative, is used predominantly for the management of chronic stable angina pectoris (CSAP). It is a selective sodium channel blocker, which inhibits the late phase of Na⁺ current in ischemia [1]. Upon oral administration, ranolazine produces a low and variable pharmacokinetic profile, resulting in poor oral bioavailability (i.e., ~35 to 50%). This is mainly attributed to its shorter half-life (~2 to 6 h), rapid clearance (>70%), and rapid hepatic first-pass metabolism by cytochrome P-450 3A (CYP3A) and CYP2D6, respectively [2–4]. Moreover, it is categorized as a Biopharmaceutics Classification System (BCS) class II drug, which exhibits low solubility and high permeability [5]. Earlier published reports have also shown that ranolazine plasma concentration is highly undesirable and fluctuate following oral administration [2]. Therefore, a unique formulation approach is strongly needed to improve the solubility, dissolution rate, permeability, and oral bioavailability of ranolazine.

✉ Darshan R. Telange
telange.darshan@gmail.com

¹ Department of Nanoscience and Nanotechnology, Rajarshi Shahu College of Pharmacy, Malvihir, Botha Road, Buldhana, Maharashtra, India

² Department of Pharmaceutics, Smt. Kishoritai Bhoyar College of Pharmacy, New Kamptee, Nagpur, Maharashtra, India

³ Department of Pharmaceutics, School of Pharmacy & Technology Management, NMIMS (Deemed to Be University), Hyderabad Campus, Hyderabad, Telangana, India

⁴ Department of Pharmaceutical Sciences and Technology, Institute of Chemical Technology, Mumbai, Mumbai, Maharashtra, India

Previous reports showed that a very few formulations have been developed and explored by scientists for improving the solubility and permeability of ranolazine. These include sustained-release tablets [2], extended-release tablets [6], microparticles [7], floating microsphere [8], and extended-release tablets [9]. Following a review of these reports, it was found that the author only reduced the dosing frequency and improved patient compliance without investigating the solubility, permeability, and systematic evaluation of ranolazine. Hence, to address this significant issue, we employed a novel and suitable formulation strategy and/or approach to improve the biopharmaceutical attributes of ranolazine.

Among all formulation approaches, the phospholipid-based coprecipitate approach is found to be a distinctive one for improving the solubility and permeability of BCS class II drugs. Previous literature has evidenced that the coprecipitate strategy significantly improved the solubility and dissolution rate of probenecid [10], indomethacin [11], carbamazepine [12], and ibuprofen [13]. Moreover, the combination of phospholipids, i.e., LIPOID SPC-3, and solvent evaporation method physico-chemically modifies the particles of the drug into coprecipitates, leading to enhancement of the biopharmaceutical properties of ranolazine. Coprecipitates are amorphous solid dispersion prepared by the solvent evaporation method [14]. This approach has created tremendous interest among scientists due to multiple benefits like controlled and rapid release, increased therapeutic efficacy, prevention of thermal decomposition of the drug and carrier, improved particle size and their composition, simple and easy preparation, and improved dissolution rate of BCS class II drugs in a lower concentration of phospholipids. LIPOID SPC-3 (free flow and non-sticky lipid) phospholipids are used in the present study, and these are reported to enhance the biopharmaceutical properties of plant bioactive and/or drug molecules [15]. The amphiphilic property of this lipid (both water- and lipid-soluble portions) entraps the drug within itself, forming a complex, and thereby improves the aqueous solubility, dissolution rate, and permeability of the drug via facilitating its transportation across the biological membrane (6. 1). The complex is also reported to enhance the poor bioavailability of drugs by inducing the alteration in the target cell membrane structure and by changing the polarity of drug molecules [16]. The liposome- and phytosome-forming ability of phospholipids entraps and/or sequesters the drug molecules within the bilayer structure during the dissolution process and further improves drug dissolution by transporting the drug to the diffusion layer, then to the bulk solution, and then to the site of absorption for rapid release of the drug to the blood circulation [17, 18]. Moreover, the phase transition (T_c) temperature of these phospholipids being lower than the experimental temperature, i.e., 37 °C, makes them disperse spontaneously when coming in contact with water, which results in an increase in

the dissolution rate of the drug. Also, the phospholipids containing a negative charge of the phosphate group can make a strong electrostatic complex with the positive charge of drug molecules, resulting in an increase of the dissolution rate of drugs with poor bioavailability [9, 10]. Besides these advantageous effects, these phospholipids also exhibit high compatibility, biodegradability, metabolic activity, and low toxicity over other lipids, representing them as the most appropriate carrier for the development of coprecipitates. This approach has been successfully used and explored for the only liposome-forming phospholipids such as L- α -dimyristoyl phosphatidylcholine (DMPC), L- α -dimyristoyl phosphatidylglycerol (DMPG), L- α -distearoyl phosphatidylcholine (DSPC), and egg phosphatidylcholine (EPC); however, the same approach is found to be lacking and unexplored for phytosome-forming phospholipids, i.e., LIPOID SPC-3, and small molecules with poor aqueous solubility like ranolazine. Additionally, the previous reports are also found to lack a systemic and comprehensive evaluation of physico-chemical and functional characterization of coprecipitate formulations. According to this, the current work was undertaken, to explore the feasibility of LIPOID SPC-3 as a coprecipitate carrier for enhancing the solubility and permeability of ranolazine.

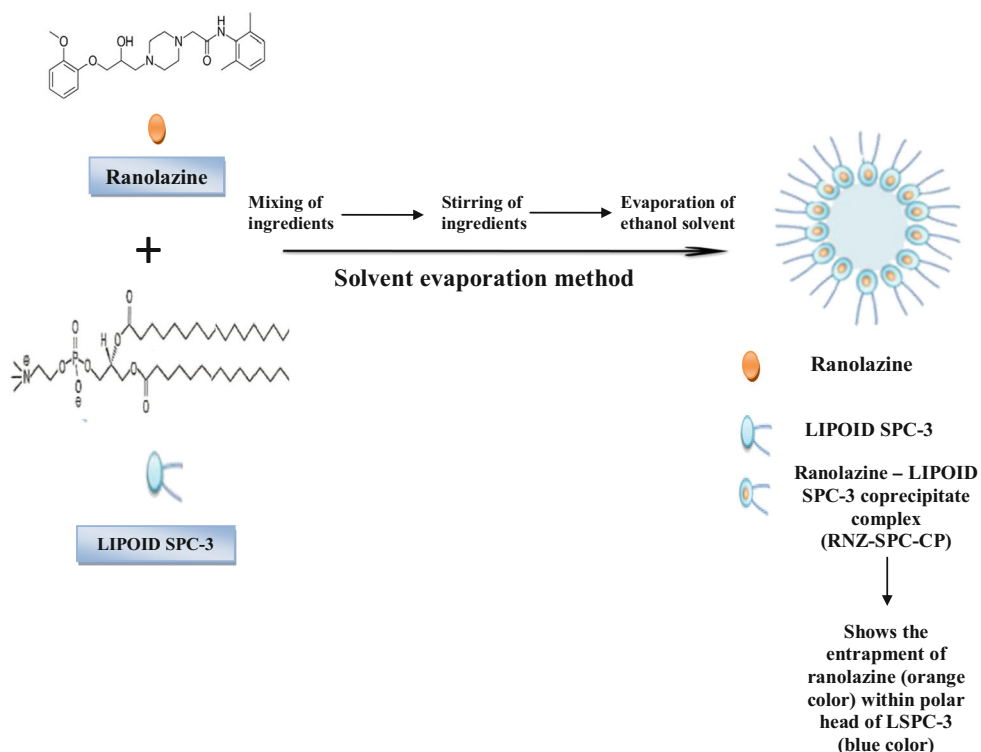
The present research is a “proof-of-concept” type of work, in which we explore the feasibility of LIPOID SPC-3 as a coprecipitate carrier for improving the solubility and permeability of ranolazine. Coprecipitate formulations of ranolazine with LIPOID SPC-3 (RNZ-SPC-CP) were prepared using the solvent evaporation method. The prepared coprecipitates were physically evaluated by particle size, zeta potential, SEM, DSC, FT-IR, powder x-ray diffractometry (PXRD), and drug estimation. Functional characterization was carried out by solubility and in vitro dissolution and ex vivo permeation studies. Moreover, the coprecipitate formulation was also tested for preliminary stability study under the influence of controlled temperature and relative humidity for 6 months.

Materials and Methods

Materials

Ranolazine (purity more than 99.86%) was obtained from Alkem Laboratories Ltd., Mumbai, India. LIPOID SPC-3 was obtained from Lipoid GmbH, Ludwigshafen, Germany. Absolute ethanol, acetone, chloroform, dichloromethane, diethyl ether, and 1,4-dioxane were purchased from Loba Chemicals Pvt., Ltd., Mumbai, India. The remaining ingredients such as potassium bromide, potassium chloride, potassium dihydrogen phosphate, sodium hydroxide, sodium dihydrogen phosphate, and sodium chloride were purchased from Sigma-Aldrich Corporation, St. Louis, MO.

Fig. 1 Schematic diagram representing the entrapment of pure ranolazine within the polar head of LSPC-3 resulting in formation of the RNZ-SPC-CP complex



Preparation of Ranolazine-LIPOID SPC-3 Coprecipitate

The RNZ-SPC-CP was prepared according to stoichiometric ratios (1:1, 1:2, 1:3, 1:4, and 1:5) using a method reported previously [10]. Briefly, the required quantity of ranolazine and LIPOID SPC-3 (LSPC-3) was accurately weighed and transferred into a 50 -mL beaker. The weighed ingredients were mixed and then dissolved in 10 mL of absolute ethanol using a magnetic stirrer until a homogenous solution was achieved. The prepared solution was allowed to evaporate at room temperature, resulting in the formation of a solid mass of RNZ-SPC-CP. The obtained solid mass was collected from the beaker and dried under vacuum at 40 °C for 24 h. The dried RNZ-SPC-CP formulation was sieved and placed into a light-resistant amber-colored glass bottle, flushed with N₂, and finally kept in desiccators for further characterization. The composition of the formulation is shown in Table 1.

Physico-chemical Characterization of Ranolazine-LIPOID SPC-3 Coprecipitate

Scanning Electron Microscopy

The surface characterization of samples such as ranolazine, LSPC-3, and RNZ-SPC-CP was carried out on SEM (model: Supra® 55, Carl Zeiss NTS Ltd., Germany). Briefly, an approximate amount of samples (~ 50 mg) was weighed and then spread as a very thin layer on double-faced carbon tape. The prepared samples were then loaded into a sputter coater

and then coated with a thin layer of gold. After this, the images were captured at suitable magnification using instrument-associated software (SmartSEM®, TV mode). The accelerating voltage throughout the scanning was maintained at 10 kV.

Particle Size and Zeta Potential Analysis

Particle size analysis of RNZ-SPC-CP formulations was carried out by photon cross-correlation spectroscopy (PCCS) with the support of dynamic light scattering (DLS) technology setup as per the method reported by our laboratory [19]. Briefly, the RNZ-SPC-CP formulation with a concentration of ~500 µg/mL in deionized water was prepared and placed into the sample chamber of the analyzer (model: NANOPHOX, Sympatec GmbH, Clausthal-Zellerfeld, Germany). The loaded sample was analyzed for particle size within the sensitivity range of 1 nm to 10 µm via adjusting its suitable optimizing

Table 1 Composition of the prepared ranolazine-LIPOID SPC-3 coprecipitate formulations

Coprecipitates	Drug (mg)	LIPOID SPC-3 (mg)
RNZ-SPC-CP1	100	100
RNZ-SPC-CP2	100	200
RNZ-SPC-CP3	100	300
RNZ-SPC-CP4	100	400
RNZ-SPC-CP5	100	500

count rate position. The results were read by the instrument-associated software.

The prepared dispersion of RNZ-SPC-CP formulations was also employed for the zeta potential analysis using Nano Particle Analyzer (model: NanoPlusTM-2, particulate system, Norcross, GA, USA) equipped with a DLS setup. The sample solution was analyzed in the sensitivity range of -200 to $+200$ mV. The temperature during the entire analysis was set to 25 °C.

Differential Scanning Calorimetry

Samples of formulation components such as ranolazine, LSPC-3, physical mixture (PM) of ranolazine and LSPC-3 (1:1), and prepared RNZ-SPC-CP were analyzed to study their thermal interaction as well as performance using a differential scanning calorimeter (model: DSC-1821e, Mettler Toledo AG, Analytical, Schwerzenbach, Switzerland) as per the procedure described earlier by our groups [20]. Briefly, the individual samples ($\sim 2.0 \pm 0.2$ mg) were accurately weighed and then sealed in an aluminum pan covered with a lid and crimper. After this, the weighed samples were loaded into the DSC instrument that had been previously calibrated concerning heat flow and capacity using standard indium (In). The sample-analyzing chamber was constantly purged with dried nitrogen gas (N_2) at a flow rate of (50 mL/min) to avoid any interference from entrapped moisture. The tested samples were allowed to be heated at a temperature range of 0 to 400 °C at a heating rate of 10 °C/min. DSC thermograms along with their associated heating parameters were read by the instrument-accompanied software (Universal Analysis 2000, V4.5A, build 4.5.0.5).

Fourier Transform Infrared Spectroscopy

An FT-IR spectrophotometer (model: FTIR-8300, Shimadzu, Kyoto, Japan) was used to analyze and understand the molecular-level functional group interaction between the samples of ranolazine, LSPC-3, PM, and RNZ-SPC-CP, respectively. Briefly, the homogenous mixture for the FT-IR analysis was prepared by mixing of individual samples with FT-IR-grade potassium bromide (KBr) in an agate mortar and pestle. The individual mixture was compressed into thin and uniform transparent discs using a mini handpress machine (model: MHP-1, P/N-200-66747-91, Shimadzu, Kyoto, Japan). The prepared discs were scanned under a wave number region of 4000 to 400 cm^{-1} , with the resolution set to 4 cm^{-1} . The instrument-received FT-IR spectra for a single sample were compared and interpreted using the FT-IR software (IRSolution FT-IR control software, version 1.10). The detailed procedure for FT-IR analysis has been followed as per earlier published literature [21].

Powder X-ray Diffractometry

The crystalline performance of ranolazine, LSPC-3, PM, and RNZ-SPC-CP was evaluated in terms of their PXRD spectra using a powder x-ray diffractometer (model: D8 Advance, Bruker AXS, Inc., Madison, WI, USA). The detailed procedure regarding the sample preparation, their evaluation, and interpretation of the spectrum was followed according to the literature reported earlier [22].

Estimation of Drug Content

A UV-visible spectrophotometry-based procedure earlier described by Choudhary et al. was used to estimate the content of ranolazine in the prepared RNZ-SPC-CP formulations [23]. Briefly, an aqueous solution for the spectral analysis of ranolazine was prepared by dissolving the approximate amount of RNZ-SPC-CP formulations (~ 100 mg of ranolazine) in 100 mL of phosphate buffer (0.05 M, pH 6.8) and stirred well. The developed solution was then filtered through a membrane filter (0.45 μm). The filtered solution was diluted suitably and analyzed for absorbance on a UV-visible spectrophotometer (model: V-630, JASCO International Co., Ltd., Tokyo, Japan) at 270 nm. Moreover, the blank solution of LSPC-3 was also prepared and compared against the sample solution to avoid the interference from the added phospholipid carrier. The content of ranolazine (%) in the RNZ-SPC-CP was calculated according to Eq. (1) described below:

$$\text{RNZ content (\%)} = \frac{\text{total RNZ (mg)} - \text{free drug (mg)}}{\text{total RNZ (mg)}} \times 100 \quad (1)$$

Functional Characterization of Ranolazine-LIPOID SPC-3 Coprecipitate

Aqueous Solubility Analysis

The samples of pure ranolazine, PM of ranolazine, and LSPC-3 and RNZ-SPC-CP formulations were analyzed for aqueous solubility using the procedure reported earlier elsewhere [24]. Briefly, an individual sample in an excess amount was weighed and then transferred into clean screw-capped glass vials containing 10 mL of distilled water. The aqueous dispersion was stoppered carefully and agitated using a rotary shaker (model: RS-24 BL, REMI Laboratory Instruments, Remi House, Mumbai, India) at 37 °C for 24 h. After agitation, the mixture was filtered (membrane filter, 0.45 μm), collected, and diluted appropriately. The resulting solution was assayed for recording the

absorbance using a UV-visible spectrophotometer (model: V-630, JASCO International Co., Ltd., Tokyo, Japan) at a maximum wavelength of 272 nm against a blank. The entire study was carried out at room temperature.

In Vitro Dissolution Studies

A paddle (USP type II)–based dissolution apparatus (model: TDT-08LX, Electrolab India Pvt. Ltd., Mumbai, India) was employed for the comparative evaluation of in vitro dissolution performance of pure ranolazine and ranolazine from the prepared RNZ-SPC-CP formulation, respectively. The dissolution studies were carried out as per the procedure previously reported in the literature [10, 11]. Briefly, the testing samples, i.e., pure ranolazine (~100 mg) or prepared RNZ-SPC-CP (~100 mg of pure ranolazine), were dispersed in a dissolution flask containing 900 mL of distilled water. After dispersing the samples, the contents of the flask were stirred at a speed of 100 RPM and the temperature of the media was maintained at 37 ± 0.5 °C throughout the study. The dissolution study was performed for 120 min. At designated time intervals (10 min), the samples were withdrawn, filtered (membrane filter, 0.45 µm), diluted, and analyzed for measuring the absorbance of the resulting solution on a UV-visible spectrophotometer (model: V-630, JASCO International Co., Ltd., Tokyo, Japan) at a maximum wavelength of 270 nm against the blank. The recorded absorbance values of each sample were used for calculation of the percentage cumulative amount of release of ranolazine and RNZ-SPC-CP formulations.

Kinetic Model–Fitting Analysis The release kinetic analysis of RNZ from RNZ-SPC-CP was estimated by the fitting of the release data into different kinetic models such as zero order, first order, and Higuchi models. The zero-order model represents the cumulative amount of drug released vs. time, and it is represented by the following equation:

$$C = K_0t$$

where K_0 describes the zero-order rate constant that is expressed in units of concentration/time and t represents the time in minutes. A graph of concentration of vs. time would yield a straight line with a slope equal to K_0 and the intercept at the origin of the axis.

The first-order model shows the release as a cumulative percentage of the drug remaining vs. time, and it is described in the following equation:

$$\log C = \log C_0 - Kt/2.303$$

where C_0 is the initial concentration of the drug, K is the first-order rate constant, and t is the time in minutes.

The Higuchi model equation shows the release as a cumulative percentage of drug released vs. the square root of time, and it is calculated using the described equation below.

$$Qt = Kt^{1/2}$$

where Qt represents the amount of drug released in time t , K is the kinetic constant, and t is the time in minutes.

Mechanism of Drug Release The RNZ release mechanism from optimized RNZ-SPC-CP was determined by subjecting the release data to the Korsmeyer-Peppas equation as shown below; it describes the release as a cumulative percentage of drug released vs. time.

$$Mt/M_\infty = Kt^n$$

where Mt/M_∞ describes the fraction of drug released, K is the rate constant, t is the time for drug release, and n is the diffusional exponent for drug release. The diffusional exponent (n) value describes the release mechanism of formulations. For example, when $n = 1$, the release can be considered zero order (case II transport), and $n = 0.5$ indicates a Fickian diffusion release; $0.5 < n < 1.0$ indicates diffusion and non-Fickian diffusion. Finally, if $n > 1$, then the apparent mechanism is super case II transport.

Fasted vs. Fed State Dissolution Comparison

The comparative release pattern of pure ranolazine or ranolazine from RNZ-SPC-CP formulations was also studied under the effect of fasted (FaSSIF) or fed state (FeSSIF) in a USP type II (paddle) dissolution apparatus (model: TDT-08LX, Electrolab India Pvt. Ltd., Mumbai, India). Dissolution studies were carried out in FaSSIF (fasted state simulated intestinal fluid) and FeSSIF (fed state simulated intestinal fluid) media, and the procedure for the preparation of this media was followed according to the procedure reported earlier [25]. Briefly, ranolazine (~100 mg) or ranolazine from RNZ-SPC-CP formulations (~100 mg of pure ranolazine) was dispersed in dissolution media of FaSSIF (500 mL) or FeSSIF (1000 mL), respectively. The media were stirred continuously at a speed of 50 RPM, with the temperature maintained at 37 ± 0.5 °C for 120 min. During the study, the small samples were removed using a micropipette and replaced with fresh dissolution media for maintaining the sink conditions. The removed samples were diluted and assayed for absorbance using a UV-visible spectrophotometer (model: V-630, JASCO International Co., Ltd., Tokyo, Japan) at a wavelength of 271 nm for FaSSIF or 270 nm for FeSSIF against blank absorbance. Sample

absorbance values were calculated and represented in the form of a percentage cumulative release.

Ex Vivo Permeability Studies

The testing samples of pure ranolazine or prepared RNZ-SPC-CP formulations were analyzed for permeation across the biological membrane using the *everted rat intestine method* described earlier in the literature [26]. The studies were performed as per the literature earlier reported by our group [19, 27]. The Institutional Animal Ethical Committee of Smt. Kishoritai Bhoyar College of Pharmacy, Kamptee, reviewed and sanctioned the protocol (*SKBCOP/IAEC/201819, dated August 19, 2018*). The study was performed under the supervision of guidelines suggested by the Committee for the Purpose of Control and Supervision of Experiments on Animals (CPCSEA). Briefly, the prepared everted rat intestine membrane was fixed between the two tapered ends of the apparatus. After that, the apparatus was filled with freshly prepared Krebs solution and then immersed into a 250-mL beaker containing testing solutions of pure ranolazine (~100 µg/mL) or RNZ-SPC-CP formulations (~100 µg/mL) in Krebs solution. The entire assembly was placed on a magnetic stirrer, and the contents were stirred at a speed of 25 RPM, with the temperature of the media maintained at 37 ± 0.5 °C for 120 min. The permeation media (inside and outside of the apparatus) was continuously aerated using carbogen (95% O₂ and 5% CO₂ mixture). At predetermined time intervals, the small samples were removed from the apparatus, filtered, diluted, and analyzed for absorbance at 271 nm on a UV-visible spectrophotometer (model: V-630, JASCO International Co., Ltd., Tokyo, Japan) against the blank, and the absorbance values of the samples were reported as percentage cumulative permeation release.

Preliminary Stability Assessment Studies

The preliminary stability assessment studies on the optimized formulation, i.e., RNZ-SPC-CP1, were carried out to study the influence of storage conditions, i.e., controlled temperature (25 ± 5 °C) and relative humidity ($60 \pm 5\%$ RH), on the dissolution and permeation rate of RNZ from the abovementioned formulations. This study was carried out as per the literature reported earlier [28]. Briefly, the RNZ-SPC-CP1 formulation was packed in a screw-capped container, with high-density polyethylene (HDPE) amber-colored bottles. The packed samples were stored in a stability chamber (model: TS00002009, Mumbai, Maharashtra, India) for 6 months. At the end of the study, the samples were removed and tested for functional characterization.

Results and Discussion

Physico-chemical Characterization of Ranolazine-LIPOID SPC-3 Coprecipitate

Scanning Electron Microscopy

The SEM analysis of pure ranolazine, LSPC-3, and prepared RNZ-SPC-CP formulations are depicted in Fig. 2 a, b, and c, respectively. Pure ranolazine (Fig. 2a) appeared as clusters of small and larger particles, with a heterogeneous surface. LSPC-3 particles (Fig. 2b) are exhibited as larger and non-uniform particles with ill-defined morphology. The prepared RNZ-SPC-CP formulations (Fig. 2c) appeared as aggregates with characteristics of small particles of pure ranolazine and large particles of LSPC-3. The formation of these aggregates confirmed that pure ranolazine and LSPC-3 physically interact with each other. Results agreed with earlier published reports [28]. Moreover, the formation of such types of aggregates was possibly due to the solvent evaporation method. These findings were found to be consistent with an earlier published report which suggests that SPC-based carriers using the solvent evaporation method produce the same types of particles following their interaction with drugs [29, 30]. Moreover, different types and grades of phospholipids may also have different effects on the shape and surface morphology of phospholipid-based formulations [29].

Particle Size and Zeta Potential Analysis

The particle size and zeta potential analysis of prepared RNZ-SPC-CP formulations are shown in Fig. 3 a and b, respectively. Particle size and zeta potential are the basic parameters used for the determination of the physical stability of sub-micron particles dispersed in the liquid media. In general, the particle size of the pharmaceutical excipients is found to be inversely proportional to their surface area/volume ratio (SA/V) [31]. In the current study, the prepared RNZ-SPC-CP formulation (Fig. 3a) showed an average particle size of $\sim 95.76 \pm 0.20$ nm, indicating the small particle size of the formulations. This lower particle size formulation shows a higher SA/V, which in turn results in increase in the release rate of drugs from coprecipitate formulations through the mechanisms of diffusion and erosion. Moreover, a particle with a size smaller than 500 nm is considered a suitable particle size for its transportation across the biological membrane via endocytosis, whereas a particle size greater than 5 µm is particularly absorbed through the lymphatic system [32, 33]. Additionally, the polydispersity index (PDI) value of the same formulation was observed to be $\sim 0.29 \pm 0.10$. An obtained lower PDI value indicates a narrow distribution of pure ranolazine within the carrier. Zeta potential (ζ) is another valuable indicator used particularly for the determination of

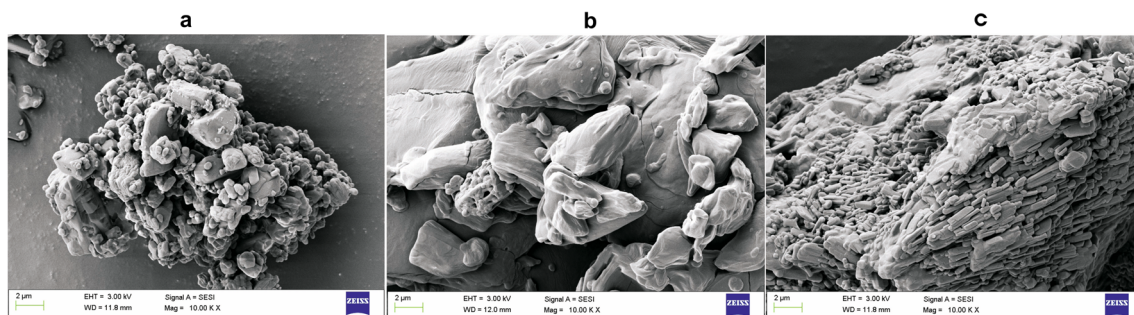


Fig. 2 SEM photomicrographs of **a** pure ranolazine, **b** LSPC-3 and **c** prepared RNZ-SPC-CP formulations

surface charges distributed around the particles. Moreover, zeta potential can also provide useful information about the behavior of particles following an oral administration [34]. Generally, the zeta potential values in the range of -30 to $+30$ mV can be considered acceptable values for the physical stability of multiparticulate systems. Prepared RNZ-SPC-CP formulations (Fig. 3b) showed zeta potential values as $\sim -24.31 \pm 0.19$ mV, indicating that it lies in between the acceptable range and, thus, confirming that the prepared formulation is physically stable. Moreover, this acceptable zeta potential value was likely due to a large portion of LSPC-3 contributing to the complexation process and generating negative charges in the aqueous environment with a neutral pH value. This possible mechanism provides sufficient negative charges on the surface of the RNZ-SPC-CP complex and makes the complex stable in the aqueous state. Additionally, the

phospholipid composition and its type may also have a strong impact on the zeta potential values. Findings were found to be consistent with earlier published reports [21, 34]. Therefore, based on this discussion, it is suggested that zeta potential plays a significant role in the stabilization of the phospholipid-based coprecipitate complex.

Differential Scanning Calorimetry

DSC is a valuable analytical tool used often in the quantitative determination of the interaction (physical and solid state) between the ingredients of the formulations. The thermograms of pure ranolazine, LSPC-3, the PM of ranolazine and LSPC-3 (ratio 1:1), and optimized RNZ-SPC-CP1 formulations are presented in Fig. 4 a, b, c, and d, respectively. The thermograms of pure ranolazine (Fig. 4a) showed a single and sharp

Fig. 3 **a** Particle size and **b** zeta potential of the prepared RNZ-SPC-CP formulations

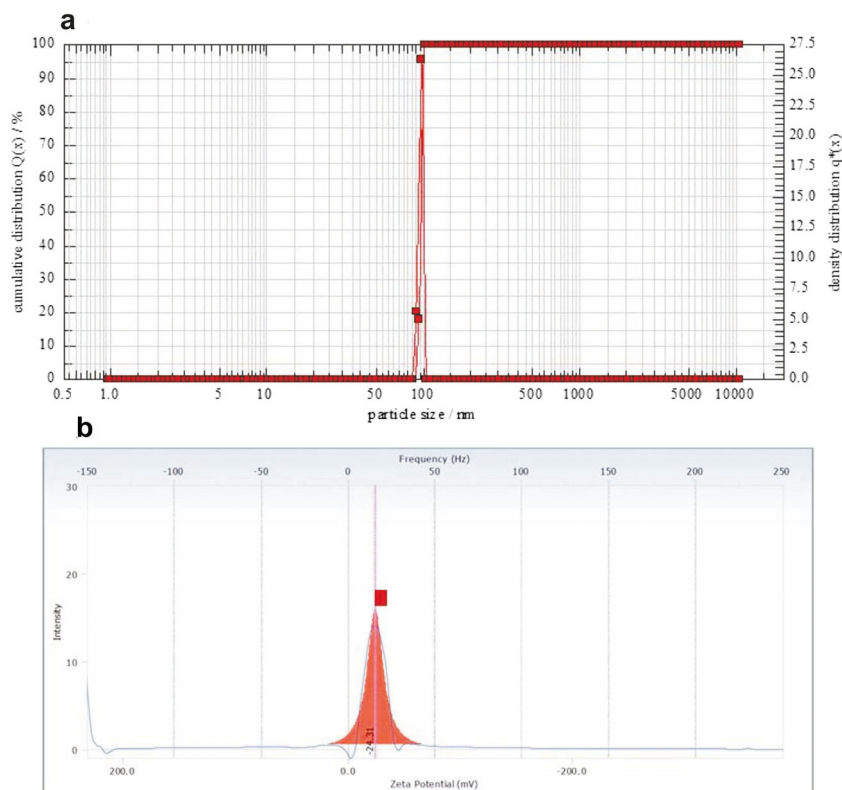
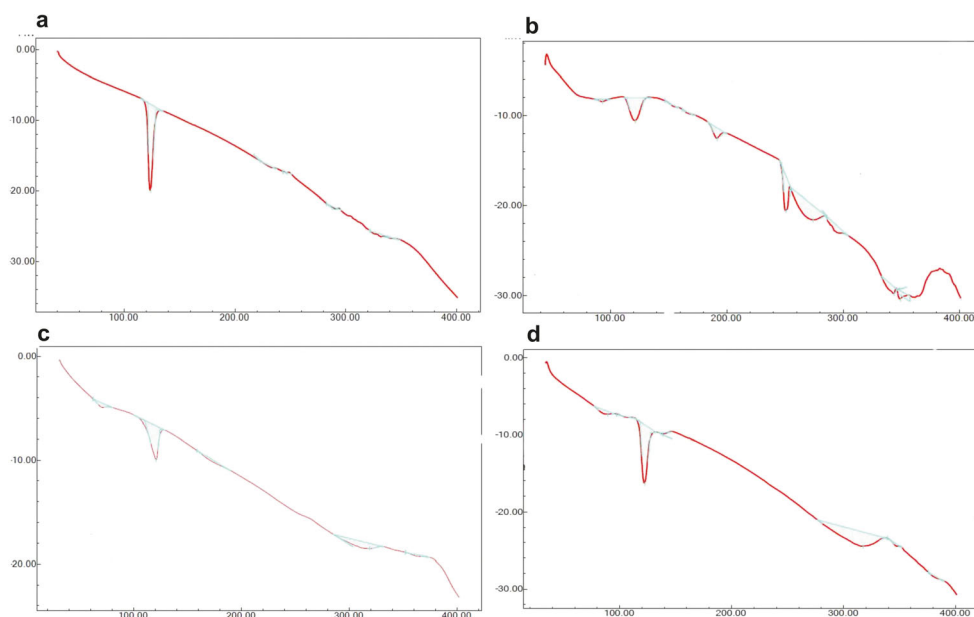


Fig. 4 DSC thermograms of **a** pure ranolazine, **b** LSPC-3, **c** the physical mixture of ranolazine and LSPC-3 (1:1), and **d** prepared RNZ-SPC-CP formulations



endothermic peak at ~ 124.13 °C; this peak signifies the melting point of pure ranolazine. The enthalpy of fusion (ΔH) for this peak was found to be ~ 79.26 J/g. Additionally, the same drug also displayed four very small intensity peaks in the region between ~ 222.78 and ~ 321.71 °C ($\Delta H \sim 6.97$ J/g). This may be likely due to the phase transition of ranolazine from its crystalline to anhydrous form. The results are well supported with earlier published reports [6]. The LSPC-3 thermograms (Fig. 4b) exhibited six dissimilar endothermic peaks. First, four small intensity peaks appeared at ~ 93.36 °C, 121.46 °C, 161.72 °C, and 191.95 °C, indicating the melting of the polar element of LSPC-3 as a function of increasing temperature. The remaining two peaks at ~ 250.90 °C and ~ 274.45 °C appeared to be mild, fused, and diffused ones compared with the initial four peaks. These peaks may be attributed to the physical transformation of the carbon-hydrogen part of LSPC-3 from the gel to the liquid crystalline state. Findings were consistent with those of phospholipids published earlier [20, 35]. The DSC thermograms of PM (1:1) (Fig. 4c) showed a combination of endothermic peaks at ~ 62.53 °C ($\Delta H \sim 6.02$ J/g), 120.65 °C ($\Delta H \sim 38.99$ J/g), 158.73 °C ($\Delta H \sim 4.86$ J/g), and 318.92 °C ($\Delta H \sim 22.44$ J/g) that correspond to pure ranolazine and LSPC-3 of the formulation. Moreover, the PM spectra showed the predominant peak of ranolazine with a small intensity compared with the peak observed for pure ranolazine; this indicates that a low amount of ranolazine is present in the PM as compared with LSPC-3 as well as possible physico-chemical interaction between them, suggesting that as the thermal temperature was achieved to a favorable position, the pure ranolazine and LSPC-3 were both melted, formed a partial mixture, and, thus, showed the peaks with low intensities, compared with pure ranolazine and LSPC-3 [35, 36]. Moreover, the last phase

transition peak of ranolazine also appeared at ~ 318.92 °C with broad and low-intensity characteristics indicating possible interaction of ranolazine with LSPC-3. Compared with the thermograms of PM, the thermograms of RNZ-SPC-CP1 formulations (Fig. 4d) displayed new endothermic peaks at ~ 89.28 °C and 122.68 °C. The overall appearance of these peaks was similar to that of PM; however, based on the endothermic peak position, the obtained peaks in these thermograms were found to be different from that of the peak position for pure ranolazine and PM. Moreover, the new peak at 122.68 °C appeared parallel to that of PM and pure ranolazine; however, it could be formed due to complete dispersion of pure ranolazine into the LSPC-3 matrix, reducing the sharp crystalline nature of the drug (i.e., partial amorphization) and converting it into an LSPC-3-based coprecipitate complex with broad and low-intensity peaks. Findings were consistent with earlier published literature [20]. Likewise, the enthalpy of fusion for major peaks of pure ranolazine, PM, and RNZ-SPC-CP1 formulations was found to be different, i.e., ~ 79.26 J/g, 38.99 J/g, and ~ 43.37 J/g. Therefore, based on the above comparative discussion, it is concluded that pure ranolazine and LSPC-3 forms strong interaction with each other, resulting in the formation of an amorphous RNZ-SPC-CP complex with different endothermic peak characteristics compared with those of the pure drug and PM.

Fourier Transform Infrared Spectroscopy

The interaction between the functional groups of various components of the formulation is confirmed by the FT-IR analysis. The FT-IR spectrum of pure ranolazine, LSPC-3, PM (1:1), and prepared RNZ-SPC-CP1 formulations are shown in Fig. 5a–d, respectively. The units are represented as cm^{-1} .

The FT-IR spectrum of pure ranolazine is displayed in Fig. 5a. In this figure, the absorption peaks observed at ~ 3328.5 , 2829.0, 1684.8, 1591.6, 1461.1, 1330.7, and 1252.4 represent the N–H stretching (primary aliphatic amine), C–H stretching, C=C stretching, C–H bending, and C–O stretching vibrations. The FT-IR spectrum of LSPC-3 (Fig. 5b) shows absorption peaks at 3362.1, 2914.8 and 2847.7, 1736.9, 1237.5, 1092.3, and 902.0, representing the O–H stretching, C–H stretching (for the long fatty acid chain), C=O stretching (fatty acid ester), P=O and P–O–C stretching, and $[-N^+(CH_2)_3]$ [37]. The FT-IR spectrum of PM (1:1), as shown in (Fig. 5c), exhibited absorption peaks at ~ 3332.2 , 2851.4, 2918.5, 1684.8, 1461.1, 1330.7, and 1252.4, indicating that these peaks had additive characteristics of pure ranolazine and LSPC-3. This additive peak suggests that both pure drug and LSPC-3 show strong physico-chemical interactions. As compared with the FT-IR spectrum of PM, that of RNZ-SPC-CP1 formulations (Fig. 5d) displayed lower absorption peaks at ~ 3328.5 , whereas compared with pure ranolazine, RNZ-SPC-CP1 showed complete disappearance of the absorption peak at ~ 2829.0 . Moreover, the absorption peak at ~ 3362.1 due to the O–H stretching vibration of LSPC-3 was found to disappear completely in the coprecipitate complex formulation. Likewise, the low absorption peak at ~ 902.0 in LSPC-3 appeared at a higher frequency at ~ 969.1 in the coprecipitate complex formulation. The peak frequencies' change observed in the spectrum of the RNZ-SPC-CP1 formulation for broadening, shifting, and appearance and/or disappearance of primary aliphatic amine (N–H stretching), O–H stretching, C–H stretching, and $[-N^+(CH_2)_3]$ peaks to lower and higher frequencies compared with those of PM, pure ranolazine, and LSPC-3 could be explained on the basis that pure ranolazine

molecularly interacted with the polar part of LSPC-3 through weak interactions, i.e., H-bonding, ion-dipole forces, and van der Waals forces, thus leading to the formation of stable RNZ-SPC-CP. Therefore, the shifting of absorption of peaks in the formulation concludes that there is a molecular interaction between ranolazine and LSPC-3, and this could be the evidence for the formation of RNZ-SPC-CP.

Powder X-ray Diffractometry

Figure 6 a, b, c, and d display the diffractogram spectra of pure ranolazine, LSPC-3, PM (1:1), and prepared RNZ-SPC-CP1 formulations on a 2θ scale, respectively. Pure ranolazine (Fig. 6a) diffractograms showed a chain of multiple numbers of sharp-pointed peaks observed at $\sim 4.95^\circ$, 10.31° , 12.22° , 14.92° , 16.42° , 16.42° , 19.27° , 21.37° , 23.39° , and 24.60° on a 2θ scale, indicating the crystalline nature of pure ranolazine. Moreover, the intensity (Lin counts on the y-axis) of these peaks appeared as ~ 490 , 400, 240, 300, 750, 250, 480, 550, and 350 counts, respectively, also confirming the crystalline nature of pure ranolazine. The PXRD spectrum of LSPC-3 (Fig. 6b) exhibited two dissimilar peaks. The first sharp and small-intensity peak developed at $\sim 5.92^\circ$ (650 counts), whereas a second broad and large-intensity peak was found at $\sim 21.57^\circ$ (2050 counts) on a 2θ scale. Two very miniature peaks also developed at 3.80° and 9.93° . Results were found to be similar to those of phospholipid literature published earlier [38]. Diffractograms of PM (Fig. 6c) displayed several combined peaks associated with small and large intensities, indicating that pure ranolazine and LSPC-3 were both physically mixed in the ratio 1:1, and

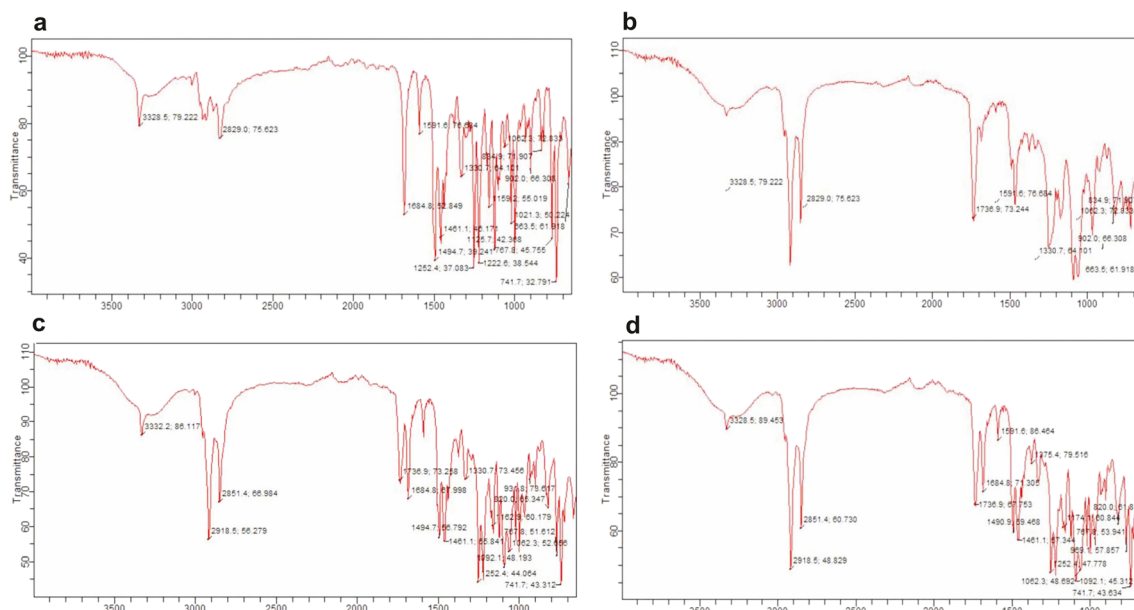


Fig. 5 FT-IR spectra of **a** pure ranolazine, **b** LSPC-3, **c** the physical mixture of ranolazine and LSPC-3 (1:1), and **d** prepared RNZ-SPC-CP formulations

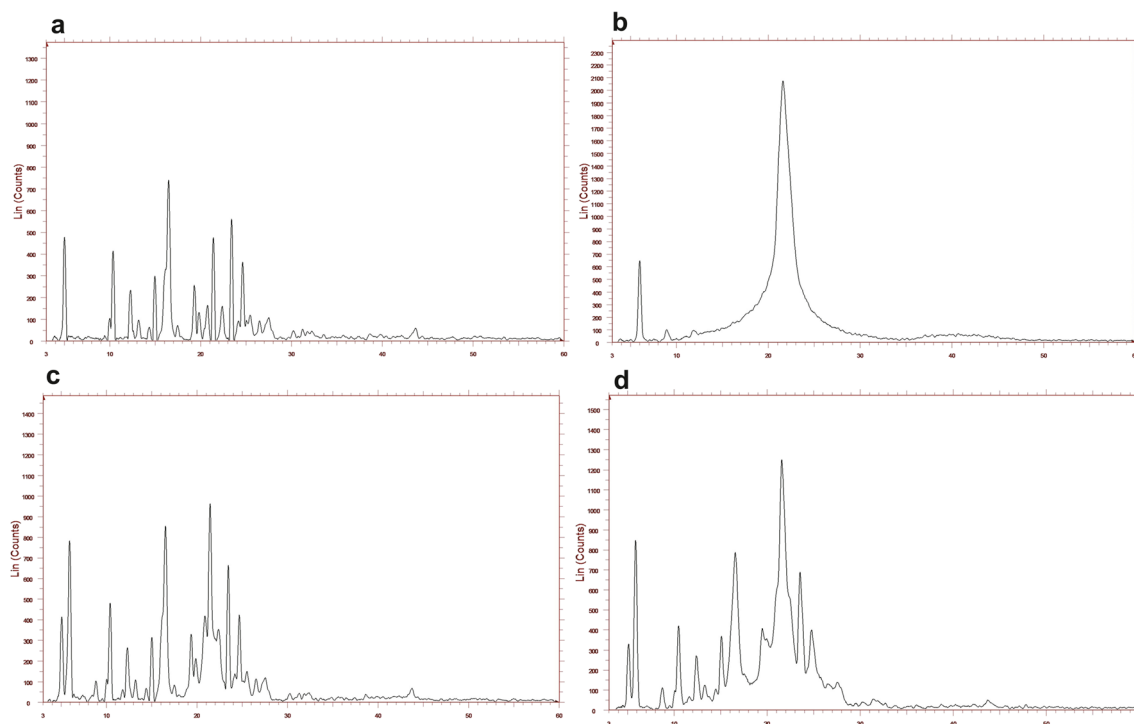


Fig. 6 The powder x-ray diffractograms of **a** pure ranolazine, **b** LSPC-3, **c** the physical mixture of ranolazine and LSPC-3 (1:1), and **d** prepared RNZ-SPC-CP formulations

therefore, the resulting peaks appeared in a combination of ranolazine as well as LSPC-3. Also, in this spectrum, the peak height/intensity of ranolazine in between the region of ~ 3 and 18° was found to be nearly similar to the peak height of the PXRD spectrum of pure ranolazine, whereas in the region of ~ 19 to 28° , the PM demonstrated a narrow range of LSPC-3-dominated peak along with the appearance of sharp peaks of pure ranolazine, and the complete appearance of these peaks was found to be parallel to that of the peak height of LSPC-3, indicating interaction between ranolazine and LSPC-3, and this was likely due to formation of in situ partial aggregates with equal contribution of both formulation components. PXRD diffractograms of optimized RNZ-SPC-CP1 formulation (Fig. 6d) exhibited few peaks of ranolazine with small, broad, and fused characteristics in the region between 3 and 20° , and their peak intensity was found to be lowered in this spectrum to around 300, 400, and 800 counts compared with higher counts, i.e., 400, 470, and 850, in PM, whereas in the region between 10 and 30° , the same formulation showed a broad range of LSPC-3-dominated peaks with a low intensity accompanied with reduction and/or disappearance of peaks as compared with PM and pure ranolazine. Formation of this spectrum could be explained that while the formulation of the pure ranolazine firstly mixed with LSPC-3 in the ratio 1:1 and then dispersed into the matrix of LSPC-3, this dispersion resulted in the partial reduction of the crystal nature

of pure ranolazine, which was finally converted into RNZ-SPC-CP formulation accompanied with amorphous characteristics [39]. Hence, the observed significant difference in the formation of a broad range of LSPC-3-dominated peaks with lower-intensity peaks in RNZ-SPC-CP compared with a narrow range of LSPC-3 peaks with a higher intensity in PM confirms that there were molecular association and interaction between ranolazine and LSPC-3, and this could be the basis for the development of RNZ-SPC-CP.

Drug Content

The analyzed ranolazine content in the prepared RNZ-SPC-CP formulations is shown in Table 2. As seen in Table 2, the formulation RNZ-SPC-CP in the ratio 1:1 exhibited the highest percentage of incorporation efficiency of ranolazine of $\sim 96.40 \pm 1.19\%$ w/w, whereas the other formulations in the ratios 1:2, 1:3, 1:4, and 1:5 showed lower percentages of ranolazine efficiency of $\sim 94.80 \pm 1.40\%$, $93.47 \pm 0.70\%$, $93.11 \pm 1.36\%$, and $92.07 \pm 1.41\%$, respectively. Among all formulations, the RNZ-SPC-CP (1:1) formulation was considered to be an optimized one for further analysis. Moreover, based on this analysis, it was found that the phospholipid carrier and solvent evaporation method could be a suitable and robust approach for the preparation of RNZ-SPC-CP with high ranolazine content.

Table 2 Drug content of ranolazine in prepared coprecipitate formulations

Coprecipitates	Drug content (% w/w)*
RNZ-SPC-CP1	96.40 ± 1.19
RNZ-SPC-CP2	94.80 ± 1.40
RNZ-SPC-CP3	93.47 ± 0.70
RNZ-SPC-CP4	93.11 ± 1.36
RNZ-SPC-CP5	92.07 ± 1.41

*All results are expressed as mean ± Std. Dev. ($n = 3$)

Functional Characterization of Ranolazine-LIPOID SPC-3 Coprecipitate

Aqueous Solubility Analysis

Table 3 displays the aqueous solubility analysis of pure ranolazine, PM (1:1), and prepared RNZ-SPC-CP formulations. Pure ranolazine showed low aqueous solubility of ~4.94 µg/mL, and this was likely due to its low solubility and the high permeability profile of the BCS class II category. PM formulations displayed somewhat higher aqueous solubility, and their solubility range was found to be between ~24 and ~30 µg/mL. The value corresponds to a nearly 6-fold increase in aqueous solubility. PM containing phospholipid ratios increasing from 1:1 to 1:3 showed significant enhancement in the solubility, and thereafter, further increasing ratios of phospholipids, i.e., 1:4 and 1:5, lowered the aqueous solubility of pure ranolazine. The modest increase in aqueous solubility of all PM was possibly attributed to the close association of the amphiphilic nature of phospholipids with ranolazine resulting in the formation of slightly modified ranolazine particles with higher aqueous solubility and wettability characteristics.

Table 3 Aqueous solubility of pure ranolazine, the physical mixture of ranolazine and LIPOID SPC-3, and ranolazine-LIPOID SPC-3 coprecipitate formulations

Coprecipitates	Aqueous solubility (µg/mL)*
Pure ranolazine	4.94 ± 0.06
PM1	30.20 ± 0.04
PM2	28.41 ± 0.07
PM3	27.50 ± 0.02
PM4	25.07 ± 0.08
PM5	24.27 ± 0.03
RNZ-SPC-CP1	92.23 ± 0.08
RNZ-SPC-CP2	90.07 ± 0.01
RNZ-SPC-CP3	87.46 ± 0.05
RNZ-SPC-CP4	84.39 ± 0.08
RNZ-SPC-CP5	80.12 ± 0.03

*All results are expressed as mean ± Std. Dev. ($n = 3$)

Apart from this, the higher amount of phospholipids in PM formulations, i.e., PM 1:4 and 1:5, may restrict the access of ranolazine particles into the aqueous media and, thus, reduces their solubility in water [11]. Moreover, the higher amount of phospholipids may also impart higher viscosity to formulations, which further reduced the solubility of the drug into the aqueous media [40]. RNZ-SPC-CP formulations improved the aqueous solubility in the range between ~80 and ~92 µg/mL. Among all formulations, the optimized RNZ-SPC-CP1 formulations (a drug to carrier ratio of 1:1) significantly ($p < 0.01$) enhanced the aqueous solubility of ranolazine to ~92.23 µg/mL. The obtained value shows an 18-fold increase in aqueous solubility as compared with those of pure ranolazine and all PM. The possible reason for the enhancement of this aqueous solubility was likely attributed to the complex formation and partial amorphization of ranolazine particles within the formulations [41, 42]. The amphiphilic character of LSPC-3 and the amorphous state of the drug within this carrier could have the possibility of increasing the aqueous solubility of ranolazine [43]. Moreover, the phospholipids are known to form self-assembly of amphiphilic structures like micelles, liposomes, and phytosomes with high incorporation of hydrophobic drug particles, resulting in the increase in the aqueous solubility of the drug via formation of a complex between the drug and phospholipids. The wetting nature of these phospholipids can also contribute to increasing the water solubility of the hydrophobic drug via surface coating [44]. The amphiphilic nature, wetting, and lowering of the interfacial tension between the drug and water functions of LSPC-3 may also contribute to increasing the hydrophilicity of drugs [40].

In Vitro Dissolution Studies

Figure 7 describes the comparative dissolution pattern of pure ranolazine, PM (1:1), and optimized RNZ-SPC-CP1 formulations tested in distilled water for 120 min. As seen in the figure, the pure ranolazine exhibited only ~21% dissolution by the end of 120 min. The low solubility and high permeability profile of ranolazine are considered to be the main reason for its low dissolution in distilled water. The PM (1:1) demonstrated a modest increase in the rate and extent of ranolazine dissolution compared with pure ranolazine. By the end of dissolution, the rate and extent of ranolazine dissolution from PM were found to be only ~35%. From this observation, it is found that the PM pursued the same dissolution fashion as observed in the solubility studies. As compared with pure ranolazine and PM (1:1), the optimized RNZ-SPC-CP1 exhibited the highest dissolution efficiency, and by the end of the dissolution period, ~85% of ranolazine was found to be released in the distilled water. The improved dissolution rate of RNZ-SPC-CP1 formulation could have been possibly due to the solvent evaporation method, LSPC-

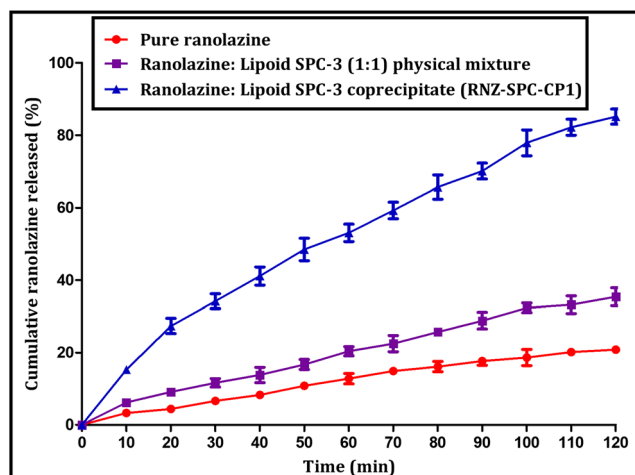


Fig. 7 The in vitro dissolution profiles of pure ranolazine, the physical mixture of ranolazine and LSPC-3 (1:1), and the prepared optimized RNZ-SPC-CP1 formulations

3 carrier, and ethanol solvent. Solvent evaporation, a well-known method, transforms the crystalline drug into a partially amorphized form and, finally, converts it into the high-energy state powder, which increases the dissolution rate of low-solubility drug particles [45]. The shorter fatty acid chain length, as well as the phase transition temperature (T_c) of LSPC-3 being lower than the experimental temperature (37 °C), may cause to increase the dissolution rate of ranolazine because of its more amorphous nature as well as the spontaneous dispersibility of LSPC-3 when coming in contact with distilled water [10, 11]. Moreover, the LSPC-3 structure was found to be similar to those of earlier used phospholipids, i.e., DMPC and DMPG. The combined impact of this phospholipid exhibits a dual effect; the first one is the complex formation between the negative charge of the phosphate group of phospholipids and positive charge of ranolazine, and the second one is liposome and phytosome formation ability, which in turn increases the dissolution rate of ranolazine in distilled water [11, 12]. Ethanol, a non-toxic and class III solvent, may remain as a trace solvent even after the vacuum drying. This trace amount of solvent can form hydrogen bonding with ranolazine and LSPC-3, resulting in the formation of the coprecipitate complex, which can increase the rate and extent of ranolazine dissolution. Moreover, ranolazine forms a strong chemical association with LSPC-3 via intermolecular bonding, and this interaction could change the physico-chemical properties of both of these compounds, resulting in a significant enhancement of the dissolution rate of ranolazine from the prepared coprecipitate complex. Results were found to be consistent with earlier published reports [13].

The obtained release data from RNZ-SPC-CP formulations were analyzed using various kinetic models such as first-order, zero-order, Higuchi, and Korsmeyer-Peppas models. Following analysis, the obtained higher correlation coefficient

value ($R^2 = 0.9731$) compared with the small value of the zero-order ($R^2 = 0.9322$) and first-order ($R^2 = 0.9550$) models suggests the Higuchi model as a best-fit kinetic model describing the dissolution of RNZ-SPC-CP formulations. Moreover, the release exponent value (n) was found to be ~ 0.48 , indicating that diffusion is the principal mechanism responsible for the release of ranolazine from RNZ-SPC-CP formulations. Moreover, based on the Korsmeyer-Peppas model, the release mechanism of the ranolazine from the optimized RNZ-SPC-CP1 complex was found to be a two-step diffusion process. First, the ranolazine molecule dissociates from the RNZ-SPC-CP complex, and second, the dissociated ranolazine molecule diffuses out from the LSPC-3 matrix into the dissolution media.

Fasted vs. Fed State Dissolution Comparison

The fasted vs. fed state dissolution profile comparison between the pure ranolazine and optimized RNZ-SPC-CP1 formulation is shown in Fig. 8. Pure ranolazine in the FaSSIF state showed a lower rate and extent of dissolution of $\sim 22\%$ at the end of 2 h of dissolution study. Compared with this, in the FeSSIF state, the pure ranolazine showed an increase in dissolution rate of $\sim 30\%$ over the same dissolution period. The optimized RNZ-SPC-CP1 formulation enhanced the dissolution rate of pure ranolazine in the FaSSIF state as well as in the FeSSIF state. However, the dissolution rate of optimized formulation in FeSSIF state was found to be increased drastically, i.e., $\sim 78\%$, as compared with only $\sim 60\%$ in the FaSSIF state over the same dissolution period. This enhanced rate and extent of dissolution of pure ranolazine and RNZ-SPC-CP1 formulation in the fed state could be attributed to positive food effects on enhancing the solubility and dissolution rate of BCS class II drugs [25, 46]. Moreover, in the fed state, the generation of taurocholate-ranolazine micelles as well as

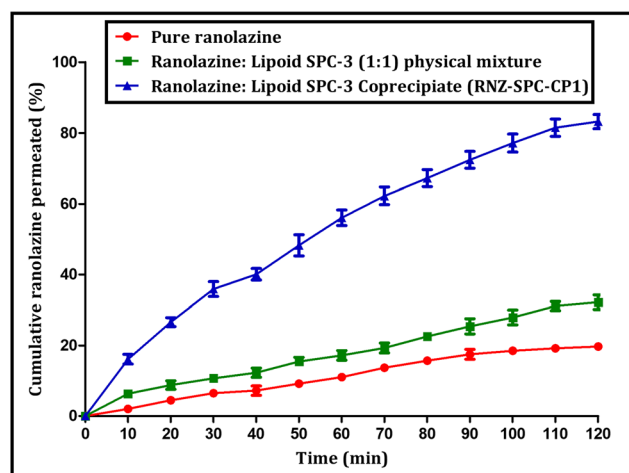


Fig. 8 The ex vivo permeation profiles of pure ranolazine, the physical mixture of ranolazine and LSPC-3 (1:1), and the prepared optimized RNZ-SPC-CP1 formulations

taurocholate-phospholipid-ranolazine micelles during dissolution could have possibly enhanced the dissolution rate of ranolazine. The results are found to be consistent with previously published reports [47].

Ex Vivo Permeability Studies

The comparative permeation efficiency of pure ranolazine and ranolazine from the optimized RNZ-SPC-CP1 formulation is depicted in Fig. 9. As seen in this figure, the pure ranolazine permeated only ~19% at the end of 2 h of the dissolution period, likely due to low permeability characteristics of pure ranolazine. The PM in a ratio of 1:1 fairly enhanced the permeation rate of ranolazine, and by the end of the permeation period, it was found to be ~32%. This was possibly attributed to a close association of the amphiphilic nature of LSPC-3. The optimized RNZ-SPC-CP1 formulation, after 1 h of study, showed ~56% permeation, and by the end of 2 h, the permeation rate was increased and found to be ~83%, compared with that of pure ranolazine and PM (1:1). This was likely attributed to amphiphilic and wetting characteristics of LSPC-3 that was used in the current study. Moreover, the amphiphilic phospholipid bilayers are also the component of the biological membrane, and therefore, the prepared phospholipid-based coprecipitate formulation shows higher miscibility with the biological membrane, resulting in the increase of the permeability of the drug across the membrane [48]. Additionally, LSPC-3 like a class of phospholipids exhibits beneficial advantages such as biocompatibility, biodegradability, metabolic activity, and low toxicity [49, 50]. These advantages of LSPC-3 serve it as an excellent carrier for the transportation of drugs across the biological barrier. Therefore, based on the biocompatible nature and safety profile in animal studies without any sign of inflammation and other negative effects [51, 52], the LSPC-3 carrier was selected and used in the preparation of the ranolazine coprecipitate complex. Overall, the results conclude that LSPC-3 improved

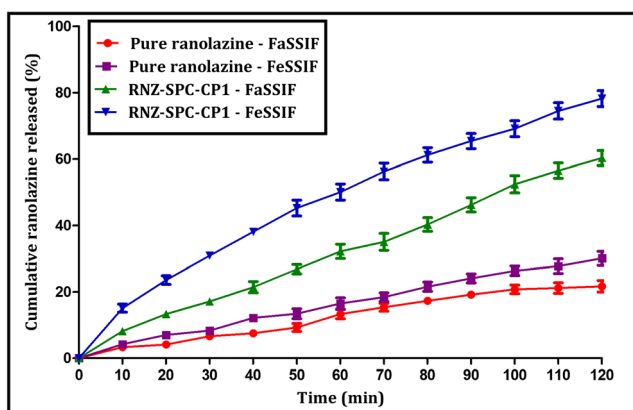


Fig. 9 The influence of fasted and fed state conditions on the dissolution behavior of pure ranolazine and the prepared optimized RNZ-SPC-CP1 formulations

the permeation rate of ranolazine and its permeation pattern was found to be similar to that of solubility and in vitro dissolution studies.

Preliminary Stability Assessment Studies

The preliminary stability evaluations under the influence of controlled temperature and relative humidity on the comparative in vitro dissolution and ex vivo permeation profile of ranolazine from the optimized RNZ-SPC-CP1 formulation are depicted in Figs. 10 and 11, respectively. The comparative in vitro dissolution patterns of optimized RNZ-SPC-CP1 at day 0 and day 180 (sixth month) are shown in Fig. 10. As seen in the figure, the dissolution pattern of the stored RNZ-SPC-CP1 formulation at day 180 was found to be parallel to that of the dissolution pattern of the initial formulation on day 0. Both dissolution patterns did not show any significant difference. However, the rate and extent of dissolution of ranolazine from stored RNZ-SPC-CP1 at day 180 was found to be decreased over that of the initial release formulation at day 0. Figure 11 shows the comparative ex vivo permeation profile of the optimized RNZ-SPC-CP1 formulation at day 0 and day 180. The permeation profile of initial RNZ-SPC-CP1 on day 0 and stored RNZ-SPC-CP1 formulation at day 180 was found to be parallel without any significant differences between them. However, the stored RNZ-SPC-CP1 formulation after the sixth month of the study demonstrated lower permeation efficiency compared with that of the initial formulation on day 0. Obtained results confirmed that the optimized formulation is robust and stable. Conversely, the shifting of the dissolution and permeation profile from that of original may be attributed to the influence of relative humidity and other unclear factors. Therefore, additional characterization studies must be warranted to understand the behavior of stored samples under the impact of stability parameters.

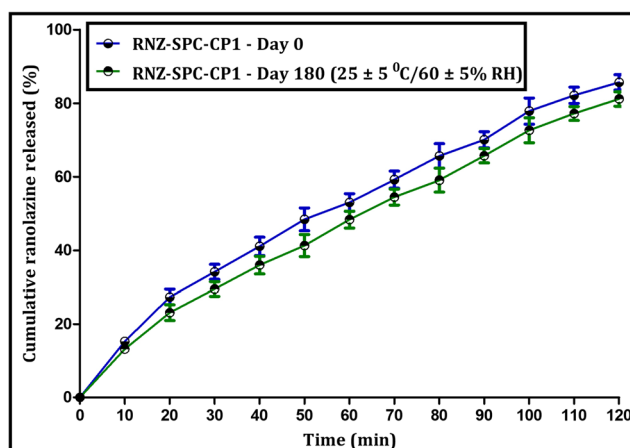


Fig. 10 Comparison of the in vitro dissolution profiles of the optimized RNZ-SPC-CP1 formulation before and after 6-month (day 180) storage at 25 ± 5 °C/60 ± 5% RH

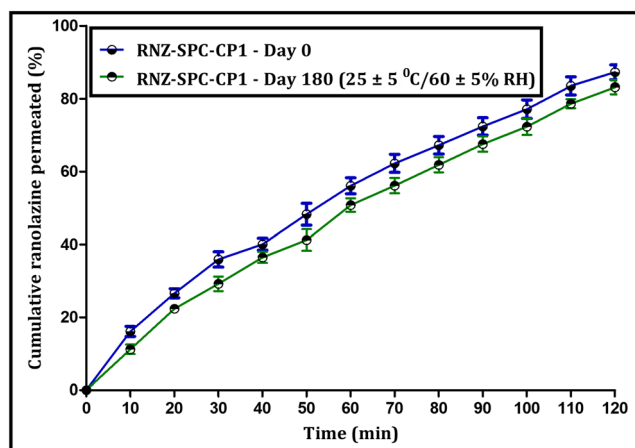


Fig. 11 Comparison of the ex vivo permeation profiles of the optimized RNZ-SPC-CP1 formulation before and after 6-month (day 180) storage at 25 ± 5 °C/ 60 ± 5 % RH

Conclusions

In this study, we explored the feasibility of LIPOID SPC-3 as a coprecipitate carrier for improving the aqueous solubility and permeability of ranolazine. The coprecipitate of ranolazine with increasing ratios of LIPOID SPC-3 was prepared using the solvent method. Formation of the RNZ-SPC-CP formulation was confirmed by physico-chemical (i.e., SEM, DSC, FT-IR, and PXRD) and functional (solubility analysis, in vitro dissolution, and ex vivo permeation) characterization studies. Optimized RNZ-SPC-CP1 formulations significantly improved the aqueous solubility (18-fold), the rate and extent of dissolution, and the permeation of ranolazine as compared with those of pure ranolazine and PM. Moreover, the same optimized formulation also increased the rate and extent of dissolution of ranolazine under the influence of food effects. Optimized RNZ-SPC-CP1 was found to be stable and robust at the end of 6-month stability studies; however, the modest impact of storage conditions appeared on the in vitro dissolution and ex vivo permeation of either the drug and/or formulations. The mechanism of this influence is still under investigation, and therefore, additional characterization studies must be required on the stability samples. Finally, the obtained appreciable results display the excellent feasibility of LIPOID SPC-3 as a coprecipitate carrier to improve the overall biopharmaceutical attributes of ranolazine and other similar drugs with poor water solubility.

Acknowledgments The corresponding author acknowledges Dr. Shirish P. Jain, Principal, Rajarshi Shahu College of Pharmacy, Buldhana, for providing the technical support for completing the manuscript on time.

CRedit Authorship Contribution Statement Darshan Telange: conceptualization, investigation, methodology, writing—original draft, writing—review and editing. Sarita Ukey: methodology, investigation, data curation. Atul Hemke: validation, data curation. Milind Umekar: project administration, resources. Anil Pethe: conceptualization, supervision, investigation, visualization. Prashant Kharkar: investigation, methodology, writing—original draft.

Compliance with Ethical Standards

The Institutional Animal Ethical Committee of Smt. Kishoritai Bhoyar College of Pharmacy, Kamptee, reviewed and sanctioned the protocol (*SKBCOP/IAEC/201819*, dated August 19, 2018). The study was performed under the supervision of guidelines suggested by the Committee for the Purpose of Control and Supervision of Experiments on Animals (CPCSEA).

Conflict of Interest The authors declare that they have no conflict of interest.

References

- Rayner-Hartley E, Sedlak T. Ranolazine: a contemporary review. *J American Hear Assoc.* 2016;5(3):1–8. <https://doi.org/10.1161/JAHA.116.003196>.
- Wolff AA, Baker F, Landridge J. Sustained release ranolazine formulations. United State Patent, US 6396062B1.
- Reddy BM, Weintraub HS, Schwartzbard AZ. Ranolazine: a new approach to treating an old problem. *Tex Heart Inst J.* 2010;37(6):641–7.
- Jerling M. Clinical pharmacokinetics of ranolazine. *Clin Pharmacokinet.* 2006;45(5):469–91.
- Bidada JP, Gonjari ID, Raut CS, Bhutada CJ. Novel spectroscopic method for estimation of ranolazine in bulk and pharmaceutical dosage forms. *Der Pharma Chemica.* 2011;3(2):1–4.
- Murthy TEGK, Mukkala VP, Suresh Bhau VV. Formulation and evaluation of ranolazine extended-release tablet: influence of polymers. *Asian J Pharm.* 2011;5:162–6. <https://doi.org/10.4103/0973-8398.91992>.
- Gowda DV, Gowrav MP, Gandadharappa HV, Khan MS. Preparation and evaluation of mixture of Eudragit and ethylcellulose microparticles loaded with ranolazine for controlled release. *J Young Pharm.* 2011;3:189–96.
- Rajkumar K, Bolmol US, Reddy ER, Sowjanya PS, Anusha P, Reddy KR. Formulation and evaluation of floating microsphere of ranolazine for the treatment of chronic angina. *Int J Pharm Sci Nanotech.* 2013;6(3):2137–44.
- Bhosale PV, Ranade AN, Awahad C. Formulation and evaluation of extended release tablet of ranolazine. *Inventi Rapid: Pharm Tech.* 2015;3:1–5.
- Habib MJ, Azadi M, Akogyeram CO. Enhancement of dissolution rate of probenecid in phospholipids coprecipitates. *Drug Dev Ind Pharm.* 1992;18(10):1117–25. <https://doi.org/10.3109/03639049209069319>.
- Habib MJ, Akohyeram C, Ahmadi B. Improved dissolution of indomethacin with phospholipids – I. *Drug Dev Ind Pharm.* 1993;19(4):499–505. <https://doi.org/10.3109/03639049309063207>.
- El-Zein H, Riad L, Abd El-Bary A. Enhancement of carbamazepine dissolution: in vitro and in vivo evaluation. *Int J Pharm.* 1998;168:209–20. [https://doi.org/10.1016/S0378-5173\(98\)00093-3](https://doi.org/10.1016/S0378-5173(98)00093-3).
- Hussain MD, Saxena V, Brausch JF, Talukder RM. Ibuprofen-phospholipids solid dispersion: improved dissolution and gastric tolerance. *Int J Pharm.* 2012;422:290–4. <https://doi.org/10.1016/j.ijpharm.2011.11.011>.
- Hu Q, Choi DS, Chokshi H, Shah N, Sandhu H. Highly efficient miniaturized coprecipitation screening (MiCoS) for amorphous solid dispersion formulation development. *Int J Pharm.* 2013;450:53–62. <https://doi.org/10.1016/j.ijpharm.2013.04.040>.
- MS EYSR, Abdallah OY. Lyophilized phytosomal nanocarriers as platforms for enhanced diosmin delivery: optimization and ex vivo

- permeation. *Int J Nanomedicine*. 2013;8:2385–97. <https://doi.org/10.2147/IJN.S45231>.
16. Barry J, Fritz M, Brender JR, Smith PES, Lee D-K, Ramamoorthy A. Determining the effects of lipophilic drugs on membrane structure by solid-state NMR spectroscopy: the case of the antioxidant curcumin. *J Am Chem Soc*. 2009;131(12):4490–8. <https://doi.org/10.1021/ja809217u>.
 17. Venkataram S, Rogers JA. Characteristics of drug phospholipid coprecipitates I: physical properties and dissolution behavior of griseofulvin-dimyristoyl phosphatidylcholine systems. *J Pharm Sci*. 1984;73:757–61. <https://doi.org/10.1002/jps.2600730613>.
 18. Biswas M, Akogyeram CO, Scott KR, Potti GK, Gallelli JF, Habib MJ. Development of carbamazepine: phospholipid solid dispersion formulations. *J Control Release*. 1993;23:239–45. [https://doi.org/10.1016/0168-3659\(93\)90005-P](https://doi.org/10.1016/0168-3659(93)90005-P).
 19. Telange DR, Bhagat SB, Patil AT, Umekar MJ, Pethe AM, Raut NA, et al. Glucosamine HCl-based solid dispersions to enhance the biopharmaceutical properties of acyclovir. *J Excipients Food Chem*. 2019;10(3):65–81.
 20. Telange DR, Nirgulkar SB, Umekar MJ, Patil AT, Pethe AM, Bali NR. Enhanced transdermal permeation and anti-inflammatory potential of phospholipids complex-loaded matrix film of umbelliferone: formulation development, physico-chemical and functional characterization. *Eur J Pharm Sci*. 2019;131:23–38. <https://doi.org/10.1016/j.ejps.2019.02.006>.
 21. Telange DR, Patil AT, Pethe AM, Fegade H, Anand S, Dave VS. Formulation and characterization of an apigenin-phospholipid phytosome (APLC) for improved solubility, in vivo bioavailability, and antioxidant potential. *Eur J Pharm Sci*. 2017;108:36–49. <https://doi.org/10.1016/j.ejps.2016.12.009>.
 22. Dhore PW, Dave VS, Saoji SD, Gupta D, Raut NA. Influence of carrier (polymer) type and drug-carrier-ratio in the development of amorphous dispersions for solubility and permeability enhancement of ritonavir. *J Excipients and Food Chem*. 2017;8(3):1–18.
 23. Choudhary A, Rana AC, Aggarwal G, Kumar V, Zakir F. Development and characterization of an atorvastatin solid dispersion formulation using skimmed milk for improved oral bioavailability. *Acta Pharm Sin B*. 2012;2(4):421–8. <https://doi.org/10.1016/j.apsb.2012.05.002>.
 24. Al-Hamidi H, Edwards AA, Mohammad MA, Nokhodchi A. To enhance dissolution rate of poorly water-soluble drugs: glucosamine hydrochloride as a potential carrier in solid dispersion formulations. *Colloids Surf B: Biointerfaces*. 2010;76(1):170–8. <https://doi.org/10.1016/j.colsurfb.2009.10.030>.
 25. Klein S. The use of biorelevant dissolution media to forecast the in vivo performance of a drug. *AAPS J*. 2010;12(3):397–406. <https://doi.org/10.1208/s12248-010-9203-3>.
 26. Dixit P, Jain DK, Dumbwani J. Standardization of an ex vivo method for determination of intestinal permeability of drugs using everted rat intestine apparatus. *J Pharmacol Toxicol Methods*. 2012;65(1):13–7. <https://doi.org/10.1016/j.vascn.2011.11.001>.
 27. Dhore PW, Dave VS, Saoji SD, Bobde YS, Mack C, Raut NA. Enhancement of the aqueous solubility and permeability of a poorly water soluble drug ritonavir via lyophilized milk-based solid dispersions. *Pharm Dev Technol*. 2017;22(1):90–102. <https://doi.org/10.1080/10837450.2016.1193193>.
 28. Telange DR, Denge RP, Patil RP, Umekar MJ, Gupta SV, Dave VS. Pentaerythritol as an excipients/solid–dispersion carrier for improved solubility and permeability of ursodeoxycholic acid. *J Excipients Food Chem*. 2018;9(3):80–95.
 29. Semalty A, Semalty M, Singh D, Rawat MSM. Development and physicochemical evaluation of pharmacosomes of diclofenac. *Acta Pharma*. 2009;59:335–44. <https://doi.org/10.2478/v10007-009-0023-x>.
 30. Semalty A, Semalty M, Singh D, Rawat MSM. Preparation and characterization of phospholipids complexes of naringenin for effective drug delivery. *J Incl Phenom Macrocycl Chem*. 2010;67:253–60. <https://doi.org/10.1007/s10847-009-9705-8>.
 31. Rarokar NR, Saoji SD, Raut NA, Taksande JB, Khedekar PB, Dave VS. Nanostructured cubosomes in a thermoresponsive depot system: an alternate approach for the controlled delivery of docetaxel. *AAPS PharmSciTech*. 2016;17:436–45. <https://doi.org/10.1208/s12249-015-0369-y>.
 32. LeFevre ME, Olivo R, Vanderhoff JW, Joel DD. Accumulation of latex in Peyer's patches and its subsequent appearance in villi and mesenteric lymph nodes. *Proc Soc Exp Biol Med*. 1978;159:298–302.
 33. Savic R, Luo L, Eisenberg A, Maysinger D. Micellar nanocontainers distribute to defined cytoplasmic organelles. *Science*. 2003;300(5619):615–8. <https://doi.org/10.1126/science.1078192>.
 34. Hou Z, Li Y, Huang Y, Zhou C, Lin J, Wang Y, et al. Phytosomes loaded with mitomycin c–soybean phosphatidylcholine complex developed for drug delivery. *Mol Pharm*. 2013;10:90–101. <https://doi.org/10.1021/mp300489p>.
 35. Cai X, Luan Y, Jiang Y, Song A, Shao W, Li Z, et al. Huperzine A-phospholipid complex-loaded biodegradable thermosensitive polymer gel for controlled drug release. *Int J Pharm*. 2012;433:102–11. <https://doi.org/10.1016/j.ijpharm.2012.05.009>.
 36. Ruan J, Liu J, Zhu D, Gong T, Yang F, Hao X, et al. Preparation and evaluation of self-nanoemulsified drug delivery systems (SNEDDSs) of matrine based on drug-phospholipid complex technique. *Int J Pharm*. 2010;386:282–90. <https://doi.org/10.1016/j.ijpharm.2009.11.026>.
 37. Li J, Liu P, Liu J-P, Yang JK, Zhang W-L, Fan Y-Q, et al. Bioavailability and foam cells permeability enhancement of Salviaanolic acid B pellets based on drug–phospholipids complex technique. *Eur J Pharm Biopharm*. 2012;83:76–86. <https://doi.org/10.1016/j.ejpb.2012.09.021>.
 38. Semalty A, Semalty M, Singh D, Rawat MSM. Phyto-phospholipid complex of catechin in value added herbal drug delivery. *J Incl Phenom Macrocycl Chem*. 2012;73:377–86. <https://doi.org/10.1007/s10847-011-0074-8>.
 39. Yue PF, Zhang WJ, Yuan HL, Yang M, Zhu WF, Cai PL, et al. Process optimization, characterization and pharmacokinetic evaluation in rats of ursodeoxycholic acid-phospholipid complex. *AAPS PharmSciTech*. 2008;9:322–9. <https://doi.org/10.1208/s12249-008-9040-1>.
 40. Chen T, Ynag J, Chen L, Qian X, Zhang Q, Fu T, et al. Use of ordered mesoporous silica-loaded phyto-phospholipid complex for BCS IV class plant drug to enhance oral bioavailability: a case report of tanshinone IIA. *RSC Adv*. 2016;6:115010–20. <https://doi.org/10.1039/C6RA22778C>.
 41. Singh D, Rawat MSM, Semalty A, Semalty M. Emodin–phospholipid complex: a potential of herbal drug in the novel drug delivery system. *J Therm Anal Calorim*. 2012;108:289–98. <https://doi.org/10.1007/s10973-011-1759-3>.
 42. Singh D, Rawat MSM, Semalty A, Semalty M. Quercetin-phospholipid complex: an amorphous pharmaceutical system in herbal drug delivery. *Curr Drug DisTechnol*. 2012;9:17–24. <https://doi.org/10.2174/157016312799304507>.
 43. Jo K, Cho JM, Kim EK, Kim HC, Kim H, Lee J. Enhancement of aqueous solubility and dissolution of celecoxib through phosphatidylcholine-based dispersion system solidified with adsorbent carriers. *Pharmaceutics*. 2019;11(1):2–14. <https://doi.org/10.3390/pharmaceutics11010001>.
 44. Singh RP, Gangadharappa HV, Mruthunjaya K. Phospholipids: unique carriers for drug delivery systems. *J Drug Deliv Sci Technol*. 2017;39:166–79. <https://doi.org/10.1016/j.jddst.2017.03.027>.

45. Leuner C, Dressman J. Improving drug solubility for oral delivery using solid dispersions. *Eur J Pharm Biopharm.* 2000;50:47–60. [https://doi.org/10.1016/s0939-6411\(00\)00076-x](https://doi.org/10.1016/s0939-6411(00)00076-x).
46. Raman S, Polli JE. Prediction of positive food effect: bioavailability enhancement of BCS class II drugs. *Int J Pharm.* 2016;506(1–2): 110–5. <https://doi.org/10.1016/j.ijpharm.2016.04.013>.
47. Fong SYK, Ibisogly A, Bauer-Brandl A. Solubility enhancement of BCS Class II drug by solid phospholipids dispersions: spray drying versus freeze-drying. *Int J Pharm.* 2015;496(2):382–91. <https://doi.org/10.1016/j.ijpharm.2015.10.029>.
48. Saoji SD, Belgamwar VS, Dharashivkar SS, Rode AA, Mack C, Dave VS. The study of the influence of formulation and process variables on the functional attributes of simvastatin–phospholipid complex. *J Pharm Innov.* 2016;11:264–78. <https://doi.org/10.1007/s12247-016-9256-7>.
49. Chen JM, Zhang L, Yuet KP, Liao G, Rhee JW, Langer R. PLGA-lecithin-PEG core shell nanoparticles for controlled drug delivery. *Biomaterials.* 2009;30(8):1627–34. <https://doi.org/10.1016/j.biomaterials.2008.12.013>.
50. Fricke G, Kromp T, Wendel A, Blume A, Zirkel J, Rebmann H. Phospholipids and lipid-based formulations in oral drug delivery. *Pharm Res.* 2010;27(8):1469–86. <https://doi.org/10.1007/s11095-010-0130-x>.
51. Xie J, Li Y, Song L, Pan Z, Ye S, Hou Z. Design of a novel curcumin-soybean phosphatidylcholine complex-based targeted drug delivery systems. *Drug Deliv.* 2017;24(1):707–19. <https://doi.org/10.1080/10717544.2017.1303855>.
52. Yu F, Ao M, Zhang X, Xia J, Li Y, Li D, et al. PEG-lipid-PLGA hybrid nanoparticles loaded with berberine-phospholipids complex to facilitate the oral delivery efficiency. *Drug Deliv.* 2017;24(1): 825–33. <https://doi.org/10.1080/10717544.2017.1321062>.

Publisher's Note Springer Nature remains neutral with regard to jurisdictional claims in published maps and institutional affiliations.



Antimutagenic Activity of Cassia Auriculata Linn Fractions along with Anticancer Activity in Male Albino Mice

Shailesh M. Kewatkar ^{a*≡}, Dipak V Bhusari ^{b[⊖]}, Madhav chakolkar ^{c[#]},
Amit Joshi ^{d[†]}, Shirish P. Jain ^{e[‡]} and Chanchal Navin Raj ^{f^{##}}

^a Rajarshi Shahu College of Pharmacy, Buldana, Maharashtra, India.

^b Rajarshi Shahu College of Pharmacy, Buldana, Maharashtra, India.

^c Rajarshi Shahu College of Pharmacy, Buldana, Maharashtra, India.

^d LNCT School of Pharmacy, Kanadiya, Indore, India.

^e Rajarshi Shahu College of Pharmacy, Buldana, Maharashtra, India.

^f Shri D. D. Vispute College of Pharmacy and Research Center, New Panvel, Maharashtra, India.

Authors' contributions

This work was carried out in collaboration among all authors. All authors read and approved the final manuscript.

Article Information

DOI: 10.9734/JPRI/2021/v33i59A34267

Open Peer Review History:

This journal follows the Advanced Open Peer Review policy. Identity of the Reviewers, Editor(s) and additional Reviewers, peer review comments, different versions of the manuscript, comments of the editors, etc are available here: <https://www.sdiarticle5.com/review-history/76966>

Original Research Article

Received 10 October 2021
Accepted 15 December 2021
Published 16 December 2021

ABSTRACT

Background: In recent years, there has been a surge in interest in studying plant-derived materials and their impact on DNA. Herbal products include a number of natural substances that may help protect cells against mutagen-induced cell damage.

Aim: The purpose of this research was to assess the genotoxic effects of Cassia Auriculata Linn flavonoids (CAF) and Cassia Auriculata Linn saponin (CAS) rich fractions on mouse bone marrow cells utilizing chromosomal aberration test and micronucleus assay.

Methodology: The suppressive impact of CAF and CAS on 7, 12-dimethylbenz (α) anthracene (DMBA) and Croton oil induced skin tumor promotion in mice with topical administration twice

[≡] Associate Professor

[⊖] HOD-Diploma

[#] Assistant Professor

[†] Principal

[‡] Research Guide

*Corresponding author: E-mail: rakeshshivatare@gmail.com;

weekly for 18 weeks is also investigated in this work. Three dosages of 100 and 200 mg/kg body weight were used. Single oral dosages of CAF and CAS Fraction at the three levels did not enhance the number of micronucleate polychromatic erythrocytes in the micronucleus experiment.

Result: In mice bone marrow cells, a single oral treatment of CAF and CAS fraction revealed no significant alterations in mitotic indices or chromosomal aberration induction. The clastogenicity of CYP was considerably decreased by pretreatment with CAF and CAS fraction. As a result, it can be stated that CAF and CAS fraction had no genotoxic impact on mouse bone marrow cells.

Conclusions: The portions of *Cassia Auriculata* have been shown to be non-genotoxic and non-clastogenic at the quantities utilized in this investigation. CAF and CAS Fraction might possibly be a promising skin tumor promotion reducing agent, according to this research.

Keywords: *Cassia Auriculata*; cyclophosphamide; Genotoxic effects; anticancer activity.

1. INTRODUCTION

Natural products, in different forms such as extracts, fractions, or as a chemical platform, continue to play an important role in the treatment of numerous illnesses [1]. Plants have historically been the most common source of medicines throughout human history, owing to their secondary metabolites, which have a wide range of pharmacological activities. The knowledge of the many medicinal powers of plants has mostly been passed down via folk traditions and subsequently proven through scientific data [1,2]. Natural bioactive compounds in the prevention and/or treatment of chronic illnesses, which have been dubbed the public health challenge of the twenty-first century, are now one of the trendiest topics in medicine [2]. Indeed, as Lunenfeld and Stratton explain, the rise in healthcare systems and life expectancy in developed countries, as well as the decrease in fertility rate due to chromosomal abnormalities, has resulted in a rapid increase in global population ageing, with an increase in chronic degenerative disease [2,3]. According to the World Health Organization (WHO, 2018), cancer is the second leading cause of death (9.6 million in 2018), with malignancies of the liver (782 000 deaths) and breast (627 000 deaths) being the most prevalent. DNA damage has long been known as a cause of cancer formation, as stated [3]. In reality, oncogenes and tumor suppressor genes are affected by mutations or chromosomal abnormalities, leading to malignant transformation of cells [4]. As a result, antimutagenic, antigenotoxic, and anticarcinogenic chemicals play a critical role in cancer prevention [4,5]. A wide range of medicinal plants and their metabolites have been studied in recent years for their potential to reduce the mutagenic and carcinogenic effects of potentially harmful chemicals [6,7]; in fact, these natural compounds can inhibit free radicals and

oxidative stress-induced DNA and cellular damage [8,9].

Many mutagens and carcinogens work by creating reactive oxygen species (ROS), which are well known for causing oxidative damage to cell structures and biomolecules such lipids, nucleic acids, and proteins in living systems [10]. As a result, the evaluation of the possible genotoxicity of conventional medications is a crucial problem, as damage towards the genetic material can result in significant changes and, as a result, an increased cancer risk or other disorders. Genetic toxicology research has spawned a slew of testing methodologies, including both vitro and in vivo, as a result of their findings. In order to determine the effects of different test chemicals on genetic material and, as a result, the danger to living creatures, including humans, several processes have been devised and tested [11,12].

Synthetic antioxidants such as butylated hydroxytoluene (BHT) and butylated hydroxyanisole (BHA) are preferred, but according to recent research by Lobo et al. [13], they may have major negative consequences on human health. Plants and medicinal plants have been advised to counteract the effects of free radicals/mutagens because they may stimulate phase II enzymes, lowering the activity of cancer and other degenerative illnesses at the initiation, promotion, and progression phases [14–17].

Tanners Senna, *Cassia auriculata* Linn (Family: *Caesalpinaceae*), is found across India's hot deciduous woods and maintains a renowned place in Ayurveda and Siddha systems of treatment. It is said to include alkaloids, terpenoids, phenols and tannins, sugar saponins, flavonoids, quinines, steroids, and proteins, among other phytoconstituents. The *C. auriculata* was found to be used to cure diabetes, joint pain and inflammation, muscular discomfort, sickness,

cold, venereal disease, hair cleaner, decrease body heat, stomach pain, vomiting, diarrhea, and toothache in an ethnobotanical survey. Anti-diabetic, anti-oxidant, hepatoprotective, anti-cancer, anti-inflammatory, anti-hyperlipidemic, and other pharmacological effects of *C. auriculata* have been reported [18-19].

2. MATERIAL AND METHOD

2.1 Collection of Plant Material

Cassia auriculata Linn. roots were obtained from farms around Walgaon Road in Amravati, Maharashtra. Safia College of Science, Peer Gate, Bhopal, Madhya Pradesh, validated this plant and assigned it the voucher specimen number 159/Bot/Safia/2010 (*Cassia auriculata* Linn.).

2.2 Material and Reagent

Sigma-Aldrich Co. provided 7,12-dimethylbenz(α)anthracene (DMBA) and acetone (United States). TCI chemicals provided the croton oil (Japan). All of the other reagents were readily accessible. The tumor initiator DMBA was dissolved in acetone at a concentration of 100 g/100μl. Croton oil was dissolved in acetone to make a % croton oil solution, which was used as a tumour promoter. Curcumin was dissolved in acetone at a dosage of 10 mg/kg as a positive control. All other chemicals were bought from Himedia Laboratories Pvt. Ltd in Mumbai, India, and were of analytical quality.

2.3 Extraction of the Plant Material

Cassia auriculata Linn. roots (2 kg) were dried in the shade before being ground into a coarse powdered substance. The powdered roots of the plant were extracted with the aid of water using the decoction technique [2020] of extraction at 40°C 5°C. The aqueous extract was then filtered through funnel, and alcohol (Ethanol) was gently added to the aqueous liquid extract to precipitate out polysaccharides found in individual plant roots. The solution was then filtered, and the filtrate was evaporated to a quarter of its original volume. After evaporating 1/4 of the total volume of the solution, it was extracted with an equivalent quantity of ethyl acetate using a separating funnel to get a fraction of root components in ethyl acetate. To improve the yield of extract, the ethyl acetate extract was acidified with 0.1 N HCl. The ethyl acetate portion of the plant's root was then evaporated to produce a precipitate, which was then dissolved

in methanol and slowly evaporated to produce crystalline powder (CAF) [20].

Similarly, saponin-rich fractions were extracted from the roots of the plants. After defatting with petroleum ether, pulverized plant material was treated with a 70:30 mixture of ethanol and water for maceration for seven days (40:60). During this time, the mixture was agitated at regular intervals. After filtering through muslin cloth and filter paper, the obtained extract was concentrated using a rotary vacuum evaporator (40°C), with care taken to ensure that the extract did not become powdered. To get the n-butanol soluble fraction, the concentrated extract was treated with n-butanol. The soluble fraction of n-butanol was then treated with cold diethyl ether. Precipitate was generated after treatment with cold diethyl ether. This precipitate-containing mixture was stored at -20°C for 24 hours. Centrifugation was used to further separate the precipitates. To get crystalline powder (CAS), these precipitates were further dissolved in methanol and then evaporated [20-21].

2.4 Animals

This study was conducted in accordance with ethical procedures and policies approved by the Institutional animal ethical committee (IAEC) of PBRI (1283/c/09/CPCSEA). *Swiss albino* mice (Male; 4-5 months; 20-30 gms) were obtained from animal house of Pinnacle Biomedical Research Institute. The animals were randomly assigned to different control and treatment groups (Six animals in each group). All experimental and housing conditions for animals were maintained as per CPCSEA guidelines. Naive animals were selected at random from animal house of PBRI. Animals were kept in group of six in propylene plastic cages with sterilized husk as bedding material. Animals were provided standard feeding pellets (Golden feeds, New Delhi) and water *ad libitum*. Temperature was maintained at 22±2°C, with light and dark cycle of 12:12 hrs. The animals were transferred to the laboratory at least 1h before experiment for proper acclimatization. The experiments were performed during day (08:00-16:00 h).

2.5 Acute Toxicity Study

Toxicology experiments were conducted on young male Swiss albino mice. Each mouse's weight was recorded. The animals were separated into two groups, each with three

animals, and then labelled. Plant extract solution was produced and delivered orally in dosages of 5, 50, 100, 200, and 500 mg/kg. Up to 36 hours, no detrimental effects or mouse death were found. For any additional pharmacological action, treatment doses of 1/10th and 1/20th of the highest tolerable safe dosage were used [22-23].

2.6 Chromosomal Aberration Assay

2.6.1 Dose and treatment

The Chromosomal aberration assay of the tested substance was performed on 36 mice, age 4 - 5 months, weight - 20-30g. Before and during the experiments, all groups of animals were kept under natural light conditions with free access to food and water (Dose- 100 mg/kg; 200 mg/kg).

2.7 Procedure

In the aforesaid group of animals, CYP was utilized as a mutagenic agent and was administered as an intraperitoneal (i.p.) injection at a single dosage of 40 mg/kg b.w 2 hours after the final administration of extract on the seventh day. The positive control group got just a single CYP i.p. injection. The negative control got merely a single 0.4 mL distilled water (d.w.) i.p. injection. For 7 days, the control groups were given p.o. extract at a rate of 200 mg/kg b.w per day for 7 days.

2.8 Chromosomal Analysis

The animals in all groups were slaughtered by cervical dislocation at the sampling time of 24 hours after treatment (colchicine was administered at a dosage of 4 mg/kg of body

weight 2 hours before to killing to halt the metaphase stage). Preston et al procedure's for cytogenetic analysis was followed. Hank's balanced salt solution was used to drain the bone marrow from both femurs (pH 7.2). To allow osmotic swelling of cells, the cells were centrifuged at 1000 rpm for 5 minutes and the pellet was re-dispersed in a hypotonic solution of 0.56 % (w/v) KCl for 30 minutes at 37°C. Swollen cells were fixed in ice-cold Carnoy's fluid, transferred to slides, and stained with phosphate-buffered 5% Giemsa solution. The mitotic index was estimated from a scan of 2000 cells per animal and 75 well-spread metaphase plates per animal in each group were tested for chromosomal abnormalities at a magnification of 100 X. Breaks, fragments, exchanges, and numerous chromosomal abnormalities were classed as chromosomal aberrations (cells with 10 or more aberrations were classified as multiple). The mitotic index, percentage of occurrence of aberrant cells, and percentage of suppression of chromosomal abnormalities were among the criteria studied. The mitotic index was determined as a proportion of dividing cells out of total bone marrow cells measured for cytotoxicity assessment. The number of abnormal cells was calculated as a proportion of the total number of damaged cells (aberrant metaphases).

The suppression percentage of chromosomal aberrations was calculated as:

$$100 - \left[\frac{\text{percent incidence of aberrant cells in extract pre-treated and CYP post treated groups}}{\text{percent incidence of aberrant cells in CYP alone treated group}} \times 100 \right] \text{ [24-26].}$$

Table 1. Dose and treatment selection for Chromosomal Aberration Assay

Group No	Group name	Treatment	Dose	No of animal/group
1	Vehicle	No treatment	Nil	06
2	Control	CYP Only	Nil	06
3	CYP+CAF	Extract + CYP	100 mg/kg	06
4	CYP+CAF	Extract + CYP	200 mg/kg	06
5	CYP+CAS	Extract + CYP	100 mg/kg	06
6	CYP+CAS	Extract + CYP	200 mg/kg	06

Table 2. Dose and treatment selection for Micronucleus assay

Group No	Group name	Treatment	Dose	No of animal/group
1	Vehicle	No treatment	Nil	06
2	Control	CYP Only	Nil	06
3	CYP+CAF	Extract + CYP	200 mg/kg	06
4	CYP+ CAS	Extract + CYP	200 mg/kg	06

2.9 Micronucleus Assay

2.9.1 Dose and treatment

The Micronucleus assay of the tested substance was performed on 36 mice, age 4 - 5 months, weight- 20-30 g. Before and during the experiments, all groups of animals were kept under natural light conditions with free access to food and water (Dose- 100 mg/kg; 200 mg/kg).

2.10 Bone Marrow MN Test and Scoring

The bone marrow MN tests were performed on the same experimental animals. Cervical dislocation was used to kill the animals. The femur and tibia were surgically removed. The modified Schmid technique was used to create bone marrow MN slides. The pellet was centrifuged at 1000 rpm and resuspended in BSA solution after marrow suspension from femur and tibia bones was produced in % bovine serum albumin (BSA). Smears were created and the slides were air-dried after a drop of this suspension was applied on clean glass slides. MN were found in the forms of RBCs, i.e., polychromatic erythrocytes as PCEs, when the slides were fixed in methanol and stained with May-Grunwald-Giemsa. MN was detected in around 2000 PCEs per animal [27-29].

2.10.1 Anticancer activity

2.10.1.1 Dose and treatment

The Anticancer activity of the tested substance was performed on 24 mice, age 4 - 5 months, weight - 20-30g. Before and during the experiments, all groups of animals were kept under natural light conditions with free access to food and water (Dose- 100 mg/kg; 200 mg/kg).

2.11 Procedure

2.11.1 Tumor induction

Different groups of 06 animals were treated with a single dose of DMBA (7,12-

dimethylbenz[a]anthracene) (100 µg/100 µl of acetone) over the shaven area of the skin of the mice. Two weeks later, croton oil (1% in 100 µl of acetone) was applied as a promoter 3 times per week until the end of the experiment (i.e., 16 weeks).

2.11.2 Parameters to be noticed

Tumor incidence: The number of mice carrying at least 1 tumor, expressed as a percentage incidence.

Tumor yield: The average number of papillomas per mouse.

Tumor Burden: The average number of tumors per tumor bearing mouse.

Body weight: The weight of the mice was measured weekly.

Average Latent Period: The lag between the application of the promoting agent and the appearance of 50% of tumors was determined. The average latent period was calculated by multiplying the number of tumors appearing each week by the time in weeks after the application of the promoting agent and dividing the sum by total number of tumors.

$$\text{Average latent period} = \sum fx / n$$

Where f is the number of tumors appearing each week, x is the numbers of weeks, and n is the total number of tumors.

2.12 Histopathological Study

Skin was fixed with buffered formalin for 24 hours. Afterward skin was embedded in paraffin wax by standard protocol. Serial section of 4 µm was cut by microtome with rotary microtome. Sections were stained with Hemtoxyline and eosin staining. Sections were observed at 40x and 100x for histological variations. Important areas were photographed using microscope with digital camera [30-32].

Table 3. Dose and treatment selection for anticancer activity

Group No	Group name	Treatment	Dose	No of animal/group
1	Control	DMBA + Croton oil	Nil	06
2	CAF + CAS	DMBA + Croton oil + Extract of CAF + CAS	200 mg/kg	06
3	CAF	DMBA + Croton oil + Extract of CAF	200 mg/kg	06
4	CAS	DMBA + Croton oil + Extract of CAS	200 mg/kg	06

3. RESULT AND DISCUSSION

3.1 Acute Toxicity Study

Acute oral toxicity is a key criterion for determining a component's safety. The acute oral toxicity of test samples was determined using the OECD 423 criteria in this study. Four dosage levels were employed, according to the guidelines: 5 mg/kg, 50 mg/kg, 300 mg/kg, and 2000 mg/kg. No mortality was reported in *Cassia auriculata* flavonoid rich extracts (CAF) up to a level of 2000 mg/kg. No fatality was seen in the case of *Cassia auriculata* saponin rich extract (CAS) up to a dosage of 300 mg/kg, but one death was recorded at a dose of 2000 mg/kg. As a result, it was determined that the LD50 of both extracts was more than 2000 mg/kg. This upper limit was also utilized to determine dosages for the current study. As a result, for future research, dosages of 1/10th and 1/20th of the maximum allowed dose, i.e., 200 mg/kg and 100 mg/kg, were used [22-23].

3.2 Chromosomal Aberration Assay

In present study effect of test samples was assessed against cyclophosphamide (CYP) induced mutagenicity. Break, Fragment, Deletion, polyploidy, pulverized and ring type of aberrations were quantified in various treatment groups. Generally, chromatid breaks can be induced in the S and G2 phases of the cell cycle, when the chromosome has split into 2 chromatids. Many chemical agents, especially alkylating agents cause predominantly chromatid-type aberrations. In vehicle treated animals total break was found to be 3.83 ± 1.72 % which was significantly elevated ($P < 0.05$) in CYP only treated animals with 31.33 ± 3.01 %. Flavonoid rich extract of *Cassia auriculata* significantly lowered percentage break up to 8.16 ± 1.47 % and 5.16 ± 1.72 % at 100 and 200 mg/kg respectively ($P < 0.05$). In saponins rich extract increased mutagenicity was observed at lower dose as well as higher doses. Fragments

are single chromatid without centromeres. In CYP treated animals 24.16 ± 2.56 % fragments were observed which were significantly higher ($P < 0.05$) as compared to vehicle treated animals in which 2.83 ± 1.47 % fragments were present [24-26].

3.3 Effect of CAF & CAS on Cyclophosphamide induced Genotoxicity

3.3.1 Study of effect of CAF& CAS in micronucleus assay

During anaphase, Mn products from entire chromosomes or central chromosomal segments were not involved in cell division. Mn formation might be used as a biomarker for exposure to both clastogenic and eugenic hazards. Mn is a useful biomarker for biological dosimetry in the event of acute radiation exposure in humans, according to studies. Radiation dosage has an effect on Mn frequency. After being exposed to ionizing radiation in the 50-500 Msv range, Fenech discovered a rise in Mn frequency in human cells. The Mn test was used to assess biological damage in populations living in locations with high levels of radioactivity, as well as in workers who are exposed to ionizing radiation on the job. Counting the amount of PCE among 1000 cells was used to assess the cytotoxic capability of CAF and CAS. Table 6 shows the number of MNPCEs among 2000 PCE, which indicates genotoxicity. At a dosage of 200 mg/kg, the number of MNPCEs among 2000 PCE generated by CAF was significant ($p < 0.001$). CAF reduced the yields of MN induced by CYP in pre-, simultaneous, and post-treatments by a statistically significant amount. Except for the two highest dosages, all of the CAF doses tested were shown to be beneficial in lowering the incidence of MN caused by CYP. There was also a significant decline in overall MN yield (MN in PCE) [27-29]. CAS were shown to be ineffective in lowering the frequency of MN.

Table 4. Acute toxicity study

Groups	No. of animals	Dose (mg/kg)	Result
<i>C. auriculata</i> root, crude flavonoids extract			
1.	3	5	Not observed (0/3)
2.	3	50	No death
3.	3	300	No death
4.	3	2000	No death
<i>C. auriculata</i> root, crude saponin extract			
5.	3	5	No death

Groups	No. of animals	Dose (mg/kg)	Result
6.	3	50	No death
7.	3	300	No death
8.	3	2000	01 Dead

Table 5. Effect of CAF & CAS on Cyclophosphamide induced Genotoxicity

S. No.	Treatment	Break	Fragment	Deletion	Polyploidy	Pulverized	Ring
1	Vehicle	3.83 ± 1.72 ^d	2.83 ± 1.47	3.66 ± 1.63	0	0	0
2	CYP	31.33 ± 3.01 ^a	24.16 ± 2.56 ^a	17.33 ± 3.26 ^a	6.66 ± 1.96 ^a	6.16 ± 1.47 ^a	5.83 ± 1.60 ^a
3	CYP+CAF (100 mg/kg)	8.16 ± 1.47 ^{abc}	7.17 ± 2.22 ^{abc}	7.83 ± 2.63 ^{abc}	2.33 ± 1.21 ^{abc}	1.83 ± 1.169 ^{abc}	2.16 ± 0.98 ^{abc}
4	CYP+CAF (200 mg/kg)	5.16 ± 1.72 ^{abc}	4.33 ± 1.86 ^{abc}	3.67 ± 1.63 ^{abc}	1.16 ± 0.75 ^{abc}	1.16 ± 1.60 ^{abc}	0.83 ± 1.16 ^{abc}
5	CYP+CAS (100 mg/kg)	37.66 ± 2.58	29.83 ± 2.71	23.16 ± 3.31	10.33 ± 2.25	10.66 ± 2.50	9.17 ± 1.47
6	CYP+CAS (200 mg/kg)	30.83 ± 2.31 ^a	23.67 ± 3.32 ^a	16.83 ± 3.31 ^a	5.83 ± 1.94 ^a	5.66 ± 1.96 ^a	5.33 ± 2.16 ^a

All Data presented in mean ± SD, ^a P<0.05 as compared to CYP+CAS treated group, ^b P<0.05 as compared to CYP treated group, ^c P<0.05 as compared to CYP+CAF treated group, ^d P<0.05 as compared to CYP+CAF treated group

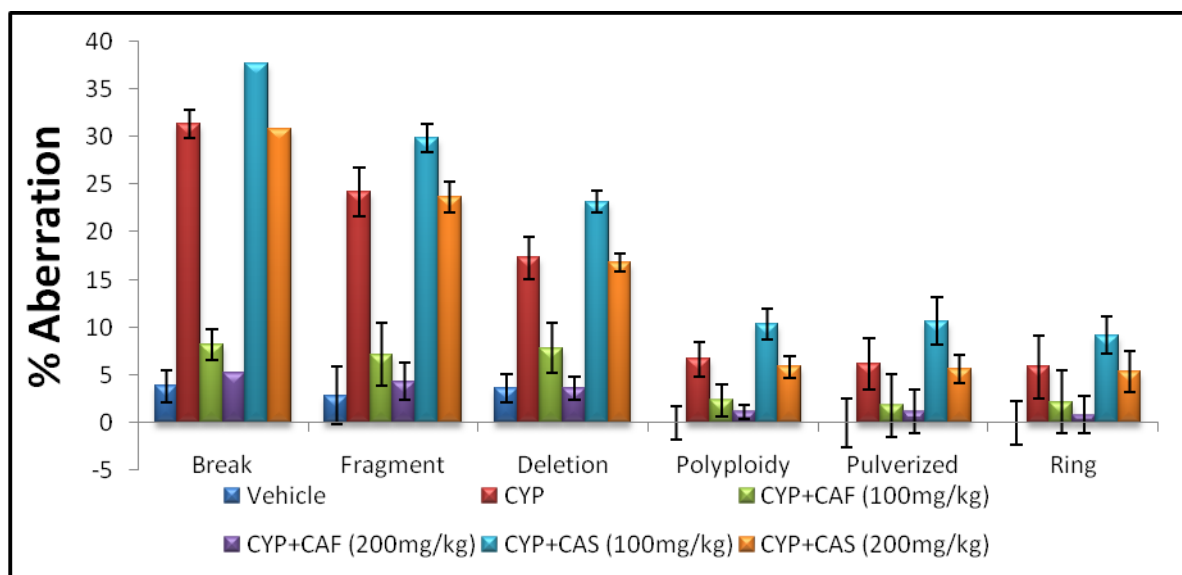


Fig. 1. Effect of CAF & CAS on Cyclophosphamide induced Genotoxicity

Table 6. Effect of CAF & CAS in Micronucleus Assay

S. No.	Treatment	MN-PCE
1.	Vehicle	0.24±0.11
2.	CYP	6.12±0.42
3.	CYP+CAF	2.48±0.63 ^{abcd}
4.	CYP+ CAS	5.92±0.54

All Data presented in mean ± SD, ^a P<0.05 as compared to CYP treated group, ^b P<0.05 as compared to CYP+ Caf treated group, ^c P<0.05 as compared to CYP+ CAS treated group

3.4 Anticancer Activity

At weekly intervals, body weight, tumor yield, percentage of tumors incidence, and tumors burden were examined and assessed. Only tumors with a diameter bigger than 1 mm that had been present for more than one week were included for data analysis. When the first tumors developed, the latency time of tumor development was established. The number of tumor-bearing mice was divided by the total number of mice in a group and multiplied by 100 percent to get the percentage of tumor incidence. The total number of tumors was divided by the number of tumor-bearing mice in a group to get the tumor burden. The volume of the tumor was calculated by multiplying the length, breadth, and height of the tumor by $\pi/6$.

At the conclusion of the trial, all groups' average body weights had increased significantly (Table 7). During the promotion stage, tumors begin to form on the skin between weeks 6 and 9. Tumor development began one week sooner in groups I and IV than in groups II and III, in the sixth week.

The incidence of tumors differed considerably between the treatment Control group and the remainder group. Statistical analysis also revealed that there is a significant variation in tumor burden across groups. Tumor burden is greatest in group I, with a value of 32.5, followed

by 18.83, 22.83, and 29.83 in groups II, III, and IV, respectively. In terms of tumor volume, there was no significant difference between groups.

However, there was a statistically significant difference in tumor volume between groups I (32.5) and II (18.83) when compared to group III, while group IV (22.83 and 29.83) was lower than group I, albeit there was no statistically significant difference between these two groups.

In terms of tumor incidence, tumor yield, and tumor burden, groups II and III performed better than the carcinogen control group (group I). The suppressing impact of group II was equivalent to that of the positive control group (group III), but the suppressing effect of group IV was even larger than that of group I, notably in terms of tumor incidence and tumor burden. Nonetheless, as compared to the carcinogen control group, Group II had a higher tumor incidence and tumor volume.

Morphological investigation (Fig. 2) revealed substantial epidermal hyperplasia (as shown by the thicker epidermal layer) as well as many keratin pearls and rete ridges in the carcinogen control-treated group in all protocols. In the skin sections of the DMBA plus croton oil-treated group, irregular distribution with finger-like projections (papilloma) suggestive of malignant development was identified.

Table 7. Result of anticancer parameters

Group	Parameters	Week 0	Week 8	Week 16
Control	Body weight (gms)	22.82±1.79	32.28±3.84	31.82±2.23
	Tumor yield	0	3.67	32.5
	Tumor incidence	0	83.33	100
	Tumor burden	0	4.4	32.5
CAF+CAS	Body weight (gms)	23.07±0.90	30.35±2.27	31.02±2.58
	Tumor yield	0	2	18.83
	Tumor incidence	0	50	100
	Tumor burden	0	4	18.83
CAF	Body weight (gms)	23.63±0.53	31.14±1.31	31.38±1.89
	Tumor yield	0	2	22.83
	Tumor incidence	0	50	100
	Tumor burden	0	4	22.83
CAS	Body weight (gms)	22.83±0.61	30.69±0.83	29.7±0.85
	Tumor yield	0	3.33	29.83
	Tumor incidence	0	50	100
	Tumor burden	0	6.67	29.83

Furthermore, pieces of the basement membrane were disturbed in several tissue slices, suggesting that the tumors had advanced to a premalignant stage. In all methods, skin tissue samples from the different extracts treated groups showed a decreased degree of epidermal hyperplasia, keratin pearls, and rete ridges. Because the basement membrane remained intact and the dermis had not been infiltrated, the tumors developed were deemed benign. As a consequence of the histology examinations, it was discovered that the level of cellular diversity in various treatment groups correlated with tumor outcomes.

In all treated groups, further histological investigation revealed varied degrees of hyperplasia and keratin pearls. In comparison to the carcinogen control (group I), the epidermis in groups II and III is less hyperplastic, but group IV has more keratin pearls and a hyperplastic epidermis that is equivalent to the carcinogen control. The tumors that develop are benign papillomas that remain contained inside an intact basement membrane with no evidence of invasion into the dermis. Premalignant lesions, on the other hand, were seen in the carcinogen control group [30-32].

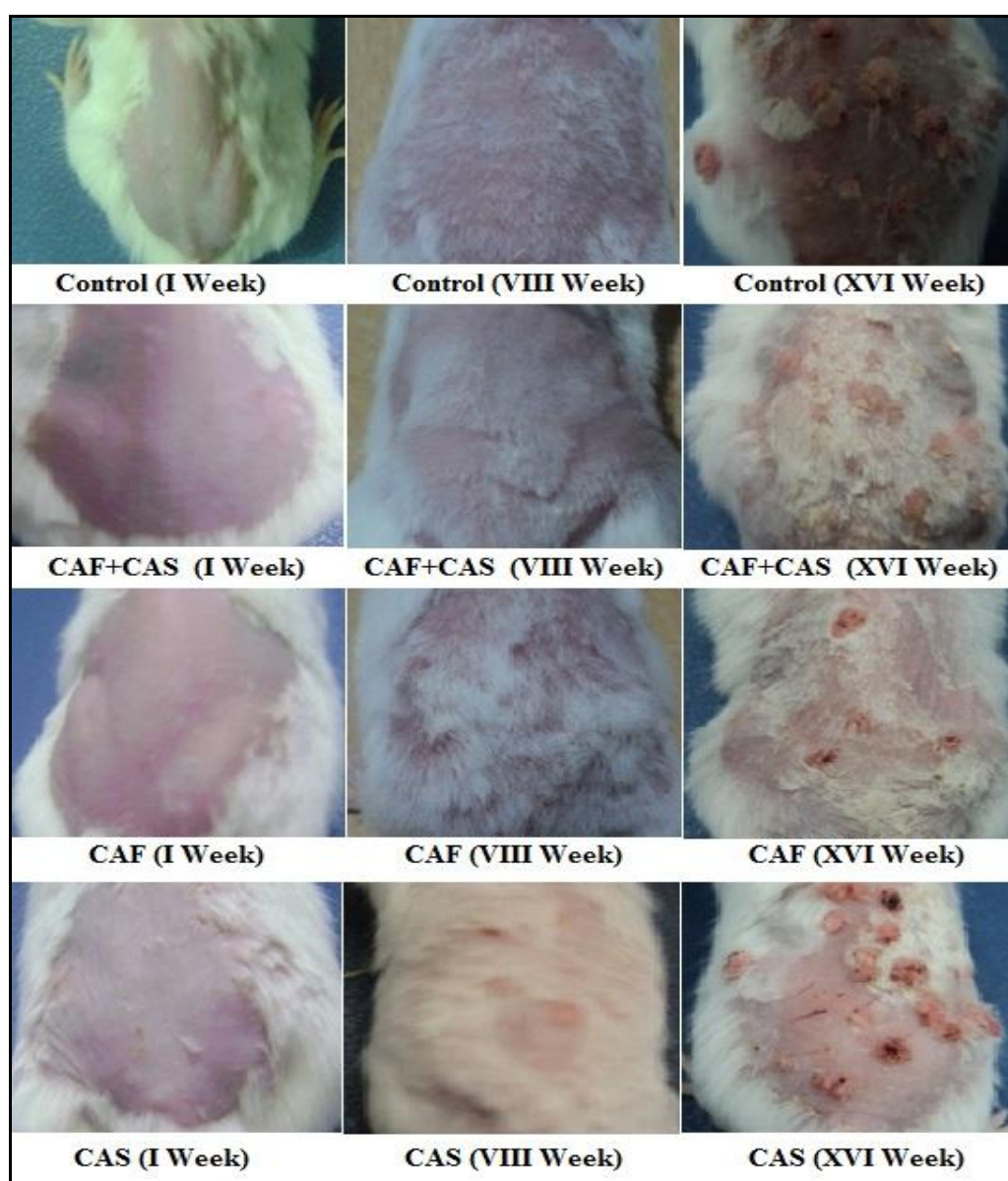


Fig. 2. Morphological examination of anticancer activity on mice

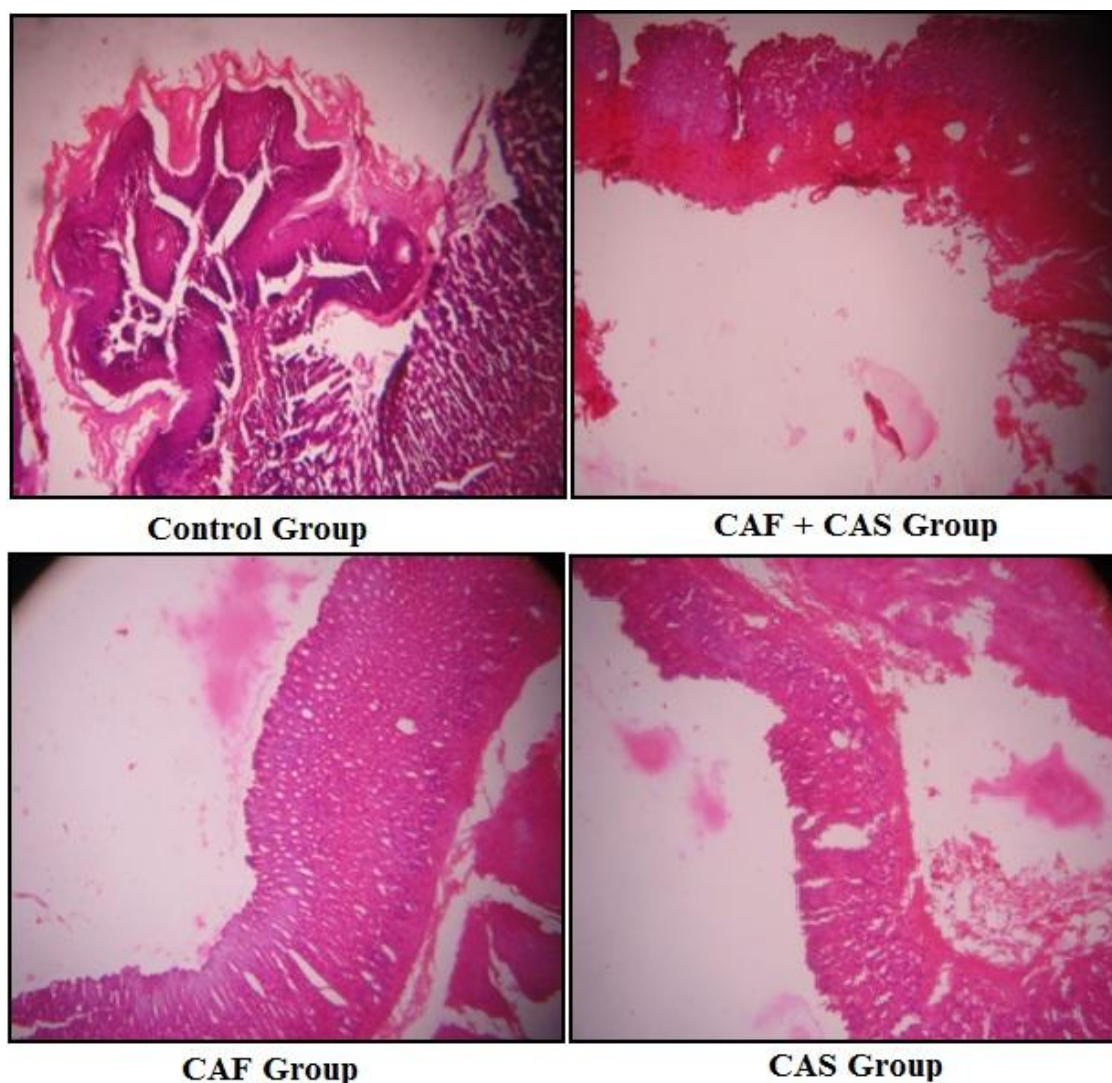


Fig. 3. Histopathological analysis of anticancer activity on mice

4. CONCLUSION

Traditional medical systems have grown in importance over the last decade as a result of their safety. According to current estimates, a significant section of the population in many developing nations depends significantly on traditional practitioners and medicinal herbs to cover their basic health care requirements. Despite the pharmaceutical industry's breakthroughs in the production of unique and highly effective medications for the treatment of a broad variety of disorders, the use of herbal remedies has increased significantly in the world's most wealthy nations. Every medicine has side effects, but a useful pharmacologically active substance should have a good balance of therapeutic and harmful or undesirable side effects. A battery of genotoxic and/or

mutagenicity tests must be done to screen the toxicity mechanism to assure the safety and effectiveness of natural compounds. There is no one test that can collect enough data to predict the chemical risks to human health. The findings of this investigation show that the *Cassia Auriculata* Linn CAF and CAS Fractions are neither genotoxic or clastogenic at the quantities employed. Our findings further suggest that pretreatment with *Cassia Auriculata* Linn CAF and CAS Fraction reduces CYP-induced clastogenicity while maintaining its cytotoxic capability. Because it prolongs the development of tumors in the skin and reduces the hyperproliferative response evoked by CYP, it can be inferred that CAF and CAS Fraction of *Cassia Auriculata* functions as a modulator of two-stage skin carcinogenesis in Swiss albino mice. Furthermore, it reduces oxidative cell

damage, which is inextricably linked to the development of cancer. Further research into the exact mode of action of the genetic toxicity of isolated compounds from this plant species is needed to gain a better understanding of the genotoxic mechanisms described herein, as well as to investigate the protective role of *Cassia Articulata*'s CAF and CAS fractions against genotoxic agents in the environment. It is necessary to understand their processes as cancer treatments.

CONSENT

It is not applicable.

ETHICAL APPROVAL

This study was conducted in accordance with ethical procedures and policies approved by the Institutional animal ethical committee (IAEC) of PBRI (1283/c/09/CPCSEA). Swiss albino mice (Male; 4-5 months; 20-30 gms) were obtained from animal house of Pinnacle Biomedical Research Institute.

COMPETING INTERESTS

Authors have declared that no competing interests exist.

REFERENCES

1. Atanasov AG, Waltenberger B, Pferschy-Wenzig EM, Linder T, Wawrosch C, Uhrin P, et al. Discovery and resupply of pharmacologically active plant-derived natural products: A review. *Biotechnology Advances*. 2015; 33(8):1582–1614. pmid:26281720
Available:https://doi.org/10.1016/j.biotechadv.2015.08.001
2. Lunenfeld B, Stratton P. The clinical consequences of an ageing world and preventive strategies. *Best Practice & Research: Clinical Obstetrics & Gynecology*. 2013;27(5):643–59. Available:https://doi.org/10.1016/j.bpobgyn.2013.02.005
3. Torgovnick A, Schumacher B. DNA repair mechanisms in cancer development and therapy. *Frontiers in Genetics*. 2015; 23(6):157. Available:https://doi.org/10.3389/fgene.2015.00157
4. Nagarathna PKM, Johnson Wesley M, Sriram Reddy P, Reena K. Review on Genotoxicity, its Molecular Mechanisms and Prevention. *International Journal of Pharmaceutical Sciences Review and Research*. 2013; 22(1): 236–243. Available:https://www.researchgate.net/publication/326733700_A_review_on_genotoxicity_in_aquatic_organisms_and_environment
5. Słoczyńska K, Powroźnik B, Pękala E, Waszkielewicz AM. Antimutagenic compounds and their possible mechanisms of action. *Journal of Applied Genetics*. 2014; 55: 273–285 pmid:24615570
Available:https://doi.org/10.1007/s13353-014-0198-9
6. Collins AR, Azqueta A, Langie SAS. Effects of micronutrients on DNA repair. *European Journal of Nutrition*. 2012; 51: 261–279. pmid:22362552
Available:https://doi.org/10.1007/s00394-012-0318-4
7. Orhan F, Gulluce M, Ozkan H, Alpsoy L. Determination of the antigenotoxic potencies of some luteolin derivatives by using a eukaryotic cell system, *Saccharomyces cerevisiae*. *Food Chemistry*. 2013; 141: 366–372. pmid:23768369
Available:https://doi.org/10.1016/j.foodchem.2013.02.089
8. Chatterjee S, Poduval TB, Tilak JC, Devasagayam TPA. A modified, economic, sensitive method for measuring total antioxidant capacities of human plasma and natural compounds using Indian saffron (*Crocus sativus*). *Clinica Chimica Acta*. 2005; 352: 155–163. Available:https://doi.org/10.1016/j.cccn.2004.09.012
9. Nsimba RY, Kikuzaki H, Konishi Y. Antioxidant activity of various extracts and fractions of *Chenopodium quinoa* and *Amaranthus* spp. seeds. *Food Chemistry*. 2008; 106: 760–766. Available:https://doi.org/10.1016/j.foodchem.2007.06.004
10. Castro L, Freeman BA. Reactive oxygen species in human health and disease. *Nutrition*. 2001; 170:161–5. Available:https://doi.org/10.1016/s0899-9007(00)00570-0
11. Attia S M. The genotoxic and cytotoxic effects of nicotine in the mouse bone marrow. *Mutation Research/ Genetic Toxicology and Environmental Mutagenesis*. 2007; 632(1-2), 29-36.

- Available: <https://doi.org/10.1016/j.mrgento.2007.04.010>
12. Nagarathna PKM, Yadav CK, Yadav SK. Evaluation of Mutagenic Effect and Antimutagenic of Dalbergia Latifolia on Swiss Albino Mice Evaluation, Asian J Pharm Clin Res, 2015;8(3):154-158
 13. V. Lobo, A. Patil, A. Phatak, N. Chandra, Free radical's antioxidants and functional foods: impact on human health, Pharmacogn. Rev. 4 (8) (2010) 118–126. Available: <https://dx.doi.org/10.4103%2F0973-7847.70902>
 14. W.K. Hong, M.B. Sporn, Recent advances in the chemoprevention of cancer, Science 278 (1997) 1073–1077. Available: <https://doi.org/10.1126/science.278.5340.1073>
 15. X.L. Tan, S.D. Spivack, Dietary chemoprevention strategies for induction of phase II xenobiotic-metabolizing enzymes in lung carcinogenesis: a review, Lung Cancer 65 (2009) 129–137. Available: <https://doi.org/10.1016/j.lungcan.2009.01.002>
 16. J.K. Kundu, Y.J. Surh, Molecular basis of chemoprevention with dietary phytochemicals: redox-regulated transcription factors as relevant targets, Phytochem. Rev. 8 (2009) 333–347. Available: <http://dx.doi.org/10.1007%2Fs11101-009-9132-x>
 17. R. Edenharder, I. Von Petersdorff, R. Rauscher, Antimutagenic effects of flavonoids, chalcones and structurally related compounds on the activity of 2-amino-3-methylimidazo [4,5-f] quinoline (IQ) and other heterocyclic amine mutagens from cooked food, Mutat. Res. Med. 287 (1993) 261–274. Available: [https://doi.org/10.1016/0027-5107\(93\)90019-C](https://doi.org/10.1016/0027-5107(93)90019-C)
 18. Salma B, Janhavi P, Muthaiah S, Veeresh P, Santhepete Nanjundaiah M, Divyashree S, Serva Peddha M. Ameliorative efficacy of the cassia auriculata root against high-fat-diet+ STZ-induced type-2 diabetes in C57BL/6 mice. ACS omega. 2020 Dec 18;6(1):492-504. Available: <https://doi.org/10.1021/acsomega.0c04940>
 19. Anu K, Devanesan S, Prasanth R, AlSalhi MS, Ajithkumar S, Singaravelu G. Biogenesis of selenium nanoparticles and their anti-leukemia activity. Journal of King Saud University-Science. 2020;32(4):2520-6. Available: <https://doi.org/10.1016/j.jksus.2020.04.018>
 20. Khyade M, Kamble S, Waman M, Padwal A, Gunjal M. Food Potential and Antioxidant Property of Cassia auriculata Seed: A Nutritionally Unexploited Legume. Current Nutrition & Food Science. 2020 Dec 1;16(9):1381-92. Available: <https://doi.org/10.2174/1573401316666200221110140>
 21. Ebringerová A, Hromádková Z. An overview on the application of ultrasound in extraction, separation and purification of plant polysaccharides. Central European Journal of Chemistry. 2010;8(2):243-57. Available: <http://dx.doi.org/10.2478/s11532-010-0006-2>
 22. Lalitha P, Sripathi SK, Jayanthi P. Acute toxicity study of extracts of Eichhornia Crassipes (Mart.) Solms. Asian J Pharm Clin Res. 2012;5(4):59-61. Available: <https://innovareacademics.in/journal/ajpcr/Vol5Issue4/1225.pdf>
 23. Halim SZ, Abdullah NR, Afzan A, Rashid BA, Jantan I, Ismail Z. Acute toxicity study of Carica papaya leaf extract in Sprague Dawley rats. Journal of Medicinal Plants Research. 2011 May 18;5(10):1867-72. Available: https://www.researchgate.net/publication/230859605_Acute_toxicity_study_of_Carica_papaya_leaf_extract_in_Sprague_Dawley_rats
 24. Gangar SC, Sandhir R, Koul A. Anticlastogenic activity of Azadirachta indica against benzo (a) pyrene in murine forestomach tumorigenesis bioassay. Acta Pol Pharm. 2010 Jul 1;67(381):90. Available: <https://pubmed.ncbi.nlm.nih.gov/20635534/>
 25. Parveen N, Shadab GG. The dual clastogenic and anti-clastogenic properties of quercetin is dose dependent. Front Biosci (School Ed). 2017 Jan 1; 9:139-53. Available: <https://doi.org/10.2741/s478>
 26. Manoharan S, Balakrishnan S, Vinothkumar V, Silvan S. Anti-clastogenic potential of carnosic acid against 7, 12-dimethylbenz (a) anthracene (DMBA)-induced clastogenesis. Pharmacological Reports. 2010 Nov 1;62(6):1170-7. Available: [http://dx.doi.org/10.1016/S1734-1140\(10\)70379-0](http://dx.doi.org/10.1016/S1734-1140(10)70379-0)
 27. Želazna K, Rudnicka K, Tejs S. In vitro micronucleus test assessment of polycyclic aromatic hydrocarbons. Environmental Biotechnology. 2011; 7:70-80.

28. Available:file:///C:/Users/Rohan%20Yadav/Downloads/httpwww_environmentalbiotechnology_plebdzialyebonline2011vol72ms161kzelazna.pdf
29. Promkum C, Butryee C, Tuntipopipat S, Kupradinun P. Anticlastogenic effect of *Eryngium foetidum* L. assessed by erythrocyte micronucleus assay. *Asian Pacific Journal of Cancer Prevention*. 2012;13(7):3343-7. Available:https://doi.org/10.7314/apjcp.2012.13.7.3343
30. Maurich T, Pistelli L, Turchi G. Anticlastogenic activity of two structurally related pterocarpanes purified from *Bituminaria bituminosa* in cultured human lymphocytes. *Mutation Research/Genetic Toxicology and Environmental Mutagenesis*. 2004;561(1-2):75-81. Available:https://doi.org/10.1016/j.mrgento.2004.03.006
31. Saini MR, Goyal PK, Chaudhary G. Antitumor activity of *Aloe vera* against DMBA/croton oil-induced skin papilloma genesis in Swiss albino mice. *Journal of Environmental Pathology, Toxicology and Oncology*. 2010; 29(2). DOI: 10.1615/JEnvironPatholToxicolOncol.v29.i2.60
32. Sharma S, Khan N, Sultana S. Effect of *Onosma echioides* on DMBA/croton oil mediated carcinogenic response, hyperproliferation and oxidative damage in murine skin. *Life sciences*. 2004 Oct 1;75(20):2391-410. Available:https://doi.org/10.1016/j.lfs.2004.04.030

© 2021 Kewatkar et al.; This is an Open Access article distributed under the terms of the Creative Commons Attribution License (<http://creativecommons.org/licenses/by/4.0>), which permits unrestricted use, distribution, and reproduction in any medium, provided the original work is properly cited.

Peer-review history:

The peer review history for this paper can be accessed here:

<https://www.sdiarticle5.com/review-history/76966>



Antimutagenic Activity of Cassia Auriculata Linn Fractions along with Anticancer Activity in Male Albino Mice

Shailesh M. Kewatkar ^{a*≡}, Dipak V Bhusari ^{b[⊙]}, Madhav chakolkar ^{c[#]},
Amit Joshi ^{d[†]}, Shirish P. Jain ^{e[‡]} and Chanchal Navin Raj ^{f[#]}

^a Rajarshi Shahu College of Pharmacy, Buldana, Maharashtra, India.

^b Rajarshi Shahu College of Pharmacy, Buldana, Maharashtra, India.

^c Rajarshi Shahu College of Pharmacy, Buldana, Maharashtra, India.

^d LNCT School of Pharmacy, Kanadiya, Indore, India.

^e Rajarshi Shahu College of Pharmacy, Buldana, Maharashtra, India.

^f Shri D. D. Vispute College of Pharmacy and Research Center, New Panvel, Maharashtra, India.

Authors' contributions

This work was carried out in collaboration among all authors. All authors read and approved the final manuscript.

Article Information

DOI: 10.9734/JPRI/2021/v33i59A34267

Open Peer Review History:

This journal follows the Advanced Open Peer Review policy. Identity of the Reviewers, Editor(s) and additional Reviewers, peer review comments, different versions of the manuscript, comments of the editors, etc are available here: <https://www.sdiarticle5.com/review-history/76966>

Original Research Article

Received 10 October 2021
Accepted 15 December 2021
Published 16 December 2021

ABSTRACT

Background: In recent years, there has been a surge in interest in studying plant-derived materials and their impact on DNA. Herbal products include a number of natural substances that may help protect cells against mutagen-induced cell damage.

Aim: The purpose of this research was to assess the genotoxic effects of Cassia Auriculata Linn flavonoids (CAF) and Cassia Auriculata Linn saponin (CAS) rich fractions on mouse bone marrow cells utilizing chromosomal aberration test and micronucleus assay.

Methodology: The suppressive impact of CAF and CAS on 7, 12-dimethylbenz (α) anthracene (DMBA) and Croton oil induced skin tumor promotion in mice with topical administration twice

[≡] Associate Professor

[⊙] HOD-Diploma

[#] Assistant Professor

[†] Principal

[‡] Research Guide

*Corresponding author: E-mail: rakeshshivatare@gmail.com;

weekly for 18 weeks is also investigated in this work. Three dosages of 100 and 200 mg/kg body weight were used. Single oral dosages of CAF and CAS Fraction at the three levels did not enhance the number of micronucleate polychromatic erythrocytes in the micronucleus experiment.

Result: In mice bone marrow cells, a single oral treatment of CAF and CAS fraction revealed no significant alterations in mitotic indices or chromosomal aberration induction. The clastogenicity of CYP was considerably decreased by pretreatment with CAF and CAS fraction. As a result, it can be stated that CAF and CAS fraction had no genotoxic impact on mouse bone marrow cells.

Conclusions: The portions of *Cassia Auriculata* have been shown to be non-genotoxic and non-clastogenic at the quantities utilized in this investigation. CAF and CAS Fraction might possibly be a promising skin tumor promotion reducing agent, according to this research.

Keywords: *Cassia Auriculata*; cyclophosphamide; Genotoxic effects; anticancer activity.

1. INTRODUCTION

Natural products, in different forms such as extracts, fractions, or as a chemical platform, continue to play an important role in the treatment of numerous illnesses [1]. Plants have historically been the most common source of medicines throughout human history, owing to their secondary metabolites, which have a wide range of pharmacological activities. The knowledge of the many medicinal powers of plants has mostly been passed down via folk traditions and subsequently proven through scientific data [1,2]. Natural bioactive compounds in the prevention and/or treatment of chronic illnesses, which have been dubbed the public health challenge of the twenty-first century, are now one of the trendiest topics in medicine [2]. Indeed, as Lunenfeld and Stratton explain, the rise in healthcare systems and life expectancy in developed countries, as well as the decrease in fertility rate due to chromosomal abnormalities, has resulted in a rapid increase in global population ageing, with an increase in chronic degenerative disease [2,3]. According to the World Health Organization (WHO, 2018), cancer is the second leading cause of death (9.6 million in 2018), with malignancies of the liver (782 000 deaths) and breast (627 000 deaths) being the most prevalent. DNA damage has long been known as a cause of cancer formation, as stated [3]. In reality, oncogenes and tumor suppressor genes are affected by mutations or chromosomal abnormalities, leading to malignant transformation of cells [4]. As a result, antimutagenic, antigenotoxic, and anticarcinogenic chemicals play a critical role in cancer prevention [4,5]. A wide range of medicinal plants and their metabolites have been studied in recent years for their potential to reduce the mutagenic and carcinogenic effects of potentially harmful chemicals [6,7]; in fact, these natural compounds can inhibit free radicals and

oxidative stress-induced DNA and cellular damage [8,9].

Many mutagens and carcinogens work by creating reactive oxygen species (ROS), which are well known for causing oxidative damage to cell structures and biomolecules such lipids, nucleic acids, and proteins in living systems [10]. As a result, the evaluation of the possible genotoxicity of conventional medications is a crucial problem, as damage towards the genetic material can result in significant changes and, as a result, an increased cancer risk or other disorders. Genetic toxicology research has spawned a slew of testing methodologies, including both vitro and in vivo, as a result of their findings. In order to determine the effects of different test chemicals on genetic material and, as a result, the danger to living creatures, including humans, several processes have been devised and tested [11,12].

Synthetic antioxidants such as butylated hydroxytoluene (BHT) and butylated hydroxyanisole (BHA) are preferred, but according to recent research by Lobo et al. [13], they may have major negative consequences on human health. Plants and medicinal plants have been advised to counteract the effects of free radicals/mutagens because they may stimulate phase II enzymes, lowering the activity of cancer and other degenerative illnesses at the initiation, promotion, and progression phases [14–17].

Tanners Senna, *Cassia auriculata* Linn (Family: *Caesalpinaceae*), is found across India's hot deciduous woods and maintains a renowned place in Ayurveda and Siddha systems of treatment. It is said to include alkaloids, terpenoids, phenols and tannins, sugar saponins, flavonoids, quinines, steroids, and proteins, among other phytoconstituents. The *C. auriculata* was found to be used to cure diabetes, joint pain and inflammation, muscular discomfort, sickness,

cold, venereal disease, hair cleaner, decrease body heat, stomach pain, vomiting, diarrhea, and toothache in an ethnobotanical survey. Anti-diabetic, anti-oxidant, hepatoprotective, anti-cancer, anti-inflammatory, anti-hyperlipidemic, and other pharmacological effects of *C. auriculata* have been reported [18-19].

2. MATERIAL AND METHOD

2.1 Collection of Plant Material

Cassia auriculata Linn. roots were obtained from farms around Walgaon Road in Amravati, Maharashtra. Safia College of Science, Peer Gate, Bhopal, Madhya Pradesh, validated this plant and assigned it the voucher specimen number 159/Bot/Safia/2010 (*Cassia auriculata* Linn.).

2.2 Material and Reagent

Sigma-Aldrich Co. provided 7,12-dimethylbenz(α)anthracene (DMBA) and acetone (United States). TCI chemicals provided the croton oil (Japan). All of the other reagents were readily accessible. The tumor initiator DMBA was dissolved in acetone at a concentration of 100 g/100μl. Croton oil was dissolved in acetone to make a % croton oil solution, which was used as a tumour promoter. Curcumin was dissolved in acetone at a dosage of 10 mg/kg as a positive control. All other chemicals were bought from Himedia Laboratories Pvt. Ltd in Mumbai, India, and were of analytical quality.

2.3 Extraction of the Plant Material

Cassia auriculata Linn. roots (2 kg) were dried in the shade before being ground into a coarse powdered substance. The powdered roots of the plant were extracted with the aid of water using the decoction technique [2020] of extraction at 40°C 5°C. The aqueous extract was then filtered through funnel, and alcohol (Ethanol) was gently added to the aqueous liquid extract to precipitate out polysaccharides found in individual plant roots. The solution was then filtered, and the filtrate was evaporated to a quarter of its original volume. After evaporating 1/4 of the total volume of the solution, it was extracted with an equivalent quantity of ethyl acetate using a separating funnel to get a fraction of root components in ethyl acetate. To improve the yield of extract, the ethyl acetate extract was acidified with 0.1 N HCl. The ethyl acetate portion of the plant's root was then evaporated to produce a precipitate, which was then dissolved

in methanol and slowly evaporated to produce crystalline powder (CAF) [20].

Similarly, saponin-rich fractions were extracted from the roots of the plants. After defatting with petroleum ether, pulverized plant material was treated with a 70:30 mixture of ethanol and water for maceration for seven days (40:60). During this time, the mixture was agitated at regular intervals. After filtering through muslin cloth and filter paper, the obtained extract was concentrated using a rotary vacuum evaporator (40°C), with care taken to ensure that the extract did not become powdered. To get the n-butanol soluble fraction, the concentrated extract was treated with n-butanol. The soluble fraction of n-butanol was then treated with cold diethyl ether. Precipitate was generated after treatment with cold diethyl ether. This precipitate-containing mixture was stored at -20°C for 24 hours. Centrifugation was used to further separate the precipitates. To get crystalline powder (CAS), these precipitates were further dissolved in methanol and then evaporated [20-21].

2.4 Animals

This study was conducted in accordance with ethical procedures and policies approved by the Institutional animal ethical committee (IAEC) of PBRI (1283/c/09/CPCSEA). *Swiss albino* mice (Male; 4-5 months; 20-30 gms) were obtained from animal house of Pinnacle Biomedical Research Institute. The animals were randomly assigned to different control and treatment groups (Six animals in each group). All experimental and housing conditions for animals were maintained as per CPCSEA guidelines. Naive animals were selected at random from animal house of PBRI. Animals were kept in group of six in propylene plastic cages with sterilized husk as bedding material. Animals were provided standard feeding pellets (Golden feeds, New Delhi) and water *ad libitum*. Temperature was maintained at 22±2°C, with light and dark cycle of 12:12 hrs. The animals were transferred to the laboratory at least 1h before experiment for proper acclimatization. The experiments were performed during day (08:00-16:00 h).

2.5 Acute Toxicity Study

Toxicology experiments were conducted on young male Swiss albino mice. Each mouse's weight was recorded. The animals were separated into two groups, each with three

animals, and then labelled. Plant extract solution was produced and delivered orally in dosages of 5, 50, 100, 200, and 500 mg/kg. Up to 36 hours, no detrimental effects or mouse death were found. For any additional pharmacological action, treatment doses of 1/10th and 1/20th of the highest tolerable safe dosage were used [22-23].

2.6 Chromosomal Aberration Assay

2.6.1 Dose and treatment

The Chromosomal aberration assay of the tested substance was performed on 36 mice, age 4 - 5 months, weight - 20-30g. Before and during the experiments, all groups of animals were kept under natural light conditions with free access to food and water (Dose- 100 mg/kg; 200 mg/kg).

2.7 Procedure

In the aforesaid group of animals, CYP was utilized as a mutagenic agent and was administered as an intraperitoneal (i.p.) injection at a single dosage of 40 mg/kg b.w 2 hours after the final administration of extract on the seventh day. The positive control group got just a single CYP i.p. injection. The negative control got merely a single 0.4 mL distilled water (d.w.) i.p. injection. For 7 days, the control groups were given p.o. extract at a rate of 200 mg/kg b.w per day for 7 days.

2.8 Chromosomal Analysis

The animals in all groups were slaughtered by cervical dislocation at the sampling time of 24 hours after treatment (colchicine was administered at a dosage of 4 mg/kg of body

weight 2 hours before to killing to halt the metaphase stage). Preston et al procedure's for cytogenetic analysis was followed. Hank's balanced salt solution was used to drain the bone marrow from both femurs (pH 7.2). To allow osmotic swelling of cells, the cells were centrifuged at 1000 rpm for 5 minutes and the pellet was re-dispersed in a hypotonic solution of 0.56 % (w/v) KCl for 30 minutes at 37°C. Swollen cells were fixed in ice-cold Carnoy's fluid, transferred to slides, and stained with phosphate-buffered 5% Giemsa solution. The mitotic index was estimated from a scan of 2000 cells per animal and 75 well-spread metaphase plates per animal in each group were tested for chromosomal abnormalities at a magnification of 100 X. Breaks, fragments, exchanges, and numerous chromosomal abnormalities were classed as chromosomal aberrations (cells with 10 or more aberrations were classified as multiple). The mitotic index, percentage of occurrence of aberrant cells, and percentage of suppression of chromosomal abnormalities were among the criteria studied. The mitotic index was determined as a proportion of dividing cells out of total bone marrow cells measured for cytotoxicity assessment. The number of abnormal cells was calculated as a proportion of the total number of damaged cells (aberrant metaphases).

The suppression percentage of chromosomal aberrations was calculated as:

$$100 - \left[\frac{\text{percent incidence of aberrant cells in extract pre-treated and CYP post treated groups}}{\text{percent incidence of aberrant cells in CYP alone treated group}} \times 100 \right] \text{ [24-26].}$$

Table 1. Dose and treatment selection for Chromosomal Aberration Assay

Group No	Group name	Treatment	Dose	No of animal/group
1	Vehicle	No treatment	Nil	06
2	Control	CYP Only	Nil	06
3	CYP+CAF	Extract + CYP	100 mg/kg	06
4	CYP+CAF	Extract + CYP	200 mg/kg	06
5	CYP+CAS	Extract + CYP	100 mg/kg	06
6	CYP+CAS	Extract + CYP	200 mg/kg	06

Table 2. Dose and treatment selection for Micronucleus assay

Group No	Group name	Treatment	Dose	No of animal/group
1	Vehicle	No treatment	Nil	06
2	Control	CYP Only	Nil	06
3	CYP+CAF	Extract + CYP	200 mg/kg	06
4	CYP+ CAS	Extract + CYP	200 mg/kg	06

2.9 Micronucleus Assay

2.9.1 Dose and treatment

The Micronucleus assay of the tested substance was performed on 36 mice, age 4 - 5 months, weight- 20-30 g. Before and during the experiments, all groups of animals were kept under natural light conditions with free access to food and water (Dose- 100 mg/kg; 200 mg/kg).

2.10 Bone Marrow MN Test and Scoring

The bone marrow MN tests were performed on the same experimental animals. Cervical dislocation was used to kill the animals. The femur and tibia were surgically removed. The modified Schmid technique was used to create bone marrow MN slides. The pellet was centrifuged at 1000 rpm and resuspended in BSA solution after marrow suspension from femur and tibia bones was produced in % bovine serum albumin (BSA). Smears were created and the slides were air-dried after a drop of this suspension was applied on clean glass slides. MN were found in the forms of RBCs, i.e., polychromatic erythrocytes as PCEs, when the slides were fixed in methanol and stained with May-Grunwald-Giemsa. MN was detected in around 2000 PCEs per animal [27-29].

2.10.1 Anticancer activity

2.10.1.1 Dose and treatment

The Anticancer activity of the tested substance was performed on 24 mice, age 4 - 5 months, weight - 20-30g. Before and during the experiments, all groups of animals were kept under natural light conditions with free access to food and water (Dose- 100 mg/kg; 200 mg/kg).

2.11 Procedure

2.11.1 Tumor induction

Different groups of 06 animals were treated with a single dose of DMBA (7,12-

dimethylbenz[a]anthracene) (100 µg/100 µl of acetone) over the shaven area of the skin of the mice. Two weeks later, croton oil (1% in 100 µl of acetone) was applied as a promoter 3 times per week until the end of the experiment (i.e., 16 weeks).

2.11.2 Parameters to be noticed

Tumor incidence: The number of mice carrying at least 1 tumor, expressed as a percentage incidence.

Tumor yield: The average number of papillomas per mouse.

Tumor Burden: The average number of tumors per tumor bearing mouse.

Body weight: The weight of the mice was measured weekly.

Average Latent Period: The lag between the application of the promoting agent and the appearance of 50% of tumors was determined. The average latent period was calculated by multiplying the number of tumors appearing each week by the time in weeks after the application of the promoting agent and dividing the sum by total number of tumors.

$$\text{Average latent period} = \sum fx / n$$

Where f is the number of tumors appearing each week, x is the numbers of weeks, and n is the total number of tumors.

2.12 Histopathological Study

Skin was fixed with buffered formalin for 24 hours. Afterward skin was embedded in paraffin wax by standard protocol. Serial section of 4 µm was cut by microtome with rotary microtome. Sections were stained with Hemtoxyline and eosin staining. Sections were observed at 40x and 100x for histological variations. Important areas were photographed using microscope with digital camera [30-32].

Table 3. Dose and treatment selection for anticancer activity

Group No	Group name	Treatment	Dose	No of animal/group
1	Control	DMBA + Croton oil	Nil	06
2	CAF + CAS	DMBA + Croton oil + Extract of CAF + CAS	200 mg/kg	06
3	CAF	DMBA + Croton oil + Extract of CAF	200 mg/kg	06
4	CAS	DMBA + Croton oil + Extract of CAS	200 mg/kg	06

3. RESULT AND DISCUSSION

3.1 Acute Toxicity Study

Acute oral toxicity is a key criterion for determining a component's safety. The acute oral toxicity of test samples was determined using the OECD 423 criteria in this study. Four dosage levels were employed, according to the guidelines: 5 mg/kg, 50 mg/kg, 300 mg/kg, and 2000 mg/kg. No mortality was reported in *Cassia auriculata* flavonoid rich extracts (CAF) up to a level of 2000 mg/kg. No fatality was seen in the case of *Cassia auriculata* saponin rich extract (CAS) up to a dosage of 300 mg/kg, but one death was recorded at a dose of 2000 mg/kg. As a result, it was determined that the LD50 of both extracts was more than 2000 mg/kg. This upper limit was also utilized to determine dosages for the current study. As a result, for future research, dosages of 1/10th and 1/20th of the maximum allowed dose, i.e., 200 mg/kg and 100 mg/kg, were used [22-23].

3.2 Chromosomal Aberration Assay

In present study effect of test samples was assessed against cyclophosphamide (CYP) induced mutagenicity. Break, Fragment, Deletion, polyploidy, pulverized and ring type of aberrations were quantified in various treatment groups. Generally, chromatid breaks can be induced in the S and G2 phases of the cell cycle, when the chromosome has split into 2 chromatids. Many chemical agents, especially alkylating agents cause predominantly chromatid-type aberrations. In vehicle treated animals total break was found to be 3.83 ± 1.72 % which was significantly elevated ($P < 0.05$) in CYP only treated animals with 31.33 ± 3.01 %. Flavonoid rich extract of *Cassia auriculata* significantly lowered percentage break up to 8.16 ± 1.47 % and 5.16 ± 1.72 % at 100 and 200 mg/kg respectively ($P < 0.05$). In saponins rich extract increased mutagenicity was observed at lower dose as well as higher doses. Fragments

are single chromatid without centromeres. In CYP treated animals 24.16 ± 2.56 % fragments were observed which were significantly higher ($P < 0.05$) as compared to vehicle treated animals in which 2.83 ± 1.47 % fragments were present [24-26].

3.3 Effect of CAF & CAS on Cyclophosphamide induced Genotoxicity

3.3.1 Study of effect of CAF& CAS in micronucleus assay

During anaphase, Mn products from entire chromosomes or central chromosomal segments were not involved in cell division. Mn formation might be used as a biomarker for exposure to both clastogenic and eugenic hazards. Mn is a useful biomarker for biological dosimetry in the event of acute radiation exposure in humans, according to studies. Radiation dosage has an effect on Mn frequency. After being exposed to ionizing radiation in the 50-500 Msv range, Fenech discovered a rise in Mn frequency in human cells. The Mn test was used to assess biological damage in populations living in locations with high levels of radioactivity, as well as in workers who are exposed to ionizing radiation on the job. Counting the amount of PCE among 1000 cells was used to assess the cytotoxic capability of CAF and CAS. Table 6 shows the number of MNPCEs among 2000 PCE, which indicates genotoxicity. At a dosage of 200 mg/kg, the number of MNPCEs among 2000 PCE generated by CAF was significant ($p < 0.001$). CAF reduced the yields of MN induced by CYP in pre-, simultaneous, and post-treatments by a statistically significant amount. Except for the two highest dosages, all of the CAF doses tested were shown to be beneficial in lowering the incidence of MN caused by CYP. There was also a significant decline in overall MN yield (MN in PCE) [27-29]. CAS were shown to be ineffective in lowering the frequency of MN.

Table 4. Acute toxicity study

Groups	No. of animals	Dose (mg/kg)	Result
<i>C. auriculata</i> root, crude flavonoids extract			
1.	3	5	Not observed (0/3)
2.	3	50	No death
3.	3	300	No death
4.	3	2000	No death
<i>C. auriculata</i> root, crude saponin extract			
5.	3	5	No death

Groups	No. of animals	Dose (mg/kg)	Result
6.	3	50	No death
7.	3	300	No death
8.	3	2000	01 Dead

Table 5. Effect of CAF & CAS on Cyclophosphamide induced Genotoxicity

S. No.	Treatment	Break	Fragment	Deletion	Polyploidy	Pulverized	Ring
1	Vehicle	3.83 ± 1.72 ^d	2.83 ± 1.47	3.66 ± 1.63	0	0	0
2	CYP	31.33 ± 3.01 ^a	24.16 ± 2.56 ^a	17.33 ± 3.26 ^a	6.66 ± 1.96 ^a	6.16 ± 1.47 ^a	5.83 ± 1.60 ^a
3	CYP+CAF (100 mg/kg)	8.16 ± 1.47 ^{abc}	7.17 ± 2.22 ^{abc}	7.83 ± 2.63 ^{abc}	2.33 ± 1.21 ^{abc}	1.83 ± 1.169 ^{abc}	2.16 ± 0.98 ^{abc}
4	CYP+CAF (200 mg/kg)	5.16 ± 1.72 ^{abc}	4.33 ± 1.86 ^{abc}	3.67 ± 1.63 ^{abc}	1.16 ± 0.75 ^{abc}	1.16 ± 1.60 ^{abc}	0.83 ± 1.16 ^{abc}
5	CYP+CAS (100 mg/kg)	37.66 ± 2.58	29.83 ± 2.71	23.16 ± 3.31	10.33 ± 2.25	10.66 ± 2.50	9.17 ± 1.47
6	CYP+CAS (200 mg/kg)	30.83 ± 2.31 ^a	23.67 ± 3.32 ^a	16.83 ± 3.31 ^a	5.83 ± 1.94 ^a	5.66 ± 1.96 ^a	5.33 ± 2.16 ^a

All Data presented in mean ± SD, ^a P<0.05 as compared to CYP+CAS treated group, ^b P<0.05 as compared to CYP treated group, ^c P<0.05 as compared to CYP+CAF treated group, ^d P<0.05 as compared to CYP+CAF treated group

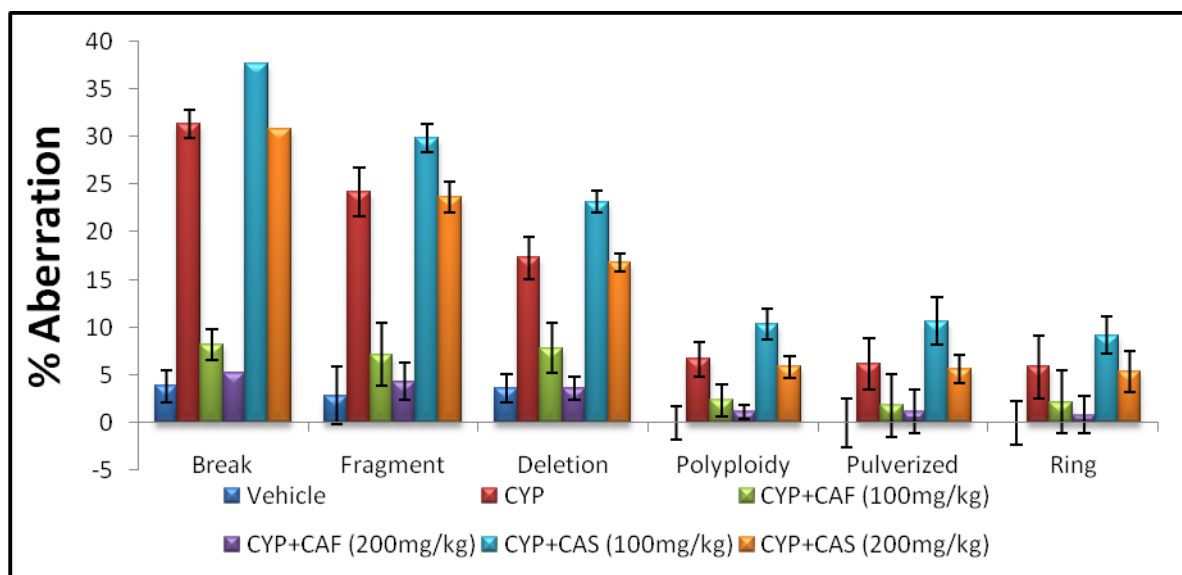


Fig. 1. Effect of CAF & CAS on Cyclophosphamide induced Genotoxicity

Table 6. Effect of CAF & CAS in Micronucleus Assay

S. No.	Treatment	MN-PCE
1.	Vehicle	0.24±0.11
2.	CYP	6.12±0.42
3.	CYP+CAF	2.48±0.63 ^{abcd}
4.	CYP+ CAS	5.92±0.54

All Data presented in mean ± SD, ^a P<0.05 as compared to CYP treated group, ^b P<0.05 as compared to CYP+ Caf treated group, ^c P<0.05 as compared to CYP+ CAS treated group

3.4 Anticancer Activity

At weekly intervals, body weight, tumor yield, percentage of tumors incidence, and tumors burden were examined and assessed. Only tumors with a diameter bigger than 1 mm that had been present for more than one week were included for data analysis. When the first tumors developed, the latency time of tumor development was established. The number of tumor-bearing mice was divided by the total number of mice in a group and multiplied by 100 percent to get the percentage of tumor incidence. The total number of tumors was divided by the number of tumor-bearing mice in a group to get the tumor burden. The volume of the tumor was calculated by multiplying the length, breadth, and height of the tumor by $\pi/6$.

At the conclusion of the trial, all groups' average body weights had increased significantly (Table 7). During the promotion stage, tumors begin to form on the skin between weeks 6 and 9. Tumor development began one week sooner in groups I and IV than in groups II and III, in the sixth week.

The incidence of tumors differed considerably between the treatment Control group and the remainder group. Statistical analysis also revealed that there is a significant variation in tumor burden across groups. Tumor burden is greatest in group I, with a value of 32.5, followed

by 18.83, 22.83, and 29.83 in groups II, III, and IV, respectively. In terms of tumor volume, there was no significant difference between groups.

However, there was a statistically significant difference in tumor volume between groups I (32.5) and II (18.83) when compared to group III, while group IV (22.83 and 29.83) was lower than group I, albeit there was no statistically significant difference between these two groups.

In terms of tumor incidence, tumor yield, and tumor burden, groups II and III performed better than the carcinogen control group (group I). The suppressing impact of group II was equivalent to that of the positive control group (group III), but the suppressing effect of group IV was even larger than that of group I, notably in terms of tumor incidence and tumor burden. Nonetheless, as compared to the carcinogen control group, Group II had a higher tumor incidence and tumor volume.

Morphological investigation (Fig. 2) revealed substantial epidermal hyperplasia (as shown by the thicker epidermal layer) as well as many keratin pearls and rete ridges in the carcinogen control-treated group in all protocols. In the skin sections of the DMBA plus croton oil-treated group, irregular distribution with finger-like projections (papilloma) suggestive of malignant development was identified.

Table 7. Result of anticancer parameters

Group	Parameters	Week 0	Week 8	Week 16
Control	Body weight (gms)	22.82±1.79	32.28±3.84	31.82±2.23
	Tumor yield	0	3.67	32.5
	Tumor incidence	0	83.33	100
	Tumor burden	0	4.4	32.5
CAF+CAS	Body weight (gms)	23.07±0.90	30.35±2.27	31.02±2.58
	Tumor yield	0	2	18.83
	Tumor incidence	0	50	100
	Tumor burden	0	4	18.83
CAF	Body weight (gms)	23.63±0.53	31.14±1.31	31.38±1.89
	Tumor yield	0	2	22.83
	Tumor incidence	0	50	100
	Tumor burden	0	4	22.83
CAS	Body weight (gms)	22.83±0.61	30.69±0.83	29.7±0.85
	Tumor yield	0	3.33	29.83
	Tumor incidence	0	50	100
	Tumor burden	0	6.67	29.83

Furthermore, pieces of the basement membrane were disturbed in several tissue slices, suggesting that the tumors had advanced to a premalignant stage. In all methods, skin tissue samples from the different extracts treated groups showed a decreased degree of epidermal hyperplasia, keratin pearls, and rete ridges. Because the basement membrane remained intact and the dermis had not been infiltrated, the tumors developed were deemed benign. As a consequence of the histology examinations, it was discovered that the level of cellular diversity in various treatment groups correlated with tumor outcomes.

In all treated groups, further histological investigation revealed varied degrees of hyperplasia and keratin pearls. In comparison to the carcinogen control (group I), the epidermis in groups II and III is less hyperplastic, but group IV has more keratin pearls and a hyperplastic epidermis that is equivalent to the carcinogen control. The tumors that develop are benign papillomas that remain contained inside an intact basement membrane with no evidence of invasion into the dermis. Premalignant lesions, on the other hand, were seen in the carcinogen control group [30-32].

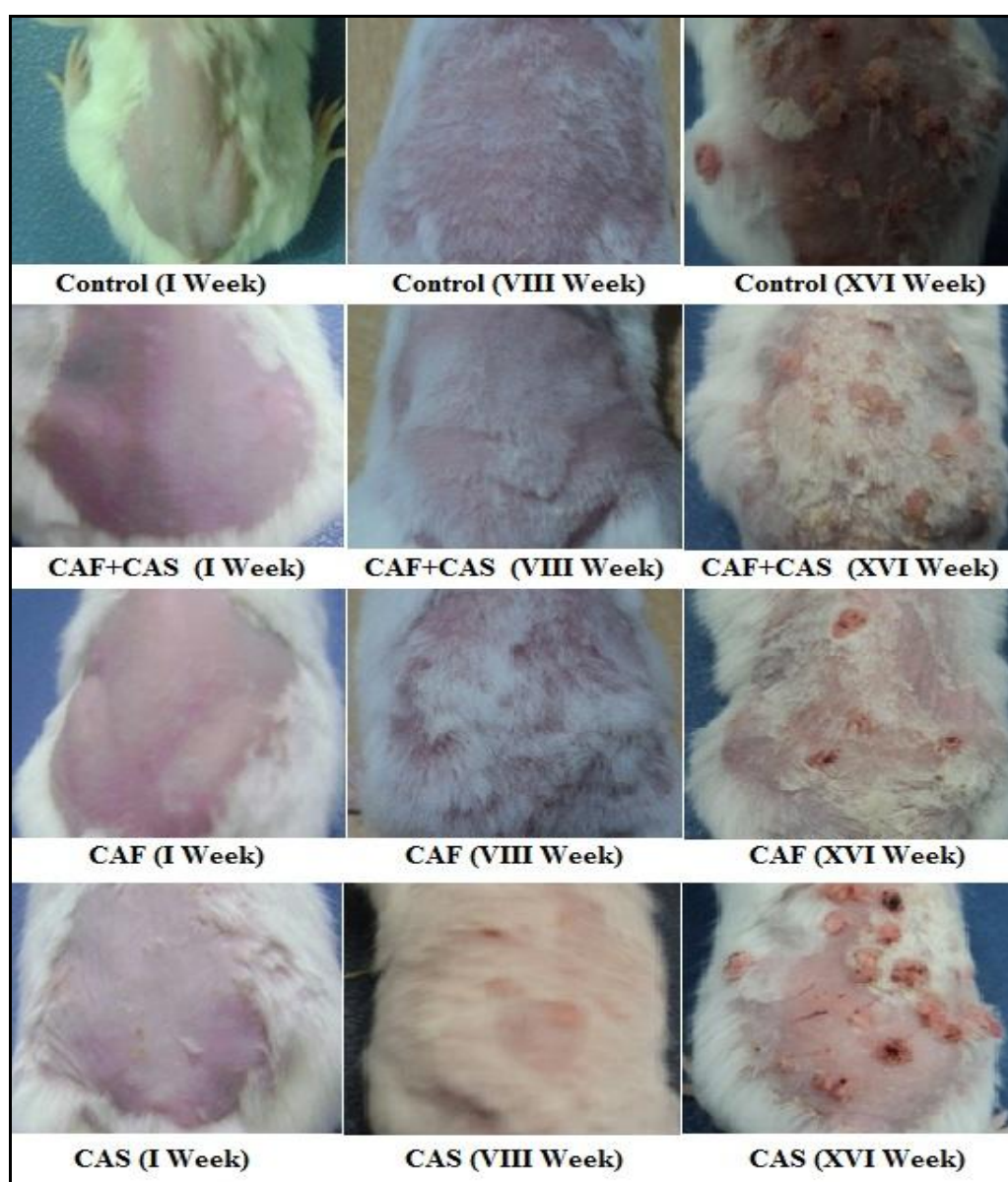


Fig. 2. Morphological examination of anticancer activity on mice

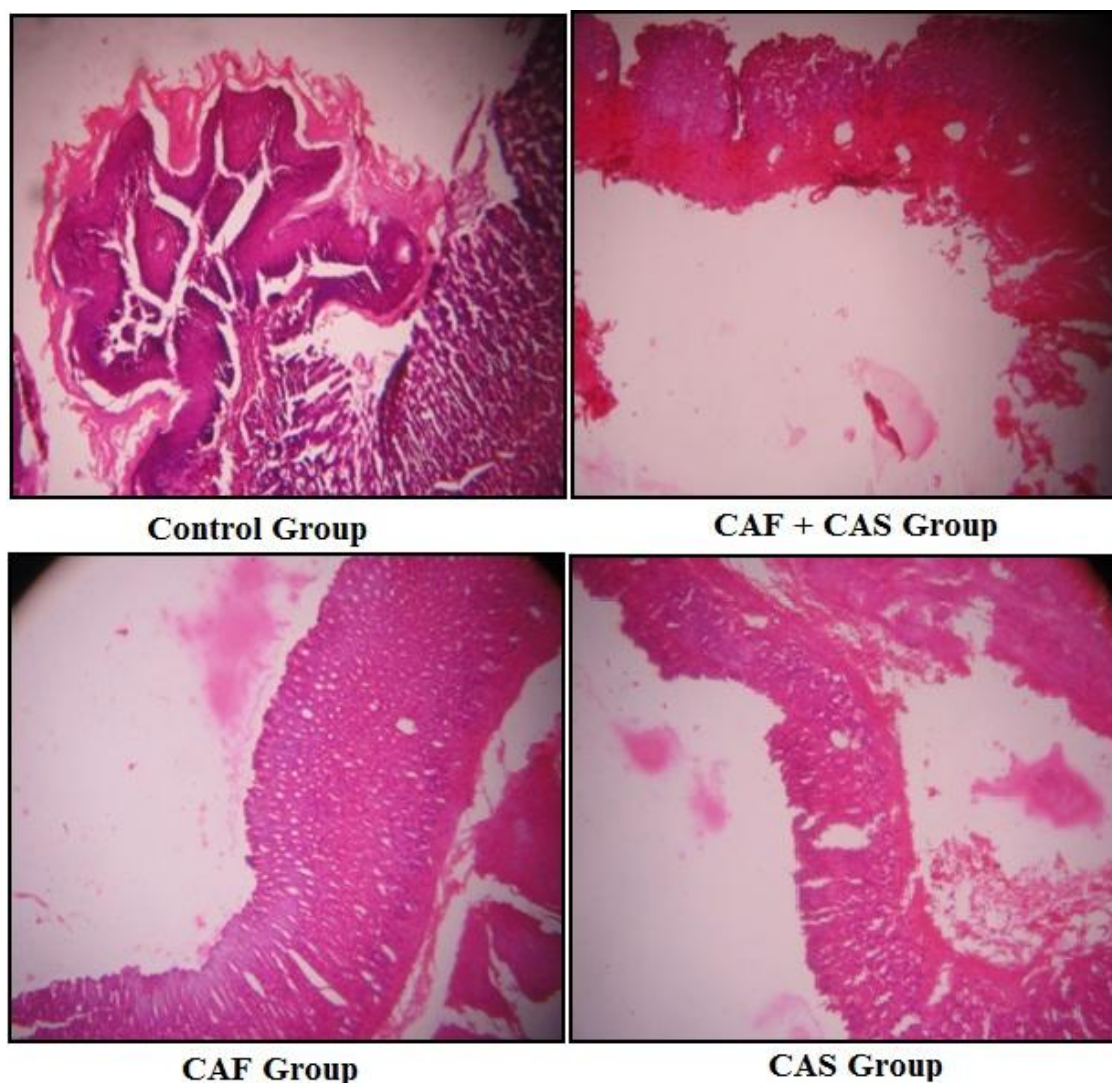


Fig. 3. Histopathological analysis of anticancer activity on mice

4. CONCLUSION

Traditional medical systems have grown in importance over the last decade as a result of their safety. According to current estimates, a significant section of the population in many developing nations depends significantly on traditional practitioners and medicinal herbs to cover their basic health care requirements. Despite the pharmaceutical industry's breakthroughs in the production of unique and highly effective medications for the treatment of a broad variety of disorders, the use of herbal remedies has increased significantly in the world's most wealthy nations. Every medicine has side effects, but a useful pharmacologically active substance should have a good balance of therapeutic and harmful or undesirable side effects. A battery of genotoxic and/or

mutagenicity tests must be done to screen the toxicity mechanism to assure the safety and effectiveness of natural compounds. There is no one test that can collect enough data to predict the chemical risks to human health. The findings of this investigation show that the Cassia Auriculata Linn CAF and CAS Fractions are neither genotoxic or clastogenic at the quantities employed. Our findings further suggest that pretreatment with Cassia Auriculata Linn CAF and CAS Fraction reduces CYP-induced clastogenicity while maintaining its cytotoxic capability. Because it prolongs the development of tumors in the skin and reduces the hyperproliferative response evoked by CYP, it can be inferred that CAF and CAS Fraction of Cassia Auriculata functions as a modulator of two-stage skin carcinogenesis in Swiss albino mice. Furthermore, it reduces oxidative cell

damage, which is inextricably linked to the development of cancer. Further research into the exact mode of action of the genetic toxicity of isolated compounds from this plant species is needed to gain a better understanding of the genotoxic mechanisms described herein, as well as to investigate the protective role of *Cassia Articulata*'s CAF and CAS fractions against genotoxic agents in the environment. It is necessary to understand their processes as cancer treatments.

CONSENT

It is not applicable.

ETHICAL APPROVAL

This study was conducted in accordance with ethical procedures and policies approved by the Institutional animal ethical committee (IAEC) of PBRI (1283/c/09/CPCSEA). Swiss albino mice (Male; 4-5 months; 20-30 gms) were obtained from animal house of Pinnacle Biomedical Research Institute.

COMPETING INTERESTS

Authors have declared that no competing interests exist.

REFERENCES

1. Atanasov AG, Waltenberger B, Pferschy-Wenzig EM, Linder T, Wawrosch C, Uhrin P, et al. Discovery and resupply of pharmacologically active plant-derived natural products: A review. *Biotechnology Advances*. 2015; 33(8):1582–1614. pmid:26281720
Available:https://doi.org/10.1016/j.biotechadv.2015.08.001
2. Lunenfeld B, Stratton P. The clinical consequences of an ageing world and preventive strategies. *Best Practice & Research: Clinical Obstetrics & Gynecology*. 2013;27(5):643–59.
Available:https://doi.org/10.1016/j.bpobgyn.2013.02.005
3. Torgovnick A, Schumacher B. DNA repair mechanisms in cancer development and therapy. *Frontiers in Genetics*. 2015; 23(6):157.
Available:https://doi.org/10.3389/fgene.2015.00157
4. Nagarathna PKM, Johnson Wesley M, Sriram Reddy P, Reena K. Review on

Genotoxicity, its Molecular Mechanisms and Prevention. *International Journal of Pharmaceutical Sciences Review and Research*. 2013; 22(1): 236–243.

Available:https://www.researchgate.net/publication/326733700_A_review_on_genotoxicity_in_aquatic_organisms_and_environment

5. Słoczyńska K, Powroźnik B, Pękala E, Waszkielewicz AM. Antimutagenic compounds and their possible mechanisms of action. *Journal of Applied Genetics*. 2014; 55: 273–285
pmid:24615570
Available:https://doi.org/10.1007/s13353-014-0198-9
6. Collins AR, Azqueta A, Langie SAS. Effects of micronutrients on DNA repair. *European Journal of Nutrition*. 2012; 51: 261–279. pmid:22362552
Available:https://doi.org/10.1007/s00394-012-0318-4
7. Orhan F, Gulluce M, Ozkan H, Alpsoy L. Determination of the antigenotoxic potencies of some luteolin derivatives by using a eukaryotic cell system, *Saccharomyces cerevisiae*. *Food Chemistry*. 2013; 141: 366–372.
pmid:23768369
Available:https://doi.org/10.1016/j.foodchem.2013.02.089
8. Chatterjee S, Poduval TB, Tilak JC, Devasagayam TPA. A modified, economic, sensitive method for measuring total antioxidant capacities of human plasma and natural compounds using Indian saffron (*Crocus sativus*). *Clinica Chimica Acta*. 2005; 352: 155–163.
Available:https://doi.org/10.1016/j.cccn.2004.09.012
9. Nsimba RY, Kikuzaki H, Konishi Y. Antioxidant activity of various extracts and fractions of *Chenopodium quinoa* and *Amaranthus* spp. seeds. *Food Chemistry*. 2008; 106: 760–766.
Available:https://doi.org/10.1016/j.foodchem.2007.06.004
10. Castro L, Freeman BA. Reactive oxygen species in human health and disease. *Nutrition*. 2001; 170:161–5.
Available:https://doi.org/10.1016/s0899-9007(00)00570-0
11. Attia S M. The genotoxic and cytotoxic effects of nicotine in the mouse bone marrow. *Mutation Research/ Genetic Toxicology and Environmental Mutagenesis*. 2007; 632(1-2), 29-36.

- Available: <https://doi.org/10.1016/j.mrgento.2007.04.010>
12. Nagarathna PKM, Yadav CK, Yadav SK. Evaluation of Mutagenic Effect and Antimutagenic of *Dalbergia Latifolia* on Swiss Albino Mice Evaluation, *Asian J Pharm Clin Res*, 2015;8(3):154-158
 13. V. Lobo, A. Patil, A. Phatak, N. Chandra, Free radical's antioxidants and functional foods: impact on human health, *Pharmacogn. Rev.* 4 (8) (2010) 118–126. Available: <https://dx.doi.org/10.4103%2F0973-7847.70902>
 14. W.K. Hong, M.B. Sporn, Recent advances in the chemoprevention of cancer, *Science* 278 (1997) 1073–1077. Available: <https://doi.org/10.1126/science.278.5340.1073>
 15. X.L. Tan, S.D. Spivack, Dietary chemoprevention strategies for induction of phase II xenobiotic-metabolizing enzymes in lung carcinogenesis: a review, *Lung Cancer* 65 (2009) 129–137. Available: <https://doi.org/10.1016/j.lungcan.2009.01.002>
 16. J.K. Kundu, Y.J. Surh, Molecular basis of chemoprevention with dietary phytochemicals: redox-regulated transcription factors as relevant targets, *Phytochem. Rev.* 8 (2009) 333–347. Available: <http://dx.doi.org/10.1007%2Fs11101-009-9132-x>
 17. R. Edenharder, I. Von Petersdorff, R. Rauscher, Antimutagenic effects of flavonoids, chalcones and structurally related compounds on the activity of 2-amino-3-methylimidazo [4,5-f] quinoline (IQ) and other heterocyclic amine mutagens from cooked food, *Mutat. Res. Med.* 287 (1993) 261–274. Available: [https://doi.org/10.1016/0027-5107\(93\)90019-C](https://doi.org/10.1016/0027-5107(93)90019-C)
 18. Salma B, Janhavi P, Muthaiah S, Veeresh P, Santhepete Nanjundiah M, Divyashree S, Serva Peddha M. Ameliorative efficacy of the cassia auriculata root against high-fat-diet+ STZ-induced type-2 diabetes in C57BL/6 mice. *ACS omega*. 2020 Dec 18;6(1):492-504. Available: <https://doi.org/10.1021/acsomega.0c04940>
 19. Anu K, Devanesan S, Prasanth R, AlSalhi MS, Ajithkumar S, Singaravelu G. Biogenesis of selenium nanoparticles and their anti-leukemia activity. *Journal of King Saud University-Science*. 2020;32(4):2520-6. Available: <https://doi.org/10.1016/j.jksus.2020.04.018>
 20. Khyade M, Kamble S, Waman M, Padwal A, Gunjal M. Food Potential and Antioxidant Property of Cassia auriculata Seed: A Nutritionally Unexploited Legume. *Current Nutrition & Food Science*. 2020 Dec 1;16(9):1381-92. Available: <https://doi.org/10.2174/1573401316666200221110140>
 21. Ebringerová A, Hromádková Z. An overview on the application of ultrasound in extraction, separation and purification of plant polysaccharides. *Central European Journal of Chemistry*. 2010;8(2):243-57. Available: <http://dx.doi.org/10.2478/s11532-010-0006-2>
 22. Lalitha P, Sripathi SK, Jayanthi P. Acute toxicity study of extracts of *Eichhornia Crassipes* (Mart.) Solms. *Asian J Pharm Clin Res*. 2012;5(4):59-61. Available: <https://innovareacademics.in/journal/ajpcr/Vol5Issue4/1225.pdf>
 23. Halim SZ, Abdullah NR, Afzan A, Rashid BA, Jantan I, Ismail Z. Acute toxicity study of *Carica papaya* leaf extract in Sprague Dawley rats. *Journal of Medicinal Plants Research*. 2011 May 18;5(10):1867-72. Available: https://www.researchgate.net/publication/230859605_Acute_toxicity_study_of_Carica_papaya_leaf_extract_in_Sprague_Dawley_rats
 24. Gangar SC, Sandhir R, Koul A. Anticlastogenic activity of *Azadirachta indica* against benzo (a) pyrene in murine forestomach tumorigenesis bioassay. *Acta Pol Pharm*. 2010 Jul 1;67(381):90. Available: <https://pubmed.ncbi.nlm.nih.gov/20635534/>
 25. Parveen N, Shadab GG. The dual clastogenic and anti-clastogenic properties of quercetin is dose dependent. *Front Biosci (School Ed)*. 2017 Jan 1; 9:139-53. Available: <https://doi.org/10.2741/s478>
 26. Manoharan S, Balakrishnan S, Vinothkumar V, Silvan S. Anti-clastogenic potential of carnosic acid against 7, 12-dimethylbenz (a) anthracene (DMBA)-induced clastogenesis. *Pharmacological Reports*. 2010 Nov 1;62(6):1170-7. Available: [http://dx.doi.org/10.1016/S1734-1140\(10\)70379-0](http://dx.doi.org/10.1016/S1734-1140(10)70379-0)
 27. Želazna K, Rudnicka K, Tejs S. In vitro micronucleus test assessment of polycyclic aromatic hydrocarbons. *Environmental Biotechnology*. 2011; 7:70-80.

28. Available:file:///C:/Users/Rohan%20Yadav/Downloads/httpwww_environmentalbiotechnology_plebdzialyebonline2011vol72ms161kzelazna.pdf
29. Promkum C, Butryee C, Tuntipopipat S, Kupradinun P. Anticlastogenic effect of *Eryngium foetidum* L. assessed by erythrocyte micronucleus assay. *Asian Pacific Journal of Cancer Prevention*. 2012;13(7):3343-7. Available:https://doi.org/10.7314/apjcp.2012.13.7.3343
30. Maurich T, Pistelli L, Turchi G. Anticlastogenic activity of two structurally related pterocarpanes purified from *Bituminaria bituminosa* in cultured human lymphocytes. *Mutation Research/Genetic Toxicology and Environmental Mutagenesis*. 2004;561(1-2):75-81. Available:https://doi.org/10.1016/j.mrgento.2004.03.006
31. Saini MR, Goyal PK, Chaudhary G. Antitumor activity of *Aloe vera* against DMBA/croton oil-induced skin papilloma genesis in Swiss albino mice. *Journal of Environmental Pathology, Toxicology and Oncology*. 2010; 29(2). DOI: 10.1615/JEnvironPatholToxicolOncol.v29.i2.60
32. Sharma S, Khan N, Sultana S. Effect of *Onosma echioides* on DMBA/croton oil mediated carcinogenic response, hyperproliferation and oxidative damage in murine skin. *Life sciences*. 2004 Oct 1;75(20):2391-410. Available:https://doi.org/10.1016/j.lfs.2004.04.030

© 2021 Kewatkar et al.; This is an Open Access article distributed under the terms of the Creative Commons Attribution License (<http://creativecommons.org/licenses/by/4.0>), which permits unrestricted use, distribution, and reproduction in any medium, provided the original work is properly cited.

Peer-review history:

The peer review history for this paper can be accessed here:

<https://www.sdiarticle5.com/review-history/76966>



Antimutagenic Activity of Cassia Auriculata Linn Fractions along with Anticancer Activity in Male Albino Mice

Shailesh M. Kewatkar ^{a*≡}, Dipak V Bhusari ^{b[⊖]}, Madhav chakolkar ^{c[#]},
Amit Joshi ^{d[†]}, Shirish P. Jain ^{e[‡]} and Chanchal Navin Raj ^{f[‡]}

^a Rajarshi Shahu College of Pharmacy, Buldana, Maharashtra, India.

^b Rajarshi Shahu College of Pharmacy, Buldana, Maharashtra, India.

^c Rajarshi Shahu College of Pharmacy, Buldana, Maharashtra, India.

^d LNCT School of Pharmacy, Kanadiya, Indore, India.

^e Rajarshi Shahu College of Pharmacy, Buldana, Maharashtra, India.

^f Shri D. D. Vispute College of Pharmacy and Research Center, New Panvel, Maharashtra, India.

Authors' contributions

This work was carried out in collaboration among all authors. All authors read and approved the final manuscript.

Article Information

DOI: 10.9734/JPRI/2021/v33i59A34267

Open Peer Review History:

This journal follows the Advanced Open Peer Review policy. Identity of the Reviewers, Editor(s) and additional Reviewers, peer review comments, different versions of the manuscript, comments of the editors, etc are available here: <https://www.sdiarticle5.com/review-history/76966>

Original Research Article

Received 10 October 2021
Accepted 15 December 2021
Published 16 December 2021

ABSTRACT

Background: In recent years, there has been a surge in interest in studying plant-derived materials and their impact on DNA. Herbal products include a number of natural substances that may help protect cells against mutagen-induced cell damage.

Aim: The purpose of this research was to assess the genotoxic effects of Cassia Auriculata Linn flavonoids (CAF) and Cassia Auriculata Linn saponin (CAS) rich fractions on mouse bone marrow cells utilizing chromosomal aberration test and micronucleus assay.

Methodology: The suppressive impact of CAF and CAS on 7, 12-dimethylbenz (α) anthracene (DMBA) and Croton oil induced skin tumor promotion in mice with topical administration twice

[≡] Associate Professor

[⊖] HOD-Diploma

[#] Assistant Professor

[†] Principal

[‡] Research Guide

*Corresponding author: E-mail: rakeshshivatare@gmail.com;

weekly for 18 weeks is also investigated in this work. Three dosages of 100 and 200 mg/kg body weight were used. Single oral dosages of CAF and CAS Fraction at the three levels did not enhance the number of micronucleate polychromatic erythrocytes in the micronucleus experiment.

Result: In mice bone marrow cells, a single oral treatment of CAF and CAS fraction revealed no significant alterations in mitotic indices or chromosomal aberration induction. The clastogenicity of CYP was considerably decreased by pretreatment with CAF and CAS fraction. As a result, it can be stated that CAF and CAS fraction had no genotoxic impact on mouse bone marrow cells.

Conclusions: The portions of *Cassia Auriculata* have been shown to be non-genotoxic and non-clastogenic at the quantities utilized in this investigation. CAF and CAS Fraction might possibly be a promising skin tumor promotion reducing agent, according to this research.

Keywords: *Cassia Auriculata*; cyclophosphamide; Genotoxic effects; anticancer activity.

1. INTRODUCTION

Natural products, in different forms such as extracts, fractions, or as a chemical platform, continue to play an important role in the treatment of numerous illnesses [1]. Plants have historically been the most common source of medicines throughout human history, owing to their secondary metabolites, which have a wide range of pharmacological activities. The knowledge of the many medicinal powers of plants has mostly been passed down via folk traditions and subsequently proven through scientific data [1,2]. Natural bioactive compounds in the prevention and/or treatment of chronic illnesses, which have been dubbed the public health challenge of the twenty-first century, are now one of the trendiest topics in medicine [2]. Indeed, as Lunenfeld and Stratton explain, the rise in healthcare systems and life expectancy in developed countries, as well as the decrease in fertility rate due to chromosomal abnormalities, has resulted in a rapid increase in global population ageing, with an increase in chronic degenerative disease [2,3]. According to the World Health Organization (WHO, 2018), cancer is the second leading cause of death (9.6 million in 2018), with malignancies of the liver (782 000 deaths) and breast (627 000 deaths) being the most prevalent. DNA damage has long been known as a cause of cancer formation, as stated [3]. In reality, oncogenes and tumor suppressor genes are affected by mutations or chromosomal abnormalities, leading to malignant transformation of cells [4]. As a result, antimutagenic, antigenotoxic, and anticarcinogenic chemicals play a critical role in cancer prevention [4,5]. A wide range of medicinal plants and their metabolites have been studied in recent years for their potential to reduce the mutagenic and carcinogenic effects of potentially harmful chemicals [6,7]; in fact, these natural compounds can inhibit free radicals and

oxidative stress-induced DNA and cellular damage [8,9].

Many mutagens and carcinogens work by creating reactive oxygen species (ROS), which are well known for causing oxidative damage to cell structures and biomolecules such lipids, nucleic acids, and proteins in living systems [10]. As a result, the evaluation of the possible genotoxicity of conventional medications is a crucial problem, as damage towards the genetic material can result in significant changes and, as a result, an increased cancer risk or other disorders. Genetic toxicology research has spawned a slew of testing methodologies, including both vitro and in vivo, as a result of their findings. In order to determine the effects of different test chemicals on genetic material and, as a result, the danger to living creatures, including humans, several processes have been devised and tested [11,12].

Synthetic antioxidants such as butylated hydroxytoluene (BHT) and butylated hydroxyanisole (BHA) are preferred, but according to recent research by Lobo et al. [13], they may have major negative consequences on human health. Plants and medicinal plants have been advised to counteract the effects of free radicals/mutagens because they may stimulate phase II enzymes, lowering the activity of cancer and other degenerative illnesses at the initiation, promotion, and progression phases [14–17].

Tanners Senna, *Cassia auriculata* Linn (Family: *Caesalpinaceae*), is found across India's hot deciduous woods and maintains a renowned place in Ayurveda and Siddha systems of treatment. It is said to include alkaloids, terpenoids, phenols and tannins, sugar saponins, flavonoids, quinines, steroids, and proteins, among other phytoconstituents. The *C. auriculata* was found to be used to cure diabetes, joint pain and inflammation, muscular discomfort, sickness,

cold, venereal disease, hair cleaner, decrease body heat, stomach pain, vomiting, diarrhea, and toothache in an ethnobotanical survey. Anti-diabetic, anti-oxidant, hepatoprotective, anti-cancer, anti-inflammatory, anti-hyperlipidemic, and other pharmacological effects of *C. auriculata* have been reported [18-19].

2. MATERIAL AND METHOD

2.1 Collection of Plant Material

Cassia auriculata Linn. roots were obtained from farms around Walgaon Road in Amravati, Maharashtra. Safia College of Science, Peer Gate, Bhopal, Madhya Pradesh, validated this plant and assigned it the voucher specimen number 159/Bot/Safia/2010 (*Cassia auriculata* Linn.).

2.2 Material and Reagent

Sigma-Aldrich Co. provided 7,12-dimethylbenz(α)anthracene (DMBA) and acetone (United States). TCI chemicals provided the croton oil (Japan). All of the other reagents were readily accessible. The tumor initiator DMBA was dissolved in acetone at a concentration of 100 g/100μl. Croton oil was dissolved in acetone to make a % croton oil solution, which was used as a tumour promoter. Curcumin was dissolved in acetone at a dosage of 10 mg/kg as a positive control. All other chemicals were bought from Himedia Laboratories Pvt. Ltd in Mumbai, India, and were of analytical quality.

2.3 Extraction of the Plant Material

Cassia auriculata Linn. roots (2 kg) were dried in the shade before being ground into a coarse powdered substance. The powdered roots of the plant were extracted with the aid of water using the decoction technique [2020] of extraction at 40°C 5°C. The aqueous extract was then filtered through funnel, and alcohol (Ethanol) was gently added to the aqueous liquid extract to precipitate out polysaccharides found in individual plant roots. The solution was then filtered, and the filtrate was evaporated to a quarter of its original volume. After evaporating 1/4 of the total volume of the solution, it was extracted with an equivalent quantity of ethyl acetate using a separating funnel to get a fraction of root components in ethyl acetate. To improve the yield of extract, the ethyl acetate extract was acidified with 0.1 N HCl. The ethyl acetate portion of the plant's root was then evaporated to produce a precipitate, which was then dissolved

in methanol and slowly evaporated to produce crystalline powder (CAF) [20].

Similarly, saponin-rich fractions were extracted from the roots of the plants. After defatting with petroleum ether, pulverized plant material was treated with a 70:30 mixture of ethanol and water for maceration for seven days (40:60). During this time, the mixture was agitated at regular intervals. After filtering through muslin cloth and filter paper, the obtained extract was concentrated using a rotary vacuum evaporator (40°C), with care taken to ensure that the extract did not become powdered. To get the n-butanol soluble fraction, the concentrated extract was treated with n-butanol. The soluble fraction of n-butanol was then treated with cold diethyl ether. Precipitate was generated after treatment with cold diethyl ether. This precipitate-containing mixture was stored at -20°C for 24 hours. Centrifugation was used to further separate the precipitates. To get crystalline powder (CAS), these precipitates were further dissolved in methanol and then evaporated [20-21].

2.4 Animals

This study was conducted in accordance with ethical procedures and policies approved by the Institutional animal ethical committee (IAEC) of PBRI (1283/c/09/CPCSEA). *Swiss albino* mice (Male; 4-5 months; 20-30 gms) were obtained from animal house of Pinnacle Biomedical Research Institute. The animals were randomly assigned to different control and treatment groups (Six animals in each group). All experimental and housing conditions for animals were maintained as per CPCSEA guidelines. Naive animals were selected at random from animal house of PBRI. Animals were kept in group of six in propylene plastic cages with sterilized husk as bedding material. Animals were provided standard feeding pellets (Golden feeds, New Delhi) and water *ad libitum*. Temperature was maintained at 22±2°C, with light and dark cycle of 12:12 hrs. The animals were transferred to the laboratory at least 1h before experiment for proper acclimatization. The experiments were performed during day (08:00-16:00 h).

2.5 Acute Toxicity Study

Toxicology experiments were conducted on young male Swiss albino mice. Each mouse's weight was recorded. The animals were separated into two groups, each with three

animals, and then labelled. Plant extract solution was produced and delivered orally in dosages of 5, 50, 100, 200, and 500 mg/kg. Up to 36 hours, no detrimental effects or mouse death were found. For any additional pharmacological action, treatment doses of 1/10th and 1/20th of the highest tolerable safe dosage were used [22-23].

2.6 Chromosomal Aberration Assay

2.6.1 Dose and treatment

The Chromosomal aberration assay of the tested substance was performed on 36 mice, age 4 - 5 months, weight - 20-30g. Before and during the experiments, all groups of animals were kept under natural light conditions with free access to food and water (Dose- 100 mg/kg; 200 mg/kg).

2.7 Procedure

In the aforesaid group of animals, CYP was utilized as a mutagenic agent and was administered as an intraperitoneal (i.p.) injection at a single dosage of 40 mg/kg b.w 2 hours after the final administration of extract on the seventh day. The positive control group got just a single CYP i.p. injection. The negative control got merely a single 0.4 mL distilled water (d.w.) i.p. injection. For 7 days, the control groups were given p.o. extract at a rate of 200 mg/kg b.w per day for 7 days.

2.8 Chromosomal Analysis

The animals in all groups were slaughtered by cervical dislocation at the sampling time of 24 hours after treatment (colchicine was administered at a dosage of 4 mg/kg of body

weight 2 hours before to killing to halt the metaphase stage). Preston et al procedure's for cytogenetic analysis was followed. Hank's balanced salt solution was used to drain the bone marrow from both femurs (pH 7.2). To allow osmotic swelling of cells, the cells were centrifuged at 1000 rpm for 5 minutes and the pellet was re-dispersed in a hypotonic solution of 0.56 % (w/v) KCl for 30 minutes at 37°C. Swollen cells were fixed in ice-cold Carnoy's fluid, transferred to slides, and stained with phosphate-buffered 5% Giemsa solution. The mitotic index was estimated from a scan of 2000 cells per animal and 75 well-spread metaphase plates per animal in each group were tested for chromosomal abnormalities at a magnification of 100 X. Breaks, fragments, exchanges, and numerous chromosomal abnormalities were classed as chromosomal aberrations (cells with 10 or more aberrations were classified as multiple). The mitotic index, percentage of occurrence of aberrant cells, and percentage of suppression of chromosomal abnormalities were among the criteria studied. The mitotic index was determined as a proportion of dividing cells out of total bone marrow cells measured for cytotoxicity assessment. The number of abnormal cells was calculated as a proportion of the total number of damaged cells (aberrant metaphases).

The suppression percentage of chromosomal aberrations was calculated as:

$$100 - \left[\frac{\text{percent incidence of aberrant cells in extract pre-treated and CYP post treated groups}}{\text{percent incidence of aberrant cells in CYP alone treated group}} \times 100 \right] \text{ [24-26].}$$

Table 1. Dose and treatment selection for Chromosomal Aberration Assay

Group No	Group name	Treatment	Dose	No of animal/group
1	Vehicle	No treatment	Nil	06
2	Control	CYP Only	Nil	06
3	CYP+CAF	Extract + CYP	100 mg/kg	06
4	CYP+CAF	Extract + CYP	200 mg/kg	06
5	CYP+CAS	Extract + CYP	100 mg/kg	06
6	CYP+CAS	Extract + CYP	200 mg/kg	06

Table 2. Dose and treatment selection for Micronucleus assay

Group No	Group name	Treatment	Dose	No of animal/group
1	Vehicle	No treatment	Nil	06
2	Control	CYP Only	Nil	06
3	CYP+CAF	Extract + CYP	200 mg/kg	06
4	CYP+ CAS	Extract + CYP	200 mg/kg	06

2.9 Micronucleus Assay

2.9.1 Dose and treatment

The Micronucleus assay of the tested substance was performed on 36 mice, age 4 - 5 months, weight- 20-30 g. Before and during the experiments, all groups of animals were kept under natural light conditions with free access to food and water (Dose- 100 mg/kg; 200 mg/kg).

2.10 Bone Marrow MN Test and Scoring

The bone marrow MN tests were performed on the same experimental animals. Cervical dislocation was used to kill the animals. The femur and tibia were surgically removed. The modified Schmid technique was used to create bone marrow MN slides. The pellet was centrifuged at 1000 rpm and resuspended in BSA solution after marrow suspension from femur and tibia bones was produced in % bovine serum albumin (BSA). Smears were created and the slides were air-dried after a drop of this suspension was applied on clean glass slides. MN were found in the forms of RBCs, i.e., polychromatic erythrocytes as PCEs, when the slides were fixed in methanol and stained with May-Grunwald-Giemsa. MN was detected in around 2000 PCEs per animal [27-29].

2.10.1 Anticancer activity

2.10.1.1 Dose and treatment

The Anticancer activity of the tested substance was performed on 24 mice, age 4 - 5 months, weight - 20-30g. Before and during the experiments, all groups of animals were kept under natural light conditions with free access to food and water (Dose- 100 mg/kg; 200 mg/kg).

2.11 Procedure

2.11.1 Tumor induction

Different groups of 06 animals were treated with a single dose of DMBA (7,12-

dimethylbenz[a]anthracene) (100 µg/100 µl of acetone) over the shaven area of the skin of the mice. Two weeks later, croton oil (1% in 100 µl of acetone) was applied as a promoter 3 times per week until the end of the experiment (i.e., 16 weeks).

2.11.2 Parameters to be noticed

Tumor incidence: The number of mice carrying at least 1 tumor, expressed as a percentage incidence.

Tumor yield: The average number of papillomas per mouse.

Tumor Burden: The average number of tumors per tumor bearing mouse.

Body weight: The weight of the mice was measured weekly.

Average Latent Period: The lag between the application of the promoting agent and the appearance of 50% of tumors was determined. The average latent period was calculated by multiplying the number of tumors appearing each week by the time in weeks after the application of the promoting agent and dividing the sum by total number of tumors.

$$\text{Average latent period} = \sum fx / n$$

Where f is the number of tumors appearing each week, x is the numbers of weeks, and n is the total number of tumors.

2.12 Histopathological Study

Skin was fixed with buffered formalin for 24 hours. Afterward skin was embedded in paraffin wax by standard protocol. Serial section of 4 µm was cut by microtome with rotary microtome. Sections were stained with Hemtoxyline and eosin staining. Sections were observed at 40x and 100x for histological variations. Important areas were photographed using microscope with digital camera [30-32].

Table 3. Dose and treatment selection for anticancer activity

Group No	Group name	Treatment	Dose	No of animal/group
1	Control	DMBA + Croton oil	Nil	06
2	CAF + CAS	DMBA + Croton oil + Extract of CAF + CAS	200 mg/kg	06
3	CAF	DMBA + Croton oil + Extract of CAF	200 mg/kg	06
4	CAS	DMBA + Croton oil + Extract of CAS	200 mg/kg	06

3. RESULT AND DISCUSSION

3.1 Acute Toxicity Study

Acute oral toxicity is a key criterion for determining a component's safety. The acute oral toxicity of test samples was determined using the OECD 423 criteria in this study. Four dosage levels were employed, according to the guidelines: 5 mg/kg, 50 mg/kg, 300 mg/kg, and 2000 mg/kg. No mortality was reported in *Cassia auriculata* flavonoid rich extracts (CAF) up to a level of 2000 mg/kg. No fatality was seen in the case of *Cassia auriculata* saponin rich extract (CAS) up to a dosage of 300 mg/kg, but one death was recorded at a dose of 2000 mg/kg. As a result, it was determined that the LD50 of both extracts was more than 2000 mg/kg. This upper limit was also utilized to determine dosages for the current study. As a result, for future research, dosages of 1/10th and 1/20th of the maximum allowed dose, i.e., 200 mg/kg and 100 mg/kg, were used [22-23].

3.2 Chromosomal Aberration Assay

In present study effect of test samples was assessed against cyclophosphamide (CYP) induced mutagenicity. Break, Fragment, Deletion, polyploidy, pulverized and ring type of aberrations were quantified in various treatment groups. Generally, chromatid breaks can be induced in the S and G2 phases of the cell cycle, when the chromosome has split into 2 chromatids. Many chemical agents, especially alkylating agents cause predominantly chromatid-type aberrations. In vehicle treated animals total break was found to be 3.83 ± 1.72 % which was significantly elevated ($P < 0.05$) in CYP only treated animals with 31.33 ± 3.01 %. Flavonoid rich extract of *Cassia auriculata* significantly lowered percentage break up to 8.16 ± 1.47 % and 5.16 ± 1.72 % at 100 and 200 mg/kg respectively ($P < 0.05$). In saponins rich extract increased mutagenicity was observed at lower dose as well as higher doses. Fragments

are single chromatid without centromeres. In CYP treated animals 24.16 ± 2.56 % fragments were observed which were significantly higher ($P < 0.05$) as compared to vehicle treated animals in which 2.83 ± 1.47 % fragments were present [24-26].

3.3 Effect of CAF & CAS on Cyclophosphamide induced Genotoxicity

3.3.1 Study of effect of CAF& CAS in micronucleus assay

During anaphase, Mn products from entire chromosomes or central chromosomal segments were not involved in cell division. Mn formation might be used as a biomarker for exposure to both clastogenic and eugenic hazards. Mn is a useful biomarker for biological dosimetry in the event of acute radiation exposure in humans, according to studies. Radiation dosage has an effect on Mn frequency. After being exposed to ionizing radiation in the 50-500 Msv range, Fenech discovered a rise in Mn frequency in human cells. The Mn test was used to assess biological damage in populations living in locations with high levels of radioactivity, as well as in workers who are exposed to ionizing radiation on the job. Counting the amount of PCE among 1000 cells was used to assess the cytotoxic capability of CAF and CAS. Table 6 shows the number of MNPCEs among 2000 PCE, which indicates genotoxicity. At a dosage of 200 mg/kg, the number of MNPCEs among 2000 PCE generated by CAF was significant ($p < 0.001$). CAF reduced the yields of MN induced by CYP in pre-, simultaneous, and post-treatments by a statistically significant amount. Except for the two highest dosages, all of the CAF doses tested were shown to be beneficial in lowering the incidence of MN caused by CYP. There was also a significant decline in overall MN yield (MN in PCE) [27-29]. CAS were shown to be ineffective in lowering the frequency of MN.

Table 4. Acute toxicity study

Groups	No. of animals	Dose (mg/kg)	Result
<i>C. auriculata</i> root, crude flavonoids extract			
1.	3	5	Not observed (0/3)
2.	3	50	No death
3.	3	300	No death
4.	3	2000	No death
<i>C. auriculata</i> root, crude saponin extract			
5.	3	5	No death

Groups	No. of animals	Dose (mg/kg)	Result
6.	3	50	No death
7.	3	300	No death
8.	3	2000	01 Dead

Table 5. Effect of CAF & CAS on Cyclophosphamide induced Genotoxicity

S. No.	Treatment	Break	Fragment	Deletion	Polyploidy	Pulverized	Ring
1	Vehicle	3.83 ± 1.72 ^d	2.83 ± 1.47	3.66 ± 1.63	0	0	0
2	CYP	31.33 ± 3.01 ^a	24.16 ± 2.56 ^a	17.33 ± 3.26 ^a	6.66 ± 1.96 ^a	6.16 ± 1.47 ^a	5.83 ± 1.60 ^a
3	CYP+CAF (100 mg/kg)	8.16 ± 1.47 ^{abc}	7.17 ± 2.22 ^{abc}	7.83 ± 2.63 ^{abc}	2.33 ± 1.21 ^{abc}	1.83 ± 1.169 ^{abc}	2.16 ± 0.98 ^{abc}
4	CYP+CAF (200 mg/kg)	5.16 ± 1.72 ^{abc}	4.33 ± 1.86 ^{abc}	3.67 ± 1.63 ^{abc}	1.16 ± 0.75 ^{abc}	1.16 ± 1.60 ^{abc}	0.83 ± 1.16 ^{abc}
5	CYP+CAS (100 mg/kg)	37.66 ± 2.58	29.83 ± 2.71	23.16 ± 3.31	10.33 ± 2.25	10.66 ± 2.50	9.17 ± 1.47
6	CYP+CAS (200 mg/kg)	30.83 ± 2.31 ^a	23.67 ± 3.32 ^a	16.83 ± 3.31 ^a	5.83 ± 1.94 ^a	5.66 ± 1.96 ^a	5.33 ± 2.16 ^a

All Data presented in mean ± SD, ^a P<0.05 as compared to CYP+CAS treated group, ^b P<0.05 as compared to CYP treated group, ^c P<0.05 as compared to CYP+CAF treated group, ^d P<0.05 as compared to CYP+CAF treated group

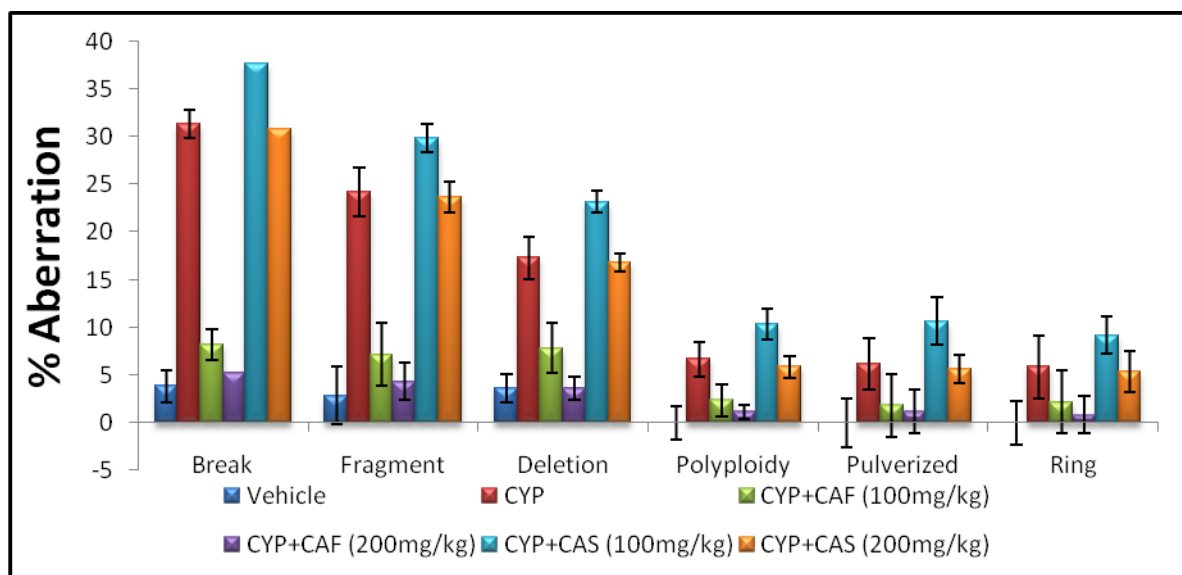


Fig. 1. Effect of CAF & CAS on Cyclophosphamide induced Genotoxicity

Table 6. Effect of CAF & CAS in Micronucleus Assay

S. No.	Treatment	MN-PCE
1.	Vehicle	0.24±0.11
2.	CYP	6.12±0.42
3.	CYP+CAF	2.48±0.63 ^{abcd}
4.	CYP+ CAS	5.92±0.54

All Data presented in mean ± SD, ^a P<0.05 as compared to CYP treated group, ^b P<0.05 as compared to CYP+ Caf treated group, ^c P<0.05 as compared to CYP+ CAS treated group

3.4 Anticancer Activity

At weekly intervals, body weight, tumor yield, percentage of tumors incidence, and tumors burden were examined and assessed. Only tumors with a diameter bigger than 1 mm that had been present for more than one week were included for data analysis. When the first tumors developed, the latency time of tumor development was established. The number of tumor-bearing mice was divided by the total number of mice in a group and multiplied by 100 percent to get the percentage of tumor incidence. The total number of tumors was divided by the number of tumor-bearing mice in a group to get the tumor burden. The volume of the tumor was calculated by multiplying the length, breadth, and height of the tumor by $\pi/6$.

At the conclusion of the trial, all groups' average body weights had increased significantly (Table 7). During the promotion stage, tumors begin to form on the skin between weeks 6 and 9. Tumor development began one week sooner in groups I and IV than in groups II and III, in the sixth week.

The incidence of tumors differed considerably between the treatment Control group and the remainder group. Statistical analysis also revealed that there is a significant variation in tumor burden across groups. Tumor burden is greatest in group I, with a value of 32.5, followed

by 18.83, 22.83, and 29.83 in groups II, III, and IV, respectively. In terms of tumor volume, there was no significant difference between groups.

However, there was a statistically significant difference in tumor volume between groups I (32.5) and II (18.83) when compared to group III, while group IV (22.83 and 29.83) was lower than group I, albeit there was no statistically significant difference between these two groups.

In terms of tumor incidence, tumor yield, and tumor burden, groups II and III performed better than the carcinogen control group (group I). The suppressing impact of group II was equivalent to that of the positive control group (group III), but the suppressing effect of group IV was even larger than that of group I, notably in terms of tumor incidence and tumor burden. Nonetheless, as compared to the carcinogen control group, Group II had a higher tumor incidence and tumor volume.

Morphological investigation (Fig. 2) revealed substantial epidermal hyperplasia (as shown by the thicker epidermal layer) as well as many keratin pearls and rete ridges in the carcinogen control-treated group in all protocols. In the skin sections of the DMBA plus croton oil-treated group, irregular distribution with finger-like projections (papilloma) suggestive of malignant development was identified.

Table 7. Result of anticancer parameters

Group	Parameters	Week 0	Week 8	Week 16
Control	Body weight (gms)	22.82±1.79	32.28±3.84	31.82±2.23
	Tumor yield	0	3.67	32.5
	Tumor incidence	0	83.33	100
	Tumor burden	0	4.4	32.5
CAF+CAS	Body weight (gms)	23.07±0.90	30.35±2.27	31.02±2.58
	Tumor yield	0	2	18.83
	Tumor incidence	0	50	100
	Tumor burden	0	4	18.83
CAF	Body weight (gms)	23.63±0.53	31.14±1.31	31.38±1.89
	Tumor yield	0	2	22.83
	Tumor incidence	0	50	100
	Tumor burden	0	4	22.83
CAS	Body weight (gms)	22.83±0.61	30.69±0.83	29.7±0.85
	Tumor yield	0	3.33	29.83
	Tumor incidence	0	50	100
	Tumor burden	0	6.67	29.83

Furthermore, pieces of the basement membrane were disturbed in several tissue slices, suggesting that the tumors had advanced to a premalignant stage. In all methods, skin tissue samples from the different extracts treated groups showed a decreased degree of epidermal hyperplasia, keratin pearls, and rete ridges. Because the basement membrane remained intact and the dermis had not been infiltrated, the tumors developed were deemed benign. As a consequence of the histology examinations, it was discovered that the level of cellular diversity in various treatment groups correlated with tumor outcomes.

In all treated groups, further histological investigation revealed varied degrees of hyperplasia and keratin pearls. In comparison to the carcinogen control (group I), the epidermis in groups II and III is less hyperplastic, but group IV has more keratin pearls and a hyperplastic epidermis that is equivalent to the carcinogen control. The tumors that develop are benign papillomas that remain contained inside an intact basement membrane with no evidence of invasion into the dermis. Premalignant lesions, on the other hand, were seen in the carcinogen control group [30-32].

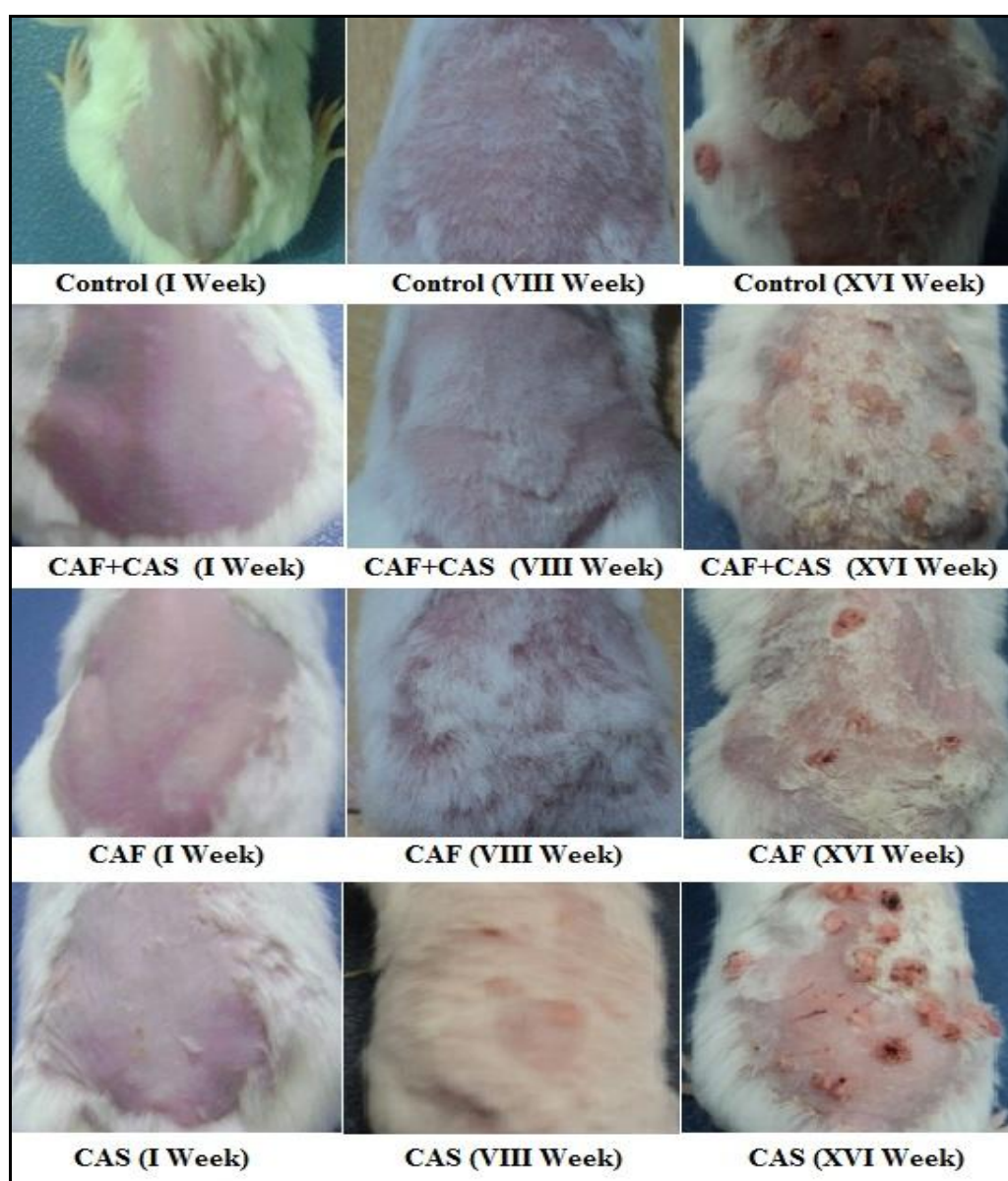


Fig. 2. Morphological examination of anticancer activity on mice

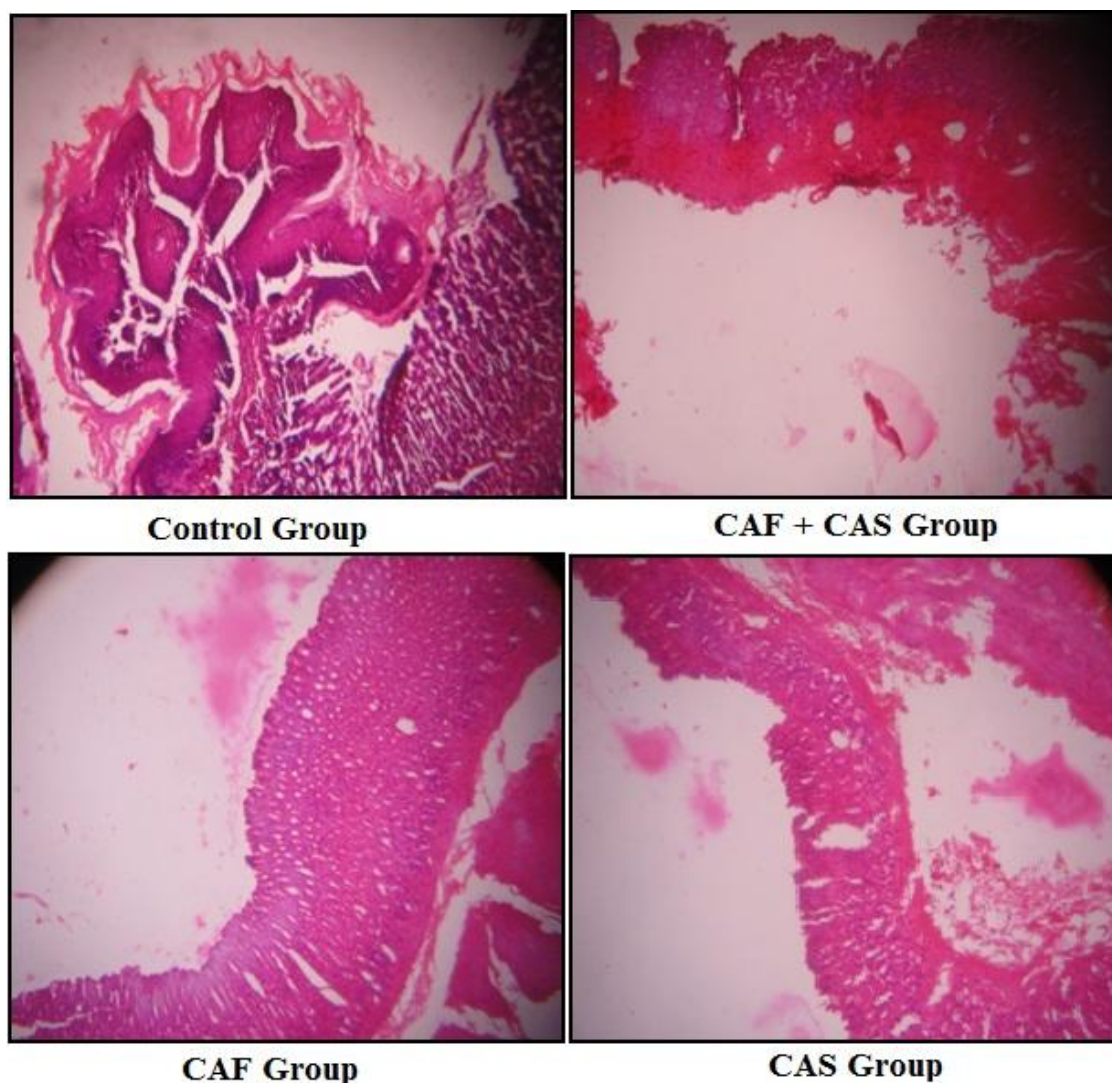


Fig. 3. Histopathological analysis of anticancer activity on mice

4. CONCLUSION

Traditional medical systems have grown in importance over the last decade as a result of their safety. According to current estimates, a significant section of the population in many developing nations depends significantly on traditional practitioners and medicinal herbs to cover their basic health care requirements. Despite the pharmaceutical industry's breakthroughs in the production of unique and highly effective medications for the treatment of a broad variety of disorders, the use of herbal remedies has increased significantly in the world's most wealthy nations. Every medicine has side effects, but a useful pharmacologically active substance should have a good balance of therapeutic and harmful or undesirable side effects. A battery of genotoxic and/or

mutagenicity tests must be done to screen the toxicity mechanism to assure the safety and effectiveness of natural compounds. There is no one test that can collect enough data to predict the chemical risks to human health. The findings of this investigation show that the *Cassia Auriculata* Linn CAF and CAS Fractions are neither genotoxic or clastogenic at the quantities employed. Our findings further suggest that pretreatment with *Cassia Auriculata* Linn CAF and CAS Fraction reduces CYP-induced clastogenicity while maintaining its cytotoxic capability. Because it prolongs the development of tumors in the skin and reduces the hyperproliferative response evoked by CYP, it can be inferred that CAF and CAS Fraction of *Cassia Auriculata* functions as a modulator of two-stage skin carcinogenesis in Swiss albino mice. Furthermore, it reduces oxidative cell

damage, which is inextricably linked to the development of cancer. Further research into the exact mode of action of the genetic toxicity of isolated compounds from this plant species is needed to gain a better understanding of the genotoxic mechanisms described herein, as well as to investigate the protective role of *Cassia Articulata*'s CAF and CAS fractions against genotoxic agents in the environment. It is necessary to understand their processes as cancer treatments.

CONSENT

It is not applicable.

ETHICAL APPROVAL

This study was conducted in accordance with ethical procedures and policies approved by the Institutional animal ethical committee (IAEC) of PBRI (1283/c/09/CPCSEA). Swiss albino mice (Male; 4-5 months; 20-30 gms) were obtained from animal house of Pinnacle Biomedical Research Institute.

COMPETING INTERESTS

Authors have declared that no competing interests exist.

REFERENCES

1. Atanasov AG, Waltenberger B, Pferschy-Wenzig EM, Linder T, Wawrosch C, Uhrin P, et al. Discovery and resupply of pharmacologically active plant-derived natural products: A review. *Biotechnology Advances*. 2015; 33(8):1582–1614. pmid:26281720
Available:https://doi.org/10.1016/j.biotechadv.2015.08.001
2. Lunenfeld B, Stratton P. The clinical consequences of an ageing world and preventive strategies. *Best Practice & Research: Clinical Obstetrics & Gynecology*. 2013;27(5):643–59.
Available:https://doi.org/10.1016/j.bpobgyn.2013.02.005
3. Torgovnick A, Schumacher B. DNA repair mechanisms in cancer development and therapy. *Frontiers in Genetics*. 2015; 23(6):157.
Available:https://doi.org/10.3389/fgene.2015.00157
4. Nagarathna PKM, Johnson Wesley M, Sriram Reddy P, Reena K. Review on Genotoxicity, its Molecular Mechanisms and Prevention. *International Journal of Pharmaceutical Sciences Review and Research*. 2013; 22(1): 236–243.
Available:https://www.researchgate.net/publication/326733700_A_review_on_genotoxicity_in_aquatic_organisms_and_environment
5. Słoczyńska K, Powroźnik B, Pękala E, Waszkielewicz AM. Antimutagenic compounds and their possible mechanisms of action. *Journal of Applied Genetics*. 2014; 55: 273–285
pmid:24615570
Available:https://doi.org/10.1007/s13353-014-0198-9
6. Collins AR, Azqueta A, Langie SAS. Effects of micronutrients on DNA repair. *European Journal of Nutrition*. 2012; 51: 261–279. pmid:22362552
Available:https://doi.org/10.1007/s00394-012-0318-4
7. Orhan F, Gulluce M, Ozkan H, Alpsoy L. Determination of the antigenotoxic potencies of some luteolin derivatives by using a eukaryotic cell system, *Saccharomyces cerevisiae*. *Food Chemistry*. 2013; 141: 366–372.
pmid:23768369
Available:https://doi.org/10.1016/j.foodchem.2013.02.089
8. Chatterjee S, Poduval TB, Tilak JC, Devasagayam TPA. A modified, economic, sensitive method for measuring total antioxidant capacities of human plasma and natural compounds using Indian saffron (*Crocus sativus*). *Clinica Chimica Acta*. 2005; 352: 155–163.
Available:https://doi.org/10.1016/j.cccn.2004.09.012
9. Nsimba RY, Kikuzaki H, Konishi Y. Antioxidant activity of various extracts and fractions of *Chenopodium quinoa* and *Amaranthus* spp. seeds. *Food Chemistry*. 2008; 106: 760–766.
Available:https://doi.org/10.1016/j.foodchem.2007.06.004
10. Castro L, Freeman BA. Reactive oxygen species in human health and disease. *Nutrition*. 2001; 170:161–5.
Available:https://doi.org/10.1016/s0899-9007(00)00570-0
11. Attia S M. The genotoxic and cytotoxic effects of nicotine in the mouse bone marrow. *Mutation Research/ Genetic Toxicology and Environmental Mutagenesis*. 2007; 632(1-2), 29-36.

- Available: <https://doi.org/10.1016/j.mrgento.2007.04.010>
12. Nagarathna PKM, Yadav CK, Yadav SK. Evaluation of Mutagenic Effect and Antimutagenic of Dalbergia Latifolia on Swiss Albino Mice Evaluation, Asian J Pharm Clin Res, 2015;8(3):154-158
 13. V. Lobo, A. Patil, A. Phatak, N. Chandra, Free radical's antioxidants and functional foods: impact on human health, Pharmacogn. Rev. 4 (8) (2010) 118–126. Available: <https://dx.doi.org/10.4103%2F0973-7847.70902>
 14. W.K. Hong, M.B. Sporn, Recent advances in the chemoprevention of cancer, Science 278 (1997) 1073–1077. Available: <https://doi.org/10.1126/science.278.5340.1073>
 15. X.L. Tan, S.D. Spivack, Dietary chemoprevention strategies for induction of phase II xenobiotic-metabolizing enzymes in lung carcinogenesis: a review, Lung Cancer 65 (2009) 129–137. Available: <https://doi.org/10.1016/j.lungcan.2009.01.002>
 16. J.K. Kundu, Y.J. Surh, Molecular basis of chemoprevention with dietary phytochemicals: redox-regulated transcription factors as relevant targets, Phytochem. Rev. 8 (2009) 333–347. Available: <http://dx.doi.org/10.1007%2Fs11101-009-9132-x>
 17. R. Edenharder, I. Von Petersdorff, R. Rauscher, Antimutagenic effects of flavonoids, chalcones and structurally related compounds on the activity of 2-amino-3-methylimidazo [4,5-f] quinoline (IQ) and other heterocyclic amine mutagens from cooked food, Mutat. Res. Med. 287 (1993) 261–274. Available: [https://doi.org/10.1016/0027-5107\(93\)90019-C](https://doi.org/10.1016/0027-5107(93)90019-C)
 18. Salma B, Janhavi P, Muthaiah S, Veeresh P, Santhepete Nanjundiah M, Divyashree S, Serva Peddha M. Ameliorative efficacy of the cassia auriculata root against high-fat-diet+ STZ-induced type-2 diabetes in C57BL/6 mice. ACS omega. 2020 Dec 18;6(1):492-504. Available: <https://doi.org/10.1021/acsomega.0c04940>
 19. Anu K, Devanesan S, Prasanth R, AlSalhi MS, Ajithkumar S, Singaravelu G. Biogenesis of selenium nanoparticles and their anti-leukemia activity. Journal of King Saud University-Science. 2020;32(4):2520-6. Available: <https://doi.org/10.1016/j.jksus.2020.04.018>
 20. Khyade M, Kamble S, Waman M, Padwal A, Gunjal M. Food Potential and Antioxidant Property of Cassia auriculata Seed: A Nutritionally Unexploited Legume. Current Nutrition & Food Science. 2020 Dec 1;16(9):1381-92. Available: <https://doi.org/10.2174/1573401316666200221110140>
 21. Ebringerová A, Hromádková Z. An overview on the application of ultrasound in extraction, separation and purification of plant polysaccharides. Central European Journal of Chemistry. 2010;8(2):243-57. Available: <http://dx.doi.org/10.2478/s11532-010-0006-2>
 22. Lalitha P, Sripathi SK, Jayanthi P. Acute toxicity study of extracts of Eichhornia Crassipes (Mart.) Solms. Asian J Pharm Clin Res. 2012;5(4):59-61. Available: <https://innovareacademics.in/journal/ajpcr/Vol5Issue4/1225.pdf>
 23. Halim SZ, Abdullah NR, Afzan A, Rashid BA, Jantan I, Ismail Z. Acute toxicity study of Carica papaya leaf extract in Sprague Dawley rats. Journal of Medicinal Plants Research. 2011 May 18;5(10):1867-72. Available: https://www.researchgate.net/publication/230859605_Acute_toxicity_study_of_Carica_papaya_leaf_extract_in_Sprague_Dawley_rats
 24. Gangar SC, Sandhir R, Koul A. Anticlastogenic activity of Azadirachta indica against benzo (a) pyrene in murine forestomach tumorigenesis bioassay. Acta Pol Pharm. 2010 Jul 1;67(381):90. Available: <https://pubmed.ncbi.nlm.nih.gov/20635534/>
 25. Parveen N, Shadab GG. The dual clastogenic and anti-clastogenic properties of quercetin is dose dependent. Front Biosci (School Ed). 2017 Jan 1; 9:139-53. Available: <https://doi.org/10.2741/s478>
 26. Manoharan S, Balakrishnan S, Vinothkumar V, Silvan S. Anti-clastogenic potential of carnosic acid against 7, 12-dimethylbenz (a) anthracene (DMBA)-induced clastogenesis. Pharmacological Reports. 2010 Nov 1;62(6):1170-7. Available: [http://dx.doi.org/10.1016/S1734-1140\(10\)70379-0](http://dx.doi.org/10.1016/S1734-1140(10)70379-0)
 27. Želazna K, Rudnicka K, Tejs S. In vitro micronucleus test assessment of polycyclic aromatic hydrocarbons. Environmental Biotechnology. 2011; 7:70-80.

28. Available:file:///C:/Users/Rohan%20Yadav/Downloads/httpwww_environmentalbiotechnology_plebdzialyebonline2011vol72ms161kzelazna.pdf
29. Promkum C, Butryee C, Tuntipopipat S, Kupradinun P. Anticlastogenic effect of *Eryngium foetidum* L. assessed by erythrocyte micronucleus assay. *Asian Pacific Journal of Cancer Prevention*. 2012;13(7):3343-7. Available:https://doi.org/10.7314/apjcp.2012.13.7.3343
30. Maurich T, Pistelli L, Turchi G. Anticlastogenic activity of two structurally related pterocarpanes purified from *Bituminaria bituminosa* in cultured human lymphocytes. *Mutation Research/Genetic Toxicology and Environmental Mutagenesis*. 2004;561(1-2):75-81. Available:https://doi.org/10.1016/j.mrgento.2004.03.006
31. Saini MR, Goyal PK, Chaudhary G. Antitumor activity of *Aloe vera* against DMBA/croton oil-induced skin papilloma genesis in Swiss albino mice. *Journal of Environmental Pathology, Toxicology and Oncology*. 2010; 29(2). DOI: 10.1615/JEnvironPatholToxicolOncol.v29.i2.60
32. Sharma S, Khan N, Sultana S. Effect of *Onosma echioides* on DMBA/croton oil mediated carcinogenic response, hyperproliferation and oxidative damage in murine skin. *Life sciences*. 2004 Oct 1;75(20):2391-410. Available:https://doi.org/10.1016/j.lfs.2004.04.030

© 2021 Kewatkar et al.; This is an Open Access article distributed under the terms of the Creative Commons Attribution License (<http://creativecommons.org/licenses/by/4.0>), which permits unrestricted use, distribution, and reproduction in any medium, provided the original work is properly cited.

Peer-review history:

The peer review history for this paper can be accessed here:

<https://www.sdiarticle5.com/review-history/76966>



Antimutagenic Activity of Cassia Auriculata Linn Fractions along with Anticancer Activity in Male Albino Mice

Shailesh M. Kewatkar ^{a*≡}, Dipak V Bhusari ^{b[⊙]}, Madhav chakolkar ^{c[#]},
Amit Joshi ^{d[†]}, Shirish P. Jain ^{e[‡]} and Chanchal Navin Raj ^{f[‡]}

^a Rajarshi Shahu College of Pharmacy, Buldana, Maharashtra, India.

^b Rajarshi Shahu College of Pharmacy, Buldana, Maharashtra, India.

^c Rajarshi Shahu College of Pharmacy, Buldana, Maharashtra, India.

^d LNCT School of Pharmacy, Kanadiya, Indore, India.

^e Rajarshi Shahu College of Pharmacy, Buldana, Maharashtra, India.

^f Shri D. D. Vispute College of Pharmacy and Research Center, New Panvel, Maharashtra, India.

Authors' contributions

This work was carried out in collaboration among all authors. All authors read and approved the final manuscript.

Article Information

DOI: 10.9734/JPRI/2021/v33i59A34267

Open Peer Review History:

This journal follows the Advanced Open Peer Review policy. Identity of the Reviewers, Editor(s) and additional Reviewers, peer review comments, different versions of the manuscript, comments of the editors, etc are available here: <https://www.sdiarticle5.com/review-history/76966>

Original Research Article

Received 10 October 2021
Accepted 15 December 2021
Published 16 December 2021

ABSTRACT

Background: In recent years, there has been a surge in interest in studying plant-derived materials and their impact on DNA. Herbal products include a number of natural substances that may help protect cells against mutagen-induced cell damage.

Aim: The purpose of this research was to assess the genotoxic effects of Cassia Auriculata Linn flavonoids (CAF) and Cassia Auriculata Linn saponin (CAS) rich fractions on mouse bone marrow cells utilizing chromosomal aberration test and micronucleus assay.

Methodology: The suppressive impact of CAF and CAS on 7, 12-dimethylbenz (α) anthracene (DMBA) and Croton oil induced skin tumor promotion in mice with topical administration twice

[≡] Associate Professor

[⊙] HOD-Diploma

[#] Assistant Professor

[†] Principal

[‡] Research Guide

*Corresponding author: E-mail: rakeshshivatare@gmail.com;

weekly for 18 weeks is also investigated in this work. Three dosages of 100 and 200 mg/kg body weight were used. Single oral dosages of CAF and CAS Fraction at the three levels did not enhance the number of micronucleate polychromatic erythrocytes in the micronucleus experiment.

Result: In mice bone marrow cells, a single oral treatment of CAF and CAS fraction revealed no significant alterations in mitotic indices or chromosomal aberration induction. The clastogenicity of CYP was considerably decreased by pretreatment with CAF and CAS fraction. As a result, it can be stated that CAF and CAS fraction had no genotoxic impact on mouse bone marrow cells.

Conclusions: The portions of *Cassia Auriculata* have been shown to be non-genotoxic and non-clastogenic at the quantities utilized in this investigation. CAF and CAS Fraction might possibly be a promising skin tumor promotion reducing agent, according to this research.

Keywords: *Cassia Auriculata*; cyclophosphamide; Genotoxic effects; anticancer activity.

1. INTRODUCTION

Natural products, in different forms such as extracts, fractions, or as a chemical platform, continue to play an important role in the treatment of numerous illnesses [1]. Plants have historically been the most common source of medicines throughout human history, owing to their secondary metabolites, which have a wide range of pharmacological activities. The knowledge of the many medicinal powers of plants has mostly been passed down via folk traditions and subsequently proven through scientific data [1,2]. Natural bioactive compounds in the prevention and/or treatment of chronic illnesses, which have been dubbed the public health challenge of the twenty-first century, are now one of the trendiest topics in medicine [2]. Indeed, as Lunenfeld and Stratton explain, the rise in healthcare systems and life expectancy in developed countries, as well as the decrease in fertility rate due to chromosomal abnormalities, has resulted in a rapid increase in global population ageing, with an increase in chronic degenerative disease [2,3]. According to the World Health Organization (WHO, 2018), cancer is the second leading cause of death (9.6 million in 2018), with malignancies of the liver (782 000 deaths) and breast (627 000 deaths) being the most prevalent. DNA damage has long been known as a cause of cancer formation, as stated [3]. In reality, oncogenes and tumor suppressor genes are affected by mutations or chromosomal abnormalities, leading to malignant transformation of cells [4]. As a result, antimutagenic, antigenotoxic, and anticarcinogenic chemicals play a critical role in cancer prevention [4,5]. A wide range of medicinal plants and their metabolites have been studied in recent years for their potential to reduce the mutagenic and carcinogenic effects of potentially harmful chemicals [6,7]; in fact, these natural compounds can inhibit free radicals and

oxidative stress-induced DNA and cellular damage [8,9].

Many mutagens and carcinogens work by creating reactive oxygen species (ROS), which are well known for causing oxidative damage to cell structures and biomolecules such lipids, nucleic acids, and proteins in living systems [10]. As a result, the evaluation of the possible genotoxicity of conventional medications is a crucial problem, as damage towards the genetic material can result in significant changes and, as a result, an increased cancer risk or other disorders. Genetic toxicology research has spawned a slew of testing methodologies, including both vitro and in vivo, as a result of their findings. In order to determine the effects of different test chemicals on genetic material and, as a result, the danger to living creatures, including humans, several processes have been devised and tested [11,12].

Synthetic antioxidants such as butylated hydroxytoluene (BHT) and butylated hydroxyanisole (BHA) are preferred, but according to recent research by Lobo et al. [13], they may have major negative consequences on human health. Plants and medicinal plants have been advised to counteract the effects of free radicals/mutagens because they may stimulate phase II enzymes, lowering the activity of cancer and other degenerative illnesses at the initiation, promotion, and progression phases [14–17].

Tanners Senna, *Cassia auriculata* Linn (Family: *Caesalpinaceae*), is found across India's hot deciduous woods and maintains a renowned place in Ayurveda and Siddha systems of treatment. It is said to include alkaloids, terpenoids, phenols and tannins, sugar saponins, flavonoids, quinines, steroids, and proteins, among other phytoconstituents. The *C. auriculata* was found to be used to cure diabetes, joint pain and inflammation, muscular discomfort, sickness,

cold, venereal disease, hair cleaner, decrease body heat, stomach pain, vomiting, diarrhea, and toothache in an ethnobotanical survey. Anti-diabetic, anti-oxidant, hepatoprotective, anti-cancer, anti-inflammatory, anti-hyperlipidemic, and other pharmacological effects of *C. auriculata* have been reported [18-19].

2. MATERIAL AND METHOD

2.1 Collection of Plant Material

Cassia auriculata Linn. roots were obtained from farms around Walgaon Road in Amravati, Maharashtra. Safia College of Science, Peer Gate, Bhopal, Madhya Pradesh, validated this plant and assigned it the voucher specimen number 159/Bot/Safia/2010 (*Cassia auriculata* Linn.).

2.2 Material and Reagent

Sigma-Aldrich Co. provided 7,12-dimethylbenz(α)anthracene (DMBA) and acetone (United States). TCI chemicals provided the croton oil (Japan). All of the other reagents were readily accessible. The tumor initiator DMBA was dissolved in acetone at a concentration of 100 g/100μl. Croton oil was dissolved in acetone to make a % croton oil solution, which was used as a tumour promoter. Curcumin was dissolved in acetone at a dosage of 10 mg/kg as a positive control. All other chemicals were bought from Himedia Laboratories Pvt. Ltd in Mumbai, India, and were of analytical quality.

2.3 Extraction of the Plant Material

Cassia auriculata Linn. roots (2 kg) were dried in the shade before being ground into a coarse powdered substance. The powdered roots of the plant were extracted with the aid of water using the decoction technique [2020] of extraction at 40°C 5°C. The aqueous extract was then filtered through funnel, and alcohol (Ethanol) was gently added to the aqueous liquid extract to precipitate out polysaccharides found in individual plant roots. The solution was then filtered, and the filtrate was evaporated to a quarter of its original volume. After evaporating 1/4 of the total volume of the solution, it was extracted with an equivalent quantity of ethyl acetate using a separating funnel to get a fraction of root components in ethyl acetate. To improve the yield of extract, the ethyl acetate extract was acidified with 0.1 N HCl. The ethyl acetate portion of the plant's root was then evaporated to produce a precipitate, which was then dissolved

in methanol and slowly evaporated to produce crystalline powder (CAF) [20].

Similarly, saponin-rich fractions were extracted from the roots of the plants. After defatting with petroleum ether, pulverized plant material was treated with a 70:30 mixture of ethanol and water for maceration for seven days (40:60). During this time, the mixture was agitated at regular intervals. After filtering through muslin cloth and filter paper, the obtained extract was concentrated using a rotary vacuum evaporator (40°C), with care taken to ensure that the extract did not become powdered. To get the n-butanol soluble fraction, the concentrated extract was treated with n-butanol. The soluble fraction of n-butanol was then treated with cold diethyl ether. Precipitate was generated after treatment with cold diethyl ether. This precipitate-containing mixture was stored at -20°C for 24 hours. Centrifugation was used to further separate the precipitates. To get crystalline powder (CAS), these precipitates were further dissolved in methanol and then evaporated [20-21].

2.4 Animals

This study was conducted in accordance with ethical procedures and policies approved by the Institutional animal ethical committee (IAEC) of PBRI (1283/c/09/CPCSEA). *Swiss albino* mice (Male; 4-5 months; 20-30 gms) were obtained from animal house of Pinnacle Biomedical Research Institute. The animals were randomly assigned to different control and treatment groups (Six animals in each group). All experimental and housing conditions for animals were maintained as per CPCSEA guidelines. Naive animals were selected at random from animal house of PBRI. Animals were kept in group of six in propylene plastic cages with sterilized husk as bedding material. Animals were provided standard feeding pellets (Golden feeds, New Delhi) and water *ad libitum*. Temperature was maintained at 22±2°C, with light and dark cycle of 12:12 hrs. The animals were transferred to the laboratory at least 1h before experiment for proper acclimatization. The experiments were performed during day (08:00-16:00 h).

2.5 Acute Toxicity Study

Toxicology experiments were conducted on young male Swiss albino mice. Each mouse's weight was recorded. The animals were separated into two groups, each with three

animals, and then labelled. Plant extract solution was produced and delivered orally in dosages of 5, 50, 100, 200, and 500 mg/kg. Up to 36 hours, no detrimental effects or mouse death were found. For any additional pharmacological action, treatment doses of 1/10th and 1/20th of the highest tolerable safe dosage were used [22-23].

2.6 Chromosomal Aberration Assay

2.6.1 Dose and treatment

The Chromosomal aberration assay of the tested substance was performed on 36 mice, age 4 - 5 months, weight - 20-30g. Before and during the experiments, all groups of animals were kept under natural light conditions with free access to food and water (Dose- 100 mg/kg; 200 mg/kg).

2.7 Procedure

In the aforesaid group of animals, CYP was utilized as a mutagenic agent and was administered as an intraperitoneal (i.p.) injection at a single dosage of 40 mg/kg b.w 2 hours after the final administration of extract on the seventh day. The positive control group got just a single CYP i.p. injection. The negative control got merely a single 0.4 mL distilled water (d.w.) i.p. injection. For 7 days, the control groups were given p.o. extract at a rate of 200 mg/kg b.w per day for 7 days.

2.8 Chromosomal Analysis

The animals in all groups were slaughtered by cervical dislocation at the sampling time of 24 hours after treatment (colchicine was administered at a dosage of 4 mg/kg of body

weight 2 hours before to killing to halt the metaphase stage). Preston et al procedure's for cytogenetic analysis was followed. Hank's balanced salt solution was used to drain the bone marrow from both femurs (pH 7.2). To allow osmotic swelling of cells, the cells were centrifuged at 1000 rpm for 5 minutes and the pellet was re-dispersed in a hypotonic solution of 0.56 % (w/v) KCl for 30 minutes at 37°C. Swollen cells were fixed in ice-cold Carnoy's fluid, transferred to slides, and stained with phosphate-buffered 5% Giemsa solution. The mitotic index was estimated from a scan of 2000 cells per animal and 75 well-spread metaphase plates per animal in each group were tested for chromosomal abnormalities at a magnification of 100 X. Breaks, fragments, exchanges, and numerous chromosomal abnormalities were classed as chromosomal aberrations (cells with 10 or more aberrations were classified as multiple). The mitotic index, percentage of occurrence of aberrant cells, and percentage of suppression of chromosomal abnormalities were among the criteria studied. The mitotic index was determined as a proportion of dividing cells out of total bone marrow cells measured for cytotoxicity assessment. The number of abnormal cells was calculated as a proportion of the total number of damaged cells (aberrant metaphases).

The suppression percentage of chromosomal aberrations was calculated as:

$$100 - \left[\frac{\text{percent incidence of aberrant cells in extract pre-treated and CYP post treated groups}}{\text{percent incidence of aberrant cells in CYP alone treated group}} \times 100 \right] \text{ [24-26].}$$

Table 1. Dose and treatment selection for Chromosomal Aberration Assay

Group No	Group name	Treatment	Dose	No of animal/group
1	Vehicle	No treatment	Nil	06
2	Control	CYP Only	Nil	06
3	CYP+CAF	Extract + CYP	100 mg/kg	06
4	CYP+CAF	Extract + CYP	200 mg/kg	06
5	CYP+CAS	Extract + CYP	100 mg/kg	06
6	CYP+CAS	Extract + CYP	200 mg/kg	06

Table 2. Dose and treatment selection for Micronucleus assay

Group No	Group name	Treatment	Dose	No of animal/group
1	Vehicle	No treatment	Nil	06
2	Control	CYP Only	Nil	06
3	CYP+CAF	Extract + CYP	200 mg/kg	06
4	CYP+ CAS	Extract + CYP	200 mg/kg	06

2.9 Micronucleus Assay

2.9.1 Dose and treatment

The Micronucleus assay of the tested substance was performed on 36 mice, age 4 - 5 months, weight- 20-30 g. Before and during the experiments, all groups of animals were kept under natural light conditions with free access to food and water (Dose- 100 mg/kg; 200 mg/kg).

2.10 Bone Marrow MN Test and Scoring

The bone marrow MN tests were performed on the same experimental animals. Cervical dislocation was used to kill the animals. The femur and tibia were surgically removed. The modified Schmid technique was used to create bone marrow MN slides. The pellet was centrifuged at 1000 rpm and resuspended in BSA solution after marrow suspension from femur and tibia bones was produced in % bovine serum albumin (BSA). Smears were created and the slides were air-dried after a drop of this suspension was applied on clean glass slides. MN were found in the forms of RBCs, i.e., polychromatic erythrocytes as PCEs, when the slides were fixed in methanol and stained with May-Grunwald-Giemsa. MN was detected in around 2000 PCEs per animal [27-29].

2.10.1 Anticancer activity

2.10.1.1 Dose and treatment

The Anticancer activity of the tested substance was performed on 24 mice, age 4 - 5 months, weight - 20-30g. Before and during the experiments, all groups of animals were kept under natural light conditions with free access to food and water (Dose- 100 mg/kg; 200 mg/kg).

2.11 Procedure

2.11.1 Tumor induction

Different groups of 06 animals were treated with a single dose of DMBA (7,12-

dimethylbenz[a]anthracene) (100 µg/100 µl of acetone) over the shaven area of the skin of the mice. Two weeks later, croton oil (1% in 100 µl of acetone) was applied as a promoter 3 times per week until the end of the experiment (i.e., 16 weeks).

2.11.2 Parameters to be noticed

Tumor incidence: The number of mice carrying at least 1 tumor, expressed as a percentage incidence.

Tumor yield: The average number of papillomas per mouse.

Tumor Burden: The average number of tumors per tumor bearing mouse.

Body weight: The weight of the mice was measured weekly.

Average Latent Period: The lag between the application of the promoting agent and the appearance of 50% of tumors was determined. The average latent period was calculated by multiplying the number of tumors appearing each week by the time in weeks after the application of the promoting agent and dividing the sum by total number of tumors.

$$\text{Average latent period} = \sum fx / n$$

Where f is the number of tumors appearing each week, x is the numbers of weeks, and n is the total number of tumors.

2.12 Histopathological Study

Skin was fixed with buffered formalin for 24 hours. Afterward skin was embedded in paraffin wax by standard protocol. Serial section of 4 µm was cut by microtome with rotary microtome. Sections were stained with Hemtoxyline and eosin staining. Sections were observed at 40x and 100x for histological variations. Important areas were photographed using microscope with digital camera [30-32].

Table 3. Dose and treatment selection for anticancer activity

Group No	Group name	Treatment	Dose	No of animal/group
1	Control	DMBA + Croton oil	Nil	06
2	CAF + CAS	DMBA + Croton oil + Extract of CAF + CAS	200 mg/kg	06
3	CAF	DMBA + Croton oil + Extract of CAF	200 mg/kg	06
4	CAS	DMBA + Croton oil + Extract of CAS	200 mg/kg	06

3. RESULT AND DISCUSSION

3.1 Acute Toxicity Study

Acute oral toxicity is a key criterion for determining a component's safety. The acute oral toxicity of test samples was determined using the OECD 423 criteria in this study. Four dosage levels were employed, according to the guidelines: 5 mg/kg, 50 mg/kg, 300 mg/kg, and 2000 mg/kg. No mortality was reported in *Cassia auriculata* flavonoid rich extracts (CAF) up to a level of 2000 mg/kg. No fatality was seen in the case of *Cassia auriculata* saponin rich extract (CAS) up to a dosage of 300 mg/kg, but one death was recorded at a dose of 2000 mg/kg. As a result, it was determined that the LD50 of both extracts was more than 2000 mg/kg. This upper limit was also utilized to determine dosages for the current study. As a result, for future research, dosages of 1/10th and 1/20th of the maximum allowed dose, i.e., 200 mg/kg and 100 mg/kg, were used [22-23].

3.2 Chromosomal Aberration Assay

In present study effect of test samples was assessed against cyclophosphamide (CYP) induced mutagenicity. Break, Fragment, Deletion, polyploidy, pulverized and ring type of aberrations were quantified in various treatment groups. Generally, chromatid breaks can be induced in the S and G2 phases of the cell cycle, when the chromosome has split into 2 chromatids. Many chemical agents, especially alkylating agents cause predominantly chromatid-type aberrations. In vehicle treated animals total break was found to be 3.83 ± 1.72 % which was significantly elevated ($P < 0.05$) in CYP only treated animals with 31.33 ± 3.01 %. Flavonoid rich extract of *Cassia auriculata* significantly lowered percentage break up to 8.16 ± 1.47 % and 5.16 ± 1.72 % at 100 and 200 mg/kg respectively ($P < 0.05$). In saponins rich extract increased mutagenicity was observed at lower dose as well as higher doses. Fragments

are single chromatid without centromeres. In CYP treated animals 24.16 ± 2.56 % fragments were observed which were significantly higher ($P < 0.05$) as compared to vehicle treated animals in which 2.83 ± 1.47 % fragments were present [24-26].

3.3 Effect of CAF & CAS on Cyclophosphamide induced Genotoxicity

3.3.1 Study of effect of CAF& CAS in micronucleus assay

During anaphase, Mn products from entire chromosomes or central chromosomal segments were not involved in cell division. Mn formation might be used as a biomarker for exposure to both clastogenic and eugenic hazards. Mn is a useful biomarker for biological dosimetry in the event of acute radiation exposure in humans, according to studies. Radiation dosage has an effect on Mn frequency. After being exposed to ionizing radiation in the 50-500 Msv range, Fenech discovered a rise in Mn frequency in human cells. The Mn test was used to assess biological damage in populations living in locations with high levels of radioactivity, as well as in workers who are exposed to ionizing radiation on the job. Counting the amount of PCE among 1000 cells was used to assess the cytotoxic capability of CAF and CAS. Table 6 shows the number of MNPCEs among 2000 PCE, which indicates genotoxicity. At a dosage of 200 mg/kg, the number of MNPCEs among 2000 PCE generated by CAF was significant ($p < 0.001$). CAF reduced the yields of MN induced by CYP in pre-, simultaneous, and post-treatments by a statistically significant amount. Except for the two highest dosages, all of the CAF doses tested were shown to be beneficial in lowering the incidence of MN caused by CYP. There was also a significant decline in overall MN yield (MN in PCE) [27-29]. CAS were shown to be ineffective in lowering the frequency of MN.

Table 4. Acute toxicity study

Groups	No. of animals	Dose (mg/kg)	Result
<i>C. auriculata</i> root, crude flavonoids extract			
1.	3	5	Not observed (0/3)
2.	3	50	No death
3.	3	300	No death
4.	3	2000	No death
<i>C. auriculata</i> root, crude saponin extract			
5.	3	5	No death

Groups	No. of animals	Dose (mg/kg)	Result
6.	3	50	No death
7.	3	300	No death
8.	3	2000	01 Dead

Table 5. Effect of CAF & CAS on Cyclophosphamide induced Genotoxicity

S. No.	Treatment	Break	Fragment	Deletion	Polyploidy	Pulverized	Ring
1	Vehicle	3.83 ± 1.72 ^d	2.83 ± 1.47	3.66 ± 1.63	0	0	0
2	CYP	31.33 ± 3.01 ^a	24.16 ± 2.56 ^a	17.33 ± 3.26 ^a	6.66 ± 1.96 ^a	6.16 ± 1.47 ^a	5.83 ± 1.60 ^a
3	CYP+CAF (100 mg/kg)	8.16 ± 1.47 ^{abc}	7.17 ± 2.22 ^{abc}	7.83 ± 2.63 ^{abc}	2.33 ± 1.21 ^{abc}	1.83 ± 1.169 ^{abc}	2.16 ± 0.98 ^{abc}
4	CYP+CAF (200 mg/kg)	5.16 ± 1.72 ^{abc}	4.33 ± 1.86 ^{abc}	3.67 ± 1.63 ^{abc}	1.16 ± 0.75 ^{abc}	1.16 ± 1.60 ^{abc}	0.83 ± 1.16 ^{abc}
5	CYP+CAS (100 mg/kg)	37.66 ± 2.58	29.83 ± 2.71	23.16 ± 3.31	10.33 ± 2.25	10.66 ± 2.50	9.17 ± 1.47
6	CYP+CAS (200 mg/kg)	30.83 ± 2.31 ^a	23.67 ± 3.32 ^a	16.83 ± 3.31 ^a	5.83 ± 1.94 ^a	5.66 ± 1.96 ^a	5.33 ± 2.16 ^a

All Data presented in mean ± SD, ^a P<0.05 as compared to CYP+CAS treated group, ^b P<0.05 as compared to CYP treated group, ^c P<0.05 as compared to CYP+CAF treated group, ^d P<0.05 as compared to CYP+CAF treated group

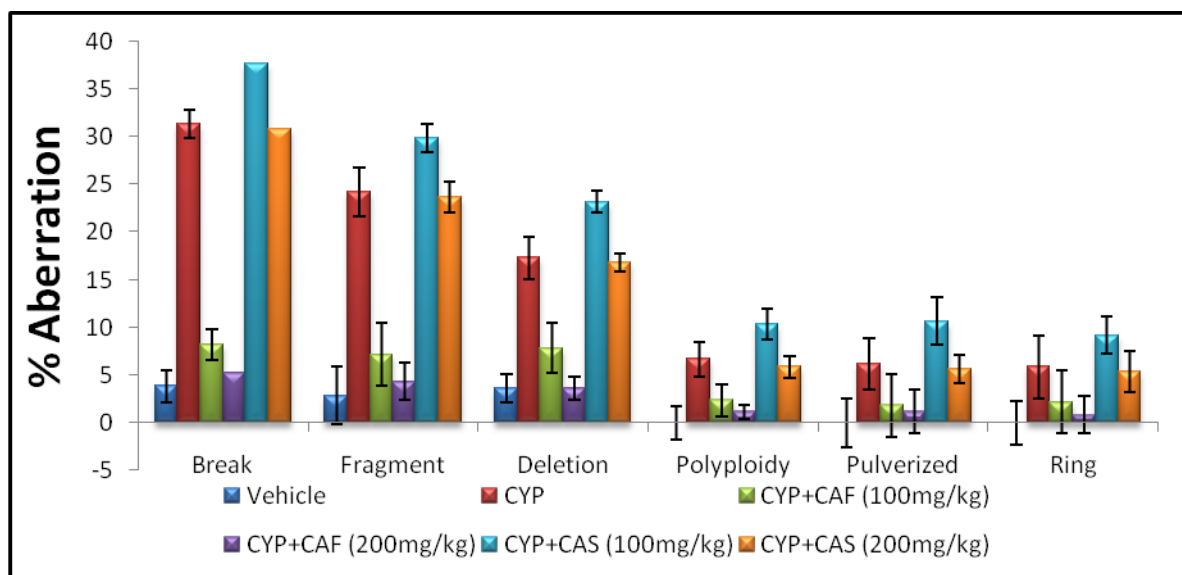


Fig. 1. Effect of CAF & CAS on Cyclophosphamide induced Genotoxicity

Table 6. Effect of CAF & CAS in Micronucleus Assay

S. No.	Treatment	MN-PCE
1.	Vehicle	0.24±0.11
2.	CYP	6.12±0.42
3.	CYP+CAF	2.48±0.63 ^{abcd}
4.	CYP+ CAS	5.92±0.54

All Data presented in mean ± SD, ^a P<0.05 as compared to CYP treated group, ^b P<0.05 as compared to CYP+ Caf treated group, ^c P<0.05 as compared to CYP+ CAS treated group

3.4 Anticancer Activity

At weekly intervals, body weight, tumor yield, percentage of tumors incidence, and tumors burden were examined and assessed. Only tumors with a diameter bigger than 1 mm that had been present for more than one week were included for data analysis. When the first tumors developed, the latency time of tumor development was established. The number of tumor-bearing mice was divided by the total number of mice in a group and multiplied by 100 percent to get the percentage of tumor incidence. The total number of tumors was divided by the number of tumor-bearing mice in a group to get the tumor burden. The volume of the tumor was calculated by multiplying the length, breadth, and height of the tumor by $\pi/6$.

At the conclusion of the trial, all groups' average body weights had increased significantly (Table 7). During the promotion stage, tumors begin to form on the skin between weeks 6 and 9. Tumor development began one week sooner in groups I and IV than in groups II and III, in the sixth week.

The incidence of tumors differed considerably between the treatment Control group and the remainder group. Statistical analysis also revealed that there is a significant variation in tumor burden across groups. Tumor burden is greatest in group I, with a value of 32.5, followed

by 18.83, 22.83, and 29.83 in groups II, III, and IV, respectively. In terms of tumor volume, there was no significant difference between groups.

However, there was a statistically significant difference in tumor volume between groups I (32.5) and II (18.83) when compared to group III, while group IV (22.83 and 29.83) was lower than group I, albeit there was no statistically significant difference between these two groups.

In terms of tumor incidence, tumor yield, and tumor burden, groups II and III performed better than the carcinogen control group (group I). The suppressing impact of group II was equivalent to that of the positive control group (group III), but the suppressing effect of group IV was even larger than that of group I, notably in terms of tumor incidence and tumor burden. Nonetheless, as compared to the carcinogen control group, Group II had a higher tumor incidence and tumor volume.

Morphological investigation (Fig. 2) revealed substantial epidermal hyperplasia (as shown by the thicker epidermal layer) as well as many keratin pearls and rete ridges in the carcinogen control-treated group in all protocols. In the skin sections of the DMBA plus croton oil-treated group, irregular distribution with finger-like projections (papilloma) suggestive of malignant development was identified.

Table 7. Result of anticancer parameters

Group	Parameters	Week 0	Week 8	Week 16
Control	Body weight (gms)	22.82±1.79	32.28±3.84	31.82±2.23
	Tumor yield	0	3.67	32.5
	Tumor incidence	0	83.33	100
	Tumor burden	0	4.4	32.5
CAF+CAS	Body weight (gms)	23.07±0.90	30.35±2.27	31.02±2.58
	Tumor yield	0	2	18.83
	Tumor incidence	0	50	100
	Tumor burden	0	4	18.83
CAF	Body weight (gms)	23.63±0.53	31.14±1.31	31.38±1.89
	Tumor yield	0	2	22.83
	Tumor incidence	0	50	100
	Tumor burden	0	4	22.83
CAS	Body weight (gms)	22.83±0.61	30.69±0.83	29.7±0.85
	Tumor yield	0	3.33	29.83
	Tumor incidence	0	50	100
	Tumor burden	0	6.67	29.83

Furthermore, pieces of the basement membrane were disturbed in several tissue slices, suggesting that the tumors had advanced to a premalignant stage. In all methods, skin tissue samples from the different extracts treated groups showed a decreased degree of epidermal hyperplasia, keratin pearls, and rete ridges. Because the basement membrane remained intact and the dermis had not been infiltrated, the tumors developed were deemed benign. As a consequence of the histology examinations, it was discovered that the level of cellular diversity in various treatment groups correlated with tumor outcomes.

In all treated groups, further histological investigation revealed varied degrees of hyperplasia and keratin pearls. In comparison to the carcinogen control (group I), the epidermis in groups II and III is less hyperplastic, but group IV has more keratin pearls and a hyperplastic epidermis that is equivalent to the carcinogen control. The tumors that develop are benign papillomas that remain contained inside an intact basement membrane with no evidence of invasion into the dermis. Premalignant lesions, on the other hand, were seen in the carcinogen control group [30-32].

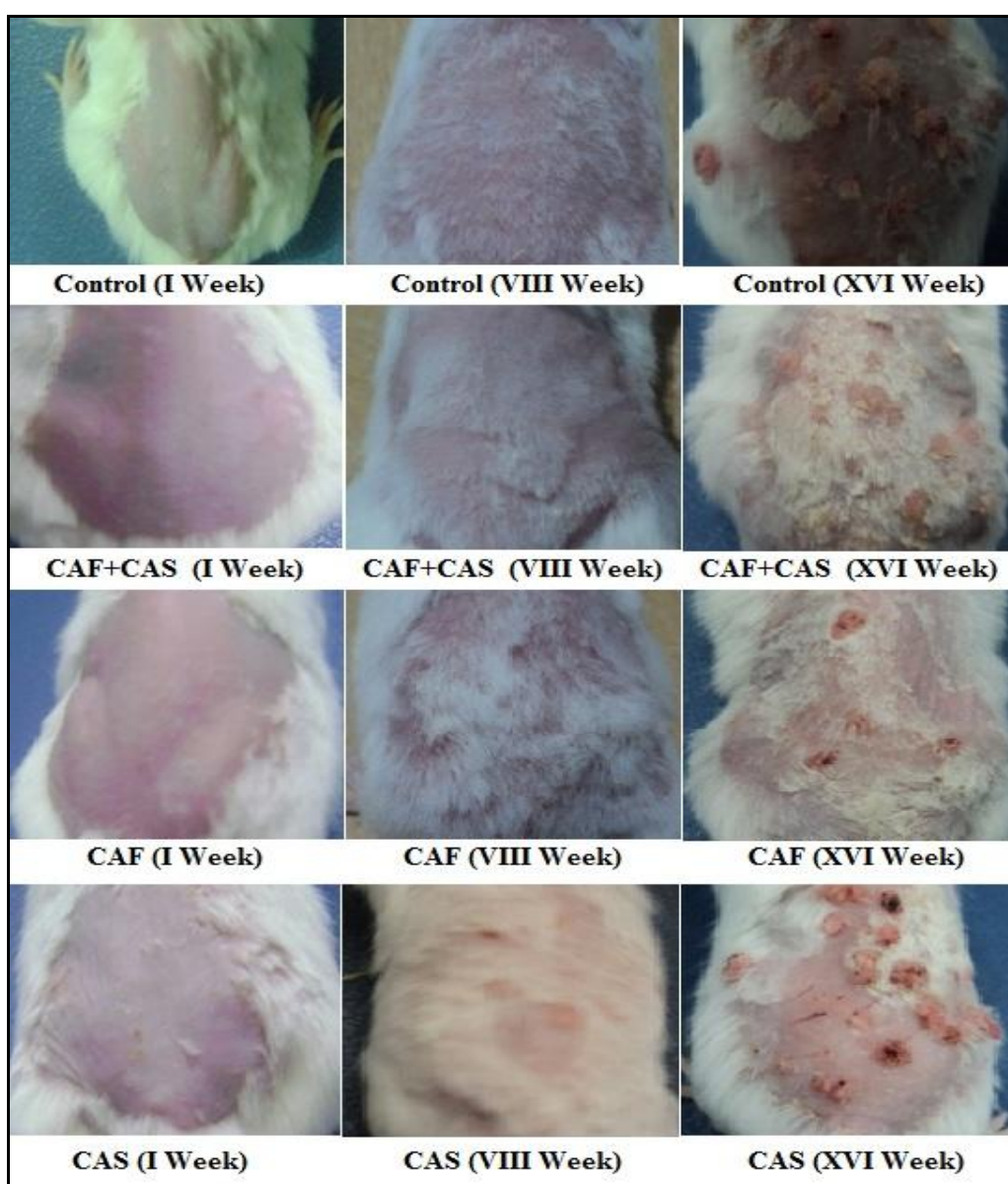


Fig. 2. Morphological examination of anticancer activity on mice

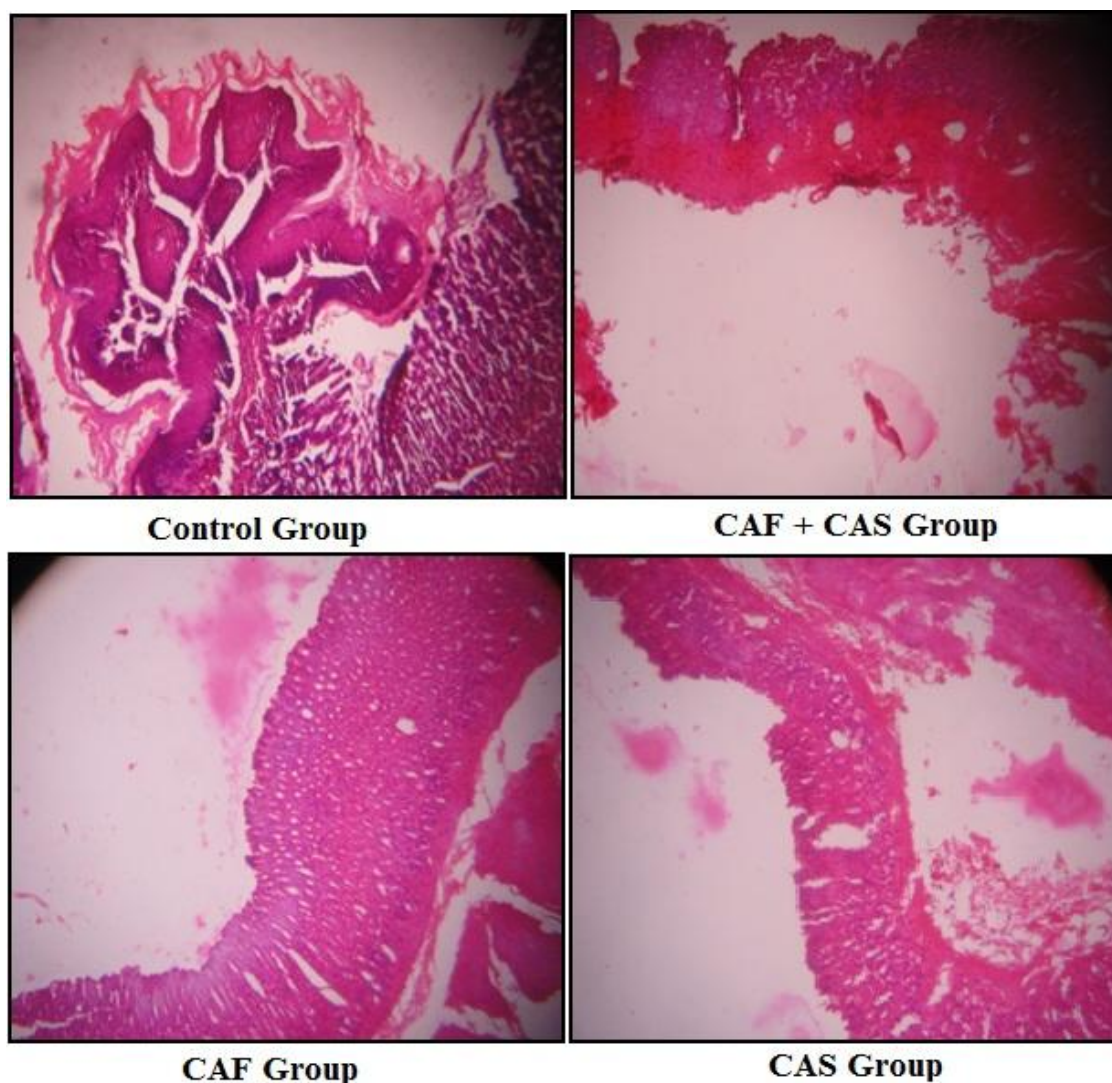


Fig. 3. Histopathological analysis of anticancer activity on mice

4. CONCLUSION

Traditional medical systems have grown in importance over the last decade as a result of their safety. According to current estimates, a significant section of the population in many developing nations depends significantly on traditional practitioners and medicinal herbs to cover their basic health care requirements. Despite the pharmaceutical industry's breakthroughs in the production of unique and highly effective medications for the treatment of a broad variety of disorders, the use of herbal remedies has increased significantly in the world's most wealthy nations. Every medicine has side effects, but a useful pharmacologically active substance should have a good balance of therapeutic and harmful or undesirable side effects. A battery of genotoxic and/or

mutagenicity tests must be done to screen the toxicity mechanism to assure the safety and effectiveness of natural compounds. There is no one test that can collect enough data to predict the chemical risks to human health. The findings of this investigation show that the *Cassia Auriculata* Linn CAF and CAS Fractions are neither genotoxic or clastogenic at the quantities employed. Our findings further suggest that pretreatment with *Cassia Auriculata* Linn CAF and CAS Fraction reduces CYP-induced clastogenicity while maintaining its cytotoxic capability. Because it prolongs the development of tumors in the skin and reduces the hyperproliferative response evoked by CYP, it can be inferred that CAF and CAS Fraction of *Cassia Auriculata* functions as a modulator of two-stage skin carcinogenesis in Swiss albino mice. Furthermore, it reduces oxidative cell

damage, which is inextricably linked to the development of cancer. Further research into the exact mode of action of the genetic toxicity of isolated compounds from this plant species is needed to gain a better understanding of the genotoxic mechanisms described herein, as well as to investigate the protective role of *Cassia Articulata*'s CAF and CAS fractions against genotoxic agents in the environment. It is necessary to understand their processes as cancer treatments.

CONSENT

It is not applicable.

ETHICAL APPROVAL

This study was conducted in accordance with ethical procedures and policies approved by the Institutional animal ethical committee (IAEC) of PBRI (1283/c/09/CPCSEA). Swiss albino mice (Male; 4-5 months; 20-30 gms) were obtained from animal house of Pinnacle Biomedical Research Institute.

COMPETING INTERESTS

Authors have declared that no competing interests exist.

REFERENCES

1. Atanasov AG, Waltenberger B, Pferschy-Wenzig EM, Linder T, Wawrosch C, Uhrin P, et al. Discovery and resupply of pharmacologically active plant-derived natural products: A review. *Biotechnology Advances*. 2015; 33(8):1582–1614. pmid:26281720
Available:https://doi.org/10.1016/j.biotechadv.2015.08.001
2. Lunenfeld B, Stratton P. The clinical consequences of an ageing world and preventive strategies. *Best Practice & Research: Clinical Obstetrics & Gynecology*. 2013;27(5):643–59.
Available:https://doi.org/10.1016/j.bpobgyn.2013.02.005
3. Torgovnick A, Schumacher B. DNA repair mechanisms in cancer development and therapy. *Frontiers in Genetics*. 2015; 23(6):157.
Available:https://doi.org/10.3389/fgene.2015.00157
4. Nagarathna PKM, Johnson Wesley M, Sriram Reddy P, Reena K. Review on

Genotoxicity, its Molecular Mechanisms and Prevention. *International Journal of Pharmaceutical Sciences Review and Research*. 2013; 22(1): 236–243.

Available:https://www.researchgate.net/publication/326733700_A_review_on_genotoxicity_in_aquatic_organisms_and_environment

5. Słoczyńska K, Powroźnik B, Pękala E, Waszkielewicz AM. Antimutagenic compounds and their possible mechanisms of action. *Journal of Applied Genetics*. 2014; 55: 273–285
pmid:24615570
Available:https://doi.org/10.1007/s13353-014-0198-9
6. Collins AR, Azqueta A, Langie SAS. Effects of micronutrients on DNA repair. *European Journal of Nutrition*. 2012; 51: 261–279. pmid:22362552
Available:https://doi.org/10.1007/s00394-012-0318-4
7. Orhan F, Gulluce M, Ozkan H, Alpsoy L. Determination of the antigenotoxic potencies of some luteolin derivatives by using a eukaryotic cell system, *Saccharomyces cerevisiae*. *Food Chemistry*. 2013; 141: 366–372.
pmid:23768369
Available:https://doi.org/10.1016/j.foodchem.2013.02.089
8. Chatterjee S, Poduval TB, Tilak JC, Devasagayam TPA. A modified, economic, sensitive method for measuring total antioxidant capacities of human plasma and natural compounds using Indian saffron (*Crocus sativus*). *Clinica Chimica Acta*. 2005; 352: 155–163.
Available:https://doi.org/10.1016/j.cccn.2004.09.012
9. Nsimba RY, Kikuzaki H, Konishi Y. Antioxidant activity of various extracts and fractions of *Chenopodium quinoa* and *Amaranthus* spp. seeds. *Food Chemistry*. 2008; 106: 760–766.
Available:https://doi.org/10.1016/j.foodchem.2007.06.004
10. Castro L, Freeman BA. Reactive oxygen species in human health and disease. *Nutrition*. 2001; 170:161–5.
Available:https://doi.org/10.1016/s0899-9007(00)00570-0
11. Attia S M. The genotoxic and cytotoxic effects of nicotine in the mouse bone marrow. *Mutation Research/ Genetic Toxicology and Environmental Mutagenesis*. 2007; 632(1-2), 29-36.

- Available: <https://doi.org/10.1016/j.mrgento.2007.04.010>
12. Nagarathna PKM, Yadav CK, Yadav SK. Evaluation of Mutagenic Effect and Antimutagenic of Dalbergia Latifolia on Swiss Albino Mice Evaluation, Asian J Pharm Clin Res, 2015;8(3):154-158
 13. V. Lobo, A. Patil, A. Phatak, N. Chandra, Free radical's antioxidants and functional foods: impact on human health, Pharmacogn. Rev. 4 (8) (2010) 118–126. Available: <https://dx.doi.org/10.4103%2F0973-7847.70902>
 14. W.K. Hong, M.B. Sporn, Recent advances in the chemoprevention of cancer, Science 278 (1997) 1073–1077. Available: <https://doi.org/10.1126/science.278.5340.1073>
 15. X.L. Tan, S.D. Spivack, Dietary chemoprevention strategies for induction of phase II xenobiotic-metabolizing enzymes in lung carcinogenesis: a review, Lung Cancer 65 (2009) 129–137. Available: <https://doi.org/10.1016/j.lungcan.2009.01.002>
 16. J.K. Kundu, Y.J. Surh, Molecular basis of chemoprevention with dietary phytochemicals: redox-regulated transcription factors as relevant targets, Phytochem. Rev. 8 (2009) 333–347. Available: <http://dx.doi.org/10.1007%2Fs11101-009-9132-x>
 17. R. Edenharder, I. Von Petersdorff, R. Rauscher, Antimutagenic effects of flavonoids, chalcones and structurally related compounds on the activity of 2-amino-3-methylimidazo [4,5-f] quinoline (IQ) and other heterocyclic amine mutagens from cooked food, Mutat. Res. Med. 287 (1993) 261–274. Available: [https://doi.org/10.1016/0027-5107\(93\)90019-C](https://doi.org/10.1016/0027-5107(93)90019-C)
 18. Salma B, Janhavi P, Muthaiah S, Veeresh P, Santhepete Nanjundaiah M, Divyashree S, Serva Peddha M. Ameliorative efficacy of the cassia auriculata root against high-fat-diet+ STZ-induced type-2 diabetes in C57BL/6 mice. ACS omega. 2020 Dec 18;6(1):492-504. Available: <https://doi.org/10.1021/acsomega.0c04940>
 19. Anu K, Devanesan S, Prasanth R, AlSalhi MS, Ajithkumar S, Singaravelu G. Biogenesis of selenium nanoparticles and their anti-leukemia activity. Journal of King Saud University-Science. 2020;32(4):2520-6. Available: <https://doi.org/10.1016/j.jksus.2020.04.018>
 20. Khyade M, Kamble S, Waman M, Padwal A, Gunjal M. Food Potential and Antioxidant Property of Cassia auriculata Seed: A Nutritionally Unexploited Legume. Current Nutrition & Food Science. 2020 Dec 1;16(9):1381-92. Available: <https://doi.org/10.2174/1573401316666200221110140>
 21. Ebringerová A, Hromádková Z. An overview on the application of ultrasound in extraction, separation and purification of plant polysaccharides. Central European Journal of Chemistry. 2010;8(2):243-57. Available: <http://dx.doi.org/10.2478/s11532-010-0006-2>
 22. Lalitha P, Sripathi SK, Jayanthi P. Acute toxicity study of extracts of Eichhornia Crassipes (Mart.) Solms. Asian J Pharm Clin Res. 2012;5(4):59-61. Available: <https://innovareacademics.in/journal/ajpcr/Vol5Issue4/1225.pdf>
 23. Halim SZ, Abdullah NR, Afzan A, Rashid BA, Jantan I, Ismail Z. Acute toxicity study of Carica papaya leaf extract in Sprague Dawley rats. Journal of Medicinal Plants Research. 2011 May 18;5(10):1867-72. Available: https://www.researchgate.net/publication/230859605_Acute_toxicity_study_of_Carica_papaya_leaf_extract_in_Sprague_Dawley_rats
 24. Gangar SC, Sandhir R, Koul A. Anticlastogenic activity of Azadirachta indica against benzo (a) pyrene in murine forestomach tumorigenesis bioassay. Acta Pol Pharm. 2010 Jul 1;67(381):90. Available: <https://pubmed.ncbi.nlm.nih.gov/20635534/>
 25. Parveen N, Shadab GG. The dual clastogenic and anti-clastogenic properties of quercetin is dose dependent. Front Biosci (School Ed). 2017 Jan 1; 9:139-53. Available: <https://doi.org/10.2741/s478>
 26. Manoharan S, Balakrishnan S, Vinothkumar V, Silvan S. Anti-clastogenic potential of carnosic acid against 7, 12-dimethylbenz (a) anthracene (DMBA)-induced clastogenesis. Pharmacological Reports. 2010 Nov 1;62(6):1170-7. Available: [http://dx.doi.org/10.1016/S1734-1140\(10\)70379-0](http://dx.doi.org/10.1016/S1734-1140(10)70379-0)
 27. Želazna K, Rudnicka K, Tejs S. In vitro micronucleus test assessment of polycyclic aromatic hydrocarbons. Environmental Biotechnology. 2011; 7:70-80.

28. Available:file:///C:/Users/Rohan%20Yadav/Downloads/httpwww_environmentalbiotechnology_plebdzialyebonline2011vol72ms161kzelazna.pdf
29. Promkum C, Butryee C, Tuntipopipat S, Kupradinun P. Anticlastogenic effect of *Eryngium foetidum* L. assessed by erythrocyte micronucleus assay. *Asian Pacific Journal of Cancer Prevention*. 2012;13(7):3343-7. Available:https://doi.org/10.7314/apjcp.2012.13.7.3343
30. Maurich T, Pistelli L, Turchi G. Anticlastogenic activity of two structurally related pterocarpanes purified from *Bituminaria bituminosa* in cultured human lymphocytes. *Mutation Research/Genetic Toxicology and Environmental Mutagenesis*. 2004;561(1-2):75-81. Available:https://doi.org/10.1016/j.mrgento.2004.03.006
31. Saini MR, Goyal PK, Chaudhary G. Antitumor activity of *Aloe vera* against DMBA/croton oil-induced skin papilloma genesis in Swiss albino mice. *Journal of Environmental Pathology, Toxicology and Oncology*. 2010; 29(2). DOI: 10.1615/JEnvironPatholToxicolOncol.v29.i2.60
32. Sharma S, Khan N, Sultana S. Effect of *Onosma echioides* on DMBA/croton oil mediated carcinogenic response, hyperproliferation and oxidative damage in murine skin. *Life sciences*. 2004 Oct 1;75(20):2391-410. Available:https://doi.org/10.1016/j.lfs.2004.04.030

© 2021 Kewatkar et al.; This is an Open Access article distributed under the terms of the Creative Commons Attribution License (<http://creativecommons.org/licenses/by/4.0>), which permits unrestricted use, distribution, and reproduction in any medium, provided the original work is properly cited.

Peer-review history:

The peer review history for this paper can be accessed here:

<https://www.sdiarticle5.com/review-history/76966>



Evaluation of the Antigenotoxic Potential of Methanolic Leaves Extract of *Triticum aestivum* in Mice

Gaurav Jain^{1*}, Shailesh M. Kewatker², Govind Nayak³ and Amit Nayak⁴

¹IES Institute of Pharmacy, IES University Campus, Kalkheda, Ratibad Main Road, Bhopal, 462044, Madhya Pradesh, India.

²Rajarshi Shahu College of Pharmacy, Buldana, 443001, Maharashtra, India.

³Lakshmi Narain College of Pharmacy, Kalchuri Nagar, Raisen Road, Bhopal, 462022, Madhya Pradesh, India.

⁴GD Goenka University, Sohna-Gurgaon Road, Sohna Gurgon, 122103, India.

Authors' contributions

This work was carried out in collaboration among all authors. All authors read and approved the final manuscript.

Article Information

DOI: 10.9734/JPRI/2021/v33i47B33088

Editor(s):

(1) Dr. Asmaa Fathi Moustafa Hamouda, Jazan University, Saudi Arabia.

(2) Dr. Mohamed Fawzy Ramadan Hassanien, Zagazig University, Egypt.

Reviewers:

(1) Walaa Ibrahim Ahmed Ibrahim, National Research Center, Egypt.

(2) J. B. Kathiriya, Kamdhenu University, India.

Complete Peer review History: <https://www.sdiarticle4.com/review-history/75916>

Original Research Article

Received 12 August 2021

Accepted 25 October 2021

Published 30 October 2021

ABSTRACT

Mutations are changes to the nucleotide sequence of the genetic material of an organism. Reactive oxygen species (ROS) play an important role in process like mutagenesis, carcinogenesis and aging by their ability to damage cellular DNA. Inhibition of mutagenesis or carcinogenesis is generally not based on one specific mechanism. Protection against cancer can occur at different stages of the complicated processes of carcinogenesis. Naturally occurring antioxidants have been extensively studied for their capacity to protect organisms and cells from oxidation. *Triticum aestivum* (*T. aestivum*) have revealed its medicinal potential for some human diseases; therefore, this study aimed to evaluate the genotoxic and antigenotoxic potential of methanolic extract. To accomplish this, the methanolic extract of *T. aestivum* was evaluated for its antigenotoxic effect using the chromosomal aberrations and micronucleus assay of bone marrow cells of mice.

*Corresponding author: E-mail: dr_gaurav.jain@iesbpl.ac.in, gauravjain20us@gmail.com;

T. aestivum extract has shown significant protection against Cyclophosphamide induced micronucleus formation and chromosomal aberrations.

Keywords: *Triticum aestivum*; cyclophosphamide; chromosomal aberrations; micronucleus assay; antigenotoxic; genotoxicity; carcinogenesis.

1. INTRODUCTION

Oxidative deoxy ribonucleic acid (DNA) damage is caused by mutagen which leads to mutagenesis. It is crucial step in the development of cancer and other degenerative processes such as cardiovascular and neurodegenerative disease as well as premature ageing [1]. The mutation in the DNA leads to the formation of faulty DNA that leads to cancer. Classical treatment for cancer in is radio or chemo therapy. But the therapies work by targeting the DNA and damaging both the malignant as well as the normal cells [2–5].

The mutagens can be prevented by many herbal therapies by maximizing the pharmacological effects and minimizing the side-effects. Therefore, many types of research have been performed to find out plants having secondary metabolites which act as antimutagens and nontoxic to the normal cells [6]. It is found that green plants are generally the primary source of antimutagens as well as toxic agents. Many plants contain mutagenic or carcinogenic substances and their use has been diagnosed for tumor formation in some patients. Recent research has affirmed that many plants used as food or in traditional medicine have mutagenic and genotoxic effects [7,8,9,10]. Genotoxicity testing is a significant part of the threat estimation of chemicals for regulatory purposes [11,12]. It is undertaken for two main reasons: a) to detect chemicals that might cause genetic damage, including point mutations in germ cells and thus increase the burden of genetic disease in the human population and b) to detect chemicals that might be carcinogenic (based on the assumption that a mutagenesis is a key event in the process of carcinogenesis) [13,14]. In crude preparations, other components are also present in addition to the active components which may be counteracting the toxic effects of the active components. These known and unknown components may act as synergists for the therapeutic effects and antagonists for the side effects of the active components as well as for other toxic components in the crude preparation [15]. In the past few years, there has

been considerable interest in natural products endowed with antimutagenic and anticarcinogenic properties.

Triticum aestivum (*T. aestivum*) has been a primary source of food from ancient times, therefore it commemorates to check whether *T.aestivum* leaves extract itself is mutagenic and also to ascertain its antigenotoxic potential. Many studies have been performed on its leaves in this context. It has been used for its antioxidant, apoptotic, antiproliferative activities on CML (K562) and MCF-7 breast cancer cell lines [16,17]. Its leaves extract was also evaluated for its chemopreventive action against DBMA and croton oil [18]. Its sprouts have also been used for antimutagenicity and its mechanism of action is also identified [19,20]. Chlorophyllin a potent antioxidant compound is extensively used for its chemopreventive, antimutagenic, anticytotoxic, antiproliferative, anticarcinogenic, antitumorigenic, apoptotic activity and its mechanism of *in vitro* action against benzo(a)pyrene is also reported [21,22,23,24–35]. Chlorophyllin is also used as a protector of mitochondrial membranes against γ -radiation and photosensitization [36]. Wheat sprout extract also induces apoptosis in human cancer cells and also induces changes in 20S proteasomes functionality [37]. The sprout is also reported for its antioxidant activity and inhibits DNA oxidative damage [38]. The nutritional relevance of its sprouts containing high levels of organic phosphates and antioxidant compounds was also studied [39]. Cytotoxic activity on HL60 and the antiproliferative effect of local health supplement wheatgrass and the mixture of fibers were investigated *in vitro* using a cancerous cell line and normal blood cell culture [40].

The objective of the work was to evaluate the antigenotoxic potential of methanolic extract of *T.aestivum* young leaves using cyclophosphamide as an inducer of genotoxicity. Cyclophosphamide is an alkylating agent possessing the clastogenic effect which produces the formation of micronuclei in bone marrow cells [41]. The Antigenotoxic effects were evaluated by microsomal aberrations and micronucleus assay models.

2. MATERIALS AND METHODS

2.1 Procurement of Seeds and Authentication of the Plant Material

The *T.aestivum* seeds for the research were purchased from Breeder Seed Production Unit Field crops, Department of Plant Breeding and Genetics, Jawahar Lal Nehru Krishi Vishwavidyalaya, Krishinagar, Jabalpur M.P. and the release order number DFP2219 was obtained. The whole plant of TA was collected in December and authenticated at Safia college of Science Bhopal, Madhya Pradesh. The herbarium of the plant was prepared and the voucher specimen number 236/BOT/SAFIA/2011 was obtained.

2.2 Preparation of Powder

T.aestivum was cultivated, and the leaves were collected on the ninth day. It was dried in shade and then powdered with a mechanical grinder. The powder was passed through sieve no.40 and stored in a labeled air-tight container for further studies.

2.3 Preparation of Extract

The maceration process involves the separation of medicinally active portions of the crude drugs. It is based on the immersion of the crude drugs in the bulk of solvent or menstrum. Solid drug material was taken in a stoppered container with about 750 mL of the methanol and allowed to stand for seven days in a warm place with frequent shaking. The mixture of crude drug containing solvent was filtered until most of the liquid drains off. The filtrate and the washing were combined to produce 1000 mL of the solution. This solution was kept aside for solidification and was dried on a hot air oven at 40 °C. The extract is then collected in a dark colored bottle [42].

2.4 Animal Care and Handling

The procurement of the animals and the studies were performed at Sapience Bioanalytical Research Lab Bhopal and the animals were acclimatized to the standard laboratory conditions in cross ventilated animal house at temperature 25±2 °C relative humidity 44–56% and light and dark cycles of 12:12 hours, fed with standard pellet diet and water *ad libitum* during experiment.

2.5 Micronucleus assay

Grouping: In the experiment, 24 mice were used. The mice were divided into 4 groups comprising of 6 animals in each group as follows:

Group I: Normal control, vehicle treated.

Group II: Negative control, cyclophosphamide (50 mg/kg i.p) treated.

Group III: *T.aestivum* extract (500mg/kg p.o.) for 7 days and cyclophosphamide.

Group IV: Only *T.aestivum* extract for 7 days.

2.6 Bone Marrow Samples

After completion of 7 days of treatment, the animals were sacrificed by cervical dislocation and bone marrow cells were harvested. Bone marrow cells were aspirated by flushing with Hank's balanced salt solution (HBSS) with the help of a syringe. The tubes were centrifuged at 1000 rpm for 5 min. The supernatant was removed. The cells in the sediment were carefully mixed by aspiration and a small drop of the viscous suspension was put on the end of a slide and spread by pulling the material behind a polished cover glass held at an angle of 45 degrees. The composition was then dried and fixed for 2-5 mins. Staining was carried out in ordinary vertical staining jars. The slides were stained for 10 mins in a may-Gruenwald giemsa solution. Then slides were rinsed in distilled water, blotted, cleaned and then dried on the slide warmer. Polychromatic erythrocytes (PCE) were scored for micronuclei under the microscope, at least 1000 PCE per animal were scored for the incidence of micronuclei. The ratio of PCE to non-chromatic erythrocytes (NCE) was determined for each animal by counting a total of 1000 erythrocytes [43–45].

2.7 Chromosomal Aberration Test

Grouping: In the experiment, a total of 24 mice were used. The mice were divided into 4 groups comprising of 6 animals in each group as follows:

Group I: Normal control, vehicle treated.

Group II: Negative control, cyclophosphamide (50 mg/kg i.p.) treated.

Group III: *T.aestivum* extract (500 mg/kg p.o.) for 7 days and cyclophosphamide (50 mg/kg p.o.).

Group IV: Only *T.aestivum* extract (500 mg/kg p.o.) for 7 days.

cyclophosphamide was injected 24 hrs before sacrificing in group II and III and colchicine (25 mg/kg i.p.) were injected to all groups before 1hr to sacrifice.

2.8 Bone Marrow Samples

After completion of 7 days of treatment, the animals were sacrificed by cervical dislocation and bone marrow cells were harvested. The suspension was flushed in the tube properly to get good cell suspension and centrifugation for 10 min at 1000 rpm. The supernatant was discarded. Pellet was treated with pre-warmed (37°C) KCl on cyclomixer. The suspension was left in a water bath (37°C) for 20 min. It was centrifuged and the supernatant was discarded. Pellet was treated with freshly prepared cornoy's fixative on cyclomixer, centrifuged and the supernatant was discarded. The above step of treatment with Cornoy's fixative was repeated 3 times to get debris free white pellet. To pellet Cornoy's fixative (quantity sufficient) was added to get a good cell suspension. Slides were made

with Air Drop Method. Stained (Giemsa-3 min, Methanol-3 min and DDW-1 Dip) and observed under the microscope in 40x10X and then in 100x10X magnifications. No. of cells having aberration and the particular aberrations were scored. A total of 1000 cells were counted [46].

3. RESULTS AND DISCUSSION

3.1 Effect of TA Extract on Micronucleus Formations in Mouse Bone Marrow Cells

PCE, NCE and micronucleus (MN) are the forms of micronucleus formation produced by administration of cyclophosphamide in the bone marrow cells of mice given in Table 1 and Figs. 1-2.

Table 1. Effect of TA extract on micronucleus formations in mouse bone marrow cells

Group	Treatment	Dose	MN/PCE ± S.E.M.	PCE/NCE± S.E.M. Ratio
I	Control	1 mg/kg p.o.	0.78±0.54	0.38±0.23
II	Cyclophosphamide	50 mg/kg i.p.	1.84±0.30a*	0.78±0.53
III	<i>T.aestivum</i> Extract + cyclophosphamide	500mg/kg p.o. + 50 mg/kg i.p.	0.97±0.26a*,b*	0.55±0.34
IV	<i>T.aestivum</i> Extract	500mg/kg p.o.	0.90±0.23	0.41±0.21

n= 6 in each group, **P*<0.05, compared with multiple groups using One-way ANOVA followed by Dunnett's multiple comparison test

a = significant difference when compared with vehicle treated group
b = significant inhibition, when compared with cyclophosphamide, treated group

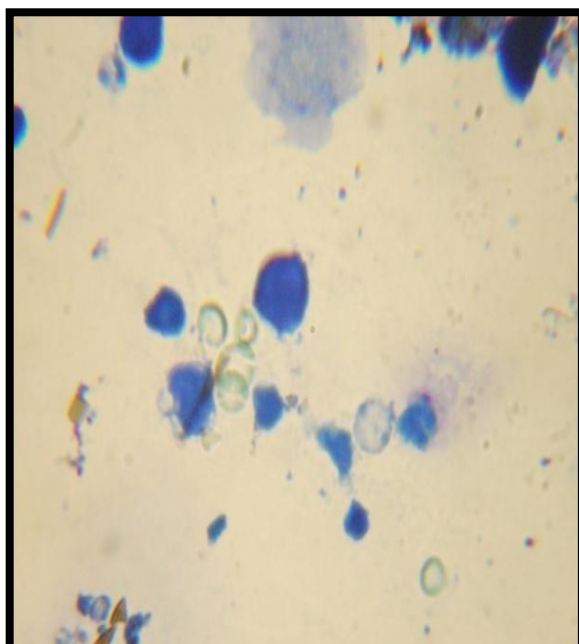


Fig. 1. Normal bone marrow cells

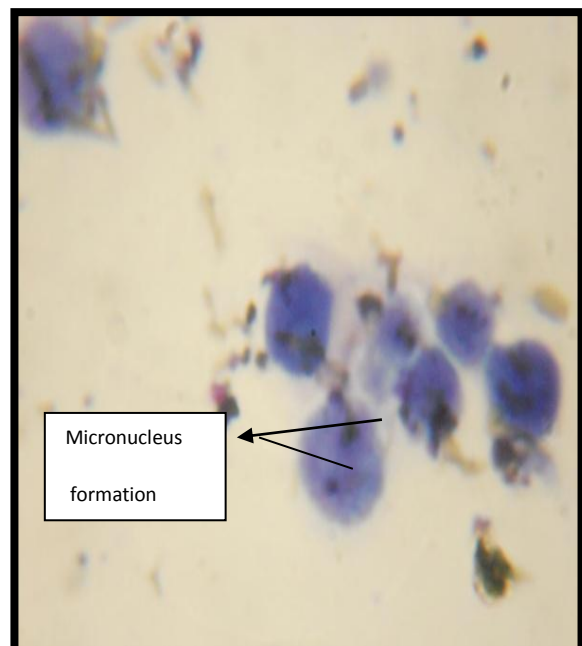


Fig. 2. Bone marrow cells with micronucleus

3.2 Effect of *T. aestivum* Extract on Chromosomal Aberration in Mouse Bone Marrow Cells

Chromosomal aberration (C.Ab.), chromatid break (C.B.), chromatid fragment (C.F.), chromatid gap (C.G.), ring formation (R.F.) and centromeric association (C.A.) are the different types of chromosomal aberrations found in the bone marrow cells shown in Fig. 4-6. They serve

as an important tool in assessing the genotoxicity produced by the drugs as their side effect. The administration of *T.aestivum* extract at the dose of 500 mg/kg body weight, 24 hours before i.p. administration of cyclophosphamide (50mg/kg) have significantly prevented the micronucleus formations (Fig. 1& 2) and chromosomal aberration in bone marrow cells of mice as compared to cyclophosphamide (Table 2).



Fig. 3. Normal

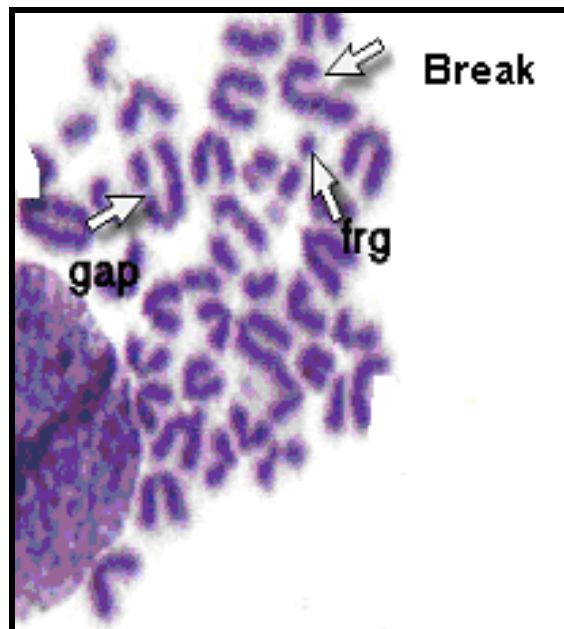


Fig. 4. Break, fragment, gap

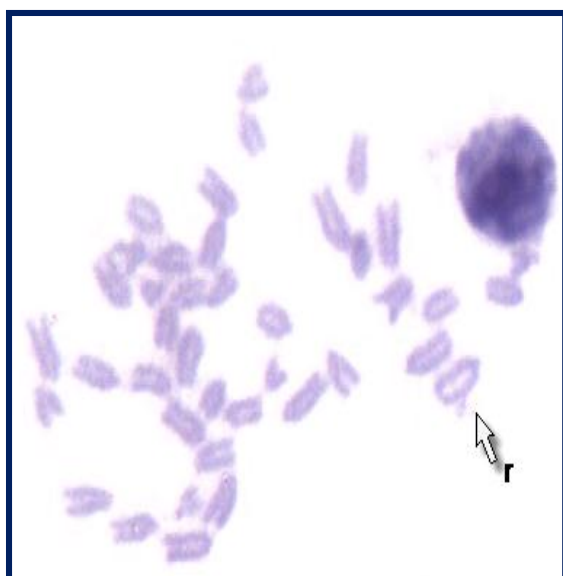


Fig. 5. Ring formation

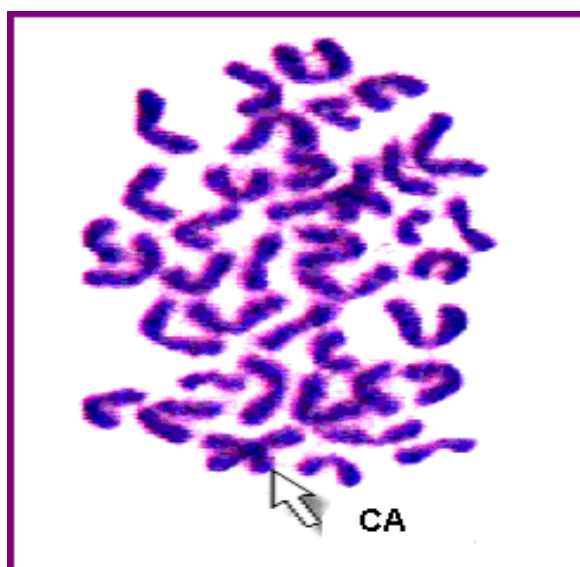


Fig. 6. Centromeric association

Fig. 3-6. Different types of chromosomal aberrations

Table 2. Effect of *T.aestivum* extract on chromosomal aberration in mouse bone marrow cells

Group	Treatment	Mean \pm S.E.M. (C. Ab.)	% C.B.	% C.F.	% C.G.	% R.F.	% C.A.
I.	Control 1 mg/kg p.o.	29.0 \pm 3.10	14	12	3	Nil	Nil
II.	Cyclophosphamide 50 mg/kg i.p.	51.3 \pm 4.48a*	24	20	7.3	4	2
III.	<i>T.aestivum</i> Extract + Cyclophosphamide 500mg/kg p.o. + 50 mg/kg i.p.	39.7 \pm 2.59a*,b**	17.7	16	4	2	Nil
IV.	<i>T.aestivum</i> Extract 500mg/kg p.o.	31.8 \pm 3.43b**	14.8	13	2	2	Nil

Data are expressed in mean \pm SEM, n= 6 (no. of six animals) in each group, *p<0.05, **p<0.01 compared with multiple groups using One-way ANOVA followed by Dunnett's multiple comparison test. a = significant difference in compared with vehicle treated group

b= significant protection in comparison with Cyclophosphamide treated group

4. CONCLUSION

T. aestivum extract has shown significant protection against cyclophosphamide induced micronucleus formation and chromosomal aberrations. It may be concluded that the antimutagenic effects of *T. aestivum* young leaves may be due to the presence of phenolic and flavonoids in the extract. Quercetin may be the key flavonoid of ethanolic extract of *T. aestivum* which may be engaged reduce the harmful effects of cyclophosphamide. These findings confirmed the health benefits of *T. aestivum* as a medicinal plant to reduce mutagenicity. Further studies are needed to check the role of phenolic and flavonoids in the antigenotoxic activity of *T. aestivum*.

CONSENT

It is not applicable.

ETHICAL APPROVAL

The experiment was approved by the institutional ethical committee and as per CPCSEA guidelines (approval no. 1413/PO/a/11/CPCSEA).

COMPETING INTERESTS

Authors have declared that no competing interests exist.

REFERENCES

1. Shahsavari G, N. Nouryazdan, G. Adibhesami, M. Birjandi, Genetic

associations and serum paraoxonase levels with atherosclerosis in western Iranian patients, Mol. Biol. Rep; 2020.

<https://doi.org/10.1007/s11033-020-05585-2>.

2. Singh S, D. Hassan, H.M. Aldawsari, N. Molugulu, R. Shukla, P. Kesharwani, Immune checkpoint inhibitors: a promising anticancer therapy, Drug Discov. Today; 2020.

<https://doi.org/10.1016/j.drudis.2019.11.003>.

3. Singh S, A.A.S. Gill, M. Nlooto, R. Karpoornath, Prostate cancer biomarkers detection using nanoparticles based electrochemical biosensors, Biosens. Bioelectron; 2019.

<https://doi.org/10.1016/j.bios.2019.03.065>.

4. Singh S, A. Numan, B. Maddiboyina, S. Arora, Y. Riadi, N.A. Alhakamy, P. Kesharwani, The emerging role of immune checkpoint inhibitors in the treatment of triple-negative breast cancer, Drug Discov. Today. 2021;1-7.

<https://doi.org/10.1016/j.drudis.2021.03.011>.

5. Singh S, A. Numan, N. Agrawal, M.M. Tambuwala, V. Singh, P. Kesharwani, Role of immune checkpoint inhibitors in the revolutionization of advanced melanoma care, Int. Immunopharmacol; 2020.

<https://doi.org/10.1016/j.intimp.2020.106417>.

6. Podstavková S, D. Vlcek, E. Miadoková, Bioactivation of promutagens by the unicellular green alga *Chlamydomonas reinhardtii*, J. Environ. Pathol. Toxicol. Oncol; 1997.

7. Higashimoto M, J. Purintrapiban, K. Kataoka, T. Kinouchi, U. Vinitketkumnuen, S. Akimoto, H. Matsumoto, Y. Ohnishi, Mutagenicity and antimutagenicity of extracts of three spices and a medicinal plant in Thailand, *Mutat. Res. Lett*; 1993. [https://doi.org/10.1016/0165-7992\(93\)90026-R](https://doi.org/10.1016/0165-7992(93)90026-R).
8. Çelik TA, Aslantürk ÖS. Cytotoxic and genotoxic effects of *Lavandula stoechas* aqueous extracts, *Biologia (Bratisl)*; 2007. <https://doi.org/10.2478/s11756-007-0051-2>.
9. Aşkin Çelik T, ÖS. ASLANTÜRK, Cytotoxic and Genotoxic Effects of Aqueous Extracts of *Rosmarinus officinalis* L., *Lavandula stoechas* L. and *Tilia cordata* Mill. on in vitro Human Peripheral Blood Lymphocytes, *Cumhur. Sci. J*; 2018. <https://doi.org/10.17776/cs.405629>.
10. Qiu D, Kurosawa M, Lin Y, Inaba YT, Matsuba S, Kikuchi K, Yagyu Y, Motohashi A, Tamakoshi, M. Mori I, Tsuji, Y, Nakamura H, Iso H, Mikami Y, Hoshiyama H, Suzuki H, Shimizu H, Toyoshima S, Tokudome Y, Ito S, Hashimoto A, Koizumi T, Kawamura Y, Watanabe T, Miki C, Date K, Sakata T, Nose N, Hayakawa T, Yoshimura A, Shibata N, Okamoto H, Shio Y, Ohno T, Kitagawa T, Kuroki K, Tajima, Overview of the epidemiology of pancreatic cancer focusing on the JACC Study, *J. Epidemiol*; 2005. <https://doi.org/10.2188/jea.15.S157>.
11. Corrigendum: BTS working party report on in vitro toxicology (Human and Experimental Toxicology (1997) 1 (15)), *Hum. Exp. Toxicol*; 1998. <https://doi.org/10.1191/096032798678909025>.
12. Danford N. The interpretation and analysis of cytogenetic data, *Methods Mol. Biol*; 2012. https://doi.org/10.1007/978-1-61779-421-6_6.
13. Guidelines for the testing of chemicals for mutagenicity. Committee on Mutagenicity of Chemicals in Food, Consumer Products and the Environment., *Rep. Health Soc. Subj. (Lond)*; 1989.
14. Zeller A, S. Pfuhler, S. Albertini, F. Bringezu, A. Czich, Y. Dietz, R. Fautz, N.J. Hewitt, A. Kirst, P. Kasper, A critical appraisal of the sensitivity of in vivo genotoxicity assays in detecting human carcinogens, *Mutagenesis*; 2018. <https://doi.org/10.1093/mutage/gey005>.
15. Koul AS, Gangar V. Sandhir Pitfalls in Journey from Traditional to Modern medicine, *Indian J. Nat. Prod. Resour*; 2005.
16. Aydos OS, A. Avci, T. Özkan, A. Karadağ, E. Gürleyik, B. Altinok, A. Sunguroğlu, Antiproliferative, apoptotic and antioxidant activities of wheatgrass (*Triticum aestivum* L.) extract on CML (K562) cell line, *Turkish J. Med. Sci*; 2011. <https://doi.org/10.3906/sag-0912-425>.
17. Tandon S. a Arora, Antioxidant Profiling of *Triticum aestivum* (wheatgrass) and its Antiproliferative Activity In MCF-7 Breast Cancer Cell Line., *J. Pharm*; 2011.
18. Arya P, M. Kumar, Chemoprevention by *Triticum aestivum* of mouse skin carcinogenesis induced by DMBA and croton oil - Association with oxidative status, *Asian Pacific J. Cancer Prev*; 2011.
19. Peryt B, J. Miłoszewska, B. Tudek, M. Zielińska, T. Szymczyk, Antimutagenic effects of several subfractions of extract from wheat sprout toward benzo[a]pyrene-induced mutagenicity in strain TA98 of *Salmonella typhimurium*, *Mutat. Res. Toxicol*; 1988. [https://doi.org/10.1016/0165-1218\(88\)90164-4](https://doi.org/10.1016/0165-1218(88)90164-4).
20. Peryt B, Szymczyk T, Lesca P. Mechanism of antimutagenicity of wheat sprout extracts, *Mutat. Res. - Fundam. Mol. Mech. Mutagen*; 1992. [https://doi.org/10.1016/0027-5107\(92\)90201-C](https://doi.org/10.1016/0027-5107(92)90201-C).
21. Tachino N, D. Guo, W.M. Dashwood, S. Yamane, R. Larsen, R. Dashwood, Mechanisms of the in vitro antimutagenic action of chlorophyllin against benzo[a]pyrene: Studies of enzyme inhibition, molecular complex formation and degradation of the ultimate carcinogen, *Mutat. Res. Regul. Pap*; 1994. [https://doi.org/10.1016/0027-5107\(94\)90154-6](https://doi.org/10.1016/0027-5107(94)90154-6).
22. Bonfili L, M. Amici, V. Cecarini, M. Cuccioloni, R. Tacconi, M. Angeletti, E. Fioretti, J.N. Keller, A.M. Eleuteri, Wheat sprout extract-induced apoptosis in human cancer cells by proteasomes modulation, *Biochimie*; 2009. <https://doi.org/10.1016/j.biochi.2009.06.001>.
23. Guo D, Horio DT, Grove JS, Dashwood RH. Inhibition by chlorophyllin of 2-amino-3-methylimidazo-[4,5-f] quinoline-induced

- tumorigenesis in the male F344 rat, *Cancer Lett*; 1995.
[https://doi.org/10.1016/0304-3835\(95\)03882-W](https://doi.org/10.1016/0304-3835(95)03882-W).
24. Wang F, Ckurshumova W, Liu J, M. Fefer, RH. Pelton, Preventing the release of copper chlorophyllin from crop spray deposits on hydrophobic surfaces, *J. Colloid Interface Sci*; 2021.
<https://doi.org/10.1016/j.jcis.2020.09.014>.
 25. Richter P, M. Krüger, B. Prasad, S. Gastiger, M. Bodenschatz, F. Wieder, A. Burkovski, W. Geißdörfer, M. Lebert, S.M. Strauch, Using colistin as a trojan horse: Inactivation of gram-negative bacteria with chlorophyllin, *Antibiotics*. (2019).
<https://doi.org/10.3390/antibiotics8040158>.
 26. Chong HS, S. Sim, T. Yamaguchi, J. Park, C. Lee, M.K. Kim, G. Lee, S.S. Yun, H.S. Lim, H.J. Suh, Simultaneous determination of sodium iron chlorophyllin and sodium copper chlorophyllin in food using high-performance liquid chromatography and ultra-performance liquid chromatography–mass spectrometry, *Food Chem*; 2019.
<https://doi.org/10.1016/j.foodchem.2018.10.015>.
 27. Li B, Z. Wu, W. Li, G. Jia, J. Lu, J. Fang, G. Chen, Chlorophyllin e4 is a novel photosensitizer against human bladder cancer cells, *Oncol. Rep.* (2012).
<https://doi.org/10.3892/or.2012.1656>.
 28. Zheng H, Y. You, M. Hua, P. Wu, Y. Liu, Z. Chen, L. Zhang, H. Wei, Y. Li, M. Luo, Y. Zeng, Y. Liu, D.X. Luo, J. Zhang, M. Feng, R. Hu, S.J. Pandol, Y.P. Han, Chlorophyllin Modulates Gut Microbiota and Inhibits Intestinal Inflammation to Ameliorate Hepatic Fibrosis in Mice, *Front. Physiol*; 2018.
<https://doi.org/10.3389/fphys.2018.01671>.
 29. Krüger M, P. Richter, S.M. Strauch, A. Nasir, A. Burkovski, C.A. Antunes, T. Meißgeier, E. Schlücker, S. Schwab, M. Lebert, What an escherichia coli mutant can teach us about the antibacterial effect of chlorophyllin, *Microorganisms*; 2019.
<https://doi.org/10.3390/microorganisms7020059>.
 30. Siwińska-Ciesielczyk K, O. Bartlewicz, P. Bartczak, A. Piasecki, T. Jesionowski, Functional titania–silica/chlorophyllin hybrids: design, fabrication, comprehensive physicochemical characteristic and photocatalytic test, *Adsorption*; 2019.
<https://doi.org/10.1007/s10450-019-00035-3>.
 31. Singh DJ, D.K. Singh, Anthelmintic activity of chlorophyllin against different larval stages of fasciola gigantica, *Rev. Inst. Med. Trop. Sao Paulo*; 2016.
<https://doi.org/10.1590/S1678-9946201658039>.
 32. Rodríguez-López MI, V.M. Gómez-López, V. Lukseviciute, Z. Luksiene, Modelling the inactivation and possible regrowth of *Salmonella enterica* treated with chlorophyllin-chitosan complex and visible light, *Food Technol. Biotechnol*; 2020.
<https://doi.org/10.17113/ftb.58.01.20.6374>.
 33. Chiniforush N, M. Pourhajibagher, S. Parker, S. Benedicenti, A. Bahador, T. Salagean, I.R. Bordea, The effect of antimicrobial photodynamic therapy using chlorophyllin-phycoyanin mixture on enterococcus faecalis: The influence of different light sources, *Appl. Sci*; 2020.
<https://doi.org/10.3390/app10124290>.
 34. Putra BTW, RS. Purwoko I, Indarto Soni. An investigation of copper chlorophyllin solution for low-cost optical devices calibration in chlorophyll measurement, *Int. J. Metrol. Qual. Eng*; 2019.
<https://doi.org/10.1051/ijmqe/2019009>.
 35. Lihuan DZ, Jingcun J. Ning W. Guozeng, C. Yiwei L, Wei Q, Jing Z, Yuanfang C. Gang, Photodynamic therapy with the novel photosensitizer chlorophyllin f induces apoptosis and autophagy in human bladder cancer cells, *Lasers Surg. Med*; 2014.
<https://doi.org/10.1002/lsm.22225>.
 36. Bloor KK, JP Kamat TPA. Devasagayam, Chlorophyllin as a protector of mitochondrial membranes against γ -radiation and photosensitization, *Toxicology*; 2000.
[https://doi.org/10.1016/S0300-483X\(00\)00278-X](https://doi.org/10.1016/S0300-483X(00)00278-X).
 37. Amici M, Bonfili L, Spina M, Cekarini V, Calzuola I, Marsili V, M. Angeletti, E. Fioretti, R. Tacconi, G.L. Gianfranceschi, A.M. Eleuteri, Wheat sprout extract induces changes on 20S proteasomes functionality, *Biochimie*; 2008.
<https://doi.org/10.1016/j.biochi.2007.12.001>.
 38. Falcioni G, Fedeli D, L. Tiano, I. Calzuola, L. Mancinelli, V. Marsili, G. Gianfranceschi, Antioxidant activity of wheat sprouts extract in vitro: Inhibition of DNA oxidative damage, *J. Food Sci*; 2002.
<https://doi.org/10.1111/j.1365-2621.2002.tb08838.x>.

39. Marsili V, Calzuola I, Gianfranceschi GL. Nutritional relevance of wheat sprouts containing high levels of organic phosphates and antioxidant compounds., *J. Clin. Gastroenterol*; 2004.
<https://doi.org/10.1097/01.mcg.0000128933.46296.0a>.
40. Alitheen NB, Oon CL, Keong YS, Chuan TK, Li HK, Yong HW Cytotoxic effects of commercial wheatgrass and fiber towards human acute promyelocytic leukemia cells (HL60), *Pak. J. Pharm. Sci*; 2011.
41. Countryman PI, Heddle JA. The production of micronuclei from chromosome aberrations in irradiated cultures of human lymphocytes, *Mutat. Res. - Fundam. Mol. Mech. Mutagen*; 1976.
[https://doi.org/10.1016/0027-5107\(76\)90105-6](https://doi.org/10.1016/0027-5107(76)90105-6).
42. Phillipson JD. Phytochemistry and pharmacognosy, *Phytochemistry*; 2007.
<https://doi.org/10.1016/j.phytochem.2007.06.028>.
43. Udrouiu I. The micronucleus test in piscine erythrocytes, *Aquat. Toxicol*; 2006.
<https://doi.org/10.1016/j.aquatox.2006.06.013>.
44. Leonardi S, Poma AM, Colafarina S, F. D'Aloisio, M. Scatigna, O, Zarivi R, Mastrantonio, L. Tobia, L. Fabiani, Early genotoxic damage through micronucleus test in exfoliated buccal cells and occupational dust exposure in construction workers: a cross-sectional study in L'Aquila, Italy, *Ecotoxicol. Environ. Saf*; 2020.
<https://doi.org/10.1016/j.ecoenv.2020.110989>.
45. Hayashi M. The micronucleus test-most widely used in vivo genotoxicity test, *Genes Environ*; 2016.
<https://doi.org/10.1186/s41021-016-0044-x>.
46. Protective Role of Diallyl Disulphide Compound (From Garlic Extract) Against Mercuric Chloride - Induced Genotoxicity and Cytotoxicity in Albino Rats, *Iran. J. Cancer Prev*; 2012.

© 2021 Jain et al.; This is an Open Access article distributed under the terms of the Creative Commons Attribution License (<http://creativecommons.org/licenses/by/4.0>), which permits unrestricted use, distribution, and reproduction in any medium, provided the original work is properly cited.

Peer-review history:

The peer review history for this paper can be accessed here:
<https://www.sdiarticle4.com/review-history/75916>



Received on 26 May 2020; received in revised form, 05 October 2020; accepted, 15 October 2020; published 01 June 2021

IN-VITRO ANTIOXIDANT AND ANTI-INFLAMMATORY ACTIVITY OF *SALIX ALBA* L. ALONG WITH SIMULTANEOUS HPTLC ANALYSIS OF SALICIN AND FERULIC ACID

R. S. Shivtare ^{*1}, S. M. Kewatkar ², R. Musale ¹, P. Lohakare ¹, D. Patil ¹, D. Choudhary ³, G. Ganu ³, D. H. Nagore ^{1,3} and S. Chitlange ⁴

Department of Pharmaceuticals ¹, JJT University, Jhunjhunu - 333001, Rajasthan, India.

Rajarshi Shahu College of Pharmacy ², Buldana - 443001, Maharashtra, India.

Mprex Healthcare ³, Pune - 411057, Maharashtra, India.

Dr. D.Y. Patil institute of Pharmaceutical Research and Sciences ⁴, Pune - 411018, Maharashtra, India.

Keywords:

Salix alba L, Salicin, Ferulic acid, High performance thin layer chromatography, Antioxidant and anti-inflammatory

Correspondence to Author:

Mr. Rakesh S. Shivtare

Research Scholar,
PhD Research Scholar,
Department of Pharmaceuticals,
JJT University, Jhunjhunu - 333001,
Rajasthan, India.

E-mail: rakeshshivtare@rerp@gmail.com

ABSTRACT: Now a day's interest towards natural and has been growing due to the unhealthy consequences of chemicals in the health industry; though, herbal substances possess several quality control and confirm pharmacological action issues. This present study was designed to determine the effects of *Salix alba* L. methanolic extract (MESAL) for its antioxidant and anti-inflammatory activity in rat models. Further to establish and validate a sensitive, fast and reproducible high performance thin layer chromatographic (HPTLC) method of two biomarker compounds Salicin and Ferulic acid from MESAL. The anti-inflammatory activity was studied by the carrageenan-induced rat paw oedema method while DPPH free radical scavenging ability was utilized to determine the antioxidant activity. Additionally, the separation was performed by HPTLC with quantification of markers (Salicin and Ferulic acid). Among the different combinations of mobile phases used, the best separation was achieved in Toluene: Ethyl acetate: Methanol: Formic Acid (5:3:1:1v/v/v/v). The MESAL exhibited antioxidant activity with a maximal inhibitory concentration (IC₅₀) value of 400 µg/ml, and exerted anti-inflammatory activity, wherein 70 % protection was shown at 400 mg/ml. In contrast, HPTLC method gave compact spots of Salicin and Ferulic acid at R_f 0.22 ± 0.02 and 0.68 ± 0.02, respectively. The MESAL displayed potent antioxidant and anti-inflammatory properties. Statistical analysis proves that the HPTLC method is repeatable and selective for the estimation of the said drugs, thus can be used for routine analysis and quality control of raw material of *Salix alba* L.

INTRODUCTION: Noteworthy work is essential to evaluate herbal drugs for their quality, safety, and efficacy; there is required for a well-defined particular strategy for routine analysis of herbal raw materials and formulations with regard to constituents responsible for their efficacy ^{1,2}.

S. alba L., universally recognized as White Willow (particularly, the bark) is the original source of salicin, a weaker precursor of aspirin ³.

The chemical component like glycosides (1.5-11%) predominantly salicylates (salicin, salicortin, populin, fragilin, tremulacin); tannins (8-20%); aromatic aldehydes and acids distinctively salidroside, vanillin, syringin, salicylic acid, caffeic and ferulic acids; Salicyl alcohol (saligenin); Flavonoids have been isolated and identified from the plant ⁴⁻⁶. *Salix alba* L. has been used as antioxidant, antiacetyl cholinesterase, anti-

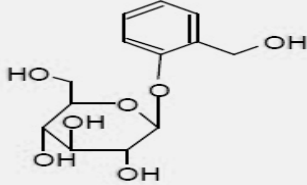
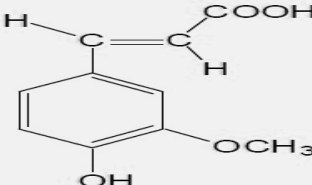
<p>QUICK RESPONSE CODE</p> 	<p>DOI: 10.13040/IJPSR.0975-8232.12(6).3176-84</p> <p>This article can be accessed online on www.ijpsr.com</p>
<p>DOI link: http://dx.doi.org/10.13040/IJPSR.0975-8232.12(6).3176-84</p>	

migraine, mouth wash agent, antiestrogenic and antigenotoxic activity⁷⁻⁸. Ferulic acid, a phenolic acid, has vast conveyance plant kingdom and is more bioavailable than other dietary flavonoids and monophenolics studied in **Table 1**. It has been detailed to be a powerful antioxidant, anti-inflammatory, and is accounted to terminate free radical chain reaction and decrease the chance for coronary heart diseases^{3, 9-14}. Salicin is the metabolic antecedent of salicylic acid; a ponder compound. Chemically talking is closely related to aspirin and includes an exceptionally comparative activity within the human body. Salicin is an alcoholic beta-glycoside that contains D-glucose **Table 1**. Having antipyretic and analgesic effects, salicin can be utilized for the treatment of fever and diseases, like arthritis¹⁵.

Tragically, deficient data is accessible concerning the dispersion of Salicin and Ferulic acid in the *S. alba* L. There is no synchronous strategy that has been detailed for quantitation of Salicin and Ferulic acid from the *S. alba* L. as well as a pharmacological activity like antioxidant and anti-inflammatory of methanolic extract of *S. alba* L.

In the present study, an endeavor has been made to create a simple, rapid, and accurate HPTLC method for estimation of the two biomarker compounds Salicin and Ferulic acid from methanolic extract of *S. alba* L. and the extracts were further evaluated to investigate *in-vitro* antioxidant and anti-inflammatory activity of methanolic extract of *S. alba* L.

TABLE 1: CHEMICAL PROPERTIES OF SALICIN AND FERULIC ACID

Particular	Details	
	Salicin	Ferulic acid
CAS number	138-52-3	1135-24-6
Chemical Formula	C ₁₃ H ₁₈ O ₇	C ₁₀ H ₁₀ O ₄
Chemical Name	2-(Hydroxymethyl)phenyl-β-D-glucopyranoside	(E)-3-(4-Hydroxy-3-methoxyphenyl)prop-2-enoic acid
Representation		
Molecular Weight	286.27	194.18
Description	NSAID. Salicylic acid prodrug	Hydroxycinnamic acid; antioxidant properties

MATERIALS AND METHODS:

Chemicals and Reagents: Standard Salicin and Ferulic acid were purchased from Natural Remedies India and used without further purification, owing to its high purity, at least 99% w/w. 2,2-Diphenyl-1-picrylhydrazyl hydrate (DPPH) was purchased from Hi-Media Lab. Pvt. Ltd., Mumbai, India. HPLC water (Millipore equipment, France) was used to prepare the stock solution. Analytical-reagent grade solvents like tween 80, ascorbic acid, Diclophenac Na, carrageenan, toluene, ethyl acetate, formic acid, and methanol were obtained from Merck Ltd (India). HPTLC aluminium plates precoated with silica gel 60F254 (20 × 20 cm, 0.2 mm thickness) were obtained from Merck, India.

Plant Material: The dried methanolic extract of *S. alba* L. was purchased from Phyto concentrate,

India. Their identity and Authentication were confirmed by the Department of Pharmacognosy Dr. D. Y. Patil institute of Pharmaceutical research and sciences, Pimpri, India, by correlating their morphological and microscopical characters with those given in the literature.

Experimental Animals: Male Wister rats weighing 150–180 g were obtained from the National Institute of Biosciences, Pune, and utilized for this examination. The animals were separated into bunches and kept in plastic cages (47 × 34 × 18 cm) beneath 12 h light/12 h dark cycle at room temperature (22 °C) with standard diet and water were given *ad libitum*. The animals were allowed to acclimatize to laboratory conditions earlier to experimentation. All experiments were conducted during the light period of 12 h of the day/night cycle. All the experiments were allowed and

conducted as per the rules of the Institutional Animal Ethical Committee.

Acute Toxicity Study: Acute oral toxicity study was carried out in accordance with the guidelines of the OECD-423 (acute toxic class method). Eighteen rats (six for each group) were used for the research of acute toxicity. Overnight the animals were kept fasting, offering only water. Different extract doses (0.5, 1, and 2 g / kg) were suspended and administered orally in 0.5 percent aqueous Tween 80. For indications of toxicity, e.g., autonomy, central nervous system, and behavioral modifications, the animals were continually noted for 12 h, and death was observed for 24 h¹⁶⁻¹⁷.

DPPH Radical Scavenging: MESAL's antioxidant activity was assessed using a photometric assay of DPPH. The test extract (2 ml) at different concentrations (100, 200, and 400 µg/ml) was mixed with 0.5 mM DPPH (in 1 ml of methanol) in a cuvette. The absorbance at 517 nm was taken after 30 min of incubation in the dark at room temperature. Ascorbic acid was utilized as a positive control. The radical scavenging activity (RSA) was calculated as a percentage of DPPH discoloration using Equation¹⁸⁻¹⁹.

$$\% \text{RSA} = [(A_0 - A_s) / A_0] \times 100$$

Where A_0 and A_s are the absorbance of the control (containing all reagents, except the test compound) and test compound respectively.

Anti-inflammatory Activity: Acute inflammation was induced by carrageenan injection into the hind paws of rats. Rats were divided into five groups (6 rats/group). The control group received 0.5% Tween 80 (1 ml/kg, p.o.) served as the vehicle only, while other groups received (100, 200 & 400 mg/kg, p.o.) and standard drug diclophenac Na (75 mg/ kg, p.o.) respectively. To develop the paw edema, 0.1 ml of 1% carrageenan was injected into the subplantar surface of the right hind paw of each rat 1 h after the administration of MESAL. The paw volume was measured initially at 1, 2, 3, 4, and 24 h after carrageenan injection using a plethys-mometer²⁰⁻²¹. The percent inhibition of edema volume was calculated using the formula as follows: %

$$\text{Inhibition} = \frac{(\text{Predrug reading} - \text{Postdrug reading}) \times 100}{\text{Predrug reading}}$$

Statistical Analysis: Data is expressed as Mean \pm SEM and was analyzed for the significance of variance by one-way ANOVA followed by Tukey multiple comparison tests using PRISM software.

Quantification of Salicin and Ferulic acid using HPTLC

Preparation of Standard Solution of Salicin and Ferulic Acid: Standard solution was prepared by dissolving Salicin and Ferulic acid in 50 mL methanol (stock solution). 1ml of stock solution was diluted to 10 mL and was used as a working standard for the analysis.

Preparation of Test Solution for Analysis: Methanolic extract of *S. alba* L. was accurately weighed in a 50 mL volumetric flask and added to 25 mL Methanol. It was allowed to sonicate for 15 min. Then make up the volume with methanol.

HPTLC-Photodensitometry: The samples were applied in the form of a band of width 6 mm with CAMAG 100 µL syringe on precoated silica gel 60F₂₅₄ aluminium plate (20cm \times 10cm with 0.2mm thickness) using Linomat 5 applicator CAMAG (Switzerland) fitted with a CAMAG 100 µL syringe. The ascending development was carried out in the mobile phase Toluene: Ethyl acetate: Methanol: Formic Acid (5:3:1:1 v/v/v/v) in a CAMAG twin trough chamber (20 \times 10 cm) previously saturated with mobile phase for 15 minutes. The volume applied on each track was 10 µL. The plate was allowed to run approximately 80 mm from the point of application. After development, plates were dried by dryer. The densitometric scanning was performed using CAMAG TLC scanner-3 operated by win CATS software V at 254 nm for Salicin and Ferulic acid. The slit dimension was 5 \times 0.45 mm with a scanning speed of 20 mm s⁻¹. An evaluation was done via peak area with linear regression.

Calibration Graph of Standard Salicin and Ferulic Acid: The stock solution of Salicin and Ferulic acid was diluted to different concentrations between of working concentration. These were applied in duplicate on the HPTLC plate for the preparation of the calibration graph. The calibration graph was plotted by using the concentrations versus the average peak area at 254 nm. The linearity of the detector response for the standards was determined by means of linear regression.

Method Validation: Validation of the analytical method was done according to the International Conference on Harmonization guideline. The method was validated for specificity, linearity, recovery, robustness, and precision²²⁻²⁷.

Specificity: Specificity was ascertained by analyzing blank, standard, and samples. The bands for Salicin and Ferulic acid from sample solutions were established by comparing the R_f and spectra of the bands to those of the standards. The peak purity of all the compounds was analyzed by comparing the spectra at three different levels, *i.e.*, start, middle, and end positions of the peak.

Precision: Precision of the method was studied by performing System, Method, and intermediate precision studies. The sample application and measurement of peak area were determined by performing seven replicate measurements of the same band using a sample solution containing Salicin and Ferulic acid.

Solution Stability: The sample solution and standard solution were prepared as per the proposed method and subjected to stability study at room temperature for 24 h. The sample solution was analyzed at initial and at 6 different time intervals up to 24 h. The change in response of Salicin and Ferulic acid in sample solution with respect to time is calculated as absolute percent difference against initial response.

Robustness: Composition of the mobile phase, the volume of the mobile phase, time from spotting to development, and time from development to scanning was involved in this study. The composition and volume of the mobile phase were varied in the range of $\pm 10\%$ of the used optimized conditions. Time variations were varied from the optimized times in the range of $\pm 20\%$.

The effect of these changes on the R_f value evaluated by calculating the relative standard deviations (RSD) for each parameter.

Accuracy (Recovery): The accuracy of the method was ascertained by spiking the preanalysed samples with known amount of Salicin and Ferulic acid (80, 100 and 120%). The average percentage recovery was estimated by applying values of peak area to the regression equations of the calibration graph.

RESULTS AND DISCUSSION:

DPPH Radical Scavenging Assay: DPPH is a stable free radical in aqueous or methanol and ethanol solution and accepts an electron or hydrogen radical to become a stable diamagnetic molecule. It is used as a substrate to evaluate the antioxidative activity of antioxidants. The reduction capability of DPPH radicals was determined by a decrease in its absorbance at 517 nm. The decrease in absorbance of DPPH radical was caused by antioxidant, and was due to the scavenging of hydrogen donation. In another study, the antioxidant properties of hot ethanolic extract of *S. alba* L. bark which was assessed by 1, 1-Diphenyl-2-Picrylhydrazyl (DPPH) free radical scavenging. The extract showed significant antioxidant activity.

Table 2 shows the dose-response of DPPH radical scavenging activity of the MESAL of 100, 200, and 400 $\mu\text{g/ml}$, compared with Ascorbic acid. It was observed that the MESAL of 400 $\mu\text{g/ml}$ had higher activity than that of the other extractives. At a concentration of 100 and 200 $\mu\text{g/ml}$ of MESAL, the scavenging activity reached 239.56 and 170.96, respectively. While at 400 $\mu\text{g/ml}$ of MESAL, the scavenging activity reached 120.47, that of the ascorbic acid was 80.92 %. From the above scavenging activity, it was found that 400 $\mu\text{g/ml}$ of MESAL having higher antioxidant activity as compared to ascorbic acid. The antioxidant activity of 400 $\mu\text{g/ml}$ of MESAL may be due to the presence of ferulic acid in their extract¹⁶⁻¹⁸.

TABLE 2: IC₅₀ FOR DPPH SCAVENGING OF MESAL

Sample name	Concentration ($\mu\text{g/ml}$)	DPPH scavenging activity
MESAL	100	239.56 \pm 5.1
	200	170.96 \pm 4.5
	400	120.47 \pm 2.5
Ascorbic acid	100	80.92 \pm 3.1

Acute Toxicity Studies of MESAL: The acute toxicity results showed that MESAL was safe up to a dose of 2000 mg/kg body weight. Based on acute toxicity data, two different dosages 100, 200 and 400 mg/kg (p.o.) were selected for *in-vivo* anti-inflammatory study¹⁶⁻¹⁷.

Anti-inflammatory Activity: carrageenan-induced inflammation is useful in detecting orally active anti-inflammatory agents; therefore, it has significant predictive value for anti-inflammatory

agents acting through mediators of acute inflammation. The development of edema induced by carrageenan injection causes an acute and local inflammatory response. In past studies, anti-inflammatory effects by plethysmometric measurement of formalin-induced paw edema on methanolic extracts of *S. alba* L. The result indicates that the extracts inhibited the paw edema size and shows inhibition of the inflammation.

As seen in **Table 2**, MESAL at 100, 200, and 400 µg/ml significantly decreased carrageenan-induced rat paw edema. The anti-inflammatory effects of 100 and 200 µg/ml dose of MESAL determined

inflammation as 0.923 and 0.817 respectively at 24 h. For the same hour, a 400 µg/ml dose of MESAL produced inflammation of 0.783. In comparison, the anti-inflammatory effect of Diclofenac at 75 mg/kg was 0.767 at the same time. These results suggest that the MESAL at 100, 200, and 400 µg/ml exhibits the anti-inflammatory property in the acute phase of inflammation, but the anti-inflammatory activity is more significant in dose 400 µg/ml, and mechanism of action may be associated with inhibition of the some of the inflammatory mediators like histamine, serotonin, bradykinins, and prostaglandins¹⁷⁻²¹.

TABLE 3: EFFECT OF MESAL ON CARRAGEENAN INDUCED RAT PAW EDEMA

Group	Average inflammation (mm) ± SEM					
	0 hour	1 hour	2 hour	3 hour	4 hour	24 hour
Control	0.760±0.029	0.913±0.046	0.920±0.017	0.928±0.024	0.913± 0.007	0.908± 0.044
MESAL 100 mg/kg	0.761±0.049	0.943±0.043	0.967±0.021	0.981±0.013	0.951±0.015	0.923±0.027
MESAL 200 mg/kg	0.756±0.010	0.872±0.030	0.890±0.019	0.871±0.008	0.849±0.023	0.817±0.036
MESAL 400 mg/kg	0.751±0.033	0.863±0.045	0.870±0.012	0.852±0.031	0.815±0.019	0.783±0.023
Diclophenac 75 mg/kg	0.752±0.019	0.871±0.038	0.804±0.041	0.792±0.037	0.785±0.031	0.767±0.026

The values are presented in the form of means ± standard error. One-way ANOVA followed by Tukey multiple comparison tests using PRISM software.

Method Optimization for the HPTLC-Densitometric Measurements: The reported methods of Salicin and Ferulic acid estimation like HPLC requires derivatization or working at a lower wavelength for sample detection due to lack of UV absorbing chromophore. HPTLC offers several advantages over reported methods²⁷. It facilitates automatic application and scanning *in-situ*. The composition of the mobile phase for the development of the chromatographic method was optimized by testing different solvent mixtures of varying polarity²⁶⁻²⁷. The solvent system consisting of Toluene: Ethyl acetate: Methanol: Formic Acid (5:3:1:1v/v/v/v) given dense, compact and well

separated bands of the drug. This mobile phase showed good resolution of Salicin and Ferulic acid peak from the different extract of *Salix alba*. Densitometric scanning of all the extracts showed compounds with *R_f* value 0.22 ± 0.02 and 0.68 ± 0.02, identified as Salicin and Ferulic acid. The present method is quicker as the time needed for plate development is reduced considerably to less than half an hour for chamber saturation and development of plate compared to the previously reported method. The scanning wavelength selected was 254 nm for Salicin and Ferulic acid. At this wavelength, the Salicin and Ferulic acid showed optimum response **Fig. 1-2**.

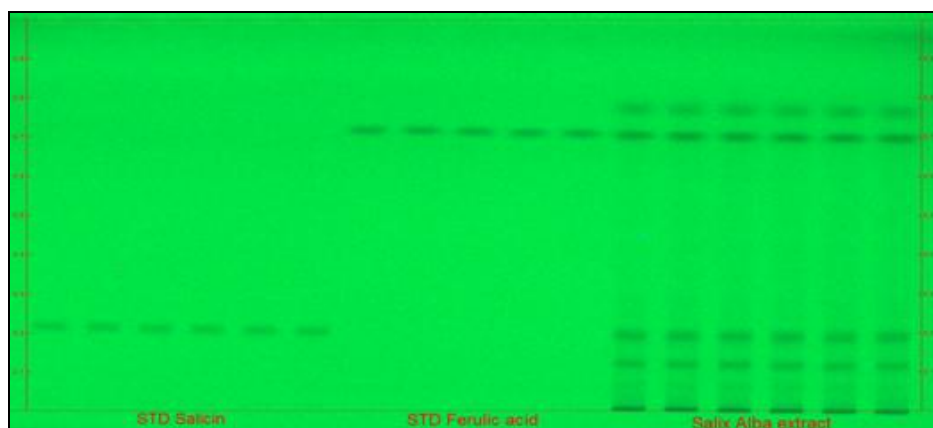


FIG. 1: HPTLC PROFILE OF SALIX ALBA L. BEFORE DERIVATIZATION UNDER UV 254 nm

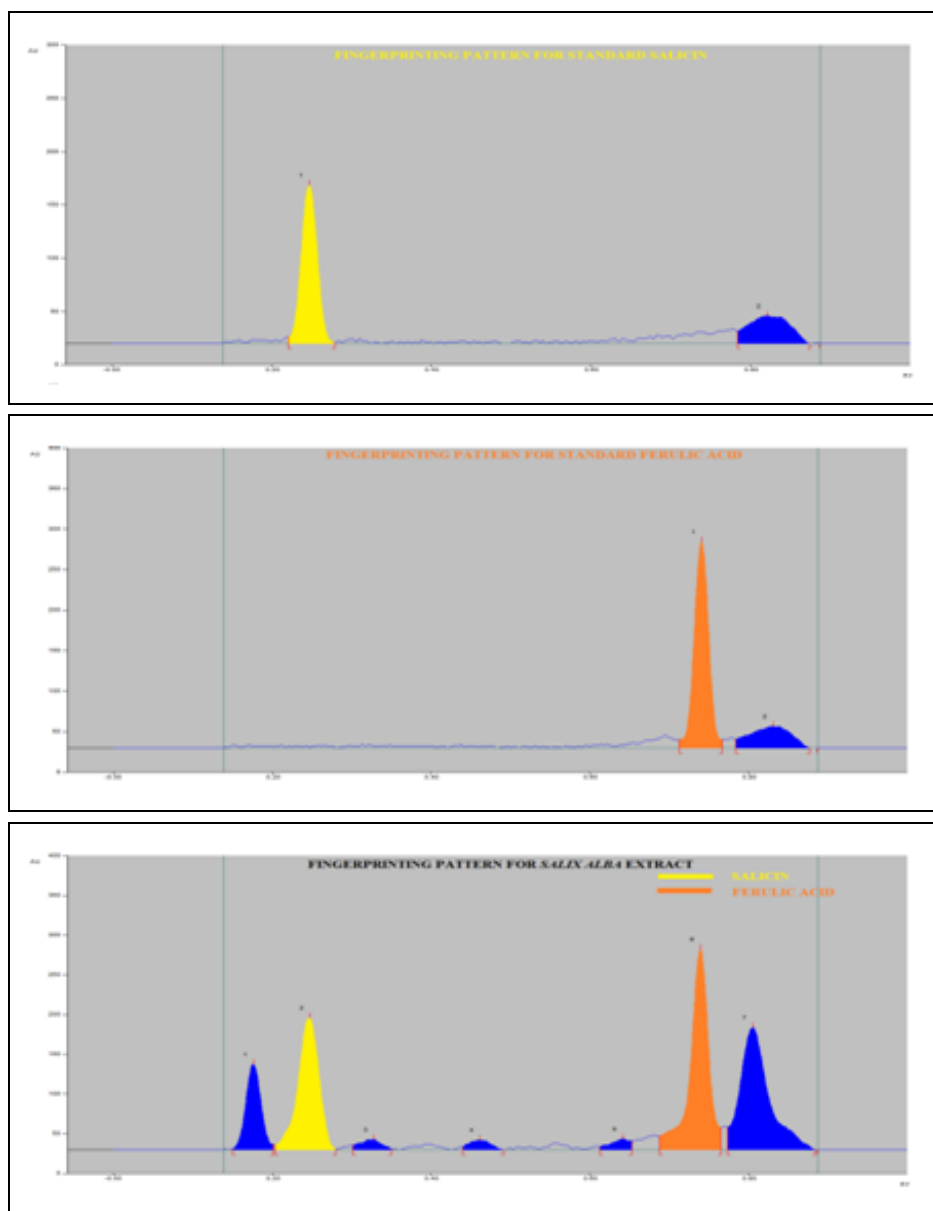


FIG. 2: COMPARATIVE CHROMATOGRAM OF STANDARD SALICIN AND FERULIC ACID WITH SALIX ALBA EXTRACT

Method Validation:

Linearity: Peak areas were found to have a good linear relationship with the concentration than the peak heights **Fig. 3**. For Salicin and Ferulic acid,

the r^2 was found 0.9984 and 0.9991. The correlation coefficients, y-intercepts, and slopes of the regression lines of the compound were calculated and presented in **Table 4**.

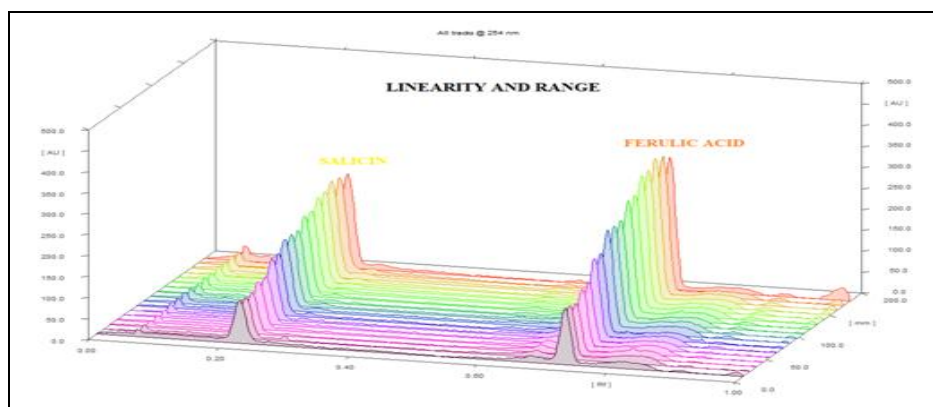


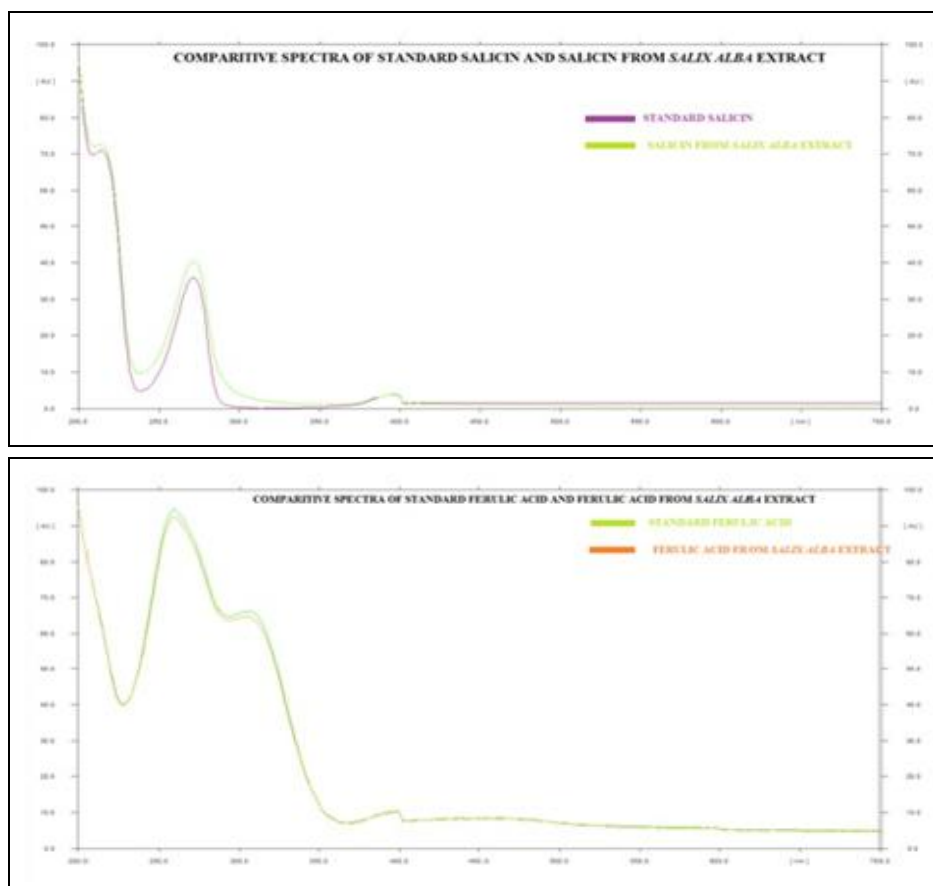
FIG. 3: 3-D CHROMATOGRAM OF LINEARITY OF SALICIN AND FERULIC ACID

TABLE 4: SUMMARY OF LINEAR REGRESSION AND VALIDATION DATA

Parameters	Salicin	Ferulic acid
Linearity range	5-50 ng/spot	10-100 ng/spot
Linear regression equation	$y = 0.19694x + 0.25244$	$y = 0.13162x + 0.16696$
Slope \pm SD	0.19694	0.13162
Intercept \pm SD	0.25244	0.16696
Correlation coefficient @	0.9994	0.9993
Determination coefficient (r^2)	0.9984	0.9991

Specificity: The peak purity tests of Salicin and Ferulic acid spots were assessed by comparing their

respective spectra at peak start, peak apex, and peak end positions of spot¹⁶. The results of spectral comparison for Salicin and Ferulic acid were found to be specific at peak start–peak apex and at peak apex–peak end, respectively. The closeness of peak purity values to 1 indicates that the spots were only attributed to a single compound. A good correlation ($r = 0.992$) was also obtained between standard and sample spectra of Salicin and Ferulic acid. The UV spectra comparison of the spots of the standards and all extracts were presented in **Fig. 4**.

**FIG. 4: COMPARITIVE SPECTRA OF SALICIN AND FERULIC ACID**

Precision: System, Method, and Intermediate precision of the developed method were expressed in terms of relative standard deviation (RSD) of the peak area. The results showed that the System, Method, and intermediate variation of the results for Salicin and Ferulic acid were within the acceptable range. The coefficients of variation for System, Method, and Intermediate precision of the method were found to be less than 2.0%. The Salicin and Ferulic acid were also analyzed by two different analysts within the same day, and the results revealed that there is good intermediate precision between analysts **Table 5**.

TABLE 5: METHOD VALIDATION PARAMETERS FOR QUANTITATION OF SALICIN AND FERULIC ACID

S. no.	Parameters	Salicin	Ferulic acid
1	Specificity	Specific	Specific
2	System precision (% RSD)	0.98	1.12
3	Method Precision (% RSD)	1.25	1.37
4	Intermediate precision (% RSD)	1.57	1.02

Solution Stability: The sample solution was prepared and was kept at room temperature ($20 \pm 2^\circ\text{C}$ and $30 \pm 2^\circ\text{C}$) on a shelf protected from direct light. The solution was analyzed after 1 h, 3 h, 6 h, 12 h, 18 h, and 24 h. Because of the time needed⁴¹⁷

for sonication and filtration, the fastest possible analysis was carried out within 20 min and hence results of the remaining analysis times were compared with it. The average peak area values are presented in **Table 6**.

TABLE 6: SOLUTION STABILITY STUDY

S. no.	Time of analysis (hrs)	Peak Area (AU)	
		Salicin	Ferulic acid
1	0	10104	23087
2	3	10202	22596
3	6	10090	22869
4	12	10078	22731
5	18	10143	22921
6	24	10105	22843

TABLE 7: ROBUSTNESS STUDY FOR THE DEVELOPED METHOD

S. no.	Parameter studied	Salicin % RSD	Ferulic acid % RSD
1	Composition of mobile phase	1.37	0.99
2	Volume of mobile phase	1.11	1.38
3	Time from spotting to development (5–60 min)	1.08	0.87
4	Time from development to scanning (5–60 min)	1.30	1.21

Accuracy (Recovery): The recovery studies were carried out at 80%, 100%, and 120% of the test concentration as per ICH guidelines. The percentage recovery of Salicin and Ferulic acid at all three levels were found to be satisfactory **Table 8**. For Salicin and Ferulic acid, the % recovery was found between 98.4-100.28%.

TABLE 8: RECOVERY STUDY OF THE METHOD FOR SALICIN AND FERULIC ACID

S. no.	Recovery level (%)	Salicin	Ferulic acid
1	80	98.4	99.28
2	100	100.28	101.36
3	120	99.13	100.23
	Average	99.27	100.29

CONCLUSION: The current studies indicate that MESAL exerts a potential antioxidant activity at a higher dose comparable to Ascorbic acid. MESAL in a dose-dependent manner exhibited anti-inflammatory activity in the rat paw edema model. The developed HPTLC/densitometric method was found to be simple, rapid, selective, quite sensitive, and suitable for simultaneous determination of Salicin and Ferulic acid in three different extracts. The method can minimize the cost of reagents and time for analysis. It also utilized the merit of applying several sample spots on the HPTLC plate, which may be more advantageous for regulatory quality control laboratories especially to facilitate the post-marketing surveillance program. In addition, the method is inexpensive and not

The average peak areas of Salicin and Ferulic acid does not vary significantly from the reference time after 1 day of sample preparation.

Robustness: The standard deviations of peak areas were calculated for the aforementioned four parameters (variation in composition of the mobile phase, volume of the mobile phase, time from spotting to development, and time from development to scanning), and coefficients of variation were found to be less than 2.0% in all cases as shown in **Table 7**. The low RSD values indicate the robustness of the method.

requires certain types of stationary phases. Thus, it can represent another good alternative for the already existing HPLC methods, especially those using certain types of detectors which are not present in most of the laboratories.

ACKNOWLEDGEMENT: The authors thank Dr. D.Y. Patil institute of Pharmaceutical research and sciences, Pune, India, for providing facilities to conduct the research.

CONFLICTS OF INTEREST: There are no conflicts of interest among all the authors with the publication of the manuscript.

REFERENCES:

- Gupta A, Maheta P, Chauhan R, Pandey S, Yadav JS and Shah S: Simultaneous quantification of bioactive triterpene acids (ursolic acid and oleanolic acid) in different extracts of *Eucalyptus globulus* (L) by HPTLC method. *Pharmacognosy Journal* 2018; 10(1): 1-8.
- Shivtare RS, Nagore DH and Nipanikar SU: HPTLC'an important tool in standardization of herbal medical product: A review. *Journal of Scientific and Innovative Research* 2013; 2(6): 1086-96.
- Kim HR, Park GN, Jung BK, Yoon WJ, Jung YH and Chang KS: Antioxidative effects of *Rhaphiolepis indica* and *Quercus salicina* from Jeju. *Journal of the Korean Applied Science and Technology* 2016; 33(1): 41-50.
- Banerjee M, Khursheed R, Yadav AK, Singh SK, Gulati M, Pandey DK, Prabhakar PK, Kumar R, Porwal O, Awasthi A and Kumari Y: A Systematic Review on Synthetic Drugs and Phytopharmaceuticals Used to Manage Diabetes. *Current Diabetes Reviews* 2020; 16(4): 340-56.

5. Kaur P, Pandey DK, Gupta RC and Dey A: Simultaneous microwave assisted extraction and HPTLC quantification of mangiferin, amarogentin, and swertiamarin in *Swertia* species from Western Himalayas. *Industrial Crops and Products* 2019; 132: 449-59.
6. Meier B, Lehmann D, Sticher O and Bettschart A: Identification and determination of 8 phenol glycosides each in *Salix purpurea* and *S. daphnoides* by modern high pressure liquid chromatography. *Pharmaceutica Acta Helveticae* 1985; 60: 269-75.
7. Dou J, Xu W, Koivisto JJ, Mobley JK, Padmakshan D, Kögler M, Xu C, Willför S, Ralph J and Vuorinen T: Characteristics of hot water extracts from the bark of cultivated willow (*Salix* sp.). *ACS Sustainable Chemistry & Engineering* 2018; 6(4): 5566-73.
8. Sulaiman GM, Hussien NN, Marzooq TR and Awad HA: Phenolic content, antioxidant, antimicrobial and cytotoxic activities of ethanolic extract of *Salix alba*. *American Journal of Biochemistry and Biotechnology* 2013; 9(1): 41-6.
9. Mancuso C and Santangelo R: Ferulic acid: pharmacological and toxicological aspects. *Food and Chemical Toxicology*; 2014; 65: 185-95.
10. Bumrungpert A, Lilitchan S, Tuntipopipat S, Tirawanchai N and Komindr S: Ferulic acid supplementation improves lipid profiles, oxidative stress, and inflammatory status in hyperlipidemic subjects: A randomized, double-blind, placebo-controlled clinical trial. *Nutrients* 2018; 10(6): 713.
11. Amić A, Marković Z, Marković JM, Milenković D and Stepanić V: Antioxidative potential of ferulic acid phenoxyl radical. *Phytochemistry* 2020; 170: 112218.
12. Zduńska K, Dana A, Kolodziejczak A and Rotsztejn H: Antioxidant properties of ferulic acid and its possible application. *Skin Pharmacology and Physiology* 2018; 31(6): 332-6.
13. Barboza JN, da Silva Maia Bezerra Filho C, Silva RO, Medeiros JV and de Sousa DP: An overview on the anti-inflammatory potential and antioxidant profile of eugenol. *Oxidative Medicine and Cellular Longevity* 2018; 1-10.
14. Bonomo MG, Cafaro C, Russo D, Calabrone L, Milella L, Saturnino C, Capasso A and Salzano G: Antimicrobial activity, antioxidant properties and phytochemical screening of *Aesculus hippocastanum* mother tincture against food-borne bacteria. *Letters in Drug Design & Discovery* 2020; 17(1): 48-56.
15. Nirumand MC, Hajjalyani M, Rahimi R, Farzaei MH, Zingue S, Nabavi SM and Bishayee A: Dietary plants for the prevention and management of kidney stones: preclinical and clinical evidence and molecular mechanisms. *International Journal of Molecular Sciences* 2018; 19(3): 765.
16. Mehta JP, Parmar PH, Vadia SH, Patel MK and Tripathi CB: *In-vitro* antioxidant and *in-vivo* anti-inflammatory activities of aerial parts of *Cassia* species. *Arabian Journal of Chemistry* 2017; 10(2): S1654-S1662.
17. Salem GA, Alamyel FB, Abushaala FA, Elnory KA, Abusheba H and Sahu RP: Evaluation of the hepatoprotective, anti-inflammatory, antinociceptive and antiepileptic activities of *Chrysanthemum trifurcatum*. *Biomedicine & Pharmacotherapy* 2019; 117: 109-23.
18. Onoja SO, Ezeja MI, Omeh YN and Onwukwe BC: Antioxidant, anti-inflammatory and antinociceptive activities of methanolic extract of *Justicia secunda* Vahl leaf, *Alexandria Journal of Medicine* 2017; 53(3): 207-13.
19. Ngoua-Meye-Misso RL, Sima-Obiang C, Ndong JDL, Ondo JP, Abessolo FO and Obame-Engonga LC: Phytochemical screening, antioxidant, anti-inflammatory and antiangiogenic activities of *Lophira procera* A. Chev. (Ochnaceae) medicinal plant from Gabon, *Egyptian Journal of Basic and Applied Sciences* 2018; 5(1): 80-86.
20. Paun G, Neagu E, Moroceanu V, Albu C, Ursu TM, Zanfirescu A, Negres S, Chirita C and Radu GL: Anti-inflammatory and antioxidant activities of the *Impatiens noli-tangere* and *Stachys officinalis* polyphenolic-rich extracts. *Revista Brasileira de Farmaco* 2018; 28(1): 57-64.
21. Santos LCDS, Guilhon CC, Moreno DSA, Alviano CS, Estevam CDS, Blank AF and Fernandes PD: Anti-inflammatory, antinociceptive and antioxidant properties of *Schinopsis brasiliensis* bark. *The Journal of Ethnopharmacology* 2018; 213: 176-82.
22. Pedan V, Weber C, Do T, Fischer N, Reich E and Rohn S: HPTLC fingerprint profile analysis of cocoa proanthocyanidins depending on origin and genotype. *Food Chemistry* 2018; 267: 277-87.
23. Stanek N and Jasicka-Misiak I: HPTLC phenolic profiles as useful tools for the authentication of honey. *Food Analytical Methods*. 2018; 11(11): 2979-89.
24. ICH Harmonised Tripartite Guideline, Validation of Analytical Procedures: Text and Methodology Q2 (R1), Nov 2005.
25. Hakim M, Rathod D, Trivedi DA, Panigrahi J, Gantait S and Patel IC: An effective validated method for HPTLC-fingerprinting of alkaloids and glycosides from multiple plant parts of three *Terminalia* spp. *Israel Journal of Plant Sciences* 2018; 65(01-02): 109-17.
26. Patil AG, Koli SP and Patil DA: Pharmacognostical standardization and HPTLC fingerprint of *Averrhoa bilimbi* (L.) fruits. *J of Pharmacy Res* 2013; 6(1): 145-50.
27. Seboletswe PS, Mkhize Z and Katata-Seru LM: HPTLC fingerprint profiling of *Protorhus longifolia* methanolic leaf extract and qualitative analysis of common biomarkers. *International Journal of Materials and Metallurgical Engineering* 2019; 13(12): 553-7.

How to cite this article:

Shivtare RS, Kewatkar SM, Musale R, Lohakare P, Patil D, Choudhary D, Ganu G, Nagore DH and Chitlange S: *In-vitro* antioxidant and anti-inflammatory activity of *Salix alba* L. along with simultaneous HPTLC analysis of salicin and ferulic acid. *Int J Pharm Sci & Res* 2021; 12(6): 3176-84. doi: 10.13040/IJPSR.0975-8232.12(6).3176-84.

All © 2013 are reserved by the International Journal of Pharmaceutical Sciences and Research. This Journal licensed under a Creative Commons Attribution-NonCommercial-ShareAlike 3.0 Unported License.

This article can be downloaded to **Android OS** based mobile. Scan QR Code using Code/Bar Scanner from your mobile. (Scanners are available on Google Playstore)



Received on 23 March 2020; received in revised form, 04 July 2020; accepted, 15 July 2020; published 01 March 2021

ANTIOXIDANT ACTIVITY OF *CASSIA AURICULATA* AND *CASSIA FISTULA* EXTRACT ALONG WITH WOUND HEALING ACTIVITY OF ITS POLYHERBAL FORMULATION

S. M. Kewatkar ^{*1}, V. V. Paithankar ², S. S. Deshpande ³, S. P. Jain ¹ and D. H. Nagore ⁴

Department of Pharmacognosy ¹, Rajarshi Shahu College of Pharmacy, Buldana - 443001, Maharashtra, India.

Department of Pharmacology ², Vidyabharti College of Pharmacy, Amravati - 444602, Maharashtra, India.

Department of Pharmacology ³, Dr. PDMC, Amravati - 444603, Maharashtra, India.

Research and Development ⁴, Mprex Healthcare, Pune - 411057, Maharashtra, India.

Keywords:

Antioxidant, *Cassia fistula*, *Cassia auriculata*, Polyherbal formulation, Wound healing activity

Correspondence to Author:

Dr. Shailesh M. Kewatkar

Associate Professor,
Rajarshi Shahu College of Pharmacy,
Buldana - 443001, Maharashtra, India.

E-mail: kewatkar.shailesh@gmail.com

ABSTRACT: Due to emergent concerns about unhealthy consequences of chemicals in the health industry, the interest towards natural and herbal substances has been growing every day. In this study, the antioxidant effect of *Cassia fistula* [CFF] and *Cassia auriculata* [CAF] extract was evaluated. Also discover wound healing activity of polyherbal formulation (CFF and CAF). The antioxidant activity of the extract was evaluated by using 2, 2-diphenyl-1-picrylhydrazyl (DPPH) free radical scavenging activity. Total phenolic content (TPC) was determined to screen the prepared extracts by using the Folin-Ciocalteu phenol reagent method. The polyherbal formulation (CFF and CAF) using the excision wound model. The CFF and CAF extracts showed variable degrees of antioxidant activity. The formulated gel accelerates the wound healing process which may be due to enhancing the cellular defense mechanisms, proliferation, suppression of inflammation, and contraction of the collagen tissue and could be delayed by reactive oxygen species or microbial infection. The results suggest that extracts have antioxidant properties, which may be a potentially promising agent and favorable for wound healing, and this plant extract used in polyherbal formulation may be useful in the management of abnormal healing.

INTRODUCTION: Wound healing is the natural process of repair that follows injury to the skin and other soft tissues. It is an interaction of the complex cascade of cellular and biochemical actions healing to the restoration of structural and functional integrity with the recovery of the strength of injured tissues ¹.

Healing involves continuous cell-cell interaction and cell-matrix interactions that allow the process to continue in different overlapping phases, which include inflammation, wound contraction, re-epithelialization, tissue remodeling, and formation of granulation tissue with angiogenesis ². These events are controlled by several mediators, including platelets, inflammatory cells, cytokines, growth factors, and matrix metalloproteinases and their inhibitors ³.

Numerous factors such as microbial infection, necrotic tissue, and interference with blood supply, lymphatic blockage, oxidative stress and disease condition such as diabetes delay the wound healing ⁴²⁰

<p>QUICK RESPONSE CODE</p> 	<p>DOI: 10.13040/IJPSR.0975-8232.12(3).1805-10</p>
<p>This article can be accessed online on www.ijpsr.com</p>	
<p>DOI link: http://dx.doi.org/10.13040/IJPSR.0975-8232.12(3).1805-10</p>	

process. The reactive oxygen species (ROS) are harmful to the wound healing process due to the destructive effects on cells and tissues. Free-radical-scavenging enzymes (FRSE) are a cytoprotective enzyme group that has a vital role in the reduction, deactivation, and removal of ROS as well as regulating the wound healing process⁴. However, if the above factors may be altered by any agent, an augmented healing rate could be achieved⁵. Nevertheless, wound healing can have severe complications that invoke high costs for therapy. Therefore, it is necessary to develop more efficient methods for improving wound healing and reduce the cost involved⁶.

Plants are an abundant source of phytochemicals, which could have wound healing and antioxidant properties. Several indigenous drugs have been described in Indian folklore medicine for the management of cuts, bruises, burns, and wounds. Moreover, the phytomedicines for wound healing are cheap, well-tolerated and affordable and supposedly effective and nontoxic as hypersensitive reactions are rarely encountered with the use of these agents⁷.

Cassia is a native medicinal plant genus, in which CFF has large biodiversity in north India and CAF in south India. CFF is a rapidly medium-sized, deciduous tree that is now widely cultivated worldwide as an ornamental tree for its beautiful, attractive yellow flowers. CFF also is known as a golden shower, and Amaltash belongs to the family Fabaceae. These plants are consisting of the various active principles of therapeutic value and possessing wide biological activity. The root is prescribed as a tonic, febrifuge, astringent, and strong purgative⁸.

CAF, commonly known as Tanners Cassia, also known as 'Taroda' in Hindi is a shrub that belongs to the Fabaceae family is import to tanner as well as workers in iron and well known for its contribution in Ayurveda as Avarai Panchaga Chooranam⁹ and Kalpa Herbal tea. The plant has been accounted to possess antipyretic¹⁰, hepatoprotective, antidiabetic, antiperoxidative and antihyperglycaemic¹¹, and microbicidal activity¹². The present study was aimed to assess the antioxidant and wound healing activity of extract CFF and CAF used in traditional Indian medicine.

MATERIALS AND METHODS:

Plant Material: The roots of *Cassia auriculata* Linn and *Cassia fistula* Linn were collected from the fields of Walgaon Road, Amravati (Maharashtra), and interiors of Bhopal (Madhya Pradesh), respectively. Both the plant have been authenticated by Safia College of Science, Bhopal, (Madhya Pradesh), and were given the voucher specimen number 159/Bot/Safia/2010 (*Cassia auriculata* Linn.) and 160/Bot/Safia/2010 (*Cassia fistula* Linn.).

Extraction of Drugs: The authenticated plant material (root) was dried in the shade, powdered, and used for extraction. The extraction was carried out with the help of water by decoction method at 40 °C ± 5 °C. Then this aqueous extract was filtered, and ethanol was added slowly into this aqueous liquid extract to precipitate out polysaccharides. Then the filtrate was evaporated to 1/4th of the total volume. Further, it was successively extracted with ethyl acetate. Then the ethyl acetate extract was acidified with 0.1 N HCl to increase the yield of the extract. Then this fraction was evaporated to get precipitate which was then dissolved in methanol and evaporated slowly to get crystalline powder. The obtained powder was purified using column chromatography by solvent by their polarity.

Evaluation Parameters for the Extract:

Determination of Extractive Value: A total of ten gm. of the powdered root was extracted with 100ml solvent using Soxhlet extraction apparatus. The percentage yield of each extract was determined.

In-vitro Antioxidant Assay Method: The phenolic compounds might be the essential plant material and could, therefore, be a natural source of antioxidants¹³. The high scavenging property of plant extract may be due to hydroxyl groups present in the phenolic compounds. Henceforth total phenolic content of the prepared extracts was determined to screen the bioactive extract.

Determination of Total Phenolic Content (TPC):

The total phenolics in extracts were determined according to Folin- Ciocalteu procedure of Singleton and Rossi¹⁴. Gallic acid was used as a standard, and the total phenolic contents were expressed as mg/g gallic acid equivalent (GAE).

Test mixture consists of one ml of extract solution (1mg/ml), 0.5ml of Folin-Ciocalteu reagent, and five ml of distilled water. The mixture incubated at room temperature for ten min. Then 1.5 ml of anhydrous sodium carbonate solution (10% w/v) was added, and the final volume made up to ten ml. The final mixture was allowed to stand at room temperature for 30 min. The absorbance measured at 760 nm using a UV-Vis spectrophotometer. The experiment was carried out in triplicate.

In-vitro Antioxidants Activity:

DPPH Free Radical Scavenging Activity: The antioxidant activity of the plant extract was estimated using a slight modification of the DPPH (2,2-diphenyl-1-picryl-hydrazyl-hydrate) radical scavenging protocol given by Chen *et al.*¹⁵ For DPPH radical scavenging activity, different concentrations of plant extract and different concentration of Ascorbic acid were prepared. Afterward, these dilutions were mixed with 0.5 ml DPPH solution (4mg in 100 ml methanol) and incubated at room temperature for 30 mins in dark conditions. After incubation, the absorbance was noted at 517 nm using methanol as a blank. Percentage inhibition was calculated using the following formulae:

$$\% \text{ inhibition} = \frac{\text{Absorbance (control)} - \text{Absorbance (test)}}{\text{Absorbance (control)}} \times 100$$

Polyherbal Gel Formulation: Carbopol 934 was dispersed in 50 ml of distilled water with constant stirring. The required quantity of plant extracts was mixed in 20 ml, and components were mixed properly to the Carbopol 934 gel with constant stirring and volume was made up to 100 ml, and triethanolamine was added dropwise to the formulation for adjustment of required skin pH (6.8-7) and obtained the gel at required consistency. The same method was followed for the preparation of the control sample without adding any extract¹⁶.

TABLE 1: FORMULAE FOR GEL PREPARATION

S. no.	Ingredient	Formulation (weight)		
		F1	F2	F3
1	Carbopol-934	3 gm	3 gm	3 gm
2	CAF	10 %	--	--
3	CFF	--	10%	--
4	CAF+CFF (1+1)	--	--	10%
5	Purified water	100 mL	100 mL	100 mL
6	Triethanolamine	QS to neutralize gel base	QS to neutralize gel base	QS to neutralize gel base

Evaluation Parameters for the Polyherbal Formulation:^{17,18}

Measurement of pH: The pH of the gel was measured by using a pH meter.

Determination of Homogeneity: All developed gels were tested for homogeneity by visual inspection after the gels have been set in the container. They were tested for their appearance and presence of any aggregates.

Determination of Viscosity: The viscosity of the gel was measured by using Brookfield viscometer with the spindle.

Determination of Color: It was done with naked eyes against a white background.

In-vivo Pharmacological Activity for Polyherbal Gel Formulation:

Animals: Healthy Wistar albino rats of either sex weighing 150-250 gm. were used for the study. All experimental and housing conditions for animals were maintained as per CPCSEA guidelines. Animals were provided standard feeding pellets (Golden feeds, New Delhi) and water *ad libitum*. The temperature was maintained at 22±2 °C, with a light and dark cycle of 12:12 h. The animals have been transferred to the laboratory for at least one hr. before the experiment for proper acclimatization. The experiments were performed during the day (08:00-16:00 h). All animal experiments were conducted with the prior permission of the Institutional animal ethical committee (IAEC) of PBRI (Regd No. 1283/c/09/CPCSEA).

Wound Healing Activity:

Excision Wound Model: The back of each animal was shaved and prepared after washing with spirit. An area of two sq.cm as described by Bhat *et al.*,¹⁹ was defined with a marker on the shaven back of the animals. The marked circular area was excised with its full thickness using a surgical sterile blade and scissors under phenobarbitone anesthesia. The Control/ formulations were applied to the wounded rats of the respective groups three times a day. The wounded rats of the first group were used as the baseline control for all the formulations. The application was repeated for 16 days post-operatively. The wound contractions were measured as the percentage of wound reduction in

the wound area for every four days. The progressive wound area reduction was monitored periodically by tracing the wound margin on paper, and the area was measured using graph paper. The wound size reduction was calculated by the formula:-

Wound contraction% = (difference in the area of the wound in mm² between the initial and on a particular post-operative day) × 100 / area of the wound in mm² immediately after the wound excision.

Statistical Analysis: The statistical significance was assessed using one-way analysis of variance (ANOVA) followed by the Holm-Sidak test and Bonferroni t-test. The values were expressed as mean ± SD, and P<0.05 was considered significant.

RESULTS AND DISCUSSION:

Total Phenolic Content: In a flavonoid-rich extract of both plants, total phenol content was also estimated. For total phenol content estimation (TPC) standard curve of Gallic acid was used and estimated as Gallic acid equivalent (GAE). Total Phenol Content in *Cassia auriculata* and *Cassia fistula* was found to be 67.32 and 63.84 µg/mg GAE, respectively.

TABLE 2: STANDARD CURVE OF GALLIC ACID

S. no.	Conc. (µg/mL)	Absorbance	Line of regression and R ₂
1	10	0.1098	
2	20	0.1763	
3	30	0.2468	Y=0.005x + 0.065
4	40	0.2981	and R ₂ = 0.976
5	50	0.3258	

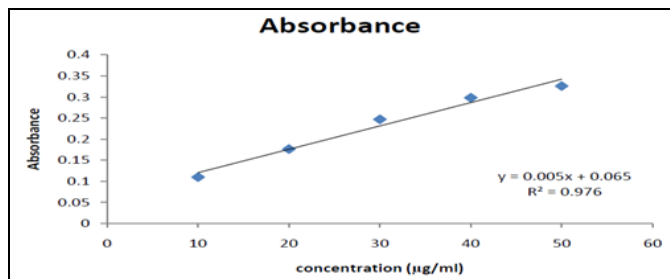


FIG. 1: STANDARD CURVE OF GALLIC ACID

TABLE 3: TOTAL PHENOLIC CONTENT

S. no.	Test sample	Absorbance	Total phenol content (GAE) µg/mL
1	CAF	0.4016	67.32
2	CFF	0.3842	63.84

DPPH Free Radical Scavenging Activity: Antioxidant potential of the flavonoid-rich extract

was ascertained by an effect on percentage inhibition of DPPH free radicals. DPPH assay was done by the concentration required for 50% inhibition (IC₅₀). Flavonoids-rich extract of *Cassia auriculata* showed a significant effect on DPPH free radicals. In the concentration range of 10 µg/ml to 100 µg/ml, the goodness of fit for a line of regression was good with R₂ = 0.976. IC₅₀ was found to be 60.97µg/ml. In the DPPH assay effect of flavonoids, a rich extract of *Cassia fistula* was not significantly different as compared to flavonoids rich extract of *Cassia auriculata*. IC₅₀ in DPPH assay was 62.19µg/ml for extract.

TABLE 4: EFFECT OF CAF IN DPPH FREE RADICAL SCAVENGING ASSAY

S. no.	Conc. (µg/mL)	% inhibition	IC ₅₀
1	10	21.46	
2	20	28.67	
3	40	32.25	60.977
4	60	48.56	
5	80	64.24	
6	100	72.5	

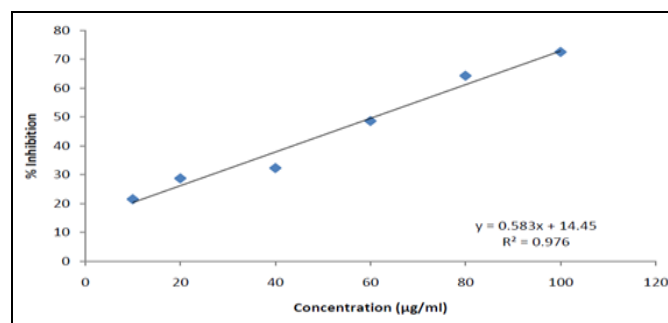


FIG. 2: EFFECT OF CAF IN DPPH FREE RADICAL SCAVENGING ASSAY

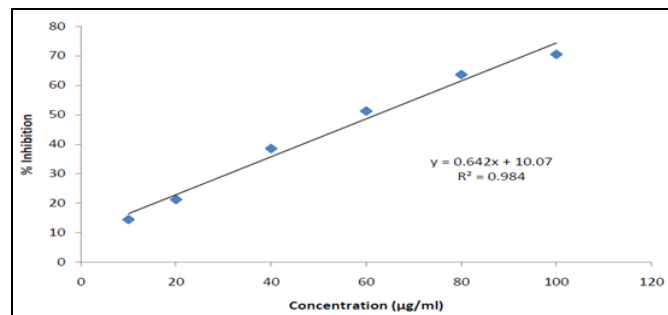


FIG. 3: EFFECT OF CFF IN DPPH FREE RADICAL SCAVENGING ASSAY

TABLE 5: EFFECT OF CFF IN DPPH FREE RADICAL SCAVENGING ASSAY

S. no.	Conc. (µg/mL)	% inhibition	IC ₅₀
1	10	14.5	
2	20	21.26	
3	40	38.55	62.196
4	60	51.26	
5	80	63.62	
6	100	70.5	

Evaluation of Polyherbal Gel Formulations:**TABLE 6: EVALUATION OF POLYHERBAL GEL FORMULATIONS**

S. no.	Treatment	% Wound Contraction (Day)			
		4	8	12	16
1	Control (gel base)	11.00±2.10	23.67±2.88	45.83±2.64	59.17±5.19
2	F1	14.33±2.25	32.17±2.14 ^{ab}	60.67±4.89 ^a	77.83±5.78 ^b
3	F2	13.83±1.60	30.17±3.43 ^{ab}	58.17±3.19 ^{ab}	70.00±5.73 ^{ac}
4	F3	15.17±1.33	32.83±2.64 ^{ab}	61.00±1.90 ^{ab}	79.17±3.31 ^b
5	Standard Cream	16.17±2.04	40.00±4.05	68.33±2.16 ^b	86.33±5.32 ^b

All Data presented in mean ± SD, ^a P<0.05 as compared to Standard cream treated a group, ^b P<0.05 as compared to gel base treated a group, ^c P<0.05 as compared to F3 treated a group

The flavonoid-rich extract had antimicrobial and antioxidant property they were incorporated in a gel base for topical use. Basic consideration was used in cancerous wounds. Carbopo l 934 was used as a gel base and Triethanolamine as a neutralizing agent for pH changes due to Carbopol. Ten % extract formulations were prepared in which F1 consisted of CAF (flavonoids rich extract of CAF), F2 of CFF (flavonoids rich extract of CFF), and F3 of CAF and CFF in equal proportion. The formulated gel accelerates the wound healing process which may be due to enhancing the cellular defense mechanisms, proliferation, suppression of inflammation, and contraction of the collagen tissue and could be delayed by reactive oxygen species or microbial infection ¹⁶.

The wound healing property of extract was ascertained by percentage contraction of the wound. The observation was done on the fourth, eighth, 12th, and 16th day. It was observed that on fourth -day formulation one and two were not having any significant effect on wound contraction as compared to the control group, but different formulation which was having an equal proportion of both extracts showed a significant effect (P<0.05) as compared to control group. Thus it could be considered that components present in both extracts, when combined in equal proportion, would be giving a synergistic effect when combined in equal proportion. Afterward, it was observed that formulation F1, F2, and F3 showed a better effect as a wound healing activity. On the eighth, 12th, and 16th day, all formulations showed a significant effect (P<0.05) as compared to the control group. The study results demonstrated that F3 was better than F2 and F1, and F2 was better than F1. Flavonoids have been possessing the antioxidant potential and free radical scavenging effect, which is believed to be one of the important

components of wound healing. Bioflavonoids are thought to benefit connective tissue by binding to elastin, preventing its degradation by elastases ²⁰. Many studies have shown that antimicrobial activities of plants can also be attributed to their flavonoids content ²¹⁻²²; hence, they are helpful in the prevention of wound infection. Most of the delay in wound healing is due to insufficient or excessive fibroblast activity. Thus, inhibition of fibroblast growth by flavonoids such as apigenin could be beneficial for the treatment of any skin injury.

CONCLUSION: The present study concludes that the polyherbal gel of the extracts of CFF and CAF has significant wound healing activity. The better activity of polyherbal formulation could be due to the synergistic action of the plant's constituents present in the formulation. The phytoconstituents like flavonoids are known to promote the wound healing process due to their anti-oxidant properties. The investigation reveals that the wound healing activity of polyherbal formulation may be due to the combined action and presence of phytoconstituents.

ACKNOWLEDGEMENT: The authors thank Rajarshi Shahu College of Pharmacy, Buldana for providing facilities to conduct the research.

CONFLICTS OF INTEREST: There are no conflicts of interest among all the authors with the publication of the manuscript.

REFERENCES:

1. Kumarasamyraja D, Jeganathan NS and Manavalan R: A review on medicinal plants with potential wound healing activity. *Int J Pharm Pharm Sci* 2012; 2: 105-07.
2. Takeo M, Lee W and Ito M: Wound healing and skin regeneration. *Cold Spring Harbor Perspectives in Medicine* 2015; 5(1): a023267.

3. Janis JE and Harrison B: Wound healing, part I; Basic science. *Plastic and Reconstructive Surgery*. 2014; 133(2): 199e-207e.
4. Dai T, Tanaka M, Huang YY and Hamblin MR: Chitosan preparations for wounds and burns: antimicrobial and wound-healing effects. *Expert Review of Anti-infective Therapy* 2011; 9(7): 857-79.
5. Esat DM, Temel S, Ozer H, Kemal UM, Kaya F, Aslan F, Celepli P, Senes M, Dogan K, Kuru S and Mutlu BA: Comparison of the effects of platelet-rich plasma prepared in various forms on the healing of dermal wounds in rats. *Wounds: a compendium of clinical research and practice*. 2016; 28(3): 99.
6. Latif MA, Zaki MZ, Leng TM, Rahman NH, Arshad SA and Hamid A: *Alocasia denudata* Engler treatment enhance open wound healing activities in Wistar rat's skin. *J Ethnopharmacol* 2015; 176: 258-67.
7. Marume A, Matope G, Katsande S, Khoza S, Mutingwende I and Mduluzi T: Wound Healing Properties of Selected Plants Used in Ethnoveterinary Medicine. *Frontiers in Pharmacology* 2017; 8: 544.
8. Khare CP: *Indian Medicinal Plants*: Springer-Verlag New York 2007. 127.
9. Prakash Yoganandam G, Gopal V and Thanka J: Aavara kudineer-A potent polyherbal siddha formulation for management of diabetes mellitus. *International Journal of Pharmaceutical Development & Technol* 2014; 4: 98-103.
10. Hossain E, Mandal SC and Gupta JK. Phytochemical screening and in-vivo antipyretic activity of the methanol leaf-extract of *Bombax malabaricum* DC (Bombacaceae). *Tropical Journal of Pharmaceutical Research* 2011; 10(1).
11. Latha M and Pari L: Antihyperglycaemic effect of *Cassia auriculata* in experimental diabetes and its effects on key metabolic enzymes involved in carbohydrate metabolism. *Clin Exp Pharmacol Physiol* 2003; 30(1-2): 38-43.
12. Swapna NL, Prasad MA and Prasad S: Efficacy of *Euphorbia tirucalli* (L) towards microbicidal activity against human pathogens. *Int J Phar Bio Sci* 2011; 2: 12-8.
13. Teleszko M and Wojdylo A: Comparison of phenolic compounds and antioxidant potential between selected edible fruits and their leaves. *Journal of Functional Foods* 2015; 14: 736-46.
14. Sulaiman CT and Balachandran I: Total phenolics and total flavonoids in selected Indian medicinal plants. *Indian Journal of Pharmaceutical Sciences* 2012; 74(3): 258.
15. Wojtunik KA, Ciesla LM and Waksmundzka-Hajnos M: Model studies on the antioxidant activity of common terpenoid constituents of essential oils by means of the 2, 2-diphenyl-1-picrylhydrazyl method. *Journal of Agricultural and Food Chemistry* 2014; 62(37): 9088-94.
16. Alqasoumi SI, Yusufoglu HS and Alam A: Anti-inflammatory and wound healing activity of *Fagonia schweinfurthii* alcoholic extract herbal gel on albino rats. *African Journal of Pharmacy and Pharmacology* 2011; 5(17): 1996-2001.
17. Sharma A, Dwivedi DS, Mishra G and Joshi H: Formulation and evaluation of herbal gel containing extracts of *Albezia lebeck* linn. *Am J PharmTech Res* 2012; 2(4): 663-68.
18. Pandey A, Jagtap JV and Polshettiwar SA: Formulation and evaluation of *in-vitro* antimicrobial activity of gel containing essential oils and effect of polymer on their antimicrobial activity. *Int J Pharm Pharm Sci* 2011; 3: 234-37.
19. Fahimi S, Abdollahi M, Mortazavi SA, Hajimehdipoor H, Abdolghaffari AH and Rezvanfar MA: Wound healing activity of a traditionally used poly herbal product in a burn wound model in rats. *Iranian Red Crescent Medical Journal*. 2015; 17(9): 1-8.
20. Sugumar S, Ghosh V, Nirmala MJ, Mukherjee A and Chandrasekaran N: Ultrasonic emulsification of eucalyptus oil nanoemulsion: antibacterial activity against *Staphylococcus aureus* and wound healing activity in Wistar rats. *Ultrasonics sonochemistry* 2014; 21(3): 1044-9.
21. Ammar I, Bardaa S, Mzid M, Sahnoun Z, Rebaï T, Attia H and Ennouri M. Antioxidant, antibacterial and *in-vivo* dermal wound healing effects of *Opuntia* flower extracts. *International Journal of Biological Macromolecules*. 2015; 81: 483-90.
22. Ye D, Zhong Z, Xu H, Chang C, Yang Z, Wang Y, Ye Q and Zhang L: Construction of cellulose/nanosilver sponge materials and their antibacterial activities for infected wounds healing. *Cellulose* 2016; 23(1): 749-63.

How to cite this article:

Kewatkar SM, Paithankar VV, Deshpande SS, Jain SP and Nagore DH: Antioxidant activity of *Cassia auriculata* and *Cassia fistula* extract along with wound healing activity of its polyherbal formulation. *Int J Pharm Sci & Res* 2021; 12(3): 1805-10. doi: 10.13040/IJPSR.0975-8232.12(3).1805-10.

All © 2013 are reserved by the International Journal of Pharmaceutical Sciences and Research. This Journal licensed under a Creative Commons Attribution-NonCommercial-ShareAlike 3.0 Unported License.

This article can be downloaded to **Android OS** based mobile. Scan QR Code using Code/Bar Scanner from your mobile. (Scanners are available on Google Playstore)



Received on 23 March 2020; received in revised form, 04 July 2020; accepted, 15 July 2020; published 01 March 2021

ANTIOXIDANT ACTIVITY OF *CASSIA AURICULATA* AND *CASSIA FISTULA* EXTRACT ALONG WITH WOUND HEALING ACTIVITY OF ITS POLYHERBAL FORMULATION

S. M. Kewatkar ^{*1}, V. V. Paithankar ², S. S. Deshpande ³, S. P. Jain ¹ and D. H. Nagore ⁴

Department of Pharmacognosy ¹, Rajarshi Shahu College of Pharmacy, Buldana - 443001, Maharashtra, India.

Department of Pharmacology ², Vidyabharti College of Pharmacy, Amravati - 444602, Maharashtra, India.

Department of Pharmacology ³, Dr. PDMC, Amravati - 444603, Maharashtra, India.

Research and Development ⁴, Mprex Healthcare, Pune - 411057, Maharashtra, India.

Keywords:

Antioxidant, *Cassia fistula*, *Cassia auriculata*, Polyherbal formulation, Wound healing activity

Correspondence to Author:

Dr. Shailesh M. Kewatkar

Associate Professor,
Rajarshi Shahu College of Pharmacy,
Buldana - 443001, Maharashtra, India.

E-mail: kewatkar.shailesh@gmail.com

ABSTRACT: Due to emergent concerns about unhealthy consequences of chemicals in the health industry, the interest towards natural and herbal substances has been growing every day. In this study, the antioxidant effect of *Cassia fistula* [CFF] and *Cassia auriculata* [CAF] extract was evaluated. Also discover wound healing activity of polyherbal formulation (CFF and CAF). The antioxidant activity of the extract was evaluated by using 2, 2-diphenyl-1-picrylhydrazyl (DPPH) free radical scavenging activity. Total phenolic content (TPC) was determined to screen the prepared extracts by using the Folin-Ciocalteu phenol reagent method. The polyherbal formulation (CFF and CAF) using the excision wound model. The CFF and CAF extracts showed variable degrees of antioxidant activity. The formulated gel accelerates the wound healing process which may be due to enhancing the cellular defense mechanisms, proliferation, suppression of inflammation, and contraction of the collagen tissue and could be delayed by reactive oxygen species or microbial infection. The results suggest that extracts have antioxidant properties, which may be a potentially promising agent and favorable for wound healing, and this plant extract used in polyherbal formulation may be useful in the management of abnormal healing.

INTRODUCTION: Wound healing is the natural process of repair that follows injury to the skin and other soft tissues. It is an interaction of the complex cascade of cellular and biochemical actions healing to the restoration of structural and functional integrity with the recovery of the strength of injured tissues ¹.

Healing involves continuous cell-cell interaction and cell-matrix interactions that allow the process to continue in different overlapping phases, which include inflammation, wound contraction, re-epithelialization, tissue remodeling, and formation of granulation tissue with angiogenesis ². These events are controlled by several mediators, including platelets, inflammatory cells, cytokines, growth factors, and matrix metalloproteinases and their inhibitors ³.

Numerous factors such as microbial infection, necrotic tissue, and interference with blood supply, lymphatic blockage, oxidative stress and disease condition such as diabetes delay the wound healing ⁴²⁶

<p>QUICK RESPONSE CODE</p> 	<p>DOI: 10.13040/IJPSR.0975-8232.12(3).1805-10</p>
<p>This article can be accessed online on www.ijpsr.com</p>	
<p>DOI link: http://dx.doi.org/10.13040/IJPSR.0975-8232.12(3).1805-10</p>	

process. The reactive oxygen species (ROS) are harmful to the wound healing process due to the destructive effects on cells and tissues. Free-radical-scavenging enzymes (FRSE) are a cytoprotective enzyme group that has a vital role in the reduction, deactivation, and removal of ROS as well as regulating the wound healing process⁴. However, if the above factors may be altered by any agent, an augmented healing rate could be achieved⁵. Nevertheless, wound healing can have severe complications that invoke high costs for therapy. Therefore, it is necessary to develop more efficient methods for improving wound healing and reduce the cost involved⁶.

Plants are an abundant source of phytochemicals, which could have wound healing and antioxidant properties. Several indigenous drugs have been described in Indian folklore medicine for the management of cuts, bruises, burns, and wounds. Moreover, the phytomedicines for wound healing are cheap, well-tolerated and affordable and supposedly effective and nontoxic as hypersensitive reactions are rarely encountered with the use of these agents⁷.

Cassia is a native medicinal plant genus, in which CFF has large biodiversity in north India and CAF in south India. CFF is a rapidly medium-sized, deciduous tree that is now widely cultivated worldwide as an ornamental tree for its beautiful, attractive yellow flowers. CFF also is known as a golden shower, and Amaltash belongs to the family Fabaceae. These plants are consisting of the various active principles of therapeutic value and possessing wide biological activity. The root is prescribed as a tonic, febrifuge, astringent, and strong purgative⁸.

CAF, commonly known as Tanners Cassia, also known as 'Taroda' in Hindi is a shrub that belongs to the Fabaceae family is import to tanner as well as workers in iron and well known for its contribution in Ayurveda as Avarai Panchaga Chooranam⁹ and Kalpa Herbal tea. The plant has been accounted to possess antipyretic¹⁰, hepatoprotective, antidiabetic, antiperoxidative and antihyperglycaemic¹¹, and microbicidal activity¹². The present study was aimed to assess the antioxidant and wound healing activity of extract CFF and CAF used in traditional Indian medicine.

MATERIALS AND METHODS:

Plant Material: The roots of *Cassia auriculata* Linn and *Cassia fistula* Linn were collected from the fields of Walgaon Road, Amravati (Maharashtra), and interiors of Bhopal (Madhya Pradesh), respectively. Both the plant have been authenticated by Safia College of Science, Bhopal, (Madhya Pradesh), and were given the voucher specimen number 159/Bot/Safia/2010 (*Cassia auriculata* Linn.) and 160/Bot/Safia/2010 (*Cassia fistula* Linn.).

Extraction of Drugs: The authenticated plant material (root) was dried in the shade, powdered, and used for extraction. The extraction was carried out with the help of water by decoction method at 40 °C ± 5 °C. Then this aqueous extract was filtered, and ethanol was added slowly into this aqueous liquid extract to precipitate out polysaccharides. Then the filtrate was evaporated to 1/4th of the total volume. Further, it was successively extracted with ethyl acetate. Then the ethyl acetate extract was acidified with 0.1 N HCl to increase the yield of the extract. Then this fraction was evaporated to get precipitate which was then dissolved in methanol and evaporated slowly to get crystalline powder. The obtained powder was purified using column chromatography by solvent by their polarity.

Evaluation Parameters for the Extract:

Determination of Extractive Value: A total of ten gm. of the powdered root was extracted with 100ml solvent using Soxhlet extraction apparatus. The percentage yield of each extract was determined.

In-vitro Antioxidant Assay Method: The phenolic compounds might be the essential plant material and could, therefore, be a natural source of antioxidants¹³. The high scavenging property of plant extract may be due to hydroxyl groups present in the phenolic compounds. Henceforth total phenolic content of the prepared extracts was determined to screen the bioactive extract.

Determination of Total Phenolic Content (TPC):

The total phenolics in extracts were determined according to Folin- Ciocalteu procedure of Singleton and Rossi¹⁴. Gallic acid was used as a standard, and the total phenolic contents were expressed as mg/g gallic acid equivalent (GAE).⁴²⁷

Test mixture consists of one ml of extract solution (1mg/ml), 0.5ml of Folin-Ciocalteu reagent, and five ml of distilled water. The mixture incubated at room temperature for ten min. Then 1.5 ml of anhydrous sodium carbonate solution (10% w/v) was added, and the final volume made up to ten ml. The final mixture was allowed to stand at room temperature for 30 min. The absorbance measured at 760 nm using a UV-Vis spectrophotometer. The experiment was carried out in triplicate.

In-vitro Antioxidants Activity:

DPPH Free Radical Scavenging Activity: The antioxidant activity of the plant extract was estimated using a slight modification of the DPPH (2,2-diphenyl-1-picryl-hydrazyl-hydrate) radical scavenging protocol given by Chen *et al.*¹⁵ For DPPH radical scavenging activity, different concentrations of plant extract and different concentration of Ascorbic acid were prepared. Afterward, these dilutions were mixed with 0.5 ml DPPH solution (4mg in 100 ml methanol) and incubated at room temperature for 30 mins in dark conditions. After incubation, the absorbance was noted at 517 nm using methanol as a blank. Percentage inhibition was calculated using the following formulae:

$$\% \text{ inhibition} = \frac{\text{Absorbance (control)} - \text{Absorbance (test)}}{\text{Absorbance (control)}} \times 100$$

Polyherbal Gel Formulation: Carbopol 934 was dispersed in 50 ml of distilled water with constant stirring. The required quantity of plant extracts was mixed in 20 ml, and components were mixed properly to the Carbopol 934 gel with constant stirring and volume was made up to 100 ml, and triethanolamine was added dropwise to the formulation for adjustment of required skin pH (6.8-7) and obtained the gel at required consistency. The same method was followed for the preparation of the control sample without adding any extract¹⁶.

TABLE 1: FORMULAE FOR GEL PREPARATION

S. no.	Ingredient	Formulation (weight)		
		F1	F2	F3
1	Carbopol-934	3 gm	3 gm	3 gm
2	CAF	10 %	--	--
3	CFF	--	10%	--
4	CAF+CFF (1+1)	--	--	10%
5	Purified water	100 mL	100 mL	100 mL
6	Triethanolamine	QS to neutralize gel base	QS to neutralize gel base	QS to neutralize gel base

Evaluation Parameters for the Polyherbal Formulation:^{17,18}

Measurement of pH: The pH of the gel was measured by using a pH meter.

Determination of Homogeneity: All developed gels were tested for homogeneity by visual inspection after the gels have been set in the container. They were tested for their appearance and presence of any aggregates.

Determination of Viscosity: The viscosity of the gel was measured by using Brookfield viscometer with the spindle.

Determination of Color: It was done with naked eyes against a white background.

In-vivo Pharmacological Activity for Polyherbal Gel Formulation:

Animals: Healthy Wistar albino rats of either sex weighing 150-250 gm. were used for the study. All experimental and housing conditions for animals were maintained as per CPCSEA guidelines. Animals were provided standard feeding pellets (Golden feeds, New Delhi) and water *ad libitum*. The temperature was maintained at 22±2 °C, with a light and dark cycle of 12:12 h. The animals have been transferred to the laboratory for at least one hr. before the experiment for proper acclimatization. The experiments were performed during the day (08:00-16:00 h). All animal experiments were conducted with the prior permission of the Institutional animal ethical committee (IAEC) of PBRI (Regd No. 1283/c/09/CPCSEA).

Wound Healing Activity:

Excision Wound Model: The back of each animal was shaved and prepared after washing with spirit. An area of two sq.cm as described by Bhat *et al.*,¹⁹ was defined with a marker on the shaven back of the animals. The marked circular area was excised with its full thickness using a surgical sterile blade and scissors under phenobarbitone anesthesia. The Control/ formulations were applied to the wounded rats of the respective groups three times a day. The wounded rats of the first group were used as the baseline control for all the formulations. The application was repeated for 16 days post-operatively. The wound contractions were measured as the percentage of wound reduction in

the wound area for every four days. The progressive wound area reduction was monitored periodically by tracing the wound margin on paper, and the area was measured using graph paper. The wound size reduction was calculated by the formula:-

Wound contraction% = (difference in the area of the wound in mm² between the initial and on a particular post-operative day) × 100 / area of the wound in mm² immediately after the wound excision.

Statistical Analysis: The statistical significance was assessed using one-way analysis of variance (ANOVA) followed by the Holm-Sidak test and Bonferroni t-test. The values were expressed as mean ± SD, and P<0.05 was considered significant.

RESULTS AND DISCUSSION:

Total Phenolic Content: In a flavonoid-rich extract of both plants, total phenol content was also estimated. For total phenol content estimation (TPC) standard curve of Gallic acid was used and estimated as Gallic acid equivalent (GAE). Total Phenol Content in *Cassia auriculata* and *Cassia fistula* was found to be 67.32 and 63.84 µg/mg GAE, respectively.

TABLE 2: STANDARD CURVE OF GALLIC ACID

S. no.	Conc. (µg/mL)	Absorbance	Line of regression and R ₂
1	10	0.1098	Y=0.005x + 0.065 and R ₂ = 0.976
2	20	0.1763	
3	30	0.2468	
4	40	0.2981	
5	50	0.3258	

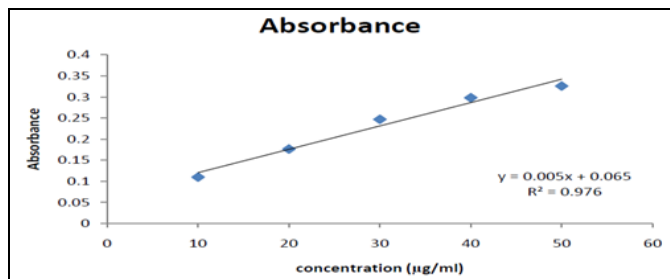


FIG. 1: STANDARD CURVE OF GALLIC ACID

TABLE 3: TOTAL PHENOLIC CONTENT

S. no.	Test sample	Absorbance	Total phenol content (GAE) µg/mL
1	CAF	0.4016	67.32
2	CFF	0.3842	63.84

DPPH Free Radical Scavenging Activity: Antioxidant potential of the flavonoid-rich extract

was ascertained by an effect on percentage inhibition of DPPH free radicals. DPPH assay was done by the concentration required for 50% inhibition (IC₅₀). Flavonoids-rich extract of *Cassia auriculata* showed a significant effect on DPPH free radicals. In the concentration range of 10 µg/ml to 100 µg/ml, the goodness of fit for a line of regression was good with R₂ = 0.976. IC₅₀ was found to be 60.97µg/ml. In the DPPH assay effect of flavonoids, a rich extract of *Cassia fistula* was not significantly different as compared to flavonoids rich extract of *Cassia auriculata*. IC₅₀ in DPPH assay was 62.19µg/ml for extract.

TABLE 4: EFFECT OF CAF IN DPPH FREE RADICAL SCAVENGING ASSAY

S. no.	Conc. (µg/mL)	% inhibition	IC ₅₀
1	10	21.46	60.977
2	20	28.67	
3	40	32.25	
4	60	48.56	
5	80	64.24	
6	100	72.5	

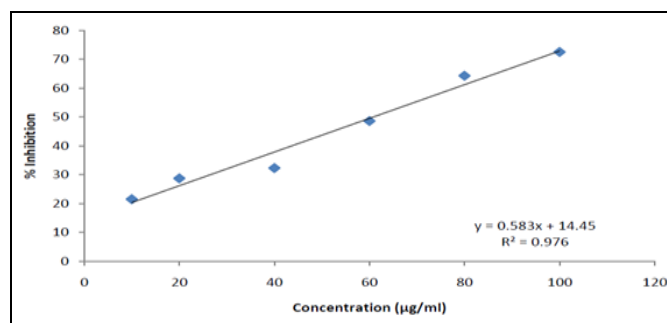


FIG. 2: EFFECT OF CAF IN DPPH FREE RADICAL SCAVENGING ASSAY

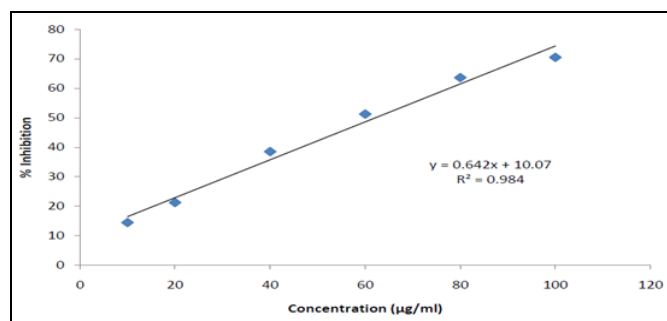


FIG. 3: EFFECT OF CFF IN DPPH FREE RADICAL SCAVENGING ASSAY

TABLE 5: EFFECT OF CFF IN DPPH FREE RADICAL SCAVENGING ASSAY

S. no.	Conc. (µg/mL)	% inhibition	IC ₅₀
1	10	14.5	62.196
2	20	21.26	
3	40	38.55	
4	60	51.26	
5	80	63.62	
6	100	70.5	

Evaluation of Polyherbal Gel Formulations:**TABLE 6: EVALUATION OF POLYHERBAL GEL FORMULATIONS**

S. no.	Treatment	% Wound Contraction (Day)			
		4	8	12	16
1	Control (gel base)	11.00±2.10	23.67±2.88	45.83±2.64	59.17±5.19
2	F1	14.33±2.25	32.17±2.14 ^{ab}	60.67±4.89 ^a	77.83±5.78 ^b
3	F2	13.83±1.60	30.17±3.43 ^{ab}	58.17±3.19 ^{ab}	70.00±5.73 ^{ac}
4	F3	15.17±1.33	32.83±2.64 ^{ab}	61.00±1.90 ^{ab}	79.17±3.31 ^b
5	Standard Cream	16.17±2.04	40.00±4.05	68.33±2.16 ^b	86.33±5.32 ^b

All Data presented in mean ± SD, ^a P<0.05 as compared to Standard cream treated a group, ^b P<0.05 as compared to gel base treated a group, ^c P<0.05 as compared to F3 treated a group

The flavonoid-rich extract had antimicrobial and antioxidant property they were incorporated in a gel base for topical use. Basic consideration was used in cancerous wounds. Carbopo l 934 was used as a gel base and Triethanolamine as a neutralizing agent for pH changes due to Carbopol. Ten % extract formulations were prepared in which F1 consisted of CAF (flavonoids rich extract of CAF), F2 of CFF (flavonoids rich extract of CFF), and F3 of CAF and CFF in equal proportion. The formulated gel accelerates the wound healing process which may be due to enhancing the cellular defense mechanisms, proliferation, suppression of inflammation, and contraction of the collagen tissue and could be delayed by reactive oxygen species or microbial infection ¹⁶.

The wound healing property of extract was ascertained by percentage contraction of the wound. The observation was done on the fourth, eighth, 12th, and 16th day. It was observed that on fourth -day formulation one and two were not having any significant effect on wound contraction as compared to the control group, but different formulation which was having an equal proportion of both extracts showed a significant effect (P<0.05) as compared to control group. Thus it could be considered that components present in both extracts, when combined in equal proportion, would be giving a synergistic effect when combined in equal proportion. Afterward, it was observed that formulation F1, F2, and F3 showed a better effect as a wound healing activity. On the eighth, 12th, and 16th day, all formulations showed a significant effect (P<0.05) as compared to the control group. The study results demonstrated that F3 was better than F2 and F1, and F2 was better than F1. Flavonoids have been possessing the antioxidant potential and free radical scavenging effect, which is believed to be one of the important

components of wound healing. Bioflavonoids are thought to benefit connective tissue by binding to elastin, preventing its degradation by elastases ²⁰. Many studies have shown that antimicrobial activities of plants can also be attributed to their flavonoids content ²¹⁻²²; hence, they are helpful in the prevention of wound infection. Most of the delay in wound healing is due to insufficient or excessive fibroblast activity. Thus, inhibition of fibroblast growth by flavonoids such as apigenin could be beneficial for the treatment of any skin injury.

CONCLUSION: The present study concludes that the polyherbal gel of the extracts of CFF and CAF has significant wound healing activity. The better activity of polyherbal formulation could be due to the synergistic action of the plant's constituents present in the formulation. The phytoconstituents like flavonoids are known to promote the wound healing process due to their anti-oxidant properties. The investigation reveals that the wound healing activity of polyherbal formulation may be due to the combined action and presence of phytoconstituents.

ACKNOWLEDGEMENT: The authors thank Rajarshi Shahu College of Pharmacy, Buldana for providing facilities to conduct the research.

CONFLICTS OF INTEREST: There are no conflicts of interest among all the authors with the publication of the manuscript.

REFERENCES:

1. Kumarasamyraja D, Jeganathan NS and Manavalan R: A review on medicinal plants with potential wound healing activity. *Int J Pharm Pharm Sci* 2012; 2: 105-07.
2. Takeo M, Lee W and Ito M: Wound healing and skin regeneration. *Cold Spring Harbor Perspectives in Medicine* 2015; 5(1): a023267.

3. Janis JE and Harrison B: Wound healing, part I; Basic science. *Plastic and Reconstructive Surgery*. 2014; 133(2): 199e-207e.
4. Dai T, Tanaka M, Huang YY and Hamblin MR: Chitosan preparations for wounds and burns: antimicrobial and wound-healing effects. *Expert Review of Anti-infective Therapy* 2011; 9(7): 857-79.
5. Esat DM, Temel S, Ozer H, Kemal UM, Kaya F, Aslan F, Celepli P, Senes M, Dogan K, Kuru S and Mutlu BA: Comparison of the effects of platelet-rich plasma prepared in various forms on the healing of dermal wounds in rats. *Wounds: a compendium of clinical research and practice*. 2016; 28(3): 99.
6. Latif MA, Zaki MZ, Leng TM, Rahman NH, Arshad SA and Hamid A: *Alocasia denudata* Engler treatment enhance open wound healing activities in Wistar rat's skin. *J Ethnopharmacol* 2015; 176: 258-67.
7. Marume A, Matope G, Katsande S, Khoza S, Mutingwende I and Mduluzi T: Wound Healing Properties of Selected Plants Used in Ethnoveterinary Medicine. *Frontiers in Pharmacology* 2017; 8: 544.
8. Khare CP: *Indian Medicinal Plants*: Springer-Verlag New York 2007. 127.
9. Prakash Yoganandam G, Gopal V and Thanka J: Aavara kudineer-A potent polyherbal siddha formulation for management of diabetes mellitus. *International Journal of Pharmaceutical Development & Technol* 2014; 4: 98-103.
10. Hossain E, Mandal SC and Gupta JK. Phytochemical screening and in-vivo antipyretic activity of the methanol leaf-extract of *Bombax malabaricum* DC (Bombacaceae). *Tropical Journal of Pharmaceutical Research* 2011; 10(1).
11. Latha M and Pari L: Antihyperglycaemic effect of *Cassia auriculata* in experimental diabetes and its effects on key metabolic enzymes involved in carbohydrate metabolism. *Clin Exp Pharmacol Physiol* 2003; 30(1-2): 38-43.
12. Swapna NL, Prasad MA and Prasad S: Efficacy of *Euphorbia tirucalli* (L) towards microbicidal activity against human pathogens. *Int J Pharm Bio Sci* 2011; 2: 12-8.
13. Teleszko M and Wojdyło A: Comparison of phenolic compounds and antioxidant potential between selected edible fruits and their leaves. *Journal of Functional Foods* 2015; 14: 736-46.
14. Sulaiman CT and Balachandran I: Total phenolics and total flavonoids in selected Indian medicinal plants. *Indian Journal of Pharmaceutical Sciences* 2012; 74(3): 258.
15. Wojtunik KA, Ciesla LM and Waksmundzka-Hajnos M: Model studies on the antioxidant activity of common terpenoid constituents of essential oils by means of the 2, 2-diphenyl-1-picrylhydrazyl method. *Journal of Agricultural and Food Chemistry* 2014; 62(37): 9088-94.
16. Alqasoumi SI, Yusufoglu HS and Alam A: Anti-inflammatory and wound healing activity of *Fagonia schweinfurthii* alcoholic extract herbal gel on albino rats. *African Journal of Pharmacy and Pharmacology* 2011; 5(17): 1996-2001.
17. Sharma A, Dwivedi DS, Mishra G and Joshi H: Formulation and evaluation of herbal gel containing extracts of *Albezia lebbeck* linn. *Am J PharmTech Res* 2012; 2(4): 663-68.
18. Pandey A, Jagtap JV and Polshettiwar SA: Formulation and evaluation of *in-vitro* antimicrobial activity of gel containing essential oils and effect of polymer on their antimicrobial activity. *Int J Pharm Pharm Sci* 2011; 3: 234-37.
19. Fahimi S, Abdollahi M, Mortazavi SA, Hajimehdipoor H, Abdolghaffari AH and Rezvanfar MA: Wound healing activity of a traditionally used poly herbal product in a burn wound model in rats. *Iranian Red Crescent Medical Journal*. 2015; 17(9): 1-8.
20. Sugumar S, Ghosh V, Nirmala MJ, Mukherjee A and Chandrasekaran N: Ultrasonic emulsification of eucalyptus oil nanoemulsion: antibacterial activity against *Staphylococcus aureus* and wound healing activity in Wistar rats. *Ultrasonics sonochemistry* 2014; 21(3): 1044-9.
21. Ammar I, Bardaa S, Mzid M, Sahnoun Z, Rebaï T, Attia H and Ennouri M. Antioxidant, antibacterial and *in-vivo* dermal wound healing effects of *Opuntia* flower extracts. *International Journal of Biological Macromolecules*. 2015; 81: 483-90.
22. Ye D, Zhong Z, Xu H, Chang C, Yang Z, Wang Y, Ye Q and Zhang L: Construction of cellulose/nanosilver sponge materials and their antibacterial activities for infected wounds healing. *Cellulose* 2016; 23(1): 749-63.

How to cite this article:

Kewatkar SM, Paithankar VV, Deshpande SS, Jain SP and Nagore DH: Antioxidant activity of *Cassia auriculata* and *Cassia fistula* extract along with wound healing activity of its polyherbal formulation. *Int J Pharm Sci & Res* 2021; 12(3): 1805-10. doi: 10.13040/IJPSR.0975-8232.12(3).1805-10.

All © 2013 are reserved by the International Journal of Pharmaceutical Sciences and Research. This Journal licensed under a Creative Commons Attribution-NonCommercial-ShareAlike 3.0 Unported License.

This article can be downloaded to **Android OS** based mobile. Scan QR Code using Code/Bar Scanner from your mobile. (Scanners are available on Google Playstore)



Comparative Pharmacognostical and Phytochemical Study of *Cassia auriculata* and *Cassia fistula*

Shailesh M. Kewatkar^{1*}, Vivek V. Paithankar², Supriya S. Deshpande³, Shirish P. Jain¹, Dheeraj H. Nagore⁴, Dipak V. Bhusari¹, Chanchal Navin Raj⁵, Madhav D. Chakolkar¹ and Trupti A. Nimburkar⁶

¹Rajarshi Shahu College of Pharmacy, Buldana – 443001, Maharashtra, India; kewatkar.shailesh@gmail.com

²Vidyabharti College of Pharmacy, Amravati – 444602, Maharashtra, India

³Dr. Panjabrao Deshmukh Medical College, Amravati – 444603, Maharashtra, India

⁴Mprex Healthcare Pvt. Ltd., Wakad – 411057, Pune, India

⁵Shri D. D. Vispute College of Pharmacy and Research Center, New Panvel – 410221, Maharashtra, India

⁶Dr. Rajendra Gode College of Pharmacy, Amravati – 444901, Maharashtra, India

Abstract

Cassia auriculata L. (CAL) popularly identified as Tanner's Cassia and *Cassia fistula* L. (CFL) is generally known as Golden Shower. Both plants belong to the Family, Fabaceae. These plants are used in skin disease, as hepatoprotective, as anticancer agent and as antioxidant agent. The intention of current article is to put forward the comparative pharmacognostical analysis of *Cassia auriculata* and *Cassia fistula* roots in terms of macroscopic evaluation, microscopic evaluation, physicochemical evaluation, extractive values and phytochemical analysis. Thin Layer Chromatography study was carried out for CAL and CFL and data pertaining to the above cited evaluations were recorded for both, CAL and CFL roots. The present study may help in differentiating among these species and these pharmacognostic parameters may serve as a tool for identification, authentication and standardization of CAL and CFL.

Keywords: *Cassia auriculata*, *Cassia fistula*, Microscopy, Phytochemical evaluation

1. Introduction

CAL is usually well-known as Tanner's Cassia, which fit in to the Family Fabaceae. The said plant is spread in Indian county and subcontinents. In Indian traditional system of medicine, the leaf and flower along with Triphala are utilized in the management of diabetic problems. The root of *cassia* is alexeteric and reported to be useful in thirst and respiratory problems. The leaves showed anthelmintic potential and they are supportive in the management of ulcers. The flowers are also reported to be useful in the treatment of throat complications^{1,2}. Preclinical and clinical research have showed that roots have ephroprotective potential, leaves also showed liver protective action along with other health benefits³⁻¹¹.

CFL normally identified as Golden Shower belonging to Family Fabaceae, also well-known as Amaltas. The herb is found throughout the country. It is scattered in numerous countries including Asia, Mexico, East Africa, South Africa and West Indies along with Brazil. The root is generally consumed as a stimulant and febrifuge. It also shows potential as a strong laxative. In ayurvedic literature, root is used in skin problems like leprosy. The flowers are useful in treating cough and related problems, even flatulence. In Unani system of medicine, the leaf of CFL diminishes the edema. The flowers are used as a purgative. The seeds are used as an emetic. The described uses of CFL are as antibacterial, liver protective, wound healing, anti feedant, larvicidal, antifungal, protease inhibitor, anticancer and antifertility, antioxidant action¹²⁻²⁰.

*Author for correspondenc

2. Materials and Methods

2.1 Procurement and Authentication of Plants

The roots of the plant CAL and CFL had been gathered from regions of Walgaon Road, Amravati, Maharashtra and some area of Bhopal, Madhya Pradesh respectively. Both the herbs have been validated by Safia College of Science, Bhopal, (MP), and the voucher specimen records were 159/Bot/Safia/2010 (CAL) and 160/Bot/Safia/2010 (CFL).

2.2 Preparation of Flavonoid Rich Fraction

The extraction of selected part of the herb for getting flavonoids rich fraction had been carried out. Roots of CAL and CFL (2 kg each) were dried under shade, and ground to get the coarse powdered material. Powdered roots of the plant were extracted with water by decoction method. While preparing the decoction, some precaution was taken regarding temperature, it was ensured that temperature did not exceed $40^{\circ}\text{C} \pm 5^{\circ}\text{C}$ as it would lead to precipitation or crystallization of various phytoconstituents which will not be soluble in any solvent for further process. The extracted aqueous sample was filtered and alcohol (ethanol) was poured to precipitate out polysaccharides which are present in the roots of the individual plant. The precipitated solution was filtered and the filtrate was evaporated to $1/4^{\text{th}}$ of the total volume. This was consecutively extracted with equivalent quantity of ethyl acetate with the aid of separating funnel to get separate fraction of root constituents. Then the ethyl acetate extract was acidified to raise the yield of the extract. The ethyl acetate fraction was evaporated to obtain a precipitate which was then dissolved in methanol and evaporated gradually to obtain crystalline powder.

The finally obtained powder was investigated for the occurrence of active phytoconstituents. The powder tested positive for Shinoda test for the Flavonoids. The positivity for flavonoids was also confirmed by TLC in appropriate solvent system. Similarly, the roots of both plants were used to obtain saponin rich fraction. Crushed plant material was macerated with ethanol: water (70:30) for seven days after defatting with petroleum ether (40:60). The extract so obtained was filtered through a muslin cloth followed by filter paper. Later this was concentrated using rotary vacuum evaporator (40°C) with precaution that extract does not get powdered. N-butanol was used to treat concentrated extract to obtain n-butanol soluble fraction. N-butanol fraction was further reacted with chilled diethyl ether to form a precipitate. This

combination with precipitate was reserved at -20°C for 24 hrs. Precipitates were further alienated by centrifugation. These precipitates were dissolved in methanol and methanol was evaporated, to get a crystalline powder²¹. Powder was analysed for the presence/absence of different phytoconstituents. Positive results for froth test and hemolysis test was observed in powders, which confirms the occurrence of saponin in powder. Further purity of powder was confirmed on the basis of TLC. It was observed that few extra spots were present in solvent system (BAW). Obtained powder was further purified using column chromatography by solvent on the basis of their polarity. Purity was again confirmed on the basis of TLC.

2.3 Macroscopical Characters

External features, dimensions and organoleptic properties of roots were studied.

2.4 Microscopical Characters

2.4.1 Collection of Specimens

The plant specimen was gathered. Precaution was taken to choose healthy sample. The root was dipped in FAA (Formalin + acetic acid + 70% ethanol). After 24 hours of fixing, the samples were dehydrated with graded series of tertiary butyl alcohol (TBA). Infiltration of the specimens was conceded by slow addition of paraffin wax until TBA solution attained saturation. Then the roots were moved into paraffin blocks.

2.4.2 Sectioning

With the help of Rotary Microtone, the paraffin entrenched specimens were sectioned. The width of the sections was $10 - 12 \mu\text{m}$. Dewaxing was conceded by customary method. Toluidine blue, a polychromatic stain was used to stain the sections. Satisfactory results were obtained by staining and some cytochemical reactions were also obtained. Cellulose walls were stained pink color with the dye, lignified cells stained blue, dark green to suberin, dark violet to mucilage, light blue to the protein bodies where essential sections were also stained with safranin and fast green and potassium iodide (for starch). Glycerine mounted temporary preparations were cleared with sodium hydroxide (NaOH) and after staining they were mounted in glycerine medium and the variant cell components were studied and measured.

2.5 Microphotography

Microscopic characterization of tissues was done with micrographs. Nikon lab photo 2 microscopic units were

used for taking photographs with different magnifications. Intense field was used for standard observation of the components. Polarizer was used to study the crystals, starch, grains and lignified cells. The results were vivid against dark background under the polarizer. Scale bars were used to indicate magnifications of the figures²³.

2.6 Physicochemical Evaluation of Crude Powdered Material^{22,23}

2.6.1 Ash Value

Ash values for the roots such as total ash value, acid insoluble and water soluble ash value were investigated.

2.6.2 Extractive Value

Extractive values for the roots such as water soluble and alcohol soluble extractive values were investigated.

2.7 Thin Layer Chromatography

2.7.1 Detection of Flavonoids and their Glycosides

Detection: At UV 365nm and visible light the developed TLC plate was observed. Flavonoids and their glycosides emerged as yellow, dark blue, orange spots. The color gels intensified on exposure of the plates to ammonia vapors. Following spraying agents were used for finding the flavonoids and their glycosides,

- Vanillin-Sulphuric acid
- Anisaldehyde-sulphuric acid

2.7.2 Detection of Saponins

Detection: The developed TLC plate was experiential in visible light and in UV at 365 nm. Following spraying agents were used for detection of saponins,

- Vanillin-Sulphuric acid
- Anisaldehyde-sulphuric acid

2.8 High performance thin layer chromatography

2.8.1 Sample Application

Commercially available pre-coated plates of silica gel GF254 were used. Flavonoid rich fractions were spotted on plates with bandwidth of 6mm. Application rate was 10µl/ min, using Linomat V applicator (Automatic TLC plate applicator, Camag, Switzerland). A sample volume of 10 and 20µl was applied.

2.8.2 Development of Chromatogram

The plate was allowed to run in twin trough chamber (20×10) using the solvent system. After developing, the plates were air dried and observed under Camag UV chamber 4.

2.8.3 Densitometric Scanning

The developed plates were scanned using densitometer at 254 nm (Camag TLC scanner – 4, combined with integration software, Win CATS 4.06, Switzerland).

3. Results

3.1 Microscopy

3.1.1 Microscopic Characters of CAL Roots

The root measuring 2.3mm diameter was studied. The surface of the root was deeply and irregularly fissured. The periderm outer part exfoliates into small, irregular fragments. The root consists of thick periderm, narrow cortex and wide and continuous secondary phloem. The secondary xylem was thick and dense (Figure 1).

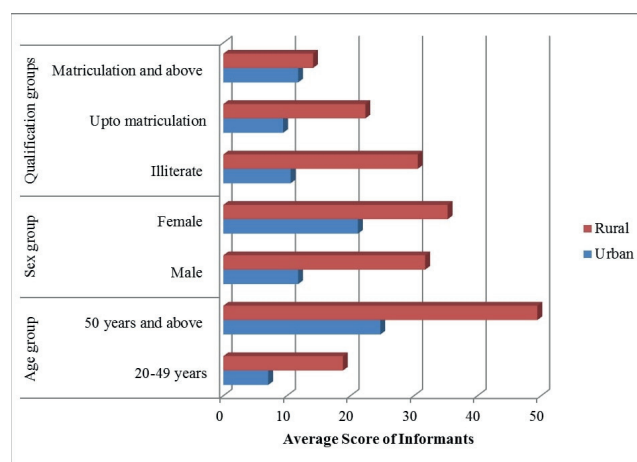
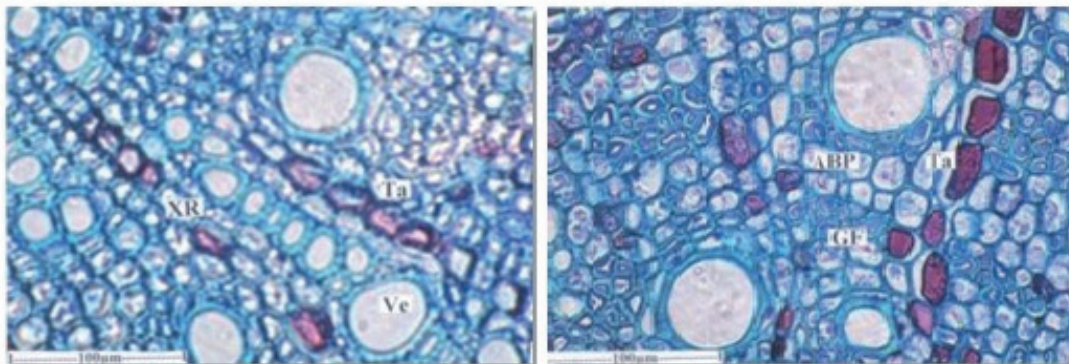


Figure 1. Transverse section of root - entire view.

The periderm consists of wide, darkly stained and thick walled phloem which was 150 cm thick. The cells contain darkly stained amorphous inclusions. The cells were tabular in shape and supervised. The inner part of the periderm had phelloderm which was 30 cm thick. It consists of thin walled radial files of tabular cells. The cortical zone was narrow comprising large, polygonal, compact thick walled cells.

Cortex was followed by secondary phloem which was 80cm thick. It includes sieve elements, phloem rays and phloem parenchyma. The inner part of the phloem consists of fairly wide, rectangular cells arranged in regular, radial files. The outer part of the phloem includes a narrow zone of collapsed phloem where the delicate cells were crushed into dark, thick tangential line. The inner part includes circular, clusters of sieve elements where the elements were narrow, thick walled cells.

Secondary xylem was about 1 mm in diameter. It consists of narrow, circular, solitary, thick walled diffusely distributed vessels (Figure 2). The vessels were 15-50 μm wide. There were tangential bands of apotrachial parenchyma cells. The parenchyma cells were wide angular and thick walled. The xylem rays were one or two cells thick, straight and they were filled with brown colored tannin. The xylem fibers were mostly gelatinous type. They had inner gelatinous or mucilaginous substance.



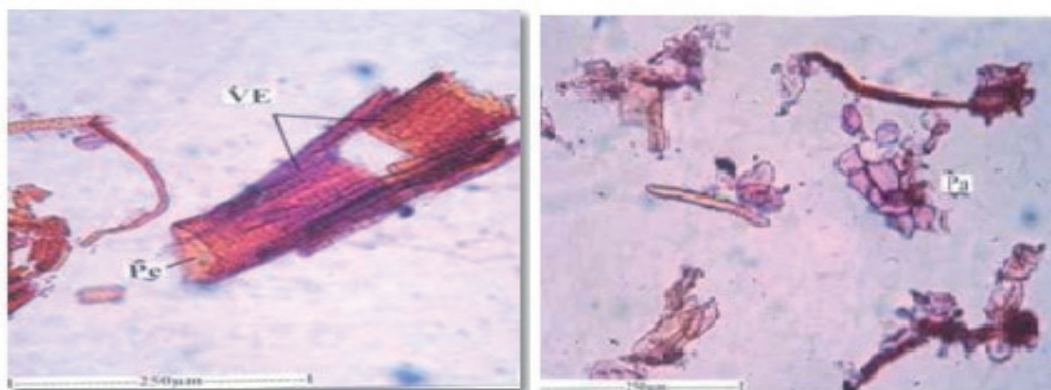
ABP- Apotrachial band of parenchyma, GF- Gelatinous Fibers, Ta- Tannin, Ve- Vessel, XR- Xylem Rays

Figure 2. T.S. of secondary xylem showing solitary vessels, apotrachial band of parenchyma and tannin filled xylem rays.

3.1.2 Powder Microscopy

The powder of the root consists of vessels elements, fibers, Sclereids and parenchyma cells. The vessel elements were cylindrical, long or short and wide. The vessel elements range from 100-200 μm long. They had dense, multiseriate, elliptical bordered pits on the lateral walls and wide circular, oblique or horizontal perforation on the end walls. The fibers were narrow and wide. The narrow

fibers were thick walled with narrow lumen. They were 710 μm long. The wide fibers were short, thin walled with wide lumen. They were 470 μm long. The Sclereids were long, narrow and fiber like. They have thick lignified walls with dense and prominent canal-like simple pits. Some of the sclereids were wider in the middle and tapering at the ends. Small polygonal thick walled parenchyma cells were seen scattered in the powder. The cells do not have any cell inclusions (Figure 3).



Pe- Perforation, Pi- Pits, VE- Vessel Elements, Pa- Parenchyma

Figure 3. Vessel elements and parenchyma cells.

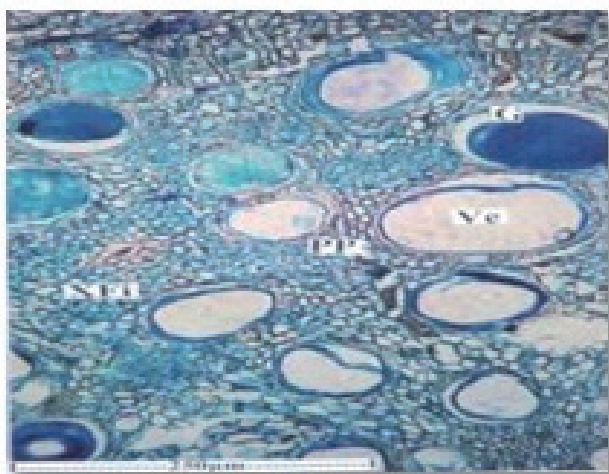
3.1.3 Microscopic Characters of CFL Roots

Root sample having minimum 2.2 mm thickness was studied. It was circular in outline with more or less smooth outline. The root consists of periderm, cortex, secondary phloem and secondary xylem cylinder.

Periderm was continuous all around the root and more or less uniform in thickness. It was 300cm thick in radial plane. The periderm includes several layers of dark brown narrowly tabular radial files of phellem cells and 2 layers of wide, square in phelloderm cells.

The cortical zone includes polygonal, compact parenchyma cells and small scattered clusters of gelatinous fibers. Some of the cortical cells also had tannin content. Secondary xylem cylinder was solid with circular outline. It also showed wide, circular, diffusely distributed vessel elements. The vessel element ranges from 40-150µm in diameter. Some of the vessel elements were filled with amorphous gummy substance. The secondary xylem also consists of xylem fibers and xylem parenchyma.

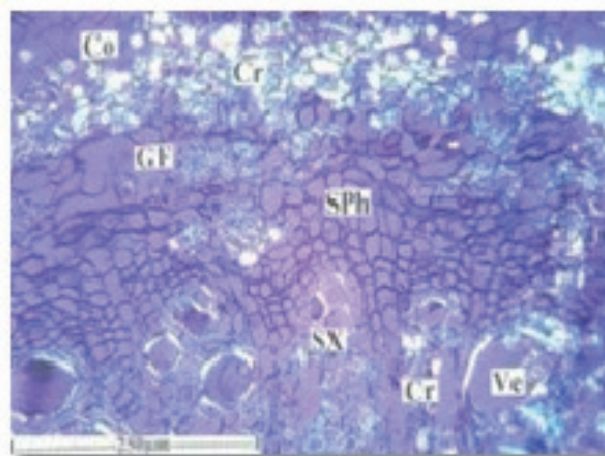
The fibers were libriform type, thick walled with narrow lumen (Figure 4). Xylem parenchyma occurs in the form of thick sheath around the vessels. They are called paratrachial parenchyma. The secondary phloem consists of outer part of collapsed phloem cells forming dark, thick, tangential lines. Intact non-collapsed phloem was found inner to the collapsed part. In this region the phloem elements were intact with small clusters of sieve elements and polygonal wide parenchyma cells. Calcium oxalate crystals were abundant in the middle cortical zone. Prismatic types of crystals were exclusively observed.



Pp- Paratrachial Parenchyma, Ve- Vessel, XFi- Xylem Fiber, G- Gum

Figure 4. Secondary xylem showing gum inclusions in the vessels.

The crystals also occur in the xylem parenchyma which encloses the vessel (Figure 5).



Co- Cortex, Cph- Collapsed phloem, Cr- Crystal, GF- Gelatinous Fibers, NCph- Non collapsed phloem, Pp- Paratrachial Parenchyma, Sph- Secondary Phloem, SX- Secondary xylem, Ve- Vessel, XFi- Xylem Fiber, G- Gum

Figure 5. Crystal distribution in the bark.

3.1.4 Powder Microscopy

The root powder included fiber, vessel elements and periderm fragments. Parenchyma cells were also occasionally seen. The fibers were of two types. Many of the fibers were wide, thin walled and short. They were 1 mm long and 40 µm wide. Some crystalline bodies of unknown chemical nature were often seen inside the wide fibers. Narrow fibers were less common they were 550µm long 10 µm thick. The walls were thick and lignified. The lumen was narrow and no inclusions were seen in the cell lumen. The vessel elements were also of two types. Some were narrow, long and resemble the wide fibers in size and shape. The narrow vessel elements had short tails at both ends. The vessel elements had minute, circular, multiseriate pits on the lateral walls. The perforation of the wide vessels was circular and horizontal in orientation. The narrow vessels elements were 280 µm long 20 µm wide. The wide vessel elements were 120 µm long and 40 µm wide.

3.2 Thin Layer Chromatography

TLC characterization of fractions of CAL and CFL has been discussed in Table 1. Flavonoids rich extracts of both the plants were subjected to HPTLC studies using solvents

of varying polarity, Rf values of the separated components were found out. The number of components separated in the extracts, their Rf values and their percentage area were represented in respective tables.

Table 1. TLC characterization of fractions of *Cassia auriculata* and *Cassia fistula*

Sr. No.	Mobile Phase	Spraying Reagent	No. of Spots		Rf Value		Inference
			CAL	CFL	CAL	CFL	
1	Chloroform: Methanol	Ammonia vapour/ VS reagent	2	1	0.24, 0.83	0.62	Flavonoids
2	Ethyl acetate: Formic acid: Glacial acetic acid: Water	Ammonia vapour/ VS reagent	2	3	0.35, 0.53	0.27, 0.42, 0.70	Flavonoids
3	Chloroform: Gallic acid: Methanol: Water	Anisaldehyde sulphuric Acid reagent	1	2	0.22	0.47, 0.71	Saponins
4	Chloroform: Methanol: Water	Vanillin phosphoric acid reagent	2	2	0.14, 0.20	0.57, 0.61	Saponins

HPTLC was carried out by using following solvent systems, ethyl acetate: acetic acid: formic acid: water [100:11:11:26] (EAFW). HPTLC Fingerprinting of CAL at 254 has been discussed in Figures 6 and 7. HPTLC Fingerprinting of

CFL at 254 shown in Figures 8 and 9. Correlation between reported and observed Rf values of various constituents has been observed in Table 2.

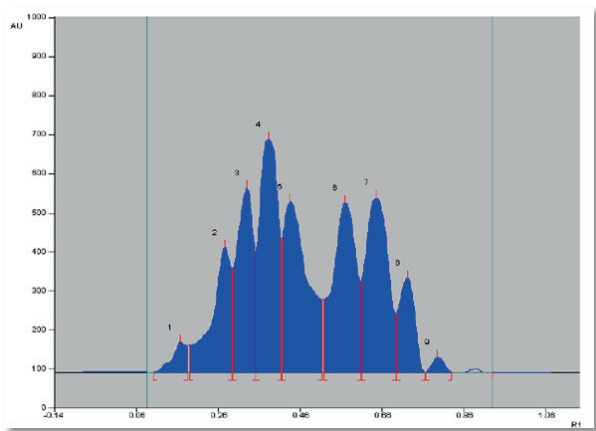


Figure 6. HPTLC fingerprinting of CAL at 254 nm.

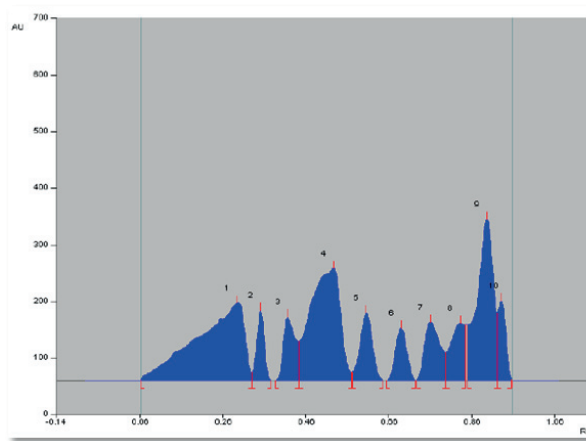


Figure 8. HPTLC Absorbance of CFL at 254 nm.

Peak	Start Position	Start Height	Max Position	Max Height	Max %	End Position	End Height	Area	Area %	Assigned substance
1	0.10 Rf	0.1 AU	0.17 Rf	76.5 AU	2.50 %	0.18 Rf	37.6 AU	2162.4 AU	1.80 %	unknown *
2	0.19 Rf	69.0 AU	0.27 Rf	318.9 AU	10.42 %	0.29 Rf	33.2 AU	12180.9 AU	10.13 %	unknown *
3	0.29 Rf	264.7 AU	0.33 Rf	472.2 AU	15.43 %	0.35 Rf	33.0 AU	15210.3 AU	12.65 %	unknown *
4	0.35 Rf	305.3 AU	0.38 Rf	596.3 AU	19.49 %	0.41 Rf	41.0 AU	21576.1 AU	17.94 %	unknown *
5	0.41 Rf	343.7 AU	0.43 Rf	436.5 AU	14.27 %	0.51 Rf	35.8 AU	21147.3 AU	17.59 %	unknown *
6	0.52 Rf	186.5 AU	0.57 Rf	433.2 AU	14.16 %	0.61 Rf	31.9 AU	19830.2 AU	16.49 %	unknown *
7	0.61 Rf	233.5 AU	0.65 Rf	446.2 AU	14.58 %	0.69 Rf	49.0 AU	19911.7 AU	16.56 %	unknown *
8	0.69 Rf	150.1 AU	0.72 Rf	241.0 AU	7.88 %	0.76 Rf	0.2 AU	7330.7 AU	6.10 %	unknown *
9	0.77 Rf	0.3 AU	0.79 Rf	38.9 AU	1.27 %	0.83 Rf	1.4 AU	900.9 AU	0.75 %	unknown *

Figure 7. HPTLC fingerprinting of CAL at 254 nm.

Peak	Start Position	Start Height	Max Position	Max Height	Max %	End Position	End Height	Area	Area %	Assigned substance
1	0.06 Rf	1.3 AU	0.29 Rf	137.0 AU	9.70 %	0.33 Rf	13.9 AU	12595.4 AU	25.11 %	unknown *
2	0.33 Rf	14.4 AU	0.35 Rf	123.4 AU	8.75 %	0.36 Rf	0.0 AU	1774.9 AU	3.54 %	unknown *
3	0.39 Rf	0.0 AU	0.42 Rf	112.0 AU	7.94 %	0.44 Rf	39.4 AU	2510.8 AU	5.01 %	unknown *
4	0.44 Rf	69.5 AU	0.53 Rf	197.7 AU	14.01 %	0.57 Rf	14.6 AU	11540.3 AU	23.01 %	unknown *
5	0.57 Rf	14.6 AU	0.61 Rf	119.6 AU	8.47 %	0.65 Rf	0.3 AU	2818.5 AU	5.62 %	unknown *
6	0.65 Rf	0.0 AU	0.69 Rf	93.0 AU	6.59 %	0.72 Rf	0.0 AU	2016.6 AU	4.02 %	unknown *
7	0.73 Rf	0.1 AU	0.76 Rf	102.9 AU	7.29 %	0.80 Rf	50.1 AU	3141.5 AU	6.26 %	unknown *
8	0.80 Rf	50.1 AU	0.83 Rf	100.6 AU	7.13 %	0.84 Rf	38.0 AU	2712.4 AU	5.41 %	unknown *
9	0.85 Rf	97.9 AU	0.90 Rf	284.4 AU	20.15 %	0.92 Rf	18.0 AU	8985.6 AU	17.91 %	unknown *
10	0.92 Rf	119.4 AU	0.93 Rf	140.9 AU	9.99 %	0.96 Rf	0.7 AU	2067.6 AU	4.12 %	unknown *

Figure 9. HPTLC fingerprinting of CFL at 254 nm.

Table 2. Correlation between reported and observed Rf value

Sr.no	Name of the Constituents	Reported Rf value	Observed Rf value
1	Chlorogenic Acid	0.45, 0.50	0.44
2	Isochlorogenic acid	0.80	0.80
3	Caffeic acid	0.90	0.92
4	Rutin	0.40	0.41
5	Apigenin 7-o-glucoside	0.75	0.76
6	Quercetin	0.35-0.75	0.29, 0.35, 0.38
7	Quercetin	0.80, 0.74	0.72, 0.84
8	Isoquercitrin	0.80, 0.60	0.57, 0.61, 0.79
9	Avicularin	0.85	0.83
10	Vitexin, 2-rhamnoside	0.45	0.33, 0.42
11	Vitexin	0.70	0.65
12	Luteolin	0.40-0.55	0.51
13	Kampeferol	0.40	0.31, 0.47
14	Flavone 6 - glycosides	0.65	0.69, 0.65, 0.67
15	Isoorientin	0.45	0.42

4. Discussion

All plants have their unique nature, structure, appearance, chemical constituents and therapeutic efficacy. Therefore, it is essential to study organoleptic properties of a medicinal plant, not only for quality control and standardization but also to recognize its structure and biology.

CAL and CFL were used by traditional practitioners for management of several ailments. Regularity of herbal products is a multifaceted task due to their diverse composition in all forms of the material. To protect reproducible quality of herbal products, appropriate control of starting material is essential. The primary step towards ensuring quality of preliminary material is

verification of the species. Now a days there has been a rapid increase in the standardization of many medicinal herbs of latent healing significance. Although many fresh techniques are available still identification of herbs by pharmacognostic properties is more liable. The macroscopic and microscopic explanation of a medicinal plant is the first step to create an identity and the purity of materials and should be conceded by undertaking any other tests, as described by World Health Organization²⁴.

Hence, it was felt desirable to pursue study on pharmacognostical and preliminary phytochemical studies of CAL and CFL roots to supplement useful information with regard to the exact identity of this plant

and, as this plant is extensively used in indigenous system of medicine.

Morphological assessment of drugs refer to valuation of drugs by taste, size, color, odor, shape and special features, like texture, touch. It is a method of qualitative evaluation based on the study of morphological and sensory summary of whole drugs. Organoleptic estimation is the conclusions drained from studies resulted due to feeling on organs of senses. All these parameters were recorded for roots of both the plants, CAL and CFL²⁵.

Microscopical techniques provide thorough information on the crude drug. Microscopical scrutiny of crude drugs from plant source is vital for the recognition of the grounded or crushed materials. Single-handed thorough microscopy could not provide complete assessment profile of a herbal drug, still it can supply underneath evidence, which when combined with other analytical parameters can be used to find the full confirmation for standardization and estimation of herbal drugs. Restricted burning of crude drugs result in an ash residue consisting of inorganic materials (metallic salts and silica). This value varies within fairly wide limits and hence a significant factor for the intention of evaluation of crude drugs. More direct contamination, such as by sand or earth, is immediately detected by the ash value. The quantity of active constituents in a given quantity of plant material when extracted with solvents is determined from the different extractive values obtained. Extractive values were used as revenue of evaluating crude drugs which were not eagerly expected by other means²⁶. Presence of bioactive components can be ascertained on the basis of various phytochemical testing. Thus in present investigation, extracts of CAL and CFL were subjected to phytochemical testing, which revealed that both plant extracts of CAL and CFL have shown the presence of various pharmacologically active chemicals such as flavonoids, saponins, glycosides, phenolic compounds, tannins. This confirmed that the targeted active molecules were present in selected extracts.

5. Conclusion

The present study reports the comparison between macroscopic, microscopic, physicochemical parameters and phytochemical parameters of CAL and CFL. These parameters may help in differentiating among these species. Thus, pharmacognostic parameters may serve as a tool for identification, authentication and standardization of CAL and CFL.

6. Acknowledgements

The authors thank Rajarshi Shahu College of pharmacy, Buldana for providing facilities to conduct the research.

7. Conflict of Interest Statement

There are no conflicts of interest among all the authors with publication of manuscript.

8. References

1. Kirtikar KR, Basu BD. Indian medicinal plants. Dehradun. International book distributors; 1999.
2. Deshpande S, Kewatkar SM, Paithankar VV. In-vitro antioxidant activity of different fraction of roots of *Cassia auriculata* Linn. Drug Invention Today. 2013; 5(2):164–8. <https://doi.org/10.1016/j.dit.2013.05.006>
3. Annie S, Rajagopal PL, Malini S. Effect of *Cassia auriculata* Linn. root extract on cisplatin and gentamicin-induced renal injury. Phytomed. 2005; 12(8): 555–60. <https://doi.org/10.1016/j.phymed.2003.11.010>. PMID:16121515
4. Rajagopal SK, Manickam P, Periyasamy V, Nama sivayam N. Activity of *Cassia auriculata* leaf extract in rats with alcoholic liver injury. J. Nutr. Biochem. 2003; 14(8):452–8. [https://doi.org/10.1016/S0955-2863\(03\)00053-6](https://doi.org/10.1016/S0955-2863(03)00053-6)
5. Gupta S, Sharma SB, Bansal SK, Prabhu KM. Antihyperglycemic and hypolipidemic activity of aqueous extract of *Cassia auriculata* L. leaves in experimental diabetes. Journal of Ethnopharmacol. 2009; 123(3):499–503. <https://doi.org/10.1016/j.jep.2009.02.019>. PMID:19473793
6. Prasanna R, Chandramoorthy HC, Ramaiyapillai P, Sakthisekaran D. In vitro evaluation of anticancer effect of *Cassia auriculata* leaf extract and curcumin through induction of apoptosis in human breast and larynx cancer cell lines. Biomed. Pre. Nutr. 2011; 1(2):153–60. <https://doi.org/10.1016/j.bionut.2010.12.006>
7. Sabu MC, Subburaju T. Effect of *Cassia auriculata* Linn. on serum glucose level, glucose utilization by isolated rat hemidiaphragm. J. Ethnopharmacol. 2002; 80(2–3):203–6. [https://doi.org/10.1016/S0378-8741\(02\)00026-0](https://doi.org/10.1016/S0378-8741(02)00026-0)
8. Kumaran A, Karunakaran RJ. Antioxidant activity of *Cassia auriculata* flowers. Fitoterapia. 2007; 78(1):46–7. <https://doi.org/10.1016/j.fitote.2006.09.031>. PMID:17071015
9. Thabrew I, Munasinghe J, Chackrewarthi S, Senarath S. The effects of *Cassia auriculata* and *Cardiospermum*

- halicacabum* teas on the steady state blood level and toxicity of carbamazepine. *J. Ethnopharmacol.* 2004; 90(1):145–50. <https://doi.org/10.1016/j.jep.2003.09.040>. PMID:14698522
10. Vijayaraj P, Muthukumar K, Sabarirajan J, Nachiappan V. Antihyperlipidemic activity of *Cassia auriculata* flowers in triton WR 1339 induced hyperlipidemic rats. *Exper. Toxicol. Pathology.* 2013; 65(1–2):135–41. <https://doi.org/10.1016/j.etp.2011.07.001>. PMID:21852078
 11. John CM, Sandrasaigaran P, Tong CK, Adam A, Ramasamy R. Immunomodulatory activity of poly phenols derived from *Cassia auriculata* flowers in aged rats. *Cellular Immun.* 2011; 271(2):474–9. <https://doi.org/10.1016/j.cellimm.2011.08.017>. PMID:21924708
 12. Duraipandiyan V, Ignacimuthu S. Antibacterial and antifungal activity of *Cassia fistula* L.: An ethno medicinal plant. *J. Ethnopharmacol.* 2007; 112(3):590–4. <https://doi.org/10.1016/j.jep.2007.04.008>. PMID:17532583
 13. Bhakta T, Mukherjee PK, Mukherjee K, Banerjee S, Mandal SC, Maity TK, Pal M, Saha BP. Evaluation of hepatoprotective activity of *Cassia fistula* leaf extract. *J. Ethnopharmacol.* 1999; 66(3):277–82. [https://doi.org/10.1016/S0378-8741\(98\)00220-7](https://doi.org/10.1016/S0378-8741(98)00220-7)
 14. Kumar MS, Sripriya R, Raghavan HV, Sehgal PK. Wound healing potential of *Cassia fistula* on infected albino rat model. *J. Surgical Res.* 2006; 131(2):283–9. <https://doi.org/10.1016/j.jss.2005.08.025>. PMID:16242721
 15. Siddhuraju P, Mohan PS, Becker K. Studies on the antioxidant activity of Indian Laburnum (*Cassia fistula* L.): A preliminary assessment of crude extracts from stem bark, leaves, flowers and fruit pulp. *Food Chem.* 2002; 79(1):61–7. [https://doi.org/10.1016/S0308-8146\(02\)00179-6](https://doi.org/10.1016/S0308-8146(02)00179-6)
 16. Manonmani G, Bhavapriya V, Kalpana S, Govindasamy S, Apparathanam T. Antioxidant activity of *Cassia fistula* (Linn.) flowers in alloxan induced diabetic rats. *J. Ethnopharmacol.* 2005; 97(1):39–42. <https://doi.org/10.1016/j.jep.2004.09.051>. PMID:15652272
 17. Duraipandiyan V, Ignacimuthu S, Paulraj MG. Antifeedant and larvicidal activities of Rhein isolated from the flowers of *Cassia fistula* L. *Saudi J. Bio. Sci.* 2011; 18(2):129–33. <https://doi.org/10.1016/j.sjbs.2010.12.009>. PMID:23961115 PMID:PMC3730718
 18. Wijaya R, Neumann GM, Condron R, Hughes AB, Polya GM. Defense proteins from seed of *Cassia fistula* includes a lipid transfer protein homologue and a protease inhibitory plant defense. *Plant Sci.* 2000; 159(2):243–55. [https://doi.org/10.1016/S0168-9452\(00\)00348-4](https://doi.org/10.1016/S0168-9452(00)00348-4)
 19. Gupta M, Mazumder UK, Rath N, Mukhopadhyay DK. Antitumor activity of methanolic extract of *Cassia fistula* L. seed against Ehrlich ascites carcinoma. *J. Ethnopharmacol.* 2000; 72(1–2):151–6. [https://doi.org/10.1016/S0378-8741\(00\)00227-0](https://doi.org/10.1016/S0378-8741(00)00227-0)
 20. Chauhan A, Agarwal M. Evaluating the antifertility potential of an aqueous extract from *Cassia fistula* seeds in male rats. *Fert. Ster.* 2010; 93(5):1706–10. <https://doi.org/10.1016/j.fertnstert.2009.09.001>. PMID:19819443
 21. Al-Meshal IA, Tariq M, Parmar NS, Ageel AM. Anti-inflammatory activity of the flavonoid fraction of khat (*Catha edulis* Forsk). *Agenc. Acti.* 1986 Jan; 17(3–4):379–80. <https://doi.org/10.1007/BF01982654>. PMID:3962788
 22. Pharmacopoeia I. Ministry of health and family welfare, Govt. of India. controller of publications, New Delhi; 1996.
 23. Khandelwal K. Practical pharmacognosy. Pragati Books Pvt. Ltd.; 2008.
 24. Venkatesh S, Reddy YR, Ramesh M, Swamy MM, Mahadevan N, Suresh B. Pharmacognostical studies on *Dodonaea viscosa* leaves. *Afr. J. Pharm. Pharmacol.* 2008; 2(4):83–8.
 25. Kokate CK, Purohit AP, Gokhale SB. Pharmacognosy. Niralia. Prakashan, Pune, India; 2002.



Comparative Pharmacognostical and Phytochemical Study of *Cassia auriculata* and *Cassia fistula*

Shailesh M. Kewatkar^{1*}, Vivek V. Paithankar², Supriya S. Deshpande³, Shirish P. Jain¹, Dheeraj H. Nagore⁴, Dipak V. Bhusari¹, Chanchal Navin Raj⁵, Madhav D. Chakolkar¹ and Trupti A. Nimburkar⁶

¹Rajarshi Shahu College of Pharmacy, Buldana – 443001, Maharashtra, India; kewatkar.shailesh@gmail.com

²Vidyabharti College of Pharmacy, Amravati – 444602, Maharashtra, India

³Dr. Panjabrao Deshmukh Medical College, Amravati – 444603, Maharashtra, India

⁴Mprex Healthcare Pvt. Ltd., Wakad – 411057, Pune, India

⁵Shri D. D. Vispute College of Pharmacy and Research Center, New Panvel – 410221, Maharashtra, India

⁶Dr. Rajendra Gode College of Pharmacy, Amravati – 444901, Maharashtra, India

Abstract

Cassia auriculata L. (CAL) popularly identified as Tanner's Cassia and *Cassia fistula* L. (CFL) is generally known as Golden Shower. Both plants belong to the Family, Fabaceae. These plants are used in skin disease, as hepatoprotective, as anticancer agent and as antioxidant agent. The intention of current article is to put forward the comparative pharmacognostical analysis of *Cassia auriculata* and *Cassia fistula* roots in terms of macroscopic evaluation, microscopic evaluation, physicochemical evaluation, extractive values and phytochemical analysis. Thin Layer Chromatography study was carried out for CAL and CFL and data pertaining to the above cited evaluations were recorded for both, CAL and CFL roots. The present study may help in differentiating among these species and these pharmacognostic parameters may serve as a tool for identification, authentication and standardization of CAL and CFL.

Keywords: *Cassia auriculata*, *Cassia fistula*, Microscopy, Phytochemical evaluation

1. Introduction

CAL is usually well-known as Tanner's Cassia, which fit in to the Family Fabaceae. The said plant is spread in Indian county and subcontinents. In Indian traditional system of medicine, the leaf and flower along with Triphala are utilized in the management of diabetic problems. The root of *cassia* is alexeteric and reported to be useful in thirst and respiratory problems. The leaves showed anthelmintic potential and they are supportive in the management of ulcers. The flowers are also reported to be useful in the treatment of throat complications^{1,2}. Preclinical and clinical research have showed that roots have ephroprotective potential, leaves also showed liver protective action along with other health benefits³⁻¹¹.

CFL normally identified as Golden Shower belonging to Family Fabaceae, also well-known as Amaltas. The herb is found throughout the country. It is scattered in numerous countries including Asia, Mexico, East Africa, South Africa and West Indies along with Brazil. The root is generally consumed as a stimulant and febrifuge. It also shows potential as a strong laxative. In ayurvedic literature, root is used in skin problems like leprosy. The flowers are useful in treating cough and related problems, even flatulence. In Unani system of medicine, the leaf of CFL diminishes the edema. The flowers are used as a purgative. The seeds are used as an emetic. The described uses of CFL are as antibacterial, liver protective, wound healing, anti feedant, larvicidal, antifungal, protease inhibitor, anticancer and antifertility, antioxidant action¹²⁻²⁰.

*Author for correspondenc

2. Materials and Methods

2.1 Procurement and Authentication of Plants

The roots of the plant CAL and CFL had been gathered from regions of Walgaon Road, Amravati, Maharashtra and some area of Bhopal, Madhya Pradesh respectively. Both the herbs have been validated by Safia College of Science, Bhopal, (MP), and the voucher specimen records were 159/Bot/Safia/2010 (CAL) and 160/Bot/Safia/2010 (CFL).

2.2 Preparation of Flavonoid Rich Fraction

The extraction of selected part of the herb for getting flavonoids rich fraction had been carried out. Roots of CAL and CFL (2 kg each) were dried under shade, and ground to get the coarse powdered material. Powdered roots of the plant were extracted with water by decoction method. While preparing the decoction, some precaution was taken regarding temperature, it was ensured that temperature did not exceed $40^{\circ}\text{C} \pm 5^{\circ}\text{C}$ as it would lead to precipitation or crystallization of various phytoconstituents which will not be soluble in any solvent for further process. The extracted aqueous sample was filtered and alcohol (ethanol) was poured to precipitate out polysaccharides which are present in the roots of the individual plant. The precipitated solution was filtered and the filtrate was evaporated to $1/4^{\text{th}}$ of the total volume. This was consecutively extracted with equivalent quantity of ethyl acetate with the aid of separating funnel to get separate fraction of root constituents. Then the ethyl acetate extract was acidified to raise the yield of the extract. The ethyl acetate fraction was evaporated to obtain a precipitate which was then dissolved in methanol and evaporated gradually to obtain crystalline powder.

The finally obtained powder was investigated for the occurrence of active phytoconstituents. The powder tested positive for Shinoda test for the Flavonoids. The positivity for flavonoids was also confirmed by TLC in appropriate solvent system. Similarly, the roots of both plants were used to obtain saponin rich fraction. Crushed plant material was macerated with ethanol: water (70:30) for seven days after defatting with petroleum ether (40:60). The extract so obtained was filtered through a muslin cloth followed by filter paper. Later this was concentrated using rotary vacuum evaporator (40°C) with precaution that extract does not get powdered. N-butanol was used to treat concentrated extract to obtain n-butanol soluble fraction. N-butanol fraction was further reacted with chilled diethyl ether to form a precipitate. This

combination with precipitate was reserved at -20°C for 24 hrs. Precipitates were further alienated by centrifugation. These precipitates were dissolved in methanol and methanol was evaporated, to get a crystalline powder²¹. Powder was analysed for the presence/absence of different phytoconstituents. Positive results for froth test and hemolysis test was observed in powders, which confirms the occurrence of saponin in powder. Further purity of powder was confirmed on the basis of TLC. It was observed that few extra spots were present in solvent system (BAW). Obtained powder was further purified using column chromatography by solvent on the basis of their polarity. Purity was again confirmed on the basis of TLC.

2.3 Macroscopical Characters

External features, dimensions and organoleptic properties of roots were studied.

2.4 Microscopical Characters

2.4.1 Collection of Specimens

The plant specimen was gathered. Precaution was taken to choose healthy sample. The root was dipped in FAA (Formalin + acetic acid + 70% ethanol). After 24 hours of fixing, the samples were dehydrated with graded series of tertiary butyl alcohol (TBA). Infiltration of the specimens was conceded by slow addition of paraffin wax until TBA solution attained saturation. Then the roots were moved into paraffin blocks.

2.4.2 Sectioning

With the help of Rotary Microtone, the paraffin entrenched specimens were sectioned. The width of the sections was $10 - 12 \mu\text{m}$. Dewaxing was conceded by customary method. Toluidine blue, a polychromatic stain was used to stain the sections. Satisfactory results were obtained by staining and some cytochemical reactions were also obtained. Cellulose walls were stained pink color with the dye, lignified cells stained blue, dark green to suberin, dark violet to mucilage, light blue to the protein bodies where essential sections were also stained with safranin and fast green and potassium iodide (for starch). Glycerine mounted temporary preparations were cleared with sodium hydroxide (NaOH) and after staining they were mounted in glycerine medium and the variant cell components were studied and measured.

2.5 Microphotography

Microscopic characterization of tissues was done with micrographs. Nikon lab photo 2 microscopic units were

used for taking photographs with different magnifications. Intense field was used for standard observation of the components. Polarizer was used to study the crystals, starch, grains and lignified cells. The results were vivid against dark background under the polarizer. Scale bars were used to indicate magnifications of the figures²³.

2.6 Physicochemical Evaluation of Crude Powdered Material^{22,23}

2.6.1 Ash Value

Ash values for the roots such as total ash value, acid insoluble and water soluble ash value were investigated.

2.6.2 Extractive Value

Extractive values for the roots such as water soluble and alcohol soluble extractive values were investigated.

2.7 Thin Layer Chromatography

2.7.1 Detection of Flavonoids and their Glycosides

Detection: At UV 365nm and visible light the developed TLC plate was observed. Flavonoids and their glycosides emerged as yellow, dark blue, orange spots. The color gels intensified on exposure of the plates to ammonia vapors. Following spraying agents were used for finding the flavonoids and their glycosides,

- Vanillin-Sulphuric acid
- Anisaldehyde-sulphuric acid

2.7.2 Detection of Saponins

Detection: The developed TLC plate was experiential in visible light and in UV at 365 nm. Following spraying agents were used for detection of saponins,

- Vanillin-Sulphuric acid
- Anisaldehyde-sulphuric acid

2.8 High performance thin layer chromatography

2.8.1 Sample Application

Commercially available pre-coated plates of silica gel GF254 were used. Flavonoid rich fractions were spotted on plates with bandwidth of 6mm. Application rate was 10µl/ min, using Linomat V applicator (Automatic TLC plate applicator, Camag, Switzerland). A sample volume of 10 and 20µl was applied.

2.8.2 Development of Chromatogram

The plate was allowed to run in twin trough chamber (20×10) using the solvent system. After developing, the plates were air dried and observed under Camag UV chamber 4.

2.8.3 Densitometric Scanning

The developed plates were scanned using densitometer at 254 nm (Camag TLC scanner – 4, combined with integration software, Win CATS 4.06, Switzerland).

3. Results

3.1 Microscopy

3.1.1 Microscopic Characters of CAL Roots

The root measuring 2.3mm diameter was studied. The surface of the root was deeply and irregularly fissured. The periderm outer part exfoliates into small, irregular fragments. The root consists of thick periderm, narrow cortex and wide and continuous secondary phloem. The secondary xylem was thick and dense (Figure 1).

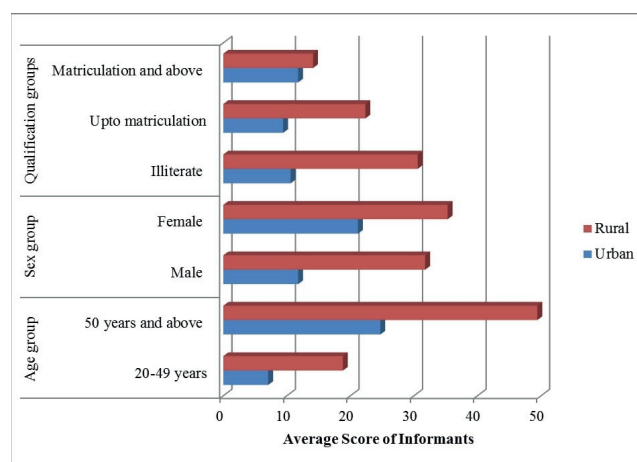
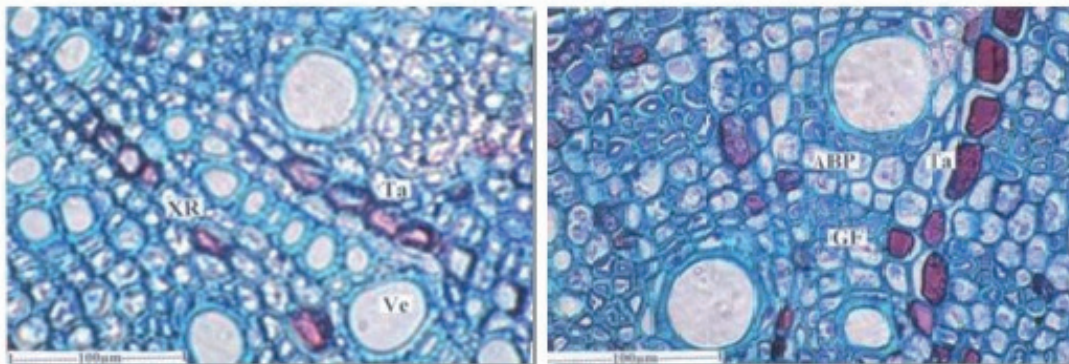


Figure 1. Transverse section of root - entire view.

The periderm consists of wide, darkly stained and thick walled phloem which was 150 cm thick. The cells contain darkly stained amorphous inclusions. The cells were tabular in shape and supervised. The inner part of the periderm had phelloderm which was 30 cm thick. It consists of thin walled radial files of tabular cells. The cortical zone was narrow comprising large, polygonal, compact thick walled cells.

Cortex was followed by secondary phloem which was 80cm thick. It includes sieve elements, phloem rays and phloem parenchyma. The inner part of the phloem consists of fairly wide, rectangular cells arranged in regular, radial files. The outer part of the phloem includes a narrow zone of collapsed phloem where the delicate cells were crushed into dark, thick tangential line. The inner part includes circular, clusters of sieve elements where the elements were narrow, thick walled cells.

Secondary xylem was about 1 mm in diameter. It consists of narrow, circular, solitary, thick walled diffusely distributed vessels (Figure 2). The vessels were 15-50 μm wide. There were tangential bands of apotrachial parenchyma cells. The parenchyma cells were wide angular and thick walled. The xylem rays were one or two cells thick, straight and they were filled with brown colored tannin. The xylem fibers were mostly gelatinous type. They had inner gelatinous or mucilaginous substance.



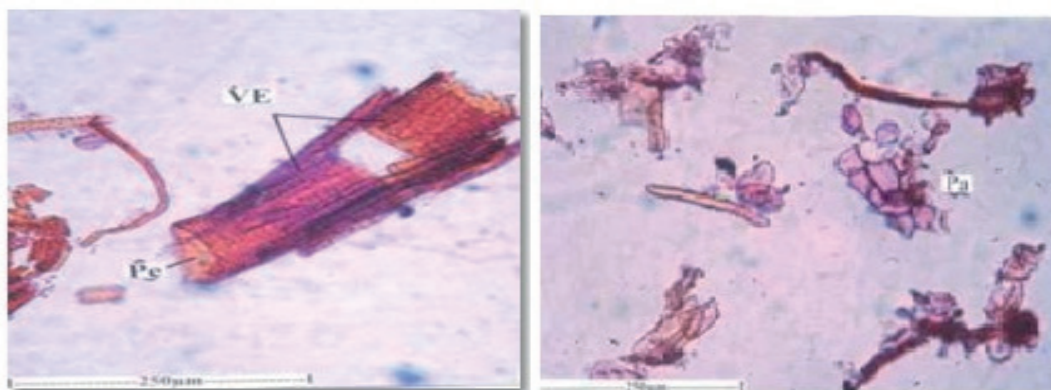
ABP- Apotrachial band of parenchyma, GF- Gelatinous Fibers, Ta- Tannin, Ve- Vessel, XR- Xylem Rays

Figure 2. T.S. of secondary xylem showing solitary vessels, apotrachial band of parenchyma and tannin filled xylem rays.

3.1.2 Powder Microscopy

The powder of the root consists of vessels elements, fibers, Sclereids and parenchyma cells. The vessel elements were cylindrical, long or short and wide. The vessel elements range from 100-200 μm long. They had dense, multiseriate, elliptical bordered pits on the lateral walls and wide circular, oblique or horizontal perforation on the end walls. The fibers were narrow and wide. The narrow

fibers were thick walled with narrow lumen. They were 710 μm long. The wide fibers were short, thin walled with wide lumen. They were 470 μm long. The Sclereids were long, narrow and fiber like. They have thick lignified walls with dense and prominent canal-like simple pits. Some of the sclereids were wider in the middle and tapering at the ends. Small polygonal thick walled parenchyma cells were seen scattered in the powder. The cells do not have any cell inclusions (Figure 3).



Pe- Perforation, Pi- Pits, VE- Vessel Elements, Pa- Parenchyma

Figure 3. Vessel elements and parenchyma cells.

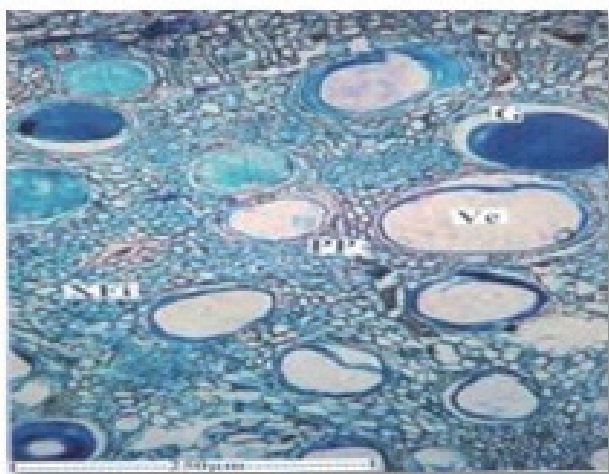
3.1.3 Microscopic Characters of CFL Roots

Root sample having minimum 2.2 mm thickness was studied. It was circular in outline with more or less smooth outline. The root consists of periderm, cortex, secondary phloem and secondary xylem cylinder.

Periderm was continuous all around the root and more or less uniform in thickness. It was 300cm thick in radial plane. The periderm includes several layers of dark brown narrowly tabular radial files of phellem cells and 2 layers of wide, square in phelloderm cells.

The cortical zone includes polygonal, compact parenchyma cells and small scattered clusters of gelatinous fibers. Some of the cortical cells also had tannin content. Secondary xylem cylinder was solid with circular outline. It also showed wide, circular, diffusely distributed vessel elements. The vessel element ranges from 40-150µm in diameter. Some of the vessel elements were filled with amorphous gummy substance. The secondary xylem also consists of xylem fibers and xylem parenchyma.

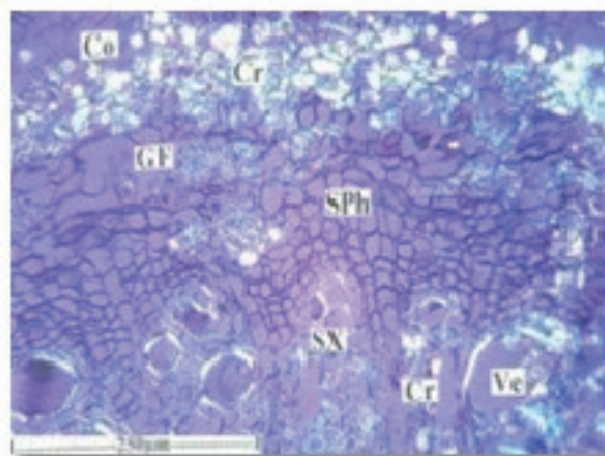
The fibers were libriform type, thick walled with narrow lumen (Figure 4). Xylem parenchyma occurs in the form of thick sheath around the vessels. They are called paratrachial parenchyma. The secondary phloem consists of outer part of collapsed phloem cells forming dark, thick, tangential lines. Intact non-collapsed phloem was found inner to the collapsed part. In this region the phloem elements were intact with small clusters of sieve elements and polygonal wide parenchyma cells. Calcium oxalate crystals were abundant in the middle cortical zone. Prismatic types of crystals were exclusively observed.



Pp- Paratrachial Parenchyma, Ve- Vessel, XFi- Xylem Fiber, G- Gum

Figure 4. Secondary xylem showing gum inclusions in the vessels.

The crystals also occur in the xylem parenchyma which encloses the vessel (Figure 5).



Co- Cortex, Cph- Collapsed phloem, Cr- Crystal, GF- Gelatinous Fibers, NCph- Non collapsed phloem, Pp- Paratrachial Parenchyma, Sph- Secondary Phloem, SX- Secondary xylem, Ve- Vessel, XFi- Xylem Fiber, G- Gum

Figure 5. Crystal distribution in the bark.

3.1.4 Powder Microscopy

The root powder included fiber, vessel elements and periderm fragments. Parenchyma cells were also occasionally seen. The fibers were of two types. Many of the fibers were wide, thin walled and short. They were 1 mm long and 40 µm wide. Some crystalline bodies of unknown chemical nature were often seen inside the wide fibers. Narrow fibers were less common they were 550µm long 10 µm thick. The walls were thick and lignified. The lumen was narrow and no inclusions were seen in the cell lumen. The vessel elements were also of two types. Some were narrow, long and resemble the wide fibers in size and shape. The narrow vessel elements had short tails at both ends. The vessel elements had minute, circular, multiseriate pits on the lateral walls. The perforation of the wide vessels was circular and horizontal in orientation. The narrow vessels elements were 280 µm long 20 µm wide. The wide vessel elements were 120 µm long and 40 µm wide.

3.2 Thin Layer Chromatography

TLC characterization of fractions of CAL and CFL has been discussed in Table 1. Flavonoids rich extracts of both the plants were subjected to HPTLC studies using solvents

of varying polarity, Rf values of the separated components were found out. The number of components separated in the extracts, their Rf values and their percentage area were represented in respective tables.

Table 1. TLC characterization of fractions of *Cassia auriculata* and *Cassia fistula*

Sr. No.	Mobile Phase	Spraying Reagent	No. of Spots		Rf Value		Inference
			CAL	CFL	CAL	CFL	
1	Chloroform: Methanol	Ammonia vapour/ VS reagent	2	1	0.24, 0.83	0.62	Flavonoids
2	Ethyl acetate: Formic acid: Glacial acetic acid: Water	Ammonia vapour/ VS reagent	2	3	0.35, 0.53	0.27, 0.42, 0.70	Flavonoids
3	Chloroform: Gallic acid: Methanol: Water	Anisaldehyde sulphuric Acid reagent	1	2	0.22	0.47, 0.71	Saponins
4	Chloroform: Methanol: Water	Vanillin phosphoric acid reagent	2	2	0.14, 0.20	0.57, 0.61	Saponins

HPTLC was carried out by using following solvent systems, ethyl acetate: acetic acid: formic acid: water [100:11:11:26] (EAFW). HPTLC Fingerprinting of CAL at 254 has been discussed in Figures 6 and 7. HPTLC Fingerprinting of

CFL at 254 shown in Figures 8 and 9. Correlation between reported and observed Rf values of various constituents has been observed in Table 2.

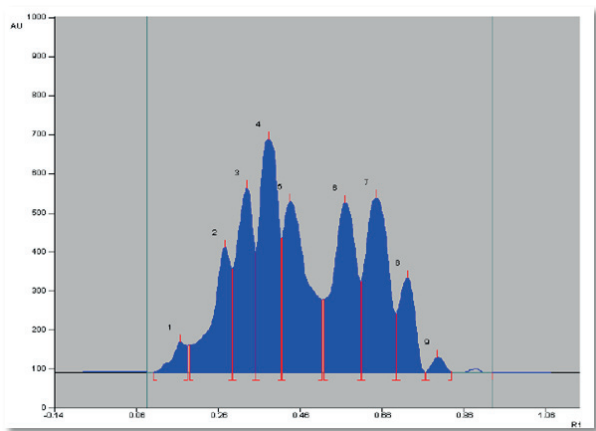


Figure 6. HPTLC fingerprinting of CAL at 254 nm.

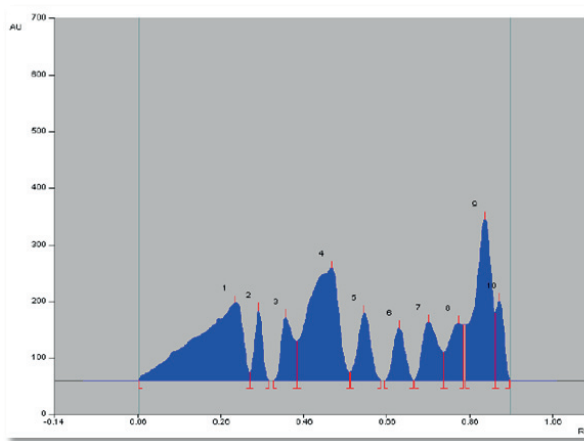


Figure 8. HPTLC Absorbance of CFL at 254 nm.

Peak	Start Position	Start Height	Max Position	Max Height	Max %	End Position	End Height	Area	Area %	Assigned substance
1	0.10 Rf	0.1 AU	0.17 Rf	76.5 AU	2.50 %	0.18 Rf	37.6 AU	2162.4 AU	1.80 %	unknown *
2	0.19 Rf	69.0 AU	0.27 Rf	318.9 AU	10.42 %	0.29 Rf	33.2 AU	12180.9 AU	10.13 %	unknown *
3	0.29 Rf	264.7 AU	0.33 Rf	472.2 AU	15.43 %	0.35 Rf	33.0 AU	15210.3 AU	12.65 %	unknown *
4	0.35 Rf	305.3 AU	0.38 Rf	596.3 AU	19.49 %	0.41 Rf	41.0 AU	21576.1 AU	17.94 %	unknown *
5	0.41 Rf	343.7 AU	0.43 Rf	436.5 AU	14.27 %	0.51 Rf	35.8 AU	21147.3 AU	17.59 %	unknown *
6	0.52 Rf	186.5 AU	0.57 Rf	433.2 AU	14.16 %	0.61 Rf	31.9 AU	19830.2 AU	16.49 %	unknown *
7	0.61 Rf	233.5 AU	0.65 Rf	446.2 AU	14.58 %	0.69 Rf	49.0 AU	19911.7 AU	16.56 %	unknown *
8	0.69 Rf	150.1 AU	0.72 Rf	241.0 AU	7.88 %	0.76 Rf	0.2 AU	7330.7 AU	6.10 %	unknown *
9	0.77 Rf	0.3 AU	0.79 Rf	38.9 AU	1.27 %	0.83 Rf	1.4 AU	900.9 AU	0.75 %	unknown *

Figure 7. HPTLC fingerprinting of CAL at 254 nm.

Peak	Start Position	Start Height	Max Position	Max Height	Max %	End Position	End Height	Area	Area %	Assigned substance
1	0.06 Rf	1.3 AU	0.29 Rf	137.0 AU	9.70 %	0.33 Rf	13.9 AU	12595.4 AU	25.11 %	unknown *
2	0.33 Rf	14.4 AU	0.35 Rf	123.4 AU	8.75 %	0.36 Rf	0.0 AU	1774.9 AU	3.54 %	unknown *
3	0.39 Rf	0.0 AU	0.42 Rf	112.0 AU	7.94 %	0.44 Rf	39.4 AU	2510.8 AU	5.01 %	unknown *
4	0.44 Rf	69.5 AU	0.53 Rf	197.7 AU	14.01 %	0.57 Rf	14.6 AU	11540.3 AU	23.01 %	unknown *
5	0.57 Rf	14.6 AU	0.61 Rf	119.6 AU	8.47 %	0.65 Rf	0.3 AU	2818.5 AU	5.62 %	unknown *
6	0.65 Rf	0.0 AU	0.69 Rf	93.0 AU	6.59 %	0.72 Rf	0.0 AU	2016.6 AU	4.02 %	unknown *
7	0.73 Rf	0.1 AU	0.76 Rf	102.9 AU	7.29 %	0.80 Rf	50.1 AU	3141.5 AU	6.26 %	unknown *
8	0.80 Rf	50.1 AU	0.83 Rf	100.6 AU	7.13 %	0.84 Rf	38.0 AU	2712.4 AU	5.41 %	unknown *
9	0.85 Rf	97.9 AU	0.90 Rf	284.4 AU	20.15 %	0.92 Rf	18.0 AU	8985.6 AU	17.91 %	unknown *
10	0.92 Rf	119.4 AU	0.93 Rf	140.9 AU	9.99 %	0.96 Rf	0.7 AU	2067.6 AU	4.12 %	unknown *

Figure 9. HPTLC fingerprinting of CFL at 254 nm.

Table 2. Correlation between reported and observed Rf value

Sr.no	Name of the Constituents	Reported Rf value	Observed Rf value
1	Chlorogenic Acid	0.45, 0.50	0.44
2	Isochlorogenic acid	0.80	0.80
3	Caffeic acid	0.90	0.92
4	Rutin	0.40	0.41
5	Apigenin 7-o-glucoside	0.75	0.76
6	Quercetin	0.35-0.75	0.29, 0.35, 0.38
7	Quercetin	0.80, 0.74	0.72, 0.84
8	Isoquercitrin	0.80, 0.60	0.57, 0.61, 0.79
9	Avicularin	0.85	0.83
10	Vitexin, 2-rhamnoside	0.45	0.33, 0.42
11	Vitexin	0.70	0.65
12	Luteolin	0.40-0.55	0.51
13	Kampeferol	0.40	0.31, 0.47
14	Flavone 6 - glycosides	0.65	0.69, 0.65, 0.67
15	Isoorientin	0.45	0.42

4. Discussion

All plants have their unique nature, structure, appearance, chemical constituents and therapeutic efficacy. Therefore, it is essential to study organoleptic properties of a medicinal plant, not only for quality control and standardization but also to recognize its structure and biology.

CAL and CFL were used by traditional practitioners for management of several ailments. Regularity of herbal products is a multifaceted task due to their diverse composition in all forms of the material. To protect reproducible quality of herbal products, appropriate control of starting material is essential. The primary step towards ensuring quality of preliminary material is

verification of the species. Now a days there has been a rapid increase in the standardization of many medicinal herbs of latent healing significance. Although many fresh techniques are available still identification of herbs by pharmacognostic properties is more liable. The macroscopic and microscopic explanation of a medicinal plant is the first step to create an identity and the purity of materials and should be conceded by undertaking any other tests, as described by World Health Organization²⁴.

Hence, it was felt desirable to pursue study on pharmacognostical and preliminary phytochemical studies of CAL and CFL roots to supplement useful information with regard to the exact identity of this plant

and, as this plant is extensively used in indigenous system of medicine.

Morphological assessment of drugs refer to valuation of drugs by taste, size, color, odor, shape and special features, like texture, touch. It is a method of qualitative evaluation based on the study of morphological and sensory summary of whole drugs. Organoleptic estimation is the conclusions drained from studies resulted due to feeling on organs of senses. All these parameters were recorded for roots of both the plants, CAL and CFL²⁵.

Microscopical techniques provide thorough information on the crude drug. Microscopical scrutiny of crude drugs from plant source is vital for the recognition of the grounded or crushed materials. Single-handed thorough microscopy could not provide complete assessment profile of a herbal drug, still it can supply underneath evidence, which when combined with other analytical parameters can be used to find the full confirmation for standardization and estimation of herbal drugs. Restricted burning of crude drugs result in an ash residue consisting of inorganic materials (metallic salts and silica). This value varies within fairly wide limits and hence a significant factor for the intention of evaluation of crude drugs. More direct contamination, such as by sand or earth, is immediately detected by the ash value. The quantity of active constituents in a given quantity of plant material when extracted with solvents is determined from the different extractive values obtained. Extractive values were used as revenue of evaluating crude drugs which were not eagerly expected by other means²⁶. Presence of bioactive components can be ascertained on the basis of various phytochemical testing. Thus in present investigation, extracts of CAL and CFL were subjected to phytochemical testing, which revealed that both plant extracts of CAL and CFL have shown the presence of various pharmacologically active chemicals such as flavonoids, saponins, glycosides, phenolic compounds, tannins. This confirmed that the targeted active molecules were present in selected extracts.

5. Conclusion

The present study reports the comparison between macroscopic, microscopic, physicochemical parameters and phytochemical parameters of CAL and CFL. These parameters may help in differentiating among these species. Thus, pharmacognostic parameters may serve as a tool for identification, authentication and standardization of CAL and CFL.

6. Acknowledgements

The authors thank Rajarshi Shahu College of pharmacy, Buldana for providing facilities to conduct the research.

7. Conflict of Interest Statement

There are no conflicts of interest among all the authors with publication of manuscript.

8. References

1. Kirtikar KR, Basu BD. Indian medicinal plants. Dehradun. International book distributors; 1999.
2. Deshpande S, Kewatkar SM, Paithankar VV. In-vitro antioxidant activity of different fraction of roots of *Cassia auriculata* Linn. Drug Invention Today. 2013; 5(2):164–8. <https://doi.org/10.1016/j.dit.2013.05.006>
3. Annie S, Rajagopal PL, Malini S. Effect of *Cassia auriculata* Linn. root extract on cisplatin and gentamicin-induced renal injury. Phytomed. 2005; 12(8): 555–60. <https://doi.org/10.1016/j.phymed.2003.11.010>. PMID:16121515
4. Rajagopal SK, Manickam P, Periyasamy V, Nama sivayam N. Activity of *Cassia auriculata* leaf extract in rats with alcoholic liver injury. J. Nutr. Biochem. 2003; 14(8):452–8. [https://doi.org/10.1016/S0955-2863\(03\)00053-6](https://doi.org/10.1016/S0955-2863(03)00053-6)
5. Gupta S, Sharma SB, Bansal SK, Prabhu KM. Antihyperglycemic and hypolipidemic activity of aqueous extract of *Cassia auriculata* L. leaves in experimental diabetes. Journal of Ethnopharmacol. 2009; 123(3):499–503. <https://doi.org/10.1016/j.jep.2009.02.019>. PMID:19473793
6. Prasanna R, Chandramoorthy HC, Ramaiyapillai P, Sakthisekaran D. In vitro evaluation of anticancer effect of *Cassia auriculata* leaf extract and curcumin through induction of apoptosis in human breast and larynx cancer cell lines. Biomed. Pre. Nutr. 2011; 1(2):153–60. <https://doi.org/10.1016/j.bionut.2010.12.006>
7. Sabu MC, Subburaju T. Effect of *Cassia auriculata* Linn. on serum glucose level, glucose utilization by isolated rat hemidiaphragm. J. Ethnopharmacol. 2002; 80(2–3):203–6. [https://doi.org/10.1016/S0378-8741\(02\)00026-0](https://doi.org/10.1016/S0378-8741(02)00026-0)
8. Kumaran A, Karunakaran RJ. Antioxidant activity of *Cassia auriculata* flowers. Fitoterapia. 2007; 78(1):46–7. <https://doi.org/10.1016/j.fitote.2006.09.031>. PMID:17071015
9. Thabrew I, Munasinghe J, Chackrevarthi S, Senarath S. The effects of *Cassia auriculata* and *Cardiospermum*

- halicacabum* teas on the steady state blood level and toxicity of carbamazepine. J. Ethnopharmacol. 2004; 90(1):145–50. <https://doi.org/10.1016/j.jep.2003.09.040>. PMID:14698522
10. Vijayaraj P, Muthukumar K, Sabarirajan J, Nachiappan V. Antihyperlipidemic activity of *Cassia auriculata* flowers in triton WR 1339 induced hyperlipidemic rats. Exper. Toxicol. Pathology. 2013; 65(1–2):135–41. <https://doi.org/10.1016/j.etp.2011.07.001>. PMID:21852078
 11. John CM, Sandrasaigaran P, Tong CK, Adam A, Ramasamy R. Immunomodulatory activity of poly phenols derived from *Cassia auriculata* flowers in aged rats. Cellular Immun. 2011; 271(2):474–9. <https://doi.org/10.1016/j.cellimm.2011.08.017>. PMID:21924708
 12. Duraipandiyan V, Ignacimuthu S. Antibacterial and antifungal activity of *Cassia fistula* L.: An ethno medicinal plant. J. Ethnopharmacol. 2007; 112(3):590–4. <https://doi.org/10.1016/j.jep.2007.04.008>. PMID:17532583
 13. Bhakta T, Mukherjee PK, Mukherjee K, Banerjee S, Mandal SC, Maity TK, Pal M, Saha BP. Evaluation of hepatoprotective activity of *Cassia fistula* leaf extract. J. Ethnopharmacol. 1999; 66(3):277–82. [https://doi.org/10.1016/S0378-8741\(98\)00220-7](https://doi.org/10.1016/S0378-8741(98)00220-7)
 14. Kumar MS, Sripriya R, Raghavan HV, Sehgal PK. Wound healing potential of *Cassia fistula* on infected albino rat model. J. Surgical Res. 2006; 131(2):283–9. <https://doi.org/10.1016/j.jss.2005.08.025>. PMID:16242721
 15. Siddhuraju P, Mohan PS, Becker K. Studies on the antioxidant activity of Indian Laburnum (*Cassia fistula* L.): A preliminary assessment of crude extracts from stem bark, leaves, flowers and fruit pulp. Food Chem. 2002; 79(1):61–7. [https://doi.org/10.1016/S0308-8146\(02\)00179-6](https://doi.org/10.1016/S0308-8146(02)00179-6)
 16. Manonmani G, Bhavapriya V, Kalpana S, Govindasamy S, Apparathanam T. Antioxidant activity of *Cassia fistula* (Linn.) flowers in alloxan induced diabetic rats. J. Ethnopharmacol. 2005; 97(1):39–42. <https://doi.org/10.1016/j.jep.2004.09.051>. PMID:15652272
 17. Duraipandiyan V, Ignacimuthu S, Paulraj MG. Antifeedant and larvicidal activities of Rhein isolated from the flowers of *Cassia fistula* L. Saudi J. Bio. Sci. 2011; 18(2):129–33. <https://doi.org/10.1016/j.sjbs.2010.12.009>. PMID:23961115 PMID:PMC3730718
 18. Wijaya R, Neumann GM, Condrón R, Hughes AB, Polya GM. Defense proteins from seed of *Cassia fistula* includes a lipid transfer protein homologue and a protease inhibitory plant defense. Plant Sci. 2000; 159(2):243–55. [https://doi.org/10.1016/S0168-9452\(00\)00348-4](https://doi.org/10.1016/S0168-9452(00)00348-4)
 19. Gupta M, Mazumder UK, Rath N, Mukhopadhyay DK. Antitumor activity of methanolic extract of *Cassia fistula* L. seed against Ehrlich ascites carcinoma. J. Ethnopharmacol. 2000; 72(1–2):151–6. [https://doi.org/10.1016/S0378-8741\(00\)00227-0](https://doi.org/10.1016/S0378-8741(00)00227-0)
 20. Chauhan A, Agarwal M. Evaluating the antifertility potential of an aqueous extract from *Cassia fistula* seeds in male rats. Fert. Ster. 2010; 93(5):1706–10. <https://doi.org/10.1016/j.fertnstert.2009.09.001>. PMID:19819443
 21. Al-Meshal IA, Tariq M, Parmar NS, Ageel AM. Anti-inflammatory activity of the flavonoid fraction of khat (*Catha edulis* Forsk). Ager. Acti. 1986 Jan; 17(3–4):379–80. <https://doi.org/10.1007/BF01982654>. PMID:3962788
 22. Pharmacopoeia I. Ministry of health and family welfare, Govt. of India. controller of publications, New Delhi; 1996.
 23. Khandelwal K. Practical pharmacognosy. Pragati Books Pvt. Ltd.; 2008.
 24. Venkatesh S, Reddy YR, Ramesh M, Swamy MM, Mahadevan N, Suresh B. Pharmacognostical studies on *Dodonaea viscosa* leaves. Afr. J. Pharm. Pharmacol. 2008; 2(4):83–8.
 25. Kokate CK, Purohit AP, Gokhale SB. Pharmacognosy. Niralia. Prakashan, Pune, India; 2002.



Comparative Pharmacognostical and Phytochemical Study of *Cassia auriculata* and *Cassia fistula*

Shailesh M. Kewatkar^{1*}, Vivek V. Paithankar², Supriya S. Deshpande³, Shirish P. Jain¹, Dheeraj H. Nagore⁴, Dipak V. Bhusari¹, Chanchal Navin Raj⁵, Madhav D. Chakolkar¹ and Trupti A. Nimburkar⁶

¹Rajarshi Shahu College of Pharmacy, Buldana – 443001, Maharashtra, India; kewatkar.shailesh@gmail.com

²Vidyabharti College of Pharmacy, Amravati – 444602, Maharashtra, India

³Dr. Panjabrao Deshmukh Medical College, Amravati – 444603, Maharashtra, India

⁴Mprex Healthcare Pvt. Ltd., Wakad – 411057, Pune, India

⁵Shri D. D. Vispute College of Pharmacy and Research Center, New Panvel – 410221, Maharashtra, India

⁶Dr. Rajendra Gode College of Pharmacy, Amravati – 444901, Maharashtra, India

Abstract

Cassia auriculata L. (CAL) popularly identified as Tanner's Cassia and *Cassia fistula* L. (CFL) is generally known as Golden Shower. Both plants belong to the Family, Fabaceae. These plants are used in skin disease, as hepatoprotective, as anticancer agent and as antioxidant agent. The intention of current article is to put forward the comparative pharmacognostical analysis of *Cassia auriculata* and *Cassia fistula* roots in terms of macroscopic evaluation, microscopic evaluation, physicochemical evaluation, extractive values and phytochemical analysis. Thin Layer Chromatography study was carried out for CAL and CFL and data pertaining to the above cited evaluations were recorded for both, CAL and CFL roots. The present study may help in differentiating among these species and these pharmacognostic parameters may serve as a tool for identification, authentication and standardization of CAL and CFL.

Keywords: *Cassia auriculata*, *Cassia fistula*, Microscopy, Phytochemical evaluation

1. Introduction

CAL is usually well-known as Tanner's Cassia, which fit in to the Family Fabaceae. The said plant is spread in Indian county and subcontinents. In Indian traditional system of medicine, the leaf and flower along with Triphala are utilized in the management of diabetic problems. The root of *cassia* is alexeteric and reported to be useful in thirst and respiratory problems. The leaves showed anthelmintic potential and they are supportive in the management of ulcers. The flowers are also reported to be useful in the treatment of throat complications^{1,2}. Preclinical and clinical research have showed that roots have ephroprotective potential, leaves also showed liver protective action along with other health benefits³⁻¹¹.

CFL normally identified as Golden Shower belonging to Family Fabaceae, also well-known as Amaltas. The herb is found throughout the country. It is scattered in numerous countries including Asia, Mexico, East Africa, South Africa and West Indies along with Brazil. The root is generally consumed as a stimulant and febrifuge. It also shows potential as a strong laxative. In ayurvedic literature, root is used in skin problems like leprosy. The flowers are useful in treating cough and related problems, even flatulence. In Unani system of medicine, the leaf of CFL diminishes the edema. The flowers are used as a purgative. The seeds are used as an emetic. The described uses of CFL are as antibacterial, liver protective, wound healing, anti feedant, larvicidal, antifungal, protease inhibitor, anticancer and antifertility, antioxidant action¹²⁻²⁰.

*Author for correspondenc

2. Materials and Methods

2.1 Procurement and Authentication of Plants

The roots of the plant CAL and CFL had been gathered from regions of Walgaon Road, Amravati, Maharashtra and some area of Bhopal, Madhya Pradesh respectively. Both the herbs have been validated by Safia College of Science, Bhopal, (MP), and the voucher specimen records were 159/Bot/Safia/2010 (CAL) and 160/Bot/Safia/2010 (CFL).

2.2 Preparation of Flavonoid Rich Fraction

The extraction of selected part of the herb for getting flavonoids rich fraction had been carried out. Roots of CAL and CFL (2 kg each) were dried under shade, and ground to get the coarse powdered material. Powdered roots of the plant were extracted with water by decoction method. While preparing the decoction, some precaution was taken regarding temperature, it was ensured that temperature did not exceed $40^{\circ}\text{C} \pm 5^{\circ}\text{C}$ as it would lead to precipitation or crystallization of various phytoconstituents which will not be soluble in any solvent for further process. The extracted aqueous sample was filtered and alcohol (ethanol) was poured to precipitate out polysaccharides which are present in the roots of the individual plant. The precipitated solution was filtered and the filtrate was evaporated to $1/4^{\text{th}}$ of the total volume. This was consecutively extracted with equivalent quantity of ethyl acetate with the aid of separating funnel to get separate fraction of root constituents. Then the ethyl acetate extract was acidified to raise the yield of the extract. The ethyl acetate fraction was evaporated to obtain a precipitate which was then dissolved in methanol and evaporated gradually to obtain crystalline powder.

The finally obtained powder was investigated for the occurrence of active phytoconstituents. The powder tested positive for Shinoda test for the Flavonoids. The positivity for flavonoids was also confirmed by TLC in appropriate solvent system. Similarly, the roots of both plants were used to obtain saponin rich fraction. Crushed plant material was macerated with ethanol: water (70:30) for seven days after defatting with petroleum ether (40:60). The extract so obtained was filtered through a muslin cloth followed by filter paper. Later this was concentrated using rotary vacuum evaporator (40°C) with precaution that extract does not get powdered. N-butanol was used to treat concentrated extract to obtain n-butanol soluble fraction. N-butanol fraction was further reacted with chilled diethyl ether to form a precipitate. This

combination with precipitate was reserved at -20°C for 24 hrs. Precipitates were further alienated by centrifugation. These precipitates were dissolved in methanol and methanol was evaporated, to get a crystalline powder²¹. Powder was analysed for the presence/absence of different phytoconstituents. Positive results for froth test and hemolysis test was observed in powders, which confirms the occurrence of saponin in powder. Further purity of powder was confirmed on the basis of TLC. It was observed that few extra spots were present in solvent system (BAW). Obtained powder was further purified using column chromatography by solvent on the basis of their polarity. Purity was again confirmed on the basis of TLC.

2.3 Macroscopical Characters

External features, dimensions and organoleptic properties of roots were studied.

2.4 Microscopical Characters

2.4.1 Collection of Specimens

The plant specimen was gathered. Precaution was taken to choose healthy sample. The root was dipped in FAA (Formalin + acetic acid + 70% ethanol). After 24 hours of fixing, the samples were dehydrated with graded series of tertiary butyl alcohol (TBA). Infiltration of the specimens was conceded by slow addition of paraffin wax until TBA solution attained saturation. Then the roots were moved into paraffin blocks.

2.4.2 Sectioning

With the help of Rotary Microtone, the paraffin entrenched specimens were sectioned. The width of the sections was $10 - 12 \mu\text{m}$. Dewaxing was conceded by customary method. Toluidine blue, a polychromatic stain was used to stain the sections. Satisfactory results were obtained by staining and some cytochemical reactions were also obtained. Cellulose walls were stained pink color with the dye, lignified cells stained blue, dark green to suberin, dark violet to mucilage, light blue to the protein bodies where essential sections were also stained with safranin and fast green and potassium iodide (for starch). Glycerine mounted temporary preparations were cleared with sodium hydroxide (NaOH) and after staining they were mounted in glycerine medium and the variant cell components were studied and measured.

2.5 Microphotography

Microscopic characterization of tissues was done with micrographs. Nikon lab photo 2 microscopic units were

used for taking photographs with different magnifications. Intense field was used for standard observation of the components. Polarizer was used to study the crystals, starch, grains and lignified cells. The results were vivid against dark background under the polarizer. Scale bars were used to indicate magnifications of the figures²³.

2.6 Physicochemical Evaluation of Crude Powdered Material^{22,23}

2.6.1 Ash Value

Ash values for the roots such as total ash value, acid insoluble and water soluble ash value were investigated.

2.6.2 Extractive Value

Extractive values for the roots such as water soluble and alcohol soluble extractive values were investigated.

2.7 Thin Layer Chromatography

2.7.1 Detection of Flavonoids and their Glycosides

Detection: At UV 365nm and visible light the developed TLC plate was observed. Flavonoids and their glycosides emerged as yellow, dark blue, orange spots. The color gels intensified on exposure of the plates to ammonia vapors. Following spraying agents were used for finding the flavonoids and their glycosides,

- Vanillin-Sulphuric acid
- Anisaldehyde-sulphuric acid

2.7.2 Detection of Saponins

Detection: The developed TLC plate was experiential in visible light and in UV at 365 nm. Following spraying agents were used for detection of saponins,

- Vanillin-Sulphuric acid
- Anisaldehyde-sulphuric acid

2.8 High performance thin layer chromatography

2.8.1 Sample Application

Commercially available pre-coated plates of silica gel GF254 were used. Flavonoid rich fractions were spotted on plates with bandwidth of 6mm. Application rate was 10µl/ min, using Linomat V applicator (Automatic TLC plate applicator, Camag, Switzerland). A sample volume of 10 and 20µl was applied.

2.8.2 Development of Chromatogram

The plate was allowed to run in twin trough chamber (20×10) using the solvent system. After developing, the plates were air dried and observed under Camag UV chamber 4.

2.8.3 Densitometric Scanning

The developed plates were scanned using densitometer at 254 nm (Camag TLC scanner – 4, combined with integration software, Win CATS 4.06, Switzerland).

3. Results

3.1 Microscopy

3.1.1 Microscopic Characters of CAL Roots

The root measuring 2.3mm diameter was studied. The surface of the root was deeply and irregularly fissured. The periderm outer part exfoliates into small, irregular fragments. The root consists of thick periderm, narrow cortex and wide and continuous secondary phloem. The secondary xylem was thick and dense (Figure 1).

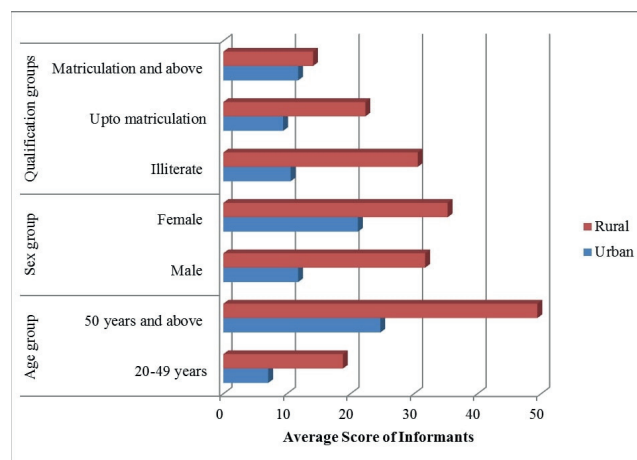
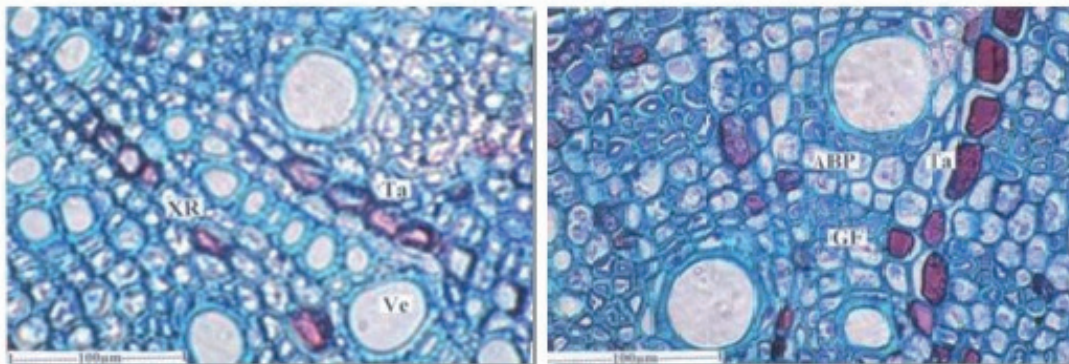


Figure 1. Transverse section of root - entire view.

The periderm consists of wide, darkly stained and thick walled phloem which was 150 cm thick. The cells contain darkly stained amorphous inclusions. The cells were tabular in shape and supervised. The inner part of the periderm had phelloderm which was 30 cm thick. It consists of thin walled radial files of tabular cells. The cortical zone was narrow comprising large, polygonal, compact thick walled cells.

Cortex was followed by secondary phloem which was 80cm thick. It includes sieve elements, phloem rays and phloem parenchyma. The inner part of the phloem consists of fairly wide, rectangular cells arranged in regular, radial files. The outer part of the phloem includes a narrow zone of collapsed phloem where the delicate cells were crushed into dark, thick tangential line. The inner part includes circular, clusters of sieve elements where the elements were narrow, thick walled cells.

Secondary xylem was about 1 mm in diameter. It consists of narrow, circular, solitary, thick walled diffusely distributed vessels (Figure 2). The vessels were 15-50 μm wide. There were tangential bands of apotrachial parenchyma cells. The parenchyma cells were wide angular and thick walled. The xylem rays were one or two cells thick, straight and they were filled with brown colored tannin. The xylem fibers were mostly gelatinous type. They had inner gelatinous or mucilaginous substance.



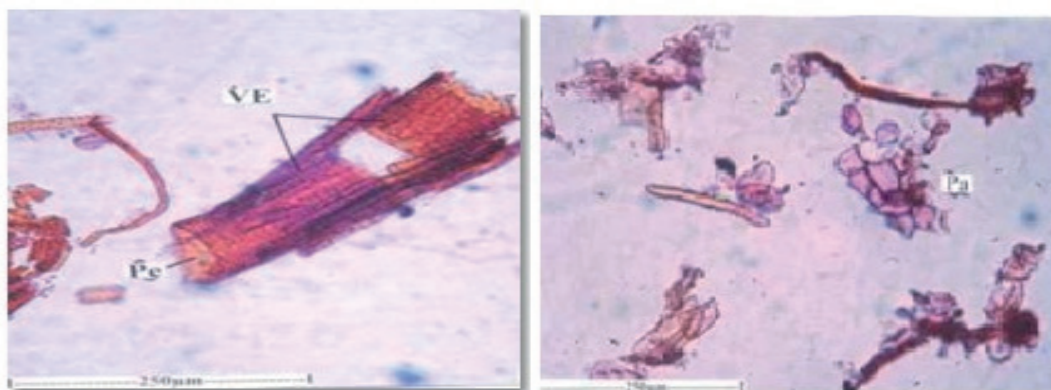
ABP- Apotrachial band of parenchyma, GF- Gelatinous Fibers, Ta- Tannin, Ve- Vessel, XR- Xylem Rays

Figure 2. T.S. of secondary xylem showing solitary vessels, apotrachial band of parenchyma and tannin filled xylem rays.

3.1.2 Powder Microscopy

The powder of the root consists of vessels elements, fibers, Sclereids and parenchyma cells. The vessel elements were cylindrical, long or short and wide. The vessel elements range from 100-200 μm long. They had dense, multiseriate, elliptical bordered pits on the lateral walls and wide circular, oblique or horizontal perforation on the end walls. The fibers were narrow and wide. The narrow

fibers were thick walled with narrow lumen. They were 710 μm long. The wide fibers were short, thin walled with wide lumen. They were 470 μm long. The Sclereids were long, narrow and fiber like. They have thick lignified walls with dense and prominent canal-like simple pits. Some of the sclereids were wider in the middle and tapering at the ends. Small polygonal thick walled parenchyma cells were seen scattered in the powder. The cells do not have any cell inclusions (Figure 3).



Pe- Perforation, Pi- Pits, VE- Vessel Elements, Pa- Parenchyma

Figure 3. Vessel elements and parenchyma cells.

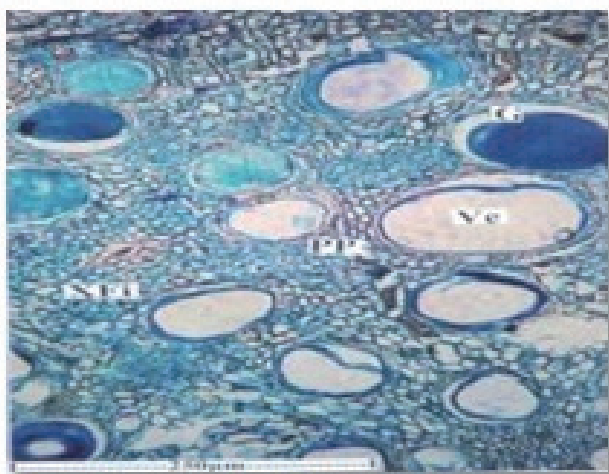
3.1.3 Microscopic Characters of CFL Roots

Root sample having minimum 2.2 mm thickness was studied. It was circular in outline with more or less smooth outline. The root consists of periderm, cortex, secondary phloem and secondary xylem cylinder.

Periderm was continuous all around the root and more or less uniform in thickness. It was 300cm thick in radial plane. The periderm includes several layers of dark brown narrowly tabular radial files of phellem cells and 2 layers of wide, square in phelloderm cells.

The cortical zone includes polygonal, compact parenchyma cells and small scattered clusters of gelatinous fibers. Some of the cortical cells also had tannin content. Secondary xylem cylinder was solid with circular outline. It also showed wide, circular, diffusely distributed vessel elements. The vessel element ranges from 40-150µm in diameter. Some of the vessel elements were filled with amorphous gummy substance. The secondary xylem also consists of xylem fibers and xylem parenchyma.

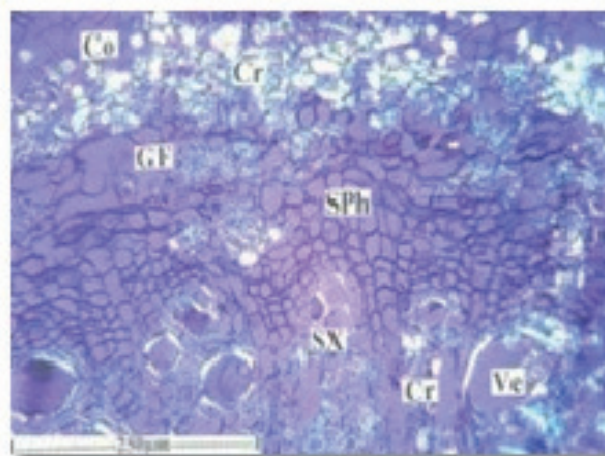
The fibers were libriform type, thick walled with narrow lumen (Figure 4). Xylem parenchyma occurs in the form of thick sheath around the vessels. They are called paratrachial parenchyma. The secondary phloem consists of outer part of collapsed phloem cells forming dark, thick, tangential lines. Intact non-collapsed phloem was found inner to the collapsed part. In this region the phloem elements were intact with small clusters of sieve elements and polygonal wide parenchyma cells. Calcium oxalate crystals were abundant in the middle cortical zone. Prismatic types of crystals were exclusively observed.



Pp- Paratrachial Parenchyma, Ve- Vessel, XFi- Xylem Fiber, G- Gum

Figure 4. Secondary xylem showing gum inclusions in the vessels.

The crystals also occur in the xylem parenchyma which encloses the vessel (Figure 5).



Co- Cortex, Cph- Collapsed phloem, Cr- Crystal, GF- Gelatinous Fibers, NCph- Non collapsed phloem, Pp- Paratrachial Parenchyma, Sph- Secondary Phloem, Sx- Secondary xylem, Ve- Vessel, XFi- Xylem Fiber, G- Gum

Figure 5. Crystal distribution in the bark.

3.1.4 Powder Microscopy

The root powder included fiber, vessel elements and periderm fragments. Parenchyma cells were also occasionally seen. The fibers were of two types. Many of the fibers were wide, thin walled and short. They were 1 mm long and 40 µm wide. Some crystalline bodies of unknown chemical nature were often seen inside the wide fibers. Narrow fibers were less common they were 550µm long 10 µm thick. The walls were thick and lignified. The lumen was narrow and no inclusions were seen in the cell lumen. The vessel elements were also of two types. Some were narrow, long and resemble the wide fibers in size and shape. The narrow vessel elements had short tails at both ends. The vessel elements had minute, circular, multiseriate pits on the lateral walls. The perforation of the wide vessels was circular and horizontal in orientation. The narrow vessels elements were 280 µm long 20 µm wide. The wide vessel elements were 120 µm long and 40 µm wide.

3.2 Thin Layer Chromatography

TLC characterization of fractions of CAL and CFL has been discussed in Table 1. Flavonoids rich extracts of both the plants were subjected to HPTLC studies using solvents

of varying polarity, Rf values of the separated components were found out. The number of components separated in the extracts, their Rf values and their percentage area were represented in respective tables.

Table 1. TLC characterization of fractions of *Cassia auriculata* and *Cassia fistula*

Sr. No.	Mobile Phase	Spraying Reagent	No. of Spots		Rf Value		Inference
			CAL	CFL	CAL	CFL	
1	Chloroform: Methanol	Ammonia vapour/ VS reagent	2	1	0.24, 0.83	0.62	Flavonoids
2	Ethyl acetate: Formic acid: Glacial acetic acid: Water	Ammonia vapour/ VS reagent	2	3	0.35, 0.53	0.27, 0.42, 0.70	Flavonoids
3	Chloroform: Gallic acid: Methanol: Water	Anisaldehyde sulphuric Acid reagent	1	2	0.22	0.47, 0.71	Saponins
4	Chloroform: Methanol: Water	Vanillin phosphoric acid reagent	2	2	0.14, 0.20	0.57, 0.61	Saponins

HPTLC was carried out by using following solvent systems, ethyl acetate: acetic acid: formic acid: water [100:11:11:26] (EAFW). HPTLC Fingerprinting of CAL at 254 has been discussed in Figures 6 and 7. HPTLC Fingerprinting of

CFL at 254 shown in Figures 8 and 9. Correlation between reported and observed Rf values of various constituents has been observed in Table 2.

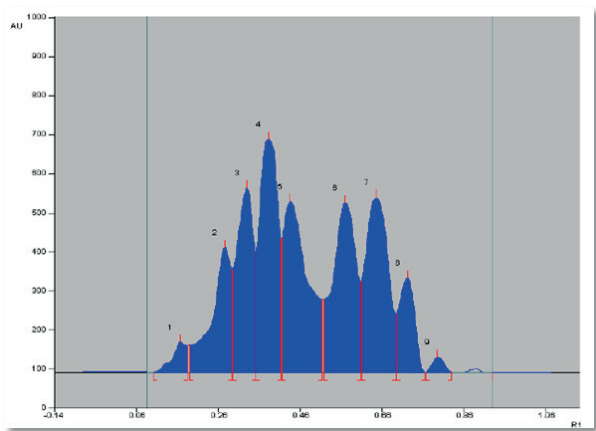


Figure 6. HPTLC fingerprinting of CAL at 254 nm.

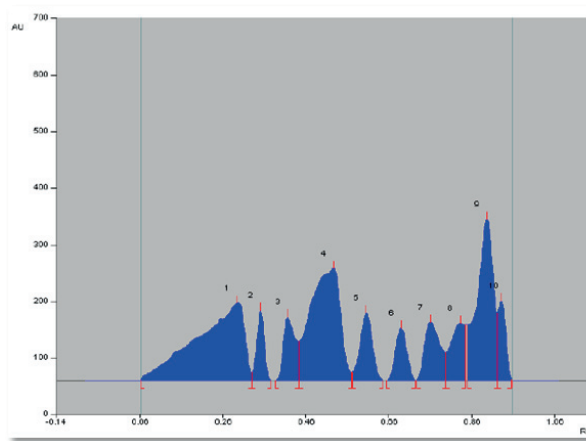


Figure 8. HPTLC Absorbance of CFL at 254 nm.

Peak	Start Position	Start Height	Max Position	Max Height	Max %	End Position	End Height	Area	Area %	Assigned substance
1	0.10 Rf	0.1 AU	0.17 Rf	76.5 AU	2.50 %	0.18 Rf	37.6 AU	2162.4 AU	1.80 %	unknown *
2	0.19 Rf	69.0 AU	0.27 Rf	318.9 AU	10.42 %	0.29 Rf	33.2 AU	12180.9 AU	10.13 %	unknown *
3	0.29 Rf	264.7 AU	0.33 Rf	472.2 AU	15.43 %	0.35 Rf	33.0 AU	15210.3 AU	12.65 %	unknown *
4	0.35 Rf	305.3 AU	0.38 Rf	596.3 AU	19.49 %	0.41 Rf	41.0 AU	21576.1 AU	17.94 %	unknown *
5	0.41 Rf	343.7 AU	0.43 Rf	436.5 AU	14.27 %	0.51 Rf	35.8 AU	21147.3 AU	17.59 %	unknown *
6	0.52 Rf	186.5 AU	0.57 Rf	433.2 AU	14.16 %	0.61 Rf	31.9 AU	19830.2 AU	16.49 %	unknown *
7	0.61 Rf	233.5 AU	0.65 Rf	446.2 AU	14.58 %	0.69 Rf	49.0 AU	19911.7 AU	16.56 %	unknown *
8	0.69 Rf	150.1 AU	0.72 Rf	241.0 AU	7.88 %	0.76 Rf	0.2 AU	7330.7 AU	6.10 %	unknown *
9	0.77 Rf	0.3 AU	0.79 Rf	38.9 AU	1.27 %	0.83 Rf	1.4 AU	900.9 AU	0.75 %	unknown *

Figure 7. HPTLC fingerprinting of CAL at 254 nm.

Peak	Start Position	Start Height	Max Position	Max Height	Max %	End Position	End Height	Area	Area %	Assigned substance
1	0.06 Rf	1.3 AU	0.29 Rf	137.0 AU	9.70 %	0.33 Rf	13.9 AU	12595.4 AU	25.11 %	unknown *
2	0.33 Rf	14.4 AU	0.35 Rf	123.4 AU	8.75 %	0.36 Rf	0.0 AU	1774.9 AU	3.54 %	unknown *
3	0.39 Rf	0.0 AU	0.42 Rf	112.0 AU	7.94 %	0.44 Rf	39.4 AU	2510.8 AU	5.01 %	unknown *
4	0.44 Rf	69.5 AU	0.53 Rf	197.7 AU	14.01 %	0.57 Rf	14.6 AU	11540.3 AU	23.01 %	unknown *
5	0.57 Rf	14.6 AU	0.61 Rf	119.6 AU	8.47 %	0.65 Rf	0.3 AU	2818.5 AU	5.62 %	unknown *
6	0.65 Rf	0.0 AU	0.69 Rf	93.0 AU	6.59 %	0.72 Rf	0.0 AU	2016.6 AU	4.02 %	unknown *
7	0.73 Rf	0.1 AU	0.76 Rf	102.9 AU	7.29 %	0.80 Rf	50.1 AU	3141.5 AU	6.26 %	unknown *
8	0.80 Rf	50.1 AU	0.83 Rf	100.6 AU	7.13 %	0.84 Rf	38.0 AU	2712.4 AU	5.41 %	unknown *
9	0.85 Rf	97.9 AU	0.90 Rf	284.4 AU	20.15 %	0.92 Rf	18.0 AU	8985.6 AU	17.91 %	unknown *
10	0.92 Rf	119.4 AU	0.93 Rf	140.9 AU	9.99 %	0.96 Rf	0.7 AU	2067.6 AU	4.12 %	unknown *

Figure 9. HPTLC fingerprinting of CFL at 254 nm.

Table 2. Correlation between reported and observed Rf value

Sr.no	Name of the Constituents	Reported Rf value	Observed Rf value
1	Chlorogenic Acid	0.45, 0.50	0.44
2	Isochlorogenic acid	0.80	0.80
3	Caffeic acid	0.90	0.92
4	Rutin	0.40	0.41
5	Apigenin 7-o-glucoside	0.75	0.76
6	Quercetin	0.35-0.75	0.29, 0.35, 0.38
7	Quercetin	0.80, 0.74	0.72, 0.84
8	Isoquercitrin	0.80, 0.60	0.57, 0.61, 0.79
9	Avicularin	0.85	0.83
10	Vitexin, 2-rhamnoside	0.45	0.33, 0.42
11	Vitexin	0.70	0.65
12	Luteolin	0.40-0.55	0.51
13	Kampeferol	0.40	0.31, 0.47
14	Flavone 6 - glycosides	0.65	0.69, 0.65, 0.67
15	Isoorientin	0.45	0.42

4. Discussion

All plants have their unique nature, structure, appearance, chemical constituents and therapeutic efficacy. Therefore, it is essential to study organoleptic properties of a medicinal plant, not only for quality control and standardization but also to recognize its structure and biology.

CAL and CFL were used by traditional practitioners for management of several ailments. Regularity of herbal products is a multifaceted task due to their diverse composition in all forms of the material. To protect reproducible quality of herbal products, appropriate control of starting material is essential. The primary step towards ensuring quality of preliminary material is

verification of the species. Now a days there has been a rapid increase in the standardization of many medicinal herbs of latent healing significance. Although many fresh techniques are available still identification of herbs by pharmacognostic properties is more liable. The macroscopic and microscopic explanation of a medicinal plant is the first step to create an identity and the purity of materials and should be conceded by undertaking any other tests, as described by World Health Organization²⁴.

Hence, it was felt desirable to pursue study on pharmacognostical and preliminary phytochemical studies of CAL and CFL roots to supplement useful information with regard to the exact identity of this plant

and, as this plant is extensively used in indigenous system of medicine.

Morphological assessment of drugs refer to valuation of drugs by taste, size, color, odor, shape and special features, like texture, touch. It is a method of qualitative evaluation based on the study of morphological and sensory summary of whole drugs. Organoleptic estimation is the conclusions drained from studies resulted due to feeling on organs of senses. All these parameters were recorded for roots of both the plants, CAL and CFL²⁵.

Microscopical techniques provide thorough information on the crude drug. Microscopical scrutiny of crude drugs from plant source is vital for the recognition of the grounded or crushed materials. Single-handed thorough microscopy could not provide complete assessment profile of a herbal drug, still it can supply underneath evidence, which when combined with other analytical parameters can be used to find the full confirmation for standardization and estimation of herbal drugs. Restricted burning of crude drugs result in an ash residue consisting of inorganic materials (metallic salts and silica). This value varies within fairly wide limits and hence a significant factor for the intention of evaluation of crude drugs. More direct contamination, such as by sand or earth, is immediately detected by the ash value. The quantity of active constituents in a given quantity of plant material when extracted with solvents is determined from the different extractive values obtained. Extractive values were used as revenue of evaluating crude drugs which were not eagerly expected by other means²⁶. Presence of bioactive components can be ascertained on the basis of various phytochemical testing. Thus in present investigation, extracts of CAL and CFL were subjected to phytochemical testing, which revealed that both plant extracts of CAL and CFL have shown the presence of various pharmacologically active chemicals such as flavonoids, saponins, glycosides, phenolic compounds, tannins. This confirmed that the targeted active molecules were present in selected extracts.

5. Conclusion

The present study reports the comparison between macroscopic, microscopic, physicochemical parameters and phytochemical parameters of CAL and CFL. These parameters may help in differentiating among these species. Thus, pharmacognostic parameters may serve as a tool for identification, authentication and standardization of CAL and CFL.

6. Acknowledgements

The authors thank Rajarshi Shahu College of pharmacy, Buldana for providing facilities to conduct the research.

7. Conflict of Interest Statement

There are no conflicts of interest among all the authors with publication of manuscript.

8. References

1. Kirtikar KR, Basu BD. Indian medicinal plants. Dehradun. International book distributors; 1999.
2. Deshpande S, Kewatkar SM, Paithankar VV. In-vitro antioxidant activity of different fraction of roots of *Cassia auriculata* Linn. Drug Invention Today. 2013; 5(2):164–8. <https://doi.org/10.1016/j.dit.2013.05.006>
3. Annie S, Rajagopal PL, Malini S. Effect of *Cassia auriculata* Linn. root extract on cisplatin and gentamicin-induced renal injury. Phytomed. 2005; 12(8): 555–60. <https://doi.org/10.1016/j.phymed.2003.11.010>. PMID:16121515
4. Rajagopal SK, Manickam P, Periyasamy V, Nama sivayam N. Activity of *Cassia auriculata* leaf extract in rats with alcoholic liver injury. J. Nutr. Biochem. 2003; 14(8):452–8. [https://doi.org/10.1016/S0955-2863\(03\)00053-6](https://doi.org/10.1016/S0955-2863(03)00053-6)
5. Gupta S, Sharma SB, Bansal SK, Prabhu KM. Antihyperglycemic and hypolipidemic activity of aqueous extract of *Cassia auriculata* L. leaves in experimental diabetes. Journal of Ethnopharmacol. 2009; 123(3):499–503. <https://doi.org/10.1016/j.jep.2009.02.019>. PMID:19473793
6. Prasanna R, Chandramoorthy HC, Ramaiyapillai P, Sakthisekaran D. In vitro evaluation of anticancer effect of *Cassia auriculata* leaf extract and curcumin through induction of apoptosis in human breast and larynx cancer cell lines. Biomed. Pre. Nutr. 2011; 1(2):153–60. <https://doi.org/10.1016/j.bionut.2010.12.006>
7. Sabu MC, Subburaju T. Effect of *Cassia auriculata* Linn. on serum glucose level, glucose utilization by isolated rat hemidiaphragm. J. Ethnopharmacol. 2002; 80(2–3):203–6. [https://doi.org/10.1016/S0378-8741\(02\)00026-0](https://doi.org/10.1016/S0378-8741(02)00026-0)
8. Kumaran A, Karunakaran RJ. Antioxidant activity of *Cassia auriculata* flowers. Fitoterapia. 2007; 78(1):46–7. <https://doi.org/10.1016/j.fitote.2006.09.031>. PMID:17071015
9. Thabrew I, Munasinghe J, Chackrewarthi S, Senarath S. The effects of *Cassia auriculata* and *Cardiospermum*

- halicacabum* teas on the steady state blood level and toxicity of carbamazepine. J. Ethnopharmacol. 2004; 90(1):145–50. <https://doi.org/10.1016/j.jep.2003.09.040>. PMID:14698522
10. Vijayaraj P, Muthukumar K, Sabarirajan J, Nachiappan V. Antihyperlipidemic activity of *Cassia auriculata* flowers in triton WR 1339 induced hyperlipidemic rats. Exper. Toxicol. Pathology. 2013; 65(1–2):135–41. <https://doi.org/10.1016/j.etp.2011.07.001>. PMID:21852078
 11. John CM, Sandrasaigaran P, Tong CK, Adam A, Ramasamy R. Immunomodulatory activity of poly phenols derived from *Cassia auriculata* flowers in aged rats. Cellular Immun. 2011; 271(2):474–9. <https://doi.org/10.1016/j.cellimm.2011.08.017>. PMID:21924708
 12. Duraipandiyan V, Ignacimuthu S. Antibacterial and antifungal activity of *Cassia fistula* L.: An ethno medicinal plant. J. Ethnopharmacol. 2007; 112(3):590–4. <https://doi.org/10.1016/j.jep.2007.04.008>. PMID:17532583
 13. Bhakta T, Mukherjee PK, Mukherjee K, Banerjee S, Mandal SC, Maity TK, Pal M, Saha BP. Evaluation of hepatoprotective activity of *Cassia fistula* leaf extract. J. Ethnopharmacol. 1999; 66(3):277–82. [https://doi.org/10.1016/S0378-8741\(98\)00220-7](https://doi.org/10.1016/S0378-8741(98)00220-7)
 14. Kumar MS, Sripriya R, Raghavan HV, Sehgal PK. Wound healing potential of *Cassia fistula* on infected albino rat model. J. Surgical Res. 2006; 131(2):283–9. <https://doi.org/10.1016/j.jss.2005.08.025>. PMID:16242721
 15. Siddhuraju P, Mohan PS, Becker K. Studies on the antioxidant activity of Indian Laburnum (*Cassia fistula* L.): A preliminary assessment of crude extracts from stem bark, leaves, flowers and fruit pulp. Food Chem. 2002; 79(1):61–7. [https://doi.org/10.1016/S0308-8146\(02\)00179-6](https://doi.org/10.1016/S0308-8146(02)00179-6)
 16. Manonmani G, Bhavapriya V, Kalpana S, Govindasamy S, Apparathanam T. Antioxidant activity of *Cassia fistula* (Linn.) flowers in alloxan induced diabetic rats. J. Ethnopharmacol. 2005; 97(1):39–42. <https://doi.org/10.1016/j.jep.2004.09.051>. PMID:15652272
 17. Duraipandiyan V, Ignacimuthu S, Paulraj MG. Antifeedant and larvicidal activities of Rhein isolated from the flowers of *Cassia fistula* L. Saudi J. Bio. Sci. 2011; 18(2):129–33. <https://doi.org/10.1016/j.sjbs.2010.12.009>. PMID:23961115 PMID:PMC3730718
 18. Wijaya R, Neumann GM, Condrón R, Hughes AB, Polya GM. Defense proteins from seed of *Cassia fistula* includes a lipid transfer protein homologue and a protease inhibitory plant defense. Plant Sci. 2000; 159(2):243–55. [https://doi.org/10.1016/S0168-9452\(00\)00348-4](https://doi.org/10.1016/S0168-9452(00)00348-4)
 19. Gupta M, Mazumder UK, Rath N, Mukhopadhyay DK. Antitumor activity of methanolic extract of *Cassia fistula* L. seed against Ehrlich ascites carcinoma. J. Ethnopharmacol. 2000; 72(1–2):151–6. [https://doi.org/10.1016/S0378-8741\(00\)00227-0](https://doi.org/10.1016/S0378-8741(00)00227-0)
 20. Chauhan A, Agarwal M. Evaluating the antifertility potential of an aqueous extract from *Cassia fistula* seeds in male rats. Fert. Ster. 2010; 93(5):1706–10. <https://doi.org/10.1016/j.fertnstert.2009.09.001>. PMID:19819443
 21. Al-Meshal IA, Tariq M, Parmar NS, Ageel AM. Anti-inflammatory activity of the flavonoid fraction of khat (*Catha edulis* Forsk). Ager. Acti. 1986 Jan; 17(3–4):379–80. <https://doi.org/10.1007/BF01982654>. PMID:3962788
 22. Pharmacopoeia I. Ministry of health and family welfare, Govt. of India. controller of publications, New Delhi; 1996.
 23. Khandelwal K. Practical pharmacognosy. Pragati Books Pvt. Ltd.; 2008.
 24. Venkatesh S, Reddy YR, Ramesh M, Swamy MM, Mahadevan N, Suresh B. Pharmacognostical studies on *Dodonaea viscosa* leaves. Afr. J. Pharm. Pharmacol. 2008; 2(4):83–8.
 25. Kokate CK, Purohit AP, Gokhale SB. Pharmacognosy. Niralia. Prakashan, Pune, India; 2002.



Comparative Pharmacognostical and Phytochemical Study of *Cassia auriculata* and *Cassia fistula*

Shailesh M. Kewatkar^{1*}, Vivek V. Paithankar², Supriya S. Deshpande³, Shirish P. Jain¹, Dheeraj H. Nagore⁴, Dipak V. Bhusari¹, Chanchal Navin Raj⁵, Madhav D. Chakolkar¹ and Trupti A. Nimburkar⁶

¹Rajarshi Shahu College of Pharmacy, Buldana – 443001, Maharashtra, India; kewatkar.shailesh@gmail.com

²Vidyabharti College of Pharmacy, Amravati – 444602, Maharashtra, India

³Dr. Panjabrao Deshmukh Medical College, Amravati – 444603, Maharashtra, India

⁴Mprex Healthcare Pvt. Ltd., Wakad – 411057, Pune, India

⁵Shri D. D. Vispute College of Pharmacy and Research Center, New Panvel – 410221, Maharashtra, India

⁶Dr. Rajendra Gode College of Pharmacy, Amravati – 444901, Maharashtra, India

Abstract

Cassia auriculata L. (CAL) popularly identified as Tanner's Cassia and *Cassia fistula* L. (CFL) is generally known as Golden Shower. Both plants belong to the Family, Fabaceae. These plants are used in skin disease, as hepatoprotective, as anticancer agent and as antioxidant agent. The intention of current article is to put forward the comparative pharmacognostical analysis of *Cassia auriculata* and *Cassia fistula* roots in terms of macroscopic evaluation, microscopic evaluation, physicochemical evaluation, extractive values and phytochemical analysis. Thin Layer Chromatography study was carried out for CAL and CFL and data pertaining to the above cited evaluations were recorded for both, CAL and CFL roots. The present study may help in differentiating among these species and these pharmacognostic parameters may serve as a tool for identification, authentication and standardization of CAL and CFL.

Keywords: *Cassia auriculata*, *Cassia fistula*, Microscopy, Phytochemical evaluation

1. Introduction

CAL is usually well-known as Tanner's Cassia, which fit in to the Family Fabaceae. The said plant is spread in Indian county and subcontinents. In Indian traditional system of medicine, the leaf and flower along with Triphala are utilized in the management of diabetic problems. The root of *cassia* is alexeteric and reported to be useful in thirst and respiratory problems. The leaves showed anthelmintic potential and they are supportive in the management of ulcers. The flowers are also reported to be useful in the treatment of throat complications^{1,2}. Preclinical and clinical research have showed that roots have ephroprotective potential, leaves also showed liver protective action along with other health benefits³⁻¹¹.

CFL normally identified as Golden Shower belonging to Family Fabaceae, also well-known as Amaltas. The herb is found throughout the country. It is scattered in numerous countries including Asia, Mexico, East Africa, South Africa and West Indies along with Brazil. The root is generally consumed as a stimulant and febrifuge. It also shows potential as a strong laxative. In ayurvedic literature, root is used in skin problems like leprosy. The flowers are useful in treating cough and related problems, even flatulence. In Unani system of medicine, the leaf of CFL diminishes the edema. The flowers are used as a purgative. The seeds are used as an emetic. The described uses of CFL are as antibacterial, liver protective, wound healing, anti feedant, larvicidal, antifungal, protease inhibitor, anticancer and antifertility, antioxidant action¹²⁻²⁰.

*Author for correspondenc

2. Materials and Methods

2.1 Procurement and Authentication of Plants

The roots of the plant CAL and CFL had been gathered from regions of Walgaon Road, Amravati, Maharashtra and some area of Bhopal, Madhya Pradesh respectively. Both the herbs have been validated by Safia College of Science, Bhopal, (MP), and the voucher specimen records were 159/Bot/Safia/2010 (CAL) and 160/Bot/Safia/2010 (CFL).

2.2 Preparation of Flavonoid Rich Fraction

The extraction of selected part of the herb for getting flavonoids rich fraction had been carried out. Roots of CAL and CFL (2 kg each) were dried under shade, and ground to get the coarse powdered material. Powdered roots of the plant were extracted with water by decoction method. While preparing the decoction, some precaution was taken regarding temperature, it was ensured that temperature did not exceed $40^{\circ}\text{C} \pm 5^{\circ}\text{C}$ as it would lead to precipitation or crystallization of various phytoconstituents which will not be soluble in any solvent for further process. The extracted aqueous sample was filtered and alcohol (ethanol) was poured to precipitate out polysaccharides which are present in the roots of the individual plant. The precipitated solution was filtered and the filtrate was evaporated to $1/4^{\text{th}}$ of the total volume. This was consecutively extracted with equivalent quantity of ethyl acetate with the aid of separating funnel to get separate fraction of root constituents. Then the ethyl acetate extract was acidified to raise the yield of the extract. The ethyl acetate fraction was evaporated to obtain a precipitate which was then dissolved in methanol and evaporated gradually to obtain crystalline powder.

The finally obtained powder was investigated for the occurrence of active phytoconstituents. The powder tested positive for Shinoda test for the Flavonoids. The positivity for flavonoids was also confirmed by TLC in appropriate solvent system. Similarly, the roots of both plants were used to obtain saponin rich fraction. Crushed plant material was macerated with ethanol: water (70:30) for seven days after defatting with petroleum ether (40:60). The extract so obtained was filtered through a muslin cloth followed by filter paper. Later this was concentrated using rotary vacuum evaporator (40°C) with precaution that extract does not get powdered. N-butanol was used to treat concentrated extract to obtain n-butanol soluble fraction. N-butanol fraction was further reacted with chilled diethyl ether to form a precipitate. This

combination with precipitate was reserved at -20°C for 24 hrs. Precipitates were further alienated by centrifugation. These precipitates were dissolved in methanol and methanol was evaporated, to get a crystalline powder²¹. Powder was analysed for the presence/absence of different phytoconstituents. Positive results for froth test and hemolysis test was observed in powders, which confirms the occurrence of saponin in powder. Further purity of powder was confirmed on the basis of TLC. It was observed that few extra spots were present in solvent system (BAW). Obtained powder was further purified using column chromatography by solvent on the basis of their polarity. Purity was again confirmed on the basis of TLC.

2.3 Macroscopical Characters

External features, dimensions and organoleptic properties of roots were studied.

2.4 Microscopical Characters

2.4.1 Collection of Specimens

The plant specimen was gathered. Precaution was taken to choose healthy sample. The root was dipped in FAA (Formalin + acetic acid + 70% ethanol). After 24 hours of fixing, the samples were dehydrated with graded series of tertiary butyl alcohol (TBA). Infiltration of the specimens was conceded by slow addition of paraffin wax until TBA solution attained saturation. Then the roots were moved into paraffin blocks.

2.4.2 Sectioning

With the help of Rotary Microtone, the paraffin entrenched specimens were sectioned. The width of the sections was $10 - 12 \mu\text{m}$. Dewaxing was conceded by customary method. Toluidine blue, a polychromatic stain was used to stain the sections. Satisfactory results were obtained by staining and some cytochemical reactions were also obtained. Cellulose walls were stained pink color with the dye, lignified cells stained blue, dark green to suberin, dark violet to mucilage, light blue to the protein bodies where essential sections were also stained with safranin and fast green and potassium iodide (for starch). Glycerine mounted temporary preparations were cleared with sodium hydroxide (NaOH) and after staining they were mounted in glycerine medium and the variant cell components were studied and measured.

2.5 Microphotography

Microscopic characterization of tissues was done with micrographs. Nikon lab photo 2 microscopic units were

used for taking photographs with different magnifications. Intense field was used for standard observation of the components. Polarizer was used to study the crystals, starch, grains and lignified cells. The results were vivid against dark background under the polarizer. Scale bars were used to indicate magnifications of the figures²³.

2.6 Physicochemical Evaluation of Crude Powdered Material^{22,23}

2.6.1 Ash Value

Ash values for the roots such as total ash value, acid insoluble and water soluble ash value were investigated.

2.6.2 Extractive Value

Extractive values for the roots such as water soluble and alcohol soluble extractive values were investigated.

2.7 Thin Layer Chromatography

2.7.1 Detection of Flavonoids and their Glycosides

Detection: At UV 365nm and visible light the developed TLC plate was observed. Flavonoids and their glycosides emerged as yellow, dark blue, orange spots. The color gels intensified on exposure of the plates to ammonia vapors. Following spraying agents were used for finding the flavonoids and their glycosides,

- Vanillin-Sulphuric acid
- Anisaldehyde-sulphuric acid

2.7.2 Detection of Saponins

Detection: The developed TLC plate was experiential in visible light and in UV at 365 nm. Following spraying agents were used for detection of saponins,

- Vanillin-Sulphuric acid
- Anisaldehyde-sulphuric acid

2.8 High performance thin layer chromatography

2.8.1 Sample Application

Commercially available pre-coated plates of silica gel GF254 were used. Flavonoid rich fractions were spotted on plates with bandwidth of 6mm. Application rate was 10µl/ min, using Linomat V applicator (Automatic TLC plate applicator, Camag, Switzerland). A sample volume of 10 and 20µl was applied.

2.8.2 Development of Chromatogram

The plate was allowed to run in twin trough chamber (20×10) using the solvent system. After developing, the plates were air dried and observed under Camag UV chamber 4.

2.8.3 Densitometric Scanning

The developed plates were scanned using densitometer at 254 nm (Camag TLC scanner – 4, combined with integration software, Win CATS 4.06, Switzerland).

3. Results

3.1 Microscopy

3.1.1 Microscopic Characters of CAL Roots

The root measuring 2.3mm diameter was studied. The surface of the root was deeply and irregularly fissured. The periderm outer part exfoliates into small, irregular fragments. The root consists of thick periderm, narrow cortex and wide and continuous secondary phloem. The secondary xylem was thick and dense (Figure 1).

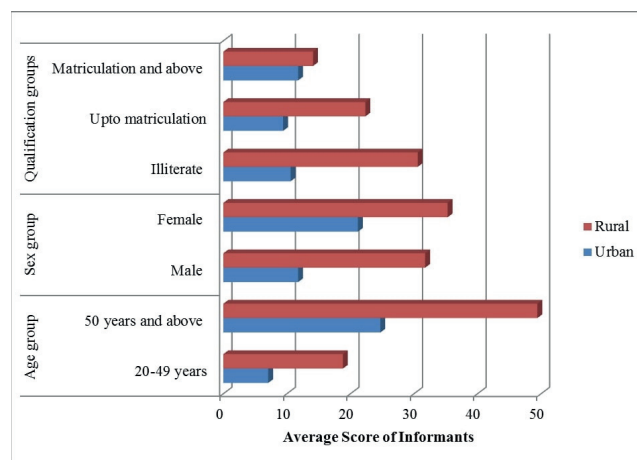
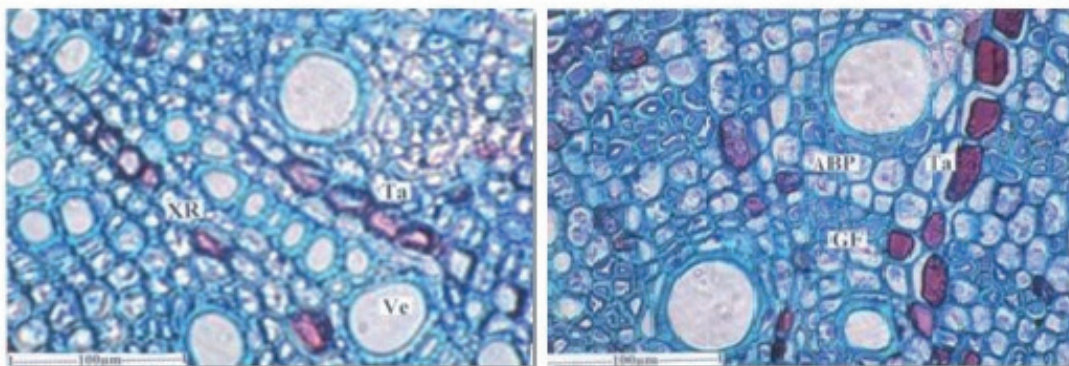


Figure 1. Transverse section of root - entire view.

The periderm consists of wide, darkly stained and thick walled phloem which was 150 cm thick. The cells contain darkly stained amorphous inclusions. The cells were tabular in shape and supervised. The inner part of the periderm had phelloderm which was 30 cm thick. It consists of thin walled radial files of tabular cells. The cortical zone was narrow comprising large, polygonal, compact thick walled cells.

Cortex was followed by secondary phloem which was 80cm thick. It includes sieve elements, phloem rays and phloem parenchyma. The inner part of the phloem consists of fairly wide, rectangular cells arranged in regular, radial files. The outer part of the phloem includes a narrow zone of collapsed phloem where the delicate cells were crushed into dark, thick tangential line. The inner part includes circular, clusters of sieve elements where the elements were narrow, thick walled cells.

Secondary xylem was about 1 mm in diameter. It consists of narrow, circular, solitary, thick walled diffusely distributed vessels (Figure 2). The vessels were 15-50 μm wide. There were tangential bands of apotrachial parenchyma cells. The parenchyma cells were wide angular and thick walled. The xylem rays were one or two cells thick, straight and they were filled with brown colored tannin. The xylem fibers were mostly gelatinous type. They had inner gelatinous or mucilaginous substance.



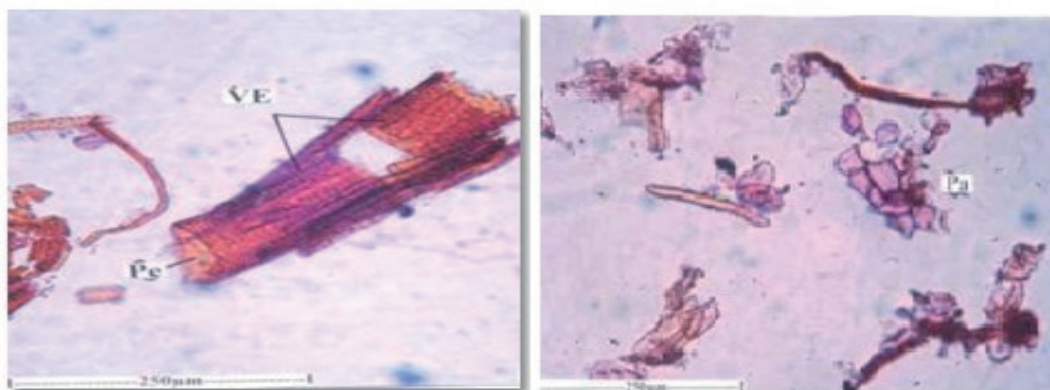
ABP- Apotrachial band of parenchyma, GF- Gelatinous Fibers, Ta- Tannin, Ve- Vessel, XR- Xylem Rays

Figure 2. T.S. of secondary xylem showing solitary vessels, apotrachial band of parenchyma and tannin filled xylem rays.

3.1.2 Powder Microscopy

The powder of the root consists of vessels elements, fibers, Sclereids and parenchyma cells. The vessel elements were cylindrical, long or short and wide. The vessel elements range from 100-200 μm long. They had dense, multiseriate, elliptical bordered pits on the lateral walls and wide circular, oblique or horizontal perforation on the end walls. The fibers were narrow and wide. The narrow

fibers were thick walled with narrow lumen. They were 710 μm long. The wide fibers were short, thin walled with wide lumen. They were 470 μm long. The Sclereids were long, narrow and fiber like. They have thick lignified walls with dense and prominent canal-like simple pits. Some of the sclereids were wider in the middle and tapering at the ends. Small polygonal thick walled parenchyma cells were seen scattered in the powder. The cells do not have any cell inclusions (Figure 3).



Pe- Perforation, Pi- Pits, VE- Vessel Elements, Pa- Parenchyma

Figure 3. Vessel elements and parenchyma cells.

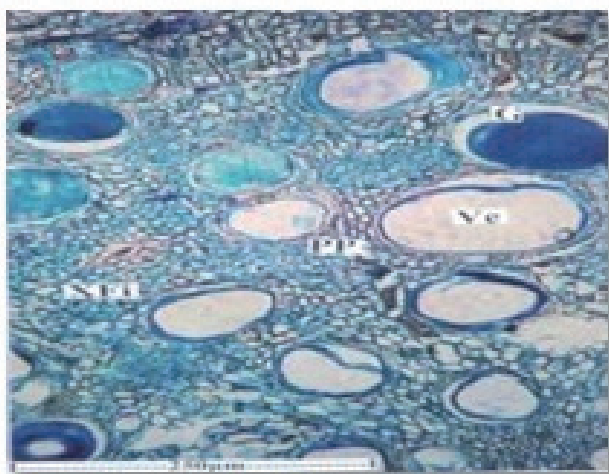
3.1.3 Microscopic Characters of CFL Roots

Root sample having minimum 2.2 mm thickness was studied. It was circular in outline with more or less smooth outline. The root consists of periderm, cortex, secondary phloem and secondary xylem cylinder.

Periderm was continuous all around the root and more or less uniform in thickness. It was 300cm thick in radial plane. The periderm includes several layers of dark brown narrowly tabular radial files of phellem cells and 2 layers of wide, square in phelloderm cells.

The cortical zone includes polygonal, compact parenchyma cells and small scattered clusters of gelatinous fibers. Some of the cortical cells also had tannin content. Secondary xylem cylinder was solid with circular outline. It also showed wide, circular, diffusely distributed vessel elements. The vessel element ranges from 40-150µm in diameter. Some of the vessel elements were filled with amorphous gummy substance. The secondary xylem also consists of xylem fibers and xylem parenchyma.

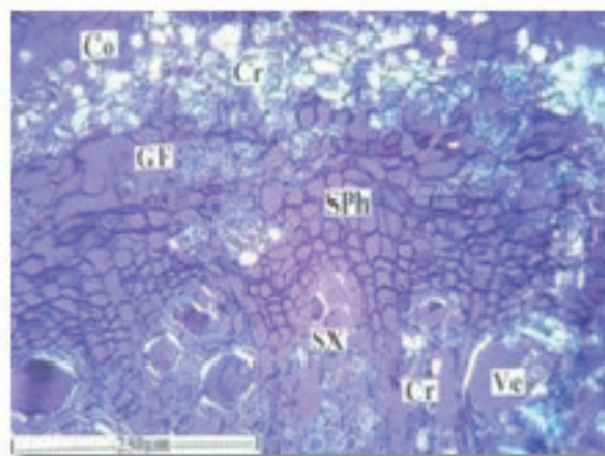
The fibers were libriform type, thick walled with narrow lumen (Figure 4). Xylem parenchyma occurs in the form of thick sheath around the vessels. They are called paratrachial parenchyma. The secondary phloem consists of outer part of collapsed phloem cells forming dark, thick, tangential lines. Intact non-collapsed phloem was found inner to the collapsed part. In this region the phloem elements were intact with small clusters of sieve elements and polygonal wide parenchyma cells. Calcium oxalate crystals were abundant in the middle cortical zone. Prismatic types of crystals were exclusively observed.



Pp- Paratrachial Parenchyma, Ve- Vessel, XFi- Xylem Fiber, G- Gum

Figure 4. Secondary xylem showing gum inclusions in the vessels.

The crystals also occur in the xylem parenchyma which encloses the vessel (Figure 5).



Co- Cortex, Cph- Collapsed phloem, Cr- Crystal, GF- Gelatinous Fibers, NCph- Non collapsed phloem, Pp- Paratrachial Parenchyma, Sph- Secondary Phloem, Sx- Secondary xylem, Ve- Vessel, XFi- Xylem Fiber, G- Gum

Figure 5. Crystal distribution in the bark.

3.1.4 Powder Microscopy

The root powder included fiber, vessel elements and periderm fragments. Parenchyma cells were also occasionally seen. The fibers were of two types. Many of the fibers were wide, thin walled and short. They were 1 mm long and 40 µm wide. Some crystalline bodies of unknown chemical nature were often seen inside the wide fibers. Narrow fibers were less common they were 550µm long 10 µm thick. The walls were thick and lignified. The lumen was narrow and no inclusions were seen in the cell lumen. The vessel elements were also of two types. Some were narrow, long and resemble the wide fibers in size and shape. The narrow vessel elements had short tails at both ends. The vessel elements had minute, circular, multiseriate pits on the lateral walls. The perforation of the wide vessels was circular and horizontal in orientation. The narrow vessels elements were 280 µm long 20 µm wide. The wide vessel elements were 120 µm long and 40 µm wide.

3.2 Thin Layer Chromatography

TLC characterization of fractions of CAL and CFL has been discussed in Table 1. Flavonoids rich extracts of both the plants were subjected to HPTLC studies using solvents

of varying polarity, Rf values of the separated components were found out. The number of components separated in the extracts, their Rf values and their percentage area were represented in respective tables.

Table 1. TLC characterization of fractions of *Cassia auriculata* and *Cassia fistula*

Sr. No.	Mobile Phase	Spraying Reagent	No. of Spots		Rf Value		Inference
			CAL	CFL	CAL	CFL	
1	Chloroform: Methanol	Ammonia vapour/ VS reagent	2	1	0.24, 0.83	0.62	Flavonoids
2	Ethyl acetate: Formic acid: Glacial acetic acid: Water	Ammonia vapour/ VS reagent	2	3	0.35, 0.53	0.27, 0.42, 0.70	Flavonoids
3	Chloroform: Gallic acid: Methanol: Water	Anisaldehyde sulphuric Acid reagent	1	2	0.22	0.47, 0.71	Saponins
4	Chloroform: Methanol: Water	Vanillin phosphoric acid reagent	2	2	0.14, 0.20	0.57, 0.61	Saponins

HPTLC was carried out by using following solvent systems, ethyl acetate: acetic acid: formic acid: water [100:11:11:26] (EAFW). HPTLC Fingerprinting of CAL at 254 has been discussed in Figures 6 and 7. HPTLC Fingerprinting of

CFL at 254 shown in Figures 8 and 9. Correlation between reported and observed Rf values of various constituents has been observed in Table 2.

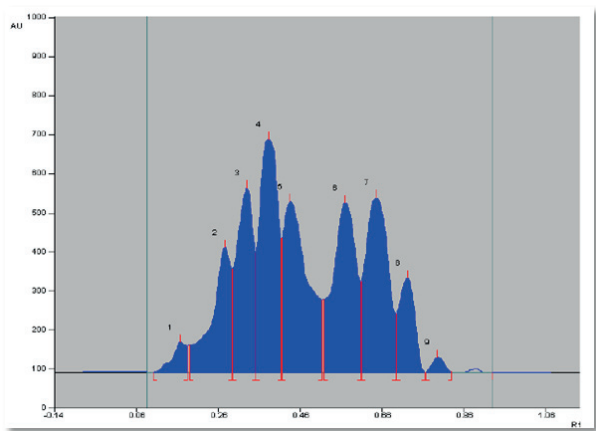


Figure 6. HPTLC fingerprinting of CAL at 254 nm.

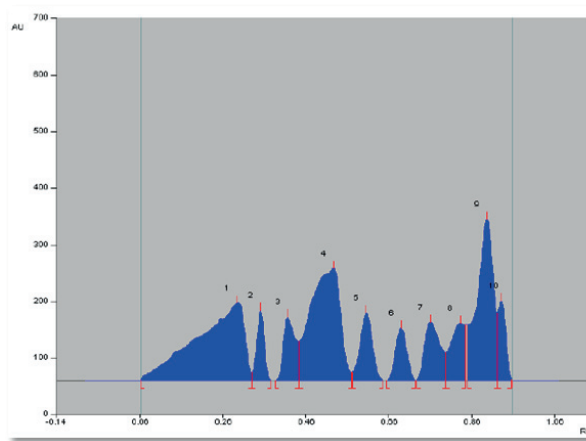


Figure 8. HPTLC Absorbance of CFL at 254 nm.

Peak	Start Position	Start Height	Max Position	Max Height	Max %	End Position	End Height	Area	Area %	Assigned substance
1	0.10 Rf	0.1 AU	0.17 Rf	76.5 AU	2.50 %	0.18 Rf	37.6 AU	2162.4 AU	1.80 %	unknown *
2	0.19 Rf	69.0 AU	0.27 Rf	318.9 AU	10.42 %	0.29 Rf	33.2 AU	12180.9 AU	10.13 %	unknown *
3	0.29 Rf	264.7 AU	0.33 Rf	472.2 AU	15.43 %	0.35 Rf	33.0 AU	15210.3 AU	12.65 %	unknown *
4	0.35 Rf	305.3 AU	0.38 Rf	596.3 AU	19.49 %	0.41 Rf	41.0 AU	21576.1 AU	17.94 %	unknown *
5	0.41 Rf	343.7 AU	0.43 Rf	436.5 AU	14.27 %	0.51 Rf	35.8 AU	21147.3 AU	17.59 %	unknown *
6	0.52 Rf	186.5 AU	0.57 Rf	433.2 AU	14.16 %	0.61 Rf	31.9 AU	19830.2 AU	16.49 %	unknown *
7	0.61 Rf	233.5 AU	0.65 Rf	446.2 AU	14.58 %	0.69 Rf	49.0 AU	19911.7 AU	16.56 %	unknown *
8	0.69 Rf	150.1 AU	0.72 Rf	241.0 AU	7.88 %	0.76 Rf	0.2 AU	7330.7 AU	6.10 %	unknown *
9	0.77 Rf	0.3 AU	0.79 Rf	38.9 AU	1.27 %	0.83 Rf	1.4 AU	900.9 AU	0.75 %	unknown *

Figure 7. HPTLC fingerprinting of CAL at 254 nm.

Peak	Start Position	Start Height	Max Position	Max Height	Max %	End Position	End Height	Area	Area %	Assigned substance
1	0.06 Rf	1.3 AU	0.29 Rf	137.0 AU	9.70 %	0.33 Rf	13.9 AU	12595.4 AU	25.11 %	unknown *
2	0.33 Rf	14.4 AU	0.35 Rf	123.4 AU	8.75 %	0.36 Rf	0.0 AU	1774.9 AU	3.54 %	unknown *
3	0.39 Rf	0.0 AU	0.42 Rf	112.0 AU	7.94 %	0.44 Rf	39.4 AU	2510.8 AU	5.01 %	unknown *
4	0.44 Rf	69.5 AU	0.53 Rf	197.7 AU	14.01 %	0.57 Rf	14.6 AU	11540.3 AU	23.01 %	unknown *
5	0.57 Rf	14.6 AU	0.61 Rf	119.6 AU	8.47 %	0.65 Rf	0.3 AU	2818.5 AU	5.62 %	unknown *
6	0.65 Rf	0.0 AU	0.69 Rf	93.0 AU	6.59 %	0.72 Rf	0.0 AU	2016.6 AU	4.02 %	unknown *
7	0.73 Rf	0.1 AU	0.76 Rf	102.9 AU	7.29 %	0.80 Rf	50.1 AU	3141.5 AU	6.26 %	unknown *
8	0.80 Rf	50.1 AU	0.83 Rf	100.6 AU	7.13 %	0.84 Rf	38.0 AU	2712.4 AU	5.41 %	unknown *
9	0.85 Rf	97.9 AU	0.90 Rf	284.4 AU	20.15 %	0.92 Rf	18.0 AU	8985.6 AU	17.91 %	unknown *
10	0.92 Rf	119.4 AU	0.93 Rf	140.9 AU	9.99 %	0.96 Rf	0.7 AU	2067.6 AU	4.12 %	unknown *

Figure 9. HPTLC fingerprinting of CFL at 254 nm.

Table 2. Correlation between reported and observed Rf value

Sr.no	Name of the Constituents	Reported Rf value	Observed Rf value
1	Chlorogenic Acid	0.45, 0.50	0.44
2	Isochlorogenic acid	0.80	0.80
3	Caffeic acid	0.90	0.92
4	Rutin	0.40	0.41
5	Apigenin 7-o-glucoside	0.75	0.76
6	Quercetin	0.35-0.75	0.29, 0.35, 0.38
7	Quercetin	0.80, 0.74	0.72, 0.84
8	Isoquercitrin	0.80, 0.60	0.57, 0.61, 0.79
9	Avicularin	0.85	0.83
10	Vitexin, 2-rhamnoside	0.45	0.33, 0.42
11	Vitexin	0.70	0.65
12	Luteolin	0.40-0.55	0.51
13	Kampeferol	0.40	0.31, 0.47
14	Flavone 6 – glycosides	0.65	0.69, 0.65, 0.67
15	Isoorientin	0.45	0.42

4. Discussion

All plants have their unique nature, structure, appearance, chemical constituents and therapeutic efficacy. Therefore, it is essential to study organoleptic properties of a medicinal plant, not only for quality control and standardization but also to recognize its structure and biology.

CAL and CFL were used by traditional practitioners for management of several ailments. Regularity of herbal products is a multifaceted task due to their diverse composition in all forms of the material. To protect reproducible quality of herbal products, appropriate control of starting material is essential. The primary step towards ensuring quality of preliminary material is

verification of the species. Now a days there has been a rapid increase in the standardization of many medicinal herbs of latent healing significance. Although many fresh techniques are available still identification of herbs by pharmacognostic properties is more liable. The macroscopic and microscopic explanation of a medicinal plant is the first step to create an identity and the purity of materials and should be conceded by undertaking any other tests, as described by World Health Organization²⁴.

Hence, it was felt desirable to pursue study on pharmacognostical and preliminary phytochemical studies of CAL and CFL roots to supplement useful information with regard to the exact identity of this plant

and, as this plant is extensively used in indigenous system of medicine.

Morphological assessment of drugs refer to valuation of drugs by taste, size, color, odor, shape and special features, like texture, touch. It is a method of qualitative evaluation based on the study of morphological and sensory summary of whole drugs. Organoleptic estimation is the conclusions drained from studies resulted due to feeling on organs of senses. All these parameters were recorded for roots of both the plants, CAL and CFL²⁵.

Microscopical techniques provide thorough information on the crude drug. Microscopical scrutiny of crude drugs from plant source is vital for the recognition of the grounded or crushed materials. Single-handed thorough microscopy could not provide complete assessment profile of a herbal drug, still it can supply underneath evidence, which when combined with other analytical parameters can be used to find the full confirmation for standardization and estimation of herbal drugs. Restricted burning of crude drugs result in an ash residue consisting of inorganic materials (metallic salts and silica). This value varies within fairly wide limits and hence a significant factor for the intention of evaluation of crude drugs. More direct contamination, such as by sand or earth, is immediately detected by the ash value. The quantity of active constituents in a given quantity of plant material when extracted with solvents is determined from the different extractive values obtained. Extractive values were used as revenue of evaluating crude drugs which were not eagerly expected by other means²⁶. Presence of bioactive components can be ascertained on the basis of various phytochemical testing. Thus in present investigation, extracts of CAL and CFL were subjected to phytochemical testing, which revealed that both plant extracts of CAL and CFL have shown the presence of various pharmacologically active chemicals such as flavonoids, saponins, glycosides, phenolic compounds, tannins. This confirmed that the targeted active molecules were present in selected extracts.

5. Conclusion

The present study reports the comparison between macroscopic, microscopic, physicochemical parameters and phytochemical parameters of CAL and CFL. These parameters may help in differentiating among these species. Thus, pharmacognostic parameters may serve as a tool for identification, authentication and standardization of CAL and CFL.

6. Acknowledgements

The authors thank Rajarshi Shahu College of pharmacy, Buldana for providing facilities to conduct the research.

7. Conflict of Interest Statement

There are no conflicts of interest among all the authors with publication of manuscript.

8. References

1. Kirtikar KR, Basu BD. Indian medicinal plants. Dehradun. International book distributors; 1999.
2. Deshpande S, Kewatkar SM, Paithankar VV. In-vitro antioxidant activity of different fraction of roots of *Cassia auriculata* Linn. Drug Invention Today. 2013; 5(2):164–8. <https://doi.org/10.1016/j.dit.2013.05.006>
3. Annie S, Rajagopal PL, Malini S. Effect of *Cassia auriculata* Linn. root extract on cisplatin and gentamicin-induced renal injury. Phytomed. 2005; 12(8): 555–60. <https://doi.org/10.1016/j.phymed.2003.11.010>. PMID:16121515
4. Rajagopal SK, Manickam P, Periyasamy V, Nama sivayam N. Activity of *Cassia auriculata* leaf extract in rats with alcoholic liver injury. J. Nutr. Biochem. 2003; 14(8):452–8. [https://doi.org/10.1016/S0955-2863\(03\)00053-6](https://doi.org/10.1016/S0955-2863(03)00053-6)
5. Gupta S, Sharma SB, Bansal SK, Prabhu KM. Antihyperglycemic and hypolipidemic activity of aqueous extract of *Cassia auriculata* L. leaves in experimental diabetes. Journal of Ethnopharmacol. 2009; 123(3):499–503. <https://doi.org/10.1016/j.jep.2009.02.019>. PMID:19473793
6. Prasanna R, Chandramoorthy HC, Ramaiyapillai P, Sakthisekaran D. In vitro evaluation of anticancer effect of *Cassia auriculata* leaf extract and curcumin through induction of apoptosis in human breast and larynx cancer cell lines. Biomed. Pre. Nutr. 2011; 1(2):153–60. <https://doi.org/10.1016/j.bionut.2010.12.006>
7. Sabu MC, Subburaju T. Effect of *Cassia auriculata* Linn. on serum glucose level, glucose utilization by isolated rat hemidiaphragm. J. Ethnopharmacol. 2002; 80(2–3):203–6. [https://doi.org/10.1016/S0378-8741\(02\)00026-0](https://doi.org/10.1016/S0378-8741(02)00026-0)
8. Kumaran A, Karunakaran RJ. Antioxidant activity of *Cassia auriculata* flowers. Fitoterapia. 2007; 78(1):46–7. <https://doi.org/10.1016/j.fitote.2006.09.031>. PMID:17071015
9. Thabrew I, Munasinghe J, Chackrewarthi S, Senarath S. The effects of *Cassia auriculata* and *Cardiospermum*

- halicacabum* teas on the steady state blood level and toxicity of carbamazepine. J. Ethnopharmacol. 2004; 90(1):145–50. <https://doi.org/10.1016/j.jep.2003.09.040>. PMID:14698522
10. Vijayaraj P, Muthukumar K, Sabarirajan J, Nachiappan V. Antihyperlipidemic activity of *Cassia auriculata* flowers in triton WR 1339 induced hyperlipidemic rats. Exper. Toxicol. Pathology. 2013; 65(1–2):135–41. <https://doi.org/10.1016/j.etp.2011.07.001>. PMID:21852078
 11. John CM, Sandrasaigaran P, Tong CK, Adam A, Ramasamy R. Immunomodulatory activity of poly phenols derived from *Cassia auriculata* flowers in aged rats. Cellular Immun. 2011; 271(2):474–9. <https://doi.org/10.1016/j.cellimm.2011.08.017>. PMID:21924708
 12. Duraipandiyan V, Ignacimuthu S. Antibacterial and antifungal activity of *Cassia fistula* L.: An ethno medicinal plant. J. Ethnopharmacol. 2007; 112(3):590–4. <https://doi.org/10.1016/j.jep.2007.04.008>. PMID:17532583
 13. Bhakta T, Mukherjee PK, Mukherjee K, Banerjee S, Mandal SC, Maity TK, Pal M, Saha BP. Evaluation of hepatoprotective activity of *Cassia fistula* leaf extract. J. Ethnopharmacol. 1999; 66(3):277–82. [https://doi.org/10.1016/S0378-8741\(98\)00220-7](https://doi.org/10.1016/S0378-8741(98)00220-7)
 14. Kumar MS, Sripriya R, Raghavan HV, Sehgal PK. Wound healing potential of *Cassia fistula* on infected albino rat model. J. Surgical Res. 2006; 131(2):283–9. <https://doi.org/10.1016/j.jss.2005.08.025>. PMID:16242721
 15. Siddhuraju P, Mohan PS, Becker K. Studies on the antioxidant activity of Indian Laburnum (*Cassia fistula* L.): A preliminary assessment of crude extracts from stem bark, leaves, flowers and fruit pulp. Food Chem. 2002; 79(1):61–7. [https://doi.org/10.1016/S0308-8146\(02\)00179-6](https://doi.org/10.1016/S0308-8146(02)00179-6)
 16. Manonmani G, Bhavapriya V, Kalpana S, Govindasamy S, Apparathanam T. Antioxidant activity of *Cassia fistula* (Linn.) flowers in alloxan induced diabetic rats. J. Ethnopharmacol. 2005; 97(1):39–42. <https://doi.org/10.1016/j.jep.2004.09.051>. PMID:15652272
 17. Duraipandiyan V, Ignacimuthu S, Paulraj MG. Antifeedant and larvicidal activities of Rhein isolated from the flowers of *Cassia fistula* L. Saudi J. Bio. Sci. 2011; 18(2):129–33. <https://doi.org/10.1016/j.sjbs.2010.12.009>. PMID:23961115 PMCID:PMC3730718
 18. Wijaya R, Neumann GM, Condrón R, Hughes AB, Polya GM. Defense proteins from seed of *Cassia fistula* includes a lipid transfer protein homologue and a protease inhibitory plant defense. Plant Sci. 2000; 159(2):243–55. [https://doi.org/10.1016/S0168-9452\(00\)00348-4](https://doi.org/10.1016/S0168-9452(00)00348-4)
 19. Gupta M, Mazumder UK, Rath N, Mukhopadhyay DK. Antitumor activity of methanolic extract of *Cassia fistula* L. seed against Ehrlich ascites carcinoma. J. Ethnopharmacol. 2000; 72(1–2):151–6. [https://doi.org/10.1016/S0378-8741\(00\)00227-0](https://doi.org/10.1016/S0378-8741(00)00227-0)
 20. Chauhan A, Agarwal M. Evaluating the antifertility potential of an aqueous extract from *Cassia fistula* seeds in male rats. Fert. Ster. 2010; 93(5):1706–10. <https://doi.org/10.1016/j.fertnstert.2009.09.001>. PMID:19819443
 21. Al-Meshal IA, Tariq M, Parmar NS, Ageel AM. Anti-inflammatory activity of the flavonoid fraction of khat (*Catha edulis* Forsk). Agen. Acti. 1986 Jan; 17(3–4):379–80. <https://doi.org/10.1007/BF01982654>. PMID:3962788
 22. Pharmacopoeia I. Ministry of health and family welfare, Govt. of India. controller of publications, New Delhi; 1996.
 23. Khandelwal K. Practical pharmacognosy. Pragati Books Pvt. Ltd.; 2008.
 24. Venkatesh S, Reddy YR, Ramesh M, Swamy MM, Mahadevan N, Suresh B. Pharmacognostical studies on *Dodonaea viscosa* leaves. Afr. J. Pharm. Pharmacol. 2008; 2(4):83–8.
 25. Kokate CK, Purohit AP, Gokhale SB. Pharmacognosy. Niralia. Prakashan, Pune, India; 2002.

PHARMACEUTICAL AND BIOPHARMACEUTICAL ASPECTS OF QUANTUM DOTS-AN OVERVIEW

SADDAM C. SHAIKH¹, SHWETA G. SABOO², PRASHANT S. TANDALE³, FAHIM S. MEMON⁴, SHARAD D. TAYADE^{4*}, M. AKIFUL HAQUE⁵, SHARUK L. KHAN⁶

¹Department of Pharmaceutics (D Pharm), Rajarshi Shahu College of Pharmacy, Buldana, Maharashtra, India 443001, ²Department of Pharmacognosy, Government College of Pharmacy, Karad, Maharashtra, India 415124, ³Department of Pharmaceutics, School of Pharmaceutical Sciences, Lovely Professional University, Punjab, India 144001, ⁴Department of Pharmaceutics, Rajarshi Shahu College of Pharmacy, Buldana, Maharashtra, India-443001, ⁵Department of Pharmaceutical Analysis, Anurag University, Venkatapur, Hyderabad, India 500088, ⁶Department of Pharmaceutical Chemistry, MUP's College of Pharmacy (B Pharm), Degaon, Risod, Washim, Maharashtra, India 444504
Emails: sharad_tayade1@rediffmail.com

Received: 23 Mar 2021, Revised and Accepted: 12 May 2021

ABSTRACT

In the twenty-first century, nanotechnology has become cutting-edge technology. It is interdisciplinary and multidisciplinary, covering numerous fields such as medicine, engineering, biology, physics, material sciences, and chemistry. The present work aims to cover the optical properties, method of preparations, surface modifications, bio-conjugation, characterization, stability, and cytotoxicity of quantum dots (QDs).

Articles were reviewed in English literature reporting the pharmaceutical and bio-pharmaceutical aspects of QDs which were indexed in Scopus, web of science, google scholar and PubMed without applying the year of publication criterion.

One significant value of utilizing nanotechnology is that one can alter and control the properties in a genuinely unsurprising way to address explicit applications' issues. In science and biomedicine, the usage of functional nanomaterials has been broadly investigated and has become one of the quick-moving and stimulating research directions. Different types of nanomaterial (silicon nanowires, QDs, carbon nanotubes, nanoparticles of gold/silver) were extensively utilized for biological purposes. Nanomedicine shows numerous advantages in the natural characteristics of targeted drug delivery and therapeutics. For instance, protection of drugs against degradation, improvement in the drug's stability, prolonged circulation time, decreased side effects, and enhanced distribution in tissues. The present review article deals with the quantum dots, their optical properties, method of preparations, surface modifications, bio-conjugation, characterization, stability, and cytotoxicity of quantum dots. The review also discusses various biomedical applications of QDs.

The QDs-based bio-nanotechnology will always be in the growing list of unique applications, with progress being made in specialized nanoparticle development, the detection of elegant conjugation methods, and the discovery of new targeting ligands.

Keywords: Quantum dots, Optical properties, Microwave-assisted method, Cytotoxicity, Cell imaging, Sentinel lymph-node mapping

© 2021 The Authors. Published by Innovare Academic Sciences Pvt Ltd. This is an open access article under the CC BY license (<https://creativecommons.org/licenses/by/4.0/>)
DOI: <https://dx.doi.org/10.22159/ijap.2021v13i4.41623>. Journal homepage: <https://innovareacademics.in/journals/index.php/ijap>

INTRODUCTION

In 1981, Ekimov and Onushenko described the Quantum dots (QDs), also called nanoscale semiconductor crystals [1]. The quantum dots are made up of material from periodic table group II-VI (CdSe) or III-V (InP) [2-6]. The most well studied and broadly utilized QDs are the cadmium selenide (Cd/Se) [3]. The cores and QDs targeting are protected by surface modification, and such changes significantly improve QDs sizes [7]. There are two kinds of fluorescent-based quantum dots, namely graphene and carbon quantum dots [8]. Quantum dots possess quantum confinement property and, on excitation from visible to infra-red wavelength, emit fluorescence [9, 10]. Usually, in the crystal core of a single QD, around 100-100,000 atoms are present. The size of QDs usually lies in between 2-10 nm diameter, which generally grows up to 5-20 nm in diameter after encapsulation of polymer [11, 12]. QDs comprise a semiconductor core, which is over-covered by shell and cap. The anatomy of QDs is represented in fig. 1 [13]. Semiconducting character and optical properties depend on the inorganic core. In QDs synthesis, the organic surfactants are developed and eventually shape ligands on the core surface [14-17]. The nature of the capping agent produced significantly relies on the final application of QDs. Frequently used ligands in QDs synthesis are alcohols, essential amines, and thiols [18, 19]. Bio-conjugation with carbohydrates, viruses, natural products, DNA fragments, and peptides assist by ligands through the covalent coupling and electrostatic or hydrophobic interactions [20, 21]. Determination of solubility, colloidal stability, control particle morphology, particle size distribution, and accumulation chiefly depends on ligands [22-24]. The present work aims to cover the optical properties, method of preparations, surface modifications,

bio-conjugation, characterization, stability, and cytotoxicity of QDs. Articles were reviewed in English literature reporting the pharmaceutical and bio-pharmaceutical aspects of QDs which were indexed in Scopus, web of science, google scholar and PubMed without applying the year of publication criterion. The keywords used for searching the literature are quantum dots, quantum dots in drug delivery system, methods of preparation of quantum dots, applications of quantum dots, recent advances in quantum dots, pharmaceutical and biopharmaceutical applications of quantum dots etc.

QDs core consists of several substances like cadmium, zinc, lead chalcogenides (CdS, CdSe, CdTe), copper salt (CuCl), arsenides (InAs, GaAs), semiconducting phosphides (InP, GaP), and nitrides (GaN). The shell of CdSe, ZnSe, PbS, ZnS, ZnTe, CdS, ZnO generally enclosed the core [3]. The core of nanomaterials guarded by outer covering from photoinitiated degradation and removing surface defects enhances the luminescence properties. Besides, cadmium, silver, copper, manganese, and rare earth metal ions can be used to dope the core of nanocrystals to enhance photoluminescence properties [25, 26]. QDs can be assembled, permitting particle shape, size, and chemical composition to be changed by suit a given application. The design and size of QDs are the properties that are frequently manipulated; this will decide if the QDs are chemically excited in NIR or UV light [27-29]. The biological targeting molecules (e. g., antibodies) or biocompatible polymeric materials (e. g., PEG) can be functionalized on the amenable external surface of QDs to improve their physiological system performance. The most commonly utilized QDs consist of graphene QDs, carbon QDs, and cadmium-based QDs [30-32]. QDs are found to be photochemically stable with symmetric, narrow, and strong fluorescence emission. QDs are

perfectly suitable for repetitive measurements or long-term observations [33–35]. After intradermal administration of dots in mouse paw, the near IR emitting dots might be noticed in the intraoperative imaging system's lymphatic system [36–39]. A report proposed that probes of quantum rods conjugated with transferring were productive for *in vitro* blood-brain barrier transmigration [40–43].

In fig. 2 composition of QDs is mentioned along with the material used [44]. The QDs are metastable and generally, through chemical surface modification, need to be stabilized. QDs show narrow-size tunable emission spectra, high extinction coefficients, and much diminishing photobleaching rates compared to organic dyes [45–48].

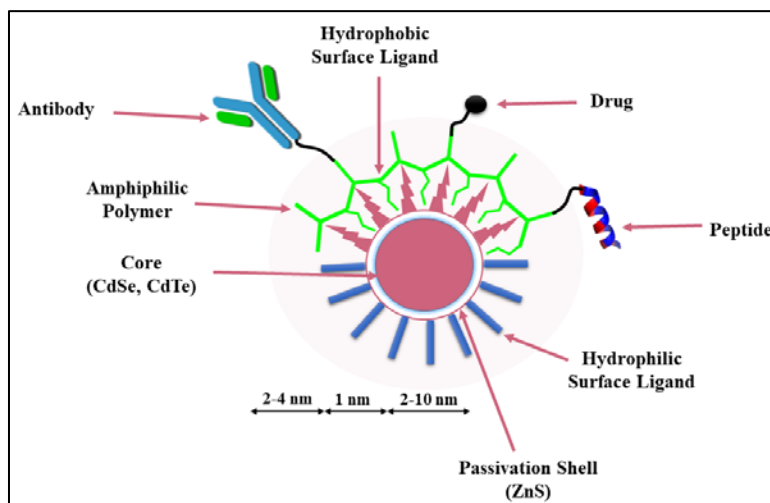


Fig. 1: The anatomy of QDs

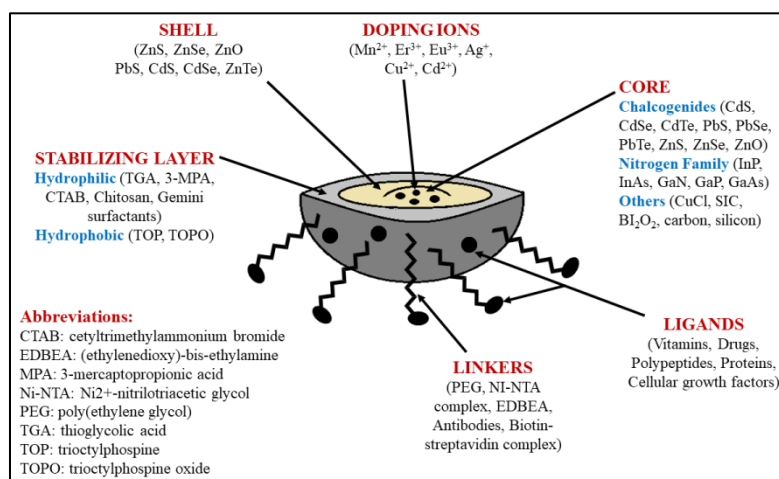


Fig. 2: The composition and material used for the synthesis of QDs

Advantages of QDs

QDs possess good physical stability and speedy degradation observed in optical imaging probes compared to QDs, whereas QDs depicted high instead of degradation. As compared to traditional dyes, QDs comprised higher photostability due to their fluorescence intensity and unique inorganic composition. QDs have a narrow emission peak and broader excitation spectra, whereas sharp emission peaks are depicted by organic dyes and narrow absorption spectrum observed with organic fluorophores. Due to these features, less energy is sufficient for the excitation of QDs irrespective of size. Hence, to excite multi-color QDs, single ultraviolet or blue wavelength beam is adequate. As compared to organic dyes, QDs show considerably longer fluorescence lifetimes and are 10-20 times brighter. Using a single source, QDs can feasibly be excited, and concurrently several targets tracked *in vivo* with the application of various probes as permitted by the multi-color QDs. With low background interference, high signal intensity depicts by the QDs conjugates due to sharp emission spectra and large Stokes Shift. QDs can be molded into various shapes, such as quantum dust, small crystals, and bead forms, and can be coated with

different biomaterials. QDs have comfortable and cost-effective manufacturing methods. Colloidal synthesis, epitaxial techniques, and lithographic techniques are various manufacturing methods of QDs [49–53].

Disadvantages of QDs

In biomedical applications, the size of the QDs has terrific importance. Through renal filtration, QDs having small size get removed from the body easily; however, there may be chances that the reticuloendothelial system takes the larger particles before reaching the targeted disease sites. The optimal activity is demonstrated by QDs having a 5-20 nm size of the polymer coating. When located in live cells, QDs aggregate and may interfere with cell function or kill the cells. Bio-conjugation of QDs results in difficult delivery of QDs into the target. QDs have unknown metabolism and excretion, leading to toxicity if it accumulates in the body tissues, spleen, liver and kidney. QDs become toxic if coated with mercaptoacetic acid. Even building material or the core of QDs (CdSe) is also toxic. Heavy metal ions

leak from the core due to oxidation and photolysis, which results in cytotoxicity [49, 50, 54–57].

Optical properties

QDs have expanded consideration because of their exceptional optical properties compared to traditional fluorescent dyes [58–60]. The distinctive optical properties of QDs permit multi-color imaging with no cross-talk in fluorescence microscopes among various detection channels. Moreover, with one single wavelength QDs having different emission maxima is excited and demand for many excitation sources is reduced. Time-resolved detection is possible because of the comparatively long fluorescence lifetime of the QDs-fluorescence, which considerably enhances the ratio (by 15 factors)

of signal-to-background concerning cell autofluorescence. QDs emission maxima can be correctly adjusted by changing QDs size. Short-wavelength light emits by smaller QDs as compared to larger particles [58, 60]. Electronic and unique optical properties in QDs are due to quantum confinement effects offering various benefits on current fluorophores, like lanthanide chelates, fluorescent proteins, and organic dyes. Properties that significantly impact fluorophore behavior and subsequently relevance to multiple circumstances consist of photostability, the width of the emission spectrum, decay lifetime, and the excitation spectrum. Concurrently, various QDs can emit different colors beneath the same excitation light to track and image numerous molecular targets [28–31]. The multi-color QDs probes can be utilized at the same time, as shown in fig. 3 [61].

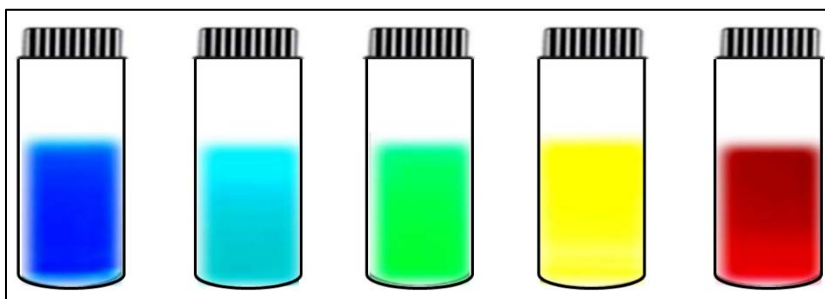


Fig. 3: In the visible range at various wavelengths, QDs displaying hues of colors

Methods of preparation

QDs are manufactured by various methods like chemical precipitation method, polyol-hydrolysis method, γ -radiation route, electron beam irradiation, photochemical synthesis [35, 36, 45, 47, 62–68]. However, few techniques of QDs fabrication are discussed below.

Organic phase method/organometallic method

Monodispersed QDs can be prepared through the organometallic process. Using this method, one can prepare monodispersed QDs with regularity in the core structure with uniform surface derivatization. Bis(trimethylsilyl) selenium and Me₂Cd is usually employed, organometallic precursors. Monodisperse CdSe achieved through organometallic reagents' pyrolysis between 250 °C to 300 °C by injecting in a hot coordinating liquid [69–71]. Different sizes of QDs formed relying upon the states of temperature. The organometallic method is right now regarded as the most vital technique to fabricate QDs. In this technique, various QDs demonstrating high quantum yield can be formed, and QDs size distribution is simply controlled by varying the reaction time or changing the temperature [72–74].

Water phase method/Aqueous solution method

Ionic perchlorates are utilized as precursors in this method. Ligands like Hydrosulphyl-containing materials, glutathione (GSH), 3-mercaptopropionic acid (3-MPA), in an aqueous medium used to prepare CdTe quantum dots. It is an eco-friendly and economical method. Likewise, the QDs formulated by the technique can be straightly given into the biological system. As compared with QDs created from the organometallic process QDs with thiol cap depicted wide size distribution and low quantum yield, poor stability in aqueous solution [75–80].

Hydrothermal method

QDs with narrow size and high quantum yields were formed by this method. This method also decreases the surface defects which were created during the synthesis process. In this method, the reagents are initially added to the hermetic container and increasing the temperature till supercritical temperature, a high pressure developed with this temperature leading to a successful reduction in the surface defects and reaction time of QDs [81–84].

Microwave-assisted method

This method was initially presented by the Kotov group and pursued by Qian and colleagues. Microwave irradiation as the heating source and water as a solvent were utilized. Heat the reaction system more than 100 °C to obtain uniform QDs and acquired a quantum yield of 17%. The organic phase synthesis formed hydrophobic QDs. But the QDs must have water solubility for the biological application. The nanocrystals produced from the water solubilization method will remain stable in biological systems and with no effect/change in the photophysical properties. Low fluorescence and less quantum yield achieved with water-soluble QDs formed in the early stage. Afterward, water-soluble QDs provide a higher quantum yield up to 50% with surface modifications and advanced synthetic procedures [85, 86]. But the huge challenge is to control the chemical and photophysical properties of QDs in water. Various methods have been established to formulate water-soluble QDs having smaller particle sizes. Ligand exchange is one method in which hydrophilic groups on QDs surface will exchange with hydrophobic groups through a ligand exchange mechanism. This method is merely using monodentate ligands; it will affect fluorescence efficiency and cause aggregation of nanoparticles. Few vacant sites were left by ligands while detaching from the surfaces, and these vacant sites work as trap centers and produce an accumulation of nanoparticles [87, 88].

This issue can be tackled utilizing ligand cross-linking and the di-thio group rather than the mono-thio group. One more method for developing water-soluble QDs is through the amphiphilic molecule incorporation, for example, phospholipids or polymers [89, 90]. The native surface of QDs ligand in the polymer encapsulation layer does not change. In the long-chain polymer molecules, the increased number of hydrophilic groups enhances the QDs dispersibility in biological buffer solutions and for conjugations of bio-probes gives chemical functional groups. The biocompatibility of QDs-polymer nanocomposites enhances and decreases their cytotoxicity due to the polymers coated on QDs. The QDs probe's photophysical properties vary with the size, structure, and chemical composition of the inorganic nanoparticle utilized for the QDs probe's development. The nanoparticle does not interact because of the lack of biological functioning with biological systems. The biomolecules like nucleic acids and proteins provide interaction with living cells used to decorate inert QDs for better biological application. QDs become more bio-compatible with living systems by incorporation of biomolecules [91–93]. The steps and design criteria used in QDs probes manufacturing are described in fig. 4 [12].

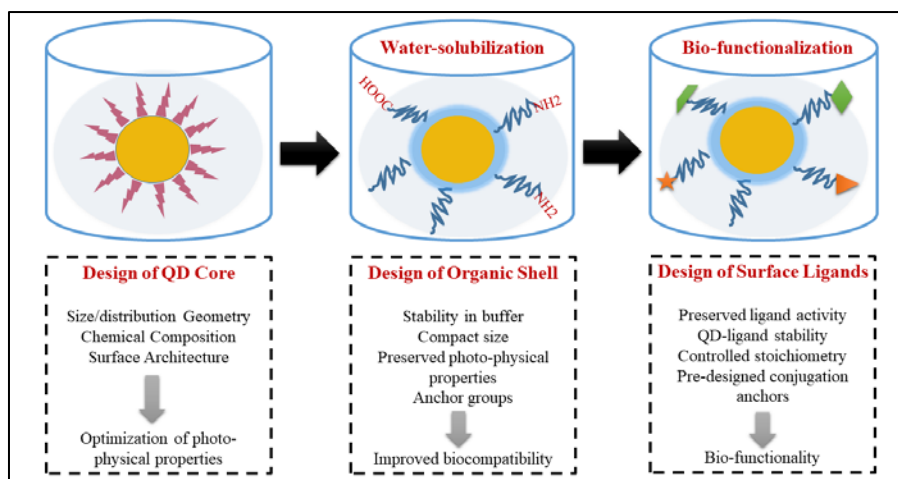


Fig. 4: The steps and design criteria used in QDs probes manufacturing

Surface modifications and Bio-conjugation of QDs

It is usually observed that the bare QDs are not practical for biological applications because of numerous reasons. Initially, in most of the synthesis approaches, QDs are water-insoluble. Thus, to obtain results from the optical properties of QDs, the surface has to be coated using a hydrophilic agent. Secondly, the core of QDs is very reactive, and with macromolecules, it undergoes potent unspecific interactions resulting in aggregation of particles and variation in fluorescence [94, 95]. Thirdly, the QDs toxicity can be significantly reduced due to the process of surface modification. The QDs have a hydrophobic surface modified by using hydrophilic agents to solubilize them in aqueous buffers. The peptides, dendrons, or oligomeric phosphines, thiol-containing molecules can be replaced with the hydrophobic surface ligands [96–98].

Further approaches employ phospholipids for modification or hydrophobic interactions between the QDs and amphiphilic polymers or encapsulate the QDs in a silica shell. Numerous potential outcomes are there in which biomolecules can be attached to the QDs. The utilization of QDs containing streptavidin is typically utilized because it is easy to link them to biotin-tagged biomolecules [99, 100]. Numerous strategies can be used to get QDs bio-conjugation consisting of covalent bond formation, multivalent chelation, or passive adsorption. There are two famous cross-linking reactions; active ester maleimide mediated amine, sulfhydryl coupling, and carbodiimide mediated amide formation. The bio-conjugation also determines by the hydrophilic coating as the required functional groups deliver by it and should be considered [101–103].

Molecules attachment for targeting

To the biomolecules like aptamers, small molecule ligands, or antibodies, the QDs must be cross-linked to make them precise to biological targets and thus employed for targeted drug delivery and diagnosis. QDs functionalization can be done by replacing biomolecules with a protein or sulfhydryl group by thiol and peptides with cysteine residues [104–107]. The QDs surface equilibrates with the thiols after incubation, and the biomolecules partially substitute the initial coating molecule. Coating of the QDs with mercapto acid can produce stable covalent bonds. Moreover, the electrostatic interactions among the macromolecules like peptides or proteins and the QDs surface can also give a facial way for modification and coating. Numerous organic functionalities are promptly attached for the QDs encapsulated in a silica shell using well-developed silane chemistry. At present different affinity reagents for QDs modification, like aptamers, small molecules, and peptides, which on cancer cells primarily identify particular overexpressed biomarkers, have been described to manufacture target drug delivery vesicles and cancer diagnosis probes [16, 64, 108–112].

Characterization of QDs

Important information regarding the morphology, structure, and physiochemical changes because of conjugation reactions can be disclosed by QDs optical characterization [113, 114]. For optical characterizations of QDs, UV-Vis and photoluminescence spectroscopy are the most utilized, non-destructive, quick, and contactless [115]. The size of QDs is finding out by employing atomic force microscopy, scanning tunneling microscopy, scanning electron microscopy, dynamic light scattering, transmission electron microscopy (TEM) studies [115–117]. The use of Raman scattering spectroscopy and photoluminescence excitation are also reported to determine the size and composition of QDs [118].

Stability of QDs

In aqueous conditions, a vital role in deciding the stability of QDs depends on the organic molecules and shell attached to the QDs surface. Finally, QDs precipitate with loss in their luminescence because of the loss of surface ligands. The stability of surface ligands can be affected by various processes. It was revealed that common surface ligands used and their photooxidation can cause desorption of hydrophilic thiols by their protonation [113]. To the cadmium chalcogenide QDs deprotonated thiols, thiolates are bound; if the QDs-ligand interface pH turns down to a particular value, protonation of ligand occurs and remove from the surface of QDs [2, 49, 102, 119]. Generally, in a low pH range, the hydrophilic thiols coated QDs precipitated in a pH range of 2 and 7, based on the chemical composition and the size of QDs [2, 45, 66, 67].

The photophysical properties and stability of QDs within the cells firmly subject to the local environment and intracellular localization. Its UV illumination over a long time leads to the photooxidation of surface ligands [46, 47, 65]. Enhancing the packing density and thickness of the ligand shell can hinder the beginning of photooxidation. The core of QDs resists photodegradation because of its inorganic nature, but the core integrity is influenced by the extended UV light exposure [86, 88, 91].

Cytotoxicity of QDs

In human beings, cadmium's half-life is around 20 y and is supposed to be carcinogenic, which can deposit in the kidney, liver, and bio-distribution in all tissues [120]. The toxicity of QDs relies on numerous chemicals, environmental and physical factors such as size, surface coating, charge, chemical composition, concentration, and free radical production, which might be deciding components of short and long-term *in vivo* side effects QDs [121]. The particles' biocompatibility has to be described, as QDs are utilized for studies including living cells and organisms [122].

QDs have not been characterized concerning their toxicity because they are new materials. The majority of the QDs contain cadmium,

which causes lethal impacts when it comes in contact with cells. Efforts need to be taken to secure the core of QDs, by developing a much lower toxicity shell, most of the time ZnS [123], which brought about a marked decrease in cytotoxic effects. The optical properties also enhance this layer; in most biological applications, core-shell systems have turned into the standard. But, to resolve the issue of cytotoxicity completely, the introduction of capping layers was still not adequate. A variety of other factors, such as the particle aggregation on the surface of the cell and even the QDs surface ligands stabilization, have been revealed to affect the cell's viability. The number of factors decides the degree of cytotoxicity, including size, dose, color, capping materials, surface chemistry, and processing parameters [124, 125]. So far, less information on QDs toxicity, particularly for *in vivo* use, is accessible. In this manner, QDs toxicity is a fundamental restriction for their utilization. Roberts reported that after administering CdSe/ZnS QDs, it caused lung injury and inflammation in rats. Likewise, Ho *et al.* detected granuloma following cadmium-based QDs administration in the lung of mice [123, 126, 127].

Biomedical applications of QDs

Cell imaging

Recently as an optional to organic dyes, QDs have been utilized for bioimaging. Furthermore, QDs have a broad absorption spectrum that makes easy excitation of two or multi-photon, particularly in the near-infrared range. Among all newly proposed imaging strategies, the bioimaging acknowledged by the confocal multi-photon excitation system is by all accounts the best solution utilizing QDs as fluorescent labels. In this imaging technique, the relatively low excitation energy is harmless for the samples. The QDs' resistance to photobleaching and bright photoluminescence allows even their real-time and long-term imaging. Recently, bioimaging of cancer cells can be done by utilizing QDs as bi-photonic fluorescent probes. Based on fluorescence imaging and magnetic resonance imaging (MRI) techniques, a multimodal tumor imaging system was given by Tan *et al.* [128]. Liu *et al.* have also fabricated other MRI nanoprobe and bimodal fluorescence with improved fluorescence and can be utilized for labeling HeLa cells [129]. The strong positive MRI contrast was used to characterize these QDs.

Bio-sensing

A new class of nanomaterials is luminescent semiconductor nanocrystals, the unique generation of fluorescent biosensors are created with the help of specific photophysical properties. Hence, the most common techniques utilized depend on fluorescence changes monitoring in immunoassays for the detection of biomolecules. The fluorescent probes have depicted extensive biosensing applications, diagnostic and clinical assays, ion detection, nucleic acid detection. Generally, the decline in QDs fluorescence emission intensity is seen in the presence of an analyte. For the detection of heavy metal ions and toxic organic substances, fluorescent nanocrystals are usually used. The L-cysteine-capped CdTe QDs synthesis and their utilization in selective trinitrotoluene recognition as the fluorescent probe was reported Chen *et al.* [130].

Photodynamic therapy

In the most recent couple of years, the photodynamic treatment (PDT) has come into sight as an advanced technique for malignancy treatment. PDT is an effective alternative to antibiotic therapy. PDT consists of a light, molecular oxygen, and photoactivable agent called photosensitizer (PS). Because of its specificity, PDT is a promising technique, simply the affected cells are exceptionally close to the PS, and until illuminated, the PS isn't cytotoxic. In photodynamic cytotoxicity, through this mechanism, the *in situ* generations of singlet oxygen (1O_2) seem to assume a crucial role because of the exceedingly productive interaction of the biomolecules with the 1O_2 species [131].

Multiplex coding

For applications demanding high throughput analysis of biomolecules, multiplex coding has tremendous potential. The small polymer multiplexed beads are embedded inside a finely controlled ratio, which provides a unique optical code. In contrast, oligonucleotides or antibodies act as molecular identifiers,

conjugated to the beads' surface [132, 133]. The intensity levels and types of fluorophores are the two variables that decide the maximum order of multiplexing possible. For instance, two fluorophores provide nine different microbeads with three intensity levels (1:1, 1:2, 3:2, 3:3). Prior efforts utilized organic fluorophores at multiplexed coding. Spectral overlaps occurred due to their broad emission spectra, and the number of fluorophores that could be used was constrained to only 2-3 dyes, leading to low multiplexing orders [134]. QDs proved to be an ideal replacement for this application because of their narrow and Gaussian-shaped emission spectra. For example, Xu *et al.* utilized QDs embedded microspheres to demonstrate the reliability and accuracy of polymerase chain reaction (PCR)-based single nucleotide polymorphism (SNP) genotyping assay [135, 136].

Bio-imaging of live cell

Live-cell imaging is a tough assignment compared with fixed cells and tissues because the thought that must be taken to keep cells alive and delivery of probes across the plasma membrane for examining intracellular targets is the challenging task. For the labeling of cell surface antigens, *in vivo* use of QDs have been shown. In recent times, the genuine favorable circumstances of QDs have been demonstrated for live-cell imaging by labeling plasma membrane receptors, for example, erbB/HER receptors and glycine receptors enabling single imaging molecules and real-time tracking of biomarkers [137-139]. The information gives new bits of knowledge into the mechanism of the ligand-receptor interaction. For delivery of QDs into the cells, different mechanisms have been utilized, for example, conjugation of QDs to cationic peptides or translocating proteins, or specific membrane receptors, via endocytosis non-specific uptake, and microinjection. Every one of these methods has effectively conveyed QDs into cells, even though it appears that the peptide-mechanism might be the most proficient [140-142].

DNA and RNA detection

QDs have become an essential tool because of resilient photoluminescence and multiple color properties for multiplexed detection of different DNA targets [138,143,144]. For DNA detection FRET technique has been one of the well-known methods. An enzyme is utilized to propel the detection sensitivity and to amplify the target. Excluding FRET, with the help of a magnetic nanoparticle-tagged DNA probe and a QDs labeled DNA probe with the DNA focus across hybridization detection, could be carried out [139, 145-148].

Gene delivery

For gene therapy, QDs depicted satisfactory performance as a promising candidate. RNA interference (RNAi) is an encouraging method with an extraordinary chance to battle disease. As RNase quickly degrades siRNAs, they have a short half-life, and they cannot cross the cell membrane because of their negative charge. For the loading of gene molecules, the fluorescent QDs have been examined as potential carriers among a large number of nanoparticles. The positively charged liposomes or polymers suppressed the negative charge of the nucleic acids. Using QDs liposome and QDs-polymer conjugates, imaging of siRNA transfection has been done successfully [149-151]. In a study performed by Lin *et al.* [152], reported that for silencing and efficient gene delivery, cadmium sulphoselenide/zinc sulfide quantum dots-polyethyleneimine (CdSSe/ZnS QDs-PEI) was found to be a proficient nanoplex formulation.

Plant bio-imaging

There is expanding use of QDs as markers in plant science for the cells or cell wall. For external agents, the cell wall is the first target location in a plant cell. Djikanovic *et al.* revealed that in the cell wall of the Picea omorika branch CdSe QDs usually attach to lignin and cellulose. Likewise, by interaction with the chains of C=C and C-C alternating bonds and interaction with the OH groups, binding to cellulose and lignin are accomplished [153, 154]. Data demonstrated that for the homogenous marking of the whole cell wall, the QDs are suitable, which is an outcome of the cell wall polymers that are structurally arranged inside the whole cell wall network. Inside the polymer structures in the cell wall composite, these qualities make possible a feasible nanoparticle penetration [155, 156].

QDs as antimicrobial agents

The various inorganic nanoparticles having antimicrobial activity have been tried. These comprised a range of metals and their oxide nanoparticles, such as zinc oxide, titanium dioxide, etc. Although upon excitation, these work on the principle of generating reactive oxygen species utilizing high wavelength lights, size-dependent optical properties are an additional benefit of QDs [157]. QDs are known to generate free radicals upon irradiation, and the core material of the semiconductor determined its quality. To the microbes, these produced free radicals are described as toxic, and also, in the process of irradiation, the liberated free heavy-metal ions are harmful to the bacteria [157–159]. Lu *et al.* depicted that excellent antimicrobial activity possessed by CdTe QDs. In their research, it was also shown that after binding to the bacteria's surface, the QDs disturbs the cellular antioxidative systems, reduces antioxidative enzyme activities, and instigate down-regulation of antioxidative genes [158].

In diagnosis and treatment of cancer

In the past several decades, cancer has attracted substantial research interest as a leading cause of human death [131, 143]. Ongoing advancements in QDs innovation have effectively had a tremendous effect on cancer imaging.

Sentinel lymph node mapping

The first lymph node or groups of nodes are the sentinel lymph nodes (SLNs) to which a primary tumor gives metastasizing cancer cells. A method that allows the recognition and the SLNs removal is known as SLN biopsy. Further lymph-node sampling is avoided if cancer is not found in the SLNs. At present, for breast cancer and melanoma staging and prognosis, SLN biopsy is in routine clinical use. Precise nodal mapping is required for success in SLN biopsy. Current mapping methods consist of utilizing peritumoral injection of radioisotopes, for example, the isosulfan blue dye, Technetium-99m-colloidal albumin, or the combination of the two agents. Kim *et al.* prepared the type II QDs and coated them with polydentate phosphine making soluble and stable QDs in serum [160]. It was observed that both in pigs and mice, the QDs were promptly identified in nearby SLN after intradermal injection. The multiple QDs under a single excitation source with different emission wavelengths may be used to identify and sort the complicated lymphatic system [161, 162].

Primary tumor detection

Prostate-specific membrane antigens (PSMA) for cancer imaging may serve as markers or targets for diagnosis. In principle, conjugating the QDs to antibodies, particularly for these antigens, helps the primary tumor recognition and identification of distant or regional metastases. Nie's group has performed some original work utilizing conjugated antibody QDs to target prostate tumor. To nude mice bearing prostate tumor xenografts, a specific PSMA antibody conjugated with Cd/Se QDs is intravenously administered. Localization of the QDs to the tumor was seen after 2 h of circulations [163, 164]. On the other hand, at 15 times higher concentration as compared to conjugated PSMA antibody QDs, when the PEG-modified QDs injected, only after 24 h circulation reached the tumor presumably by diffusion, a much longer time interval [165, 166].

An efficient lymphatic drainage system lacks in the tumor, and blood vessels are leaky; hence at the tumor site, the passive diffusion occurred because of enhanced permeability and retention of QDs. In the clinical setting, to accomplish a maximal impact on cancer diagnosis, research must be progress in the direction of small tumor identification and localization, which are currently not detected through conventional imaging methods [167–169].

QDs as drug nano-carriers

In the previous decade, with the development of surface modification technique, QDs with water-soluble capping stabilizer, for example, polyethylene glycol polymer, mercaptoethylamine, and mercaptoacetic acid are conjugate promptly with drug molecules

through electrostatic interaction or covalent bonds, giving complex nanomedicine with QDs as drug carriers [8, 14, 22, 24].

Other applications

QDs have additionally been observed to be valuable in the study of microorganisms. Kloepper *et al.* revealed that fungi and bacterial glycoproteins could be targeted with QDs conjugates [170]. Numerous different pathogens such as *Salmonella Typhi*, *Giardia lamblia* and *Cryptosporidium parvum*, and *Listeria monocytogenes* were targeted using QDs [157–159].

Additionally, for *Escherichia coli*, the QDs were utilized as cell membrane permeable indicators. It might be possible that QDs surface graft with the therapeutic enzymes and activate them producing free radicals (for example, singlet oxygen) or by light by optically cycling the QDs. For determining the content of spironolactone in the tablet, the first applications of QDs were exhibited by Liang and colleagues [171]. In neuroscience research, QDs stand for a new device of enormous potential. The studies that are restricted by the limited anatomy of neuronal and glial interactions are helpful. Photostability, multiplexing potential and inorganic nature are the features of QDs that make them significant worth for drug discovery [8, 11, 15, 21]. Outstanding review articles are available in the literature for additional information on QDs fundamentals and applications.

CONCLUSION

In nanomedicine, the potential applications of QDs span the areas of nano-diagnostics, drug delivery, therapy, and imaging. In the last place, the most promising applications are intracellular imaging, tissue imaging, multiplexed diagnostics, tumor detection, infectious agent detection, immunohistochemistry, and fluoro-immunoassays. Despite all their potential in nanomedicine, QDs are still away from large-scale utilization because of toxicity concerns, regulatory and commercialization issues. The QDs-based bio-nanotechnology will always be a growing list of amazing applications with progress being made in specialized nanoparticle development and the detection of elegant conjugation methods, discovering new targeting ligands.

LIST OF ABBREVIATIONS

QDs: Quantum Dots; 3-MPA: 3-mercaptopropionic acid; TEM: Transmission Electron Microscopy; MRI: Magnetic Resonance Imaging; PDT: Photodynamic Treatment; PS: Photosensitizer; 1O₂: Singlet Oxygen; PCR: Polymerase Chain Reaction; SNP: Single Nucleotide Polymorphism; RNAi: RNA Interference; SLNs: Sentinel Lymph Nodes; PSMA: Prostate-specific Membrane Antigens

ACKNOWLEDGEMENT

None

FUNDING

Nil

AUTHORS CONTRIBUTIONS

SCS: conceptualization and literature survey; SGS: literature survey on optical properties of QDs and writing; SDT: a literature review on methods of preparation of QDs and article writing; FSM: literature survey on applications of QDs and writing; SLK: overall literature survey, manuscript writing and referencing; PST: proofreading and contributed in writing style. All authors read and approved the final manuscript.

CONFLICT OF INTERESTS

The authors declare that they have no competing interests.

REFERENCES

- Matea CT, Mocan T, Tabaran F, Pop T, Mosteanu O, Puia C, *et al.* Quantum dots in imaging, drug delivery and sensor applications. *Int J Nanomed* 2017;12:5421–31.
- Moreels I, Justo Y, Geyter B De, Haustraete K, Martins JC, Hens Z. Quantum dots: a surface chemistry study. *ACS Nano* 2012;5:2004–12.

3. Dabbousi BO, Rodriguez Viejo J, Mikulec FV, Heine JR, Mattoussi H, Ober R, *et al.* (CdSe)ZnS core-shell quantum dots: synthesis and characterization of a size series of highly luminescent nanocrystallites. *J Phys Chem B* 1997;101:9463–75.
4. Maxwell T, Nogueira Campos MG, Smith S, Doomra M, Thwin Z, Santra S. Quantum dots. In: *Nanoparticles for biomedical applications: fundamental concepts, biological interactions and clinical applications*; 2019. p. 243–65.
5. Senthil Kumar M, Valarmathi S, Bhima P, Prudhvi Devabaktuni S, Raja A, Vallabhaneni SD. Quantum dots. *Int J Pharm Technol* 2012;4:1929–49.
6. Bawendi MG, Steigerwald ML, Brus LE. The quantum mechanics of larger semiconductor clusters (“Quantum dots”). *Annu Rev Phys Chem* 1990;41:477–96.
7. Biju V. Chemical modifications and bioconjugate reactions of nanomaterials for sensing, imaging, drug delivery and therapy. *Chem Soc Rev* 2014;43:744–64.
8. Portney NG, Ozkan M. Nano-oncology: drug delivery, imaging, and sensing. *Anal Bioanal Chem* 2006;384:620–30.
9. Godbole NN, Galgatte UC, Chaudhari PD. Development and *in vitro* evaluation of quantum dots as a carrier for delivery of 5-fluorouracil. *Int J Pharm Pharm Sci* 2016;8:289–96.
10. SLJ, Gupta NV. Diabetic retinopathy: an inclusive review on current treatment and management approaches. *Asian J Pharm Clin Res* 2018;11:54.
11. Qi L, Gao X. Emerging application of quantum dots for drug delivery and therapy. *Expert Opinion Drug Delivery* 2008;5:263–7.
12. Zrazhevskiy P, Sena M, Gao X. Designing multifunctional quantum dots for bioimaging, detection, and drug delivery. *Chem Soc Rev* 2010;39:4326–54.
13. Maysinger D, Lovric J, Eisenberg A, Savic R. Fate of micelles and quantum dots in cells. *Eur J Pharm Biopharm* 2007;65:270–81.
14. Caruthers SD, Wickline SA, Lanza GM. Nanotechnological applications in medicine. *Curr Opin Biotechnol* 2007;18:26–30.
15. Wagner AM, Knipe JM, Orive G, Peppas NA. Quantum dots in biomedical applications. *Acta Biomaterialia* 2019;94:44–63.
16. Kong FY, Zhang JW, Li RF, Wang ZX, Wang WJ, Wang W. Unique roles of gold nanoparticles in drug delivery, targeting and imaging applications. *Molecules* 2017;22:1445.
17. Wang Q, Huang X, Long Y, Wang X, Zhang H, Zhu R, *et al.* Hollow luminescent carbon dots for drug delivery. *Carbon* 2013;59:192–9.
18. Wegner KD, Hildebrandt N. Quantum dots: Bright and versatile *in vitro* and *in vivo* fluorescence imaging biosensors. *Chem Soc Rev* 2015;44:4792–834.
19. Lee JH, Yigit MV, Mazumdar D, Lu Y. Molecular diagnostic and drug delivery agents based on aptamer-nanomaterial conjugates. *Adv Drug Delivery Rev* 2010;62:592–605.
20. Xu G, Zeng S, Zhang B, Swihart MT, Yong KT, Prasad PN. New generation cadmium-free quantum dots for biophotonics and nanomedicine. *Chem Rev* 2016;116:12234–327.
21. Chinnathambi S, Chen S, Ganesan S, Hanagata N. Silicon quantum dots for biological applications. *Adv Healthcare Mater* 2014;3:10–29.
22. Probst CE, Zrazhevskiy P, Bagalkot V, Gao X. Quantum dots as a platform for nanoparticle drug delivery vehicle design. *Adv Drug Delivery Rev* 2013;65:703–18.
23. Frecker T, Bailey D, Arzeta Ferrer X, McBride J, Rosenthal SJ. Review-quantum dots and their application in lighting, displays, and biology. *ECS J Solid State Sci Technol* 2016;5:R3019–31.
24. Lin J, Chen X, Huang P. Graphene-based nanomaterials for bioimaging. *Adv Drug Delivery Rev* 2016;105:242–54.
25. Ramamurthy SK, Sridhar C. Parthenium mediated synthesis of zinc oxide nanoparticles and its characterization. *Int J Appl Pharm* 2019;11:113–6.
26. Sivapriya V, Ponnarmadha S, Azeezand NA, Sudarshanadeepa V. Novel nanocarriers for ethnopharmacological formulations. *Int J Appl Pharm* 2018;10:26–30.
27. Jinhao GAO, Hongwei GU, Bing XU. Multifunctional magnetic nanoparticles: design, synthesis, and biomedical applications. *Acc Chem Res* 2009;42:1097–107.
28. Cassette E, Helle M, Bezdetnaya L, Marchal F, Dubertret B, Pons T. Design of new quantum dot materials for deep tissue infrared imaging. *Adv Drug Delivery Rev* 2013;65:719–31.
29. Martinez Carmona M, Gun’Ko Y, Vallet Regi M. ZnO nanostructures for drug delivery and theranostic applications. *Nanomaterials* 2018;8:268.
30. Boakye Yiadom KO, Kesse S, Opoku Damoah Y, Filli MS, Aquib M, Joelle MMB, *et al.* Carbon dots: applications in bioimaging and theranostics. *Int J Pharm* 2019;564:308–17.
31. Liu ML, Chen B Bin, Li CM, Huang CZ. Carbon dots: synthesis, formation mechanism, fluorescence origin and sensing applications. *Green Chem* 2019;21:449–71.
32. Delehanty JB, Mattoussi H, Medintz IL. Delivering quantum dots into cells: Strategies, progress and remaining issues. *Anal Bioanal Chem* 2009;393:1091–105.
33. Bilan R, Fleury F, Nabiev I, Sukhanova A. Quantum dot surface chemistry and functionalization for cell targeting and imaging. *Bioconjugate Chem* 2015;26:609–24.
34. Hild WA, Breunig M, Goepperich A. Quantum dots-nano-sized probes for the exploration of cellular and intracellular targeting. *Eur J Pharm Biopharm* 2008;68:153–68.
35. Bulte JWM, Modo MMJ. Design and applications of nanoparticles in biomedical imaging. Design and applications of nanoparticles in biomedical imaging; 2016. p. 1–469.
36. Azzazy HME, Mansour MMH, Kazmierczak SC. From diagnostics to therapy: prospects of quantum dots. *Clin Biochem* 2007;40:917–27.
37. Massey M, Wu M, Conroy EM, Algar WR. Mind your P’s and Q’s: the coming of age of semiconducting polymer dots and semiconductor quantum dots in biological applications. *Curr Opin Biotechnol* 2015;34:30–40.
38. Jaleel JA, Pramod K. Artful and multifaceted applications of carbon dot in biomedicine. *J Controlled Release* 2018;269:302–21.
39. Gittard SD, Miller PR, Boehm RD, Ovsianikov A, Chichkov BN, Heiser J, *et al.* Multiphoton microscopy of transdermal quantum dot delivery using two-photon polymerization-fabricated polymer microneedles. *Faraday Discuss* 2011;149:171–85.
40. Zuo P, Lu X, Sun Z, Guo Y, He H. A review on syntheses, properties, characterization and bioanalytical applications of fluorescent carbon dots. *Microchim Acta* 2016;183:519–42.
41. Ding C, Zhu A, Tian Y. Functional surface engineering of C-dots for fluorescent biosensing and *in vivo* bioimaging. *Acc Chem Res* 2014;47:20–30.
42. Homan K, Mallidi S, Cooley E, Emelianov S. Combined photoacoustic and ultrasound imaging of metal nanoparticles *in vivo*. *Nanoimaging* 2011;3:225–49.
43. Gao X, Du C, Zhuang Z, Chen W. Carbon quantum dot-based nanopores for metal ion detection. *J Materials Chem C* 2016;4:6927–45.
44. Geszke Moritz M, Moritz M. Quantum dots as versatile probes in medical sciences: synthesis, modification and properties. *Mater Sci Eng* 2013;33:1008–21.
45. Molaei MJ. A review on nanostructured carbon quantum dots and their applications in biotechnology, sensors, and chemiluminescence. *Talanta* 2019;196:456–78.
46. Bajwa N, Mehra NK, Jain K, Jain NK. Pharmaceutical and biomedical applications of quantum dots. *Artif Cells Nanomed Biotechnol* 2016;44:758–68.
47. Dey N, Rao M. Quantum dot: novel carrier for drug delivery. *Int J Res Pharm Biomed Sci* 2011;2:448–58.
48. Mo D, Hu L, Zeng G, Chen G, Wan J, Yu Z, *et al.* Cadmium-containing quantum dots: properties, applications, and toxicity. *Appl Microbiol Biotechnol* 2017;101:2713–33.
49. Nakahara M, Ohmi T. Quantum computing with quantum dots. In: *Quantum Computing*; 2008. p. 377–98.
50. Wu P, Yan XP. Doped quantum dots for chemo/biosensing and bioimaging. *Chem Soc Rev* 2013;42:5489–521.
51. Biju V, Itoh T, Ishikawa M. Delivering quantum dots to cells: bioconjugated quantum dots for targeted and nonspecific extracellular and intracellular imaging. *Chem Soc Rev* 2010;39:3031–56.
52. Gaponik N, Talapin DV, Rogach AL, Hoppe K, Shevchenko EV, Kornowski A, *et al.* Thiol-capping of CdTe nanocrystals: An alternative to organometallic synthetic routes. *J Phys Chem B* 2002;106:7177–85.
53. Emin S, Singh SP, Han L, Satoh N, Islam A. Colloidal quantum dot solar cells. *Sol Energy* 2011;85:1264–82.

54. Chen W, Lv G, Hu W, Li D, Chen S, Dai Z. Synthesis and applications of graphene quantum dots: a review. *Nanotechnol Rev* 2018;7:157–85.
55. Campuzano S, Yanez Sedeno P, Pingarron JM. Carbon dots and graphene quantum dots in electrochemical biosensing. *Nanomaterials* 2019;9:634.
56. Lim SY, Shen W, Gao Z. Carbon quantum dots and their applications. *Chem Soc Rev* 2015;44:362–81.
57. Barroso MM. Quantum dots in cell biology. *J Histochem Cytochem* 2011;59:237–51.
58. Klimov VI, Mikhailovsky AA, Xu S, Malko A, Hollingsworth JA, Leatherdale CA, *et al.* Optical gain and stimulated emission in nanocrystal quantum dots. *Science* 2000;290:314–7.
59. Kim S, Fisher B, Eisler HJ, Bawendi M. Type-II quantum dots: CdTe/CdSe(core/shell) and CdSe/ZnTe(core/shell) heterostructures. *J Am Chem Soc* 2003;125:11466–7.
60. Chan WCW, Maxwell DJ, Gao X, Bailey RE, Han M, Nie S. Luminescent quantum dots for multiplexed biological detection and imaging. *Curr Opin Biotechnol* 2002;13:40–6.
61. True LD, Gao X. Quantum dots for molecular pathology: their time has arrived. *J Mol Diagnostics* 2007;9:7–11.
62. Moloney MP, Govan J, Loudon A, Mukhina M, Gun'ko YK. Preparation of chiral quantum dots. *Nat Protoc* 2015;10:558–73.
63. Ghaderi S, Ramesh B, Seifalian AM. Fluorescence nanoparticles “quantum dots” as drug delivery system and their toxicity: a review. *J Drug Targeting* 2011;19:475–86.
64. Nurunnabi M, Parvez K, Nafujjaman M, Revuri V, Khan HA, Feng X, *et al.* Bioapplication of graphene oxide derivatives: drug/gene delivery, imaging, polymeric modification, toxicology, therapeutics and challenges. *RSC Adv* 2015;5:42141–61.
65. Obonyo O, Fisher E, Edwards M, Douroumis D. Quantum dots synthesis and biological applications as imaging and drug delivery systems. *Crit Rev Biotechnol* 2010;30:283–301.
66. Bilan R, Nabiev I, Sukhanova A. Quantum dot-based nanotools for bioimaging, diagnostics, and drug delivery. *Chem BioChem* 2016;17:2103–14.
67. Gulia S, Kakkar R. ZnO quantum dots for biomedical applications. *Adv Materials Lett* 2013;4:876–87.
68. Liu X, Pang J, Xu F, Zhang X. Simple approach to synthesize amino-functionalized carbon dots by carbonization of chitosan. *Sci Rep* 2016;6:31100.
69. Coe S, Woo WK, Bawendi M, Bulovic V. Electroluminescence from single monolayers of nanocrystals in molecular organic devices. *Nature* 2002;420:800–3.
70. Swarnkar A, Marshall AR, Sanehira EM, Chernomordik BD, Moore DT, Christians JA, *et al.* Quantum dot-induced phase stabilization of α -CsPbI₃ perovskite for high-efficiency photovoltaics. *Science* 2016;354:92–5.
71. Bak S, Kim D, Lee H. Graphene quantum dots and their possible energy applications: a review. *Curr Appl Physics* 2016;16:1192–201.
72. Grisorio R, Debellis D, Suranna GP, Gigli G, Giansante C. The dynamic organic/inorganic interface of colloidal PbS quantum dots. *Angew Chem Int Ed* 2016;55:6628–33.
73. Seguin R, Schliwa A, Rodt S, Potschke K, Pohl UW, Bimberg D. Size-dependent fine-structure splitting in self-organized InAs/GaAs quantum dots. *Phys Rev Lett* 2005;95:257402.
74. Bhattacharya P, Ghosh S, Stiff Roberts AD. Quantum dot optoelectronic devices. *Annu Rev Mater Res* 2004;34:1–40.
75. Li H, He X, Kang Z, Huang H, Liu Y, Liu J, *et al.* Water-soluble fluorescent carbon quantum dots and photocatalyst design. *Angew Chem Int Ed* 2010;49:4430–4.
76. Darbandi M, Thomann R, Nann T. Single quantum dots in silica spheres by microemulsion synthesis. *Chem Mater* 2005;17:5720–5.
77. Tang L, Ji R, Cao X, Lin J, Jiang H, Li X, *et al.* Deep ultraviolet photoluminescence of water-soluble self-passivated graphene quantum dots. *ACS Nano* 2012;6:5102–10.
78. Wang F, Pang S, Wang L, Li Q, Kreiter M, Liu CY. One-step synthesis of highly luminescent carbon dots in noncoordinating solvents. *Chem Mater* 2010;22:4528–30.
79. Ahirwar S, Mallick S, Bahadur D. Electrochemical method to prepare graphene quantum dots and graphene oxide quantum dots. *ACS Omega* 2017;2:8343–53.
80. Nann T. Phase-transfer of CdSe@ZnS quantum dots using amphiphilic hyperbranched polyethyleneimine. *Chem Commun* 2005;13:1735–6.
81. Tian P, Tang L, Teng KS, Lau SP. Graphene quantum dots from chemistry to applications. *Materials Today Chem* 2018;10:221–58.
82. Baruah S, Dutta J. Hydrothermal growth of ZnO nanostructures. *Sci Technol Adv Mater* 2009;10:013001.
83. Wang Q, Zheng H, Long Y, Zhang L, Gao M, Bai W. Microwave-hydrothermal synthesis of fluorescent carbon dots from graphite oxide. *Carbon NY* 2011;49:3134–40.
84. Prasannan A, Imae T. One-pot synthesis of fluorescent carbon dots from orange waste peels. *Ind Eng Chem Res* 2013;52:15673–8.
85. Park SY, Thongsai N, Chae A, Jo S, Kang EB, Paoprasert P, *et al.* Microwave-assisted synthesis of luminescent and biocompatible lysine-based carbon quantum dots. *J Ind Eng Chem* 2017;47:329–35.
86. He Y, Zhong Y, Peng F, Wei X, Su Y, Lu Y, *et al.* One-pot microwave synthesis of water-dispersible, ultraphoto- and pH-stable, and highly fluorescent silicon quantum dots. *J Am Chem Soc* 2011;133:14192–5.
87. Sumanth Kumar D, Jai Kumar B, Mahesh HM. Quantum nanostructures (QDs): an overview. In: *Synthesis of Inorganic Nanomaterials*; 2018. p. 59–88.
88. Liu Y, Xiao N, Gong N, Wang H, Shi X, Gu W, *et al.* One-step microwave-assisted polyol synthesis of green luminescent carbon dots as optical nanoprobes. *Carbon* 2014;68:258–64.
89. Singh I, Arora R, Dhiman H, Pahwa R. Carbon quantum dots: Synthesis, characterization and biomedical applications. *Turkish J Pharm Sci* 2018;15:219–30.
90. Wang X, Feng Y, Dong P, Huang J. A mini-review on carbon quantum dots: preparation, properties, and electrocatalytic application. *Front Chem* 2019;7:671.
91. Qian H, Qiu X, Li L, Ren J. Microwave-assisted aqueous synthesis: A rapid approach to prepare highly luminescent ZnSe(S) alloyed quantum dots. *J Phys Chem B* 2006;110:9034–40.
92. Rangel Mendez JR, Matos J, Chazaro Ruiz LF, Gonzalez Castillo AC, Barrios Yanez G. Microwave-assisted synthesis of C-doped TiO₂ and ZnO hybrid nanostructured materials as quantum-dots sensitized solar cells. *Appl Surf Sci* 2018;434:744–55.
93. Lehnen T, Zopes D, Mathur S. Phase-selective microwave synthesis and inkjet printing applications of Zn₂SnO₄ (ZTO) quantum dots. *J Mater Chem* 2012;22:17732–6.
94. Vasudevan D, Gaddam RR, Trinchì A, Cole I. Core-shell quantum dots: properties and applications. *J Alloys Compounds* 2015;636:395–404.
95. Wu YL, Lim CS, Fu S, Tok AIY, Lau HM, Boey FYC, *et al.* Surface modifications of ZnO quantum dots for bio-imaging. *Nanotechnology* 2007;18:215604.
96. Monopoli MP, Pitek AS, Lynch I, Dawson KA. Nanomaterial interfaces in biology. In: *Nanomaterial Interfaces in Biology: Methods and Protocols, Methods in Molecular Biology*; 2013;1025:137155.
97. Yuan CT, Chou WC, Chuu DS, Chang WH, Lin HS, Ruaan RC. Fluorescence properties of colloidal CdSe/ZnS quantum dots with various surface modifications. *J Med Biol Eng* 2006;26:131–5.
98. Krogmeier JR, Kang HG, Clarke ML, Yim P, Hwang J. Probing the dynamic fluorescence properties of single water-soluble quantum dots. *Opt Commun* 2008;281:1781–8.
99. Kumar P, Kukkar D, Deep A, Sharma SC, Bharadwaj LM. Synthesis of mercaptopropionic acid stabilized CDS quantum dots for bioimaging in breast cancer. *Adv Mater Lett* 2012;3:471–5.
100. Borse V, Sadawana M, Srivastava R. CdTe quantum dots: aqueous phase synthesis, stability studies and protein conjugation for development of biosensors. In: *Nanophotonics VI*; 2016;9884:988423.
101. Singla R, Guliani A, Kumari A, Yadav SK. Metallic nanoparticles, toxicity issues and applications in medicine. In: *Nanoscale materials in targeted drug delivery, theragnosis and tissue regeneration*; 2016. p. 41–80.
102. Dobhal G, Garima. Quantum dot bioconjugates for the detection of extracellular vesicles in saliva and breath. MSc Thesis; 2019. Available from <http://researcharchive.vuw.ac.nz/handle/10063/8119>. [Last accessed on 10 Mar 2021].

103. Tian B, Al-Jamal WT, Stuart M, Kostarelos K. Doxorubicin-loaded and antibody-conjugated liposome-QD hybrid vesicles for targeted cancer therapy and imaging. In: *Nanotechnology 2010: Bio Sensors, Instruments, Medical, Environment and Energy-Technical Proceedings of the 2010 NSTI Nanotechnology Conference and Expo, NSTI-Nanotech 2010*; 3:380-1.
104. Pardo J, Peng Z, Leblanc RM. Cancer targeting and drug delivery using carbon-based quantum dots and nanotubes. *Molecules* 2018;23:378.
105. Howarth M, Takao K, Hayashi Y, Ting AY. Targeting quantum dots to surface proteins in living cells with biotin ligase. *Proc Natl Acad Sci USA* 2005;102:7583-8.
106. Liu W, Howarth M, Greytak AB, Zheng Y, Nocera DG, Ting AY, *et al.* Compact biocompatible quantum dots functionalized for cellular imaging. *J Am Chem Soc* 2008;130:1274-84.
107. Smith AM, Duan H, Mohs AM, Nie S. Bioconjugated quantum dots for *in vivo* molecular and cellular imaging. *Adv Drug Delivery Rev* 2008;60:1226-40.
108. Ghasemi Y, Peymani P, Afifi S. Quantum dot: magic nanoparticle for imaging, detection and targeting. *Acta Biomed l'Ateneo Parm* 2009;80:156-65.
109. Kim D, Kim DH, Lee JH, Grossman JC. Impact of stoichiometry on the electronic structure of PbS quantum dots. *Phys Rev Lett* 2013;110:196802.
110. Rhyner MN, Smith AM, Goo X, Mao H, Yang L, Nie S. Quantum dots and multifunctional nanoparticles: new contrast agents for tumor imaging. *Nanomedicine* 2006;1:209-17.
111. Liu W, Hak SC, Zimmer JP, Tanaka E, Frangioni JV, Bawendi M. Compact cysteine-coated CdSe(ZnCdS) quantum dots for *in vivo* applications. *J Am Chem Soc* 2007;129:14530-1.
112. Liu DS, Phipps WS, Loh KH, Howarth M, Ting AY. Quantum dot targeting with lipoic acid ligase and HaloTag for single-molecule imaging on living cells. *ACS Nano* 2012;6:11080-7.
113. Drbohlavova J, Adam V, Kizek R, Hubalek J. Quantum dots-characterization, preparation and usage in biological systems. *Int J Mol Sci* 2009;10:656-73.
114. Murray CB, Kagan CR, Bawendi MG. Self-organization of CdSe nanocrystallites into three-dimensional quantum dot superlattices. *Science* 1995;270:1335-8.
115. Micic OI, Curtis CJ, Jones KM, Sprague JR, Nozik AJ. Synthesis and characterization of InP quantum dots. *J Phys Chem* 1994;98:4966-9.
116. Lipovskii A, Kolobkova E, Petrikov V, Kang I, Olkhovets A, Krauss T, *et al.* Synthesis and characterization of PbSe quantum dots in phosphate glass. *Appl Phys Lett* 1997;71:3406-8.
117. Knittel F, Gravel E, Cassette E, Pons T, Pillon F, Dubertret B, *et al.* On the characterization of the surface chemistry of quantum dots. *Nano Lett* 2013;13:5075-8.
118. Micic OI, Sprague JR, Curtis CJ, Jones KM, Machol JL, Nozik AJ, *et al.* Synthesis and characterization of InP, GaP, and GaInP2 quantum dots. *J Phys Chem* 1995;99:7754-9.
119. Passaseo A. Quantum dots: introduction. *Science* 2010;4:1-25.
120. Derfus AM, Chan WCW, Bhatia SN. Probing the cytotoxicity of semiconductor quantum dots. *Nano Lett* 2004;4:11-8.
121. Hoshino A, Fujioka K, Oku T, Suga M, Sasaki YF, Ohta T, *et al.* Physicochemical properties and cellular toxicity of nanocrystal quantum dots depend on their surface modification. *Nano Lett* 2004;4:2163-9.
122. Zhao F, Zhao Y, Liu Y, Chang X, Chen C, Zhao Y. Cellular uptake, intracellular trafficking, and cytotoxicity of nanomaterials. *Small* 2011;7:1322-37.
123. Su Y, Hu M, Fan C, He Y, Li Q, Li W, *et al.* The cytotoxicity of CdTe quantum dots and the relative contributions from released cadmium ions and nanoparticle properties. *Biomaterials* 2010;31:4829-34.
124. Chong Y, Ma Y, Shen H, Tu X, Zhou X, Xu J, *et al.* The *in vitro* and *in vivo* toxicity of graphene quantum dots. *Biomaterials* 2014;35:5041-8.
125. Tsay JM, Michalet X. New light on quantum dot cytotoxicity. *Chem Biol* 2005;12:1159-61.
126. Wu C, Wang C, Han T, Zhou X, Guo S, Zhang J. Insight into the cellular internalization and cytotoxicity of graphene quantum dots. *Adv Healthc Mater* 2013;2:1613-9.
127. Guo G, Liu W, Liang J, He Z, Xu H, Yang X. Probing the cytotoxicity of CdSe quantum dots with surface modification. *Mater Lett* 2007;61:1641-4.
128. Tan YF, Chandrasekharan P, Maity D, Yong CX, Chuang KH, Zhao Y, *et al.* Multimodal tumor imaging by iron oxides and quantum dots formulated in poly (lactic acid)-d-alpha-tocopheryl polyethylene glycol 1000 succinate nanoparticles. *Biomaterials* 2011;32:2969-78.
129. Liu Y, Ai K, Yuan Q, Lu L. Fluorescence-enhanced gadolinium-doped zinc oxide quantum dots for magnetic resonance and fluorescence imaging. *Biomaterials* 2011;32:1185-92.
130. Chen Y, Chen Z, He Y, Lin H, Sheng P, Liu C, *et al.* L-cysteine-capped CdTe QD-based sensor for simple and selective detection of trinitrotoluene. *Nanotechnology* 2010;21:125502.
131. Juzenas P, Chen W, Sun YP, Coelho MAN, Generalov R, Generalova N, *et al.* Quantum dots and nanoparticles for photodynamic and radiation therapies of cancer. *Adv Drug Delivery Rev* 2008;60:1600-14.
132. Han M, Gao X, Su JZ, Nie S. Quantum-dot-tagged microbeads for multiplexed optical coding of biomolecules. *Nat Biotechnol* 2001;19:631-5.
133. Lagerholm BC, Wang M, Ernst LA, Ly DH, Liu H, Bruchez MP, *et al.* Multicolor coding of cells with cationic peptide coated quantum dots. *Nano Lett* 2004;4:2019-22.
134. Li J, Zhao XW, Zhao YJ, Gu ZZ. Quantum-dot-coated encoded silica colloidal crystals beads for multiplex coding. *Chem Commun* 2009;17:2329-31.
135. Tholouli E, Sweeney E, Barrow E, Clay V, Hoyland JA, Byers RJ. Quantum dots light up pathology. *J Pathol* 2008;216:275-85.
136. Xia Z, Xing Y, So MK, Koh AL, Sinclair R, Rao J. Multiplex detection of protease activity with quantum dot nanosensors prepared by intein-mediated specific bioconjugation. *Anal Chem* 2008;80:8649-55.
137. Zheng XT, Ananthanarayanan A, Luo KQ, Chen P. Glowing graphene quantum dots and carbon dots: properties, syntheses, and biological applications. *Small* 2015;11:1620-36.
138. Bourlinos AB, Stassinopoulos A, Anglos D, Zboril R, Karakassides M, Giannelis EP. Surface functionalized carbogenic quantum dots. *Small* 2008;4:455-8.
139. Kagan CR, Murray CB, Nirmal M, Bawendi MG. Electronic energy transfer in CdSe quantum dot solids. *Phys Rev Lett* 1996;76:1517-20.
140. Valizadeh A, Mikaeili H, Samiei M, Farkhani SM, Zarghami N, Kouhi M, *et al.* Quantum dots: synthesis, bioapplications, and toxicity. *Nanoscale Res Lett* 2012;7:480.
141. Luo PG, Sahu S, Yang ST, Sonkar SK, Wang J, Wang H, *et al.* Carbon "quantum" dots for optical bioimaging. *J Mater Chem B* 2013;1:2116-27.
142. Bakker MA, Mehl S, Hiltunen T, Harju A, Divincenzo DP. Validity of the single-particle description and charge noise resilience for multielectron quantum dots. *Phys Rev B-Condens Matter Mater Phys* 2015;91:155425.
143. Choi YE, Kwak JW, Park JW. Nanotechnology for early cancer detection. *Sensors* 2010;10:428-55.
144. Walling MA, Novak JA, Shepard JRE. Quantum dots for live cell and *in vivo* imaging. *Int J Mol Sci* 2009;10:441-91.
145. Qian ZS, Shan XY, Chai LJ, Ma JJ, Chen JR, Feng H. DNA nanosensor based on biocompatible graphene quantum dots and carbon nanotubes. *Biosens Bioelectron* 2014;60:64-70.
146. Obliosca JM, Liu C, Batson RA, Babin MC, Werner JH, Yeh HC. DNA/RNA detection using DNA-templated few-atom silver nanoclusters. *Biosensors* 2013;3:185-200.
147. Su S, Fan J, Xue B, Yuwen L, Liu X, Pan D, *et al.* DNA-conjugated quantum dot nanoprobe for high-sensitivity fluorescent detection of DNA and micro-RNA. *ACS Appl Mater Interfaces* 2014;6:1152-7.
148. Tikhomirov G, Hoogland S, Lee PE, Fischer A, Sargent EH, Kelley SO. DNA-based programming of quantum dot valency, self-assembly and luminescence. *Nat Nanotechnol* 2011;6:485-90.
149. Kim SS, Ye C, Kumar P, Chiu I, Subramanya S, Wu H, *et al.* Targeted delivery of siRNA to macrophages for anti-inflammatory treatment. *Mol Ther* 2010;18:993-1001.
150. Bonoiu A, Mahajan SD, Ye L, Kumar R, Ding H, Yong KT, *et al.* MMP-9 gene silencing by a quantum dot-siRNA nanoplex

- delivery to maintain the integrity of the blood brain barrier. *Brain Res* 2009;1282:142–55.
151. Bruun J, Larsen TB, Jøck RI, Eliassen R, Holm R, Gjetting T, *et al.* Investigation of enzyme-sensitive lipid nanoparticles for delivery of siRNA to blood-brain barrier and glioma cells. *Int J Nanomed* 2015;10:5995–6008.
152. Lin G, Chen T, Zou J, Wang Y, Wang X, Li J, *et al.* Quantum dots-siRNA nanoplexes for gene silencing in central nervous system tumor cells. *Front Pharmacol* 2017;8:182.
153. Djikanovic D, Kalauzi A, Jeremic M, Xu J, Micic M, Whyte JD, *et al.* Interaction of the CdSe quantum dots with plant cell walls. *Colloids Surf B* 2012;91:41–7.
154. Wang J, Yang Y, Zhu H, Braam J, Schnoor JL, Alvarez PJJ. Uptake, translocation, and transformation of quantum dots with cationic versus anionic coatings by *Populus deltoides* × *nigra* cuttings. *Environ Sci Technol* 2014;48:6754–62.
155. Zhang D, Hua T, Xiao F, Chen C, Gersberg RM, Liu Y, *et al.* Uptake and accumulation of CuO nanoparticles and CdS/ZnS quantum dot nanoparticles by *schoenoplectus tabernaemontani* in hydroponic mesocosms. *Ecol Eng* 2014;70:114–23.
156. Wang Q, Chen J, Zhang H, Lu M, Qiu D, Wen Y, *et al.* Synthesis of water-soluble quantum dots for monitoring carrier-DNA nanoparticles in plant cells. *J Nanosci Nanotechnol* 2011;11:2208–14.
157. Dong X, Liang W, Mezirani MJ, Sun YP, Yang L. Carbon dots as potent antimicrobial agents. *Theranostics* 2020;10:671–86.
158. Lu Z, Li CM, Bao H, Qiao Y, Toh Y, Yang X. Mechanism of antimicrobial activity of CdTe quantum dots. *Langmuir* 2008;24:5445–52.
159. Ristic BZ, Milenkovic MM, Dakic IR, Todorovic Markovic BM, Milosavljevic MS, Budimir MD, *et al.* Photodynamic antibacterial effect of graphene quantum dots. *Biomaterials* 2014;35:4428–35.
160. Kim S, Lim YT, Soltesz EG, De Grand AM, Lee J, Nakayama A, *et al.* Near-infrared fluorescent type II quantum dots for sentinel lymph node mapping. *Nat Biotechnol* 2004;22:93–7.
161. Frangioni JV, Kim SW, Ohnishi S, Kim S, Bawendi MG. Sentinel lymph node mapping with type-II quantum dots. *Methods Mol Biol* 2007;374:147–59.
162. Pons T, Pic E, Lequeux N, Cassette E, Bezdetnaya L, Guillemin F, *et al.* Cadmium-free CuInS₂/ZnS quantum dots for sentinel lymph node imaging with reduced toxicity. *ACS Nano* 2010;4:2531–8.
163. Smith AM, Dave S, Nie S, True L, Gao X. Multicolor quantum dots for molecular diagnostics of cancer. *Expert Rev Mol Diagnostics* 2006;6:231–44.
164. Shao L, Gao Y, Yan F. Semiconductor quantum dots for biomedical applications. *Sensors* 2011;11:11736–51.
165. Luo G, Long J, Zhang B, Liu C, Ji S, Xu J, *et al.* Quantum dots in cancer therapy. *Expert Opinion Drug Delivery* 2012;9:47–58.
166. Nie S, Xing Y, Kim GJ, Simons JW. Nanotechnology applications in cancer. *Annual Rev Biomed Eng* 2007;9:257–88.
167. Wagner MK, Li F, Li J, Li XF, Le XC. Use of quantum dots in the development of assays for cancer biomarkers. *Anal Bioanal Chem* 2010;397:3213–24.
168. Nida DL, Rahman MS, Carlson KD, Richards Kortum R, Follen M. Fluorescent nanocrystals for use in early cervical cancer detection. *Gynecol Oncol* 2005;99(3 Suppl 1):S89–94.
169. Iga AM, Robertson JHP, Winslet MC, Seifalian AM. Clinical potential of quantum dots. *J Biomed Biotechnol* 2007;2007:76087.
170. Kloepper JA, Mielke RE, Wong MS, Nealson KH, Stucky G, Nadeau JL. Quantum dots as strain- and metabolism-specific microbiological labels. *Appl Environ Microbiol* 2003;69:4205–13.
171. Liang J, Huang S, Zeng D, He Z, Ji X, Ai X, *et al.* CdSe quantum dots as luminescent probes for spironolactone determination. *Talanta* 2006;69:126–30.

PHARMACEUTICAL AND BIOPHARMACEUTICAL ASPECTS OF QUANTUM DOTS-AN OVERVIEW

SADDAM C. SHAIKH¹, SHWETA G. SABOO², PRASHANT S. TANDALE³, FAHIM S. MEMON⁴, SHARAD D. TAYADE^{4*}, M. AKIFUL HAQUE⁵, SHARUK L. KHAN⁶

¹Department of Pharmaceutics (D Pharm), Rajarshi Shahu College of Pharmacy, Buldana, Maharashtra, India 443001, ²Department of Pharmacognosy, Government College of Pharmacy, Karad, Maharashtra, India 415124, ³Department of Pharmaceutics, School of Pharmaceutical Sciences, Lovely Professional University, Punjab, India 144001, ⁴Department of Pharmaceutics, Rajarshi Shahu College of Pharmacy, Buldana, Maharashtra, India-443001, ⁵Department of Pharmaceutical Analysis, Anurag University, Venkatapur, Hyderabad, India 500088, ⁶Department of Pharmaceutical Chemistry, MUP's College of Pharmacy (B Pharm), Degaon, Risod, Washim, Maharashtra, India 444504
Emails: sharad_tayade1@rediffmail.com

Received: 23 Mar 2021, Revised and Accepted: 12 May 2021

ABSTRACT

In the twenty-first century, nanotechnology has become cutting-edge technology. It is interdisciplinary and multidisciplinary, covering numerous fields such as medicine, engineering, biology, physics, material sciences, and chemistry. The present work aims to cover the optical properties, method of preparations, surface modifications, bio-conjugation, characterization, stability, and cytotoxicity of quantum dots (QDs).

Articles were reviewed in English literature reporting the pharmaceutical and bio-pharmaceutical aspects of QDs which were indexed in Scopus, web of science, google scholar and PubMed without applying the year of publication criterion.

One significant value of utilizing nanotechnology is that one can alter and control the properties in a genuinely unsurprising way to address explicit applications' issues. In science and biomedicine, the usage of functional nanomaterials has been broadly investigated and has become one of the quick-moving and stimulating research directions. Different types of nanomaterial (silicon nanowires, QDs, carbon nanotubes, nanoparticles of gold/silver) were extensively utilized for biological purposes. Nanomedicine shows numerous advantages in the natural characteristics of targeted drug delivery and therapeutics. For instance, protection of drugs against degradation, improvement in the drug's stability, prolonged circulation time, deceased side effects, and enhanced distribution in tissues. The present review article deals with the quantum dots, their optical properties, method of preparations, surface modifications, bio-conjugation, characterization, stability, and cytotoxicity of quantum dots. The review also discusses various biomedical applications of QDs.

The QDs-based bio-nanotechnology will always be in the growing list of unique applications, with progress being made in specialized nanoparticle development, the detection of elegant conjugation methods, and the discovery of new targeting ligands.

Keywords: Quantum dots, Optical properties, Microwave-assisted method, Cytotoxicity, Cell imaging, Sentinel lymph-node mapping

© 2021 The Authors. Published by Innovare Academic Sciences Pvt Ltd. This is an open access article under the CC BY license (<https://creativecommons.org/licenses/by/4.0/>)
DOI: <https://dx.doi.org/10.22159/ijap.2021v13i4.41623>. Journal homepage: <https://innovareacademics.in/journals/index.php/ijap>

INTRODUCTION

In 1981, Ekimov and Onushenko described the Quantum dots (QDs), also called nanoscale semiconductor crystals [1]. The quantum dots are made up of material from periodic table group II-VI (CdSe) or III-V (InP) [2-6]. The most well studied and broadly utilized QDs are the cadmium selenide (Cd/Se) [3]. The cores and QDs targeting are protected by surface modification, and such changes significantly improve QDs sizes [7]. There are two kinds of fluorescent-based quantum dots, namely graphene and carbon quantum dots [8]. Quantum dots possess quantum confinement property and, on excitation from visible to infra-red wavelength, emit fluorescence [9, 10]. Usually, in the crystal core of a single QD, around 100-100,000 atoms are present. The size of QDs usually lies in between 2-10 nm diameter, which generally grows up to 5-20 nm in diameter after encapsulation of polymer [11, 12]. QDs comprise a semiconductor core, which is over-covered by shell and cap. The anatomy of QDs is represented in fig. 1 [13]. Semiconducting character and optical properties depend on the inorganic core. In QDs synthesis, the organic surfactants are developed and eventually shape ligands on the core surface [14-17]. The nature of the capping agent produced significantly relies on the final application of QDs. Frequently used ligands in QDs synthesis are alcohols, essential amines, and thiols [18, 19]. Bio-conjugation with carbohydrates, viruses, natural products, DNA fragments, and peptides assist by ligands through the covalent coupling and electrostatic or hydrophobic interactions [20, 21]. Determination of solubility, colloidal stability, control particle morphology, particle size distribution, and accumulation chiefly depends on ligands [22-24]. The present work aims to cover the optical properties, method of preparations, surface modifications,

bio-conjugation, characterization, stability, and cytotoxicity of QDs. Articles were reviewed in English literature reporting the pharmaceutical and bio-pharmaceutical aspects of QDs which were indexed in Scopus, web of science, google scholar and PubMed without applying the year of publication criterion. The keywords used for searching the literature are quantum dots, quantum dots in drug delivery system, methods of preparation of quantum dots, applications of quantum dots, recent advances in quantum dots, pharmaceutical and biopharmaceutical applications of quantum dots etc.

QDs core consists of several substances like cadmium, zinc, lead chalcogenides (CdS, CdSe, CdTe), copper salt (CuCl), arsenides (InAs, GaAs), semiconducting phosphides (InP, GaP), and nitrides (GaN). The shell of CdSe, ZnSe, PbS, ZnS, ZnTe, CdS, ZnO generally enclosed the core [3]. The core of nanomaterials guarded by outer covering from photoinitiated degradation and removing surface defects enhances the luminescence properties. Besides, cadmium, silver, copper, manganese, and rare earth metal ions can be used to dope the core of nanocrystals to enhance photoluminescence properties [25, 26]. QDs can be assembled, permitting particle shape, size, and chemical composition to be changed by suit a given application. The design and size of QDs are the properties that are frequently manipulated; this will decide if the QDs are chemically excited in NIR or UV light [27-29]. The biological targeting molecules (e. g., antibodies) or biocompatible polymeric materials (e. g., PEG) can be functionalized on the amenable external surface of QDs to improve their physiological system performance. The most commonly utilized QDs consist of graphene QDs, carbon QDs, and cadmium-based QDs [30-32]. QDs are found to be photochemically stable with symmetric, narrow, and strong fluorescence emission. QDs are

perfectly suitable for repetitive measurements or long-term observations [33–35]. After intradermal administration of dots in mouse paw, the near IR emitting dots might be noticed in the intraoperative imaging system's lymphatic system [36–39]. A report proposed that probes of quantum rods conjugated with transferring were productive for *in vitro* blood-brain barrier transmigration [40–43].

In fig. 2 composition of QDs is mentioned along with the material used [44]. The QDs are metastable and generally, through chemical surface modification, need to be stabilized. QDs show narrow-size tunable emission spectra, high extinction coefficients, and much diminishing photobleaching rates compared to organic dyes [45–48].

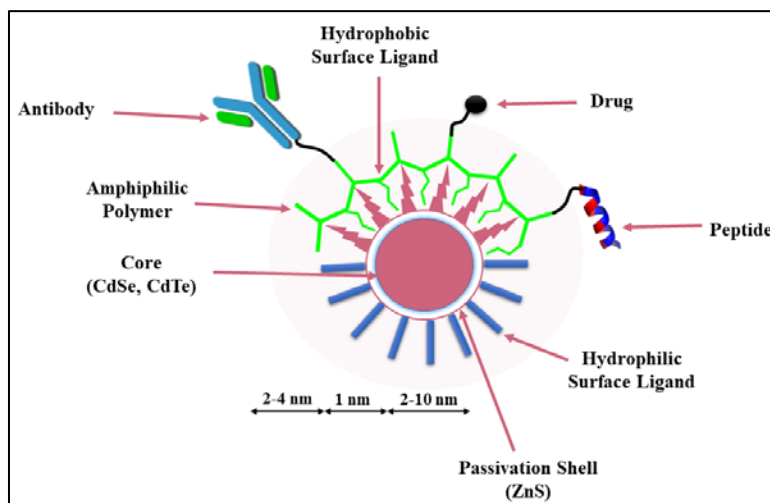


Fig. 1: The anatomy of QDs

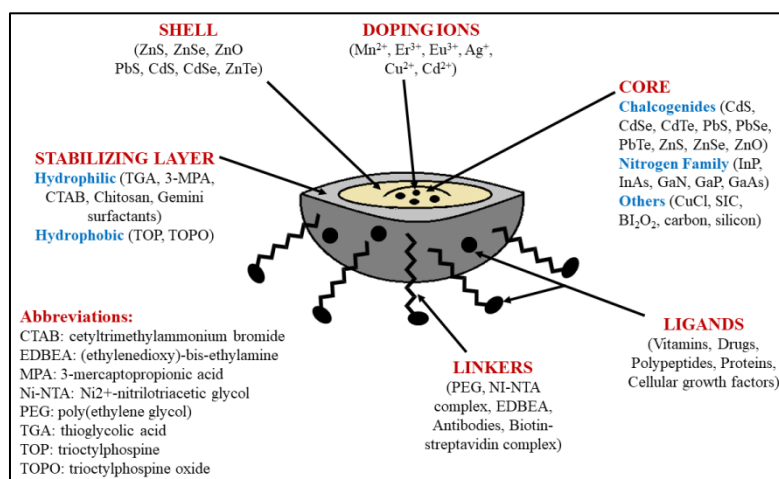


Fig. 2: The composition and material used for the synthesis of QDs

Advantages of QDs

QDs possess good physical stability and speedy degradation observed in optical imaging probes compared to QDs, whereas QDs depicted high instead of degradation. As compared to traditional dyes, QDs comprised higher photostability due to their fluorescence intensity and unique inorganic composition. QDs have a narrow emission peak and broader excitation spectra, whereas sharp emission peaks are depicted by organic dyes and narrow absorption spectrum observed with organic fluorophores. Due to these features, less energy is sufficient for the excitation of QDs irrespective of size. Hence, to excite multi-color QDs, single ultraviolet or blue wavelength beam is adequate. As compared to organic dyes, QDs show considerably longer fluorescence lifetimes and are 10-20 times brighter. Using a single source, QDs can feasibly be excited, and concurrently several targets tracked *in vivo* with the application of various probes as permitted by the multi-color QDs. With low background interference, high signal intensity depicts by the QDs conjugates due to sharp emission spectra and large Stokes Shift. QDs can be molded into various shapes, such as quantum dust, small crystals, and bead forms, and can be coated with

different biomaterials. QDs have comfortable and cost-effective manufacturing methods. Colloidal synthesis, epitaxial techniques, and lithographic techniques are various manufacturing methods of QDs [49–53].

Disadvantages of QDs

In biomedical applications, the size of the QDs has terrific importance. Through renal filtration, QDs having small size get removed from the body easily; however, there may be chances that the reticuloendothelial system takes the larger particles before reaching the targeted disease sites. The optimal activity is demonstrated by QDs having a 5-20 nm size of the polymer coating. When located in live cells, QDs aggregate and may interfere with cell function or kill the cells. Bio-conjugation of QDs results in difficult delivery of QDs into the target. QDs have unknown metabolism and excretion, leading to toxicity if it accumulates in the body tissues, spleen, liver and kidney. QDs become toxic if coated with mercaptoacetic acid. Even building material or the core of QDs (CdSe) is also toxic. Heavy metal ions

leak from the core due to oxidation and photolysis, which results in cytotoxicity [49, 50, 54–57].

Optical properties

QDs have expanded consideration because of their exceptional optical properties compared to traditional fluorescent dyes [58–60]. The distinctive optical properties of QDs permit multi-color imaging with no cross-talk in fluorescence microscopes among various detection channels. Moreover, with one single wavelength QDs having different emission maxima is excited and demand for many excitation sources is reduced. Time-resolved detection is possible because of the comparatively long fluorescence lifetime of the QDs-fluorescence, which considerably enhances the ratio (by 15 factors)

of signal-to-background concerning cell autofluorescence. QDs emission maxima can be correctly adjusted by changing QDs size. Short-wavelength light emits by smaller QDs as compared to larger particles [58, 60]. Electronic and unique optical properties in QDs are due to quantum confinement effects offering various benefits on current fluorophores, like lanthanide chelates, fluorescent proteins, and organic dyes. Properties that significantly impact fluorophore behavior and subsequently relevance to multiple circumstances consist of photostability, the width of the emission spectrum, decay lifetime, and the excitation spectrum. Concurrently, various QDs can emit different colors beneath the same excitation light to track and image numerous molecular targets [28–31]. The multi-color QDs probes can be utilized at the same time, as shown in fig. 3 [61].

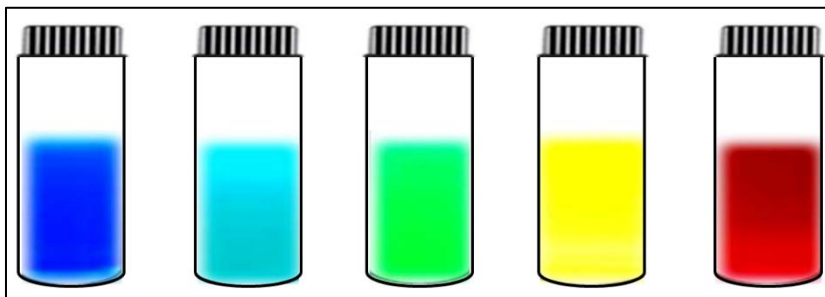


Fig. 3: In the visible range at various wavelengths, QDs displaying hues of colors

Methods of preparation

QDs are manufactured by various methods like chemical precipitation method, polyol-hydrolysis method, γ -radiation route, electron beam irradiation, photochemical synthesis [35, 36, 45, 47, 62–68]. However, few techniques of QDs fabrication are discussed below.

Organic phase method/organometallic method

Monodispersed QDs can be prepared through the organometallic process. Using this method, one can prepare monodispersed QDs with regularity in the core structure with uniform surface derivatization. Bis(trimethylsilyl) selenium and Me₂Cd is usually employed, organometallic precursors. Monodisperse CdSe achieved through organometallic reagents' pyrolysis between 250 °C to 300 °C by injecting in a hot coordinating liquid [69–71]. Different sizes of QDs formed relying upon the states of temperature. The organometallic method is right now regarded as the most vital technique to fabricate QDs. In this technique, various QDs demonstrating high quantum yield can be formed, and QDs size distribution is simply controlled by varying the reaction time or changing the temperature [72–74].

Water phase method/Aqueous solution method

Ionic perchlorates are utilized as precursors in this method. Ligands like Hydrosulphyl-containing materials, glutathione (GSH), 3-mercaptopropionic acid (3-MPA), in an aqueous medium used to prepare CdTe quantum dots. It is an eco-friendly and economical method. Likewise, the QDs formulated by the technique can be straightly given into the biological system. As compared with QDs created from the organometallic process QDs with thiol cap depicted wide size distribution and low quantum yield, poor stability in aqueous solution [75–80].

Hydrothermal method

QDs with narrow size and high quantum yields were formed by this method. This method also decreases the surface defects which were created during the synthesis process. In this method, the reagents are initially added to the hermetic container and increasing the temperature till supercritical temperature, a high pressure developed with this temperature leading to a successful reduction in the surface defects and reaction time of QDs [81–84].

Microwave-assisted method

This method was initially presented by the Kotov group and pursued by Qian and colleagues. Microwave irradiation as the heating source and water as a solvent were utilized. Heat the reaction system more than 100 °C to obtain uniform QDs and acquired a quantum yield of 17%. The organic phase synthesis formed hydrophobic QDs. But the QDs must have water solubility for the biological application. The nanocrystals produced from the water solubilization method will remain stable in biological systems and with no effect/change in the photophysical properties. Low fluorescence and less quantum yield achieved with water-soluble QDs formed in the early stage. Afterward, water-soluble QDs provide a higher quantum yield up to 50% with surface modifications and advanced synthetic procedures [85, 86]. But the huge challenge is to control the chemical and photophysical properties of QDs in water. Various methods have been established to formulate water-soluble QDs having smaller particle sizes. Ligand exchange is one method in which hydrophilic groups on QDs surface will exchange with hydrophobic groups through a ligand exchange mechanism. This method is merely using monodentate ligands; it will affect fluorescence efficiency and cause aggregation of nanoparticles. Few vacant sites were left by ligands while detaching from the surfaces, and these vacant sites work as trap centers and produce an accumulation of nanoparticles [87, 88].

This issue can be tackled utilizing ligand cross-linking and the di-thio group rather than the mono-thio group. One more method for developing water-soluble QDs is through the amphiphilic molecule incorporation, for example, phospholipids or polymers [89, 90]. The native surface of QDs ligand in the polymer encapsulation layer does not change. In the long-chain polymer molecules, the increased number of hydrophilic groups enhances the QDs dispersibility in biological buffer solutions and for conjugations of bio-probes gives chemical functional groups. The biocompatibility of QDs-polymer nanocomposites enhances and decreases their cytotoxicity due to the polymers coated on QDs. The QDs probe's photophysical properties vary with the size, structure, and chemical composition of the inorganic nanoparticle utilized for the QDs probe's development. The nanoparticle does not interact because of the lack of biological functioning with biological systems. The biomolecules like nucleic acids and proteins provide interaction with living cells used to decorate inert QDs for better biological application. QDs become more bio-compatible with living systems by incorporation of biomolecules [91–93]. The steps and design criteria used in QDs probes manufacturing are described in fig. 4 [12].

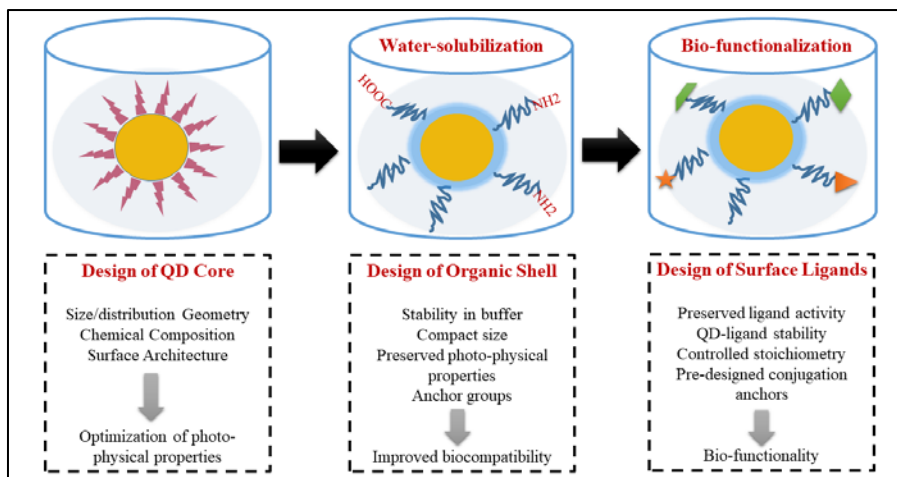


Fig. 4: The steps and design criteria used in QDs probes manufacturing

Surface modifications and Bio-conjugation of QDs

It is usually observed that the bare QDs are not practical for biological applications because of numerous reasons. Initially, in most of the synthesis approaches, QDs are water-insoluble. Thus, to obtain results from the optical properties of QDs, the surface has to be coated using a hydrophilic agent. Secondly, the core of QDs is very reactive, and with macromolecules, it undergoes potent unspecific interactions resulting in aggregation of particles and variation in fluorescence [94, 95]. Thirdly, the QDs toxicity can be significantly reduced due to the process of surface modification. The QDs have a hydrophobic surface modified by using hydrophilic agents to solubilize them in aqueous buffers. The peptides, dendrons, or oligomeric phosphines, thiol-containing molecules can be replaced with the hydrophobic surface ligands [96–98].

Further approaches employ phospholipids for modification or hydrophobic interactions between the QDs and amphiphilic polymers or encapsulate the QDs in a silica shell. Numerous potential outcomes are there in which biomolecules can be attached to the QDs. The utilization of QDs containing streptavidin is typically utilized because it is easy to link them to biotin-tagged biomolecules [99, 100]. Numerous strategies can be used to get QDs bio-conjugation consisting of covalent bond formation, multivalent chelation, or passive adsorption. There are two famous cross-linking reactions; active ester maleimide mediated amine, sulfhydryl coupling, and carbodiimide mediated amide formation. The bio-conjugation also determines by the hydrophilic coating as the required functional groups deliver by it and should be considered [101–103].

Molecules attachment for targeting

To the biomolecules like aptamers, small molecule ligands, or antibodies, the QDs must be cross-linked to make them precise to biological targets and thus employed for targeted drug delivery and diagnosis. QDs functionalization can be done by replacing biomolecules with a protein or sulfhydryl group by thiol and peptides with cysteine residues [104–107]. The QDs surface equilibrates with the thiols after incubation, and the biomolecules partially substitute the initial coating molecule. Coating of the QDs with mercapto acid can produce stable covalent bonds. Moreover, the electrostatic interactions among the macromolecules like peptides or proteins and the QDs surface can also give a facial way for modification and coating. Numerous organic functionalities are promptly attached for the QDs encapsulated in a silica shell using well-developed silane chemistry. At present different affinity reagents for QDs modification, like aptamers, small molecules, and peptides, which on cancer cells primarily identify particular overexpressed biomarkers, have been described to manufacture target drug delivery vesicles and cancer diagnosis probes [16, 64, 108–112].

Characterization of QDs

Important information regarding the morphology, structure, and physiochemical changes because of conjugation reactions can be disclosed by QDs optical characterization [113, 114]. For optical characterizations of QDs, UV-Vis and photoluminescence spectroscopy are the most utilized, non-destructive, quick, and contactless [115]. The size of QDs is finding out by employing atomic force microscopy, scanning tunneling microscopy, scanning electron microscopy, dynamic light scattering, transmission electron microscopy (TEM) studies [115–117]. The use of Raman scattering spectroscopy and photoluminescence excitation are also reported to determine the size and composition of QDs [118].

Stability of QDs

In aqueous conditions, a vital role in deciding the stability of QDs depends on the organic molecules and shell attached to the QDs surface. Finally, QDs precipitate with loss in their luminescence because of the loss of surface ligands. The stability of surface ligands can be affected by various processes. It was revealed that common surface ligands used and their photooxidation can cause desorption of hydrophilic thiols by their protonation [113]. To the cadmium chalcogenide QDs deprotonated thiols, thiolates are bound; if the QDs-ligand interface pH turns down to a particular value, protonation of ligand occurs and remove from the surface of QDs [2, 49, 102, 119]. Generally, in a low pH range, the hydrophilic thiols coated QDs precipitated in a pH range of 2 and 7, based on the chemical composition and the size of QDs [2, 45, 66, 67].

The photophysical properties and stability of QDs within the cells firmly subject to the local environment and intracellular localization. Its UV illumination over a long time leads to the photooxidation of surface ligands [46, 47, 65]. Enhancing the packing density and thickness of the ligand shell can hinder the beginning of photooxidation. The core of QDs resists photodegradation because of its inorganic nature, but the core integrity is influenced by the extended UV light exposure [86, 88, 91].

Cytotoxicity of QDs

In human beings, cadmium's half-life is around 20 y and is supposed to be carcinogenic, which can deposit in the kidney, liver, and bio-distribution in all tissues [120]. The toxicity of QDs relies on numerous chemicals, environmental and physical factors such as size, surface coating, charge, chemical composition, concentration, and free radical production, which might be deciding components of short and long-term *in vivo* side effects QDs [121]. The particles' biocompatibility has to be described, as QDs are utilized for studies including living cells and organisms [122].

QDs have not been characterized concerning their toxicity because they are new materials. The majority of the QDs contain cadmium,

which causes lethal impacts when it comes in contact with cells. Efforts need to be taken to secure the core of QDs, by developing a much lower toxicity shell, most of the time ZnS [123], which brought about a marked decrease in cytotoxic effects. The optical properties also enhance this layer; in most biological applications, core-shell systems have turned into the standard. But, to resolve the issue of cytotoxicity completely, the introduction of capping layers was still not adequate. A variety of other factors, such as the particle aggregation on the surface of the cell and even the QDs surface ligands stabilization, have been revealed to affect the cell's viability. The number of factors decides the degree of cytotoxicity, including size, dose, color, capping materials, surface chemistry, and processing parameters [124, 125]. So far, less information on QDs toxicity, particularly for *in vivo* use, is accessible. In this manner, QDs toxicity is a fundamental restriction for their utilization. Roberts reported that after administering CdSe/ZnS QDs, it caused lung injury and inflammation in rats. Likewise, Ho *et al.* detected granuloma following cadmium-based QDs administration in the lung of mice [123, 126, 127].

Biomedical applications of QDs

Cell imaging

Recently as an optional to organic dyes, QDs have been utilized for bioimaging. Furthermore, QDs have a broad absorption spectrum that makes easy excitation of two or multi-photon, particularly in the near-infrared range. Among all newly proposed imaging strategies, the bioimaging acknowledged by the confocal multi-photon excitation system is by all accounts the best solution utilizing QDs as fluorescent labels. In this imaging technique, the relatively low excitation energy is harmless for the samples. The QDs' resistance to photobleaching and bright photoluminescence allows even their real-time and long-term imaging. Recently, bioimaging of cancer cells can be done by utilizing QDs as bi-photonic fluorescent probes. Based on fluorescence imaging and magnetic resonance imaging (MRI) techniques, a multimodal tumor imaging system was given by Tan *et al.* [128]. Liu *et al.* have also fabricated other MRI nanoprobe and bimodal fluorescence with improved fluorescence and can be utilized for labeling HeLa cells [129]. The strong positive MRI contrast was used to characterize these QDs.

Bio-sensing

A new class of nanomaterials is luminescent semiconductor nanocrystals, the unique generation of fluorescent biosensors are created with the help of specific photophysical properties. Hence, the most common techniques utilized depend on fluorescence changes monitoring in immunoassays for the detection of biomolecules. The fluorescent probes have depicted extensive biosensing applications, diagnostic and clinical assays, ion detection, nucleic acid detection. Generally, the decline in QDs fluorescence emission intensity is seen in the presence of an analyte. For the detection of heavy metal ions and toxic organic substances, fluorescent nanocrystals are usually used. The L-cysteine-capped CdTe QDs synthesis and their utilization in selective trinitrotoluene recognition as the fluorescent probe was reported Chen *et al.* [130].

Photodynamic therapy

In the most recent couple of years, the photodynamic treatment (PDT) has come into sight as an advanced technique for malignancy treatment. PDT is an effective alternative to antibiotic therapy. PDT consists of a light, molecular oxygen, and photoactivable agent called photosensitizer (PS). Because of its specificity, PDT is a promising technique, simply the affected cells are exceptionally close to the PS, and until illuminated, the PS isn't cytotoxic. In photodynamic cytotoxicity, through this mechanism, the *in situ* generations of singlet oxygen (1O_2) seem to assume a crucial role because of the exceedingly productive interaction of the biomolecules with the 1O_2 species [131].

Multiplex coding

For applications demanding high throughput analysis of biomolecules, multiplex coding has tremendous potential. The small polymer multiplexed beads are embedded inside a finely controlled ratio, which provides a unique optical code. In contrast, oligonucleotides or antibodies act as molecular identifiers,

conjugated to the beads' surface [132, 133]. The intensity levels and types of fluorophores are the two variables that decide the maximum order of multiplexing possible. For instance, two fluorophores provide nine different microbeads with three intensity levels (1:1, 1:2, 3:2, 3:3). Prior efforts utilized organic fluorophores at multiplexed coding. Spectral overlaps occurred due to their broad emission spectra, and the number of fluorophores that could be used was constrained to only 2-3 dyes, leading to low multiplexing orders [134]. QDs proved to be an ideal replacement for this application because of their narrow and Gaussian-shaped emission spectra. For example, Xu *et al.* utilized QDs embedded microspheres to demonstrate the reliability and accuracy of polymerase chain reaction (PCR)-based single nucleotide polymorphism (SNP) genotyping assay [135, 136].

Bio-imaging of live cell

Live-cell imaging is a tough assignment compared with fixed cells and tissues because the thought that must be taken to keep cells alive and delivery of probes across the plasma membrane for examining intracellular targets is the challenging task. For the labeling of cell surface antigens, *in vivo* use of QDs have been shown. In recent times, the genuine favorable circumstances of QDs have been demonstrated for live-cell imaging by labeling plasma membrane receptors, for example, erbB/HER receptors and glycine receptors enabling single imaging molecules and real-time tracking of biomarkers [137-139]. The information gives new bits of knowledge into the mechanism of the ligand-receptor interaction. For delivery of QDs into the cells, different mechanisms have been utilized, for example, conjugation of QDs to cationic peptides or translocating proteins, or specific membrane receptors, via endocytosis non-specific uptake, and microinjection. Every one of these methods has effectively conveyed QDs into cells, even though it appears that the peptide-mechanism might be the most proficient [140-142].

DNA and RNA detection

QDs have become an essential tool because of resilient photoluminescence and multiple color properties for multiplexed detection of different DNA targets [138,143,144]. For DNA detection FRET technique has been one of the well-known methods. An enzyme is utilized to propel the detection sensitivity and to amplify the target. Excluding FRET, with the help of a magnetic nanoparticle-tagged DNA probe and a QDs labeled DNA probe with the DNA focus across hybridization detection, could be carried out [139, 145-148].

Gene delivery

For gene therapy, QDs depicted satisfactory performance as a promising candidate. RNA interference (RNAi) is an encouraging method with an extraordinary chance to battle disease. As RNase quickly degrades siRNAs, they have a short half-life, and they cannot cross the cell membrane because of their negative charge. For the loading of gene molecules, the fluorescent QDs have been examined as potential carriers among a large number of nanoparticles. The positively charged liposomes or polymers suppressed the negative charge of the nucleic acids. Using QDs liposome and QDs-polymer conjugates, imaging of siRNA transfection has been done successfully [149-151]. In a study performed by Lin *et al.* [152], reported that for silencing and efficient gene delivery, cadmium sulphoselenide/zinc sulfide quantum dots-polyethyleneimine (CdSSe/ZnS QDs-PEI) was found to be a proficient nanoplex formulation.

Plant bio-imaging

There is expanding use of QDs as markers in plant science for the cells or cell wall. For external agents, the cell wall is the first target location in a plant cell. Djikanovic *et al.* revealed that in the cell wall of the Picea omorika branch CdSe QDs usually attach to lignin and cellulose. Likewise, by interaction with the chains of C=C and C-C alternating bonds and interaction with the OH groups, binding to cellulose and lignin are accomplished [153, 154]. Data demonstrated that for the homogenous marking of the whole cell wall, the QDs are suitable, which is an outcome of the cell wall polymers that are structurally arranged inside the whole cell wall network. Inside the polymer structures in the cell wall composite, these qualities make possible a feasible nanoparticle penetration [155, 156].

QDs as antimicrobial agents

The various inorganic nanoparticles having antimicrobial activity have been tried. These comprised a range of metals and their oxide nanoparticles, such as zinc oxide, titanium dioxide, etc. Although upon excitation, these work on the principle of generating reactive oxygen species utilizing high wavelength lights, size-dependent optical properties are an additional benefit of QDs [157]. QDs are known to generate free radicals upon irradiation, and the core material of the semiconductor determined its quality. To the microbes, these produced free radicals are described as toxic, and also, in the process of irradiation, the liberated free heavy-metal ions are harmful to the bacteria [157–159]. Lu *et al.* depicted that excellent antimicrobial activity possessed by CdTe QDs. In their research, it was also shown that after binding to the bacteria's surface, the QDs disturbs the cellular antioxidative systems, reduces antioxidative enzyme activities, and instigate down-regulation of antioxidative genes [158].

In diagnosis and treatment of cancer

In the past several decades, cancer has attracted substantial research interest as a leading cause of human death [131, 143]. Ongoing advancements in QDs innovation have effectively had a tremendous effect on cancer imaging.

Sentinel lymph node mapping

The first lymph node or groups of nodes are the sentinel lymph nodes (SLNs) to which a primary tumor gives metastasizing cancer cells. A method that allows the recognition and the SLNs removal is known as SLN biopsy. Further lymph-node sampling is avoided if cancer is not found in the SLNs. At present, for breast cancer and melanoma staging and prognosis, SLN biopsy is in routine clinical use. Precise nodal mapping is required for success in SLN biopsy. Current mapping methods consist of utilizing peritumoral injection of radioisotopes, for example, the isosulfan blue dye, Technetium-99m-colloidal albumin, or the combination of the two agents. Kim *et al.* prepared the type II QDs and coated them with polydentate phosphine making soluble and stable QDs in serum [160]. It was observed that both in pigs and mice, the QDs were promptly identified in nearby SLN after intradermal injection. The multiple QDs under a single excitation source with different emission wavelengths may be used to identify and sort the complicated lymphatic system [161, 162].

Primary tumor detection

Prostate-specific membrane antigens (PSMA) for cancer imaging may serve as markers or targets for diagnosis. In principle, conjugating the QDs to antibodies, particularly for these antigens, helps the primary tumor recognition and identification of distant or regional metastases. Nie's group has performed some original work utilizing conjugated antibody QDs to target prostate tumor. To nude mice bearing prostate tumor xenografts, a specific PSMA antibody conjugated with Cd/Se QDs is intravenously administered. Localization of the QDs to the tumor was seen after 2 h of circulations [163, 164]. On the other hand, at 15 times higher concentration as compared to conjugated PSMA antibody QDs, when the PEG-modified QDs injected, only after 24 h circulation reached the tumor presumably by diffusion, a much longer time interval [165, 166].

An efficient lymphatic drainage system lacks in the tumor, and blood vessels are leaky; hence at the tumor site, the passive diffusion occurred because of enhanced permeability and retention of QDs. In the clinical setting, to accomplish a maximal impact on cancer diagnosis, research must be progress in the direction of small tumor identification and localization, which are currently not detected through conventional imaging methods [167–169].

QDs as drug nano-carriers

In the previous decade, with the development of surface modification technique, QDs with water-soluble capping stabilizer, for example, polyethylene glycol polymer, mercaptoethylamine, and mercaptoacetic acid are conjugate promptly with drug molecules

through electrostatic interaction or covalent bonds, giving complex nanomedicine with QDs as drug carriers [8, 14, 22, 24].

Other applications

QDs have additionally been observed to be valuable in the study of microorganisms. Kloepper *et al.* revealed that fungi and bacterial glycoproteins could be targeted with QDs conjugates [170]. Numerous different pathogens such as *Salmonella Typhi*, *Giardia lamblia* and *Cryptosporidium parvum*, and *Listeria monocytogenes* were targeted using QDs [157–159].

Additionally, for *Escherichia coli*, the QDs were utilized as cell membrane permeable indicators. It might be possible that QDs surface graft with the therapeutic enzymes and activate them producing free radicals (for example, singlet oxygen) or by light by optically cycling the QDs. For determining the content of spironolactone in the tablet, the first applications of QDs were exhibited by Liang and colleagues [171]. In neuroscience research, QDs stand for a new device of enormous potential. The studies that are restricted by the limited anatomy of neuronal and glial interactions are helpful. Photostability, multiplexing potential and inorganic nature are the features of QDs that make them significant worth for drug discovery [8, 11, 15, 21]. Outstanding review articles are available in the literature for additional information on QDs fundamentals and applications.

CONCLUSION

In nanomedicine, the potential applications of QDs span the areas of nano-diagnostics, drug delivery, therapy, and imaging. In the last place, the most promising applications are intracellular imaging, tissue imaging, multiplexed diagnostics, tumor detection, infectious agent detection, immunohistochemistry, and fluoro-immunoassays. Despite all their potential in nanomedicine, QDs are still away from large-scale utilization because of toxicity concerns, regulatory and commercialization issues. The QDs-based bio-nanotechnology will always be a growing list of amazing applications with progress being made in specialized nanoparticle development and the detection of elegant conjugation methods, discovering new targeting ligands.

LIST OF ABBREVIATIONS

QDs: Quantum Dots; 3-MPA: 3-mercaptopropionic acid; TEM: Transmission Electron Microscopy; MRI: Magnetic Resonance Imaging; PDT: Photodynamic Treatment; PS: Photosensitizer; 1O₂: Singlet Oxygen; PCR: Polymerase Chain Reaction; SNP: Single Nucleotide Polymorphism; RNAi: RNA Interference; SLNs: Sentinel Lymph Nodes; PSMA: Prostate-specific Membrane Antigens

ACKNOWLEDGEMENT

None

FUNDING

Nil

AUTHORS CONTRIBUTIONS

SCS: conceptualization and literature survey; SGS: literature survey on optical properties of QDs and writing; SDT: a literature review on methods of preparation of QDs and article writing; FSM: literature survey on applications of QDs and writing; SLK: overall literature survey, manuscript writing and referencing; PST: proofreading and contributed in writing style. All authors read and approved the final manuscript.

CONFLICT OF INTERESTS

The authors declare that they have no competing interests.

REFERENCES

- Matea CT, Mocan T, Tabaran F, Pop T, Mosteanu O, Puia C, *et al.* Quantum dots in imaging, drug delivery and sensor applications. *Int J Nanomed* 2017;12:5421–31.
- Moreels I, Justo Y, Geyter B De, Haustraete K, Martins JC, Hens Z. Quantum dots: a surface chemistry study. *ACS Nano* 2012;5:2004–12.

3. Dabbousi BO, Rodriguez Viejo J, Mikulec FV, Heine JR, Mattoussi H, Ober R, *et al.* (CdSe)ZnS core-shell quantum dots: synthesis and characterization of a size series of highly luminescent nanocrystallites. *J Phys Chem B* 1997;101:9463–75.
4. Maxwell T, Nogueira Campos MG, Smith S, Doomra M, Thwin Z, Santra S. Quantum dots. In: *Nanoparticles for biomedical applications: fundamental concepts, biological interactions and clinical applications*; 2019. p. 243–65.
5. Senthil Kumar M, Valarmathi S, Bhima P, Prudhvi Devabaktuni S, Raja A, Vallabhaneni SD. Quantum dots. *Int J Pharm Technol* 2012;4:1929–49.
6. Bawendi MG, Steigerwald ML, Brus LE. The quantum mechanics of larger semiconductor clusters (“Quantum dots”). *Annu Rev Phys Chem* 1990;41:477–96.
7. Biju V. Chemical modifications and bioconjugate reactions of nanomaterials for sensing, imaging, drug delivery and therapy. *Chem Soc Rev* 2014;43:744–64.
8. Portney NG, Ozkan M. Nano-oncology: drug delivery, imaging, and sensing. *Anal Bioanal Chem* 2006;384:620–30.
9. Godbole NN, Galgatte UC, Chaudhari PD. Development and *in vitro* evaluation of quantum dots as a carrier for delivery of 5-fluorouracil. *Int J Pharm Pharm Sci* 2016;8:289–96.
10. SLJ, Gupta NV. Diabetic retinopathy: an inclusive review on current treatment and management approaches. *Asian J Pharm Clin Res* 2018;11:54.
11. Qi L, Gao X. Emerging application of quantum dots for drug delivery and therapy. *Expert Opinion Drug Delivery* 2008;5:263–7.
12. Zrazhevskiy P, Sena M, Gao X. Designing multifunctional quantum dots for bioimaging, detection, and drug delivery. *Chem Soc Rev* 2010;39:4326–54.
13. Maysinger D, Lovric J, Eisenberg A, Savic R. Fate of micelles and quantum dots in cells. *Eur J Pharm Biopharm* 2007;65:270–81.
14. Caruthers SD, Wickline SA, Lanza GM. Nanotechnological applications in medicine. *Curr Opin Biotechnol* 2007;18:26–30.
15. Wagner AM, Knipe JM, Orive G, Peppas NA. Quantum dots in biomedical applications. *Acta Biomaterialia* 2019;94:44–63.
16. Kong FY, Zhang JW, Li RF, Wang ZX, Wang WJ, Wang W. Unique roles of gold nanoparticles in drug delivery, targeting and imaging applications. *Molecules* 2017;22:1445.
17. Wang Q, Huang X, Long Y, Wang X, Zhang H, Zhu R, *et al.* Hollow luminescent carbon dots for drug delivery. *Carbon* 2013;59:192–9.
18. Wegner KD, Hildebrandt N. Quantum dots: Bright and versatile *in vitro* and *in vivo* fluorescence imaging biosensors. *Chem Soc Rev* 2015;44:4792–834.
19. Lee JH, Yigit MV, Mazumdar D, Lu Y. Molecular diagnostic and drug delivery agents based on aptamer-nanomaterial conjugates. *Adv Drug Delivery Rev* 2010;62:592–605.
20. Xu G, Zeng S, Zhang B, Swihart MT, Yong KT, Prasad PN. New generation cadmium-free quantum dots for biophotonics and nanomedicine. *Chem Rev* 2016;116:12234–327.
21. Chinnathambi S, Chen S, Ganesan S, Hanagata N. Silicon quantum dots for biological applications. *Adv Healthcare Mater* 2014;3:10–29.
22. Probst CE, Zrazhevskiy P, Bagalkot V, Gao X. Quantum dots as a platform for nanoparticle drug delivery vehicle design. *Adv Drug Delivery Rev* 2013;65:703–18.
23. Frecker T, Bailey D, Arzeta Ferrer X, McBride J, Rosenthal SJ. Review-quantum dots and their application in lighting, displays, and biology. *ECS J Solid State Sci Technol* 2016;5:R3019–31.
24. Lin J, Chen X, Huang P. Graphene-based nanomaterials for bioimaging. *Adv Drug Delivery Rev* 2016;105:242–54.
25. Ramamurthy SK, Sridhar C. Parthenium mediated synthesis of zinc oxide nanoparticles and its characterization. *Int J Appl Pharm* 2019;11:113–6.
26. Sivapriya V, Ponnarmadha S, Azeezand NA, Sudarshanadeepa V. Novel nanocarriers for ethnopharmacological formulations. *Int J Appl Pharm* 2018;10:26–30.
27. Jinhao GAO, Hongwei GU, Bing XU. Multifunctional magnetic nanoparticles: design, synthesis, and biomedical applications. *Acc Chem Res* 2009;42:1097–107.
28. Cassette E, Helle M, Bezdetnaya L, Marchal F, Dubertret B, Pons T. Design of new quantum dot materials for deep tissue infrared imaging. *Adv Drug Delivery Rev* 2013;65:719–31.
29. Martinez Carmona M, Gun’Ko Y, Vallet Regi M. ZnO nanostructures for drug delivery and theranostic applications. *Nanomaterials* 2018;8:268.
30. Boakye Yiadom KO, Kesse S, Opoku Damoah Y, Filli MS, Aquib M, Joelle MMB, *et al.* Carbon dots: applications in bioimaging and theranostics. *Int J Pharm* 2019;564:308–17.
31. Liu ML, Chen B Bin, Li CM, Huang CZ. Carbon dots: synthesis, formation mechanism, fluorescence origin and sensing applications. *Green Chem* 2019;21:449–71.
32. Delehanty JB, Mattoussi H, Medintz IL. Delivering quantum dots into cells: Strategies, progress and remaining issues. *Anal Bioanal Chem* 2009;393:1091–105.
33. Bilan R, Fleury F, Nabiev I, Sukhanova A. Quantum dot surface chemistry and functionalization for cell targeting and imaging. *Bioconjugate Chem* 2015;26:609–24.
34. Hild WA, Breunig M, Goepperich A. Quantum dots-nano-sized probes for the exploration of cellular and intracellular targeting. *Eur J Pharm Biopharm* 2008;68:153–68.
35. Bulte JWM, Modo MMJ. Design and applications of nanoparticles in biomedical imaging. Design and applications of nanoparticles in biomedical imaging; 2016. p. 1–469.
36. Azzazy HME, Mansour MMH, Kazmierczak SC. From diagnostics to therapy: prospects of quantum dots. *Clin Biochem* 2007;40:917–27.
37. Massey M, Wu M, Conroy EM, Algar WR. Mind your P’s and Q’s: the coming of age of semiconducting polymer dots and semiconductor quantum dots in biological applications. *Curr Opin Biotechnol* 2015;34:30–40.
38. Jaleel JA, Pramod K. Artful and multifaceted applications of carbon dot in biomedicine. *J Controlled Release* 2018;269:302–21.
39. Gittard SD, Miller PR, Boehm RD, Ovsianikov A, Chichkov BN, Heiser J, *et al.* Multiphoton microscopy of transdermal quantum dot delivery using two-photon polymerization-fabricated polymer microneedles. *Faraday Discuss* 2011;149:171–85.
40. Zuo P, Lu X, Sun Z, Guo Y, He H. A review on syntheses, properties, characterization and bioanalytical applications of fluorescent carbon dots. *Microchim Acta* 2016;183:519–42.
41. Ding C, Zhu A, Tian Y. Functional surface engineering of C-dots for fluorescent biosensing and *in vivo* bioimaging. *Acc Chem Res* 2014;47:20–30.
42. Homan K, Mallidi S, Cooley E, Emelianov S. Combined photoacoustic and ultrasound imaging of metal nanoparticles *in vivo*. *Nanoimaging* 2011;3:225–49.
43. Gao X, Du C, Zhuang Z, Chen W. Carbon quantum dot-based nanopores for metal ion detection. *J Materials Chem C* 2016;4:6927–45.
44. Geszke Moritz M, Moritz M. Quantum dots as versatile probes in medical sciences: synthesis, modification and properties. *Mater Sci Eng* 2013;33:1008–21.
45. Molaei MJ. A review on nanostructured carbon quantum dots and their applications in biotechnology, sensors, and chemiluminescence. *Talanta* 2019;196:456–78.
46. Bajwa N, Mehra NK, Jain K, Jain NK. Pharmaceutical and biomedical applications of quantum dots. *Artif Cells Nanomed Biotechnol* 2016;44:758–68.
47. Dey N, Rao M. Quantum dot: novel carrier for drug delivery. *Int J Res Pharm Biomed Sci* 2011;2:448–58.
48. Mo D, Hu L, Zeng G, Chen G, Wan J, Yu Z, *et al.* Cadmium-containing quantum dots: properties, applications, and toxicity. *Appl Microbiol Biotechnol* 2017;101:2713–33.
49. Nakahara M, Ohmi T. Quantum computing with quantum dots. In: *Quantum Computing*; 2008. p. 377–98.
50. Wu P, Yan XP. Doped quantum dots for chemo/biosensing and bioimaging. *Chem Soc Rev* 2013;42:5489–521.
51. Biju V, Itoh T, Ishikawa M. Delivering quantum dots to cells: bioconjugated quantum dots for targeted and nonspecific extracellular and intracellular imaging. *Chem Soc Rev* 2010;39:3031–56.
52. Gaponik N, Talapin DV, Rogach AL, Hoppe K, Shevchenko EV, Kornowski A, *et al.* Thiol-capping of CdTe nanocrystals: An alternative to organometallic synthetic routes. *J Phys Chem B* 2002;106:7177–85.
53. Emin S, Singh SP, Han L, Satoh N, Islam A. Colloidal quantum dot solar cells. *Sol Energy* 2011;85:1264–82.

54. Chen W, Lv G, Hu W, Li D, Chen S, Dai Z. Synthesis and applications of graphene quantum dots: a review. *Nanotechnol Rev* 2018;7:157–85.
55. Campuzano S, Yanez Sedeno P, Pingarron JM. Carbon dots and graphene quantum dots in electrochemical biosensing. *Nanomaterials* 2019;9:634.
56. Lim SY, Shen W, Gao Z. Carbon quantum dots and their applications. *Chem Soc Rev* 2015;44:362–81.
57. Barroso MM. Quantum dots in cell biology. *J Histochem Cytochem* 2011;59:237–51.
58. Klimov VI, Mikhailovsky AA, Xu S, Malko A, Hollingsworth JA, Leatherdale CA, *et al.* Optical gain and stimulated emission in nanocrystal quantum dots. *Science* 2000;290:314–7.
59. Kim S, Fisher B, Eisler HJ, Bawendi M. Type-II quantum dots: CdTe/CdSe(core/shell) and CdSe/ZnTe(core/shell) heterostructures. *J Am Chem Soc* 2003;125:11466–7.
60. Chan WCW, Maxwell DJ, Gao X, Bailey RE, Han M, Nie S. Luminescent quantum dots for multiplexed biological detection and imaging. *Curr Opin Biotechnol* 2002;13:40–6.
61. True LD, Gao X. Quantum dots for molecular pathology: their time has arrived. *J Mol Diagnostics* 2007;9:7–11.
62. Moloney MP, Govan J, Loudon A, Mukhina M, Gun'ko YK. Preparation of chiral quantum dots. *Nat Protoc* 2015;10:558–73.
63. Ghaderi S, Ramesh B, Seifalian AM. Fluorescence nanoparticles “quantum dots” as drug delivery system and their toxicity: a review. *J Drug Targeting* 2011;19:475–86.
64. Nurunnabi M, Parvez K, Nafujjaman M, Revuri V, Khan HA, Feng X, *et al.* Bioapplication of graphene oxide derivatives: drug/gene delivery, imaging, polymeric modification, toxicology, therapeutics and challenges. *RSC Adv* 2015;5:42141–61.
65. Obonyo O, Fisher E, Edwards M, Douroumis D. Quantum dots synthesis and biological applications as imaging and drug delivery systems. *Crit Rev Biotechnol* 2010;30:283–301.
66. Bilan R, Nabiev I, Sukhanova A. Quantum dot-based nanotools for bioimaging, diagnostics, and drug delivery. *Chem BioChem* 2016;17:2103–14.
67. Gulia S, Kakkar R. ZnO quantum dots for biomedical applications. *Adv Materials Lett* 2013;4:876–87.
68. Liu X, Pang J, Xu F, Zhang X. Simple approach to synthesize amino-functionalized carbon dots by carbonization of chitosan. *Sci Rep* 2016;6:31100.
69. Coe S, Woo WK, Bawendi M, Bulovic V. Electroluminescence from single monolayers of nanocrystals in molecular organic devices. *Nature* 2002;420:800–3.
70. Swarnkar A, Marshall AR, Sanehira EM, Chernomordik BD, Moore DT, Christians JA, *et al.* Quantum dot-induced phase stabilization of α -CsPbI₃ perovskite for high-efficiency photovoltaics. *Science* 2016;354:92–5.
71. Bak S, Kim D, Lee H. Graphene quantum dots and their possible energy applications: a review. *Curr Appl Physics* 2016;16:1192–201.
72. Grisorio R, Debellis D, Suranna GP, Gigli G, Giansante C. The dynamic organic/inorganic interface of colloidal PbS quantum dots. *Angew Chem Int Ed* 2016;55:6628–33.
73. Seguin R, Schliwa A, Rodt S, Potschke K, Pohl UW, Bimberg D. Size-dependent fine-structure splitting in self-organized InAs/GaAs quantum dots. *Phys Rev Lett* 2005;95:257402.
74. Bhattacharya P, Ghosh S, Stiff Roberts AD. Quantum dot optoelectronic devices. *Annu Rev Mater Res* 2004;34:1–40.
75. Li H, He X, Kang Z, Huang H, Liu Y, Liu J, *et al.* Water-soluble fluorescent carbon quantum dots and photocatalyst design. *Angew Chem Int Ed* 2010;49:4430–4.
76. Darbandi M, Thomann R, Nann T. Single quantum dots in silica spheres by microemulsion synthesis. *Chem Mater* 2005;17:5720–5.
77. Tang L, Ji R, Cao X, Lin J, Jiang H, Li X, *et al.* Deep ultraviolet photoluminescence of water-soluble self-passivated graphene quantum dots. *ACS Nano* 2012;6:5102–10.
78. Wang F, Pang S, Wang L, Li Q, Kreiter M, Liu CY. One-step synthesis of highly luminescent carbon dots in noncoordinating solvents. *Chem Mater* 2010;22:4528–30.
79. Ahirwar S, Mallick S, Bahadur D. Electrochemical method to prepare graphene quantum dots and graphene oxide quantum dots. *ACS Omega* 2017;2:8343–53.
80. Nann T. Phase-transfer of CdSe@ZnS quantum dots using amphiphilic hyperbranched polyethyleneimine. *Chem Commun* 2005;13:1735–6.
81. Tian P, Tang L, Teng KS, Lau SP. Graphene quantum dots from chemistry to applications. *Materials Today Chem* 2018;10:221–58.
82. Baruah S, Dutta J. Hydrothermal growth of ZnO nanostructures. *Sci Technol Adv Mater* 2009;10:013001.
83. Wang Q, Zheng H, Long Y, Zhang L, Gao M, Bai W. Microwave-hydrothermal synthesis of fluorescent carbon dots from graphite oxide. *Carbon NY* 2011;49:3134–40.
84. Prasannan A, Imae T. One-pot synthesis of fluorescent carbon dots from orange waste peels. *Ind Eng Chem Res* 2013;52:15673–8.
85. Park SY, Thongsai N, Chae A, Jo S, Kang EB, Paoprasert P, *et al.* Microwave-assisted synthesis of luminescent and biocompatible lysine-based carbon quantum dots. *J Ind Eng Chem* 2017;47:329–35.
86. He Y, Zhong Y, Peng F, Wei X, Su Y, Lu Y, *et al.* One-pot microwave synthesis of water-dispersible, ultraphoto- and pH-stable, and highly fluorescent silicon quantum dots. *J Am Chem Soc* 2011;133:14192–5.
87. Sumanth Kumar D, Jai Kumar B, Mahesh HM. Quantum nanostructures (QDs): an overview. In: *Synthesis of Inorganic Nanomaterials*; 2018. p. 59–88.
88. Liu Y, Xiao N, Gong N, Wang H, Shi X, Gu W, *et al.* One-step microwave-assisted polyol synthesis of green luminescent carbon dots as optical nanoprobes. *Carbon* 2014;68:258–64.
89. Singh I, Arora R, Dhiman H, Pahwa R. Carbon quantum dots: Synthesis, characterization and biomedical applications. *Turkish J Pharm Sci* 2018;15:219–30.
90. Wang X, Feng Y, Dong P, Huang J. A mini-review on carbon quantum dots: preparation, properties, and electrocatalytic application. *Front Chem* 2019;7:671.
91. Qian H, Qiu X, Li L, Ren J. Microwave-assisted aqueous synthesis: A rapid approach to prepare highly luminescent ZnSe(S) alloyed quantum dots. *J Phys Chem B* 2006;110:9034–40.
92. Rangel Mendez JR, Matos J, Chazaro Ruiz LF, Gonzalez Castillo AC, Barrios Yanez G. Microwave-assisted synthesis of C-doped TiO₂ and ZnO hybrid nanostructured materials as quantum-dots sensitized solar cells. *Appl Surf Sci* 2018;434:744–55.
93. Lehnen T, Zopes D, Mathur S. Phase-selective microwave synthesis and inkjet printing applications of Zn₂SnO₄ (ZTO) quantum dots. *J Mater Chem* 2012;22:17732–6.
94. Vasudevan D, Gaddam RR, Trinchì A, Cole I. Core-shell quantum dots: properties and applications. *J Alloys Compounds* 2015;636:395–404.
95. Wu YL, Lim CS, Fu S, Tok AIY, Lau HM, Boey FYC, *et al.* Surface modifications of ZnO quantum dots for bio-imaging. *Nanotechnology* 2007;18:215604.
96. Monopoli MP, Pitek AS, Lynch I, Dawson KA. Nanomaterial interfaces in biology. In: *Nanomaterial Interfaces in Biology: Methods and Protocols, Methods in Molecular Biology*; 2013;1025:137155.
97. Yuan CT, Chou WC, Chuu DS, Chang WH, Lin HS, Ruaan RC. Fluorescence properties of colloidal CdSe/ZnS quantum dots with various surface modifications. *J Med Biol Eng* 2006;26:131–5.
98. Krogmeier JR, Kang HG, Clarke ML, Yim P, Hwang J. Probing the dynamic fluorescence properties of single water-soluble quantum dots. *Opt Commun* 2008;281:1781–8.
99. Kumar P, Kukkar D, Deep A, Sharma SC, Bharadwaj LM. Synthesis of mercaptopropionic acid stabilized CDS quantum dots for bioimaging in breast cancer. *Adv Mater Lett* 2012;3:471–5.
100. Borse V, Sadawana M, Srivastava R. CdTe quantum dots: aqueous phase synthesis, stability studies and protein conjugation for development of biosensors. In: *Nanophotonics VI*; 2016;9884:988423.
101. Singla R, Guliani A, Kumari A, Yadav SK. Metallic nanoparticles, toxicity issues and applications in medicine. In: *Nanoscale materials in targeted drug delivery, theragnosis and tissue regeneration*; 2016. p. 41–80.
102. Dobhal G, Garima. Quantum dot bioconjugates for the detection of extracellular vesicles in saliva and breath. MSc Thesis; 2019. Available from <http://researcharchive.vuw.ac.nz/handle/10063/8119>. [Last accessed on 10 Mar 2021].

103. Tian B, Al-Jamal WT, Stuart M, Kostarelos K. Doxorubicin-loaded and antibody-conjugated liposome-QD hybrid vesicles for targeted cancer therapy and imaging. In: *Nanotechnology 2010: Bio Sensors, Instruments, Medical, Environment and Energy-Technical Proceedings of the 2010 NSTI Nanotechnology Conference and Expo, NSTI-Nanotech 2010*; 3:380-1.
104. Pardo J, Peng Z, Leblanc RM. Cancer targeting and drug delivery using carbon-based quantum dots and nanotubes. *Molecules* 2018;23:378.
105. Howarth M, Takao K, Hayashi Y, Ting AY. Targeting quantum dots to surface proteins in living cells with biotin ligase. *Proc Natl Acad Sci USA* 2005;102:7583-8.
106. Liu W, Howarth M, Greytak AB, Zheng Y, Nocera DG, Ting AY, *et al.* Compact biocompatible quantum dots functionalized for cellular imaging. *J Am Chem Soc* 2008;130:1274-84.
107. Smith AM, Duan H, Mohs AM, Nie S. Bioconjugated quantum dots for *in vivo* molecular and cellular imaging. *Adv Drug Delivery Rev* 2008;60:1226-40.
108. Ghasemi Y, Peymani P, Afifi S. Quantum dot: magic nanoparticle for imaging, detection and targeting. *Acta Biomed l'Ateneo Parm* 2009;80:156-65.
109. Kim D, Kim DH, Lee JH, Grossman JC. Impact of stoichiometry on the electronic structure of PbS quantum dots. *Phys Rev Lett* 2013;110:196802.
110. Rhyner MN, Smith AM, Goo X, Mao H, Yang L, Nie S. Quantum dots and multifunctional nanoparticles: new contrast agents for tumor imaging. *Nanomedicine* 2006;1:209-17.
111. Liu W, Hak SC, Zimmer JP, Tanaka E, Frangioni JV, Bawendi M. Compact cysteine-coated CdSe(ZnCdS) quantum dots for *in vivo* applications. *J Am Chem Soc* 2007;129:14530-1.
112. Liu DS, Phipps WS, Loh KH, Howarth M, Ting AY. Quantum dot targeting with lipoic acid ligase and HaloTag for single-molecule imaging on living cells. *ACS Nano* 2012;6:11080-7.
113. Drbohlavova J, Adam V, Kizek R, Hubalek J. Quantum dots-characterization, preparation and usage in biological systems. *Int J Mol Sci* 2009;10:656-73.
114. Murray CB, Kagan CR, Bawendi MG. Self-organization of CdSe nanocrystallites into three-dimensional quantum dot superlattices. *Science* 1995;270:1335-8.
115. Micic OI, Curtis CJ, Jones KM, Sprague JR, Nozik AJ. Synthesis and characterization of InP quantum dots. *J Phys Chem* 1994;98:4966-9.
116. Lipovskii A, Kolobkova E, Petrikov V, Kang I, Olkhovets A, Krauss T, *et al.* Synthesis and characterization of PbSe quantum dots in phosphate glass. *Appl Phys Lett* 1997;71:3406-8.
117. Knittel F, Gravel E, Cassette E, Pons T, Pillon F, Dubertret B, *et al.* On the characterization of the surface chemistry of quantum dots. *Nano Lett* 2013;13:5075-8.
118. Micic OI, Sprague JR, Curtis CJ, Jones KM, Machol JL, Nozik AJ, *et al.* Synthesis and characterization of InP, GaP, and GaInP2 quantum dots. *J Phys Chem* 1995;99:7754-9.
119. Passaseo A. Quantum dots: introduction. *Science* 2010;4:1-25.
120. Derfus AM, Chan WCW, Bhatia SN. Probing the cytotoxicity of semiconductor quantum dots. *Nano Lett* 2004;4:11-8.
121. Hoshino A, Fujioka K, Oku T, Suga M, Sasaki YF, Ohta T, *et al.* Physicochemical properties and cellular toxicity of nanocrystal quantum dots depend on their surface modification. *Nano Lett* 2004;4:2163-9.
122. Zhao F, Zhao Y, Liu Y, Chang X, Chen C, Zhao Y. Cellular uptake, intracellular trafficking, and cytotoxicity of nanomaterials. *Small* 2011;7:1322-37.
123. Su Y, Hu M, Fan C, He Y, Li Q, Li W, *et al.* The cytotoxicity of CdTe quantum dots and the relative contributions from released cadmium ions and nanoparticle properties. *Biomaterials* 2010;31:4829-34.
124. Chong Y, Ma Y, Shen H, Tu X, Zhou X, Xu J, *et al.* The *in vitro* and *in vivo* toxicity of graphene quantum dots. *Biomaterials* 2014;35:5041-8.
125. Tsay JM, Michalet X. New light on quantum dot cytotoxicity. *Chem Biol* 2005;12:1159-61.
126. Wu C, Wang C, Han T, Zhou X, Guo S, Zhang J. Insight into the cellular internalization and cytotoxicity of graphene quantum dots. *Adv Healthc Mater* 2013;2:1613-9.
127. Guo G, Liu W, Liang J, He Z, Xu H, Yang X. Probing the cytotoxicity of CdSe quantum dots with surface modification. *Mater Lett* 2007;61:1641-4.
128. Tan YF, Chandrasekharan P, Maity D, Yong CX, Chuang KH, Zhao Y, *et al.* Multimodal tumor imaging by iron oxides and quantum dots formulated in poly (lactic acid)-d-alpha-tocopheryl polyethylene glycol 1000 succinate nanoparticles. *Biomaterials* 2011;32:2969-78.
129. Liu Y, Ai K, Yuan Q, Lu L. Fluorescence-enhanced gadolinium-doped zinc oxide quantum dots for magnetic resonance and fluorescence imaging. *Biomaterials* 2011;32:1185-92.
130. Chen Y, Chen Z, He Y, Lin H, Sheng P, Liu C, *et al.* L-cysteine-capped CdTe QD-based sensor for simple and selective detection of trinitrotoluene. *Nanotechnology* 2010;21:125502.
131. Juzenas P, Chen W, Sun YP, Coelho MAN, Generalov R, Generalova N, *et al.* Quantum dots and nanoparticles for photodynamic and radiation therapies of cancer. *Adv Drug Delivery Rev* 2008;60:1600-14.
132. Han M, Gao X, Su JZ, Nie S. Quantum-dot-tagged microbeads for multiplexed optical coding of biomolecules. *Nat Biotechnol* 2001;19:631-5.
133. Lagerholm BC, Wang M, Ernst LA, Ly DH, Liu H, Bruchez MP, *et al.* Multicolor coding of cells with cationic peptide coated quantum dots. *Nano Lett* 2004;4:2019-22.
134. Li J, Zhao XW, Zhao YJ, Gu ZZ. Quantum-dot-coated encoded silica colloidal crystals beads for multiplex coding. *Chem Commun* 2009;17:2329-31.
135. Tholouli E, Sweeney E, Barrow E, Clay V, Hoyland JA, Byers RJ. Quantum dots light up pathology. *J Pathol* 2008;216:275-85.
136. Xia Z, Xing Y, So MK, Koh AL, Sinclair R, Rao J. Multiplex detection of protease activity with quantum dot nanosensors prepared by intein-mediated specific bioconjugation. *Anal Chem* 2008;80:8649-55.
137. Zheng XT, Ananthanarayanan A, Luo KQ, Chen P. Glowing graphene quantum dots and carbon dots: properties, syntheses, and biological applications. *Small* 2015;11:1620-36.
138. Bourlinos AB, Stassinopoulos A, Anglos D, Zboril R, Karakassides M, Giannelis EP. Surface functionalized carbogenic quantum dots. *Small* 2008;4:455-8.
139. Kagan CR, Murray CB, Nirmal M, Bawendi MG. Electronic energy transfer in CdSe quantum dot solids. *Phys Rev Lett* 1996;76:1517-20.
140. Valizadeh A, Mikaeili H, Samiei M, Farkhani SM, Zarghami N, Kouhi M, *et al.* Quantum dots: synthesis, bioapplications, and toxicity. *Nanoscale Res Lett* 2012;7:480.
141. Luo PG, Sahu S, Yang ST, Sonkar SK, Wang J, Wang H, *et al.* Carbon "quantum" dots for optical bioimaging. *J Mater Chem B* 2013;1:2116-27.
142. Bakker MA, Mehl S, Hiltunen T, Harju A, Divincenzo DP. Validity of the single-particle description and charge noise resilience for multielectron quantum dots. *Phys Rev B-Condens Matter Mater Phys* 2015;91:155425.
143. Choi YE, Kwak JW, Park JW. Nanotechnology for early cancer detection. *Sensors* 2010;10:428-55.
144. Walling MA, Novak JA, Shepard JRE. Quantum dots for live cell and *in vivo* imaging. *Int J Mol Sci* 2009;10:441-91.
145. Qian ZS, Shan XY, Chai LJ, Ma JJ, Chen JR, Feng H. DNA nanosensor based on biocompatible graphene quantum dots and carbon nanotubes. *Biosens Bioelectron* 2014;60:64-70.
146. Obliosca JM, Liu C, Batson RA, Babin MC, Werner JH, Yeh HC. DNA/RNA detection using DNA-templated few-atom silver nanoclusters. *Biosensors* 2013;3:185-200.
147. Su S, Fan J, Xue B, Yuwen L, Liu X, Pan D, *et al.* DNA-conjugated quantum dot nanoprobe for high-sensitivity fluorescent detection of DNA and micro-RNA. *ACS Appl Mater Interfaces* 2014;6:1152-7.
148. Tikhomirov G, Hoogland S, Lee PE, Fischer A, Sargent EH, Kelley SO. DNA-based programming of quantum dot valency, self-assembly and luminescence. *Nat Nanotechnol* 2011;6:485-90.
149. Kim SS, Ye C, Kumar P, Chiu I, Subramanya S, Wu H, *et al.* Targeted delivery of siRNA to macrophages for anti-inflammatory treatment. *Mol Ther* 2010;18:993-1001.
150. Bonoiu A, Mahajan SD, Ye L, Kumar R, Ding H, Yong KT, *et al.* MMP-9 gene silencing by a quantum dot-siRNA nanoplex

- delivery to maintain the integrity of the blood brain barrier. *Brain Res* 2009;1282:142–55.
151. Bruun J, Larsen TB, Jøck RI, Eliassen R, Holm R, Gjetting T, *et al.* Investigation of enzyme-sensitive lipid nanoparticles for delivery of siRNA to blood-brain barrier and glioma cells. *Int J Nanomed* 2015;10:5995–6008.
152. Lin G, Chen T, Zou J, Wang Y, Wang X, Li J, *et al.* Quantum dots-siRNA nanoplexes for gene silencing in central nervous system tumor cells. *Front Pharmacol* 2017;8:182.
153. Djikanovic D, Kalauzi A, Jeremic M, Xu J, Micic M, Whyte JD, *et al.* Interaction of the CdSe quantum dots with plant cell walls. *Colloids Surf B* 2012;91:41–7.
154. Wang J, Yang Y, Zhu H, Braam J, Schnoor JL, Alvarez PJJ. Uptake, translocation, and transformation of quantum dots with cationic versus anionic coatings by *Populus deltoides* × *nigra* cuttings. *Environ Sci Technol* 2014;48:6754–62.
155. Zhang D, Hua T, Xiao F, Chen C, Gersberg RM, Liu Y, *et al.* Uptake and accumulation of CuO nanoparticles and CdS/ZnS quantum dot nanoparticles by *schoenoplectus tabernaemontani* in hydroponic mesocosms. *Ecol Eng* 2014;70:114–23.
156. Wang Q, Chen J, Zhang H, Lu M, Qiu D, Wen Y, *et al.* Synthesis of water-soluble quantum dots for monitoring carrier-DNA nanoparticles in plant cells. *J Nanosci Nanotechnol* 2011;11:2208–14.
157. Dong X, Liang W, Mezziani MJ, Sun YP, Yang L. Carbon dots as potent antimicrobial agents. *Theranostics* 2020;10:671–86.
158. Lu Z, Li CM, Bao H, Qiao Y, Toh Y, Yang X. Mechanism of antimicrobial activity of CdTe quantum dots. *Langmuir* 2008;24:5445–52.
159. Ristic BZ, Milenkovic MM, Dakic IR, Todorovic Markovic BM, Milosavljevic MS, Budimir MD, *et al.* Photodynamic antibacterial effect of graphene quantum dots. *Biomaterials* 2014;35:4428–35.
160. Kim S, Lim YT, Soltesz EG, De Grand AM, Lee J, Nakayama A, *et al.* Near-infrared fluorescent type II quantum dots for sentinel lymph node mapping. *Nat Biotechnol* 2004;22:93–7.
161. Frangioni JV, Kim SW, Ohnishi S, Kim S, Bawendi MG. Sentinel lymph node mapping with type-II quantum dots. *Methods Mol Biol* 2007;374:147–59.
162. Pons T, Pic E, Lequeux N, Cassette E, Bezdetnaya L, Guillemin F, *et al.* Cadmium-free CuInS₂/ZnS quantum dots for sentinel lymph node imaging with reduced toxicity. *ACS Nano* 2010;4:2531–8.
163. Smith AM, Dave S, Nie S, True L, Gao X. Multicolor quantum dots for molecular diagnostics of cancer. *Expert Rev Mol Diagnostics* 2006;6:231–44.
164. Shao L, Gao Y, Yan F. Semiconductor quantum dots for biomedical applications. *Sensors* 2011;11:11736–51.
165. Luo G, Long J, Zhang B, Liu C, Ji S, Xu J, *et al.* Quantum dots in cancer therapy. *Expert Opin Drug Delivery* 2012;9:47–58.
166. Nie S, Xing Y, Kim GJ, Simons JW. Nanotechnology applications in cancer. *Annual Rev Biomed Eng* 2007;9:257–88.
167. Wagner MK, Li F, Li J, Li XF, Le XC. Use of quantum dots in the development of assays for cancer biomarkers. *Anal Bioanal Chem* 2010;397:3213–24.
168. Nida DL, Rahman MS, Carlson KD, Richards Kortum R, Follen M. Fluorescent nanocrystals for use in early cervical cancer detection. *Gynecol Oncol* 2005;99(3 Suppl 1):S89–94.
169. Iga AM, Robertson JHP, Winslet MC, Seifalian AM. Clinical potential of quantum dots. *J Biomed Biotechnol* 2007;2007:76087.
170. Kloepfer JA, Mielke RE, Wong MS, Nealson KH, Stucky G, Nadeau JL. Quantum dots as strain- and metabolism-specific microbiological labels. *Appl Environ Microbiol* 2003;69:4205–13.
171. Liang J, Huang S, Zeng D, He Z, Ji X, Ai X, *et al.* CdSe quantum dots as luminescent probes for spironolactone determination. *Talanta* 2006;69:126–30.

A Review on: Fast Dissolving Oral Film

Mr. Vijay P. Ingle, Prof. Sharad D. Tayade, Dr. Shirish P. Jain

Rajarshi Shahu College of Pharmacy, Buldana, Maharashtra, India

ABSTRACT

Recently, fast dissolving oral films have started gaining fame and acceptance as new drug delivery systems, which aim to enhance safety and efficacy of a drug molecule to achieve better patient compliance. It is a robust form a drug delivery system where the film is placed on the top or the floor of the tongue. When put on the tongue, this film dissolves instantaneously, releasing the drug which dissolves in the saliva. Buccal drug delivery has lately become an important route of drug administration. But many of the patients (paediatrics and geriatrics) are unwilling to take solid preparations due to fear of choking. This has made the pharmaceutical industry look for alternatives routes of drug delivery like film drug delivery. Fast dissolving oral drug delivery system have started gaining popularity and acceptance as new drug delivery system, because they are easy to administer, better patient compliance, rapid drug absorption, and sudden onset of drug action with instant bioavailability is possible. This review reflects information regarding formulation ingredient, technologies and evaluation test employed in the preparation of fast dissolving oral films.

KEYWORDS: *Fast dissolving oral films, buccal drug delivery, paediatric patients, geriatrics patients*

INTRODUCTION

Among the different routes, the most agreeable routes, for the patient is oral route. Most of the pharmaceutical companies have directed their research activity in developing viable dosage alternatives from oral route for paediatrics, geriatrics, noncompliant or nauseous patients. Almost 90% of the drugs are administered to the body via oral route for the treatment of various disorders and diseases as it is regarded as the safest, most economical method of drug delivery and have the highest patient compliance. The drug is either dissolved or swallowed, which then enters into the systemic circulation to produce the desired effect. Fast dissolving oral film, a novel drug delivery system for the oral delivery of the drug is an ultrathin film prepared using hydrophilic polymers that rapidly dissolves on the top or floor of the tongue or buccal cavity. It is an ultrathin strip (50-150 microns thick) of postage stamp size with an active agent and other excipient developed on the basis on transdermal patch technology. These fast-dissolving oral films have persistent to extend in sales and launched and patient compliance and convenient products effectively addressing issues for pharmaceuticals as well as

How to cite this paper: Mr. Vijay P. Ingle | Prof. Sharad D. Tayade | Dr. Shirish P. Jain "A Review on: Fast Dissolving Oral Film" Published in International Journal of Trend in Scientific Research and Development (ijtsrd), ISSN: 2456-6470, Volume-5 | Issue-5, August 2021, pp.300-310, URL: www.ijtsrd.com/papers/ijtsrd43836.pdf



Copyright © 2021 by author (s) and International Journal of Trend in Scientific Research and Development Journal. This is an Open Access article distributed under the terms of the Creative Commons Attribution License (CC BY 4.0) (<http://creativecommons.org/licenses/by/4.0>)



nutraceuticals that have been traditionally administered as oral solid dosages.

Today, fast oral films are a well proven and world-wide accepted technology for the systemic delivery of active pharmaceutical ingredients (APIs)^[1,2]. To overcome this oral fast disintegrating drug delivery system were developed, these systems were initially developed within the late seventies as an alternative to tablets, capsules and syrups for paediatric and geriatric patients who experience difficulties in swallowing traditional oral solid dosage forms. These dosage forms either dissolve or disintegrate generally within a 3 minute in mouth, without need of water. Oral fast disintegrating dosage form have started gaining popularity and acceptance as new drug delivery system due to better patient compliance^[3] Technology Catalysts forecasts the market for drug products in oral thin film formulations to be valued at \$500 million in 2007 and could reach \$2 billion in near future^[4,5,6]. However only a few products consisting bitter molecules have been able to be commercialized because of the complexity associated with the ODT. A large number of drugs can be formulated as mouth dissolving films.

Innovative products may increase the therapeutic possibilities in the following indications^[7,8].

- Pediatrics (Antitussives, Expectorants, Antiasthmatics)
- Geriatrics (Antiepileptic, Expectorants)
- Gastrointestinal diseases
- Nausea (due to Cytostatic therapy)
- CNS (Antiparkinsonism therapy)

Fast dissolving drug delivery system (FDDS)

Fast dissolving drug delivery system is a new generation delivery system also known as fast dissolving/disintegrating film for the oral delivery of the drug which came into existence in the late 1970s as an alternative to tablets, capsules, syrups and other formulation for paediatric and geriatric patients who experience difficulties in swallowing traditional solid dosage forms which combines both the advantages of conventional tablet and of liquid formulation^[4] FDDS is easy to administer and provides better patient compliance in the elderly, paediatric, mentally retarded, nauseated and uncooperative patients^[9] This delivery system consists of the solid dosage form that dissolve quickly i.e. within a matter of seconds in the oral cavity without the administration of water. The delivery system consists of a very thin oral strip which is simply placed on the patients tongue or any other oral mucosal tissue and instantly gets wetted by saliva^[10] The film rapidly hydrates onto the site of application. It then rapidly dissolves and disintegrates to release the medication for oro-mucosal absorption. The robustness of the film depends upon the type and amount of polymer used and general dissolution time for orally dissolving film is 5-20 min as per pharmacopoeia.^[11,12] They also provide quick onset of action within few seconds as the oro-mucosal absorption of the drug occurs directly from the site of administration to the systemic circulation avoiding the first-pass metabolism to produce the desired effect.^[13]

Special features of oral thin films^[14,15]

- Thin elegant
- Available in various sizes and shapes
- Un-obstructive
- Excellent mucoadhesion.
- Fast disintegration and rapid release.

Ideal properties of fast dissolving films^[16,17,18]

- It should be compatible with the other ingredients.
- The therapeutic dose of the drug should not be greater than 40mg.
- It should be less friable and have good mechanical strength to withstand the post manufacturing handling.
- It should quickly dissolve to release drug instantaneously in mouth.
- It should have an acceptable taste with pleasing mouth feel.

Anatomy of oral cavity

The structure and anatomy of oral cavity is studied for understanding the environment provided for delivering drugs [Fig. 1]. The oral mucosa allows direct access of drug to the systemic circulation and avoids first pass metabolism. The epithelium of the oral cavity is quite similar to that of the skin, with slight differences with regard to keratinization, protective and lubricant mucous which is spread across its surface.^[19] The permeability of oral mucosa is 4–1000 times greater than that of the skin. The oral cavity is divided into two regions: outer being the oral vestibule bounded by the lips and cheeks; the hard and soft palates, the floor of the mouth and tonsils.^[20] Oral drug delivery has been known for decades as the most widely utilized route of administration among all the routes that have been explored for the systemic delivery of drugs via various pharmaceutical products of different dosageforms.^[21]

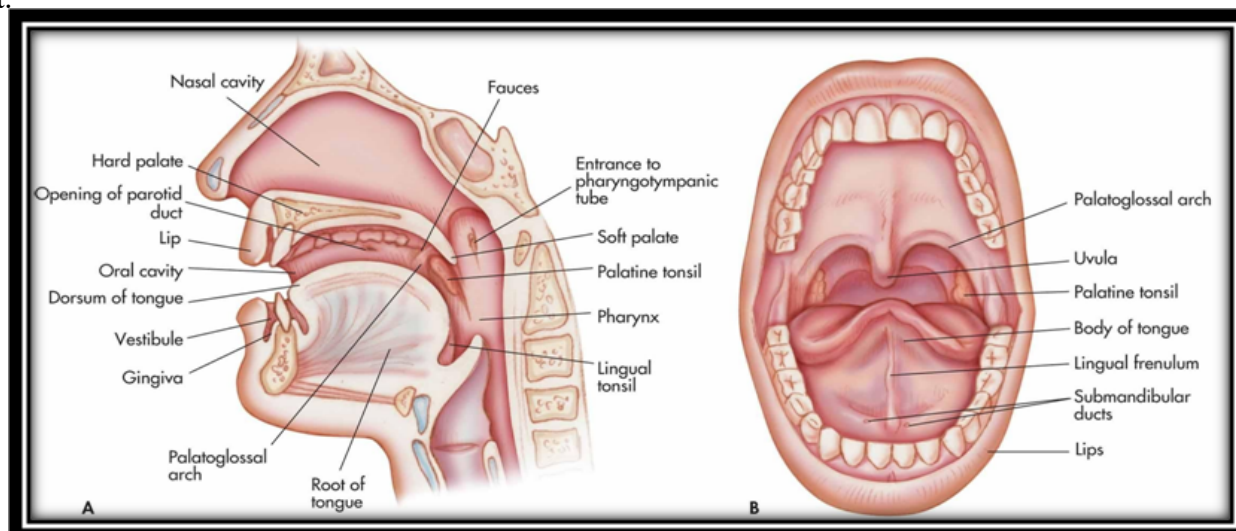


Figure 1: Anatomy of the oral cavity

Advantages of fast dissolving films^[22]

- Taste masking
- Enhanced stability
- Improve bioavailability for certain therapeutic ingredient.
- Rapid onset of action.
- No risk of choking.
- Convenient dosing or accurate dosing.
- No need of water to swallow or chewed.
- Pleasant mouth feel, leave negligible or no residue in the mouth after administration.
- Beneficial in cases such as motion sickness, acute pain, sudden allergic attack, asthmatic attack and coughing, where an ultra-rapid onset of action is required.
- Stability for longer duration of time, since the drug remains in solid dosage form till it is consumed.
- Flexible and portable in nature so they provide ease in handling, transportation and storage.

Disadvantages of fast dissolving films^[23]

- Drugs which are unstable at buccal pH cannot be administered.
- Drugs which irritate the mucosa cannot be administered by this route.
- A drug with small dose requirement can only be administered.
- Taste masking- Most drugs have the bitter taste, and need taste masking.
- It also shows the fragile, granule property.
- It is hygroscopic in nature so it must be kept in dry places.

Table 1: Comparison between Fast Dissolving Oral films and Dissolving Tablets^[24,25]

The comparison between Fast Dissolving Oral Films and Fast Dissolving Tablets was given table 1.

Sr. no	Fast Dissolving Oral Film	Fast Dissolving Tablet
1.	Large surface area gives greater dissolution.	Less surface area gives lesser dissolution than FDOF.
2.	Patient compliance is more.	Patient compliance is less than FDOF.
3.	Fast dissolving films are of thickness 0.015-.05 inches.	Fast dissolving tablets is of the same size of a conventional tablet.
4.	Only low dose can be incorporated in the formulation.	High dose can also be incorporated in the formulation.

Formulation Components of FDOFs**Active pharmaceutical ingredient**^[26]

A film composition contains 1-30% w/w of the active pharmaceutical ingredient. Always use low dose active pharmaceutical ingredients because high dose of drug is difficult to incorporate in fast dissolving film. A number of drugs can be used as fast dissolving film including anti-histamine, anti-diarrheal, anti-depressants, vasodilators, anti-asthmatic, anti-emetic, etc.^[23] Dimenhydrinate can also be incorporated into ODFs for taste masking. Common examples of drugs incorporated into ODFs are salbutamol sulfate, rizatriptan benzoate, verapamil, ondansetron, dexamethasone, rofecoxib, cetirizine, pilocarpine, tianeptine sodium, indomethacin, etc. are mentioned in edin.^[27]

Film forming polymer^[28,29]

Polymer are the most important ingredient of the fast-dissolving oral film. Generally, 45% w/w of polymer is used which is based on total weight of dry film. The selection of polymer is one of the most important and critical parameters for the successful development of oral films because of their tensile strength which depends upon the type and amount of polymer used. Mainly hydrophilic polymers are used in the oral strips as they rapidly disintegrate in the oral cavity as they come in contact with saliva. Currently, both natural and synthetic polymers are used for the preparation of fast dissolving film.

Table 2: List of polymers used in oral thin films ^[30]

Group	Class	Example
Natural	Carbohydrate	Pullulan, pectin, sodium alginate, maltodextrin, sodium starch glycolate.
	Proteins	Gelatine
	Resin	Polymerized rosin. (novel film former)
Synthetic	Cellulose Derivatives	Hydroxypropyl methylcellulose (E3, E5, E15, K3, K15, K50), Methylcellulose. (A3, A6, A15), Carboxy methylcellulose secekol-30, Sodium carboxymethyl cellulose. Microcrystalline cellulose.
	Vinyl polymer	Poly vinyl pyrrolidone (K-90, K-30), Poly vinyl alcohol, Poly ethylene oxide.
	Acrylic polymer	Eudragit (RD-100, 9,10, 11, 12 and RL- 100)

Ideal Properties of The Film Forming Polymers.

^[31,32]

1. The polymer employed should be non-toxic, non-irritant and devoid of any leachable impurities.
2. It would be ideal to have a polymer that would have local enzyme inhibition action.
3. It should have good wetting and spread ability property.
4. The polymer should exhibit sufficient peel, shear and tensile strengths.
5. The polymer should be cheap and readily available.
6. It should not cause any secondary infections in the oral mucosa/ dental region.
7. It should have a good mouth feel property.
8. It should be tasteless.
9. It should have long shelf life.

Plasticizers (0-20%)

Plasticizer helps to improve the flexibility and reduces the brittleness of the strip by reducing the glass transition temperature of the polymer. The selection of plasticizer depends on its compatibility with the polymer and the type of solvent used in the formulation ^[33,34]. Commonly used plasticizers are glycerol, propylene glycol, low molecular weight polyethylene glycols (PEGs), phthalate derivatives like dimethyl, diethyl, and dibutyl phthalate, citrate derivatives such as tributyl, triethyl, acetyl citrate, triacetin and castor oil. The plasticizers concentration of 0–20 % w/w of dry polymer weight is used by avoiding the film cracking, splitting and peeling of the strip ^[35,36]. The use of certain plasticizers may also affect the absorption rate of the drug ^[37]. The properties of plasticizer are important to decrease the glass transition temperature of the polymer in the range of 40–60°C for a nonaqueous solvent system and below 75 °C for aqueous systems ^[38]. Cellulosic hydrophilic polymers were easily plasticized with hydroxyl-containing plasticizers like PEG, propylene

glycol, glycerol, and polyols. In contrast, less hydrophilic cellulosic polymers were plasticized with esters of citric acid and phthalic acid ^[39]. Glycerol acts as a better plasticizer for polyvinyl alcohol while diethylene glycol can be used for both Hypromellose as well as polyvinyl alcohol films.

Surfactants

^[40,41]

Surfactants are used as wetting or solubilising or dispersing agent so that the film is getting dissolved within seconds and release active agent immediately. Commonly employed are poloxamer 407, benzalkonium chloride, etc. Out of these most predominantly used surfactant is poloxamer 407.

Sweetening agents

^[42,43,44]

Sucrose is the most commonly used sweeteners in FDOFs. Sucrose is very soluble in water and being colourless does not impart any undesirable colour to the final formulation. Some of the commonly employed sweeteners are dextrose, sucrose, fructose, glucose, isomaltose, etc. Artificial sweeteners like saccharine, cyclamate, aspartame (first generation), sucralose, alitame and neotame (second generation) can also be used. The sweetness of fructose is perceived rapidly in the mouth as compared to sucrose and dextrose. Fructose is sweeter than sorbitol and mannitol and thus used widely as a sweetener. Low molecular weight carbohydrates and specially sucrose are most commonly used sweeteners. Sucrose is very soluble in water and being colourless does not impart any undesirable colour to the final formulation. It is stable over the pH range 4–8. It masks the taste of both salty and bitter drugs. Polyhydric alcohols such as sorbitol, mannitol, and malt can be used in combination as they additionally provide good mouth-feel and cooling sensation. Polyhydric alcohols are less carcinogenic and do not have bitter after taste which is a vital aspect in formulating oral preparations. The artificial sweeteners have gained more popularity in pharmaceutical preparations. Saccharin, cyclamate

and aspartame are the first generation of the artificial sweeteners followed by acesulfame-K, sucralose, alitame and neotame which fall under the second-generation artificial sweeteners. Acesulfame-K and sucralose have more than 200- and 600-time sweetness. Neotame and alitame have more than 2000- and 8000-time sweetening power as compared to sucrose. Rebiana which is an herbal sweetener, derived from plant *Stevia rebaudiana* (South American plant) has more than 200 -300-time sweetness.

Saliva stimulating agents^[45]

Saliva stimulating agents are used to increase the rate of production of saliva that would help in the faster disintegration of the rapid dissolving strip formulations. Examples of salivary stimulants are citric acid, malic acid, lactic acid, ascorbic acid and tartaric acid. Among these the most preferred one is citric acid. These agents are used alone or in combination between 2 to 6% w/w of weight of the film.

Flavouring agents^[46]

Flavours used in the formulation must be non-toxic, soluble, stable and compatible with the excipients. The quantity of flavouring agent required to mask the taste depends on the flavour type and its strength. Commonly employed are fruity flavours (vanilla, cocoa, chocolate, citrus), flavour oils (peppermint oil, cinnamon oil, oil of nutmeg). Flavours can also be chosen from oleo resins, synthetic flavour oils and extract derived from various parts of the plants like fruits, flowers etc. The amount of flavour needed to mask the taste depends on the flavour type and its strength.

Colouring agents

Generally incorporated colouring agents are FD&C colours, natural colours, pigments such as titanium dioxide, etc. The colouring agents should not exceed concentration levels of 1% w/w.^[47,48] Some saliva stimulating agents may also be added to enhance the disintegration and to get rapid release. Some of these agents are citric acid, tartaric acid, malic acid, ascorbic acid and succinic acid.

Manufacturing methods

To manufacture fast dissolving oral films, following methods are generally employed:

- A. Semisolid casting
- B. Rolling
- C. Solvent casting
- D. Hot melt extrusion
- E. Solid dispersion extrusion

A. Semisolid casting^[49]

In this method at first a solution of water-soluble film forming polymer is prepared. Then the resulting solution is added to a solution of acid insoluble polymer (e.g., cellulose acetate phthalate) which was prepared in ammonium or sodium hydroxide. The ratio of the acid insoluble polymer to film forming polymer should be 1:4. A gel mass is obtained on addition of suitable amount of plasticizer. By the means of heat-controlled drums, finally the gel mass is casted in to the films or ribbons.

B. Rolling method^[50]

In this method the film is prepared by preparation of a pre-mix, addition of an active and subsequent formation of a film. Prepare pre-mix with film forming polymer, polar solvent and other additives except a drug. Add pre mix to master batch feed tank. Fed it via a 1st metering pump and control valve to either or both of the 1st and 2nd mixer. Add required amount of drug to the desired mixer. Blend the drug with master batch pre mix to give a uniform matrix. Then a specific amount of uniform matrix is then fed to the pan through 2nd metering pumps. The film is finally formed on the substrate and carried away via the support roller. The wet film is then dried using controlled bottom drying.

C. Solvent casting^[51,52,53]

In this method water soluble polymers are dissolved in water and the drug along with other ingredients is dissolved in suitable solvent. Then both the solutions are mixed, stirred, finally casted into the petri plate and dried.

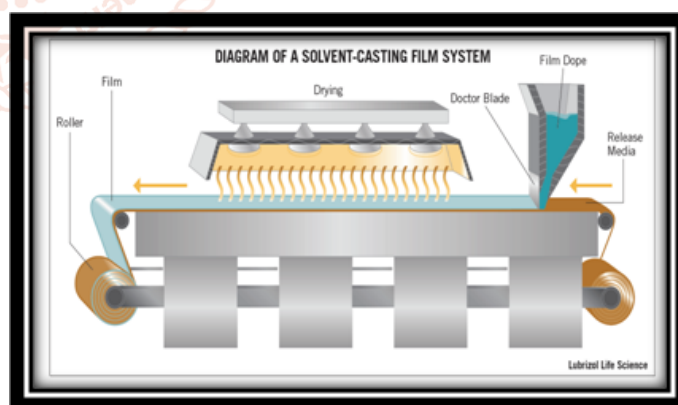


Figure 2: Solvent Casting.

Advantages:

- Better uniformity of thickness and better clarity than extrusion.
- Film has fine gloss and freedom from defects such as die lines.
- Film has more flexibility and better physical properties.
- Finished film thickness is 12-100um

Disadvantages:

- The polymer must be soluble in a volatile solvent or water.
- A stable solution with a reasonable minimum solid content and viscosity should be formed.
- Formation of homogeneous film and release from the casting support must be possible.

D. Hot melt extrusion ^[54]

The processing temperature should be 80°C in 1st zone, 115°C in 2nd zone, 100°C in 3rd zone and 65°C in

4th zone. The screw speed should set at 15 rpm to set the granule inside the extruder for approximately 3-4 min. Drug and polymer are blended in sigma blade mixer 10 min. Plasticizer is added slowly. Granulation of mixture in the presence of anti-sticking agent. Granules are store overnight and sieved through 250um sieve. Dried granules are fed into the extruder. Processing is done for 3-4 min. At temperature as mentioned above. Extrudate is pressed at temperature at 65°C to obtain a film of thickness 200um.

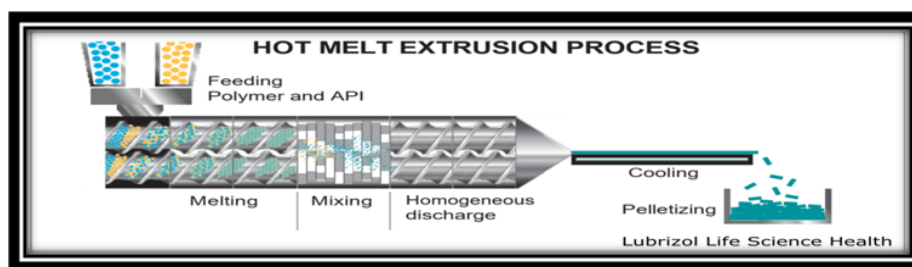


Figure 3: Holt melt extrusion

Advantages:

- Without the use of any solvent or water.
- Fewer processing steps.
- Compressibility properties of the API may not be of importance.
- A better alternative for poorly soluble drugs.
- Have stability at varying pH and moisture levels.
- Better content uniformity.
- Improved bioavailability of poorly soluble compounds.

Disadvantages:

- Thermal degradation due to use of high temperature.
- Flow properties of the polymer are essential to processing.
- A limited number of available polymers.
- All excipients must be devoid of water or any other volatile solvent.
- Required high power input

E. Solid dispersion extrusion

The term solid dispersion refers to the dispersion of one or more active ingredients in an inert carrier in a solid state in the presence of amorphous hydrophilic polymers. Drug is dissolved in suitable liquid solvent. Then solution is incorporated into the melt of polyethylene glycol, obtainable below 70°C finally the solid dispersion is shaped into the films by means of dies.

CHARACTERIZATION OF DISSOLVING FILMS ^[55,56,57]

Morphology study

The morphology of the film is studied using Scanning Electron Microscopy (SEM), at a definite magnification.

Thickness

It can be measured by micrometre screw gauge at different locations. It is crucial to determine uniformity in the thickness of the film as this is directly related to the accuracy of dose in the strip.

Organoleptic evaluation

For this purpose, in vitro methods of utilizing taste sensors and specially designed apparatus are being used. These invitro taste assessment apparatus for high throughput taste screening of oral pharmaceutical formulations.

Mechanical properties

Three mechanical properties namely tear resistance, elastic modulus and tensile strength percentage elongation are ca

Tear resistance

Principally very low rate of loading 51mm is employed and is designed to measure the force to initiate tearing. The maximum stress or force (that is generally found near the onset of tearing) necessary to tear the specimen is noted as the tear resistance value in newtons (or pounds-force).

Elastic modulus

It is calculated by formula

Elastic modulus = force at corresponding strain × 1 / cross sectional area of corresponding strain

Tensile strength

Tensile strength is the maximum stress applied to a point at which the strip specimen breaks. It is calculated by formula.

Tensile strength = Load at failure × 100/film thickness × film width

Folding endurance

Folding endurance is determined by repeated folding of the strip at the same place till the strip breaks. The number of times the film is folded without breaking is computed as the folding endurance value.

Percentage elongation

It is calculated by formula

% Elongation = Increase in length of strip x100 / initial length of strip

Swelling property

Each film sample is weighed and placed in a preweighed stainless steel wire mesh. Then the mesh containing sample is submerged into 15ml medium (simulated saliva solution) in a plastic container. Increase in the weight of the film was determined at preset time interval until a constant weight was observed.

Degree of swelling = $\frac{W_t - W_o}{W_o}$

Where,

W_t is weight of film at time t, and W_o is weight of film at time zero.

Weight variation

Weight variation is studied by individually weighing 10 randomly selected films and by calculating the average weight.

Disintegration time

Disintegration of orally fast dissolving films requires US disintegration apparatus. The disintegration time limit of 30 seconds or less for orally disintegrating tablet described in Centre for Drug Evaluation and Research (CDER) guidance can be applied to fast dissolving oral strips. Disintegration time will vary depending on the formulation but typically the disintegration ranges from 5 to 30 secs. Although, no official guidance for oral fast disintegrating films strip.

Dissolution test

Dissolution testing can be performed using the standard basket or paddle apparatus described in any of the pharmacopoeia. The dissolution medium will essentially be selected as per the sink condition and highest dose of the API. Many times, the dissolution test can be difficult due to tendency of the strip to float onto the dissolution medium when the paddle apparatus is employed.

Stability studies

Stability studies have to be carried out at accelerated condition (65% relative humidity and 35°C temperature) in the humidity chamber.

Packaging of Fast Dissolving Film.^[58]

In the pharmaceutical industry it is vital that the package selected adequately preserve the integrity of the product. Expensive packaging, specific processing, and special care are required during manufacturing and storage to protect the dosage of other fast dissolving dosage forms. A variety of packaging options are available for fast dissolving films. Single packaging is mandatory for films, which are pharmaceutical products; an aluminium pouch is the most commonly used packaging format. APR-Labtech has developed the Rapid card, a proprietary and patented packaging system, which is specially designed for the Rapid films. The rapid card has same size as a credit card and holds three rapid films on each side. Every dose can be taken out individually.

The material selected must have the following characteristics

- They must protect the preparation from environmental conditions.
- They must be FDA approved.
- They must meet applicable tamper-resistant requirement
- They must be non-toxic.
- They must not be reactive with the product.
- They must not impart to the product tastes or odours.

Foil, paper or plastic pouches:

The flexible pouch is a packaging concept capable of providing not only a package that is temper-resistance, but also by the proper selection of material, a package with a high degree of environmental protection. A flexible pouch is usually formed during the product filling operation by either vertical or horizontal forming, filling, or sealing equipment. The pouches can be single pouches or aluminium pouches.

Single pouch and Aluminium pouch:

Soluble film drug delivery pouch is a peelable pouch for “quick dissolve” soluble films with high barrier properties. The pouch is transparent for product display. Using a 2-structure combination allows for one side to be clear and the other to use a cost-effective foil lamination. The foil lamination has essentially zero transmission of both gas and moisture. The package provides a flexible thin film alternative for nutraceutical and pharmaceutical applications. The single dose pouch provides both product and dosage protection. Aluminium pouch is the most commonly used pouch.

Blister card with multiple units:

The blister container consists of two components: the blister, which is the formed cavity that holds the product, and the lid stock, which is the material that

seals to the blister. The blister package is formed by heat –softening a sheet of thermoplastic resin and vacuum-drawing the softened sheet of plastic into a contoured mold. After cooling the sheet is released from the mold and proceeds to the filling station of the packaging machine. The semi –rigid blister previously formed is filled with the product and lidded with the heat sealable backing material. The film selection should be based upon the degree of protection required. Generally, the lid stock is made of aluminium foil. The material used to form the cavity is typically a plastic, which can be designed to protect the dosage form from moisture.



Figure 4: Blister Card

Barrier Films:

Many drug preparations are extremely sensitive to moisture and therefore require high barrier films. Several materials may be used to provide moisture protection such as Polychloro trifluoro ethylene (PCTFE) film, Polypropylene. Polypropylene does not stress crack under any conditions. It is an excellent gas and vapour barrier. Lack of clarity is still a drawback.

Application of Fast Dissolving Films ^[59,60]

Oral mucosal delivery via buccal, sublingual, and mucosal route by use of FDFs could become a preferential delivery method for therapies in which rapid absorption is desired, including those used to manage pain, allergies, sleep difficulties, and central nervous system disorders. Dissolvable FDFs evolved over the past few years from the confection and oral care markets in the form of breath strips and became a novel and widely accepted form by consumers for delivering vitamins and personal care products.

Topical applications

The use of dissolvable films may be feasible in the delivery of active agents such as analgesics or antimicrobial ingredients for wound care and other applications.

Gastro retentive dosage systems

Dissolvable films are being considered in dosage forms for which water soluble and poorly soluble molecules of various molecular weights are contained in a film format. Dissolution of the films could be triggered by the pH or enzyme secretions of the gastrointestinal tract, and could potentially be used to treat gastrointestinal disorders.

Diagnostic devices

Dissolvable films may be loaded with sensitive reagents to allow controlled release when exposed to a biological fluid or to create isolation barriers for separating multiple reagents to enable a timed reaction within a diagnostic device.

CONCLUSION

Recently FDF has gained popularity as dosage form and is most acceptable and accurate oral dosage form which bypass the hepatic system and show moretherapeutic response. The pharmaceutical companies prefer this dosage form due to both patient compliance (especially paediatric and geriatric) as well as industrial acceptability of a liquid. Oral films can replace the over-the-counter drug, generic and brand name from market due to lower cost and consumer preference. This technology is a good tool for product life cycle management for increasing the patient life of existing products. FDOFs are also having great potential of delivering the medicinal agent systemically as well locally and have several advantages over many dosage forms even over the fast-disintegrating tablets. This explain the extenstensive research actively going on this technology. So, this technology is growing in fast pace challenging most of the pharmaceutical companies to develop oral films for a wide range of active pharmaceutical ingredients.

REFERENCES

- [1] Puja chaurasiya, Rajesh Kharel, R Manasa, Deepa V, Rajashekhar, K.A Shridhar. A review on oral fast dissolving films A Novel Drug Delivery System. Asian Journal of Research Chemistry and Pharmaceutical science 4(6), 1601-175.
- [2] Mahalingam k Mohad Nazish. Fast dissolving sublingual film- A review. Indian Journal of Novel Drug Delivery 8(2), Apr-June, 2016, 54-61.
- [3] Mary Elizabeth RN, Martelli BS. Sublingual and buccal medication administration. Encyclopedia of Nursing and Allied Health, 20050229
- [4] Lea L. Sublingual Administration. Colon Health 1996; 13.

- [5] Harris, D. and J.R. Robinson, 1992. Drug delivery via the mucous membranes of the oral cavity. *J. Pharmaceutical Sci.*, 81: 1-10.
- [6] Chauhan NS, Tomar A, Sharma K, Mittal A, Bajaj U. Formulation and evaluation of fast dissolving oral film of dicyclomine as potential route of buccal delivery. *Int. J. Drug Dev. Res.*, 2012; 4(2):408-417.
- [7] Frey P. Films strips and pharmaceuticals, pharm mf. & package. Sourcer, winter; 2006. P. 92-93.
- [8] Shojaei, A.H., 1998. Buccal Mucosa as A Route for Systemic Drug Delivery: A Review. *J. Pharmacy and Pharmaceutical Sci.*, 1(1): 15-30.
- [9] Oral, quickly disintegrating film, which cannot spit out, for an antiemetic or an anti migraine agent. Petra O, Thomas K, Kai-Thomas K, Karin K. US2008/0213343 A1, 2008.
- [10] Choudhary DR, Patel V, Patel H, Kundawala. Exploration of film forming properties of film formers used in the formulation of rapid dissolving films. *Int J Chem tech Res*, 2011; 3(2):531-3.
- [11] Priya YD, Chowdary YA, Murthy, Murthy TEGK, Seshagiri B. Approaches for taste masking of bitter drugs. *J Adv Drug Res*, 2011; 1(2):58-67.
- [12] Kunte S, Tandale P. Fast dissolving strip: a novel approach for delivery of Verapamil. *J Pharm Bioall Sci.*, 2010; 2(4):325-8.
- [13] Sloboda M, Bharnatt S. Formulation flexibility broadens the scope for oral thin film technology. *Adhesive Res*, 2011; 22-4.
- [14] Reema P, Richard GZ. Dissolvable film. US 2007/0042023 A1 2007:1-8.
- [15] Bhyan B, Jangra S, Kaur M, Singh H. Orally fast dissolving film: Innovation in formulation and technology. *Int. J. Pharm. Sci. Rev. Res.*, 2011; 9(2):50-57.
- [16] Bala R, Pravin Pawar, Sushil Khanna, Sandeep Arora. Orally dissolving strip: A new approach to oral drug delivery system. *Int. J. Pharm. Invest*, 2013; 3(2); 67-76.
- [17] Kulkarni AS, Deokule HA. Exploration of different polymers for use in the formulation of oral fast dissolving strips. *J. Current Pharm. Res.*, 2010; 2(1):33-35.
- [18] Heer D, Aggarwal G, Kumar SLH. Recent trends of fast dissolving drug delivery system- An overview of formulation technology. *Pharmacophore*, 2013; 4(1): 1-9.
- [19] Mahajan A, Chhabra N, Aggarwal G. Formulation and Characterization of Fast Dissolving Buccal Films: A Review. *Der Pharm Lett.*, 2011; 3(1): 152165. 29.
- [20] Controlled Drug Delivery Concepts and Advances. Vyas SP, Khar RK. New Delhi: Vallabh Prakashan; 2002; 1: 157-160
- [21] Gandhi SD, Pandya PR, Umbarkar R, Tambawala T, Shah MA. Mucoadhesive drug delivery systems an unusual maneuver for site-specific drug delivery system.. *Pharm Sci Monit an Int J Pharm Sci.*, 2011; 2(3): 132-52.
- [22] Theory and Practice of Contemporary Pharmaceutics. Ghosh TK, Jasti BR, editors. CRC Press, 2005; 282-367: 150-155.
- [23] Choudhary DR, Patel VA, Chhalotiya UK, Patel HV, Kundawala AJ. Development and characterization of pharmacokinetic parameters of fast-dissolving films containing levocetirizine. *Sci. Pharm*, 2012; 80: 779-787.
- [24] Heer D, Aggarwal G, Kumar SLH. Recent trends of fast dissolving drug delivery system- An overview of formulation technology. *Pharmacophore*, 2013; 4(1): 1-9. 28
- [25] Mitchell and M.D. Read, 2005. *Pharmaceutical Technology*, pp: 1-6.
- [26] Arya A, Chandra A, Sharma V, Pathak K. Fast dissolving oral films: An innovative drug delivery system and dosage form. *Int. J. Chem Tech. Res.*, 2010; 2(1): 576-583
- [27] Muhammad Irfan, Sumeira Rabel, Quratulain Bukhtar, Muhammad Imran Qadir, Farhat Jabeen, Ahmed Khan. Orally disintegrating films: A modern expansion in drug delivery system. *Saudi Pharmaceutical Journal*, 2016; 24: 537-546.
- [28] Chauhan I, Yasir M, Nagar P. Insights into polymers: film formers in mouth dissolving films. *Drug Invent. Today*, 2012; 3: 56-73.
- [29] Pein M, Breitkreutz, J. Development of a tastemasked orodispersible film containing dimenhydrinate. *Preis. Pharmaceutics*, 2012; 4: 551- 562.

- [30] Corniello C. Quick Dissolving Strip; from concept to commercialization. *Drug Development Technology*, 2006; 6: 68-71.
- [31] Kalyan S, Bansal M. Recent trends in the development of oral dissolving film. *Int. J. Pharm tech Res.*, 2012; 4: 725-733. 43.
- [32] Iruzo F and Cupone EI: Diclofenac fast dissolving film: suppression of bitterness by a taste-sensing system. *Drug Dev. Ind. Pharmacy*, 2010; 1-8.
- [33] Gavaskar Basani, Kumar Subhash Vijaya, guru Sharan: Overview on fast dissolving films, *Int Jr of Pharmacy and Pharmaceutical Sciences* 2009; 2: 29-33.
- [34] Interactions in cellulose derivative films for oral drug delivery. Sakellariou, P.; Rowe, R.C. *Prog. Polym. Sci.*, 1995, 20, 889-942.
- [35] 41. Fast Dissolving Oral Films: A Review Naga Sowjanya Juluru *International Journal Of Advances In Pharmacy, Biology And Chemistry Vol. 2(1), Jan- Mar 2013.*
- [36] Handbook of Pharmaceutical Excipients. Wale. A and Weller. P J., 2nd edition, 1994, 24, 27, 352,448.
- [37] Film coating theory and practice. Banker, G.S. *J. Pharm. Sci.*, 1966, 55, 81-89.
- [38] The effect of polymer molecular weight on the incidence of film cracking and splitting on film-coated tablets. Rowe, F.C.; Forse, S.F. *J. Pharm. Pharmacol.*, 1980, 32(8), 583-584.
- [39] The effect of plasticizer type and concentration on the incidence of bridging of intagliations on film-coated tablets. Rowe, R.C.; Forse, S.F. *J. Pharm. Pharmacol.*, 1981, 33(3), 174-175.
- [40] Effect of inert tablet ingredients on drug absorption I. Effect of polyethylene glycol 4000 on the intestinal absorption of four barbiturates. Singh, P.; Guillory, J.K.; Sokoloski, T.D; Benet, L.Z.; Bhatia, V.N. *J. Pharm. Sci.*, 1966, 55(1), 6-68
- [41] Formation of films from polymer dispersions. Brown, G.L. *J. Polym. Sci.*, 1956, 22 (102), 423-434. 40. Orally dissolving film strips (ODFS): the final evolution of Orally dissolving dosage forms. Hariharan, M.; Bogue, A. *Drug Del. Technol.*, 2009, 9(2), 24.29.
- [42] Muhammad Irfan, Ahmad Khan Orally Disintegrating Films: A modern expansion in drug delivery system. *Saudi Ph Jr volume 24, Issue 5, Sept 2016: 537-546.*
- [43] Shimoda H and Taniguchi K: Preparation of fast dissolving oral thin film containing dexamethasone: A possible application to antiemesis during cancer chemotherapy. *European Journal of Pharmaceutics and Biopharmaceutics*, 2009; 73: 361-365.
- [44] Development of ebiana, a natural, non-caloric sweetener, Prakash.G.E, DuBois.J.F, Clos.K.L, Wilkens and Fosdick. L.E., *Food Chem. Toxicol.* 2008, 46, S75-S82. 45
- [45] Nishimura M, Matsuura K, Sukioka T, Yamashita H, Inagaki N, Sugiyama T and Itoh Y: In-vitro and in-vivo characteristics of prochlorperazine oral disintegrating film. *International Journal of Pharmaceutical Sciences*, 2009; 98-102.
- [46] Gohel MC and Sharma R: Development of taste masked film of valdecoxib for oral use. *Indian Journal of Pharmaceutical Sciences*, 2010; 320-323.
- [47] Madgulkar A, Khar RK, Harindran J, Mujumdar DK, Nagarsenker MS. Dosage form design *Pharmaceutical and Formulation Consideration In: Allen LV, Popovich NG, Ansel HC, editors. Ansel's Pharmaceutical Dosage forms and Drug Delivery Systems: South Asian Edition 9th Ed Wolters Kluwer (India) Pvt Ltd, New Delhi, 2011; 134-136.*
- [48] Siddiqui N, Garg G, Sharma P. A Short Review on "A Novel Approach in Oral Fast Dissolving Drug Delivery System and Their Patents. *Advances in Biological Research*, 2011; 5(6): 291-303.
- [49] Dixit RP, Puthli SP, Oral strip technology: Overview and future potential. *Journal of Controlled Release*, 2009; 139: 94-107.
- [50] Iruzo F and Cupone EI: Fast dissolving films made of maltodextrins. *European Journal of Pharmaceutics and Biopharmaceutics*, 2008; 70: 895-900
- [51] Vishwakarma DK, Tripathi AK, Yogesh P and Maddheshiya B: Review article on mouth dissolving film. *Journal of Global Pharma Technology*, 2011; 3(1): 1-8.
- [52] Rathi V, Senthil V, Kammili L and Hans R: A brief review on oral film technology. *International Journal of Research in Ayurveda and Pharmacy*, 2011; 2(4): 1138-1147.

- [53] Deepak Sharma, Diljit Kaur, Shivani Verma, Davindar Singh, Mandeep Singh, Gurmeet Singh, Rajeev Garg Fast Dissolving Oral Films Technology: A Recent Trend For An Innovative Oral Drug Delivery System, Int Jr of Drug Delivery 7 (2015) 60-75.
- [54] Siddiqui N, Garg G, Sharma P. A Short Review on "A Novel Approach in Oral Fast Dissolving Drug Delivery System and Their Patents. Advances in Biological Research, 2011; 5(6): 291-303.
- [55] Bharthi P, Gopalrao M, Akila R. Characterization and Applications of Pullulan and Chitosan produced by fermentation. J Microbio Biotech Res. Pvt. Ltd., 5(2): 21-27.
- [56] Subhash Vijaya Kumar, Basanti Gavaskar, Guru Sharan, Madhusudhan Rao Y, Overview on Fast Dissolving Films. International Journal of Pharmacy and Pharmaceutical Sciences, 2010; 2(3): 29-33.
- [57] Patel Nibha K, Pancholi SS, An Overview on Sublingual Route for Systemic Drug Delivery. International Journal of Research in Pharmaceutical and Biomedical Sciences, 2012; 3(2): 913-23.
- [58] Aggarwal Jyoti. Singh Gurpreet. Saini Seema. Rana AC, Fast Dissolving Films: A Novel Approach to Oral Drug Delivery. International Research Journal of Pharmacy, 2011; 2(12): 69-74.
- [59] Vishwkarma DK, Tripathi AK, Yogesh P and Maddheshiya B, Review Article on Mouth Dissolving Film. Journal of Global Pharma Technology, 2011; 3(1): 1-8.
- [60] Patel AR, Prajapati DS and Raval JA: Fast dissolving films (FDFS) as a newer venture in fast dissolving dosage forms. International Journal of Drug Development and Research, 2010.



A Review on: Fast Dissolving Oral Film

Mr. Vijay P. Ingle, Prof. Sharad D. Tayade, Dr. Shirish P. Jain

Rajarshi Shahu College of Pharmacy, Buldana, Maharashtra, India

ABSTRACT

Recently, fast dissolving oral films have started gaining fame and acceptance as new drug delivery systems, which aim to enhance safety and efficacy of a drug molecule to achieve better patient compliance. It is a robust form a drug delivery system where the film is placed on the top or the floor of the tongue. When put on the tongue, this film dissolves instantaneously, releasing the drug which dissolves in the saliva. Buccal drug delivery has lately become an important route of drug administration. But many of the patients (paediatrics and geriatrics) are unwilling to take solid preparations due to fear of choking. This has made the pharmaceutical industry look for alternatives routes of drug delivery like film drug delivery. Fast dissolving oral drug delivery system have started gaining popularity and acceptance as new drug delivery system, because they are easy to administer, better patient compliance, rapid drug absorption, and sudden onset of drug action with instant bioavailability is possible. This review reflects information regarding formulation ingredient, technologies and evaluation test employed in the preparation of fast dissolving oral films.

KEYWORDS: *Fast dissolving oral films, buccal drug delivery, paediatric patients, geriatrics patients*

INTRODUCTION

Among the different routes, the most agreeable routes, for the patient is oral route. Most of the pharmaceutical companies have directed their research activity in developing viable dosage alternatives from oral route for paediatrics, geriatrics, noncompliant or nauseous patients. Almost 90% of the drugs are administered to the body via oral route for the treatment of various disorders and diseases as it is regarded as the safest, most economical method of drug delivery and have the highest patient compliance. The drug is either dissolved or swallowed, which then enters into the systemic circulation to produce the desired effect. Fast dissolving oral film, a novel drug delivery system for the oral delivery of the drug is an ultrathin film prepared using hydrophilic polymers that rapidly dissolves on the top or floor of the tongue or buccal cavity. It is an ultrathin strip (50-150 microns thick) of postage stamp size with an active agent and other excipient developed on the basis on transdermal patch technology. These fast-dissolving oral films have persistent to extend in sales and launched and patient compliance and convenient products effectively addressing issues for pharmaceuticals as well as

nutraceuticals that have been traditionally administered as oral solid dosages.

Today, fast oral films are a well proven and world-wide accepted technology for the systemic delivery of active pharmaceutical ingredients (APIs)^[1,2]. To overcome this oral fast disintegrating drug delivery system were developed, these systems were initially developed within the late seventies as an alternative to tablets, capsules and syrups for paediatric and geriatric patients who experience difficulties in swallowing traditional oral solid dosage forms. These dosage forms either dissolve or disintegrate generally within a 3 minute in mouth, without need of water. Oral fast disintegrating dosage form have started gaining popularity and acceptance as new drug delivery system due to better patient compliance^[3] Technology Catalysts forecasts the market for drug products in oral thin film formulations to be valued at \$500 million in 2007 and could reach \$2 billion in near future^[4,5,6]. However only a few products consisting bitter molecules have been able to be commercialized because of the complexity associated with the ODT. A large number of drugs can be formulated as mouth dissolving films.

How to cite this paper: Mr. Vijay P. Ingle | Prof. Sharad D. Tayade | Dr. Shirish P. Jain "A Review on: Fast Dissolving Oral Film" Published in International Journal of Trend in Scientific Research and Development (ijtsrd), ISSN: 2456-6470, Volume-5 | Issue-5, August 2021, pp.300-310, URL: www.ijtsrd.com/papers/ijtsrd43836.pdf



Copyright © 2021 by author (s) and International Journal of Trend in Scientific Research and Development Journal. This is an Open Access article distributed under the terms of the Creative Commons Attribution License (CC BY 4.0) (<http://creativecommons.org/licenses/by/4.0>)



Innovative products may increase the therapeutic possibilities in the following indications^[7,8].

- Pediatrics (Antitussives, Expectorants, Antiasthmatics)
- Geriatrics (Antiepileptic, Expectorants)
- Gastrointestinal diseases
- Nausea (due to Cytostatic therapy)
- CNS (Antiparkinsonism therapy)

Fast dissolving drug delivery system (FDDS)

Fast dissolving drug delivery system is a new generation delivery system also known as fast dissolving/disintegrating film for the oral delivery of the drug which came into existence in the late 1970s as an alternative to tablets, capsules, syrups and other formulation for paediatric and geriatric patients who experience difficulties in swallowing traditional solid dosage forms which combines both the advantages of conventional tablet and of liquid formulation^[4] FDDS is easy to administer and provides better patient compliance in the elderly, paediatric, mentally retarded, nauseated and uncooperative patients^[9] This delivery system consists of the solid dosage form that dissolve quickly i.e. within a matter of seconds in the oral cavity without the administration of water. The delivery system consists of a very thin oral strip which is simply placed on the patients tongue or any other oral mucosal tissue and instantly gets wetted by saliva^[10] The film rapidly hydrates onto the site of application. It then rapidly dissolves and disintegrates to release the medication for oro-mucosal absorption. The robustness of the film depends upon the type and amount of polymer used and general dissolution time for orally dissolving film is 5-20 min as per pharmacopoeia.^[11,12] They also provide quick onset of action within few seconds as the oro-mucosal absorption of the drug occurs directly from the site of administration to the systemic circulation avoiding the first-pass metabolism to produce the desired effect.^[13]

Special features of oral thin films^[14,15]

- Thin elegant
- Available in various sizes and shapes
- Un-obstructive
- Excellent mucoadhesion.
- Fast disintegration and rapid release.

Ideal properties of fast dissolving films^[16,17,18]

- It should be compatible with the other ingredients.
- The therapeutic dose of the drug should not be greater than 40mg.
- It should be less friable and have good mechanical strength to withstand the post manufacturing handling.
- It should quickly dissolve to release drug instantaneously in mouth.
- It should have an acceptable taste with pleasing mouth feel.

Anatomy of oral cavity

The structure and anatomy of oral cavity is studied for understanding the environment provided for delivering drugs [Fig. 1]. The oral mucosa allows direct access of drug to the systemic circulation and avoids first pass metabolism. The epithelium of the oral cavity is quite similar to that of the skin, with slight differences with regard to keratinization, protective and lubricant mucous which is spread across its surface.^[19] The permeability of oral mucosa is 4–1000 times greater than that of the skin. The oral cavity is divided into two regions: outer being the oral vestibule bounded by the lips and cheeks; the hard and soft palates, the floor of the mouth and tonsils.^[20] Oral drug delivery has been known for decades as the most widely utilized route of administration among all the routes that have been explored for the systemic delivery of drugs via various pharmaceutical products of different dosageforms.^[21]

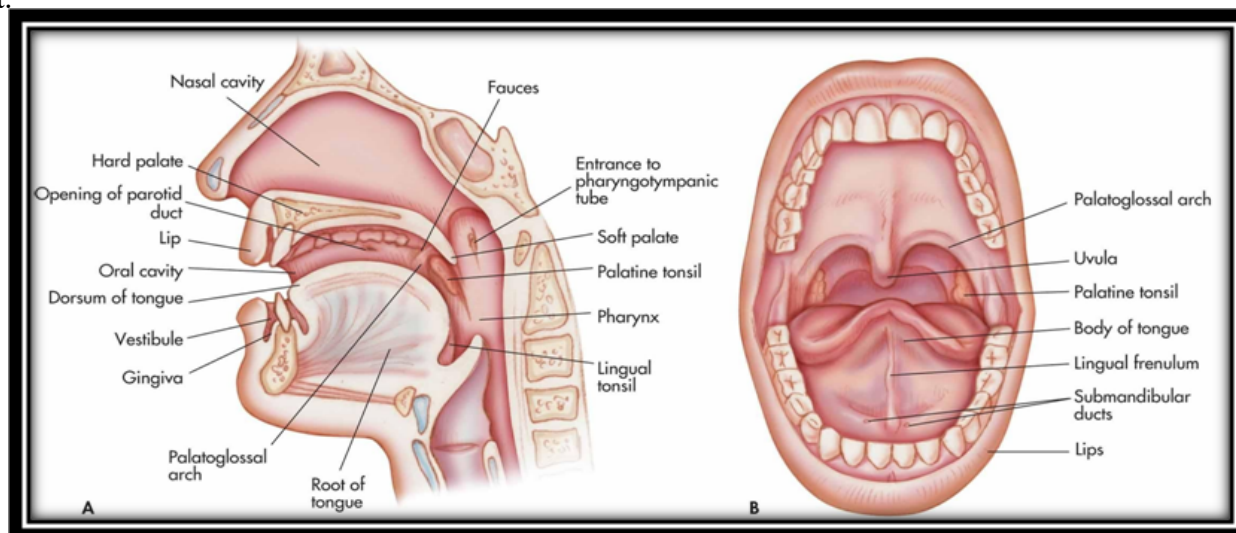


Figure 1: Anatomy of the oral cavity

Advantages of fast dissolving films^[22]

- Taste masking
- Enhanced stability
- Improve bioavailability for certain therapeutic ingredient.
- Rapid onset of action.
- No risk of choking.
- Convenient dosing or accurate dosing.
- No need of water to swallow or chewed.
- Pleasant mouth feel, leave negligible or no residue in the mouth after administration.
- Beneficial in cases such as motion sickness, acute pain, sudden allergic attack, asthmatic attack and coughing, where an ultra-rapid onset of action is required.
- Stability for longer duration of time, since the drug remains in solid dosage form till it is consumed.
- Flexible and portable in nature so they provide ease in handling, transportation and storage.

Disadvantages of fast dissolving films^[23]

- Drugs which are unstable at buccal pH cannot be administered.
- Drugs which irritate the mucosa cannot be administered by this route.
- A drug with small dose requirement can only be administered.
- Taste masking- Most drugs have the bitter taste, and need taste masking.
- It also shows the fragile, granule property.
- It is hygroscopic in nature so it must be kept in dry places.

Table 1: Comparison between Fast Dissolving Oral films and Dissolving Tablets^[24,25]

The comparison between Fast Dissolving Oral Films and Fast Dissolving Tablets was given table 1.

Sr. no	Fast Dissolving Oral Film	Fast Dissolving Tablet
1.	Large surface area gives greater dissolution.	Less surface area gives lesser dissolution than FDOF.
2.	Patient compliance is more.	Patient compliance is less than FDOF.
3.	Fast dissolving films are of thickness 0.015-.05 inches.	Fast dissolving tablets is of the same size of a conventional tablet.
4.	Only low dose can be incorporated in the formulation.	High dose can also be incorporated in the formulation.

Formulation Components of FDOFs**Active pharmaceutical ingredient**^[26]

A film composition contains 1-30% w/w of the active pharmaceutical ingredient. Always use low dose active pharmaceutical ingredients because high dose of drug is difficult to incorporate in fast dissolving film. A number of drugs can be used as fast dissolving film including anti-histamine, anti-diarrheal, anti-depressants, vasodilators, anti-asthmatic, anti-emetic, etc.^[23] Dimenhydrinate can also be incorporated into ODFs for taste masking. Common examples of drugs incorporated into ODFs are salbutamol sulfate, rizatriptan benzoate, verapamil, ondansetron, dexamethasone, rofecoxib, cetirizine, pilocarpine, tianeptine sodium, indomethacin, etc. are mentioned in edin.^[27]

Film forming polymer^[28,29]

Polymer are the most important ingredient of the fast-dissolving oral film. Generally, 45% w/w of polymer is used which is based on total weight of dry film. The selection of polymer is one of the most important and critical parameters for the successful development of oral films because of their tensile strength which depends upon the type and amount of polymer used. Mainly hydrophilic polymers are used in the oral strips as they rapidly disintegrate in the oral cavity as they come in contact with saliva. Currently, both natural and synthetic polymers are used for the preparation of fast dissolving film.

Table 2: List of polymers used in oral thin films ^[30]

Group	Class	Example
Natural	Carbohydrate	Pullulan, pectin, sodium alginate, maltodextrin, sodium starch glycolate.
	Proteins	Gelatine
	Resin	Polymerized rosin. (novel film former)
Synthetic	Cellulose Derivatives	Hydroxypropyl methylcellulose (E3, E5, E15, K3, K15, K50), Methylcellulose. (A3, A6, A15), Carboxy methylcellulose secekol-30, Sodium carboxymethyl cellulose. Microcrystalline cellulose.
	Vinyl polymer	Poly vinyl pyrrolidone (K-90, K-30), Poly vinyl alcohol, Poly ethylene oxide.
	Acrylic polymer	Eudragit (RD-100, 9,10, 11, 12 and RL- 100)

Ideal Properties of The Film Forming Polymers.

^[31,32]

1. The polymer employed should be non-toxic, non-irritant and devoid of any leachable impurities.
2. It would be ideal to have a polymer that would have local enzyme inhibition action.
3. It should have good wetting and spread ability property.
4. The polymer should exhibit sufficient peel, shear and tensile strengths.
5. The polymer should be cheap and readily available.
6. It should not cause any secondary infections in the oral mucosa/ dental region.
7. It should have a good mouth feel property.
8. It should be tasteless.
9. It should have long shelf life.

Plasticizers (0-20%)

Plasticizer helps to improve the flexibility and reduces the brittleness of the strip by reducing the glass transition temperature of the polymer. The selection of plasticizer depends on its compatibility with the polymer and the type of solvent used in the formulation ^[33,34]. Commonly used plasticizers are glycerol, propylene glycol, low molecular weight polyethylene glycols (PEGs), phthalate derivatives like dimethyl, diethyl, and dibutyl phthalate, citrate derivatives such as tributyl, triethyl, acetyl citrate, triacetin and castor oil. The plasticizers concentration of 0–20 % w/w of dry polymer weight is used by avoiding the film cracking, splitting and peeling of the strip ^[35,36]. The use of certain plasticizers may also affect the absorption rate of the drug ^[37]. The properties of plasticizer are important to decrease the glass transition temperature of the polymer in the range of 40–60°C for a nonaqueous solvent system and below 75 °C for aqueous systems ^[38]. Cellulosic hydrophilic polymers were easily plasticized with hydroxyl-containing plasticizers like PEG, propylene

glycol, glycerol, and polyols. In contrast, less hydrophilic cellulosic polymers were plasticized with esters of citric acid and phthalic acid ^[39]. Glycerol acts as a better plasticizer for polyvinyl alcohol while diethylene glycol can be used for both Hypromellose as well as polyvinyl alcohol films.

Surfactants

^[40,41]

Surfactants are used as wetting or solubilising or dispersing agent so that the film is getting dissolved within seconds and release active agent immediately. Commonly employed are poloxamer 407, benzalkonium chloride, etc. Out of these most predominantly used surfactant is poloxamer 407.

Sweetening agents

^[42,43,44]

Sucrose is the most commonly used sweeteners in FDOFs. Sucrose is very soluble in water and being colourless does not impart any undesirable colour to the final formulation. Some of the commonly employed sweeteners are dextrose, sucrose, fructose, glucose, isomaltose, etc. Artificial sweeteners like saccharine, cyclamate, aspartame (first generation), sucralose, alitame and neotame (second generation) can also be used. The sweetness of fructose is perceived rapidly in the mouth as compared to sucrose and dextrose. Fructose is sweeter than sorbitol and mannitol and thus used widely as a sweetener. Low molecular weight carbohydrates and specially sucrose are most commonly used sweeteners. Sucrose is very soluble in water and being colourless does not impart any undesirable colour to the final formulation. It is stable over the pH range 4–8. It masks the taste of both salty and bitter drugs. Polyhydric alcohols such as sorbitol, mannitol, and malt can be used in combination as they additionally provide good mouth-feel and cooling sensation. Polyhydric alcohols are less carcinogenic and do not have bitter after taste which is a vital aspect in formulating oral preparations. The artificial sweeteners have gained more popularity in pharmaceutical preparations. Saccharin, cyclamate

and aspartame are the first generation of the artificial sweeteners followed by acesulfame-K, sucralose, alitame and neotame which fall under the second-generation artificial sweeteners. Acesulfame-K and sucralose have more than 200- and 600-time sweetness. Neotame and alitame have more than 2000- and 8000-time sweetening power as compared to sucrose. Rebiana which is an herbal sweetener, derived from plant *Stevia rebaudiana* (South American plant) has more than 200 -300-time sweetness.

Saliva stimulating agents^[45]

Saliva stimulating agents are used to increase the rate of production of saliva that would help in the faster disintegration of the rapid dissolving strip formulations. Examples of salivary stimulants are citric acid, malic acid, lactic acid, ascorbic acid and tartaric acid. Among these the most preferred one is citric acid. These agents are used alone or in combination between 2 to 6% w/w of weight of the film.

Flavouring agents^[46]

Flavours used in the formulation must be non-toxic, soluble, stable and compatible with the excipients. The quantity of flavouring agent required to mask the taste depends on the flavour type and its strength. Commonly employed are fruity flavours (vanilla, cocoa, chocolate, citrus), flavour oils (peppermint oil, cinnamon oil, oil of nutmeg). Flavours can also be chosen from oleo resins, synthetic flavour oils and extract derived from various parts of the plants like fruits, flowers etc. The amount of flavour needed to mask the taste depends on the flavour type and its strength.

Colouring agents

Generally incorporated colouring agents are FD&C colours, natural colours, pigments such as titanium dioxide, etc. The colouring agents should not exceed concentration levels of 1% w/w.^[47,48] Some saliva stimulating agents may also be added to enhance the disintegration and to get rapid release. Some of these agents are citric acid, tartaric acid, malic acid, ascorbic acid and succinic acid.

Manufacturing methods

To manufacture fast dissolving oral films, following methods are generally employed:

- A. Semisolid casting
- B. Rolling
- C. Solvent casting
- D. Hot melt extrusion
- E. Solid dispersion extrusion

A. Semisolid casting^[49]

In this method at first a solution of water-soluble film forming polymer is prepared. Then the resulting solution is added to a solution of acid insoluble polymer (e.g., cellulose acetate phthalate) which was prepared in ammonium or sodium hydroxide. The ratio of the acid insoluble polymer to film forming polymer should be 1:4. A gel mass is obtained on addition of suitable amount of plasticizer. By the means of heat-controlled drums, finally the gel mass is casted in to the films or ribbons.

B. Rolling method^[50]

In this method the film is prepared by preparation of a pre-mix, addition of an active and subsequent formation of a film. Prepare pre-mix with film forming polymer, polar solvent and other additives except a drug. Add pre mix to master batch feed tank. Fed it via a 1st metering pump and control valve to either or both of the 1st and 2nd mixer. Add required amount of drug to the desired mixer. Blend the drug with master batch pre mix to give a uniform matrix. Then a specific amount of uniform matrix is then fed to the pan through 2nd metering pumps. The film is finally formed on the substrate and carried away via the support roller. The wet film is then dried using controlled bottom drying.

C. Solvent casting^[51,52,53]

In this method water soluble polymers are dissolved in water and the drug along with other ingredients is dissolved in suitable solvent. Then both the solutions are mixed, stirred, finally casted into the petri plate and dried.

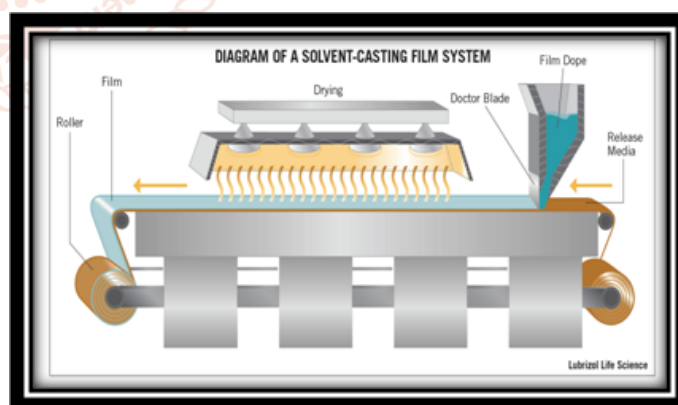


Figure 2: Solvent Casting.

Advantages:

- Better uniformity of thickness and better clarity than extrusion.
- Film has fine gloss and freedom from defects such as die lines.
- Film has more flexibility and better physical properties.
- Finished film thickness is 12-100um

Disadvantages:

- The polymer must be soluble in a volatile solvent or water.
- A stable solution with a reasonable minimum solid content and viscosity should be formed.
- Formation of homogeneous film and release from the casting support must be possible.

D. Hot melt extrusion ^[54]

The processing temperature should be 80°C in 1st zone, 115°C in 2nd zone, 100°C in 3rd zone and 65°C in

4th zone. The screw speed should set at 15 rpm to set the granule inside the extruder for approximately 3-4 min. Drug and polymer are blended in sigma blade mixer 10 min. Plasticizer is added slowly. Granulation of mixture in the presence of anti-sticking agent. Granules are store overnight and sieved through 250um sieve. Dried granules are fed into the extruder. Processing is done for 3-4 min. At temperature as mentioned above. Extrudate is pressed at temperature at 65°C to obtain a film of thickness 200um.

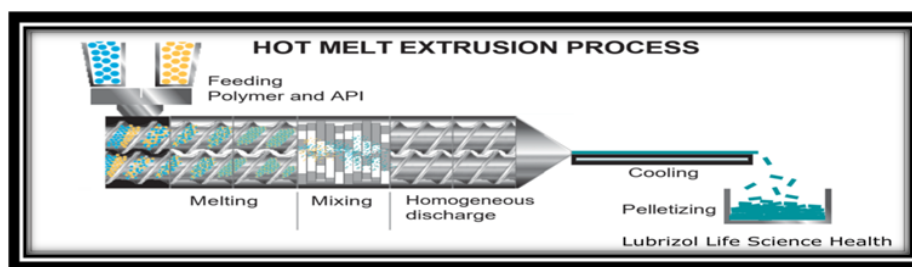


Figure 3: Holt melt extrusion

Advantages:

- Without the use of any solvent or water.
- Fewer processing steps.
- Compressibility properties of the API may not be of importance.
- A better alternative for poorly soluble drugs.
- Have stability at varying pH and moisture levels.
- Better content uniformity.
- Improved bioavailability of poorly soluble compounds.

Disadvantages:

- Thermal degradation due to use of high temperature.
- Flow properties of the polymer are essential to processing.
- A limited number of available polymers.
- All excipients must be devoid of water or any other volatile solvent.
- Required high power input

E. Solid dispersion extrusion

The term solid dispersion refers to the dispersion of one or more active ingredients in an inert carrier in a solid state in the presence of amorphous hydrophilic polymers. Drug is dissolved in suitable liquid solvent. Then solution is incorporated into the melt of polyethylene glycol, obtainable below 70°C finally the solid dispersion is shaped into the films by means of dies.

CHARACTERIZATION OF DISSOLVING FILMS ^[55,56,57]

Morphology study

The morphology of the film is studied using Scanning Electron Microscopy (SEM), at a definite magnification.

Thickness

It can be measured by micrometre screw gauge at different locations. It is crucial to determine uniformity in the thickness of the film as this is directly related to the accuracy of dose in the strip.

Organoleptic evaluation

For this purpose, in vitro methods of utilizing taste sensors and specially designed apparatus are being used. These invitro taste assessment apparatus for high throughput taste screening of oral pharmaceutical formulations.

Mechanical properties

Three mechanical properties namely tear resistance, elastic modulus and tensile strength percentage elongation are ca

Tear resistance

Principally very low rate of loading 51mm is employed and is designed to measure the force to initiate tearing. The maximum stress or force (that is generally found near the onset of tearing) necessary to tear the specimen is noted as the tear resistance value in newtons (or pounds-force).

Elastic modulus

It is calculated by formula

Elastic modulus = force at corresponding strain × 1 / cross sectional area of corresponding strain

Tensile strength

Tensile strength is the maximum stress applied to a point at which the strip specimen breaks. It is calculated by formula.

Tensile strength = Load at failure × 100/film thickness × film width

Folding endurance

Folding endurance is determined by repeated folding of the strip at the same place till the strip breaks. The number of times the film is folded without breaking is computed as the folding endurance value.

Percentage elongation

It is calculated by formula

% Elongation = Increase in length of strip x100 / initial length of strip

Swelling property

Each film sample is weighed and placed in a preweighed stainless steel wire mesh. Then the mesh containing sample is submerged into 15ml medium (simulated saliva solution) in a plastic container. Increase in the weight of the film was determined at preset time interval until a constant weight was observed.

Degree of swelling = $\frac{W_t - W_o}{W_o}$

Where,

W_t is weight of film at time t, and W_o is weight of film at time zero.

Weight variation

Weight variation is studied by individually weighing 10 randomly selected films and by calculating the average weight.

Disintegration time

Disintegration of orally fast dissolving films requires US disintegration apparatus. The disintegration time limit of 30 seconds or less for orally disintegrating tablet described in Centre for Drug Evaluation and Research (CDER) guidance can be applied to fast dissolving oral strips. Disintegration time will vary depending on the formulation but typically the disintegration ranges from 5 to 30 secs. Although, no official guidance for oral fast disintegrating films strip.

Dissolution test

Dissolution testing can be performed using the standard basket or paddle apparatus described in any of the pharmacopoeia. The dissolution medium will essentially be selected as per the sink condition and highest dose of the API. Many times, the dissolution test can be difficult due to tendency of the strip to float onto the dissolution medium when the paddle apparatus is employed.

Stability studies

Stability studies have to be carried out at accelerated condition (65% relative humidity and 35°C temperature) in the humidity chamber.

Packaging of Fast Dissolving Film.^[58]

In the pharmaceutical industry it is vital that the package selected adequately preserve the integrity of the product. Expensive packaging, specific processing, and special care are required during manufacturing and storage to protect the dosage of other fast dissolving dosage forms. A variety of packaging options are available for fast dissolving films. Single packaging is mandatory for films, which are pharmaceutical products; an aluminium pouch is the most commonly used packaging format. APR-Labtech has developed the Rapid card, a proprietary and patented packaging system, which is specially designed for the Rapid films. The rapid card has same size as a credit card and holds three rapid films on each side. Every dose can be taken out individually.

The material selected must have the following characteristics

- They must protect the preparation from environmental conditions.
- They must be FDA approved.
- They must meet applicable tamper-resistant requirement
- They must be non-toxic.
- They must not be reactive with the product.
- They must not impart to the product tastes or odours.

Foil, paper or plastic pouches:

The flexible pouch is a packaging concept capable of providing not only a package that is temper-resistance, but also by the proper selection of material, a package with a high degree of environmental protection. A flexible pouch is usually formed during the product filling operation by either vertical or horizontal forming, filling, or sealing equipment. The pouches can be single pouches or aluminium pouches.

Single pouch and Aluminium pouch:

Soluble film drug delivery pouch is a peelable pouch for “quick dissolve” soluble films with high barrier properties. The pouch is transparent for product display. Using a 2-structure combination allows for one side to be clear and the other to use a cost-effective foil lamination. The foil lamination has essentially zero transmission of both gas and moisture. The package provides a flexible thin film alternative for nutraceutical and pharmaceutical applications. The single dose pouch provides both product and dosage protection. Aluminium pouch is the most commonly used pouch.

Blister card with multiple units:

The blister container consists of two components: the blister, which is the formed cavity that holds the product, and the lid stock, which is the material that

seals to the blister. The blister package is formed by heat –softening a sheet of thermoplastic resin and vacuum-drawing the softened sheet of plastic into a contoured mold. After cooling the sheet is released from the mold and proceeds to the filling station of the packaging machine. The semi –rigid blister previously formed is filled with the product and lidded with the heat sealable backing material. The film selection should be based upon the degree of protection required. Generally, the lid stock is made of aluminium foil. The material used to form the cavity is typically a plastic, which can be designed to protect the dosage form from moisture.



Figure 4: Blister Card

Barrier Films:

Many drug preparations are extremely sensitive to moisture and therefore require high barrier films. Several materials may be used to provide moisture protection such as Polychloro trifluoro ethylene (PCTFE) film, Polypropylene. Polypropylene does not stress crack under any conditions. It is an excellent gas and vapour barrier. Lack of clarity is still a drawback.

Application of Fast Dissolving Films ^[59,60]

Oral mucosal delivery via buccal, sublingual, and mucosal route by use of FDFs could become a preferential delivery method for therapies in which rapid absorption is desired, including those used to manage pain, allergies, sleep difficulties, and central nervous system disorders. Dissolvable FDFs evolved over the past few years from the confection and oral care markets in the form of breath strips and became a novel and widely accepted form by consumers for delivering vitamins and personal care products.

Topical applications

The use of dissolvable films may be feasible in the delivery of active agents such as analgesics or antimicrobial ingredients for wound care and other applications.

Gastro retentive dosage systems

Dissolvable films are being considered in dosage forms for which water soluble and poorly soluble molecules of various molecular weights are contained in a film format. Dissolution of the films could be triggered by the pH or enzyme secretions of the gastrointestinal tract, and could potentially be used to treat gastrointestinal disorders.

Diagnostic devices

Dissolvable films may be loaded with sensitive reagents to allow controlled release when exposed to a biological fluid or to create isolation barriers for separating multiple reagents to enable a timed reaction within a diagnostic device.

CONCLUSION

Recently FDF has gained popularity as dosage form and is most acceptable and accurate oral dosage form which bypass the hepatic system and show moretherapeutic response. The pharmaceutical companies prefer this dosage form due to both patient compliance (especially paediatric and geriatric) as well as industrial acceptability of a liquid. Oral films can replace the over-the-counter drug, generic and brand name from market due to lower cost and consumer preference. This technology is a good tool for product life cycle management for increasing the patient life of existing products. FDOFs are also having great potential of delivering the medicinal agent systemically as well locally and have several advantages over many dosage forms even over the fast-disintegrating tablets. This explain the extensive research actively going on this technology. So, this technology is growing in fast pace challenging most of the pharmaceutical companies to develop oral films for a wide range of active pharmaceutical ingredients.

REFERENCES

- [1] Puja chaurasiya, Rajesh Kharel, R Manasa, Deepa V, Rajashekhar, K.A Shridhar. A review on oral fast dissolving films A Novel Drug Delivery System. Asian Journal of Research Chemistry and Pharmaceutical science 4(6), 1601-175.
- [2] Mahalingam k Mohad Nazish. Fast dissolving sublingual film- A review. Indian Journal of Novel Drug Delivery 8(2), Apr-June, 2016, 54-61.
- [3] Mary Elizabeth RN, Martelli BS. Sublingual and buccal medication administration. Encyclopedia of Nursing and Allied Health, 20050229
- [4] Lea L. Sublingual Administration. Colon Health 1996; 13.

- [5] Harris, D. and J.R. Robinson, 1992. Drug delivery via the mucous membranes of the oral cavity. *J. Pharmaceutical Sci.*, 81: 1-10.
- [6] Chauhan NS, Tomar A, Sharma K, Mittal A, Bajaj U. Formulation and evaluation of fast dissolving oral film of dicyclomine as potential route of buccal delivery. *Int. J. Drug Dev. Res.*, 2012; 4(2):408-417.
- [7] Frey P. Films strips and pharmaceuticals, pharm mf. & package. Sourcer, winter; 2006. P. 92-93.
- [8] Shojaei, A.H., 1998. Buccal Mucosa as A Route for Systemic Drug Delivery: A Review. *J. Pharmacy and Pharmaceutical Sci.*, 1(1): 15-30.
- [9] Oral, quickly disintegrating film, which cannot spit out, for an antiemetic or an anti migraine agent. Petra O, Thomas K, Kai-Thomas K, Karin K. US2008/0213343 A1, 2008.
- [10] Choudhary DR, Patel V, Patel H, Kundawala. Exploration of film forming properties of film formers used in the formulation of rapid dissolving films. *Int J Chem tech Res*, 2011; 3(2):531-3.
- [11] Priya YD, Chowdary YA, Murthy, Murthy TEGK, Seshagiri B. Approaches for taste masking of bitter drugs. *J Adv Drug Res*, 2011; 1(2):58-67.
- [12] Kunte S, Tandale P. Fast dissolving strip: a novel approach for delivery of Verapamil. *J Pharm Bioall Sci.*, 2010; 2(4):325-8.
- [13] Sloboda M, Bharnatt S. Formulation flexibility broadens the scope for oral thin film technology. *Adhesive Res*, 2011; 22-4.
- [14] Reema P, Richard GZ. Dissolvable film. US 2007/0042023 A1 2007:1-8.
- [15] Bhyan B, Jangra S, Kaur M, Singh H. Orally fast dissolving film: Innovation in formulation and technology. *Int. J. Pharm. Sci. Rev. Res.*, 2011; 9(2):50-57.
- [16] Bala R, Pravin Pawar, Sushil Khanna, Sandeep Arora. Orally dissolving strip: A new approach to oral drug delivery system. *Int. J. Pharm. Invest*, 2013; 3(2); 67-76.
- [17] Kulkarni AS, Deokule HA. Exploration of different polymers for use in the formulation of oral fast dissolving strips. *J. Current Pharm. Res.*, 2010; 2(1):33-35.
- [18] Heer D, Aggarwal G, Kumar SLH. Recent trends of fast dissolving drug delivery system- An overview of formulation technology. *Pharmacophore*, 2013; 4(1): 1-9.
- [19] Mahajan A, Chhabra N, Aggarwal G. Formulation and Characterization of Fast Dissolving Buccal Films: A Review. *Der Pharm Lett.*, 2011; 3(1): 152165. 29.
- [20] Controlled Drug Delivery Concepts and Advances. Vyas SP, Khar RK. New Delhi: Vallabh Prakashan; 2002; 1: 157-160
- [21] Gandhi SD, Pandya PR, Umbarkar R, Tambawala T, Shah MA. Mucoadhesive drug delivery systems an unusual maneuver for site-specific drug delivery system.. *Pharm Sci Monit an Int J Pharm Sci.*, 2011; 2(3): 132-52.
- [22] Theory and Practice of Contemporary Pharmaceutics. Ghosh TK, Jasti BR, editors. CRC Press, 2005; 282-367: 150-155.
- [23] Choudhary DR, Patel VA, Chhalotiya UK, Patel HV, Kundawala AJ. Development and characterization of pharmacokinetic parameters of fast-dissolving films containing levocetirizine. *Sci. Pharm*, 2012; 80: 779-787.
- [24] Heer D, Aggarwal G, Kumar SLH. Recent trends of fast dissolving drug delivery system- An overview of formulation technology. *Pharmacophore*, 2013; 4(1): 1-9. 28
- [25] Mitchell and M.D. Read, 2005. *Pharmaceutical Technology*, pp: 1-6.
- [26] Arya A, Chandra A, Sharma V, Pathak K. Fast dissolving oral films: An innovative drug delivery system and dosage form. *Int. J. Chem Tech. Res.*, 2010; 2(1): 576-583
- [27] Muhammad Irfan, Sumeira Rabel, Quratulain Bukhtar, Muhammad Imran Qadir, Farhat Jabeen, Ahmed Khan. Orally disintegrating films: A modern expansion in drug delivery system. *Saudi Pharmaceutical Journal*, 2016; 24: 537-546.
- [28] Chauhan I, Yasir M, Nagar P. Insights into polymers: film formers in mouth dissolving films. *Drug Invent. Today*, 2012; 3: 56-73.
- [29] Pein M, Breitreutz, J. Development of a tastemasked orodispersible film containing dimenhydrinate. *Preis. Pharmaceutics*, 2012; 4: 551- 562.

- [30] Corniello C. Quick Dissolving Strip; from concept to commercialization. *Drug Development Technology*, 2006; 6: 68-71.
- [31] Kalyan S, Bansal M. Recent trends in the development of oral dissolving film. *Int. J. Pharm tech Res.*, 2012; 4: 725-733. 43.
- [32] Iruzo F and Cupone EI: Diclofenac fast dissolving film: suppression of bitterness by a taste-sensing system. *Drug Dev. Ind. Pharmacy*, 2010; 1-8.
- [33] Gavaskar Basani, Kumar Subhash Vijaya, guru Sharan: Overview on fast dissolving films, *Int Jr of Pharmacy and Pharmaceutical Sciences* 2009; 2: 29-33.
- [34] Interactions in cellulose derivative films for oral drug delivery. Sakellariou, P.; Rowe, R.C. *Prog. Polym. Sci.*, 1995, 20, 889-942.
- [35] 41. Fast Dissolving Oral Films: A Review Naga Sowjanya Juluru *International Journal Of Advances In Pharmacy, Biology And Chemistry Vol. 2(1)*, Jan- Mar 2013.
- [36] Handbook of Pharmaceutical Excipients. Wale. A and Weller. P J., 2nd edition, 1994, 24, 27, 352,448.
- [37] Film coating theory and practice. Banker, G.S. *J. Pharm. Sci.*, 1966, 55, 81-89.
- [38] The effect of polymer molecular weight on the incidence of film cracking and splitting on film-coated tablets. Rowe, F.C.; Forse, S.F. *J. Pharm. Pharmacol.*, 1980, 32(8), 583-584.
- [39] The effect of plasticizer type and concentration on the incidence of bridging of intagliations on film-coated tablets. Rowe, R.C.; Forse, S.F. *J. Pharm. Pharmacol.*, 1981, 33(3), 174-175.
- [40] Effect of inert tablet ingredients on drug absorption I. Effect of polyethylene glycol 4000 on the intestinal absorption of four barbiturates. Singh, P.; Guillory, J.K.; Sokoloski, T.D; Benet, L.Z.; Bhatia, V.N. *J. Pharm. Sci.*, 1966, 55(1), 6-68
- [41] Formation of films from polymer dispersions. Brown, G.L. *J. Polym. Sci.*, 1956, 22 (102), 423-434. 40. Orally dissolving film strips (ODFS): the final evolution of Orally dissolving dosage forms. Hariharan, M.; Bogue, A. *Drug Del. Technol.*, 2009, 9(2), 24.29.
- [42] Muhammad Irfan, Ahmad Khan Orally Disintegrating Films: A modern expansion in drug delivery system. *Saudi Ph Jr* volume 24, Issue 5, Sept 2016: 537-546.
- [43] Shimoda H and Taniguchi K: Preparation of fast dissolving oral thin film containing dexamethasone: A possible application to antiemesis during cancer chemotherapy. *European Journal of Pharmaceutics and Biopharmaceutics*, 2009; 73: 361-365.
- [44] Development of ebiana, a natural, non-caloric sweetener, Prakash.G.E, DuBois.J.F, Clos.K.L, Wilkens and Fosdick. L.E., *Food Chem. Toxicol.* 2008, 46, S75-S82. 45
- [45] Nishimura M, Matsuura K, Sukioka T, Yamashita H, Inagaki N, Sugiyama T and Itoh Y: In-vitro and in-vivo characteristics of prochlorperazine oral disintegrating film. *International Journal of Pharmaceutical Sciences*, 2009; 98-102.
- [46] Gohel MC and Sharma R: Development of taste masked film of valdecoxib for oral use. *Indian Journal of Pharmaceutical Sciences*, 2010; 320-323.
- [47] Madgulkar A, Khar RK, Harindran J, Mujumdar DK, Nagarsenker MS. Dosage form design *Pharmaceutical and Formulation Consideration In: Allen LV, Popovich NG, Ansel HC, editors. Ansel's Pharmaceutical Dosage forms and Drug Delivery Systems: South Asian Edition 9th Ed Wolters Kluwer (India) Pvt Ltd, New Delhi, 2011; 134-136.*
- [48] Siddiqui N, Garg G, Sharma P. A Short Review on "A Novel Approach in Oral Fast Dissolving Drug Delivery System and Their Patents. *Advances in Biological Research*, 2011; 5(6): 291-303.
- [49] Dixit RP, Puthli SP, Oral strip technology: Overview and future potential. *Journal of Controlled Release*, 2009; 139: 94-107.
- [50] Iruzo F and Cupone EI: Fast dissolving films made of maltodextrins. *European Journal of Pharmaceutics and Biopharmaceutics*, 2008; 70: 895-900
- [51] Vishwakarma DK, Tripathi AK, Yogesh P and Maddheshiya B: Review article on mouth dissolving film. *Journal of Global Pharma Technology*, 2011; 3(1): 1-8.
- [52] Rathi V, Senthil V, Kammili L and Hans R: A brief review on oral film technology. *International Journal of Research in Ayurveda and Pharmacy*, 2011; 2(4): 1138-1147.

- [53] Deepak Sharma, Diljit Kaur, Shivani Verma, Davindar Singh, Mandeep Singh, Gurmeet Singh, Rajeev Garg Fast Dissolving Oral Films Technology: A Recent Trend For An Innovative Oral Drug Delivery System, Int Jr of Drug Delivery 7 (2015) 60-75.
- [54] Siddiqui N, Garg G, Sharma P. A Short Review on "A Novel Approach in Oral Fast Dissolving Drug Delivery System and Their Patents. Advances in Biological Research, 2011; 5(6): 291-303.
- [55] Bharthi P, Gopalrao M, Akila R. Characterization and Applications of Pullulan and Chitosan produced by fermentation. J Microbio Biotech Res. Pvt. Ltd., 5(2): 21-27.
- [56] Subhash Vijaya Kumar, Basanti Gavaskar, Guru Sharan, Madhusudhan Rao Y, Overview on Fast Dissolving Films. International Journal of Pharmacy and Pharmaceutical Sciences, 2010; 2(3): 29-33.
- [57] Patel Nibha K, Pancholi SS, An Overview on Sublingual Route for Systemic Drug Delivery. International Journal of Research in Pharmaceutical and Biomedical Sciences, 2012; 3(2): 913-23.
- [58] Aggarwal Jyoti. Singh Gurpreet. Saini Seema. Rana AC, Fast Dissolving Films: A Novel Approach to Oral Drug Delivery. International Research Journal of Pharmacy, 2011; 2(12): 69-74.
- [59] Vishwkarma DK, Tripathi AK, Yogesh P and Maddheshiya B, Review Article on Mouth Dissolving Film. Journal of Global Pharma Technology, 2011; 3(1): 1-8.
- [60] Patel AR, Prajapati DS and Raval JA: Fast dissolving films (FDFS) as a newer venture in fast dissolving dosage forms. International Journal of Drug Development and Research, 2010.

